Springer Series in Surface Sciences 59

Joseph C. Woicik *Editor*

Hard X-ray Photoelectron Spectroscopy (HAXPES)

Springer

Springer Series in Surface Sciences

Volume 59

Series editors

Roberto Car, Princeton, USA
Gerhard Ertl, Berlin, Germany
Hans-Joachim Freund, Berlin, Germany
Hans Lüth, Jülich, Germany
Mario Agostino Rocca, Genova, Italy

This series covers the whole spectrum of surface sciences, including structure and dynamics of clean and adsorbate-covered surfaces, thin films, basic surface effects, analytical methods and also the physics and chemistry of interfaces. Written by leading researchers in the field, the books are intended primarily for researchers in academia and industry and for graduate students.

More information about this series at http://www.springer.com/series/409

Joseph C. Woicik
Editor

Hard X-ray Photoelectron Spectroscopy (HAXPES)

Editor
Joseph C. Woicik
Brookhaven National Laboratory
National Institute of Standards
and Technology
Upton, NY
USA

ISSN 0931-5195 ISSN 2198-4743 (electronic)
Springer Series in Surface Sciences
ISBN 978-3-319-24041-1 ISBN 978-3-319-24043-5 (eBook)
DOI 10.1007/978-3-319-24043-5

Library of Congress Control Number: 2015950038

Springer Cham Heidelberg New York Dordrecht London
© Springer International Publishing Switzerland 2016
This work is subject to copyright. All rights are reserved by the Publisher, whether the whole or part of the material is concerned, specifically the rights of translation, reprinting, reuse of illustrations, recitation, broadcasting, reproduction on microfilms or in any other physical way, and transmission or information storage and retrieval, electronic adaptation, computer software, or by similar or dissimilar methodology now known or hereafter developed.
The use of general descriptive names, registered names, trademarks, service marks, etc. in this publication does not imply, even in the absence of a specific statement, that such names are exempt from the relevant protective laws and regulations and therefore free for general use.
The publisher, the authors and the editors are safe to assume that the advice and information in this book are believed to be true and accurate at the date of publication. Neither the publisher nor the authors or the editors give a warranty, express or implied, with respect to the material contained herein or for any errors or omissions that may have been made.

Printed on acid-free paper

Springer International Publishing AG Switzerland is part of Springer Science+Business Media
(www.springer.com)

Preface

Photoelectron spectroscopy has its roots in the Nobel Prize-winning work of Albert Einstein and Kai Siegbahn. It is therefore both an honor and a humbling experience to produce a book that documents the excitement of the newest developments in this field.

According to Einstein's discovery of the law of the photoelectric effect, considered to be the dawn of the quantum age, the conservation of energy between the incoming photon and the outgoing photoelectron in the photoemission process allows the technique to uniquely measure the chemical and electronic structure of atoms, molecules, and solids. However, despite Seigbahn's original development of the technique for chemical analysis with high-energy X-rays, the use of low-energy photons with energies up to only about 1.5 keV by modern researchers, at both laboratory and synchrotron sources, results in extremely short photoelectron inelastic mean-free paths. As a result, this limited information depth has historically restricted experiments to the study of surfaces and shallow interfaces, or what is referred to in the literature as traditional surface science.

It is therefore no surprise that recent advances in both photon source and electron-spectrometer instrumentation have driven experiments into the extended 2–10 keV photon energy range resulting in what is now called *hard* X-ray photoelectron spectroscopy (HAXPES). Due to its relatively unlimited electron escape depths, HAXPES has emerged as a powerful tool that has general application to the study of the true bulk and buried interface properties of complex materials systems. Its areas of application are thus growing exponentially compared to more traditional measurements at lower photon energies.

In addition to the many advantages of being able to study "real" samples taken directly from air without the need for ion sputtering or other surface preparation, HAXPES has opened up other research areas that are included in this book such as:

- The study of highly correlated and spintronic electron systems with surface and interface compositions and structures that are different from their bulk.
- The combination of energy and angle measurements (X-ray standing wave, photoelectron diffraction, and angle-resolved valence photoemission) to produce elementally, chemically, and spatially specific electronic structure information.
- The study of realistic prototypical multilayer device structures under both *ambient* and *operando* conditions.
- The tuning of the photoelectron inelastic mean-free path and the X-ray penetration depth to study buried layers, interfaces, and nanoparticles with the specific nanometer and mesoscopic length scales relevant to modern industry, as, for example, today's semiconductor hetero-structures.

The brightness of third- and higher generation X-ray sources has also opened the possibilities of both high-resolution two-dimensional chemical imaging with depth resolution (photoelectron microscopy) in addition to time-resolved photoemission.

This volume provides the first complete, up-to-date summary of the state of the art in HAXPES. It is therefore a must-read for scientists interested in harnessing its powerful capabilities for their own research. Chapters written by experts include historical work, modern instrumentation, theoretical developments, and real-world applications that cover the fields of physics, chemistry, and materials science and engineering. In consideration of the rapid development of the technique, several chapters include highlights that illustrate future opportunities as well.

Upton, USA Joseph C. Woicik

Contents

1 Hard X-ray Photoemission: An Overview and Future Perspective 1
Charles S. Fadley

2 The First Development of Photoelectron Spectroscopy and Its Relation to HAXPES 35
Svante Svensson, Evelyn Sokolowski and Nils Mårtensson

3 HAXPES at the Dawn of the Synchrotron Radiation Age 43
Piero Pianetta and Ingolf Lindau

4 Hard-X-ray Photoelectron Spectroscopy of Atoms and Molecules 65
Marc Simon, Maria Novella Piancastelli and Dennis W. Lindle

5 Inelastic Mean Free Paths, Mean Escape Depths, Information Depths, and Effective Attenuation Lengths for Hard X-ray Photoelectron Spectroscopy 111
C.J. Powell and S. Tanuma

6 Hard X-ray Angle-Resolved Photoelectron Spectroscopy (HARPES) 141
Alexander X. Gray

7 One Step Model Description of HARPES: Inclusion of Disorder and Temperature Effects 159
Jürgen Braun, Ján Minár and Hubert Ebert

8 Recoil Effects in X-ray Photoelectron Spectroscopy 175
Yosuke Kayanuma

9 Depth-Dependence of Electron Screening, Charge Carriers and Correlation: Theory and Experiments 197
Munetaka Taguchi and Giancarlo Panaccione

10 The Influence of Final-State Effects on XPS Spectra from First-Row Transition-Metals 217
Andrew P. Grosvenor, Mark C. Biesinger, Roger St. C. Smart and Andrea R. Gerson

11 Optimizing Polarization Dependent Hard X-ray Photoemission Experiments for Solids 263
J. Weinen, T.C. Koethe, S. Agrestini, D. Kasinathan, F. Strigari, T. Haupricht, Y.F. Liao, K.-D. Tsuei and L.H. Tjeng

12 Photoelectron Emission Excited by a Hard X-ray Standing Wave 277
Jörg Zegenhagen, Tien-Lin Lee and Sebastian Thiess

13 Depth Profiling and Internal Structure Determination of Low Dimensional Materials Using X-ray Photoelectron Spectroscopy 309
Sumanta Mukherjee, Pralay K. Santra and D.D. Sarma

14 Probing Perovskite Interfaces and Superlattices with X-ray Photoemission Spectroscopy 341
Scott A. Chambers

15 HAXPES Measurements of Heterojunction Band Alignment 381
Conan Weiland, Abdul K. Rumaiz and Joseph C. Woicik

16 HAXPES Studies of Advanced Semiconductors 407
Patrick S. Lysaght and Joseph C. Woicik

17 Liquid/Solid Interfaces Studied by Ambient Pressure HAXPES 447
Z. Liu and H. Bluhm

18 HAXPES Applications to Advanced Materials 467
Keisuke Kobayashi

19 Photoelectron Microscopy and HAXPES 533
Raymond Browning

20 Femtosecond Time-Resolved HAXPES 555
Lars-Philip Oloff, Masaki Oura, Ashish Chainani and Kai Rossnagel

Index 569

Contributors

S. Agrestini Max Planck Institute for Chemical Physics of Solids, Dresden, Germany

Mark C. Biesinger Surface Science Western, The University of Western Ontario, London, ON, Canada

H. Bluhm Lawrence Berkeley National Laboratory, Chemical Sciences Division, Berkeley, CA, USA

Jürgen Braun Department of Chemie, Ludwig-Maximilians-Universität München, Munich, Germany

Raymond Browning Shoreham, NY, USA

Ashish Chainani RIKEN Spring-8 Center, Hyogo, Japan

Scott A. Chambers Physical Sciences Division, Pacific Northwest National Laboratory, Richland, WA, USA

Hubert Ebert Department of Chemie, Ludwig-Maximilians-Universität München, Munich, Germany

Charles S. Fadley Department of Physics, University of California Davis, Davis, CA, USA; Materials Sciences Division, Lawrence Berkeley National Laboratory, Berkeley, CA, USA

Andrea R. Gerson Minerals and Materials Science and Technology (MMaST), Mawson Institute, University of South Australia, Adelaide, SA, Australia; Blue Minerals Consultancy, Adelaide, SA, Australia

Alexander X. Gray Department of Physics, Temple University, Philadelphia, PA, USA

Andrew P. Grosvenor Department of Chemistry, University of Saskatchewan, Saskatoon, Canada

T. Haupricht II. Physikalisches Institut, Universität zu Köln, Cologne, Germany

D. Kasinathan Max Planck Institute for Chemical Physics of Solids, Dresden, Germany

Yosuke Kayanuma Materials and Structures Laboratory, Tokyo Institute of Technology, Nagatsuta, Yokohama, Japan

Keisuke Kobayashi Hiroshima Synchrotron Radiation Center, Hiroshima University, Higashi-Hiroshima City, Japan; Quantum Beam Science Directorate, Japan Atomic Energy Agency, Sayo-Cho, Hyogo, Japan; Research Institute of KUT, Kochi University of Technology, Kami City, Kochi, Japan

T.C. Koethe II. Physikalisches Institut, Universität zu Köln, Cologne, Germany

Tien-Lin Lee Diamond Light Source Limited, Diamond House, Didcot, Oxfordshire, UK

Y.F. Liao National Synchrotron Radiation Research Center, Taiwan, China

Ingolf Lindau SLAC National Accelerator Laboratory, Menlo Park, CA, USA

Dennis W. Lindle Department of Chemistry, University of Nevada, Las Vegas, NV, USA

Z. Liu Advanced Light Source, Lawrence Berkeley National Laboratory, Berkeley, CA, USA; State Key Laboratory of Functional Materials for Informatics, Shanghai Institute of Microsystem and Information Technology, Chinese Academy of Sciences, Shanghai, China; Condensed Matter Physics and Photon Science Division, School of Physical Science and Technology, ShanghaiTech University, Shanghai, China

Patrick S. Lysaght SEMATECH, Albany, NY, USA

Nils Mårtensson Department of Physics and Astronomy, Uppsala, Sweden

Ján Minár Department of Chemie, Ludwig-Maximilians-Universität München, Munich, Germany; New Technologies—Research Center, University of West Bohemia, Pilsen, Czech Republic

Sumanta Mukherjee Solid State and Structural Chemistry Unit, Indian Institute of Science, Bengaluru, India

Lars-Philip Oloff Institute of Experimental and Applied Physics, University of Kiel, Kiel, Germany; RIKEN Spring-8 Center, Hyogo, Japan

Masaki Oura RIKEN Spring-8 Center, Hyogo, Japan

Giancarlo Panaccione Istituto Officina Dei Materiali (IOM)-CNR, Laboratorio TASC, Trieste, Italy

Maria Novella Piancastelli Laboratoire de Chimie Physique-Matière et Rayonnement, CNRS and UPMC, Cedex 05 Paris, France; Department of Physics and Astronomy, Uppsala University, Uppsala, Sweden

Piero Pianetta SLAC National Accelerator Laboratory, Menlo Park, CA, USA

C.J. Powell Materials Measurement Science Division, National Institute of Standards and Technology, Gaithersburg, MD, USA

Kai Rossnagel Institute of Experimental and Applied Physics, University of Kiel, Kiel, Germany; RIKEN Spring-8 Center, Hyogo, Japan

Abdul K. Rumaiz National Synchrotron Light Source II, Brookhaven National Laboratory, Upton, NY, USA

Pralay K. Santra Solid State and Structural Chemistry Unit, Indian Institute of Science, Bengaluru, India; Department of Chemical Engineering, Stanford University, Stanford, USA

D.D. Sarma Solid State and Structural Chemistry Unit, Indian Institute of Science, Bengaluru, India; Department of Physics and Astronomy, Uppsala University, Uppsala, Sweden

Marc Simon Laboratoire de Chimie Physique-Matière et Rayonnement, CNRS and UPMC, Cedex 05 Paris, France

Roger St. C. Smart Minerals and Materials Science and Technology (MMaST), Mawson Institute, University of South Australia, South Australia, Australia

Evelyn Sokolowski Tystberga, Sweden

F. Strigari II. Physikalisches Institut, Universität zu Köln, Cologne, Germany

Svante Svensson Department of Physics and Astronomy, Uppsala, Sweden

Munetaka Taguchi RIKEN SPring-8 Center, Hyogo, Japan; Nara Institute of Science and Technology (NAIST), Ikoma, Nara, Japan

S. Tanuma National Institute for Materials Science, Tsukuba, Ibaraki, Japan

Sebastian Thiess Deutsches Elektronen-Synchrotron, Hamburg, Germany

L.H. Tjeng Max Planck Institute for Chemical Physics of Solids, Dresden, Germany

K.-D. Tsuei National Synchrotron Radiation Research Center, Taiwan, China

Conan Weiland Materials Measurements Laboratory, National Institute of Standards and Technology, Gaithersburg, MD, USA

J. Weinen Max Planck Institute for Chemical Physics of Solids, Dresden, Germany

Joseph C. Woicik Materials Measurement Laboratory, National Institute of Standards and Technology, Gaithersburg, MD, USA

Jörg Zegenhagen Diamond Light Source Limited, Diamond House, Didcot, Oxfordshire, UK

Chapter 1
Hard X-ray Photoemission: An Overview and Future Perspective

Charles S. Fadley

Abstract The various aspects of hard X-ray photoemission are reviewed, including in particular more newly developed directions of measurement, but also with references to other chapters in this book or prior publications in which additional details can be found. An overview of the different dimensions of the technique, including a look at promising future directions, is presented.

1.1 Introduction

Although hard X-ray photoemission (HXPS, HAXPES, HX-PES,…) in fact has a long history, as reviewed elsewhere in this book by Svensson, Sokolowski, and Martensson, by Pianetta and Lindau, who pioneered it with synchrotron radiation (SR) excitation at SSRL [1], and by Kobayashi, who discusses the first undulator-based activities at SPring-8, it is really only in the last 15 years or so that the development of beamlines, spectrometers, and even laboratory sources, has led to its rapid growth. By now, various statistics indicate the rapid growth of the technique. The number of papers appearing and the citations to them are growing exponentially, as shown from the Web of Science statistics in Fig. 1.1, which certainly represent conservative numbers due to the fact that authors may not always use our search keywords in publications, and in fact probably do this less with time as the technique becomes more commonly used. Some overall numbers

C.S. Fadley (✉)
Department of Physics, University of California Davis, Davis, CA 95616, USA
e-mail: fadley@physics.ucdavis.edu

C.S. Fadley
Materials Sciences Division, Lawrence Berkeley National Laboratory, Berkeley
CA 94720, USA

© Springer International Publishing Switzerland 2016
J.C. Woicik (ed.), *Hard X-ray Photoelectron Spectroscopy (HAXPES)*,
Springer Series in Surface Sciences 59, DOI 10.1007/978-3-319-24043-5_1

Measures of the growth and impact of hard x-ray photoemission

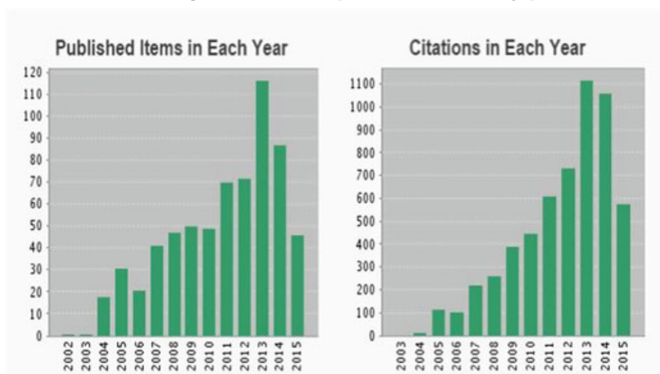

Fig. 1.1 A Web of Science plot of the number of publications and citations versus time involving the keywords “hard X-ray photoelectron spectroscopy” or “hard X-ray photoemission” or “high energy photoelectron spectroscopy” or “high kinetic energy photoelectron diffraction” or “hard X-ray photoelectron microscopy” or “HXPS” or “HAXPES” or “HX-PES” or “HAXPEEM”. This data is from June, 2015

from this search in June, 2015 are about 640 publications, 1000 citations per year, 5600 citations in total, 9 cites/paper, and an h-index of 38. These publications have furthermore appeared in leading high-impact journals. There are also currently approximately 20 synchrotron radiation beamlines running or in construction/ commissioning that are at least partly dedicated to HXPS, in alphabetical order at: ALS, BESSY II, CLS, Diamond, Petra III, NSRRC, NSLS-2, Soleil, and SPring-8, with by far the largest number at SPring-8, still the leading facility in this technique. Commercial systems permitting in-laboratory monochromatized HXPS are also now available. Finally, there has been a continuing series of international workshops and by now international conferences on HXPS, with programs and proceedings often online [2–10].

Beyond this, and more importantly, the technique has by now been applied to the full range of forefront materials issues in physics and chemistry, including bulk, surface, and buried interface studies, as beautifully demonstrated in various chapters in this book, e.g., by Browning—photoelectron microscopy of various materials types; Chambers-oxide heterostructures; Gray—dilute magnetic semiconductors; Kobayashi—a broad range of advanced materials and device structures; Liu and Bluhm—ambient pressure photoemission studies of surfaces and interfaces, including very recent use of hard X-ray excitation [11]; Taguchi and Panaccionne, plus Tjeng et al.—strongly correlated materials; Mukherjee, Santra and Sarma—nanostructures; Weiland, Rumaiz, and Woicik, plus Lysaght and Woicik—band alignments and semiconductors, and Zegenhagen, Lee, and Thiess—oxides and superconductors. In addition, it is clear that HXPS can be very fruitfully applied in atomic and molecular physics, as overviewed by Simon, Piancastelli, and Lindle. I here also note with deep sadness our loss last year of Dennis Lindle, a true pioneer

in applying hard X-ray excitation to atomic and molecular physics with his work at the Advanced Light Source.

I will not attempt here to repeat what is already so well reviewed and presented in the above-cited chapters devoted to applications of HXPS, but will limit this overview to discussing the basic principles of the technique, including its strengths, weaknesses, some new directions, and challenges for future experimental and theoretical developments. This discussion will thus more directly relate to other chapters on the fundamental physics of photoemission in the hard X-ray regime by Braun, Ebert, and Minar—photoemission theory; Browning-photoelectron microscopy; Grosvenor et al.—final-state effects; Kayanuma-recoil effects; Powell and Tanuma—inelastic mean free paths; and Rossnagel et al.—time-resolved measurements. Some additional new measurement methods will be pointed out, for example, involving standing-wave (SW) or near-total-reflection (NTR) excitation from multilayer heterostructures, which are not covered elsewhere in this book.

Finally, the reader is directed to several other overviews and special journal issues involving HXPS and its relationship to conventional XPS at less than 2 keV that have been published [12–14], including some from my group [15–20], and to which specific references will subsequently be made.

In concluding this introduction, it is worth noting the various measuring modalities in photoemission in general, which are illustrated in Fig. 1.2, all of which will be discussed individually in the following sections.

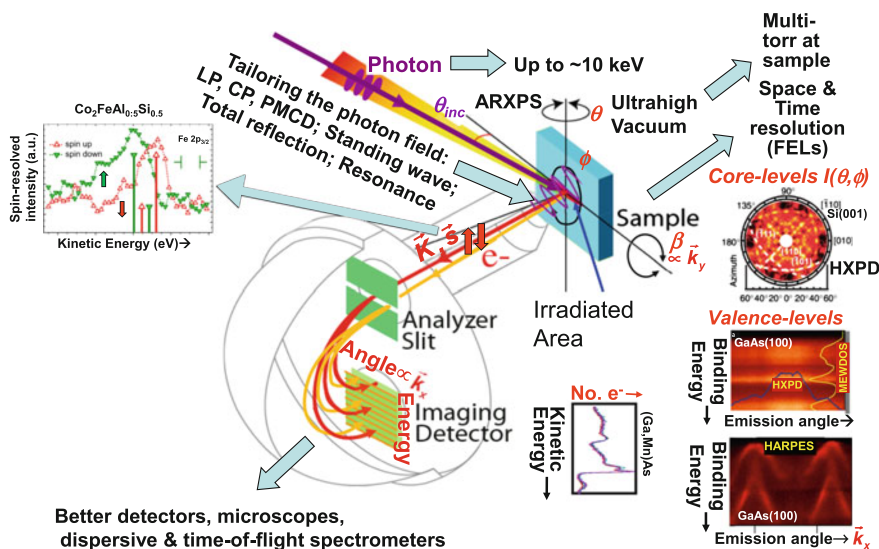

Fig. 1.2 Schematic illustration of the different measurement modalities in photoemission, with *inset* examples discussed later in this and other chapters of this book. The core schematic from which this figure is derived is from Y. Takata

1.2 Basic Effects and Considerations—Advantages, Disadvantages, and Challenges

1.2.1 Probing Depth

Of course, the ability to probe more deeply into a sample and reduce the importance of surface effects is a primary reason for using hard X-ray excitation in photoemission. Hard X-ray is here defined as >2 keV, since that is typically the energy above which crystal monochromators, instead of grating monochromators, must be used. Some prefer to call the range of ca. 2–10 keV that is most commonly used in HXPS measurements "tender" X-rays.

The probing depth is controlled by the inelastic mean free path (IMFP), and Fig. 1.3 shows a compilation of values for 41 elements calculated from optical data and leading to the much-used TPP-2 M formula for estimating them, from the work of Tanuma et al. [21]. This method and its application to HXPS are discussed in more detail in the chapter by Tanuma and Powell.

The conclusions from this and other recent experimental work [22, 23] are that the only reliable way to increase bulk or buried layer and interface sensitivity for all material types is to go to higher photon energies in the soft X-ray (ca. 0.5–2 keV) or hard X-ray (ca. 2–10 keV) regime. Going to very low photon energies with laser excitation is also often discussed as a method for enhancing bulk sensitivity [24], but it seems clear that this will not be a universal benefit for all materials, and may only be true for those with a significant bandgap. Further experimental and theoretical study of this last point is needed.

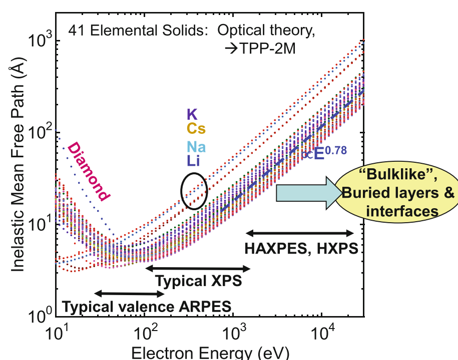

Fig. 1.3 Energy dependence of electron inelastic mean free paths as calculated from optical properties for 41 elements, with values closely related to the TTP-2M formula (From [21])

1.2.2 Ease of Spectral Analysis

There are several ways in which spectral analysis is simpler at higher photon energies:

- The inelastic backgrounds under spectra are significantly reduced, thus making the allowance for them in fitting to derive various peak intensities easier.
- Auger spectra are in general further apart, thus creating less overlap with photoelectron peaks whose detailed analysis is desired.
- Peak intensity analyses:

  The analysis of peak intensities via standard formulas for core photoelectron emission, such as that shown in (1.1) and Fig. 1.4 for a typical $n\ell j$ level in atom Q, with an incident flux of $I_{h\nu}(x, y, z, \hat{\varepsilon})$, radiation polarization of $\hat{\varepsilon}$, an IMFP of $\Lambda_e(E_{kin})$, and a spectrometer acceptance solid angle over the surface of $\Omega(E_{kin}, x, y)$,

$$I(Qn\ell j) = C\int_0^\infty I_{h\nu}(x,y,z,\hat{\varepsilon})\rho_Q(x,y,z)\frac{d\sigma_{Qn\ell j}(h\nu,\hat{\varepsilon})}{d\Omega} \times \exp\left[-\frac{z}{\Lambda_e(E_{kin})\sin\theta}\right]\Omega(E_{kin},x,y)dxdydz \tag{1.1}$$

  and as used e.g. in angle-resolved XPS (ARXPS) depth profile analyses, are simpler because:

  - The IMFPs $\Lambda_e(E_{kin})$ of different peaks, although kinetic energy dependent, can have much less variation than with lower energy excitation, because the higher kinetic energies of less-bound electronic levels are closer in relative values.
  - The instrument response function, indicated as the solid-angle of acceptance $\Omega(E_{kin}, x, y)$ in Fig. 1.4, will also tend to be more nearly constant over a set of peaks with high, and thus very nearly equal, kinetic energies.
  - The effects of elastic scattering in smearing out the photoelectron intensity distribution, indicated by the scattering factor $f(\theta_{scatt})$ in Fig. 1.4, will be less pronounced, due to the generally increasing forward focusing effect as energy is increased.
  - The effect of refraction in crossing the inner potential barrier V_0 will be less as energy is increased.
  - The effects of surface-associated inelastic scattering will also be reduced as the kinetic energy increases [25].
  - In <u>valence</u> photoemission, it is also well known [26, 27] that the photoelectric cross section becomes more and more dominated by the core region of each atom as energy is increased, thus permitting an approximate decomposition of a valence spectrum in the high-energy XPS or density-of-states (DOS) limit into a sum of partial intensities based on orbital-projected DOSs and atomic differential cross sections, as indicated in (1.2) below:

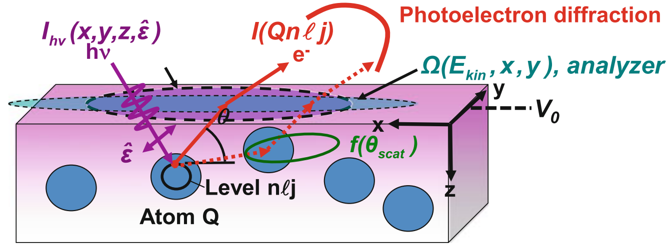

$I(Qn\ell j) =$

$$C\int_0^\infty I_{hv}(x,y,z,\hat{\varepsilon})\rho_Q(x,y,z)\frac{d\sigma_{Qn\ell j}(hv,\hat{\varepsilon})}{d\Omega}\exp\left[-\frac{z}{\Lambda_e(E_{kin})\sin\theta}\right]\Omega(E_{kin},x,y)dxdydz$$

$I_{hv}(x,y,z,\hat{\varepsilon})$ ray flux, $\hat{\varepsilon}$ = polarization

$\rho_Q(x,y,z)$ = density of atoms Q → quantitative analysis

$\frac{d\sigma_{Qn\ell j}(hv,\hat{\varepsilon})}{d\Omega}$ = energy-dependent differential photoelectric cross section for subshell $Qn\ell j$

$\Lambda_e(E_{kin})$ = energy-dependent inelastic attenuation length + elastic scattering: $f(\theta_{scatt})$

→ Effective Attenuation Length (EAD) → Mean Emission Depth (MED)

$\Omega(E_{kin},x,y)$ = energy-dependent analyzer acceptance solid angle = transmission function

V_0 = inner potential

Fig. 1.4 Core photoelectron emission, with a general sample and experimental configuration indicated, along with the standard formula for analyzing intensities, also appearing in (1.1)

$$\begin{aligned} I_{total}(E_{kin}) &= \sum_{Qn\ell j} I(E_{kin}, Qn\ell j) \\ &= \sum_{Qn\ell j} C' \int_0^\infty I_{hv}(x,y,z,\hat{\varepsilon})\rho_{Qn\ell j}(E_b,x,y,z)\frac{d\sigma_{Qn\ell j}(hv,\hat{\varepsilon})}{d\Omega} \\ &\quad \times \exp\left[-\frac{z}{\Lambda_e(E_{kin})\sin\theta}\right]\Omega(E_{kin},x,y)dxdydz \end{aligned} \tag{1.2}$$

with $\rho_{Qn\ell j}(E_b,x,y,z)$ the projected density of states for the $Qn\ell j$ orbital at a given binding energy and position in the sample.

Thus, the simple formulas shown in (1.1) or in (1.2) will be more quantitative for HXPS in many situations, permitting simpler spectral analyses of both core and valence spectra.

It is important finally to note that a user-friendly program exists for calculating spectra for core-level emission, namely Simulation of Electron Spectra for Surface Analysis (SESSA), whose input databases have recently been extended to cover hard X-ray excitation [28, 29]. This program includes all of the physical effects indicated in Fig. 1.4, with elastic scattering assumed to be from an array of randomly positioned atoms, although it does not include refraction effects in crossing the inner potential.

1.2.3 Photoelectric Cross Sections, Including Polarization Effects

Beyond these considerations however, is the clear challenge that photoelectric cross sections decrease dramatically as photon energy, or equivalenty kinetic energy E_{kin} is increased [30–32], varying in a high-energy asymptotic limit roughly as $\sigma_{Qn\ell j}(E_{kin}) \propto (E_{kin})^{-7/2} = (E_{kin})^{-3.5}$ for s subshells and $\propto(E_{kin})^{-9/2} = (E_{kin})^{-4.5}$ for p, d, and f subshells, but with more accurate calculations for specific cases in the two references mentioned. Figure 1.5 illustrates this decrease with calculated cross sections [30] for the subshells of Mn and O over 1–10 keV spanning the most common HXPS range. Thus, the development of HXPS has required the design of beamlines, including enhanced intensity with undulator excitation [33], and laboratory sources with the highest possible intensities, as well as spectrometers with the highest solid angles of acceptance, with the latter for example now going up to ±30° in commercial hemispherical electrostatic instruments and up to ±45° in custom-designed systems [34]. The possibility of time-of-flight analysis to further increase intensities is also being discussed [35, 36]. However, with present SR HXPS facilities, it is still possible to saturate any existing detector for intense core levels, and research and development thus needs to be done for higher-throughput electron detectors capable of the GHz-regime [37], as compared to the current ~1 MHz for 2D detection, and ~10 MHz for 1D detection.

Another important consequence of this energy variation for valence-level studies is that subshells with lower ℓ for a given n that thus exhibit more oscillations in the core region decay in intensity less rapidly than those with higher ℓ. Figure 1.5 illustrates that, for example, Mn 3s decays less rapidly than Mn 3p, and Mn 3p less

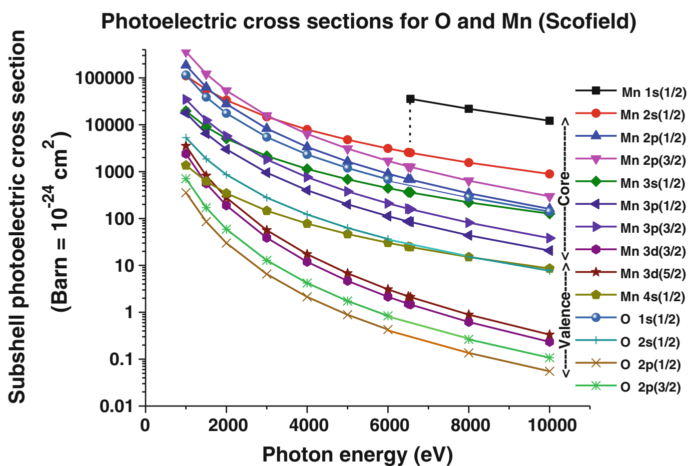

Fig. 1.5 Relativistic subshell cross sections for Mn and O as a function of photon energy over the region 1–10 keV (From [30])

rapidly than Mn 3d. A similar thing is found for O 2s, which decays less rapidly than O 2p. These variations already make the asymptotic formulas above, which do not discriminate p, d, and f cross sections, look inaccurate for typical HXPS energies. In fact, the exponents derived with cross section ratios from Fig. 1.5 at 8 and 10 keV, by assuming that (Cross section at hν = 10,000)/(Cross section at hν = 8000) = $(E_{kin}$ at 10,000 eV$)^m/(E_{kin}$ at 8000 eV$)^m$ yield values of m = −2.4 to −2.6 for Mn 1s, Mn 2s, Mn 3s, and Mn 4s, or about 5/2, with O 1s and O 2s being somewhat higher at m = 3.0, or about 6/2. Mn 2p and Mn 3p show m = −3.3 to −3.4, and O 2p larger values of m = −3.9 to −4.0, or about 7/2–8/2. Lastly, Mn 3d has the largest value at m = −4.2 to −4.3, approaching the asymptotic limit of 9/2. Thus, these values only roughly agree with, and span a greater range than, the asymptotic numbers above, and of course clearly show the trends with ℓ for a given n already mentioned.

Other more complex but important variations in relative intensity also occur if one considers the important case of valence-electron spectra. For example, by 10 keV the valence spectrum of a sample with both Mn and O in it (as would be typical for a transition metal (TM) oxide) is expected to be dominated by O 2p and Mn 4s character.

Another cross-section effect that must be allowed for as energy increases is the increasing importance of non-dipole terms [31, 32, 38] (see also chapter by Simon, Piancastelli, and Lindle). These can be broken into two types, depending on whether core-like intensities are involved or momentum-resolved angle-resolved photoemission (ARPES) valence intensities are being analyzed. In the first case, standard correction parameters to the usual dipole formula are available for a number of atoms and energies [31, 32, 38], and these can be interpolated and extrapolated for a given case at hand. For ARPES, or more appropriately, soft- and hard-X-ray ARPES (SARPES and HARPES, respectively), a correction due to the photon momentum is needed in the momentum-conservation equation, as discussed elsewhere [15, 18, 19, 39, 40], later in this chapter, and in the chapter by Gray in this book. This is a simple correction to do as well, provided that the experimental geometry is precisely defined.

As another more recently realized aspect of hard X-ray photoelectric cross sections, it has recently been shown by Drube et al. that interchannel coupling effects that are essentially resonant photoemission with deep core levels can significantly influence the relative intensities of shallower core levels. For example, the Ag $3d_{3/2,5/2}$ intensities at binding energies of ~374 and 368 eV are influenced by as much as 30 % in scanning the photon energy over the Ag $2p_{1/2,3/2}$ resonances at ~3560 and 3250 eV. Thus, it may be necessary to avoid such resonances by as much as a few hundred eV if a simple quantitative analysis according to equations such as those in (1.1) or (1.2) is to be valid.

As more and more hard X-ray beamlines are permitting the variation of polarization through the use of diamond phase retarders [41, 42], it is important to note the strong effects that this can have on the differential photoelectric cross sections. This is particularly important for valence-level spectra in which the different orbital contributions can be resolved in energy through the projected densities of states, as

indicated in (1.2). As a simple illustration of this, Figs. 1.6 and 1.7 show some calculated differential cross sections for the Cu $3d_{z2}$ and O $2p_z$ orbitals, at two energies of 0.8 and 5 keV and three different polarization orientations along x, y, and z. These have been calculated in a non-relativistic limit using equations published some time ago [43], with extrapolations of radial matrix elements and phase shifts for the $\ell \pm 1$ interfering channels to 5 keV using the data in [43], and an online program due to Nemšák et al. that permits calculating them for an arbitrary experimental geometry [44]. Of course, for any s subshell in the dipole limit, the cross section looks like a p wave oriented along the polarization direction, that is of the functional form given at the left of Fig. 1.7, since there is only one channel in the final state, and so will have a node for emission perpendicular to the polarization vector for all three orientations in this figure.

From these calculations for more complex non-s subshells, it is clear that varying polarization away from the special case of being parallel to the electron emission

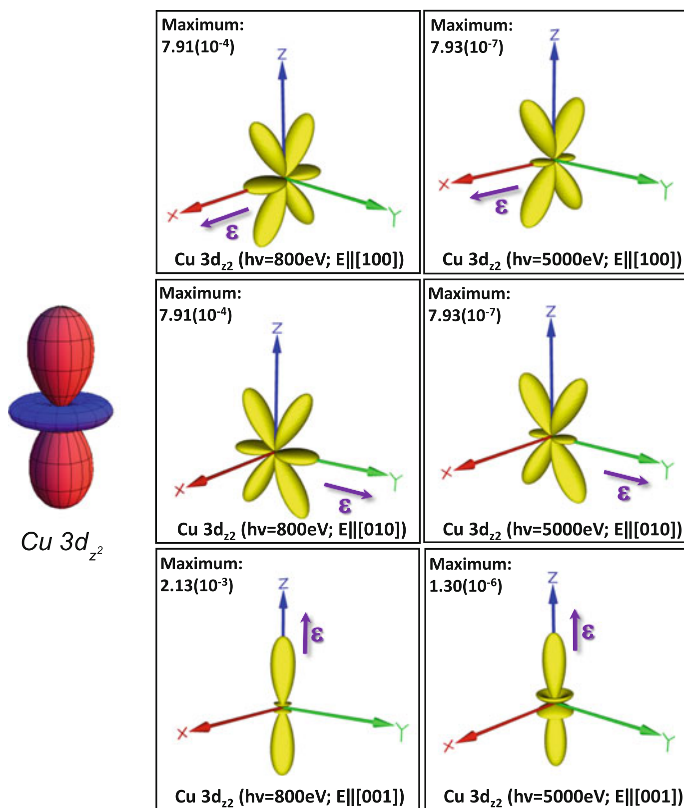

Fig. 1.6 Non-relativistic dipole-approximation cross sections for the Cu $3d_{z2}$ orbital, for three different polarization directions and at 800 and 5000 eV photon energies. The maximum value of each contour is indicated in the *inset* (From [44])

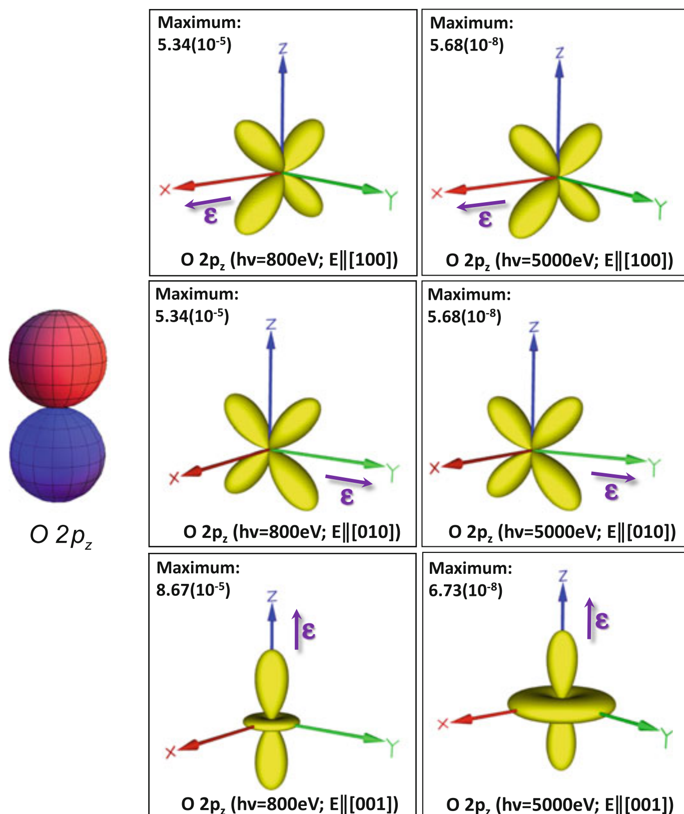

Fig. 1.7 As Fig. 1.6, but for the O $2p_z$ cross sections (From [44])

direction (a special case which is known to yield cross sections of exactly the same form as the orbital shape angular shape [43]), can yield dramatic changes. For example, the Cu $3d_{z2}$ cross section tends to look somewhat like the orbital for z polarization, but is completely different in x and y polarization. There are also some significant changes as the energy is increased from 800 to 5000, particularly for x and y polarization. Similar things are true for the O $2p_z$ cross section, again tending to look like the orbital for z polarization, but changing dramatically so as to have nodes along the orbital direction with x and y polarization. Although more accurate relativistic calculations allowing for non-dipole effects would no doubt be somewhat different from these results, the changes with polarization and energy in Figs. 1.6 and 1.7 would be expected to be semi-quantitatively maintained.

As one simple illustration of the utility of polarization in valence-band studies, it is pointed out in in recent publications [42, 45], and in the chapter by Tjeng et al., that it can be useful to emit electrons perpendicular to the polarization direction in order to suppress the strong TM 4s contributions in TM oxide valence spectra, so as to more directly see the transition metal 3d contributions (cf. Fig. 1.5). Figures 1.6

and 1.7 make it clear that other polarization-emission geometries could be useful in enhancing or de-enhancing the contributions of different orbitals. Making use of such variations in cross sections with polarization is of course also a type of linear dichroism, and will be a very useful technique in future HXPS studies.

Finally, it is important to note that elastic scattering, as indicated schematically in Fig. 1.4, will minimally tend to smear out the various features seen in purely atomic cross sections such as those in Figs. 1.6 and 1.7, but also for any atomically ordered system to produce strong modulations due to photoelectron diffraction, as discussed further below.

1.2.4 Chemical Shifts, Multiplet Splittings, and Satellites in Core-Level Spectra

It is obvious that core-spectra in HXPS can be mined for the same kinds of information as in soft X-ray excited spectra: chemical state from chemical shifts, orbital occupations and spin from multiplet structure, and local bonding information from satellites, whether they are described as shake-up or final-state screening in nature. But it was realized early on by Horiba et al. in work on a colossal magnetoresistive manganite [46], subsequently in work on high temperature superconductors [47] and later on dilute magnetic semiconductors (DMSs) [48] that going to higher energies permits observing extremely sharp low-binding-energy satellites on transition-metal 2p spectra, and that these can be interpreted in terms of bulk screening by highly delocalized valence electrons near the Fermi level [49]. An example of this kind of data for the DMS $Ga_{0.97}Mn_{0.03}As$ is shown in Fig. 1.8, for which the Mn $2p_{3/2}$ peak shows a very strong screening satellite of this type. These final-state effects provide yet another handle on valence electronic structure and have been found to be sensitive for example to the presence of ferromagnetic order [46, 48]. The spectrum in Fig. 1.8 also exhibits a multiplet splitting for the Mn 3s spectrum that can be used to estimate the spin on this atom. These final state effects and their interpretation are reviewed in the chapter by Grosvenor et al. and also discussed in the chapter by Taguchi and Panaccione.

1.2.5 Recoil Effects

Recoil effects in HXPS were first explored by Takata et al. [50], and are discussed in detail in the chapter by Kayanuma. They have been found to affect both core level- and valence level-spectra [50–52], and must be considered as sources of both peak shifts to effectively higher binding energies, and peak broadening. Figure 1.9b provides a simple way to estimate the maximum magnitude of the peak shift, in the simplest assumption that it is a single-atom phenomenon. However, it is also clear

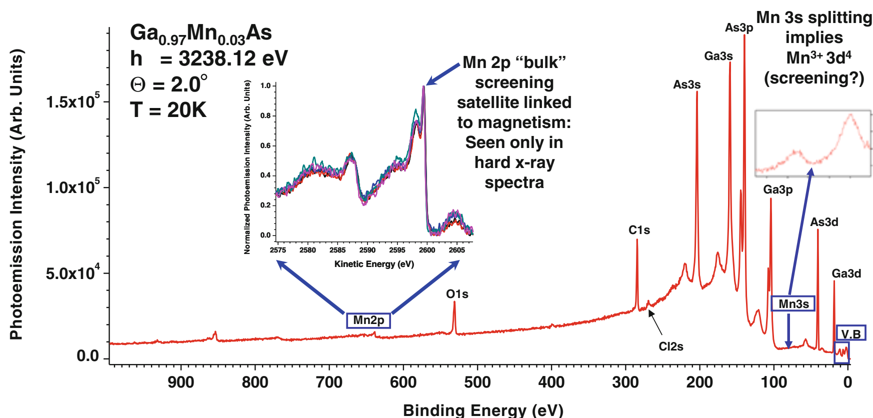

Fig. 1.8 Survey spectrum from the dilute magnetic semiconductor $Ga_{0.97}Mn_{0.03}As(001)$ with 3.2 keV excitation, and with *enlarged insets* from scanning longer on Mn 2p and 3s. Mn 2p reveals a sharp final-state screening peak only seen with hard X-ray excitation. Mn 3s show a doublet due to multiplet splitting that can be used to estimate the spin of Mn. Data from SPring-8 (From [40])

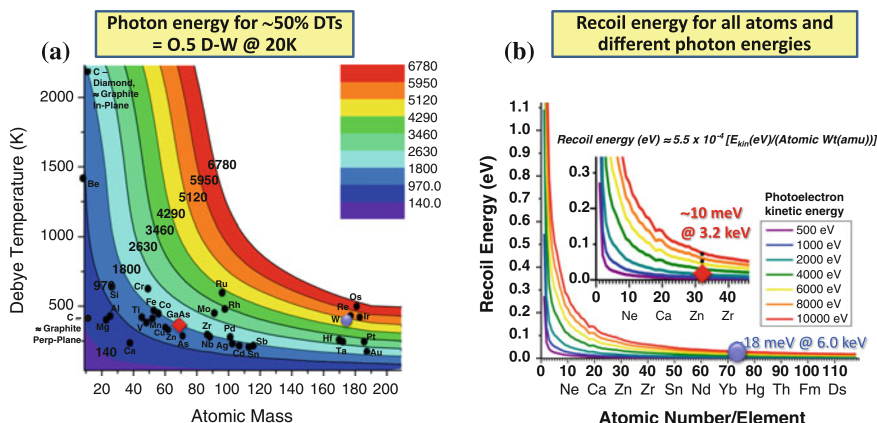

Fig. 1.9 Calculated parameters for estimating the feasibility of ARPES at higher energies, including (**a**) contours for various photon energies to yield a photoemission Debye-Waller factor W(T) of 0.5 at 20 K, and **b** the recoil energy for all atoms as a function of photon energy. Values for two first demonstration cases W and GaAs studied with hard X-rays [39] are highlighted (From [55])

from work to date that it is the detailed vibrational coupling of a given atom to its near neighbors that controls the magnitude of the recoil shift [52], suggesting what has been called "recoil spectroscopy" as a local probe of such local bonding effects, including those in valence spectra [53].

A particularly illuminating recent example of the observation of recoil effects in gas-phase HXPS is for Ne 1s emission [54], for which the p-wave nature of the

cross section means that the emission of the photoelectrons is strongly biased toward being either parallel or anti-parallel to the polarization vector, as shown in Fig. 1.10a. But if the photoelectrons and the subsequent KLL Auger electrons are detected along the polarization as shown, then the Auger electrons will be Doppler shifted in energy depending on the direction of emission of the photoelectrons. The turning on of this effect is seen as photon energy is increased into the 10 keV regime in Fig. 1.10b. Such effects are presumably also present in solids as well, and will be a source of broadening in Auger peak widths at higher energies. This and other aspects of HXPS in atomic and molecular physics are discussed in the chapter by Simon, Piancastelli, and Lindle.

As a final comment on recoil, the use of a Debye-Waller (D-W) factor to estimate the recoil-free fraction for a given excitation is directly related to the analysis of Mössbauer spectra [50], and also to the degree to which HXPS valence spectra can be expected to exhibit momentum-resolved electronic structure via direct transitions in angle-resolved photoemission (ARPES) [55]. Figure 1.9a in fact permits estimating the fraction of momentum-resolved transitions as a function of Debye temperature, atomic mass, and photon energy. When the D-W factor is very small, one speaks of being in the XPS limit or more precisely the matrix-element-weighted density of states (MEWDOS) limit. This continuum between the ARPES limit at low temperature and/or low energy and the XPS limit at high temperature and/or high energy is discussed further below, in prior publications [18, 39, 40, 55], and in the chapter by Gray.

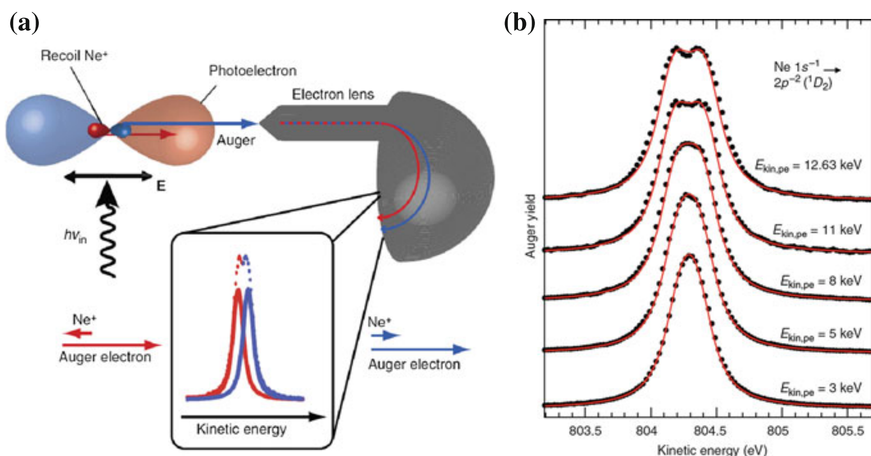

Fig. 1.10 Doppler effect on Auger emission from a free atom. **a** The two basic recoil directions of Ne 1s emission relative to the polarization directions of the incident X-ray, depending on whether the photoelectron is emitted toward the spectrometer or away from it. The expectation for this effect on a subsequent Auger emission spectrum is indicated in the *inset*. **b** Actual Auger spectra for the transition Ne^{+1} $1s^{-1}$ → Ne^{+2} $2p^{-2}$ ($^1D_2$) + Auger electron, as photon energy is increased. Data from Soleil (From [54])

1.2.6 Circular and Linear Dichroism

Making use of linear polarization to accentuate different orbital contributions has been discussed above under cross sections, but beyond this is the well-known magnetic circular dichroism (MCD) in magnetic systems, first observed in soft X-ray photoemission from Fe by Schneider et al. [56], and first observed in HXPS from Fe_3O_4 and Zn-doped Fe_3O_4 by Ueda et al. [57]. To distinguish photoemission MCD from the more commonly practiced X-ray absorption MCD (XMCD), it seems worthwhile to designate the photoemission variant as PMCD. Although the much-used sum rules of XMCD have no simple analogues in PMCD, PMCD data nonetheless permits assessing magnetic order, including at buried interfaces. Linear magnetic dichroism in photoemission (PMLD) has also been measured, and often is referred to with the suffix AD to denote that it is measured in angular distributions. Note to Editor: There are terms in the figure caption that I noticed are not defined in the text. Some PMCD results from the first HXPS study are presented in Fig. 1.11 [57], and in Fig. 1.12c–e from a more recent study of a buried layer of $Co_2FeAl_{0:5}Si_{0.5}$ [58].

PMCD has in fact been used in connection with soft X-ray standing-wave excitation (to be introduced below) to probe the depth distribution of magnetic order through buried interfaces of Fe/Cr [59] and Fe/MgO [60], and such measurements should be possible with hard X-ray excitation.

1.2.7 Spin-Resolved Spectra

Adding the spin dimension to HXPS is an obvious next step that would increase the ability to probe magnetic systems enormously, and first measurements of spin-resolved spectra have already been made on the same buried layer containing Fe [58], as shown in Fig. 1.12a–c.

Novel imaging spin detectors [61, 62] and other more efficient spin detectors that should be suitable for HXPS [63] are also being developed that promise a factor of ~100, if not more, in speed, and some of these are being implemented for HXPS

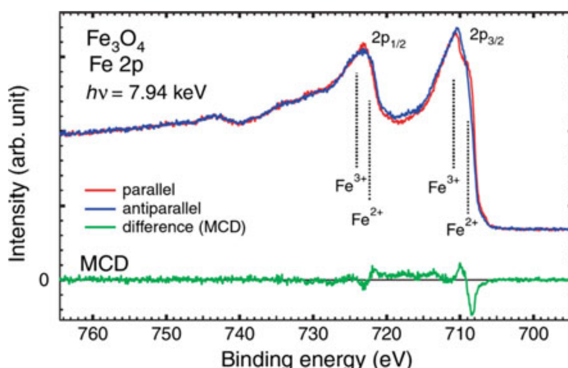

Fig. 1.11 Hard X-ray photoemission MCD (*PMCD*) for Fe 2p core-level emission from a 10 nm-thick Fe_3O_4 film. Data from SPring-8 (From [57])

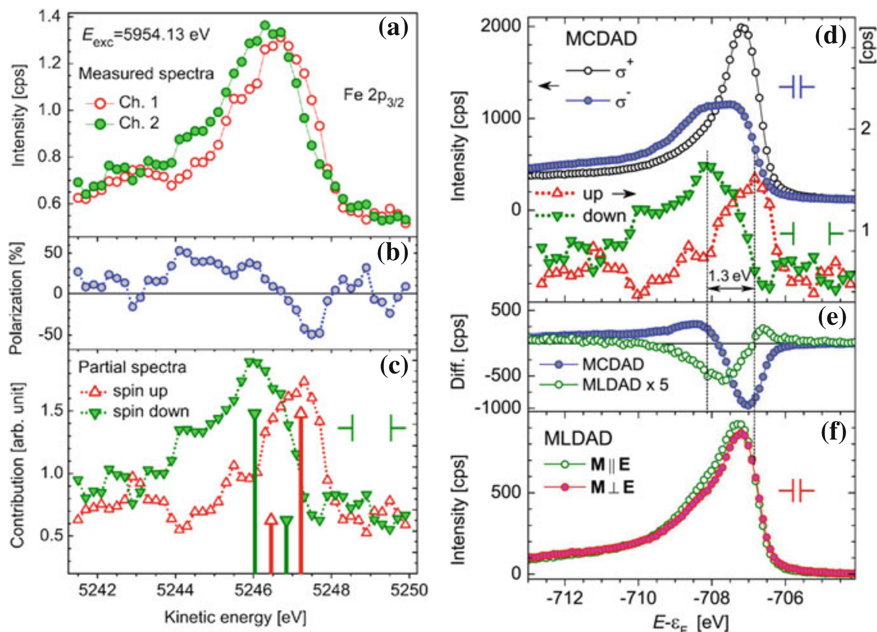

Fig. 1.12 **a**–**c** Spin-resolved spectra and **d**–**e** photoemission MCD (*PMCD*) and MLD (*PMLD*) from Fe $2p_{3/2}$ in a buried layer of $Co_2FeAl_{0:5}Si_{0.5}$ with 5.9 keV excitation. **a** Count rates in spin detector channels, **b** spin polarization derived from the curves in (**a**), and **c** spin-resolved spectra. **d**–**f** Comparison of spin-resolved Fe $2p_{3/2}$ spectra with (**c**) PMCD and (**d**), (**e**) PMLD from the same sample. Data from SPring-8 (From [58])

facilities at present. Thus, an exciting element of future studies will no doubt involve more use of spin resolution.

1.2.8 Photoelectron Diffraction

X-ray photoelectron diffraction (XPD) in core-level emission is a well-developed technique for determining local atomic structure in an element-resolved way, with over 50,000 citations in a Web of Science search based on “photoelectron diffraction”. Various reviews of XPD making use of soft X-ray excitation have appeared in the literature [64–66]. In the chapter by Chambers, he illustrates the use of XPD for characterizing oxide heterostructures. The literature on hard X-ray photoelectron diffraction is much more limited, but growing, very much due to Kobayashi et al. [67].

An initial theoretical study [68] of HXPD pointed out that the traditional multiple-scattering cluster model for calculating XPD, as for example, used in the online Electron Diffraction in Atomic Clusters (EDAC) program [69] may not be the most rapidly convergent for HXPD, in which a larger no. of atoms contribute

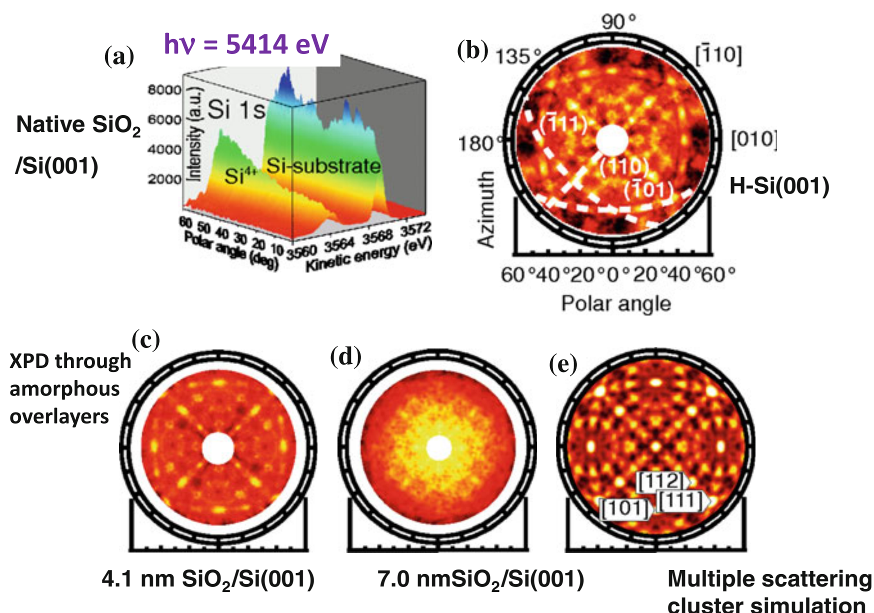

Fig. 1.13 Hard X-ray photoelectron diffraction from Si with varying thicknesses of SiO_2 on top and an excitation energy of 5414.7 eV from a monochromatized laboratory Cr Kα_1 source. The spectrometer here accepted a very wide angle of $\sim\pm40°$. **a** Si 1s spectra from a Si(001) single-crystal covered by a SiO_2 layer recorded at a certain azimuth. Note the single-shot ability to do ARXPS for depth profiling. **b–d** Two-dimensional HXPD patterns of Si 1s at a kinetic energy of 3569 eV from a Si crystal **b** terminated by H, **c** covered by a 4.1-nm-thick SiO_2 layer and **d** covered by a 7.0-nm-thick SiO_2 layer. The *dashed lines* in **b** indicate Kikuchi bands along the (110) and (111) planar directions. **e** A calculated pattern from a multiple-scattering cluster calculation. Data from a laboratory HXPS system (From [34])

due to the larger IMFPs, and the individual electron-atom scattering events become much more forward peaked, with these combined effects leading to diffraction patterns more properly interpreted as overlapping Kikuchi bands [68]. Thus, a dynamical diffraction approach is more appropriate in the high-energy limit. This prior study pointed out the possible sensitivity of HXPD to the site type of an atom, e.g. as a dopant, and this is a promising future direction for its application. One preliminary study of this type has been done, for Mn in GaAs [70].

As an example of HXPD results, Fig. 1.13 shows some data from Si with various thicknesses of SiO_2 on top, as obtained from a laboratory system using Cr Kα excitation at 5.4 keV [71]. Here, the data are compared to cluster calculations. It is evident that the amorphous SiO_2 overlayer attenuates and smears out the HXPD modulations, but that they are still present to some degree even with 7 nm of amorphous SiO_2 on top. A much more detailed set of such data for ZnO, as compared to both cluster and dynamical diffraction theory, is presented in Fig. 18.28 of the chapter by Kobayashi.

It is thus clear that HXPD will be a very useful aspect of future studies of any single-crystal or epitaxial, or even azimuthally textured, sample, with spectrometers of extremely wide angular acceptance now permitting very rapid data accumulation [71].

1.2.9 Time-Resolved Hard X-ray Photoemission

Another exciting future direction for HXPS is in the ultrafast domain, in which processes on electronic timescales of femtoseconds can be studied. New X-ray free-electron lasers (FELs) with harmonics in the several hundred eV to several keV range are beginning to provide such an opportunity, e.g. at SACLA of SPring-8, the XFEL of DESY, and the LCLS-2 project of SLAC.

Critical in such studies with any FEL is that the space charge of low-energy secondaries above the surface does not cause unacceptable peak shifts or broadenings in spectra, but by now, combinations of experimental data and detailed theoretical modeling have led to readily employable criteria for attenuating the peak flux on the sample so as to control these [72, 73]. Recently, IR-pump/X-ray probe time-resolved photoemission spectra have been obtained at SACLA with 8 keV excitation for V 1s emission from VO_2 and Ti 1s emission from $SrTiO_3$, in what has been called trHAXPES [73]. Essential for the practical future feasibility of such experiments is increasing the pulse frequency by two orders of magnitude or more, such that the peak flux in each pulse can be reduced below the space-charge threshold, while still being able to obtain spectra in a reasonable amount of time. As one possible example of what might be looked at in the time domain, it has been pointed out that the screening of hole states involved in core emission could exhibit different timescales, in particular for the example of the spin-up and spin-down multiplets of a Gd 4s spectrum in Gd during the ferromagnetic to paramagnetic transition [74], but with many other types of screening satellite, as for example that in the Mn 2p spectrum of Mn-doped GaAs in Fig. 1.8, also being candidates for this type of time-resolved measurement.

A second possibility in the time domain involves soft- or hard-X-ray excitation of photoelectron holography from oriented gas-phase molecules, in order to produce so-called “molecular movies” of dissociation or reaction, as has been proposed recently [75, 76].

The future prospects for such time-resolved studies are discussed in much more detail in the chapter by Rossnagel et al., and it is clear that this represents an exciting future dimension in hard X-ray photoemission.

1.2.10 Hard X-ray Photoelectron Microscopy

Adding lateral resolution to HXPS measurements promises to yield a truly three-dimensional picture of a sample, including the added depth penetration for studying multilayer structures and device prototypes. One approach being pursued

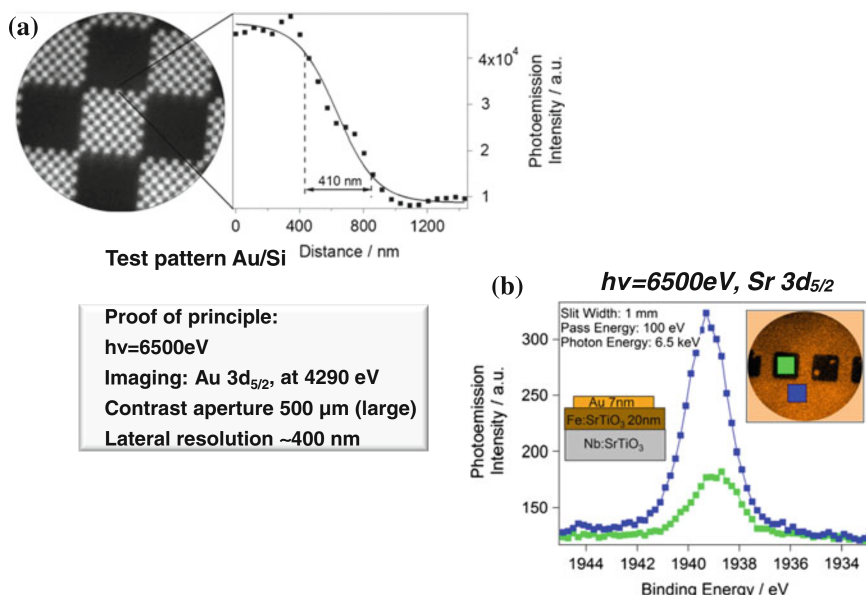

Fig. 1.14 Hard X-ray photo electron microscopy (*HAXPEEM*). **a** *Left* A Au/Si calibration sample imaged on the Au $3d_{5/2}$ photo emission line at a kinetic energy of 4290 eV. *Right* A line scan across a square edge and a 16/84 % profile fit, indicating a resolution of about 400 nm. **b** Selected area hard X-ray photoemission spectra from a patterned Au/$SrTiO_3$ sample, with cross section shown in the *left inset*. Definition of regions of interest in the *right inset*. Data from Petra III (From [77, 78])

in this is to use the electron optical system of a specially-modified photoelectron microscope (PEEM) to yield what has been termed HAXPEEM [77, 78]. Some first results from this approach are shown in Fig. 1.14, where 1.14a shows an image of a reference checkerboard Au–Si pattern that has been used to determine the resolution at 6500 eV photon energy of $\sim$400 nm, and 1.14b shows energy-resolved Sr 3d spectra from an Fe-doped $SrTiO_3$ layer on which a 70 nm thick pad of Au has been grown. Figure 1.14b thus demonstrates that lateral and element-specific resolution is possible through the thick Au overlayer. From an electron optical point of view, it should be possible to improve the resolution into the $\sim$100 nm regime in the future. A wide range of applications of HAXPEEM at this sub-micron resolution level should be possible [78].

An additional useful dimension to HAXPEEM, could be using standing-wave excitation to enhance depth resolution, as demonstrated already with soft X-ray excitation [79, 80], and discussed in a separate section below.

The chapter by Browning discusses this and other possible methods of achieving lateral resolution in hard X-ray photoemission.

1.3 Standing-Wave and Near-Total-Reflection Measurements

1.3.1 Introduction

In this section, the use of various X-ray optical effects to tailor the form of the X-ray wavefield depth distribution so as to achieve greater depth resolution in studies of buried layers or interfaces is discussed. This will involve both the creation of standing waves (SWs) and the concentration of the wavefield near the surface in going into the near-total-reflection (NTR) regime. SW hard X-ray photoemission is discussed in the chapter by Zegenhagen, Lee, and Thiess for the specific case of Bragg reflection from crystal planes, so the focus here will be on Bragg reflection from macroscopic multilayer structures.

In either core-level or valence-level studies in the DOS limit, the basic variation of photoelectron intensity is given by (1.1) or (1.2) respectively, where it is the spatial variation of the X-ray wavefield intensity $I_{h\nu}(x, y, z, \hat{\varepsilon})$ that is altered through X-ray optical effects. For SW studies this is done principally by varying the incidence angle or photon energy relative to the Bragg condition for a set of Bragg planes in a crystal or a multilayer heterostructure, or a sample grown on a suitable multilayer. This acts to sweep the SW by one half of its intensity period λ_{SW} in a direction perpendicular to the reflecting planes, the z coordinate in Figs. 1.4 and 1.15. As noted from the equations in this figure, the SW period is very close to the period of the multilayer d_{ML}, regardless of the X-ray wavelength = $\lambda_{h\nu} \equiv \lambda_{x}$, thus providing a sort of "sub-nm ruler" as the SW is scanned vertically through the sample. For NTR studies, enhanced depth probing is achieved by sweeping the incidence angle from somewhat above the critical angle θ_{crit} at which significant reflection begins to occur to a cutoff angle at which all intensities go to zero. An NTR scan also can involve buried-interface reflections if the critical angles for interfaces above them are larger, and thus SW creation, so the SW and NTR methods have overlapping strengths in providing depth resolution through the analysis of such effects.

1.3.2 Standing-Wave Hard X-ray Photoemission from Multilayer Reflections

Figure 1.15 illustrates the SW method for the case of X-ray Bragg reflection from a multilayer sample, including the two methods mentioned above for scanning the SW through the sample, as well as a third in which one layer of the sample is grown in a wedge form, the incidence angle is held fixed at the Bragg angle, and the SW can be moved through the sample simply by scanning the X-ray beam spot along the slope of the wedge [59]. This type of measurement has been reviewed elsewhere [19, 20, 81, 82].

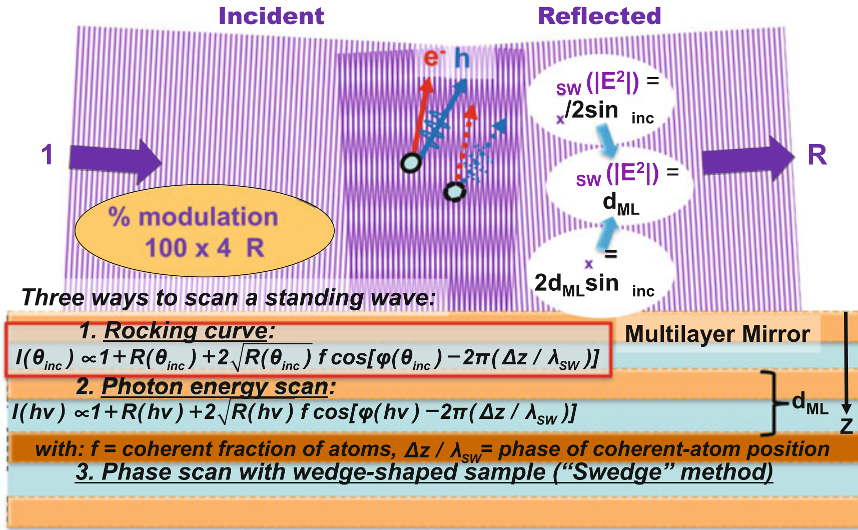

Fig. 1.15 Schematic illustration of the formation of a standing wave (*SW*) in first-order Bragg reflection from a multilayer mirror, together with the equations leading to the standing wave period $\lambda_{SW} \approx$ the multilayer period d_{ML}. The standing wave can be scanned through the sample, which might be the mirror, or grown on top of the mirror, in the three ways indicated: an angle scan or rocking curve, a photon energy scan, or a wedge scan. The equations describing the intensity of the SW are also indicated. (From [19])

The basic physics of creating a standing wave in Bragg reflection from crystal planes is discussed in the chapter by Zegenhagen, Lee, and Thiess, including various applications of this very promising type of measurement, so will not be considered further. However, it is important to note that, for the case of reflection from the nm-scale layers to be considered here, the different materials can be described by a macroscopic index of refraction $n = 1 - \delta - i\beta$, in which β represents absorption and is directly related to the X-ray exponential attenuation length $\Lambda_{hv} = \lambda_{hv}/4\pi\beta$, $\theta_{crit} = sqrt(2\delta)$ for a surface in contact with vacuum, and the wavefield can be calculated by repeatedly applying the Fresnel equations to each significant material interface, including all effects of multiple scattering at these interfaces. This type of calculation is described in detail elsewhere, including a specially written program Yang X-ray Optics (YXRO) that can compute both photoelectron and X-ray emission intensities using (1.1) and is available for online use [83].

A number of soft-X-ray studies have been published using the SW-multilayer method, including overviews [19, 20, 81, 82], and in which the technique has been applied to TM oxide heterostructures [84–86] and magnetic multilayer structures related to spintronics[59, 60, 87, 88], but the focus here will be on examples involving hard X-ray excitation [19, 20, 84, 86–89].

In one particularly illustrative multilayer SW study, a sample consisting of repeated $SrTiO_3$ and $La_{0.7}Sr_{0.33}MnO_3$ bilayers was studied, with rocking curve

measurements being performed on core levels of all of the atoms present, including surface C-containing contaminants. The multilayer was composed of 48 [84] (or in another study 120 [86]) bilayers consisting of alternating 4 unit cells of the band insulator $SrTiO_3$ and 4 unit cells of the half-metallic ferromagnet $La_{0.7}Sr_{0.3}MnO_3$. Both non-resonant hard X-ray excitation at 5950 eV (SPring-8) and resonant soft X-ray excitation at 833.2 eV (ALS) near the La $3d_{5/2}$ absorption edge that maximizes reflectivity were used. The sample configuration and experimental geometry are shown in Fig. 1.16a. The detailed analysis of these RC data appears elsewhere, but as some indication of the effects seen, Fig. 1.16b shows the final results of fitting X-ray optical calculations based on the YXRO program [83] to the experimental rocking curves for all elements. Note the presence of both the primary Bragg reflection rocking curve from the multilayer period d_{ML}, and the Kiessig fringes associated with reflection from the top and bottom of the multilayer stack over a distance D_{ML} (as illustrated in Fig. 1.16a). Theory clearly describes this data, including both types of features, extremely well, and the resulting structure of the multilayer so derived is shown in Fig. 1.16d. Notable here is that it was also found that the multilayer period varied continuously from top to bottom, by about 6 % only, as indicated in Fig. 1.16c, and a subtle structural element thus was cleanly resolvable via this SW analysis. This structural conclusion was also subsequently

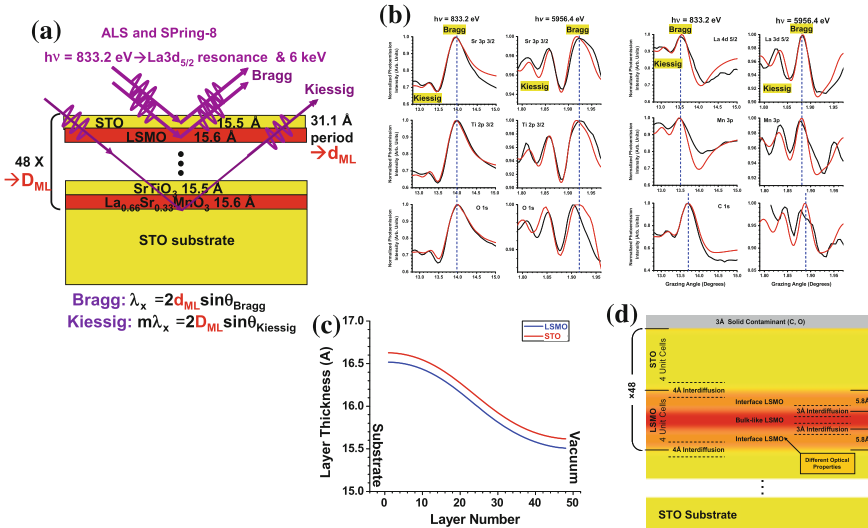

Fig. 1.16 **a** A 48-bilayer multilayer of $SrTiO_3/La_{0.7}Sr_{0.3}MnO_3$ studied with both soft X-ray and hard X-ray standing wave photoemission, with conditions for both 1st-order Bragg and mth-order Kiessig reflections indicated. **b** Results of an X-ray optical analysis of both soft and hard X-ray rocking curves of core-level intensities from all elements in the sample, with the final best-fit to theory being for a multilayer period d_{ML} that changes about 6 % with depth as shown in (**c**), and with interface concentration/roughness profiles as in (**d**). The results in (**c**) and (**d**) have also recently been quantitatively confirmed by TEM/HAADF/EELS (From [84, 86])

confirmed by transmission electron microscopy with energy loss spectroscopy [86]. The soft X-ray core-level spectra also finally revealed an interface binding energy shift for Mn 3p, but not Mn 3s, that can be explained via a crystal-field distortion near the interface [84].

Similar multilayer SW studies with hard X-ray excitation have also been carried out on spintronic systems consisting of MgO on Fe [87] and MgO on FeCoB [88] and a semiconductor system of TiN layer grown on top of a Si/Mo multilayer mirror [89]. In these studies also, subtle chemical shifts of core levels were seen as the SW scans through a buried interface.

It is thus clear that such multilayer SW measurements with hard X-ray excitation can provide unique types depth-resolved information concerning buried layers and interfaces, with a broad range of future applications.

1.3.3 Hard X-ray Photoemission at Near Total Reflection

Beyond these Bragg-reflection standing-wave effects are making use of those which occur as the incidence angle is tuned into near total reflection (NTR), with this possessing the advantage that it can be applied to any material, but in particular, simpler bilayer or trilayer samples that are easier to grow. This type of measurement was stimulated by a pioneering X-ray optics study by Henke [90], followed by experiments involving depth profiles of concentrations [91, 92], with much later studies further developing the method, and pointing out some general advantages of this approach (lower inelastic backgrounds, tunable surface sensitivity, use of Kiessig interference fringes) [93–95]. The terms grazing incidence XPS (GIXPS) or total reflection XPS (TRXPS) have been used in these studies, but NTR will be used here.

An updated application of this NTR approach is shown in Fig. 1.17, which presents some HXPS experimental data and theoretical calculations for a bilayer sample of ferroelectric $BiFeO_3$ on top of a Ce-doped Mott insulator ($Ca_{0.96}$, $Ce_{0.04}$) MnO_3 (BFO on CCMO) [96], a system recently studied as leading to strong ferroelectric control of the Mott insulator transition in the 2D electron gas at the interface between them [97]. The photon energy was 2.8 keV. The intensities of various core level intensities have been monitored as a function of incidence angle : C 1s from the surface contaminant overlayer, Bi 4f from BFO, and two components of Ca 2p from CCMO that are clearly resolved in the spectra of Fig. 1.17a, obtained at angles for which the calculations of electric field intensity in Fig. 1.17b for the final optimized sample geometry in Fig. 1.17c indicate enhanced sensitivity to the BFO/CCMO interface (higher binding energy) or the bulk of the CCMO (lower binding energy). The angular-dependent raw data for these four intensities are shown in Fig. 1.17d, and they clearly show differences in both the final decrease to zero at total reflection and the oscillatory standing-wave interference phases seen for higher angles. Noteworthy in Fig. 1.17d is the systematic change in the low-angle cutoff for atomic species at different depths, a generally useful effect even at this qualitative level. The comparison of theory for the optimized sample

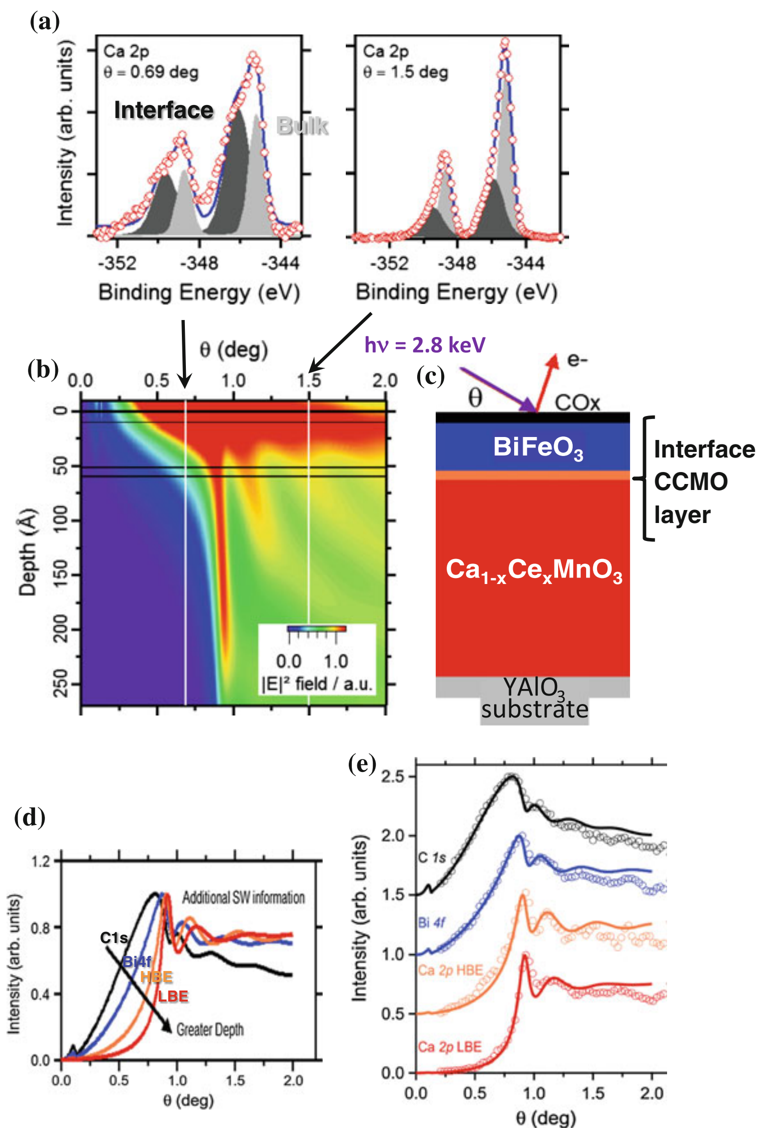

Fig. 1.17 Using near total reflection (*NTR*) HXPS on a complex oxide system, for a bilayer of $BiFeO_3$ and Ce-doped $CaMnO_3$, grown on an $YAlO_3$ substrate. **a** The Ca 2p spectra at two incidence angles emphasizing the high-binding-energy (interface) and low-binding-energy (bulk) CCMO regions. **b** The calculated electric field strength as a function of depth and incidence angle for the sample configuration in (**c**), which was derived by fitting X-ray optical theory to Ca 2p, Bi 2p, and C 1s intensities as a function of angle. **d** The experimental intensity variation of C 1s, Bi 4f, HBE Ca 2p and LBE Ca 2p with incidence angle over the NTR region. **e** The optimized final fits of X-ray optical calculations to the data in (**d**), for the sample configuration in (**c**). Data from the ALS (From [96])

geometry and experiment in Fig. 1.17e further shows excellent agreement, and the ~10 Å thickness of the 2DEG in the CCMO associate with the higher-binding energy Ca peak derived by fitting the NTR experiment to theory agrees well with a separate analysis of small shifts in TEM-EELS Mn-L_3 near-edge features, further confirming the utility of NTR photoemission in buried interface studies. The oscillations here are due to reflections and interference at the surface and the two buried interfaces in the sample, and the peaks in intensity near 0.9° to the spreading of the X-ray beam along the spectrometer entrance slit direction and the concentration of electric field near the surface, the latter an effect first observed and explained by Henke [90]. Important additional features are the differences in phase of the oscillations for Bi and Ca shown in Fig. 1.17d, which are useful through the process of optimizing the sample geometry to fit experiment in deriving depth-dependent interface information for this and other similar future samples.

Such NTR measurements thus represent another promising direction for buried interface and buried layer characterization with HXPS.

1.4 Valence-Level Studies, Including Angle-Resolved Photoemission

Valence-level studies using conventional XPS or HXPS have almost all been carried out in the MEWDOS or XPS limit, in which very useful information on momentum-integrated electronic structure can be obtained, and several such studies are reviewed in the chapters by Kobayashi and Tjeng. Such data, which will always be at higher energy and/or temperature, can often be fruitfully analyzed using (1.2), as discussed for example in prior single-crystal Bragg-reflection standing-wave work by Woicik et al. [98–101], and in the chapter by Zegenhagen, Lee, and Thiess.

However, interest is growing in doing more bulk sensitive momentum-resolved ARPES in both the soft X-ray (SARPES) and hard X-ray (HARPES) regime, for several reasons reviewed elsewhere [18–20, 102]. Momentum resolution in this context refers to so-called direct transitions (DTs) from $\vec{k}_i$ to $\vec{k}_f$ according to $\vec{k}_i = \vec{k}_f - \vec{k}_{h\nu} - \vec{g}_n$, where $\vec{k}_{h\nu} = 2\pi\nu/c$ is the photon wave vector and $\vec{g}_n$ is the relevant reciprocal lattice vector, and the low-energy ARPES version of this equation of $\vec{k}_i = \vec{k}_f - \vec{g}_n$ has been modified to allow for the photon momentum because of effects beyond the dipole approximation, as discussed also in an earlier section. For a given experimental geometry, this non-dipole correction is easily made.

Gray et al. first showed that momentum-resolved ARPES is possible with hard X-ray excitation, for the examples of W at 6 keV, and GaAs plus Mn-doped GaAs at 3.2 keV [39, 40], thus providing a novel probe of truly bulk electronic structure. Such HARPES measurements are reviewed in detail in the chapter by Gray, and certainly represent a promising future direction in HXPS studies.

The data analysis of HARPES, and its theoretical interpretation, must allow for the momentum-smearing effects of phonon creation and annihilation, as estimated

e.g. through the Debye-Waller factors of Fig. 1.9a. Simple first-order correction procedures to experimental data for both phonon and HXPD effects are discussed elsewhere [39, 40]. The most quantitative theoretical interpretation of HARPES is via the so-called one-step or "time-reversed LEED" method that has been used in prior studies, as pioneered by Gray et al. [39, 40]. This method has furthermore been improved to include phonon effects more precisely in recent work [103], and is discussed in more detail in the chapter by Braun, Ebert, and Minar, with phonon effects discussed in connection with their Figs. 7.1 and 7.2.

I will here focus only on an additional possible dimension of such HARPES measurements in which a single-crystal Bragg reflection is used to create a standing wave that is scanned perpendicular to the set of $hk\ell$ planes responsible for the reflection. This is thus the same sort of experiment discussed in the chapter by Zegenhagen, Lee, and Thiess, but with the addition of momentum resolution. The goal is thus to determine electronic structure that is both element- and momentum resolved. The SW wavelength is now given by $d_{hk\ell}$, the spacing between these planes, and the scanning is here done through the second method indicated in Fig. 1.15, that is, by scanning the photon energy through the Bragg condition.

As a first indication of the feasibility of such SW-HARPES, some encouraging proof-of-principle results results have been obtained recently for the systems of GaAs(001) and (Ga,Mn)As(001) (two materials studied previously with HARPES in [39, 40]), using an HXPS facility especially suited for this at Diamond [104]. Some of these results are summarized in Fig. 1.18. In Fig. 1.18a, very broad angular range single-detector HARPES images (cf. Fig. 1.2) for $Ga_{0.95}Mn_{0.05}As$ and GaAs, obtained near the (311) reflection from (001)-oriented surfaces with a photon energy of about 3650 eV, are compared. The entire VB spectrum in energy is probed, and over about 7 BZs in momentum. There are conspicuous differences between the undoped and doped samples: a general smearing of features in the doped sample, as seen previously over a much more limited BZ range [39, 40], but also and more significantly, enhanced intensities in the doped sample at several specific points, as circled in yellow, including in particular what is interpreted as a Mn-induced impurity band near the Fermi energy (E_F). In Fig. 1.18b, SW photon energy scans of the Ga 3d, As 3d and Mn 2p intensities from the doped sample over the (311) reflection are shown, with clear evidence of separate Bragg reflections from both the substrate GaAs (the sharper features) and the doped layer (the broader features), separated by a few eV due to slightly different lattice constants, and broader for the doped layer due to its finite thickness of only ~ 100 nm, compared to the GaAs substrate. In addition, the Ga and Mn curves are essentially identical, clearly indicating that the Mn occupies substitutional, rather than interstitial, sites. These two curves are furthermore different from that of As, due to the difference in position in the unit cell.

Going further, core-level SW energy scans such as those in Fig. 1.18b, obtained simultaneously with HARPES results in similar small energy steps over the substrate Bragg features, can be used to project the HARPES images onto the atomic makeup at each point in binding energy and $\vec{k}$. This proceeds based on the use of (1.2), as

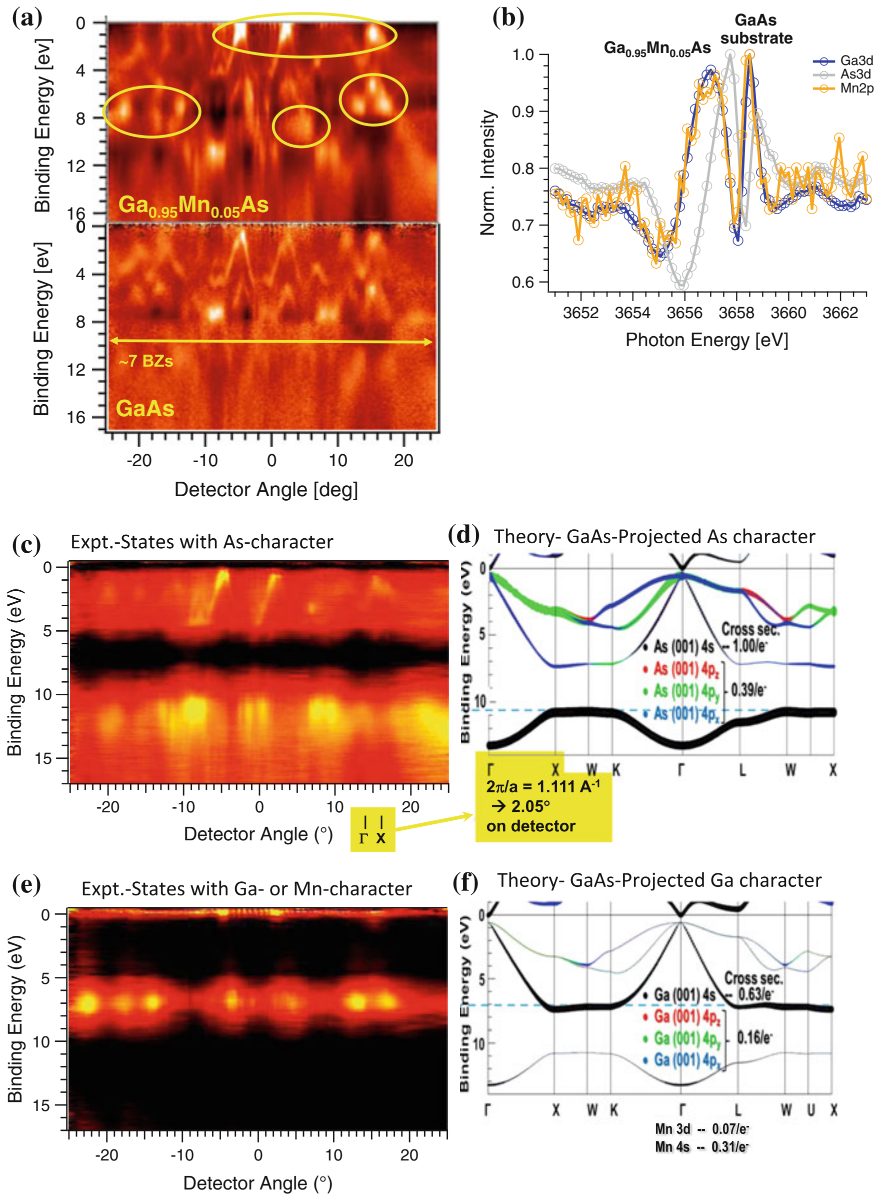

Fig. 1.18 Standing-wave HARPES based on crystal Bragg reflection. **a** HARPES results for $Ga_{0.95}Mn_{0.005}As$ and undoped GaAs, with *circled* features that are strongly enhanced for the dilute magnetic semiconductor (*DMS*). Approximately 7 Brillouin zones are sampled. **b** A photon-energy scan of Ga 3d, As 3d, and Mn 2p intensities through the (311) reflection for $Ga_{0.95}Mn_{0.05}As$, exhibiting two separate Bragg reflections, as indicated. **c** and **e** Orbital-projected standing-wave HARPES results for As and Ga + Mn, respectively, based on the core-level photon energy scans from $Ga_{0.95}Mn_{0.05}As$ in panel (**b**). For the mean exciting energy of hν = 3657 eV, the photoelectron wave vector is $k_f = 30.96$ Å^{-1}, and the resulting Γ-X distance along the detector in degrees is indicated. **d** and **f** Orbital-projected LDA band structures for As and Ga respectively, from [39] and [40], with the Γ-X distance for GaAs again indicated. Data from Diamond (From [104])

done in previous studies at the MEWDOS limit [99], and the additional assumption that the core-level scans are representative of the SW form at each atom, such that each pixel is a linear superposition of intensities from As and Ga(Mn)

$$I_{HARPES}(E_B, \vec{k}, h\nu) \approx I_{As}(E_B, \vec{k}, h\nu) + I_{Ga(Mn)}(E_B, \vec{k}, h\nu), \qquad (1.3)$$

and comparing this equation using a normalized least-squares approach for the full photon energy scan to

$$I_{core}(E_B, \vec{k}, h\nu) = f_{As}(E_B, \vec{k}) I_{As3d}(h\nu) + (1 - f_{As}(E_B, \vec{k})) I_{Ga3d(Mn2p)}(h\nu) \qquad (1.4)$$

so as to finally yield $f_{As} and\ f_{Ga}$ = $(1 - f_{As})$ over the full HARPES E_B, $\vec{k}$ image, pixel-by-pixel. The raw data such as that in the top panel of Fig. 1.18a are then multiplied by either f_{As} or f_{Ga}, yielding the results in Fig. 1.18c, e, respectively. These two projected images are markedly different, showing bands of maximum intensity and bands of minimum intensity that are out of phase with one another. Note also the preservation of enhanced Ga- or Mn-character near the Fermi level in Fig. 1.18e due to the Mn impurity band. Since the two atoms Ga and Mn occupy the same site type, we cannot project Mn alone, although some kind of resonant experiment might permit this in the future.

As confirmation that these projected SW-HARPES images are a valid representation of the atom-projected electronic structure, Figs. 1.18d, f show theoretical projected GaAs band structures from the prior HARPES study [39, 40], with the different orbitals involved specified and the thickness of the curve indicating relative population. There is excellent qualitative agreement as to those regions that should exhibit more As character, and those that should exhibit Ga (or Mn) character. The relative size of the Γ-X distance in the BZ between experiment and theory is indicated for reference. An important point in using the above method for analyzing such results that has been mentioned in connection with (1.2) is that it has long been realized through various theoretical studies that the matrix elements and cross sections for valence photoemission are increasingly controlled by the inner spatial regions of each atom involved [26, 27], thus making the use of core-level intensities on the same atom at nearly the same kinetic energy a good approximation for such SW projection procedures.

Although a complex type of measurement requiring special instrumentation and precise sample manipulation, SW-HARPES measurements represent a promising future technique in the study of complex quantum materials.

1.5 Measurements at Higher Ambient Pressures

The chapter by Liu and Bluhm discusses in detail the rapidly growing technique of near ambient- or high-pressure photoemission spectroscopy (APPS, APXPS, APPES, HPPES, NAP-XPS,…) [105, 106], in which a combination of strong

◀ **Fig. 1.19** Combining standing-wave and ambient-pressure photoemission (SWAPPS). **a** The sample configuration, with some relevant dimensions noted. **b** An O 1s spectrum, resolved into four unambiguous components by peak fitting of the rocking curves for this spectrum. **c** The rocking curves for the four types of oxygen indicated in (**b**). **d** and **e** The Cs 4d spectrum and analogous overlapping Na 2p and O 2s spectra, with peak fitting. **f** The rocking curves for Cs 4d and Na 2p derived from spectra such as those in (**d**) and (**e**). **g** A typical C 1s spectrum, showing the two components, one at low binding energy (*LBE*) and one at higher binding energy (*HBE*). **h** The rocking curves for the two C 1s components. Data from the ALS (From [107])

differential pumping and special electron optics in the entry lens to a hemispherical analyzer is used to permit going to pressures at the sample surface that are now up to 20 Torr, with future projections to much higher values. Thus, much more realistic measurements can be made of various important surface reactions in catalysis, corrosion, environmental science, and many other areas of science and technology.

I will thus not comment in detail on APPS, but simply point out a recently developed connection to the standing-wave technique mentioned above in what has been termed SWAPPS [107, 108]. This first application of SWAPPS used soft X-ray excitation and was to a liquid-like ~1 nm thick aqueous film containing NaOH and CsOH on a surface of Fe_2O_3 hematite, grown on a Si/Mo soft X-ray mirror as the SW generator, as illustrated in Fig. 1.19a. Rocking curves were measured for the core-level intensities from all of the species present, including four types of oxygen and gas-phase water above the surface, which could be resolved due to chemical shifts, as shown in Fig. 1.19b. In Fig. 1.19c, it is remarkable that all four oxygen components show the effects of the SW scanning through the surface, including even the gas-phase water, and that they each have distinct shapes, exhibiting also what are found to be Kiessig fringes. Figure 1.19f now compares the rocking curves for Cs 4d and Na 2p, as derived from spectra such as those in Fig. 1.19d, e, and reveals a small but reliable shift of 0.04° in the steeply sloping regions of the two curves near the Bragg angle of the multilayer, but also a different shape in the wings away from these regions, with Cs having higher intensity both below and above the Bragg angle. Figure 1.19g, h further show two different types of contaminant C, at high- and low-binding energy (HBE and LBE), and they have distinctly different rocking curves. Going further, these rocking curves have been compared to X-ray optical calculations while varying the layer thicknesses, positions, and linear interface regions in the sample structure, and the optimum structure as fit to these data, shown in Fig. 1.20i, yields the comparisons shown in Fig. 1.20a–h. Some significant conclusions from this study are thus that Cs and Na do not have the same distribution, but Cs is rather excluded from near the Fe_2O_3-aqueous interface, and that the two C species have very different distributions, with the HBE distributed throughout the full aqueous layer and LBE being limited to a hydrophobic surface film.

Beyond these soft X-ray results, it has also been pointed out that using hard X-ray excitation both permits looking through thicker surface layers at buried interface, and going to higher pressures due to the longer IMFPs of the emitted photoelectrons [11], such that thin liquid films in equilibrium with the electrolyte in

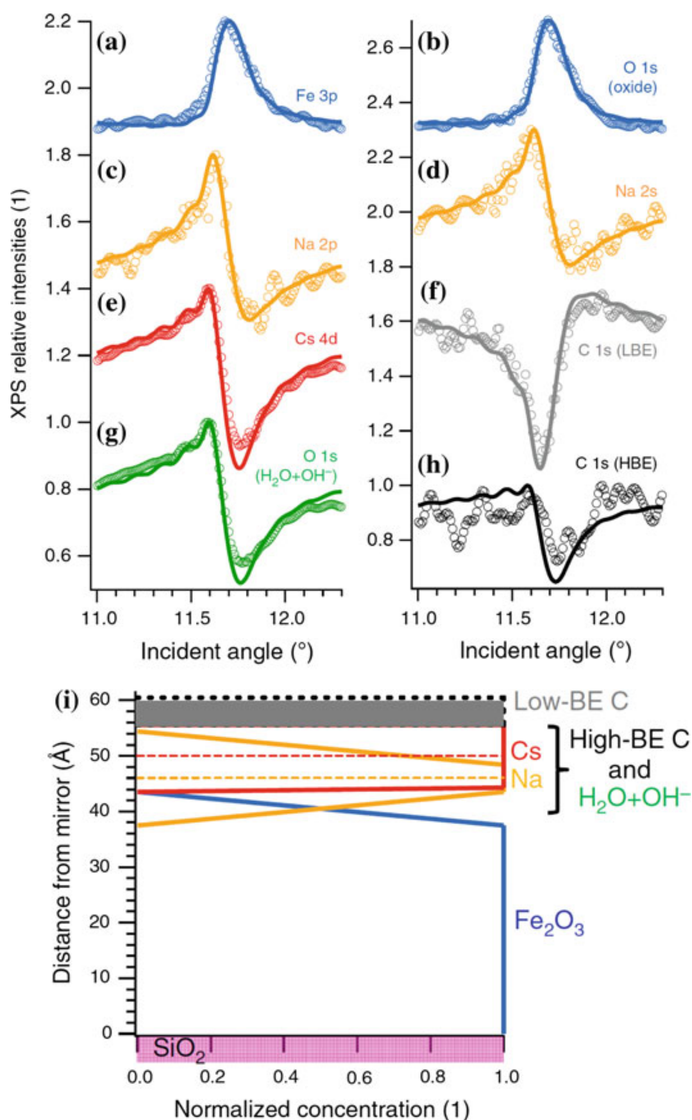

Fig. 1.20 Standing-wave ambient pressure photoemission (SWAPPS). **a**–**h** A comparison of the experimental rocking curves for various core-level intensities with theoretical calculations based on the optimized sample configuration shown in (**i**). **a** Fe 3p, **b** O 1s (oxide), **c** Na 2p, **d** Na 2s, **e** Cs 4d, **f** low binding energy (*LBE*) C 1s, **g** O 1s (OH^- + H_2O), **h** high binding energy (*HBE*) C 1s. **i** The concentration profiles for the optimized sample configuration. Data from the ALS (From [107])

an electrochemical cell can be studied, thus opening up exciting new possibilities in APPS. The combination of hard X-rays and SW excitation has also recently been demonstrated in an electrochemical cell for the first time [108].

These results thus point to the use of hard X-ray SWAPPS measurements for studying the interface region of surface reactions at realistic pressures in a much more precise and both element- and chemical state-resolved way than has previously been possible.

1.6 Concluding Remarks

It is thus clear that hard X-ray photoemission is a rapidly developing and versatile technique, which in fact by now encompasses all of the modalities represented in Fig. 1.2. Its ability to probe more deeply into any condensed matter system leads to an enormous range of applications from complex bulk materials to multilayer nanostructures to *in operando* device prototypes, as amply illustrated by the other chapters in this book. The higher energies involved are also of inherent interest in atomic and molecular studies, again as discussed later in this book.

Some more specific summary comments are: The quantitative analysis of HXPS core and valence data is in several respects simpler, including ARXPS for depth profiling and decomposition of valence spectra into their element-specific components. Adding polarization variation provides additional orbital and magnetic sensitivity. Spin resolution begins to be applied to magnetic systems, with promise of much more efficient detectors in the near future. Hard X-ray photoelectron diffraction (HXPD) provides bulk- and element-sensitive structural information that is qualitatively different from that in the soft X-ray regime, including its connection to Kikuchi bands. The use of standing wave (SW)- and near total reflection (NTR)-measurements yields unique information on buried interfaces and layers. Angle-resolved valence-level studies can also yield momentum-resolved electronic structure through hard X-ray ARPES (HARPES), and perhaps through Bragg-reflection SW excitation both momentum- and element-resolved electronic structure. Ambient pressure photoemission (APPS) benefits from higher energies in attaining higher pressures and penetrating thicker surface films to look at buried interfaces. Finally, combining hard x-ray SW excitation with APPS in SWAPPS shows promise of providing information with unprecedented detail on the solid/liquid interface.

Acknowledgements The work in my group discussed here has been supported by the Director, Office of Science, Office of Basic Energy Sciences, Materials Sciences and Engineering Division, of the U.S. Department of Energy under Contract No. DE-AC02-05CH11231, through the Materials Sciences Division of the Lawrence Berkeley National Laboratory (LBNL), and by the Laboratory Directed Research and Development program of LBNL. Additional support has come from Army Research Office MURI grant W911-NF-09-1-0398 for oxide heterostructure research; from the Jülich Research Center, Peter Grünberg Institute (PGI-6); and from the Labex PALM APTCOM Project of the Triangle de Physique (Paris), No. ANR-10-LABX-0039.

My special gratitude also goes to Alexander X. Gray and Slavomir Nemšák for their significant contributions to much of the recent work described herein, and to S.N. for his assistance in the preparation of this manuscript. I am also grateful to the various co-authors in my group and elsewhere who have contributed so much to our work in HXPS, including various scientists who have provided excellent assistance with measurements at the Advanced Light Source, BESSY, ESRF, Petra III, Soleil, SPring-8, and the Swiss Light Source.

References

1. P. Pianetta, I. Lindau, Nature **250**, 215 (1974)
2. HAXPES03-ESRF, Nucl. Inst. Meth. A **547**, 1–238 (2005)
3. HAXPES06- SPring8, http://haxpes2006.spring8.or.jp/program.html
4. HAXPES-ALS (2008), http://ssg.als.lbl.gov/ssgdirectory/fedorov/workshops/index.html
5. HAXPES09-NSLS, http://www0.bnl.gov/ps/nsls/workshops/2009/haxpes/
6. HAXPES11-DESY (2009), http://haxpes2011.desy.de
7. HAXPES-ESRF (2012), http://www.esrf.eu/files/live/sites/www/files/events/conferences/2012/users-meeting-2012-workshops/xsw-haxpes-workshop/Programme.pdf
8. HAXPES13-Uppsala, http://www2.physics.uu.se/external/haxpes2013/
9. HAXPES15-Taiwan, http://www.nsrrc.org.tw/haxpes-2015
10. HAXPES17-Berkeley, To be held 11–15 Sept. 2017
11. S. Axnanda et al., Sci. Rep. **5**, 09788 (2015)
12. J. Zegenhagen (ed), in Nuclear Instruments and Methods A vol. 547, pp. 24–41 (2005). Papers from First HXPS Conference
13. L. Kover (ed), J. Electron Spectrosc. **178–179**, 1–448 (2010), dedicated issue on XPS and HXPS
14. W. Drube (ed) J. Electron. Spectrosc. **190**, 125–314 (2013), dedicated issue on HXPS
15. C.S. Fadley, Nuclear Instruments and Methods A **547**, 24–41 (2005), special issue edited by J. Zegenhagen, C. Kunz
16. C.S. Fadley, Nucl. Inst. Meth. A **601**, 8 (2009)
17. C.S. Fadley, J. Electron Spectroc. **178–179**, 2 (2010)
18. C.S. Fadley, Synchrotron Radiation News **25**, 26 (2012)
19. C.S. Fadley, J. Electron Spectrosc. **190**, 165 (2013)
20. C.S. Fadley, S. Nemšák, J. Electron Spectrosc. **195**, 409 (2014)
21. S. Tanuma, C.J. Powell, D.R. Penn, Surf. Interf. Analysis **43**, 689 (2011)
22. F. Offi, S. Iacobucci, P. Vilmercati, A. Rizzo, A. Goldoni, M. Sacchi, G. Panaccione, Phys. Rev. B **77**, 201101R (2008)
23. F. Offi, S. Iacobucci, L. Petaccia, S. Gorovikov, P. Vilmercati, A. Rizzo, A. Ruocco, A. Goldoni, G. Stefani, G. Panaccione, J. Phys. Condens. Matter **22**, 305002 (2010)
24. R. Yoshida et al., Physica C **469**, 1034 (2009)
25. W.S.M. Werner, L. Köver, S. Egri, J. Toth, D. Varga, Surf. Sci. **585**, 85 (2005)
26. C.S. Fadley, Basic concepts of X-ray photoelectron spectroscopy, in *Electron Spectroscopy: Theory, Techniques, and Applications*, ed. by C.R. Brundle, A.D. Baker (Academic Press, London, 1978)., vol. II, Chap. 1, pp. 56–57. Available as download from http://www.physics.ucdavis.edu/fadleygroup/BasicConceptsofXPS.pdf
27. C. Solterbeck, W. Schattke, J.-W. Zahlmann-Nowitzki, K.-U. Gawlik, L. Kipp, M. Skibowski, C.S. Fadley, M.A. Van Hove, Phys. Rev. Lett. **79**, 4681 (1997)
28. W. Smekal, W.S.M. Werner, C.J. Powell, Surf. Interface Anal. **3**, 1059 (2005)
29. W.S.M. Werner, W. Smekal, T. Hisch, J. Himmelsbach, C.J. Powell, J. Electron Spectrosc. **190**, 137 (2013)

30. P.H. Scofield, Lawrence Livermore Laboratory Report UCRL-51326 (1973). Available at http://www.physics.ucdavis.edu/fadleygroup/Scofield.CrossSections.UCRL51326.pdf
31. M.B. Trzhaskovskaya, V.I. Nefedov, V.G. Yarzhemsky, At. Data Nucl. Data Tables **77**, 97 (2001)
32. M.B. Trzhaskovskaya, V.I. Nefedov, V.G. Yarzhemsky, At. Data Nucl. Data Tables **82**, 257 (2002)
33. K. Kobayashi et al., Appl. Phys. Lett. **83**, 2005 (2003)
34. I. Piš, M. Kobata, T. Matsushita et al., Anal. Sci. **26**, 227 (2010)
35. J. Buck et al., Proceedings of SPIE **8504**, 85040U (2012)
36. W.Wurth, S. Svensson, N. Mårtensson, private communication
37. J.M. Bussat et al., IEEE Trans. Nucl. Sci. **51**, 2341 (2004)
38. R. Guillemin, O. Hemmers, D.W. Lindle, S.T. Manson, Radiat. Phys. Chem. **75**, 2258 (2006)
39. A.X. Gray et al., Nat. Mater. **10**, 759 (2011)
40. A.X. Gray et al., Nat. Mater. **11**, 957 (2012)
41. A. Sekiyama, New J. Phys. **12**, 043045-1-11 (2010)
42. A. Sekiyama, A. Higashiya, S. Imada, J. Electron Spectrosc. **190**, 201 (2013)
43. S. Goldberg, S. Kono, C.S. Fadley, J. Electron Spectrosc. **21**, 285 (1985)
44. S. Nemšák, N. Kaduwela, C.S. Fadley, Program based on equations from Ref. 32, with beta test version. Accessible at http://.naomi.nocube.sk/; S. Nemšák, private communication
45. J. Weinen et al., J. Electron Spectrosc. **198**, 6 (2015)
46. K. Horiba, M. Taguchi, A. Chainani et al., Phys. Rev. Lett. **93**, 236401 (2004)
47. M. Taguchi et al., Phys. Rev. Lett. **95**, 177002 (2005)
48. J. Fujii et al., Phys. Rev. Lett. **107**, 187203 (2011)
49. M. Van Veenendaal, Phys. Rev. B **74**, 085118 (2006)
50. Y. Takata et al., Phys. Rev. B **75**, 233404 (2007)
51. Y. Takata, Phys. Rev. Lett. **101**, 137601 (2008)
52. S. Suga et al., New J. Phys. **11**, 073025 (2012)
53. Y. Kayanuma, I. Fukahori, S. Tanaka, Y. Takata, J. Electron Spectrosc. **184**, 468 (2011)
54. M. Simon et al., Nat. Comm. **5**, 4069 (2014)
55. C. Papp, L. Plucinski et al., Phys. Rev. B **84**, 045433 (2011)
56. C.M. Schneider, U. Pracht, W. Kuch, A. Chassé, J. Kirschner Phys. Rev. Lett. **54**, R15618 (1996)
57. S. Ueda et al., Appl. Phys. Express **1**, 077003 (2008)
58. G. Stryanyuk et al., Jpn. J. Appl. Phys. **51**, 016602 (2012)
59. S.-H. Yang et al., J. Phys. Cond. Matt. **14**, L406 (2002)
60. S.-H. Yang et al., Phys. Rev. B **84**, 184410 (2011)
61. C. Tusche et al., Appl. Phys. Lett. **99**, 032505 (2011)
62. V.N. Strocov, V.N. Petrov, J.H. Dil, J. Synchrotron Rad. **22**, 708 (2015)
63. C. Joswiak et al., Rev. Sci. Instr. **81**, 053904 (2010)
64. D.P. Woodruff, Rep. Prog. Phys. **57**, 1029 (1994)
65. C.S. Fadley, M.A. Van Hove, Z. Hussain, A.P. Kaduwela, J. Electron Spectrosc. **75**, 273 (1995)
66. C.S. Fadley, J. Electron Spectrosc. **178–179**, 2 (2010)
67. K. Kobayashi, M. Kobata, I. Masaaki, H. Iwai, J. Electron Spectrosc. **190**, 210 (2013), and earlier references therein
68. A. Winkelmann, J. Garcia de Abajo, C.S. Fadley, New J. Phys. **10**, 113002 (2008)
69. F.J. Garcia de Abajo, Online photoelectron diffraction program. Available at http://nanophotonics.csic.es/widgets/edac/
70. I. Bartos et al., Phys. Rev. B **83**, 235327 (2011)
71. M. Kobata et al., Surf. Interface Anal. **43**, 1632 (2011)
72. S. Hellman et al., Phys. Rev. B **85**, 075109 (2012)
73. L.-P. Oloff et al., New J. Phys. **16**, 123045 (2014)
74. E.D. Tober et al., J. Electron Spectrosc. **189**, 152 (2013)

75. F. Krasniqi, B. Najjari, L. Struder, D. Rolles, A. Voitkiv, J. Ullrich, Phys. Rev. A **81**, 033411 (2010)
76. X.S. Sun, A.X. Gray, A.P. Kaduwela, C.S. Fadley, Phys. Rev. A **89**, 053415 (2014)
77. C. Wiemann et al., Appl. Phys. Lett. **100**, 223106 (2012)
78. M. Patt et al., Rev. Sci. Inst. **85**, 113704 (2014)
79. F. Kronast, Appl. Phys. Lett. **93**, 243116 (2008)
80. A.X. Gray et al., Appl. Phys. Lett. **97**, 062503 (2010)
81. S.-H. Yang, B.C. Sell, C.S. Fadley, J. Appl. Phys. **103**, 07C519 (2008)
82. S.-H. Yang, B.C. Sell, B.S. Mun, C.S. Fadley, Probing buried layers and interfaces with soft X-ray standing wave spectroscopies, in ed. by J. Zegenhagen, A. Kazimirov, The X-ray Standing Wave Technique: Principles and Applications, Vol. 7 in the Series on Synchrotron Radiation and Applications (World Scientific, Singapore, 2013)
83. S.-H. Yang, A.X. Gray, A.M. Kaiser, B.S. Mun, J.B. Kortright, C.S. Fadley, J. Appl. Phys. **113**, 073513 (2013); A versatile downloadable software package for calculating such effects, the Yang X-ray Optics (YXRO) program, is also available at https://sites.google.com/a/lbl.gov/yxro/home
84. A.X. Gray et al., Phys. Rev. B **82**, 205116 (2010)
85. A.M. Kaiser et al., Phy. Rev. Letters **107**, 116402 (2011)
86. A.X. Gray et al., Europhys. Lett. **104**, 17004 (2013). Reprint with Supplementary Information at http://www.physics.ucdavis.edu/fadleygroup/SWARPES_EPL_104_17004_2013.reprint.pdf
87. S. Döring et al., Phys. Rev. B **83**, 165444 (2011)
88. A.A. Greer et al., Appl. Phys. Lett. **101**, 202402 (2012)
89. C. Papp, G. Conti et al., J. Appl. Phys. **112**, 114501 (2012)
90. B.L. Henke, Phys. Rev. A **6**, 94 (1972)
91. M. Mehta, C.S. Fadley, Phys. Lett. **55A**, 59 (1975)
92. M. Mehta, C.S. Fadley, Chem. Phys. Lett. **46**, 225 (1977)
93. M.J. Chester, T. Jach, S. Thurgate, J. Vac. Sci. Tech. **B11**, 1609 (1993)
94. J. Kawai, S. Hayakawa, Y. Kitajima, Y. Gohshi, Adv. X-ray Chem. Anal. Jpn. 26s, 97–102 (1995)
95. J. Kawai, J. Electron Spectrosc. Relat. Phenom. **178–179**, 268 (2010)
96. M. Marinova, J.E. Rault et al., Nano Lett. **15**, 2533 (2015)
97. H. Yamada et al., Sci. Repts. **3**, 2834 (2013)
98. J.C. Woicik, E.J. Nelson, P. Pianetta, Phys. Rev. Lett. **84**, 773 (2000)
99. J.C. Woicik, E.J. Nelson, T. Kendelewicz et al., Phys. Rev. B **63**, 041403(R) (2001)
100. J.C. Woicik, E.J. Nelson, D. Heskett et al., Phys. Rev. B **64**, 125115 (2001)
101. J.C. Woicik, E.J. Nelson, L. Kronik et al., Phys. Rev. Lett. **89**, 077401 (2002)
102. V. Strocov et al., J. Synchrotron Rad. **21**, 32 (2014) and earlier references therein
103. J. Braun, J. Minar et al., Phys. Rev. B **88**, 205409 (2013)
104. S. Nemšák et al., to be published
105. M. Salmeron, R. Schlögl, Surf. Sci. Rep. **63**, 169 (2008)
106. D.E. Starr, Z. Liu, M. Hävecker, A. Knop-Gericke, H. Bluhm, Chem. Soc. Rev. **42**, 5833 (2013)
107. S. Nemšák, A. Shavorskiy et al., Nature Comm. **5**, 5441 (2014)
108. O. Karslıoğlu, S. Nemšák, et al., Faraday Soc. Disc. 180, 35 (2015). doi:10.1039/C5FD00003C

Chapter 2
The First Development of Photoelectron Spectroscopy and Its Relation to HAXPES

Svante Svensson, Evelyn Sokolowski and Nils Mårtensson

Abstract The pioneering work on electron spectroscopy in Uppsala in the 1950s is discussed, focussing primarily on some of the experimental issues. The first experiments were performed using equipment essentially developed for detection of beta radiation. The X-ray sources used to excite the spectra utilized CrK_{α} and CuK_{α} radiation, i.e. today the experiments would be classified as Hard X-ray Photo Electron Spectroscopy (HAXPES).

The present book deals with one of the sub-fields of electron spectroscopy, HAXPES, which reads out Hard X-ray Photo Electron Spectroscopy. This field has grown rapidly during the last years due to the implementation of brilliant synchrotron radiation sources, to the development of highly resolving crystal monochromators, and last but not least to the development of electron spectrometers operating at very kinetic energies with resolving power in the range of 10^5. The importance of HAXPES was expressed at the HAXPES 2011 conference in Hamburg where the conference chairman Wolfgang Drube made the following statement: "I believe that HAXPES is the ESCA of the future". However, when discussing the early years of electron spectroscopy we would add: *HAXPES is also the roots of ESCA*. We will describe how the pioneering work of the group of Siegbahn in 1954–1958 was performed using hard X-rays for the excitation and hence that the experimental situation was the same as in modern HAXPES. In the HAXPES 2013 international conference we commemorated the 50 years anniversary of the discovery of the chemical shift. At this occasion one of the authors ES was interviewed about the pioneering years of photoelectron spectroscopy.

S. Svensson (✉) · N. Mårtensson
Department of Physics and Astronomy, Box 516, 751 20 Uppsala, Sweden
e-mail: svante.svensson@fysik.uu.se

N. Mårtensson
e-mail: nils.martensson@fysik.uu.se

E. Sokolowski
Tvär-Ramsdal 1, 611 99 Tystberga, Sweden
e-mail: evelyn.sokolowski@swipnet.se

© Springer International Publishing Switzerland 2016

J.C. Woicik (ed.), *Hard X-ray Photoelectron Spectroscopy (HAXPES)*,
Springer Series in Surface Sciences 59, DOI 10.1007/978-3-319-24043-5_2

Modern photoelectron spectroscopy originates from the work of the so called "iron free group" built up when Kai Siegbahn got the chair in physics in Uppsala, Sweden. He had a background in nuclear physics and had been focussing on the development of beta spectrometers, notably for studying internal conversion.[1] He had developed a new type of magnetic spectrometer, not using a homogenous field, but a field that was radially decreasing. Such a field provided a "double focussing" of the electrons and therefore the transmission of Siegbahn's spectrometer was more than an order of magnitude higher than that of conventional instruments at the time.

The goal of the studies of the internal conversion was to obtain accurate nuclear binding energies. However, for this purpose one had to correct for the atomic binding energies of the deep core levels involved. When Siegbahn reviewed these atomic binding energies in the beginning of the 1950s he realized that such tables were both uncertain and incomplete. He then got the idea to use a redesigned beta spectrometer and the photoelectric effect to measure core level binding energies with higher precision.

The apparatus of the group was an improved nuclear physics instrument—a beta electron spectrometer—modified to allow measurements of "low energy" electrons. "Low energy" for Kai Siegbahn at that time meant below 20 keV. The increased transmission due to the double focussing was crucial for the detection of the photoelectrons. One can also notice that the instrument could not at all detect electrons with lower kinetic energies than 2 keV. The electron detector was a Geiger-Müller tube covered by a thin window, not transparent at lower energies.

The group of Kai Siegbahn was carefully composed. He had been a professor in nuclear physics at the Royal Institute of Technology in Stockholm. When he got the chair as professor in Physics at Uppsala University 1954—he was by this nomination a successor of the very first physics professor in Sweden—he had the photoelectron spectroscopy project in mind. He offered an assistant position in Uppsala to one of the authors (ES) who at that time was a research student at the Nobel Institute of Physics in Stockholm and had a background in nuclear physics and beta spectroscopy. In Uppsala he recruited a research student who had started in X-ray spectroscopy—Carl Nordling. By this choice he had competence both to operate the beta spectrometer and to build and operate the X-ray source. Figure 2.1 shows the pioneering group gathered around the electron spectrometer.

The nuclear physics roots of modern electron spectroscopy is clearly seen from Fig. 2.2, which shows the principles of the "iron free" magnetic focussing

[1]Internal conversion (IC) is a nuclear process. An excited nucleus can interact with an inner shell electron and give the excess energy to the latter. This can happen when the orbital of the inner shell electron has a large probability to be at the nucleus, i.e. the process is strong for K-shells. Internal conversion is not a nuclear decay and therefore the resulting nucleus has the same composition of nuclear particles as before the emission of the IC electron. After the IC process the atom has a vacancy in the atomic shell and this vacancy will be filled in an Auger process. IC gives rise to sharp electron lines in the continuous beta spectrum.

Fig. 2.1 Carl Nordling, ES and Kai Siegbahn in the laboratory with the “Iron free beta spectrometer”. This was the first spectrometer where lines were observed in a photoelectron spectrum. The instrument was more than one order of magnitude more sensitive than earlier constructions due to the double focussing magnetic field and the careful control of external magnetic fields

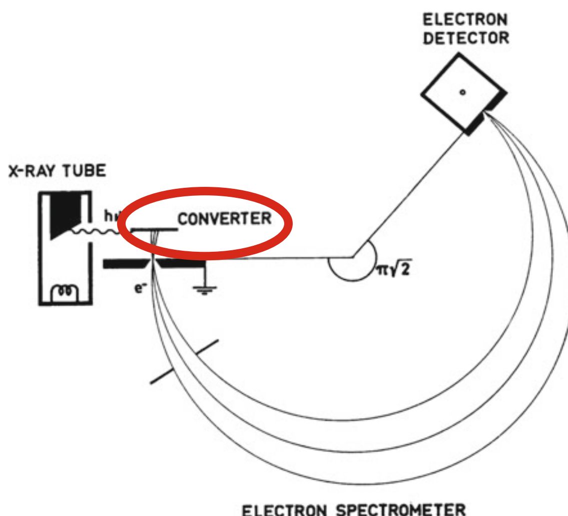

Fig. 2.2 Siegbahn’s sketch of the principles for the “iron free” instrument [1]

instrument [1]. It is interesting to note that—what a modern author would refer to as the sample—Siegbahn indicates as a “converter”. This is obviously a device that converts X-rays to photoelectrons. This shows that the primary interest for Siegbahn at this time was focused on correcting nuclear binding energies rather than on studying the properties of a sample.

The first modern core photoelectron spectrum, showing discrete lines was published in Physical Review 1957 [2]. Figure 2.3 shows the Cu 1s photoelectron lines excited by $MoK\alpha_1$ (17.479 keV) and $MoK\alpha_2$ (17.374 keV) X-rays, respectively. The excitation energy of around 17.5 keV and the kinetic energy of about 8.5 keV represents higher energies than used in most HAXPES experiments today.

From the spectrum in Fig. 2.3 they obtained Cu 1s binding energies of 8985.3 eV ± 1 eV, and 8985.7 eV±1.5 eV, for the two electron lines, respectively. In a magnetic spectrometer of this type the absolute kinetic energies were measured. No electric fields were used and the kinetic energies were derived from the current in the magnetic coils of the spectrometer. Consequently it was necessary to determine the meaning of zero kinetic energy. This was carefully discussed in [3, 4], where core level binding energies were determined for a number of metals. Several important calibration issues were penetrated. It was found that the measured kinetic energies, and thereby the derived binding energies, are related to a “vacuum zero level” inside the spectrometer. It was also realized that the relevant binding energy scale for a metal is referred to the Fermi level of the sample. In order to determine the Fermi level referenced binding energies it was therefore necessary to measure the work function of the spectrometer. Furthermore, one had to establish a good electrical contact between the spectrometer and the sample. Today, with modern electron spectrometers the Fermi level referenced binding energies can be achieved directly, as a difference in retardation voltage between the Fermi edge of a metallic calibration sample and the studied core photoelectron line.

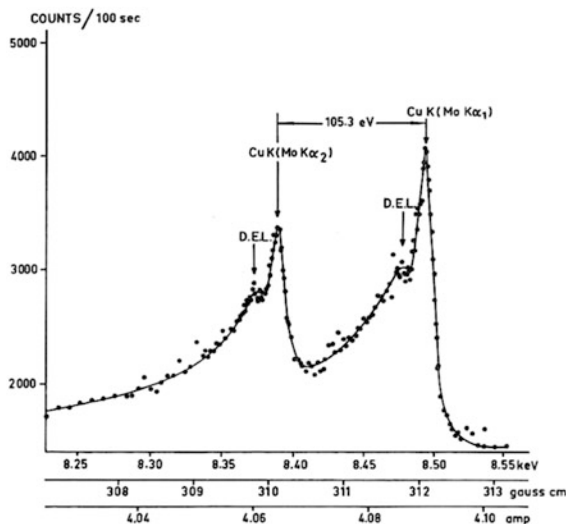

Fig. 2.3 The first published modern core photoelectron spectrum. It was obtained in 1956 but was in press in January 1957 [2]. The sample was metallic Cu evaporated on a backing. The Cu 1s core electron lines excited by $MoK\alpha_1$ (17.479 keV) and $MoK\alpha_2$ (17.374 keV) X-rays are observed. The structures noted D.E.L. were attributed to “discrete energy losses in the source”. Here the “converter” is discussed as a “source”

Using these calibration procedures the Cu 1s binding energy values above gave Fermi level referenced binding energies of 8980.8 and 8981.2 eV, respectively. Also the influence of residual magnetic fields was discussed, and additional calibration procedures were implemented [3]. This gave a final value of 8979.7 eV for the Cu 1s core level binding energy in metallic Cu. This is very close to the present value of 932.57(20) eV [5] + 8047.865(8) eV [6] = 8980.4(2) eV, obtained by summing the $2p_{3/2}$ binding energy for Cu metal and the $K\alpha_1$ X-ray emission energy, showing the quality of the original measurements and calibration procedures.

When comparing the measured and derived Cu 1s binding energies one also needs to consider the recoil effect, i.e. the fact that the outgoing photoelectron shares the available photon energy with the remaining system. In this context it is interesting to note that the concept of recoil was well understood by the original ESCA group. A discussion of the magnitude of this effect was given already in the original ESCA monograph from 1967 [1], and it was realized that the effect could be substantial for light elements and high kinetic energies. This discussion was natural, considering the fact that Siegbahn was trained as a nuclear scientist. In the present case, with a photoelectron kinetic energy of about 8.5 keV, the maximum correction will be less than 0.1 eV, for ionization of the Cu atom.

As photoelectron spectroscopy turned more and more to soft X-rays the recoil effects became insignificant. However, in connection with a detailed discussion of core level binding energies for light elements in the gas phase, the influence of the recoil was explicitly included [7]. The recoil phenomenon was also discussed in a theoretical report by Flynn [8].

With the development of modern HAXPES it was realized that the recoil effects are affecting both to the electron line profiles and positions. There was an interesting parallel work by Takata et al. [9] and Kukk et al. [10]. Both groups were active at the SpRING-8 laboratory in Japan but they studied very different types of samples. Kukk et al. looked at core photoionization from gases and Takata et al. studied solid graphite. This may explain why there was no cross referencing between the two independent developments. We also note that in the modern revival of the recoil discussions no references were made to the original studies by Siegbahn’s group.

The remarkable growth of research based on electron spectroscopy is to a large extent connected to the use of the core level binding energy shifts. The history of the discovery of the chemical shift is interesting. The first evidence of a chemical shift in core level photoelectron spectroscopy was made already in 1957 when the “iron free group” realized that they obtained different values for the Cu 1s binding energy for different samples. By carefully studying the samples with X-ray diffraction it was concluded that the Cu 1s signal from CuO appeared at higher binding energy than the Cu 1s signal from Cu metal, see Fig. 2.4. For Cu_2O they obtained no significant shift.

These findings were published in 1958 [11, 12]. The title of [11] was “Evidence of Chemical Shifts of the Inner Electronic Levels in a Metal Relative to Its Oxides (Cu, Cu_2O, CuO).” This reflects the fact that the authors could not exclude other explanations to the observed shifts. The pioneering group was aware of the

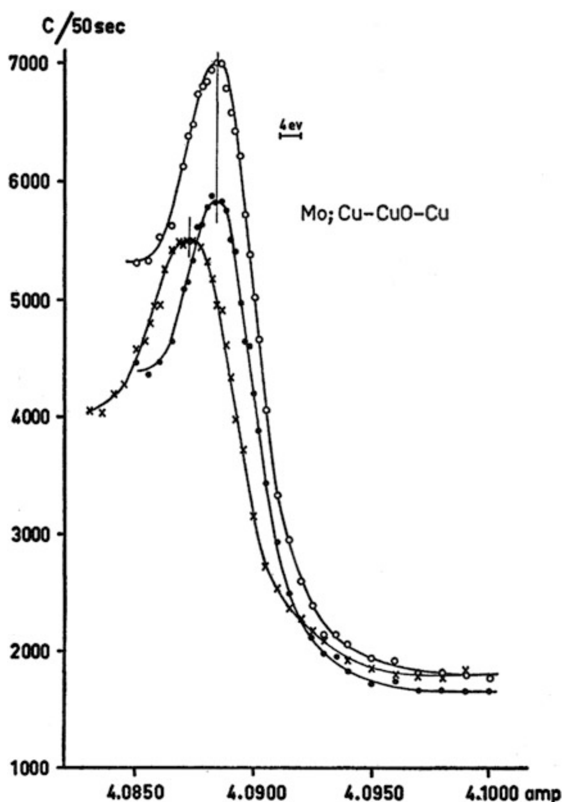

Fig. 2.4 The first indication of what was assumed to be a core level binding energy shift measured by electron spectroscopy. The figure is taken from [11]. The Cu 1s photoelectrons were excited by Mo K α_1 X-rays. The curves plotted with *open* and *filled circles* are the photo-lines of metallic copper. The photo-line of the cupric oxide, was plotted with *crosses*. The shift is clearly observable. However, the shift is about 4 eV, by far too large and the probable explanation is charging of the sample

possibility that e.g. sample charging could affect the observed effect. A more detailed description of the history of the chemical shift will be given elsewhere [13]. Today we know that the chemical shift between Cu and CuO is only of the order of 1 eV [14]. We can therefore conclude that the main part of the observed shift for CuO was indeed due to sample charging. The small shift for Cu_2O is consistent with the modern value [14].

The shift the group observed in 1958 was to a large extent not due to a shift of the core levels, but was of course a chemical effect. Cu metal, CuO and Cu_2O have different conductivities and thus charge differently. However, the observation the group made was not in vain, since the authors pointed out the possibility for chemical shifts of the core levels. This was important. Almost 20 years earlier a graduate student in Uppsala had studied the X-ray absorption spectra for N_2, N_2O and nitrogen in celluloid [15]. However, neither the graduate student Magnusson, nor his supervisors understood the significance of what we today would call a N1s-π* excitation. He denoted the very clear lines he observed as an “absorption line” within quotation marks. He was looking for absorption edges. Even less he could imagine a chemical shift of several eV, as was clearly seen for the two chemically inequivalent atoms in N_2O. He considered the sharp features as

complications when determining the position of the absorption edges, and made the remark: “As already pointed out, no high degree of accuracy is claimed for the results in the matter of the base-point, and such a difference as would seem to be indicated by the measurements, need not necessarily have any real foundation”.

In order to firmly establish the existence of chemical shifts in photoelectron spectroscopy a much more clear and unambiguous result was needed. Such a result was not achieved until five years later, when a shift between photoelectrons from two inequivalent sulphur atoms in the same molecule was observed [16]. The choice of the molecule was a result of pure serendipity [17]. At this time progress was slow and Siegbahn had started to discuss an ending of the project [18]. Therefore, the two younger members of the group, Carl Nordling and Stig Hagström, worked desperately to get out as much as possible, and one weekend they had run out of samples. They went around at the department and in the photographer’s room they found a fixation salt—sodium thiosulphate. This sample contained two chemically inequivalent sulphur atoms in the same molecule, which gave rise to two shifted peaks in the S2p spectrum. The success story of ESCA could start.

As soon as the chemical shift effect was firmly established Siegbahn launched the acronym ESCA—Electron Spectroscopy for Chemical Analysis. During the next few years the group expanded rapidly and a hectic activity started. In less than three years the impressive scientific content of the famous first ESCA volume [1] was achieved. Much of the work presented in this book was performed using hard X-rays, in other words it is to a large extent a book about HAXPES. However, from that time until the recent development of synchrotron radiation based HAXPES, photoelectron spectroscopy was almost exclusively using VUV radiation and soft X-rays.

In summary, we have reviewed the pioneering years of photoelectron spectroscopy. The original group originated from a nuclear physics environment and the long term scope of the project was to improve nuclear binding energy data. The electron kinetic energies were such that we with modern terminology would use the acronym HAXPES. The work of the pioneering group is discussed up to the discovery of the chemical shift of core level binding energies. Already at this early stage of photoelectron spectroscopy many important issues were identified, carefully examined and implemented by the pioneering group.

Acknowledgements SS and NM want to thank the Swedish Research Council (VR) for support. Professor Erik Karlsson at the Department of Physics and Astronomy in Uppsala is acknowledged for giving personal impressions from the time of the discovery of the chemical shift.

References

1. C.N.K. Siegbahn, A. Fahlman, R. Nordberg, K. Hamrin, J. Hedman, G. Johansson, T. Bergmark, S.-E. Karlsson, I. Lindgren, B. Lindberg, *ESCA, Atomic, Molecular and Solid State Structure Studied by Means of Electron Spectroscopy* (Almqvist and Wiksells, Uppsala, 1967)
2. C. Nordling, E. Sokolowski, K. Siegbahn, Phys. Rev. **105**, 1676 (1957)

3. E. Sokolowski, Ark. Fys. **15**, 1 (1959)
4. C. Nordling, Ark. Fys. **15**, 397 (1959)
5. A. Lebugle, U. Axelsson, R. Nyholm, N. Martensson, Phys. Scr. **23**, 825 (1981)
6. E.G. Kessler, R.D. Deslattes, D. Girard, W. Schwitz, L. Jacobs, O. Renner, Phys. Rev. A **26**, 2696 (1982)
7. T.D. Thomas, R.W. Shaw Jr, J. Electron Spectrosc. Relat. Phenom. **5**, 1081 (1974)
8. C.P. Flynn, Phys. Rev. B **14**, 5294 (1976)
9. Y. Takata et al., Phys Rev B **75** (2007)
10. E. Kukk et al., Phys. Rev. Lett. **95**, 133001 (2005)
11. C. Nordling, E. Sokolowski, K. Siegbahn, Ark. Fys. **13**, 483 (1958)
12. E. Sokolowski, C. Nordling, K. Siegbahn, Phys. Rev. **110**, 776 (1958)
13. N. Martensson, E. Sokolowski, S. Svensson, J. Electron. Spectrosc. Rel. Phen. **193**, 27 (2014)
14. G. Deroubaix, P. Marcus, Surf. Interface Anal. **18**, 39 (1992)
15. T. Magnusson, *Investigations into Absorption Spectra in the Extremely Soft X-ray Region* (Almquist & Wiksell, Uppsala, 1938), pp. 59
16. S. Hagström, C. Nordling, K. Siegbahn, Phys. Lett. **9**, 235 (1964)
17. C. Nordling, Current Contents **23**, 10 (1992)
18. S. Hagström, (Private Communication, 2004)

Chapter 3
HAXPES at the Dawn of the Synchrotron Radiation Age

Piero Pianetta and Ingolf Lindau

Abstract Some of the earliest X-ray Photoemission Spectroscopy (XPS) studies with high-energy X-rays took place in the 1970s as a way of demonstrating the feasibility of using synchrotron radiation from a multi-GeV storage ring to study materials. These developments took place at the SPEAR storage ring at the Stanford Linear Accelerator Center and showed that synchrotron radiation could be tamed but that the technologies of the time would not allow hard X-ray photoemission to become a tool for routine experiments. However, soft X-rays did fulfill that promise and dominated the XPS research for the next several decades with important contributions to the study of surfaces and interfaces. With the advent of second and particularly third generation synchrotron sources, XPS with high-energy X-rays has become a practical tool for the study of bulk properties and buried interfaces. The development of these techniques will be discussed as will the need for both hard and soft X-rays to provide complimentary details on bulk and surface properties of materials.

3.1 Introduction

Hard X-ray Photoemission Spectroscopy (HAXPES) employing multi-keV X-rays as the excitation source has emerged as a powerful tool for understanding the bulk properties of materials as well as for the study of buried interfaces [1]. This is an interesting development given that most of the early X-ray photoelectron spectroscopy (XPS) research was done at photon energies at or below 1.54 keV

P. Pianetta (✉) · I. Lindau
SLAC National Accelerator Laboratory, 2575 Sand Hill Road, Menlo Park, CA 94025, USA
e-mail: pianetta@slac.stanford.edu

I. Lindau
e-mail: lindau@slac.stanford.edu

© Springer International Publishing Switzerland 2016

J.C. Woicik (ed.), *Hard X-ray Photoelectron Spectroscopy (HAXPES)*,
Springer Series in Surface Sciences 59, DOI 10.1007/978-3-319-24043-5_3

(the Al K-alpha line) and much of that work was in the soft X-ray range to emphasize surface properties [2]. The motivations for these choices of photon energies were both scientific, since surfaces were and continue to be critically important to many technologies, as well as the result of the technologies available for performing the XPS experiments. As the field has matured with more powerful X-ray sources and more efficient electron energy analyzers, the benefits of being able to probe bulk properties with XPS has become apparent and HAXPES is becoming a standard tool in the field [1]. This chapter will present a historical perspective of one of first examples of HAXPES using synchrotron radiation in the 1970s illustrating the difficulties of these early experiments and the evolution over the next several decades to a mature technique.

Interest in synchrotron radiation as a source for spectroscopy began in the 1960s and was focused in the ultraviolet part of the spectrum [3–6]. In the early 1970s the importance of synchrotron radiation to study materials in the hard X-ray part of the spectrum was becoming appreciated first through the use of synchrotrons notably at DESY in Hamburg. Since synchrotrons, by design, accelerated the electrons after every injection and then dumped them from the ring, the resulting synchrotron radiation had an intensity and spectrum that varied at the injection rate making experiments challenging [7]. However, in the early 1970s multi-GeV storage rings that could maintain the electrons in a fixed energy and current were being developed for high energy physics and would make the practical utilization of synchrotron radiation in a parasitic mode of operation a reality [8]. At Stanford University, more precisely at the Stanford Linear Accelerator Center or SLAC, a state of the art high-energy physics storage ring operating at 2.5 GeV, SPEAR, began operation in 1972. The sole purpose of this storage ring was to collide relativistic electron and positron beams to study uncharted territory in particle physics that would ultimately lead to the discovery of the J/psi and tau particles [9, 10]. In 1968, before SPEAR was built, Stanford professor, W.E. Spicer, realizing that the “waste products” of the particles circulating in the storage ring could be harnessed, wrote a letter to the SLAC director, W. Panofsky, to explore the possibilities for the use of synchrotron radiation for solid-state studies with particular mention of Electron Spectroscopy for Chemical Analysis or ESCA [11]. Spicer was a professor of electrical engineering at Stanford and a pioneer in the field of photoelectron spectroscopy for the valence bands of solids which had come out of his early work at RCA Laboratories on photocathodes [12, 13]. Joined by S. Doniach of the Stanford Applied Physics Department, he garnered the support of Panofsky and B. Richter with strong support from E. Garwin and G. Fischer of SLAC. This collaboration resulted in the addition of a tangent port and fixed beam stop to SPEAR by the time it went into operation in 1972 [14]. Although this would not be the first storage ring used for synchrotron radiation studies, the vision at Stanford was to make SPEAR the first multi-GeV storage ring to provide X-rays to a large community of users [8].

3.2 Initial Scientific Motivation

The next necessary step was for the prospective users to build a beam line to extract and make use of the radiation coming out of the storage ring which brings us to the topic of this chapter. There was a strong interest in using the synchrotron radiation for high-resolution photoemission to study the surface and interface properties of a variety of materials. This formed the first guiding point for the experimental design. The second, and sometimes overriding principle, was that the high-energy physics experiments were the priority of the SPEAR storage ring and the synchrotron radiation studies could not disrupt that research. This led to the constraint that the synchrotron radiation experiments would not share the storage ring vacuum. Finally, the time frame for these first experiments was less than one year to build the beam line and extract first beam plus four months for obtaining experimental results. After obtaining initial funding from the Stanford Center for Materials research to build an exit port, a "Pilot Project" was funded by the National Science Foundation to support this effort. The authors (IL as a postdoc and PP as a graduate student) joined Spicer and Doniach on the project with the task of building the beam line with the technical support of the SLAC Technical Division [15].

After consideration of the various technical and time constraints, the decision was taken that the first experiment would be high-resolution photoemission studies of the Au 4f levels at the excitation energy of 8 keV. This decision had the benefit of allowing the use of beryllium windows to isolate the photoemission apparatus from the storage ring as well as greatly simplifying sample preparation due to the bulk sensitivity of the photoemitted electrons.

3.3 Source Characteristics

Starting with the source, synchrotron radiation is generated when a charged particle is accelerated perpendicular to its direction of motion. The total radiated power is proportional the fourth power of the electron energy and inversely with the radius of curvature of the electron orbit [16, 17]. At the time of the first experiments that will be discussed here, the SPEAR storage ring operated at 2.5 GeV and up to 40 mA [18, 19]. The source originated from a bending magnet with a radius of R = 12.7 m and a source size of 1.59 mm vertical by 3.22 mm horizontal [20]. With the given beam parameters, the power radiated over all photon energies was 1.7 Watts per horizontal mrd as given by:

$$\mathrm{P(watts/mrd)} = 14.1 * \mathrm{I(mA)} * \mathrm{E(GeV)}^4/\mathrm{R(m)}$$

where I is the beam current in mA, E is the energy in GeV, and R is the radius of curvature of the electron trajectory in meters.

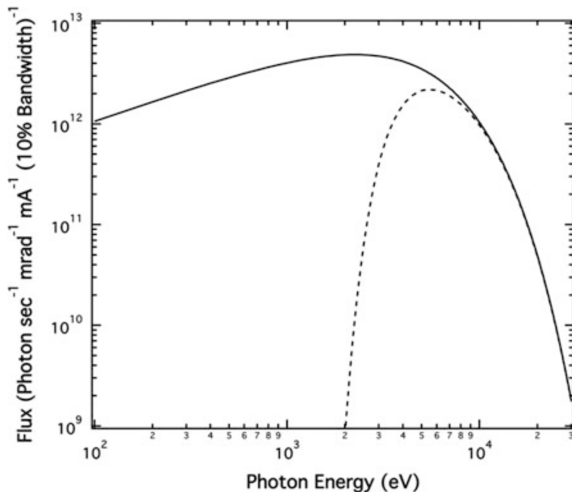

Fig. 3.1 Synchrotron radiation spectrum from SPEAR operating at 2.5 GeV with a current of 40 mA and a critical energy of 2.7 keV (*solid line*). *Dashed line* shows the spectrum transmitted through the Be window assembly consisting of two 250 μ windows plus two 65 μ absorbers

For a bending magnet, the synchrotron radiation spectrum extends smoothly from the infrared into the hard X-ray regions as shown in Fig. 3.1. For a multi-GeV storage ring such as SPEAR, there is significant X-ray flux at and above 10 keV. The characteristic energy at which half of the radiated power is above and half below is defined as the critical energy, ε_c, given by $2.2E^3/R$. For SPEAR operating at 2.5 GeV, $\varepsilon_c = 2.7$ keV. The vertical divergence is given by the critical angle $\theta_c = 1/\gamma\ (E_c/E)^{1/3}$ so that at the critical energy, the vertical divergence would be $1/\gamma = mc^2/E = 0.2$ mrd for SPEAR operating at 2.5 GeV. At energies above the critical angle, the angular distribution narrows further as $E^{-1/3}$. For a bending magnet source, as was used in this work, the opening angle in the horizontal is determined by the radius of the electron beam trajectory and can be shown to be about ten times larger than that in the vertical plane [21]. As will be discussed below, the source size and divergence directly impact the monochromator resolution and throughput. As a result, monochromators on bending magnet beam lines are designed to deflect in the vertical direction. The S-polarization of the synchrotron radiation is another factor that leads to vertically deflecting monochromators but since it did not impact these experiments, it will not be discussed in detail [22].

3.4 Beam Line Design

The vacuum isolation for the storage ring was provided by a pair of 250 μ Be windows with an independently pumped volume between the two windows to provide redundancy. The Be windows were designed to operate at the maximum anticipated SPEAR operating energy of 4.2 GeV. Since the innermost window

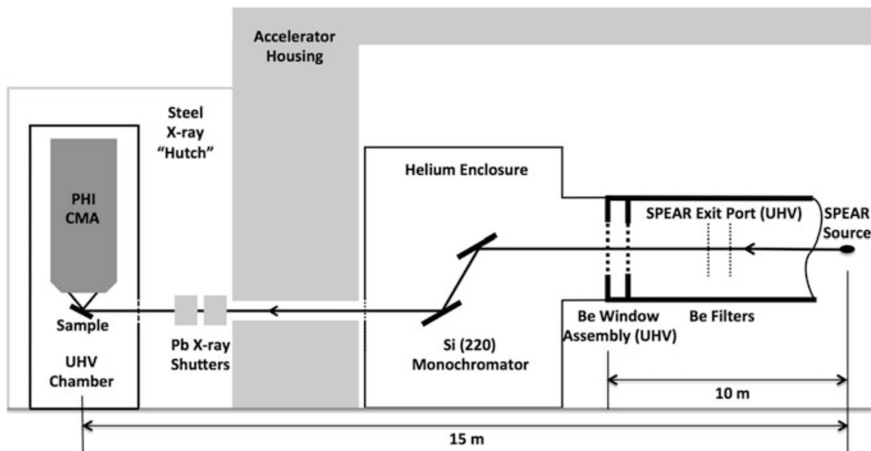

Fig. 3.2 Schematic of the experimental apparatus showing the source point, the SPEAR exit port including Be absorbers and window module, monochromator in helium enclosure, concrete accelerator housing, X-ray beam shutters located in the X-ray "hutch" with the sample chamber that included a Be entrance window and a cylindrical mirror analyzer. Note that the space between the exit window of the helium enclosure and the ultra-high vacuum (*UHV*) sample chamber was an air path

would absorb all of the low energy radiation, this window would be damaged at the highest anticipated operating powers, it was necessary to add two 65 μ Be foils to absorb the low energy radiation [21, 23]. In the next generation of beam lines, the Be absorbers were replaced by carbon foils which could handle much larger power loads. The X-ray flux transmitted through the Be window assembly is also shown in Fig. 3.1. Note the low energy cut-off due to the Be window assembly.

As shown in the schematic diagram of Fig. 3.2, the Be window module was located 10 m from the source point at the end of the ultra-high vacuum chamber attached to the SPEAR ring. A photograph of this part of the beam line is shown in Fig. 3.3 which was located inside an alcove on the side of the SPEAR ring created by rearranging the shielding blocks as shown in Fig. 3.4. This figure also shows SPEAR with its control room and power-supply building located inside the circumference, the alcove on the outer circumference that housed the X-ray monochromator and the experimental steel "hutch" that enclosed the electron spectrometer. The X-rays proceeded through the Be windows into a helium system that included the X-ray monochromator. The X-ray beam exited the alcove through a 6″ hole placed 12″ below the SPEAR median plane in the downstream 24″ thick concrete shielding block. The large vertical deflection of the beam was achieved with the monochromator and was required by the SLAC Radiation Physics group to prevent the high intensity white synchrotron-radiation beam or any scattered radiation to exit the accelerator housing. This geometry also simplified the alignment and the construction of the hutch. The hutch was located outdoors as shown and covered with plastic sheeting when it rained. The control room for this experiment

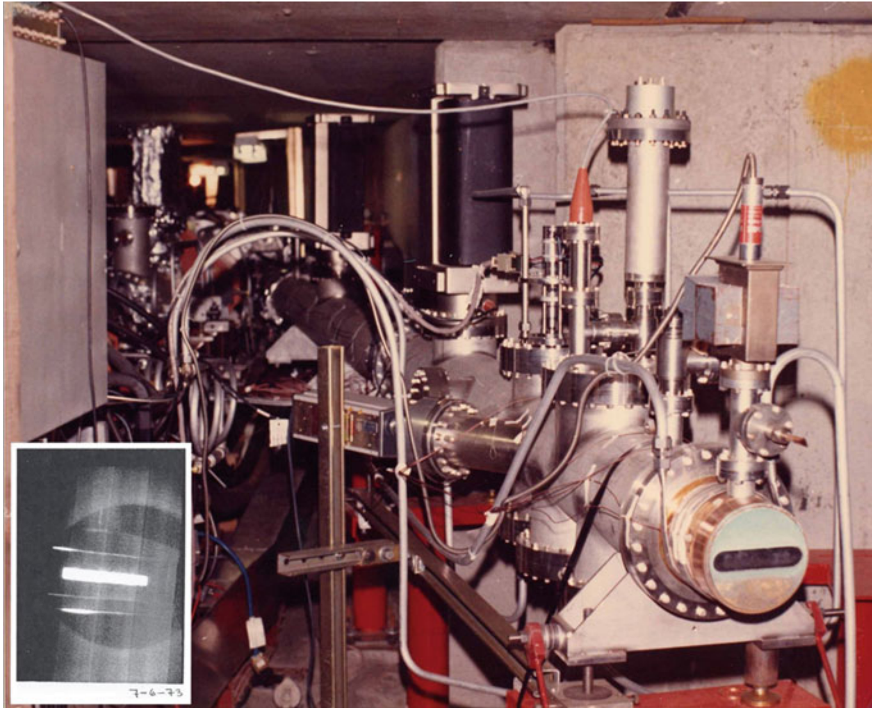

Fig. 3.3 Photograph taken after the first round experiments in July 1973 of the SPEAR exit port located in the accelerator housing showing the Be exit window, and associated UHV equipment. The window assembly shows corrosion on the water cooled copper exit chamber from ozone created by the large X-ray flux passing through the Be window. The *inset* shows a picture of a phosphor screen illuminated by the first X-rays extracted from SPEAR on July 6, 1973

was to the left, out of the view of the photograph, and was housed in a commercial office trailer. The excavation taking place was for the concrete slab that would become the Stanford Synchrotron Radiation Project and would begin operations in 1974 [15].

As already mentioned above, the vertical collimation and S-polarization of the synchrotron beam readily led to the choice of a vertically deflecting double-crystal monochromator in the parallel geometry. This geometry also resulted in parallel input and output beams thus simplifying the experimental geometry. The large vertical separation between the two crystals required that the monochromator be operated at a fixed energy in order to maintain a relatively simple mechanical system. The fixed energy was nonetheless able to satisfy the experimental requirements of the XPS experiment. The crystals used in the monochromator were Si(220) crystals at 23.5° to yield an 8 keV X-ray beam. The crystals were 2″ long by 1″ wide in order to intercept the full vertical X-ray beam and 1 mrad of the beam in the horizontal [21]. Given the mirror technology of the time and the time constraints placed on the implementation of this beam line, no focusing mirrors were

Fig. 3.4 Picture of the SPEAR accelerator housing modified by rearranging shielding blocks to add an alcove that housed the exit port and monochromator shown in Fig. 3.2. The *white box* attached to the outside of the accelerator housing is the X-ray hutch that housed the sample chamber and, as shown in the picture, was located outdoors and covered by a plastic sheet when it rained. In parallel with the Pilot Project photoemission experiments, construction was taking place to build the first SSRL experimental hall

used. Since the monochromator was located inside of the accelerator enclosure it was controlled remotely. The monochromatic X-ray beam exited the He filled monochromator enclosure through a thin (25 μ) aluminum window and went through the accelerator housing into the hutch via an air path that could be interrupted by a pair of interlocked safety shutters. The beam entered the photoemission chamber through a thin (50 μ), 0.5″ diameter Be window.

3.5 Experimental Station

The photoemission chamber consisted of an ion-pumped ultra-high vacuum, UHV, system with a Physical Electronics (PHI) double-pass cylindrical mirror analyzer (CMA), a sample flange and evaporators for preparing thin film samples. Precision power supplies were used to set the energy of the CMA and standard pulse counting electronics consisting of an amplifier/discriminator/scaler were used for data

acquisition. The PHI CMA was chosen because it had a relatively large transmission compared to many analyzers of the time and could be operated at high resolution by using the retarding mode. In addition, sample alignment was simplified by the CMA's well-defined focal spot, which could be found by maximizing the signal when moving the sample along the analyzer axis [24].

This particular CMA projected a 1.5 mm focal spot onto the sample at zero volts retarding field and had an energy resolution of 0.6 % of the pass energy. For these experiments, a pass energy of 20 eV was used in order to best optimize the throughput versus resolution. At this pass energy, the resolution was calculated to be 0.12 eV. It should be noted that the maximum kinetic energy that could be measured by this CMA was 3 keV as set by the breakdown voltage of the CMA. Given the photon energy of 8 keV, an additional positive bias of approximately 5 keV was applied to the sample in order to access the Au $4f_{5/2}$ and $4f_{7/2}$ levels whose binding energies are nominally 88 and 84 eV, respectively [25]. It should also be noted that a retarding potential will reduce the focal spot on the sample by the factor $(V_{pass}/V_{initial})^{1/2}$ due to refraction in the CMA's retarding grids [24]. For the Au 4f levels excited by 8 keV photons and a CMA pass energy of 20 eV, the focal spot on the sample becomes 75 μ. Although the smaller focal spot reduced the throughput of the system, it served as the effective exit slit of the monochromator and improved the resolution as will be discussed below.

3.6 First Experimental Results

The first spectrum collected to test the overall performance of the system was of the Au 4f levels shown in Fig. 3.5. This measurement gave a glimpse into what could be obtained by using a multi-GeV storage ring as a source. Although the counting rates were low as a result of the primitive nature of the experiment, the narrow line widths obtained for the 4f levels were quite remarkable at the time and could be used to estimate for the first time their intrinsic line width. From an instrumental point of view, these results led to equally interesting insights into the optical properties of the synchrotron radiation from SPEAR and why such high resolutions could be obtained with relatively simple instrumentation.

Since the synchrotron radiation spectrum from a bending-magnet source has a broad energy distribution, a monochromator is necessary to obtain the required spectral resolution. For 8 keV X-rays, a double-crystal monochromator in the parallel geometry simply converts the angular distribution of the incident photon beam into an energy distribution about the energy determined by the nominal Bragg angle, θ, according to the relation $dE = E \cot(\theta)\, d\theta$. One of the advantages provided by synchrotron radiation is the narrow radiation cone resulting from the relativistic electrons as well as the fact that the electrons in the storage ring have a well defined relationship between their position and angular divergence. This relationship is referred to as the phase space of the source [26, 27]. For a bend-magnet source these advantages are best seen in the vertical plane and result in the majority of

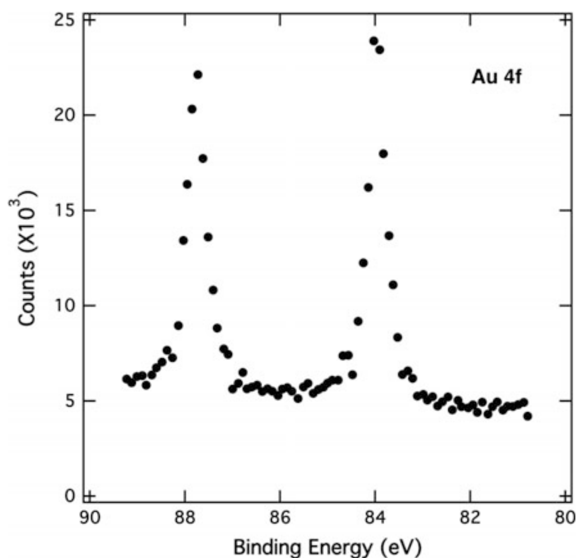

Fig. 3.5 Spectrum of Au 4f levels measured at a photon energy of 8 keV

monochromators being vertically deflecting. This configuration also allows us to ignore the horizontal divergence in calculating the energy resolution of the monochromator since it contributes only in second order [21].

If we consider an extended point source (Fig. 3.6), photons emitted from the top and bottom of the source will hit the central axis so that the angular divergence at the sample will be proportional to the source size divided by the distance to the sample. However, in the case of the synchrotron radiation source, the SPEAR electron beam was diverging at the source point so that the electrons at the top of

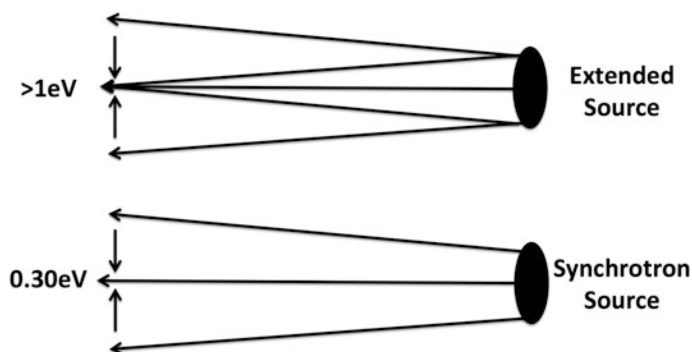

Fig. 3.6 Schematic illustrating how the characteristic divergence of the X-rays emanating from the synchrotron source versus those from an extended-point source results in a smaller range of angles reaching the sample and thus provides a higher energy resolution

the source point had a positive divergence and those at the bottom had a negative divergence. This unique characteristic of the synchrotron beam was to provide an effective dispersion of the monochromatic beam across the sample so that with the 75 μ effective exit slit provided by the CMA, a photon resolution of 0.3 eV could be obtained versus the greater than 1 eV resolution that would have come from an equivalent extended point source. A more rigorous description of the source properties using phase-space considerations and their effect on the energy resolution in these experiments is available elsewhere [21].

During the design phase of the original experiment, we had not yet understood the phase-space characteristics of the SPEAR beam. As a result, we had incorporated a second, channel-cut crystal monochromator into the design, which was in an antiparallel geometry to the first monochromator [21, 28]. This would have had the affect of only passing the rays coming in a narrow angular range from the source and thus ensuring the required high-energy resolution. It was fortunate that the phase space of the synchrotron source made the use of the second monochromator unnecessary since the flux could have been reduced to unusable levels. It is interesting to note that with a modern high-brightness undulator source, the use of a second, antiparallel double-crystal monochromator becomes advantageous since it can deliver a high-resolution X-ray beam that uses the maximum phase space of the source and fills the acceptance of a modern energy analyzer that has been designed to operate at high energies.

In these first experiments, the natural line widths were obtained for the Au 4f and Ag 3d core levels of 0.28 and 0.35 eV, respectively, and a much greater understanding of the source properties was developed. This work ultimately was one contributing factor to the development of the National Science Foundation funded Stanford Synchrotron Radiation Project (SSRP) with a complement of five beam lines including facilities for vacuum ultra-violet (VUV), soft X-ray, Extended X-ray Absorption Fine Structure (EXAFS) and biological small angle-scattering [18].

3.7 Soft X-ray Photoemission: Early Developments

Although these results did show that high-resolution XPS studies could be done at 8 keV using a multi-GeV colliding beam storage ring, the counting rates of 40 counts per second on a very strong peak even with improvements on the optics would not lead to practical research programs. This led to a shift in research emphasis to soft X-rays as the next generation of beam lines using monochromators with colorful names such as the Grasshopper [29, 30] became available. The Grasshopper monochromator delivered photon fluxes $\sim 10^{10}$ photons/s over the energy range 100–600 eV with a resolution of ~ 0.2 eV at 100 eV. These fluxes coupled with the higher photoelectric cross sections in this energy range [31–33] as well as the high surface sensitivity [34] made soft X-rays the ideal tool for studying surfaces and thin interfaces which were a major area of research. Figure 3.7 shows spectra for the Au 4f levels taken over a range of photon energies from 80 to 180 eV. These spectra not

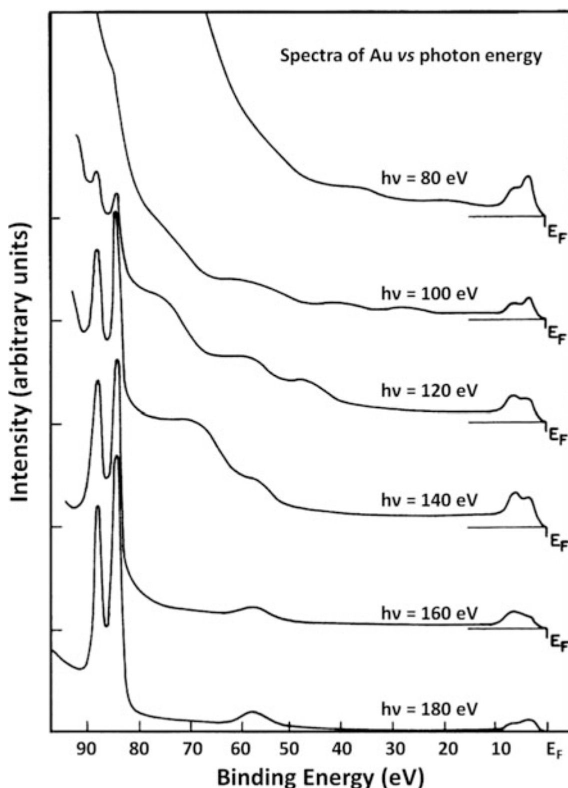

Fig. 3.7 Electron-energy distributions from gold for excitation energies between 80 and 180 eV. The horizontal scale gives the binding energies referred to the Fermi level, $E_F = 0$

only provided information on the natural line widths of the core levels as did the 8 keV spectra but they also showed the influence of the photoelectric cross section near threshold. The high counting rates resulted in low-noise data and thus measurements with higher sensitivity and precision. The relative cross section for the Au 4f levels from threshold (84 eV) to 280 eV obtained by integrating the area under the Au 4f core levels is shown in Fig. 3.8.

Given that much of the research at the time focused on surfaces and very thin interfaces, the trend of using soft X-rays for photoelectron spectroscopy continued for the next two decades. The surface sensitivity and narrow line widths that can be readily obtained at the lower photon energies are invaluable where ultra-thin surface layers are of interest. Figure 3.9 shows an escape-depth curve measured for GaAs showing that at a kinetic energy of 60 eV, the minimum in the escape depth is approximately 5 Å, which is exactly what is needed when studying phenomena that take place within the first surface layer [35].

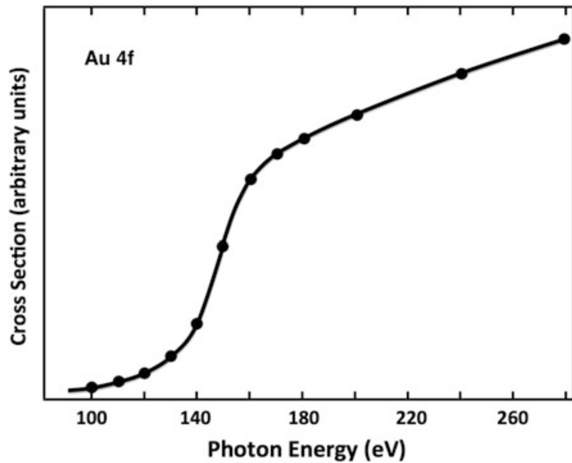

Fig. 3.8 Photoionization cross-section of the 4f level as a function of photon energy from threshold (E_B = 84. 0 eV) to 280 eV

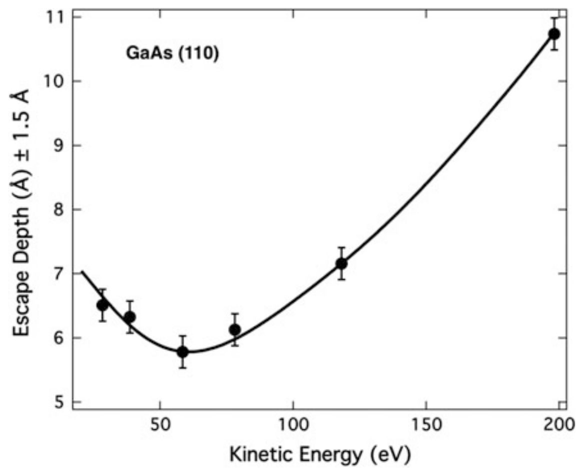

Fig. 3.9 Plot of escape depth versus kinetic energy for the GaAs (110) surface. Error bars on the graph represent the measurement error while the ±1.5 Å uncertainty in the escape-depth value results from the uncertainty in the calculated thickness of the top-most layer [35]

3.8 Soft X-ray Photoemission: Application to Photocathodes

One example that illustrates the importance of short escape depths is the study of the surface cleaning required to prepare InP for use in Negative Electron Affinity (NEA) photocathodes. These devices are used as night vision devices whose low work-function surfaces enable the conversion of incident infrared radiation to electrons which can then be imaged [36]. These devices require a pristine surface free from any traces of oxidation in order to achieve the low required work functions along with long enough lifetime to be used in practical devices. Their preparation involves the deposition of two monolayers of Cs with intercalated oxygen in a

cesium peroxide, Cs_2O_2, configuration in order to achieve an optimum photoelectric yield [37]. Oxygen contamination will drive a chemical reaction on the surface that converts the cesium peroxide into cesium superoxide which raises the work function to levels that destroy the photoelectric yield. In the first stage of the preparation, the InP wafers were originally cleaned in a sulfuric-peroxide solution to remove the native oxide. This process was the same as what had worked for GaAs NEA devices but was found not to provide the required performance in the InP devices. The reason was obvious when the surfaces were examined with soft X-ray photoemission as shown in Fig. 3.10. The presence of In and P oxides in the form of indium phosphate was clearly seen [38]. This was not the case with GaAs surfaces cleaned in this manner which did not exhibit oxidation of the Group III element, i.e., Ga in the case of GaAs. The presence of oxides on the InP surface had not been observed using conventional Al Kα XPS, typically used for industrial applications, due to the larger escape depths from the higher kinetic energies of these low binding energy core levels coupled with the lower energy resolution of a conventional XPS system. The electron kinetic energies achieved with the soft X-rays resulted in escape depths of only one monolayer and thus much higher sensitivities for surface species.

Once these oxides had been observed, it was straightforward to add a second etching step to eliminate the surface oxide, leaving only a fractional monolayer of elemental P that was readily removed by moderate heating as seen in Fig. 3.11.

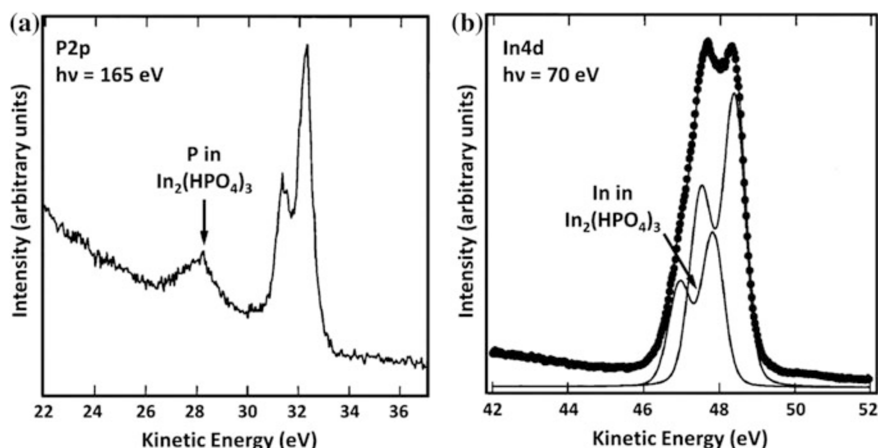

Fig. 3.10 **a** P 2p and **b** In 4d spectra after the one-step chemical-etching process using a solution of 4:1:100 H_2SO_4:H_2O_2:H_2O (raw data: *bullet*, fit: *lines*, background is subtracted from individual components). A clear, well separated oxide peak is observed for the P 2p core level with a 3.9 eV shift to lower kinetic energy relative to the bulk peak while the In 4d core level requires a two component fit to observe the oxide peak which is located at 0.47 eV lower kinetic energy. The respective kinetic energies of the P 2p and In 4d levels of 32 eV and 48 eV yield an escape depth of approximately 6 Å that provides enough surface sensitivity to observe the oxide layers

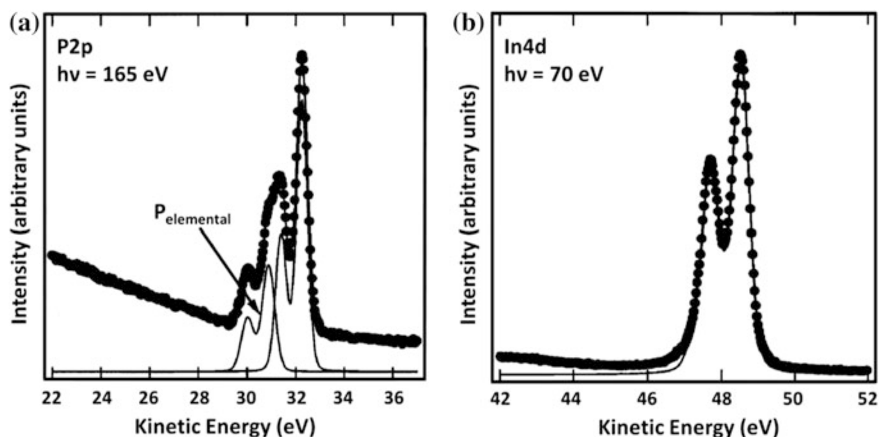

Fig. 3.11 P 2p (**a**) and In 4d (**b**) spectra after the two-step process using the solution of 4:1:100 H_2SO_4:H_2O_2:H_2O, followed by a water rinse and then a solution of 1:3 HCl:H_2O (raw data: *bullet*, fit: *lines*, background is subtracted from individual components). The P 2p spectrum can be fit with two components. The smaller peak, referred to as $P_{\mathbf{elemental}}$, on the lower kinetic-energy side corresponds to P either in clusters or bonded to P atoms on the InP surface. In both cases, the P is also bonded to H. Only a single component is required to fit the In 4d spectrum

The elemental P was probably in the form of hydrogen-covered P clusters or P atoms bonded to the surface P atoms in the InP. The resulting surfaces not only were free from oxygen but the In 4d core level exhibited a surface core-level shift indicating that the surface was atomically clean as shown in Fig. 3.12 [38].

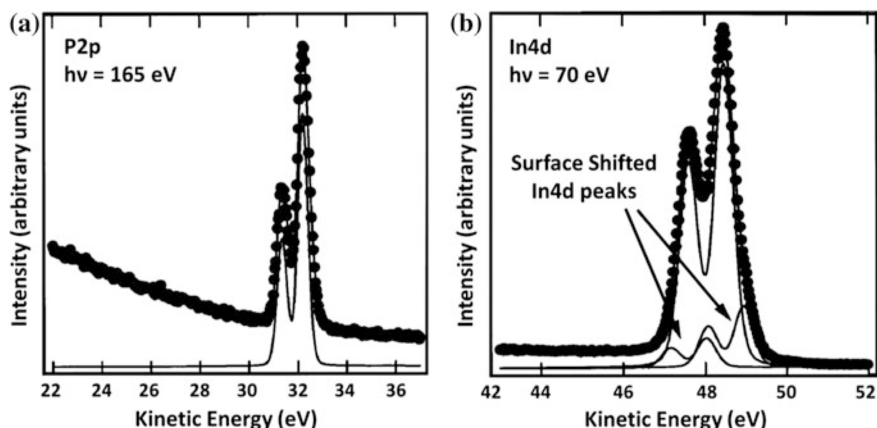

Fig. 3.12 P 2p (**a**) and In 4d (**b**) spectra after the two-step process followed by annealing at 330 °C (raw data: *bullet*, fit: *lines*, background is subtracted from individual components). Only one component is needed to fit the P 2p data. The In 4d data requires three components, with the middle component as the bulk contribution and two components on either side of the bulk peak as surface components

3.9 Development of Modern HAXPES

Although the information obtained in such studies using lower energy photons continues to be technologically relevant and necessary for many problems, there are many situations in present day technology where the layers of interest are beyond 0.2 nm from the surface and are often located 2–10 nm below the surface. In those cases, soft X-rays can only be used if some form of etching is employed to remove the surface layers leaving open the question of the effect of the etching on the measurement as well as the precision of the etching [39]. This is exactly where the much larger escape depths provided by HAXPES come to the fore. HAXPES effectively reduces the effect of sample preparation on the measurement and also makes the measurement of buried interfaces possible. However, it should be noted that thin buried interfaces are still a challenge. Since HAXPES measurements integrate the signal over the larger escape depth, it is often difficult to differentiate the signal of a thin interface from the background whether it is buried or originates from the surface. The study of such interfaces still requires some form of etching to bring the interface close enough to the surface that core levels providing higher surface sensitivity can be utilized. Of course, the higher surface sensitivity can be achieved either with soft X-rays or by choosing a higher binding energy core level if harder X-rays are employed.

For completeness, the development at SSRL in the 1980s of the JUMBO beam line should be mentioned. This beam line provided focused X-rays in the 800–4000 eV range at fluxes and resolutions suitable for photoemission, X-ray induced Auger spectroscopy, EXAFS, and photon-stimulated desorption measurements. Although this beam line was productive over the twenty years of its operation, it could have made more of an early impact on HAXPES had high throughput electron-energy analyzers been available in the early stages of its development. A more detailed discussion is beyond the scope of this chapter so the reader is referred to the literature on its operation [40] as related to, photoemission [41], EXAFS [42], and photon stimulated Auger [43] studies.

During the last twenty years, significant improvements have been made to the synchrotron sources themselves along with improvements in mirror technologies and high-throughput photoelectron-energy analyzers that are capable of working with high-electron energies. These improvements have increased the fluxes on the sample from $1e^6$ photons/s in the original experiments to over $1e^{11}$ photons/s resulting in counting rates well beyond the 40 counts/s seen in Fig. 3.5. Such counting rates not only make the study of core levels routine, they also make the study of valence bands and Fermi edges a reality overcoming their much lower cross sections. One such system, the National Institute of Standards and Technology (NIST) HAXPES end station operating on beam line X24A at the National Synchrotron Light Source (NSLS) [44] is shown in Fig. 3.13. This system uses a 200 mm radius Scienta HR4000 hemispherical electron-energy analyzer [45] and can analyze electrons with energies as high as 10 keV. In a typical XPS experiment at a photon energy of 2.14 keV, the analyzer is operated with a 0.3 mm

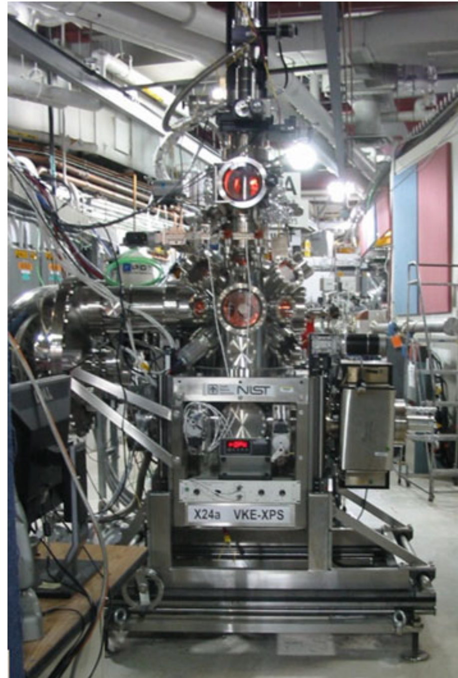

Fig. 3.13 Photograph of the NIST end station on X24A at the NSLS showing the electron-energy analyzer on the left oriented 90° from the beam axis. The sample manipulator comes down from the top through a preparation chamber located above the analysis chamber. The chamber has been designed for rapid introduction of samples into the UHV

detector aperture and a pass energy of 200 eV, yielding an analyzer resolution of 0.15 eV. The total instrumental resolution obtained from a measurement of the Ag $3d_{5/2}$ core level and the Ag Fermi edge was 0.26 eV limited primarily by the monochromator photon-energy resolution.

Although this is a state of the art analysis chamber, the overall performance was limited by the performance of the beam line because it utilized a bending-magnet source. The next generation of HAXPES beam lines, incorporating both soft- and hard-X-ray capabilities, achieve improved high-energy performance through the use of high-brightness undulator sources and state-of-the-art-monochromator designs. There are three such facilities of which two are under construction at BESSY II [46] and NSLS II [45] and a third, at the Diamond Light Source that is operating [47, 48]. The HAXPES facility at the Diamond Light Source, beam line I09, is illustrated in Fig. 3.14.

In Beam Line I09, the hard X-rays are produced by an in-vacuum undulator with a magnetic period of 27 mm in the 3 GeV storage ring operated in a top-up mode. The undulator radiation is monochromatized by a pair of liquid-nitrogen cooled Si (111) crystals designed to work from 2.1 to 20+ keV and to cope with a high-power density of approximately 30 W/mm^2. The energy width of the photon beam can be further reduced to selected values to suit the experimental needs using a set of interchangeable Si channel-cut crystals employing different higher-order Bragg reflections. Three horizontally deflecting mirrors are used to focus the X-ray beam

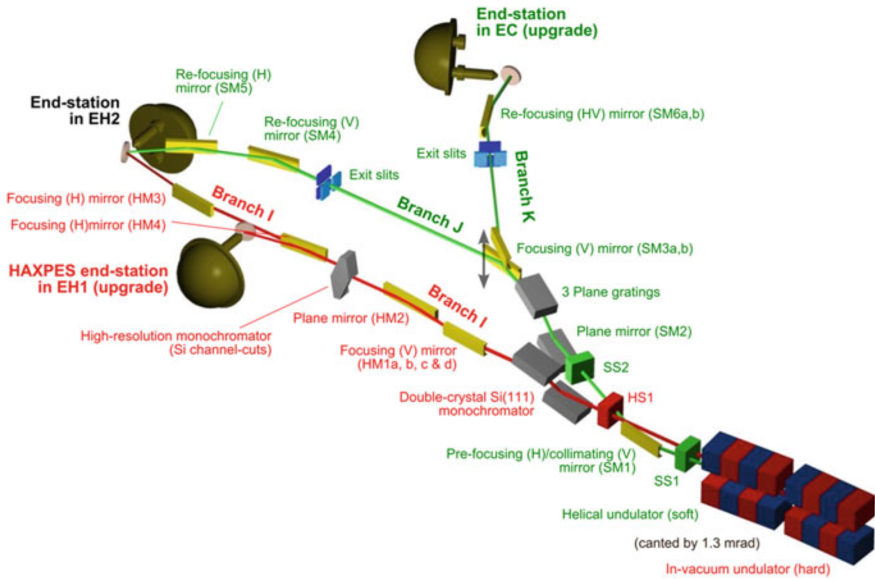

Fig. 3.14 Schematic diagram of the I09 HAXPES facility at the Diamond Light Source showing how photons from both the soft X-ray plane-grating monochromator (*PGM*) from Branch J and crystal monochromator from Branch I can be combined on the same sample at the end station in EH2 [49]

to a size of 15 μm (V) × 30 μm (H) at the sample and to reject the higher-order harmonic radiation. The small vertical-beam size ensures all emitted electrons magnified by the analyser lens in a transmission mode pass the analyser slit. The strong horizontal focusing allows a flat sample to be measured at an incident angle less than 2°, a geometry commonly used in the HAXPES community to achieve an intensity boost of photoelectrons more than 30 fold. Effective harmonic suppression minimizes the background level beyond the Fermi edge and facilitates the resolution of weak features in a valence-band spectrum. A beam-position monitor before the sample ensures long-term stability of the focused X-ray beam position with respect to the focal spot of the analyser. The HAXPES end-station is equipped with a VG Scienta analyser that can measure electrons up to 10 keV over an angular range of 60°. Energy spectra across the full angular range can be recorded in a single shot by a CCD camera with an angular resolution better than 0.5°.

3.10 Selected HAXPES Results

The typical energy resolution that is readily available on a modern HAXPES beamline is demonstrated in Fig. 3.15, which shows the gold valence-band and Fermi edge measured at 50 K. With the help of a secondary Si(333) channel-cut

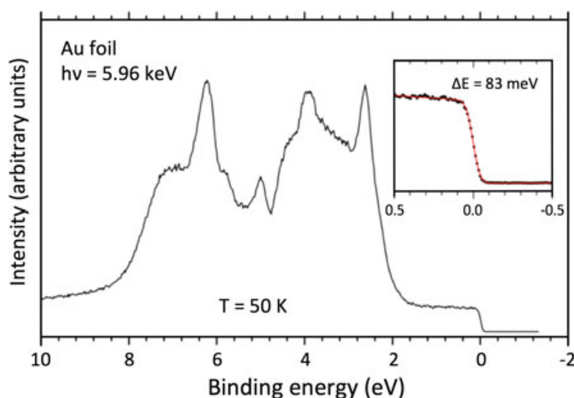

Fig. 3.15 Gold valence band spectrum taken at 5.96 keV at Beam Line I09 at the Diamond Light Source in less than 10 min. This spectrum illustrates the high throughput and resolution achievable with an optimized high-energy beam line

crystal monochromator, a resolving power close to 10^5 is achievable near 6 keV while the full valence band spectrum can be acquired in less than 10 min. The ability of modern HAXPES to unveil weak electronic states in or above a valence band is further demonstrated in Fig. 3.16, where the broad and sharp features within the band gap of Nb doped $SrTiO_3$, which have recently drawn much attention in the condensed-matter physics community and are thought to be associated with beam-induced oxygen vacancies and the formation of an electron gas, respectively, are clearly resolved at 2.5 keV with an acquisition time less than 30 min. In addition to the high-energy radiation, I09 is uniquely designed to deliver also soft X-rays down to 100 eV to the same end-station. This extended energy range offers the opportunity to vary more widely information depth and photoionization cross sections, and opens up the possibility for combining complementary X-ray techniques, such as HAXPES, X-ray Standing Waves (XSW), Resonant Photoemission

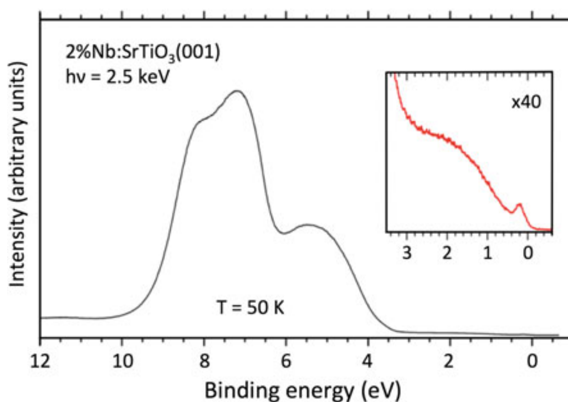

Fig. 3.16 Spectrum of the broad and sharp features within the band gap of Nb doped $SrTiO_3$ taken at Beam Line I09 at 2.5 keV showing the ability of an optimized HAXPES station to detect very weak states

(ResPES), Soft X-ray Angle Resolved Photoemission (SX-ARPES), Near Edge Absorption Fine Structure (NEXAFS), and Photoelectron Diffraction (PhD/XPD) in the same experiment. Since operational in June 2013, the beamline has been serving a fast growing user community interested in studying interactions of organic molecules adsorbed on solid surfaces, two-dimensional materials (e.g., graphene, BN and MoS_2), capture of small molecules in ionic liquids, density of valence states of novel materials (e.g., transparent conducting oxides), electronic properties at buried interfaces of metal oxide heterostructures, and chemical compositions and band alignment of energy materials (solar cells, Li-ion battery and nuclear fuel) [49].

3.11 Concluding Remarks

It is clear that significant advancements have been made from the early synchrotron photoemission measurements at 8 keV to what has developed into a useful measurement tool in HAXPES beam lines around the world. This achievement is a direct result of advancements in both the sources as well as the photoelectron energy analyzers which have revolutionized the ability to use hard X-rays for valence band as well as core level studies. A whole new range of applications for characterization of bulk properties and buried layers, which make up a large fraction of structures used for practical applications, is now possible. However, it is clear from the examples discussed that the requirement for high surface sensitivity remains as does the need for soft X-rays.

Acknowledgements The authors acknowledge the support of the Stanford Synchrotron Radiation Lightsource, SLAC National Accelerator Laboratory, which is supported by the U.S. Department of Energy, Office of Science, Office of Basic Energy Sciences under Contract No. DE-AC02-76SF00515. The authors are grateful to Tien-Lin Lee of the Diamond Lightsource for providing the description and results from BL I09 at the Diamond Lightsource.

References

1. K. Kobayashi, Nucl. Instrum. Methods Phys. Res. A **601**, 32 (2009)
2. G.V. Marr (ed.), Handbook on Synchrotron Radiation: Vacuum Ultraviolet and Soft X-ray Processes (North-Holland, Amsterdam, 1987)
3. K. Codling, J. Synchrotron Rad. **4**, 316 (1997)
4. D.W. Lynch, J. Synchrotron Rad. **4**, 334 (1997)
5. I.H. Munro, J. Synchrotron Rad. **4**, 344 (1997)
6. T. Sasaki, J. Synchrotron Rad. **4**, 359 (1997)
7. H.E. Huxley, K.C. Holmes, J. Synchrotron Rad. **4**, 366 (1997)
8. H. Winick, A. Bienenstock, Ann. Rev. Nucl. Part. Sci. **28**, 33 (1978)
9. B. Richter, Rev. Modern Phys. **49**, 251 (1977)
10. M.L. Perl et al., Phys. Rev. Lett. **35**, 1489 (1975)

11. W.E. Spicer, http://www.slac.stanford.edu/history/images/arc279.jpg
12. W.E. Spicer, Phys. Rev. **112**, 114 (1958)
13. C.N. Berglund, W.E. Spicer, Phys. Rev. **4A**, A1030 and 1044 (1964)
14. G.E. Fischer, Study of a Possible Construction Program of a National Synchrotron Radiation Facility at the SLAC Electron-Positron Storage Ring (SPEAR), SPEAR-NOTE-152, December 1972
15. S. Doniach, K. Hodgson, I. Lindau, P. Pianetta, H. Winick, J. Synchrotron Rad. **4**, 380–395 (1997)
16. R. A. Mack, Report No. CEAL-1027, Cambridge Electron Accelerator Laboratory (1966)
17. K. Wille, Rep. Prog. Phys. **54**, 1005 (1991)
18. H. Winick, *Proceedings of the IXth International Conference on High Energy Accelerators*, Stanford Linear Accelerator Center, Stanford California 1974, p. 685
19. H. Winick, *Synchrotron Radiation Research* (Plenum Press, New York, 1980), p. 28
20. R. Scholl, J. Voss, H. Wiedemann, M. Allen, J.-E. Augustin, A. Boyarski, W. Davies-White, N. Dean, G. Fischer, J.L. Harris, L. Karvonen, R.R. Larsen, M.J. Lee, P. Morton, R. McConnell, J.M. Patterson, J. Rees, B. Richter, A. Sabersky, IEEE Trans. Nucl. Sci. **20**, 752 (1973)
21. P. Pianetta, I. Lindau, J. Electron Spectrosc. **11**, 13 (1977)
22. B.E. Warren, *X-ray Diffraction* (Addison-Wesley Publishing Company, Reading, Mass, 1969)
23. E.W. Hoyt, P. Pianetta, SLAC TN-73-10, Stanford Linear Accelerator Center (1973)
24. P.W. Palmberg, J. Vac. Sci. Technol. **12**, 379 (1975)
25. J.F. Moulder, W.F. Stickle, P.E. Sobol, K.D. Bomben, *Handbook of X-ray Photoelectron Spectroscopy* (Physical Electronics Inc., Eden Prairie, 1995), p. 182
26. A.P. Sabersky, Part. Accel. **5**, 199 (1973)
27. A.P. Banford, *The Transport of Charged Particle Beams* (E. and F.N. Spon Ltd., London, 1966)
28. H. Beaumont, M. Hart, J. Phys. E **7**, 823 (1974)
29. F.C. Brown, R.Z. Bachrach, N. Lien, Nucl. Instrum. Methods **152**, 73 (1978)
30. H. Petersen, C. Jung, C. Hellwig, W.B. Peatman, W. Gudat, Rev. Sci. Instrum. **66**, 1 (1995)
31. J.J. Yeh, I. Lindau, At. Data Nucl. Data Tables **32**, 1 (1985)
32. J.H. Scofield, Lawrence Livermore National Laboratory Report UCRL-51326, 1973
33. M. Gorgoi, F. Schäfers, S. Svensson, N. Mårtensson, J. Electron Spectrosc. **190**, 153 (2013)
34. S. Tanuma, C.J. Powell, D.R. Penn, Surf. Interface Anal. **36**, 1 (2004)
35. P. Pianetta, I. Lindau, C.M. Garner, W.E. Spicer, Phys. Rev. B **18**, 2792 (1978)
36. J.S. Escher, in NEA Semiconductor Photoemitters in Semiconductors and Semimetals, Vol. 15, ed. by R.K. Willardson, A.C. Beer (Academic Press, New York, 1981) p. 195
37. D.-I. Lee, Y. Sun, Z. Liu, S. Sun, S. Peterson, P. Pianetta, J. Appl. Phys. **102**, 074909 (2007)
38. Y. Sun, Z. Liu, F. Machuca, P. Pianetta, W.E. Spicer, J. Appl. Phys. **97**, 124902 (2005)
39. R. Kasnavi, Y. Sun, R. Mo, P. Pianetta, P.B. Griffin, J.D. Plummer, J. Appl. Phys. **87**, 2255 (2000)
40. Z. Hussain, E. Umbach, D.A. Shirley, J. Stohr, J. Feldhaus, Nucl. Instrum. Methods **195**, 115 (1982)
41. M.H. Hecht, F.J. Grunthaner, B.B. Pate, P. Pianetta, M. Engelhardt, W. Jansen, C. Bryson, Nucl. Instrum. Methods **A246**, 806 (1986)
42. J. Stohr, R. Jaeger, S. Brennan, Surf. Sci. **117**, 503 (1982)
43. J.C. Woicik, B.B. Pate, P. Pianetta, Phys. Rev. B **39**, 8593 (1989)
44. C. Weiland, A.K. Rumaiz, P. Lysaght, B.A. Karlin, J.C. Woicik, D.A. Fischer, J. Elect. Spec. and Rel. Phenom. **190**, 193 (2013)
45. R. Reininger, J.C. Woicik, S.L. Hulbert, D.A. Fischer, Nucl. Instr. and Meth. A **649**, 49 (2011)
46. R. Follath, M. Hävecker, G. Reichardt, K. Lips, J. Bahrdt, F. Schäfers, P. Schmid, J. Phys: Conf. Ser. **425**, 212003 (2013)

47. J.J. Mudd, T.-L. Lee, V. Muñoz-Sanjosé, J. Zúñiga-Pérez, D. Hesp, J.M. Kahk, D.J. Payne, R. G. Egdell, C.F. McConville, Phys. Rev. B **89**, 035203 (2014)
48. J. Sforzini, L. Nemec, T. Denig, B. Stadtmüller, T.-L. Lee, C. Kumpf, S. Soubatch, U. Starke, P. Rinke, V. Blum, F.C. Bocquet, F.S. Tautz, Phys. Rev. Lett. **114**, 106804 (2015)
49. T.-L. Lee, Diamond Lightsource (private communication)

Chapter 4
Hard-X-ray Photoelectron Spectroscopy of Atoms and Molecules

Marc Simon, Maria Novella Piancastelli and Dennis W. Lindle

Abstract We review here the current status of atomic and molecular HAXPES, both experimentally and theoretically. After the era of the ESCA technique, atomic and molecular HAXPES experienced several decades when the emphasis in gas-phase research was in the soft-X-ray range, mainly due to the lack of suitable experimental conditions. In the last few years, at some of the newer synchrotron radiation sources, hard-X-ray beamlines have been developed which provide state-of-the-art instrumentation for the atomic and molecular community. A substantial impulse to the field has also been recently given by the new X-ray free-electron lasers (FELs). Therefore, the high-brightness and high-resolution sources needed for a thriving gas-phase HAXPES community are now available. We concentrate here on experimental results based on the use of SR and, more recently, FELs as ionizing sources. Available parallel theoretical developments are also included. We define the hard-X-ray photon-energy range as 1 keV or higher. We provide a summary of early theoretical work in atomic and molecular HAXPES, and then an overview on HAXPES performed at first- and second-generation SR sources and at current-generation facilities. Scientific topics of particular interest in the hard-X-ray range include nondipole effects, recoil due to the photoelectron's momentum, new interference phenomena, ultrafast nuclear motion on the femto- and sub-femtosecond scale, and double-core-hole studies. We conclude with a look at future directions in these areas and a few others of potential interest for HAXPES.

M. Simon (✉) · M.N. Piancastelli
Laboratoire de Chimie Physique-Matière et Rayonnement, CNRS and UPMC, 11 Rue Pierre et Marie Curie, 75231 Cedex 05 Paris, France
e-mail: marc.simon@upmc.fr

M.N. Piancastelli
Department of Physics and Astronomy, Uppsala University, Box 516, 75120 Uppsala, Sweden

D.W. Lindle
Department of Chemistry, University of Nevada, Las Vegas, 4505 S. Maryland Pkwy, Box 4003, Las Vegas, NV 89154-4003, USA

© Springer International Publishing Switzerland 2016

J.C. Woicik (ed.), *Hard X-ray Photoelectron Spectroscopy (HAXPES)*,
Springer Series in Surface Sciences 59, DOI 10.1007/978-3-319-24043-5_4

4.1 Introduction

Electron emission following irradiation is intrinsic to the interaction between light and matter, and the photoelectric effect [1] has received a great deal of attention over the past century. As a result, photoelectron spectroscopy (PES) has developed into a well-established and powerful technique for investigating and characterizing quantitatively the electronic structure of matter: in this Chapter, we focus primarily on neutral atoms and molecules. The power of PES stems from its ability to probe, via the measurement of electron kinetic energies, orbital structure in valence and core levels in a wide variety of species, providing a direct experimental method to probe the quantum mechanics of the system under study. As a result, PES has been used successfully for decades to provide stringent tests of our understanding of basic physical processes underlying gas-phase interactions with radiation.

The high-energy version of PES, now referred to as hard-X-ray photoelectron spectroscopy or HAXPES, received major attention in the middle of last century with the development of the technique Electron Spectroscopy for Chemical Analysis (ESCA) [2, 3]. Naturally, the technique is based on the photoelectric effect, induced by single-photon absorption, leading to the ejection of one core electron due to the high photon energy of the X-rays used. One key to the power of ESCA is that the energy needed for the ejection of an inner-shell electron [its binding energy (BE)] is characteristic of each atomic species, so core-level photoionization allows direct determination of the elemental composition of a sample. Furthermore, the same element in different chemical environments will show a small, but distinctive, shift in its BE, a well-known property known as the "chemical shift." For these developments, Kai Siegbahn was awarded the 1981 Nobel Prize in Physics.

More recently, however, HAXPES has seen only limited use in the study of atomic and molecular species, in large part because the focus in gas-phase studies for the past few decades has been in the VUV and soft-X-ray regions of the electromagnetic spectrum, where significant advances in sources (i.e., synchrotron radiation) and electron spectrometers for lower kinetic energies allowed rapid advances in energy resolution and signal rate. While some pioneering work was done during this period, it is only in the past few years that HAXPES of atoms and molecules has begun to catch up to the excellent capabilities available in the VUV and soft-X-ray ranges.

It is the purpose of this Chapter to review the current status of atomic and molecular HAXPES, both experimentally and theoretically. However, because ESCA, and its brethren using traditional excitation methods (i.e., X-ray tubes), have been summarized extensively in the past [2], the present discussion is limited to experiments from the synchrotron-radiation (SR) era and, more-recently, to those using free-electron lasers (FELs). Applicable theories from any era are included because, in most cases, theory preceded, by many years, comparable experimental work, especially for atoms. Naturally, this report focuses on results in the hard-X-ray photon-energy range, which we have arbitrarily defined as 1 keV or higher. This is a

lower energy than usually considered to be in the 'hard' X-ray region, but a more-conventional choice of 5 keV or so would have rendered this chapter moot because virtually no gas-phase SR-based experiments have been reported at these higher energies. Finally, to maintain the theme of HAXPES, many interesting and informative results using primarily ion or X-ray-emission spectroscopies, as well as the latter's kin, resonant inelastic X-ray scattering (RIXS), have been excluded from the discussion.

The remainder of this Chapter is organized as follows. Section 4.2 provides a summary of early theoretical work in atomic and molecular HAXPES, along with separate subsections on HAXPES performed at first- and second-generation SR sources and at current-generation facilities. The following four sections focus on specific scientific topics of particular interest in the hard-X-ray range: (1) nondipole effects in Sect. 4.3; (2) the effects of recoil due to the photoelectron's momentum in Sect. 4.4; (3) new interference phenomena in Sect. 4.5; and (4) double-core-hole studies in Sect. 4.6. Finally, Sect. 4.7 concludes with a look at future directions in these areas and a few others of potential interest for HAXPES.

4.2 Haxpes in the Synchrotron Era

The ability to tune the photon energy that became available with the advent of SR sources led to new capabilities beyond the powerful ESCA technique. However, doing photoemission from gas-phase samples in the hard-X-ray range was a very challenging endeavor with first- and second-generation SR sources. As a result, early work in HAXPES focused mostly on calculations of the photoelectric effect; a significant body of theory predates many of the SR-based experiments. Most of these theoretical results are described in Sect. 4.2.1, although some of the more-recent studies, as appropriate, are incorporated in relevant sections later in this Chapter. Experimentally, early pioneering efforts in HAXPES are summarized in Sect. 4.2.2. More-recent experimental studies, performed with the most-advanced light sources now in operation, are discussed in Sect. 4.2.3.

4.2.1 Theory Applied to HAXPES

4.2.1.1 High-Energy Studies

Theoretical treatment of the photoelectric effect initially focused on atomic *K*-shell photoionization probabilities (or cross sections, σ) at very high energies (MeV), for two reasons [4]. First, at MeV photon energies, photoionization from the *K* shell dominates the photoeffect, accounting for about 80 % of the total ionization cross section. Second, the effect of nuclear screening is small only for the innermost 1*s* electrons, allowing early *K*-shell calculations to assume a simple Coulomb

potential due to a nucleus of charge +Ze. Thus, the initial state could be treated as a hydrogen-like bound state for every atom. More-sophisticated potentials were, in general, too complicated to evaluate numerically before the advent of modern computers. Nevertheless, calculations of HAXPES cross sections date to the heyday of quantum mechanics in the first half of the twentieth century. Perhaps the most-accurate calculation from this period was by Hulme et al. [5], who reported numerical *K*-shell cross sections using a Coulomb-potential model for Fe, Sn, and Po at two photon energies: 354 and 1130 keV. Summaries of other theoretical work from this early period can be found elsewhere [6–9].

In 1960, Pratt [8] extended studies of *K*-shell cross sections, developing an analytical formula valid in the high-energy limit (~1 MeV). This work also neglected nuclear screening. In essence, Pratt's model and its predecessors represent one form of what is now referred to as the independent particle approximation (IPA), the assumption that electrons in a multielectron system do not interact directly with one another. Put simply, the IPA asserts that photoionization, away from any thresholds or resonances, can be treated in a single-channel picture which omits electron-electron interactions entirely. In other words, the IPA suggests that at most hard-X-ray energies, electron-correlation effects should be negligible, allowing theorists to eliminate the relevant *e-e* term(s) from the appropriate Hamiltonian. Later that same year, Pratt [9] extended this work to atomic *L*-subshell cross sections using the same model to derive analytical formulae valid in the high-energy limit. However, for the *L* shell, nuclear screening had to be taken into account. This was accomplished by using an effective nuclear charge, Z_{eff}, in place of Z in the calculations.

Enhancements in the Theory

Building on Pratt's work [8, 9], the 1960s witnessed a number of refinements in the calculation of high-energy atomic cross sections. The first improvement was to extend the calculations to somewhat lower energies (hundreds of keV), using both unscreened [10] and screened [11] numerical treatments of the *K* shell. The latter, more-comprehensive, study included wide ranges of Z [from $Z = 13$ (Al) to $Z = 92$ (U)] and photon energy (200 keV–2 MeV). It also provided some of the first reliable calculations of differential cross sections, i.e., cross sections as a function of angle of emission relative to the photon trajectory, thus characterizing the angular distributions of photoemitted electrons. These results were followed by a variety of calculations of *K*-shell and *L*-subshell cross sections and angular distributions at energies from 1 keV to 1.3 MeV, mostly for heavier elements [4, 12, 13, 14, 15], eventually including calculations for the *M* subshells of Fe, Sn, and U as well [16]. For a better understanding of the basic concepts behind the theory and calculation of atomic HAXPES at photon energies above 10 keV, the reader is referred to an early review by Pratt et al. [17]. As this review notes, at these energies the cross sections and angular distributions depend only on the very small-r portion of the atomic wavefunction of the ionized electron, as well as on its ground-state angular

momentum. Furthermore, effects of nuclear screening can be accounted for by considering the normalization factors of the bound and continuum states of the ionized electron.

Some years later, using more-refined techniques and improved theoretical and calculational methods, one group of researchers was able to add more complexities into the high-energy studies. For example, a series of papers [18–20] on the elements C, Sn, and U in the 1–100 keV photon-energy range looked at subshell cross sections and spin-orbit branching ratios [e.g., $\sigma(2p_{3/2})/\sigma(2p_{1/2})$] for all shells in each atom. One general conclusion from this work was that for most elements, beyond the lightest ones, the subshell branching ratios seldom equal the statistical value, even at the highest energies [18, 19]. As these calculations were performed using a relativistic model, and because high-energy photoionization involves only the small-r portion of a wavefunction, tiny relativistic differences of the wavefunctions for different spin-orbit states (e.g., $2p_{1/2}$ and $2p_{3/2}$) near the nucleus are amplified in the branching ratios, leading to non-statistical behavior [19]. In contrast, for s subshells, it was found that a basic nonrelativistic calculation worked quite well to high energies ($\sim$20 keV), indicating cancellation among the various effects that lead to non-statistical branching ratios for the other subshells [20].

Cross-Section Minima

One topic of theoretical interest at high energies is the existence of minima in subshell cross sections that exist because a quantum-mechanical amplitude governing the subshell photoionization process changes sign as a function of energy, thus causing the corresponding matrix element (the square of the amplitude), and its contribution to the total subshell cross section, to pass through zero at a specific photon energy. The most common of such phenomena was described by Cooper in 1962 [21]. So-called Cooper minima can occur for any subshell with a radial node in its ground-state wavefunction (e.g., $2s$, $3p$, $4d$, but not $1s$, $2p$, $3d$), if the angular momentum of the photoionized electron increases (e.g., $3p \rightarrow \varepsilon d$, but not $3p \rightarrow \varepsilon s$). Cooper minima are known to be byproducts of the effects of nuclear screening in multielectron systems [22] to vary strongly as a function of n, ℓ, and $\boldsymbol{Z}$, and to typically occur relatively close to photoionization thresholds. For example, calculations of subshell branching ratios in Sn exhibit pronounced variations due to the presence of Cooper minima [18]. Further work on ns subshells of U [23] demonstrated that the energy positions of Cooper minima become constant as n increases, because as $n \rightarrow \infty$, atomic ground-state wavefunctions change very little, except in the outermost lobe that has minimal influence on the positions of the Cooper minima. Finally, at extremely high energies, on the order of mc^2, a different kind of zero occurs in photoionization [24]. These relativistic zeroes are distinguished from Cooper minima because they do not depend on n or $\boldsymbol{Z}$, but only on the initial angular momentum of the ionized electron, ℓ, according to a simple formula given by LaJohn and Pratt [24].

4.2.1.2 Lower-Energy Studies

Cross Sections

Theoretical efforts at lower energies, more applicable to the photon energies available at SR facilities, also began in the 1960s. While the earliest lower-energy cross-section calculations assumed the IPA (no *e*-*e* correlation), as had been done previously at higher energy, they still required the use of non-hydrogen-like wavefunctions, where nuclear screening is properly taken into account. The first studies focused on the outer shells of high-$\boldsymbol{Z}$ atoms [25] and on the 3*p* and 3*d* subshells of several elements [26] at energies from 100 eV to a few keV. The latter paper [26] also provided a good tutorial about atomic potentials and wavefunctions relevant to the discussion of photoionization. The general topic of PES below 10 keV was reviewed some years ago by Fano and Cooper [22], providing an excellent summary of many of the basic concepts. There are also early tabulations of cross sections for photon energies below 1.5 keV [27, 28]. These compilations used basic IPA-based calculations, and they covered all applicable subshells throughout the Periodic Table, up to and including uranium. These works are notable because they are still used today in many applications, even though they are four decades old.

More recent cross-section studies include a look at 1*s* photoionization in argon just above threshold [29], 1*s*, 2*p*, 3*p*, and 3*d* photoionization in Ne, Ar, Fe, and U up to 100 keV [30], and 3*s* and 3*p* photoionization in Ni up to 10 keV [31]. All three of these calculations reported results within the IPA, and the first and third also included non-IPA results using a theoretical technique called the random-phase approximation [used as either the random-phase approximation with exchange (RPAE) or the relativistic random-phase approximation (RRPA)], which explicitly includes electron-electron interactions in its formulation. In the argon case, inclusion of this interaction improved agreement with measured absorption cross section, illustrating that the electron departing from the K shell interacts with the outer electrons as it leaves. For nickel, in contrast, inclusion of electron-electron interactions did not resolve a discrepancy with measurements performed on solid and thin-film samples.

Photoelectron Angular Distributions Within the Dipole Approximation

Another important theoretical effort begun in the 1960s was to better understand the differential cross section for photoionization, i.e., the angular distribution of photoelectrons, at lower photon energies. The key assumption underpinning this work is the electric-dipole ($\boldsymbol{E}1$) approximation (DA), where one assumes a uniform electromagnetic field over the dimensions of the absorbing charge distribution, leading to easily characterized and quantified behavior. Generally, use of the DA for lower-energy photon spectroscopies has been justified by the following two

arguments: (1) the photoelectron velocity is small compared to the speed of light, rendering relativistic effects small; and (2) the photon wavelength is much larger than the "classical" size of the orbitals from which electrons are ejected, mitigating higher-order effects in photoionization. Qualitatively, the DA assumes that the photon field, $exp(i\mathbf{k}_p \cdot \mathbf{r})$, expanded as $1 + i\mathbf{k}_p \cdot \mathbf{r} + \ldots$, can be truncated to unity, if $\mathbf{k}_p \cdot \mathbf{r}$ is small [7]. In this simplification, all higher-order interactions, such as electric quadrupole ($\boldsymbol{E}2$) and magnetic dipole ($\boldsymbol{M}1$), are neglected. For photoionization cross sections, the DA turns out to be valid up to many keV because the $\boldsymbol{E}2^2$ and $\boldsymbol{M}1^2$ terms are negligible, compared to $\boldsymbol{E}1^2$, due to a factor of $1/\alpha^2$.

From the early work of Bragg, Compton, and Auger, among others, the spatial distribution of emitted photoelectrons has been the subject of extended experimental and theoretical efforts. It was soon understood that the probability of electron ejection as a function of angle is an excellent probe of quantum-mechanical channels available to a photoemission process because it is sensitive to phase differences among these channels. For photoelectron angular distributions in the DA, Bethe and Salpeter [7], using parity and angular-momentum conservation laws described by Yang [32], expressed the asymmetry of photoemission for a one-electron atom. Generalization of this description to many electron atoms was made by Cooper and Zare [33], providing the well-known expression for the differential cross section for photoelectrons ionized by 100 % linearly polarized light:

$$d\sigma/d\Omega(h\nu) = \sigma(h\nu)/4\pi[1 + {}^{1}\!/_{2}\beta(h\nu) \cdot (3\cos^2\theta - 1)], \tag{4.1}$$

where the differential cross section, $d\sigma/d\Omega$, is the probability for photoelectrons to be emitted into the solid angle $d\Omega$. The energy-dependent parameters $\sigma(h\nu)$ and $\beta(h\nu)$ are the subshell photoionization cross section and the *dipolar* angular-distribution parameter, respectively, and the angle θ is between the photoelectron emission direction and the polarization vector of the X-rays. Similar equations can be written for partially linearly polarized or unpolarized and circularly polarized light. The parameter β can range from +2 (a $\cos^2\theta$ distribution, like a *p* orbital along the polarization vector) to −1 (a torus perpendicular to the polarization vector). Equation (4.1) makes it clear that dipolar photoelectron angular distributions are axially symmetrical around the X-ray polarization axis, and that any anisotropy is completely described by the parameter β.

Application of the DA to measurements of angular distributions of photoelectrons can be used to provide much useful information about the photoionization process beyond measuring just cross sections. One virtue of measuring angular distributions is their sensitivity to phase shifts among degenerate photoemission (continuum) channels, providing a stronger challenge to theory than cross sections alone, which average over phase shifts. Stringent tests of basic theory are important because theory, not experiment, is commonly used in tabulations of partial cross sections [27, 28] and angular-distribution parameters [34–36] used in numerous applications.

Aside from these compilations, all performed with a basic IPA model, there have been few calculations of photoelectron angular distributions for photon energies above 1 keV. One notable case is an IPA study of the Kr $n = 3, 4$ subshells [37]

done for comparison to experiments performed at a variety of soft-X-ray energies in the 200–1500 eV range with X-ray tubes [38]. Both subshell cross sections and angular distributions were determined and showed excellent agreement with the experiments. Furthermore, Cooper [37] reported several expressions useful for comparison to and interpretation of angle-resolved photoemission experiments. Later, cross-sections and angular-distribution calculations were performed for the Hg $3p$ and $3d$ subshell cross sections [39], in anticipation of proposed experiments that never came to fruition.

Electron-Electron Correlation and Satellites

Going beyond the IPA, one must consider the impact of electron-electron interactions on the photoionization process. One of the most well-known effects of the breakdown of the IPA is the presence of correlation satellites in photoemission spectra. In the one-electron or single-particle picture of the IPA, one expects to see only photoemission peaks ("main lines") with characteristic kinetic energies that correspond to the removal of a single electron from a given subshell in the target. Almost invariably, however, one also sees one or more weaker lines (usually 10 % or less of the main-line intensity or cross section) at slightly lower kinetic energies (higher binding energies), the so-called satellite lines. These correlation satellites exist solely because of the multielectron nature of the target. They typically involve one-photon electronic transitions in which one electron is ionized while a second (usually valence) electron is simultaneously excited to a different orbital [consider Ne $(1s^2 2s^2 2p^6) + h\nu \rightarrow \mathrm{Ne}^+(1s^1 2s^2 2p^5 3p^1) + e^-$ as an example]. The final ionic state of such satellites is often referred to as a "shake-up" state because of the notion that the excited electron (a $2p$ electron in this example) is shaken up by removal (ionization) of a $1s$ electron. In fact, this is an apt term, because photoionization of a $1s$ electron suddenly changes the amount of screening experienced by the outer electrons, causing the valence orbitals in the ionic state to be more-compact than those in the ground state (they "relax"). This relaxation leads to finite overlap between different orbitals and to some probability that a valence electron ($2p$) will end up in an excited orbital ($3p$).

While satellites provide a window on the multielectron nature of atoms (and molecules), they also pose a challenge to theory, due to the need to explicitly include electron correlation in any calculation. An informative overview of the theoretical framework required to model satellite intensities (cross sections) was published by Manson [40], who described how to derive intensities relative to the main-line cross section using the general concept of configuration interaction to model electron-correlation phenomena. This paper notes that correlation can occur in the ground state (initial-state configuration interaction—ISCI), in the final state (final-ionic-state configuration interaction—FISCI), and in the continuum state that includes the ionized photoelectron (continuum-state configuration interaction—CSCI, also known as interchannel coupling). A proper theoretical treatment of satellites in HAXPES should therefore incorporate all three types of configuration

interaction. Finally, this work marked the first time that the concept of interchannel coupling among different continuum channels was applied to PES. Some years later, a detailed study [41] of correlation effects just above the Ar *K* edge ($\sim$3.2 keV) showed that relaxation due to the ionization of a core electron must be included to calculate accurate cross sections. While this work did not explicitly address satellite lines in HAXPES, it was able to determine the positions and intensities of two-electron resonances near the Ar *K* edge (e.g., $1s^1 \ldots 3p^5 3d^2$), which can be thought of as Rydberg states below satellite thresholds.

Spin Polarization

A theoretical framework for calculating electron-spin polarization induced by high-energy photoemission of *np* subshells was developed in 1999 [42]. Explicit equations in terms of radial matrix elements and phase-shift differences were derived for the relevant spin-polarization parameters. These general results were illustrated for photon energies up to 20 keV, using C, Ne, Ar, Fe, and Kr as examples.

Molecular HAXPES

One of the few molecular HAXPES calculations pertains to the simplest molecule, H_2 [43]. This work was done in response to a photoabsorption measurement of molecular hydrogen performed at 5.4 and 8.4 keV using X-ray tubes [44]. The salient experimental finding was that the absolute cross section for photoionization of the molecule is 40–50 % larger than twice the photoionization cross section of atomic hydrogen. (*n.b.*, for both H and H_2, each with only a single occupied orbital, photoabsorption and photoionization cross sections are one and the same.) Cooper [43] explained this difference as due to the significantly different normalization factors for the bound orbitals in atomic H versus molecular H_2. This is a rare result in atomic physics in which a measurable effect is attributed solely to normalization of quantum-mechanical wavefunctions.

4.2.2 The Synchrotron-Radiation Era

4.2.2.1 The Auger Resonant-Raman Effect

The power of tuning the photon energy was demonstrated in the first HAXPES measurement reported using SR. In this work [45], excitation and ionization of Xe $2p_{3/2}$ electrons in the near-threshold region ($\sim$4.8 keV) demonstrated behavior indicative of the radiationless Auger resonant-Raman effect, the analog of the well-known Raman effect often studied with lasers, but focused on resonant-Auger

emission following core-shell excitation in an atom or molecule. The primary signatures of the Auger resonant-Raman effect in an atom are linear dispersion of the kinetic energy of the resonant-Auger peaks in the HAXPES spectra as a function of photon energy and narrowing of the resonant-Auger peaks when the photon energy is tuned to the maximum of the resonance.

The physics behind is the following. The linear dispersion of the resonant-Auger peaks is a consequence of energy conservation: the ejected electron "remembers" the excitation photon energy value, and, if the experimental conditions allow one to vary such energy within the width of the resonance, then the resonant-Auger peaks disperse accordingly. The line narrowing derives from the fact that the width of the resonant-Auger peaks reflects the width of the exciting radiation, rather than the natural lifetime width of the core hole.

These measurements were motivated by the then-recent discovery of X-ray resonant-Raman scattering [46–48]. This first HAXPES measurement was done using a commercial cylindrical-mirror analyzer (CMA) at the first-/second-generation light source, the Stanford Synchrotron Radiation Laboratory (SSRL). The results were used about a decade later to help make the case for developing atomic and molecular HAXPES capabilities at third-generation SR sources [49].

Working at the then-second-generation National Synchrotron Light Source (NSLS) at Brookhaven National Laboratory, LeBrun et al. [50] reported measurements on resonant-Auger transitions near the Ar *K* edge. Using higher energy resolution and a refined theoretical treatment, the authors identified for the first time effects of coherent excitation of multiple Rydberg states, as well as the continuum, due to the relatively broad lifetime width (0.66 eV) of Ar-1*s* hole states.

4.2.2.2 Shake-up Satellites

A few years later, working at SSRL, but using home-built electron time-of-flight analyzers, David Shirley's group studied the $3p \rightarrow 4p$ shake-up satellite above the Ar *K*-shell threshold [51]. The measurements covered a kinetic-energy region that bridged from the adiabatic regime, just above the satellite threshold, towards the sudden-limit regime, far above threshold, exhibiting a gradual increase in the relative intensity of the satellite relative to the main 1*s* photoemission line, in accord with earlier measurements for shallow core levels in the soft-X-ray region [52]. The measurements also showed excellent agreement with shake-up calculations [53].

The following year, Bernd Crasemann's group and collaborators extended these results by studying satellites in the Ar *K* Auger and resonant-Auger spectra using a wide range of photon energies from below the $3p \rightarrow 4p$ satellite threshold to 2 keV above it [54]. The measurements allowed them not only to study the energy behavior of the relative intensity of the shake-up satellite, but also the energy behavior of the "shake-off" process, in which a single photon induces simultaneous ionization of two electrons, in this case a 1*s* electron and a 3*s* or 3*p* electron. In addition to confirming the earlier results [51], their work showed for the first time that the near-threshold energy dependence of shake-up and shake-off processes are

quite different, as was expected from theoretical considerations. The results also indicated that shake-off in argon is about three times more likely than shake-up. The shake-up measurements agreed well with theory [53], while the asymptotic shake-off probability was much larger than expected.

In 1998, Southworth et al. [55] used a double-pass CMA at the NSLS to measure HAXPES spectra of the Ar *K* satellites with much-improved resolution, observing several shake-up peaks. The overall structure of the spectra showed excellent agreement with a configuration-interaction theory [55]. The authors also noted that the cross sections of "conjugate" shake-up processes (e.g., $3p \rightarrow 4s$), so called because the excited electron changes ℓ during the shake-up process, were negligible at photon energies more than 100 eV above the Ar *K* edge.

4.2.2.3 Post-collision Interaction

The Crasemann group later extended their pioneering study in the vicinity of the Xe $2p_{3/2}$ edge with more photon energies and better resolution [56]. While confirming the earlier observations of the Auger resonant-Raman effect, the authors also obtained quantitative measurements of post-collision interaction (PCI), the interaction of a slow core photoelectron and a subsequent fast Auger electron emitted when the core hole is filled by a radiationless Auger transition. The physical picture is the following: the slow photoelectron starts its course, but then the faster Auger electron overtakes it, causing a sudden change in the potential: the slow photoelectron initially 'feels' the potential of a singly charged ion, but, following emission of an Auger electron, the photoelectron suddenly 'feels' the influence of a doubly charged ion. Essentially, this is another type of electron-electron interaction. The primary signature of PCI is a loss of kinetic energy by the photoelectron, accompanied by a concomitant gain in kinetic energy by the Auger electron due to energy conservation. In the case of photoionization just above the core-level threshold, it is even possible for the photoelectron to be recaptured into an unoccupied Rydberg orbital of the ion, due to its loss of energy. Exactly this sort of kinetic-energy shift was observed as the photon energy was tuned across the Xe $2p_{3/2}$ threshold [56]. Accompanying the experiment, the authors also introduced the first fully quantum-mechanical treatment of PCI.

4.2.2.4 Molecular HAXPES

The first molecular HAXPES study was performed by the Shirley group at the S 1*s* edge of SF_6 [57]. While these measurements had only moderate electron kinetic-energy resolution, they nevertheless identified a number of new behaviors related to resonant-Auger decay, doubly excited states, and above-threshold resonances. At the strong S $1s \rightarrow 6t_{1u}$ resonance below threshold, the results suggested primarily spectator-type decay, so called because the initially excited electron (in the $6t_{1u}$ orbital) acts as a "spectator" to the subsequent core-hole decay; the electron

remains in the $6t_{1u}$ orbital in the final state of the decay process. Just above the K edge, some features were identified as doubly excited states leading to satellite thresholds by virtue of their decay, in part, into final states other than S $1s^{-1}$. Finally, unusual resonances in SF_6 well above the S K edge were reproduced by multiple-scattering calculations, but not by EXAFS calculations, suggesting a complicated character that has still not been discerned.

4.2.2.5 Coincidence Measurements

Levin et al. [58, 59] performed the first HAXPES measurement incorporating coincidence techniques, in this case between ions and energy-resolved resonant-Auger electrons in the region of the Ar K edge. The coincident ion yields obtained were greatly simplified by defining the initial decay of the 1s vacancy state and they exhibited a much more pronounced photon-energy dependence than had been seen previously in non-coincident ion-yield measurements. Indeed, measuring the Ar^{+3} ion in coincidence with K-$L_{2,3}L_{2,3}$ resonant-Auger electrons illustrated that these ions appear only within a 5-eV window centered on the $1s \rightarrow 4p$ subthreshold resonance. With the help of Monte-Carlo simulations, the authors were able to identify the presence of shake-off of the initially excited Rydberg electron accompanying the resonant-Auger emission, double-Auger processes, and recapture of the 1s photoelectron via PCI just above threshold. Subsequently, these coincident measurements were compared to detailed calculations in the framework of lowest-order scattering theory [60]. The calculations agreed well with the measurements, confirming the importance of shake-off processes and PCI, and providing a solid basis for understanding complex core-hole decays in the hard-X-ray region. Finally, the argon measurements led to a first attempt at resonant-Auger—ion-coincidence measurements on a molecule, CF_3Cl at the Cl K edge [61].

Further work on argon at the NSLS [62] used a different type of coincidence measurement, between a K-$L_{2,3}$ ($K\alpha$) X-ray emitted by a 1s-excited or -ionized argon atom and a secondary $L_{2,3}$-MM Auger electron emitted after the initial radiative decay. As with electron-ion coincidence, the subsequent electron spectra were greatly simplified by defining the initial decay pathway for the core-excited atom. Comparison with Hartree-Fock calculations identified effects due to shake-up and PCI, in complement to the earlier results [58].

4.2.3 Results at Current Facilities

4.2.3.1 Breakdown of the Independent Particle Approximation

Working at the Advanced Light Source (ALS), a third-generation SR facility at Lawrence Berkeley National Laboratory, a HAXPES study of neon valence photoionization demonstrated the breakdown of the IPA at high energies [63]. In this

combined experimental and theoretical study, the primary evidence for breakdown of the IPA was the ratio of the Ne 2s and 2p photoionization cross sections, σ_{2s}/σ_{2p}, as a function of photon energy up to 1.5 keV.

In Fig. 4.1 we show the ratio of the 2s to 2p cross sections in Ne [63]. The spike in the calculations corresponds to the crossing of the Ne 1s threshold. At the highest energy measured, the ratio is ~25 % smaller than predicted by a single-channel, or IPA, calculation (dotted curve), and the discrepancy is expected to increase at higher energies. However, when the 2*s* and 2*p* continuum channels are coupled in a RRPA framework, the calculated ratio agrees perfectly with the measurements (solid curve), indicating that electron correlation plays a critical role at high energy. This counterintuitive result can be understood by considering that, at high energies, photoionization cross sections are known to drop off with energy ($E = h\nu - BE$) as $E^{-(7/2+\ell)}$ in a hydrogenic model, where ℓ is the angular momentum of the ionized electron [64, 65]. Thus, at high enough energy, the Ne 2*s* photoionization cross section will *always* dominate the Ne 2*p* cross section. It is also known that inter-channel coupling between a strong continuum channel and a weak continuum channel leads to the behavior of the weak channel being dictated by the behavior of the strong channel; thus, the high energy behavior of Ne 2*p* photoionization does not follow the IPA predictions. This unexpected result was confirmed in similar experimental and theoretical studies of argon valence photoionization [66] and 3*s*, 3*p*, and 3*d* photoionization in krypton [67]. Breakdown of the IPA is expected for photoionization of any subshell with $\ell > 0$ throughout the Periodic Table. Indeed, it led the authors of one of the studies [66] to state that “the IPA is not valid for most

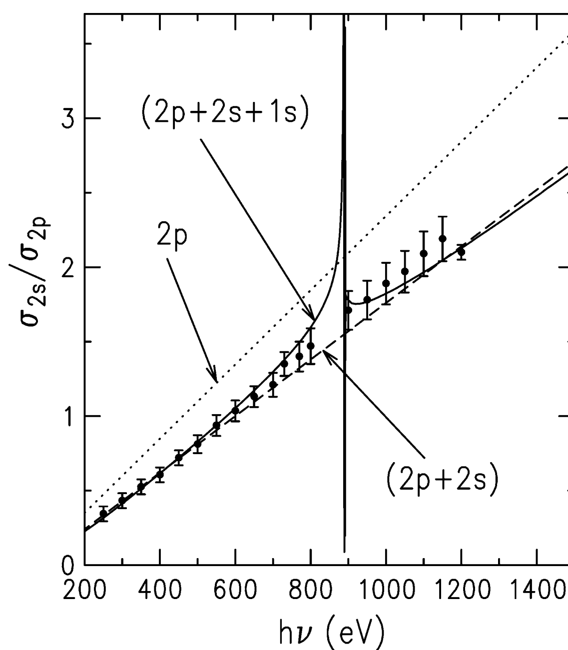

Fig. 4.1 Ratio of the 2*s* to 2*p* cross section for Ne. The calculations employed the RRPA formalism with the single excitation channels arising from 2*p*, 2*s*, and 1*s* coupled (*solid curve*); 2*p* and 2*s* coupled (*dashed curve*); and 2*p* and 2*s* *uncoupled* to each other (*dotted curve*) (from [63], reproduced with permission)

subshells of most atoms at most energies." These results spurred a number of developments [68–71] that have helped place the breakdown of the IPA at high energies on a firm theoretical footing.

4.2.3.2 Molecular Resonant-Auger Emission

More recently, at the SPring-8 SR facility in Japan, a series of gas-phase studies have been performed in the vicinity of the Si 1*s* edge ($\sim$1.85 keV) in a variety of silicon-containing compounds. The first experiments were on 1-trifluorosilyl-2-trimethylsilylethane [$F_3SiCH_2CH_2Si(CH_3)_3$, FSMSE] [72, 73]. This large molecule exhibits several interesting behaviors. For example, the two silicon atoms in the molecule are in very different chemical environments, so, as might be expected, the corresponding Si 1*s* photoemission peaks have quite different chemical shifts; the Si 1*s* HAXPES spectra show two peaks separated by about 4 eV. The photoabsorption spectrum contains three distinct peaks below these two Si 1*s* ionization thresholds, indicating the complex nature of the valence molecular structure of FSMSE. Resonant-Auger spectra collected at these resonances exhibit different degrees of spectator *vs*. "participator" decay, where the term participator refers to cases in which the initially excited electron is involved in the decay process, shifting to a different orbital. If this different orbital is higher in energy, it is referred to as shake-up in the resonant-Auger process, whereas if the different orbital is at lower energy, it is called "shake-down." Excitations at the three different subthreshold resonances in FSMSE also exhibit different probabilities for shake-up and shake-down. The authors cite these behaviors as evidence for site-specific resonant-Auger behavior in a large molecule, where the different chemical environments for the two silicon atoms (one bonded to three fluorine atoms, the other to three methyl groups) are presumed to lead to these variations. Finally, this work introduced 2-D resonant-Auger maps, created by plotting together a large number of near-threshold PES spectra collected as a function of small increments in photon energy, to gas-phase HAXPES.

This work was followed by a series of papers on SiF_4 at the Si *K* edge [74–76], all of which included 2-D HAXPES maps. In this simpler molecule, Si 1*s* excitation to the unoccupied molecular orbital $6t_2$ or to atomic-like Rydberg orbitals leads to different behavior in the resonant-Auger spectra. Specifically, Rydberg excitation may lead to shake-down of the excited electron into a molecular orbital, as well as shake-up into higher Rydberg states, whereas only shake-up is energetically allowed for $6t_2$ excitation [74]. The authors also note that improved energy resolution allows them to use the resonant-Auger spectra to disentangle overlapping excited states observed in photoabsorption, providing a more-detailed view of the electronic structure of the molecule. In contrast to this result, a companion experiment on $Si(CH_3)_4$ [75] did not exhibit any shake-down after Si 1*s* $\rightarrow$ Rydberg excitation. The authors attributed this difference to the fact that the unoccupied orbitals (molecular and Rydberg) in SiF_4 are expected to mix rather strongly, and thus the excited electron will have a higher propensity for changing orbitals during

the subsequent decay process. Finally, the same team performed a similar measurement on $SiCl_4$ [77]. In this case, most of the resonant-Auger decay at the molecular resonance ($9t_2$ for $SiCl_4$) appears to be via spectator transitions, with little evidence of shake-up or shake-down. The authors included density-functional theory (DFT) calculations with this work, which helped to provide a clearer understanding of the excited-state orbitals in the molecule.

4.2.3.3 Electron-Ion Coincidence Measurements

Working at SOLEIL, the French SR facility, Guillemin et al. [78] measured Ar 1*s* photoelectrons in coincidence with argon ions in the photon-energy region just above the *K*-shell threshold. They observed strong PCI shifts in the electron spectra depending on the ultimate degree of ionization of the argon atom, i.e., on the degree of Auger decay following the initial photoionization process. Comparison to theory illustrated that the shifts were related to the ultrafast rates of Auger decay relative to the escape of the slow photoelectron, as expected for PCI.

The experimental (circles) and theoretical (solid lines) results for Ar ions up to Ar^{5+} are shown in Fig. 4.2 [78]. The authors followed up this work with photoelectron-ion coincidence measurements of OCS at the S *K* edge [79], where they observed similar behavior to what was seen in argon. In both cases, PCI shifts observed in the coincident HAXPES spectra were related to the overall degree of ionization of the atom or molecule.

4.2.3.4 Molecular-Frame Photoelectron Angular Distributions

In the soft-X-ray range, it is now fairly common for experiments to measure so-called molecular-frame photoelectron angular distributions (MFPADs), using instruments based on the cold-target recoil-ion momentum-spectroscopy (COLTRIMS) technique or some similar method, such as vector correlation [80–83]. These techniques can perform full coincidence measurements among all the ions and electrons produced by photoionization and fragmentation of a molecule in the gas phase, allowing researchers to construct diagrams of photoelectron angular distributions emitted within the frame of the molecule, rather than just in the laboratory frame. The first, and thus far only, MFPAD measurement in the hard-X-ray range was performed at a few photon energies above the S *K* edge of OCS [84]. The results generally agreed well with DFT calculations [84] and, moreover, demonstrated that such measurements can be done following deep-core-level ionization, despite the larger degree of total ionization produced compared to soft-X-ray energies. In Fig. 4.3 the theoretical and experimental MFPADs are shown, taken at 10 eV above the ionization threshold [84]. Comparison of these results to similar measurements on OCS above other core subshells (O 1*s*, S 2*p*) showed that the S 1*s* and S 2*p* edges exhibit very similar results, suggesting MFPADs collected using hard X-rays are a viable approach.

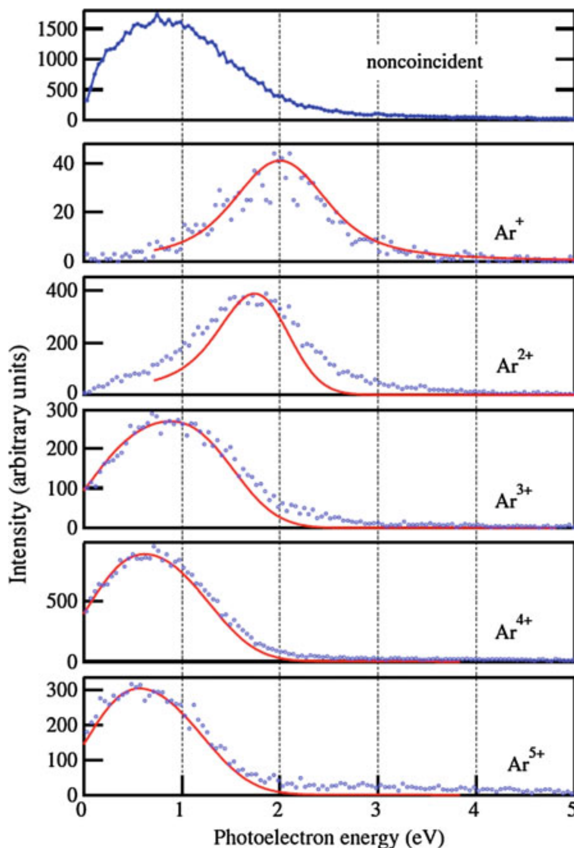

Fig. 4.2 Experimental (*circles*) and theoretical (*solid*) partial photoelectron spectra measured in coincidence with Ar^{n+} ions ($n = 1 - 5$) for excess energy 2 eV above ionization potential (IP). The *top curve* shows the noncoincident photoelectron spectrum (from [78], reproduced with permission)

4.2.3.5 Ultrafast Nuclear Motion

A recent paper [85] uses CH_3Cl as an example to demonstrate that characteristic molecular Auger resonant-Raman effects, such as *nonlinear* dispersion and line narrowing, can be observed using both RIXS and HAXPES at the Cl *K* edge. Both such effects indicate that the chemical bond during the lifetime of the core hole is stretched, and therefore nuclear motion can take place even in a timescale of ∼1 fs, which is the core-hole lifetime. This work is the first clear observation of ultrafast dynamics (bond stretching) using HAXPES. Differences between the results of these complementary radiative and nonradiative methods can be used to gain subtle information about potential curves for the intermediate and final states of the two processes.

In Fig. 4.4 we show the dispersion curves, the relative dispersion and the line width for one specific decay feature in the resonant Auger spectrum (right) or in the RIXS data (left). We observe that the behavior is similar, although the two final states are different (one neutral in RIXS, Cl K-L-type, the other one singly charged

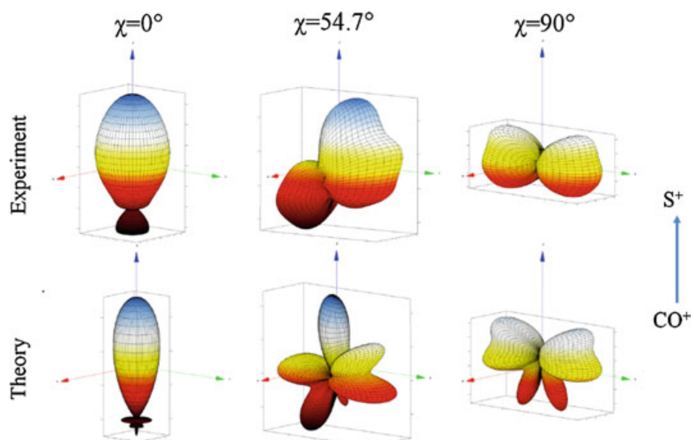

Fig. 4.3 Experimental and theoretical 3D MFPADs at 10 eV above threshold, for three different molecular orientations (from [84], reproduced with permission)

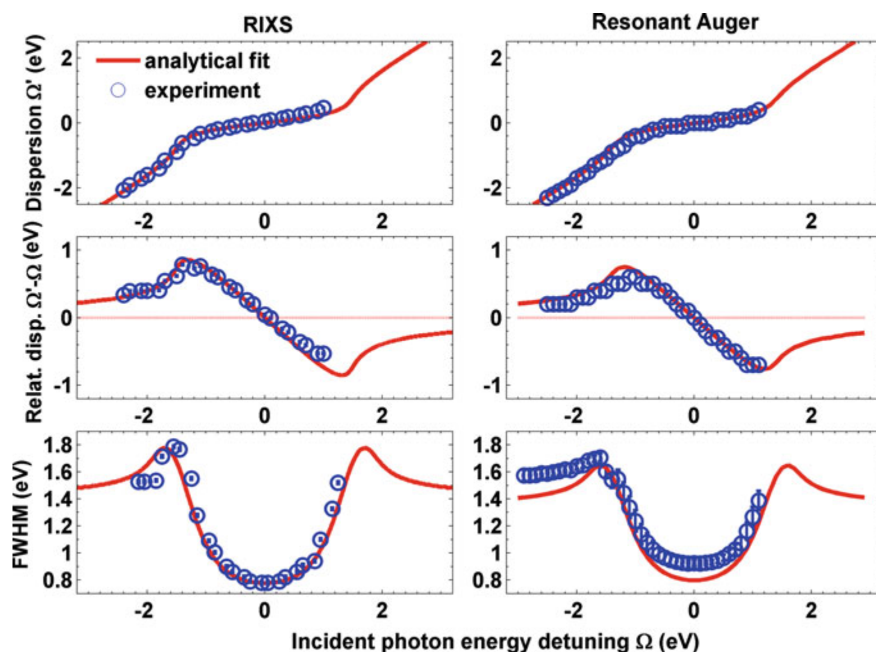

Fig. 4.4 *Top* dispersion; *centre* dispersion relative to the linear dispersion; *bottom* FWHM of the Cl K–L RIXS (*left*) and Cl KLL resonant Auger (*right*) lines as a function of the incident photon energy detuning with respect to the resonance energy. *Solid lines* show simulations for RIXS or resonant-Auger cross section convoluted with the beamline and the spectrometer instrumental function (from [85], reproduced with permission)

in resonant Auger, Cl KLL-type). We observe also that the line narrowing is slightly less pronounced in the resonant Auger data, indicating a different interplay between the potential curves of the intermediate and final states [85].

4.3 Nondipole Effects in HAXPES

The reader is referred to the summary of the well-known DA provided in Section "Photoelectron Angular Distributions Within the Dipole Approximation".

4.3.1 Beyond the Dipole Approximation

Virtually all of the work on nondipole PES described in this chapter focuses on the simplest possible enhancement beyond the DA, i.e., the first-order-nondipole approximation, in which nondipole effects are treated in a perturbative manner [86–92]. At this order, the expansion of $exp(i\mathbf{k}_p \cdot \mathbf{r})$ is truncated after the second term: $1 + \mathbf{k}_p \cdot \mathbf{r}$. Several parameterizations, all equivalent, are available in the literature [86–94]. Due to its ease of comparison with the geometries of modern experiments, the parameterization of Cooper [90] for the differential cross section in the first-order-nondipole approximation (for 100 % linearly polarized light) has been widely adopted:

$$
\begin{aligned}
d\sigma/d\Omega(h\nu) = \sigma(h\nu)/4\pi\{[1 + {}^1\!/\!_2\beta(h\nu) \cdot (3\cos^2\theta - 1)] \\
+ [\delta(h\nu) + \gamma(h\nu)\cos^2\theta] \cdot \sin\theta\cos\phi\},
\end{aligned}
\tag{4.2}
$$

where the first two (dipole) terms are the same as in (4.1). In SR experiments, where the photon beam is horizontal, ϕ is the angle between the propagation vector of the radiation and the projection of the photoelectron vector into the vertical plane containing the X-ray beam. The energy- and subshell-dependent *nondipolar* angular-distribution parameters $\delta(h\nu)$ and $\gamma(h\nu)$ arise from interference terms between the $\boldsymbol{E1}$ interaction and the $\boldsymbol{E2}$ and $\boldsymbol{M1}$ interactions, including their relative phases (see Appendix A in Cooper [92]); "pure" $\boldsymbol{E2}$ and $\boldsymbol{M1}$ effects are not included, hence cross sections are *not* affected at this level of approximation.

The $\boldsymbol{E}1 \cdot \boldsymbol{E}2$ and $\boldsymbol{E}1 \cdot \boldsymbol{M}1$ cross terms generally are non-negligible and can be, in some cases, as large as the dipole $\boldsymbol{E}1^2$ terms. However, these terms contribute only to odd multipoles, leaving the dipolar β parameter unaffected. The presence of the third term in (4.2) leads to *forward/backward asymmetries* in photoejection probability relative to the photon propagation vector $\mathbf{k}$. Because of the presence of cos ϕ in this term, these first-order-nondipole effects do not influence measurements in the so-called 'dipole plane' perpendicular to the propagation vector of the radiation ($\phi = 90°$). In addition, $\boldsymbol{M}1$ interactions vanish in non-relativistic cases, meaning that

deviations from the DA are more likely due to $\boldsymbol{E}1 \cdot \boldsymbol{E}2$ terms. The nondipole parameters can take on any value, but may be restricted by the value of β (e.g., δ = 0 when β = 2). This is in contrast to β, which is restricted to the range $-1 \le \beta \le 2$ regardless of the order of approximation. Finally, to provide scale, a magnitude of ±1 for γ (the sign indicates forward or backward asymmetry) yields approximately a *factor-of-two* redistribution in the number of photoelectrons as a function of direction.

4.3.1.1 Early Developments

Historically, early experiments in PES [95] used photon energies in the hard-X-ray range ($h\nu > 5$ keV). Attention quickly focused on the forward/backward anisotropy observed in photoemission from metal films under irradiation from γ-rays and X-rays from radioactive sources. Deviations from the DA in angle-resolved photoemission at lower X-ray energies, also in the form of forward/backward asymmetries, were first observed by Krause [38] and Wuilleumier and Krause [52] in measurements on rare gases using unpolarized Mg and Al $K\alpha$ X-rays. Early explanations of these results involved the retardation effect, i.e., the effect of finite velocity of the ionizing radiation [37], now recognized as a manifestation of nondipole effects. Soon, explicit retardation calculations [96] exhibited good agreement with the experimental data.

4.3.1.2 General Theoretical Advances

Since the earliest theoretical description [37], extensive efforts have been made to advance the general theory of what are now referred to as 'nondipole effects' in a variety of directions, of which a few examples are noted here. A few years after the initial experimental observations of nondipole angular distributions [38, 52], hazards in using the nonrelativistic DA for all atoms at high energies and for higher-$\boldsymbol{Z}$ atoms even at lower energies were highlighted [96]. At very high photon energies, breakdown of the DA is essentially complete, requiring use of the full Taylor-series expansion for the photon interaction. Under these circumstances the differential cross section can be described by an infinite sum of spherical harmonics [87, 97], where each term includes an independent angular-distribution parameter. In 1980, the general theoretical treatment was enhanced [98] to include spin-polarization, and explicit formulae for angular distributions of photoelectrons emitted from closed-shell atoms were derived. The importance of Cooper minima in dipole photoionization to observing nondipole processes was pointed out by Wang et al. in 1982 [99], who were also the first to show that the nondipole (i.e., quadrupole) channels can experience Cooper minima as well, which was confirmed experimentally with soft X-rays in 2008 [100]. Kabachnik and Sazhina demonstrated in 1996 [101] how nondipole effects can modify the angular distributions of Auger electrons, even though the Auger process occurs subsequent to the original

photoionization event. LaJohn and Pratt [102] showed the importance of atomic screening parameters to the theoretical description of nondipole effects. The general theoretical treatment of nondipole effects was further extended in 1999 to include effects on the spin polarization of the photoelectrons [42], and then in 2001 to include photoemission from polarized atoms and for experiments using magnetic dichroism [103]. More recently, the existence of zeroes in nondipole transition amplitudes at relativistic photon energies was demonstrated [104]. Beyond atomic systems, recent advances have introduced detailed expressions for nondipole photoionization of molecules [105, 106], subsequently including general expressions for fixed-in-space molecules [107].

4.3.2 Atoms

After the initial experimental and computational results noted above, there were no new experimental studies for about two decades, after advances in both X-ray sources and electron-detection schemes were achieved. In the interim, however, significant theoretical and computational effort was undertaken to further elucidate nondipole photoionization. Fairly early, extensive calculations were done over a wide range of $\boldsymbol{Z}$ using a relativistic IPA approach for photon energies as high as 500 keV [97]. In fact, use of the IPA would continue to dominate theoretical studies of nondipole effects for years to come. The same group did similar studies focused on Hg and U [108] and C, Sn, and U [19] up to 100 keV a few years later, then lower-energy calculations, up to 5 keV, for elements with $\boldsymbol{Z} < 40$ [88, 89]. Somewhat later, this group revisited the C, Sn, and U results, extending them up to 200 keV, and showing that, for s subshells only, the combination of relativistic, retardation, and nondipole effects mostly cancel each other to fairly high energies [20] . Notably, this is not true for subshells with $\ell > 0$. Additional nondipole calculations were performed for U [109] up to 200 keV and for C, Ne, Ar, Fe, and Kr up to 20 keV [42]. Finally, a compilation of nondipole angular distribution parameters for several elements at 3 keV photon energy was published in 1990 [87].

4.3.2.1 First SR Experiments

In the mid-1990s, more-extensive measurements began with two instruments specifically designed to measure nondipole effects in gas-phase photoemission using X-ray SR [110, 111]. Focusing on noble-gas core levels (Ar *K* and Kr *K* and *L*) and tunable photon energies in the 2–22 keV range, one group investigated nondipole effects in photoelectron angular distributions [110, 112, 113].

Their results for Ar 1s nondipolar asymmetry parameter are shown in Fig. 4.5 [110]. Incidentally, this was the first gas-phase HAXPES experiment done at a third-generation SR facility. This work demonstrated excellent agreement with IPA predictions [90–92], as well as with later calculations using Dirac-Fock [114] and

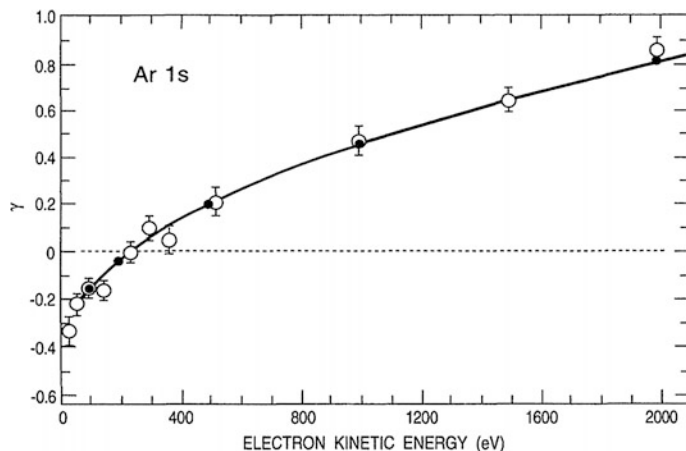

Fig. 4.5 Dependence on electron kinetic energy of measured values of the Ar 1s nondipolar asymmetry parameter γ (*open circles*) compared with Cooper's calculated values (*solid circles* with spline-fit line) (from [110], reproduced with permission)

RPAE [115] methods, confirming dependence of nondipole effects on atomic number and the orbital angular momentum of the emitted electron. These measurements also demonstrated that nondipole effects do not necessarily vanish at threshold. At some kinetic energies, the nondipole angular distributions were observed to be backward directed ($\gamma < 0$), nicely illustrating that nondipole effects are not simply due to a classical transfer of photon momentum to the photoelectron, but result from quantum-mechanical interactions among continuum wavefunctions.

Probing limits of the DA at lower energies (up to 1.2 keV), a second group measured nondipolar angular distributions in Ne 2*s* and 2*p* valence photoionization [116–119]. Nondipole effects were observed at all energies studied, as seen in Fig. 4.6 [117] and agreed fairly well with both IPA [92] and random-phase-approximation [120] predictions, bringing into question the usual assumption (at that time) of the DA in experimental applications of PES near 1 keV.

As noted above, early interpretations of angular distributions in valence-shell-photoemission measurements of neon were treated in a retardation model. The later results on neon prompted a reinterpretation [121] of the early data using the modern nondipole formalism [(4.2), and related equations for unpolarized X-rays]. Not surprisingly, agreement with the more-recent measurements was very good. At even lower photon energies, several other measurements have demonstrated that nondipole effects are visible even in the VUV range. Aside from fundamental interest in the limits of the DA, these observations in atoms suggested relative photoemission peak intensities in many HAXPES measurements could be influenced significantly by nondipole interactions. Indeed, many applications of HAXPES, including gas-phase, surface-science, and materials-science work, likely need to account for breakdowns in the DA.

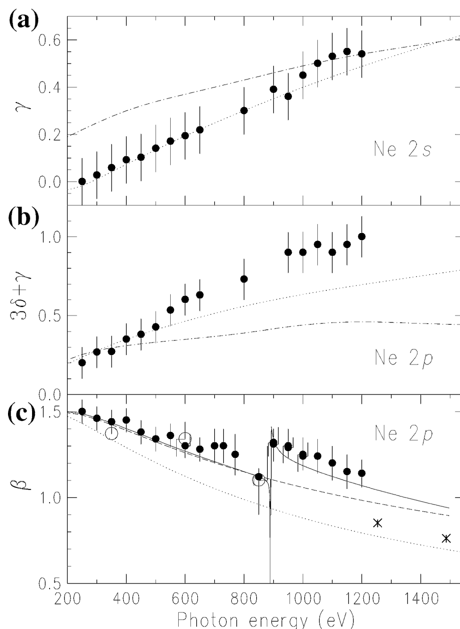

Fig. 4.6 **a** γ parameter for Ne 2s photoemission; **b** 3δ + γ parameters for Ne 2p photoemission; **c** *β* parameter for Ne 2p photoemission (from [117], reproduced with permission)

4.3.2.2 Modern Theoretical Developments

The mid-1990s measurements led to growing interest in nondipole effects at the theoretical level, resulting in a number of more-comprehensive calculations. In the hard-X-ray region, Nefedov et al. published two papers that covered most of the occupied subshells over wide ranges of ***Z***, with photoelectron kinetic energies up to 5 keV [122, 123]. These calculations were performed using a Dirac-Fock IPA model. Shortly after, Amusia et al. focused on n*s* and n*p* subshells in the rare gases at lower kinetic energies (up to 1.6 keV), using both IPA and RPAE methods [124]. Their results agreed well with the then-recent measurements. At about the same time, two similar studies were published, also using both IPA and RPAE formulations, one on Cr 3*d* up to 6 keV [125], the other on the 2*p* subshells of Ne and atomic nitrogen [126]. Altogether, these three papers, in addition to a theoretical study at lower photon energies [127], demonstrated that the IPA is generally less accurate, thus highlighting the importance of electron correlation, manifested as interchannel coupling among continuum-state channels, for a proper description of nondipole photoemission. Indeed, these results indicated that correlation effects can be quite large. For example, in Cr 3*d*, the nondipole angular-distribution parameters showed a 50 % deviation between the RPAE and IPA results at 6 keV [125]. As was already well-known at the time, interchannel coupling is ubiquitous in atomic photoionization within the DA, i.e., in terms of its effects on cross sections and dipolar angular distributions. Indeed, the general lack of validity of the IPA within the DA [66] presaged a similar finding for nondipole effects, challenging the notion that the IPA should always be valid for quadrupole channels.

4.3.2.3 Second-Order Nondipole Effects

To this point, the discussion has been strictly limited to first-order nondipole corrections in which ***E*2**- and ***M*1**-related matrix elements are present only through interference with the dipole terms. However, in the hard-X-ray region, this limitation is likely to lead to an inadequate description of photoelectron angular distributions. Indeed, for a single case, Ne 2*p* photoionization [117], the measured first-order-nondipole parameters were found to be 30 % larger than IPA predictions above 1 keV, a discrepancy ultimately attributed, through close collaboration between theory and experiment [128], to the influence of *second-order-nondipole* processes. Second-order corrections include pure-electric-quadrupole terms, $\boldsymbol{E2^2}$, as well as several interference terms: e.g., ***E*1–*E*3**, ***E*1–*M*2**, ***E*2–*M*1**. Including nondipole effects through second order involves truncating the expansion of *exp* $(i\mathbf{k}_p \cdot \mathbf{r})$ after the third term [of order $(\mathbf{k}_p \cdot \mathbf{r})^2$]. At this level of approximation, the differential cross section for photoionization can be written as [128]:

$$d\sigma/d\Omega(h\nu) = \sigma(h\nu)/4\pi\{1 + {}^1\!/\!_2[\beta(h\nu) + \Delta\beta(h\nu)]\cdot(3\cos^2\theta - 1) + [\delta(h\nu) + \gamma(h\nu)\cos^2\theta]\cdot\sin\theta\cos\phi + {}^1\!/\!_2\eta(h\nu)\cdot(3\cos^2\theta - 1)\cdot\cos2\phi + \mu(h\nu)\cdot\cos2\phi + \xi(h\nu)\cdot(1+\cos2\phi)\cdot P_4(\cos\theta\}, \tag{4.3}$$

introducing four new second-order-nondipole angular-distribution parameters, $\Delta\beta(h\nu)$, $\eta(h\nu)$, $\mu(h\nu)$, and $\xi(h\nu)$, with different angular dependencies. The expression $P_4(\cos\theta)$ refers to the fourth-order Legendre polynomial. Of the six terms on the right-hand side of (4.3), the first two include the usual DA expression (4.1), the third is due solely to first-order nondipole effects (4.2), and the last three terms are due solely to second-order-nondipole processes. In addition, $\Delta\beta$ in the second term is due solely to second-order effects, but it is not distinguishable experimentally from the dipole parameter β. As noted above, the second-order-nondipole parameters arise from terms involving the ***E*1**, ***E*2**, and ***M*1** interactions, as well as the electric-octupole (***E*3**) and magnetic-quadrupole (***M*2**) interactions; typically, the ***E*1–*E*3** (octupole-dipole) and $\boldsymbol{E2^2}$ ("pure" electric-quadrupole) terms are expected to be most important. These parameters can take on any value, but may be restricted by the values of the lower-order parameters, and three of them must satisfy $\eta(h\nu) + \mu(h\nu) + \xi(h\nu) = 0$, meaning that only two new independent second-order parameters can be determined experimentally.

Because of the complex angular dependence of (4.3), the second-order parameters are difficult to extract using existing experimental setups. However, Hemmers et al. [117] were able to measure indirectly the influence of second-order effects in the angular distribution of Ne 2*p* photoelectrons up to 1.2 keV in photon energy. The data were convincing enough to stimulate theoretical interest, and the experiment and calculation demonstrating second-order-nondipole contributions was published jointly in 2000 [128]. The authors noted there is nothing peculiar about neon, and future observations of second-order influences are expected in many other systems. Finally, more-extensive calculations of second-order-nondipole angular-distribution papers have been published for rare gases [129].

4.3.3 Molecules

Compared to atoms, very few molecular nondipole experiments have been published, and molecular theory still has to be fully developed to describe the higher-order photoionization processes in these more complex systems. Indeed, the only molecular study above 1 keV is a comparison of Br 1*s* photoemission from Br_2 and $CBrF_3$ to Kr 1*s* photoemission and to atomic-Br calculations performed within the IPA [130]. Overall, the significant nondipole effects observed for Br 1*s* photoelectrons agreed very well with both the atomic-Br theory and the results from Kr, exhibiting little or no effect attributable to the influence of the molecular environment. This finding was explained as a result of the fact that the X-ray wavelengths used to ionize the Br 1*s* electrons (<1 Å) were smaller than the lengths of the molecular bonds, presumably mitigating any impact of the molecular environment. We note that significant effects due to the molecular nature of the target have been reported at much longer wavelengths [131–136], but this energy range is outside the scope of this Chapter.

4.3.4 Condensed-Phase Systems

A few experiments on atoms or molecules on surfaces have demonstrated that nondipole effects also can be apparent for condensed species. The results were obtained from the interferometric X-ray standing-wave (XSW) technique: a standing wave is generated by overlap between the incident X-rays and X-rays reflected from the substrate. By scanning either the incident angle or the photon energy, the phase of the standing wave shifts and the resulting X-ray absorption varies with the location of an adsorbed atom relative to the substrate. This absorption signature is monitored most directly by measuring the photoemission intensity of the adsorbed species, providing the additional advantage of chemical selectivity. Naturally, photoelectron detection may be influenced by photoelectron angular distributions, and thus by nondipole effects in the hard-X-ray range.

Vartanyants and Zegenhagen [137–139] were the first to analyze, theoretically, the influence of nondipole contributions to the photoelectron yield in XSW measurements. Using a normal-incidence XSW technique, Fisher et al. [140] measured nondipolar effects in the angular distribution of core-level photoemission for atomic iodine adsorbed on Cu(111). By performing photoemission measurements at two different angles relative to the incident radiation, the authors demonstrated that nondipole contributions have a substantial influence on surface structures determined with X-ray standing-waves. The nondipolar effects were $\sim$60 %, much larger than predicted [137]. Considering these results, Woodruff [141] noted that if the spectra were analyzed without considering nondipole effects, then the location of the iodine atom would be determined with a large systematic error of 0.3 Å.

Later, Jackson et al. [142] devised a new and rather simple method, taking advantage of the sensitivity of photoemission-monitored XSW to quadrupole-dipole interferences, to determine nondipole parameters for most elements, and illustrated the method by measuring specific values for C, O, and F 1*s* photoemission. Schreiber et al. [143] used photoemission-monitored XSW to measure relatively strong nondipole effects in C 1s and O 1s photoemission from a sample of perylene-3,4,9,10-tetracarboxylic dianhydride (PTCDA) ($C_{24}H_8O_6$) adsorbed on Ag(111). Finally, by monitoring the angle-resolved photoelectron yield as a function of photon energy near the (11–1) Bragg back-reflection condition of crystalline Ge, the contribution of nondipole effects to Ge 3*p*, Ge 3*d*, and Ge valence-band XSW photoelectron emission was measured. Changes due to nondipole emission were reported in both amplitude and phase of the Ge structure factor relative to the true Ge atomic distribution, and compared to theory [144].

4.4 Recoil Effects in Haxpes

Energy and momentum conservation require that the linear momentum of a photoelectron departing a residual gas-phase ion must be equal to the linear momentum imparted to the ion. For an atom, this results only in a change in the degree of translational momentum for the atomic ion. For a molecule, however, in addition to any change in translational momentum, some of the energy (momentum) may end up as vibrational or rotational excitation of the residual molecular ion, leading to a violation of the Franck-Condon Principle for molecular photoionization. Colloquially, this phenomenon is referred to as “photoelectron recoil,” and the corresponding “recoil momentum” is “imparted” to the ion due to momentum conservation. The first observations of recoil were made at relatively low photon, and thus kinetic, energies, but it is clear that recoil effects will be larger in HAXPES experiments performed at higher photon energies. As a result, HAXPES of molecules, adsorbates, and even solids, will need to consider the influences of recoil effects. The reader is referred to two recent reviews for a more in-depth discussion of this phenomenon [145, 146], including descriptions of the classical and quantum-mechanical models used to analyze PES spectra. Furthermore, recoil will be treated in another chapter of this book (by Y. Kayanuma).

Recoil effects in molecular photoemission were first predicted in 1978 by Domcke and Cederbaum [147] using a quantum-mechanical formalism. The first observation, in C 1*s* photoemission from CH_4 [148] was not made until many years later, after electron-spectroscopy techniques had advanced significantly. The effects in CH_4 appeared as a slight distortion in the vibrationally resolved C 1s PES spectrum that was enhanced as the photon energy was increased from near threshold to 1.2 keV.

The results are shown in Fig. 4.7, where the change in the vibrational substructure of the C 1s photoelectron spectral feature is clearly seen [148]. At low

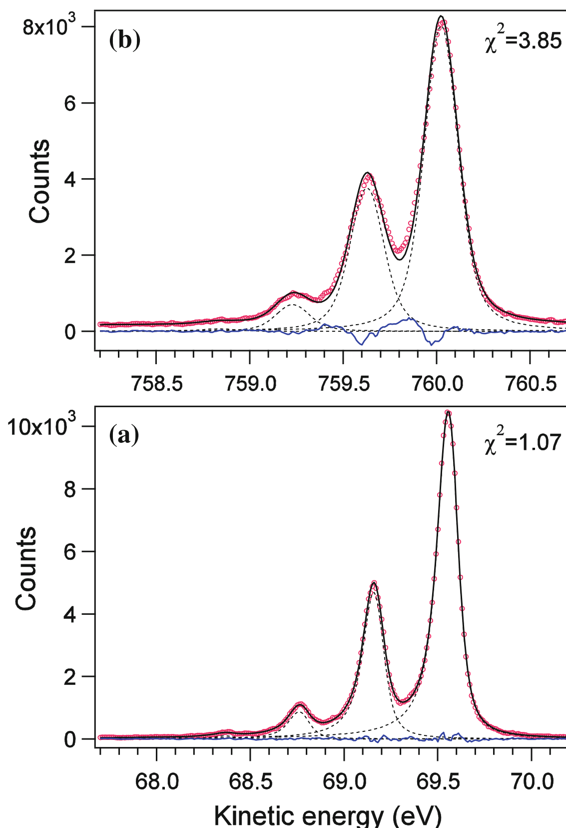

Fig. 4.7 Carbon 1s photoelectron spectra of methane, taken at **a** 360 eV and **b** 1050 eV. *Circles* experiment, *solid lines* modeled spectra, *dashed lines* individual peaks (from [148], reproduced with permission)

photon energies, the spectra included vibrational contributions from only the symmetric-stretching mode, whereas at higher energies the spectra could be fit adequately only by inclusion of contributions from the asymmetric-stretching and bending vibrational modes. These latter modes appear because they include relative motion of the carbon atom with respect to the remainder of the molecule, modes that can only be excited due to recoil momentum. Quantitative modelling of the spectra were achieved using basic classical and quantum-mechanical concepts based ultimately on the conservation of momentum.

Subsequent to this first experiment, C 1*s* photoionization of a different tetrahedral molecule, CF_4, provided a much clearer observation of recoil effects [149]. Several spectra in Fig. 4.8 illustrate the larger recoil effects observed as a function of photon energy [149]. As predicted classically [148], the presence of heavier F atoms around the central carbon, instead of lighter hydrogen atoms, enhances the impact of recoil because the fraction of the momentum transferred to internal motion of the molecular ion increases as the fraction of the molecular mass due to

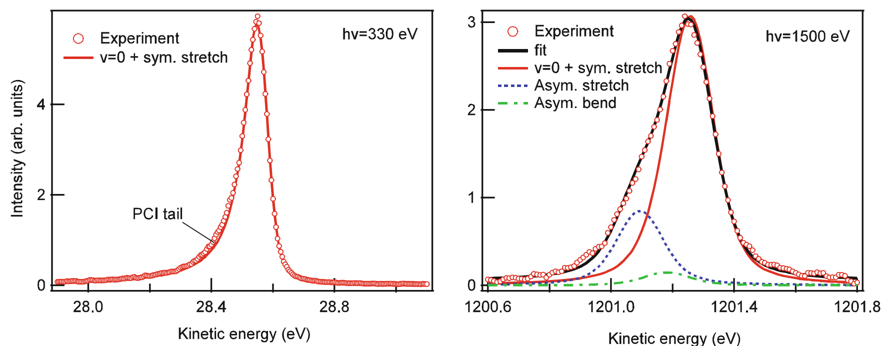

Fig. 4.8 Carbon 1*s* photoelectron spectra of CF_4 at the photon energies indicated. The *open circles* represent the data, the heavy *solid lines* represent least-squares fits to the data using theoretical predictions of the recoil-induced vibrational excitation, and the light *solid lines* show the contribution from the vibrationally unexcited state (from [149b], reproduced with permission)

the initially ionized atom decreases. As a result, the non-Franck-Condon vibrational structure is much more significant in CF_4 than in CH_4 for the same photoelectron kinetic energy. Similarly to methane, it is the asymmetric-stretching mode that is primarily enhanced by recoil, not the symmetric-stretching mode, which does not involve motion of the C atom relative to the center of mass of the molecule.

In contrast to CH_4 and CF_4, which are very well-described by a classical picture, the CO molecule provides an interesting counterexample [150]. Of course, CO has only one vibrational mode, i.e., bond stretching, and even at low photon energies just above the C 1s threshold, the v = 1 vibrationally excited state of the ion has an appreciable intensity (>50 %) in comparison to the v = 0 state. At the highest photon energies studied (up to 1.5 keV), however, the degree of vibrational excitation actually decreases, exhibiting the opposite effect of what is expected due to increasing recoil momentum imparted by the ionized photoelectron. At present, these is no satisfactory explanation for this unexpected result, but it is speculated that it may be due to an interference phenomenon between the "normal Franck-Condon excitation and the recoil-induced excitation" of the v = 1 state [150]. Additional experimental and theoretical work will be needed to clarify this situation.

Finally, in a study of neon at photon energies above 10 keV, the highly energetic 1*s* photoelectron induces significant recoil in the residual neon ion. This induced translational motion leads to observable Doppler shifts in the kinetic energies of subsequent Auger electrons emitted by the ion [151]. The effect is illustrated in Fig. 4.9 [151], where a gradual broadening and finally a splitting of an Auger peak as a function of the emitted photoelectron kinetic energy is clearly seen. This it is expected to be a general phenomenon that could be used to measure angular distributions of high-energy photoelectrons, or perhaps to measure the polarization of radiation with MeV energies.

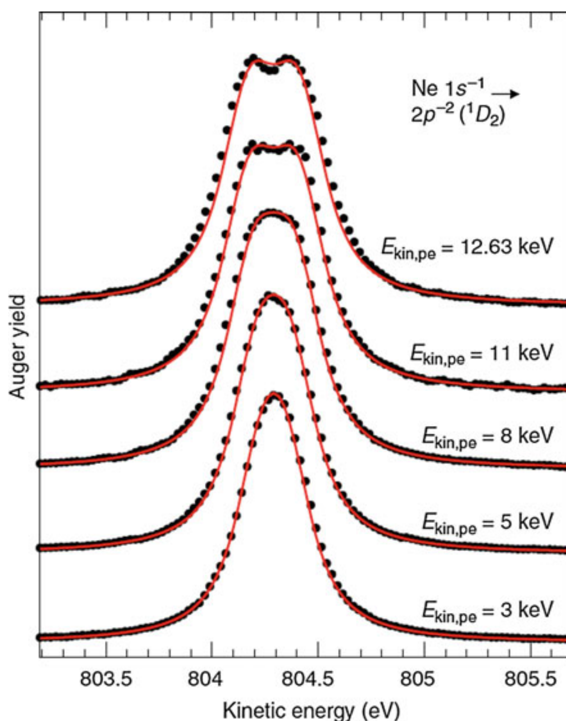

Fig. 4.9 The Ne $1s^{-1} \rightarrow 2p^{-2}(^1D_2)$ Auger transition. The spectra show the results measured subsequent to photoionization with different kinetic energies of the photoelectron between 3 and 12.63 keV. The *solid line* through the data points is a simulation based on a simple model (from [151], reproduced with permission)

4.5 Electronic State-Interference Phenomena

The excitation of an inner-shell electron to a virtual orbital or to the ionization continuum leads to core-hole states which then relax by radiative or non-radiative decays. In general, the deeper the core hole is, the shorter the lifetime, and therefore the larger the natural broadening of the corresponding excited state. If the spacing between core-excited states is of the same order of magnitude as their line width, interferences between several decay channels involving the overlapping excited states and leading to the same final states are possible. For relatively shallow core holes, the lifetime broadening can be comparable to the vibrational spacing of the core-excited state. Such conditions have been verified in some simple molecules for which the contributions of the lifetime-vibrational interferences (LVI) in the resonant Auger spectra have been identified (see e.g., [152, 153] and references therein). This phenomenon causes changes in the vibrational distribution of the final states by modulating the population of the various intermediate-state vibrational levels. Energy shifts can also be observed, due to constructive or destructive interference.

Electronic-state lifetime interferences were described theoretically within a scattering-theory formulation, for the determination of the resonant Auger decay

and X-ray emission cross sections [154]. Experimentally, electronic state-lifetime interferences have also been taken into account for Ne, where a photon-energy dependence of the shake processes was observed in the decay spectra taken at excitation energies between the two $1s^{-1}3p$ and $1s^{-1}4p$ resonances [155]. However, the lack of suitable experimental conditions has hindered up to now the possibility of observing the phenomenon for deep shells.

In a recent paper [156], a study on the argon 1s electron promotion to the first empty orbitals or to the ionization continuum is reported, with state-of-the-art resolution.

A result of the theoretical and experimental analysis in [156] is the clear asymmetry in the pseudo partial cross sections of the $2p^{-2}4p$ and $2p^{-2}5p$ final states reached after resonant Auger decay, together with a relative shift in their maxima. The relative intensities of such final states are shown in Fig. 4.10. These findings are attributed to electronic state-lifetime interference effects. Namely, due to the large lifetime broadening, several intermediate states are coherently excited, which causes interference in the decay processes when the same final states are reached. Such interference manifests itself in the line profile and energy position of final states. It was already theoretically predicted [157], but the corresponding experimental observation was hindered due to the relatively poor experimental conditions previously available.

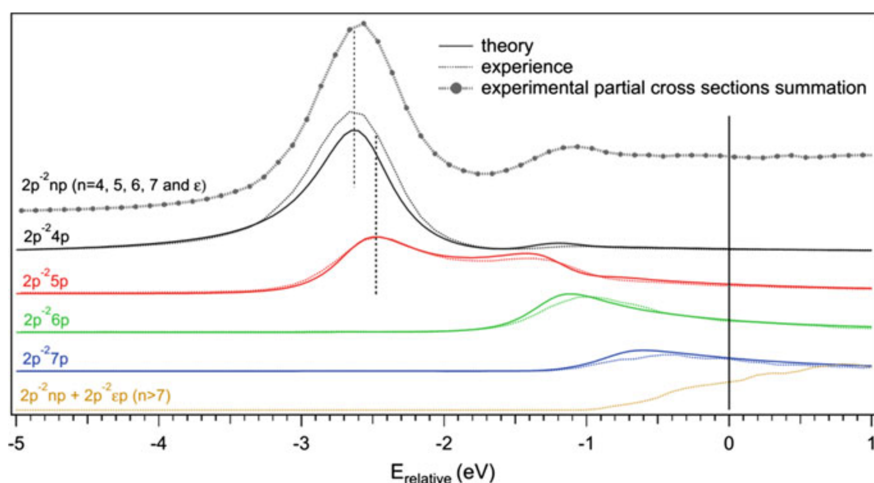

Fig. 4.10 Comparison of experimental (*dashed*) and theoretical (*line*) calculations of the partial cross sections for the lowest-lying Ar K-$L_{23}L_{23}$ resonant Auger lines. The partial cross sections are plotted as a function of photo-excitation energy relative to the Ar K-shell edge. The intensity scale of the theoretical values is normalized to the 4p resonance of the $2p^{-2}5p$ final state. The summation of all partial cross sections including $2p^{-2}np$ ($n > 7$) and $2p^{-2}$ final states is also shown (from [156], reproduced with permission)

4.6 Double-Core-Hole States

Photoemission studies of atoms and molecules with two simultaneous core vacancies, despite the femtosecond-scale decay times, have rapidly expanded in the past few years with the advent of new capabilities in electron spectroscopy and new sources of X-rays, such as the latest generation of synchrotron-radiation (SR) beamlines and X-ray free-electron lasers (FELs). This section briefly describes the current status of this growing area of research.

4.6.1 Atoms

Early work on double-core-hole (DCH) states in rare gases focused on photoabsorption and X-ray-emission studies, and even with these techniques, the results were difficult to obtain experimentally with the X-ray sources available at the time. Perhaps due to the limited availability of experimental data, only a few theoretical calculations were performed until recently, and they focused on Ar *KL* DCH states, both the neutral double-Rydberg states and the singly ionized $K^{-1}L^{-1}n\ell^{+1}$ states [158–160]. In all cases, the theoretical results showed good agreement with the measurements available at the time.

Following these pioneering efforts, complementary photoemission measurements in atoms had to await the development of the X-ray FEL at the Linac Coherent Light Source (LCLS). The very first publication [161] on gases from this next-generation light source focused on sequential multiphoton ionization of the neon atom, using up to 6 X-ray photons to fully strip an atom of its 10 electrons. Primary evidence for the production of $1s^{-2}$ DCH ("hollow-atom") states was a combination of ion-yield spectroscopy and detailed theoretical predictions of the cascade of decays from such states. Corroborating evidence came from HAXPES measurements ($h\nu$ up to 2 keV) using the electron—time-of-flight technique to collect the spectra. Because this technique collects almost all electron kinetic energies simultaneously, the spectra also included Auger electrons emitted by the DCH states, a clear signature that such states were produced.

More-refined results on sequentially produced DCH states in neon [162, 163], also using the LCLS, have since been obtained using a magnetic-bottle electron analyzer with nearly 4π of solid-angle collection. In a magnetic bottle time-of-flight spectrometer, electrons ejected in nearly any direction are guided by the divergent field of a strong permanent magnet into a solenoid, whose field lines they follow to a multi-channel-plate detector. The method of partial covariance mapping was applied to these new data to extract a more-complete picture of the ionization processes involved in the decay of the DCH states. The authors note that similar analysis techniques will be needed in order to use X-ray FEL sources to image large systems, such as biomolecules. Neon, then, can act as a fundamental example of how to achieve this sort of detailed analysis.

4.6.2 Molecules

For molecular DCH states, Cederbaum et al. [164] predicted some time ago that the presence and location of one core hole affects the energy to produce a second core hole, as well as influencing the decay of the resulting DCH states. These states can be formed either with both vacancies on a single atomic site (SS) in the molecule or with the two vacancies on different atomic sites (two-site, TS). While experimentally more challenging, an important motivation for studying TS-DCH states is because they probe the local chemical environment more sensitively than either single-core-hole (SCH) or SS-DCH states. This enhanced sensitivity originates from the fact that the double ionization potential of TS-DCH states is coupled directly to the changes induced in the valence charge distribution at the different atomic sites due to the presence of the other core vacancy [164–166]. Ultimately, the capability to measure binding energies of TS-DCH states will provide an extremely sensitive probe of the chemical environment in a molecule. Two recent reviews, one on molecular experiments [167] and the other on theoretical developments [168], are recommended for the reader seeking more detail on the topics in this section.

4.6.2.1 SR Studies

The first SR-based HAXPES experiment demonstrating the observation of DCH states in molecules was published in 2010 on CH_4 and NH_3 [169]. Naturally, production of these states via single-photon absorption has a very low cross section ($\sim 10^{-3}$ of the SCH cross section for SS-DCH, and $\sim 10^{-5}$ for TS-DCH [169, 170]), requiring instrumentation with high collection efficiency for success. This first experiment used a magnetic-bottle spectrometer based on time-of-flight analysis and multi-coincidence detection to collect up to five electrons from a single event in order to achieve the high efficiency needed. The key results are based on triple-coincidence measurements of two photoelectrons and one Auger electron after C K^{-2} or N K^{-2} DCH ionization, thus determining directly the ionization energy necessary to remove both 1*s* electrons from each molecule. The same group later did a similar measurement on H_2O [171].

Complementary results on DCH states in N_2 created by single-photon photoabsorption using SR were soon published by Lablanquie et al. [170]. Similar results were also presented for O 1*s* SS-DCH states in the molecules CO, CO_2, and O_2. All of these results were obtained with a magnetic-bottle spectrometer similar to the one mentioned above, but this work focused on coincidence detection of four electrons (2 photoelectrons, 2 Auger electrons) from the same event. The experiments succeeded not only in determining DCH photoionization probabilities, but they also revealed other information, such as chemical shifts and the dynamics of the formation and decay of the DCH states. As previously noted, compared to SCH states, DCH states show significantly enhanced chemical shifts. Large shifts were seen in

this work, and they were reproduced quite well by theory [170]. Another result from this work is a spectrum of DCH states, obtained by taking a histogram of the coincidence data summed over the kinetic energies of the two photoelectrons, which is directly analogous to a conventional SCH photoemission spectrum. An interesting result from comparing the SCH and DCH spectra is that the satellite structure is considerably more intense in the DCH case, which was attributed to the stronger perturbation affecting the valence electrons when two core electrons are removed instead of just one.

The first observation of a TS-DCH state using single-photon excitation, although it is an extremely low-probability process, was reported by Lablanquie et al. [172] in a study of C_2H_2. While the authors clearly observed SS-DCH states, as they were able to do in their earlier paper [170] for other molecules, by focusing on 3-electron (2 photoelectrons, one Auger electron) coincidences, they could see a very weak photoemission peak corresponding to a TS-DCH state. The energy of this peak also matched extremely well with the predicted value [172].

Recently, Nakano et al. [173] have done more-extensive studies on the molecular series C_2H_{2n}, using triple-electron coincidence measurements to look at the $K^{-2}V^{+1}$ SS-DCH "satellite" states (V = valence). The term satellite is used to indicate that these states can be thought of as shake-up states in which the 'shaken' electron is one of the two C 1*s* electrons in the DCH state. In effect, the resulting spectra of singly ionized molecular states can be thought of as constituting the Near-Edge X-ray Absorption Fine Structure (NEXAFS) spectrum of a molecule with a single C *K* vacancy, offering a new means of studying the spectroscopy of exotic species.

In Fig. 4.11 we show experimental (left) and calculated (right) $K^{-2}V$ spectra for the series of molecules C_2H_6–C_2H_4–C_2H_2, with the related spectral assignment [173].

4.6.2.2 FEL Studies

The first FEL-based HAXPES experiment on DCH states in molecules focused on N_2 and was performed at the LCLS [174]. While creation of DCHs using SR relies entirely on generally weak electron-correlation effects, FEL-based studies take advantage of the high instantaneous brightness of the source to achieve sequential two-photon or multiphoton absorption. With enough brightness and a sufficiently short photon pulse, it is feasible to produce multiple core-electron vacancies within the time scale dictated by the rapid Auger-decay process inherent to core vacancies. This first experiment [174] searched for evidence for production of both SS-DCH and TS-DCH states in molecular nitrogen. Using photon energies of 1.0 and 1.1 keV and a relatively long (280 fs) FEL pulse duration compared to the N_2 Auger-decay lifetime (6.4 fs), the authors observed complex photoelectron spectra representing a multitude of ionization and decay pathways, not all of which are attributable to either SS-DCH or TS-DCH states. Detailed analysis of the complex spectra clearly identified a photoemission peak near the theoretically predicted [174] kinetic energy for photoionization of a 1*s* electron from a nitrogen atom in the

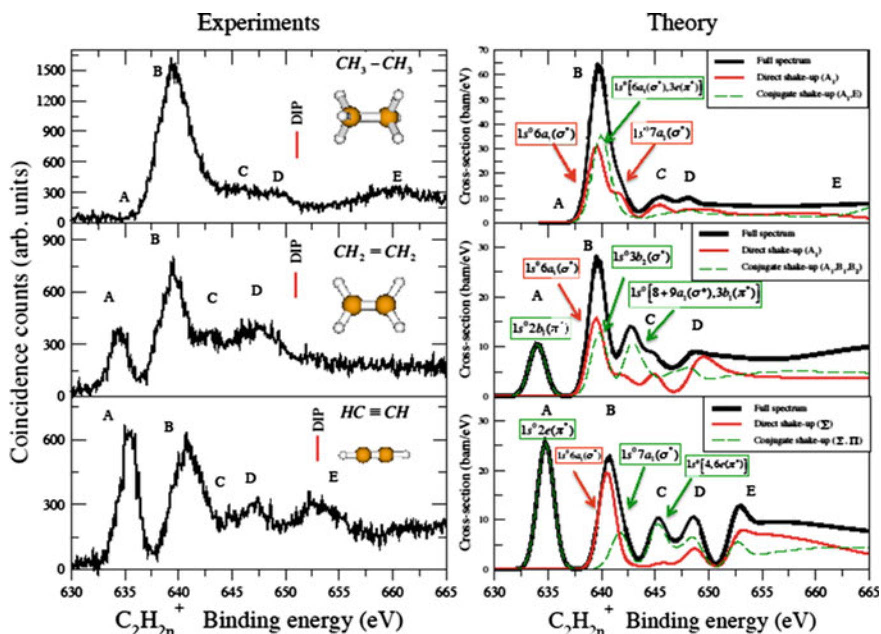

Fig. 4.11 *Left* Experimental $K^{-2}V$ spectra recorded at a photon energy of 770 eV. The position of the core double ionization potential (DIP) is indicated. *Right* Absolute theoretical $K^{-2}V$ cross sections (from [173], reproduced with permission)

molecule that had already had the other 1*s* electron removed (i.e., SS-DCH). However, this energy is close to the calculated positions of peaks associated with core ionization of triply ionized atomic nitrogen, and these processes cannot be distinguished in the HAXPES spectra. In contrast, the predicted position of the similar photoelectron peak for a TS-DCH state lies in a congested area of the spectra and could not be identified; only an upper limit on the production of such states could be determined.

The first unambiguous observation of a TS-DCH state using multiphoton excitation at a FEL was reported the same year in measurements on CO [175]. The related spectra are shown in Fig. 4.12, together with the identification of the SS-DCH and TS-DCH states. This result was achieved by tuning the X-ray pulse intensity and duration to provide partial control of the multiphoton excitation processes at a femtosecond level. By using X-ray pulse durations comparable to the Auger decay rates in the molecule, the intensity of the X-rays from the LCLS is high enough to allow core electrons on different atoms to each absorb a photon in competition with Auger decay. By choosing a duration time shorter than the typical SCH state lifetime, the SCH Auger cascade is suppressed, and the formation of DCH states is actively enhanced. The production of a TS-DCH state was then characterized by HAXPES and Auger-electron spectroscopy, and its energy agreed well with calculations [165]. This work also was able to provide a first demonstration of the future

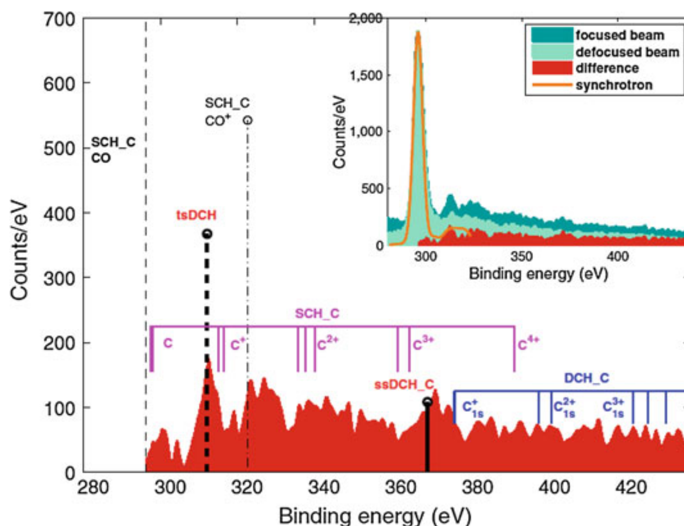

Fig. 4.12 Photoelectron spectra of carbon recorded at 700 eV photon energy, approximately 10 fs pulse duration. Calculated state energies and intensities are marked by vertical *thick lines* with head markers: tsDCH (*dashed line*), ssDCH (*solid line*), and SCH of CO^+ with a valence hole (*dash-dotted*) (from [175], reproduced with permission)

feasibility of using TS-DCH states for chemical applications. Following up on this work, the authors performed similar measurements of SS-DCH and TS-DCH states for a number of small molecules, in order to begin a systematic study of chemical shifts [176, 177]. The main goal was to demonstrate the predictive power of DCH spectroscopy in unraveling details of charge fluctuation after core ionization, essentially a modern reinterpretation of the chemical shift first described in the early ESCA measurements [2].

4.6.2.3 Theory

On the theoretical side, work by Santra et al. [178] underlined the importance of sequential two-photon absorption to create DCH states. Subsequently, Tashiro et al. thoroughly investigated *K*-shell DCH states of many small closed-shell [165] and open-shell [166] molecules. They inferred that the interatomic relaxation energy, a crucial parameter for probing the chemical environment, may be obtained by measuring both the relevant SCH ionization potentials and the TS-DCH double ionization potentials. Working on somewhat larger systems, Kryzhevoi et al. [179] investigated SCH and DCH states in para-, meta-, and ortho-aminophenol, clearly showing that these isomers may be distinguishable by DCH spectroscopy. In even larger systems, DFT has been applied to nucleobase molecules to calculate DCH and SCH states [180].

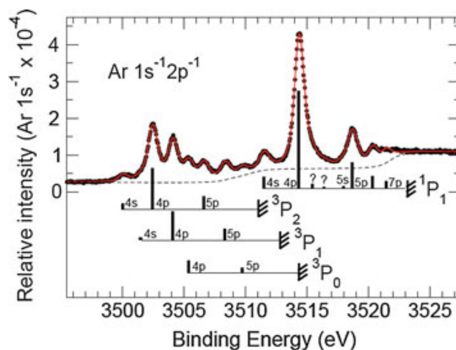

Fig. 4.13 The $1s^{-1}2p^{-1}$ DCH shake-up photoelectron spectrum of argon, relative to the intensity of Ar $1s^{-1}$ photoionization. The *solid curve* through the data points is a fit, and the *dashed curve* represents the background. The *bar* diagrams indicate positions and intensities of Rydberg series converging to the four different ionization thresholds (from [181], reproduced with permission)

4.6.2.4 Recent SR Developments

A very recent HAXPES study at synchrotron SOLEIL has unraveled the possibility of detecting Ar^+ $1s^{-1}2p^{-1}n\ell^{+1}$ ($n \geq 4$) and Ar^+ $1s^{-1}2s^{-1}n\ell^{+1}$ states, where ℓ represents either an *s* or *p* Rydberg electron. These are single-ion states, so only one photoelectron is emitted, producing what could be described as a core "shake-up" state, e.g., 1*s* photoionization accompanied by shake-up of a core 2*p* electron to the $n\ell$ Rydberg orbital. In this case, an entire Rydberg series could be measured, from which double-core ionization thresholds could be determined accurately. A different perspective, if one assumes the 1*s* and 2*p* core holes are coupled weakly, is to consider the series of $1s^{-1}2p^{-1}n\ell$ states as similar to the photoabsorption of an Ar^+ ion with a vacancy in the 2*p* subshell, i.e., the spectrum observed in HAXPES would be analogous to the NEXAFS spectrum of a singly ionized argon atom [181].

In Fig. 4.13 we show the detailed photoelectron spectrum in the region of Ar^+ $1s^{-1}2p^{-1}n\ell^{+1}$ with the related assignment [181]. We can assign four Rydberg series converging to the four thresholds of the Ar^+ $1s^{-1}2p^{-1}$double core-hole states.

4.7 Future Prospects in Atomic and Molecular Haxpes

As noted in Sect. 4.1, after the era of the ESCA technique, atomic and molecular HAXPES experienced several decades when the emphasis in gas-phase research was in the soft-X-ray range and when successful experiments were extremely difficult with the existing X-ray sources and PES instrumentation. Recently, this situation has changed dramatically. At some of the newer SR sources, hard-X-ray beamlines are being or have been developed that provide access and instrumentation for the atomic and molecular community. The past few years have also seen the

operation of the first X-ray FEL, with more likely to come in the future. So, the high-brightness and high-resolution sources needed for a thriving gas-phase HAXPES community are now available. These new facilities can be coupled with new analyzers designed and developed specifically to study high-energy electrons, while maintaining the high-resolution and high-throughput necessary for meaningful results. It is our opinion that gas-phase HAXPES is approaching a period of rapid growth, both in the number of practitioners and in the number of new phenomena to be discovered with the technologies now available. This renaissance in the field is surely to be accompanied by resurgence in interest in theoretical efforts as novel experimental results appear.

The remainder of this section takes a look into the crystal ball and offers a few examples of possible advances in experimental atomic and molecular HAXPES in the near future. The topics include the focus areas described in the previous three sections, as well as two others (ultrafast dynamics and studies of fixed-in-space molecules) that have received much interest in the soft-X-ray range, but, as of yet, little has been reported in the hard-X-ray range.

4.7.1 Nondipole Effects

The best way to study nondipole effects in gases is with angle-resolved PES, and HAXPES is a natural choice because, at higher energies, the momentum of the photon increases, enhancing the likelihood of significant nondipole influences on the photoionization process. This is also a fertile direction to pursue because of the paucity of results in the hard-X-ray range.

In atoms, at least in the rare gases, the current situation is one of excellent agreement between theory and experiment, suggesting that there is little left to learn in these textbook cases. However, the number of experimental measurements to date is perhaps too few to jump to this conclusion, and further studies are warranted on the rare gases in a few cases. For example, all of the HAXPES measurements reported thus far are on 1*s*, 2*s*, or 2*p* subshells of Ne, Ar, or Kr, and agreement with theory is near-perfect. In the heavier rare gases, it is known that *d* subshells often have more interchannel coupling and other correlation effects that may influence nondipole effects, and this seems like a reasonable extension of existing experiments. Another area where surprises may await is in the vicinity of resonances and thresholds, where channels often couple and new effects appear. No HAXPES results of this nature have yet been reported. Going beyond the rare gases, for which theory seems to have a good handle, no measurements have been reported on open-shell atoms, obviously due to the difficulty of such experiments. However, if they become feasible, it is likely that new effects, related to the open-shell electronic structure, would be observed.

Nondipole studies in molecular HAXPES have been limited to Br 1*s* photoemission from two compounds, Br_2 and $CBrF_3$, in which the nondipole behavior of the Br 1*s* photoelectrons was indistinguishable from that expected of the bromine

atom. Again, this is a very limited data set from which to draw any conclusions, and further work needs to be done on a wider variety of molecules, with a focus on different elements and different subshells, including the valence shell.

In the hard-X-ray regime, it is more likely that nondipole effects beyond first-order will become more prominent as the photon momentum increases. In fact, at photon energies beyond 5–10 keV, second-order-nondipole amplitudes are likely to be as large as those for first-order, and even comparable to the dipole amplitudes. However, as one can deduce from (4.3) in Sect. 4.3, the geometry of most current gas-phase PES and HAXPES instruments is unsuitable to measure higher-order effects, so new experimental geometries for SR experiments will be required for progress in this area. On the other hand, multi-photon processes, common using X-rays from a FEL, will naturally enhance the importance of second- and high-order nondipole processes. As far as we know, no such measurements have been attempted.

4.7.2 Recoil Effects

The existing examples of recoil effects in molecular HAXPES provide an interesting contrast. On the one hand, there are examples like CH_4 and CF_4, where the results agree extremely well with an essentially classical picture of momentum conservation when a photoelectron departs a molecule. On the other hand, there is the example of CO, in which the behavior is exactly opposite to what this classical picture predicts. Clearly more examples are called for, both in the geometry of the molecules studies and in the relative masses of the constituent atoms, in order to understand the systematics of this phenomenon. The use of HAXPES is an obvious choice for such experiments, but it will be necessary to strive for the highest possible photon and kinetic-energy resolutions feasible.

Another option would be to measure high resolution Auger spectra at very high photon energy. The recoil effect leaves the ion in vibrational and/or rotational excitation which is probed by the Auger spectrum. Such studies have been started with the CO molecule up to 12 keV of photon energy [182].

4.7.3 Double-Core-Hole Studies

Section 4.5 outlined the heroic experimental efforts undertaken so far to observe DCH photoionization in molecules. These pioneering experiments either had to use complex multi-electron coincidence techniques using SR or required beamtime at an X-ray FEL to be successful. In our view, the next advance for these studies is to develop capabilities to study DCH states via single-channel HAXPES at a SR facility, in which measurement of a single photoelectron can reveal the spectroscopy

of these highly excited molecular states. Of course, such studies will require a very efficient experimental setup including a high-brightness and high-resolution source and an efficient PES apparatus. Fortunately, such combinations exist, and we are aware of current experiments that are pursuing this type of study.

Based on the Ar prototypical case [181], it is easy to imagine similar measurements on DCH states in Ne ($1s^{-2}n\ell$), and Kr ($2p^{-1}3d^{-1}n\ell$), to name a few. More generally, molecules also should exhibit singly charged DCH states, such as chlorine-containing compounds (CH_3Cl, CF_3Cl), silicon compounds (SiF_4, $SiCl_4$), as well as species studied already (CO, N_2, C_2H_2). The advent of single-channel HAXPES studies of DCH states at SR facilities should open up a whole new field of research. Studies of molecules also open the possibility of studying TS-DCH states in more detail than has been possible previously.

Finally, production of DCH states is easier with an X-ray FEL source. The challenge, in this case, is understanding the complex spectra obtained, because many single-photon and multiphoton processes occur simultaneously and contribute to the HAXPES spectra. For future DCH studies at a FEL, significant progress may require incorporating coincidence techniques in order to unravel the contributions from specific DCH states.

4.7.4 Ultrafast Dynamics

To date, only one HAXPES measurement has clearly demonstrated the effects of ultrafast nuclear motion following hard-X-ray excitation [85]. The deep core excited CH_3Cl molecule around the chlorine K shell does exhibit the carbon-chlorine chemical bond elongation in the 1-femtosecond time range. In contrast, observations of ultrafast dynamics and fragmentation have enjoyed a bountiful history in the soft-X-ray regime. The seminal paper in this area focused on inner-shell excitation of HBr [183]. This work illustrated that excitation of a Br $3d$ electron to the strongly anti-bonding σ* orbital in the molecule leads to competition between emission of an electron via resonant-Auger decay of the molecular core-excited state and ultrafast photofragmentation of the molecule into neutral H and Br*. The core-excited Br* atoms were identified by their characteristic atomic resonant-Auger decay peaks, which are narrower and shifted in energy relative to the molecular resonant-Auger lines. The generality of this phenomenon was soon demonstrated by studies of similar halogenated compounds [184].

As a starting point for discussion, we review a few highlights of ultrafast-dynamics research in the soft-X-ray range. First of all, a trio of experiments [185–187] explored the consequences of ultrafast dissociation with higher resolution, finding that some features in the PES spectra showed behavior characteristic of the Auger resonant-Raman effect. Kukk et al. [185] observed that the molecular resonant-Auger peaks exhibited line narrowing, whereas the atomic resonant-lines, appearing after ultrafast fragmentation occurred, did not. By tuning the photon

energy across the relevant anti-bonding resonance, Simon et al. [187] noted that participator resonant-Auger decay dispersed linearly with photon energy, while lines due to spectator decay did not. Similarly, detuning from the resonance leads to significant changes in the relative intensities of atomic versus molecular resonant-Auger decay in HCl [188], with the atomic lines decreasing at energies away from the peak of the resonance. This observation is in accord with the notion of an "effective duration time," first described by [188], and the results have been treated with different theoretical models [189–191]. Finally, Feifel et al. [192] demonstrated that under certain conditions, it is possible to observe interference phenomena between the atomic and molecular resonant-Auger lines, if the overall final states of the different decay processes are the same.

Two results in the hard-X-ray range, but not involving HAXPES measurements, deserve mention. First, ion-yield measurements at the Cl *K* edge of HCl [193] showed a strong propensity for the production of neutral H atoms at the Cl $1s \rightarrow 6\sigma^*$ anti-bonding resonance, suggesting the possibility of ultrafast fragmentation in competition with the decay of the Cl *K* hole, despite its ~1 fs lifetime. Second, RIXS measurements at the I $2p$ edges of CH_3I observed line-narrowing and nonlinear-dispersion effects [194], albeit small ones, characteristic of ultrafast nuclear motion, even though the lifetime of the core-excited state is only ~200 as.

These latter non-HAXPES experiments provide hope that the effects of ultrafast dynamics should be visible in HAXPES spectra of small molecules. Certainly, the showcase system of HCl would be a good starting point, based both on the mystery of the existing ion-yield measurements [193] and on the extensive theoretical effort that has been applied to this molecule at lower energies near the Cl $2p$ edge. Likewise, CH_3I, having already exhibited ultrafast nuclear motion via RIXS, should be a viable candidate for similar evidence in HAXPES. Also, the soft-X-ray results that showed different behavior for spectator and participator resonant-Auger decay [186] and interference between atomic and molecular resonant-Auger lines [192] suggest possible directions of research in molecular HAXPES. Finally, a variety of molecules should be studied in order to identify any trends as a function of the excitation process, geometry, and mass of the atomic constituents.

4.7.5 Molecular-Frame Photoelectron Angular Distributions (MFPADs)

The only hard-X-ray measurements of MFPADs were performed on OCS [78] and CS_2 [195]. They demonstrated the feasibility of such experiments in this energy range, even though the average degree of ionization following emission of a S $1s$ photoelectron is around four. This high degree of ionization guarantees nearly complete fragmentation of the molecule into cationic species, meaning that there are typically a large number of charged particles (4–8) that could be measured in coincidence. On the other hand, this implies a much richer domain of possible

fragmentation patterns, electron-electron interactions, and other phenomena, that could be studied in the hard-X-ray range. We expect this type of multi-coincidence experiment to yield a plethora of new HAXPES results over the next few years.

Acknowledgments The authors wish to thank S.T. Manson for a careful reading of the manuscript, and B. Krässig, S. Carniato, O. Hemmers and E. Kukk for providing good-quality copies of their figures.

References

1. A. Einstein, Ann. Phys. **17**, 132 (1905)
2. K. Siegbahn, C. Nordling, G. Johansson, J. Hedman, P.F. Hedén, K. Hamrin, U. Gelius, T. Bergmark, L.O. Werme, R. Manne, Y. Baer, *ESCA Applied to Free Molecules* (North-Holland, Amsterdam, 1971)
3. N. Mårtensson, S. Svensson, U. Gelius, J. Phys. B: At. Mol. Opt. Phys. **20**, 6243 (1987). (And references therein)
4. W.R. Alling, W.R. Johnson, Phys. Rev. **139**, 1050 (1965)
5. H.R. Hulme, J. McDougall, R.A. Buckingham, R.H. Fowler, Proceedings of the Royal Society of London series A—Mathematical and Physical Sciences 149 0131 (1935)
6. W. Heitler, *The Quantum Theory of Radiation* (Clarendon Press, Oxford, 1954)
7. H.A. Bethe, E.E. Salpeter, *Quantum Mechanics of One- and Two-Electron Atoms* (Springer 1957)
8. R.H. Pratt, Phys. Rev. **117**, 1017 (1960)
9. R.H. Pratt, Phys. Rev. **119**, 1619 (1960)
10. S. Hultberg, B. Nagel, P. Olsson, Arkiv. Fysik. **20**, 555 (1961)
11. R.H. Pratt, Phys. Rev. **134**, A898 (1964)
12. J.J. Matese, W.R. Johnson, Phys. Rev. **140**, A1 (1965)
13. G. Rakavy, A. Ron, Phys. Lett. **19**, 207 (1965)
14. H. Hall, E. Sullivan, Phys. Rev. **152**, 4 (1967)
15. G. Rakavy, A. Ron, Phys. Rev. **159**, 50 (1967)
16. R.D. Schmickley, R.H. Pratt, Phys. Rev. **164**, 104 (1967)
17. R.H. Pratt, A. Ron, H.K. Tseng, Rev. Modern Phys. **45**, 273 (1973)
18. A. Ron, Y.S. Kim, R.H. Pratt, Phys. Rev. A **24**, 1260 (1981)
19. Y.S. Kim, R.H. Pratt, A. Ron, Phys. Rev. A **24**, 1889 (1981)
20. A. Ron, I.B. Goldberg, J. Stein, S.T. Manson, R.H. Pratt, R.Y. Yin, Phys. Rev. A **50**, 1312 (1994)
21. J.W. Cooper, Phys. Rev. **128**, 681 (1962)
22. U. Fano, J.W. Cooper, Rev. Mod. Phys. **40**, 441 (1968)
23. M.S. Wang, R.H. Pratt, Phys. Rev. A **29**, 174 (1984)
24. L.A. LaJohn, R.H. Pratt, Phys. Rev. A **67**, 032701 (2003)
25. F. Combet Farnoux, C. R. Acad. Sci. **264B**, 1728 (1967)
26. S.T. Manson, J.W. Cooper, Phys. Rev. **165**, 126 (1968)
27. E. Storm, H.I. Israel, NDT **A7**, 565 (1970)
28. J.H. Scofield, J. Electron Spectrosc. Relat. Phenom. **8**, 129 (1976). (And references therein)
29. S.T. Manson, AIP Conf. Proc. **94**, 321 (1982)
30. Q. Dong, Y. Kuang, R.H. Pratt, Nuclear Instrum. Meth. A **280**, 189 (1989)
31. MYa. Amusia, L.V. Chernysheva, V.G. Yarzhemsky, J. Exp. Theo. Phys. Lett. **97**, 704 (2013)
32. C.N. Yang, Phys. Rev. **74**, 764 (1948)
33. J. Cooper, R.N. Zare, J. Chem. Phys. **48**, 942 (1968)

34. R.F. Reilman, A. Msezane, S.T. Manson, J. Electron Spectrosc. Relat. Phenom. **8**, 389 (1976)
35. I.M. Band, Y.I. Kharitomov, M.B. Trhaskovskaya, At. Data Nucl. Data Tables **23**, 443 (1979)
36. J.J. Yeh, I. Lindau, At. Data Nucl. Data Tables **32**, 1 (1985)
37. J.W. Cooper, S.T. Manson, Phys. Rev. **177**, 157 (1969)
38. M. Krause, Phys. Rev. **177**, 151 (1969)
39. V. Radojevic, W.R. Johnson, Phys. Lett. A **97**, 335 (1983)
40. S.T. Manson, J. Electron Spectrosc. Relat. Phenom. **9**, 21 (1976)
41. J.W. Cooper, Phys. Rev. A **38**, 3417 (1988)
42. A. Bechler, R.H. Pratt, J. Phys. B: At. Mol. Opt. Phys. **32**, 2889 (1999)
43. J.W. Cooper, Phys. Rev. A **9**, 2236 (1974)
44. B. Craseman, P.E. Koblas, T.C. Wang, H.E. Birdseye, M.H. Chen, Phys. Rev. A **9**, 1143 (1974)
45. G.S. Brown, M.H. Chen, B. Crasemann, G.E. Ice, Phys. Rev. Lett. **45**, 1937 (1980)
46. C.J. Sparks, Phys. Rev. Lett. **33**, 262 (1974)
47. P. Eisenberger, P.M. Platzman, H. Winick, Phys. Rev. Lett. **36**, 623 (1976)
48. Y.B. Bannett, I. Freund, Phys. Rev. Lett. **34**, 372 (1975)
49. D.W. Lindle, B. Crasemann, Nucl. Instrum. Meth. B **56**, 441 (1991)
50. T. Lebrun, S.H. Southworth, G.B. Armen, M.A. MacDonald, Y. Azuma, Phys. Rev. A **60**, 4667 (1999)
51. P.H. Kobrin, S.H. Southworth, C.M. Truesdale, D.W. Lindle, U. Becker, D.A. Shirley, Phys. Rev. A **29**, 194 (1984)
52. F. Wuilleumier, M.O. Krause, Phys. Rev. A **10**, 242 (1974)
53. K.G. Dyall, J. Phys. B: At. Mol. Opt. Phys. **16**, 3137 (1983)
54. G.B. Armen, T. Åberg, Kh. R. Karim, J.C. Levin, B. Crasemann, G.S. Brown, M.H. Chen, G.E. Ice, Phys. Rev. Lett. **54**, 182 (1985)
55. S.H. Southworth, T. LeBrun, Y. Azuma, K.G. Dyall, J. Electron Spectrosc. Relat. Phenom. **94**, 33 (1998)
56. G.B. Armen, T. Åberg, J.C. Levin, B. Crasemann, M.H. Chen, G.E. Ice, G.S. Brown, Phys. Rev. Lett. **54**, 1142 (1985)
57. T.A. Ferrett, D.W. Lindle, P.A. Heimann, H.G. Kerkhoff, U.E. Becker, D.A. Shirley, Phys. Rev. A **34**, 1916 (1984)
58. J.C. Levin, C. Biedermann, N. Keller, L. Liljeby, C.-S. O, R. T. Short, I. A. Sellin, D.W. Lindle, Phys. Rev. Lett. **65**, 988 (1990)
59. J.C. Levin, C. Biedermann, N. Keller, L. Liljeby, R.T. Short, I.A. Sellin, D.W. Lindle, Nucl. Instr. Meth. B **56/57**, 124 (1991)
60. G.B. Armen, J.C. Levin, I.A. Sellin, Phys. Rev. A **53**, 772 (1996)
61. D.W. Lindle, W.L. Manner, L. Steinbeck, E. Villalobos, J.C. Levin, I.A. Sellin, J. Electron Spectrosc. Relat. Phenom. **67**, 373 (1994)
62. U. Arp, T. LeBrun, S.H. Southworth, M.A. MacDonald, M. Jung, Phys. Rev. A **55**, 4273 (1997)
63. E.W.B. Dias, H.S. Chakraborty, P.C. Deshmukh, S.T. Manson, O. Hemmers, P. Glans, D.L. Hansen, H. Wang, S.B. Whitfield, D.W. Lindle, R. Wehlitz, J.C. Levin, I.A. Sellin, R.C.C. Perera, Phys. Rev. Lett. **78**, 4553 (1997)
64. A.F. Starace, in Handbuch der Physik, edited by W. Mehlhorn (Springer, Berlin, 1982), Vol. 31, pp. 1–121
65. M.Ya. Amusia, *Atomic Photoeffect* (Plenum Press, New York, 1990)
66. D.L. Hansen, O. Hemmers, H. Wang, D.W. Lindle, P. Focke, I.A. Sellin, C. Heske, H.S. Chakraborty, P.C. Deshmukh, S.T. Manson, Phys. Rev. A **60**, R2641 (1999)
67. H.S. Chakraborty, D.L. Hansen, O. Hemmers, P.C. Deshmukh, P. Focke, I.A. Sellin, C. Heske, D.W. Lindle, S.T. Manson, Phys. Rev. A **63**, 042708 (2001)
68. M.Ya. Amusia, N.B. Avdonina, E.G. Drukarev, S.T. Manson, R.H. Pratt, Phys. Rev. Lett. **85**, 4703 (2000)

69. N.B. Avdonina, E.G. Drukarev, R.H. Pratt, Phys. Rev. A **65**, 052705 (2002)
70. E.G. Drukarev, R.H. Pratt, Phys. Rev. A **72**, 062701 (2005)
71. E.G. Drukarev, R.H. Pratt, Phys. Rev. A **80**, 013406 (2009)
72. I.H. Suzuki, A. Nitta, H. Fukuzawa, K. Ueda, O. Takahashi, Y. Tamenori, S. Nagaoka, J. Chem. Phys. **131**, 164309 (2009)
73. S. Nagaoka, A. Nitta, Y. Tamenori, H. Fukuzawa, K. Ueda, O. Takahashi, T. Kakiuchi, Y. Kitajima, K. Mase, I.H. Suzuki, J. Electron Spectrosc. Relat. Phenom. **175**, 14 (2009)
74. I.H. Suzuki, Y. Kono, A. Ikeda, T. Ouchi, K. Ueda, O. Takahashi, I. Higuchi, Y. Tamenori, S. Nagaoka, Phys. Rev. A **82**, 045401 (2010)
75. I.H. Suzuki, Y. Kono, A. Ikeda, T. Ouchi, K. Ueda, O. Takahashi, I. Higuchi, Y. Tamenori, S. Nagaoka, J. Chem. Phys. **134**, 084312 (2011)
76. I.H. Suzuki, Y. Kono, A. Ikeda, M. Oi, T. Ouchi, K. Ueda, Y. Tamenori, O. Takahashi, S. Nagaoka, J. Chem. Phys. **138**, 024302 (2013)
77. I.H. Suzuki, Y. Kono, K. Sakai, M. Kimura, K. Ueda, Y. Tamenori, O. Takahashi, S. Nagaoka, J. Phys. B: At. Mol. Opt. Phys. **46**, 075101 (2013)
78. R. Guillemin, S. Sheinerman, C. Bomme, T. Marin, L. Journel, T. Marchenko, R.K. Kushawaha, N. Trcera, M.N. Piancastelli, M. Simon, Phys. Rev. Lett. **109**, 013001 (2012)
79. C. Bomme, R. Guillemin, S. Sheinerman, T. Marin, L. Journel, T. Marchenko, R.K. Kushawaha, N. Trcera, M.N. Piancastelli, M. Simon, J. Phys. B: At. Mol. Opt. Phys. **46**, 215101 (2013)
80. E. Shigemasa, J. Adachi, M. Oura, A. Yagishita, Phys. Rev. Lett. **74**, 359 (1995)
81. A.V. Golovin, F. Heiser, C.J.K. Quayle, P. Morin, M. Simon, O. Gessner, P.-M. Guyon, U. Becker, Phys. Rev. Lett. **79**, 4554 (1997)
82. A. Lafosse, M. Lebech, J.C. Brenot, P.M. Guyon, O. Jagutzki, L. Spielberger, M. Vervloet, J.C. Houver, D. Dowek, Phys. Rev. Lett. **84**, 5987 (2000)
83. T. Jahnke, L. Foucar, J. Titze, R. Wallauer, T. Osipov, E.P. Benis, A. Alnaser, O. Jagutzki, W. Arnold, S.K. Semenov, N.A. Cherepkov, L.Ph.H. Schmidt, A. Czasch, A. Staudte, M. Schöffler, C.L. Cocke, M.H. Prior, H. Schmidt-Böcking, R. Dörner, Phys. Rev. Lett. **93**, 083002 (2004)
84. C. Bomme, R. Guillemin, T. Marin, L. Journel, T. Marchenko, N. Trcera, R.K. Kushawaha, M.N. Piancastelli, M. Simon, M. Stener, P. Decleva, J. Phys. B: At. Mol. Opt. Phys. **45**, 194005 (2012)
85. M.N. Piancastelli, G. Goldsztejn, T. Marchenko, R. Guillemin, R.K. Kushawaha, L. Journel, S. Carniato, J.-P. Rueff, D. Céolin, M. Simon, J. Phys. B: At. Mol. Opt. Phys. **47**, 124031 (2014)
86. J.H. Scofield, Phys. Rev. A **40**, 3054 (1989)
87. J.H. Scofield, Phys. Scripta **41**, 59 (1990)
88. A. Bechler, R.H. Pratt, Phys. Rev. A **39**, 1774 (1989)
89. A. Bechler, R.H. Pratt, Phys. Rev. A **42**, 6400 (1990)
90. J.W. Cooper, Phys. Rev. A **42**, 6942 (1990)
91. J.W. Cooper, Phys. Rev. A **45**, 3362 (1992)
92. J.W. Cooper, Phys. Rev. A **47**, 1841 (1993)
93. M.Ya. Amusia, P.U. Arifov, A.S. Baltenkov, A.A. Grinberg, S.G. Shapiro, Phys. Lett. A **47**, 66 (1974)
94. M. Ya. Amusia, A.S. Baltenkov, A.A. Grinberg, S.G. Shapiro, Zh. Éksp. Teor. Fiz. 68 28 (1975) Sov. Phys. JETP **41**, 14 (1975)
95. P. Auger, F. Perrin, J. Phys. Rad. **8**, 93 (1927)
96. A. Ron, R.H. Pratt, H.K. Tseng, Chem. Phys. Lett. **47**, 377 (1977)
97. H.K. Tseng, R.H. Pratt, S. Yu, A. Ron, Phys. Rev. A **17**, 1061 (1978)
98. K.N. Huang, Phys. Rev. A **22**, 223 (1980)
99. M.S. Wang, Y.S. Kim, R.H. Pratt, A. Ron, Phys. Rev. A **25**, 857 (1982)
100. P.C. Deshmukh, T. Banerjee, H.R. Varma, O. Hemmers, R. Guillemin, D. Rolles, A. Wolska, S.W. Yu, D.W. Lindle, W.R. Johnson, S.T. Manson, J. Phys. B: At. Mol. Opt. Phys. **41**, 021002 (2008)

101. N.M. Kabachnik, I.P. Sazhina, J. Phys. B: At. Mol. Opt. Phys. **29**, L515 (1996)
102. L.A. LaJohn, R.H. Pratt, Phys. Rev. A **58**, 4989 (1998)
103. A.N. Grum-Grzhimailo, J. Phys. B: At. Mol. Opt. Phys. **34**, L359 (2001)
104. L.A. LaJohn, R.H. Pratt, Rad. Phys. Chem. **71**, 665 (2004)
105. A.N. Grum-Grzhimailo, J. Phys. B: At. Mol. Opt. Phys. **36**, 2385 (2003)
106. N.A. Cherepkov, S.K. Semenov, Int. J. Quantum Chem. **107**, 2889 (2007)
107. A.N. Grum-Grzhimailo, R.R. Lucchese, X.-J. Liu, G. Prümper, Y. Morishita, N. Saito, K. Ueda, J. Electron Spectrosc. Relat. Phenom. **155**, 100 (2007)
108. Y.S. Kim, R.H. Pratt, A. Ron, H.K. Tseng, Phys. Rev. A **22**, 567 (1980)
109. R.H. Pratt, L. LaJohn, Nucl. Instrum. Meth. B **99**, 1 (1995)
110. B. Krässig, M. Jung, D.S. Gemmell, E.P. Kanter, T. LeBrun, S.H. Southworth, L. Young, Phys. Rev. Lett. **75**, 4736 (1995)
111. O. Hemmers, S.B. Whitfield, P. Glans, H. Wang, D.W. Lindle, R. Wehlitz, I.A. Sellin, Rev. Sci. Instrum. **69**, 3809 (1998)
112. M. Jung, B. Krässig, D.S. Gemmell, E.P. Kanter, T. LeBrun, S.H. Southworth, L. Young, Phys. Rev. A **54**, 2127 (1996)
113. B. Krässig, J.-C. Bilheux, R.W. Dunford, D.S. Gemmell, S. Hasegawa, E.P. Kanter, S.H. Southworth, L. Young, L.A. LaJohn, R.H. Pratt, Phys. Rev. A **67**, 022707 (2003)
114. M.B. Trzhaskovskaya, V.K. Nikulin, V.I. Nefedov, V.G. Yarzhemsky, J. Phys. B: At. Mol. Opt. Phys. **34**, 3221 (2001)
115. M. Ya Amusia, A.S. Baltenkov, Z. Felfli, A.Z. Msezane, Phys. Rev. **A59**, R2544 (1999)
116. O. Hemmers, P. Glans, D.L. Hansen, H. Wang, S.B. Whitfield, D.W. Lindle, R. Wehlitz, J.C. Levin, I.A. Sellin, R.C.C. Perera, Synchrotron Rad. News **9**, 40 (1996)
117. O. Hemmers, G. Fisher, P. Glans, D.L. Hansen, H. Wang, S.B. Whitfield, R. Wehlitz, J.C. Levin, I.A. Sellin, R.C.C. Perera, E.W.B. Dias, H.S. Chakraborty, P.C. Deshmukh, S.T. Manson, D.W. Lindle, J. Phys, B: At. Mol. Opt. Phys **30**, L727 (1997)
118. O. Hemmers, M. Blackburn, T. Goddard, P. Glans, H. Wang, S.B. Whitfield, R. Wehlitz, I.A. Sellin, D.W. Lindle, J. Electron Spectrosc. Relat. Phenom. **123**, 257 (2002)
119. D.W. Lindle, O. Hemmers, P. Glans, D.L. Hansen, H. Wang, S.B. Whitfield, R. Wehlitz, J.C. Levin, I.A. Sellin, R.C.C. Perera, Indian J. Phys. **B71**, 325 (1997)
120. W.R. Johnson, A. Derevianko, K.T. Cheng, V.K. Dolmatov, S.T. Manson, Phys. Rev. A **59**, 3609 (1999)
121. D.W. Lindle, O. Hemmers, J. Electron Spectrosc. Relat. Phenom. **100**, 297 (1999)
122. V.I. Nefedov, V.G. Yarzhemsky, I.S. Nefedova, M.B. Trzhaskovskaya, J. Electron Spectrosc. Relat. Phenom. **113**, 191 (2000)
123. V.I. Nefedov, V.G. Yarzhemsky, I.S. Nefedova, M.B. Trzhaskovskaya, I.M. Band, J. Electron Spectrosc. Relat. Phenom. **107**, 123 (2000)
124. M.Ya. Amusia, A.S. Baltenkov, L.V. Chernysheva, Z. Felfli, A.Z. Msezane, Phys. Rev. A **63**, 052506 (2001)
125. V.K. Dolmatov, S.T. Manson, Phys. Rev. A **63**, 022704 (2001)
126. V.K. Dolmatov, A.S. Baltenkov, S.T. Manson, Phys. Rev. A **64**, 042718 (2001)
127. W.R. Johnson, K.T. Cheng, Phys. Rev. A **63**, 022504 (2001)
128. A. Derevianko, O. Hemmers, S. Oblad, P. Glans, H. Wang, S.B. Whitfield, R. Wehlitz, I.A. Sellin, W.R. Johnson, D.W. Lindle, Phys. Rev. Lett. **84**, 2116 (2000)
129. A. Derevianko, W.R. Johnson, K.T. Cheng, At. Data Nucl. Data Tables **73**, 153 (1999)
130. S.H. Southworth, R.W. Dunford, E.P. Kanter, B. Krässig, L. Young, L.A. LaJohn, R.H. Pratt, Rad. Phys. Chem. **75**, 1574 (2006)
131. O. Hemmers, H. Wang, P. Focke, I.A. Sellin, D.W. Lindle, J.C. Arce, J.A. Sheehy, P.W. Langhoff, Phys. Rev. Lett. **87**, 273003 (2001)
132. R. Guillemin, O. Hemmers, D.W. Lindle, E. Shigemasa, K. Le Guen, D. Céolin, C. Miron, N. Leclercq, P. Morin, M. Simon, P.W. Langhoff, Phys. Rev. Lett. **89**, 033002 (2002)
133. O. Hemmers, R. Guillemin, D. Rolles, A. Wolska, D.W. Lindle, E.P. Kanter, B. Krässig, S.H. Southworth, R. Wehlitz, P.W. Langhoff, V. McKoy, B. Zimmermann, J. Electron Spectrosc. Relat. Phenom. **144**, 155 (2005)

134. K. Hosaka, J. Adachi, A.V. Golovin, M. Takahashi, T. Teramoto, N. Watanabe, A. Yagishita, S.K. Semenov, N.A. Cherepkov, J. Phys. B: At. Mol. Opt. Phys. **39**, L25 (2006)
135. K. Hosaka, J. Adachi, A.V. Golovin, M. Takahashi, T. Teramoto, N. Watanabe, T. Jahnke, Th Weber, M. Schöffler, L. Schmidt, T. Osipov, O. Jagutzki, A.L. Landers, M.H. Prior, H. Schmidt-Böcking, R. Dörner, A. Yagishita, S.K. Semenov, N.A. Cherepkov, Phys. Rev. A **73**, 022716 (2006)
136. P. Bolognesi, D. Toffoli, P. Decleva, V. Feyer, L. Pravica, L. Avaldi, J. Phys. B: At. Mol. Opt. Phys. **41**, 221002 (2008)
137. I.A. Vartanyants, J. Zegenhagen, Nuovo Cimento **19D**, 617 (1997)
138. I.A. Vartanyants, J. Zegenhagen, Phys. St. Sol. B **215**, 819 (1999)
139. I.A. Vartanyants, J. Zegenhagen, Solid State Commun. **115**, 161 (2000)
140. C.J. Fisher, R. Ithin, R.G. Jones, G.J. Jackson, D.P. Woodruff, B.C.C. Cowie, J. Phys.: Condens. Matter **10**, L623 (1998)
141. D.P. Woodruff, J. Electron Spectrosc. Relat. Phenom. **100**, 259 (1999)
142. G.J. Jackson, B.C.C. Cowie, D.P. Woodruff, R.G. Jones, M.S. Kariapper, C. Fisher, A.S.Y. Chan, M. Butterfield, Phys. Rev. Lett. **84**, 2346 (2000)
143. F. Schreiber, K.A. Ritley, I.A. Vartanyants, H. Dosch, J. Zegenhagen, B.C.C. Cowie, Surf. Sci. **486**, L519 (2001)
144. E.J. Nelson, J.C. Woicik, P. Pianetta, I.A. Vartanyants, J.W. Cooper, Phys. Rev. B **65**, 165219 (2002)
145. E. Kukk, T.D. Thomas, K. Ueda, J. Electron Spectrosc. Relat. Phenom. **183**, 53 (2011)
146. E. Kukk, K. Ueda, C. Miron, J. Electron Spectrosc. Relat. Phenom. **185**, 278 (2012)
147. W. Domcke, L.S. Cederbaum, J. Electron Spectrosc. Relat. Phenom. **13**, 161 (1978)
148. E. Kukk, K. Ueda, U. Hergenhahn, X.-J. Liu, G. Prümper, H. Yoshida, Y. Tamenori, C. Makochekanwa, T. Tanaka, M. Kitajima, H. Tanaka, Phys. Rev. Lett. **95**, 133001 (2005)
149. (a) T.D. Thomas, E. Kukk, R. Sankari, H. Fukuzawa, G. Prümper, K. Ueda, R. Püttner, J. Harries, Y. Tamenori, T. Tanaka, M. Hoshino, H. Tanaka, J. Chem. Phys. **128**, 144311 (2008); (b) E. Kukk, T. D. Thomas, K. Ueda, J. Phys.: Conf. Ser. **194,** 012007 (2009)
150. T.D. Thomas, J. Electron Spectrosc. Relat. Phenom. **189**, 3 (2013)
151. M. Simon, R. Püttner, T. Marchenko, R. Guillemin, R.K. Kushawaha, L. Journel, G. Goldsztejn, M.N. Piancastelli, J.M. Ablett, J.-P. Rueff, D. Céolin, Nature Comm. **5**, 4069 (2014)
152. M. Neeb, J.-E. Rubensson, M. Biermann, W. Eberhardt, J. Electron Spectrosc. Relat. Phenom. **67**, 261 (1994)
153. M.N. Piancastelli, J. Electron Spectrosc. Relat. Phenom. **107**(1), 1 (2000)
154. A. Cesar, H. Ågren, Phys. Rev. A **45**, 2833 (1992)
155. J.-E. Rubensson, M. Neeb, A. Bringer, M. Biermann, W. Eberhardt, Chem. Phys. Lett. **257**, 447 (1996)
156. D. Céolin, T. Marchenko, R. Guillemin, L. Journel, R. Kushawaha, S. Carniato, S.-M. Huttula, J.-P. Rueff, G.B. Armen, M.N. Piancastelli, M. Simon, Phys. Rev. A **91**, 022502 (2015)
157. G.B. Armen, H. Aksela, T. Åberg, S. Aksela, J. Phys. B: At. Mol. Opt. Phys. **33**, R49 (2000)
158. U. Kuetgens, J. Hormes, Phys. Rev. A **44**, 264 (1991)
159. M. Deutsch, N. Maskil, W. Drube, Phys. Rev. A **46**, 3963 (1992)
160. M. Štuhec, A. Kodre, M. Hribar, D. Glavič-Cindro, I. Arčon, W. Drube, Phys. Rev. A **49**, 3104 (1994)
161. L. Young, E.P. Kanter, B. Krassig, Y. Li, A.M. March, S.T. Pratt, R. Santra, S.H. Southworth, N. Rohringer, L.F. DiMauro, G. Doumy, C.A. Roedig, N. Berrah, L. Fang, M. Hoener, P.H. Bucksbaum, J.P. Cryan, S. Ghimire, J.M. Glownia, D.A. Reis, J.D. Bozek, C. Bostedt, M. Messerschmidt, Nature **466**, 7302 (2010)
162. L.J. Frasinski, V. Zhaunerchyk, M. Mucke, R.J. Squibb, M. Siano, J.H.D. Eland, P. Linusson, P.v.d. Meulen, P. Salén, R.D. Thomas, M. Larsson, L. Foucar, J. Ullrich, K. Motomura, S. Mondal, K. Ueda, T. Osipov, L. Fang, B.F. Murphy, N. Berrah, C. Bostedt,

J.D. Bozek, S. Schorb, M. Messerschmidt, J.M. Glownia, J.P. Cryan, R.N. Coffee, O. Takahashi, S. Wada, M.N. Piancastelli, R. Richter, K.C. Prince, R. Feifel, Phys. Rev. Lett. **111**, 073002 (2013)
163. V. Zhaunerchyk, M. Mucke, P. Salén, P.v.d. Meulen, M. Kaminska, R.J. Squibb, L. J. Frasinski, M. Siano, J.H.D. Eland, P. Linusson, R.D. Thomas, M. Larsson, L. Foucar, J. Ullrich, K. Motomura, S. Mondal, K. Ueda, T. Osipov, L. Fang, B.F. Murphy, N. Berrah, C. Bostedt, J.D. Bozek, S. Schorb, M. Messerschmidt, J.M. Glownia, J.P. Cryan, R.N. Coffee, O. Takahashi, S. Wada, M.N. Piancastelli, R. Richter, K.C. Prince, R. Feifel, J. Phys. B: At. Mol. Opt. Phys. **46**, 164034 (2013)
164. L.S. Cederbaum, F. Tarantelli, A. Sgamellotti, J. Schirmer, J. Chem. Phys. **85**, 6513 (1986)
165. M. Tashiro, M. Ehara, H. Fukuzawa, K. Ueda, C. Buth, N.V. Kryshevoi, L.S. Cederbaum, J. Chem. Phys. **132**, 184302 (2010)
166. M. Tashiro, M. Ehara, K. Ueda, Chem. Phys. Lett. **496**, 217 (2010)
167. M.N. Piancastelli, Eur. Phys. J. Special Topics **222**, 2035 (2013)
168. K. Ueda, O. Takahashi, J. Electron Spectrosc. Relat. Phenom. **185**, 301 (2012). (And references therein)
169. J.H.D. Eland, M. Tashiro, P. Linusson, M. Ehara, K. Ueda, R. Feifel, Phys. Rev. Lett. **105**, 213005 (2010)
170. P. Lablanquie, F. Penent, J. Palaudoux, L. Andric, P. Selles, S. Carniato, K. Bučar, M. Žitnik, M. Huttula, J.H.D. Eland, E. Shigemasa, K. Soejima, Y. Hikosaka, I.H. Suzuki, M. Nakano, K. Ito, Phys. Rev. Lett. **106**, 063003 (2011)
171. M. Mucke, J.H.D. Eland, O. Takahashi, P. Linusson, D. Lebrun, K. Ueda, R. Feifel, Chem. Phys. Lett. **558**, 82 (2013)
172. P. Lablanquie, T.P. Grozdanov, M. Žitnik, S. Carniato, P. Selles, L. Andric, J. Palaudoux, F. Penent, H. Iwayama, E. Shigemasa, Y. Hikosaka, K. Soejima, M. Nakano, I.H. Suzuki, K. Ito, Phys. Rev. Lett. **107**, 193004 (2011)
173. M. Nakano, P. Selles, P. Lablanquie, Y. Hikosaka, F. Penent, E. Shigemasa, K. Ito, S. Carniato, Phys. Rev. Lett. **111**, 123001 (2013)
174. L. Fang, M. Hoener, O. Gessner, F. Tarantelli, S.T. Pratt, O. Kornilov, C. Buth, M. Gühr, E.P. Kanter, C. Bostedt, J.D. Bozek, P.H. Bucksbaum, M. Chen, R. Coffee, J. Cryan, M. Glownia, E. Kukk, S.R. Leone, N. Berrah, Phys. Rev. Lett. **105**, 083005 (2010)
175. N. Berrah, L. Fang, B. Murphy, T. Osipov, K. Ueda, E. Kukk, R. Feifel, P.v.d. Meulen, P. Salén, H.T. Schmidt, R.D. Thomas, M. Larsson, R. Richter, K.C. Prince, J.D. Bozek, C. Bostedt, S.-I. Wada, M.N. Piancastelli, M. Tashiro, M. Ehara, Proc. Natl. Acad. Sci. U.S.A. **108**, 16912 (2011)
176. P. Salén, P.v.d. Meulen, H.T. Schmidt, R.D. Thomas, M. Larsson, R. Feifel, M.N. Piancastelli, L. Fang, B. Murphy, T. Osipov, N. Berrah, E. Kukk, K. Ueda, J.D. Bozek, C. Bostedt, S. Wada, R. Richter, V. Feyer, K.C. Prince, Phys. Rev. Lett. **108**, 153003 (2012)
177. M. Larsson, P. Salén, P.v.d. Meulen, H.T. Schmidt, R.D. Thomas, R. Feifel, M.N. Piancastelli, L. Fang, B. Murphy, T. Osipov, N. Berrah, E. Kukk, K. Ueda, J.D. Bozek, C. Bostedt, S. Wada, R. Richter, V. Feyer, K.C. Prince, J. Phys. B: At. Mol. Opt. Phys. **46**, 164034 (2013)
178. R. Santra, N.V. Kryzhevoi, L.S. Cederbaum, Phys. Rev. Lett. **103**, 013002 (2009)
179. N.V. Kryzhevoi, R. Santra, L.S. Cederbaum, J. Chem. Phys. **135**, 084302 (2011)
180. O. Takahashi, M. Tashiro, M. Ehara, K. Yamasaki, K. Ueda, J. Phys. Chem. A **115**, 12070 (2011)
181. R. Püttner, G. Goldsztejn, D. Céolin, J.-P. Rueff, T. Moreno, R. K. Kushawaha, T. Marchenko, R. Guillemin, L. Journel, D. W. Lindle, M. N. Piancastelli, M. Simon, Phys. Rev. Lett. **114**, 093001 (2015)
182. D. Céolin *et al*., to be published
183. P. Morin, I. Nenner, Phys. Rev. Lett. **56**, 1913 (1986)
184. P. Morin, I. Nenner, Phys. Scr. **T17**, 171 (1987)

185. E. Kukk, H. Aksela, S. Aksela, F. Gel'mukhanov, H. Ågren, S. Svensson, Phys. Rev. Lett. **76**, 3100 (1996)
186. O. Björneholm, S. Sundin, S. Svensson, R.R.T. Marinho, A. Naves de Brito, F. Gel'mukhanov, H. Ågren, Phys. Rev. Lett. **79**, 3150 (1997)
187. M. Simon, C. Miron, N. Leclercq, P. Morin, K. Ueda, Y. Sato, S. Tanaka, Y. Kayanuma, Phys. Rev. Lett. **79**, 3857 (1997)
188. F. Gel'mukhanov, H. Ågren, Phys. Rev. A **54**, 379 (1996)
189. E. Pahl, L.S. Cederbaum, H.-D. Meyer, F. Tarantelli, Phys. Rev. Lett. **80**, 1865 (1998)
190. Z.W. Gortel, R. Teshima, D. Menzel, Phys. Rev. A **60**, 2159 (1999)
191. F. Gel'mukhanov, H. Ågren, Phys. Rep. **312**, 87 (1999)
192. R. Feifel, F. Burmeister, P. Sałek, M.N. Piancastelli, M. Bässler, S.L. Sorensen, C. Miron, H. Wang, I. Hjelte, O. Björneholm, A. Naves de Brito, F. Gel'mukhanov, H. Ågren, S. Svensson, Phys. Rev. Lett. **85**, 3133 (2000)
193. D.L. Hansen, M.E. Arrasate, J. Cotter, G.R. Fisher, K.T. Leung, J.C. Levin, R. Martin, P. Neill, R.C.C. Perera, I.A. Sellin, M. Simon, Y. Uehara, B. Vanderford, S.B. Whitfield, D. W. Lindle, Phys. Rev. A **57**, 2608 (1998)
194. T. Marchenko, L. Journel, T. Marin, R. Guillemin, S. Carniato, M. Žitnik, M. Kavčič, K. Bučar, A. Mihelič, J. Hoszowska, W. Cao, M. Simon, J. Chem. Phys. **134**, 144308 (2011)
195. R. Guillemin, P. Decleva, M. Stener, C. Bomme, T. Marin, L. Journel, T. Marchenko, R.K. Kushawaha, K. Jänkälä, N. Trcera, K.P. Bowen, D.W. Lindle, M.N. Piancastelli, M. Simon, Nature Communications **6**, 6166 (2015)

Chapter 5
Inelastic Mean Free Paths, Mean Escape Depths, Information Depths, and Effective Attenuation Lengths for Hard X-ray Photoelectron Spectroscopy

C.J. Powell and S. Tanuma

Abstract An overview is given of recent work on the determination of inelastic mean free paths, mean escape depths, information depths, and effective attenuation lengths for applications in hard X-ray photoelectron spectroscopy (HAXPES). Sources of data are provided for these parameters and useful predictive equations are given. Information is given on databases available from the National Institute of Standards and Technology (NIST) for HAXPES applications.

5.1 Introduction

Hard X-ray photoelectron spectroscopy (HAXPES) is a method of growing importance for a wide variety of scientific and technological applications, as described in other chapters of this volume. For HAXPES studies of solids, a key sample parameter is the electron inelastic mean free path (IMFP) which is a convenient (inverse) measure of the probability of inelastic scattering for the detected photoelectrons. As we will see, the IMFP is a function of material and photoelectron energy. A principal motivation for HAXPES is to conduct experiments at sufficiently high X-ray energies so that the IMFPs for the samples of interest are large enough for useful photoelectron signals to be obtained from thin-film samples

C.J. Powell (✉)
Materials Measurement Science Division, National Institute of Standards and Technology, Gaithersburg, MD 20899-8370, USA
e-mail: cedric.powell@nist.gov

S. Tanuma
National Institute for Materials Science, 1-2-1 Sengen, Tsukuba 305-0047 Ibaraki, Japan

© Springer International Publishing Switzerland 2016

J.C. Woicik (ed.), *Hard X-ray Photoelectron Spectroscopy (HAXPES)*,
Springer Series in Surface Sciences 59, DOI 10.1007/978-3-319-24043-5_5

that would not be observable using conventional XPS instruments with Al or Mg Kα X-ray sources. For example, the properties of certain buried films or interfaces may be significant, and it is then necessary to be able to detect photo-electrons from the films or interfaces of interest that may be tens of nanometers below the sample surface. An important advantage of HAXPES is that the film or the interface information of interest can often be obtained without the need for removal of surface layers by ion sputtering (with the consequent risk that the sample composition will be altered and important sample properties modified).

In addition to the IMFP, there are three related parameters that are often relevant for HAXPES experiments: the effective attenuation length (EAL), the mean escape depth (MED), and the information depth (ID). While the IMFP is a basic material parameter, the EAL, MED, and ID depend not only on the IMFP but also on the instrumental configuration and the magnitudes of elastic-scattering effects on the trajectories of the detected electrons. Since these parameters are often confused or misunderstood, we first give definitions of each term [1] in Sect. 5.2. We then present examples of recent calculations of IMFPs for electron energies up to 30 keV in Sect. 5.3. Information is given there on IMFPs for selected elemental solids and inorganic compounds, comparisons of calculated and measured IMFPs, and two useful analytical equations for estimating IMFPs. Sections 5.4 and 5.5 contain brief information on MEDs and IDs. Section 5.6 gives more detailed information on determination of EALs since this parameter is often used to determine film thick-nesses. Two empirical equations are presented for estimating EALs and a summary is given of detailed EAL calculations for thin films of $SiO_{1.6}N_{0.4}$ and $HfO_{1.9}N_{0.1}$ on Si. These calculations are based on simulated photoelectron intensities from the National Institute of Standards and Technology (NIST) Database for Simulation of Electron Spectra for Surface Analysis (SESSA) [2, 3]. EALs were determined using two algorithms in common use, and systematic differences were found depending on the algorithm, the overlayer material, and the XPS configuration. We also summarize EALs determined from HAXPES experiments and compare them with values obtained from one of the EAL predictive equations. Finally, we give brief information on SESSA and four other NIST databases that are useful for HAXPES applications.

5.2 Definitions of IMFP, EAL, MED, and ID

The International Organisation for Standardisation (ISO) has published the fol-lowing definitions for the IMFP, EAL, MED, and ID [1]:

Inelastic mean free path: average distance that an electron with a given energy travels between successive inelastic collisions.
Effective attenuation length: parameter which, when introduced in place of the inelastic mean free path into an expression derived for AES and XPS on the assumption that elastic-scattering effects are negligible for a given quantitative

application, will correct that expression for elastic-scattering effects. This definition has two notes that provide additional information [1]. First, the EAL may have different values for different quantitative applications of AES and XPS. However, the most common use of EAL is the determination of overlayer-film thicknesses from measurement of the changes of substrate Auger-electron or photoelectron signal intensities after deposition of a film or as a function of emission angle. For emission angles of up to about 60° (with respect to the surface normal), it is often satisfactory to use a single value of this parameter. For larger emission angles, the EAL can depend on this angle. Second, since there are different uses of EAL, it is recommended that users specify clearly the particular application and the definition of the parameter for that application (e.g., by giving an equation or by providing a reference to a particular source).

Mean escape depth: average depth normal to the surface from which the specified particles or radiations escape as defined by [1],

$$D = \int_0^\infty z\phi(z,\alpha)dz \Big/ \int_0^\infty \phi(z,\alpha)dz, \tag{5.1}$$

where $\phi(z,\alpha)$ is the emission depth distribution function (EDDF) for depth z from the surface into the material and for angle of emission α with respect to the surface normal. The DDF is defined [1], for a measured signal of particles or radiation emitted from a surface, as the probability that the particle or radiation leaving the surface in a specified state and in a specified direction originated from a specified depth measured normally from the surface into the material.

Information depth: maximum depth, normal to the surface, from which useful information is obtained. This definition has three notes that provide additional information [1]. First, the information depths for different surface-analysis methods may differ significantly. The ID for each technique depends on the material being analyzed, the particular signals being recorded from that material, and the instrument configuration. Second, the ID can be identified with the sample thickness from which a specified percentage (e.g., 95 % or 99 %) of the detected signal originates. Finally, the ID may be determined from a measured, calculated, or estimated emission DDF for the signal of interest.

5.3 Inelastic Mean Free Paths for Electron Energies Between 50 eV and 30 keV

5.3.1 Calculated IMFPs for Elemental Solids

The IMFP is the basic material property that determines the surface or bulk sensitivity of HAXPES measurements. Photoelectrons can be inelastically scattered as

they travel from the atom of origin through the sample material with some reaching the sample surface and subsequently being detected by an analyzer. The most probable type of inelastic scattering is excitation of the valence electrons. These excitations include plasmon excitation (mostly occurring in the so-called free-electron-like solids such as Mg, Al, Si, Ge, and Sn) and single-electron excitations in many solids. Smaller contributions to the total inelastic-scattering cross section come from excitations of inner-shell excitations (of the type commonly observed in X-ray absorption spectra). As we shall see, it is not necessary for us to identify specific types of inelastic scattering in solids. Instead, we will show how IMFPs in bulk solids can be calculated from experimental optical data. In a 2009 review, Powell and Jablonski [4] discussed the surface sensitivity of X-ray photoelectron spectroscopy (XPS) and we will focus here on more recent developments.

Tanuma et al. [5] have reported calculations of IMFPs for 41 elemental solids (Li, Be, graphite, diamond, glassy C, Na, Mg, Al, Si, K, Sc, Ti, V, Cr, Fe, Co, Ni, Cu, Ge, Y, Nb, Mo, Ru, Rh, Pd, Ag, In, Sn, Cs, Gd, Tb, Dy, Hf, Ta, W, Re, Os, Ir, Pt, Au, and Bi) in 2011 for electron energies between 50 eV and 30 keV using the Penn algorithm [6]. Experimental optical data, typically for photon energies between 0.1 eV or 1 eV and 30 keV, were utilized to compute the optical energy-loss function (ELF) for each material [5]. In most cases, the optical data were obtained from optical experiments but in some cases ELFs were obtained from transmission electron energy-loss experiments. It was necessary to use atomic photoabsorption data for some spectral regions, typically for photon energies above 50 eV where atomic processes largely determine the optical constants [5].

The differential cross section for inelastic scattering can be written using Hartree atomic units ($m_e = e = \hbar = 1$) as:

$$\frac{d^2\sigma}{d\omega dq} = \frac{1}{\pi NE}\mathrm{Im}\left[\frac{-1}{\varepsilon(q,\omega)}\right]\frac{1}{q}, \tag{5.2}$$

where σ is the inelastic cross section, ω is the energy loss, q is the momentum transfer, N is the number of atoms per unit volume, E is the electron energy, and $\mathrm{Im}[-1/\varepsilon(q,\omega)]$ is the energy loss function (ELF) of the target material. In the Penn algorithm [6], the ELF can be related to the optical ELF as follows:

$$\mathrm{Im}\left[\frac{-1}{\varepsilon(q,\omega)}\right] = \int_0^\infty d\omega_p g(\omega_p)\mathrm{Im}\left[\frac{-1}{\varepsilon^L(q,\omega;\omega_p)}\right], \tag{5.3}$$

where

$$g(\omega) = \frac{2}{\pi\omega}\mathrm{Im}\left[\frac{-1}{\varepsilon(\omega)}\right], \tag{5.4}$$

ε^L denotes the Lindhard model dielectric function for a free-electron gas with plasmon energy $\omega_p\left(=\sqrt{4\pi n}\right)$, n is the electron density, $g(\omega_p)$ is a coefficient introduced to satisfy the condition $\mathrm{Im}[-1/\varepsilon(q=0,\omega)] = \mathrm{Im}[-1/\varepsilon(\omega)]$, and $\mathrm{Im}[-1/\varepsilon(\omega)]$ is the optical energy-loss function. A total inelastic-scattering cross section for a particular electron energy E can be obtained from double integrations of (5.2) and use of (5.3) and (5.4). The corresponding IMFP, λ_i, can then be computed from $\lambda_i = 1/N\sigma$.

The internal consistency of each set of optical ELF data was checked with the oscillator-strength sum rule (or f-sum rule) and the perfect-screening (ps) sum rule (also obtained as a limiting form of a Kramers-Kronig integral of the ELF) [5, 7]. The resulting average root-mean-square (RMS) errors were 4.2 and 7.7 % for the f-sum rule and ps sum rule, respectively [5].

IMFPs were calculated at equal energy intervals on a logarithmic scale corresponding to increments of 10 % from 10 eV to 30 keV. Figure 5.1 shows illustrative IMFP results (solid circles) for Si, Fe, Cu, Ag, W, and Au [5]. The Penn algorithm is expected to give reasonable results for energies above 50 eV [8] but we show less-reliable IMFPs for lower energies in Fig. 5.1 to indicate trends. Sources of uncertainties of IMFPs calculated from the Penn algorithm are discussed elsewhere [4, 5, 9, 10].

The IMFP dependence on energy was analyzed for each material with a modified form of the Bethe equation for inelastic electron scattering in matter [11, 12]:

$$\lambda_i = \frac{E}{E_p^2[\beta \ln(\gamma E) - (C/E) + (D/E^2)]} \quad (\mathrm{nm}), \tag{5.5}$$

where λ_i is the IMFP, E is the electron energy (in eV), $E_p = 28.8(N_v\rho/M)^{1/2}$ is the bulk plasmon energy (in eV), N_v is the number of valence electrons per atom or molecule, ρ is the bulk density (in g/cm^2), M is the atomic or molecular weight, and β, γ, C, and D are parameters. Satisfactory fits were made with (5.5) to the calculated IMFPs for the 41 elemental solids at energies between 54.6 eV and 29.733 keV. The solid lines in Fig. 5.1 show plots of these fits for the six chosen solids and Table 5.1 gives the fit parameters. For the group of 41 elemental solids, the average RMS difference between the calculated IMFPs and the fitted values with (5.5) was 0.48 % [5]. Equation (5.5) is thus a convenient analytical representation of the calculated IMFPs (e.g., for interpolation).

We now comment on comparisons of the Tanuma et al. [5] "optical" IMFPs with values reported from other calculations and measurements. Tanuma et al. compared their calculated IMFPs for Al and Cu with corresponding values reported by Mao et al. [13] who also used the Penn algorithm in their calculations. Excellent agreement was obtained for Al and slight differences were found for Cu at energies less than 100 eV; the latter differences were probably due to the selection of different sets of ELF data in each calculation.

IMFPs can be obtained from measurements of ratios of elastically backscattered electrons from a sample of interest and a reference material for which the IMFP is

known, a technique known as elastic-peak electron spectroscopy (EPES) [4, 10]. These ratios, determined for a range of incident electron energies, are then compared with corresponding ratios from Monte Carlo simulations in which the sample

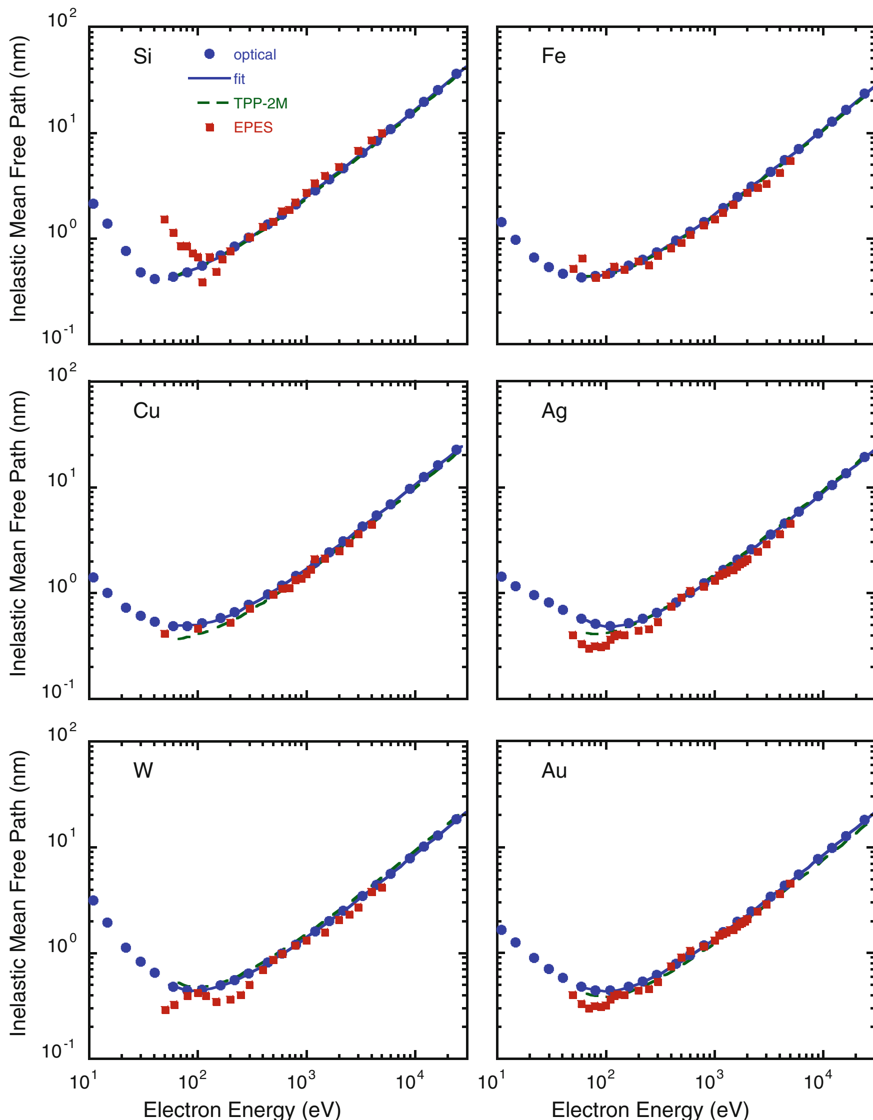

Fig. 5.1 Plots of electron inelastic mean free paths as a function of electron energy for Si, Fe. Cu, Ag, W, and Au [4]. The *solid circles* show calculated IMFPs from the Penn algorithm [6], and the *solid lines* show fits to these IMFPs with the modified Bethe equation (5.5) and the derived parameters in Table 5.1. The *long-dashed lines* indicate IMFPs calculated from the TPP-2M equation (5.5) and (5.6). The *solid squares* show IMFPs obtained from the EPES experiments of Tanuma et al. [14]

Table 5.1 Values of E_p and the parameters β, γ, C, and D found in the fits of (5.5) to the calculated IMFPs for Si, Fe, Cu, Ag, W, and Au

Element	E_p (eV)	β (eV^{-1} nm^{-1})	γ (eV^{-1})	C (nm^{-1})	D (eV nm^{-1})
Si	16.59	0.311	0.1186	11.04	303
Fe	30.59	0.151	0.0715	9.81	337
Cu	35.87	0.117	0.0535	6.80	258
Ag	29.80	0.196	0.0628	19.33	650
W	22.86	0.372	0.0417	15.43	556
Au	29.92	0.213	0.0524	14.24	481

IMFP is a parameter. Ni, Cu, Ag, or Au are often chosen as reference materials since these materials showed good consistencies in comparisons of IMFPs calculated from optical data and IMFPs determined from EPES experiments [10]. Two groups [14–16] have reported IMFPs for elemental solids from EPES experiments, with Tanuma et al. [14] providing IMFPs for 13 elemental solids for energies between 50 eV and 5 keV and Werner et al. [15, 16] providing IMFPs for 24 elemental solids for energies between 50 eV and 3.4 keV. The average RMS difference between the optical IMFPs of Tanuma et al. [5] and the EPES IMFPs of Tanuma et al. [14] was 12 % (for the 11 solids that were common to both data sets), while the average RMS difference between the optical IMFPs of Tanuma et al. [5] and the EPES IMFPs of Werner et al. [15, 16] was 15 % (for the 17 solids that were common to both data sets). Figure 5.1 shows comparisons of IMFPs from the EPES experiments of Tanuma et al. [14] with the corresponding IMFP calculations to indicate the satisfactory agreement between the experimental results and the recent calculations for Si, Fe, Cu, Ag, W, and Au.

Werner et al. [17] analyzed reflection electron energy-loss spectra (REELS) for 17 elemental solids and derived their optical constants for photon energies between 0.5 and 70.5 eV. With these results and atomic photoabsorption data for higher photon energies, Werner et al. computed ELFs and then IMFPs using the Penn algorithm for energies between 100 eV and 10 keV. The average RMS deviation between these REELS IMFPs and the optical IMFPs of Tanuma et al. was 5.9 % [4]. Werner et al. also commented that their REELS IMFPs were “indistinguishably similar” to those obtained from optical constants calculated using density functional theory [17].

Powell and Jablonski [4] concluded that IMFPs calculated from optical data have uncertainties of up to about 10 %. In principle, they might have smaller uncertainties but better estimates await the development of improved experimental tests. It would also be helpful to have optical data with smaller uncertainties. It is also clear that better understanding is needed of differences that can occur at energies below about 100 eV between IMFPs calculated from the Penn algorithm and those obtained from an alternative approach, the Mermin [18] model for the dielectric function [19]. Chantler and Bourke have reported systematic differences between IMFPs from the Penn algorithm and IMFPs deduced from analyses of

X-ray absorption fine structure (XAFS) for Cu and Mo for electron energies less than 120 eV [20, 21]. Da et al. have recently shown that use of an "extended Mermin" method leads to better agreement between calculated IMFPs for Cu and Mo and experimental IMFPs (from EPES and XAFS determinations) for energies above 50 eV [22]. Their approach considers not only valence-electron and inner-shell excitations but also phonon excitations [22].

5.3.2 Calculated IMFPs for Inorganic Compounds

Figure 5.2 shows preliminary results of IMFPs calculated for SiO_2, GaAs, InP, and PbS by Tanuma et al. [23]. These IMFPs were calculated from experimental optical

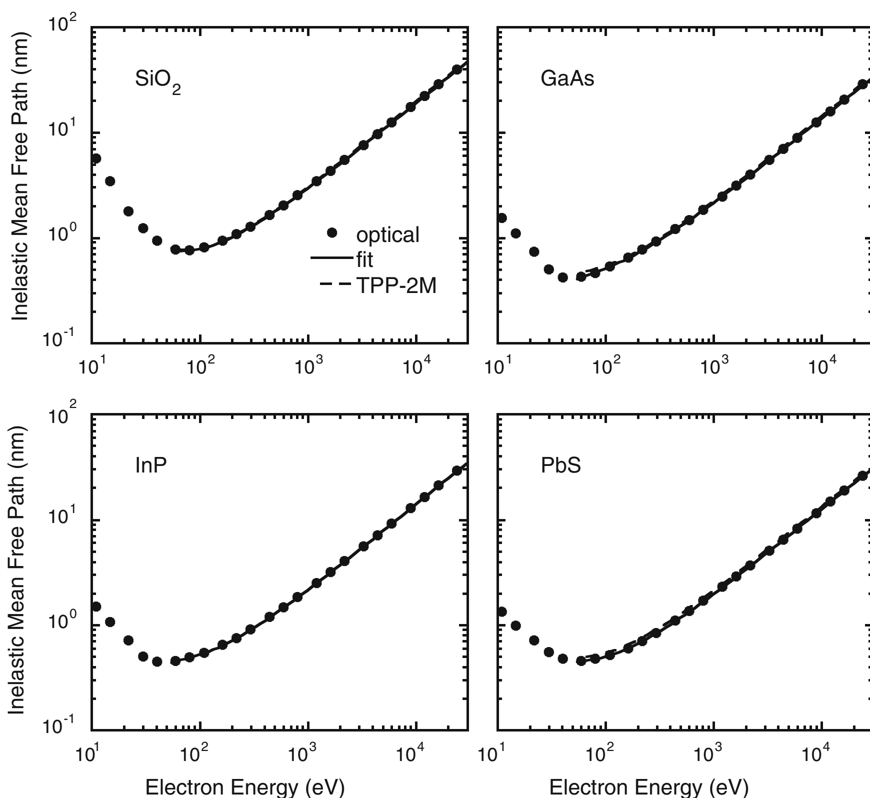

Fig. 5.2 Plots of electron inelastic mean free paths as a function of electron energy for SiO_2, GaAs, InP, and PbS [23]. The *solid circles* show calculated IMFPs from the Penn algorithm [6], and the *solid lines* show fits to these IMFPs with the modified Bethe equation (5.5) and the derived parameters in Table 5.2. The *long-dashed lines* indicate IMFPs calculated from the TPP-2M equation (5.5) and (5.6)

Table 5.2 Values of E_p and the parameters β, γ, C, and D found in the fits of (5.5) to the calculated IMFPs for SiO_2, GaAs, InP, and PbS

Compound	E_p (eV)	β (eV^{-1} nm^{-1})	γ (eV^{-1})	C (nm^{-1})	D (eV nm^{-1})
SiO_2	22.02	0.153	0.101	12.38	323.5
GaAs	15.63	0.428	0.0898	21.95	823.7
InP	14.77	0.441	0.1339	38.28	1170
PbS	16.26	0.417	0.1097	34.88	1063

data for SiO_2 and from calculated ELFs for the other compounds (from the Wien2K [24] and FEFF [25] codes) using the Penn algorithm in the same way as for the elemental solids. The solid lines in Fig. 5.2 show satisfactory fits to the calculated IMFPs for energies between 50 eV and 30 keV with (5.5) and the parameter values in Table 5.2. The dashed lines in Fig. 5.2 indicate IMFPs calculated from the TPP-2M equation, i.e., (5.5) with parameter values obtained from (5.6), for the same energy range. Small differences between the solid and dashed lines are only apparent for GaAs at low energies and for PbS.

5.3.3 *Predictive Formulae for IMFPs*

Tanuma et al. [26] analyzed IMFPs for a group of 27 elemental solids and a group of 14 organic solids that had been calculated earlier from optical data for electron energies between 50 eV and 2 keV. Simple expressions were found for the four parameters (5.5) in terms of material properties:

$$\beta = -1.0 + 9.44/\left(E_p^2 + E_g^2\right)^{0.5} + 0.69\rho^{0.1}, \left(\mathrm{eV}^{-1}\ \mathrm{nm}^{-1}\right) \tag{5.6a}$$

$$\gamma = 0.191\rho^{-0.5}, \left(\mathrm{eV}^{-1}\right) \tag{5.6b}$$

$$C = 19.7 - 9.1U, \left(\mathrm{nm}^{-1}\right) \tag{5.6c}$$

$$D = 534 - 208U, \left(\mathrm{eV\,nm}^{-1}\right) \tag{5.6d}$$

$$U = N_v\rho/M = E_p^2/829.4, \tag{5.6e}$$

where E_g is the bandgap energy (in eV) for nonconductors. Equations (5.5) and (5.6) represent the TPP-2M formula of Tanuma et al. for estimating IMFPs in other materials [13]. The long-dashed lines in Fig. 5.1 show plots of IMFPs from (5.2) and (5.3) for the six illustrative solids. For the group of 41 solids, the average RMS deviation between the IMFPs from the TPP-2M equation and the calculated IMFPs

between 50 eV and 30 keV was 12.3 %. There were relatively large RMS deviations for diamond, graphite, and cesium (71.7, 47.9, and 36.7 %, respectively); possible reasons for these large deviations have been proposed [27]. If the deviations for these three solids are ignored, the average RMS deviation for the remaining 38 elemental solids was 9.2 % [5].

Seah [28] has recently proposed another analytical expression, designated the S1 equation, for estimating IMFPs:

$$\lambda_i = \frac{(4 + 0.44Z^{0.5} + 0.104E^{0.872})a^{1.7}}{Z^{0.3}(1 - W)}(\text{nm}), \tag{5.7}$$

where E is expressed in eV, a is the average interatomic spacing given by

$$a^3 = \frac{10^{21}M}{\rho N_A(g + h)}\left(\text{nm}^3\right), \tag{5.8}$$

Z is the atomic number of the solid (or the average atomic number for a compound), $W = 0.06H$ or $0.02E_g$, H is the heat of reaction in eV/atom for a compound ($W = 0$ for an elemental solid), and N_A is the Avogadro constant, The terms g and h in (5.8) represent stoichiometry coefficients for an assumed binary compound G_gH_h; for an elemental solid, $g = 1$ and $h = 0$. Seah found that the average RMS deviation between IMFPs from (5.7) and (5.8) and the IMFPs of Tanuma et al. [5] for 41 elemental solids was 8.5 % for electron energies between 100 eV and 10 keV [26]. In a similar comparison between IMFPs from (5.7) and (5.8) and the early IMFPs of Tanuma et al. [29] for 15 inorganic compounds that had been adjusted for sum-rule errors [26], the RMS deviation was 8.3 % for energies between 100 eV and 2 keV. The RMS deviation between IMFPs from (5.7) and (5.8) and the IMFPs of Tanuma et al. [26] for 14 organic compounds was 7.9 % for energies between 100 eV and 2 keV. The Seah S1 expression is expected to be useful for energies between 100 eV and 10 keV [28].

Figure 5.3 shows plots of ratios of IMFPs from the TPP-2M formula (5.5) and (5.6), solid circles, and from the Seah S1 formula (5.7) and (5.8), solid squares, to the corresponding optical IMFPs of Tanuma et al. [5] as a function of electron energy for Si, Fe, Cu, Ag, W, and Au. For Si, W, and Au, the IMFP ratios for both predictive IMFP equations are close to unity for energies between 200 eV and 10 keV. For Fe and Cu, however, the IMFP ratios from the Seah S1 equation are systematically lower than the ratios based on the TPP-2M equation, while the reverse is found for Ag at energies above 200 eV. Overall, the differences between IMFPs from the two predictive equations and the optical IMFPs in Fig. 5.3 correspond to those expected from the RMS deviations between predicted and optical values for the 41 elemental solids. Figure 5.4 is a similar plot of ratios of IMFPs from the two predictive equations to the optical IMFPs of Tanuma et al. [23] for SiO_2, GaAs, InP, and PbS. These IMFP ratios are qualitatively similar to those in Fig. 5.3.

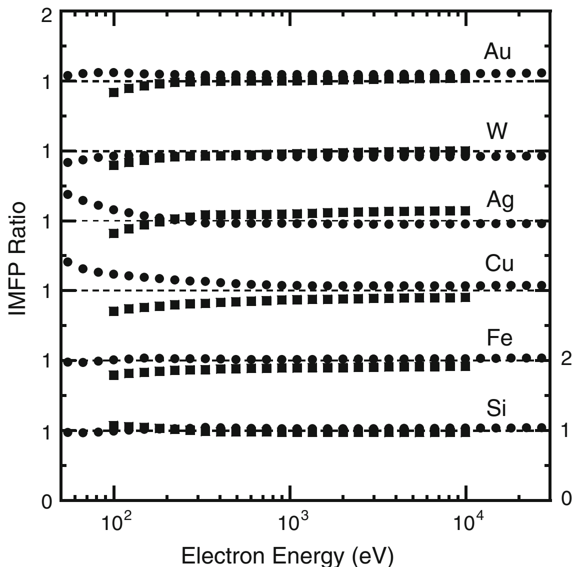

Fig. 5.3 Plot of IMFP ratios [TPP-2M values (*circles*) to optical values, and Seah S1 values (*squares*) to optical values] as a function of electron energy for Si, Fe, Cu, Ag, W, and Au. Successive plots have been displaced vertically for clarity. The right-hand ordinate scale is for Si

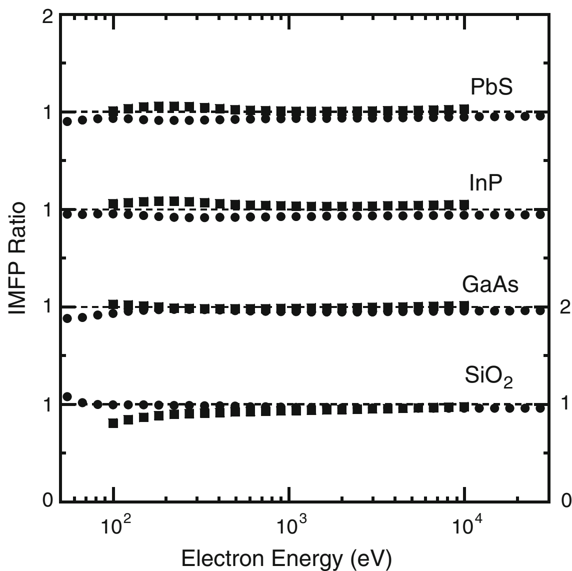

Fig. 5.4 Plot of IMFP ratios [TPP-2M values (*circles*) to optical values, and Seah S1 values (*squares*) to optical values] as a function of electron energy for SiO_2, GaAs, InP, and PbS. Successive plots have been displaced vertically for clarity. The right-hand ordinate scale is for SiO_2

5.4 Mean Escape Depths

The mean escape depth (MED) is a convenient measure of the surface or bulk sensitivity of HAXPES measurements that depends on both the IMFP and the average photoelectron emission angle. As we shall see, the MED also depends on the magnitude of elastic-scattering effects in the samples of interest [4].

The MED can be calculated from (5.1) if the emission depth distribution function (EDDF) is known. Jablonski and Powell [30] determined EDDFs and MEDs for 12 photoelectron lines excited by unpolarized X-rays from Mg Kα or Al Kα sources and 9 Auger lines from five elemental solids (Si, Cu, Ag, W, and Au) and 4 photoelectron lines from four inorganic compounds (ZrO_2, $ZrSiO_4$, HfO_2, and $HfSiO_4$). The EDDFs were obtained from solution of the kinetic Boltzmann equation within the transport approximation [30]. Their MEDs could be fitted to a simple linear equation for electron energies between 61 and 2016 eV and for electron emission angles between 0° and 50° with a mean percentage deviation of 0.25 %,

$$D = \lambda_i \cos\alpha(1 - 0.736\omega), \tag{5.9}$$

where ω is the single-scattering albedo,

$$\omega = \lambda_i/(\lambda_i + \lambda_t), \tag{5.10}$$

and λ_t is the transport mean free path (TMFP). The TMFP is defined as the average distance that an energetic particle must travel before its momentum in its original direction of motion is reduced to 1/*e* of its initial value by elastic scattering alone [1]. TMFP values can be calculated from the corresponding values of transport cross sections which in turn can be calculated from differential cross sections for elastic scattering [4]. TMFPs as well as IMFPs can be conveniently obtained from two NIST databases [2, 31]. The MED from (5.6) is the product of two factors. The first of these is $\lambda_i \cos\alpha$ which would be the MED if elastic-scattering effects were negligible. The second factor is $(1 - 0.736\omega)$ which is the correction needed to account for elastic scattering.

The single-scattering albedo is a useful measure of the effects of elastic scattering in XPS. Figure 5.5 shows plots of ω from (5.10) as a function of electron energy for Si, Fe, Cu, Ag, W, and Au. For energies less than about 1 keV, the dependence of ω on energy is complex, ranging from a monotonic decrease with increasing energy for Si to a maximum at about 200 eV for Cu while for Au there is a minimum at about 200 eV and a maximum at about 1 keV. For energies above about 1 keV, we see that ω decreases with increasing energy and generally increases with increasing *Z*. It is the latter energy region that is most relevant to HAXPES since the usual experimental objective is to excite photoelectrons with sufficient energy (or IMFP) for characterizations of films or interfaces that are deeper than those accessible by XPS with conventional Al or Mg Kα X-ray sources. For a photoelectron energy of 5 keV, ω is about 0.25 for W and Au in Fig. 5.5, about 0.15 for Ag, and about 0.04 for Si. Although (5.9) was derived for unpolarized X-rays and for photoelectron energies less than 2 keV, we use it to provide estimates of elastic-scattering effects on MEDs for higher energies. The corrections from (5.9) for these effects are then 18, 11, and 3 % for W and Au, Ag, and Si, respectively, at 5 keV. At energies higher than 30 keV, elastic-scattering effects are expected to become negligible, i.e., $\lambda_t \to \infty$ and $\omega \to 0$.

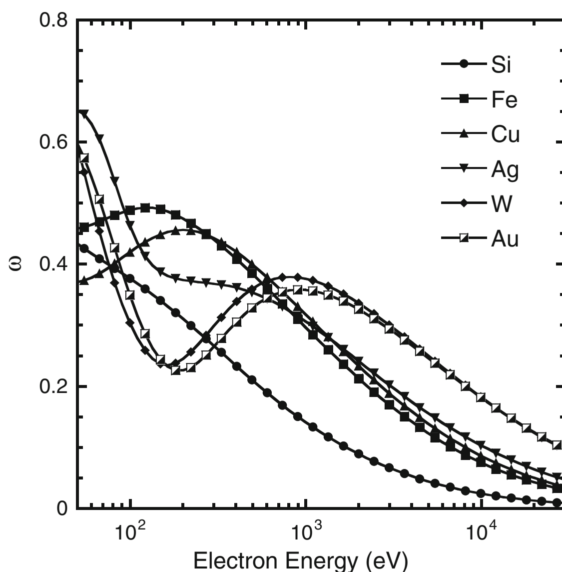

Fig. 5.5 Plot of the single-scattering albedo, ω, from (5.10) as a function of electron energy for Si, Fe, Cu, Ag, W, and Au

Tanuma et al. [32] have reported results of EDDF and MED calculations from Monte Carlo simulations for linearly polarized X-rays incident on substrates of Si, Cu, and Au. They performed simulations for an X-ray angle of incidence of 85° (with respect to the sample normal) and various X-ray energies to give photoelectron energies between 50 eV and 10 keV. They determined MEDs for values of the dipole asymmetry parameter, β, of −1.0, −0.5, 0, 0.5, 1.0, 1.5, and 2.0. The MEDs at a particular photoelectron emission angle from each solid depend in part on the angular distribution of photoelectrons emitted from a particular atom (i.e., on the value of β) and in part on the magnitude of elastic-scattering effects (i.e., on the magnitude of ω). For the XPS configuration considered by Tanuma et al., non-dipole effects on the photoelectron angular distributions were negligible. While most of the MEDs from the Monte Carlo simulations of Tanuma et al. were similar to those found by Jablonski and Powell [28] from transport-approximation calculations [i.e., (5.9)], Tanuma et al. found that the following modified expression fitted their results with a relative RMS deviation of 2.0 %:

$$D = 0.981\lambda_i \cos \alpha(1 - 0.736\omega)g(\beta), \tag{5.11a}$$

where

$$g(\beta) = 1.00 - 0.102\beta + 0.0577\beta^2 - 0.0133\beta^3. \tag{5.11b}$$

The MED values for Au from (5.11) were about 8 % less than those obtained from (5.9) when $\omega > 0.3$ (i.e., for photoelectron energies less than about 100 eV and for photoelectron energies between 500 eV and 3 keV, as shown in Fig. 5.5).

5.5 Information Depths

The information depth (ID) is a measure of the sampling depth for a particular experiment that depends on the IMFP (i.e., the sample), the average photoelectron emission angle (i.e., the experimental configuration), and the magnitude of elastic-scattering effects in the sample. Jablonski and Powell [30] determined IDs from transport-approximation calculations for 16 photoelectron lines and 9 Auger-electron lines from Si, Cu, Ag, W, Au, ZrO_2, $ZrSiO_4$, HfO_2, and $HfSiO_4$. These IDs, S, could be fitted to a simple linear equation for electron energies between 61 eV and 2016 eV and for electron emission angles between 0° and 50° with a mean percentage deviation of 0.54 %,

$$S = \lambda_i \cos\alpha(1 - 0.787\omega)\ln\left[\frac{1}{1 - (P/100)}\right] \tag{5.12}$$

where P is the specified percentage of the detected signal which originates within the ID. The final factor in (5.12) largely determines the ratio of the ID to the MED from (5.9) for a given material and HAXPES configuration, and is 2.3, 3.0, and 4.61 for values of $P = 90$, $P = 95$, and $P = 99$, respectively.

5.6 Effective Attenuation Lengths

The effective attenuation length (EAL) is generally understood to be a measure of the opacity of a material for a beam of electrons of a given energy. Due to the effects of elastic scattering, however, photoelectrons from a substrate material that are emitted in a particular direction are not necessarily attenuated exponentially with thickness of an overlayer material, as would be expected from the Beer-Lambert law. Nevertheless, the EAL is a useful parameter for describing photoelectron-signal attenuation at least approximately for defined conditions of overlayer-film thickness and photoelectron-emission angle. Although other applications are possible [33, 34], the most common use for the EAL is determination of overlayer film thicknesses and this application will be emphasized here.

5.6.1 Empirical Formulae for EALs

Jablonski and Powell [30] determined EALs from transport-approximation calculations for 16 photoelectron lines and 9 Auger-electron lines from Si, Cu, Ag, W, Au, ZrO_2, $ZrSiO_4$, HfO_2, and $HfSiO_4$. These EALs, L, could be fitted to a simple

linear equation for electron energies between 61 eV and 2016 eV and for electron emission angles between 0° and 50° with a mean percentage deviation of 0.61 %:

$$L = \lambda_i(1 - 0.735\omega). \quad (5.13a)$$

Equation (5.13a) represents average EAL values determined for a range of film thicknesses corresponding to P values of 90, 95, and 99 %. Values of ω can be obtained from (5.10).

Very recently, Jablonski and Powell [35] reported EAL calculations for Si 2s, Cu $2p_{3/2}$, Ag $3d_{5/2}$, and Au $4f_{7/2}$ photoelectrons excited by unpolarized Mg Kα, Al Kα, Zr Lα, and Ti Kα X-rays, where the photoelectron energies ranged from 321 eV to 4.426 keV. These EALs, appropriate for determining overlayer-film thicknesses, were calculated from the transport-approximation (TA) formalism and from Monte Carlo (MC) simulations using photoionization cross sections from the dipole and non-dipole approximations. Satisfactory consistency was found between EALs determined from the TA formalism and from MC simulations, while differences between EALs for Au $4f_{7/2}$ photoelectrons from the dipole and non-dipole approximations were between 1 % (for Mg and Al Kα X-rays) and 2.5 % (for Ti Kα X-rays) for photoelectron emission angles less than 50°. As in their earlier work for electron energies less than 2 keV [30], they found an essentially identical relation to (5.13a):

$$L = \lambda_i(1 - 0.739\omega) \quad (5.13b)$$

Equation (5.13b) was obtained from a linear fit to EALs calculated from both the transport approximation and MC simulations using both the dipole and non-dipole approximations and for overlayer-film thicknesses corresponding to P values of 90, 95, and 99 %. The root-mean-square difference between these average EALs and those from (5.13b) was 1.44 %. This expression should be useful in determinations of film thicknesses by HAXPES for photoelectron energies up to about 5 keV. Nevertheless, further investigations need to be made to determine the effects of X-ray polarization on the calculated EALs.

Seah [36] has proposed an analytical expression for the EAL, designated the S3 equation, similar to the one he developed for the IMFP (5.7):

$$L = \frac{(5.8 + 0.0041Z^{1.7} + 0.088E^{0.93})a^{1.82}}{Z^{0.38}(1 - W)}\,(\text{nm}). \quad (5.14)$$

This formula is based on a fit to the calculated IMFPs of Tanuma et al. [5, 8, 26] multiplied by the correction for elastic-scattering effects given by (5.13a), that is, the factor $(1 - 0.735\omega)$. Equation (5.14) was recommended for use for electron energies between 100 eV and 30 keV. Seah found that the average RMS deviation between EALs from (5.14) and those determined from (5.13a) and the IMFPs of

Tanuma et al. [5] for 41 elemental solids, Tanuma et al. [8] for 15 inorganic compounds, and Tanuma et al. [26] for 14 organic compounds was 8.0 % for electron energies between 100 eV and 10 keV [36]. While (5.14) is easy to use, Jablonski and Powell [35] concluded that (5.13b) was more reliable.

5.6.2 *Calculated EALs from SESSA Simulations*

Powell et al. [37] recently reported more detailed calculations of EALs for thin films of $SiO_{1.6}N_{0.4}$ and $HfO_{1.9}N_{0.1}$ on Si. These calculations were made with the NIST SESSA database [2, 3] for two XPS configurations, one in which there was a fixed angle of 55° between the incident X-rays and the average emission angle of the detected photoelectrons (the "sample-tilting" configuration) and the other in which photoelectrons were detected in parallel for a 60° range of emission angles (the "Theta Probe" configuration [38–40]). In the former configuration, the sample is tilted to vary the emission angle, thereby varying the surface sensitivity of the XPS measurements [as indicated by (5.9), (5.11), and (5.12)]. For the Theta Probe configuration, the X-ray incidence angle is 30° and the plane of X-ray incidence is at 70° with respect to the emission plane (defined by the entrance optics of the electron energy analyzer and the surface normal). The angle between the direction of X-ray incidence and a particular emission angle thus varies with emission angle.

The SESSA database was used to determine photoelectron intensities (for excitation by Al Kα X-rays) from 0.5, 1.5, 2.5, 3.5 and 4.5 nm films of each oxide at photoelectron emission angles in 5° steps between 0° and 75° for the sample-tilting configuration and between 21.875° and 78.125° in steps of 3.75° for the Theta Probe configuration [37]. The analyzer acceptance geometry was chosen as a cone with a semi-angle of 12° for the sample-tilting configuration and as a wedge with a polar angle of 3.75° and an azimuthal angle of 5° for the Theta Probe configuration.

EALs were determined using two algorithms in common use, one in which substrate Si $2p_{3/2}$ photoelectron intensities were determined as a function of overlayer film thickness at a particular photoelectron emission angle ("Method 1") and the other in which the ratio of the Si $2p_{3/2}$ intensities from the $SiO_{1.6}N_{0.4}$ film and the substrate or the ratio of the Hf $4f_{7/2}$ intensity from the $HfO_{1.9}N_{0.1}$ film to the Si $2p_{3/2}$ intensity from the substrate were analyzed as a function of photoelectron emission angle for a given film thickness ("Method 2") [37]. Both methods involve simple expressions that had been developed with the assumption that elastic-scattering effects were negligible. Since elastic scattering was switched 'on' in the SESSA simulations, the following analysis emulates EAL determinations from measured intensities. It is then possible to compare EALs for the two materials from methods 1 and 2 as well as to compare EALs for the two XPS configurations.

Method 1 for determining EALs is based on changes of a substrate photoelectron signal intensity, I_t, as a function of overlayer film thickness, t, for a given photoelectron emission angle, α. The EAL is then calculated from

$$L = t/[\cos\,\alpha(\ln I_0 - \ln I_t)], \tag{5.15}$$

where I_0 is the substrate photoelectron signal intensity for a bare substrate (i.e., zero film thickness). It is useful to plot $(\ln I_0 - \ln I_t)\cos\,\alpha$ as a function of t for particular values of α. If these plots are judged to be sufficiently linear for useful ranges of t and α, the derived values of L can then be used as EALs for these conditions with (5.15) to measure film thicknesses. Due to the effects of elastic scattering, deviations from linearity in these plots are typically found for larger film thicknesses and larger emission angles [33, 34].

Figure 5.6 is an illustrative plot of $(\ln I_0 - \ln I_t)\cos\,\alpha$ versus t for thin films of $HfO_{1.9}N_{0.1}$ on Si obtained from the simulated Si $2p_{3/2}$ photoelectron intensities for the sample-tilting configuration and the indicated average photoelectron emission angles [37]. We see that these plots show near-linear regions but that there are deviations from linearity with increasing film thickness that become more pronounced with increasing emission angles. Qualitatively similar results were found for thin films of $SiO_{1.6}N_{0.4}$ on Si although the deviations from linearity in plots like those in Fig. 5.6 were not as pronounced as for the case of $HfO_{1.9}N_{0.1}$ films [37].

Linear fits were made to selected regions of the plots in Fig. 5.6 to derive average values of the EAL, L_{ave1}, from (5.15) for Method 1 [37]. These fits were made for all $HfO_{1.9}N_{0.1}$ film thicknesses for which the emission angles were

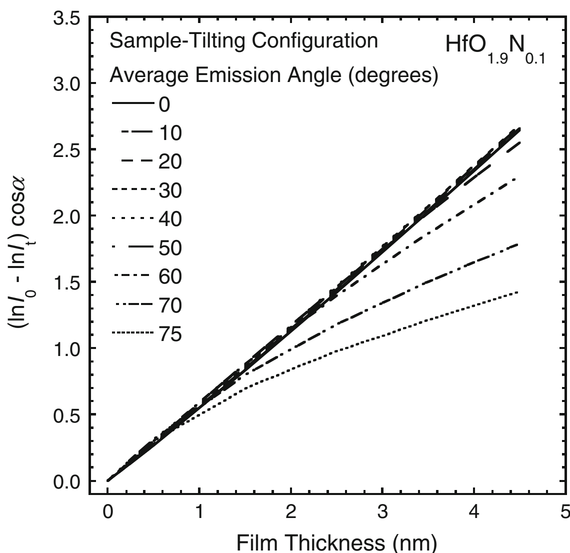

Fig. 5.6 Plot of $(\ln I_0 - \ln I_t)\cos\alpha$ versus film thickness for $HfO_{1.9}N_{0.1}$ films on Si obtained from simulated substrate Si $2p_{3/2}$ photoelectron intensities excited by Al Kα X-rays for the sample-tilting configuration and various average photoelectron emission angles [37]

between 0° and 45°, for film thicknesses up to 3.5 nm for emission angles of 50° and 55°, for thicknesses up to 2.5 nm for emission angles of 60° and 65°, and for thicknesses of up to 1.5 nm for emission angles of 70° and 75°. Similar fits were made for $SiO_{1.6}N_{0.4}$ films using the results for all film thicknesses except for emission angles of 70° and 75° where the fits were made for thicknesses up to 3.5 nm for $\alpha = 70°$ and up to 2.5 nm for $\alpha = 75°$. We note that the maximum film thicknesses chosen for each fit at the larger emission angles corresponded to an intensity reduction of the Si $2p_{3/2}$ substrate signal to about 5 % of its original value; it is unlikely that weaker substrate signals would be utilized in practical measurements.

Figure 5.7 shows plots of the ratios of L_{ave1} to the IMFPs of the substrate Si $2p_{3/2}$ photoelectrons in each oxynitride film as a function of emission angle for both the sample-tilting and the Theta Probe configurations [37]. These IMFPs were found to

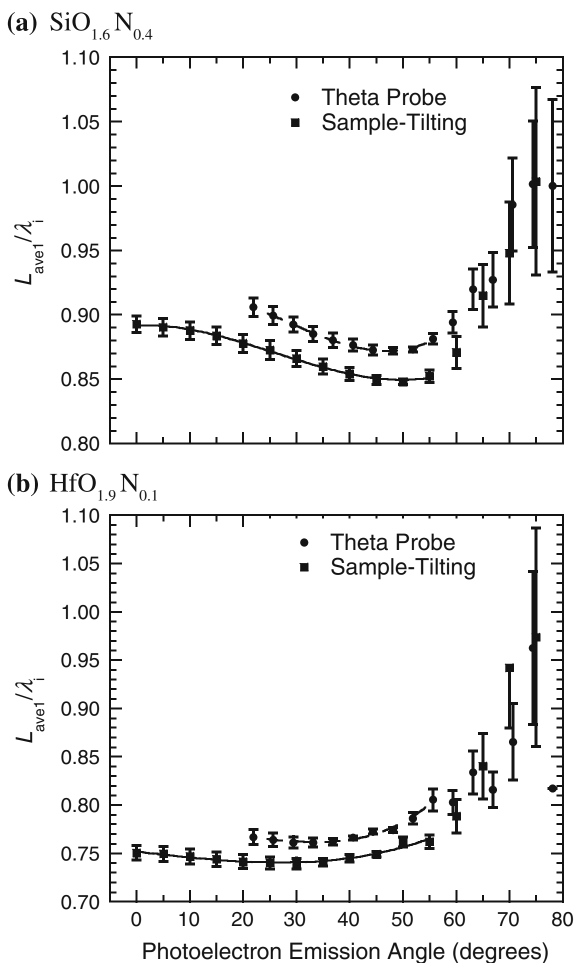

Fig. 5.7 Plots of L_{ave1}/λ_i (*symbols*) as a function of average photoelectron emission angle for substrate Si $2p_{3/2}$ photoelectrons excited by Al Kα X-rays with an energy of 1387.4 eV in thin films of **a** $SiO_{1.6}N_{0.4}$ and **b** $HfO_{1.9}N_{0.1}$ on Si for the Theta Probe configuration (*filled circle*) and the sample-tilting configuration (*filled square*). The error *bars* indicate one-standard-deviation uncertainties of the derived values of L_{ave1} from the linear fits described in the text. The *lines* show fits with a cubic equation to guide the eye [37]

be 3.90 nm for $SiO_{1.6}N_{0.4}$ and 2.21 nm for $HfO_{1.9}N_{0.1}$ at a photoelectron kinetic energy of 1387.4 eV from (5.5) and (5.6) [26]. If elastic-scattering effects were negligible, the EAL would equal the IMFP. Instead, we see that values of L_{ave1}/λ_i are about 0.90 for $SiO_{1.6}N_{0.4}$ and about 0.75 for $HfO_{1.9}N_{0.1}$ at emission angles less than about 55°. That is, elastic-scattering effects are stronger in $HfO_{1.9}N_{0.1}$ than in $SiO_{1.6}N_{0.4}$; these changes will be discussed further below. Moreover, small but significant differences in the values of L_{ave1}/λ_i, about 3 % for $SiO_{1.6}N_{0.4}$ and between 2 and 5 % for $HfO_{1.9}N_{0.1}$, are found for the sample-tilting and Theta Probe configurations at emission angles between 0° and 55°. Finally, there is a large increase in the values of L_{ave1}/λ_i for emission angles larger than 55°.

Method 2 for determining EALs is based on ratios of photoelectron peak intensities from the film and from the substrate, often as a function of emission angle [37]. The EAL is then calculated from

$$L = \frac{t}{\ln[F + (R_{t,\alpha}/R_0)]\cos\alpha}, \tag{5.16a}$$

where $R_{t,\alpha}$ is the ratio of peak intensities for the film and the substrate for a particular thickness and emission angle and R_0 is the ratio of these intensities for a thick film and a bare substrate. Method 2 has often been utilized for thin films of an oxide such as SiO_2 on a substrate of the same element (i.e., Si). For this application, the photoelectrons from the film and the substrate have nearly the same kinetic energy (e.g., 1383.4 and 1387.4 eV, respectively), and the term F in (5.16a) is very close to unity. More generally, F in (5.16a) is

$$F = \frac{\exp(-t/L_{Hf}\cos\alpha)}{\exp(-t/L_{Si}\cos\alpha)}, \tag{5.16b}$$

where, for the case of $HfO_{1.9}N_{0.1}$ films on Si, L_{Hf} and L_{Si} are EALs for substrate Si $2p_{3/2}$ photoelectrons and Hf $4f_{7/2}$ photoelectrons, respectively, in $HfO_{1.9}N_{0.1}$ for which the kinetic energies are 1387.4 and 1472.4 eV. Since F will be close to unity if the kinetic energies of the two selected photoelectron lines are not too different, L_{Si} and L_{Hf} in (5.16b) were estimated with the NIST Electron Effective-Attenuation-Length Database [31] and found to be 1.77 and 1.85 nm, respectively [37]. Average values of F from (5.16b) ranged from 1.015 for a film thickness of 0.5 nm to 1.144 for a film thickness of 4.5 nm. A value of L from (5.16a) for $HfO_{1.9}N_{0.1}$ films on Si will be an average EAL for the average photoelectron energy of 1429.9 eV. Method 2 is a convenient method for determining EALs since the ratio $R_{t,\alpha}$ does not depend on the presence of surface contamination.

It is useful to plot $\ln[F + (R_{t,\alpha}/R_0)]/t$ versus $1/\cos\alpha$ to show clearly the similarities and differences of the plots for different film thicknesses [37]. If these plots are judged to be sufficiently linear for useful ranges of t and α, the derived values of L can be utilized as EALs to measure film thicknesses with (5.16) for these conditions. In practice, deviations from linearity can occur due to the effects of elastic scattering, particularly at larger film thicknesses and emission angles. Figure 5.8

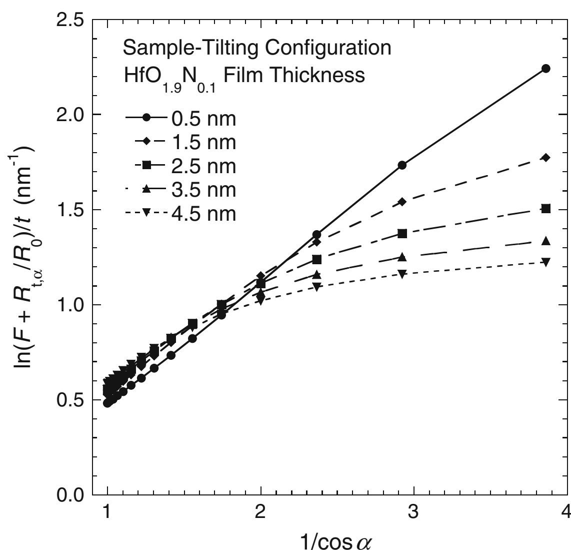

Fig. 5.8 Plots of $\ln[F + (R_{t,\alpha}/R_0)]/t$ versus $1/\cos\alpha$ for $HfO_{1.9}N_{0.1}$ films on Si obtained from simulated substrate Si $2p_{3/2}$ photoelectron intensities excited by Al Kα X-rays for the sample-tilting configuration and various film thicknesses [37]

shows plots of $\ln[F + (R_{t,\alpha}/R_0)]/t$ versus $1/\cos\alpha$ for $HfO_{1.9}N_{0.1}$ films on Si for different film thicknesses [37]. Values of R_0 in (5.16) were determined from separate simulations of Si $2p_{3/2}$ intensities for a bare Si substrate and of Hf $4f_{7/2}$ intensities for a 100 nm $HfO_{1.9}N_{0.1}$ film. We see that the plots in Fig. 5.8 are roughly linear for emission angles up to about 55° (for which $1/\cos\alpha$ is 1.74). At larger emission angles, deviations from linearity occur to an increasing extent for thicker films. Similar trends are found for thin films of $SiO_{1.6}N_{0.4}$ on Si although the deviations from linearity are less pronounced [37].

One-parameter linear fits (through the origin) were made to selected regions of the plots in Fig. 5.8 to derive average values of the EAL, L_{ave2}, for $HfO_{1.9}N_{0.1}$ from (5.16) for Method 2 [37]. These fits were judged satisfactory for angular ranges between 0° and 55° for film thicknesses of 0.5 and 1.5 nm, between 0° and 50° for a film thickness of 2.5 nm, and between 0° and 45° for film thicknesses of 3.5 and 4.5 nm. Similar fits were made for $SiO_{1.6}N_{0.4}$ films for emission angles between 0° and 55°.

Figure 5.9 shows plots of the ratio of derived values of L_{ave2} to the average IMFP for the two photoelectron lines in each oxynitride (3.895 nm at an average kinetic energy of 1385.4 eV for $SiO_{1.6}N_{0.4}$ and 2.265 nm at an average energy of 1429.9 eV for $HfO_{1.9}N_{0.1}$) as a function of film thickness for the sample-tilting and Theta Probe configurations [37]. As for the EALs from Method 1 in Fig. 5.7, we see that the EALs from Method 2 in Fig. 5.9 are systematically different for the sample-tilting and Theta Probe configurations. These differences are between 1 and 2 % for $SiO_{1.6}N_{0.4}$ and between 2 and 3 % for $HfO_{1.9}N_{0.1}$. The differences between EAL values for the two configurations (for each EAL algorithm) are associated with the effects of angular anisotropy in the photoionization cross section for the Theta Probe configuration [37].

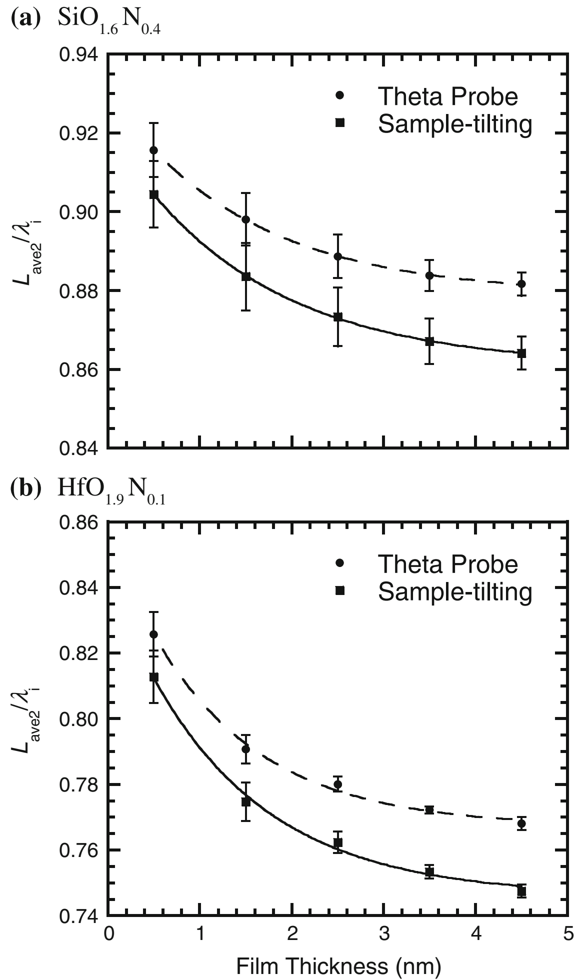

Fig. 5.9 Plots of L_{ave2}/λ_i (*symbols*) as a function of film thickness for **a** $SiO_{1.6}N_{0.4}$ and **b** $HfO_{1.9}N_{0.1}$ on Si for the Theta Probe configuration (*filled circle*) and the sample-tilting configuration (*filled square*). The error *bars* indicate one-standard-deviation uncertainties of the derived values of L_{ave2} from the linear fits described in the text. The *lines* show fits with a simple analytical equation to guide the eye [37]

The values of L_{ave2}/λ_i in Fig. 5.9b for $HfO_{1.9}N_{0.1}$ with the sample-tilting configuration decrease from 0.813 ± 0.008 for a film thickness of 0.5 nm to 0.748 ± 0.002 for a film thickness of 4.5 nm (where the stated uncertainties represent one-standard-deviation uncertainties in the derived values of L_{ave2}/λ_i from the linear fits with (5.16) to the selected regions of data plotted in Fig. 5.8). This decrease (8 %) is larger than the corresponding decrease of 4 % for $SiO_{1.6}N_{0.4}$ in Fig. 5.9a. The values of L_{ave2}/λ_i in Fig. 5.9b also differ from those of L_{ave1}/λ_i for $HfO_{1.9}N_{0.1}$ in Fig. 5.7b which range from 0.751 ± 0.008 for $\alpha = 0°$ to 0.740 ± 0.005 for $\alpha = 30°$ and 0.783 ± 0.012 for $\alpha = 55°$ (where the latter uncertainties are one-standard-deviation uncertainties in the derived values of L_{ave1}/λ_i from the linear fits with (5.15) to the selected regions of data in Fig. 5.6). These differences (and similar differences for $SiO_{1.6}N_{0.4}$) are due to elastic-scattering effects and the

fact that (5.15) provides an average EAL for a range of film thicknesses at a particular emission angle whereas (5.16) provides an average EAL for a range of emission angles at a particular thickness. Although the same sets of simulated intensities were analyzed in deriving EALs from Methods 1 and 2, the resulting average EALs can be different due to different weightings of the intensities in the various fits. While the values of L_{ave2}/λ_i for $HfO_{1.9}N_{0.1}$ in Fig. 5.9b were for a higher average energy (1429.9 eV) than for the values of L_{ave1}/λ_i in Fig. 5.7b (1385.4 eV), the ratios of the EAL to the IMFP should not vary appreciably over such a small energy range. We also note that the relatively strong dependence of the L_{ave2}/λ_i values for $HfO_{1.9}N_{0.1}$ on film thickness in Fig. 5.9b compared to the corresponding variation for $SiO_{1.6}N_{0.4}$ in Fig. 5.9a is another indication of the relatively larger effects of elastic scattering in $HfO_{1.9}N_{0.1}$ compared to $SiO_{1.6}N_{0.4}$.

Figures 5.7 and 5.9 demonstrate that EALs can depend in a complicated way on overlayer thickness, photoelectron emission angle, XPS configuration, and the particular algorithm used for the EAL determination. These dependencies also vary with the overlayer material, that is, on the strength of elastic-scattering effects. Although simple analytic predictive formulae for the EAL such as (5.13) and (5.14) are convenient for providing estimates of EALs, they obviously cannot be expected to show details of the EAL variations revealed by the SESSA simulations that were summarized in Figs. 5.7 and 5.9. Nevertheless, we find that values of the single-scattering albedo from (5.10) are 0.116 and 0.256 for $SiO_{1.6}N_{0.4}$ and $HfO_{1.9}N_{0.1}$, respectively, at an energy of 1387 eV (the energy of Si $2p_{3/2}$ photoelectrons excited by Al Kα X-rays). In this evaluation, IMFPs were determined using (5.5) and (5.6) and TMFPs were obtained from obtained from [31]. The corresponding ratios of L/λ_i from (5.13) are then 0.915 and 0.812 for $SiO_{1.6}N_{0.4}$ and $HfO_{1.9}N_{0.1}$, respectively; these values are close to but larger than the values of L_{ave1}/λ_i and L_{ave2}/λ_i plotted in Figs. 5.7 and 5.9. Values of L/λ_i were similarly determined from the Seah expressions, (5.7) and (5.14), and found to be 0.897 and 0.821 for $SiO_{1.6}N_{0.4}$ and $HfO_{1.9}N_{0.1}$, respectively. The former value agrees reasonably with values of L_{ave1}/λ_i and L_{ave2}/λ_i for $SiO_{1.6}N_{0.4}$ plotted in Figs. 5.7 and 5.9 while the latter value is generally larger than the corresponding values for $HfO_{1.9}N_{0.1}$ in Figs. 5.7 and 5.9.

We note that plots for $SiO_{1.6}N_{0.4}$ like those for $HfO_{1.9}N_{0.1}$ in Fig. 5.8 are qualitatively similar to those obtained from measured Si 2p photoelectron intensities for a 3.9 nm SiO_2 film on Si [41]. Nevertheless, there are systematic differences between these and other careful measurements [42] and the corresponding results from SESSA simulations [43]. These differences could be due to possible variations in the fraction of intrinsic or shakeup intensity accompanying Si 2p photoionization with SiO_2 thickness or photoelectron emission angle and/or to possible variations in the inelastic-scattering probabilities in the vicinity of the Si/SiO_2 and SiO_2/vacuum interfaces, also as a function of SiO_2 thickness or photoelectron emission angle [37, 42–44]. Neither of these effects is included in the SESSA simulations. Nevertheless, the results shown in Figs. 5.7 and 5.9 illustrate the usefulness of SESSA for determining systematic effects of film thickness, emission angle, XPS configuration, and EAL algorithm on EALs.

5.6.3 EAL Measurements

Most early EAL measurements (i.e., those performed prior to 1980) were made using the Method 1 algorithm [4, 33, 34]. Thin overlayer films were deposited on a substrate and measurements were made of the intensities of photoelectrons or Auger electrons from the substrate as a function of overlayer thickness. It was natural then to assume that the overlayer material formed uniform layers, and to assume that the observed signal intensities would depend exponentially on overlayer thickness. In fact, deviations from the expected exponential behavior were taken as evidence that the films must be nonuniform, and the results were discarded. It was not until the advent of scanning probe microscopes and low-energy electron microscopes in the 1980s that the complexities of thin-film growth became more apparent. It was also around this time that the role of elastic scattering was recognized [45], i.e., that the EAL was not the same as the IMFP. Kim and Seah [42] have recently reported careful EAL determinations for photoelectrons excited by Al Kα X-rays using the Method 2 algorithm for thin films of SiO_2 on Si.

Few EAL measurements have been published based on HAXPES experiments [46–49]. Like most subsequent efforts, Dallera et al. [46] utilized EAL Method 1 and reported EALs for Al 1s photoelectrons from an AlAs layer covered by various thicknesses of GaAs for kinetic energies between about 740 eV and 6 keV. Their GaAs EALs were proportional to the square root of the electron energy, and ranged from about 1 nm at an energy of about 750 eV to about 5.3 nm at an energy of about 6 keV. Sacchi et al. [47] determined EALs for wedge-shaped films of Co, Cu, Ge, and Gd_2O_3 on a Si substrate. Attenuation measurements were made of Si 1s, Si 2s, and Si 2p photoelectrons at kinetic energies between 4 and 6.15 keV; some additional measurements were made of photoelectron signals from the overlayer film. We comment further on their results below. Gray et al. [48] reported EALs for thin films of lanthanum niobate on either an $LaAlO_3$ substrate or a $(LaAlO_3)_{0.3}(Sr_2AlTaO_6)_{0.7}$ substrate for energies of selected substrate photoelectron peaks from about 4.4 keV to about 5.9 keV. Their EALs were about 16 % less than EALs that were estimated from IMFPs for $LaAlO_3$ calculated with the TPP-2M equation (5.5) and (5.6) and the correction for elastic-scattering effects (5.13). Finally, Rubio-Zuazo and Castro [49] obtained EALs for Au films on a Cu substrate for photoelectron energies between 1 and 15 keV; comments on these results are also given below. They employed EAL Method 1 and some additional measurements of signals from the Au overlayer. Their experimental setup is noteworthy in that they were able to perform in situ X-ray diffraction measurements for determination of the Au film thickness and roughness as the films were grown. Rubio-Zuazo and Castro reported that their Au EALs were proportional to $E^{0.627}$; this energy dependence, however, is weaker than expected from the Seah S3 formula (5.14). Sacchi et al. performed similar X-ray reflectivity measurements on their films ex situ [47].

5.6.4 Comparisons Between Measured EALs and Calculated EALs

We now make comparisons of the EAL measurements for elemental solids of Sacchi et al. [47] and of Rubio-Zuazo and Castro [49] with the corresponding calculated IMFPs of Tanuma et al. [5] and EALs determined from these IMFPs with (5.13b). While (5.13b) was developed only for energies below 5 keV, we will apply it for energies up to 10 keV since it shows reductions in the effects of elastic scattering (i.e., smaller percentage differences between IMFPs and EALs with increasing energy) that are expected from Fig. 5.5. In using (5.13b), we will thus be ignoring the complications of EALs varying with different film thicknesses, emission angles, XPS configurations, and EAL algorithms that were described in Sect. 5.6.2 since these effects should also become smaller with increasing energy. We will also be ignoring the effects of X-ray polarization on the EALs.

We utilized TMFPs from the the NIST Electron Effective-Attenuation-Length Database [31] to compute values of the single-scattering albedo from (5.10) for the electron energies chosen by Tanuma et al. between 992 eV and 9.897 keV [5]. Figure 5.10 shows plots of these calculated IMFPs (dashed lines) and EALs (solid lines) for (a) Co, (b), Cu, (c) Ge, and (d) Au. We first note that the calculated IMFPs for Cu and Au in Fig. 5.10 agree well with corresponding IMFPs obtained from EPES experiments [14] that were shown in Fig. 5.1. In addition, Powell and Jablonski [10] concluded that IMFPs calculated from optical data by at least two groups for Cu, Ge, and Au agreed satisfactorily with IMFPs derived from EPES experiments by at least two groups.

The error bars on the measured EALs in Fig. 5.10 were determined by each experimental group. Sacchi et al. [47] stated that their EAL uncertainties were determined from their exponential fits to plots of a selected substrate peak as a function of overlayer thickness; these uncertainties are assumed to represent one-standard-deviation values. Rubio-Zuazo and Castro reported EAL uncertainties from variations in their exponential-fit parameters for extreme values of overlayer thicknesses that were derived from the measured thicknesses and the corresponding roughness values [49]; the latter values were identified as possible thickness uncertainties.

The EAL comparison for Co in Fig. 5.10a indicates that the measured EALs [47] are systematically larger than the calculated EALs from (5.13) by between 28 % at 4.079 keV and 12 % at 5.77 keV. The reason for these differences is not known although it could be associated with an unexpected kink in a plot of Co film thicknesses from X-ray reflectivity data versus position along their sample wedge [47]. The measured EALs for Cu [47] in Fig. 5.10b agree closely with the calculated EALs. For Ge, the measured EALs [47] in Fig. 5.10c are systematically lower than the calculated EALs. Finally, the comparison of the measured EALs [49] for Au in Fig. 5.10d shows good agreement with the calculated EALs at the highest energies (8.75–9.69 keV) but there are systematic differences at lower energies. The calculated IMFPs of Tanuma et al. [5] for Au, however, agree well other IMFP data [10, 14]. Powell et al. [50] have recently shown that the differences between the

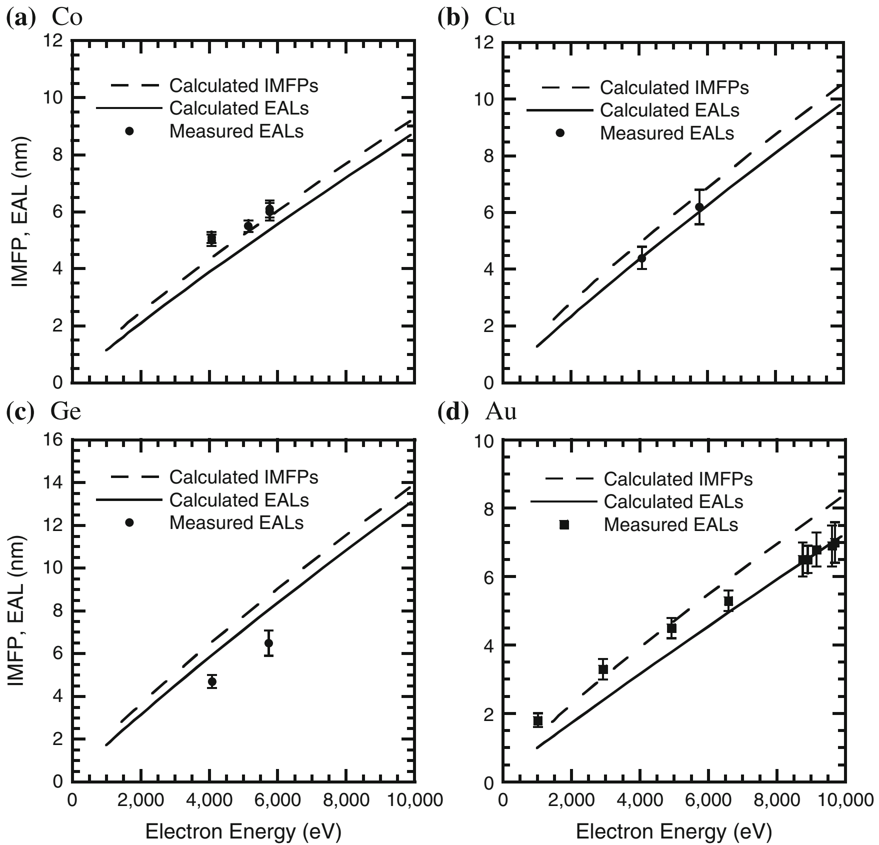

Fig. 5.10 Comparisons of the calculated inelastic mean free paths of Tanuma et al. [5] (*dashed lines*), the effective attenuation lengths calculated from (5.10) and (5.13b) (*solid lines*), and the measured effective attenuation lengths reported by Sacchi et al. [47] (*filled circle*) and by Rubio-Zuazo and Castro [49] (*filled square*) for **a** Co, **b** Cu, **c** Ge, and **d** Au

calculated EALs for Au in Fig. 5.10d and the measured EALs of Rubio-Zuazo and Castro [49] can be explained by assuming that their films were islands rather than continuous films. They used the NIST SESSA database [2, 3] to determine the fractional area of the assumed Au islands corresponding to the observed attenuation of Cu substrate 1s and 2s photoelectrons for an X-ray energy of 10.008 keV. As expected, the fractional Au area increased from about 20 % for a film thickness of 0.2 nm to a fractional area of about 90 % for a film thickness of 9.3 nm [50].

Table 5.3 lists values of the single-scattering albedo from (5.10) for the four elemental solids shown in Fig. 5.10 at the extremes of the energy range shown for the calculated IMFPs of Tanuma et al. [5] and calculated EALs from (5.13b). At the lowest energy, 992 eV, the values of ω range from 0.252 for Ge to 0.356 for Au. The calculated EALs are then less than the corresponding IMFPs by between 18.5 % for Ge and 26.1 % for Au. At the highest energy, 9.987 keV, the values of ω

Table 5.3 Values of the single-scattering albedo, ω, from (5.10) and the corresponding percentage decreases of the EALs [calculated using (5.13b)] from the calculated IMFPs of Tanuma et al. [5] for Co, Cu, Ge, and Au at electron energies of 992 eV and 9.857 keV

Element	E = 992 eV		E = 9.987 keV	
	ω	Percentage decrease	ω	Percentage decrease
Co	0.290	21.4	0.075	5.5
Cu	0.316	23.5	0.088	6.5
Ge	0.252	18.5	0.072	5.3
Au	0.356	26.1	0.185	13.6

are between 0.072 for Ge and 0.185 for Au, and the calculated EALs are then smaller than the related IMFPs by between 5.3 and 13.6 %.

Finally, we comment briefly on the EALs for GaAs that were reported by Dallera et al. [46]. Their EALs, ranging from about 1 nm at an energy of about 750 eV to about 5.3 nm at an energy of about 6 keV, are significantly smaller than the corresponding calculated IMFPs [23] which range from 1.70 nm at 735 eV to 8.94 nm at 6 keV. Since the average atomic number of GaAs (32) is the same as the atomic number of Ge, we can calculate ω at a given energy from the TMFP for Ge [31] and the IMFP for GaAs. From (5.13), we then expect that the calculated EALs for energies of 735 eV and 6 keV would be 1.35 and 8.29 nm, respectively. We have no explanation for the substantial differences (from 25 to 40 %) between the measured and calculated EALs.

5.7 NIST Databases for HAXPES

NIST provides five databases that are useful for XPS applications, and brief descriptions will now be given of these databases. The NIST X-ray Photoelectron Spectroscopy Database [51] contains more than 33,000 new data records with information taken from publications that met the NIST evaluation criteria [51]. Each record typically contains information on measured photoelectron binding energies, Auger-electron kinetic energies, Auger parameters, chemical shifts, doublet separations, and surface or interface core-level shifts together with citation information. Newer records contain information on the specimen material, the conditions of measurement, and the analysis of the data. The database can be used for the identification of unknown lines, retrieval of data for selected elements (binding energy, Auger kinetic energy, chemical shift, and surface or interface core-level shift), retrieval of data for selected compounds (according to chemical name, selected groups of elements, or chemical classes), display of Wagner plots, and retrieval of data by scientific citation. Reference photoelectron binding energies, reference Auger-electron kinetic energies, and reference Auger parameters are available for many elemental solids. These reference energies, derived from analyses of Handbook data [52], are useful in calculations of chemical shifts.

The NIST Electron Elastic-Scattering Cross-Section Database [53] provides differential elastic-scattering cross sections, total elastic-scattering cross sections, phase shifts, and transport cross sections for elements with atomic numbers from 1 to 96 and for electron energies between 50 eV and 300 keV (in steps of 1 eV). The cross sections in the database were calculated using the Dirac-Hartree-Fock atomic potential for each element [54]. Knowledge of elastic-scattering effects is important for the development of theoretical models for quantitative analyses by XPS, Auger-electron spectroscopy (AES), electron microprobe analysis, and analytical electron microscopy. The software package is designed to facilitate simulations of electron transport for these and similar applications in which electron energies from 50 eV to 300 keV are utilized. An evaluation of calculated and measured elastic-scattering cross-sections data has been published by Jablonski et al. [54].

The NIST Electron Inelastic-Mean-Free-Path Database [55] provides IMFPs principally for use in surface analysis by AES and XPS. IMFPs are available for electron energies between 50 eV and 10 keV although most of the available data are for energies less than 2 keV. The database includes IMFPs calculated from experimental optical data and IMFPs measured by EPES. If no calculated or measured IMFPs are available for a material of interest, values can be estimated from the predictive IMFP formulae of Tanuma et al. [(5.5) and (5.6)] and of Gries [56]. Powell and Jablonski [4, 10] have published evaluations of calculated and measured IMFPs.

The NIST Electron Effective-Attenuation-Length Database [31] provides EALs in solid elements and compounds at user-selected electron energies between 50 eV and 2 keV. The database was designed mainly to provide EALs for applications in surface analysis by AES and conventional XPS, i.e., for XPS instruments with Al or Mg Kα X-ray sources. EALs are calculated using an algorithm based on electron-transport theory for measurement conditions specified by the user [33, 34]. A critical review on the EAL has been published by Jablonski and Powell [33, 34].

The NIST Database for the Simulation of Electron Spectra for Surface Analysis (SESSA) [2, 3] facilitates quantitative interpretation of AES and XPS spectra and improves the accuracy of quantitation in routine analysis. This database contains extensive physical data needed to perform quantitative interpretation of an electron spectrum for a specimen of given composition and a user-specified measurement configuration. A simulation module provides spectra and peak intensities for a sample consisting of a substrate and a variable number of overlayer films (with compositions and thicknesses specified by the user); a newer version provides similar information for nanostructures such as islands, lines, spheres, and layered spheres on surfaces. This database provides physical data such as IMFPs and TMFPs for electron energies up to 20 keV, and so is a valuable resource for HAXPES applications. Moreover, SESSA allows a user to specify the polarization of the incident X-ray beam in HAXPES and provides parameters for determining the non-dipole contributions to photoionization cross sections.

Figure 5.11 shows the home screen of the graphical user interface for SESSA. The design of the software allows the user to enter the required information in a reasonably simple way. The modular structure of the user interface closely matches

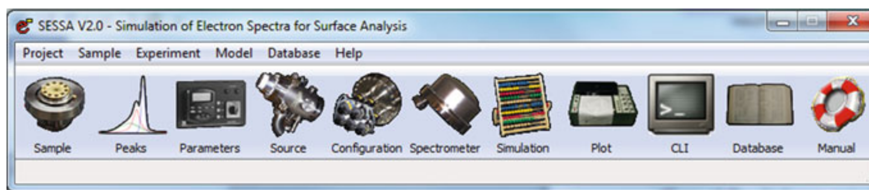

Fig. 5.11 Home screen of the graphical user interface for the NIST SESSA database [2, 3]

that of the usual control units on a real instrument. Any user who is familiar with a typical XPS spectrometer can perform a retrieval/simulation operation with the SESSA software in a few minutes for a specimen with a given composition and morphology. A command line interface can also control the software; this feature allows users to load sequences of commands that facilitate a series of simulations for similar sample materials, similar instrumental conditions, or similar simulation conditions.

Werner et al. [57] have published examples of SESSA applications for HAXPES. Powell et al. [58] have recently shown that SESSA can be used to determine XPS detection limits for thin-film materials such as a thin film on a substrate or buried at varying depths in another material for common XPS measurement conditions. If an XPS detection limit for a minor species in a homogeneous solid is known or can be estimated [59], SESSA simulations can provide a means for converting these detection limits to the corresponding XPS detection limits for that species as a thin film on or buried in the chosen solid [58].

5.8 Summary

An overview has been given of recent work for the determination of IMFPs, MEDs, IDs, and EALs with emphasis placed on HAXPES applications. Sources of data have been provided for these parameters and useful predictive equations have been given for parameter estimation where no alternative data sources are available. Comparisons have been made between calculated and measured IMFPs and EALs. Finally, information is given on NIST databases for HAXPES applications.

References

1. ISO 18115-1, Surface Chemical Analysis—Vocabulary—Part 1. General terms and terms used in spectroscopy, International Organization for Standardization, Geneva (2010); this document can be accessed at http://avs.org/Education-Outreach/Technical-Resources, http://www.emsl.pnl.gov/capabilities/spectroscopy/surface_analysis, and http://www.aist.go.jp/aist_e/aist_laboratories/6metrology/iso.html

2. W.S.M. Werner, W. Smekal, C.J. Powell, NIST Database for the Simulation of Electron Spectra for Surface Analysis, Version 1.3, Standard Reference Data Program Database 100, U.S. Department of Commerce, National Institute of Standards and Technology, Gaithersburg, MD (2011); http://www.nist.gov/srd/nist100.cfm
3. W. Smekal, W.S.M. Werner, C.J. Powell, Surf. Interface Anal. **37**, 1059 (2005)
4. C.J. Powell, A. Jablonski, Nucl. Instrum. Methods Phys. Res. A **601**, 54 (2009)
5. S. Tanuma, C.J. Powell, D.R. Penn, Surf. Interface Anal. **43**, 689 (2011)
6. D.R. Penn, Phys. Rev. B **35**, 482 (1987)
7. S. Tanuma, C.J. Powell, D.R. Penn, J. Electron Spectrosc. Relat. Phenom. **62**, 95 (1993)
8. S. Tanuma, C.J. Powell, D.R. Penn, Surf. Interface Anal. **17**, 911 (1991)
9. S. Tanuma, C.J. Powell, D.R. Penn, Surf. Interface Anal. **20**, 77 (1993)
10. C.J. Powell, A. Jablonski, J. Phys. Chem. Ref. Data **19**, 28 (1999)
11. H. Bethe, Ann. der Physik **5**, 325 (1930)
12. M. Inokuti, Rev. Mod. Phys. **43**, 297 (1971)
13. S.F. Mao, Y.G. Li, R.G. Zeng, Z.J. Ding, J. Appl. Phys. 104, 114907 (2008); erratum 105, 099902 (2009)
14. S. Tanuma, T. Shiratori, T. Kimura, K. Goto, S. Ichimura, C.J. Powell, Surf. Interface Anal. **37**, 833 (2005)
15. W.S.M. Werner, C. Tomastik, T. Cabela, G. Richter, H. Störi, Surf. Sci. **470**, L123 (2000)
16. W.S.M. Werner, C. Tomastik, T. Cabela, G. Richter, H. Störi, J. Electron Spectrosc. Relat. Phenom. **113**, 127 (2001)
17. W.S.M. Werner, K. Glantschnig, C. Ambrosch-Draxl, J. Phys. Chem. Ref. Data **38**, 1013 (2009)
18. N.D. Mermin, Phys. Rev. B **1**, 2362 (1970)
19. J.D. Bourke, C.T. Chantler, J. Phys. Chem. A **116**, 3202 (2012)
20. J.D. Bourke, C.T. Chantler, Phys. Rev. Lett. **104**, 206601 (2010)
21. C.T. Chantler, J.D. Bourke, J. Phys. Chem. Lett. **1**, 2422 (2010)
22. B. Da, H. Shinotsuka, H. Yoshikawa, Z.J. Ding, S. Tanuma, Phys. Rev. Lett. **113**, 063201 (2014)
23. S. Tanuma et al. (to be published)
24. http://www.wien2k.at
25. http://www.feffproject.org
26. S. Tanuma, C.J. Powell, D.R. Penn, Surf. Interface Anal. **21**, 165 (1994)
27. S. Tanuma, C.J. Powell, D.R. Penn, Surf. Interface Anal. **37**, 1 (2005)
28. M.P. Seah, Surf. Interface Anal. **44**, 497 (2012)
29. S. Tanuma, C.J. Powell, D.R. Penn, Surf. Interface Anal. **17**, 929 (1991)
30. A. Jablonski, C.J. Powell, J. Vac. Sci. Technol. A **27**, 253 (2009)
31. C.J. Powell, A. Jablonski, NIST Electron Effective-Attenuation-Length Database, Version 1.3, Standard Reference Data Program Database 82, U.S. Department of Commerce, National Institute of Standards and Technology, Gaithersburg, MD (2011); http://www.nist.gov/srd/nist82.cfm
32. S. Tanuma, H. Yoshikawa, H. Shinotsuka, R. Ueda, J. Electron Spectrosc. Relat. Phenom. **190**, 127 (2013)
33. A. Jablonski, C.J. Powell, Surf. Sci. Rep. **47**, 33 (2002)
34. C.J. Powell, A. Jablonski, Surf. Interface Anal. **33**, 211 (2002)
35. A. Jablonski, C.J. Powell, J. Electron Spectrosc. Relat. Phenom. **199**, 27 (2015)
36. M.P. Seah, Surf. Interface Anal. **44**, 1353 (2012)
37. C.J. Powell, W.S.M. Werner, W. Smekal, Surf. Interface Anal. **45**, 628 (2013)
38. G. Tasneem, C. Tomastik, S. Gerhold, W.S.M. Werner, W. Smekal, C.J. Powell, Surf. Interface Anal. **43**, 934 (2010)
39. R. Champaneria, P. Mack, R. White, J. Wolstenholme, Surf. Interface Anal. **35**, 1028 (2003)

40. Certain commercial products are identified to specify the experimental conditions. This identification does not imply that the products are endorsed or recommended by the National Institute of Standards and Technology, or that they are necessarily the most suitable for the purposes described
41. M.P. Seah, R. White, Surf. Interface Anal. **33**, 960 (2002)
42. K.J. Kim, M.P. Seah, Surf. Interface Anal. **39**, 512 (2007)
43. C.J. Powell, W.S.M. Werner, W. Smekal, Appl. Phys. Lett. **89**, 252116 (2006)
44. N. Pauly, S. Tougaard, Surf. Sci. **605**, 1556 (2011)
45. O.A. Baschenko, V.I. Nefedov, J. Electron Spectrosc. Relat. Phenom. **27**, 109 (1982)
46. C. Dallera, L. Duo, G. Panaccione, G. Paolicelli, B. Cowie, J. zegenhagen, and L. Braicovich, Appl. Phys. Lett. **85**, 4532 (2004)
47. M. Sacchi, F. Offi, P. Torelli, A. Fondacaro, C. Spezzani, M. Cautero, G. Cautero, S. Huotari, M. Grioni, R. Delaunay, M. Fabrizioli, G. Vanko, G. Monaco, G. Paolicelli, G. Stefani, G. Panaccione, Phys. Rev. B **71**, 155117 (2005)
48. A.X. Gray, A. Janotti, J. Son, J.M. LeBeau, S. Ueda, Y. Yamashita, K. Kobayashi, A.M. Kaiser, R. Sutarto, H. Wadati, G.A. Sawatzky, C.G. Van de Walle, S. Stemmer, C.S. Fadley, Phys. Rev. B **84**, 075104 (2011)
49. J. Rubio-Zuazo, G.R. Castro, J. Electron Spectrosc. Relat. Phenom. **184**, 384 (2011)
50. C.J. Powell, W.S.M. Werner, W. Smekal (to be published)
51. A.V. Naumkin, A. Kraut-Vass, S.W. Gaarenstroom, C.J. Powell, NIST X-ray Photoelectron Spectroscopy Database, Version 4.1, Standard Reference Data Program Database 64, U.S. Department of Commerce, National Institute of Standards and Technology, Gaithersburg, MD (2012); http://srdata.nist.gov/xps
52. C.J. Powell, J. Electron Spectrosc. Relat. Phenom. **185**, 1 (2012)
53. F. Salvat, A. Jablonski, C.J. Powell, NIST Electron Elastic-Scattering Cross-Section Database, Version 3.2, Standard Reference Data Program Database 64, U.S. Department of Commerce, National Institute of Standards and Technology, Gaithersburg, MD (2010); http://www.nist.gov/srd/nist64.cfm
54. A. Jablonski, F. Salvat, C.J. Powell, J. Phys. Chem. Ref. Data **33**, 409 (2004)
55. C.J. Powell, A. Jablonski, NIST Electron Inelastic-Mean-Free-Path Database, Version 1.2, Standard Reference Data Program Database 71, U.S. Department of Commerce, National Institute of Standards and Technology, Gaithersburg, MD (2010); http://www.nist.gov/srd/nist71.cfm
56. W.H. Gries, Surf. Interface Anal. **24**, 38 (1996)
57. W.S.M. Werner, W. Smekal, T. Hisch, J. Himmelsbach, C.J. Powell, J. Electron Spectrosc. Relat. Phenom. **190**, 137 (2013)
58. C.J. Powell, W.S.M. Werner, W. Smekal, J. Vac. Sci. Technol. A **32**, 050603 (2014)
59. A.G. Shard, Surf. Interface Anal. **46**, 175 (2014)

Chapter 6
Hard X-ray Angle-Resolved Photoelectron Spectroscopy (HARPES)

Alexander X. Gray

Abstract This chapter will provide an overview of the basic principles of hard X-ray angle-resolved photoelectron spectroscopy (HARPES), which has recently emerged as a powerful technique for studying momentum-resolved bulk electronic structure of novel materials, buried interfaces and heterostructures. HARPES provides access to the bulk electronic structure of solids due to the high inelastic mean-free paths (IMFP) of the valence-band electrons emitted at high excitation energies. The first results of HARPES measurements at excitation energies of 3.24 and 5.95 keV will be presented. The systems that will be discussed are W, as a model transition-metal system to study basic principles in such HARPES experiments; GaAs, as a technologically-relevant material to illustrate the broad applicability of this new technique; and $Ga_{1-x}Mn_xAs$, as a novel dilute ferromagnetic semiconductor material. The experimental results will be compared to free-electron final-state model calculations and more precise one-step photoemission theory including matrix element effects. Some likely future applications areas will also be discussed.

6.1 Introduction and Basic Concepts of Angle-Resolved Photoelectron Spectroscopy

It would be unjust to delve into the discussion of all the advantages of HARPES without first at least briefly reviewing the conventional ARPES technique, which uses ultraviolet and soft X-ray excitation (usually $h\nu < 100$ eV), or more recently going up to the 1000 eV regime. To this day, ARPES offers the most direct way of

---

A.X. Gray (✉)
Department of Physics, Temple University, Philadelphia, PA 19122, USA
e-mail: axgray@temple.edu

© Springer International Publishing Switzerland 2016

J.C. Woicik (ed.), *Hard X-ray Photoelectron Spectroscopy (HAXPES)*,
Springer Series in Surface Sciences 59, DOI 10.1007/978-3-319-24043-5_6

probing the electronic structure of solids, since the unprocessed output of the experiment is the map of photoelectron intensities as a function of electron kinetic energy (and thus binding energy E_B) and electron crystal momentum or wave vector. This magnificent straightforwardness of the measurement owes itself to the manner in which photoelectrons disperse as they leave the surface of the sample and travel through the analyzer. The latter has been discussed in-depth earlier in this book—by virtue of traveling between the two biased hemispheres of the analyzer after leaving a specially tuned retarding lens, photoelectrons are spatially dispersed along the y-axis of the detector based on their kinetic energies (see Fig. 6.1a). The former, namely the *angular* dispersion, or the dispersion along the x-axis of the detector as depicted in Fig. 6.1a, will be discussed below.

In principle, by measuring the kinetic energy E_{kin} of the photoelectron, one simultaneously obtains information about the photoelectron momentum $\boldsymbol{p}$, whose absolute value in the non-relativistic limit is given by $p = \sqrt{2mE_{kin}}$. The photoelectron momentum vector, of course, will have a component which is perpendicular to the surface of the sample, and another component which is parallel to that surface, as illustrated in Fig. 6.1b. The perpendicular component of the photoelectron momentum vector $\boldsymbol{p}_\perp$ is not conserved across the surface of the sample due to the surface potential V_0 that must be surmounted in leaving the solid. However, the component of the photoelectron momentum which is parallel to the sample surface $\boldsymbol{p}_{||}$, is conserved, and is related to the kinetic energy and the polar photoelectron take-off angle θ_{TOA} via $\boldsymbol{p}_{||} = \hbar \boldsymbol{k}_{||} = \sqrt{2mE_{kin}} \cdot \sin\theta_{TOA}$, where $\boldsymbol{k}_{||}$ is the

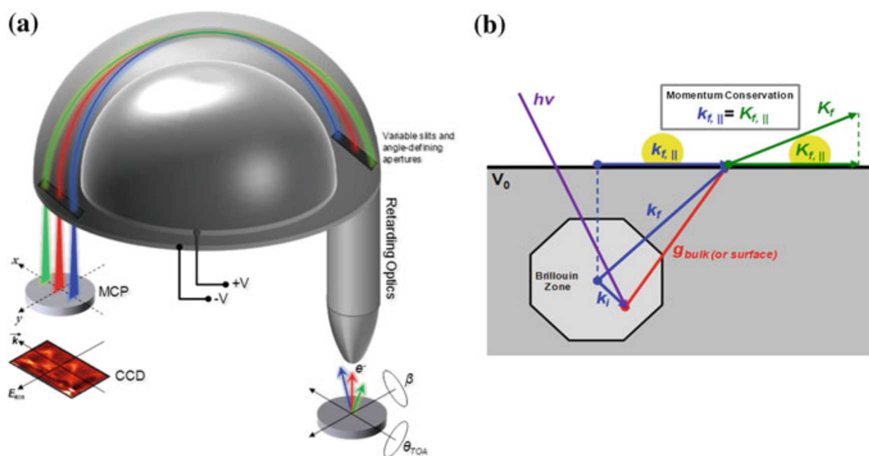

Fig. 6.1 **a** Schematic diagram of a hemispherical electrostatic analyzer and its primary components. **b** Schematic diagram of the photoemission process in k-space. Wave vector component of the final photoelectron momentum parallel to the surface of the sample is conserved

surface-parallel component of the electron wave vector. As a result of this relationship, detailed electronic dispersion $E_B(\boldsymbol{k}_{\|})$ can be obtained simply by tracking the changes in binding energies of the valence-band peaks as functions of the take-off angle θ_{TOA}. For an electron analyzer equipped with a two-dimensional detector, this task becomes even easier, since the electrons exiting the sample at various take-off angles will be dispersed along the x-axis of the microchannel plate (MCP) as illustrated in Fig. 6.1a. The momentum resolution of such measurement will usually be determined by the finite acceptance angle of the electron analyzer Ω_0 at the exit of the lens, and the detailed imaging properties of the lens.

In addition to recording the electronic dispersion $E_B(\boldsymbol{k}_{\|})$ as a function of the take-off angle θ_{TOA}, one can also do the same experiment by varying the polar take-off angle β_{TOA}, which is orthogonal to θ_{TOA}, as depicted in Fig. 6.1a. This way, both surface-parallel components of the electron wave vector $\boldsymbol{k}$, k_x and k_y can be mapped-out as function of binding energy. As a result, what one gets is a three-dimensional dataset (k_x, k_y, E_B), which represents a finite volume of the energy-momentum space for a given solid, containing all the information about the valence-band electronic structure and the Fermi surface.

ARPES had, and continues to have, major impacts on solid-state physics in emerging fields, such as the studies of topological insulators [1–3], cuprate superconductors [4–6], and graphene [7–9]. As of 2014, tens of thousands publications can be found on the internet on the subject of ARPES [10].

6.2 Angle-Resolved Photoelectron Spectroscopy in the Hard X-ray Regime: Challenges and Limitations

The major disadvantage of the conventional ARPES technique is its extreme surface-sensitivity, due to the very low inelastic mean-free paths of the electrons photoemitted using ultraviolet and soft X-ray radiation ($h\nu$ < 100 eV). As a quantitative example, widely-used TPP-2M formula [11–13] predicts that the IMFP for tungsten will be 4.2 Å at $h\nu$ = 25 eV, and 4.8 Å at $h\nu$ = 100 eV [14–16]. Such short probing depths correspond to just a few atomic layers below the surface of the sample, and thus the spectrum will be dominated by the signal coming mainly from the surface. Due to this shortcoming, in-situ cleaving or sample-growth is often required in order to avoid any kind of surface oxidation, adsorption or desorption, and contamination prior to the measurement. In fact, even in ultra-high vacuum, the surface adsorption or desorption rate for some solids can be rapid enough to make a sample change its properties in a matter of hours [17]. This suggests that going to higher photon energies with hard X-ray excitation and the resulting larger electron inelastic mean-free paths will provide a more accurate picture of bulk electronic structure, and reduce the surface contribution to the spectrum, thus diminishing the necessity for elaborate sample preparation. However, going to higher photon

energies, and particularly into the hard X-ray regime, opens up a whole new "Pandora's box" of problems and limitations, which will be discussed in the sections below.

6.2.1 *Phonon Effects and the Debye-Waller Factor*

Firstly, as the photon energy, and therefore the kinetic energy, of the photoelectrons increases, the effects of phonon creation and annihilation begin to play an important role in the experiment. In any angle-resolved photoemission experiment, the two major contributions to the spectrum will be due to the direct transitions, for which the crystal momentum is conserved, and due to the phonon-assisted non-direct transitions, for which the atomic vibrations diminish the degree of translational symmetry in the crystal [18, 19]. In a direct transition, initial occupied one-electron Bloch-wave state with the wave vector $\boldsymbol{k_i}$ can only make a transition to a final state with wave vector $\boldsymbol{k_f} = \boldsymbol{k_i} + \boldsymbol{g_n}$ where $\boldsymbol{g_n}$ is a reciprocal lattice vector for the given crystal structure. Therefore, the contribution from the direct transitions alone utilizes the full advantage of the momentum conservation equations mentioned earlier, thus resulting in a clean electronic dispersion $E_B(\boldsymbol{k}_{||})$. Conversely, the contribution due to the phonon-assisted transitions smears out the band structure and suppresses the dispersive direct-transition features. The relative intensities of these two contributions depend on both the photoelectron kinetic energy and the temperature of the sample.

With a good degree of precision, the percentage of transitions that are direct can be estimated by a photoemission Debye-Waller (D-W) factor, which is given by $W(T) \approx \exp[-\frac{1}{3}g^2\langle U^2(T)\rangle]$, where $\boldsymbol{g}$ is the reciprocal lattice vector representing the change in the initial photoelectron wave vector due to a given direct transition, and $\langle U^2(T)\rangle$ is the one-dimensional mean-squared vibrational displacement at temperature T. In other words, the phonon-related smearing of the dispersive direct-transition features becomes more significant at higher temperatures (via the $\langle U^2(T)\rangle$ term) and higher excitation energies (via the $\boldsymbol{g}^2$ term). More detailed basic treatment of the phonon-assisted transitions in the valence-band photoemission spectra can be found in the classic 1980s papers by Shevchik [18, 19] and by Hussain et al. [20–25]. Latest state-of-the art treatise of the phonon effects in HAXPES and HARPES by using the *one-step model* of photoemission is described by Minár et al. [26–28], and is presented in Chap. 7 of this book.

To illustrate the material-dependent character of the phonon effects in HARPES, Fig. 6.2 displays four typical plots of the Debye-Waller factors for Ca, C, Ge, and W valence-band photoemission calculated as functions of kinetic energy and temperature [29, 30]. This type of chart can be used as a helpful metric in determining the optimal photon energy and temperature for a HARPES experiment, such that a reasonable fraction of direct transitions is present in the spectra. For example, looking at the chart for Ca, it is clear that even with cryogenic cooling only 20 % or

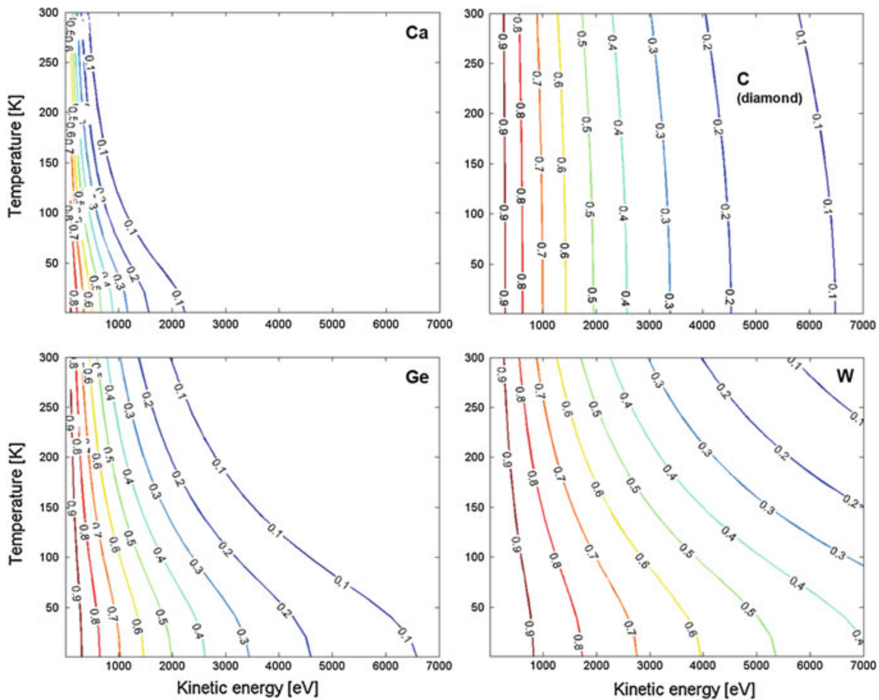

Fig. 6.2 Charts of the Debye-Waller factors for Ca, C, Ge, and W valence-band photoemission calculated as functions of kinetic energy and temperature (From [29, 30])

less of the signal will originate from the ***k***-conserving transitions. In fact, in order to get 50 %, even at the temperature of 20 K, one has to go into the soft X-ray regime, down to about 700 eV, where the IMFP is about 26.1 Å.

Other elements, such as C (applicable to diamond, but not graphite), are more forgiving, and will allow one to go as high as 2 keV in order to get 45–50 % of the direct transitions in the spectrum. For diamond, going to 2 keV will yield an IMFP of about 49.5 Å. It is important to note that the equipotential D-W lines for C are almost vertical, so that ultralow temperatures may not in fact be needed to take maximum advantage of higher energy band mapping. Similar nearly temperature-independent behavior is observed to various degrees in most elements for ultra-low temperatures (<30 K), which is a consequence of zero-point motion [29]. This happens to be a very helpful effect, since it implies that HARPES experiments can be performed in most modern synchrotron-based and laboratory-based endstations equipped with liquid He cooling.

Germanium is an example of the material for which temperature starts playing an important role in the multi-keV regime. 50 % direct transitions can be obtained at liquid-helium temperatures at as high as 2 keV, where the IMFP is about 38.4 Å; looking at Ge here is also relevant to the closely related material GaAs (same average atomic mass and very similar Debye temperature), which is discussed later

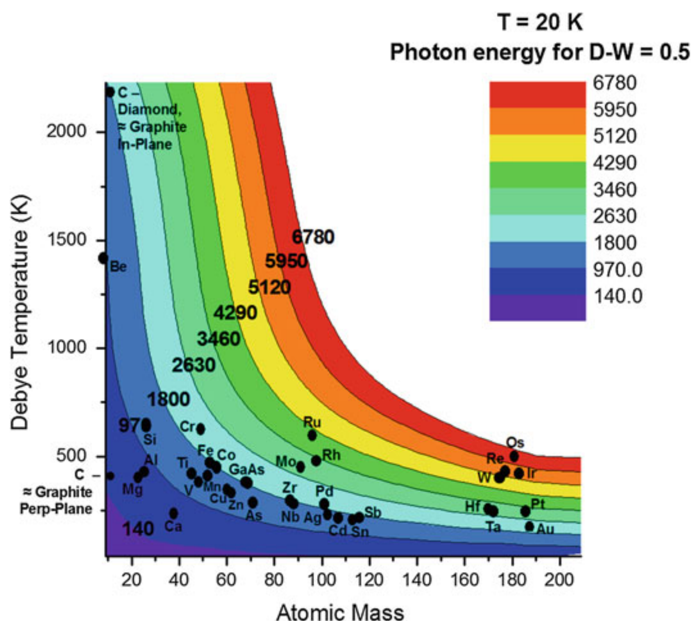

Fig. 6.3 Photon energies which at the temperature of 20 K yield Debye-Waller factors of 0.5 (50 % direct transitions) as a function of atomic mass and Debye temperature. Plotting the positions of about 40 elements on this chart shows that HARPES studies should be possible for many materials in the 1–3 keV energy range, and for some materials such as Rh, Ru, W, Ir, Re and Os in the 3–6 keV range with an average IMFP of as high as ∼55 Å at 6 keV

in this chapter. However, going to liquid-nitrogen temperatures (∼70 K) at the same photon energy will reduce the fraction of the direct transitions to 40 %. Finally, W is well-known to be among the few elements which are best at suppressing phonon effects in ARPES due to their high Debye temperature and atomic mass. About 45 % of the signal originating from the ***k***-conserving transitions is observed at the temperature of 20 K and the photon energy of 6 keV, where the IMFP in tungsten is estimated to be about 60.7 Å; W is another system studied with HARPES and discussed later in this chapter.

In order to assess the degree of phonon smearing for various materials, Fig. 6.3 shows the photon energies which at the temperature of 20 K yield Debye-Waller factors of 0.5 (50 % direct transitions) as a function of atomic mass and Debye temperature. After plotting the positions of about 40 elements on this chart, it becomes evident that HARPES studies should be possible for many materials in the 1–3 keV energy range, and for some materials such as Rh, Ru, W, Ir, Re and Os in the 3–6 keV range with an average IMFP of as high as ∼55 Å at 6 keV. Based on the GaAs measurements which are discussed later in this chapter, however, it is clear that these kinds of Debye-Waller estimates are too pessimistic for some materials, and thus that the photon energies for HARPES may be higher than the above estimates.

6.2.2 Brillouin Zone Averaging and Shifts Due to the Photon Momentum and Recoil

Another source of band “smearing” or Brillouin-zone averaging is the angular acceptance of the analyzer [22]. For a given angular acceptance, or more precisely angular resolution, ΔΩ, as the magnitude of the wave vector $\boldsymbol{k_f}$ associated with the final photoelectron momentum increases, the set of initial electron wave vectors that are being probed inside the Brillouin zone is significantly broadened. Thus, the definition of points in the Brillouin zone becomes smeared out. This effect is illustrated by the shaded disks in Fig. 6.4 (from [24]), which represent the angular broadening effect on a typical set of direct transitions in W due to a ΔΩ of ±1.5°. At higher energies this broadening effect is going to be enhanced and more Brillouin-zone averaging will be observed. Therefore, going to higher photon energies, while trying to maintain reasonable resolution in $\boldsymbol{k}$, will require photoelectron analyzers with smaller solid-angle resolutions, and in fact the spectrometer that was used for the first proof-of-principle HARPES measurements has an estimated resolution of about 0.25–0.30°, as discussed later in this chapter.

Figure 6.4 also illustrates another effect which becomes prominent at higher photon energies—the shift in the position of the final-state photoelectron wave vector $\boldsymbol{k_f}$ due to the photon momentum wave vector $k_{h\nu} = 2\pi\nu/c$. In the usual units of Å^{-1}, the magnitude of $k_{h\nu}$ can be easily calculated using $k_{h\nu} = 0.000507 \times E_{h\nu}$ (in eV), and from this it is clear that for low photon energies the effects of $k_{h\nu}$ are

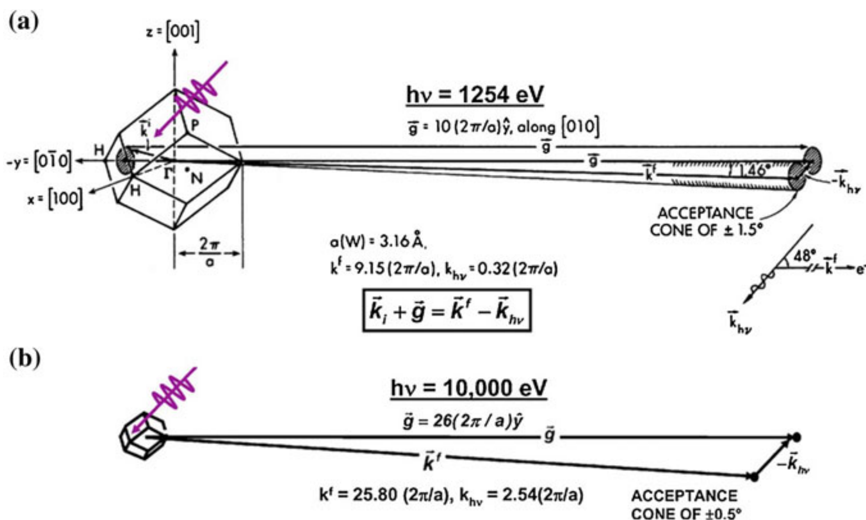

Fig. 6.4 **a** W(001) Brillouin zone with a scale drawing of a $\boldsymbol{k}$-conserving (direct) transition at the photon energy of 1254 eV, and the corresponding photon wave vector. **b** Same type of direct transition, but at the photon energy of 10,000 eV. The effect of the photon wave vector on the final photoelectron wave vector is much stronger (From [24])

negligible. In the multi-keV regime, however, the dipole approximation starts to lose its relevance, and the magnitude of the photon momentum must be taken into account in the momentum conservation equation $\boldsymbol{k_f} = \boldsymbol{k_i} + \boldsymbol{g} + \boldsymbol{k_{h\nu}}$. Figure 6.4a, b illustrate schematically the angular shift in the direction of the final photoelectron momentum due to the photon-electron interaction at 1254 and 10,000 eV [24]. In fact, first proof-of-principles HARPES measurements of W(110) which are discussed later in this chapter serve as a clear demonstration that the magnitude of the photon wave vector $k_{h\nu}$ is an important consideration in determining which region of the Brillouin zone is being mapped by the two-dimensional detector in the HARPES experiment.

In addition to the shifts in the Brillouin zone, the kinetic energy of the photoemitted electron will also be "shifted" (reduced) by a recoil effect, a phenomenon wherein photoelectrons emitted from a lighter element loses kinetic energy to the atomic nucleus in accordance with the conservation of momentum [31]. The recoil energy E_{Recoil}, although negligible in soft X-ray regime, becomes more prominent at higher kinetic energies, and especially for lighter elements, as evident from the simple formula which can be used to estimate it:

$$E_{Recoil} \approx \frac{\hbar^2 k_f^2}{2M} \approx 5.5 \times 10^{-4} \left[\frac{E_{Kinetic}(\mathrm{eV})}{M(\mathrm{amu})} \right]$$

6.2.3 Diminished Photoelectric Cross-Sections

One last major difficulty which is relevant for both angle-integrated and angle-resolved measurements in the hard X-ray regime is the diminution of the photoelectric cross sections with higher excitation energies. In the multi-keV regime we encounter this unfortunate limitation related to the fact that the photoelectric cross sections fall off continuously with increasing photon energy, approximately as $\sigma_{\mathrm{Qnlj}}(h\nu) \sim (\mathrm{E_{kin}})^{-7/2}$ for *s* subshells and as $\sigma_{\mathrm{Qnlj}}(h\nu) \sim (\mathrm{E_{kin}})^{-9/2}$ for *p*, *d*, and *f* subshells [32]. For the angle-resolved valence-band studies, the distinction between the *s*-like and *d*-like orbitals plays an important role. Due to the higher number of oscillations in the radial wavefunction, *s*-like orbitals will interact with the higher-energy photons more compared to the *p*, *d* or *f*-like orbitals. In other words, subshells with lower angular momentum quantum number *l* and higher *n* will dominate the spectrum [33]. While the *sp*-like states are more important in general with respect to transport properties, learning something about the *d*- and *f*-like states thus has to be more indirect, via *d*- and *f*-hybridization with *s*- and *p*-states [34].

In spite of these challenges, with the recent advent of new high-energy third-generation synchrotron facilities and the development of new high-energy electron analyzers it is now becoming possible to carry out angle-resolved valence-band measurements in the soft and hard X-ray regimes. In particular, Plucinski et al. in 2008 have successfully measured band dispersion in W at 260

and 870 eV [29]. Later, in 2009, Venturini et al. performed soft X-ray measurements of Ag valence-bands at 552, 698, and 1040 eV [35]. Finally, in 2011, Papp et al. have demonstrated band structure of W using MgKα source with the photon energy of 1253.6 eV [36]. Today, a dedicated soft X-ray ARPES (SARPES) beamtime operates at the Swiss Light Source (PSI) [37, 38], and the feasibility of HARPES has been experimentally demonstrated at several hard X-ray beamlines in the world [39]. The overall energy resolutions (down to ~50 meV), as well as the angular resolutions of these newly-developed facilities (down to ~0.2–0.3°) make it possible to meaningfully study dispersive energy bands at up to 3–6 keV excitation energies, and with wavevector resolutions of 0.1–0.2 $Å^{-1}$. The following sections of this chapter will provide an overview the first "true multi-keV" HARPES measurements of W, GaAs and $Ga_{1-x}Mn_xAs$ obtained with the excitation energies of 5.95 and 3.24 keV [40, 41].

6.3 First Experimental Results and Discussion

6.3.1 W(110)—Proof of Principle Experiments at 5.95 keV

The first *true* hard X-ray HARPES experiments were carried out at the synchrotron radiation facility SPring-8 in Japan, using W single crystal with (110) orientation as a well-understood model system [22, 23, 42–44] and the excitation energy of 5.95 keV. W was particularly well-suited for such proof of principle experiments due to its high Debye temperature and high atomic weight, leading to high Debye-Waller factors (up to 0.45) at low temperatures (~30 K) and thus substantial signal contribution from the direct transitions, as discussed earlier in this chapter. The average probing depth of 56–61 Å (18–19 unit cells of W) which was determined via the widely-used TPP-2M formula [11–13] is about 13 times larger than the probing depth for 100 eV-electrons and about 42 times larger than that for 20 eV-electrons. Thus, compared to the prior experiments carried out with typical ARPES excitation energies, at 5.95 keV we expect to obtain much more accurate information about the true bulk electronic structure of W.

Two-dimensional HAXPES images of W (110) taken at two different temperatures, 300 and 30 K, are shown in Fig. 6.5a, b respectively [40]. Each panel is a single 2D detector image spanning approximately 12° in momentum space (x-axis of the detector) and 12 eV of binding energy (y-axis). Diminution of the phonon effects with cryogenic cooling is immediately noticeable when comparing the two images. At room temperature (300 K) the Debye-Waller factor, and thus the approximate fraction of the direct transitions, is estimated to be ~0.09 [29, 30], resulting in nearly total smearing of dispersive bands, and leaving non-dispersive modulation due to the matrix-element-weighted density of states (MEW-DOS) along the binding-energy axis, which is shown with the yellow curve. Additional modulation along the detector-angle axis can be attributed to core-like X-ray photoelectron diffraction (XPD) [45 and references therein]. In sharp contrast with

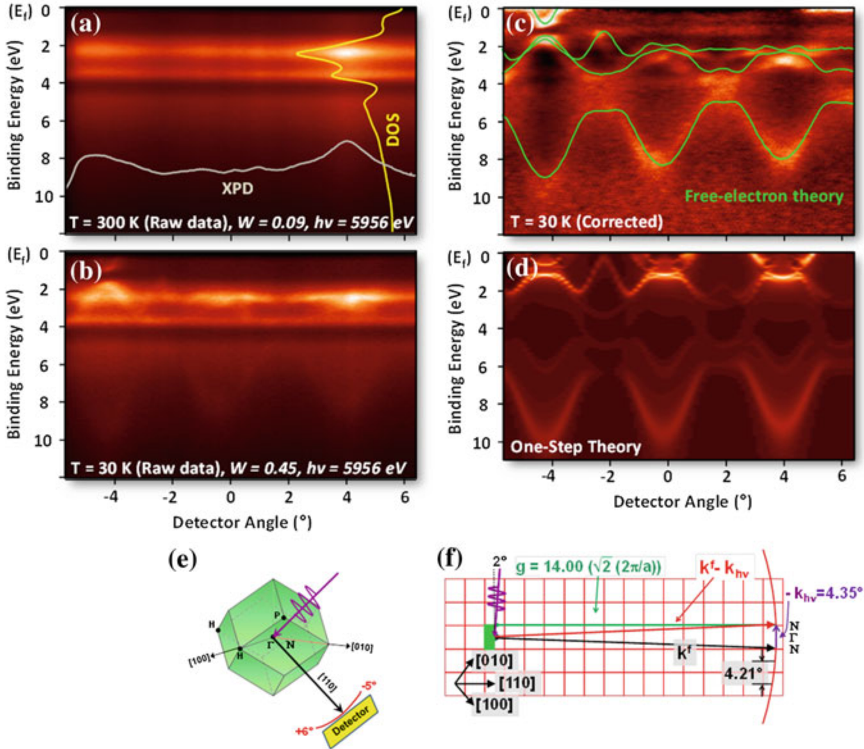

Fig. 6.5 **a** Room temperature HARPES measurement from W(110). The spectra are dominated by modulations due to the density of states (DOS) in energy (*yellow curve*) and X-ray photoelectron diffraction (XPD) effects in angle (*grey curve*). Dispersive features are not observed due to the low fraction of direct transitions at room temperature in this hard X-ray regime. The Debye-Waller factor here is only 0.09. **b** The same measurement as in (**a**), but at 30 K. Phonon effects are suppressed at low temperature and dispersive features are now apparent. The Debye-Waller factor here is 0.45. **c** Data from (**b**), normalized via a 2-step process so as to remove the DOS and XPD effects, thus enhancing dispersive valence-band features. The *solid curves* superimposed on the experimental data are the results of band-structure-to-free-electron final-state model calculations. **d** One-step photoemission calculations of the HARPES spectra taking into account matrix-element effects. **e** The experimental geometry relative to the first Brillouin zone. **f** An extended Brillouin zone picture of the HARPES measurement for W (From [40])

the room-temperature data, image in Fig. 6.5b which was recorded at the temperature of 30 K shows clear angular dispersion on top of the MEW-DOS and XPS effects. Appearance of such dispersive bands is expected from a simple Debye-Waller factor calculation which yields a 0.45 fraction of the direct transitions in the HARPES image, as discussed earlier. The non-dispersive modulations due to MEW-DOS and XPD which partially obscure the bands in Fig. 6.5b can be removed via a two-step normalization procedure using the averaged room-temperature contours (gray and yellow curves in Fig. 6.5a). The resulting corrected image is shown in Fig. 6.5c, where the overlaying green curves are the results of

theoretical calculations based on a simple model which couples the W band structure (as calculated with the Wien2k program [46]) with free-electron final-states.

Quasi-periodical nature of the bands in the HARPES image can be easily understood using the extended Brillouin zone picture sketched in Fig. 6.5e, f, with all the relevant wave vectors shown to scale. Basic wave vector conservation arguments explained in detail elsewhere [40] imply that the bands seen in Fig. 6.5b, c are being sampled along the red arc traversed by $\left[\overrightarrow{k_f} - \overrightarrow{k_{hv}}\right]$, and thus also by $\overrightarrow{k_i}$ in the reduced Brillouin zone. Thus, for a detector window of about 12°, segment of an entire Brillouin zone between N-Γ-N points is sampled three times in a single detector image.

Figure 6.5d shows the results of much more accurate state-of-the-art one-step theory based on an LDA layer-KKR approach with a time-reversed LEED final-state [26–28]. Such calculations include all matrix element effects, all multiple scattering effects in the initial and final states, the effect of the photon momentum vector, and the escape depth of the photoelectrons via an imaginary part in the potential function. Details of this theoretical approach are discussed in-depth in Chap. 7 of this book. For the current results, the resemblance of the experimental data to the one-step theory in is indeed remarkable.

In summary, the proof of principle HARPES measurements of W(100) with the photon energy of 5.95 keV produced clear dispersive bands, in agreement with the free-electron final-state theory calculations and more sophisticated fully-relativistic one-step theory of photoemission. These first HARPES measurements provide a clear picture of the possibilities and challenges of HARPES, elucidating the need for cryogenic cooling and correction for both phonon-produced MEW-DOS-like features and XPD-like features. Using these results from W as a measure for the feasibility of HARPES measurements in general, it can be concluded as a conservative estimate that a Debye-Waller factor of about 0.45 or greater is required to obtain a sufficient fraction of direct transitions that are amenable to fairly easy further data analysis.

6.3.2 GaAs(001)—Proof of Principle Experiments at 3.24 keV

In order to demonstrate immediate applicability of HARPES to the bulk-sensitive band mapping of a real technologically-relevant material, the second system measured by Gray et al. at SPring-8 was a prototypical semiconductor GaAs in (001) orientation [40]. Due to its high electron mobility GaAs finds broad applicability in a multitude of fast-switching electronic devices and is considered to be a promising candidate for future high-efficiency solar-cell technology and spintronic devices [47–52]. Due to the lower Debye temperature and effective atomic mass of GaAs the measurements were carried out at lower photon energy of 3.24 keV.

At cryogenic temperatures (20 K) the Debye-Waller factor of GaAs is estimated to be about 0.31, as discussed earlier in this chapter, which is somewhat lower than that for the previous case of W. However, the average probing depth (IMFP) of ~57 Å at 3.24 keV, as calculated by the TPP-2M formula, is comparable to that of W at 5.95 keV. Thus, once again, even at a lower phonon energy the measurement should provide an insight into the true bulk electronic structure, looking as far as 10 unit cells beneath the surface.

The results of the measurements are summarized in Fig. 6.6a–d in a format similar to that for W(110), and show clear dispersive bands in the binding energy range between ~0.5 and ~7.5 eV, as well as more localized core-like bands at ~12 eV dominated by the As 4 s states and exhibiting intensity modulations due to the XPD effects [40]. It is important to note that even the raw low-temperature data in Fig. 6.6b clearly show dispersing bands which are even more prominent in the raw data than those for W with a higher Debye-Waller factor. This surprising finding points at a potentially beneficial material dependence in phonon broadening that requires a better theoretical explanation. Once again, excellent agreement between the experimental data and the one-step theory of photoemission (Fig. 6.6d), as well as the free-electron final-state theory (green curves in Fig. 6.6c) is observed. Due to the lower photon energy used for this experiment and thus a

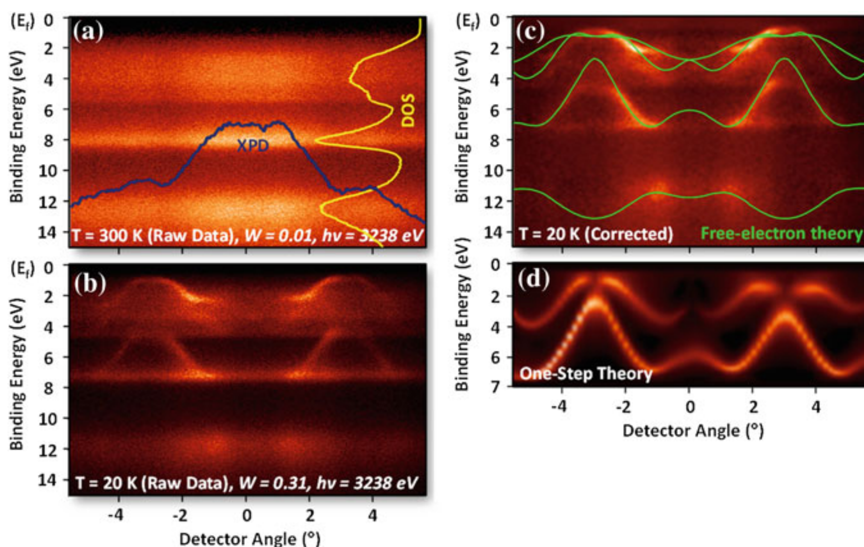

Fig. 6.6 **a** Room temperature measurement from GaAs(001), with Debye-Waller factor 0.01 and average curves representing DOS and XPD again shown. **b** The same measurement as in (**a**), but at 20 K, with Debye-Waller factor of 0.31. **c** Same measurement, corrected so as to remove the DOS and XPD effects. The *solid curves* superposed on the experimental data are the results of the free-electron final-state calculations. **d** One-step photoemission calculations of the HARPES spectra (From [40])

shorter resulting final photoelectron momentum wavevector, the Brillouin zone segment between Γ-K-X points is traversed only twice in the detector image (compared to three times for W at 5.95 keV). This, of course, is still a big improvement over conventional ARPES experiments carried out at lower photon energies, and thus typically spanning only 1/4 to 1/8 of a single Brillouin zone.

6.3.3 $Ga_{1-x}Mn_xAs$—First Application of HARPES at 3.24 keV

The first true application of HARPES was motivated by a long-standing controversy regarding the nature of the electronic states producing ferromagnetic coupling in dilute magnetic semiconductor $Ga_{1-x}Mn_xAs$ [41]. The two primary competing theories attribute the Mn-induced ferromagnetism to either the so-called *double-exchange* mechanism in which case the Mn states form a narrow impurity band which is cleanly separated from the GaAs host valence bands, or the *p-d exchange* in which case the Mn states overlap in energy with the host GaAs states [53–57]. In principle, such information regarding the valence-band states should be readily accessible by X-ray photoelectron spectroscopy. However, the conventionally accepted surface preparation methods for $Ga_{1-x}Mn_xAs$ [58, 59] destroy the crystallinity in the first few layers, thus precluding a clean measurement of the bulk valence-band electronic structure. Thus, HARPES presented a unique opportunity to look through these damaged surface layers into the bulk of the sample, and to resolve this controversy.

Figure 6.7 compares the results of the one-step theory calculations for **a** GaAs and **b** $Ga_{0.97}Mn_{0.03}As$ to the experimental valence-band HARPES data in **c** and **d**, respectively. As discussed earlier in the chapter, the experimental valence-band spectra have been normalized by energy- and angle-averaged curves in order to minimize the effects of MEW-DOS and XPD modulations across the detector and to "bring-out" the dispersive bands. The agreement between the calculations and the experimental data is remarkable. As expected, the probed Brillouin zone region is repeated twice in the detector image which spans about 15° of the arc traversed by vector $\left[\overrightarrow{k_f} - \overrightarrow{k_{h\nu}}\right]$. Mn impurities that disturb the long-range translational order of the host GaAs crystal result in smearing of the bands in $Ga_{0.97}Mn_{0.03}As$, which is observed in experiment and is confirmed by the one-step theory calculations.

The most important information is revealed in Fig. 6.8, which compares the experimental *angle-integrated* valence-band spectra for GaAs and $Ga_{0.97}Mn_{0.03}As$ (**a**) to the theoretical spectra obtained via the one-step theory calculations (**b**). The differences between the angle-integrated spectra shown as blue curves in panels **a** and **b**, and magnified in panels **c** and **d**, essentially, represent the Mn-induced differences in the MEW-DOS of GaAs and $Ga_{0.97}Mn_{0.03}As$. Once again, the agreement between the experiment and the theory is remarkable, apart from the lack of some sharper features in the experimental spectra appearing in the theory

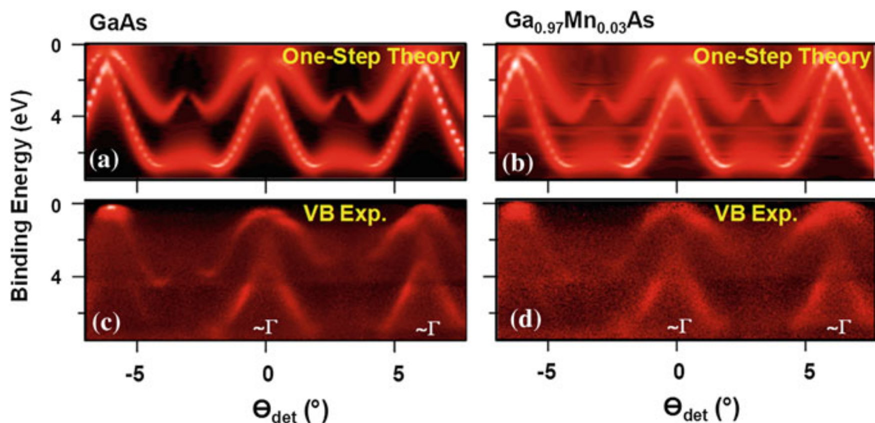

Fig. 6.7 **a** and **b** Results of one-step hard-X-ray angle-resolved photoemission (HARPES) calculations for GaAs and $Ga_{0.97}Mn_{0.03}As$ respectively. **c** and **d** Experimental HARPES data obtained for GaAs and $Ga_{0.97}Mn_{0.03}As$ respectively (From [41])

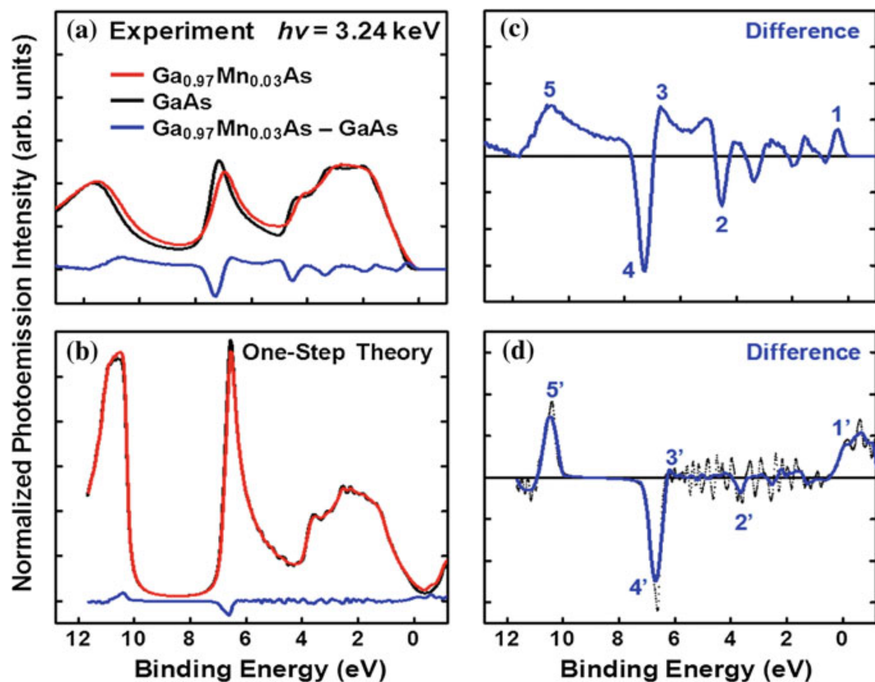

Fig. 6.8 **a** Experimental angle-integrated valence-band spectra for GaAs and $Ga_{0.97}Mn_{0.03}As$. **b** Theoretical spectra obtained via the one-step theory calculations. **c** and **d** Intensity difference spectra between $Ga_{0.97}Mn_{0.03}As$ and GaAs for the experimental data and the one-step theory results (From [41])

between 2 and 6 eV. This is likely caused by the combined effects of total experimental resolution and residual disorder-induced broadening. Feature labeled 1 in experiment and 1′ in theory represents the contribution of the Mn bands near the Fermi edge, or the so-called Mn impurity band. Further analysis of the angle-resolved data [41] confirms the model in which the Mn-induced impurity band is merged with the valence bands. This indicates that ferromagnetism in $Ga_{0.97}Mn_{0.03}As$ must be considered to arise from both *p–d* exchange and *double-exchange*, thus providing a more unifying picture of this controversial material. This conclusion is also supported by the first-principles spin-resolved total and projected DOS calculations [41]. The remarkable result that such small compositional change (3 % Mn) could be detected and quantitatively analyzed makes HARPES a very promising new technique with a wide potential applicability.

6.4 Summary and Future Outlook

This chapter provides an overview of the basic principles, considerations and challenges of hard X-ray angle-resolved photoelectron spectroscopy, or HARPES. Recent proof-of-principle studies demonstrate that angle-resolved band mapping is indeed possible with high energy X-rays in the multi-keV regime, thus allowing for more bulk-sensitive electronic structure determinations. Although the energy resolution in HARPES, presently in the range of couple of hundreds of meV, may not reach the typical values of energy resolution of conventional ARPES (1 meV or smaller), significant efforts are being undertaken to improve the detection schemes which clearly indicate that values of less than 50 meV are achievable in the near future. Resolution in $\overrightarrow{k_f}$ will ultimately be limited by the analyzer lens characteristics, but since a smaller angular range is needed to span the Brillouin zone in one direction in HARPES (e.g. only 4.1° for W at 6 keV and 6.2° for GaAs at 3.2 keV), a smaller cone of angle could be used, with this making it easier for the lens to achieve higher angular resolution.

Despite some of these technical challenges the unique advantages of true bulk sensitivity and of using samples "as prepared" open up new possibilities in the field of condensed matter physics and materials science, as demonstrated in the case of $Ga_{1-x}Mn_xAs$. High energies make it possible to probe an entire Brillouin zone for a given material in "one shot" by either rotating the spectrometer with respect to the sample, or by simply varying the photon energy. In addition to this, HARPES opens the door for future angle-resolved studies of buried layers and interfaces in multilayer structures, as demonstrated recently using soft X-ray ARPES, or SARPES [60]. Finally, imminent advances in the instrumentation and data analysis techniques will undoubtedly lead to the addition of new dimensions, such as time and spin.

References

1. Y.L. Chen, J.G. Analytis, J.-H. Chu, Z.K. Liu, S.-K. Mo, X.L. Qi, H.J. Zhang, D.H. Lu, X. Dai, Z. Fang, S.C. Zhang, I.R. Fisher, Z. Hussain, Z.-X. Shen, Science **325**, 178 (2009)
2. D. Hsieh, Y. Xia, L. Wray, D. Qian, A. Pal, J.H. Dil, J. Osterwalder, F. Meier, G. Bihlmayer, C.L. Kane, Y.S. Hor, R.J. Cava, M.Z. Hasan, Science **323**, 919 (2009)
3. Y. Xia, D. Qian, D. Hsieh, L. Wray, A. Pal, H. Lin, A. Bansil, D. Grauer, Y.S. Hor, R.J. Cava, Z. Hasan, Nat. Phys. **5**, 398 (2009)
4. A.G. Loeser, Z.-X. Shen, D.S. Dessau, D.S. Marshall, C.H. Park, P. Fournier, A. Kapitulnik, Science **273**, 325 (1996)
5. A. Lanzara, P.V. Bogdanov, X.J. Zhou, S.A. Kellar, D.L. Feng, E.D. Lu, T. Yoshida, H. Eisaki, A. Fujimori, K. Kishio, J.-I. Shimoyama, T. Noda, S. Uchida, Z. Hussain, Z.-X. Shen, Nature **412**, 510 (2001)
6. A. Damascelli, Z. Hussain, Z.X. Shen, Rev. Mod. Phys. **75**, 473 (2003)
7. A. Bostwick, T. Ohta, T. Seyller, K. Horn, E. Rotenberg, Nat. Phys. **3**, 36 (2007)
8. T. Ohta, A. Bostwick, J.L. McChesney, T. Seyller, K. Horn, E. Rotenberg, Phys. Rev. Lett. **98**, 206802 (2007)
9. S.Y. Zhou, G.-H. Gweon, A.V. Fedorov, P.N. First, W.A. de Heer, D.-H. Lee, F. Guinea, A.H. Castro Neto, A. Lanzara, Nat. Mater. **6**, 770 (2007)
10. Google Scholar search result. Keyword “ARPES”, June 2014
11. S. Tanuma, C.J. Powell, D.R. Penn, Surf. Interface Anal. **37**, 1–14 (2005)
12. S. Tanuma, T. Shiratori, T. Kimura, K. Goto, S. Ichimura, C.J. Powell, Surf. Interface Anal. **37**, 833–845 (2005)
13. S. Tanuma, C.J. Powell, D.R. Penn, Surf. Interface Anal. **43**, 689 (2011)
14. C.J. Powell, A. Jablonski, I.S. Tilinin, S. Tanuma, D.R. Penn, J. Electron Spectrosc. Relat. Phenom. **98**, 1 (1999)
15. A. Jablonski, C.J. Powell, J. Vac. Sci. Technol. A **27**, 253 (2009)
16. C.J. Powell, J. Electron Spectrosc. Relat. Phenom. **182**, 11 (2010)
17. D.P. Woodruff, T.A. Delchar, *Modern Techniques of Surface Science* (Cambridge University Press, Cambridge, 1986)
18. N.J. Shevchik, J. Phys. C **10**, L555 (1977)
19. N.J. Shevchik, Phys. Rev. B **16**, 3428 (1977)
20. Z. Hussain, N.F.T. Hall, L.F. Wagner, S.P. Kowalczyk, C.S. Fadley, K.A. Thompson, R.L. Dod, Solid State Commun. **25**, 907 (1978)
21. Z. Hussain, S. Kono, R.E. Connelly, C.S. Fadley, Phys. Rev. Lett. **44**, 895 (1980)
22. Z. Hussain, C.S. Fadley, S. Kono, L.F. Wagner, Phys. Rev. B **22**, 3750 (1980)
23. Z. Hussain, E. Umbach, J.J. Barton, J.G. Tobin, D.A. Shirley, Phys. Rev. B **25**, 672 (1982)
24. R.C. White, C.S. Fadley, M. Sagurton, Z. Hussain, Phys. Rev. B **34**, 5226 (1986)
25. R.C. White, C.S. Fadley, M. Sagurton, P. Roubin, D. Chandesris, J. Lecante, C. Guillot, Z. Hussain, Phys. Rev. B **35**, 1147 (1987)
26. J. Braun, J. Minár, F. Matthes, C.M. Schneider, H. Ebert, Phys. Rev. B **82**, 024411 (2010)
27. J. Minár, J. Braun, H. Ebert, J. Electron Spectrosc. Relat. Phenom. **190**, 159 (2013)
28. J. Braun, J. Minár, S. Mankovsky, V.N. Strocov, N.B. Brookes, L. Plucinski, C.M. Schneider, C.S. Fadley, H. Ebert, Phys. Rev. B **88**, 205409 (2013)
29. L. Plucinski, J. Minár, B.C. Sell, J. Braun, H. Ebert, C.M. Schneider, C.S. Fadley, Phys. Rev. B **78**, 035108 (2008)
30. L. Plucinski, private communication
31. Y. Takata, Y. Kayanuma, S. Oshima, S. Tanaka, M. Yabashi, K. Tamasaku, Y. Nishino, M. Matsunami, R. Eguchi, A. Chainani, M. Oura, T. Takeuchi, Y. Senba, H. Ohashi, S. Shin, T. Ishikawa, Phys. Rev. Lett. **101**, 137601 (2008)
32. C.S. Fadley, Nucl. Instrum. Methods Phys. Res., Sect. A **547**, 24 (2005)
33. J.C. Woicik et al., Phys. Rev. Lett. **89**, 077401 (2002)

34. S. Hüfner, *Photoelectron Spectroscopy: Principles and Applications*, 2nd edn. (Springer Verlag, Berlin, 1996)
35. F. Venturini, J. Minár, J. Braun, H. Ebert, N.B. Brookes, Phys. Rev. B **77**, 045126 (2008)
36. C. Papp, L. Plucinski, J. Minár, J. Braun, H. Ebert, C.M. Schneider, C.S. Fadley, Phys. Rev. B **84**, 045433 (2011)
37. V.N. Strocov, T. Schmitt, U. Flechsig, T. Schmidt, A. Imhof, Q. Chen, J. Raabe, R. Betemps, D. Zimoch, J. Krempasky, X. Wang, M. Grioni, A. Piazzalunga, L. Patthey, J. Synchrotron Rad. **17**, 631 (2010)
38. V.N. Strocov, X. Wang, M. Shi, M. Kobayashi, J. Krempasky, C. Hess, T. Schmitt, L. Patthey, J. Synchrotron Rad. **21**, 32 (2014)
39. Programs and abstract archives from two recent hard X-ray photoemission workshops (HAXPES 2011 and 2013): http://indico.desy.de/ConferenceDisplay.py?confId=3713 and http://www-conference.slu.se/haxpes2013/
40. A.X. Gray, C. Papp, S. Ueda, B. Balke, Y. Yamashita, L. Plucinski, J. Minár, J. Braun, E. Ylvisaker, C.M. Schneider, W.E. Pickett, H. Ebert, K. Kobayashi, C.S. Fadley, Nat. Mater. **10**, 759 (2011)
41. A.X. Gray, J. Minár, S. Ueda, P.R. Stone, Y. Yamashita, J. Fujii, J. Braun, L. Plucinski, C.M. Schneider, G. Panaccione, H. Ebert, O.D. Dubon, K. Kobayashi, C.S. Fadley, Nat. Mater. **11**, 957 (2012)
42. N.E. Christensen, B. Feuerbacher, Phys. Rev. B **10**, 2349–2372 (1974)
43. B. Feuerbacher, N.E. Christensen, Phys. Rev. B **10**, 2373–2390 (1974)
44. J. Feydt, A. Elbe, H. Engelhard, G. Meister, Phys. Rev. B **58**, 14007–14012 (1998)
45. M.A.V. Alvarez, H. Ascolani, G. Zampieri, Phys. Rev. B **54**, 14703–14712 (1996)
46. P. Blaha, K. Schwarz, G. Madsen, D. Kvasnicka, J. Luitz, *WIEN2k, An Augmented Plane Wave + Local Orbitals Program for Calculating Crystal Properties (Karlheinz Schwarz* (Technical University, Wien, 2001). ISBN 3-9501031-1-2
47. H.J. Zhu, M. Ramsteiner, H. Kostial, M. Wassermeier, H.-P. Schönherr, K.H. Ploog, Phys. Rev. Lett. **87**, 016601 (2001)
48. G. Brammertz, M. Caymax, M. Meuris, M. Heyns, Y. Mols, S. Degroote, M. Leys, Appl. Phys. Lett. **83**, 180–182 (2003)
49. P.D. Ye, G.D. Wilk, B. Yang, J. Kwo, S.N.G. Chu, S. Nakahara, H.-J.L. Gossmann, J. P. Mannaerts, M. Hong, K.K. Ng, J. Bude, Appl. Phys. Lett. **83**, 180–182 (2003)
50. M. Ieong, B. Doris, J. Kedzierski, K. Rim, M. Yang, Science **306**, 2057–2060 (2004)
51. R. Chau, S. Datta, M. Doczy, B. Doyle, B. Jin, J. Kavalieros, A. Majumdar, M. Metz, M. Radosavljevic, IEEE Trans. Nanotechnol. **4**, 153–158 (2005)
52. J.D. Wu, Y.S. Huang, G. Brammertz, K.K. Tiong, J. Appl. Phys. **106**, 023505 (2009)
53. H. Ohno, A. Shen, F. Matsukura, A. Oiwa, A. Endo, S. Katsumoto, Y. Iye, Appl. Phys. Lett. **69**, 363 (1996)
54. H. Ohno, Science **281**, 951 (1998)
55. Y. Ohno, D.K. Young, B. Beschoten, F. Matsukura, H. Ohno, D.D. Awschalom, Nature **402**, 790 (1999)
56. T. Jungwirth, J. Sinova, A.H. MacDonald, B.L. Gallagher, V. Novák, K.W. Edmonds, A.W. Rushforth, R.P. Campion, C.T. Foxon, L. Eaves, E. Olejník, J. Mašek, S.-R. Eric Yang, J. Wunderlich, C. Gould, L.W. Molenkamp, T. Dietl, H. Ohno, Phys. Rev. B **76**, 125206 (2007)
57. K. Burch, D.D. Awschalom, D.N. Basov, J. Magn. Magn. Mater. **320**, 3207 (2008)
58. K.W. Edmonds, K.Y. Wang, R.P. Campion, A.C. Newmann, N.R.S. Farley, B.L. Gallagher, C.T. Foxon, Appl. Phys. Lett. **81**, 4991 (2002)
59. K. Olejník, M.H.S. Owen, V. Novák, J. Mašek, A.C. Irvine, J. Wunderlich, T. Jungwirth, Phys. Rev. B **78**, 054403 (2008)
60. M. Kobayashi, I. Muneta, T. Schmitt, L. Patthey, S. Ohya, M. Tanaka, M. Oshima, V.N. Strocov, Appl. Phys. Lett. **101**, 242103 (2012)

Chapter 7
One Step Model Description of HARPES: Inclusion of Disorder and Temperature Effects

Jürgen Braun, Ján Minár and Hubert Ebert

Abstract Angle integrated as well as angle resolved photoemission in the soft and hard X-ray regime became a very important tool to investigate the bulk properties of various materials. In practise enhanced bulk sensitivity can be achieved by so called threshold photoemission. Increased bulk sensitivity may suggest that LSDA band structure or density of states calculations can be directly compared to the measured spectra. However, various important effects, like matrix elements, the photon momentum or phonon excitations, are this way neglected. Here, we present a generalization of the one-step model that describes the excitation of the photoelectron, its transport to the surface and the escape into the vacuum in a coherent way. First, a short introduction to the main features of the one-step model implementation within the Munich SPR-KKR program package is given. The capability to account for correlation effects and chemical disorder using the LSDA+DMFT (dynamical mean field theory) scheme in combination with the coherent potential approximation (CPA) method will be demonstrated by various examples. Special emphasis is put on the description of phonon-assisted transitions which lead to the so-called XPS-limit in the hard X-ray and/or high temperature regime.

J. Braun · J. Minár (✉) · H. Ebert
Department of Chemie, Ludwig-Maximilians-Universität München, 81377 Munich, Germany
e-mail: jan.minar@cup.uni-muenchen.de

J. Braun
e-mail: juergen.braun@cup.uni-muenchen.de

H. Ebert
e-mail: hubert.ebert@cup.uni-muenchen.de

J. Minár
New Technologies—Research Center, University of West Bohemia, Univerzitni 8, 306 14 Pilsen, Czech Republic

© Springer International Publishing Switzerland 2016

J.C. Woicik (ed.), *Hard X-ray Photoelectron Spectroscopy (HAXPES)*,
Springer Series in Surface Sciences 59, DOI 10.1007/978-3-319-24043-5_7

7.1 Introduction

Angle-resolved photoemission (ARPES) has developed over the past several decades into the technique of choice for determining the electronic structure of any new crystalline material, and it is thus in some respects a very mature tool in materials physics [1, 2]. It has always been realized, however, that the results obtained are restricted in sensitivity to the surface-near region of the systems studied, due to the short inelastic mean free path (IMFPs) of $\sim$5–10 Å of the low energy photoelectrons, which are typically in the range from 10 to 150 eV [3]. To overcome this limitation of surface sensitivity, there is now considerable interest in using X-rays in the soft X-ray sub-keV or even hard X-ray multi-keV regime to access deeper-lying layers in a sample, thus sampling more bulk-like properties [4–17, 20–23]. One can thus think of soft X-ray ARPES (SARPES) or hard X-ray ARPES (HARPES), respectively. These techniques have to date been applied to a wide variety of materials, including free-electron like and transition metals [4, 11], strongly correlated oxides and high T_C materials [6, 7], heavy fermion systems [6], mixed-valent Ce compounds [9], dilute magnetic semiconductors [16, 21, 23], layered transition metal dichalcogenides [15] and as well as systems showing the Rashba effect [17]. Additional advantages in such experiments are being able to tune to core-level resonances so as to identify the atomic-orbital makeup of ARPES features [23], to map three-dimensional Fermi surfaces [15], and to take advantage of the longer IMFPs, which translate into less smearing of dispersive features along the emission direction (usually near the surface normal) [14].

Going higher in energy, however, comes with some additional challenges for interpretation of the data [4, 10, 14]. Deviations from the dipole approximation in photoelectron excitation mean that the momentum of the photon can result in a non-negligible shift of the position of the initial-state wave vector in the reduced Brillouin zone (BZ) [11]. Also, phonon creation and annihilation during photoemission hinders the unambiguous identification of the initial state in the BZ via wave vector conservation [4, 5, 10, 11, 13, 14, 16].

In the following we review the one-step model of photoemission taking special care of several aspects, which must be considered beyond the standard one-step model approach to be able to interprete and predict SARPES and HARPES spectra in a quantitative way. Furthermore, we present a variety of recent applications of our generalized formalism.

7.1.1 General Theory of Photoemission

In this section, the main features of general photoemission theory will be eludicated. The calculation ofthe photocurrent starts from first order time-dependent perturbation theory. Assuming a small perturbation Δ, the transition probability per unit time w between two N-electron states $|\Psi_f>$ and $|\Psi_i>$ of the same Hamiltonian H, is given by Fermi's golden rule:

$$w = \frac{2\pi}{\hbar} | < \Psi_f | \Delta | \Psi_i > |^2 \delta(E_f - E_i - \hbar\omega), \tag{7.1}$$

where E_f and E_i denote the energies of the N-electron states and $\hbar\omega$ the excitation energy. This equation can be also derived within the Keldysh Green function approach and can be represented in the lowest order as a triangular like skeleton diagram (see e.g. Fujikawa and Arai [18, 19]). In second quantization the interaction operator Δ is defined as follows

$$\Delta = \sum_{k,m} \Delta_{k,m} \mathbf{a}_{\mathbf{k}}^{\dagger} \mathbf{a}_m, \tag{7.2}$$

where $\Delta_{k,m}$ denotes a one-particle matrix element between two single-particle states ϕ_k and ϕ_m. The initial and final states are then defined as $|\Psi_i> \; = |\Psi_N^0>$ and $|\Psi_f> \; = \mathbf{a}_f^{\dagger} |\Psi_{N-1}^s>$ where $|\Psi_{N-1}^s>$ denotes an excited N − 1 particle state and $|\Psi_N^0>$ defines the ground state of the many-particle system. For the explicit formulation of the final state the so called sudden approximation is used. This means the photoelectron is described by a single-particle state and the interaction with the excited N − 1 state $|\Psi_{N-1}^s>$ is completely neglected. In other words $\mathrm{a}_f |\Psi_N^0> \; = 0$. Using these approaches for the initial and final states the transition probability results to

$$w_s = \frac{2\pi}{\hbar} | < \Psi_{N-1}^s | \sum_{k,m} \Delta_{k,m} \mathbf{a}_f \mathbf{a}_{\mathbf{k}}^{\dagger} \mathbf{a}_m | \Psi_N^0 > |^2 \delta(E_N - E_{N-1} - \hbar\omega), \tag{7.3}$$

where the delta-function describes the energy conservation in the photo-excitation process generated by a certain photon energy $\hbar\omega$. Performing some standard manipulations on (7.3) it follows for $w = \sum_s w_s$:

$$w = \frac{2\pi}{\hbar} \sum_{m,m'} \Delta_{f,m}^{\dagger} A_{m,m'}(E_n) \Delta_{f,m'}, \tag{7.4}$$

where

$$A_{m,m'}(E_n) = \frac{2}{\hbar} \sum_s < \Psi_N^0 | \mathbf{a}_m^{\dagger} | \Psi_{N-1}^s > \delta(E_N - E_{N-1} - \hbar\omega) < \Psi_{N-1}^s | \mathbf{a}_{m'} | \Psi_N^0 > , \tag{7.5}$$

represents the one-electron spectral function of the initial state. Using further the relation

$$A_{m,m'}(E_n) = -\frac{1}{\pi} \mathrm{Im}\; G_{m,m'}^R(E_n) \tag{7.6}$$

between the spectral function and the one-electron retarded Green function the intensity of the photocurrent follows to

$$I(\hbar\omega) = -\frac{1}{\pi}\mathrm{Im}\sum_{m,m'}\left\langle \phi_f|\Delta^\dagger|\phi_m\right\rangle G^R_{m,m'}(E_n)\langle\phi_{m'}|\Delta|\phi_f\rangle. \tag{7.7}$$

With the help of the operator representation for G^R

$$G^R(E_n) = \sum_{m,m'} |\phi_m > G^R_{m,m'}(E_n) < \phi_{m'}| \tag{7.8}$$

we arrive at the final expression

$$I(\hbar\omega) = -\frac{1}{\pi}\mathrm{Im} < \phi_f|\Delta^\dagger G^R(E_n)\Delta|\phi_f > \tag{7.9}$$

for the photocurrent $I(\hbar\omega)$. Replacing the retarded one-electron Green function by the one-particle Green function and reformulating (7.9) in the space representation one arrives at the one step model description of the photocurrent as derived among others by Pendry [31] (see (7.10) and [37]).

7.2 Fully Relativistic One-Step Model of Temperature-Dependent Photoemission

Photoemission spectroscopy (PES) as an extremely important experimental tool, which provides detailed information on the electronic structure of a probed system, can be seen as a stringent benchmark for the success of any electron structure theory. PES in its angle-integrated form (AIPES) reflects the density of states (DOS) rather directly in the high photon energy regime (XPS). Therefore, it is quite common to probe density functional theory (DFT) based calculations by comparing the theoretical DOS directly to the AIPES spectra [24–26].

However, this approach ignores the influence of the specific matrix elements that in general will introduce element- and energy-dependent weights to the partial DOS. In case of ARPES the situation is even move complicated as the surface in combination with the local dipole selection rules may have a very pronounced impact on the spectra [27]. This situation demands for a coherent description on the basis of the one-step model [28]. To achieve a reliable interpretation of experimental data, however, it is inevitable to deal with so-called matrix-element effects which considerably modify the raw spectra. Especially, the wave-vector and energy dependence of the transition-matrix elements has to be accounted for. These issues are known to be indispensible and therefore cannot be neglected. They result from strong multiple-scattering processes in the final states which dominate the electron dynamics in the low-energy regime of typically 1–200 eV. With increasing photon

energy the final states tend to be more and more free electron like [29]. The transition-matrix elements also include the effects of selection rules which are not accounted for in a calculated raw spectrum. In other words, the main task of a photoemission theory is to close the gap between a raw spectrum obtained from DFT-like electronic-structure calculations and corresponding experimental data. The most successful theoretical approach is found in the one-step model with its implementation worked out by Pendry and co-workers [30–32]. In the following a short overview will be given on recent extensions of the one-step model which are connected with correlation effects, disordered alloys and temperature-dependent effects important for soft- and hard X-ray photoemission.

The main idea of the one-step model is to describe the actual excitation process, the transport of the photoelectron to the crystal surface as well as the escape into the vacuum [33] as a single quantum-mechanically coherent process including all multiple-scattering events. Treating the initial and final states within the fully relativistic version of the layer-dependent KKR method [34, 35] as implemented in the Munich SPR-KKR package [36], it is a straight forward task to describe the photoemission process from complex layered structures like thin films and multilayers.

In order to get a numerical implementation of (7.9), Pendry reformulated this expression into the following form for the photocurrent within the one-step model of PES [31]:

$$I^{PES} \propto \mathrm{Im}\,\langle \varepsilon_f, \boldsymbol{k}_\parallel | G_2^+ \,\Delta G_1^+\, \Delta^\dagger G_2^- | \varepsilon_f, \boldsymbol{k}_\parallel \rangle. \tag{7.10}$$

As we showed in the previous section this expression can be derived from Fermi's golden rule for the transition probability per unit time [28, 37]. Considering an energy-, angle- and spin-resolved photoemission experiment the state of the photoelectron at the detector is written as $|\epsilon_f, \boldsymbol{k}_\parallel\rangle$, where $\boldsymbol{k}_\parallel$ is the component of the wave vector parallel to the surface, and ϵ_f is the kinetic energy of the photoelectron. The spin character of the photoelectron is implicitly included in $|\epsilon_f, \boldsymbol{k}_\parallel\rangle$ which is understood as a four-component Dirac spinor. The advanced Green function G_2^- in (7.10) characterizes the scattering properties of the material at the final-state energy ϵ_f. Via $|\Psi_f\rangle = G_2^- |\epsilon_f, \boldsymbol{k}_\parallel\rangle$ all multiple-scattering corrections are formally included. We construct the final state within spin-polarized low-energy electron diffraction (SPLEED) theory considering a single plane wave $|\epsilon_f, \boldsymbol{k}_\parallel\rangle$ advancing onto the crystal surface. In the UV-regime kinematic and dynamic effects in the multiple scattering for both, initial and final states, are taken into account because both effects are strong and dominate the electron dynamics. Here the scattering events due to the lattice structure are understood as kinematic effects that produce the typical LEED spots, whereas the dynamic effects generate the intensity profiles in the different LEED spots [30]. Dynamic effects are taken into account by the so called X-matrix [30]. This quantity represents energy-dependent multiple scattering within a single layer. For photon energies in the soft- and hard X-ray regime this quantity tends to zero so that $(1 - X)^{-1}$ tends to one because multiple scattering events are strongly suppressed at higher photon energies. Usually this fact is

considered in first-order by the so called single-scatterer approximation. Within our HARPES calculations we go well beyond this approximation using the full kinematic version of the single-layer scattering matrix for $X \approx 0$. Based on this approach the conventional LEED-formalism [30] is applied to calculate the final-state wave-field in the kinematic limit, considering therefore quantitatively Bragg scattering of the photoelectron within the reciprocal lattice. This kinematic approach allows to describe the photoelectron as a time-reversed SPLEED state in analogy to UV-photoemission and in consequence allows to account for photoelectron diffraction effects in a reasonable approximation.

A detailed description of the generalized one-step model for disordered magnetic alloys including correlation effects by means of the dynamical mean field theory (DMFT) can be found in [20, 38, 39]. Calculations based on this approach have been used to successfully interpret ARPES data over the full energy range in recent years [10, 11, 13, 16, 20, 28, 39, 40]. However, the main limitation of angle resolved SARPES and HARPES are phonon induced transitions leading to the so called XPS limit. Shevchik [41] showed that the photoemission intensities at a given energy E and vector $\mathbf{k}$ can be approximately divided into zero-phonon direct transitions $I^{\mathrm{DT}}(\mathrm{E}, \mathbf{k})$ and phonon-assisted non-direct transitions $I^{\mathrm{NDT}}(E, \mathbf{k})$. As a rough guide to the degree of direct-transition behavior expected in an ARPES experiment, one can use a temperature-dependent Debye-Waller factor $W(T)$ which qualitatively represents the fraction of direct transitions [4, 5, 10, 14, 41–43]. As a first approach that aimed to go beyond this simple scheme for temperature-dependent ARPES, Larsson and Pendry [44] introduced a scheme called Debye-Waller model which incorporates the effect of lattice vibrations on the electron single site scattering t-matrix. More than 15 years later Zampieri et al. [45] introduced a cluster approach to model the temperature-dependent excitation of valence band electrons for photon energies of about 1 keV. More recently Fujikawa [46, 47] discussed phonon effects on ARPES spectra on the basis of nonequilibrium Green function theory. Recently we generalised the one-step model of photoemission in order to accurately model phonon effects over the full energy range from normal low-energy ARPES to HARPES [48]. Most importantly our approach converges for high temperatures and/or photon energies to the so called XPS-limit in photoemission, this means it leads to the expected development of matrix-element-weighted density-of-states (MEW-DOS) like features in the intensity distribution [13, 40]. We use an alloy analogy model [48] which includes vibrational atomic displacements via the coherent potential approximation (CPA), where vibrations of different lattice sites are assumed to be uncorrelated and averaged in the sense of CPA over various possible displacements which are calculated within Debye theory. Using the CPA-formulation of the one-step model [38, 49] provides a self-consistent temperature-dependent averaging of the photoemission matrix elements. In other words, we describe in a quantitative way the breakdown of the $\mathbf{k}$-conserving rules due to phonon-assisted transitions, the driving mechanism that leads finally to the XPS-limit.

7.3 Applications

7.3.1 Thermal Effects and XPS Limit

In Fig. 7.1, we compare results of our calculations directly to experimental data for W(110) with soft X-ray excitation at 870 eV [10]. W has a Debye temperature of 400 K and a atomic mass of 183.84 u close to Au and Pt. In Fig. 7.1(i), we show experimental results for four different sample temperatures: (a) 300 K, (b) 470 K, (c) 607 K and (d) 780 K [10]. For all four temperatures dispersive features are clearly seen but with significant smearing and an increase of MEW-DOS-like intensity features as temperature is raised. Also shown in Fig. 7.2a, b are vertical and horizonal cuts, respectively, through the 2D data of Fig. 7.1(i). These cuts yield Fig. 7.2a-energy distribution curves (EDCs) and Fig. 7.2b-momentum distribution curves (MDCs) to illustrate more directly the changes in both types of distributions with temperature. Also, various spectral features are labeled by the numbers 1–6 in these figures. Figure 7.1(ii) again presents fully relativistic one-step calculations which are done with our new alloy analogy model, whereas Fig. 7.1(iii) shows conventional one-step calculations in which phonon excitations are considered in a simplified way through a temperature-dependent single-site scattering t-matrix [43]. Although at the lowest temperature of 300 K, the two different theoretical approaches yield very similar results, as expected for a Debye–Waller factor of 0.70, the temperature dependence of the experimental data is much better described by our temperature-dependent one-step calculations. The simpler calculation based on the single-site scattering Debye-Waller model [43] predicts neither the smearing of dispersing features nor the growth of MEW-DOS features for higher binding energies, but shows instead only the monotonous decrease of direct transition intensities with increasing temperature [10]. Phonon induced smearing only appears via temperature-dependent matrix elements which cause a decrease of the direct part of the photocurrent due to a redistribution of spectral weight. Although for 780 K and a 870 eV photon energy the XPS-limit is not fully established for W, the indirect contribution of the temperature-dependent CPA-like photocurrent dominates the corresponding angle-resolved soft X-ray spectra. This is clearly observable from both the experimental and theoretical data, which are nearly in quantitative agreement. Figure 7.2a, c compare in more detail the temperature dependence of experimental and theoretical spectra in the form of EDCs for a fixed emission angle of ≈104° which is 14° from the surface normal. Figure 7.2b, d present the same comparison for MDCs at a fixed binding energy of ≈2 eV. The points labeled 1, 2, 4, 5 and 6 denote d-like electronic states, whereas point 3 labels bands that are more free-electron like and a mixture of s and d states. The experimental and theoretical data in Fig. 7.1 show pronounced smearing of features in both EDCs and MDCs as the temperature is raised, but some remnant direct-transition behavior is clearly still present, even at 780 K. The dashed lines shown in Fig. 7.2c, d indicate conventional one-step calculations using the single-site scattering Debye-Waller model [43]. As expected, only slight changes

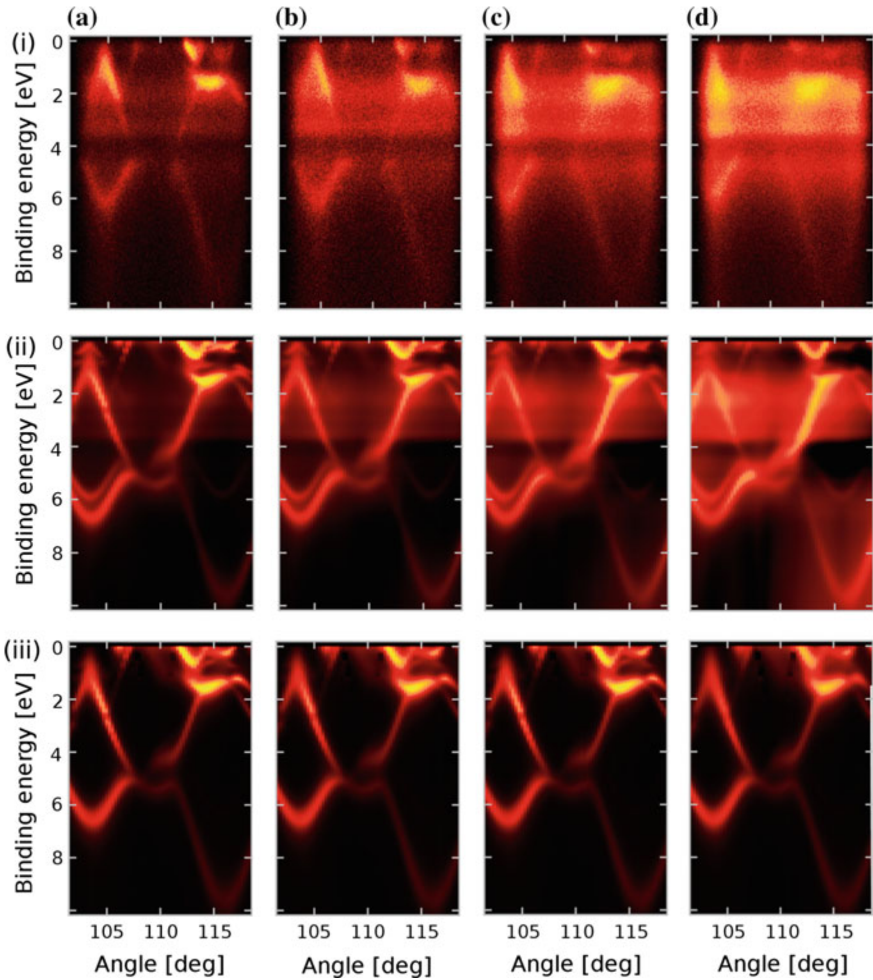

Fig. 7.1 (*i*) Plots of measured intensity versus emission angle for 870 eV excitation energy from the valence bands of W(110) approximately along the Γ–N direction for four temperatures of **a** 300 K, **b** 470 K, **c** 607 K, and **d** 780 K (from [10]), where 90° corresponds to normal emission. (*ii*) Corresponding intensity distributions calculated from temperature-dependent one-step theory based on the CPA formulation. (*iii*) Conventional ARPES calculations of the direct contribution $I^{\mathrm{DT}}(E, \mathrm{k})$ by use of complex scattering phase shifts and the Debye-Waller model. Figure reproduced from [48]

appear in the form of the EDCs and MDCs as a function of temperature. In contrast, the EDCs and MDCs strongly depend on temperature when using the alloy analogy approach, although in general the MDCs in experiment and those of the conventional as well as CPA approaches change less than the EDCs. Significant broadening of spectral features and shift of spectral weight, not at all present in the conventional single-site scattering matrix Debye-Waller model [43], can be observed. The EDC at the highest temperature has not converged to a

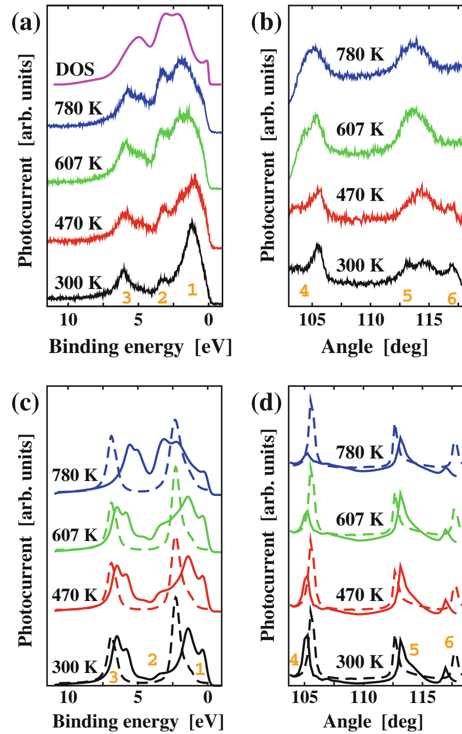

Fig. 7.2 **a** Measured temperature-dependent energy distribution curves (EDCs). A comparison to the W DOS (the topmost curve) is also given. **b** Measured temperature-dependent momentum distribution curves (MDCs). **c**, **d** Corresponding theoretical results for (**c**) EDCs and (**d**) MDCs. *Dashed lines* indicate conventional one-step calculations, *solid lines* indicate calculations within the new alloy analogy model. Figure reproduced from [48]

MEW-DOS-like curve and the corresponding MDC still has structure in it. In the XPS-limit all MDCs would exhibit only X-ray photoelectron diffraction (XPD), with a different type of angular distribution [10, 16, 20, 40, 45]. This is obviously not the case. This is expected, because the Debye-Waller factor of 0.41 at 780 K indicates that a certain number of transitions should still be direct. Our calculations thus correctly predict a diminution of the features expected due to direct transitions, and also a significant broadening of features in the EDCs or MDCs. The additional weak and smooth background observed in the experimental data thus must be ascribed to additional phonon effects, perhaps through multiple phonon excitations.

7.3.2 Correlation Effects

It is widely accepted to interpret a measured photoelectron spectrum by referring to the results of band-structure calculations that are based on DFT and the local spin-density approximation (LSDA) [50, 51]. Such an interpretation is questionable for moderately and even more for strongly correlated systems. To overcome these deficiencies we have developed a generalized approach by accounting properly for electronic correlations beyond the LSDA. For this purpose a general nonlocal,

site-diagonal, complex and energy-dependent self-energy Σ^{DMFT} [25, 26, 52], has been included self-consistently in the fully relativistic spin-polarized Korringa–Kohn–Rostoker multiple scattering theory [36]. Within this scheme the self-energy is determined by a self-consistent DMFT calculation [53, 54]. This method is straightforwardly applicable for electronic structure calculations of 3D- and 2D-systems with perfect lateral translational periodicity and arbitrary number of atoms per unit cell. Furthermore, the computational scheme has been extended to the case of disordered alloys [53, 54], to include many-body correlation effects in the electronic structure and photoemission calculations of this class of complex materials. Application of this approach to the hard-X-ray angle integrated photoemission is demonstrated in Fig. 7.3 where we show HAXPES spectra for the

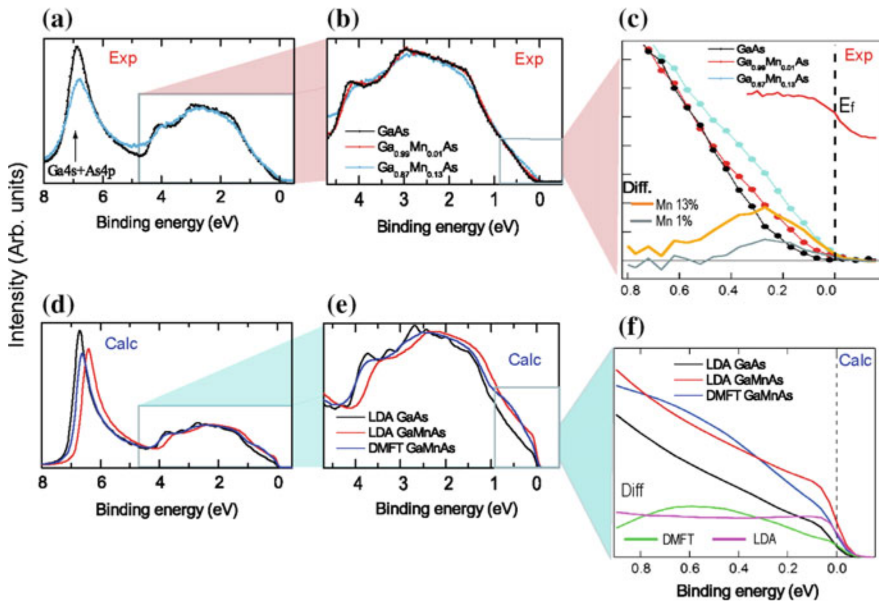

Fig. 7.3 **a**, **c** HARPES spectra (5953 eV) energy for different Mn doping in GaAs. The GaAs spectra have been aligned to the (GaMn)As spectra using the binding energy position of the As 4s core level. No background subtraction was applied. **a** Extended valence band PES (T = 20 K), including the As 4s, Ga 4s, and As 4p shallow core levels of GaAs(100) and 13 % Mn-doped GaAs. **b** Zoom of the valence band region (T = 100 K), showing the spectra from pure GaAs (*black dots*), 1 and 13 % Mn-doped GaAs (*red* and *blue dots*, respectively). **c** High-resolution spectra measured in the vicinity of Fermi level E_F. Difference spectra, corresponding to the Mn contribution only, are shown in *orange* (13 % Mn spectrum (*blue dots*) minus pure GaAs spectrum (*black dots*)) and *grey* (1 % Mn spectrum (*red dots*) minus pure GaAs spectrum (*black dots*)). The reference Fermi level of Au is displayed, with the offset. **d** Calculated angle-integrated PES (including matrix elements) for photon energy and geometry (p polarization) as used in the experiment. **e** Calculated valence-band spectra of GaAs(100) using LDA (*black curve*) and (Ga, Mn)As (13 %) using both LDA (*red curve*) and DMFT (*blue curve*). **f** Zoom of the vicinity of Fermi level E_F with calculated difference spectra, as in **c**, for LDA (*violet curve*) and DMFT (*green curve*). Figure reproduced from [21]

diluted magnetic semiconductor $Ga_{1-x}Mn_xAs$. An essential element for a better understanding of the nature of ferromagnetism in such dilute magnetic semiconductors is the direct measurement of the bulk valence electronic states. A difficulty in obtaining such a direct measurement by conventional UV photoemission, which is very surface sensitive, has been that the preparation of the surface often destroys the crystallinity in the first few layers, and may also distort its stoichiometry. Recently, this problem could be solved by angle resolved [16] and angle integrated [21] bulk sensitive hard X-ray photoemission. In Fig. 7.3 we show experimental (a–c) and theoretical curves (d–f) based on the one-step model of angle integrated photoemission. To describe the presence of Mn dopant we used the CPA approach in combination with the DMFT. Our calculations agree quantitatively with the experimental data over a wide range of binding energies. In particular, we found close to Fermi level E_F a peak with its maximum lying at 250 meV below the Fermi edge, which is described by LDA+DMFT rather than by use of simple LDA calculations. From the calculations we infer that the maximum in the difference signal has mainly Mn-3d (t_{2g}) character. A strong hybridization is present with a mixture of mainly As 4p states localized around the impurity, and Mn 4p states. It is important to emphasize that the Mn-related DOS near the Fermi edge, although significantly smaller, is nonzero within the energy resolution.

7.3.3 Rashba Surface States as Seen by HARPES

Rashba physics has raised enormous scientific interest during the last decade because of the high potential for technological applications. As a bridge between conventional Rashba systems and topological insulators the W(110) surface turned out to be a unique system showing up with highly anisotropic surface features which exhibit peculiar energy dispersions and spin-polarization structures. This has been documented already in the literature by experimental and first theoretical photoemission investigations. Remarkably, in W(110), the Rashba-split surface features are d-type surface resonances in contrast to conventional Rashba systems where the spin-orbit split surface states exclusively exhibit sp-like character [55–57]. In the following we demonstrate that SARPES and HARPES can also be used to study surface relevant questions. It is known from ARPES and inverse photoemission [58–60] that the intensity distributions of surface states strongly decrease with increasing photon energy. The reason is found in the strong dependence of the cross-section of the surface state photoemission on the photon energy [58]. In fact, two general types of mechanisms exist which are responsible for the cross-section variation. The first one is of atomic nature and is based on the spatial extent of the wave functions. The wave functions of real Shockley as well as Tamm states are mainly located in front of the first atomic layer. The second one is a solid state effect and is due to a release of momentum selections rules for the momentum perpendicular to the surface [58]. If the photon energy is increased to the soft or even hard X-ray regime the enhanced bulk sensitivity [61], which is due to the

increase in the inelastic mean free path (IMFP) [13, 16, 20, 40, 61] has to be considered as well. Real surface states contribute to the layer-resolved photocurrent with an intensity distribution only nonzero for the first few atomic layers. As a consequence the contribution to the total spectral weight decreases with increasing number of layers contributing to the photocurrent. The combined effect of energy-dependent cross-sections and greater IMFP causes then a strong decrease of surface state photoemission as the photon energy increases. For surface resonances the situation can be very different if the coupling to the bulk continuum is relatively strong. This is because the cross-section dependence of surface-resonance emission on the momentum selection rules is significantly reduced due to their bulk-like behavior. Furthermore, a typical surface resonance shows up with a valuable spectral weight within the first three or even four atomic layers. Especially, on W (110) the surface emission has a considerable bulk contribution [57] triggered by the symmetry gap around $\overline{\Gamma}$. As a consequence the spectral weight of the resonance could be much larger than that of a real surface state with the result that a surface resonance can be observable at soft X-ray or even hard X-ray energies. In this sense one can use S(H)ARPES measurements or calculations to estimate the fraction of bulk-like photoemission as part of surface related intensity distributions. This is somewhat opposed to the so-called determinant criterion [63] that serves as a test for the surface sensitivity of a given intensity distribution.

We performed HARPES calculations shown in Fig. 7.4 to reveal the bulk-like part of the highly anisotropic surface resonance. In the upper row (left panel) we show an intensity plot calculated for p-polarized light along the $\overline{\Gamma}$-$\overline{S}$ direction at $h\nu = 0.5$ keV, which is a typical soft X-ray energy. The surface resonance is clearly observable but with its maximum intensity around $\overline{\Gamma}$, i.e. within the spin-orbit induced gap. All other surface-related features have more or less vanished in intensity. This trend continues when one inspects the middle panel where we present the corresponding calculation for a photon energy of 1.0 keV, which defines an excitation energy on the border between the SARPES and HARPES region. The true HARPES case is presented at the right panel. For a photon energy of 3.0 keV the surface emission is completely suppressed and only bulk-like emission survives. Surprisingly, the surface resonance is still observable at $h\nu = 3.0$ keV. This tells us that this surface-related feature is different from conventional surface states. Although, no dependence on the photon energy is visible, we have a clear cut argument against a pure bulk state. This result is very uncommon for simple metals but it was recently discovered also in the surface emission of topological insulators like Bi_2Se_3(0001) or Sb_2Te_3(0001) [64].

The bottom row shows the corresponding spin-polarization pattern of the Rashba component for all three excitation energies. The polarization calculated under HARPES conditions appears as the most symmetric one. For lower excitation energies the polarization pattern appears to be less symmetric if one moves from negative to positive $\mathbf{k}_{||}$ values. This observation reflects the fact that the symmetry of the $\overline{\Gamma}$–$\overline{S}$ direction is lower than the symmetry of the $\overline{\Gamma}$–$\overline{N}$ and $\overline{\Gamma}$–$\overline{H}$ directions.

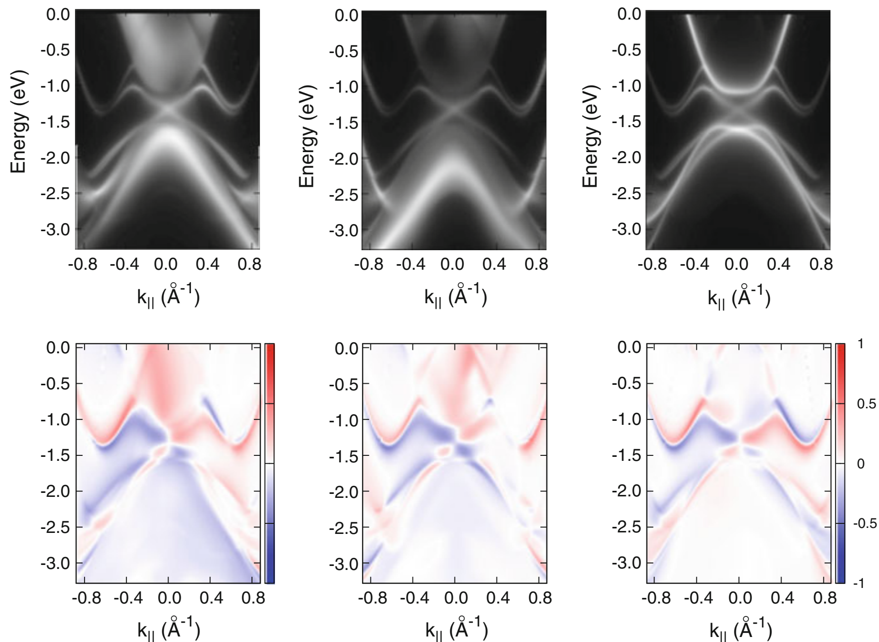

Fig. 7.4 *Top row*: Photoemission intensities calculated for different photon energies with linear p-polarized light along the $\overline{\Gamma}-\overline{S}$ direction. *Left panel*: Intensity map calculated at hν = 0.5 keV. *Middle panel*: Intensity map calculated at hν = 1.0 keV and *Right panel*: Intensity map calculated at hν = 3.0 keV. *Bottom row*: Corresponding spin polarizations in the Rashba configuration: in-plane, perpendicular to the reaction plane. Figure reproduced from [62]

In other words, the spectra at lower photon energies reflect more the surface than the bulk symmetry due to the combined effect of energy-dependent cross-sections and reduced IMFP [13, 16, 20, 40, 61].

7.4 Summary

We have shown several examples of photoemission calculations which reflect the wide range of applicability of the one-step model of photoemission. In its latest version, which is directly implemented in the SPR-KKR program package quantitative spectroscopical investigations may range from 10 eV up to 10 keV concerning the photon energy. This gives not only direct access to the UV-regime but also to the so called HARPES-regime of angle resolved photoemission. Due to the LSDA + DMFT method the range of applicability has been greatly enhanced ranging now from simple paramagnetic metals to complex layered compounds inhibiting strong electronic correlations. The recent extent of the one-step model to disordered magnetic alloys and finite temperatures round up the range of

applicability to a variety of complex 3D- as well as 2D-materials and allows investigations on surface related features for low photon energies as well as bulk-sensitive analyses for higher photon energies. As it holds for photocurrent calculations in the HARPES regime, phonon-related effects are also very important when analysing the intensity distributions which are obtained for energies around the Fermi level. The nearly quantitative agreement between experiment and theory, which is documented in this contribution, illustrates that our approach can work as a powerful analysis tool for various soft X-ray as well as hard X-ray ARPES investigations in the future.

Acknowledgments We thank the Deutsche Forschungsgemeinschaft (Projekt FOR1346, SPP1666, EB 154/23 and EB 154/20) and the Bundesminsisterium für Bildung und Forschung through BMBF: 05K13WMA for financial support. J. Minár would like to thank the CENTEM project, reg. no. CZ.1.05/2.1.00/03.0088, cofunded by the ERDF as part of the Ministry of Education, Youth and Sports OP RDI programme and, in the follow-up sustainability stage, supported through CENTEM PLUS (LO1402) by financial means from the Ministry of Education, Youth and Sports under the National Sustainability Programme I. We thank C.S. Fadley (US Davis), C.M. Schneider (Jülich), N.B. Brookes (Grenoble), G. Panaccione (Trieste), V. Strocov (PSI) and M. Donath (Münster) for helpful discussions and their continuous cooperation.

References

1. A. Damascelli, Z. Hussain, Z.X. Shen, Rev. Mod. Phys. **75**, 473 (2003)
2. D.H. Lu, I.M. Vishik, M. Yi, Y. Chen, R.G. Moore, Z.X. Shen, Annu. Rev. Cond. Mat. Phys. **3**, 129 (2012)
3. S. Tanuma, C.J. Powell, D.R. Penn, Surf. Interface Anal. **43**, 689 (2011)
4. Z. Hussain, C.S. Fadley, S. Kono, L.F. Wagner, Phys. Rev. B **22**, 3750 (1980)
5. Ch. Sondergaard, Ph. Hofmann, Ch. Schultz, M.S. Moreno, J.E. Gayone, M.A. Vicente Alvarez, G. Zampieri, S. Lizzit, A. Baraldi, Phys. Rev. B **63**, 233102 (2001)
6. A. Sekiyama, S. Suga, J. Electron Spectrosc. Relat. Phenom. **137**, 681 (2004)
7. A. Yamasaki, A. Sekiyama, S. Imada, M. Tsunekawa, A. Higashiya, A. Shigemoto, S. Suga, Nucl. Instr. Meth. Phys. Res. A **547**, 136 (2005)
8. T. Yokoya, T. Nakamura, T. Matsushita, T. Muro, Y. Takano, M. Nagao, T. Takenouchi, H. Kawarada, T. Oguchi, Nature **438**, 647 (2005)
9. M. Yano, A. Sekiyama, H. Fujiwara, T. Saita, S. Imada, T. Muro, Y. Onuki, S. Suga, Phys. Rev. Lett. **98**, 036405 (2007)
10. L. Plucinski, J. Minár, B.C. Sell, J. Braun, H. Ebert, C.M. Schneider, C.S. Fadley, Phys. Rev. B **78**, 035108 (2008)
11. F. Venturini, J. Minár, J. Braun, H. Ebert, N.B. Brookes, Phys. Rev. B **77**, 045126 (2008)
12. S. Suga, A. Sekiyama, J. Electron Spectrosc. Relat. Phenom. **181**, 48 (2010)
13. A.X. Gray, C. Papp, S. Ueda, B. Balke, Y. Yamashita, L. Plucinski, J. Minár, J. Braun, E.R. Ylvisaker, C.M. Schneider, W.E. Pickett, H. Ebert, K. Kobayashi, C.S. Fadley, Nat. Mater. **10**, 759 (2011)
14. C.S. Fadley, Synchrotron Radiat. News **25**, 26 (2012)
15. V.N. Strocov, M. Shi, M. Kobayashi, C. Monney, X. Wang, J. Krempasky, Th Schmitt, L. Patthey, H. Berger, P. Blaha, Phys. Rev. Lett. **109**, 086401 (2012)
16. A.X. Gray, J. Minár, S. Ueda, P.R. Stone, Y. Yamashita, J. Fujii, J. Braun, L. Plucinski, C.M. Schneider, G. Panaccione, H. Ebert, O.D. Dubon, K. Kobayashi, C.S. Fadley, Nat. Mater. **11**, 957 (2012)

17. G. Landolt, S.V. Eremeev, Y.M. Koroteev, B. Slomski, S. Muff, T. Neupert, M. Kobayashi, V. N. Strocov, Th Schmitt, Z.S. Aliev, M.B. Babanly, I.R. Amiraslanov, E.V. Chulkov, J. Osterwalder, J.H. Dil, Phys. Rev. Lett. **109**, 116403 (2012)
18. T. Fujikawa, H. Arai, J. Elec. Spec. Rel. Phenom. **123**, 19 (2002)
19. T. Fujikawa, H. Arai, J. Electron Spectrosc. Relat. Phenom. **174**, 85 (2009)
20. J. Minár, J. Braun, H. Ebert, J. Electron Spectrosc. Relat. Phenom. **190**, 159 (2013)
21. J. Fujii, B.R. Salles, M. Sperl, S. Ueda, M. Kobata, K. Kobayashi, Y. Yamashita, P. Torelli, M. Utz, C.S. Fadley, A.X. Gray, J. Braun, H. Ebert, I. Di Marco, O. Eriksson, P. Thunström, G.H. Fecher, H. Stryhanyuk, E. Ikenaga, J. Minár, C.H. Back, G. van der Laan, G. Panaccione, Phys. Rev. Lett. **111**, 097201 (2013)
22. A.X. Gray, J. Minár, L. Plucinski, M. Huijben, A. Bostwick, E. Rotenberg, S.-H. Yang, J. Braun, A. Winkelmann, G. Conti, D. Eiteneer, A. Rattanachata, A.A. Greer, J. Ciston, C. Ophus, G. Rijnders, D.H.A. Blank, D. Doenning, R. Pentcheva, C.M. Schneider, H. Ebert, C. S. Fadley, Europhys. Lett. **104**, 116403 (2013)
23. M. Kobayashi, I. Muneta, Y. Takeda, Y. Harada, A. Fujimori, J. Krempasky, Th. Schmitt, S. Ohya, M. Tanaka, M. Oshima, V.N. Strocov, http://arxiv.org/abs/1302.0063v1
24. K. Held, I.A. Nekrasov, G. Keller, V. Eyert, N. Blümer, A.K. McMahan, R.T. Scalettar, T. Pruschke, V.I. Anisimov, D. Vollhardt, Phys. Stat. Sol. (b) **243**, 2599 (2006)
25. G. Kotliar, S.Y. Savrasov, K. Haule, V.S. Oudovenko, O. Parcollet, C.A. Marianetti, Rev. Mod. Phys. **78**, 865 (2006)
26. K. Held, Adv. Phys. **56**, 829 (2007)
27. F. Manghi, V. Bellini, J. Osterwalder, T.J. Kreutz, P. Aebi, C. Arcangeli, Phys. Rev. B **59**, R10409 (1999)
28. J. Braun, Rep. Prog. Phys. **59**, 1267 (1996)
29. V.N. Strocov, M. Shi, M. Kobayashi, C. Monney, X. Wang, J. Krempasky, T. Schmitt, L. Patthey, H. Berger, P. Blaha, Phys. Rev. Lett. **109**, 086401 (2012)
30. J.B. Pendry, *Low Energy Electron Diffraction* (Academic Press, London, 1974)
31. J.B. Pendry, Surf. Sci. **57**, 679 (1976)
32. J.F.L. Hopkinson, J.B. Pendry, D.J. Titterington, Comp. Phys. Commun. **19**, 69 (1980)
33. C.N. Berglund, W.E. Spicer, Phys. Rev. **136**, A1030 (1964)
34. K. Kambe, Z. Naturf. **22a**, 322 (1967)
35. J.M. MacLaren, S. Crampin, D.D. Vvedensky, J.B. Pendry, Phys. Rev. B **40**, 12164 (1989)
36. H. Ebert, D. Ködderitzsch, J. Minár, Rep. Prog. Phys. **74**, 096501 (2011)
37. G. Borstel, Appl. Phys. A **38**, 193 (1985)
38. J. Braun, J. Minár, F. Matthes, C.M. Schneider, H. Ebert, Phys. Rev. B **82**, 024411 (2010)
39. J. Minár, J. Braun, H. Ebert, J. Electron Spectrosc. Relat. Phenom. **189**, 129 (2013)
40. C. Papp, L. Plucinski, J. Minár, J. Braun, H. Ebert, C.M. Schneider, C.S. Fadley, Phys. Rev. B **84**, 045433 (2011)
41. N.J. Shevchik, Phys. Rev. B **16**, 3428 (1977)
42. R. Feder, J. Phys. C Solid State Phys. **14**, 2049 (1981)
43. R. Paniago, R. Matzdorf, G. Meister, A. Goldmann, J. Braun, G. Borstel, Surf. Sci. **347**, 46 (1996)
44. C.G. Larrson, J.B. Pendry, J. Phys. C Solid State Phys. **14**, 3089 (1981)
45. M.A.V. Alvarez, H. Ascolani, G. Zampieri, Phys. Rev. B **54**, 14703 (1996)
46. T. Fujikawa, J. Electron Spectrosc. Relat. Phenom. **173**, 51 (2009)
47. T. Fujikawa, J. Electron Spectrosc. Relat. Phenom. **173**, 51 (2009)
48. J. Braun, J. Minár, S. Mankovsky, V.N. Strocov, N.B. Brookes, L. Plucinski, C.M. Schneider, C.S. Fadley, H. Ebert, Phys. Rev. B **88**, 205409 (2013)
49. B. Ginatempo, P.J. Durham, B.I. Gyorffy, J. Phys. Cond. Mat. **1**, 6483 (1989)
50. P. Hohenberg, W. Kohn, Phys. Rev. **136**, B 864 (1964)
51. W. Kohn, L.J. Sham, Phys. Rev. **140**, A 1133 (1965)
52. A. Georges, G. Kotliar, W. Krauth, M.J. Rozenberg, Rev. Mod. Phys. **68**, 13 (1996)
53. J. Minár, L. Chioncel, A. Perlov, H. Ebert, M.I. Katsnelson, A.I. Lichtenstein, Phys. Rev. B **72**, 045125 (2005)

54. J. Minár, J. Phys. Cond. Mat. **23**, 253201 (2011)
55. K. Miyamoto, A. Kimura, K. Kuroda, T. Okuda, K. Shimada, H. Namatame, M. Taniguchi, M. Donath, Phys. Rev. Lett. **108**, 066808 (2012)
56. K. Miyamoto, A. Kimura, T. Okuda, K. Shimada, H. Iwasawa, H. Hayashi, H. Namatame, M. Taniguchi, M. Donat, Phys. Rev. B **86**, 161411(R) (2012)
57. H. Mirhosseini, M. Flieger, J. Henk, New J. Phys. **15**, 033019 (2013)
58. Th Fauster, F.J. Himpsel, Phys. Rev. B **30**, 1874 (1984)
59. R. Matzdorf, R. Paniago, G. Meister, A. Goldmann, Ch. Zubrägel, J. Braun, G. Borstel, Surf. Sci. **352–354**, 670 (1996)
60. G.H. Fecher, J. Braun, N.A. Cherepkov, L.V. Chernysheva, Th Jentzsch, J. Morais, A. Oelsner, Ch. Ostertag, J. Paul, H. Ufer, G. Schönhense, Eur. Phys. J. B **11**, 161 (1999)
61. H. Ebert, J. Minár, J. Braun, S. Mankovskyy, J. Elect. Spec. Rel. Phenom. **184**, 91 (2011)
62. J. Braun, K. Miyamoto, A. Kimura, T. Okuda, M. Donath, H. Ebert, J. Min. New J. Phys. **16**, 015005 (2014)
63. J. Braun, M. Donath, Europhys. Lett. **59**, 592 (2002)
64. R. Claessen, *Private Communication* (2013)

Chapter 8
Recoil Effects in X-ray Photoelectron Spectroscopy

Yosuke Kayanuma

Abstract Recent advances in hard X-ray photoelectron spectroscopy (HAXPES) have made it possible to measure electronic energy levels with resolution as high as 80 meV for photon energies extending to as high as 10 keV. For such high energy photoelectrons, the recoil momentum imparted to the atoms is no longer negligible, even though the momentum of the incident photon can safely be neglected. Here, the recoil effects in HAXPES of solids as well as gas-phase molecules are reviewed. It is shown that by comparison of the experimental data with quantum mechanical theories based on appropriate models of matter, information on the local environments of the emitter atoms in the material is obtained.

8.1 Introduction

The foundation of the principles of photoelectron spectroscopy can be traced back to the celebrated article of Einstein in 1905 [1], in which the kinetic energy E_{kin} of a photoelectron is given by the conservation law of energy as

$$E_{kin} = h\nu - W, \tag{8.1}$$

where $h\nu$ is the incident photon energy and W is the binding energy with respect to the vacuum level. Although this is one of the simplest equations to appear in the literature, it has the unequaled power of enabling us to determine the binding energy of the electrons in materials by subtraction of two observable quantities, $h\nu$ and E_{kin}.

Y. Kayanuma (✉)
Materials and Structures Laboratory, Tokyo Institute of Technology,
Nagatsuta, Yokohama, Japan
e-mail: kayanuma.y.aa@m.titech.ac.jp

© Springer International Publishing Switzerland 2016

J.C. Woicik (ed.), *Hard X-ray Photoelectron Spectroscopy (HAXPES)*,
Springer Series in Surface Sciences 59, DOI 10.1007/978-3-319-24043-5_8

There is another conservation law that also needs to be in the elementary process of photoemission: the momentum of the whole system should be conserved. An incident photon of energy $h\nu$ has the momentum $p_i = h\nu/c$, where c is the velocity of light. The ejected electron has the momentum $p = \sqrt{2mE_{kin}}$ within the nonrelativistic approximation, where m is the mass of the electron. In the case of a relatively shallow bound state with high-energy photons, we may neglect W because it is small compared to $h\nu$ in (8.1) for a rough estimation. Then, for an incident photon with an energy on the order of 10 keV, the momentum of the photon is estimated to be less than the momentum of the photoelectron by an order of magnitude and can safely be neglected. However, the momentum of the photoelectron may not be negligible in the hard X-ray region. The photoelectron "kicks" the emitter atom when ejected, which is called the photoelectron recoil effect. This means the (8.1) needs to be modified because the additional terms corresponding to the recoil energy must be considered.

The possibility of observing the recoil effects of photoelectrons was noted theoretically in the early days of X-ray photoelectron spectroscopy (XPS) [2, 3]. However, this process did not receive much attention, mainly because of the limitation of the experimental resolution in the hard X-ray region, which is where the recoil effect becomes discernible. Therefore, it was a little surprising when researchers found an anomalous shift and broadening in the hard X-ray photoelectron spectrum (HAXPES) measured for the $1s$ core level of graphite [4]. The anomalous shift and broadening are caused by the recoil effect of photoelectrons. In solids, most XPS studies investigating core levels in recent years have focused on high-resolution measurements using hard X-rays from third-generation synchrotron light sources [5]. One of the reasons for this trend is the necessity to obtain precise data about bulk solids by avoiding surface effects. The identification of recoil effects may pose a new problem in the interpretation of experimental XPS data.

The recoil of a photoelectron results in a peak shift as well as the broadening of the spectrum. First, let us estimate the magnitude of these effects by considering a simple model of an atom with mass M in thermal equilibrium in the gas phase. It is assumed that the atom is moving with momentum $\vec{P}$ and hit by a photon of energy $h\nu$. In the final state, an electron with mass m is ejected from the bound state of energy ϵ_c to the free state with momentum $\vec{p}$. Through conservation of energy and momentum, we find

$$\epsilon_c + h\nu + \frac{\vec{P}^2}{2M} = \frac{\vec{p}^2}{2m} + \frac{\left(\vec{P} - \vec{p}\right)^2}{2M}. \tag{8.2}$$

The observed kinetic energy of the photoelectron is then

$$E_{kin} \equiv \frac{\vec{p}^2}{2m} = \epsilon_c + h\nu - \frac{\vec{p}^2}{2M} + \frac{\vec{P} \cdot \vec{p}}{M}. \tag{8.3}$$

Taking the thermal average over the initial distribution of $\vec{P}$, we find the shift of the apparent binding energy $\Delta E = h\nu + \epsilon_c - \langle E_{kin} \rangle$,

$$\Delta E = \left\langle \frac{\vec{p}^2}{2M} \right\rangle = \frac{m}{M} \langle E_{kin} \rangle. \tag{8.4}$$

From the equipartition law, the second moment of the spectrum is evaluated as

$$\langle (E_{kin} - \langle E_{kin} \rangle)^2 \rangle = \frac{\left\langle \left(\vec{P} \cdot \vec{p}\right)^2 \right\rangle}{M^2} = 2\Delta E k_B T. \tag{8.5}$$

This is simply the Doppler broadening.

If an atom is embedded in a solid at low temperatures, the thermal energy $k_B T$ should be replaced by the energy of the typical phonon $\hbar\bar{\omega}$. As a measure of the magnitude of the recoil effect, one may define the effective coupling constant S as

$$S = \Delta E / \hbar\bar{\omega}. \tag{8.6}$$

This is an analogue of the Huang-Rhys factor in electron-phonon interactions. The value e^{-S} then represents the relative amplitude of the recoilless transition, and is an analogue of the Debye-Waller factor at low temperatures [6].

For a carbon atom with the mass ratio m/M = 1/22000, ΔE becomes roughly 0.36 eV for $\langle E_{kin} \rangle = 8$ keV. This is readily observable by the present level of experimental resolution. The mass ratio 1/22000 is equivalent to that of a person with weight of 75 kg to a cargo vessel of 1650 t. When the person dives into the water from the ship, the recoil movement of the ship, albeit small, is real and should be observable.

The recoil energy transferred to the emitter atom will be dissipated by the excitation of phonons in the solids. In molecules in the gas phase, the recoil energy is dissipated at a translational mode of the center of mass, and excitation of ro-vibronic modes within the molecule. These effects will distort the line shape of the HAXPES in addition to causing a peak shift. As a result, the line shape containing the recoil effect bears information on the local environments of the atoms in materials. The presence of recoil effects in HAXPES is therefore not an annoyance but a new spectroscopic tool, provided the data are obtained with sufficient resolution and analyzed carefully.

Here, recent experimental findings on the recoil effects in HAXPES are reviewed together with theoretical analyses. It is shown that good agreement is obtained between the experimental data and quantum mechanical theories based on appropriate models of matter, which provides insight into the electron-matter interactions in materials.

8.2 Recoil Effects in Solids

8.2.1 Core-Level HAXPES

Figure 8.1a shows C 1*s* core-level spectra of highly oriented pyrolytic graphite (HOPG) measured at room temperature with soft X-ray excitation (340 and 870 eV) and hard X-ray excitation (5950 and 7940 eV) [4]. The measurements to obtain these spectra were performed at SPring-8 using synchrotron radiation. The total instrumental energy resolution determined for the soft and hard X-rays were 100 and 120 meV, respectively. The spectra were obtained in normal emission geometry; the photoelectron detection angle relative to the sample surface was 90° and 85° for soft and hard X-rays, respectively. The peak position of the spectrum obtained with $h\nu = 340$ eV shifts to higher binding energy compared to that with $h\nu = 870$ eV. This originates from the difference in the chemical shift of the core level caused by the excitation-energy dependence of the probing depth. The spectrum measured with $h\nu = 340$ eV is dominated by surface effects, while that for $h\nu = 870$ eV is considered to be probing the bulk material [7]. With increasing

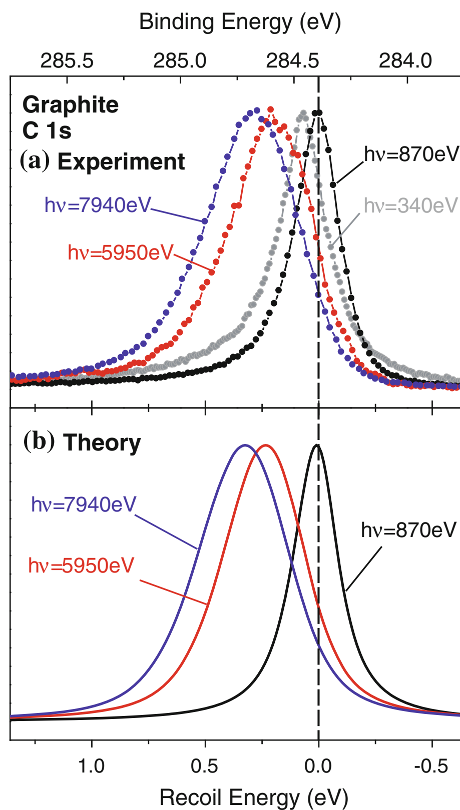

Fig. 8.1 **a** Photon-energy dependence of C 1*s* core-level spectra of graphite. The emission angles are 90° ($h\nu = 340$ and 870 eV) and 85° ($h\nu = 5950$ and 7940 eV) relative to the sample surface. **b** Theoretical spectra that takes into account the recoil effect using an anisotropic Debye model [4]

excitation energy, the peak position shifts to higher binding energy. It is also obvious that the spectrum becomes broadened and asymmetrical. Although there are a range of possible origins of the spectral broadening such as plasmon excitation and phonon excitation, these can be excluded because they cannot explain the *excitation energy dependent* peak shift and broadening. Thus, the peak changes are caused by the recoil effect.

The theoretical treatment of the recoil effect in the core-level HAXPES of solids is formulated as follows [4]. The interaction with the X-rays aside from irrelevant factors is given by

$$H_I = \left(a + a^\dagger\right)\vec{\kappa} \cdot \vec{p}, \tag{8.7}$$

where a is the annihilation operator for the X-rays with energy $h\nu$ and polarization vector $\vec{\kappa}$ (unit vector), and $\vec{p}$ is the momentum of the electron. In the above equation, we have assumed the dipole approximation. For the case of interaction with extremely high-energy photons, the higher terms of the multipole expansion cannot be ignored. It has been shown [8] that for hydrogen-like atoms, the ratio of the contribution to the photoelectric cross section by the quadratic term to that by the dipole term is estimated to be the order of $h\nu/mc^2$. For X-rays with energy on the order of 10 keV, therefore, we can safely rely on the dipole approximation.

The initial state of the transition is given by $|\Psi_i\rangle = |h\nu\rangle \otimes |\psi_c\rangle \otimes |i\rangle$, in which $|h\nu\rangle$ is the one-photon state, $|\psi_c\rangle$ is the core-electron state with energy ϵ_c, and $|i\rangle$ is a phonon state of the crystal. We assume that a core electron of the atom at the lattice point $\vec{R}^0$ is ejected by the X-rays. The actual nuclear position $\vec{R}$ is given by $\vec{R} = \vec{R}^0 + \vec{u}$, where $\vec{u}$ is the fluctuation of the atom. An important point is that the wave function of the core electron is given by the form $\langle\vec{r}|\psi_c\rangle = \psi_c\left(\vec{r} - \vec{R}\right)$. Although this dependence of the core-electron wave function on the nuclear position $\vec{R}$ seems to be a trivial fact, it plays a key role in the theory of recoil effect. This form of the wave function means that the core electron follows the instantaneous nuclear position adiabatically. The local translational symmetry is thus guaranteed, and the conservation of momentum directly appears without any *ad hoc* assumption of the dynamical equations. The final state of the transition is given by $|\Psi_f\rangle = |0\rangle \otimes |\varphi_K\rangle \otimes |f\rangle$, in which $|0\rangle$ is the vacuum of the photon, $|\varphi_K\rangle$ is the plane wave of the photoelectron, $\langle\vec{r}|\varphi_K\rangle = (2\pi)^{-3/2}\exp\left(i\vec{K} \cdot \vec{r}\right)$, with energy $\hbar^2K^2/2m$, and $|f\rangle$ is a phonon state.

In the evaluation of the matrix element $\langle\Psi_f|H_I|\Psi_i\rangle$, we change the integration variable from $\vec{r}$ to $\vec{r} - \vec{R}$ and find

$$\langle\Psi_f|H_I|\Psi_i\rangle = \vec{\kappa} \cdot \vec{\zeta}\langle f|\mathrm{e}^{-i\vec{K}\cdot\vec{R}}|i\rangle, \tag{8.8}$$

in which

$$\vec{\zeta} = (2\pi)^{-3/2} \int d^3 r \mathrm{e}^{-i\vec{K}\cdot\vec{r}} \left(-i\hbar \frac{\partial}{\partial \vec{r}} \right) \psi_c(\vec{r}). \tag{8.9}$$

The photoelectron spectrum is calculated by the usual second-order perturbation. After some manipulations, we obtain the following expression for the photoelectron spectrum as a function of the relative binding energy E measured from the recoilless value,

$$I(E) = \frac{|\vec{\kappa}\cdot\vec{\zeta}|^2}{2\pi\hbar} \int_{-\infty}^{\infty} \mathrm{d}t \mathrm{e}^{-Et/\hbar - \Gamma|t|/\hbar} F(t), \tag{8.10}$$

in which the correlation function $F(t)$ is given by the canonical average over the phonons,

$$F(t) = \langle \mathrm{e}^{i\vec{K}\cdot\vec{u}(t)} \mathrm{e}^{-i\vec{K}\cdot\vec{u}} \rangle, \tag{8.11}$$

where $\vec{u}(t)$ is the Heisenberg representation of $\vec{u}$ at time t, and Γ is the lifetime broadening factor. In the evaluation of (8.11), $\vec{u}$ is expanded by the phonon operators for the normal modes of the crystal, and we obtain after an exercise $F(t) = \exp[G(t)]$ where

$$G(t) = \sum_q \alpha_q^2 \left\{ \left[2n(\omega_q) + 1 \right] \left(\cos\omega_q t - 1 \right) - i \sin\omega_q t \right\}, \tag{8.12}$$

with

$$\alpha_q^2 = \left(\frac{\hbar}{2N\tilde{M}\omega_q} \right) |\vec{K}\cdot\vec{\eta}_q|^2 \tag{8.13}$$

and

$$n\left(\omega_q\right) = 1/\left(\mathrm{e}^{\hbar\omega_q/k_B T} - 1 \right).$$

In the above equations, q represents the branch index and wave vector of the phonons, $\tilde{M}$ is the mass of a unit cell, N is the number of unit cells, and $\vec{\eta}_q$ is the polarization vector of the phonons. As shown in (8.10), the photoelectron spectrum $I(E)$ is a convolution of a structure function with the Lorentz function. The former consists of the recoilless line, i.e. the zero-phonon line, and its phonon sidebands.

The analogy of the above expression with that for the Mössbauer effect [9] is noticeable. In the radiative decay of an unstable excited state of nuclei, the emitted γ-ray kicks the mother atom. For atoms in free space, the recoil momentum shifts the energy of the γ-ray to lower energy side because of the Doppler effect, which

results in the prohibition of the resonant reabsorption of the γ-ray by the other atoms. The Mössbauer effect is the revival of the resonant absorption for the samples in which the radioactive atoms are embedded in crystal lattices. In such cases, a part of the recoil momentum is accepted by the rigid crystal lattice, and the spectrum of the emitted γ-ray now consists of a sharp recoilless line and its phonon sidebands. In the case of recoil effect in the core-level XPS, the zero-phonon line is indiscernible in many cases because of the lifetime broadening of the core-excited states, unlike the Mössbauer effect.

It is well known that graphite has highly anisotropic phonon dispersions. An important aspect of the photoelectron recoil effect is that the photoelectron spectrum depends on the relative angle of the $\vec{K}$-vector of the emitted electron to the lattice vector, because the effective coupling constant α_q is proportional to the inner product between $\vec{K}$ and the lattice displacement vector $\vec{\eta}_q$ as shown in (8.13). In actual calculations, we adopt an anisotropic Debye model for graphite. The stretching (in-plane) mode and bending (out-of plane) mode are assumed to be independent with different Debye cutoff frequencies of $\hbar\omega_{s,D} = 150\,\text{meV}$ and $\hbar\omega_{b,D} = 75\,\text{meV}$ [10], respectively. The summation over $\vec{q}$ in (8.12) is transformed into the integration over the anisotropic density of states for the two modes.

Theoretical spectra of the C 1s normal-angle emission photoelectrons of graphite are plotted as a function of recoil energy in Fig. 8.1b. The lifetime broadening (full width at half maximum) is taken to be 160 meV [7, 11]. The spectra are convoluted with a Gaussian function corresponding to an experimental resolution of 120 meV. The agreement with experimental data is good even though there are no adjustable parameters. In this case, the bending-mode phonons are excited. Each spectrum has an asymmetric line shape with a low-energy tail. This asymmetry is caused by the quantum nature of phonons; the phonon side band forms a Poisson distribution rather than a Gaussian distribution, just like the optical absorption spectra for the electron-phonon coupled systems [6]. Although the measurement was carried out at room temperature, the broadening originates almost from the zero-point vibration [12]. Note that at 870-eV excitation, the asymmetric broadening is discernible even though the peak shift is quite small.

Figure 8.2a depicts experimental photoelectron spectra for HOPG C 1s [4] measured with 7940-eV excitation at emission angles of 85° and 30° relative to the sample surface. The emission angle is controlled by tilting the graphite plane against the X-ray beam, because $\vec{\zeta} \| \vec{K}$ for the 1s core level as shown in (8.9). The peak shifts to slightly lower binding energy and becomes broader in the grazing emission spectrum compared with normal emission. Theoretical spectra are shown in Fig. 8.2b. The theoretical spectra reproduce the observed emission-angle dependence well. The broader peak in the grazing angle emission than the normal emission is attributed to the stiffness against lattice distortion in the direction parallel to the surface compared with that in the normal direction. This can be understood in the following way. In the potential well for atomic motions, the uncertainty in coordinate space is smaller for a stronger spring constant than a weaker one. This in turn results in larger uncertainty in the momentum space. Because the spectral widening

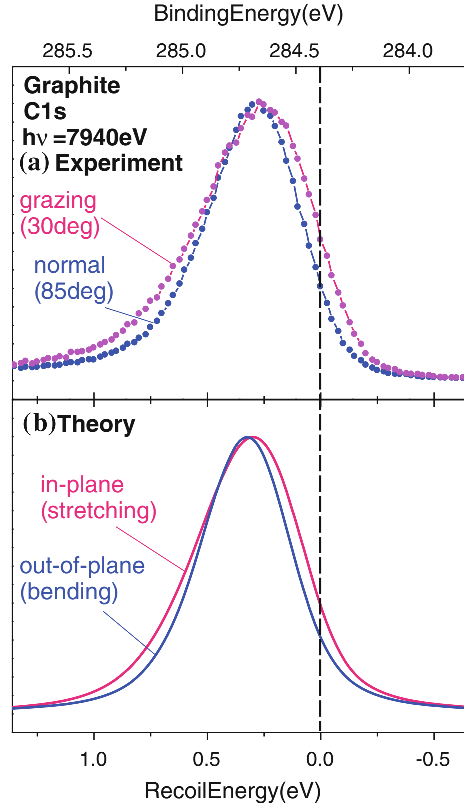

Fig. 8.2 a C 1*s* core-level spectra of graphite measured at a photon energy of 7940 eV and the emission angles of 85° (normal) and 30° (grazing) relative to the sample surface. **b** Theoretically obtained spectra with Debye energies of $\hbar\omega_{b,D} = 75\,\text{meV}$ and $\hbar\omega_{s,D} = 150\,\text{meV}$ for bending and stretching modes, respectively [4]

is caused by the Doppler broadening from zero-point vibrations, it becomes wider in the grazing angle emission for which the relevant spring constant is larger than the normal emission. The small difference of the peak position between normal and the grazing-angle spectra is also attributed to the quantum effect; the larger the quantum of phonons is, the larger the relative amplitude of the recoilless transition is, because the effective coupling constant S becomes smaller. This is seen if one takes the Debye cutoff frequency for a typical phonon frequency $\bar{\omega}$ in (8.6). Therefore, the peak shift is smaller in the grazing-angle emission. Note that ΔE given in (8.4) is, strictly speaking, the first moment of the spectrum, which does not necessarily coincide with the peak position because of the asymmetry. Although the gross spectral shape of the recoil effect can be understood by the semiclassical approximation [13], it is necessary to use a full quantum-mechanical analysis taking into account the solid-state effect for such high-resolution spectroscopy.

Vos et al. [14] noticed the universality of the angle dependence of the recoil effect in graphite observed in large angle electron scattering [15], neutron scattering [16] and HAXPES [4]. In scattering experiments, the direction of momentum transfer $\vec{q}$ can be controlled by choosing the events between the transmission configuration (here $\vec{q}$ is parallel to the graphite plane) and reflection configuration ($\vec{q}$

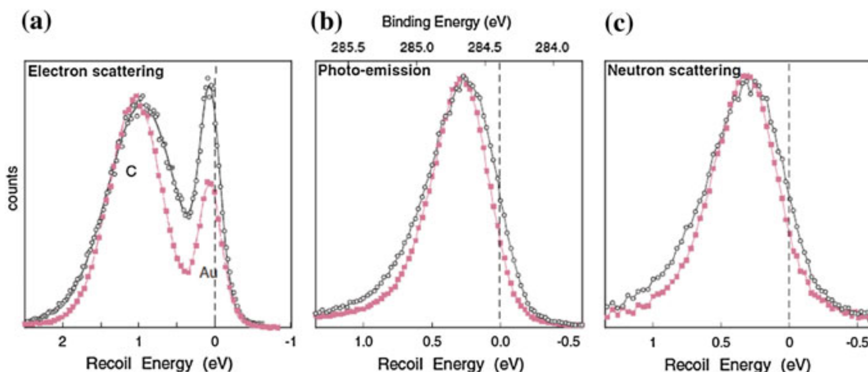

Fig. 8.3 Spectra for HOPG samples obtained from three types of scattering experiments **a** electron scattering, **b** 1*s* photoemission and **c** neutron scattering. The momentum transfer is perpendicular (*filled squares*) and parallel (*open circles*) to the graphite planes [14]

is perpendicular to the plane) by tilting the HOPG samples for a fixed scattering angle. Figure 8.3a presents spectra for electron scattering measured in the transmission configuration (open circles) and reflection configuration (filled squares) against recoil energy [15]. This electron scattering experiment was performed at 40 keV with a scattering angle of 44.3°, which corresponds to a momentum transfer of 41.7 a.u. To calibrate the zero point of energy loss, a small amount of Au was added to the sample, which provided a separate peak that is very close to (but not coincident with) the zero-energy loss. The photoemission data illustrated in Fig. 8.3b are the same as in Fig. 8.2a. Meanwhile, Fig. 8.3c contains the data for neutron scattering [16] for transmission (open circles) and reflection (filled squares).

Despite the differences in the physical processes underlying these three experiments, the similarity of their spectral features is startling. The recoil loss spectra corresponding to the momentum transfer along the graphite plane always give broader peaks with slightly smaller shifts compared with those for perpendicular momentum transfer. Actually, all three sets of experimental data are well fitted by the anisotropic Debye model without any adjustable parameters. In the neutron scattering experiment performed by Fielding et al. [16], the value of the momentum transfer (23.4 a.u.) is very similar to that for the photoemission experiment [4] (23.8 a.u.). Therefore, it is meaningful to compare the data shown in (b) and (c) not only qualitatively but also quantitatively. The agreement of the data in (b) and (c) is good. The agreement of the theoretical calculations based on the single-site approximation with the experimental data indicates that the correlation of the recoil effects in the photoemission and particle scatterings discussed by Fujikawa et al. [17] plays only a minor role.

The recoil effect in the core-level HAXPES has also been ascertained in other materials with relatively light elements such as the B 1*s* of MgB_2 ($M = 11$) and Al

$2p$ (M = 27), where systematic shifts and broadening of the spectra are clearly observed [18].

8.2.2 Valence-Band HAXPES

In the recoil effect of photoelectron emission, it is assumed that the electron kicks one atom when ejected. Therefore, it may not be surprising if one observes the recoil shift of the binding energy in core-level HAXPES, because the core electron is tightly bound to a particular atom. It is an intriguing question whether or not the valence electrons in a crystal in a Bloch state exhibit recoil effects. In particular, the recoil effect about nearly free electrons in the conduction band of simple metals is unclear. Because the nearly free electrons in metals have delocalized wave functions extending all over the crystals, the recoil effect would not seem to be present at first glance.

It is instructive to reconsider here the role of the conservation of momentum in the photoemission processes. It should be noted that a free electron can never be photoemitted because it is impossible to satisfy both of the conservation laws of energy and momentum. In order to satisfy the conservation of momentum, there must be third particles, i.e. nuclei, in addition to the photon and the electron. In the traditional theory of the photoemission, the initial state wave function $\psi(\vec{r})$ in solids is assumed to have the form $\psi(\vec{r}) = \sum_i f_i(\vec{r} - \vec{R}_i^0)$, where $\vec{R}_i^0$ is a constant parameter representing the coordinate of relevant nucleus. Behind this form, it is implicitly assumed that the nuclei have infinitely heavy masses. The above wave function then yields a finite cross section of the photoemission without violating the conservation of momentum. It is worthwhile to note that the fact that one observes the valence-band photoemission in the HAXPES for metals itself indicates that the nearly free electrons actually *see* the lattice structure, because higher order

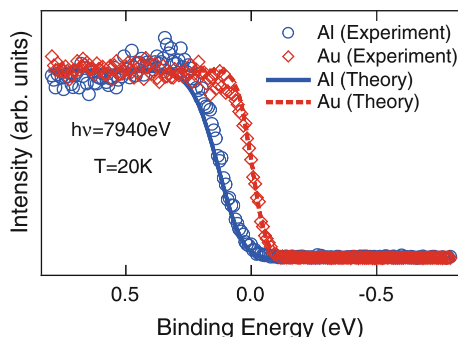

Fig. 8.4 Photoelectron spectra near the Fermi edge for Al (*circles*) and Au (*squares*) with an excitation energy of 7940 eV. The *solid* and *dotted lines* indicate the theoretical curves calculated by the Debye model [19]

Umklapp processes are needed in order to be compatible with the momentum conservation law.

Figure 8.4 shows photoelectron spectra around the Fermi edge of Au (squares) and Al (circles) measured at 20 K at excitation energy of 7940 eV [19]. The binding energy scale is calibrated by assuming that the recoil energy in Au (M = 197) is negligible. As clearly seen, the Fermi edge of Al (M = 27) is shifted to higher binding energy from that of Au. Because the Fermi level of metals should coincide in energy with each other in XPS measurements, this apparent shift of Al Fermi level relative to Au must be caused by the recoil effect, and it is therefore direct experimental evidence of its existence for Bloch electrons. Furthermore, the inclination of the edge slope is reduced for Al compared with that for Au. The conventional fitting using the Fermi-Dirac function indicates an energy shift of 120 meV for Al relative to that for Au, and Gaussian widths of 160 meV for Al and 120 meV for Au. The broadening of the line width for Al is also a sign of the recoil effect.

Soft X-ray spectra of Au (squares) and Al (circles) measured at 50 K with an excitation energy of 880 eV are presented in Fig. 8.5. In the wide-range plot (Fig. 8.5a), it is difficult to recognize the difference between the spectra of Au and Al. However, in the expanded spectra (Fig. 8.5b), the energy shift and broadening

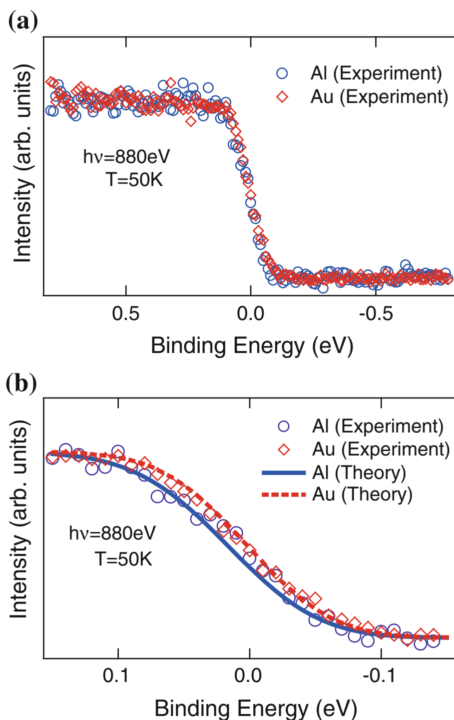

Fig. 8.5 **a** Photoelectron spectra near the Fermi edge for Al (*circles*) and Au (*squares*) with an excitation energy of 880 eV. **b** Expanded-scale plot of the spectra. The *solid* and *dotted lines* indicate the theoretical curves [19]

of the Fermi-edge profile are certainly observed. Fitting analysis clarified that there is an energy shift of 12 meV for Al relative to Au.

First we present a formal theory to analyze the experimental data, and then discuss its physical meaning. Consider the transition probability $I(\vec{k}, \vec{K})$ in which a Bloch electron with wave vector $\vec{k}$ is emitted to the free-electron state with wave vector $\vec{K}$ by an X-ray photon with energy $h\nu$. Without the recoil effect, the component of the wave vector parallel to the surface is conserved in the periodic-zone scheme. The perpendicular component is not conserved, but is determined by the conservation of energy. In the presence of the recoil effect, this is written as

$$h\nu + \epsilon_k + \epsilon_i = E_K + \epsilon_f, \tag{8.14}$$

in which ϵ_k is the energy of the Bloch electron measured from the vacuum level, and ϵ_i and ϵ_f are the energies of the phonons in the initial and final states, respectively. The initial and final states of the transition are also the same as given in the previous subsection: the only difference is that in the initial state $|\Psi_i\rangle$, the electronic wave function is given by the Bloch state $|\psi_k\rangle$ instead of the core-electron state $|\psi_c\rangle$. The Bloch state $\langle \vec{r}|\psi_k\rangle \equiv \psi_k(\vec{r})$ is expanded by the Wannier function as

$$\psi_k(\vec{r}) = N^{-1/2} \sum_i \mathrm{e}^{i\vec{k}\cdot\vec{R}_i} w\left(\vec{r} - \vec{R}_i\right), \tag{8.15}$$

where $\vec{R}_i$ is the lattice vector at site i. We assume that $\vec{R}_i$ is a dynamical variable fluctuating around the fixed lattice point $\vec{R}_i^0$ as $\vec{R}_i = \vec{R}_i^0 + \vec{u}_i$ with $\vec{u}_i$ being a displacement vector. This lattice fluctuation usually gives rise to a local change of the band energy of the deformation potential type. We neglect this electron-lattice interaction for simplicity. The interaction Hamiltonian H_I with the X-rays is given by (8.7).

The transition probability $I\left(\vec{k}, \vec{K}\right)$ is given by Fermi's golden rule,

$$I\left(\vec{k}, \vec{K}\right) = \left\langle \sum_f |\langle \Psi_f | H_I | \Psi_i \rangle|^2 \delta\left(E_K + \epsilon_f - h\nu - \epsilon_k - \epsilon_i\right) \right\rangle, \tag{8.16}$$

in which the summation runs over the final phonon states and $\langle \cdots \rangle$ means the canonical average over the initial phonon states. The electronic part of the transition matrix element is given by

$$\langle \varphi_K | H_I | \psi_k \rangle = \vec{\kappa} \cdot \vec{\zeta} \frac{1}{\sqrt{N}} \sum_i \mathrm{e}^{-i(\vec{K}-\vec{k})\cdot\vec{R}_i^0} \mathrm{e}^{-i\vec{K}\cdot\vec{u}_i}, \tag{8.17}$$

in which the transition dipole moment $\vec{\zeta}$ is given in the same form as that in (8.9) with the core-level wave function $\psi_c(\vec{r})$ being replaced by $w(\vec{r})$. Note that in the absence of the recoil effect $\vec{u}_i = 0$, the conservation of the k-vector is recovered with the modulus of the reciprocal lattice vectors. Using the same technique as before, the transition probability $I(\vec{k}, \vec{K})$ can be written as a Fourier transform of a generating function. In the case of valence-band photoemission, there appears an infinite sum of the correlation functions $F_i(t)$,

$$F_i(t) = \langle e^{i\vec{K}\cdot\vec{u}_i(t)} e^{-i\vec{K}\cdot\vec{u}_0} \rangle,$$

which describes the spatiotemporal correlation between phonons created at 0-site at $t = 0$ and those at i-site at time t. Because of the dispersion of the phonon spectrum, the contribution from the off-diagonal terms $i \neq 0$ is much smaller than that from the diagonal term $i = 0$. Taking into account only the diagonal term $F_0(t)$ in accordance with the incoherent scattering approximation [20], we arrive at an expression similar to (8.10),

$$I(\epsilon, E) = \frac{1}{2\pi\hbar} \int_{-\infty}^{\infty} dt e^{i(E-\epsilon)t/\hbar} F_0(t), \tag{8.18}$$

where we have changed variables from $\vec{k}$ and $\vec{K}$ to the binding energy $\epsilon = -\epsilon_k - \phi$ and the apparent binding energy $E = h\nu - E_K - \phi$ (ϕ is the work function), respectively. The actual spectrum is calculated by taking the average over the initial distribution of the electrons

$$I(E) = \int d\epsilon I(\epsilon, E) f(\mu - \epsilon) D(\epsilon),$$

where $f(\epsilon)$ is the Fermi distribution function, μ is the chemical potential, and $D(\epsilon)$ is the density of states near the Fermi edge, which is approximated to be nearly constant. Finally, $I(E)$ is convoluted with the Gaussian broadening function because of the resolution of the apparatus.

The theoretical curves for HAXPES for Au and Al with an excitation energy of 7940 eV are shown in Fig. 8.4. The Debye energies are $\hbar\omega_D(\text{Al}) = 36.8\,\text{eV}$ and $\hbar\omega_D(\text{Au}) = 14.2\,\text{meV}$, respectively. The broadening caused by the experimental resolution was fixed to 108 meV (FWHM) from the fitting of the Au line shape. As shown in Fig. 8.4, the agreement of the experimental data with the theoretical curve is good. The apparent Fermi energy of Al is shifted by 120 meV compared with that of Au because of the recoil effect. Equation (8.4) estimates this shift to be 138 meV, so the theory correctly reproduces the experimental value. The reduction from 138–120 meV can be explained by the quantum effect of the phonons. In the case of HAXPES using X-rays with energy as high as 7940 eV, even the observed Fermi energy of Au is shifted by about 24 meV from its true value. Figure 8.5 presents the

results for excitation with an energy of 880 eV on an expanded scale. Although the difference between the spectra for Al and Au is very small, it does exist and agrees with the theoretical calculation as shown in Fig. 8.5b.

8.2.3 Site-Specific Recoil Effect in Compounds

One of the purposes of XPS of solids is to elucidate element-selective information on the electronic states in the valence band. Resonant photoelectron spectroscopy (RPES) has proved to be a powerful tool to obtain such information [21]. Analysis of the experimental data measured by RPES requires knowledge of the core excited states as the intermediate state of transition. Sometimes this complicates the analysis because of intermediate-state interactions. Observation of recoil effects in valence-band photoemission spectra then suggests a fascinating possibility to use HAXPES as a tool to extract information on the local density of states associated with the atomic species on which the hole localizes [22].

The valence band of a composite crystal is often made of hybridized orbitals originating from atoms with both light and relatively heavy masses. Typical examples are the oxides of transition metals or rare earth species. Although the valence electrons occupy the coherently hybridized and delocalized states in the ground state, the valence-band holes will be localized on each atomic orbital at the moment the kinetic energy of the photoelectron by the hard X-rays is measured. This is a lesson that the recoil effect of the valence band in Al shown in Fig. 8.4 teaches us. By calculation of a simple model of a binary compound, it was shown that the spectral deformation caused by the recoil effect in valence-band HAXPES is described by a combination of the local density of states associated with the atomic species, the ionization cross sections of the atomic orbitals and the modulation factor related to the recoil effect [22]. This theoretical prediction will be applicable to the evaluation of the degree of hybridization of the 3*d* or 4*f* orbital of transition metal ions with 2*p* of ligand oxygen atoms at the Fermi edge in various oxide materials. The shift and broadening of the Fermi edge indicates the relative contribution from each atomic species. The material dependence of the recoil effects in the valence band of vanadium oxide compounds has recently been reported [23].

A recent experiment on the recoil diffraction of backscattered electrons in Al_2O_3 [24] should be mentioned. The researchers found that the electron energy loss spectrum caused by the nuclear recoil effect contains the site-specific information: the energy-loss peaks are assigned to scattering by Al or O. This opens up a possibility of element-resolved crystallographic measurements.

8.2.4 Localization of Bloch Electrons by High-Energy Probing

The valence electrons in solids have delocalized wave-like nature described by Bloch functions. Specifically, the conduction electrons in simple metals are considered to be a typical example of nearly free electrons. Actually, many physical properties of simple metals such as their electric conductivity, heat capacity or optical response in the visible or infrared region can be well understood by considering a model of free-electron gas with effective masses. In contrast, the existence of the recoil effect at the Fermi edge in Al seems to indicate that the electrons are tightly bound to individual atoms. Let us discuss how this apparent discrepancy can be resolved.

Even the nearly free electron states in solids must have rapidly oscillating parts in the vicinity of the atomic cores because of the requirement of orthogonality to the core levels. The simplest approximation to incorporate this requirement is the orthogonalized plane-wave (OPW) approximation [25], in which the wave function for the Bloch state is given by

$$\psi_k(\vec{r}) = \psi_k^0(\vec{r}) - \sum_{i=1}^{N} \sum_{core} \langle \psi_{i,core} | \psi_k^0 \rangle \psi_{core}(\vec{r} - \vec{R}_i), \tag{8.19}$$

aside from the normalization constant, where $\psi_k^0(\vec{r})$ is the plane wave and $\psi_{core}(\vec{r} - \vec{R}_i)$ is the core state at site i. In Fig. 8.6, the spatial profile of the OPW function is schematically plotted together with the wave function of the high energy free electron state which is the final state of photoemission. In the evaluation of the transition amplitude $\langle \varphi_K | H_I | \psi_k \rangle$, the contribution from the plane-wave part in $\psi_k(\vec{r})$ will be very small because of the great mismatch of the wavelength, $|\vec{K}| \gg |\vec{k}|$ in HAXPES, and the main contribution will come from the rapidly changing part of the core-level wave function in the OPW. Thus, the valence emission originates only from the close vicinity to the atomic cores, even though the wave functions are

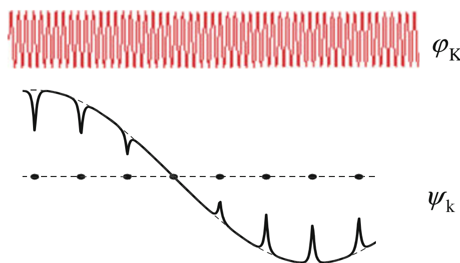

Fig. 8.6 Schematic diagram of the wave functions of the nearly free electron ψ_k in the orthogonalized plane-wave approximation and the photoelectron φ_K

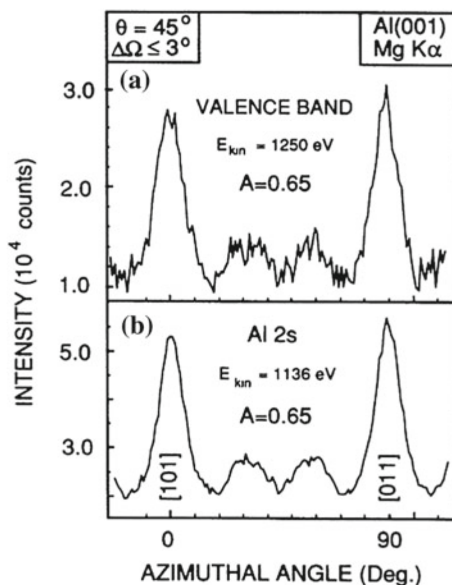

Fig. 8.7 **a** XPD azimuthal pattern of integrated valence band measured for a (001) single crystal of Al using Mg Kα radiation. **b** Same as (**a**) for electrons detected from the 2*s* core line [26]

widely delocalized. It may be said, therefore, that even the nearly free electrons in metals are tightly bound to atoms, if one uses a high-energy probe to detect them.

In connection with this conjecture on the *localization* of valence electrons by a high-energy probe, two topics are worth mentioning. The first is the X-ray photoelectron diffraction (XPD) of Al. Osterwalder et al. [26] found that the azimuthal pattern of the integrated valence-band XPS by Mg Kα excitation of Al is essentially the same as that for the 2*s* core line, as shown in Fig. 8.7. This means that the holes in the valence band of Al are somehow localized at the atomic site like the core holes in the final state of high-energy photoemission. This is in sharp contradiction to the well-established free electron-like picture of the valence electrons of Al. The sensitivity to the atomic displacement through the orthogonality requirement and the decoherence caused by the phonon emission from the recoil effect together induce the hole localization for high-energy excitation.

The second topic is the recent developments in the X-ray standing-wave (XSW) technique [27]. An XSW is formed by the coherent superposition of two plane waves of X-rays. Evidence for XSWs was first reported by Batterman [28], who formed an XSW inside a Ge crystal by superposition of incident and Bragg-reflected X-ray beams. The advent of third-generation synchrotron radiation sources has made it easier to obtain sufficiently collimated and monochromatic X-ray plane waves. By controlling the phase of the superposition of the incident and elastically scattered waves, it has become possible to use XSWs as a new spectroscopic tool to obtain information about electronic states with spatial resolution in

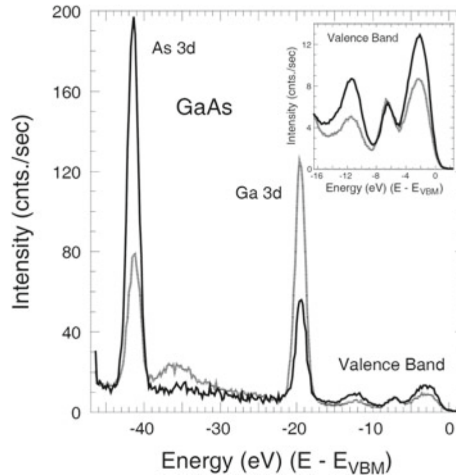

Fig. 8.8 Comparison of the photoemission spectra, referenced to the valence-band maximum, for the GaAs(111) (*shaded line*) and GaAs(–1–1–1) (*bold line*) reflections over the kinetic-energy range of the Ga 3*d*, As 3*d*, and crystal valence-electron emissions recorded at photon energy $h\nu = 1900$ eV. The *inset* compares the valence-band region of the spectra. The features at the lowest and highest energies of the valence band are enhanced when the maxima of the electric-field intensity are placed on the As atomic planes, whereas the feature at intermediate kinetic energy is enhanced when the maxima of the electric-field intensity are placed on the Ga atomic planes [30]

the order of the X-ray wave length [27]. This is done by adjusting the position of the maxima of the XSW to the plane of target atoms, and by measuring the signals from inelastic scatterings such as photoelectrons or X-ray fluorescence. The XSW technique has been used for site-specific investigation of interfaces, surfaces and bulk crystals [29].

Figure 8.8 shows high-resolution photoelectron spectra for cystalline GaAs recorded utilizing the GaAs(111) and GaAs(–1–1–1) reflections at the same photon energy $h\nu = 1900$ eV [30]. This energy was chosen to locate the maxima of the X-ray standing-wave field on either the cation or anion sites for this heteropolar crystal. As evident from the figure, either the Ga 3*d* or As 3*d* core-level emissions are enhanced by over a factor 2 when the Ga or As atomic planes are preferentially excited. Additionally, note the large differences in line shape between the valence-band structures (see inset). The valence-band features at the lowest and highest energies are enhanced when the maxima of the electric-field intensity are placed on the As atomic sites, the feature at intermediate kinetic energy is enhanced when the maxima of the electric-field intensity are placed on the Ga atomic sites.

From the theoretical calculations of Cohen and Chelikowsky [31], it is well established that the three lobes observed in the valence-band spectrum of GaAs,

typical of the covalent semiconductors, are directly related to the crystalline band structure; they arise from the hybridization of Ga and As 4*s* and 4*p* atomic orbitals. The first lobe at lowest energy corresponds to electronic states that are strongly localized on the As anion site and originate from the As 4*s* and 4*p* level. The second lobe is more complex; its character changes from Ga 4*s* to As 4*p* with increasing energy going from the band edge to the band maximum. The third lobe encompasses the top two valence bands; it extends to the valence-band maximum and is mostly of As 4*p* character. Clearly, these conclusions based on the density functional theory calculations are supported by these raw data.

Similar analysis has been used to study the chemical bonding in the transition-metal oxide crystal rutile TiO_2, where careful analysis of the angular-momentum dependent photoelectron cross sections of different valence orbitals led to a fundamental understanding of the chemical bonding [32].

8.3 Recoil Effect in Molecules

The recoil effects in XPS have been rather consciously investigated with respect to molecules in the gas phase [33]. In the core-level XPS of molecules, the recoil momentum is delivered to the translational mode (a trivial effect), vibrational modes, and rotational modes. As noticed by Domcke and Cederbaum [3], one of the spectroscopic signatures of the molecular recoil effect is the violation of the Franck-Condon principle of vibronic excitation, because the emitted electron transfers the momentum impulsively to the emitter atom.

The first experimental measurement of the recoil-induced deviation of the vibronic progression in the photoelectron emission was performed for the C 1*s* photoelectrons of methane [34]. The vibrational structure of methane has been studied in detail both theoretically and experimentally [35]. At the C 1*s* ionization, it exhibits a single vibrational excitation of the symmetric stretching mode of the C–H bond. The recoil effect would be observed as a spectral change of the vibronic lines in accordance with the change of excitation energy. However, this choice of sample proved poor. The ratio of the momentum transferred to the relative mode is small when the mass ratio of the emitter atom to the total mass is large, as can be easily understood by classical mechanics [33]. Because the C atom has 75 % of the total molecular mass of methane, most of the recoil momentum is delivered to the center-of-mass motion. In fact, as shown in the lower panels in Fig. 8.9, the change of the vibronic spectrum of CH_4 is quite small when the excitation energy is varied from 360 to 1050 eV.

So, Thomas and coworkers [36] examined C 1*s* emission in CF_4 molecules. In this case, the C atom constitutes only 13.5 % of the molecular mass. In addition, the Franck-Condon factor for the symmetric stretching mode is quite small in CF_4. As shown in the upper left panel of Fig. 8.9, the photoelectron spectrum at 330 eV is in fact well fitted by a single $v = 0$ vibronic line. The spectrum obtained for 1500 eV excitation is shown in the upper right panel. Additional vibronic structure is clearly

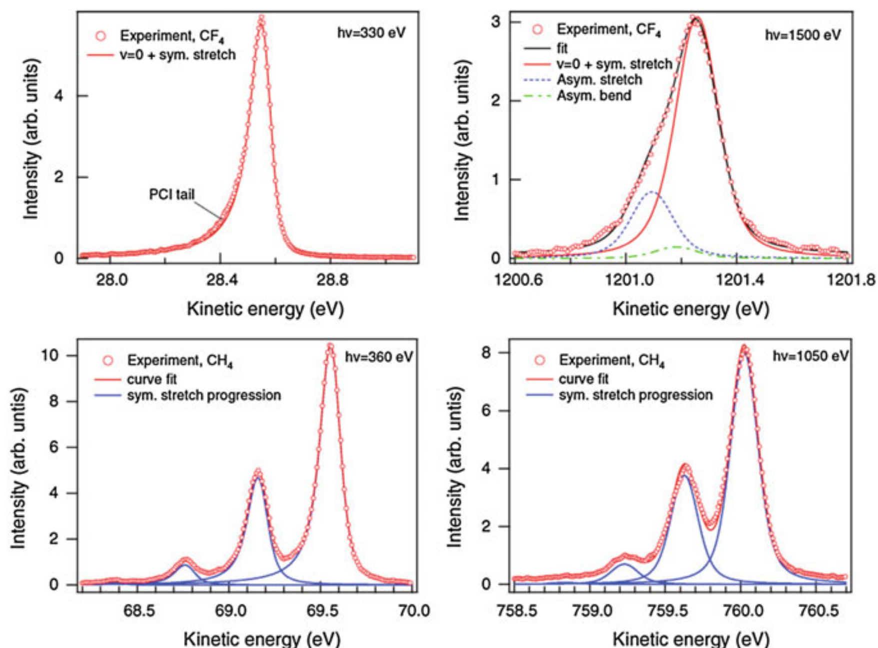

Fig. 8.9 C 1*s* photoelectron spectra for CH_4 (*bottom*) and CF_4 (*top*) molecules, near the ionization threshold (*left*) and at high photon energies. *Circles*—experiment, *solid lines* through data points—*curve* fitting results [33]

observed in the low-energy part of the spectrum as a shoulder. This shoulder is caused by the excitation of the asymmetric modes by the recoil effect, which is evidence for the symmetry breaking because of the momentum transfer to the emitter atom.

The recoil effect caused by the Auger electron after deep-core excitation to the ionization threshold has also been observed in the gas phase for Ne_2 dimers [37]. In this case, the nuclear motion is probed by the interatomic Coulombic decay (ICD). The angle dependence of the coincidence of fragmentation of Ne_2 ions and the ICD electrons reveals the effect of the momentum transfer of the Auger electrons to the dimer.

8.4 Summary and Outlook

High-resolution HAXPES measurements have clearly revealed the existence of recoil effects in solids and molecules. Recoil effects have been established not only in core-level HAXPES but also in the valence-band HAXPES of typical metals with nearly free electrons. The recoil effects become salient for materials containing light atoms. A number of important elements, such as C, N, and O belong to this

category. Because the recoil effects reflect the spring constant of vibration around the emitter atom as shown in previous sections, it may be a new tool to probe the local environment of site-specified atomic species in matter. In some materials, light-element ions are considered to be located in highly anisotropic configuration. A typical example is the Li ions in the electrodes of ionic batteries. Core-level HAXPES may be used to probe the anisotropy of the mobility of Li ions by measuring the emission-angle dependence of their spectra.

In the quest for bulk sensitivity, angle-resolved photoelectron spectroscopy (ARPES) is being extended to the hard X-ray region [38]. The existence of recoil effects then poses a fundamental question on the range of applicability of hard X-ray ARPES [29], because the recoil-generated phonons may interfere with the coherence and localize the hole in the valence band even at zero temperature. In this respect, the site-specific measurement of the valence band by the XSW technique has been briefly reviewed. The point is that the interaction of the valence electrons with hard X-rays is localized to the close vicinity to the atomic core. This is a common feature with the recoil effect of valence-electrons. The localization-delocalization problem has been a subject of long-lasting interest in solid-state physics. It will be worthwhile to investigate this problem in light of the recoil effect in HAXPES by state-of-the-art high-resolution spectroscopy.

References

1. A. Einstein, Ann. der Physik **17**, 132 (1905)
2. C.P. Flynn, Phys. Rev. Lett. **37**, 1445 (1976)
3. W. Domcke, L. Cederbaum, J. Electron Spectrosc. Relat. Phenom. **13**, 161 (1978)
4. Y. Takata, Y. Kayanuma, M. Yabashi, K. Tamasaku, Y. Nishino, D. Miwa, Y. Harada, K. Horiba, S. Shin, S. Tanaka, E. Ikenaga, K. Kobayashi, Y. Senba, H. Ohashi, T. Ishikawa, Phys. Rev. B **75**, 233404 (2007)
5. C.S. Fadley, J. Electron Spectrosc. Relat. Phenom. **178–179**, 2 (2010). (L. Kövér, ibid. **178-179**, 241(2010))
6. Y. Toyozawa, *Optical Processes in Solids* (Cambridge University Press, Cambridge 2003)
7. T. Balasubramanian, J.N. Andersen, L. Wallden, Phys. Rev. B **64**, 205420 (2001)
8. H. Wagenfeld, Phys. Rev. **144**, 216 (1966)
9. A.A. Maradudin, P.A. Flinn, J.M. Radcliffe, Ann. Phys. (N.Y.) **26**, 81 (1964)
10. L. Wirtz, A. Rubio, Solid State Commun. **131**, 141 (2004)
11. K.C. Prince, T. Ulrych, M. Peloi, B. Ressel, V. Chab, C. Crotti, C. Comicioli, Phys. Rev. B **62**, 6866 (2000)
12. Y. Takata, S. Tanaka, Y. Kayanuma, It is ascertained that the width of C 1*s* photoelectron spectrum with 7940 eV excitation measured at $T = 15$ K becomes narrower by only a small amount than that measured at room temperature (unpublished)
13. T. Fujikawa, R. Suzuki, L. Kövér, J. Electron Spectrosc. Relat. Phenom. **151**, 170 (2006)
14. M. Vos, M.R. Went, Y. Kayanuma, S. Tanaka, Y. Takata, J. Mayers, Phys. Rev. B **78**, 024301 (2008)
15. M. Vos, M.R. Went, Phys. Rev. B **74**, 205407 (2006)
16. A.L. Fielding, D.N. Timms, J. Mayers, Europhys. Lett. **44**, 255 (1998)
17. T. Fujikawa, H. Arai, R. Suzuki, H. Shinotsuka, J. Kövér, N. Ueno, J. Electron Spectrosc. Relat. Phenom. **162**, 146 (2008)

18. Takata et al. have measured the shift of the binding energy ΔE=340meV for B 1s of MgB_2 and ΔE=115meV for Al 2p with X-ray excitation energy 7940eV (unpublished)
19. Y. Takata, Y. Kayanuma, S. Oshima, S. Tanaka, M. Yabashi, K. Tamasaku, Y. Nishino, M. Matsunami, R. Eguchi, A. Chainani, M. Oura, T. Takeuchi, Y. Senba, H. Ohashi, S. Shin, T. Ishikawa, Phys. Rev. Lett. **101**, 137601 (2008)
20. L. van Hove, Phys. Rev. **95**, 249 (1954)
21. A. Sekiyama, T. Iwasaki, K. Matsuda, Y. Saitoh, Y. Ohnuki, S. Suga, Nature **403**, 396 (2000)
22. Y. Kayanuma, I. Fukahori, S. Tanaka, Y. Takata, J. Electron Spectrosc. Relat. Phenom. **184**, 468 (2011)
23. S. Suga, A. Sekiyama, H. Fujiwara, Y. Nakatsu, T. Miyamachi, S. Imada, P. Baltzer, S. Niitaka, H. Takagi, K. Yoshimura, M. Yabashi, K. Tamasaku, A. Higashiya, T. Ishikawa, New J. Phys. **11**, 073025 (2009)
24. A. Winkelmann, M. Vos, Phys. Rev. Lett. **106**, 085503 (2011)
25. C. Herring, Phys. Rev. **57**, 1169 (1940)
26. J. Osterwalder, T. Greber, S. Hüfner, L. Schlapbach, Phys. Rev. Lett. **64**, 2683 (1990)
27. For contemporary reviews on various aspects of XSW, *The X-ray Standing Wave Technique, Principles and Applications*, ed. by J. Zegenhagen, A. Kazimirov (World Scientific, 2013)
28. B.W. Batterman, Phys. Rev. **133**, A759 (1964)
29. C.S. Fadley, J. Electron Spectrosc. Relat. Phenom. **190**, 165 (2013)
30. J.C. Woicik, E.J. Nelson, T. Kendelewicz, P. Pianetta, Phys. Rev. B **63**, 041403(R) (2001)
31. M.L. Cohen, J.R. Chelikowsky, *Electronic Structure and Optical Properties of Semiconductors*, Chap. 6, vol. 75 (Springer Series in Solid State Sciences, Springer, Berlin, 1988)
32. J.C. Woicik, E.J. Nelson, L. Kronik, M. Jain, J.R. Chelikowsky, D. Heskett, L.E. Berman, G. S. Herman, Phys. Rev. Lett. **89**, 077401 (2002)
33. E. Kukk, T.D. Thomas, K. Ueda, J. Electron Spectrosc. Relat. Phenom. **183**, 53 (2011)
34. E. Kukk, K. Ueda, U. Hergenhan, X.-J, Liu, G. Prümper, H. Yoshida, Y. Tamenori, C. Makochekanwa, T. Tanaka, M. Kitajima, H. Tanaka, Phys. Rev. Lett. **95**, 133001 (2005)
35. T.X. Carroll, N. Berrah, J. Bozek, J. Hahne, E. Kukk, L.J. Saehre, T.D. Thomas, Phys. Rev. A **59**, 3386 (1999)
36. T.D. Thomas, E. Kukk, R. Sankari, H. Fukuzawa, G. Prümper, K. Ueda, R. Püttner, J. Harries, Y. Tamenori, T. Tanaka, M. Hoshino, H. Tanaka, J. Chem. Phys. **128**, 144311 (2008)
37. K. Kredi et al., Phys. Rev. Lett. **103**, 033001 (2009). (For theoretical analysis, see also Ph. V. Demekhin, S. Scheit, L.S. Cederbaum, J. Chem. Phys. **131**, 164301 (2009))
38. A.X. Gray, C. Papp, S. Ueda, B. Balke, Y. Yamashita, L. Plucinski, J. Minar, J. Braun, E.R. Ylvisaker, C.M. Schneider, W.E. Pickket, H. Ebert, K. Kobayashi, C.S. Fadley, Nat. Mater. **10**, 729 (2011)

Chapter 9
Depth-Dependence of Electron Screening, Charge Carriers and Correlation: Theory and Experiments

Munetaka Taguchi and Giancarlo Panaccione

Abstract Core-level Photoemission Spectroscopy (PES) has played a very important role in our understanding of the electronic structure of correlated transition metal and rare-earth compounds. The appearance of strong satellite structures accompanying the main PES spectra in correlated systems is well known, and systematic variations in the position and intensities of these satellites provide us with important clues to their electronic structures. In spite of these successes, the surface sensitivity of PES has often led to controversies regarding surface versus bulk electronic structure, and hence, hard X-ray photoelectron spectroscopy (HAXPES) is very important and promising. HAXPES is a bulk sensitive probe of the electronic structure due to its ability to overcome surface sensitivity of conventional PES. Unlike soft X-ray PES, $2p$ core-level HAXPES have shown additional well-screened features with significant intensity at the low binding energy side of the main peak. These features were explained well by the configuration-interaction model including a screening channel derived from coherent states near Fermi energy. Here, we review these advances and examine the application of HAXPES to studies of the strongly correlated electron systems, especially for $3d$ transition metal compounds. The details of the well-screened features are also discussed.

M. Taguchi (✉)
RIKEN SPring-8 Center, Sayo, Hyogo 679-5148, Japan
e-mail: mtaguchi@ms.naist.jp

M. Taguchi
Nara Institute of Science and Technology (NAIST), 89165 Takayama, Ikoma, Nara 630-0192, Japan

G. Panaccione
Istituto Officina Dei Materiali (IOM)-CNR, Laboratorio TASC, Area Science Park, S.S.14, Km 163.5, 34149 Trieste, Italy
e-mail: giancarlo.panaccione@elettra.eu

© Springer International Publishing Switzerland 2016

J.C. Woicik (ed.), *Hard X-ray Photoelectron Spectroscopy (HAXPES)*,
Springer Series in Surface Sciences 59, DOI 10.1007/978-3-319-24043-5_9

9.1 Introduction

Photoelectron spectroscopy (PES) is an indispensable tool for studying the properties of condensed matter. Over the last decade the Hard X-Ray PES (HAXPES) technique made a major impact in unraveling the electronic properties of solids, encompassing a large field of applications, from fundamental to applied science [1, 2]. Recent advances in the development of synchrotron radiation beamlines made possible to exploit HAXPES with an extremely large dynamic range in photon energy (2–15 keV) and the necessary high flux and energy resolution (10^{11}/10^{12} photons/s on the sample in a bandwidth of 50–300 meV) to overcome the strong reduction of photoionization cross section at high energy [3–10], Paying the price of a minimum energy resolution in the order of $\sim$50 meV, yet good enough to obtain reliable comparison with the standard surface sensitive PES experiments, HAXPES proves an information depth up to 15–20 nm for electron kinetic energy ≥5 keV, corresponding to truly bulk sensitivity with chemical selectivity [3–10]. A paradigmatic example of the merit of HAXPES comes from the study of strongly correlated materials, like Transition Metal Oxides (TMO). In these systems, a general agreement has been reached on the fact that the surface sensitivity of standard PES becomes a limitation when the need is to obtain information about bulk electronic properties; this limitation is particularly important when dealing with electron correlation, where structural distortion, stoichiometry changes, strong reactivity to external agent and major atomic and/or electronic reconstruction often appear at surfaces, preventing to obtain meaningful and reliable informations about the solid as a whole. Moreover, bulk properties cannot necessarily be predicted from those observed at larger or smaller scales and are not simply scalable from surface and interface ones [11].

Thus, the analysis of the true bulk electronic structure in many oxides, Mott-Hubbard and mixed valence systems, heavy Fermion compounds, and anomalous metals/doped semiconductors have been successfully addressed by HAXPES in recent years both experimentally and theoretically [8]. In this chapter we discuss selected examples, with the aim of: (a) focusing on the HAXPES-only features recently found in TMOs, revealing profound differences between surface and bulk electronic screening and correlation, (b) underlining the importance of HAXPES in establishing a link between experiment and theory, and (c) describing some of the potentialities of the HAXPES technique. It is important to underline that HAXPES benefits not only of high bulk sensitivity but also of a direct access to electronic states near the Fermi level, i.e. to the energy scale of the electronic correlation [12]. However, the present contribution focuses mainly on core-level results and theoretical methods; a thorough discussion on valence band HAXPES can be found in other chapters of the present volume.

9.2 Transition Metal Oxides and 'Bulk-Only' Features

In TMOs, minute changes—the energy scale of the relevant processes lies in the meV regime—of the electron, spin, and orbital degrees of freedom correspond to a drastic variation of their macroscopic properties, with materials passing from insulating to metallic and even to superconducting behavior, or changing their long range magnetic state [13, 14]. Whether one considers the simple classical oxides such as NiO, CoO, FeO, V_2O_3, VO_2 and Cr_2O_3, or more complex ones such as high temperature superconductors, these systems represent a challenge for understanding by both theory and experiment [13, 14]. Both classes cannot be tackled without the large probing depth of HAXPES. The use of high photon (thus high kinetic) energy does not only mean to probe more deeply in the solid, but also to access core-levels and make use of chemical shifts, multiplets, satellites, and other fine structures in these spectra as an additional and important source of information other than valence band only.

In this context, it is particularly significant that a totally new class of satellites structure has been observed in HAXPES spectra of 3*d* based TMOs and more recently in diluted magnetic semiconductors. The first observation of a bulk-only HAXPES feature in 3*d*-TMOs has been reported by Horiba et al. [15]. Figure 9.1 shows Mn 2*p* core-level spectra of $LaMnO_3$ at 300 K measured with different probing depths by changing the photon energy and emission angle. At $h\nu = 5.95$ keV, a clear shoulder appears at the low binding energy side of Mn $2p_{3/2}$ (arrow). The intensity of such shoulder decreases for larger emission angles (i.e. when surface sensitivity is enhanced) and almost disappears at low photon energy (e.g. increased surface sensitivity due to the lower kinetic energy). The observed behavior clearly points to a bulk feature. In a similar experiment on $La_{0.7}Sr_{0.3}MnO_3$, Mn 2*p* core-level measured in the HAXPES regime also display

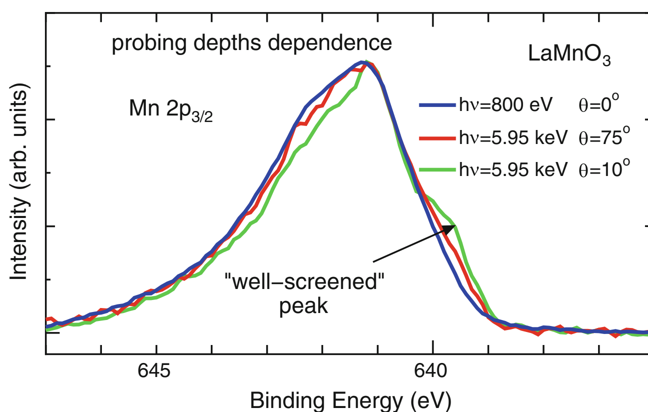

Fig. 9.1 Mn $2p_{3/2}$ core-level spectra of $LaMnO_3$ measured with different probing depth by changing photon energy (800 eV and 5.95 keV) and emission angle (0°, 10°, and 75°) [15]. 0° corresponds to normal emission

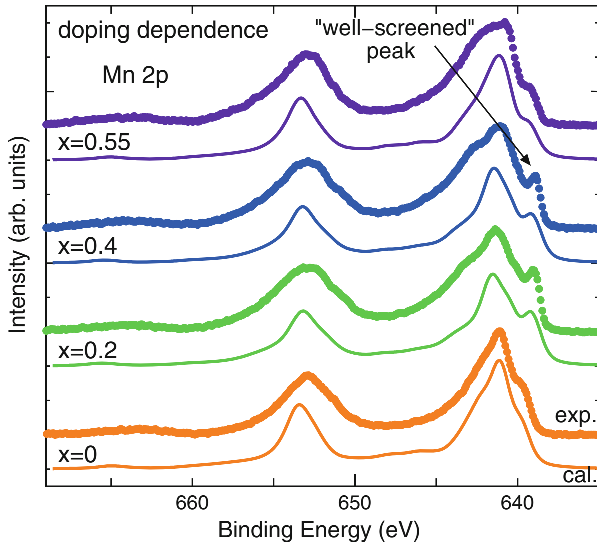

Fig. 9.2 HAXPES spectra of Mn 2*p* core-level of $La_{1-x}Sr_xMnO_3$ with extended cluster model calculations [15]

the low energy extra feature observed in Fig. 9.1 [16]. Interestingly, such structure disappears above T_c, corresponding to the passage between a metallic ferromagnetic phase to an insulator paramagnetic one. Furthermore, the dramatic changes with Sr doping have been also observed. Figure 9.2 shows Mn 2*p* core-level spectra of $La_{1-x}Sr_xMnO_3$ (LSMO) at 300 K measured with different Sr doping [15]. Here, by substituting the tri-valence element La with di-valence element Sr in $LaMnO_3$, some holes are introduced into the system. Since it has been widely recognized that the hole-doping plays an important role in determining the transport properties and the complex behaviors of magnetic and structural transitions of LSMO, it suggests the strong correlation between the observed changes of extra features and the physical properties.

The bulk-derived extra or "well-screened" feature exhibits the following characteristics: the separation between the main peak and the well-screened feature increases with hole doping until $x = 0.4$, but reduces for $x = 0.55$. This behavior is similar to the physical properties, that is, with increasing x, the hole doping produces a ferromagnetic phase with increasing T_c and reduced resistivity until $x = 0.4$. On further hole doping, a magnetic transition from the ferromagnetic metal to the antiferromagnetic metal state is induced for $x > 0.5$. These changes observed in HAXPES Mn $2p_{3/2}$ spectra at low binding energy side have not been observed in earlier soft X-ray PES spectra of bulk polycrystals, single crystals as well as thin films of manganites. All these results strongly indicates that a well-screened feature observed in HAXPES originate from truly bulk properties. Moreover, these well-screened features cannot be interpreted in the usual cluster model or Anderson

impurity model applied to transition metal (TM) compounds. 'Well-screened' features in the core-level of strongly correlated systems have been observed in the past, mainly in 4*d* and 4*f* base system and have been interpreted following the approach of Gunnarsson, Fuggle et al. [17–19]. The observation of Horiba et al., however, raised new questions on 3*d*-TMOs. To address this issue, Taguchi et al. have proposed new theoretical model which includes an additional screening mechanism from electronic states near the Fermi level [20]. The comparison between the HAXPES spectra and the optimized calculations are also shown in Fig. 9.2. Although, the detail of the calculation will be shown in next section, the calculation reproduces well the intensity and position of the well-screened feature of HAXPES spectra for all *x* values. Furthermore, the results shown in Fig. 9.2 have been confirmed by other experimental results, and similar satellites have been observed in other core-levels of LSMO, e.g. Mn 3*s* [16].

9.3 Theory of Well Screened Satellites (Evolution of the Screening, Hybridization Parameters, Etc.)

In this section, we describe theoretical aspects of core-level HAXPES spectra, with emphasis on the basic understanding of the underlying physics. Before looking into the details, let us first make one general remark. As we mentioned in the previous section, HAXPES spectra shows totally new class of satellite peaks in the 2*p* core-level for many TMOs. Those additional peaks strongly depend on the doping, metallic or insulating states (bulk or surface). However, it should be noted that the difference between spectral shapes of metallic and insulating states (or bulk and surface states) never imply the difference between core electronic states of metal and insulator (or bulk and surface states). Basically, there is no difference in core-level electronic states between them. If that is the case, what factors have led to the difference? The key factors for this question are the core hole and the screening. In the core-level photoemission process, a core electron is excited by an incident X-ray and ejected from the solid as a photoelectron. A core hole can be defined as the absence of a deep core electron in a core-level. The system with core hole will be in extremely unstable states, because of the positive charge of core hole. After the core electron excitation, the valence or conduction electrons around the core hole are polarized and try to screen the core hole in order to get back to a stable state. Since the character of the valence or conduction electrons are different in between metal and insulator (or bulk and surface states), the behavior of screenings are also different. This difference of screening is reflected in the core-level spectrum as a spectral asymmetry and satellites.

For the analysis of core-level and valence band PES spectra, one of the most widely used and prime theoretical model is a cluster model (or Anderson impurity model). In this model, we consider only a central TM atom with localized 3*d* state, but at the same time appropriate linear combinations of ligand 2*p* orbitals on

neighboring sites, and the hybridization between local $3d$ states and ligand states is taken into account. The Hamiltonian of the conventional cluster model for $3d$ TM compounds is given by

$$\begin{aligned} H_I = & \sum_{\Gamma\sigma} \varepsilon_{3d}(\Gamma) d^{\dagger}_{\Gamma\sigma} d_{\Gamma\sigma} + \sum_{m\sigma} \varepsilon_{2p} p^{\dagger}_{m\sigma} p_{m\sigma} \\ & + \sum_{\Gamma\sigma} \varepsilon_{p}(\Gamma) a^{\dagger}_{\Gamma\sigma} a_{\Gamma\sigma} + \sum_{\Gamma\sigma} V(\Gamma)(d^{\dagger}_{\Gamma\sigma} a_{\Gamma\sigma} + a^{\dagger}_{\Gamma\sigma} d_{\Gamma\sigma}) \\ & + U_{dd} \sum_{(\Gamma\sigma)\neq(\Gamma'\sigma')} d^{\dagger}_{\Gamma\sigma} d_{\Gamma\sigma} d^{\dagger}_{\Gamma'\sigma'} d_{\Gamma'\sigma'} \\ & - U_{dc} \sum_{\Gamma m\sigma\sigma'} d^{\dagger}_{\Gamma\sigma} d_{\Gamma\sigma}(1 - p^{\dagger}_{m\sigma'} p_{m\sigma'}) \\ & + H_{\mathrm{mult}}. \end{aligned} \tag{9.1}$$

Here $\varepsilon_{3d}(\Gamma)$, ε_{2p} and $\varepsilon_p(\Gamma)$ represent the energies of TM $3d$, TM $2p$ and ligand state such as oxygen $2p$ states, respectively, with the irreducible representation Γ of the local symmetry around the TM atom. The indices m and σ are the orbital and the spin states. $V(\Gamma)$, U_{dd}, and $-U_{dc}$ are the hybridization between the TM $3d$ and the ligand states, the on-site repulsive Coulomb interaction between TM $3d$ states and the attractive core hole potential, respectively. The Hamiltonian H_{mult} describes the intra-atomic multiplet coupling between TM $3d$ states and that between TM $3d$ and TM $2p$ states. The spin-orbit interactions for TM $2p$ and $3d$ states are also included in H_{mult}.

This approach is well established for explaining soft X-ray PES spectra for various strongly correlated electron systems in general [21–24]. However, as mentioned above, the same model was found to be insufficient to explain the extra peak in HAXPES results. In order to address these problems, Taguchi et al. have introduced an additional state near Fermi level labeled 'C' as a new screening channel described by H_{II} term in addition to the usual cluster model (H_I term),

$$H_{II} = \sum_{\Gamma\sigma} \varepsilon_c(\Gamma) c^{\dagger}_{\Gamma\sigma} c_{\Gamma\sigma} + \sum_{\Gamma\sigma} V^*(\Gamma)(d^{\dagger}_{\Gamma\sigma} c_{\Gamma\sigma} + c^{\dagger}_{\Gamma\sigma} d_{\Gamma\sigma}). \tag{9.2}$$

An effective coupling parameter $V^*(\Gamma)$ for describing the interaction strength between TM $3d$ orbitals and the C state is introduced, analogous to the hybridization $V(\Gamma)$. The charge transfer energy from the additional state to the TM $3d$ orbital is Δ^*, whereas the usual charge transfer energy Δ (from the ligand state to the TM $3d$ orbitals) is defined as the energy difference of the configuration-averaged energies $E(3d^{n+1}\underline{L}) - E(3d^n)$.

The 'C' states represent the coherent state for Ti_4O_7, [25] V_2O_3 [20, 26] and VO_2, [27] and the doping-induced states for doped $LaMnO_3$ [15, 28] which develop into electronic states at and near the Fermi level. For the late TM compounds such as high-T_c cuprates and NiO, it represents the Zhang-Rice singlet and doublet

states, respectively [29, 30]. Note that this extended cluster model can be applied even to insulating system like NiO. We would like to emphasize that the model is valid, irrespective of the condition whether the 'C' state develops into metallic states which cross the Fermi level. The essential point is that it is necessary to include the additional screening state with a different screening energy V^* (for C state positioned at Δ^*) compared to the conventional ligand screening energy V (for L state positioned at Δ).

As a typical example, a schematic energy diagram of the optical transition of $2p$ core-level HAXPES for LSMO is shown in Fig. 9.3a. The configuration-averaged energies of the ionic configurations have been used which mean that multiplet, crystal field, and hybridization effects are neglected in the diagram. It should be kept in mind, however, that all these effects shift and spread the levels. The $3d^6\underline{L}^2$, $3d^6\underline{C}^2$, and $3d^6\underline{LC}$ configurations are not depicted for simplicity. The $3d^4$ state gives the biggest contribution to the ground state and the $3d^5\underline{C}$ lies just above $3d^4$ ones in the initial state. As for the final state, the core hole potential pulls down both the $2p^53d^5\underline{L}$ and $2p^53d^5\underline{C}$ states which lie below the $2p^53d^4$ state. Since Δ^* is smaller than Δ, the

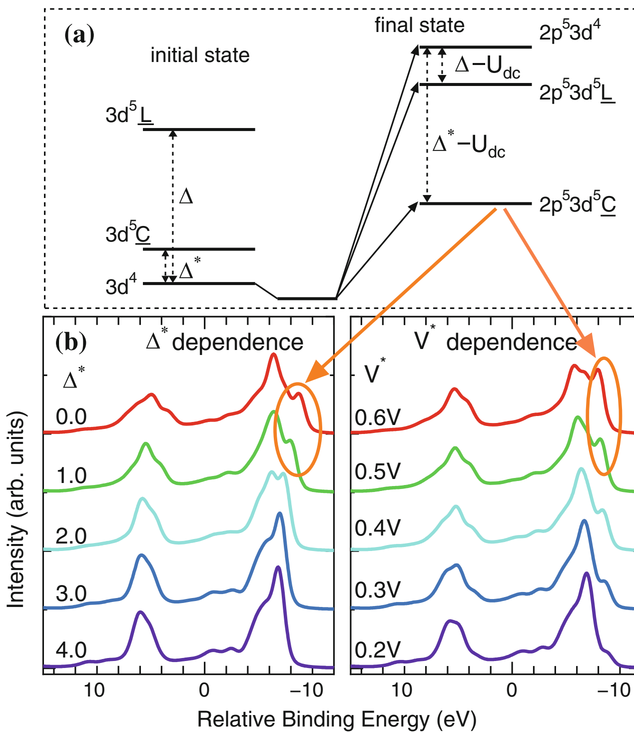

Fig. 9.3 **a** Schematic illustration of energy levels and total energy level diagram of $2p$ core-level PES for LSMO. **b** Δ^* and V^* dependence of theoretical calculations for the HAXPES. The other parameter values are fixed

$2p^5 3d^5 \underline{C}$ is the lowest energy state. As a consequence, the main lines are due to a mixture of $2p^5 3d^5 \underline{L}$ and $2p^5 3d^4$, whereas the lowest binding energy satellites are mainly due to the coherently screened $2p^5 3d^5 \underline{C}$ final states. The curves of Fig. 9.3b give an overall impression of the influence of the parameters on spectral line-shape. The separation between $2p^5 3d^5 \underline{C}$ and $2p^5 3d^5 \underline{L}$ peaks increases, as expected, with decreasing of the Δ^* and increasing of the hybridization V^* between $3d^4$ and $3d^5 \underline{C}$ configurations. The strength of hybridization V^* also influences their relative intensities. Basically, the smaller value of Δ^* forms a peak at much lower binding energy side. In Fig. 9.4a, b, we give the comparison between new theory (solid line) and conventional cluster model calculation (dashed line) for LSMO and NiO, respectively. While the conventional cluster model calculation can not reproduce the experimentally observed well-screened feature at low binding energy, the inclusion of additional screening from electronic state near E_F solves the problem in both cases.

Next, we would like to stress the importance of the core hole potential and the screening effect in the core-level spectra. This situation is very well shown in the two extreme cases (see Fig. 9.5). In the case without screening (i.e. small or zero values of U_{dc}), the valence or conduction electrons around the core hole site are not

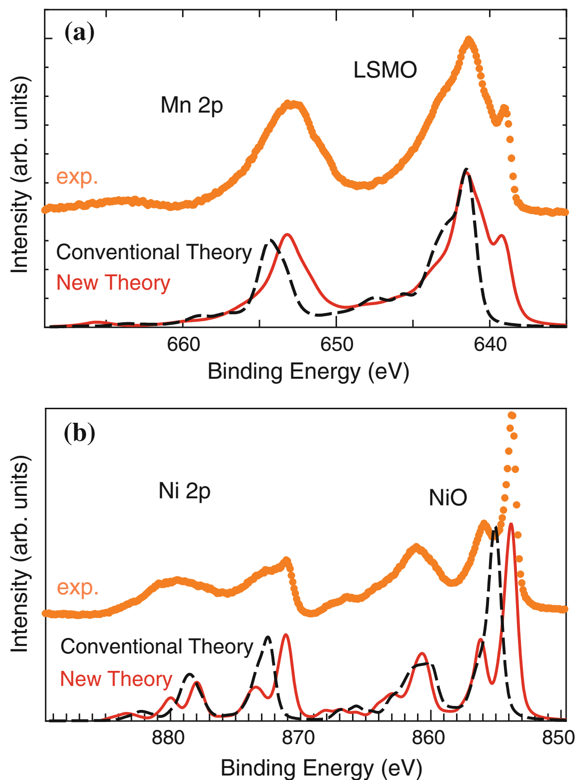

Fig. 9.4 Comparison of new theory and the conventional cluster model calculation together with the experimental spectra. **a** Calculated $2p$ core-level PES spectra for LSMO. **b** Calculated $2p$ core-level PES spectra for NiO

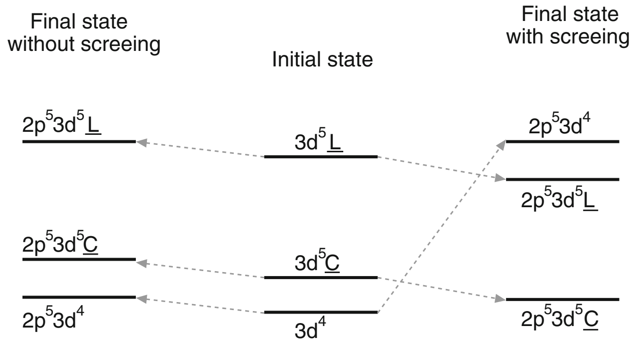

Fig. 9.5 Schematic energy diagram for $2p$ core-level PES for LSMO. *Arrows* indicate the transitions in both core-level spectra with screening and without screening

polarized and the electronic structure does not change. Thus, the ordering of each configurations in the final state is the same as that of initial states configurations (the left hand panel in Fig. 9.5). On the other hand, if the screening is strong enough (i.e. large values of U_{dc}), the valence or conduction electrons around core hole are polarized and the electronic structure changes drastically. As a result, in the final states with the screening, the ordering of the final state configurations are changed because of large U_{dc} (i.e. the $2p^5 3d^5 \underline{L}$ and $2p^5 3d^5 \underline{C}$ states lie clearly below $2p^5 3d^4$ state), as shown in the right panel of Fig. 9.5. The change of the ordering of the final state configurations results in the strong well-screened satellites. This is the reason why the clear well-screened satellite is observed with significant intensity.

Before ending this section, we briefly look back on the historical background of theoretical model for core-level spectroscopy in order to stress the importance of newly developed theory. As we mentioned before, conventional single-site impurity Anderson model or cluster model have been used as a standard theory of core-level spectroscopy for the strongly correlated electron systems. These models are based on Kotani–Toyozawa (KT) theory [31–33] and Gunnarsson–Schönhammer (GS) theory [22, 34]. First, Kotani and Toyozawa succeeded in analyzing $3d$ core-level PES spectrum of La elemental metal by taking into account the conduction screening effects of $4f$ electron due to a core hole [31–33]. After that, KT theory has been extended further to analysis of XAS and PES spectra of mixed-valence Ce intermetallic compounds by Gunnarsson and Schönhammer. They performed theoretical analysis of three peak structures observed in Ce $3d$ core-level PES spectra, with particular focus on cases where the $4f$ level degeneracy N_f is large [22, 34]. After that, GS theory has also been applied to insulating compounds with $4f$ and $3d$ electron systems by replacing a conduction band with a completely filled valence band. In GS theory, the spectral intensity is expanded in the power series of $1/N_f$. The main point is shown in Fig. 9.6. It should be kept in mind that, there is no essential difference in description of PES spectra between metal and insulator in GS theory framework. For insulating systems, the ground state of Ce compounds are described by $(1/N_f)^0$ order

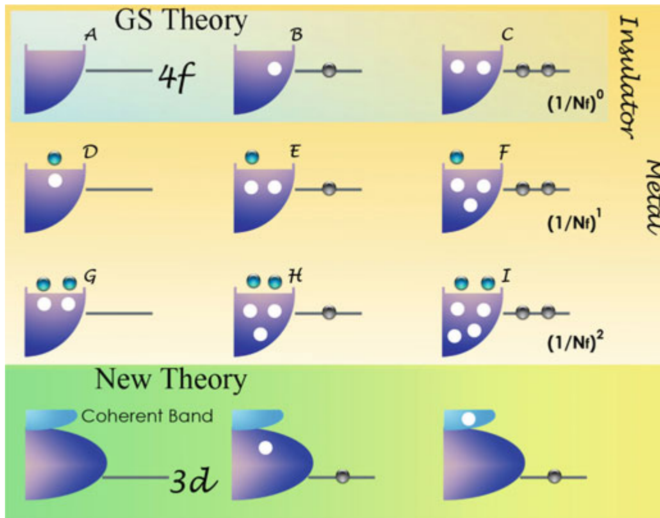

Fig. 9.6 Schematic basis states used to diagonalize the Hamiltonian in GS theory and newly developed theory by Taguchi et al.

basis states like $4f^0$, $4f^1\underline{v}$, and $4f^2\underline{v}^2$ configurations. For metallic systems, the higher-order terms ($(1/N_f)^1$ and $(1/N_f)^2$) (which includes electron-hole pairs) are necessary. However, since $N_f\,(1/N_f)$ is considerably large (small), it is very difficult to see the contribution of electron-hole pairs directly in the core-level PES spectra and we can get almost converged results by using rather small basis set. In fact, most of the reported experimental spectra have not shown any essential changes between insulator and metal both in $4f$ and $3d$ electron systems with exception of the asymmetric line shape due to electron-hole pair shake-up (the Doniach-Šunjic' line shape). On that occasion, we had the misconception that we cannot observe changes of core-level spectra between metal and insulator, until quite recently. The situation has been changed completely by the extra-peak in HAXPES experiments and its corresponding new theory. It became clear that the low binding energy extra peak cannot be explained by GS theory (which includes electron-hole pair excitations) and it required new theoretical framework beyond GS theory. We can also see this point from a different viewpoint. The original conduction screening mechanism in KT and GS theory was replaced by ligand screening mechanism from occupied valence band electron when it has been applied to insulating $3d$ and $4f$ systems. In new theoretical framework, the original conduction screening proposed by KT theory is now resurrected as the screening from the coherent state near E_F.

Recent theoretical studies of the multi-site cluster (MSC) model offer an alternative interpretation on the basis of a nonlocal screening scenario [35, 36]. The question whether such features reflect the screening from the coherent states, or the nonlocal screening of the MSC model, and whether these models can be effectively

mapped into each other or not, remains to be answered in general. However, at least in high T_c cuprates, the MSC model has confirmed that the screening from the ZR singlet bound state at the top of the VB is the origin of the lower binding energy feature in the Cu 2*p* core-level HAXPES [35].

9.4 Metal to Insulator Transition: The Vanadates

Unraveling what ultimately drives the electronic and magnetic properties of 3*d*-based TMOs is strictly linked to a direct measure of the electronic distribution over the metal orbitals. In particular, the metal to insulator transition (MIT) is one of the most intriguing aspect in the physics of TMOs. Such a transition is due to a subtle interplay between various interactions with comparable energy scales, such that the system can be driven from one state to another by a small external parameter. In the study of MIT of strongly correlated systems, the oxides of vanadium, specifically V_2O_3 and VO_2 are the archetypes, where small variation of temperature and doping produce a rich and complicated phase diagram [13, 14, 37, 38]. The difference between surface and bulk electronic properties in the study of MIT has been a longstanding issue for both theory and experiments. V_2O_3 presents a Mott transition as a function of both temperature and pressure (or doping), and it is placed right at the border between the metallic and the insulating phase. At ambient temperature and pressure, pure V_2O_3 crystallizes in the α-corundum structure and undergoes a first order transition at 150 K, passing from the paramagnetic metallic (PM) phase to the antiferromagnetic insulating (AFI) phase, with monoclinic structure. Across the MIT, one observes a change in resistivity of several orders of magnitude and a large volume increase. That, in pure V_2O_3, means that crossing the MIT is destructive, and can result in sample turning to powder. The experimental analysis of pure V_2O_3 is particularly difficult not only because of the destruction of the sample, but also because surfaces are difficult to anneal, polish and etch. In general, surface preparation in V_2O_3 substantially alters its chemical/structural properties.

Despite a large amount of photoemission studies in more than two decades, only very recently PES experiments using soft X-rays in the metallic phase of V_2O_3 [39] and VO_2 [40] yield valence band spectra in which the so-called coherent peak is substantially larger than the incoherent peak, very much unlike the surface sensitive spectra taken with UV light. Such observation closed the gap between experiment and theory, and DMFT calculation were able to estimate the Hubbard U correlation value. A few years later, HAXPES came into play: Taguchi et al. [20] reported for the first time the appearance of an extra peak in the V 2*p* emission spectra of the metallic phase of $V_{1.98}Cr_{0.02}O_3$, not visible in low energy photoemission spectra (see the feature ‘A’ in Fig. 9.7a). Furthermore, sharp screened satellites have been observed in the vanadium 2*p* and 3*p* core-level spectra, pertaining to the metallic phase [41]. As the system enters in the insulating phase, the well screened peak disappears (see Figs. 9.7a and 9.8). Figure 9.7b shows our theoretical spectrum for the paramagnetic (PM) phase, compared to the experimental spectrum at 220 K.

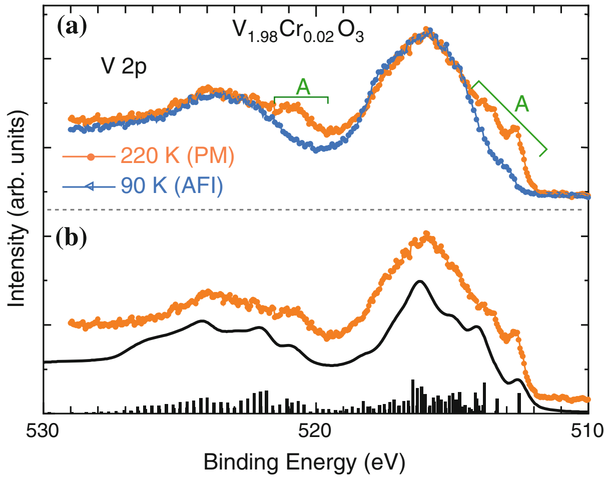

Fig. 9.7 V 2*p* core-level PES spectra of $V_{1.98}Cr_{0.02}O_3$: **a** Comparison between T = 220 K (PM phase) and T = 90 K (AFI phase). **b** Experimental V 2*p* PES spectrum of $V_{1.98}Cr_{0.02}O_3$ in the PM phase compared with a calculated spectrum, with an integrated background

Theory and experiment show very satisfactory agreement for the complete multiplet structure and the low binding energy satellites. HAXPES experiments vs. temperature, crossing the MIT in pure V_2O_3, provided experimental proof of: (a) the correlation between sharp satellites observed in core-level spectra and the coherent intensity measured at the Fermi level, (b) the presence of a large transfer of spectral weight, occurring at the MIT, in both valence band (gap opening) and core-level spectra (Fig. 9.8) and (c) the transfer of spectral weight observed across the MIT in the valence band region, where a satisfactory agreement with DMFT calculation is found, setting the limit for the Hubbard U correlation term to $U = 4.2$ eV [20, 41, 42]. Such features are not visible in surface sensitive soft X-ray PES experiments.

9.5 Late TM Compounds

In the charge-transfer (CT) type TMOs, the O 2*p* band appears between the lower and upper Hubbard bands, and the gap is usually formed between the O 2*p* and the upper Hubbard 3*d* band. In contrast to the early TM compounds, insulating NiO is a typical example of CT insulator while the high-T_c cuprates are CT insulators driven metallic by doping. It is well-known that these two compounds involve the formation of Zhang-Rice states positioned at the top of the valence band [43–52]. They arise from a competition between O 2*p*—Ni (or Cu) 3*d* hybridization and the Ni (or Cu) on-site Coulomb interaction.

First, experimental results of Ni 2*p* core-level HAXPES and soft X-ray PES of NiO are shown in Fig. 9.9 [29]. The core-level spectra were normalized at the

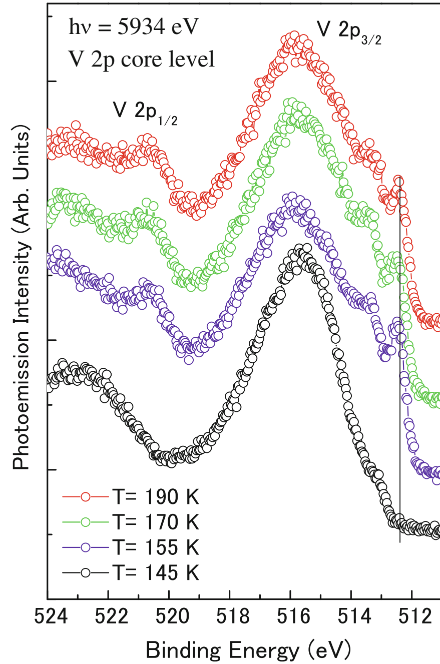

Fig. 9.8 Evolution of the well screened satellites in V $2p_{3/2}$ core-level of V_2O_3 versus temperature, while crossing the MIT. The peak, present with same intensity and shape in the metallic phase, disappears as soon as the T_{MIT} is reached, confirming a sudden transition

feature C, since it is well known that the feature C is insensitive to the surface preparation. In comparison with soft X-ray PES, the intensity of the feature A for bulk sensitive HAXPES was found to be enhanced by a factor of 1.35 with respect to the soft X-ray PES. Experiments in Fig. 9.9 clearly show that the feature A was appreciably changed between the HAXPES and soft X-ray PES. Extended cluster model described in the previous subsection can be applied to insulating NiO by replacing a coherent band or doping induced state with Zhang-Rice bound state labeled '*Z*'. The calculated spectrum is shown in Fig. 9.9. The experimental features are reproduced well by the calculation over the whole energy range. From the calculations, it was concluded that the dominant spectral weight in the feature A arises from the $2p^5 3d^9 \underline{Z}$ state, while the contribution of the $2p^5 3d^9 \underline{L}$ is dominant for the feature B. The satellite C is mainly due to the $2p^5 3d^8$ state. It should be mentioned that Hariki et al. recently explained this double peak structure of NiO in terms of dynamical mean field theory, [53] consistent with the picture of Taguchi et al.

Another example in which Zhang-Rice states play an important role is high T_c cuprates. Theoretical studies have predicted that the Zhang-Rice singlet (ZRS) should show a signature in Cu 2*p* PES of the cuprates. The Zhang-Rice singlet state is considered very important for superconductivity but has not been observed by conventional soft X-ray PES. Furthermore, while many Cu 2 *p* core-level soft X-ray PES of high T_c cuprates have been performed, the spectra show very little change upon doping. These puzzles bring into question the role of the depth

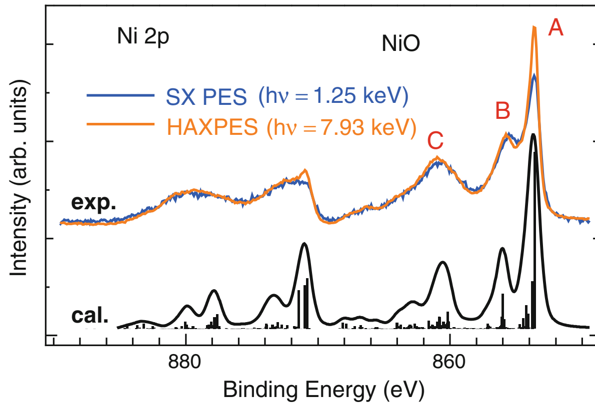

Fig. 9.9 *Upper panel* Comparison between experimental Ni 2*p* core-level HAXPES and soft X-ray PES. *Lower panel* Cluster model calculation for Ni 2*p* spectrum [29]

sensitivity of PES. Figure 9.10a shows Cu 2 *p* core-level HAXPES of single crystal electron-doped $Nd_{1.85}Ce_{0.15}CuO_4$ (NCCO), hole doped $La_{1.85}Sr_{0.15}CuO_4$ (LSCO) and La_2CuO_4 (LCO) [30]. The HAXPES spectra of NCCO, LCO, and LSCO are

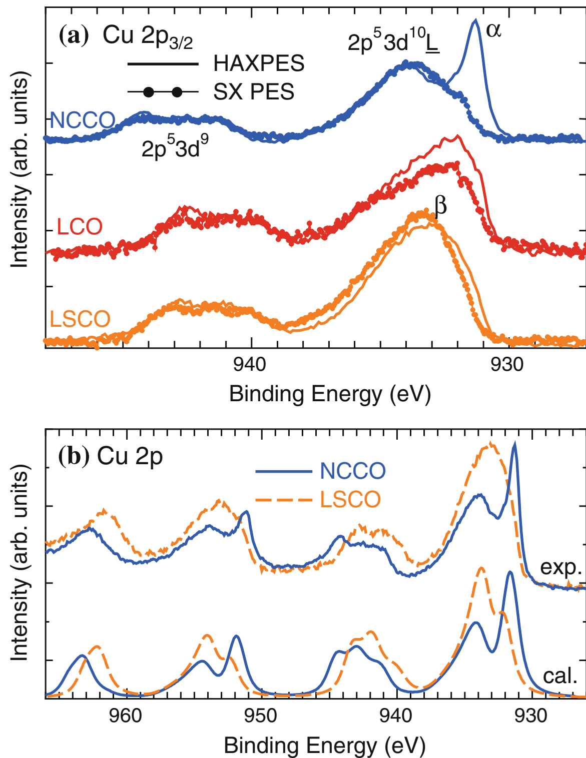

Fig. 9.10 **a** Comparison between experimental Cu 2*p* HAXPES (*solid line*) and soft X-ray PES (*line with symbols*) for electron-doped NCCO, undoped LCO and hole doped LSCO. **b** Model calculations for the Cu 2*p* core-level PES of NCCO and LSCO (*lower panel*) compared with experiments (*upper panel*) [29]

clearly different for each materials, emphasizing their differences in their ground states. Especially, the HAXPES for NCCO shows a sharp low binding energy feature α which is not observed in NCCO soft X-ray PES.

The calculated results are shown in Fig. 9.10b with experiments of LSCO and NCCO. The calculations reproduce well the main peaks and satellite structure. The sharp peak at low binding energy in NCCO originates from core hole screening by doping induced states at E_F, the $2p^5 3d^{10}\underline{Z}$ state. The obtained parameter values show small differences for LSCO and NCCO. The most important parameter is Δ^*, which represents the energy difference between the upper Hubbard band and doping induced states. The small values of Δ^* for NCCO (=0.25 eV) indicates that the doping induced states lie just below the upper Hubbard band, whereas a large Δ^* (=1.35 eV) of LSCO describes the situation for doping induced states lying near the top of the valence band, with the upper Hubbard band separated by Δ^*.

9.6 Diluted Magnetic Semiconductors

Dilute magnetic semiconductors (DMS) hold promise for creating spin-dependent devices that operate on the same principle as (e.g.) electrical transistors, but that employ the electron-spin for signal storage and processing [54, 55]. One limit to realize DMS-based spintronics devices is that the temperature at which long range magnetic order is observed (T_c) occurs well below room temperature. GaMnAs is the prototype of a DMS and, to date, the highest T_c temperature is <200 K. The value of T_c in GaMnAs, since the discovery of ferromagnetism (FM) made in 1996 by Ohno et al. [56], has increased, mainly due to post-growth annealing techniques, but the newer materials are rich of defects. Interstitial Mn and AsGa antisites, both acting as a double donor, hinder the full contribution to FM of the free holes provided by substitutional Mn. Moreover, diffusion of the interstitial Mn to the surface has been pointed out. Still, DMS pose a number of unique challenges to the understanding of the physics governing their properties, as e.g. (i) a thorough description of the new band structure resulting from the Mn doping, (ii) a reliable control of surface and interface effects (clustering, diffusion of Mn), (iii) a precise evaluation of magnetic properties as a function of Mn doping. Concerning the spectroscopic investigation of GaMnAs magnetic properties, the relationship between sample preparation conditions and disorder/diffusion effects has considerable implications on the understanding of the magnetic and electronic properties of GaMnAs. HAXPES performed at medium photon energy (4.5 keV), [57] suggest an evolution of the Mn $2p$ signal as a function of annealing temperature. Recent studies of electrical gating of As-based DMS compounds have indicated the presence of a nearly 1.5 nm wide depletion zone at the surface of these materials. The depletion zone changes the hole density profile in a thin DMS channel so dramatically, that a sizable reduction of T_c (>50 %) is observed [58]. Such observations clarify well how important is the use of HAXPES to understand what

factors control this behavior and what could be done to overcome the possible limitations induced by the surface towards nano-spintronics applications. (Ga, Mn) As bears a competition between localized/metallic behavior in the vicinity of the transition, as revealed by recent STM results versus doping [59]. Knowing the sensitivity of core-level to screening effects, HAXPES can be very fruitful in providing a measure of the localization/metallicity of such systems. Indeed, the comparison between core-level and valence band spectra in HAXPES versus both doping and preparation conditions was able to demonstrate that the electronic structure of the bulk and the surface of (Ga, Mn)As are profoundly different. In Fig. 9.11, Mn $2p_{3/2}$ HAXPES spectra reveal the presence of a sharp well screened feature (d^6 electronic configuration) in the low binding energy region of the Mn $2p$ peaks. Such satellite is found for the first time for a metallic element in a semiconducting environment. As in the case of $3d$ TMOs, the well screened feature is not detected by soft X-ray PES [60, 61]. The intensity of the satellite peak increases below the T_c (60 K) of the (GaMn)As, in a reversible way, suggesting an important role played by electronic localization-hybridization when crossing the ferromagnetic transition. Comparison with model calculations were able to identify the character of the Mn $3d$ electronic states [60, 61]. A final important open question addressing the nature of the well screened structures, and hence the screening ability of electrons in correlated systems. As already mentioned, well

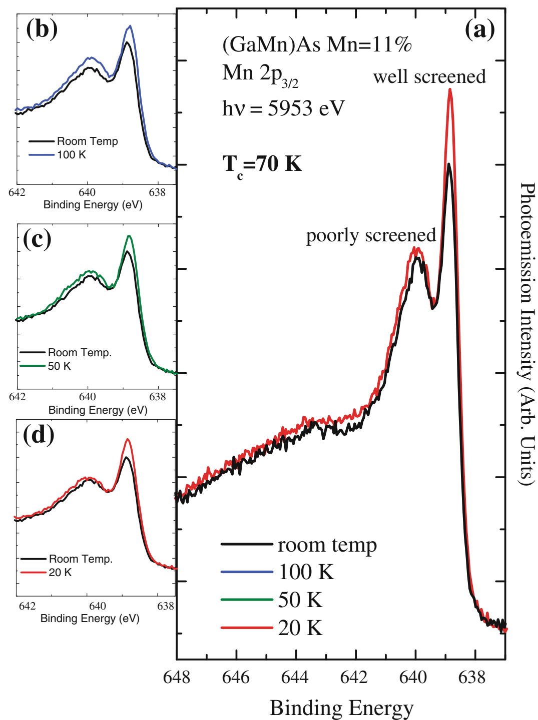

Fig. 9.11 Mn *2p* HAXPES spectra of (Ga,Mn)As (13 % Mn, T_c 80 K) versus temperature (panel **a**). **b**–**d** Expanded view of the $2p_{3/2}$ region, showing the difference of the spectra at room temperature with those at low temperatures. A clear redistribution of spectral weight is found, where the intensity of the well-screened peak increases, when lowering the temperature, with respect to the normal peak at higher binding energy

screened or satellites originating from a non-local channels have been observed by soft X-ray PES in many *f*-based systems as well as for 4*d*-TMOs. The case of ruthenates is a paradigmatic example: a transition from itinerant to localized character, corresponding to the variation of well screened satellites versus doping, is clearly observed both in the low and the high kinetic energy region [62]. Only for 3*d*-TMOs, the use of HAXPES is 'mandatory' for detecting the non local satellites. It is tempting to associate this discrepancy with the different extensions of the electronic wavefunction, i.e. the screening ability in 3*d*, more localized, is more easily perturbed by the change of the electronic structure passing from surface to bulk. However, both theory and experiment, so far, did not address such issue in a quantitative manner.

9.7 Summary

HAXPES reveals new features in the core-level of 3*d*-based TMOs (vanadates, manganites, cuprates) and DMS not visible at surface sensitive, excitation energy. In particular, the additional low-binding-energy features of 2*p* core-level lines, the so-called well screened satellites, have been connected with both metallic and ferromagnetic properties; extra peaks disappear when the system enters in the insulating phase and are not detectable at low kinetic energy, thus suggesting a clear and distinct behavior of the electronic screening at the surface and in the bulk of the materials. Still, both experiment and theory face many open questions. A key question regarding the presence or absence of the well screened satellites refers to the possibility of using such structures as the spectroscopic 'signatures' of a metallic-like behavior in systems close to a metal-insulator transition, and/or the use of such signature for quick and reliable 'quality-control' of samples produced to device applications. In this case, samples would be produced in a less controlled experimental conditions (both from the morphological and crystalline point of view), the bulk sensitivity guaranteed by HAXPES may turn into an easier method of control. Well screened features could be then identified as a general benchmark of the magnetic and/or metallic status of a specific class of materials. In order to make this approach 'robust' enough, the value of a 'critical thickness', i.e. the probing depth at which such peaks appear, and if such new structure appears suddenly or gradually, must be determined and it is presently unknown. A second important issue concerns the interpretation in terms of final-state screening properties: if the linewidth of the screened peak bears a degree of proportionality with the bandwidth W or not; due to the increase of electron localization in passing from volume to surface, one would expect a line narrowing in surface sensitive PES, reflecting the progressive reduction of W. As in the case described in the previous sections for TMOs, the well screened feature observed in the Mn core-level of (Ga, Mn)As is not detected in soft X-ray PES [60, 61].

In summary, in less than ten years from its 'birth', HAXPES became a well established spectroscopic technique, bringing a valuable contribution to our

understanding of complex and correlated solid systems. We are confident that the combined use of theory and experiment will further boost its application in the years to come.

Acknowledgments We sincerely thank all our collaborators of HAXPES studies over viewed in this review. MT acknowledges the support of T. Ishikawa and the X-ray optics group of RIKEN and thanks A. Chainani, M. Matsunami, K. Horiba, R. Eguchi, T. Takeuchi, N. Kamakura and S. Shin, for fruitful collaborations. GP would like to thank the colleagues of the VOLPE project: P. Torelli, F. Offi. F. Borgatti, G. Monaco, G. Paolicelli, A. Fondacaro, M. Sacchi, P. Lacovig, G. Cautero, M. Cautero, the Id16 beamline team and in particular R. Verbeni and C. Henriquet. G. Panaccione thanks G. van der Laan, C.H. Back, R. Egdell and D. Payne for fruitful discussion and suggestion. MT and GP wish to dedicate this article to Dr. Takata's memory. This work was partially supported by KAKENHI (No. 20540324).

References

1. C.S. Fadley, J. Electron Spectrosc. Relat. Phenom. **178–179**, 2 (2010)
2. G. Panaccione, K. Kobayashi, Surf. Sci. **3–4**, 125 (2012)
3. W. Drube, Th Eickhoff, H. SchulteSchrepping, J. Heuer, AIP Conf. Proc. **705**, 1130 (2002)
4. J. Danger, P. Le Fèvre, H. Magnan, D. Chandesris, S. Bourgeois, J. Jupille, T. Eickhoff, W. Drube, Phys. Rev. Lett. **88**, 243001 (2002)
5. K. Kobayashi, M. Yabashi, Y. Takata, T. Tokushima, S. Shin, K. Tamasaku, D. Miwa, T. Ishikawa, H. Nohira, T. Hattori, Y. Sugita, O. Nakatsuka, A. Sakai, S. Zaima, Appl. Phys. Lett. **83**, 1005 (2003)
6. Y. Takata, K. Tamasaku, T. Tokushima, D. Miwa, S. Shin, T. Ishikawa, M. Yabashi, K. Kobayashi, J.J. Kim, T. Yao, T. Yamamoto, M. Arita, H. Namatame, M. Taniguchi, Appl. Phys. Lett. **84**, 4310 (2004)
7. S. Thiess, C. Kunz, B.C.C. Cowie, T.-L. Lee, M. Renier, J. Zegenhagen, Solid State Commun. **132**, 589 (2004)
8. C. Dallera, L. Duo, L. Braicovich, G. Panaccione, G. Paolicelli, B. Cowie, J. Zegenhagen, Appl. Phys. Lett. **85**, 4532 (2004)
9. P. Torelli, M. Sacchi, G. Cautero, M. Cautero, B. Krastanov, P. Lacovig, P. Pittana, R. Sergo, R. Tommasini, A. Fondacaro, F. Offi, G. Paolicelli, G. Stefani, M. Grioni, R. Verbeni, G. Monaco, G. Panaccione, Rev. Sci. Instrum. **76**, 023909 (2005)
10. M. Sacchi, F. Offi, P. Torelli, A. Fondacaro, C. Spezzani, M. Cautero, G. Cautero, S. Huotari, M. Grioni, R. Delaunay, M. Fabrizioli, G. Vanko, G. Monaco, G. Paolicelli, G. Stefani, G. Panaccione, Phys. Rev. B **71**, 155117 (2005)
11. A. Sekiyama, T. Iwasaki, K. Matsuda, Y. Saitoh, Y. Onuki, S. Suga, Nature **403**, 396 (2000)
12. G. Panaccione, M. Cautero, G. Cautero, A. Fondacaro, M. Grioni, P. Lacovig, G. Monaco, F. Offi, G. Paolicelli, M. Sacchi, M. Stojic, G. Stefani, R. Tommasini, P. Torelli, J. Phys. Condens. Matter **17**, 2671 (2005)
13. N.F. Mott, *Metal Insulator Transition* (Taylor and Francis, London, 1990)
14. M. Imada, A. Fujimori, Y. Tokura, Rev. Mod. Phys. **70**, 1039 (1998)
15. K. Horiba, M. Taguchi, A. Chainani, Y. Takata, E. Ikenaga, D. Miwa, Y. Nishino, K. Tamasaku, M. Awaji, A. Takeuchi, M. Yabashi, H. Namatame, M. Taniguchi, H. Kumigashira, M. Oshima, M. Lippmaa, M. Kawasaki, H. Koinuma, K. Kobayashi, T. Ishikawa, S. Shin, Phys. Rev. Lett. **93**, 236401 (2004)
16. F. Offi, N. Mannella, T. Pardini, G. Panaccione, A. Fondacaro, P. Torelli, M.W. West, J.F. Mitchell, C.S. Fadley, Phys. Rev. B **77**, 17442 (2008)
17. J. Fuggle, M. Campagna, Z. Zolnierek, R. Lässer, A. Platau, Phys. Rev. Lett. **45**, 1597 (1980)

18. O. Gunnarsson, K. Schönhammer, Phys. Rev. Lett. **50**, 604 (1983)
19. M.A. van Veenendaal, G. Sawatzky, Phys. Rev. Lett. **70**, 2459 (1993)
20. M. Taguchi, A. Chainani, N. Kamakura, K. Horiba, Y. Takata, M. Yabashi, K. Tamasaku, Y. Nishino, D. Miwa, T. Ishikawa, S. Shin, E. Ikenaga, T. Yokoya, K. Kobayashi, T. Mochiku, K. Hirata, K. Motoya, Phys. Rev. B **71**, 155102 (2005)
21. G. van der Laan, C. Westra, C. Haas, G.A. Sawatzky, Phys. Rev. B **23**, 4369 (1981)
22. O. Gunnarsson, K. Schönhammer, Phys. Rev. B **28**, 4315 (1983)
23. A. Fujimori, F. Minami, Phys. Rev. B **30**, 957 (1984)
24. J. Zaanen, G.A. Sawatzky, J.W. Allen, Phys. Rev. Lett. **55**, 418 (1985)
25. M. Taguchi, A. Chainani, M. Matsunami, R. Eguchi, Y. Takata, M. Yabashi, K. Tamasaku, Y. Nishino, T. Ishikawa, S. Tsuda, S. Watanabe, C.-T. Chen, Y. Senba, H. Ohashi, K. Fujiwara, Y. Nakamura, H. Takagi, S. Shin, Phys. Rev. Lett. **104**, 106401 (2010)
26. N. Kamakura, M. Taguchi, A. Chainani, Y. Takata, K. Horiba, K. Yamamoto, K. Tamasaku, Y. Nishino, D. Miwa, E. Ikenaga, M. Awaji, A. Takeuchi, H. Ohashi, Y. Senba, H. Namatame, M. Taniguchi, T. Ishikawa, K. Kobayashi, S. Shin, Europhys. Lett. **68**, 557 (2004)
27. R. Eguchi, M. Taguchi, M. Matsunami, K. Horiba, K. Yamamoto, Y. Ishida, A. Chainani, Y. Takata, M. Yabashi, D. Miwa, Y. Nishino, K. Tamasaku, T. Ishikawa, Y. Senba, H. Ohashi, Y. Muraoka, Z. Hiroi, S. Shin, Phys. Rev. B **78**, 075115 (2008)
28. H. Tanaka, Y. Takata, K. Horiba, M. Taguchi, A. Chainani, S. Shin, D. Miwa, K. Tamasaku, Y. Nishino, T. Ishikawa, E. Ikenaga, M. Awaji, A. Takeuchi, T. Kawai, K. Kobayashi, Phys. Rev. B **73**, 094403 (2006)
29. M. Taguchi, M. Matsunami, Y. Ishida, R. Eguchi, A. Chainani, Y. Takata, M. Yabashi, K. Tamasaku, Y. Nishino, T. Ishikawa, Y. Senba, H. Ohashi, S. Shin, Phys. Rev. Lett. **100**, 206401 (2008)
30. M. Taguchi, A. Chainani, K. Horiba, Y. Takata, M. Yabashi, K. Tamasaku, Y. Nishino, D. Miwa, T. Ishikawa, T. Takeuchi, K. Yamamoto, M. Matsunami, S. Shin, T. Yokoya, E. Ikenaga, K. Kobayashi, T. Mochiku, K. Hirata, J. Hori, K. Ishii, F. Nakamura, T. Suzuki, Phys. Rev. Lett. **95**, 177002 (2005)
31. A. Kotani, Y. Toyozawa, J. Phys. Soc. Jpn. **35**, 1073 (1973)
32. A. Kotani, Y. Toyozawa, J. Phys. Soc. Jpn. **35**, 1082 (1973)
33. A. Kotani, Y. Toyozawa, J. Phys. Soc. Jpn. **37**, 912 (1974)
34. O. Gunnarsson, K. Schönhammer, Phys. Rev. B **31**, 4815 (1985)
35. K. Okada, A. Kotani, J. Phys. Soc. Jpn. **74**, 653 (2005)
36. M.A. van Veenendaal, Phys. Rev. B **74**, 085118 (2006)
37. A. Georges, G. Kotliar, W. Krauth, M.J. Rozenberg, Rev. Mod. Phys. **68**, 13 (1996)
38. G. Kotliar, D. Vollhardt, Phys. Today **57**, 53 (2004)
39. S.-K. Mo, J.D. Denlinger, H.-D. Kim, J.-H. Park, J.W. Allen, A. Sekiyama, A. Yamasaki, K. Kadono, S. Suga, Y. Saitoh, T. Muro, P. Metcalf, G. Keller, K. Held, V. Eyert, V.I. Anisimov, D. Vollhardt, Phys. Rev. Lett. **90**, 186403 (2003)
40. T.C. Koethe, Z. Hu, M.W. Haverkort, C. Schüßler-Langeheine, F. Venturini, N.B. Brookes, O. Tjernberg, W. Reichelt, H.H. Hsieh, H.-J. Lin, C.T. Chen, L.H. Tjeng, Phys. Rev. Lett. **97**, 116402 (2006)
41. G. Panaccione, M. Altarelli, A. Fondacaro, A. Georges, S. Huotari, P. Lacovig, A. Lichtenstein, P. Metcalf, G. Monaco, F. Offi, L. Paolasini, A. Poteryaev, O. Tjernberg, M. Sacchi, Phys. Rev. Lett. **97**, 116401 (2006)
42. H. Fujiwara, A. Sekiyama, S.-K. Mo, J.W. Allen, J. Yamaguchi, G. Funabashi, S. Imada, P. Metcalf, A. Higashiya, M. Yabashi, K. Tamasaku, T. Ishikawa, S. Suga, Phys. Rev. B **84**, 075117 (2011)
43. F.C. Zhang, T.M. Rice, Phys. Rev. B **37**, 3759 (1988)
44. J. van Elp, H. Eskes, P. Kuiper, G.A. Sawatzky, Phys. Rev. B **45**, 1612 (1992)
45. M.A. van Veenendaal, H. Eskes, G.A. Sawatzky, Phys. Rev. B **47**, 11462 (1993)
46. M.A. van Veenendaal, G.A. Sawatzky, Phys. Rev. B **49**, 3473 (1994)
47. J. Bala, A.M. Oleś, J. Zaanen, Phys. Rev. Lett. **72**, 2600 (1994)
48. J. Bala, A.M. Oleś, J. Zaanen, Phys. Rev. B. **61**, 13573 (2000)

49. X. Ren, I. Leonov, G. Keller, M. Kollar, I. Nekrasov, D. Vollhardt, Phys. Rev. B **74**, 195114 (2006)
50. J. Kuneš, V.I. Anisimov, A.V. Lukoyanov, D. Vollhardt, Phys. Rev. B **75**, 165115 (2007)
51. J. Kuneš, V.I. Anisimov, S.L. Skornyakov, A.V. Lukoyanov, D. Vollhardt, Phys. Rev. Lett. **99**, 156404 (2007)
52. Q. Yin, A. Gordienko, X. Wan, S.Y. Savrasov, Phys. Rev. Lett. **100**, 066406 (2008)
53. A. Hariki, Y. Ichinozuka, T. Uozumi, J. Phys. Soc. Jpn. **82**, 043710 (2013)
54. I. Zutic, J. Fabian, S. Das, Sarma. Rev. Mod. Phys. **76**, 323 (2004)
55. A.H. Macdonald, P. Schiffer, N. Samarth, Nat. Mater. **4**, 195 (2005)
56. H. Ohno, A. Shen, F. Matsukura, A. Oiwa, A. Endo, S. Katsumoto, Y. Iye, Appl. Phys. Lett. **69**, 363 (1996)
57. B. Schmid, A. Müller, M. Sing, R. Claessen, J. Wensch, C. Gould, K. Brunner, L. Molenkamp, Phys. Rev. B **78**, 075319 (2008)
58. M. Sawicky, D. Chiba, A. Korbecka, Y. Nishitani, J.A. Majewski, F. Matsukura, T. Dietl, H. Ohno, Nat. Phys. **6**, 22 (2009)
59. A. Richardella, P. Roushan, S. Mack, B. Zhou, D.A. Huse, D.D. Awschalom, A. Yazdani, Science **327**, 665 (2010)
60. J. Fujii, M. Sperl, S. Ueda, K. Kobayashi, Y. Yamashita, M. Kobata, P. Torelli, F. Borgatti, M. Utz, C.S. Fadley, A.X. Gray, G. Monaco, C.H. Back, G. van der Laan, G. Panaccione, Phys. Rev. Lett. **107**, 187203 (2011)
61. J. Fujii, B.R. Salles, M. Sperl, S. Ueda, M. Kobata, K. Kobayashi, Y. Yamashita, P. Torelli, M. Utz, C.S. Fadley, A.X. Gray, J. Braun, H. Ebert, I. Di Marco, O. Eriksson, P. Thunström, G.H. Fecher, H. Stryhanyuk, E. Ikenaga, J. Minár, C.H. Back, G. van der Laan, G. Panaccione, Phys. Rev. Lett. **111**, 097201 (2013)
62. G. Panaccione, U. Manju, F. Offi, E. Annese, I. Vobornik, P. Torelli, Z.H. Zhu, M.A. Hossain, L. Simonelli, A. Fondacaro, P. Lacovig, A. Guarino, Y. Yoshida, G.A. Sawatzky, A. Damascelli, New J. Phys. **13**, 053059 (2011)

Chapter 10
The Influence of Final-State Effects on XPS Spectra from First-Row Transition-Metals

Andrew P. Grosvenor, Mark C. Biesinger, Roger St. C. Smart and Andrea R. Gerson

Abstract The first row transition metals (FRTM) and their compounds are of immense importance to the worldwide economy. In 2009, 2.3 billion (metric) tonnes of iron ore, 21.5 million tonnes (Mt) of chromium, 11.1 Mt of zinc, 9.6 Mt of manganese, 6.2 Mt of titanium, 1.6 Mt of nickel, 1.6 Mt of copper, 62,000 tonnes of cobalt and 54,000 tonnes of vanadium were produced from mining operations around the world [1].

10.1 Introduction

The first row transition metals (FRTM) and their compounds are of immense importance to the worldwide economy. In 2009, 2.3 billion (metric) tonnes of iron ore, 21.5 million tonnes (Mt) of chromium, 11.1 Mt of zinc, 9.6 Mt of manganese, 6.2 Mt of titanium, 1.6 Mt of nickel, 1.6 Mt of copper, 62,000 tonnes of cobalt and 54,000 tonnes of vanadium were produced from mining operations around the world [1]. Their use in alloys for building materials and consumer products is ubiquitous. They are important components of catalysts, batteries, magnetic

A.P. Grosvenor (✉)
Department of Chemistry, University of Saskatchewan, 110 Science Place,
Saskatoon S7N 5C9, Canada
e-mail: andrew.grosvenor@usask.ca

M.C. Biesinger
Surface Science Western, The University of Western Ontario, 999 Collip Circle,
London, ON N6G 0J3, Canada

R.St.C. Smart · A.R. Gerson
Minerals and Materials Science and Technology (MMaST), Mawson Institute,
University of South Australia, Mawson Lakes, South Australia 5095, Australia

Present Address:
A.R. Gerson
Blue Minerals Consultancy, 13 Mill Terrace, Middleton, South Australia 5213, Australia

© Springer International Publishing Switzerland 2016

J.C. Woicik (ed.), *Hard X-ray Photoelectron Spectroscopy (HAXPES)*,
Springer Series in Surface Sciences 59, DOI 10.1007/978-3-319-24043-5_10

materials, pigments, specialty chemicals, and in the emerging nano-materials field. To be able to define the bulk and surface chemistry of these materials is fundamental to improvements in research and applied industrial process innovation. The surface chemistry of FRTM and their compounds is central to applications in, for instance, thin films, alloys, coatings, catalysts, nano-structured materials, oxides, corrosion/degradation and mineral separation. X-ray photoelectron spectroscopy (XPS) is used to study surfaces. Variations in the lineshape and binding energy (BE) of FRTM XPS spectra are used to draw conclusions on the ground-state electronic configurations and chemical behaviour of a FRTM in the surfaces of different materials. Although it is well known that ground-state effects, such as a decrease or increase in oxidation-state of the absorbing atom, are reflected as changes in lineshape or binding energy of an XPS spectrum, final-state effects in the XPS measurement process can also play a role. Therefore, to properly interpret an XPS spectrum, the influence of both ground-state and final-state effects must be understood. In particular, interpretation of M 2*p* (M = metal) XPS spectra of the economically important first row transition metals is important and widely used by material scientists, corrosion scientists and surface scientists. However, the current interpretation of the complex structures seen in these spectra, usually based on single binding energy assignments, carries significant uncertainties and can be incorrect in some cases. A lack of high quality literature references has impeded progress in understanding the chemistry occurring at transition metal surfaces. The purpose of this Chapter is to introduce the concepts of final-state XPS spectral effects; describe how such effects can influence the lineshape and binding energy obtained; and improve interpretation of FRTM spectra for more reliable surface chemical assignment.

10.1.1 An Introduction to Final-State Effects

Binding energies and their shifts in XPS spectra contain information about both the initial state potential experienced by localized core electrons and final-state or relaxation effects resulting from intra- and extra-atomic processes during the emission of a core electron. In X-ray photoelectron spectra of many of the FRTM and their compounds, interpretation can be complicated by several final-state effects that produce peaks or intensity additional to the main element emission and can alter the measured binding energy of the main emission normally used to identify the element and its chemical state. To introduce these effects, which will be discussed in more detail in the following sections, the final-state effects that result in additional peaks or intensity in XPS spectra (multiplet splitting, shake-up peaks, the asymmetric lineshape of spectra from conducting materials, and plasmon loss peaks) will be introduced first, followed by a discussion of how binding energy shifts may occur.

10.1.1.1 Effects on Lineshapes

Multiplet splitting arises when an atom contains unpaired electrons (e.g. Cr(III), $3p^63d^3$) in the valence levels. When a core electron vacancy is created by photoionization, there can be multiple couplings between the now unpaired electron in the core orbital with the unpaired electrons in the outer valence shell. This can create a number of final states, which are usually observed in the photoelectron spectrum as a multi-peak envelope [2]. This splitting arises from the coupling of the magnetic fields set up by the unpaired valence electron(s) and the unpaired core electron present as a result of photoemission, with the resulting high spin (parallel spins) and low spin (apposed spins) components moving to greater and lesser binding energies, respectively [3].

Shake-up peaks are a result of the finite probability that an ion (after photoionization) will be left in a specific excited energy state a few eV above the ground state through excitation of the ion by the outgoing photoelectron [4]. In this process, the kinetic energy of the emitted photoelectron is reduced and this will be measured as a “shake-up” peak at a higher binding energy than the main emission peak. Shake-up satellite peaks are common with paramagnetic states having unpaired valence electron configurations [5]. The shake-up observed for transition metal compounds can also be described as an interaction in the final state involving significant ligand-metal charge transfer that results in an extra $3d$ or a $4f$ electron configuration compared to the initial state. The classic example of shake-up structure is observed in the $2p_{3/2}$ spectrum for Cu(II) species, such as that for $Cu(OH)_2$ and CuO. In the case of CuO, there is a shake-up of a $3d$ electron leading to a $2p^53d^9$ configuration [6]. The intensity and structure of the shake-up features can aid in the assignment of chemical states where, for instance, Cu(II) species in $Cu(OH)_2$ and CuO show different shake-up structures. Shake-up structures are also important in the analysis of Mn, Fe, Co and Ni species [5, 7–9]. It is important to note that the intensity of these satellite peaks comprises part of the overall intensity of the specific XPS emission and should be included with the main peak in quantitative estimates. This is often not done.

For highly conductive samples, such as metals or graphite, there is a distribution of unfilled levels in the continuous conduction band that are available for shake-up-like events following core electron photoemission. When this occurs, instead of a discrete structure, like that seen for shake-up satellites, an asymmetric peak shape to higher binding energy of the main peak is evident [10]. Furthermore, for some conductive materials, plasmon loss peaks may occur in which loss of a specific amount of kinetic energy is due to the interaction between the photoelectron and electrons in a conduction band (plasmons). Plasmons occur in well-defined quanta arising from group oscillations of the conduction electrons [2], and those attributed to the bulk of the material and its surface can sometimes be separately identified as relatively weak peaks at higher binding energy than the main emission [7].

10.1.1.2 Shifts in Binding Energies

In the simplest model, shifts in measured binding energy (BE) of the absorbing atom (i), E_{bi}, due to inter- and intra-atomic chemical influences, relative to a defined reference potential ($(E_b{}^o)$), are a combination of terms as described using the modified charge potential model:

$$\Delta E_b = \Delta(E_{bi} - E_b^0) = \left(k\Delta q_i + \Delta\sum_{\mathrm{i}\neq\mathrm{j}}\frac{q_\mathrm{j}}{r_\mathrm{ij}}\right) - \left(\Delta E_i^{\mathrm{IA}} + \Delta E_i^{\mathrm{EA}}\right) + V_s^4. \quad (10.1.1)$$

Shifts in the ground-state energies are caused by changes in the valence charge of the absorbing atom (q_i in $k\Delta q_i$, where k is a parameter due to interactions between core and valence electrons) and in its chemical environment ($\Delta\sum_{\mathrm{i}\neq\mathrm{j}}\frac{q_\mathrm{j}}{r_\mathrm{ij}}$, here r_{ij} is the distance to atom j, which has a charge of q_j), which are intra- and extra-atomic effects, respectively [4]. Ground-state effects are generally understood to represent the “chemical shift” as a result of the ground state electronic structure and are a function of the valence structure of the core atom, which is in turn a function of bonding to neighbouring atomic valence states. Charged or polar surfaces introduce the additional general potential, V_s, that alters $E_{\mathrm{b}i}$. In practice, however, this bias is compensated by measuring the 1s core level BE for carbon atoms, which are usually present as surface contamination, as reference.

In the final state, however, after a photoelectron has been ejected from atom i and an unscreened core-hole has been produced, the system will rearrange its remaining electrons to minimize its energy by intra-atomic and extra-atomic relaxation. Final-state intra-atomic relaxation effects, ΔE_i^{IA}, are associated with the screening of the core hole by the other electrons in the atom resulting in shifts in the measured binding energy of the main emission. Extra-atomic relaxation of electrons from surrounding atoms, represented by ΔE_i^{EA}, is sensitive to changes in the chemical environment, whereas intra-atomic relaxation of electrons localized on the atom of interest is not, and $\Delta E_i{}^{\mathrm{IA}}$ is often negligible [4].

To obtain these relaxation energies, it is now well established that the contribution from final-state relaxation can be estimated separately from the ground-state energy by combining the measured core binding energy of the photoelectron with a corresponding Auger kinetic energy measured in the same XPS spectrum to form the Auger parameter. The seminal conception of the Auger parameter was made in 1971 by Wagner [11, 12]. In its now common form, the modified Auger parameter (α'—now known as the Auger parameter) is defined as:

$$\Delta\alpha' = \Delta E_b + \Delta E_k \quad (10.1.2)$$

where ΔE_b and ΔE_k are the shifts in binding and kinetic energies of the dominant core electron and Auger electron lines for a particular element, respectively, relative to those from some standard reference species. Using terminology adopted by

Wagner and Taylor, ΔE_b can be expressed as $\Delta E_b = -\Delta E_i - \Delta R$, where positive values of ΔE_i, ground state contributions, and ΔR, final state contributions, result in a shift to lower binding energy [13]. If linear screening is assumed, which reflects the quadratic dependence of the relaxation energy on the number of core holes, and core level shifts between two different chemical environments are assumed to be the same, then, in the simplest analysis [13]:

$$\Delta E_k = \Delta E_i + 3\Delta R \tag{10.1.3}$$

In this case, the modified Auger parameter becomes [13, 14]

$$\Delta \alpha' = \Delta E_b + \Delta E_k = 2\Delta R \tag{10.1.4}$$

This simple model has become a valuable tool in the assignment of chemical states for a wide variety of surface species and in the separation of ground-state effects from final-state effects in shifts in XPS binding energies [14].

10.2 Multiplet Splitting

Now that the general changes in lineshape and BE that can result from final-state effects have been described, a more detailed description of these final-state effects will be provided. In the following sections, emphasis will be placed on final-state effects in XPS spectra from first-row transition-metal containing materials. The interpretation of chemical states of transition metals from X-ray photoelectron spectra of the most intense $2p$ envelope is recognised in the literature to carry a high degree of uncertainty due to the complex extended multiplet structures, shake-up structures, plasmon loss structures and overlap between the various chemical state signals [5, 7, 8]. Confident assignment of the correct multiplet envelope and other structures to each chemical state is necessary for quantitative estimates of the relative proportions of different oxidation states and species for processing of materials, minerals, ceramics and many other technologies. For example, in previous work [7], it was shown that there are very different line shapes resulting from free ion structures in contrast to strong ligand charge-transfer multiplet complexes for different compounds of the same transition metal with the same nominal oxidation state. In this chapter, we present an attempt to classify these different cases and correlate theoretical estimates of free ion and charge-transfer multiplet envelopes with the X-ray photoelectron spectra for materials containing primarily polar-covalent/ionic metal-ligand bonds (i.e., metal oxides).

10.2.1 Intra- versus Inter-Atomic Core Hole Shielding Effects

The first experimental reports of multiplet splitting in XPS spectra of gases [15] and solid materials [16, 17] appeared in 1969–70. The first comprehensive theoretical Hartree-Fock treatment of the multiplet structure of transition metal 2*p* spectra was carried out by Gupta and Sen a few years later [18, 19]. This work assumed a free ion state for the transition metal; only ground state intra-atomic effects were considered, which included spin-orbit splitting. Hence, crystal field effects from ligands, which may change the spacing and intensity of the multiplet peaks present, were not included. The calculations also assumed that the 2*p* electron shell is still complete (i.e., that no photoionisation has taken place). Modulation of the 2*p* emission is therefore modelled relative to an arbitrary zero of energy. Since the ground state of the free ions is generally a high-spin state, the spectra calculated are expected to more closely resemble those observed in high-spin complexes. The 2p XPS spectra calculated by Gupta and Sen are presented in Fig. 10.1 for all of the FRTM [19].

Gupta and Sen speculated that if excited states were taken into account, “calculations will automatically and naturally also predict the so-called shake-up satellites” [18]. This statement was based on the expectation that the presence of the satellite is caused by a ‘shake-up’ event, i.e., excitation of an unpaired 3*d* electron to a higher bound energy level (possibly 4*s*). This results in the kinetic energy of the 2*p* electron being reduced by the excitation energy of the unpaired 3*d* electron. Thus, two peaks result, one for the 2*p* excitation and one for the combined effect of the 3*d* and 2*p* excitations. Due to the reduced kinetic energy, the satellite occurs at a higher apparent BE.

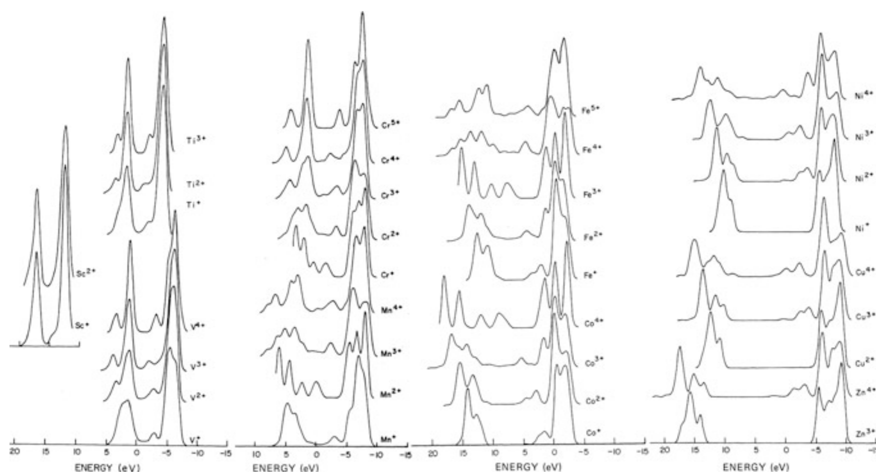

Fig. 10.1 Simulated free ion 2p spectra for the first row transition metals (Adapted from [19])

The following paragraphs will focus on the theoretical analysis of XPS spectra from NiO along with some comments on the spectra from other Ni-bearing materials, including Ni metal. This section is not intended to be a complete review but to highlight current models and continuing discussion. The predicted XPS 2*p* spectral profiles for NiO (i.e., Ni^{2+}), along with the full set of FRTM, are shown in Fig. 10.1 [19]. NiO adopts the face centered cubic rock salt structure with space group *Fm-3m*. Below ≈530 K (Néel temperature), NiO in its ground state is an antiferromagnetic insulator (band gap 3.8 eV [20]) with parallel spins in the (111) planes. Ni^{2+} is present in a $t_{2g}^{6}e_{g}^{2}$ configuration with a spin multiplicity of 3 [21]. The upper valence band of NiO is dominated by O 2*p* orbitals [22].

Subsequent simulations have improved upon the ability to predict line-shapes for various transition metal compounds. For example, Zaanen et al. [23] presented an impurity-like many-body analysis ("cluster approximation") of the $2p_{3/2}$ spectra of nickel dihalides. Modeled peak shapes were a reasonable match with the experimental data available at the time. However, comparison to present data shows that significant structure is unaccounted for (c.f. [7, 23]). It is suggested that charge-transfer energies vary significantly across the series and that Coulomb interaction energies (energy between the core hole and the valence electrons) are the greatest energies in the system. Okada and Kotani [24] used a model that includes multiplet and configuration interactions. Part of this work included modeling of the nickel dihalides, again with reasonable comparison to the experimental spectra of the time but with clearly missing structure compared to current data (c.f. [7, 23]). This model was also applied to a variety of transition metal monoxides [24]. Peak shapes were reasonably similar to experimental data with moderate variations in peak positions and intensities.

The Ni 3*s* XPS spectrum has been the subject of subsequent calculations in an effort to reduce the computational complexity as compared to Ni 2*p* (for Ni 3*s* $l = 0$, no spin-orbit splitting) even though the relatively low intensity of this peak can make verification in XPS spectra more difficult. It was initially proposed that intra-atomic spin redistributions are unlikely to play a substantial role for high-spin final states [25, 26] and hence *j–j* coupling effects were not considered. Formative calculations for NiO did not allow for relaxation of the local Ni geometry and effects were averaged over the local environment [25]. The observed satellite peak was proposed to be associated with a significant charge transfer from O 2*p* to Ni 3*d*. Three effects were proposed to contribute to the greater binding energy of the charge transfer related satellite: (1) The more favourable Madelung potential for high charge ions; (2) the energy associated with removing an electron from O^{2-}; and (3) the benefit of adding an electron resulting in $3d^{n+1}$, with the first two effects dominating to give rise to an increased satellite binding energy [25]. It was also suggested that the contribution of this satellite to transition metal spectra increases in importance (i.e., reduced ΔE_b and increased intensity) from left to right across the periodic table as the relative energetic importance of (3) increases [25].

In a later study, absolute BE values were calculated for NiO and mixed inter- and intra-atomic core-hole screening effects were considered through application of a

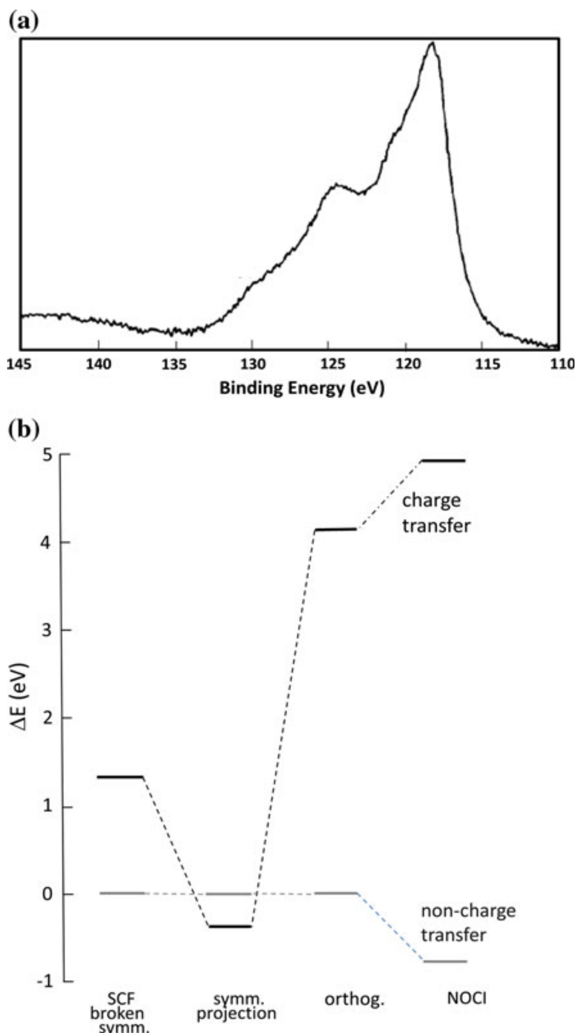

Fig. 10.2 **a** Ni 3*s* XPS spectrum from NiO (adapted from [28]); **b** Representation of energy changes between different modes of calculation. From *left* to *right*: for the charge transfer configuration: self-consistent field wavefunction with broken symmetry (C_{4V}) and with symmetry projection (O_h); after orthogonalization; and NOCI for both the charge transfer and non-charge transfer configurations (Adapted from [27])

non-orthogonalised configuration interaction (NOCI) calculation [27]. The experimental Ni 3*s* BE in NiO is 118.2 eV [28] (Fig. 10.2a). The BE calculated using a NOCI approach was 122.3 eV based on a $[NiO_6]^{10-}$ cluster within a 50 point charge array (Fig. 10.2b) [27]. Furthermore, a less intense satellite at a BE approximately 5.7 eV higher was also predicted (as compared to the experimental value of 6.1 eV higher) and resulted to a considerable extent from a charge transfer to give a $3s^13d^{n+1}L$ state with a lesser degree of charge transfer for the main line that was proposed to be predominately $3s^13d^n$ in character [27, 28].

The electronic structures of a wide range of transition-metal compounds, including Cu, Ni, Co, Fe and Mn oxides and sulphides, were modelled by Bocquet

et al. [29] using a cluster-type configuration-interaction analysis of the core-level 2p X-ray photoemission spectra. Including the d–d exchange interaction (retaining only diagonal terms) and an anisotropic metal-ligand hybridization in the model reproduced these spectra reasonably well and was used to deduce quantitative values for the ligand-to-metal charge-transfer energy, the on-site d-d Coulomb repulsion energy, and the metal-ligand transfer integrals. Van Veenendaal and Sawatsky [30], however, showed that modelling of the Ni 2*p* peak-shape for NiO must include more than a single NiO_6 cluster due to non-local screening effects. A model using a Ni_7O_{36} cluster gave very good agreement with experimental data. Atanasov and Reinen [31] also included non-local electronic effects in their modelling of core-level photoemission, UV and optical electronic absorption spectra of nickel oxides. Ni 3*s* core-level line-shapes were presented by these authors and appear to have reasonable agreement with acquired spectra. Takahashi et al. [32] used ab initio calculations to model the electronic structure of NiO near the Fermi level. Their results are in good agreement with the experimental results obtained by photoelectron spectroscopy and Bremsstrahlung isochromat spectroscopy.

Grosvenor et al. [7] recently presented an analysis of the peak-shapes of Ni $2p_{3/2}$ in Ni metal, NiO, $Ni(OH)_2$ and NiOOH. In the Ni metal $2p_{3/2}$ spectrum, two peaks at 3.7 and 6 eV above the main peak were identified as plasmon loss peaks, in agreement with the original suggestion by Baer et al. [33]. Analysis of losses in EELS [34] and REELS spectra (using AES at low voltages) for plasmons and inter-band transitions corresponded to the satellite structures in Ni metal 2p spectra. This interpretation has been challenged by Karis et al. [35] using new high-kinetic-energy photoemission spectroscopy (HIKE), or hard X-ray photoelectron spectroscopy (HAXPES), in third generation synchrotron studies of Ni 1s (and 2p) spectra not previously accessible due to the lack of suitable excitation sources to reach this deep core level. The Ni 1*s* core electron binding energy of 8.33 keV is usually inaccessible using laboratory X-ray photoelectron spectrometers. These authors have found different satellite energies for the different core levels. The satellite positions are 4.0, 4.6, and 6.0 eV for the 1*s*, $2p_{1/2}$, and $2p_{3/2}$ core levels, respectively. The pronounced shell dependence is taken as evidence against the interpretation that the satellites are only due to plasmon losses. The Ni 2*p* core-level hard X-ray photoelectron spectrum presented in this study was obtained using an excitation energy of 6.030 eV with an electron inelastic mean-free path of the resulting Ni 2p photoelectron approaching 10 nm so that the surface contribution was consequently almost negligible in these measurements. The EELS and REELS spectra reported by others, however, only measured surface contributions [7, 34]. Hence, Karis et al. suggest that the difference in satellite energy can be described within the 3*d* shake-up model and that the shift of the 1*s* satellite is due to the difference in 1*s* core hole screening and localization [35].

Karis et al. have supported this interpretation with spectra calculated using a DFT configuration interaction model for the initial and final states as a mixture of $3d^8$, $3d^9$, and $3d^{10}$ configurations using the commonly accepted initial state of 16 $\% d^8$ + 47 $\% d^9$ + 37 $\% d^{10}$ as representation of the metallic nickel ground state [35]. The 1*s* core hole state is described by a configuration closer to the initial state

than the 2*p* core hole state. The measured and computed photoelectron spectra using the charge transfer multiplet theory compare very well. At the $2p_{3/2}$ and $2p_{1/2}$ edges, the computed satellite appears at 6.0 and 4.6 eV respectively, while at the 1*s* edge it appears at 4.0 eV coinciding with the experimental values.

For the Ni oxides and hydroxides, Grosvenor et al. [7] found that the. Ni 2p spectra from $Ni(OH)_2$ and NiOOH were fitted quite well to a Gupta and Sen [18, 19] multiplet line-shape. NiO, which shows a well resolved set of peaks, could only be satisfactorily fitted by a Gupta and Sen line-shape by allowing variation in the binding energy positions of the multiplet contributions to the main peak. For all three compounds, a broad peak associated with other intrinsic losses at a higher binding energy than the main peak multiplets had to be added to model the valley between the main peak and the satellite structures, as is consistent with the inter-band losses discussed in the extensive review by Hagelin-Weaver et al. [34, 36].

It has been pointed out in later work [37] that, at best, the use of Gupta and Sen's multiplet structures in empirical data can only be used with some adjustment of the multiplet features. That work used an ab initio calculation to model the many body effects of the *p*-shell photoelectron spectra of a free Cr(III) ion [37]. The results are reasonable but still do not exactly match the experimentally obtained line-shapes (cf. Fig. 10.3 in [37]). Modelling of the free Cr ion accounted for important features in the Cr $2p_{3/2}$ XPS spectrum of α-Cr_2O_3 including spin-orbit splitting energy [37]. However, the theory only accounts for the grossest features of the Cr 3*p* spectrum. Further refinements were deemed necessary [38], which included a previously neglected inter-atomic many body effect (the "frustrated Auger configuration (FAC)"). Its use affects the multiplet splitting and absolute binding energy and can also lead to new satellite structure. These results suggest that it is possible to model the multiplet envelope without explicitly including charge transfer from the ligands [38]. Application of the FAC, in this instance (intra-atomic) $3p3d \rightarrow 3s4f$, has also resulted in an extremely good simulation of the spectral intensities and spacing of the multiplet structures of Mn 3*s* XPS spectra [38]. It is proposed that analogous FAC events may also play an important role in the complete understanding of the XPS spectra of other transition metals.

Whereas there has been extensive theoretical examination of XPS spectra for metal oxides, for which only a selected few have been described here, very little theoretical examination of metal sulfide spectra has occurred. Conversely, metal sulfides have been relatively well characterised in XPS measurements due to their importance in geochemistry and minerals processing. The most common polymorph of iron disulfide (FeS_2) is pyrite, with space group $Pa\overline{3}$. Its crystal structure resembles face centered cubic rocksalt, where the Na and Cl sites are occupied by Fe ions and the center of gravity of the S anion pairs, respectively. As a consequence, the Fe atoms are situated at the centres of distorted octahedra. The bonding in pyrite is best described by d^2sp^3 hybridisation of the Fe valence orbitals, resulting in an octahedral coordination of the S atoms around the Fe atoms, with the S atoms tetrahedrally coordinated to three Fe atoms and one S atom. A considerable number

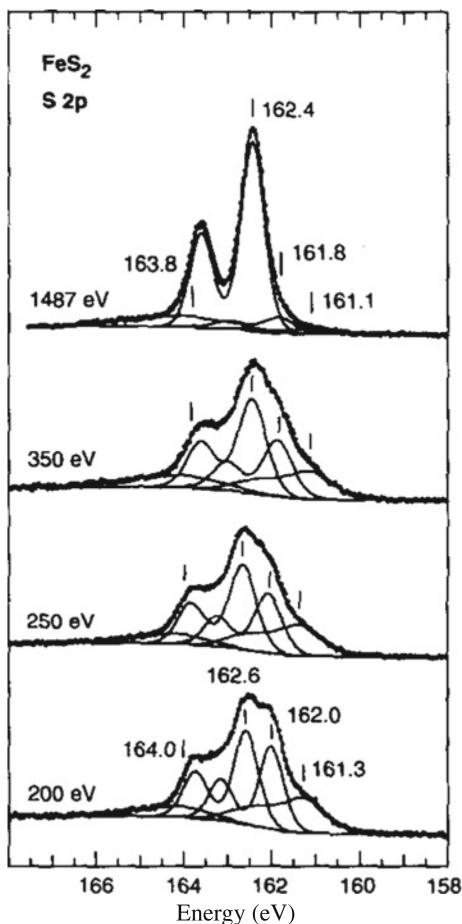

Fig. 10.3 S 2*p* XPS spectra from different incident energies. The fitted components are shown as *solid lines*. The components at 161.3 and 162.0 eV clearly decrease in relative intensity with increasing incident X-ray energy (Reprinted from [39] with permission from Elsevier)

of high-resolution XPS studies of pyrite have been made. Synchrotron radiation measurements have identified two S 2*p* doublets (with the S $2p_{3/2}$ peaks at 161.3 and 162.0 eV) that diminish on decreasing surface sensitivity (Fig. 10.3) [39]. These were initially attributed to the two S atoms in the disulfide ion closest to the surface. This theory, however, has been called into question with the alternate proposal that the 161.3 eV peak is due to S–S bond breakage [40].

The dominant Fe $2p_{3/2}$ line from pyrite is located at 707.2 eV with further higher BE components thought to be due to surface oxidation [40] although the dominant Fe peak has also been reported to be present at 706.7 eV [41]. Bulk and surface sensitive XPS spectra (using synchrotron radiation) have been recorded for Fe $2p_{3/2}$. The low spin bulk Fe^{2+} contribution was fitted by a single peak. It was proposed that both surface Fe^{2+} and Fe^{3+} high spin states existed (Fig. 10.4) [42]. Both were fitted in the manner suggested by Gupta and Sen [19], but the proposed

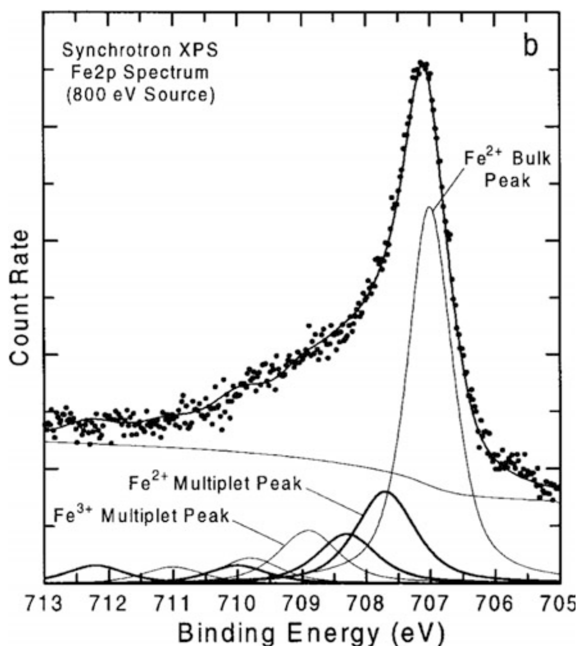

Fig. 10.4 Synchrotron Fe 2*p* spectra of pyrite showing the bulk low spin Fe^{2+} peak plus proposed high spin surface Fe^{2+} and Fe^{3+} multiplets (Reprinted from [42] with permission from the Mineralogical Society of America)

analogue of Cr^{5+} was used in the absence of the simulation for high spin Fe^{2+} [42]. This interpretation should be revisited in light of more sophisticated and accurate XPS simulations for transition metals in metal oxides.

10.2.2 Fitting of Spectra from First Row Transition Metals by Multiplet Envelopes

As was explained in previous sections, multiplet splitting arises when an atom contains unpaired electrons (e.g. Cr(III), $3p^6 3d^3$). When a core electron vacancy is created by photoionization, there can be coupling between the unpaired electron in the core with the unpaired electrons in the outer shell. This can create a number of final states, which will be seen in the photoelectron spectrum as a multi-peak envelope [2]. Figure 10.5 shows the multiplet structure associated with the Cr $2p_{3/2}$ peak for a vacuum fractured Cr_2O_3 specimen. The early Hartree-Fock calculation of the multiplet structure of core *p*-valence levels of free ion state first row transition metals by Gupta and Sen [19] graphically shows their multiplet structures (see Fig. 10.1 for examples). These calculations are an excellent starting point for the examination of multiplet structure observed for transition metal compounds. However, they apply to free ion states only and, in transition metals and their compounds, there may be ligand charge transfer effects that will change the spacing

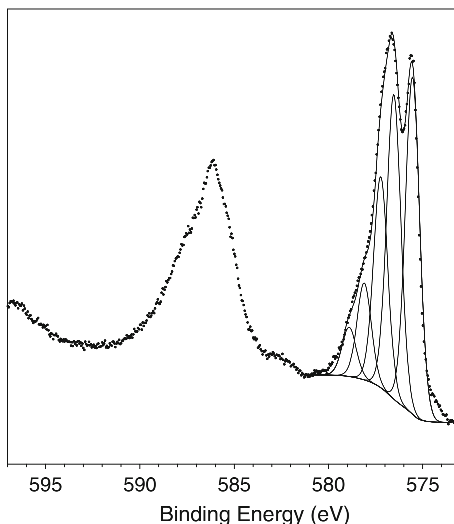

Fig. 10.5 Cr 2p XPS spectrum of a sample of vacuum cleaved Cr_2O_3

and intensity of the multiplet peaks present in their spectra. These relative changes can be utilized for transition metal compounds to differentiate those more closely approximating free ions from those in which charge transfer from the bonded neighbouring ions may have changed both the effective oxidation state and multiplet splitting of the core transition metal [5, 7, 9, 43]. This change in local electronic structure has been used to explain the differences between the XPS spectra of nickel oxide and its oxy/hydroxides [7].

Table 10.1 summarizes the various first-row transition metal (FRTM) species that show multiplet splitting in their XPS spectra. Spectra from Sc, Ti, V, Cu and Zn species generally do not exhibit multiplet splitting, but if it is present, then it is generally not well resolved or is observed as peak broadening. Cr, Fe, Mn, Co and Ni species show significant multilplet spitting. It will be shown in this Section that it is necessary to employ the entire peak-shape of the compounds under study to identify and quantify those species present in the analysis of samples containing a mix of species that show multiplet structure in their spectra (see for example Fig. 10.6 in Sect. 10.2.2.1).

Chemical state determination using XPS has become routine for most of the elements in the periodic table. Binding energy databases such as the NIST Database [44] or the Phi Handbook [2] generally provide sufficient data for the determination of the chemical state for uncomplicated (i.e., single peak) spectra. However, the M 2*p* spectra from the transition metals pose a number of problems that these databases do not adequately cover (e.g. multi-peak spectra with, specifically, shake-up structure, plasmon loss structure and multiplet splitting, all of which can complicate interpretation of the chemical states).

The starting point to using 2*p* spectra for determining the relative contributions of a transition metal in different oxidation states is to define the separation of the

Table 10.1 First row transition metal species that show multiplet splitting in their XPS spectra

e- (3d+4s)	0	1	2	3	3	4	4	5	5	6	6	7	7	8	8	9	9	10	10	11	12
Electronic Configuration	[Ar]	[Ar] 3d1	[Ar] 3d2	[Ar] 3d3	[Ar] 3d1 4s2	[Ar] 3d4	[Ar] 3d2 4s2	[Ar] 3d5	[Ar] 3d3 4s2	[Ar] 3d6	[Ar] 3d5 4s1	[Ar] 3d7	[Ar] 3d5 4s2	[Ar] 3d8	[Ar] 3d6 4s2	[Ar] 3d9	[Ar] 3d7 4s2	[Ar] 3d10	[Ar] 3d8 4s2	[Ar] 3d10 4s1	[Ar] 3d10 4s2
Sc	Sc(III)				Sc(0)																
Ti	Ti(IV)	Ti(III)	Ti(II)				Ti(0)														
V	V(V)	V(IV)	V(III)	V(II)					V(0)												
Cr	Cr(VI)		Cr(IV)	Cr(III)		Cr(II)					Cr(0)										
Mn	Mn(VII)	Mn(VI)		Mn(VI)		Mn(III)		Mn(II)					Mn(0)								
Fe								Fe(III)		Fe(II)*					Fe(0)						
Co										Co(III)		Co(II)					Co(0)				
Ni												Ni(III)		Ni(II)*					Ni(0)		
Cu																Cu(II)		Cu(I)		Cu(0)	
Zn																		Zn(II)			Zn(0)

This is for high spin compounds. For low spin Fe(II) and low spin Ni(II) electrons are paired and no multiplet splitting is observed

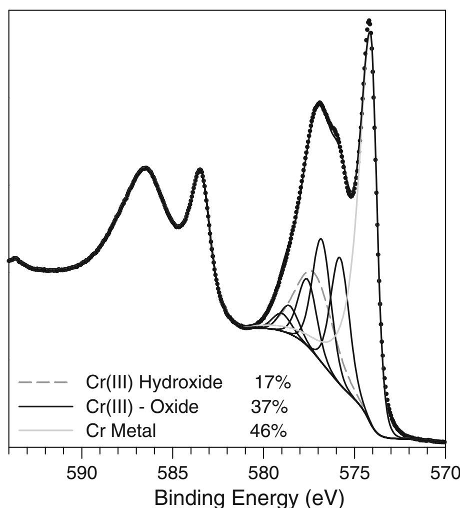

Fig. 10.6 An example of a Cr 2*p* spectrum fitted with parameters from Table 10.2. This spectrum is from a sample of a vacuum sputter deposited decorative chromium plated plastic and shows a thin layer of Cr_2O_3 and "$Cr(OH)_3$" (Adapted from [8])

$2p_{3/2}$ and $2p_{1/2}$ spin-orbit splitting. In many cases, this separation is large enough to consider only the more intense $2p_{3/2}$ signal with all of its structure, as the two spectral components are not overlapped. The databases attempt to assign oxidation states from the binding energy of the $2p_{3/2}$ signal assuming a single identifiable peak maximum. This assumption has been shown to be invalid for many transition metal spectra, e.g. Cr [43], Fe [5], and Ni [7]. Reviews of the current literature of XPS analysis of specific first-row transition metals (Cr, Mn, Fe, Co, Ni) are presented in the following sections to illustrate the uncertainties and complexities of interpretation of chemical states from XPS spectra, and how these spectra can be fitted by multiplet peaks to aid in the understanding of the chemistry of materials.

10.2.2.1 Chromium

A primary objective of the interpretation of Cr 2*p* XP spectra is usually to determine the relative percentages present of the 0, II, III, IV and VI oxidation states in order to follow oxidation processes. In the past, misinterpretation of Cr 2*p* spectra has occurred due to the complex multiplet splitting that occurs for Cr(III) compounds. Stypula and Stoch [45] misinterpreted the Cr(III) line shape and consequently identified both Cr^{3+} and "Cr^{n+} containing compounds". Desimoni et al. [46] presented a survey of Cr containing reference materials; however, all $2p_{3/2}$ peaks were fitted with a single peak of varying FWHM. The use of a single peak to represent the broad (non-symmetrical) peak shape of multiplet split Cr(III) species is used in numerous publications [47–51]. Halada and Clayton [52] and Grohmann et al. [53] attempted to use an asymmetric peak shape to model Cr(III) compounds. Halada and Clayton [52] have also analyzed a number of reference compounds including a prepared CrO_2 sample which was suggested to give rise to a single peak $2p_{3/2}$

binding energy at ≈575.2 eV. This appears to be contrary to accepted chemical shift theory which suggests that Cr(IV) species have a binding energy higher than that for Cr(III) species. Halada and Clayton also fitted a number of peaks in the spectra to various different species [52]. It is likely that some of these "species" would be more correctly interpreted as multiplet structure.

The poorer resolution of older XPS instruments may be one reason that a single peak shape has been taken to be of practical use. However, this may also play a part in misinterpretations of the species present. With newer generation instruments, the fine multiplet structure is more often well resolved and must be taken into account. Some earlier publications [54, 55] and most later publications [43] have recognized this and employ multiple peaks to represent the various Cr(III) peak shapes.

For most publications, curve fitting of the different chemical states is rarely attempted. However, previous work [43] has shown that systematic curve fitting of the various chemical states is possible provided suitable standard samples are examined and peak fitting parameters are fully reported. The work presented below based the fitting of the multiplet peak structures of well-resolved standard spectra on the theoretical modeling of Gupta and Sen [19].

Fitting parameters for Cr $2p_{3/2}$ spectra (Table 10.2) are based on spectra taken from a series of well-characterized standard compounds [8]. These fitting parameters have been slightly modified from those reported in previous work [43]. New analyses of Cr_2O_3 (powder), $FeCr_2O_4$ (chromite), $CoCr_2O_4$ and $NiCr_2O_4$ have been carried out and are incorporated here. Fitting parameters for Cr(0), Cr(III) oxide, Cr(III) hydroxide, and Cr(VI) components were determined and these take into account asymmetry in the metal peak, a broader envelope of peaks attributed to multiplet splitting of the Cr(III) compounds, and a single peak (no unpaired electrons) for Cr(VI) compounds. Cr(III) oxide shows discrete multiplet structure whereas the hydroxide shows only a broad peak shape. The asymmetry determined for the metal peak is based on spectra from an argon ion sputter cleaned pure metal surface. Quantification of Cr(VI) species (single peak at 579.5 eV from average of literature data, FWHM of 1.3–1.5 eV to incorporate a variety of Cr(VI) species; or 579.6 eV for a standard CrO_3 sample, FWHM of 1.3–1.4 eV) is complicated by the overlap with the multiplet splitting of Cr(III) species. This is likely to result in an increase in the detection limit for Cr(VI), when present in a matrix dominated by Cr(III), to around 10 % of the total Cr. Any contribution attributed to Cr(VI) below this value should be treated as below detection limits. An example of this type of fitting is presented in Fig. 10.6 which shows a Cr *2p* spectrum from a vacuum sputter-deposited Cr decorative coating. The percentage of the species present has been estimated from this fitting.

Fitting parameters for of $FeCr_2O_4$ (chromite) $CoCr_2O_4$, and $NiCr_2O_4$ can be incorporated into a fitting scheme when these compounds may be present. The corresponding Fe 2*p* or Co 2*p* or Ni 2*p* spectra should also indicate the presence of these compounds in the appropriate (stoichiometric) amounts. Due to the close overlap of peak positions and overall spectral shape for Cr_2O_3 and $FeCr_2O_4$, it is likely that meaningful separation by curve fitting of these two species requires extremely good spectral signal to noise [8].

Table 10.2 Cr $2p_{3/2}$ spectral fitting parameters: binding energy (eV), percentage of total area, FWHM value (eV) for each pass energy, and spectral component separation (eV) [8]

Compound	Peak 1 (eV)	%	Peak 2 (eV)	Δ Peak2 - Peak1 (eV) a)	%	Peak 3 (eV)	Δ Peak3 - Peak2 (eV)	%	Peak 4 (eV)	Δ Peak4 - Peak3 (eV)	%	Peak 5 (eV)	Δ Peak5 - Peak4 (eV)	%	FWHM, 10 eV Pass Energy	FWHM, 20 eV Pass Energy	
Cr(0)	574.2	100													0.80	0.90	b)
Cr(III) Oxide	575.7	36	576.7	1.01	35	577.5	0.78	19	578.5	1.00	8	578.9	0.41	5	0.88	0.94	c)
Cr(III) Hydroxide	577.3	100													2.58	2.60	d)
FeCr2O4 (Chromite)	575.9	41	577.0	1.09	39	577.9	0.88	13	578.9	1.04	7				1.12	1.20	
NiCr2O4	575.2	35	576.2	1.02	34	577.0	0.81	18	578.1	1.05	9	579.2	1.13	4	1.09		
Cr(VI) Mixed Species	579.5	100													1.40	1.50	e)
Cr(VI) Oxide	579.6	100													1.28	1.38	f)

a) Binding energies are significant to 0.1eV but an additional figure is added because energy splittings are much more accurate than the absolute binding energies.
b) Asymmetric peakshape and FWHM defined by standard chromium metal sample (LA(1.3,4,5))
c) FWHM for multiplet splitting single peaks can be estimated by metal FWHM
d) This BE value is for an aged hydroxide, freshly prepared hydroxide has a BE of 577.1 eV.
e) Binding energy from Literature average, broadened FWHM to incorporate a variety of Cr(VI) species
f) Binding energy and FWHM from standard CrO3 sample

10.2.2.2 Manganese

Manganese, having six stable oxidation states (0, II, III, IV, VI and VIII), three oxidation states with significant multiplet splitting (II, III, IV), one oxidation state with less defined splitting or broadening (VI), and overlapping binding energy ranges for these multiplet splitting structures presents a serious challenge for both qualitative and quantitative analysis. Oku et al. [56] published a series of spectra of a variety of manganese oxide species. These spectra show excellent peak structure and are useful for qualitative assignment of Mn oxidation states. Some discussion of multiplet splitting is presented with some prominent peak binding energy values reported, but no attempt at fitting of these structures was made.

Nesbitt and Banerjee have used curve fitting of Mn $2p_{3/2}$ spectra, based on the multiplet splitting proposed by Gupta and Sen [19] to interpret MnO_2 precipitation [57] and reactions on birnessite ($MnO_{1.7}(OH)_{0.25}$ or $MnO_{1.95}$) mineral surfaces [58–60]. These papers provide excellent detail of FWHM values, multiplet splitting separations and peak weightings for easy reproduction of their curve fitting procedure.

Fitting parameters for recent spectra [8] of the metal and powder standards MnO, Mn_2O_3, MnO_2, K_2MnO_4 and $KMnO_4$, are presented in Table 10.3 with spectra for these standards given in Fig. 10.7. Fittings from in-vacuum fractured minerals specimens of manganite (MnOOH) and pyrolusite (MnO_2) are also presented. The asymmetric Mn $2p_{3/2}$ main metal peak is found at 638.64 ± 0.06 eV with a $2p_{3/2}$ to $2p_{1/2}$ splitting of 11.10 ± 0.02 eV. This compares well to a NIST database average of 639.7 ± 1.0 eV and 11.15 ± 0.15 eV. Recent work [61] at the UE56/2-PGMI beamline at BESSY (synchrotron radiation facility) has shown a well resolved second peak at ≈1 eV above the main peak which is attributed to an intra-atomic multiplet effect associated with Mn atoms with a large local moment. This peak is also visible in the well resolved XPS spectrum shown in Fig. 10.7. It is fitted with a similar asymmetric peak shape as for the main peak, with an area of around 15 % of the main peak.

Mn_2O_3 has a Mn $2p_{3/2}$ spectrum similar in binding energy range to MnOOH. The peak shape is slightly different for Mn_2O_3 which shows a small higher binding energy peak at 646.2 eV. Fitting parameters (Table 10.3) for MnOOH are similar to those from Nesbitt and Banerjee [57–60]. The Mn $2p_{3/2}$ spectrum from MnO_2 is fitted with 6 peaks of equal FWHM, compared to 5 peaks used by Nesbitt and Banerjee [57–60]. This is likely to be due to the much better instrument resolution used for the more recent analysis of this sample. As expected, vacuum fractured pyrolusite has a similar spectrum to the MnO_2 powder sample. Peak FWHM values are slightly greater (0.92 eV and 0.99 eV at 10 eV and 20 eV pass energies) and the relative concentration of Mn^{3+} is increased as well (≈10 % Mn^{3+} in MnO_2 powder and ≈15 % in pyrolusite). The small peak at the lower binding energy region of the spectra for both MnO_2 and pyrolusite can be shown to be a Mn^{3+} component and not part of the MnO_2 multiplet structure. Calculated spectra [19] do not show this peak and the relative peak intensity changes between the two samples. A timed analysis of MnO_2 powder has shown that while MnO_2 is relatively stable in the incident X-ray beam (Al Kα 15 mA, 14 kV), the Mn^{3+} peak does grow from 6 to

Table 10.3 Mn $2p_{3/2}$ spectral fitting parameters: binding energy (eV), percentage of total area, FWHM value (eV) for each pass energy, and spectral component separation (eV) [8]

Compound	Peak 1 (eV)	%	Peak 2 (eV)	∆ Peak2 - Peak1 (eV) a)	%	Peak 3 (eV)	∆ Peak3 - Peak2 (eV)	%	Peak 4 (eV)	∆ Peak4 - Peak3 (eV)	%	Peak 5 (eV)	∆ Peak5 - Peak4 (eV)	%	Peak 6 (eV)	∆ Peak6 - Peak5 (eV)	%	FWHM, 10 eV Pass Energy	FWHM, 20 eV Pass Energy	
Mn(0)	638.6	87.0	639.6	1.00	13.0													0.74	0.79	b)
Mn(II) MnO	640.2	24.0	641.1	0.97	27.8	642.1	0.93	22.1	643.0	0.95	12.5	644.2	1.14	4.7	645.9	1.75	9.1	1.21	1.23	c)
Mn(III) Mn2O3	640.8	18.9	641.9	1.10	44.5	643.1	1.27	25.3	644.6	1.50	8.5	646.2	1.62	3.1				1.65	1.75	
Mn(III) Manganite (MnOOH)	641.0	24.0	641.7	0.70	24.0	642.5	0.81	27.8	643.5	1.02	17.5	644.9	1.37	6.7				1.34	1.35	
Mn(IV) MnO2	641.9	41.7	642.7	0.86	26.5	643.4	0.70	15.5	644.2	0.75	9.1	645.0	0.85	4.9	646.0	1.00	2.5	0.84	0.91	
Mn(IV) Pyrolusite (MnO2)	641.8	41.0	642.7	0.87	27.4	643.5	0.75	16.1	644.3	0.81	8.9	645.2	0.91	4.6	646.2	1.03	2.1	0.92	0.99	
Mn(VI) K2MnO4	643.8	100.0																1.31	1.40	
Mn(VII) KMnO4	645.5	100.0																0.98	1.08	

a) Binding energies are significant to 0.1eV but an additional figure is added because energy splittings are much more accurate than the absolute binding energies.
b) Both peaks have an asymmetric peakshape and FWHM defined by standard manganese metal sample (LA(1.1,3.2,3))
c) Peak 6 is a shake-up peak with FWHM of 3.5 eV (at both pass energies)

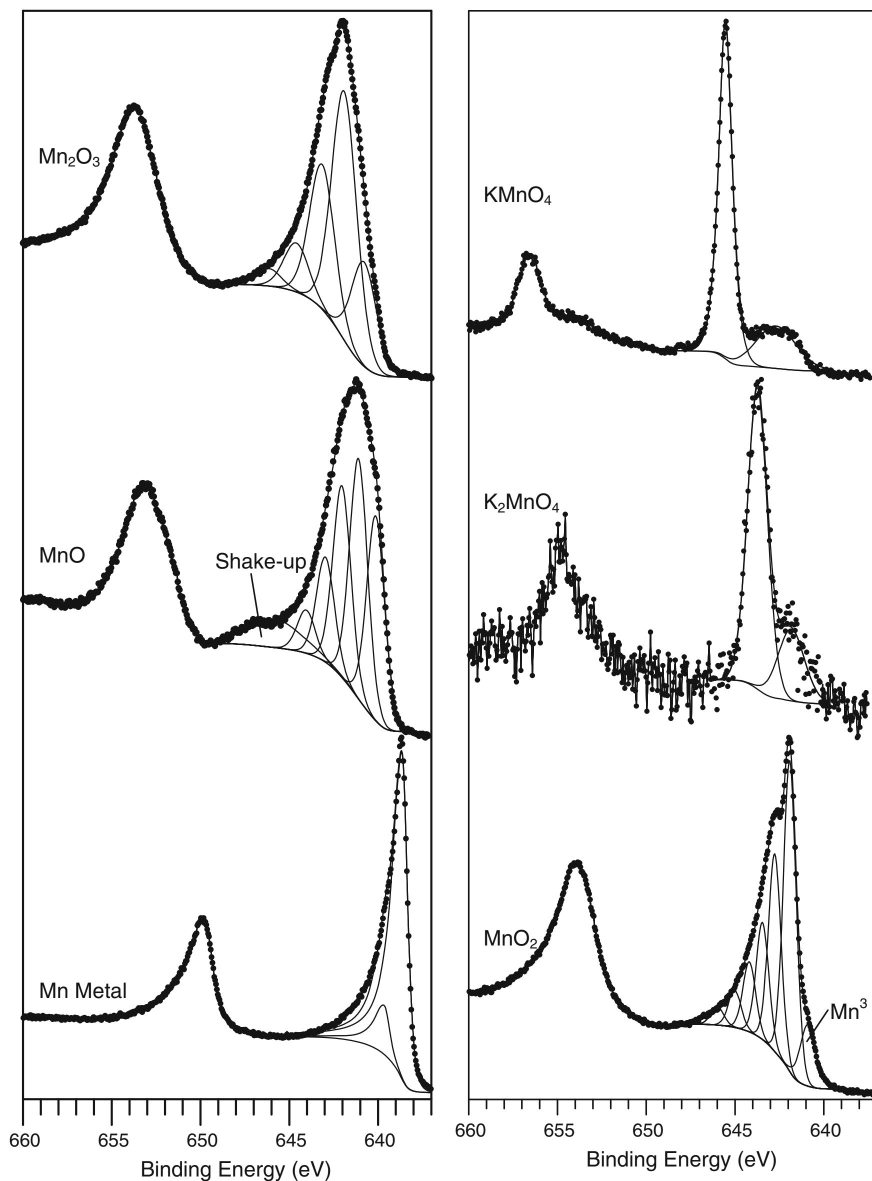

Fig. 10.7 Mn 2*p* spectra for (*left*, *bottom*) Mn metal, (*left*, *middle*) MnO, (*left*, *top*) Mn_2O_3, (*right*, *bottom*) MnO_2, (*right*, *middle*) K_2MnO_4, and (*right*, top) $KMnO_4$ (Reprinted from [8] with permission from Elsevier)

14 % of the total spectrum after 48 h of X-ray exposure. K_2MnO_4 gives rise to a slightly broadened peak (FWHM of 1.31 eV and 1.40 eV at 10 eV and 20 eV pass energies) at 634.8 eV compared to $KMnO_4$ (0.98, 1.08 eV) at 645.5 eV.

10.2.2.3 Iron

Peak shape and peak binding energy comparisons to standard compounds can be used to derive oxide composition for the analysis of photoelectron spectra of relatively pure iron oxides. McIntyre and Zetaruk's [9] paper is widely cited and is still an excellent starting point for qualitative iron oxide determination. A comparison of peak shapes to the theoretically calculated multiplet split peak shapes from Gupta and Sen [19] are discussed with relatively good agreement found. Pratt et al. [62] used a series of multiplet peaks to curve fit oxidized iron sulfide (pyrrhotite) surfaces. However, Lin et al. [63] used broad peak shapes instead to quantify Fe(0), Fe (II) and Fe(III) components in a series of thin oxide films. The authors used the shake-up satellites as approximate guides for the positioning of the main 2*p* peaks.

Grosvenor et al. [5] fitted the various iron oxide, hydroxide, and halide peak shapes with a close approximation to the Gupta and Sen [19] multiplet structure. Multiplet FWHM, peak splitting energies, and weightings are presented in this work. An analysis of satellite to main peak separation is also given. All Fe(II) (high spin only as low spin Fe(II) does not exhibit multiplet splitting) and Fe(III) species can be fitted with Gupta and Sen multiplet structures. Variation in peak spacing and intensity occur for different ligands. Broad satellite peaks of varying intensities at binding energies above the main Fe $2p_{3/2}$ structure are present in the spectra for all high spin compounds. However, this paper [5] only presents the main multiplet lines, excluding the details needed to fit the broader higher binding energy satellite structures.

Table 10.4 presents full fitting parameters including the multiplet and satellite structure [8]. A Shirley background encompassing only the $2p_{3/2}$ portion of the spectrum was used for these fits. Also included in Table 10.4 are new spectral fitting parameters for $FeCr_2O_4$ and $NiFe_2O_4$, species that are important for the examination of oxide films on Fe–Cr–Ni alloys, as well as data for new analyses of α-Fe_2O_3 and γ-Fe_2O_3. Fitting parameters for $FeCO_3$, which has been noted in certain corrosion products, are also presented in Table 10.4.

While these values and reference spectra [6–8] are useful for identification of pure oxide or oxy-hydroxide species, curve fitting of mixed systems quickly becomes complicated due to spectral overlap. For example, it can be seen that various Fe(III) compounds have a similar range of Fe 2*p* binding energies and vary mostly in peak shape and satellite intensities. Any attempt at fitting two or more Fe (III) species to a spectrum will consequently contain an inherent degree of error. As well, overlap of the Fe(III) satellite structure with the Fe(0) and Fe(II) Fe $2p_{1/2}$ portion of the spectrum will result in setting the higher binding energy background endpoint placement at a point that will not cover the satellite structure of the Fe(III) species. This will require any fitting of mixed chemical state systems containing Fe(III) species to omit the higher binding energy Fe(III) satellite from the envelope of peaks, which will increase the error associated with the curve fitting. The fitting of a spectrum from pure Fe_3O_4 will also need to omit the higher binding Fe(III) energy satellite contribution as is reflected in the values presented in Table 10.4. Finally, determination of the Fe species present, especially in a mix of Fe(III)

Table 10.4 Fe $2p_{3/2}$ spectral fitting parameters: binding energy (eV), percentage of total area, FWHM value (eV) and spectral component separation (eV) [8]

Compound	Peak 1 (eV)	FWHM, 10 eV Pass Energy	%	Peak 2 (eV)	∆ Peak2 - Peak1 (eV) a)	FWHM, 10 eV Pass Energy	%	Peak 3 (eV)	∆ Peak3 - Peak2 (eV)	FWHM, 10 eV Pass Energy	%	Peak 4 (eV)	∆ Peak4 - Peak3 (eV)	FWHM, 10 eV Pass Energy	%	Peak 5 (eV)	∆ Peak5 - Peak4 (eV)	FWHM, 10 eV Pass Energy	%	Peak 6 (eV)	∆ Peak6 - Peak5 (eV)	FWHM, 10 eV Pass Energy	%	
Fe(0)	706.6	0.88	100.0																					b)
FeO	**708.4**	**1.4**	**24.2**	**709.7**	**1.3**	**1.6**	**30.1**	**710.9**	**1.2**	**1.6**	**14.5**	**712.1**	**1.2**	**2.9**	**25.6**	**715.4**	**3.3**	**2.5**	**5.6**					
α-Fe2O3	709.8	1.0	26.1	710.7	0.9	1.2	22.0	711.4	0.7	1.2	17.4	712.3	0.9	1.4	11.1	713.3	1.0	2.2	14.8	719.3	6.0	2.9	8.6	
γ-Fe2O3	709.8	1.2	27.4	710.8	1.0	1.3	27.4	711.8	1.0	1.4	20.3	713.0	1.2	1.4	9.1	714.1	1.1	1.7	5.1	719.3	5.2	2.2	10.0	
Ave. Fe2O3	**709.8**	**1.1**	**26.8**	**710.8**	**1.0**	**1.3**	**24.7**	**711.6**	**0.8**	**1.3**	**18.9**	**712.7**	**1.1**	**1.4**	**10.1**	**713.7**	**1.1**	**2.0**	**10.0**	**719.3**	**5.6**	**2.6**	**9.3**	
Std. Dev.	0.0	0.1	0.9	0.1	0.1	0.1	3.8	0.3	0.2	0.1	2.1	0.5	0.2	0.0	1.4	0.6	0.1	0.4	6.9	0.0	0.6	0.5	1.0	
α-FeOOH	710.2	1.3	26.7	711.2	1.0	1.2	25.3	712.1	0.9	1.4	21.0	713.2	1.1	1.4	12.1	714.4	1.2	1.7	7.2	719.8	5.4	3.0	7.7	
γ-FeOOH	710.3	1.4	27.3	711.3	1.0	1.4	27.6	712.3	1.0	1.4	20.1	713.3	1.0	1.4	10.5	714.4	1.1	1.8	5.4	719.5	5.1	2.8	8.9	
Ave. FeOOH	**710.3**	**1.4**	**27.0**	**711.3**	**1.0**	**1.3**	**26.5**	**712.2**	**0.9**	**1.4**	**20.6**	**713.3**	**1.1**	**1.4**	**11.3**	**714.4**	**1.1**	**1.8**	**6.3**	**719.7**	**5.3**	**2.9**	**8.3**	
Std. Dev.	0.1	0.1	0.4	0.1	0.0	0.1	1.6	0.1	0.1	0.0	0.6	0.1	0.1	0.0	1.1	0.0	0.1	0.1	1.3	0.2	0.2	0.1	0.8	
Average Fe(III)	**710.0**	**1.2**	**26.9**	**711.0**	**1.0**	**1.3**	**25.6**	**711.9**	**0.9**	**1.4**	**19.7**	**713.0**	**1.1**	**1.4**	**10.7**	**714.1**	**1.1**	**1.9**	**8.1**	**719.5**	**5.4**	**2.7**	**8.8**	
Std. Dev.	0.3	0.2	0.6	0.3	0.0	0.1	2.6	0.4	0.1	0.1	1.6	0.5	0.1	0.0	1.3	0.5	0.1	0.2	4.5	0.2	0.4	0.4	0.9	
Fe3O4 2+	708.4	1.2	16.6	709.2	0.8	1.2	14.8																	d)
Fe3O4 3+	710.2	1.4	23.7	711.2	1.0	1.4	17.8	712.3	1.1	1.4	12.2	713.4	1.1	1.4	5.7	714.5	1.1	3.3	9.1	c)				d)
FeCr2O4 (Chromite)	709.0	2.0	40.5	710.3	1.2	1.5	12.9	711.2	0.9	1.5	17.8	712.3	1.2	1.5	8.3	713.8	1.4	3.6	20.6					e)
NiFe2O4	709.5	2.0	34.1	710.7	1.3	2.0	33.2	712.2	1.4	2.0	22.3	713.7	1.6	2.0	10.4									
FeCO3 (Siderite)	709.8	1.5	24.3	711.1	1.3	1.5	13.2	712.0	0.9	3.6	41.9	715.6	3.6	3.4	20.0	719.4	3.8	1.5	0.70					

a) Binding energies are significant to 0.1eV but an additional figure is added because energy splittings are much more accurate than the absolute binding energies.

b) Asymmetric peakshape and FWHM defined by standard iron metal sample (LA(1.2,4.8,3))

c) Satellite structure for 3+ though likely present will be buried under Fe 2+ Fe 2p1/2 portion of spectrum

d) Sum of 2+ and 3+ areas is 100

e) Taken with a 20 eV pass energy

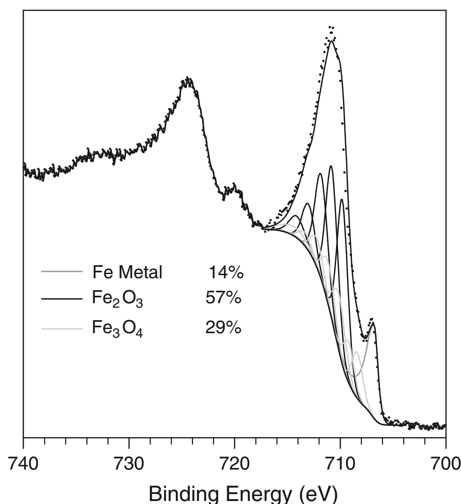

Fig. 10.8 Curve fitted Fe 2*p* spectrum of a mixed metal/oxide system of Fe based nano-particles dispersed on a glass substrate (Adapted from [8])

species, should include corroborating evidence from O 1*s* analysis and even other analytical techniques such as Raman spectroscopy or, for thin crystalline films, grazing angle X-ray diffraction (XRD).

Figure 10.8 presents an example of curve fitting of a mixed iron metal/oxide nano-particle system dispersed on a glass substrate. The resulting fit suggests a mix of metal, Fe_3O_4, and Fe_2O_3 components. The higher binding energy satellite peaks for Fe_2O_3 are omitted from the fitting, as are the assumed satellites for the Fe_3O_4 components. This will effectively cause a slight overestimation of the metal compared to the two oxide components. The O 1*s* spectrum confirmed that the bulk of the O was present as a lattice oxide with only a small amount of hydroxide-like O being detected.

Figure 10.9 shows spectra of two polished carbon steel surfaces with electrochemically grown oxide (2.5 h, −0.2 V vs. SCE, pH 10.6, borate buffer solution) that was treated with a 24 h bath of (A) 10^{-3} M and (B) 10^{-5} M H_2O_2 [8]. To determine the most representative Fe speciation, the spectra were fitted with a variety of components. The peak fit residuals were examined after fitting with the metal component as well as the following species: (1) FeO, γ-Fe_2O_3, and FeOOH (average of two species), residuals of 4.28 and 3.79, for A and B respectively; (2) Fe_3O_4 and γ-Fe_2O_3, residuals of 5.52 and 4.77; (3) Fe_3O_4 and Fe(III) average, residuals of 5.80 and 4.68; (4) FeO and γ-Fe_2O_3, residuals of 4.98 and 6.62; (5) Fe_3O_4, γ-Fe_2O_3 and FeOOH (average of two species), residuals of 4.61 and 4.02; (6) Fe_3O_4 and FeOOH (average of two species), residuals of 15.51 and 11.46; and (7) FeO, α-Fe_2O_3 and FeOOH (average of two species), residuals of 5.26 and 4.44. This iterative approach suggests that the best fit is found using a mix of FeO, γ-Fe_2O_3 and FeOOH components and is consistent with corrosion potential (E_{CORR}) results [64] on these surface layers where maghemite, rather than hematite, is implied. The error in the quantitation of this fit is likely to be large but complex

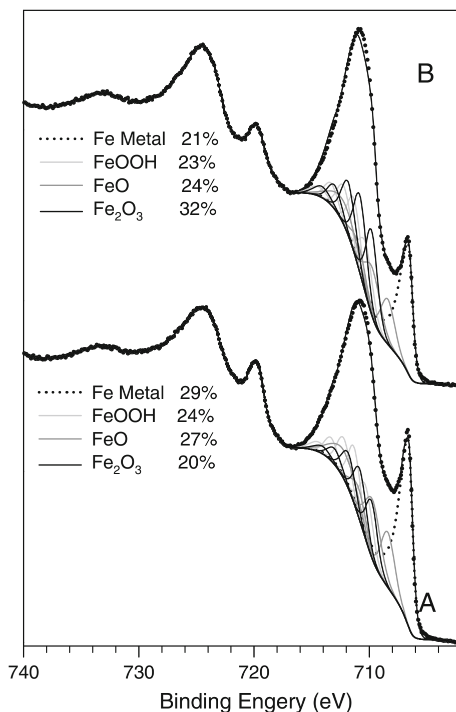

Fig. 10.9 Curve fitted Fe 2*p* spectra of two similar samples of polished carbon steel surfaces with an electrochemically grown surface oxide (2.5 h, −0.2 V vs. SCE, pH 10.6, borate buffer solution) that has been treated with a 24 h bath of (*A*) 10^{-3} M and (*B*) 10^{-5} M H_2O_2 (Adapted from [8])

fitting is still useful when comparisons of multiple samples with similar preparations are made (as is done here). An analysis of the O 1*s* spectra revealed that an increase in lattice oxide as compared to hydroxide is seen for sample A as compared to sample B, in agreement with the trend seen in the Fe $2p_{3/2}$ spectra.

Compared to the other transition metal species studied here, the complex multiple species fitting of Fe is the most problematic. With so many possible species having overlapping binding energies, erroneous interpretation can result. A sample with two distinct species can likely be fitted accurately, three species much less so, while four or more species must be looked at as indicative but unreliable. It is worth stating that corroborating evidence is desirable for this type of Fe surface chemical state speciation.

10.2.2.4 Cobalt

There appear to be few instances of good quality high-resolution Co 2*p* spectra presented in the literature. Fitting appears to be inconsistent with generally only a qualitative approach to the analysis of the spectral changes reported. Fitting of a broad main peak combined with a portion of the satellite structure has been one approach [65, 66] although fitting parameter details are not presented in enough detail to emulate. Recent work [67] has proposed that the satellite structure in the

Co metal (and CoP; cobalt phosphide) spectra is a result of plasmon loss, although this interpretation may need to be revisited considering the more recent analysis of the satellite structure in HAXPES Ni 2p spectra from Ni metal [35]. In the recent study of the Co metal spectrum, it was fitted with an asymmetric main peak and two plasmon loss peaks at 3.0 and 5.0 eV above the main peak, which constitutes the surface and bulk plasmons, respectively, with FWHM values of 3.0 eV in both cases [67].

Obtaining a pure CoO specimen can be problematic. Initial analysis of a commercial CoO sample by one of the authors of this chapter showed the surface to be extensively oxidized to Co_3O_4 even though the bulk powder XRD spectrum showed only CoO. This appears to be a common problem with two published databases [2, 68] showing similar Co_3O_4 oxidized surfaces for CoO. Attempts to reduce this surface oxide by heating the sample to 950 °C (4 h) under argon were unsuccessful. A second sample purchased from the same supplier contained larger lumps of the compound that when ground by mortar and pestle and analyzed by XPS gave spectra that were more consistent with literature results. To confirm this, spectra from three different literature sources [69–71] were digitized, curve fitted, and compared to these results. The areas of the main peak centered at ≈780 eV relative to the satellite peak at ≈786 eV were compared and were shown to be equivalent. The results presented in this work show significantly better resolution than previous work using non-monochromatic sources [69–72] and/or older spectrometers [73].

Co metal, CoO, $Co(OH)_2$ and Co_3O_4 spectra are presented in Fig. 10.10 with spectral fitting parameters given in Table 10.5. Fitting parameters for CoOOH from a fit of a digitized spectrum from the recent work of Yang et al. [74] are also presented, as are parameters for a new analysis of $CoCr_2O_4$. As for Fe, the binding energy overlap of the various oxide and hydroxide forms will greatly increase the absolute error in speciation quantitation. However, curve fitting procedures such as those presented here should be useful for a more meaningful interpretation for a series of similar Co containing samples. A second concern is the overlap of the higher binding energy $2p_{3/2}$ multiplet or satellite structures of the various oxides and hydroxides with the metal $2p_{1/2}$ peak at 793.1 eV. This overlap, when the metal is present, requires the use of an offset for the higher binding energy background endpoint similar to that used for Ni as described previously [75] and in the next section.

10.2.2.5 Nickel

There is a large body of work based on the use of XPS to examine nickel surfaces, nickel oxides, and nickel alloys [76–79]. Varying methods of chemical state identification are used with moderate to good success. McIntyre et al. [80] presented line-shapes of standard NiO and $NiFe_2O_4$ which were then used to study Inconel 600 alloys under very mild oxidation conditions. Matienzo et al. [81] presented a survey of analyses of numerous nickel compounds (including a large

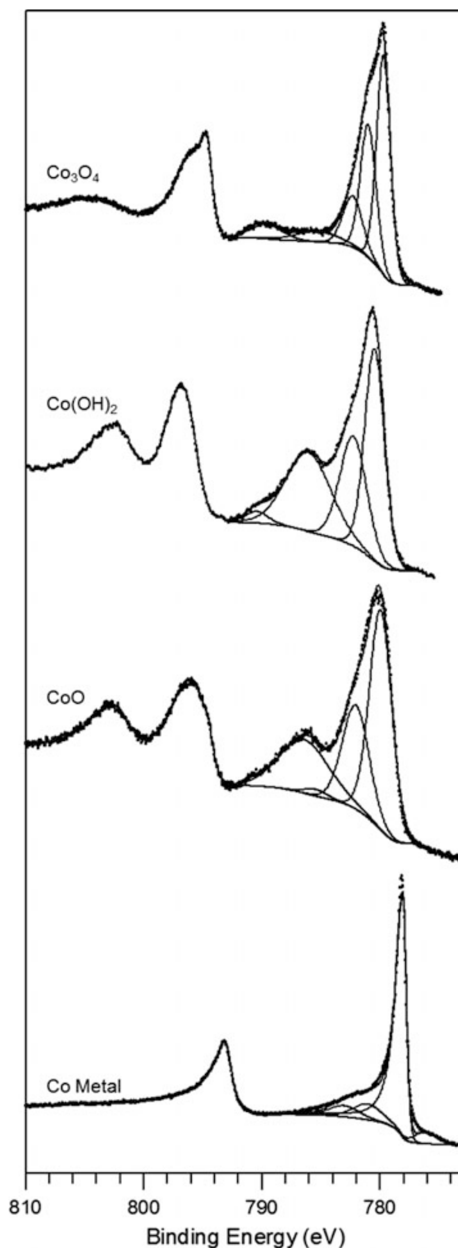

Fig. 10.10 Co 2p spectra for (*bottom* to *top*) Co metal, CoO, $Co(OH)_2$ and Co_3O_4 (Reprinted from [8] with permission from Elsevier)

number of nickel complexes) and gave single peak positions for both the $2p_{3/2}$ and $2p_{1/2}$ peaks.

Roberts and Smart [82] investigated changes in the defect structure of NiO surfaces by XPS. Changes in the O 1*s* and Ni 2*p* spectra were followed after heat

Table 10.5 Co $2p_{3/2}$ spectral fitting parameters: binding energy (eV), percentage of total area, FWHM value (eV) for each pass energy, and spectral component separation (eV) [8]

Compound	Peak 1 (eV)	%	Peak 1 FWHM, 10 eV Pass Energy	Peak 1 FWHM, 20 eV Pass Energy	Peak 2 (eV)	Δ Peak2 - Peak1 (eV) a)	%	Peak 2 FWHM, 10 eV Pass Energy	Peak 2 FWHM, 20 eV Pass Energy	Peak 3 (eV)	Δ Peak3 - Peak2 (eV)	%	Peak 3 FWHM, 10 eV Pass Energy	Peak 3 FWHM, 20 eV Pass Energy	Peak 4 (eV)	Δ Peak4 - Peak3 (eV)	%	Peak 4 FWHM, 10 eV Pass Energy	Peak 4 FWHM, 20 eV Pass Energy	Peak 5 (eV)	Δ Peak5 - Peak4 (eV)	%	Peak 5 FWHM, 10 eV Pass Energy	Peak 5 FWHM, 20 eV Pass Energy	
Co(0)	778.1	81.0	0.70	0.75	781.1	3.00	11.0	3.00	3.00	783.1	2.0	8.0	3.00	3.00											b)
CoO	780.0	46.6	2.23	2.24	782.1	2.10	25.7	2.59	2.66	785.5	3.40	1.6	2.42	2.29	786.5	1.00	26.1	5.28	4.98						
Co(OH)2	780.4	38.1	2.01	2.04	782.2	1.80	26.6	2.60	2.55	786.0	3.79	33.0	4.47	4.47	790.4	4.40	2.4	2.33	2.33						
CoOOH	780.1	61.4		1.48	781.4	1.32	24.5		1.48	783.1	1.68	5.2		1.48	790.1	7.07	8.9		3.30						c)
Co3O4	779.6	40.5	1.38	1.39	780.9	1.30	29.1	1.55	1.62	782.2	1.30	15.2	1.94	2.18	785.2	3.00	8.1	4.28	4.44	789.5	4.30	7.2	3.15	3.29	

a) Binding energies are significant to 0.1eV but an additional figure is added because energy splittings are much more accurate than the absolute binding energies.
b) Asymmetric peakshape (Peak 1) and FWHM defined by standard cobalt metal sample LA(1.2,5,5), LMM B Auger peak seen at 766.2 eV, 2.2 eV FWHM
c) From a fit of a digitized copy from reference 54.

treatment. A Ni $2p_{3/2}$ peak at 856.1 eV was attributed to the presence of Ni(III) species. Carley et al. [83] showed that Ni(III) species can be found within a potassium doped Ni(110)-O surface. Moroney et al. [84] studied the thermal decomposition of β-NiO(OH) and 'nickel peroxide'. They concluded that the two compounds are chemically identical, as both convert in vacuum to defective NiO at 773 K (500 °C).

Grosvenor et al. [7] presented an initial investigation of the multiplet splitting structure of $Ni(OH)_2$, NiOOH and NiO Ni 2*p* spectra as well as the plasmon loss structure associated with the metal Ni 2*p* spectrum. $Ni(OH)_2$ and NiOOH were found to be fitted quite well to a Gupta and Sen multiplet line-shape [7, 19]. NiO, which shows a well resolved set of peaks, could only be satisfactorily fitted with a Gupta and Sen line-shape by allowing variation in the binding energy positions of the multiplet contributions to the main peak [7].

For much of the earlier work, the importance of multiplet splitting and satellite structure in the interpretation of the Ni 2*p* line shape was understood but limited models for fitting these structures were available as reviewed in Sect. 10.2.1 [80, 85]. Recent experimental and theoretical advances have considerably improved the fitting process. Recent publications [7, 8, 75] summarize some of the important milestones in these works which will not be duplicated here; however, the curve fitting method [8, 75] will be summarized. This recent work [75, 86], and other works [83, 87], shows how spectral subtraction using quality reference spectra can be used to identify small amounts of Ni(III) within the complex spectral profile of NiO in thin oxide films.

These curve fitting techniques use specified empirical fitting parameters that take into account the unique peak shapes of the various Ni compounds. Spectra are fitted with the asymmetric line shape and plasmon loss peaks for Ni metal and an empirical fit of the NiO and $Ni(OH)_2$ line shapes from parameters derived from standard samples (Table 10.6). The binding energy differences, FWHM, and area ratios were constrained for each species. The absolute binding energy values were allowed to vary by ±0.1 eV to allow for error associated with charge referencing to adventitious C 1*s*. Overlap of the high binding energy satellite structure from Ni $(OH)_2$ (and to a lesser extent NiO) with the $2p_{1/2}$ metal peak, which is composed of an asymmetric main peak and contributions from plasmon loss structure, can make the definition of an appropriate spectral background using only the $2p_{3/2}$ portion of the spectrum problematic. This work has shown that a Shirley-type background applied across the entire 2*p* ($2p_{3/2}$ and $2p_{1/2}$) portion of the spectrum works reasonably well (even though fitting of only the $2p_{3/2}$ portion of the spectrum is carried out). In many cases, an offset of the higher binding energy end of the background can be used to improve the fit of the peak shapes. The appropriate background offset is determined using an iterative approach while monitoring a residual plot of the $2p_{3/2}$ area. It is necessary during spectral acquisition to use a window of sufficient width (848.0–890.0 eV) to accurately assess the end of the Ni $2p_{1/2}$ envelope for positioning of the background endpoint. Examples of fitted spectra are presented in Fig. 10.11.

Table 10.6 Ni $2p_{3/2}$ spectral fitting parameters: binding energy (eV), percentage of total area, FWHM value (eV) for each pass energy, and spectral component separation (eV) [8]

Compound	Peak 1 (eV) a)	%	Peak 1, FWHM, 10 eV Pass Energy	Peak 1, FWHM, 20 eV Pass Energy	Peak 2 (eV)	Δ Peak2 - Peak1 (eV) a)	%	Peak 2, FWHM, 10 eV Pass Energy	Peak 2, FWHM, 20 eV Pass Energy	Peak 3 (eV)	Δ Peak3 - Peak2 (eV)	%	Peak 3, FWHM, 10 eV Pass Energy	Peak 3, FWHM, 20 eV Pass Energy	Peak 4 (eV)	Δ Peak4 - Peak3 (eV)	%	Peak 4, FWHM, 10 eV Pass Energy	Peak 4, FWHM, 20 eV Pass Energy	
Ni Metal from [5]	852.6	79.6	1.00	1.02	856.3	3.65	5.6	2.48	2.48	858.7	2.38	14.8	2.48	2.48						b) d)
Ni Metal - New Line Shape	852.6	81.2	0.94	0.95	856.3	3.65	6.3	2.70	2.70	858.7	2.38	12.5	2.70	2.70						c) d)
NiO	853.7	14.3	0.98	1.02	855.4	1.71	44.2	3.20	3.25	860.9	5.44	34.0	3.85	3.76	864.0	3.10	3.6	1.97	2.04	
Ni(OH)2	854.9	7.4	1.12	1.16	855.7	0.77	45.3	2.25	2.29	857.7	2.02	3.0	1.59	1.59	860.5	2.79	1.4	1.06	1.06	
Gamma NiOOH	854.6	13.8	1.40		855.3	0.70	12.4	1.50		855.7	0.36	9.7	1.40		856.5	0.78	20.7	1.40		
Beta NiOOH (3+ Portion)	854.6	9.2	1.40		855.3	0.70	8.3	1.50		855.7	0.36	6.4	1.40		856.5	0.78	13.8	1.40		e)
Beta NiOOH (2+ Portion)	854.9	2.5	1.12		855.7	0.77	15.1	2.25		857.7	2.02	1.0	1.59		860.5	2.79	0.5	1.06		e)
NiCr2O4	853.8	7.0	1.22	1.30	855.8	1.95	20.5	1.82	1.86	856.5	0.71	24.7	3.91	3.81	861.0	4.50	2.3	1.27	1.33	
NiFe2O4	854.5	17.3	1.35	1.36	856.0	1.52	38.2	3.03	2.98	861.4	5.41	38.5	4.49	4.50	864.7	3.29	2.8	3.04	3.01	

Table 10.6 (continued)

Compound	Peak 5 (eV)	Δ Peak5 - Peak4 (eV)	%	Peak 5, FWHM, 10 eV Pass Energy	Peak 5, FWHM, 20 eV Pass Energy	Peak 6 (eV)	Δ Peak6 - Peak5 (eV)	%	Peak 6, FWHM, 10 eV Pass Energy	Peak 6, FWHM, 20 eV Pass Energy	Peak 7 (eV)	Δ Peak7 - Peak6 (eV)	%	Peak 7, FWHM, 10 eV Pass Energy	Peak 7, FWHM, 20 eV Pass Energy	
Ni Metal from [5]																b) d)
Ni Metal - New Line Shape																c) d)
NiO	866.3	2.38	3.9	2.60	2.44											
Ni(OH)2	861.5	1.00	39.2	4.64	4.65	866.5	4.96	3.7	3.08	3.01						
Gamma NiOOH	857.8	1.33	8.7	1.90		861.0	3.20	23.3	4.00		864.4	3.38	11.4	4.40		
Beta NiOOH (3+ Portion)	857.8	1.33	5.8	1.90		861.0	3.20	15.6	4.00		864.4	3.38	7.6	4.40		e)
Beta NiOOH (2+ Portion)	861.5	1.00	13.1	4.64		866.5	4.96	1.2	3.08							e)
NiCr2O4	861.3	0.26	39.4	4.34	4.31	866.0	4.73	6.1	2.07	2.13						
NiFe2O4	867.0	2.27	3.2	2.61	2.66											

a) Binding energies are significant to 0.1eV but an additional figure is added because energy splittings are much more accurate than the absolute binding energies.
b) Asymmetric peakshape for peak 1 defined by standard nickel metal sample, CasaXPS peakshape parameter = A(0.4,0.55,10)GL(30)
c) Asymmetric peakshape for peak 1 defined by standard nickel metal sample, CasaXPS peakshape parameter = LA(1.1,2.2,10)
d) Metal peak is corrected to Au 4f7/2 set to 83.95 eV. All other peaks are charge corrected to C 1s (C-C, C-H, adventitious carbon) set to 284.8eV.
e) Beta NiOOH has a ratio of 2:1 Ni(III):Ni(II). Peak percentages for the 3+ and 2 + portions for Beta NiOOH total 100%.

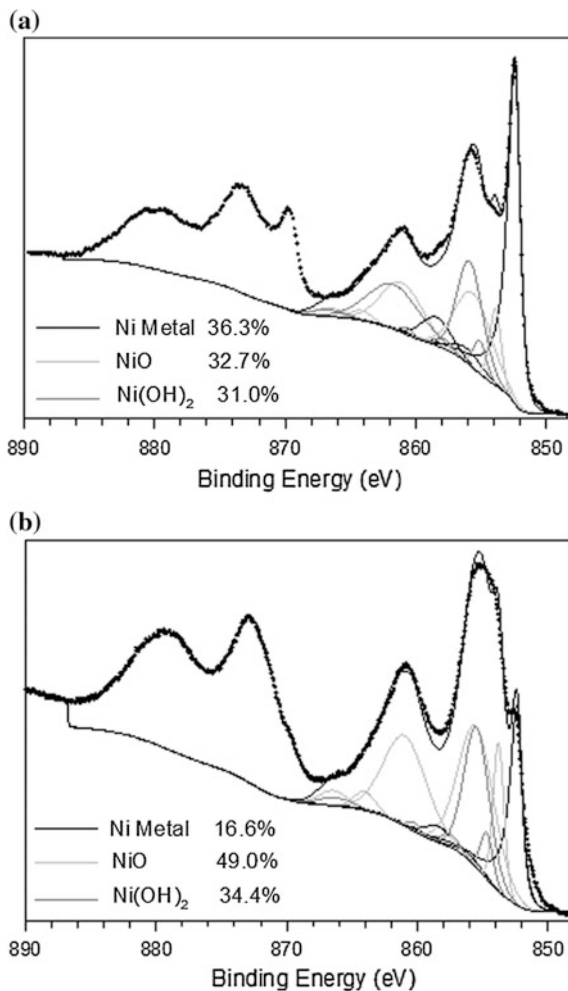

Fig. 10.11 **a** Ni 2p spectra of INCO (Type 123) nickel powder and **b** an ultrafine nickel powder. A Shirley background under the entire Ni 2p spectrum with an offset on the higher binding energy endpoint was used for both spectra (Adapted from [75])

10.3 Intra- and Extra-Atomic Relaxation Mechanisms

The previous sections have sought to review the practical methods of analysing final state effects in FRTM and their compounds; in this section, details of how final state effects influence binding energies will be presented. XPS binding energies are sensitive to the chemical environment because they are related to the interactions between the atom of interest and its first coordination shell, i.e., its nearest neighbour atoms. Longer-range interactions with more distant atoms can also influence these energies, though these effects are often much less pronounced [4, 88]. The observed binding energy of a photoelectron from atom *i*, ΔE_{bi}, which results from both ground- and final-state energies, can be described by the modified charge potential

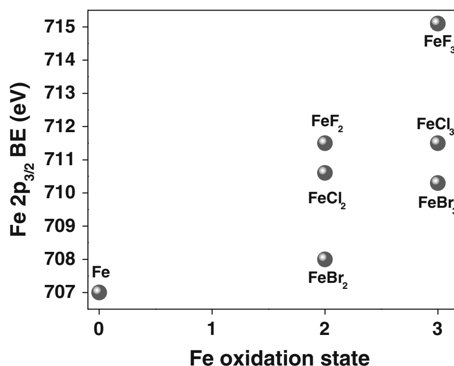

Fig. 10.12 Change in Fe $2p_{3/2}$ binding energy depending on oxidation state and composition (Adapted from [5])

model described in Sect. 10.1.1.2 (10.1.1). Many factors influence binding energies, and isolating the main contributions can be difficult.

Binding energy shifts can be very informative when examining the electronic structure of materials; however, it is important when defining the surface chemistry of first row transition metals, and their compounds, to understand if observed shifts result from ground-state or final-state effects. Before describing how final-state effects can influence XPS binding energies, and how they can be separated from ground-state effects, it seems appropriate to provide examples of how ground-state effects can shift binding energies. Rewriting (10.1.1) to exclude final-state effects gives:

$$\Delta E_{bi} = k\Delta q_i + \Delta \sum_{\mathrm{i}\neq \mathrm{j}} \frac{\mathrm{q_j}}{\mathrm{r_{ij}}} \qquad (10.3.1)$$

An increase in the charge of the absorbing atom (q_i) results in decreased screening of the nuclear charge, leading to the core (and valence) electrons of the absorbing atom being more tightly bound. The result of this is that more energy is required to remove an electron from the atom (ion), and this is observed as an increase in the photoelectron binding energy. For example, applying the multiplet fitting method described above for transition-metal 2p XPS spectra to high-spin Fe-containing materials has resulted in the determination of highly accurate Fe $2p_{3/2}$ binding energies for FeX_y compounds (X = halide), which are plotted in Fig. 10.12 versus the Fe oxidation state [5]. As can be easily observed, the average BE increases with increasing oxidation state, but it can also be observed that the Fe $2p_{3/2}$ binding energy changes significantly when the Fe oxidation state is held constant and the ligand that is bound to Fe is changed. The Fe-ligand bond covalency changes considerably depending on the electronegativity of the ligand, which affects the Fe charge [89]. The Fe charge is defined here as representing a combination of the Fe oxidation state and Fe-X bond covalency. With increasing bond covalency, the Fe charge is reduced, resulting in a lower Fe $2p_{3/2}$ binding energy (cf. the Fe $2p_{3/2}$ binding energies from FeF_y, $FeCl_y$, and $FeBr_y$ in Fig. 10.12). A shift to lower binding energy because of an increase in the bond

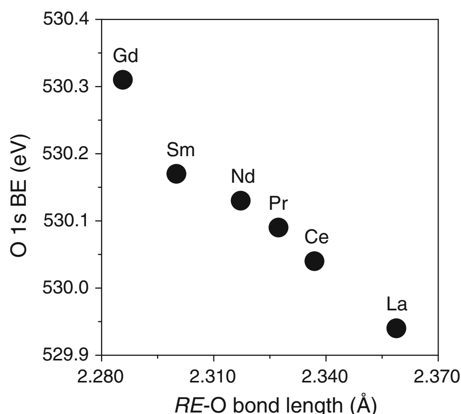

Fig. 10.13 Plot of O 1s binding energy (BE) versus RE–O bond length in *RE*FeAsO (RE = La–Nd, Sm, Gd) (Adapted from [90])

covalency could be described as resulting from ground state effects in (10.1.2) by attributing the shift to a decrease in the magnitude of the Fe charge (q_i). However, as has been shown previously, and will be presented below, changes in XPS binding energies due to apparent changes in the covalency of the bond between the absorbing atom and nearest-neighbours can also result from combined extra- and intra-atomic final-state relaxation.

Along with binding energy shifts resulting from changes in oxidation state, the ground-state binding energy can also shift because of extra-atomic (nearest and next-nearest neighbour) effects. The screening of the nuclear charge of the absorbing atom can be influenced by electrons from near and nearest-neighbours, as described by the $\Delta\sum_{i\neq j}\frac{q_j}{r_{ij}}$ term in the modified charge potential model (10.1.1). The binding energy can change depending on the charge of the neighbouring atom (q_j) and/or the distance between the neighbouring atoms and the absorbing atom (r_{ij}). An example of the effect of bond distance on XPS binding energies is the shift in the O 1s BE that was observed in the *RE*FeAsO (*RE* = Ce, Pr, Nd, Sm, Gd) system (Fig. 10.13) [90]. These materials have received considerable attention, as the F-substituted materials (i.e., *RE*$FeAsO_{1-x}F_x$) have been observed to exhibit superconducting behaviour [91–94]. The O ions are tetrahedrally coordinated to rare-earth (*RE*) ions within the structure [90]. It was observed in this study that the O 1s BE (Fig. 10.13) decreased in energy with increasing *RE*-O bond length [90]. This shift cannot be specifically attributed to a decrease in O charge as the *RE* ions studied all have similar electronegativity values [89]. Instead, it was proposed that the increase in the *RE*-O bond length decreased the contribution of the nearest-neighbour *RE* ions to the screening of the O ($\Delta\sum_{i\neq j}\frac{q_j}{r_{ij}}$), which led to a decrease of the O 1s BE [90].

Ground-state effects resulting from a change in formal oxidation state play a significant role in shifting XPS binding energies. For example, the difference in Fe $2p_{3/2}$ BE between $FeCl_2$ and $FeCl_3$ is ≈+1 eV [5]. However, final-state effects can shift the binding energy by similar magnitudes. It has been determined that the Ti

2p, Si 2p, and O 1s binding energies in $(TiO_2)_x(SiO_2)_{1-x}$ shift because of final-state effects with increasing value of x (similar materials are reviewed in more detail in Sect. 10.3.1.2) [95, 96]. The Ti $2p_{3/2}$ binding energy decreased by >1 eV on progressing from $(TiO_2)_{0.1}(SiO_2)_{0.9}$ to TiO_2, which is of similar magnitude to the ground state shift of the Fe $2p_{3/2}$ binding energy when comparing $FeCl_2$ to $FeCl_3$ [6, 95]. Changes in the coordination environment (i.e., coordination number) have also recently been shown to lead to binding energy shifts because of final-state effects, which is a result of a change in the screening of the core-hole produced by excitation of a photoelectron [97]. Examples of how final-state effects can contribute to XPS binding energy shifts are presented below along with a discussion of how ground-state and final-state effects can be separated.

10.3.1 *Examples of Binding Energy Shifts Due to Final-State Relaxation*

10.3.1.1 Understanding the Influence of Ground-State and Final-State Effects on the Ni $2p_{3/2}$ Binding Energy from Nickel Halides

As presented in Sect. 10.1.1.2, multiple contributions can result in shifts in XPS binding energies (cf. 10.1.1). Shifts in binding energy between materials because of final-state relaxation effects are likely the least acknowledged cause of binding energy shifts. One of the reasons why final-state effects are not often discussed when reporting binding energy shifts can be attributed to the difficulty in separating ground-state and final-state effects by examination of core-line XPS spectra alone.

To understand if a binding energy shift between two materials primarily results from ground-state or final-state effects requires the examination of more than just core-line XPS spectra. The combination of Auger and core-line emissions in XPS spectra has been extensively used to determine the amount of ground-state and final-state effects that contribute to the measured binding energy using the modified Auger parameter (10.1.2)–(10.1.4) [14, 98]. The physical basis for the Auger parameter lies in the nature of the final states created during photoelectron and Auger electron emission. In an Auger process, the atom is left in a doubly-ionized final state, which experiences more relaxation than the final state produced by emission of a photoelectron, where there is only a single core-hole [99]. Understandably, final-state effects play a larger role in Auger kinetic energies than photoelectron binding energies. Shifts in ground-state energies generally influence XPS binding energies and Auger kinetic energies equally; however, it should be recognized that this is not always the case [14]. Examination of the XPS and Auger spectra using Wagner plots, which compares the kinetic energy of the Auger emission to the binding energy of the XPS emission from the same surface, can provide information on the relative contributions of ground-state and final-state effects to shifts in XPS binding energies [14].

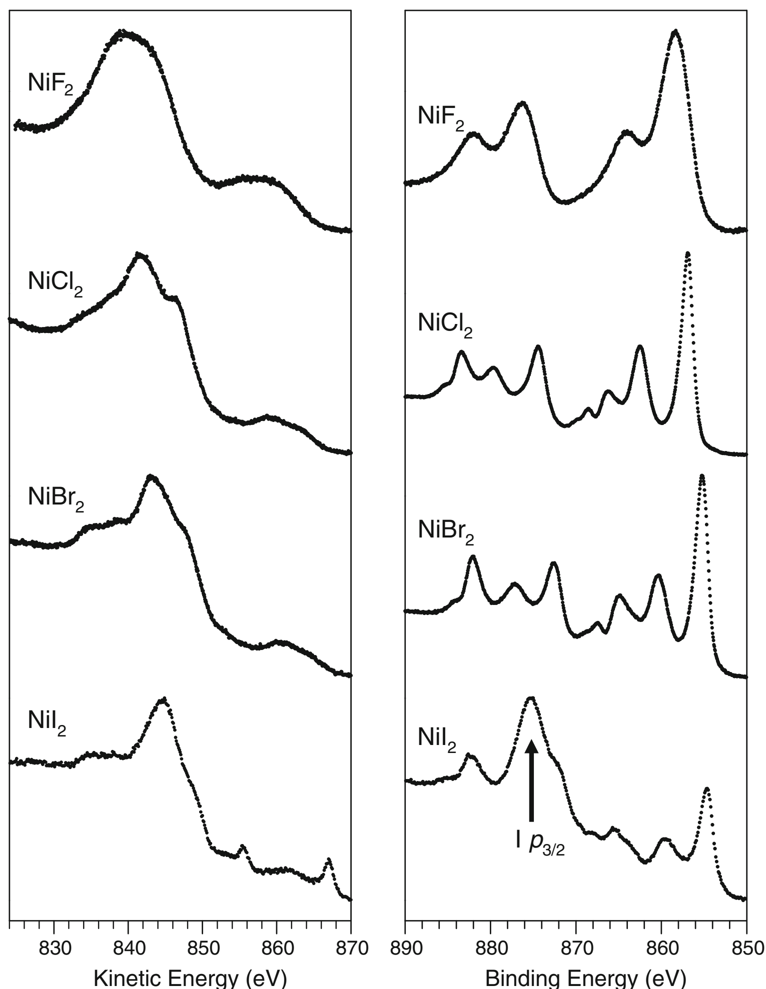

Fig. 10.14 Ni LMM Auger (*left*) and Ni 2p XPS (*right*) spectra for NiF_2, $NiCl_2$, $NiBr_2$ and NiI_2. Note the overlap of I $3p_{3/2}$ peak with the Ni 2p spectrum for NiI_2 (Reproduced from [98] with permission of the PCCP Owner Societies)

A recent study combined the analysis of Ni 2p core-line peaks and Ni LMM Auger peaks in the same XPS spectra to understand final-state relaxation contributions to the Ni 2p XPS binding energies from Ni oxides, hydroxides, oxyhydroxides and halides [98]. The analysis of the halides will be used here to outline the method. Examination of Ni $2p_{3/2}$ XPS spectra from nickel halides (Fig. 10.14) showed that the binding energy decreased on progressing from NiF_2 to NiI_2, as might be expected based on a bond covalency argument and assuming only ground-state effects. Analysis of the Ni LMM Auger spectra (Fig. 10.14) showed that the spectra shifted to higher kinetic energy and became narrower on

Table 10.7 Ni $2p_{3/2}$ and Ni LMM peak maximum positions, Auger parameter (α'), ΔEb, ΔEk, $\Delta\alpha'$, ΔR and ΔE_i values [98]

Compound	Ni 2p3/2 peak maximum E_b (eV)	Ni LMM auger peak maximum E_k (eV)	Auger parameter (eV) (α')	ΔE_b (Ni $2p_{3/2}$; relative to Ni metal)	ΔE_k (Ni LMM)	$\Delta\alpha'$	ΔR	ΔE_i
Ni Metal	852.54	846.22	1698.76					
NiF_2	858.12	839.74	1697.86	5.58	−6.48	−0.90	−0.45	−5.13
$NiCl_2$	856.77	841.88	1698.65	4.23	−4.34	−0.11	−0.06	−4.17
$NiBr_2$	855.27	843.25	1698.52	2.73	−2.97	−0.24	−0.12	−2.61
NiI_2	854.46	845.23	1699.69	1.92	−0.99	0.93	0.46	−2.38

progressing from NiF_2 to NiI_2. By comparing the ΔE_b (relative shift in binding energy) and ΔE_k (relative shift in kinetic energy) values, the modified Auger parameter was calculated, which allowed for a determination of the contribution of ground-state and final-state effects (i.e., relaxation) to the shift observed in the Ni $2p_{3/2}$ XPS binding energy (Table 10.7) [98]. It was possible to calculate the contributions of ground-state and final-state effects to the shift in the Ni $2p_{3/2}$ binding energy from the Ni halides by use of (10.1.3) and (10.1.4) presented in Sect. 10.1.1.2.

Figure 10.14 shows the succession of nickel halide Ni 2p and LMM Auger spectra from the nickel halides. The Ni $2p_{3/2}$ peak increases in binding energy from the iodide through to the fluoride, which would suggest an increasing positive charge. This is supported by the strong relationship between Ni $2p_{3/2}$ binding energy and electronegativity of the ligand, as one might expect, and as has been shown previously [6]. The chloride and bromide show similar Ni 2p peak structures. Subtraction of the overlap of the I $3p_{3/2}$ peak from the Ni 2p peak structure gives a similar structure to the chloride and bromide for the Ni $2p_{3/2}$. The degree of covalency for these compounds has been calculated to be $NiI_2 > NiBr_2 > NiCl_2$ [100]. This change in bonding is reflected in the halide LMM Auger spectra (Fig. 10.14), which show progressive changes from the chloride to the iodide. Specifically, the higher kinetic energy shoulder on the main peak diminishes from the chloride to the iodide. The overall Auger peak width also decreases from the chloride to the iodide and is correlated with a reduction in effective d-hole concentration [101, 102]. The fluoride does not fit into this trend with a peak width between that of the chloride and the bromide.

Analysis of the ground- and final-state effects for the halides (Table 10.7) shows that the binding and kinetic energy shifts of the nickel halides are dominated by ground-state effects, ΔE_i, which are much larger (−5.15 to −2.45 eV) than final state effects, ΔR (−0.45 to +0.45 eV). These ground-state effects induce a shift to lower binding energy, as described by $\Delta E_b = -\Delta E_i - \Delta R$, on progressing from NiF_2 to NiI_2. The ground-state effect decreases in magnitude from fluoride to iodide, which suggests a progressively decreasing positive ground state valence state, as would be expected based on electronegativity arguments [89].

Final-state effects, ΔR, due to the polarizability of the larger halide ions, particularly the diffuse iodide ion, are seen in the positive ΔR relaxation shift to lower binding energy [98]. The shift to lower binding because of final-state effects offset the shift to higher binding because of ground-state effects. There is also support in this study for the direct use of relative bond lengths from diffraction analysis in interpreting differences in ΔR between related compounds rather than more general electronegativity or similar parameters alone [98].

10.3.1.2 Deciphering Final-State and Ground-State Effects in XPS Binding Energy Shifts from $(ZrO_2)_x(TiO_2)_y(SiO_2)_{1-x-y}$

Amorphous transition-metal silicates (e.g. $(MO_2)_x(SiO_2)_{1-x}$; M = Ti, Zr, Hf) have been the subject of many investigations because of their tuneable properties and industrial applications. Many of the properties of these materials depend on the metal content, which can be adjusted to control the refractive index, thermal expansion coefficient, hardness, chemical durability, and dielectric constant of the materials [103–112]. Amorphous $(ZrO_2)_x(TiO_2)_y(SiO_2)_{1-x-y}$ and $(ZrO_2)_x(SiO_2)_{1-x}$ (quaternary and ternary metal silicates, respectively) have been synthesized by sol-gel methods and investigated by X-ray absorption near-edge spectroscopy (XANES) and XPS [97]. Complementary techniques, such as Auger spectroscopy and XANES, were needed in this study to separate ground- and final-state effects, and to identify the major contributions to observed shifts in binding energy. The important difference between XANES and XPS lies in the final state produced by each method. In XPS, the final state of the system being probed is electron deficient and has an unscreened core-hole owing to the removal of a core-electron from the atom. Because of this, relaxation effects due to the core-hole are greater in XPS than in XANES where the core-electron is promoted to conduction states and can partially screen the core-hole [113–115]. Thus, when the ground-state is identical, and electrons of equal energy (i.e., the same orbital) are probed by both techniques (e.g., Ti $2p_{3/2}$ XPS and Ti L_3-edge XANES), the difference in the final-state of analogous XPS and XANES excitations can be exploited to resolve ground- and final-state effects in XPS binding energies.

To study how increasing the total metal content affects the electronic structure of these materials, XPS core-line spectra from $(ZrO_2)_x(TiO_2)_y(SiO_2)_{1-x-y}$ were collected (cf. Fig. 10.15) [96]. The binding energy of the photoelectron peak maximum is plotted as a function of total metal content in Fig. 10.16. Binding energies from ternary silicates ($(ZrO_2)_x(SiO_2)_{1-x}$ and $(TiO_2)_x(SiO_2)_{1-x}$) are also plotted to show the close agreement with values obtained from the quaternary silicates at similar total metal content (i.e., ≤0.1 eV difference when the total metal content is identical) [95, 96]. All core-line photoelectron peaks (Zr $3d_{5/2}$, Ti $2p_{3/2}$, Si 2p, and O 1s) showed a significant decrease in binding energy with increasing total metal content (x + y, mol.% ZrO_2 + TiO_2), but show little to no variation in binding energy when the total metal content was fixed and the Zr:Ti ratio was varied. As the total metal

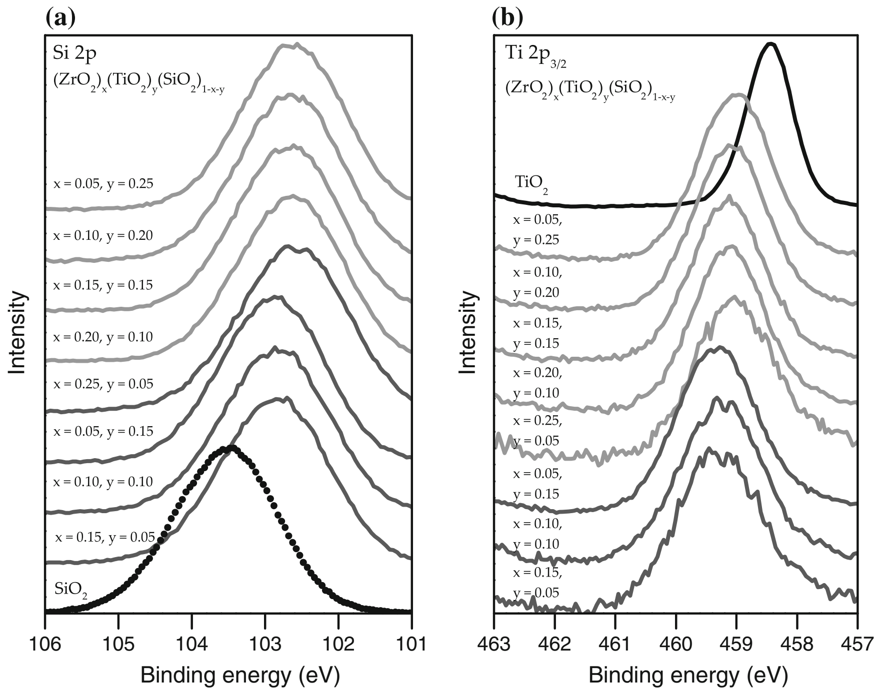

Fig. 10.15 **a** Si 2p and **b** Ti $2p_{3/2}$ XPS core-line spectra of the quaternary silicates and binary oxides (Adapted from [96])

content increases, the variation of the quaternary binding energies at a fixed total metal content increases.

It is clear that there are large decreases in binding energy with increasing total metal content, but the underlying cause of the binding energy shift cannot be determined by analysis of only the XPS binding energies. For example, substitution of Si^{4+} atoms by more electropositive Ti^{4+} or Zr^{4+} atoms ($\chi_{Si} = 1.74$, $\chi_{Ti} = 1.32$, $\chi_{Zr} = 1.22$) [89] may increase final-state relaxation experienced by electrons in the material, increasing ΔE_i^{EA} in (10.1.1) and decreasing the binding energy. This substitution could also lead to more electron density at and/or around the absorbing atom in the ground-state, decreasing $k\Delta q_i$ and/or $\Delta \sum_{i \neq j} \frac{q_j}{r_{ij}}$ in (10.1.1) and decreasing the binding energy [4, 116, 117]. Additionally, the incorporation of metals into these materials will increase the average bond distances (ionic radii: $r_{Si4+\ (CN:4)} = 0.26$, $r_{Ti4+\ (CN:5)} = 0.51$, $r_{Zr4+\ (CN:8)} = 0.84$), which could also affect $\Delta \sum_{i \neq j} \frac{q_j}{r_{ij}}$ [4, 116, 118].

To determine the origin of the binding energy shifts in the XPS core-line spectra from $(ZrO_2)_x(TiO_2)_y(SiO_2)_{1-x-y}$ and $(ZrO_2)_x(SiO_2)_{1-x}$, soft X-ray XANES spectra (Ti $L_{2,3}$-, and Si $L_{2,3}$-edge; Fig. 10.17) were collected and compared to the corresponding XPS spectra (Ti 2p, and Si 2p). Ti $L_{2,3}$-edge spectra result from the

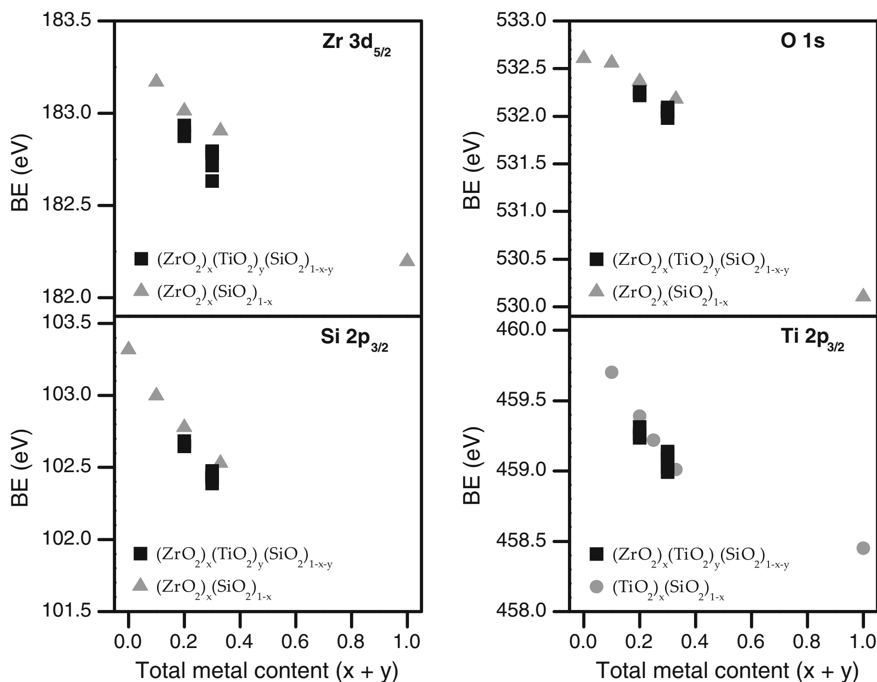

Fig. 10.16 The binding energy (BE) of the photoelectron peak maximum decreases with increasing total metal content (mol.% ZrO_2 + TiO_2) (Adapted from [95, 96])

excitation of Ti 2p electrons to unoccupied Ti 3d states, and are sensitive to both the local coordination number and the electronic structure [113, 119]. Previous studies have assigned the multiple peaks of the L_3 or L_2 components to transitions with energies reflective of the splitting in Ti 3d orbital energies [120]. Ti L_3-edge absorption energies were examined to probe the Ti 2p ground-state energies to separate ground- and final-state effects in the XPS Ti $2p_{3/2}$ binding energy shifts. Ti L_3-edge spectra (Fig. 10.17a) showed no change in the L_3-edge absorption energy (<0.1 eV; determined by the maximum in the first derivative shown in Fig. 10.17a), suggesting that ground-state effects are not responsible for the Ti 2p binding energy shift observed by XPS. Si $L_{2,3}$-edge spectra were also collected to probe changes in the Si ground-state electronic structure (Fig. 10.17). The Si $L_{2,3}$-edge spectra have features due primarily to Si 2p → 3s transitions at lower energies (feature A in Fig. 10.17), followed by a broader region at higher energies involving largely 2p → 3d transitions (feature A in Fig. 10.17b) [121–124]. Comparison of the spectra collected at the Si $L_{2,3}$-edge reveals only subtle changes in the lineshape (such as a slight broadening of the peaks with increasing metal content) and a < 0.1 eV change in absorption energy across all samples (Fig. 10.17b). The lack of significant changes in the Si $L_{2,3}$-edge absorption energies (<0.1 eV shift; determined by the

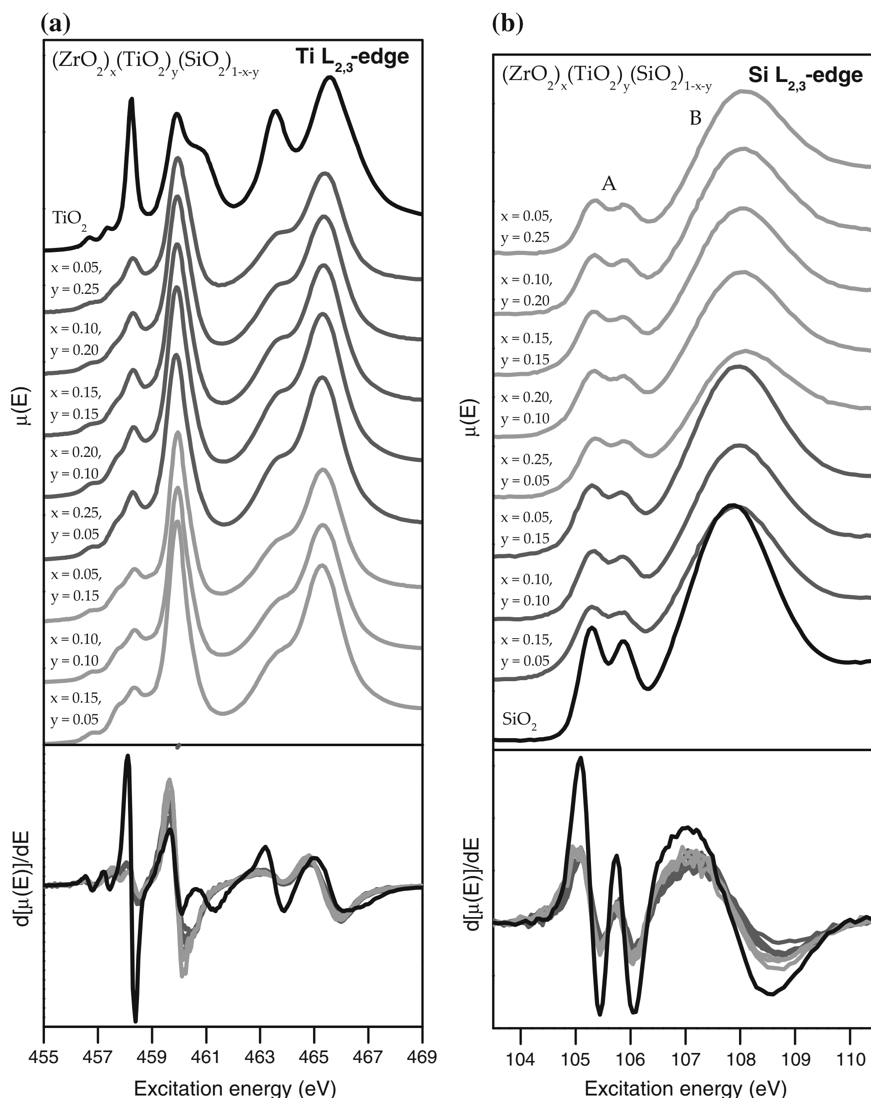

Fig. 10.17 **a** Ti $L_{2,3}$-edge and **b** Si $L_{2,3}$-edge XANES spectra of the quaternary silicates. In both sets of spectra, a <0.1 eV shift in the absorption-edge energy was observed across the series, as determined by examination of the first-derivative of the spectra (*bottom panel* in each figure) (Adapted from [96])

maximum in the first derivative shown in Fig. 10.17b) is testament to the lack of ground-state shifts in the Si 2p XPS binding energies with substitution.

The XPS core-line spectra showed a large decrease in the photoelectron binding energies of all elements in $(ZrO_2)_x(TiO_2)_y(SiO_2)_{1-x-y}$ with increasing total metal content. Meanwhile, XANES spectra (Ti $L_{2,3}$- and Si $L_{2,3}$-edge) showed no changes

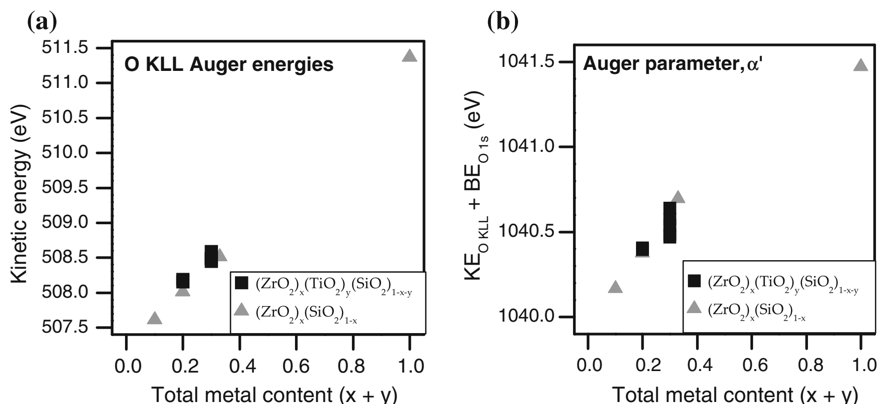

Fig. 10.18 **a** O KLL Auger peak maxima and **b** Auger parameters of the quaternary and ternary silicates (Adapted from [96])

in absorption energies, implying that ground-state effects are not a major contributor in the XPS binding energy shifts. This leaves changes in extra-atomic final-state relaxation (ΔE_i^{EA}) as the driving cause of these binding energy shifts. The binding energy shifts in the silicates are caused by substitution of Si for Ti or Zr atoms, which are much less electronegative ($\chi_{Si} = 1.74$, $\chi_{Ti} = 1.32$, $\chi_{Zr} = 1.22$) [89, 117]. As metal atoms replace Si, and the average electronegativity of the Si/Zr/Ti site decreases, the electron density becomes less tightly bound. Consequently, electron density from the chemical environment surrounding the absorbing atom can relax to a greater extent around the core-hole produced during an XPS experiment, lowering the final-state energy and leading to a decrease in the binding energy.

To confirm that final-state effects are responsible for the BE shifts, the O KLL Auger transition was monitored and the Auger parameter, one of the few experimental measures of relaxation, was extracted (Fig. 10.18) [14, 99, 125]. The peak maxima for the O KLL Auger spectra from the quaternary silicates are shown in Fig. 10.18a. These Auger kinetic energies values were added to the previously presented O 1s binding energies (Fig. 10.16) to obtain the Auger parameter (Fig. 10.18b). A plot of the Auger parameter versus total metal content (irrespective

Table 10.8 O 1s and O KLL peak maximum positions, Auger parameter (α′), ΔEb, ΔEk, Δα′, ΔR, and ΔE_i values from $(ZrO_2)_x(SiO_2)_{1-x}$ [96]

x in $(ZrO_2)_x(SiO_2)_{1-x}$	O 1s peak maximum E_b (eV)	O KLL auger peak maximum E_k (eV)	Auger parameter (eV) (α′)	ΔE_b (relative to x = 0.1)	ΔE_k	Δα′	ΔR	ΔE_i
0.1	532.55	507.6	1040.15	0	0	0	0	0
0.2	532.4	508	1040.4	−0.15	0.4	0.25	0.125	0.025
0.33	532.2	508.55	1040.75	−0.35	0.95	0.6	0.3	0.05
1	530.1	511.4	1041.5	−2.45	3.8	1.35	0.675	1.775

of metal identity) yields a positive linear relationship, confirming that ΔE_i^{EA}, the degree of extra-atomic final-state relaxation, in $(ZrO_2)_x(TiO_2)_y(SiO_2)_{1-x-y}$ and $(ZrO_2)_x(SiO_2)_{1-x}$ increases with total metal content [96]. As the electronegativities of Zr and Ti are similar, the identity of the metal was not found to be important in this case. Using (10.1.2)–(10.1.4), the O 1s XPS spectra, and the O KLL Auger spectra, the contribution of ground-state (ΔE_i) and final-state (ΔR) effects were also calculated. The values of ΔE_i and ΔR from $(ZrO_2)_x(SiO_2)_{1-x}$ (relative to $(ZrO_2)_{0.1}(SiO_2)_{0.9}$) are presented in Table 10.8. These values confirm that final-state effects play an important role in shifting the XPS binding energies from these materials.

10.4 Summary and Conclusions

The first-row transition-metals (FRTM) are a very technologically important set of elements and the 2p core-line spectra from FRTM are some of the most intensely analysed of all XPS spectra. Information on the surface chemistry of these elements is extremely valuable to materials design and performance optimization; however, defining accurate information on the chemical state of a FRTM in different compounds from XPS spectra can be complicated because of the influence of both ground-state and final-state effects. As reviewed here, the FRTM XPS spectra can have complicated lineshapes because of multiplet splitting and satellite peaks. To determine accurate binding energy values, it is necessary to fit the spectra by including multiplet structures and satellite peaks. Practical methods for this fitting have been developed and now provide much more confident identification of binding energies for each element in its metallic and ionised forms.

Once an accurate binding energy is determined from properly fitted XPS spectra, it is then necessary to understand if the binding energy is dominated by ground-state or final-state effects (or both). Changes in bond covalency, charge, and coordination environment can result in shifts in binding energies because of ground-state effects and/or final-state effects. Complementary information from the analysis of Auger spectra and the Auger parameter, XANES spectra, and examination of the structure by XRD is required to properly determine if final-state or ground-state effects are most important to an observed shift in binding energy.

References

1. U.S. Geological Survey Data, Department of the Interior/USGS, (http://www.usgs.gov) 2011
2. J.F. Moulder, W.F. Stickle, P.E. Sobol, K.D. Bomben, *Handbook of X-ray Photoelectron Spectroscopy* (Perkin-Elmer Corp, Eden Prairie, MN, 1992)
3. P.A.W. van der Heide, J. Electron Spectrosc. Relat. Phenom. **164**, 8 (2008)

4. D. Briggs, *Surface Analysis of Polymers by XPS and Static SIMS* (Cambridge University Press, Cambridge, UK, 1998)
5. A.P. Grosvenor, B.A. Kobe, M.C. Biesinger, N.S. McIntyre, Surf. Interface Anal. **36**, 1564 (2004)
6. F. de Groot, A. Kotani, *Core Level Spectroscopy of Solids* (CRC Press, Boca Raton, 2008)
7. A.P. Grosvenor, M.C. Biesinger, R.St.C. Smart, N.S. McIntrye, Surf. Sci. **600**, 1771 (2006)
8. M.C. Biesinger, B.P. Payne, A.P. Grosvenor, L.W.M. Lau, A.R. Gerson, R.St.C. Smart, Appl. Surf. Sci. *257*, 2717 (2011)
9. N.S. McIntyre, D.G. Zetaruk, Anal. Chem. **49**, 1521 (1977)
10. N. Fairley, XPS Lineshapes and Curve Fitting, in *Surface Analysis by Auger and X-ray Photoelectron Spectroscopy*, ed. by D. Briggs, J.T. Grant (IM Publications, Chichester, UK, 1983)
11. C.D. Wagner, in *Electron Spectroscopy: Proceedings of the International Conference Held at Asilomar, Pacific Grove, CA, USA, 7–10 September, 1971*, ed. D.A. Shirley, North-Holland, Amsterdam, p 861 (1972)
12. C.D. Wagner, Anal. Chem. **44**, 967 (1972)
13. C.D. Wagner, J.A. Taylor, J. Electron Spectrosc. Relat. Phenom. **28**, 211 (1982)
14. G. Moretti, Surf. Sci. **618**, 3 (2013)
15. J. Hedman, P.F. Heden, C. Nordling, K. Siegbahn, Phys. Lett. **29A**, 178 (1969)
16. C.S. Fadley, D.A. Shirley, A.J. Freeman, P.S. Bagus, J.V. Mallow, Phys. Rev. Lett. **23**, 1397 (1969)
17. C.S. Fadley, D.A. Shirley, Phys. Rev. A **2**, 1109 (1970)
18. R.P. Gupta, S.K. Sen, Phys. Rev. B **10**, 71 (1974)
19. R.P. Gupta, S.K. Sen, Phys. Rev. B **12**, 15 (1975)
20. P.A. Cox, *Transition Metal Oxides: An Introduction to Their Electronic Structure and Properties, The International Series of Monographs on Chemistry No 27* (Clarendon, Oxford, 1995)
21. M.D. Towler, N.L. Allan, N.M. Harrison, V.R. Saunders, W.C. Mackrodt, E. Aprà, Phys. Rev. B **50**, 5041 (1994)
22. T. Bredow, A.R. Gerson, Phys. Rev. B **61**, 5194 (2000)
23. J. Zaanen, C. Westra, G.A. Sawatzky, Phys. Rev. B **33**, 8060 (1986)
24. K. Okada, A. Kotani, J. Phys. Soc. Jpn. **61**, 4619 (1992)
25. P.S. Bagus, H.J. Freund, T. Minerva, G. Pacchioni, F. Parmigiani, Chem. Phys. Lett. **251**, 90 (1996)
26. E.-K. Viinikka, Y. Öhm, Phys. Rev. B **11**, 4168 (1975)
27. P.S. Bagus, R. Broer, C. de Graaf, W.C. Nieuwpoort, J. Electron. Spec. Rel. Phenom. **98–99**, 303 (1999)
28. P.S. Bagus, G. Pacchioni, F. Pamigiani, Chem. Phys. Lett. **207**, 569 (1993)
29. A.E. Bocquet, T. Mizokawa, T. Saitoh, H. Namatame, A. Fujimori, Phys. Rev. B **46**, 3771 (1992)
30. M.A. Van Veenendaal, G.A. Sawatzky, Phys. Rev. Lett. **70**, 2459 (1993)
31. M. Atanasov, D. Reinen, J. Electron Spectrosc. Relat. Phenom. **86**, 185 (1997)
32. H. Takahashi, F. Munakata, M. Yamanaka, J. Phys.: Condens. Matter **7**, 1583 (1995)
33. Y. Baer, P.F. Heden, J. Hedman, M. Klasson, C. Nordling, K. Siegbahn, Phys. Scr. **1**, 55 (1970)
34. H.A.E. Hagelin-Weaver, J.F. Weaver, G.B. Hoflund, G.N. Salaita, J. Electron Spectrosc. Relat. Phenom. **134**, 139 (2004)
35. O. Karis, S. Svensson, J. Rusz, P.M. Oppeneer, M. Gorgoi, F. Schäfers, W. Braun, W. Eberhardt, N. Mårtensson, Phys. Rev. B **78**, 233105 (2008)
36. H.A.E. Hagelin-Weaver, J.F. Weaver, G.B. Hoflund, G.N. Salaita, J. Alloys Compd. **389**, 34 (2005)
37. E.S. Ilton, W.A de Jong, P.S. Bagus, Phys. Rev. B. **68**, 125106 (2003)
38. P.S. Bagus, R. Broer, E.S. Ilton, Chem. Phys. Lett. **394**, 150 (2004)
39. M. Bronold, Y. Tomm, W. Jaegermann, Surf. Sci. **314**, L931 (1994)

40. H.W. Nesbitt, G.M. Bancroft, A.R. Pratt, M.J. Scaini, Am. Mineral. **1998**, 83 (1067)
41. H. van der Heide, R. Hemmel, C.F. van Bruggen, C. Haas, J. Solid State Chem. **33**, 17 (1980)
42. H.W. Nesbitt, M. Scaini, H. Höchst, G.M. Bancroft, A.G. Schaufuss, R. Szargan, Am. Mineral. **85**, 850 (2000)
43. M.C. Biesinger, C. Brown, J.R. Mycroft, R.D. Davidson, N.S. McIntyre, Surf. Interface Anal. **36**, 1550 (2004)
44. C.D. Wagner, A.V. Naumkin, A. Kraut-Vass, J.W. Allison, C.J. Powell, J.R. Jr. Rumble, *NIST Standard Reference Database 20, Version 3.4* (Web Version) (http://srdata.nist.gov/xps/). (2003)
45. B. Stypula, J. Stoch, Corros. Sci. **36**, 2159 (1994)
46. E. Desimoni, C. Malitesta, P.G. Zambonin, J.C. Rivière, Surf. Interface Anal. **13**, 173 (1988)
47. V. Maurice, W.P. Yang, P. Marcus, J. Electrochem. Soc. **141**, 3016 (1994)
48. D.R. Rosseinsky, G.K. Muthakia, C.L. Honeybourne, R.L. Ewen, Transition Met. Chem. **20**, 88 (1995)
49. E. Kemnitz, A. Kohne, I. Grohmann, A. Lippitz, W.E.S. Unger, J. Catal. **159**, 270 (1996)
50. X.Y. Li, E. Akiyama, H. Habazaki, A. Kawashima, K. Asami, K. Hashimoto, Corros. Sci. **39**, 1365 (1997)
51. M. Tetsuya, K. Takao, J. Shimomura, Appl. Surf. Sci. ***121/122***, 120 (1997)
52. G.P. Halada, C.R. Clayton, J. Electrochem. Soc. **138**, 2921 (1991)
53. I. Grohmann, E. Kemnitz, A. Lippitz, Surf. Interface Anal. **23**, 887 (1995)
54. N.S. McIntyre, T.C. Chan, C. Chen, Oxid. Met. **33**, 457 (1990)
55. A.R. Pratt, N.S. McIntyre, Surf. Interface Anal. **24**, 529 (1996)
56. M. Oku, K. Hirokawa, S. Ikeda, J. Electron Spec. Rel. Phenom. **7**, 465 (1975)
57. H.W. Nesbitt, D. Banerjee, Am. Mineral. **83**, 305 (1998)
58. D. Banerjee, H.W. Nesbitt, Geochim. Cosmochim. Acta **63**, 3025 (1999)
59. D. Banerjee, H.W. Nesbitt, Geochim. Cosmochim. Acta **63**, 1671 (1999)
60. D. Banerjee, H.W. Nesbitt, Geochim. Cosmochim. Acta **63**, 1703 (1999)
61. A.K. Shukla, P. Krüger, R.S. Dhaka, D.I. Sayago, K. Horn, S.R. Barman, Phys. Rev. B **75**, 235419 (2007)
62. A.R. Pratt, I.J. Muir, H.W. Nesbitt, Geochim. Cosmochim. Acta **58**, 827 (1994)
63. T.C. Lin, G. Seshadri, J.A. Kelber, Appl. Surf. Sci. **119**, 83 (1997)
64. K. Daub, X. Zhang, D. Shoesmith, J.C. Wren, *Meet Abtr. – Electrochem. Soc.*, 2009, *901*, 643
65. J.C. Dupin, Thin Solid Films **384**, 23 (2001)
66. A. Foelske, H.H. Strehblow, Surf. Interface Anal. **29**, 548 (2000)
67. A.P. Grosvenor, S.D. Wik, R.G. Cavell, A. Mar, Inorg. Chem. **44**, 8988 (2005)
68. B.V. Crist, *Handbook of Monochromatic XPS Spectra*, vol. 2 (XPS International Inc., Commercially Pure Binary Oxides, 1999)
69. N.S. McIntrye, M.G. Cook, Anal. Chem. **47**, 2208 (1975)
70. J. van Elp, J.L. Wieland, H. Eskes, P. Kuiper, G.A. Sawatzky, F.M.F. De Groot, T.S. Turner, Phys. Rev. B **44**, 6090 (1991)
71. M.A. Langell, F. Gevrey, M.W. Nydegger, Appl. Surf. Sci. **153**, 114 (2000)
72. V.M. Jiminez, J.P. Espinos, A.R. González-Elipe, Surf. Interface Anal. **26**, 62 (1998)
73. H. Yang, J. Ouyang, A. Tang, J. Phys. Chem. B **111**, 8006 (2007)
74. J. Yang, H. Liu, W.N. Martens, R.L. Frost, J. Phys. Chem. C **114**, 111 (2010)
75. M.C. Biesinger, B.P. Payne, L.W.M. Lau, A. Gerson, R.St.C. Smart, Surf. Interface Anal. **41**, 324 (2009)
76. St.G. Christoskova, N. Danova, M. Georgieva, O.K. Argirov, D. Mehandzhiev, Appl. Catal. A-Gen. **128**, 219 1995
77. R. Danoix-Souchet, A. D'Huysser, Surf. Interface Anal. **25**, 747 (1997)
78. N. Kitakasu, V. Maurice, C. Hinnen, P. Marcus, Surf. Sci. **407**, 36 (1998)
79. M. Chigane, M. Ishikawa, J. Chem. Soc. Faraday Trans. **94**, 3665 (1998)
80. N.S. McIntyre, D.G. Zetaruk, D. Owen, *Appl. Surf. Sci.* ***2***, 55 (1978)

81. L.J. Matienzo, L.I., Yin, S.O. Grim, W.E. Swartz, Inorg. Chem. ***12***, 2762 (1973)
82. M.W. Roberts, R.St.C. Smart, J. Chem. Soc. Faraday Trans. **80**, 2957 (1984)
83. A.F. Carley, S.D. Jackson, J.N. O'Shea, M.W. Roberts, Surf. Sci. **440**, L868 (1999)
84. L.M. Moroney, R.St.C. Smart, M.W. Roberts, J. Chem. Soc. Faraday Trans. **79**, 1769 (1983)
85. M.W. Roberts, R.St.C. Smart, J. Chem. Soc. Faraday Trans. **80**, 2957 (1984)
86. B.P. Payne, M.C. Biesinger, N.S. McIntyre, J. Electron Spec. Rel. Phenom. **175**, 55 (2009)
87. B.P. Payne, A.P. Grosvenor, M.C. Biesinger, B.A. Kobe, N.S. McIntyre, Surf. Interfece Anal. **9**, 582 (2007)
88. A.P. Grosvenor, R.G. Cavell, A. Mar, J. Solid State Chem. **181**, 2549 (2008)
89. A.L. Allred, E.G. Rochow, J. Inorg. Nucl. Chem. **5**, 264 (1958)
90. P.E.R. Blanchard, R.G. Cavell, A. Mar, J. Solid State Chem. **183**, 1477 (2010)
91. H. Takahashi, K. Igawa, K. Arii, Y. Kamihara, M. Hirano, H. Hosono, Nature **453**, 376 (2008)
92. G.F. Chen, Z. Li, D. Wu, G. Li, W.Z. Hu, J. Dong, P. Zheng, J.L. Luo, N.L. Wang, Phys. Rev. Lett. **100**, 247002 (2008)
93. Z.A. Ren, J. Yang, W. Lu, W. Yi, G.C. Che, X.L. Dong, L.L. Sun, Z.X. Zhao, Mater. Res. Innov. **12**, 105 (2008)
94. Z.-A. Ren, J. Yang, W. Lu, W. Yi, X.-L. Shen, Z.-C. Li, G.-C. Che, X.-L. Dong, L.-L. Sun, F. Zhou, Z.-X. Zhao, Europhys. Lett. **82**, 57002 (2008)
95. M. W. Gaultois, A. P. Grosvenor, J. Mat. Chem. **21**, 1829 (2011)
96. M.W. Gaultois, A.P. Grosvenor, Phys. Chem. Chem. Phys. **14**, 205 (2012)
97. M.W. Gaultois, A.P. Grosvenor, J. Phys. Chem. C **114**, 19822 (2010)
98. M.C. Biesinger, L.W. M. Lau, A.R. Gerson, R.St.C. Smart, Phys. Chem. Chem. Phys. **14**, 2434 (2012)
99. C.D. Wagner, Faraday Discuss. Chem. Soc. **60**, 291 (1975)
100. M.G. Brik, Phys. B **387**, 69 (2007)
101. P.T. Andrews, T. Collins, P. Weightman, J. Phys. C: Solid State Phys. **14**, L957 (1981)
102. G. van der Laan, B.T. Thole, G.A. Sawatzky, M. Verdaguer, Phys. Rev. B: Condens. Matter **37**, 6587 (1988)
103. M.A. Villegas, A. de Pablos, J.M. Fernandez-Navarro, Glass Technol. **35**, 276 (1994)
104. G. Mountjoy, D.M. Pickup, R. Anderson, G.W. Wallidge, M.A. Holland, R.J. Newport, M.E. Smith, Phys. Chem. Chem. Phys. **2**, 2455 (2000)
105. G.W. Wallidge, R. Anderson, G. Mountjoy, D.M. Pickup, P. Gunawidjaja, R.J. Newport, M. E. Smith, J. Mater. Sci. **39**, 6743 (2004)
106. K. Kamiya, S. Sakka, J. Mater. Sci. **15**, 2937 (1980)
107. T. Hayashi, T. Yamada, H. Saito, J. Mater. Sci. **18**, 3137 (1983)
108. K. Kamiya, S. Sakka, Y. Tatemichi, J. Mater. Sci. **15**, 1765 (1980)
109. C.J. Brinker, G.W. Scherer, *Sol–Gel Science: The Physics and Chemistry of Sol–Gel Processing* (Academic Press, Boston, 1990)
110. D. Poitras, S. Larouche, L. Martinu, Appl. Opt. **41**, 5249 (2002)
111. G. Mountjoy, M.A. Holland, G.W. Wallidge, P. Gunawidjaja, M.E. Smith, D.M. Pickup, R. J. Newport, J. Phys. Chem. B **107**, 7557 (2003)
112. D. Brassard, D.K. Sarkar, M.A. El Khakani, L. Ouellet, J. Vac. Sci. Technol., A **24**, 600 (2006)
113. R.D. Leapman, L.A. Grunes, P.L. Fejes, Phys. Rev. B **26**, 614 (1982)
114. R.L. Opila, G.D. Wilk, M.A. Alam, R.B. van Dover, B.W. Busch, Appl. Phys. Lett. **81**, 1788 (2002)
115. A. Nilsson, R.E. Palmer, H. Tillborg, B. Hernnas, R.J. Guest, N. Martensson, Phys. Rev. Lett. **68**, 982 (1992)
116. P.S. Bagus, F. Illas, G. Pacchioni, F. Parmigiani, J. Electron Spectrosc. Relat. Phenom. **100**, 215 (1999)
117. E.J. Little, M.M. Jones, J. Chem. Educ. **37**, 231 (1960)
118. R.D. Shannon, Acta. Crystallogr. Sect. A: Cryst. Phys. Diffr. Theor. Gen. Crystallogr. **32**, 751 (1976)

119. J.P. Crocombette, F. Jollet, J. Phys.: Condens. Matter **6**, 10811 (1994)
120. G.S. Henderson, X. Liu, M.E. Fleet, Phys. Chem. Miner. **29**, 32 (2002)
121. C. Weigel, G. Calas, L. Cormier, L. Galoisy, G.S. Henderson, J. Phys.: Condens. Matter **20**, 135219 (2008)
122. D. Li, G.M. Bancroft, M. Kasrai, M.E. Fleet, X.H. Feng, K.H. Tan, Am. Mineral. **79**, 785 (1994)
123. L.A.J. Garvie, P.R. Buseck, Am. Mineral. **84**, 946 (1999)
124. J.A. van Bokhoven, T. Nabi, H. Sambe, D.E. Ramaker, D.C. Koningsberger, J. Phys.: Condens. Matter **13**, 10247 (2001)
125. G. Moretti, J. Electron Spectrosc. Relat. Phenom. **95**, 95 (1998)

Chapter 11
Optimizing Polarization Dependent Hard X-ray Photoemission Experiments for Solids

J. Weinen, T.C. Koethe, S. Agrestini, D. Kasinathan, F. Strigari, T. Haupricht, Y.F. Liao, K.-D. Tsuei and L.H. Tjeng

Abstract Polarization dependent hard X-ray photoemission (HAXPES) experiments are a very powerful tool to identify the nature of the orbitals contributing to the valence band. To optimize this type of experiments we have set up a photoelectron spectroscopy system consisting of two electron energy analyzers mounted such that one detects the photoelectrons propagating parallel to the polarization vector (E) of the light and the other perpendicular. This method has the advantage over using phase retarders (to rotate the E-vector of the light) that the full intensity and full polarization of the light is available for the experiments. Using NiO as an example, we are able to identify reliably the Ni 3*d* spectral weight of the valence band and at the same time demonstrate the importance of the Ni 4*s* for the chemical stability of the compound. We have also discovered the limitations of this type of polarization dependent experiments: the polarization dependence is less than

J. Weinen · S. Agrestini · D. Kasinathan · L.H. Tjeng (✉)
Max Planck Institute for Chemical Physics of Solids, Nöthnitzer Str. 40,
01187 Dresden, Germany
e-mail: hao.tjeng@cpfs.mpg.de

J. Weinen
e-mail: jonas.weinen@cpfs.mpg.de

S. Agrestini
e-mail: stefano.agrestini@cpfs.mpg.de

D. Kasinathan
e-mail: deepa.kasinathan@cpfs.mpg.de

T.C. Koethe · F. Strigari · T. Haupricht
II. Physikalisches Institut, Universität zu Köln, Zülpicher Straße 77,
50937 Cologne, Germany
e-mail: koethe@ph2.uni-koeln.de

F. Strigari
e-mail: strigari@ph2.uni-koeln.de

T. Haupricht
e-mail: tim@haupricht.de

© Springer International Publishing Switzerland 2016

J.C. Woicik (ed.), *Hard X-ray Photoelectron Spectroscopy (HAXPES)*,
Springer Series in Surface Sciences 59, DOI 10.1007/978-3-319-24043-5_11

expected on the basis of calculations for free atoms and we can ascribe this incompleteness of the polarization dependence to the presence of appreciable side-scattering effects of the outgoing electrons, even at these high kinetic energies in the 6–8 keV range.

11.1 Introduction

With bulk sensitivity being an important characteristic of HAXPES, another useful aspect of this technique appears to be the very pronounced dependence of the spectra on the polarization of the light. This can in principle be used to identify the character of the orbitals contributing to the valence band [1–4]. In fact, if this can be made quantitative, one can obtain a very detailed understanding of the electronic structure of the material under study, especially when guided by theoretical ab initio calculations. The polarization dependent HAXPES experiments reported so far [1–4] made use of phase retarders to rotate the polarization of the light. The efficiency of the retarders to generate vertically polarized light, however, is about 0.8 only [1–4]. This hampers a reliable determination of the limits of polarization dependent HAXPES due to the inaccuracies in the characterization of the efficiency of the phase retarders.

In our HAXPES project we followed a different route: instead of rotating the polarization of the light, we altered the position of the electron energy analyzer, i.e. we used two different experimental geometries, one in which the analyzer is placed horizontally in the direction of the linear polarization of the light and the other vertically and thus perpendicular to the light polarization (Fig. 11.1). This set-up has the advantage that all the spectra can be taken with the full light polarization provided by the undulator beam line. We have carried out a test experiment on NiO as a model system for strongly correlated oxides. We can identify clearly the Ni 3*d* spectral weight of the valence band and at the same time demonstrate the importance of the Ni 4*s* for the chemical stability of the compound. We have also quantified the limitations of the polarization analysis: the polarization dependence is less than expected on the basis of calculations for free atoms. We ascribe this incompleteness of the polarization dependence to the presence of appreciable side-scattering effects of the outgoing electrons, even at these high kinetic energies in the 6–8 keV range [5].

Y.F. Liao · K.-D. Tsuei
National Synchrotron Radiation Research Center, 101 Hsin-Ann Road,
Hsinchu Science-Park Hsinchu, Taiwan 30077, China
e-mail: liao.yenfa@nsrrc.org.tw

K.-D. Tsuei
e-mail: tsuei@nsrrc.org.tw

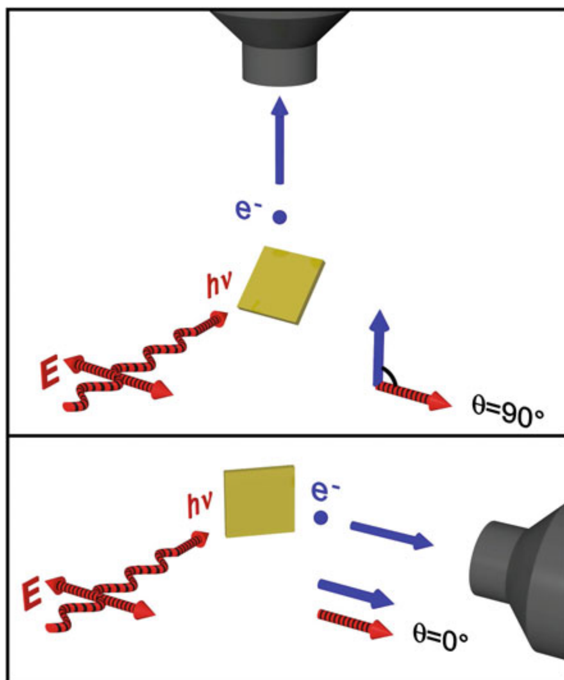

Fig. 11.1 Experimental geometry for different angles θ between the photon beam (*red, striped*) electrical field vector $\boldsymbol{E}$ and the momentum of the analyzed photoelectrons (*blue*). $\boldsymbol{E}$ is always horizontal, in the plane of the synchrotron storage ring, the photoelectron analyzer is always mounted perpendicular to the photon beam. *Top* Analyzer mounted vertically, $\theta = 90°$. *Bottom* Analyzer mounted horizontally, $\theta = 0°$

11.2 Experimental

The experiments have been carried out at the recently installed Max-Planck-NSRRC HAXPES set-up at the Taiwan undulator beamline BL12XU at SPring-8, Japan. The photon beam is linearly polarized with the electrical field vector in the plane of the storage ring (i.e. horizontal). The photon energy is about 6.5 keV. The beam is monochromatized in two stages: a diamond crystal diverts a photon beam with about 1 eV bandwidth to the HAXPES side branch and a channel-cut monochromator is introduced to produce the desired photon resolution. Several silicon single crystal channel-cut monochromators are available, allowing to select the photon resolution within the range of 75–220 meV. A pair of K-B mirrors focuses the beam on the sample position, achieving a spot size at the sample of $40\,\mu\text{m} \times 40\,\mu\text{m}$. The ultra-high vacuum experimental chamber is mounted on a motorized table which allows to easily and precisely align the setup. Also the sample manipulator is fully motorized. The sample is mounted on a continuous-flow cryostat which allows to use liquid helium for cooling to 10 K.

An MB Scientific A-1 HE analyzer was used for the measurements. In the horizontal geometry, the analyzer was mounted parallel to the photon beam's electrical field vector and perpendicular to the Poynting vector of the light. The maximum angular acceptance was limited to ±15.3° (30.5° total acceptance) by the circular opening of the first lens element. The photon energy and the overall energy

resolution was determined using a gold reference sample. The Fermi level was at 6474.4 eV kinetic energy and the overall energy resolution was set to 390 meV. For the measurements in the vertical geometry, the spectrometer was mounted perpendicular to the photon beam and to its electrical field vector. The maximum angular acceptance was limited to ±8.3° (16.6° total acceptance) by the circular opening of the first lens element. A silver reference sample was used to determine the photon energy and energy resolution. The Fermi level was at 6482.4 eV kinetic energy and the overall energy resolution was set to 350 meV.

For both geometries, an analyzer entrance slit/aperture set was used which limited the angular acceptance in the energy dispersive direction to ±1.65°. Applying the Helmholtz-Lagrange relation [6], this corresponds to an acceptance of about ±3.5° at the lens entrance. The acceptance angle in the direction parallel to the analyzer entrance slit (i.e. perpendicular to the energy dispersive direction) is determined by the circular opening of the first element as specified above. A NiO single crystal from SurfaceNet, Germany, was used (vertical geometry: as introduced, horizontal: cleaved in situ). It was aligned in a grazing incidence and near normal emission geometry. The temperature was 300 K, the pressure in the measurement chamber was $2-3 \times 10^{-8}$ mbar.

We have also performed X-ray photoemission (XPS) measurements for the NiO valence band using a Scienta SES-100 electron energy analyzer and a Vacuum Generators twin crystal monochromatized Al-K_α $h\nu = 1486.6\,\mathrm{eV}$ source. The overall energy resolution was set to 350 meV, as determined using the Fermi cutoff of a silver reference. The pressure in this spectrometer was 2×10^{-10} mbar during the measurements, and the NiO single crystal was cleaved in situ to obtain a clean surface.

11.3 Core Levels

Figure 11.2 displays the HAXPES Ni 2*p* and O 1*s* core level spectra of NiO taken with the photoelectron momentum parallel (red curves) and perpendicular (blue curves) to the polarization vector of the light. The parallel versus perpendicular spectra are normalized with respect to the Ni 2*p* main peak intensity. No corrections have been made to the spectra apart from a constant background subtraction. The line shape of the Ni 2*p* spectra is essentially identical to the ones published using also lower photon energies [7–12]. The O 1*s* spectrum shows a narrow single line demonstrating that the NiO sample is clean and of good quality. The relevant information that is contained in Fig. 11.2 is that the O 1*s* intensity is much lower for the perpendicular (blue curve) than for the parallel (red curve) polarization. This is qualitatively in agreement with the observations for *s*-orbitals in experiments in which the polarization has been varied using a phase retarder [1–4].

Making use of the fact that the degree of the photon polarization is identical for the two experimental geometries, we now can be quantitative concerning the

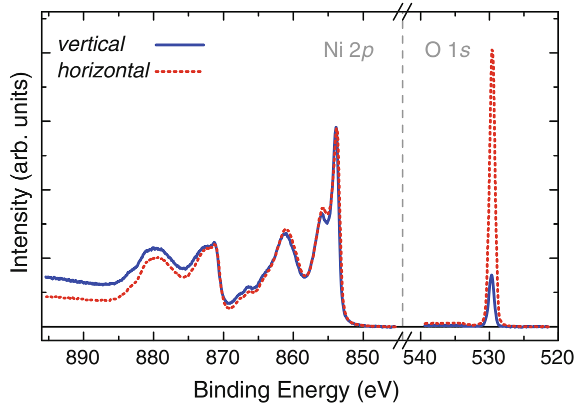

Fig. 11.2 HAXPES (photon energy 6.5 keV) spectra of NiO Ni 2*p* and O 1*s* core levels with $\theta = 90°$ (*vertical*) and $\theta = 0°$ (*horizontal*)

physics underlying the change of the O 1*s* intensity with the photoelectron momentum. The expression for the angular dependence for the differential photoionization cross section is given by Trzhaskovskaya et al. [13, 14]:

$$\frac{d\sigma}{d\Omega} = \frac{\sigma}{4\pi}\left[1 + \beta P_2(\cos\theta) + (\gamma\cos^2\theta + \delta)\sin\theta\cos\varphi\right] \tag{11.1}$$

where σ is the subshell photoionization cross section and P_2 the second Legendre polynomial. θ is the angle between the photoelectron momentum and the polarization vector of the light, φ the angle between the photon momentum vector and the plane spanned by the photoelectron momentum vector and the electrical field vector. β, γ, and δ are the angular distribution parameters. In our setup, we have for the horizontal analyzer $\theta = 0°$ (φ undefined) and for the vertical analyzer $\theta = 90°$ and $\varphi = 90°$. The expression (11.1) now simplifies to

$$\frac{d\sigma}{d\Omega} = \frac{\sigma}{4\pi}\{1 + \beta P_2(\cos\theta)\} \tag{11.2}$$

or

$$\frac{d\sigma}{d\Omega} = \frac{\sigma}{4\pi}\left\{1 + \frac{\beta}{2}(3\cos^2\theta - 1)\right\} = \frac{\sigma}{4\pi}\left\{1 + \beta\left(\frac{1}{4} + \frac{3}{4}\cos 2\theta\right)\right\}. \tag{11.3}$$

A polar plot of this angular dependence is shown in Fig. 11.3 for several values of β.

Ideally, in the atomic limit, β is 2 for *s* orbitals, so that for the perpendicular orientation, i.e. $\theta = 90°$, the intensity for the O 1*s* spectrum is expected to be zero. This is clearly not the case. Normalized to the Ni 2*p* intensities, the intensity ratio of the O 1*s* signal taken with perpendicular and parallel orientation is 0.16. Cross-section calculations for atomic orbitals provide a β value of about 0.98 for Ni 2*p* at $h\nu = 6.5\,\text{keV}$ [13, 14] (angular distribution parameters are interpolated from

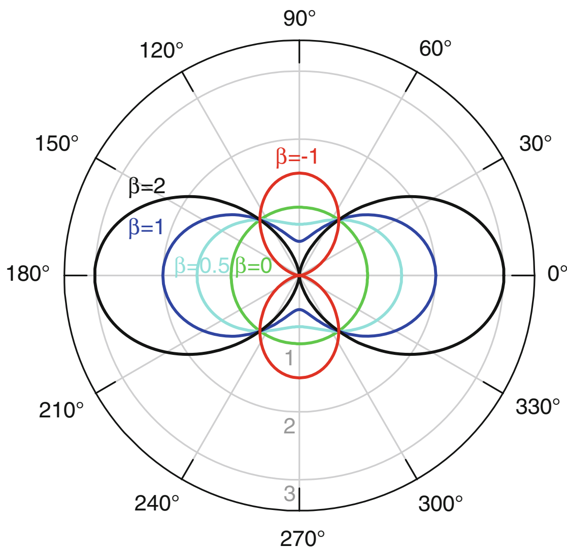

Fig. 11.3 Polar plot of the cross section angular dependence for various values of β

tabulated values), so that the Ni 2p intensity ratio for vertical versus horizontal orientation should be close to 0.258 using (11.3). The real experimental O 1s intensity ratio is therefore 0.16 × 0.258 = 0.041. This is substantially larger than the expected value of 0.008 using (11.3) for the interpolated β value of about 1.952 for O 1s at $h\nu = 6.5\,\text{keV}$ [13, 14].

To identify the origin of this discrepancy we will first investigate the effect of the acceptance angle of the electron energy analyzers. We first of all note that the third term in the sum in (11.1) still can be omitted for the two geometries used in our experiment when we consider the effect of the acceptance angles: for the horizontal geometry, the acceptance angle in both the analyzer entrance slit and energy dispersive directions enters as variations of the θ angle symmetrically around $\theta = 0$, and will not integrate a non-zero value for the third term since sin θ is an odd function of θ. For the vertical geometry, the acceptance angle in the analyzer entrance slit direction enters as variations in the φ angle symmetrically around $\varphi = 90°$. Since cos φ is an odd function around $\varphi = 90°$, the third term will not show up. The acceptance angle in the energy dispersive direction then also becomes irrelevant. We still can therefore use the simpler (11.3).

In order to calculate the cross-section average over the acceptance angle, we integrate (11.3) from $\theta - \alpha$ to $\theta + \alpha$ and divide by 2α, where $\pm\alpha$ denotes the acceptance angle. We arrive at:

$$\frac{d\sigma}{d\Omega} = \frac{\sigma}{4\pi}\left\{1 + \beta\left(\frac{1}{4} + \frac{3}{4}\cos 2\theta\,\frac{\sin 2\alpha}{2\alpha}\right)\right\} \tag{11.4}$$

The relevant acceptance angle for the horizontal geometry is determined essentially by the acceptance along the analyzer entrance slit direction, i.e. ±15.3°, since this is much larger than the acceptance along the energy dispersive direction, i.e. ±3.5°. For the vertical geometry on the other hand, the acceptance along the analyzer entrance slit direction does not alter θ, so the relevant number here is the acceptance along the energy dispersive direction, i.e. ±3.5°. Using these numbers and (11.4), we have a theoretical Ni 2*p* intensity ratio for vertical versus horizontal orientation of 0.264 and 0.01 for the O 1*s*. The real experimental O 1*s* intensity ratio is $0.16 \times 0.264 = 0.042$. Clearly, this is much larger than expected on the basis of the cross-section tables including the effect of the analyzer acceptance angles. In fact, in order to obtain a value of 0.042 we need for the analyzer in the vertical geometry acceptance angles of the order of ±18°, which is physically not possible with the ±8.3° acceptance dictated by the opening of the first lens. Apparently, we have to conclude that the acceptance angles of the analyzer do not form the limiting factor for the suppression of the O 1*s* signal in the vertical orientation.

11.4 Valence Band

In order to investigate to what extent these findings also affect HAXPES experiments on the valence band and especially the quantitative analysis of their polarization dependence, we also set out to collect the valence band spectrum of NiO. Figure 11.4 displays the HAXPES spectrum taken with the vertical and horizontal geometries, together with the spectrum taken with the standard XPS [15] using monochromatized $h\nu = 1486.6$ eV photons, as reference.

Starting with the XPS, we would like to note that this spectrum is very similar to the ones reported earlier in the literature [16–18] and that it shows the characteristic features labeled as A, B, C, and D, which are all related to the multiplet structure of the Ni 3*d* spectral weight [16–18]. The HAXPES spectra, interestingly, have different lineshapes with clear extra features labeled S1 and S2. In the vertical geometry, the intensities of these extra features are modest, but in the horizontal geometry, the features dominate the spectrum.

To identify the origin of the S1 and S2 structures, we have performed LDA band structure calculations using the full-potential code with the basis set of local atomic-like orbitals (FPLO) [19]. The resulting total and partial densities of states (DOS) are depicted in the bottom panel of Fig. 11.4. Of particular interest is the Ni 4*s* partial DOS. We can clearly observe that the peak positions of the Ni 4*s* and O 2*p* bands coincide very well with structures S1 and S2. Indeed, looking at the tables [13, 14], the ratio of the subshell photoionization cross section of the Ni 4*s* relative to that of the Ni 3*d* increases from 0.12 at $h\nu = 1486.6$ eV, to 0.99 at $h\nu = 5$ keV, and to 3.61 at $h\nu = 10$ keV, meaning that the contribution of the Ni 4*s* to the spectrum is negligible in XPS and that it becomes significant in the HAXPES experiment. The finding that HAXPES is much more sensitive to valence *s* orbitals

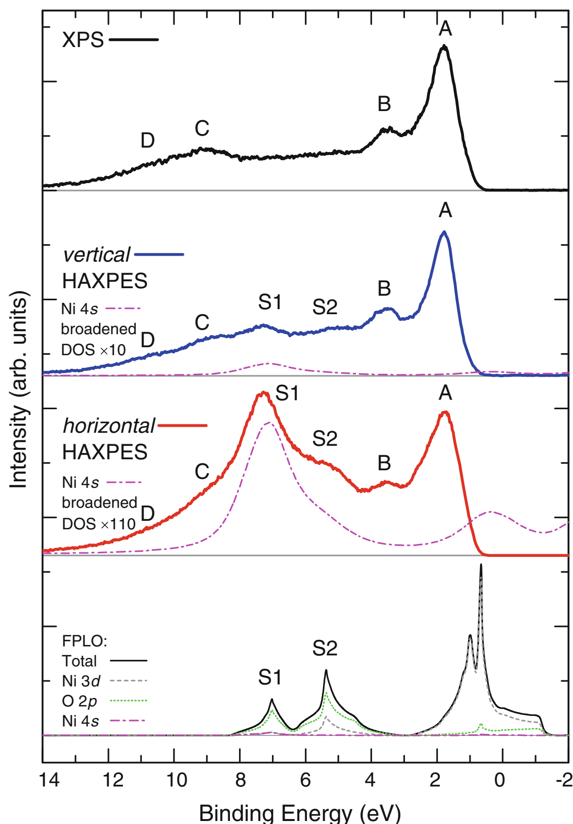

Fig. 11.4 XPS [15] (photon energy 1.487 keV) and HAXPES (6.5 keV) spectra of NiO valence band with $\theta = 90°$ (*vertical*) and $\theta = 0°$ (*horizontal*). LDA total and partial density of states from FPLO band structure calculations

is consistent with earlier reports and has been used to identify the partial density of states of the *s* orbital in semiconductors and metals [20–25].

This result in fact shows that HAXPES unveils an important part of the chemical bonding between the Ni and the O in the formation of NiO, namely the hybridization between the Ni 4*s* conduction band and the O 2*p* valence band. This provides an extra energy gain on top of the bonding energy due to the Ni 3*d* and O 2*p* hybridization. This Ni 4*s* − O 2*p* hybridization is analogous to that of Mg 3*s* and O 2*p* in MgO [26, 27]. We would like to note that it is rather surprising that the LDA calculation can explain so well the experimentally observed structure S1. It is well known that due to the strongly correlated nature of the Ni 3*d* electrons the description of the electronic structure by theory is still a great challenge. Features A, B, C, and D require an explanation that includes at least aspects of configuration interaction and atomic multiplet effects [16–18]. The Ni 3*d* states and their hybridization with the O 2*p* will therefore result in an O 2*p* spectral weight that may be significantly different from the LDA O 2*p* partial DOS. The Ni 4*s* that couples to this O 2*p* may consequently show spectral weight at quite different energies than

predicted by the LDA. It is therefore invaluable that the Ni 4*s* states can indeed be made visible experimentally. From the fact that the LDA does give a reasonable match to the experiment for the Ni 4*s* we can apparently deduce that the O 2*p* states that hybridize with the Ni 4*s* have a rather weak mixing with the Ni 3*d*. In hindsight, we may indeed see a justification for this in the form of a rather small Ni 3*d* and very high O 2*p* partial DOS in the LDA band that form the S1 structure.

We now analyze quantitatively the polarization dependence of the Ni 4*s* contribution to the spectrum. With the spectra normalized to the Ni 3*d* peak height at 2 eV binding energy, i.e. peak A, in the experiment and normalized to the Ni 3*d* peak height at 1 eV binding energy in the calculation, we can make an estimate for the relative contribution of the Ni 4*s* to the spectra. After broadening the calculated DOS with a 0.35 eV Gaussian to account for the experimental resolution and 1.9 eV Lorentzian for the life time (full width at half maximum values), we find for the vertical geometry that a multiplication by a factor of 10 of the Ni 4*s* DOS gives a reasonable match for the intensity of structure S1 and S2. For the horizontal geometry, we need a multiplication factor of approximately 110. From the cross section tables we expect the Ni 3*d* to have an intensity ratio for vertical versus horizontal orientation of about 0.58. Here we make use of (11.4), with $\beta = 0.39$ for Ni 3*d* at $h\nu = 6.5\,\mathrm{keV}$ [13, 14]. The effect of the analyzer acceptance angle is included. We then find experimentally that the ratio for the Ni 4*s* polarization dependence is given by $10/110 \times 0.58 = 0.053$. This is a very large contrast which demonstrates the power of polarization dependence to identify the contribution of *s* orbitals to the valence band. Using the polarization dependence rather than the photon energy dependence of the photoionization cross section has the advantage that one does not also vary the probing depth as is the case when comparing HAXPES with XPS.

Yet, on the basis of atomic cross-section calculation, we expect even a larger contrast, namely a Ni 4*s* intensity ratio of about 0.004 with $\beta = 1.984$ for Ni 4*s* [13, 14]. The reduction of the Ni 4*s* is thus much less than can be expected on the basis of the atomic calculations including the effect of the analyzer acceptance angles. This finding is consistent with the above described observations for the O 1*s*. Again, in order to obtain the value of 0.053 we need somehow effective acceptance angles of the order of ±18° for the measurement, and this is clearly not related to the instrumental conditions. A possible explanation for this non-perfect polarization dependence can perhaps be found in the (quasi-elastic) scattering processes which take place following the creation of the photoelectron [28–31]. Although forward scattering will be dominant at high kinetic energies, a non-negligible amount of side scattering processes will make it possible to change the propagation direction of part of the photoelectrons such that they enter the analyzer which they otherwise will not be able to do. The effective acceptance angle of the order of ±18° that we would need, as mentioned above, reflects this process. We note that experiments using 700 eV photons on VO_2 reveal only a weak polarization dependence for the O 1s [32] as shown in Fig. 11.5, supporting the explanation on the basis of such scattering processes: the kinetic energy of the photoelectrons (ca. 170 eV) is so low, that side or

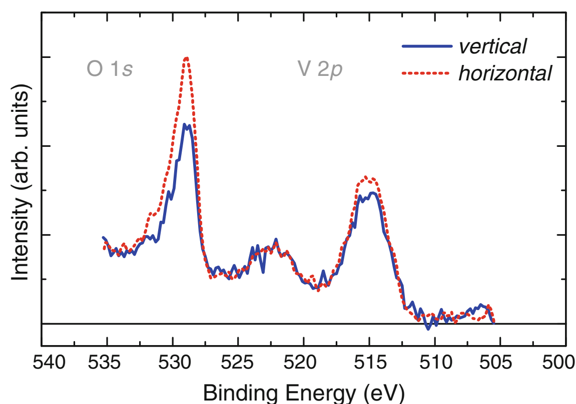

Fig. 11.5 PES (photon energy 700 eV) spectra of VO_2 core levels with $\theta = 90°$ (*vertical*) and $\theta = 0°$ (*horizontal*). The suppression of the O 1*s* is much weaker than at higher energies

even back scattering events dominate, leading to an almost complete loss of the relationship between the propagation direction of the photoelectron upon creation and the direction of the photoelectron when it enters the analyzer.

Fig. 11.6 HAXPES endstation at SPring-8 Taiwan Beamline 12XU sideline

11.5 Conclusions

Although the polarization dependence in the HAXPES experiments is not as much as we have expected on the basis of atomic cross-section calculations, i.e. a reduction to 0.042 or 0.053 instead of 0.01 or 0.004, we nevertheless can state that it is extremely large: the reduction is from 1.00 to 0.042 or 0.053. In other words, we can achieve a contrast of about 20:1 for *s* orbitals. This is more than sufficient for determining the character of the orbitals forming the valence band of solids as we have shown for the case of NiO. Based on the results of these experiments, we now have modified our HAXPES set-up such that two photoelectron energy analyzers are mounted simultaneously: one analyzer is placed horizontally (in the direction of the linear polarization of the light) and the other vertically (and thus perpendicular to the light polarization). Figure 11.6 shows a photograph of this new set-up. Although a simultaneous measurement of both polarizations is even possible, our aim is more to facilitate high-quality polarization dependence experiments without the need to interrupt the measurement to rotate the set-up, which usually is accompanied by stopping the vacuum pumps or even breaking the vacuum.

Acknowledgement We would like to thank G. Panaccione for valuable discussions. We acknowledge Lucie Hamdan and Thomas Mende for their skillful technical assistance. This work was supported by the Deutsche Forschungsgemeinschaft through SFB 608 and FOR 1346.

References

1. A. Sekiyama, J. Yamaguchi, A. Higashiya, M. Obara, H. Sugiyama, M.Y. Kimura, S. Suga, S. Imada, I.A. Nekrasov, M. Yabashi, K. Tamasaku, T. Ishikawa, New J. Phys. **12**(4), 043045 (2010). doi:10.1088/1367-2630/12/4/043045
2. S. Ouardi, G.H. Fecher, X. Kozina, G. Stryganyuk, B. Balke, C. Felser, E. Ikenaga, T. Sugiyama, N. Kawamura, M. Suzuki, K. Kobayashi, Phys. Rev. Lett. **107**, 036402 (2011). doi:10.1103/PhysRevLett.107.036402
3. Y. Nakatsu, A. Sekiyama, S. Imada, Y. Okamoto, S. Niitaka, H. Takagi, A. Higashiya, M. Yabashi, K. Tamasaku, T. Ishikawa, S. Suga, Phys. Rev. B **83**, 115120 (2011). doi:10.1103/PhysRevB.83.115120
4. S. Ouardi, G.H. Fecher, C. Felser, J. Electron Spectrosc. **190**, 249 (2013). doi:10.1016/j.elspec.2013.09.001
5. J. Weinen, T.C. Koethe, C.F. Chang, S. Agrestini, D. Kasinathan, Y.F. Liao, H. Fujiwara, C. Schüßler-Langeheine, F. Strigari, T. Haupricht, G. Panaccione, F. Offi, G. Monaco, S. Huotari, K.D. Tsuei, L.H. Tjeng, J. Electron Spectrosc. Rel. Phen. **198**, 6 (2015). doi:http://dx.doi.org/10.1016/j.elspec.2014.11.003. URL:http://www.sciencedirect.com/science/article/pii/S0368204814002370
6. F. Offi, A. Fondacaro, G. Paolicelli, A. De Luisa, G. Stefani, Nucl. Instrum. Methods Phys. Res., Sect. A **550**(12), 454 (2005). doi:http://dx.doi.org/10.1016/j.nima.2005.04.086. URL: http://www.sciencedirect.com/science/article/pii/S0168900205012544
7. M. Oku, H. Tokuda, K. Hirokawa, J. Electron Spectrosc. **53**(4), 201 (1991). doi:10.1016/0368-2048(91)85039-V

8. A.E. Bocquet, T. Mizokawa, T. Saitoh, H. Namatame, A. Fujimori, Phys. Rev. B **46**, 3771 (1992). doi:10.1103/PhysRevB.46.3771
9. S. Uhlenbrock, C. Scharfschwerdt, M. Neumann, G. Illing, H.J. Freund, J. Phys.: Condens. Mat. **4**(40), 7973 (1992). URL:http://stacks.iop.org/0953-8984/4/i=40/a=009
10. L. Sangaletti, L.E. Depero, F. Parmigiani, Solid State Commun. **103**(7), 421 (1997). doi:10.1016/S0038-1098(97)00185-3
11. S. Altieri, L.H. Tjeng, A. Tanaka, G.A. Sawatzky, Phys. Rev. B **61**, 13403 (2000). doi:10.1103/PhysRevB.61.13403
12. M. Taguchi, M. Matsunami, Y. Ishida, R. Eguchi, A. Chainani, Y. Takata, M. Yabashi, K. Tamasaku, Y. Nishino, T. Ishikawa, Y. Senba, H. Ohashi, S. Shin, Phys. Rev. Lett. **100**, 206401 (2008). doi:10.1103/PhysRevLett.100.206401
13. M.B. Trzhaskovskaya, V.I. Nefedov, V.G. Yarzhemsky, Atom. Data Nucl. Data **77**(1), 97 (2001). doi:10.1006/adnd.2000.0849
14. M.B. Trzhaskovskaya, V.K. Nikulin, V.I. Nefedov, V.G. Yarzhemsky, Atom. Data Nucl. Data **92**(2), 245 (2006). doi:10.1016/j.adt.2005.12.002
15. T.J.T. Haupricht, Transition metal impurities in wide bandgap oxides: fundamental model systems for strongly correlated oxides. Ph.D. thesis, Universität zu Köln (2011)
16. J. van Elp, H. Eskes, P. Kuiper, G.A. Sawatzky, Phys. Rev. B **45**, 1612 (1992). doi:10.1103/PhysRevB.45.1612
17. A. Fujimori, F. Minami, Phys. Rev. B **30**, 957 (1984). doi:10.1103/PhysRevB.30.957
18. G.A. Sawatzky, J.W. Allen, Phys. Rev. Lett. **53**, 2339 (1984). doi:10.1103/PhysRevLett.53.2339
19. K. Koepernik, H. Eschrig, Phys. Rev. B **59**, 1743 (1999). doi:10.1103/PhysRevB.59.1743
20. J.C. Woicik, E.J. Nelson, L. Kronik, M. Jain, J.R. Chelikowsky, D. Heskett, L.E. Berman, G. S. Herman, Phys. Rev. Lett. **89**, 077401 (2002). doi:10.1103/PhysRevLett.89.077401. URL: http://link.aps.org/doi/10.1103/PhysRevLett.89.077401
21. K. Kobayashi, Y. Takata, T. Yamamoto, J.J. Kim, H. Makino, K. Tamasaku, M. Yabashi, D. Miwa, T. Ishikawa, S. Shin, T. Yao, Jpn J. Appl. Phys. **43**(8A), L1029 (2004). URL:http://stacks.iop.org/1347-4065/43/i=8A/a=L1029
22. G. Panaccione, G. Cautero, M. Cautero, A. Fondacaro, M. Grioni, P. Lacovig, G. Monaco, F. Offi, G. Paolicelli, M. Sacchi, N. Stojić, G. Stefani, R. Tommasini, P. Torelli, J. Phys. Condens. Matter **17**(17), 2671 (2005). URL:http://stacks.iop.org/0953-8984/17/i=17/a=015
23. D.J. Payne, R.G. Egdell, G. Paolicelli, F. Offi, G. Panaccione, P. Lacovig, G. Monaco, G. Vanko, A. Walsh, G.W. Watson, J. Guo, G. Beamson, P.A. Glans, T. Learmonth, K.E. Smith, Phys. Rev. B **75**, 153102 (2007). doi:10.1103/PhysRevB.75.153102. URL:http://link.aps.org/doi/10.1103/PhysRevB.75.153102
24. J.C. Woicik, M. Yekutiel, E.J. Nelson, N. Jacobson, P. Pfalzer, M. Klemm, S. Horn, L. Kronik, Phys. Rev. B **76**, 165101 (2007). doi:10.1103/PhysRevB.76.165101. URL:http://link.aps.org/doi/10.1103/PhysRevB.76.165101
25. K. Kobayashi, Nuclear instruments and methods in physics research section a: accelerators, spectrometers, detectors and associated equipment **601**(12), 32 (2009). doi:http://dx.doi.org/10.1016/j.nima.2008.12.188. URL:http://www.sciencedirect.com/science/article/pii/S016890020802010X. Special issue in honour of Prof. Kai Siegbahn
26. L.H. Tjeng, A.R. Vos, G.A. Sawatzky, Surf. Sci. **235**(23), 269 (1990). doi:10.1016/0039-6028(90)90802-F
27. U. Schönberger, F. Aryasetiawan, Phys. Rev. B **52**, 8788 (1995). doi:10.1103/PhysRevB.52.8788. Also see the references therein
28. A.X. Gray, C. Papp, S. Ueda, B. Balke, Y. Yamashita, L. Plucinski, J. Minár, J. Braun, E.R. Ylvisaker, C.M. Schneider, W.E. Pickett, H. Ebert, K. Kobayashi, C.S. Fadley, Nat. Mater. **10**(10), 759 (2011). doi:10.1038/nmat3089
29. M.A. Vicente Alvarez, H. Ascolani, G. Zampieri, Phys. Rev. B **54**, 14703 (1996). doi:10.1103/PhysRevB.54.14703

30. N.J. Shevchik, Phys. Rev. B **16**, 3428 (1977). doi:10.1103/PhysRevB.16.3428
31. R.C. White, C.S. Fadley, M. Sagurton, Z. Hussain, Phys. Rev. B **34**, 5226 (1986). doi:10.1103/PhysRevB.34.5226
32. T.C. Koethe, J.C. Cezar, N.B. Brookes, Z. Hu, L.H. Tjeng, unpublished

Chapter 12
Photoelectron Emission Excited by a Hard X-ray Standing Wave

Jörg Zegenhagen, Tien-Lin Lee and Sebastian Thiess

Abstract The following chapter describes the basics and some applications for the case that photoelectrons are emitted from a hard X-ray interference field instead of by a travelling wave. The dipole approximation holds astonishingly well even for hard X-rays as far as the magnitude of the transition matrix element is concerned. However, the forward-backward asymmetry caused by higher order multipole terms needs to be considered when the photoelectron is emitted by the coherent action of two X-ray waves travelling in different directions. This has implications on the chosen experimental set-up which will be briefly discussed together with other experimental aspects. Finally, some examples of X-ray standing wave analysis using hard X-ray photoelectron spectroscopy will be presented yielding the geometric and electronic structure of (crystalline) materials with pm resolution.

12.1 Introduction

In the 1960s, verifying the predictions of the dynamical theory of X-ray diffraction (DTXD) [1–3], Boris Batterman demonstrated that an X-ray standing wave (XSW) with the periodicity of the lattice planes (correctly speaking: diffraction planes[1]) is formed during Bragg reflection of hard X-rays [4]. A few

[1]Note the difference between diffraction plane, i.e. the plane defined by $\mathbf{k}_0$ and $\mathbf{k}_h$ and diffraction planes, which are parallel to a corresponding set of Miller planes, for example (333), (444), (555), etc. which are all parallel to the (111) Miller planes. Diffraction planes are not necessarily atomic planes. Their spacing d_{hkl}/m is defined by Bragg's law $2d_{hkl}\sin\Theta = m\lambda$ where d_{hkl} is the spacing of the (hkl) Miller planes.

J. Zegenhagen (✉) · T.-L. Lee
Diamond Light Source Limited, Diamond House, Didcot, Oxfordshire OX11 0DE, UK
e-mail: jorg.zegenhagen@diamond.ac.uk

T.-L. Lee
e-mail: Tien-Lin.Lee@diamond.ac.uk

S. Thiess
Deutsches Elektronen-Synchrotron, Notkestraße 85, 22607 Hamburg, Germany
e-mail: sebastian.thiess@desy.de

© Springer International Publishing Switzerland 2016

J.C. Woicik (ed.), *Hard X-ray Photoelectron Spectroscopy (HAXPES)*,
Springer Series in Surface Sciences 59, DOI 10.1007/978-3-319-24043-5_12

years later he showed that the photo-absorption can be made position selective [5] when using such an X-ray interference field instead of a travelling wave for the photo excitation. At the time, he used the emitted X-ray fluorescence as a probe for the strength of the photoabsorption, though. The principle of this method, commonly referred to as the XSW technique, is shown in Figs. 12.1 and 12.2.

Interestingly enough, but nowadays mostly forgotten, K. Siegbahn conceived the ESCA (electron spectroscopy for chemical analysis) technique in the 1960s using in the beginning X-rays in the 10 keV range as excitation source [6]. Thus, ESCA using hard X-rays, that is HAXPES, and the XSW technique were conceived at pretty much the same time. In a typical photoelectron spectroscopy (PES) experiment, the electron emission is of course excited by a transient electromagnetic wave and thus the absorbing atom and its surroundings are exposed to the same constant electric field intensity.

The motivation of Batterman's first experiment was just to prove that an XSW exists in a crystal during Bragg reflection, but then he realized that the XSW is rather useful as a novel structural probe [5]. Nowadays, the XSW technique is understood as highly valuable extension of many spectroscopic techniques, notably PES, adding high spatial resolution to the already powerful spectrum of features [7]. For employing the full strength of the XSW technique, especially the extensive Fourier analysis of the distribution of atoms in the unit cell or on the surface of a substrate [8, 9], the methods requires the use of hard X-rays. Higher spatial resolution requires shorter wavelengths, i.e. higher X-ray energies. Furthermore, due to the properties of crystal optics, it is straight forward to produce monochromatic X-rays with rather small band-pass, easily reaching below 10 meV, at higher X-ray energies [10, 11]. Thus, the advantage of combining the XSW technique especially with hard X-ray PES (HAXPES) is obvious. However, it took quite a while until the two techniques, which were almost conceived in parallel, came together and joined forces.

In the early days of the XSW technique, fluorescence spectroscopy was employed as the spectroscopic technique of choice, simply because PES requires the sample to be placed in vacuum, which represents an additional complication (and limitation for some applications). However, it should be noted that relatively early simple total yield electron detectors such as gas avalanche detectors were used for XSW experiments [12].

In the early 1980s, the strength of using the XSW technique for surface studies was demonstrated [13] locating Br on Si(110) in methanol solution. In the development of the XSW technique, a major leap forward was the application of synchrotron radiation [14]. Shortly after, the XSW method was then adapted for surface studies in ultra high vacuum (UHV) in the mid 1980s by several groups [15, 16], also employing photoelectrons as the detection channel [17, 18].

The fact that the XSW technique allows pm spatial resolution is a direct consequence of the (largely) valid dipole approximation (DA) of the photo-absorption

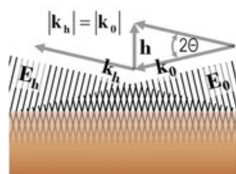

Fig. 12.1 Bragg reflection of a plane wave, characterized by momentum $\mathbf{k_0}$ and electric field $\mathbf{E_0}$ giving rise to a reflected wave $\mathbf{k_h}$ and $\mathbf{E_h}$ and the formation of a standing wave (interference field) in the overlap region

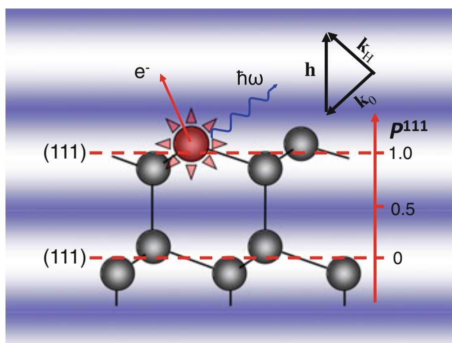

Fig. 12.2 Schematic of an XSW produced by a Si(111) reflection. The (111) diffraction planes which are also Miller planes are indicated. An atom, photo excited by the maxima of the field intensity, emits a photoelectron and then X-ray fluorescence upon relaxation

process [19]. In the DA, the strength of the photo-absorption is exactly proportional to the electric field strength at the center of the absorbing atom. Thus, using XSW the atomic distribution is probed, in contrast to X-ray diffraction experiment, probing the charge distribution. At higher X-ray energies, the dipole approximation is unfortunately compromised and multipole contributions cause a forward/backward asymmetry in the photoelectron emission (cf. Fig. 12.3). This must be considered when interpreting the result of an PES/XSW experiment in particular in case of backreflection as will be briefly discussed further below.

12.2 X-ray Standing Wave and Photo-Absorption

The XSW technique is in essence an X-ray interference technique. Scanning the interference field, the intensity of the photoelectron emission, following the absorption by a specific atom, reveals the position of this atom with respect to the XSW

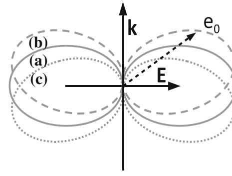

Fig. 12.3 The photoelectron (e_0) emission profile is symmetric with respect to the E-field vector in case of pure dipolar emission (*a*) and shifted along photon propagation **k** forward (*b*) or backward (*c*) when quadrupole contributions become sizeable, i.e. shifted in opposite directions for the incident and reflected beam in case of back-reflection

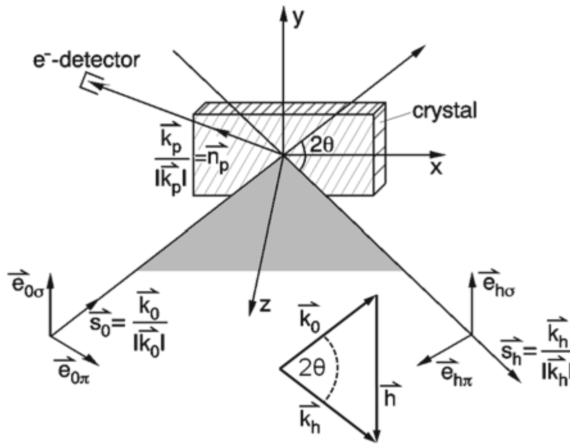

Fig. 12.4 Schematic of photoelectron emission from a crystal under Bragg reflection. The incident and reflected electromagnetic waves $\mathbf{E_0}$ and $\mathbf{E_h}$ are characterized by the wave vectors $\mathbf{k_0}$ and $\mathbf{k_h}$, respectively. The X-ray polarization is indicated by the vectors $\mathbf{e_{0\sigma}}$, $\mathbf{e_{0\pi}}$ and $\mathbf{e_{h\sigma}}$, $\mathbf{e_{h\pi}}$. The angle 2θ, i.e. twice the Bragg angle, is the angle between the wave vectors $\mathbf{k_0}$ and $\mathbf{k_h}$. The escaping photoelectron is characterised by the vector $\mathbf{k_p}$

pattern. The interference field, the standing wave, is considered here being created by Bragg diffraction from a single crystal and atomic positions are thus determined on the scale of its unit cell.

12.2.1 X-ray Standing Wave Formation

An X-ray wavefield is created by the superposition of the incident and Bragg reflected X-ray waves (cf. Fig. 12.1) with the electric field vectors $\mathbf{E}_0 = \mathbf{e}_0 E_0$ and $\mathbf{E}_h = \mathbf{e}_h E_h$, respectively with

$$\mathbf{E}_0 = \mathbf{e}_0 E_0 \mathrm{e}^{i(\omega_0 t - \mathbf{k}_0 \mathbf{r})} \quad \text{and} \quad \mathbf{E}_h = \mathbf{e}_h E_h \mathrm{e}^{i(\omega_h t - \mathbf{k}_h \mathbf{r})}$$

as shown schematically in Fig. 12.1. Here $\mathbf{e}_0$ and $\mathbf{e}_h$ are polarization vectors and $\mathbf{k}_0$ and $\mathbf{k}_h$ are the X-ray propagation vectors with

$$|\mathbf{k}_0| = |\mathbf{k}_h| = |\mathbf{k}| = k = 2\pi\lambda^{-1}$$

where λ is the X-ray wavelength. The two E-field vectors are related by an amplitude and a phase factor via

$$E_h = \sqrt{R} E_0 \exp(i\upsilon)$$

with R being the reflectivity

$$R = \frac{I_h}{I_0} = \frac{|E_h|^2}{|E_0|^2}.$$

The propagation vectors of the two plane waves are related by

$$\mathbf{k}_h = \mathbf{k}_0 + \mathbf{h} \qquad (12.1)$$

as shown in Fig. 12.1.

The XSW in the overlap region is given by

$$\mathbf{E} = \mathbf{E}_0 + \mathbf{E}_h = \mathrm{e}^{i\omega t}\left[\mathbf{e}_0 E_0 \mathrm{e}^{(-i\mathbf{k}_0 \mathbf{r})} + \mathbf{e}_h \sqrt{R} E_0 \mathrm{e}^{i\upsilon} \mathrm{e}^{(-i\mathbf{k}_h \mathbf{r})}\right]$$

Assuming for simplicity $\mathbf{e}_0 \| \mathbf{e}_h$ and using the cosine theorem the wavefield intensity I can be cast into the simple form:

$$I^h = |\mathbf{E}|^2 = I_0\left(1 + R + 2\sqrt{R}\cos(\upsilon - \mathbf{hr})\right)$$

The dimensionless scalar product $\mathbf{hr}$ describes the spatial modulation of the wavefield intensity along $\mathbf{h}$ with the spacing $d_h = 2\pi h^{-1}$, where $h = |\mathbf{h}|$. Normal to $\mathbf{h}$ the wavefield intensity is constant (cf. Figs. 12.1 and 12.2). Calculating reflectivity, wavefield intensities, the phase υ and other parameters requires the DTXD [1–3]. The wavefield exists above the surface to a distance limited by the temporal coherence length of the X-ray beam. Besides using the Bragg reflection from a single crystal one can also use multilayers [20] or the total reflection from a mirror surface [21].

12.2.2 Photoelectron Emission from a Hard X-ray Standing Wave

The photo-absorption of an XSW has been described thoroughly [7, 22] and is only recalled briefly, adopting largely the description given in the recently published book on the XSW technique [7]. The coordinate r of an electron of an atom, excited from $|i>$ to $<f|$, is given by $\mathbf{r} = \mathbf{r}_a + \mathbf{r}_e^a$, where $\mathbf{r}_a$ points to the center of the atom and $\mathbf{r}_e^a$ points to the electron (from the center of the atom), which is emitted. As reference frame for $\mathbf{r}_a$ serves the origin of the unit cell of the crystal.

The matrix element of the photo-absorption process of the interference field is the sum of the complex matrix elements of the absorption corresponding to each wave E_0 and E_h,

$$M_{fi} = E_0 <f|\mathrm{e}^{i\mathbf{k_0}\cdot\mathbf{r}}(\mathbf{e_0}\cdot\hat{\mathbf{p}})|i> \; + E_h <f|\mathrm{e}^{i\mathbf{k_h}\cdot\mathbf{r}}(\mathbf{e_h}\cdot\hat{\mathbf{p}})|i> , \tag{12.2}$$

or

$$M_{fi} = E_0 \exp(i\mathbf{k_0}\cdot\mathbf{r}_a)[M_{fi}(\mathbf{s_0}) + \left(\frac{E_h}{E_0}\right)\mathrm{e}^{i\mathbf{h}\cdot\mathbf{r}_a}M_{fi}(\mathbf{s_h})], \tag{12.3}$$

where $\mathbf{s}_0 = \mathbf{k_0}/|\mathbf{k_0}|$, $\mathbf{s_h} = \mathbf{k_h}/|\mathbf{k_h}|$, the momentum operator $\hat{\mathbf{p}} = -i\hbar\nabla$ and

$$\begin{aligned} M_{fi}(\mathbf{s_0}) &= \; <f|\exp(i\mathbf{k_0}\mathbf{r}_e^a)(\mathbf{e_0}\hat{\mathbf{p}})|i> , \\ M_{fi}(\mathbf{s_h}) &= \; <f|\exp(i\mathbf{k_h}\mathbf{r}_e^a)(\mathbf{e_h}\hat{\mathbf{p}})|i> \end{aligned} \tag{12.4}$$

are the corresponding matrix elements. The cross section of the process and hence the expected intensity of the photoelectron yield $Y(\Omega)$ is proportional to the square modulus of the matrix element, given for each (linear) polarization state by

$$Y_a^h(\Omega) \propto \mathrm{d}\sigma/\mathrm{d}\Omega \propto |M_{fi}|^2,$$

where

$$|M_{fi}|^2 = |E_0|^2\left\{S_{00} + S_{hh}R + 2\sqrt{R}Re[S_{0h}\mathrm{e}^{i(\nu+\mathbf{h}\mathbf{r}_a)}]\right\}. \tag{12.5}$$

with

$$S_{00} = |M_{fi}(\mathbf{s_0})|^2,\; S_{hh} = |M_{fi}(\mathbf{s_h})|^2,\; S_{0h} = M_{fi}(\mathbf{s_0})^* M_{fi}(\mathbf{s_h}). \tag{12.6}$$

Here, S_{00} and S_{hh} are real numbers, but S_{0h} may be complex and can give rise to an additional phase shift $\psi = \arg\,[S_{0h}/S_{00}]$.

After normalization, the photoelectron yield can thus be expressed as

$$Y_a^h(\Omega) = 1 + S_R R + 2|S_I|\sqrt{R}\cos(\upsilon - \mathbf{hr_a} + \psi), \tag{12.7}$$

by introducing the new parameters

$$S_R = \frac{S_{hh}}{S_{00}}, S_I = |S_I|\mathrm{e}^{i\psi} = \frac{S_{0h}}{S_{00}}. \tag{12.8}$$

Typically non-dipole contributions beyond quadrupole (Q) can safely be neglected, and the matrix elements are given by

$$M_{fi}(\mathbf{s_0}) \simeq M_{fi}^D + M_{fi}^Q(\mathbf{s_0}), M_{fi}(\mathbf{s_h}) \simeq M_{fi}^D + M_{fi}^Q(\mathbf{s_h}). \tag{12.9}$$

Only the quadrupole term depends on the propagation vectors $\mathbf{s_0}$, $\mathbf{s_h}$ but dipole and quadrupole terms are in general complex and can thus interfere with each other. Thus, additional to the interference of the two coherent X-ray waves E_0 and E_h, the interference of the multipole matrix elements M_{fi}^D and M_{fi}^Q needs to be considered.

12.2.3 XSW and Structural Information: Fourier Analysis

In reality a large number N_A of specific atoms A will be excited by the XSW. The total recorded yield $I_{A,T}^h$ is the summation of the yields of all individual atoms. Normalized, it is expressed as

$$Y_{A,T}^h = N_A^{-1} \sum_j^{N_A} \left\{ 1 + S_R R + 2S_I\sqrt{R}\cos(\upsilon - \mathbf{hr}_{Aj} + \psi) \right\} \tag{12.10}$$

Substituting the summation by an integral and introducing the distribution function $G(r)$, we can write

$$Y_{A,T}^h = N_A^{-1} \int_{\mathbf{r}} \mathrm{d}\mathbf{r} G_A(\mathbf{r}) \left\{ 1 + S_R R + 2S_I\sqrt{R}\cos(\upsilon - \mathbf{hr}_A + \psi) \right\} \tag{12.11}$$

The summation/integration of cosine functions yields again a cosine function with a certain amplitude $F_A^h \leq 1$ and phase P_A^h i.e.

$$Y_{A,T}^h = 1 + S_R R + 2\sqrt{R} S_I F_A^h \cos(\upsilon - 2\pi P_A^h + \psi) \tag{12.12}$$

with

$$2\pi P_A^h = hz_{Ah} = \mathbf{hr}_A \quad (12.13)$$

Casting the yield function in this form,[2] it becomes evident that the two parameters F_A^h and P_A^h (coherent fraction and coherent position) in (12.12) represent in fact the amplitude and phase of one of the coefficients of the Fourier transform of $G_A(\mathbf{r})$ [8, 9], i.e.,

$$G_A(\mathbf{h}) = G_A^h = F_A^h \mathrm{e}^{-i\mathbf{hr}_A} = F_A^h \mathrm{e}^{-i2\pi P_A^h} \quad (12.14)$$

An image of the analyzed distribution of atoms A can be created by Fourier back transformation [23, 24].

$$G_{A,XSW}(\mathbf{r}) = 1 + 2\sum_h F_A^h \cos[2\pi P_A^h - \mathbf{hr}] \quad (12.15)$$

Since the available h-values and thus Fourier coefficients are restricted (to the allowed Bragg reflections), length scales beyond the dimensions of the unit cell are not accessible.

12.2.4 Structural Analysis: Simple Interpretation

Employing sufficient reflections and performing a Fourier analysis, structural information can be obtained without any a priori assumptions or models. However, in particular because of the availability of phase information, XSW data of just one or few reflections can be sufficient to learn about the location of a particular atom in, or with respect to, the unit cell of the substrate. Bond-lengths are restricted and thus the surface distance of an adsorbate can be determined using just one reflection with the diffraction planes parallel to the surface. The coherent position P_A^H (cf. Fig. 12.2) can be regarded as the "average" position of the adsorbate (normalized by the diffraction plane spacing). The coherent fraction $f_A^H = D_A^H \cdot F_A^H$ is a measure of the width of the distribution around this mean position [9, 25]. All three parameters are dimensionless given on a scale 0–1, where the Debye-Waller factor D_A^H accounts for positional broadening due to thermal vibrations.

[2] The electron yield I_A^h detected in an XSWs experiment is given by $I_A^h = I_{A,0} Y_{A,T}^h$ where $I_{A,0}$, called off-Bragg yield, is proportional to the number of sampled atoms and other parameter such as photoelectric cross section, solid angle, beam intensity and more.

12.2.5 Influence of Multipole Contributions

The influence of multipole contributions on the XSW yield is the stronger the higher the Bragg angle and particularly strong for light elements. It depends also strongly on the electron analyzer position and quadrupole contributions can be suppressed when the detected electrons have been emitted in the polarization direction of the X-rays. Figure 12.5 shows the calculated values for S_R, S_I and ψ for five light elements for backreflection XSW and 1s photoemission as a function of

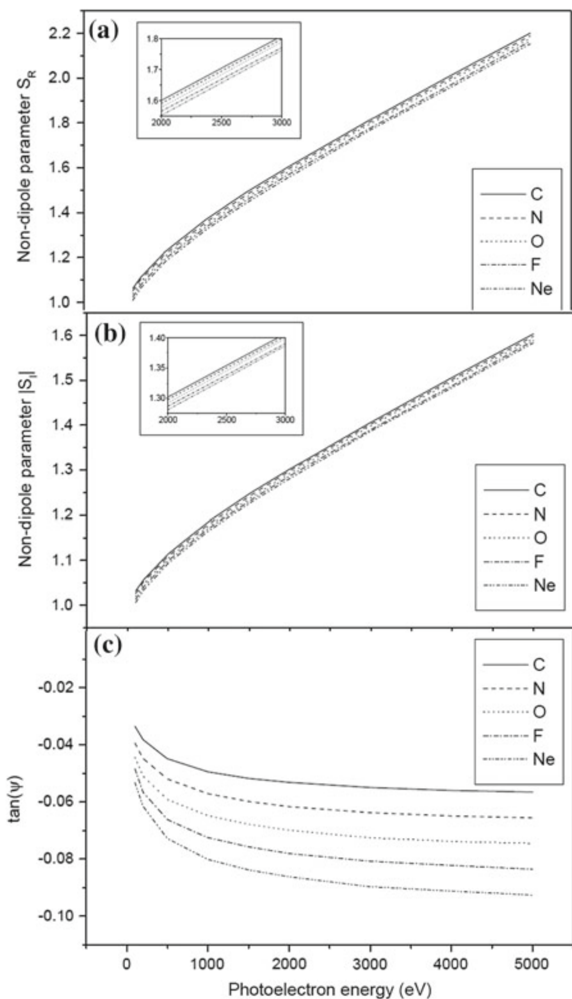

Fig. 12.5 Dependence of non-dipole parameters on photoelectron energy calculated for *1s*-state photoelectron emission and backreflection. The photoelectron escape angle was fixed to the $\theta_p = 45°$. **a** Non-dipole parameter S_R. **b** Non-dipole parameter $|S_I|$. **c** The phase tan (ψ) calculated utilizing phase shifts for each atom and energy [26, 27]

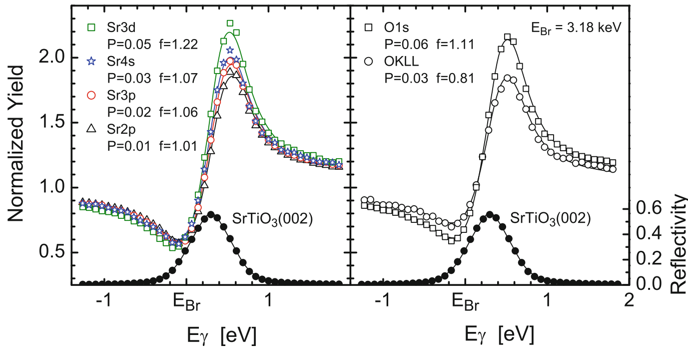

Fig. 12.6 Photoelectron and Auger electron yield recorded from a $SrTiO_3(001)$ crystal at an angle $\theta_p = 45°$ with respect to the beam polarization employing a (002) Bragg reflection in backscattering geometry at $E_\gamma = 3.18$ keV. Shown are the experimental data (*symbols*) and fits to the data (*lines*) with an analytical expression given by (12.12) with $S_R = S_I = 1.$ and $\psi = 0$. The $SrTiO_3(111)$ reflection curve (*closed symbols*) and a fit (*line*) according to the dynamical theory of X-ray diffraction is shown in the lower diagram

photoelectron emission energies up to 5 keV. The influence of quadrupole contributions is obviously very strong on S_R and S_I which differ largely from unity.[3]

The influence on the phase ψ is less pronounced. However, if sizeable multipole contributions were neglected and the a specific electron yield would be fitted with the equation

$$Y_T^h = 1 + R + 2\sqrt{R}f\cos(\upsilon - 2\pi P) \tag{12.16}$$

instead of (12.12), i.e. assuming pure dipole emission with $S_R = S_I = 1.$ and $\psi = 0$, not only the coherent fraction $f^h \neq F^H$ (cf Fig. 12.6) but also the coherent position P^h would be wrong and the structural information would thus be incorrect.

Figure 12.6 documents the influence of multipole contributions on the XSW yield. The XSW analysis of the oxygen KLL Auger yield from a $SrTiO_3$ crystal shows the true coherent position P and coherent fraction, i.e. $f^h = F^h$ in Fig. 12.6) since the Auger electron emission is isotropic and (far from absorption edges) not influenced by multipole contributions. Within error bars, the coherent position is zero as expected since for the (002) reflection all atoms are located on the (002) diffraction planes and secondary excitation does not influence the coherent position.[4] When fitting the O 1*s* signal using (12.16) by neglecting multipole contributions and setting $S_R = S_I = 1.$ and $\psi = 0$, the coherent position P deviates significantly from zero and obviously f, being larger than unity, does not correspond to the real coherent fraction F^h.

[3]For details of how the parameters S_R, S_I and ψ are calculated, the reader is referred to the original publication [24].

[4]A minor influence by a modified surface layer leading to $P =\neq 0$ cannot be excluded.

Even the photoelectron emission of heavier elements can be significantly influenced as shown in the upper panel of Fig. 12.6 for the XSW yield of different Sr core levels recorded from a $SrTiO_3$ crystal. Fitting the yield with (12.16) by setting again $S_R = S_I = 1.$ and $\psi = 0$, the fit to all three core levels yields different values for the coherent position P and the seeming coherent fraction f, with all f-values being larger than 0.81 and even larger than unity, which is physically impossible.

12.3 Experimental Considerations

In addition to the experimental conditions which are typically required for HAXPES experiments, there are some specifics when combining HAXPES with the XSW technique. This concerns the preparation of the X-ray beam, that is the plane X-ray wave, as well as the properties of the sample and its geometrical arrangement. Noteworthy, for both techniques a good (high) energy resolution is very beneficial. However, the XSW technique requires in addition a collimated beam (not necessary for HAXPES), which excludes strong focusing.

12.3.1 X-ray Source and Optics

The formation of the X-ray standing wave, that is a planar X-ray wavefield, is facilitated by Bragg reflection. In the early days of the XSW technique, using X-ray lab sources or 1st generation synchrotrons, the production of a plane wave was not straight forward. Producing a (pseudo) plane wave requires an optical scheme where the monochromator delivers a narrow bandpass and a collimated beam (see e.g. [14, 17, 28]). When this was not possible, non-dispersive crystal arrangements needed to be used (see e.g. [7] Chap. 13). This rendered the experimental set-up for XSW measurements complicated, with little versatility. Typically, for different sample crystals and reflections used, specific monochromator crystal combinations were necessary.[5] Thus, practicality was severely limiting the number of accessible Bragg reflections i.e. Fourier components.

With the help of the highly, brilliant, strongly collimated and intense X-ray beams from third generation synchrotron sources, the optical requirements are nowadays much easier to meet. Commonly a liquid nitrogen cooled Si(111) monochromator takes the high heat load from the insertion device. High energy resolution can be achieved with a secondary monochromator. This monochromator arrangement can be used for a large number of reflections (=Fourier components),

[5]If a divergent beam with a wide bandpass is incident on a crystal the different wavelengths are reflected at different angles, they are dispersed. When this rainbow like x-ray beam is incident on a sample crystal, incident wavelengths and angles only match if the crystal has exactly the same diffraction plane spacing (see e.g. [30]).

provided that the energy band and divergence of the X-ray beam is (much) smaller than the most narrow reflection curve used for the XSW experiment. Utilizing the small source size of present storage rings, if necessary, the angular divergence of the insertion device beam can be further decreased with the help of collimating optics, such as compound refractive lenses or similar. Any decrease in bandwidth is of course accompanied by a corresponding decrease in intensity, which can be tolerated because of the high flux from 3rd generation X-ray sources. In a recent publication Lee et al. [29] demonstrated how a proper optical arrangement allows to utilize a large number (close to 20) reflections for a complete analysis of the distribution of Mn in the GaAs unit cell.

12.3.2 Geometrical Consideration

When detecting photoelectrons the polarization of the X-ray beam, the diffraction geometry and the direction of the electron emission need to be considered, which will be briefly discussed in the following.

Evaluating the matrix elements $M_{fi}(s)$ in the dipole approximation one obtains for the parameters $S_{\alpha\beta}$,

$$\begin{aligned} S_{00} &= (\sigma^D/4\pi)[1 + \beta P_2(\mathbf{e_{0s}n_p})], \\ S_{hh} &= (\sigma^D/4\pi)[1 + \beta P_2(\mathbf{e_{hs}n_p})], \\ S_{0h} &= (\sigma^D/4\pi)[(1 - \beta/2)(\mathbf{e_{0s}e_{hs}}) + 3/2\beta(\mathbf{e_{0s}n_p})(\mathbf{e_{hs}n_p})]. \end{aligned} \tag{12.17}$$

Here σ^D is the dipole cross section, β is the dipole asymmetry parameter [31–33] and $P_2(x) = 0.5(3x^2 - 1)$ is the second order Legendre polynomial. The geometry for an XSW-HAXPES experiment, indicating the used parameters, is schematically shown in Fig. 12.4.

In the σ-polarization scattering geometry (cf. Fig. 12.4) the polarization vectors $\mathbf{e_0}$ and $\mathbf{e_h}$ are collinear. In this case we obtain for the parameters $S_{\alpha\beta}$ (12.17),

$$S_{00} = S_{hh} = S_{0h} = (\sigma^D/4\pi)[1 + \beta P_2(\mathbf{e}_\sigma \mathbf{n_p})]. \tag{12.18}$$

and consequently $S_R = |S_I| = 1$.

For π-polarization, the incident and diffracted electric field vectors lie in the scattering plane, the polarization vectors $\mathbf{e}_0$ and $\mathbf{e_h}$ are misaligned by twice the magnitude of the Bragg-angle 2θ (see Fig. 12.4) and the matrix element is a function of the angular momenta of the initial $|i>$ and final $|f>$ state electron wave functions.

For an s to p transition, $\beta = 2$ (to a very good approximation [31–33]), and we obtain for the parameters $S_{\alpha\beta}$ (12.17),

$$
\begin{aligned}
S_{00} &= 3(\sigma^D/4\pi)(\mathbf{e_{0\pi}n_p})^2 = 3(\sigma^D/4\pi)\cos^2\vartheta_{p0},\\
S_{hh} &= 3(\sigma^D/4\pi)(\mathbf{e_{h\pi}n_p})^2 = 3(\sigma^D/4\pi)\cos^2\vartheta_{ph},\\
S_{0h} &= 3(\sigma^D/4\pi)(\mathbf{e_{0\pi}n_p})(\mathbf{e_{h\pi}n_p}) = 3(\sigma^D/4\pi)\cos\vartheta_{p0}\cos\vartheta_{ph},
\end{aligned}
\tag{12.19}
$$

where ϑ_{p0} and ϑ_{ph} are the polar angles of the emitted electron relative to $\mathbf{e_{0\pi}}$ and $\mathbf{e_{h\pi}}$, respectively.

The photoelectron yield $Y_p(\Omega)$ [cf. (12.5)] is now expressed as

$$
Y_p(\Omega) \propto \cos^2\vartheta_{p0} + \cos^2\vartheta_{ph} R + 2\cos\vartheta_{p0}\cos\vartheta_{ph}\sqrt{R}F^h\cos(\upsilon - 2\pi P^h). \tag{12.20}
$$

If the detector is at a position satisfying the condition: $\vartheta_{p0} = 90°$ (in this case $\cos\vartheta_{p0} = 0$ and $S_{00} = 0$) or $\vartheta_{ph} \approx 90°$ (i.e. $\cos\vartheta_{ph} = 0$ and $S_{hh} \simeq 0$), the interference term $\sqrt{R}F^h\cos(\nu - 2\pi P^h)$ will be suppressed and $Y_p \propto R$ or $Y_p = const.$, respectively. Thus, using the π-geometry for the XSW-HAXPES measurements, the choice of the position of the photoelectron detector will drastically influence the shape of the photoelectron yield curve. This was shown experimentally [34] recording the L_I photoelectron yield from iodine adsorbed on a Ge(111) single crystal [35]. Using an aperture in front of the cylindrical mirror analyzer, the photoelectrons were detected in different directions with respect to the polarization vectors of the incident and reflected X-rays. The strong dependence of the yield shape on the direction of the photoelectron emission is obvious in Fig. 12.7 when detecting the electrons more in the direction of the polarization vector of the incident or reflected beam.

For σ-geometry, the shape of the yield curve resulting from an XSW measurements is not influenced by the specific positioning of the electron analyzer as long as multipole contributions in the photoelectron emission are negligible.\

12.3.3 Experimental Arrangement and Crystal Quality

When utilizing HAXPES under standing wave excitation by Bragg reflection, a crystalline substrate is needed as object of study. The mosaicity of this crystal should not be (much) larger than the angular range of Bragg reflection. This width is rather narrow (cf. Fig. 12.8), but increases strongly when Θ approaches 90°.[6] For example, the width of the Ge(111) reflection becomes of the order of a degree (11 mrad) at a Bragg angle of 88° (E_γ = 1.9 keV) whereas it's width is just 3/1000 of a degree (0.06 mrad) at 10.9° (E_γ = 10 keV). Using Bragg reflection close to 90° has of course

[6]This can easily be understood from Bragg's law $2d\sin(\Theta) = m\lambda$; at $\Theta = 90°$ the sine function is flat and a small change in λ necessitates a large change in Θ.

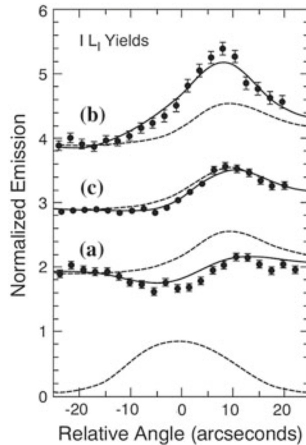

Fig. 12.7 The iodine L_I photoelectron (kinetic energy 1560 eV) yield as a function of glancing angle around the maximum reflectivity of the Ge(111) Bragg reflection at around 6.75 keV for a π-scattering geometry, recorded with a cylindrical mirror analyzer with different adjustments of its angular aperture: For curve a, the aperture selects photoelectrons with a larger momentum component in the direction of the polarization vector of the incident beam $e_{0\pi}$; for curve b, the aperture is adjusted to select photoelectrons emitted with a larger momentum component in the direction of the polarization vector of the reflected beam $e_{h\pi}$, cf. Fig. 12.4; for curve c, the aperture was removed, and a wide range of emission angles was selected. On the bottom the *Ge*(111) reflectivity is shown. The calculated yield curves (*solid lines*) assume an *s* to *p* dipole transition; the dashed curves are given by (12.12) with $S_R = |S_I| = 1$ and $\psi = 0$ from [34]

the consequences that the excitation energy $E_\gamma \pm \Delta E_\gamma$ of the X-ray is almost fixed. Exactly at 90°, and neglecting small refraction corrections, $E_\gamma = hc/2d_{hkl} = 1.2398$ keVnm/$2d_{hkl}$.

For backscattering XSW measurements, which are typically performed at Bragg angles a few degrees below 90°, it is commonly preferred to scan the Bragg reflection in energy rather than in angle [36, 37]. For the example shown in Fig. 12.8 the width of the rocking curve in energy is 2.98 eV, which can be scanned conveniently with a Si(111) monochromator which delivers, using the collimated beam of a third generation undulator source, an energy resolution of 1.3 eV at 10 keV.

The term normal incidence XSW (NIXSW) is in use for this method, which is misleading since Bragg reflections may be employed with a diffraction vector **H** which is inclined with the surface normal **n**. Thus, the X-ray beam is (nearly) normally incident on the diffraction plane, but not on the surface. When using diffraction planes inclined with the surface, it is generally advisable to use a geometry such that the angle of incidence with the surface equals the exit angle, as shown schematically in Fig. 12.9 to avoid complications in the data analysis because of "asymmetrical reflection". Space constraints do not permit elaborating this case further and the reader is referred for more information to the literature, e.g. to Chap. 13 in [7] or for even more details to the DTXD [1–3].

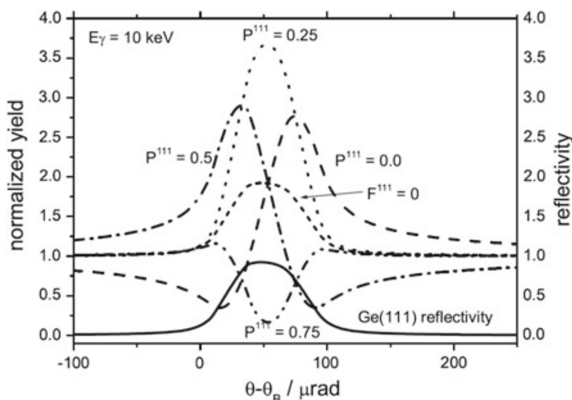

Fig. 12.8 Ge(111) reflection at 10 keV using the beam from a Si(111) monochromator. The photoelectron mission is calculated according to (12.12). Displayed are the yield curves for atoms located at different position $P^H = z_H/d_H$ (cf. Fig. 12.2) for a delta function profile ($F^{111} = 1.$). When passing the reflection curve from low to high energy the wavefield moves in direction $-\mathbf{H}$ by half a diffraction plane spacing, leading to characteristic yield profiles. The reflectivity R and phase ν [cf. (12.12)] are calculated with the help of the dynamical theory of X-ray diffraction [1–3]. Shown is also a yield curve for a random distribution of atoms ($F^{111} = 0$)

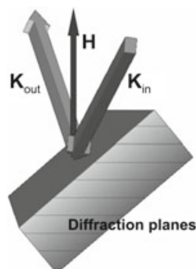

Fig. 12.9 Preferred geometry when using diffraction planes which are inclined with the surface plane. With respect to the surface, the angle of incidence of the beam is the same as the exit angle. Furthermore, the electric field vectors (not shown) of the incident and reflected beam should be parallel with the diffraction planes (σ-polarization)

12.4 Structural Analysis with HAXPES and XSW

Already in the early days of the XSW technique electron detection had been used, however with little or no energy resolution [12], as already mentioned in the introduction. Electrons excited by a hard XSW were detected later with moderate energy and thus depth resolution for analyzing the strain introduced in silicon by implantation of BF_2 [38] and As [39]. Using electrons excited by hard X-rays with little energy discrimination, the information gained can hardly be depth specific,

since the origin and nature of the electrons (photo, Auger, Compton) is not known. Moderate depth resolution can be achieved if the sample material is made of light elements such as B and F, as in the papers cited above, or e.g. carbon, where practically all electrons have the same origin i.e. C 1s.

The XSW technique in combination with PES has been used in the beginning exclusively for surface studies, in particular for the structural analysis of surface adsorbates. The first papers were published by Durbin et al. [17, 40] studying Au on Si(111) and the clean Si(111) surface. However, Auger electrons, detected in these studies, must not be exclusively the result of excitation by the X-ray photon beam. Soft X-ray fluorescence and Auger electron signals can also be excited by sufficiently energetic inelastic background from the sample. Consequently such signals do not carry reliably the information of the movement of the XSW with respect to the emitting atoms as D. Pacilé et al. showed in 2004 by comparing photoelectron and soft Auger electron emission [41]. Peculiarities of the differential photoelectron emission excited by an XSW also need to be considered to avoid errors in the structural analysis. As shown explicitly above, the orientation of the photoelectron analyzers to polarization vectors of the radiation has to be taken into account (a) if π-polarization is used [34, 35] and (b) in general if multipole contributions are significant [22, 42].

12.4.1 Surface Adsorbates

Of the almost 1500 papers published (at the time of the writing) using the XSW technique more than half (≈800) are dedicated to surface studies and of these ≈30 % (≈250) employ electron spectroscopy. In general, surface studies are not really of major interest for the HAXPES technique. However, if one wants to conduct a thorough structural analysis of a surface system using the XSW technique, one necessarily needs higher excitation energies in order to access higher order reflections. Thus, in discussing the combination of XSW and HAXPES, surface studies should not be omitted.

The strength of the XSW technique in surface science is a direct consequence of its combination with powerful spectroscopic techniques. Thus, an adsorbate is identified by spectroscopy and its structure can thus selectively be measured. In particular PES adds a very valuable benefit. Via the combination of XSW and ESCA different chemical species of the same element can be identified and their positions on the surface selectively determined. This was demonstrated in 1995 by Sugiyama et al. [43] and later by Jackson et al. [44]. Since then the chemical state sensitive XSW analysis has been very successful for the structural analysis of adsorbed organic molecules [45]. In this respect, we will report briefly as an example the results of a very recently published application, namely the XSW analysis of an anorganic carbon form i.e. the structure of graphene on SiC(0001) [46].

Graphene grows on the Si(0001) surface on top of a buffer layer with a $6\sqrt{3} \times 6\sqrt{3}$ structure [47] (cf. Fig. 12.10). This intermediate layer contains two

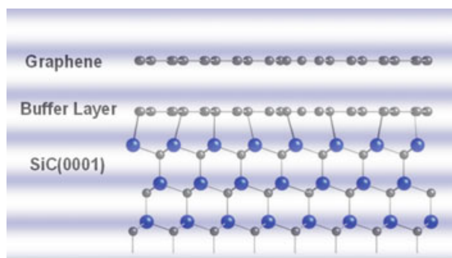

Fig. 12.10 Schematic of the structure of graphene on SiC(0001), which grows on top of an intermediate carbon layer, which contains two non-equivalent carbon atoms with a 2:1 ratio. The XSW is indicated

non-equivalent carbon atoms. Thus, for graphene on SiC(0001) one has to take in total four different, non-equivalent carbon species into account: One in the bulk, two in the intermediate layer, and one in the graphene. Photoelectron spectra of carbon and silicon excited by 2.45 keV X-rays are shown in Fig. 12.11.

All four C1s peaks can be separated and the surface distance of each of the three surface adsorbate components (S1, S2, EG) can be determined from the XSW data, shown in Fig. 12.12. The analysis of the carbon and silicon signals from the bulk does not provide any new information. However, the fits to the data determined the

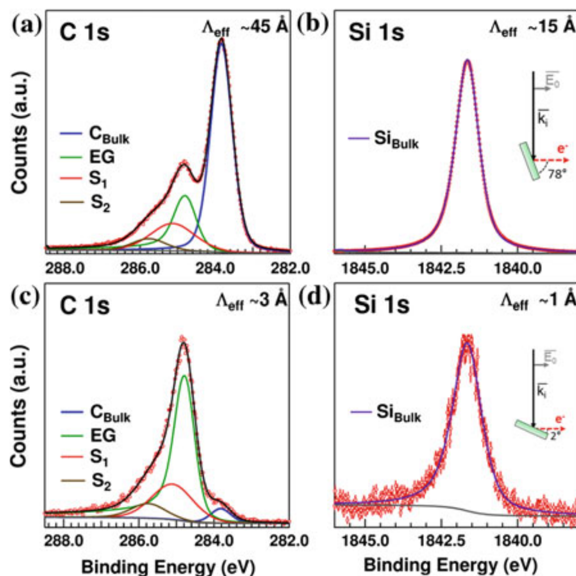

Fig. 12.11 Photoelectron spectra of 1.3 monolayer graphene (EG) on SiC(0001) recorded at non-grazing (**a**) and (**b**) and grazing (**c**) and (**d**) electron escape angles. The intermediate carbon layer, contains two non-equivalent carbon atoms with a 2:1 ratio labelled S1 and S2 respectively. The excitation energy used was 2.45 keV. Figure taken from [46]

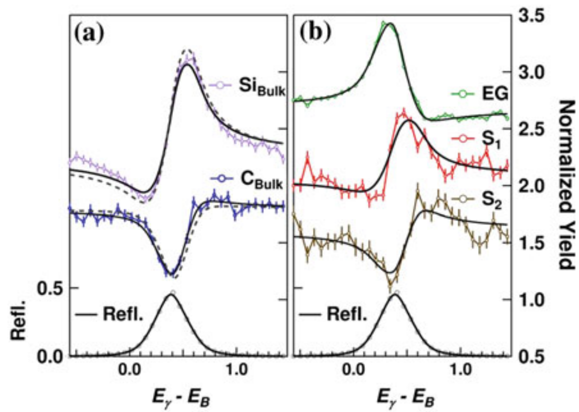

Fig. 12.12 Results of an XSW scan for graphene (EG) on SiC(0001) around the Bragg energy of 2.45 keV. Shown is also the reflectivity. Symbols are data and lines are fits to the data using (12.12). Figure taken from [46]

positions of the Si and C exactly as expected, demonstrating the quality of the surface as well as the accuracy of the XSW structural results. For more details, the reader is referred to the original publication [46].

12.4.2 Substrate Surface Structure

Analyzing the reconstruction of clean surfaces is not straightforward for the XSW method, because in most cases, the surface atoms can not be clearly distinguished from the substrate bulk. Durbin et al. had attempted to analyze the structure of the Si(111)-(7 × 7) surface by gaining surface sensitivity with the help of the shallow escape depth of 90 eV Si LVV Auger electrons [40]. However, as mentioned above, these Auger electrons can be excited by inelastic background from the bulk of the sample. Furthermore, the depth from which the signal originates and thus the contribution of different layers is not precisely known and can also be influenced by other effects such as diffraction of the low energy electrons.

A modified approach was used by Woicik et al. [48] (and later by Herrera-Gomez et al. [49]) in determining the reconstruction of InP(110) (and the GaP(110): Bi surface structure). In the zincblende structure of the III–V semiconductors, the atoms of both elements are located on the (220) lattice planes (in contrast e.g. to the (111) planes). The authors also detected soft Auger lines to determine the substrate surface structure, which are likely affected by signals from the bulk. They tried to take this into account by assuming that the soft Auger signal T is made of two contributions, S and B. Correspondingly the XSW yield $Y_T = Y_T(\Delta E)$ is made of two contributions $Y_T = Y_S + \alpha Y_B$, where S is the signal originating only from the surface, B is the bulk signal, exciting the soft Auger line, and α is a scaling factor. The bulk signal B was determined with the help of the electron background just above the Auger lines. Since any XSW yield function is determined by two free parameters, fitting T to the Auger yield leads only to a correct result with the help of additional

assumptions. For this example, the authors needed to assume that the surface atoms occupy only one site with a coherent fraction of unity. In this case, fitting Y_T gives the scaling parameter α and the coherent position P_S^H of the surface atom. It is beyond the scope of this short review to go into more detail and the reader is referred to the literature for more details XSW analysis [7, 9, 25]. Woicik and coworkers also employed low energy photoelectrons for analysing the clean, In and Ag covered Si(111) surface structure by detecting low energy Si 1s photoelectrons [50–52], which is a better approach than detecting Auger electrons. However, the accuracy of the analysis can still suffer from uncertainties in the electron escape depth and thus the contribution of the different atomic layers to the signal.

The analysis of graphene on SiC in the previous chapter serves as a good example of how the structure of the (reconstructed) surface of a substrate can be determined unambiguously. Since surface atoms are missing binding partners they generally exhibit a shift in binding energy. This chemical shift needs to be large with respect to the intrinsic line width and/or the overall energy resolution to be resolved. In the case of graphene on SiC, the carbon atoms of the $6\sqrt{3} \times 6\sqrt{3}$ reconstructed SiC crystal surface could be distinguished by spectroscopy i.e. they exhibited a sufficiently large difference in binding energy with their bulk counterparts.

12.4.3 Buried Interfaces

Epitaxial thin films have become indispensable in modern technology. In addition, interfaces of epitaxial systems have attracted increasing attention. The interface structure is crucial for the structural quality (and other properties) of the film. Furthermore, the interface itself can display astonishingly new properties[7] which are determined by the specific atomic structure and chemical bonds at the interface. For instance, by tailoring the interface structure, extremely high critical currents have been achieved in thin films of the 90 K high temperature superconductor (HTS) $YBa_2Cu_3O_{7-\delta}$ grown on $SrTiO_3(001)$ [53, 54]. More recently, interfaces of wide band gap metal-oxide insulators have displayed remarkable properties such as high mobility conductivity, superconductivity and more [55].

The structure and interface structure of ultra thin films (3.5 and 17.5 nm) of the HTS $GdBa_2Cu_3O_{7-\delta}$ (GBCO, orthorhombic, a = 0.3859 nm, b = 0.3885 nm, c = 1.1759 nm) grown on $NdGaO_3(001)$ was investigated a while ago [56]. With the chemical sensitivity and enhanced probing depth of high-energy photoelectrons, the atomic structures of film (e.g. lattice constant) and interface with the substrate (for the 3.5 nm sample) could be characterized.

[7]As Herbert Kroemer phrased it in his Nobel lecture, December 8, 2000: "Often it may be said that *the interface is the device*".

The GdBCO thin films were grown on single-crystal $NdGaO_3(001)$ substrates by pulsed laser deposition (PLD). $NdGaO_3$ has an orthorhombic structure ($a = 0.5428$ nm, $b = 0.5498$ nm, $c = 0.7708$ nm), but one can define an almost cubic ("pseudo-cubic") perovskite unit cell with $a = b = 0.3863$ nm and $c = 0.3855$ nm, which will be used in the following. XSW measurements were done by scanning the Si(111) monochromator through the (004) ("pseudo cubic") Bragg reflection at 3.23 keV ± ΔE of the NGO substrate in back reflection geometry. For the The O 1*s* and Cu 2*p* core-level spectra, different components could be identified. The components that exhibited high coherent fractions, were arising from well-ordered (intrinsic) parts of the oxide films. Components of the O 1*s* and Cu 2*p* spectra that showed low coherent fractions were arising from reacted, degraded parts (non-intrinsic) of the films. Figure 12.13 shows the spectrum and the XSW analysis for O 1*s* components.

The comparable large mean-free paths of the photoelectrons permitted in addition the analysis of the signal of the Nd and Ga atoms near the buried interface below the 3.5-nm film. The measurements suggested an essentially bulk-terminated $NdGaO_3$ (NGO) surface. Combined with the information from the GBCO, the

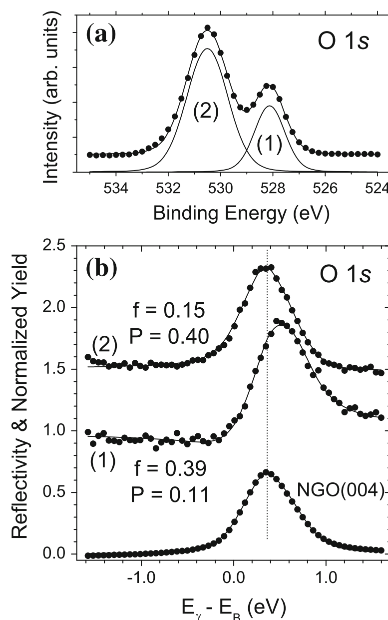

Fig. 12.13 O 1*s* Results of HAXPES/XSW investigations for a 3.5-nm GdBCO film on $NdGaO_3(001)$. **a** The photoelectron spectrum shows two components with the smaller component (1) originating from the intrinsic part of the film whereas the larger one (2) is from contaminated parts of the film due to air exposure. **b** The XSW data (*symbols*) and best fits to the data (*lines*) for the $NdGaO_3(004)$ reflection. Figure taken from [56]

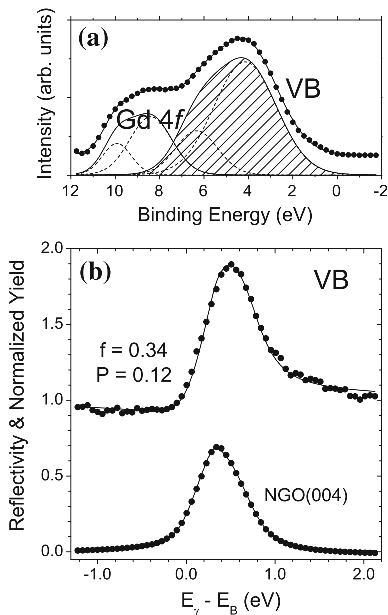

Fig. 12.14 O 1*s* HAXPES/XSW results of the valence band of a 3.5-nm GdBCO film on $NdGaO_3(001)$. **a** The photoelectron spectrum of the GdBCO valence band region including the Gd 4*f* photoelectron lines. **b** The XSW data (*symbols*) and best fits to the data (*lines*) of the GdBCO valence band (*hashed area*) for the $NdGaO_3(004)$ reflection. Figure taken from [56]

X-ray standing wave results revealed an interface with the CuO plane attached to the NdO plane, with a Cu-Nd distance of 0.18 nm.[8] The XSW results also showed that the 3.5 nm GBCO film had grown pseudomorphically strained on the NGO surface whereas the thicker, 17.5-nm film, was found to be already partially relaxed. Interestingly enough, for $YBa_2Cu_3O_{7-\delta}$ on $SrTiO_3(001)$, it had been found that the superconductor binds with the BaO plane to the TiO_2 plane of the substrate [57] (Fig. 12.15).

It was also possible to analyze the $GdBa_2Cu_3O_{7-\delta}$ valence band. The results are reproduced in Fig. 12.14. The X-ray standing wave measurement yielded values of coherent fraction F^H and coherent position P^H nearly identical to the values for the intrinsic part of the Cu 2*p* core level. This showed that the dominant contribution to the valence band in this high-temperature cuprate originates from the Cu (Cu 3*d*). For more detailed information, the reader is referred to the original publication [56].

12.4.4 XSW Imaging of the Nucleation of a Complex Oxide

Early scanning tunneling microscopy (STM) investigations had revealed that sub-monolayer films of $YBa_2Cu_3O_{7-\delta}$ deposited on $SrTiO_3(001)$ by pulsed laser deposition (PLD) do not grow in the 1.2 nm tall orthorhombic structure but in the

[8]This surface distance should not be confused with the bond length.

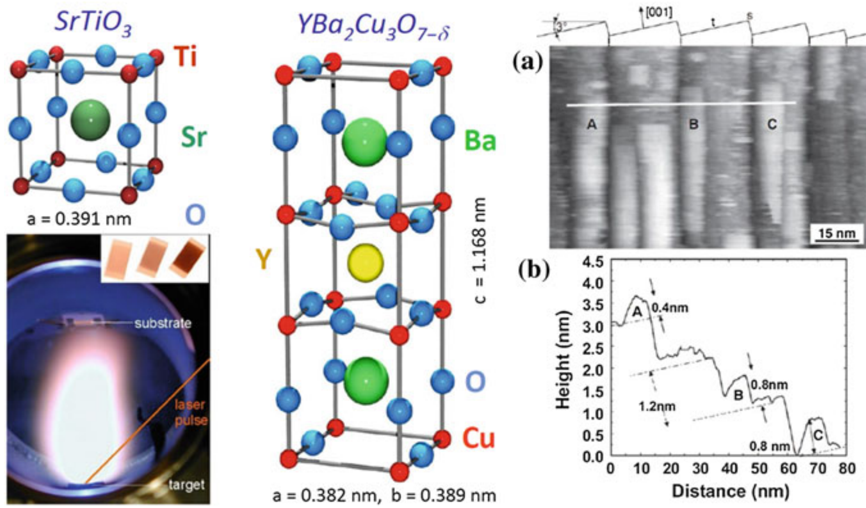

Fig. 12.15 Growth of $YBa_2Cu_3O_{7-\delta}$ on $SrTiO_3(001)$. *Left hand* A photograph of the PLD process and the 5 × 10 mm substrates with $YBa_2Cu_3O_{7-\delta}$ films. *Right hand* An STM image and cross section taken from [59]

form of smaller, 0.4 and 0.8 nm high sub-units [58, 59] (cf. Fig. STO-YBCO). With the additional help of scanning tunnelling spectroscopy it was suggested that these nuclei are a perovskite-like material [59].

In order to verify this assignment, the early stages of growth of $YBa_2Cu_3O_{7-\delta}$ on $SrTiO_3(001)$ were investigated by XSW imaging [60]. Half a monolayer of $YBa_2Cu_3O_{7-\delta}$ was deposited in 0.5 mbar oxygen atmosphere on atomically clean $SrTi_3(001)$ held at 760 °C by PLD. The sample was post-annealed at 450° in 0.8 bar oxygen for 20 min and then transferred under vacuum to the UHV analysis chamber at the ID32 beamline at the ESRF [61]. To obtain sufficient resolution, XSW scans of seven $SrTiO_3$ reflections in the energy range from 2.75 to 5.49 keV were performed in backreflection geometry. Photoelectron spectra of core levels of all six elements were recorded. The XSW modulations of the extracted net counts for all elements are shown in Fig. 12.16. A fit to each of the yield curves using (12.12) provided the amplitude F_A^H and phase P_A^H of the Fourier coefficient of the distribution function for each reflection **H** and element A.

As shown in Fig. 12.17, the images of all six elements could be constructed with the help of (12.15).[9] Since the $SrTiO_3$ was used for generating the reflections, the largest length scale available is the unit cell size of the $SrTiO_3$, which is perfectly appropriate for resolving the internal structure of the 0.4 and 0.8 nm nuclei. Obviously, the deposited $YBa_2Cu_3O_{7-\delta}$ material adopts the perovskite structure.

[9]Utilizing additionally the cubic symmetry of the $SrTiO_3$.

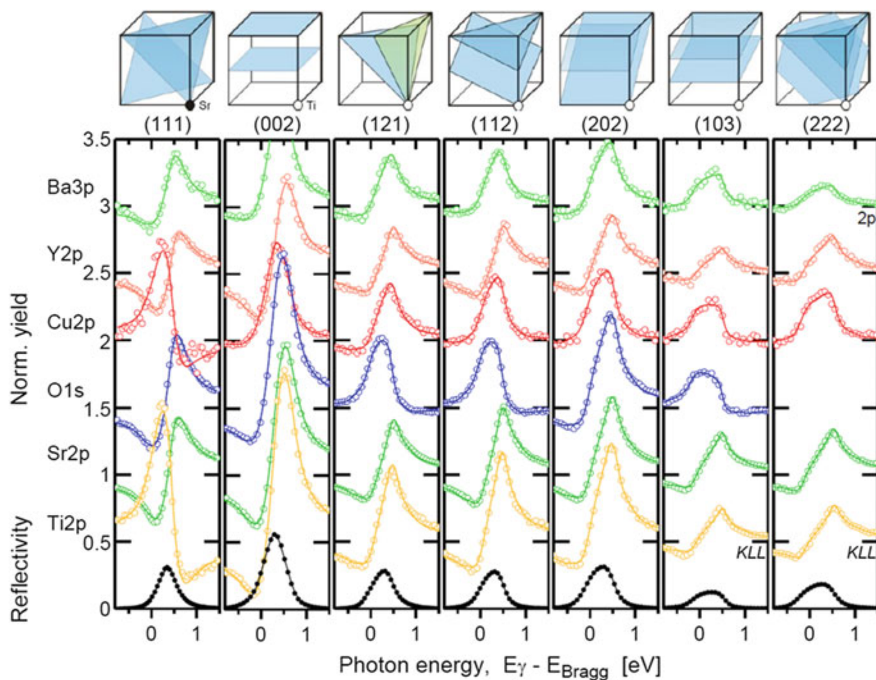

Fig. 12.16 Results of the XSW HAXPES measurements of 0.5 ML $YBa_2Cu_3O_{7-\delta}$ on $SrTiO_3(001)$; *Symbols* Data, lines: fits to the data. The corresponding reflectivity *curves* are shown on the *bottom*. The geometry of the used reflections is indicated on the *top*

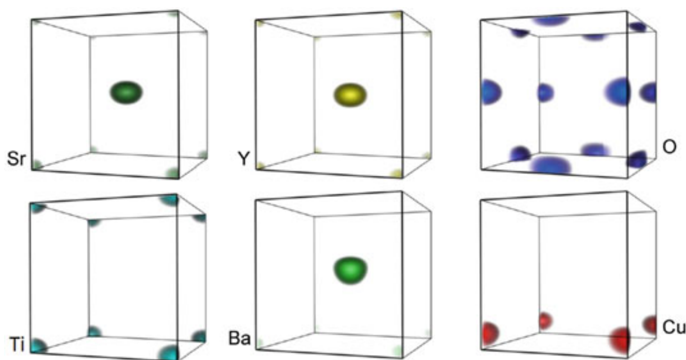

Fig. 12.17 Results of the image reconstruction for 0.5 ML $YBa_2Cu_3O_{7-\delta}$ on $SrTiO_3(001)$ shown with respect to the 0.391 nm cubic $SrTiO_3$ unit cell

The oxygen structure is also clearly resolved. However, it should be noted that the oxygen of the adsorbate cannot be distinguished from the oxygen of the substrate and both are represented together in the image.

12.5 Site Selective Valence Band Photoelectron Emission: Electronic Structure

PES is a well known tool for learning about the electronic structure of materials. With the help of the XSW method, one can obtain site selective electronic information. Site specific valence band (VB) and conduction band (CB) analysis with the help of XSW was pioneered by Woicik and coworkers [62].

Figure 12.18 shows the XSW measurement of the VB emission of a copper single crystal in comparison with the Cu 3p core line. For anyone not fully familiar with the consequences of the dipole approximation the result may be rather astonishing since the yield in both cases is practically the same, suggesting that the valence electrons are localized at the center of the atoms. This is, of course, a misled conclusion. The result is in fact just the consequence of the fact that the dipole approximation is largely valid even for hard X-rays. The absorption probability is highest where the gradient of the core potential is the steepest i.e. close to the core.[10] Without the strong Coulomb force of the core, momentum conservation is not possible. The absorbed photon with spin 1 causes a $\Delta l = \pm 1$ transition, but no angular momentum is transferred to the electron and the photon is absorbed at and the electron emitted from the center of the atom. If there are some differences in the yields of the core level and the VB, they can be explained by multipole contributions to the photoelectron emission.

The valence electrons are delocalized, because the VB of condensed mater is the result of the hybridization of the wavefunctions of all atoms upon forming a chemical bond. Thus, for any part of the VB, contributions from all of the atoms of all different elements within the crystalline unit cell must be considered, rather than emission from a single type of atom. However, since the XSW technique allows to probe the photoemission site selectively in the crystal unit cell, VB emission studied with the XSW technique allows to probe from which (atomic) site the different regions of the VB (predominantly) arise. This was first demonstrated by Nelson et al., analysing the VB of a GaAs crystal [63]. XSW VB analysis is treated explicitly and comprehensively in Chaps. 11, 12 and 26 of the World Scientific edition on XSW [7].

Recently, we used this approach to decompose the VB emission of $SrTiO_3$ [64]. Decomposing the $SrTiO_3$ VB into its constituent contributions from three elements, required two reflections, i.e. the $SrTiO_3$ (111) and (112). Because of less than perfect samples, the XSW was set up at Bragg angles close to 90° at excitation energies $E_\gamma = 2.753$ and 3.891 keV, respectively. The result of the scans of the $SrTiO_3$ VB using the (111) reflection, which allows to separate the Ti and SrO sites, are shown in Fig. 12.19. When the maxima (minima) of the XSW are at the Ti-position, the Ti core level yield is maximal (minimal) and the Sr and O core level yield is at minimum (maximum). This allows direct interpretation of specific VB

[10]The absorption probability, i.e. cross section also depends strongly on the shape of the electron wavefunction close to the core.

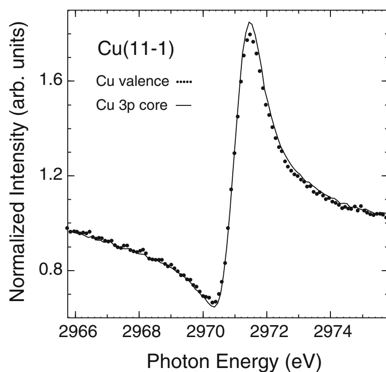

Fig. 12.18 Photon energy dependence of the Cu 3p core (*solid line*) and the Cu valence (*dots*) electron emissions around the Cu(11-1) Bragg back-reflection condition. The curves have been scaled only by a constant to make equal their yields away from the Bragg condition. Figure taken from [62]

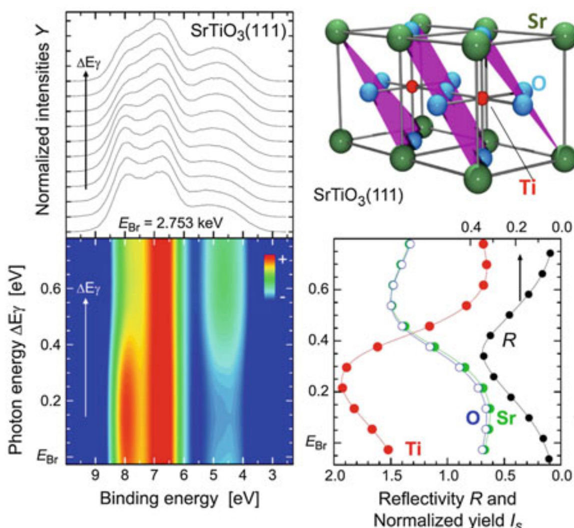

Fig. 12.19 *Left panel* Constant initial state spectra of the $SrTiO_3$ VB recorded when passing the $SrTiO_3$(111) reflection in backreflection geometry around $E_\gamma = 2.753$ keV as line profile (*top*) and colour coded (*bottom*). The movement of the XSW through the unit cell of the crystal is accompanied by drastic changes in the VB shape. *Right panel* Schematic of the (111) standing wave planes in the $SrTiO_3$ unit cell (*top*). The $SrTiO_3$(111) reflectivity and the XSW modulations of the oxygen, titanium and strontium core levels (*right*). When the maxima (minima) of the XSW are at the Ti-position, the Ti core level yield is maximal (minimal) and the Sr and O core level yield is at minimum (maximum). This allows direct assignment of VB features to Ti- and Sr, O-sites

features and the assignment to emission from the Ti or Sr,O crystallographic sites. In a second step, emission from the metal and oxygen sites could be separated using the (112) reflection.

Site specific XSW valence band data can be directly compared with the local density of states when taking X-ray atomic subshell cross sections and the specific electron emission profile into account [31–33]. The corresponding quantitative comparison with ab initio angular momentum decomposed DFT bandstructure calculations shown in Fig. 12.20 shows excellent agreement. The theoretical l-resolved local density of states (lpDOS) was fitted to the experimental data using

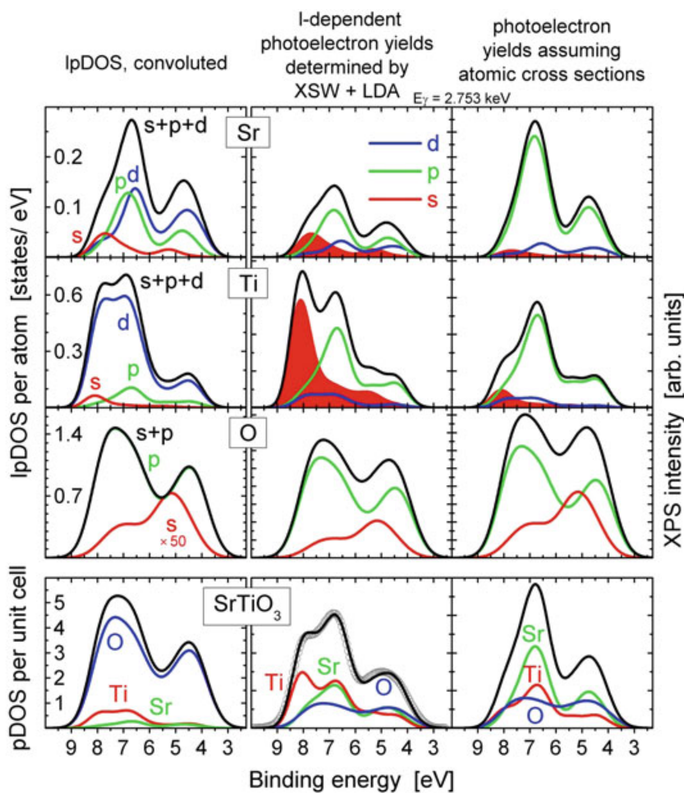

Fig. 12.20 The $SrTiO_3$ valence band decomposition. Shown in the *left panel* is the calculated angular momentum resolved local density of states (Gaussian broadened to reflect the experimental instrumental resolution). The *right panel* shows the lpDOS calculated by theory and weighted with theoretical cross sections. The *center panel* shows the calculated lpDOS best-fit to the experimental data for Sr, Ti and O (*black lines*) using cross sections as scaling parameters. The experimental XSW decomposition into spectral weight originating from Ti, Sr, and O is shown on the *bottom* of the central panel as well as the overall experimental (*dots*) and calculated (*black line*) VB. For the decomposition, the $SrTiO_3$ (111) and the (112) reflections were used with a Bragg angle close to 90° at excitation energies E_γ = 2.753 and 3.891 keV, respectively

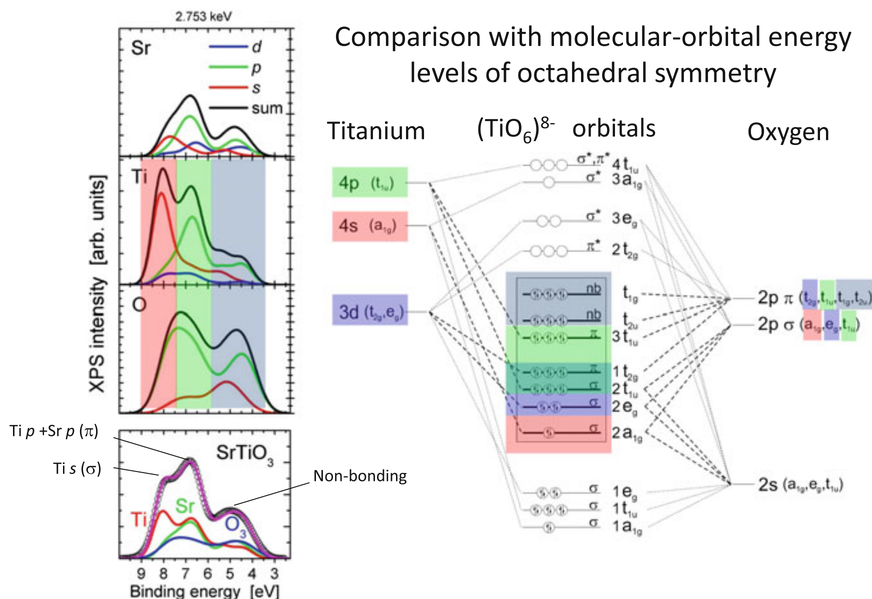

Fig. 12.21 Decomposed $SrTiO_3$ valence band and comparison with schematic molecular-orbital energy levels for octahedral symmetry (after Fischer [66])

just one scaling factor (the cross section for each lpDOS).[11] This is shown in the center panel of Fig. 12.20. Some of the as determined cross sections deviate significantly from the results of relativistic Hartree-Slater calculations for the free atoms [65]. This is shown in the right panel of Fig. 12.20 where the calculated lpDOS is plotted, scaled with theoretical cross sections [31–33]. In this case, the partial yield and the VB yield as a whole do not agree with the experimental results at all.

It is instructive to interpret the XSW VB results for $SrTiO_3$ in terms of a generic energy level scheme for atomic and molecular orbitals for a transition metal (here Ti) oxide as published by Fischer [66]. It allows a straightforward assignment of three different regions of the $SrTiO_3$ VB to the σ-, π- and non-bonding TiO_6 molecular orbitals as shown in Fig. 12.21.

It is equally instructive to compare the $SrTiO_3$ XSW VB decomposition with the corresponding results for TiO_2 obtained earlier by Woicik et al. [67]. On a first view, the oxygen and titanium derived pDOS appear to be rather similar for rutile and strontiumtitanate. However, closer inspection of the O and Ti lpDOS (both left panels in Fig. 12.22) reveals some minor but interesting differences. For the $SrTiO_3$, the Ti derived σ- but also the π-bonding features are stronger pronounced and

[11]In order to fit with the experimental partial yield, the calculated lpDOS had to be convoluted with a Gaussian significantly wider than given by the experimental resolution, in particular for oxygen.

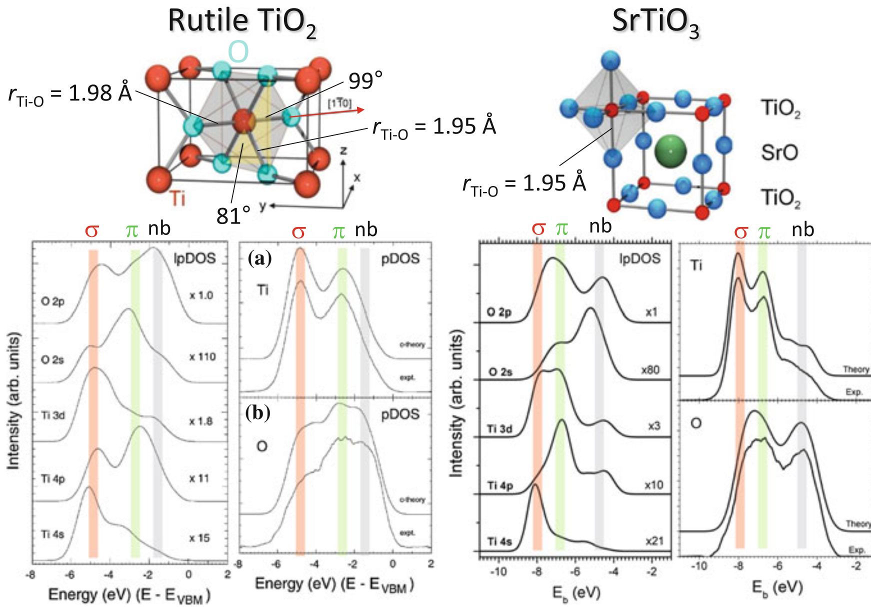

Fig. 12.22 TiO_2 and $SrTiO_2$ unit cells and comparison of the oxygen and titanium contributions to the TiO_2 and $SrTiO_3$ valence bands

concentrated at higher binding energy than in the case of the rutile. This can be explained by the fact that the TiO_6 octahedra are distorted in the tetrahedral TiO_2 whereas they are perfectly symmetric in the cubic $SrTiO_3$.

12.6 Conclusion and Outlook

The XSW method adds structural resolution to all of the strong features of PES, allowing the model independent Fourier analysis of the structure of specific atoms or atomic species. The technique thus benefits directly from the recent development of HAXPES, since higher order Fourier components (smaller diffraction plane spacings) require higher X-ray excitation energies, yielding in turn higher kinetic energy electrons in case of emission from lighter elements or shallower core levels. XSW VB studies provide site specific electronic information, which is not available by any other technique. Furthermore, by using HAXPES, the information is truly bulk representative when studying the electronic structure of crystals. It is expected that the combination of XSW and HAXPES will become even more fruitful and productive in the near future when fully exploiting features of the new generation of HAXPES analyzers such as angular dispersive and position sensitive lens modes and time of flight spectrometers, which allow three dimensional k-space imaging

[68]. With the help of 2D detectors rapid spatially and/or angularly resolved HAXPES measurements will yield position sensitive and depth selective electronic and structural information on the atomic scale with pm-resolution.

References

1. M.V. Laue, Röntgenstrahl-Interferenzen (Akademische Verlagsgesellschaft, Becker & ErlerKolm.-Ges., Leipzig, 1941; Akademische Verlagsgesellschaft, Frankfurt, 1960)
2. B. Batterman, H. Cole, Rev. Mod. Phys. **36**, 681 (1964)
3. A. Authier, *Dynamical Theory of X-ray Diffraction* (IUCr Monographs on Crystallography Oxford Science Publications, 2001)
4. B.W. Batterman, Phys. Rev. **133**, A759 (1964)
5. B.W. Batterman, Phys. Rev. Lett. **22**, 703 (1969)
6. K. Siegbahn, Nucl. Instrum. Meth. Phys. Res. A **547**, 1 (2005)
7. J. Zegenhagen, A.Y. Kazimirov (eds.) *The X-ray Standing Waves Technique: Principles and Applications* (World Scientific, 2013)
8. N. Hertel, G. Materlik, J. Zegenhagen, Z. Phys, B **58**, 199 (1985)
9. J. Zegenhagen, Surf. Sci. Rep. **18**, 199 (1993)
10. Y. Shvyd'ko, *X-ray Optics: High-Energy-Resolution Application* (Springer, Berlin, Heidelberg, 2004)
11. T. Ishikawa, Nucl. Instr. Meth. A **547**, 42 (2005)
12. E.A. Sozontov, M.V. Kruglov, B.G. Zakharov, Phys. Stat. Sol. A **66**, 303 (1981)
13. P.L. Cowan, J.A. Golovchenko, M.F. Robbins, Phys. Rev. Lett. **44**, 1680 (1980)
14. G. Materlik, J. Zegenhagen, Phys. Lett. A **104**, 47 (1984)
15. P. Funke, G. Materlik, Solid State Commun. **54**, 921 (1985)
16. J.R. Patel, P.E. Freeland, J.A. Golovchenko, A.R. Kortan, D.J. Chadi, G.-X. Quian, Phys. Rev. Lett. **57**, 3077 (1986)
17. S.M. Durbin, L.E. Berman, B.W. Batterman, J.M. Blakeley, J. Vacuum Sci. Technol. A **3**, 973 (1985)
18. T. Ohta, Y. Kitajima, H. Kuroda, T. Takahashi, S. Kikuta, Nucl. Instr. Meth. A **246**, 760 (1986)
19. In the dipole approximation, the exponential $e^{2\pi i\mathbf{kr}}$ of the E-field operator in the Matrix element, describing the photoelectric process, is simply replaced by 1, the first term of its corresponding representation in a Taylor series $(1 + 2\pi i\mathbf{kr} - \pi^2(\mathbf{kr})^2 - \ldots)$
20. T.W. Barbee, W.K. Warburton, Mater. Lett. **3**, 17 (1984)
21. M.J. Bedzyk, D.H. Bilderback, G.M. Bommarito, M. Caffrey, J.S. Schildkraut, Science **241**, 1788 (1988)
22. I.A. Vartanyants, J. Zegenhagen, Solid State Comm. **113**, 299 (1999)
23. Z. Zhang, P. Fenter, L. Cheng, N.C. Sturchio, M.J. Bedzyk, M.L. Machesky, D. J. Wesolowski, Surf. Sci. **554**, L95 (2004)
24. J. Zegenhagen, Surf. Sci. **554**, 77 (2004)
25. J. Zegenhagen, in *Surface Science Techniques*, eds. by G. Bracco, B. Holst, Surface Structure Analysis with X-ray Standing Waves (Springer Series in Surface Science, Springer, Berlin, 2013), p. 249
26. A. Jablonski, F. Salvat, C.J. Powell, *NIST Electron Elastic Scattering Cross-Section Database-Version 3.0* (National, Institute of Standarts and Technology, Gaithersburg, MD, 2002)
27. I. Vartanyants, T.-L. Lee, S. Thiess, J. Zegenhagen, Nucl. Instr. Meth. A **547**, 196 (2005)
28. S.K. Andersen, J.A. Golovchenko, G. Mair, Phys. Rev. Lett. **37**, 1141 (1976)
29. T.-L. Lee, C. Bihler, W. Schoch, W. Limmer, J. Daeubler, S. Thiess, J. Zegenhagen, Phys. Rev. B. **81**, 235202 (2010)

30. J. Zegenhagen, G. Materlik, W. Uelhoff, J. X-ray Sci. Technol. **2**, 214 (1990)
31. M.B. Trzhaskovskaya, V.I. Nefedov, V.G. Yarzhemsky, At. Data Nucl. Data Tables **77**, 97 (2001)
32. M.B. Trzhaskovskaya, V.I. Nefedov, V.G. Yarzhemsky, ibid. **82**, 257 (2002)
33. M.B. Trzhaskovskaya, V.K. Nikulin, V.I. Nefedov, V.G. Yarzhemsky, At. Data Nucl. Data Tables **92**, 245 (2006)
34. L.E. Berman, M.J. Bedzyk, Phys. Rev. Lett. **63**, 1172 (1989)
35. M.J. Bedzyk, Q. Shen, M.E. Keeffe, G. Navrotski, L.E. Berman, Surf. Sci. **220**, 419 (1989)
36. T. Ohta, H. Sekiyama, Y. Kitayima, H. Kuroda, T. Takahashi, S. Kikuta, Jpn. J. Appl. Phys. **24**, L475 (1985)
37. D.P. Woodruff, D.L. Seymour, C.F. McConville, C.E. Riley, M.D. Crapper, N.P. Prince, Phys. Rev. Lett. **58**, 1460 (1987)
38. C. Bocchi et al., J. Vac. Sci. Technol., B **20**, 1436 (2002)
39. C. Bocchi et al., J. Vacuum Sci. Technol. B **23**, 1504 (2005)
40. S.M. Durbin, L.E. Berman, B.W. Batterman, J.M. Blakely, Phys. Rev. Lett. **56**, 236 (1986)
41. D. Pacilé, M. Papagno, A. Cupolillo, G. Chiarello, L. Papagno, J. Electron Spectrosc. Related Phenom. **135**, 201 (2004)
42. I.A. Vartanyants, J. Zegenhagen, Nuovo Cimento **19D**, 617 (1997)
43. M. Sugiyama, S. Maeyama, S. Heun, M. Oshima, Phys. Rev. B **51**, 14778 (1995)
44. G.J. Jackson, J. Ludecke, D.P. Woodruff, A.S.Y. Chan, N.K. Singh, J. McCombie, R.G. Jones, B.C.C. Cowie, V. Formoso, Surf. Sci. **441**, 515 (1999)
45. G. Heimel et al., Nature Chem. **5**, 187 (2013)
46. J.D. Emery, B. Detlefs, H.J. Karmel, L.O. Nyakiti, D.K. Gaskill, M.C. Hersam, J. Zegenhagen, M.J. Bedzyk, Phys. Rev. Lett. **111**, 215501 (2013)
47. A.J. Van Bommel, J.E. Crombeen, A. Van Tooren, Surf. Sci. **48**, 463 (1975)
48. J.C. Woicik, T. Kendelewicz, K.E. Miyano, P.L. Cowan, C.E. Bouldin, B.A. Karlin, P. Pianetta, W.E. Spicer, Phys. Rev. Lett. **68**, 341 (1992)
49. A. Herrera-Gomez, J.C. Woicik, T. Kendelewicz, K.E. Miyano, W.E. Spicer, Phys. Rev. B **75**, 165318 (2007)
50. J.C. Woicik et al., J. Vacuum Sci. Technol. A **11**, 2359 (1993)
51. J.C. Woicik, T. Kendelewicz, A. Herrera-Gomez, K.E. Miyano, P.L. Cowan, C.E. Bouldin, P. Pianetta, W.E. Spicer, Phys. Rev. Lett. **71**, 1204 (1993)
52. J.C. Woicik, T. Kendelewicz, S.A. Yoshikawa, K.E. Miyano, G.S. Herman, P.L. Cowan, P. Pianetto, W.E. Spicer, Phys. Rev. B **53**, 15425 (1996)
53. T. Haage, J. Zegenhagen, J.Q. Li, H.-U. Habermeier, M. Cardona, Ch. Jooss, R. Warthmann, A. Forkl, H. Kronmüller, Phys. Rev. B **56**, 8404 (1997)
54. C. Jooss, R. Warthmann, H. Kronmüller, T. Haage, H.-U. Habermeier, J. Zegenhagen, Phys. Rev. Lett. **82**, 632 (1999)
55. H.Y. Hwang, Y. Iwasa, M. Kawasaki, B. Keimer, N. Nagaosa, Y. Tokura, Nat. Mater. **11**, 103 (2012)
56. T.-L. Lee, S. Warren, L. Cao, S. Thiess, B.C.C. Cowie, J. Zegenhagen, Nucl. Instrum. Meth. A **547**, 216 (2005)
57. J. Zegenhagen, T. Siegrist, E. Fontes, L.E. Berman, J.R. Patel, Solid State Commun. **93**, 763 (1995)
58. T. Haage, Q.D. Jiang, M. Cardona, H.-U. Habermeier, J. Zegenhagen, Appl. Phys. Lett. **68**, 2427 (1996)
59. T. Haage, J. Zegenhagen, H.-U. Habermeier, M. Cardona, Phys. Rev. Lett. **80**, 4225 (1998)
60. Sebastian Thiess, Ph.D thesis, University Hamburg (2007)
61. J. Zegenhagen, B. Detlefs, T.-L. Lee, S. Thiess, H. Isern, L. Petit, L. André, J. Roy, Y. Mi, I. Joumard, J. Electron Spectrosc. Related Phenom. **178–179**, 258 (2010)
62. J.C. Woicik et al., Phys. Rev. B **64**, 125115 (2001)
63. E. Nelson, J. Woicik, P. Pianetta, J. Synchr. Rad. **6**, 341 (1998)
64. S. Thiess, T.-L. Lee, F. Bottin, J. Zegenhagen, Solid State Comm. **150**, 553 (2010)

65. J.H. Scofield, Theoretical photoionization cross-sections from 1 to 1500 keV, Lawrence Livermore Report UCRL-51326(1973)
66. D.B. Fischer, Phys. Rev. B **5**, 4219 (1972)
67. J.C. Woicik, E.J. Nelson, Leeor Kronik, Manish Jain, James R. Chelikowsky, D. Heskett, L.E. Berman, G.S. Herman, Phys. Rev. Lett. **89**, 077401 (2002)
68. R. Ovsyannikov, P. Karlsson, M. Lundqvist, C. Lupulescu, W. Eberhardt, A. Föhlisch, S. Svensson, N. Mårtensson, J. Electron Spectrosc. Related Phenom. **191**, 92 (2013)

Chapter 13
Depth Profiling and Internal Structure Determination of Low Dimensional Materials Using X-ray Photoelectron Spectroscopy

Sumanta Mukherjee, Pralay K. Santra and D.D. Sarma

Abstract Properties of any heterostructured material depend critically on the specific composition profile of the constituent elements in the sample. X-ray photoelectron spectroscopy (XPS) is particularly well suited to probe elemental composition of any system. Tunable photon energies, available from any synchrotron centre, allow one to map out the compositional variation through a sample in a manner that can be termed non-invasive and non-destructive depth profiling. In addition, XPS is also able to provide depth resolved electronic structure information by directly mapping out occupied states at and near the Fermi energy. Recent developments at various synchrotron centers, providing access up to very high energy (~ 10 keV) photons with a good resolution and flux, have made it possible to estimate such compositional and electronic structure depth profiles with a greater accuracy for a wider range of materials. In this book chapter, we describe in detail the use of X-ray photoelectron spectroscopy in a selection of heterostructures, in order to illustrate the power of this technique.

S. Mukherjee · P.K. Santra · D.D. Sarma (✉)
Solid State and Structural Chemistry Unit, Indian Institute of Science,
Bengaluru 560012, India
e-mail: sarma@sscu.iisc.ernet.in

P.K. Santra
Department of Chemical Engineering, Stanford University, Stanford, USA

D.D. Sarma
Department of Physics and Astronomy, Uppsala University, Box 534,
Uppsala 751 21, Sweden

© Springer International Publishing Switzerland 2016

J.C. Woicik (ed.), *Hard X-ray Photoelectron Spectroscopy (HAXPES)*,
Springer Series in Surface Sciences 59, DOI 10.1007/978-3-319-24043-5_13

13.1 Introduction

Tailoring functionalities by constraining dimensionalities of materials, typically down to the range of a few nanometers, has become a well-developed field over the last few decades [1–3]. Major technological advancement in diverse fields such as electronics, robotics, alternative energy sources, catalysis, sensor technology, aeronautics, medical diagnostics and therapeutics are dependent on the ability to control material synthesis at such extremely small sizes. Since most material properties are highly size-sensitive at such small length scales [3–6], there has been an enormous effort to design and optimize synthesis for a precise control of the size [4, 7, 8] and shape [9–13] of various materials. Apart from the control of size and shapes, a large variety of heterostructured nanoparticles [14–24] with diverse internal structures (or composition profiles) has also been produced to meet specific requirements for a range of applications. A few examples are coating of silica on certain functional nanomaterial to make them water soluble [25], a requisite for medical usage or a coating of high bandgap semiconductor nanomaterial on a low band gap nanomaterial to obtain better photophysical properties [19, 26]. Core/shell [5, 14–18, 27–29], homogeneous and heterogeneous alloy [19, 30–32], core/shell/shell [20, 21, 33, 34], and coupled dots [22, 23] are some more examples of diversity of internal structures in such heterostructured systems, which are becoming increasingly popular to improve their specific properties. It is easy to anticipate that enhanced desirable properties achieved via the synthesis of different heterostrutures mentioned above must be controlled by the variation of different constituent elements across the heterostructure. For example, properties of a simple core-shell material with a sharp boundary between the core and shell materials are expected to be different from a core-shell material having alloying/mixing across the core/shell interface. Many a times, the structure of a synthesized nanomaterial is implicitly assumed to be the one targeted by the specific synthesis strategy, with evidences being drawn from a variety of indirect techniques, *e.g.* by monitoring the changes in position of the photoluminescence (PL) peak in case of a core-shell nanoparticle system [18]. It has been illustrated [19, 20] in recent times that, such assumptions are not always valid. On the other hand slight changes in the composition profile across the interface of the synthesize nanomaterial were shown to markedly alter certain properties *e.g.* PL properties and PL intermittency [19, 35–39]. Therefore, it becomes necessary to have a detailed knowledge of the internal structure of such materials [19, 35–37] in order to, not only understand the origin of extraordinary properties of such nanomaterials with a possibility of complex internal structures, but also to tailor synthesis for improved targeted properties based on rational approaches arising from that understanding.

As in the case of nanomaterials discussed above, internal structure in terms of composition profile of different constituents is also important in various two-dimensional (2D) multilayered thin film heterojuctions, specifically, where interface characteristics are important in controlling specific properties. Probably the most remarkable example of such heterostructures are 2D thin films semiconductor

heterostructures forming diodes and transistors, which are integral parts of all electronic devices. Other examples include tunneling magneto-resistance (TMR) based modern day magnetic devices, where interface play an important role controlling the coherency of tunneling current in such systems [40–44]. Among various 2D thin film electronic devices, one of the most exciting and emerging research fields is the heterostructure of various oxide materials, where a rich variety of unexpected phenomena has been observed in recent times [45–48]. One such example is the interface between two insulating nonmagnetic oxides, namely $LaAlO_3$ and $SrTiO_3$, which shows properties ranging from high mobility metals to superconductivity and magnetism [45, 48–50] depending on the specific synthesis conditions. This underlines once again the need to understand the interfaces of heterosructures in depth and greater details.

In this book chapter, we discuss an unconventional way of determining the composition profiles in complex heterogeneous low dimensional materials (nanoparticles, thin films) using variable kinetic energy X-ray photoelectron spectroscopy (XPS), which has become an important technique with recent improvement in various synchrotron centers providing high and widely tunable photon energies with high fluxes and resolutions [51–61]. This chapter is divided in three main sections: (a) basic principle and common use of XPS in studying different nanoparticle and thin film systems; (b) principle of variable energy XPS to determine the internal composition profile of complex nanostructures with a few examples and understanding different optoelectronic properties from the derived internal structure; and (c) usefulness of recently developed hard X-ray photoelectron spectroscopy (HAXPES) [51–61] in determining the internal interface structure of nanoparticles and thin film heterostructures. Finally, we end this book chapter with a conclusion and future outlook section.

13.2 X-ray Photoelectron Spectroscopy and Early Applications in Studying Nanoparticles

X-ray photoelectron spectroscopy (XPS), a highly surface sensitive technique, is an established tool to determine the electronic structure of various materials. Since the method of photoelectron spectroscopy is directly related to the electronic energy states of a material, it can give many useful information like charge, valence state, band structures etc. besides identifying the elemental composition in the sample volume that it probes. The basic principle of XPS is related to the photoelectric effect [62]. In this technique, monochromatic photons of known energy are irradiated on the sample, leading to absorption of the photon by a bound electron and causing its emission; this process of ejecting *photoelectrons* happens for all electronic energy levels of all elements present in the material with different probabilities, characterized by the corresponding photoemission cross-sections, provided the photon energy is larger than the binding energy of that level including the work

function of the material. Let us assume that on absorbing a photon with sufficient energy, *hν*, an electron from one of the occupied energy levels, with a binding energy of *BE*, is ejected from the system with a kinetic energy of *KE*. The kinetic energy of the ejected photoelectron, is related to its *BE* as shown in (13.1)

$$KE = h\nu - (BE + \phi) \tag{13.1}$$

where ϕ is the work function of the spectrometer. Therefore, by measuring the *KE* of the photoelectron, the *BE* of the electron prior to the photoionization process can be determined. The *BE* of a photoelectron emitted from a specific electronic energy level of an element in a sample depends on the chemical state of the element in the given material. Even small changes in the chemical environment can influence the *BE* and such changes in the *BE* of an electronic level arising from the change in the chemical environment around the specific element is known as chemical shift [63, 64], which is often characteristic of the valence state or effective charge state of the element in the given material within a related family of compounds. This particular way of using chemical shifts to determine chemical states of different elements in matters has been so extensively used that the technique is often termed separately as 'electron spectroscopy for chemical analysis' (or popularly known as ESCA) [63, 64]. Sokolowski et al. have discussed the development of ESCA in Chap. 2 of this book in details.

With a decrease in the size of any material, the surface-to-bulk ratio increases, enhancing contributions from the surface to every property compared to its bulk contribution. Thus, a detailed knowledge of surface properties becomes essential to understand such low dimensional systems. Being one of the most surface sensitive techniques, XPS has become a very useful tool to characterize electronic structures of materials of lower dimensionalities. It has been applied very frequently to qualitatively ascertain the formation [15, 65–67] and the quality of the synthesized nanoparticles as well as to understand their surface characteristics and compositions [67–76]. A few illustrative examples of the use of XPS in nanoparticle systems are discussed below.

In one of the earliest investigations on the effect of a decreasing size on the metalicity of Pd and Ag nanoclusters, Vijayakrishnan et al. used XPS to show that decreasing sizes lead to an opening of band gap at the Fermi level below a critical size of the nanoclusters, evidencing a characteristics of metal-insulator transitions in such systems [77]. In another XPS study [71] of PbI_2 nanoparticles, a huge excess of I 3d signal was observed compared to Pb 4f, which suggests that iodide ions plays an important role in stabilizing the PbI_2 nanocrystallites in different solvents. Roy et al. used XPS in conjunction with step-wise argon-ion etching of the surface of a luminescent porous silicon sample to probe the composition in the surface and sub-surface region [70]. However, it is to be noted that this approach can only provide qualitative and often relative information and is not reliable to quantify the results with a great accuracy due to the preferential etching of certain elements compared to others. Jasieniak et al. have used different techniques to synthesize either Cd or Se rich CdSe nanoparticles and the formation of such nanoparticles

were confirmed from the core level photoelectron spectra of Cd 3d or S 2p [72], which shows additional features related to the presence of excess Cd or Se at the surface of such nanocrystal systems. In a similar study on Cd rich CdSe nanoparticles [76], XPS was used to extract the composition of the surface with excess Cd, which was shown to be crucial to optimize the PL efficiency of those nanoparticle systems. XPS has also been used to understand the surface passivation of nanoparticles by various organic ligands, often used for better stability and good size distribution of nanoparticles. XPS studies of trioctylphosphine oxide (TOPO) passivated CdSe nanoparticles of different sizes revealed evidence for the surface binding of TOPO only to the surface Cd, leaving the surface Se intact; this was further supported by the observation of preferential oxidation of Se [73]. XPS chemical shift has often been used to characterize attachment between two different kinds of nanoparticle systems for example Au with TiO_2 or MoO_3 with TiO_2 [78, 79], such complex systems being specifically required for applications in catalysis or in photovoltaic solar cells. In one of the earliest use of synchrotron radiation to carry out variable energy XPS of semiconductor nanocrystals, Kulkarni et al. showed the presence of different S species on CdS nanoparticles stabilized with thioglyecerol as the passivating agent [74, 75]. In the same way, many qualitative information like formation, surface chemistry, elemental composition, and interfacial carrier dynamics under photo irradiation have also been obtained from various heterostructured nanoparticles systems using XPS.

13.3 Description of the Internal Structure Using XPS

In general, XPS studies including few examples mentioned above, did not involve any *quantitative* determination of the internal structure, say of a nanoparticle. Common characterization techniques, like transmission electron microscopy (TEM) [28], X-ray diffraction (XRD), photoluminescence emission spectroscopy, Raman spectroscopy [36, 80, 81] etc. have been used to probe the internal structure, but these provide only qualitative information about the internal structure. More advanced techniques such as scanning transmission electron microscopy (STEM) coupled with either energy dispersive X-ray spectroscopy (EDX) or electron energy loss spectroscopy (EELS) can provide more quantitative information on the compositional variation across interfaces in some specific cases [82]. In certain 2D thin film heterostructures, high angle annular dark field (HAADF) imaging in TEM can also provide information on the elemental distribution [49]. In the following sections, we shall describe a nontraditional use of XPS to *quantitatively* determine the internal structure of a variety of heterostructures.

While different nondestructive and quantitative methods [83–92] of determining internal structures of a number of systems have been developed using XPS over the last few decades, we shall discuss in greater details one such method [88] that is versatile, having been applied to a wide variety of systems, discussing more briefly the other methods wherever relevant.

The quantitative determination of the internal structure of a heterostructure relies on the intensity [88, 93–97] of the photoemission signal arising from different energy levels of all elements present in the sample. In XPS, the photoemission signal intensity depends on various parameters as discussed in the following. In order to be detected as a photoemission signal, the photoelectron must travel from the atomic site of photoabsorption to the analyzer without suffering any inelastic process according to the energy conservation indicated by (13.1). During this travel through the material, the photoelectron has a finite probability to interact with the sample, for example, with other electrons present. These collisions can be elastic, thus retaining the same *KE* of the photoelectron and thereby contributing to the photoelectron spectra. Alternately, these can also be inelastic, which causes a decrease in the photoelectron *KE*; such electrons are lost from the main photoelectron spectra being detected as the background [98, 99] of the photoemission signal. These processes are schematically shown in Fig. 13.1a. The probability of the inelastic scattering, can be defined in terms of the average distance, λ, between two inelastic collisions for the same photoelectron, thus defining a mean free path of the photoelectron. The probability of a photoelectron coming out from the sample without any inelastic scattering follows an exponential dependence on the depth at which the original photoabsorption process takes place, and with that the differential photoemission signal intensity, $dI_{z'}$, originating from a volume of 'dv' at a depth z' from the surface can be expressed as [88, 93–96]

$$dI_{z'} = I_0 \exp\left(\frac{-l}{\lambda}\right) dv = I_0 \exp\left(\frac{-z'}{\lambda \cos \alpha}\right) dv \qquad (13.2)$$

where, 'l' is the path length of the photoelectron to travel to the surface of the material from the originating point in the direction of the electron analyzer and α is

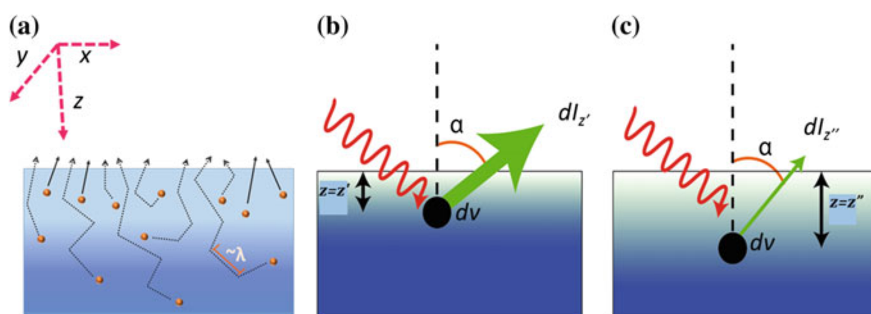

Fig. 13.1 **a** Schematic illustration showing the increasing probability of collision of photoelectrons with increasing depth of their generation, thereby, decreasing their escaping probability exponentially. The average length scale, λ, represents the mean free path of the photoelectrons. **b** and **c** Photoelectrons generated from a volume element 'dv' present at different depth, z' and z'', from the surface of the material show different intensities in the photoemission signal, with the intensity dropping off exponentially with z. Adapted from [88]

the angle between the electron detection and surface normal; I_0 is the proportionality constant dependent on various factors, such as the photon flux (P), transmission function of the spectrometer, and the photoemission cross-section (σ) or the photoionization probability for the atomic level in question (Fig. 13.1b). It is clear from the above equation that the differential contribution dI to the total intensity I of a particular electronic energy level (core level) decreases exponentially with an increase in z, and consequently, ~95 % of the total photoemission signal comes from the surface region of 3λ thickness if the angle of detection (α) is considered to be zero. The remaining 5 % originates from the region deeper into the sample. While this immediately explains the surface sensitive nature of the XPS technique (λ being in the range of few nm), it is interesting to note here that increasing the angle of detection with respect to the surface normal makes it even more surface sensitive, since the photoelectron then needs to escape more tangential to the surface, therefore, requiring a longer path length (l) within the material for the same depth z' as shown in Fig. 13.1b. For example, for α = 45°, a 3λ thick surface region contributes as much as 98.5 % of the total signal. It is also clear from (13.2) that the surface vs bulk sensitivity of this technique can also be controlled by systematically changing the mean free path λ of the photoelectron, as can indeed be done by changing the photon energy, hv; we shall discuss this aspect in the next section of this chapter. The total intensity, I, of the photoelectron signal of a particular core level at a given photon energy, hv, including all parameters can be obtained by integrating (13.2) over the entire volume and expressing I_0 in terms of its component parameters, as given below

$$I(hv) \propto K \cdot P(hv) \cdot T(KE)\sigma(hv) \int_v N(x, y, z) \exp\left(\frac{-z}{\lambda(KE)\cos\alpha}\right) dx\, dy\, dz \quad (13.3)$$

where the prefactor K takes care of the geometry of the measurements (such as the angular acceptance of the analyzer), P is the flux of the incident photon beam and T is the transmission function of the analyzer. The parameters K, P and T are characteristics of the instrument and measurement conditions, the sample specific information is coded in the parameter $N(x, y, z)$, the number density of the specific element distributed in the sample, in addition to the parameter $\sigma(hv)$, representing the hv-dependent photoionization cross-section of the specific core level of the element in question. It is obvious that the distribution, $N(x, y, z)$, of all elements define the internal structure of any given sample. Therefore, the problem of determining the internal structure reduces to extracting $N(x, y, z)$ from the photoemission signal. Since photoemission signals are sensitive to the chemical state of the element probed, variable energy XPS not only can provide the internal structure in terms of mapping the elemental distribution, it can also provide information on the chemical state of the element with spatial resolution, as will be discussed in the following sections.

13.4 Inelastic Mean Free Path, λ, of Photoelectrons

As mentioned earlier, the mean free path, λ, of the photoelectron is the average distance between two inelastic collisions and it depends on the *KE* of the photoelectron. The dependency of λ with *KE* can be given approximately by Wagner, Davis and Riggs equation [100] as

$$\lambda \approx m\,(KE)^n \tag{13.4}$$

when *KE* is expressed in electronvolt (eV) and λ in angstroms (Å). This purely empirical equation with ($m = 0.5$ and $n = 0.5$) is found to be reasonably valid for a wide range of *KE* above ~ 150 eV in the soft X-ray region (<1000 eV). While for very high *KE* regions (>2000 eV) the values for m and n are found to be ~ 0.11 and ~ 0.75 [100–102]. There are several other ways to calculate the mean free path of the photoelectron, for example using TPP and TPP-2 formula [100, 103, 104]; these have been discussed in Chap. 5 by Powell and Tanuma. For a specific core level of an element in a given sample, it is easy to change the *KE* of the photoelectron by changing the incident $h\nu$ according to (13.1); this implies that $\lambda(h\nu)$ varies approximately as $(h\nu - BE)^n$ and therefore, can be tuned by suitable choice of $h\nu$. With recent advancement on the synchrotron sources, it is possible to tune the photon energy almost continuously over a wide range, thereby achieving a continuous tuning of the *KE* and λ of any photoelectron originating from any specific core level. In the early days of photoelectron spectroscopy, λ values typically ranged from 0.5 to 2 nm ($3\lambda_{max} \sim 6$ nm) depending on the *BE* of the core level with the use of laboratory sources like Al Kα (1486.6 eV) and Mg Kα (1253.4 eV); presently, with the advent of sophisticated synchrotron facilities, the possibility of continuously varying λ using such variable photon energy source forms the main basis of mapping out the chemical compositions, defined by $N(x, y, z)$ of all the elements, at various depths within the sample, thereby enabling characterization of the internal structure of a large number of systems. We have pointed out earlier that it is possible to change the *effective* mean free path ($\lambda \cdot \cos\alpha$) by varying the detection angle, α, keeping $h\nu$ (and consequently, λ) at a fixed value. This method of internal elemental composition mapping by varying the detection angle has often been used for internal structure determination of thin films [90, 91, 105]. While such method has inherent limitations [91, 102] and suitable only when the 2D film thickness to be estimated is considerably smaller than the λ of the photoelectrons [90, 102], the alternate method [88, 102] of using variable $h\nu$ is robust and applicable to a wide variety of geometry, for example for spherically shaped nanoparticle systems where the method based on variation of detection angle, α would be ineffective.

13.5 Intensity Variation of Different Core Levels/Elements with photon energy, *hν*, in Heterostructures

The idea to probe a sample at different depths using variable energy XPS has been explained [88] in this section with the help of schematic Fig. 13.1. Let us consider the absorption of a photon with sufficient energy of $h\nu$ at a depth of z' from the sample surface, thereby causing emission of a photoelectron that is detected with an intensity of $dI_{z'}$ at an angle of α from the surface normal, as shown in Fig. 13.1b. With no loss in generality, let us consider that another photon with same energy $h\nu$, causes a photoelectron from another atom of the same element and core level to originate at a depth of z'' and detected with an intensity of $dI_{z''}$ at the same angle of α from the surface normal as shown in Fig. 13.1c. From (13.2), the intensity ratio of the two photoelectrons originating at two different depths can be expressed as

$$\frac{dI_{z'}}{dI_{z''}}(h\nu) = \exp\left(\frac{z'' - z'}{\lambda(h\nu)\cos\alpha}\right) \tag{13.5}$$

As $z'' > z'$, the intensity contribution from the deeper volume element at z'', will be lower compared to that from z' ($dI_{z''} < dI_{z'}$). The above equation also shows that an increase in λ by increasing $h\nu$ will lead to a systematic decrease in the intensity ratio $\frac{dI_{z'}}{dI_{z''}}(h\nu)$, due to an increase in the relative contribution from the deeper region of the sample compared to regions that are closer to the surface. Now, instead of one element if the sample is made of two different elements **A** and **B** and the two volume elements at two different depths, z′ and z″ contains the elements **A** and **B**, respectively, then in terms of total intensity contribution to the photoemission signals from some core levels (13.3) of the two elements, the intensity ratio can be written as

$$\frac{I_A}{I_B}(h\nu) = \frac{T_A}{T_B}(KE)\frac{\sigma_A}{\sigma_B}(h\nu)\frac{\int_v N_A(x,y,z)\exp\left(\frac{-z}{\lambda_A(KE)\cos\alpha}\right)dx\,dy\,dz}{\int_v N_B(x,y,z)\exp\left(\frac{-z}{\lambda_B(KE)\cos\alpha}\right)dx\,dy\,dz} \tag{13.6}$$

The immediate benefit of taking intensity ratio is that the contributions of uncertain instrumental factors, (e.g. K, P), mentioned earlier in (13.3), are not required to be considered any more, the expression for the intensity ratio being independent of those factors. The remaining parameters, namely the transmission functions T's and cross-sections, σ's in (13.6) can be estimated as a function of $h\nu$ [106–108], leaving only the number densities $N_A(x,y,z)$ and $N_B(x,y,z)$ as the unknown variables. It is clear from (13.6) that, for different heterostructures, characterized by different number density profile of the constituent elements, the variation of intensity ratio I_A/I_B as a function of $h\nu$ will be different, and by measuring I_A/I_B at many different $h\nu$, it is possible to determine the number densities, defining the internal structure of a given heterostructure. This is further illustrated in

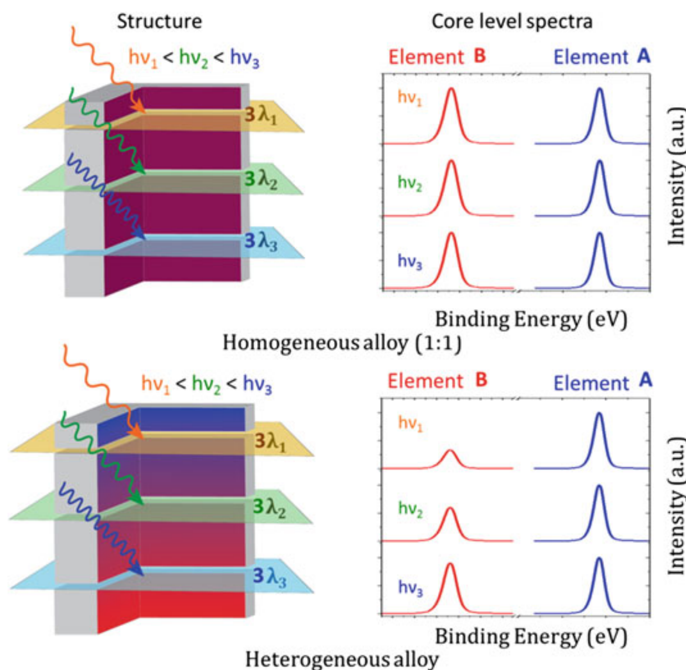

Fig. 13.2 Schematic illustration of spectral dependence on photon energy for two systems having different internal structures. One system is chosen to represent a homogeneous alloy of two elements (say **A**, indicated in *blue color* and **B**, indicated in *red color*), while the other one has a graded alloy structure with the core rich in **B** and the surface in **A**. The graphs on the *right side* show schematically changes in the relative intensities with increasing photon energy. Horizontal slices from the *top* represents changing mean escape depth, λ, with a changing photon energy where $h\nu_1 < h\nu_2 < h\nu_3$, giving rise to $\lambda_1 < \lambda_2 < \lambda_3$. Adapted from [88]

the Fig. 13.2, where we have considered two hypothetical materials with flat surfaces consisting of two elements **A** (indicated by blue) and **B** (indicated by red). For the sake of simplicity, let us consider that the photoemission cross-sections of the specific core levels of these two elements σ_A and σ_B are equal and also the *KE* of the emitted photoelectrons have similar values and, therefore, $T_A = T_B$ and $\lambda_A = \lambda_B = \lambda$ in (13.6). In the first scenario, we consider our hypothetical material to be a homogenous alloy of elements **A** and **B**, implying that these elements are distributed uniformly within the material, as shown in the upper left schematics. The other hypothetical material also consists of elements **A** and **B**, but they form a gradient alloy structure with only element **A** on the surface and only element **B** at a certain depth with the composition changing uniformly in-between. With a low photon energy of $h\nu_1$, the primary contribution to the photoemission signal will come from a thin slice of the sample, as shown in the Fig. 13.2, with the slice thickness governed by the mean free path, λ_1, of the photoelectron with the photon energy of $h\nu_1$. In case of the homogenous alloy, the intensity ratio of core levels of **A** and **B**, $\boldsymbol{I_A/I_B}$ will be independent of $h\nu$, as can be seen from (13.6) with

$N_A(x, y, z)/N_B(x, y, z)$ being a constant dependent only on the composition of the homogeneous alloy, but independent of *x*, *y*, and *z* over the entire volume of the sample.

However, the same intensity ratio will be critically dependent on $h\nu$ in case of the graded alloy sample with $N_A(x, y, z)/N_B(x, y, z)$ being dependent on *z*; clearly for a small λ_1, the thin slice probed in the experiment contains a dominant contribution of **A** as illustrated in Fig. 13.2 for the graded alloy structure with the blue color representing the element **A**. Thus, the photoemission signal will be largely dominated by the contribution of **A** with a smaller contribution from **B** with the lowest photon energy of $h\nu_1$. With a progressive increase in the photon energy $(h\nu_3 > h\nu_2 > h\nu_1)$, the mean free path of the photoelectrons will also increase $(\lambda_3 > \lambda_2 > \lambda_1)$. The intensity ratio $\boldsymbol{I_A/I_B}$ will not change with photon energy for the homogeneous alloy, as shown in upper right schematic spectral distribution. However, the relative intensity ratio $\boldsymbol{I_A/I_B}$ will increase with increasing photon energy for the gradient alloy (lower right schematic graph). From this illustrative example, it is clear that the variation in signal intensity ratio of different elements obtained at different $h\nu$ will provide information of the internal structure of the materials with dimensions comparable to the mean free path (λ) of the photoelectrons. It is important to note here that a heterostructure does not necessarily need two different elements, it can be made of different spatial distribution of two different chemical states (**A** and **A′**) (for example different valence states), characterized by a slightly different *BE* (chemical shift) of the same core level spectra, of one element (**A**). In such situations (13.6) will have the following form

$$\frac{I_A}{I_{A'}}(h\nu) = \frac{\int_v N_A(x, y, z) \exp\left(\frac{-z}{\lambda(KE)\cos\alpha}\right) dx\, dy\, dz}{\int_v N_{A'}(x, y, z) \exp\left(\frac{-z}{\lambda(KE)\cos\alpha}\right) dx\, dy\, dz} \tag{13.7}$$

and can be used the same way for internal structure determination. We shall provide examples of each of the situations described above in the following sections.

At this stage we provide a real illustrative example, to show the sensitivity of this approach in delineating complex nanostructures with additional information coming from the phenomenon of chemical shift that was alluded to earlier in this chapter. We adopt results from [109] and a sequence of photoemission signals from PbSe nanocrystals passivated with TOPO in Fig. 13.3 for a series of photon energy. The two peaks apparently at 130 and 132.8 eV binding energies are both associated with P 2p core level from TOPO. It is clear from the spectra, the P related intensities are dominant in the extremely surface sensitive limit of low photon energies, establishing P to be present predominantly at the surface of the sample. This is consistent with TOPO being a superficial capping agent for these nanocrystals. Interestingly, the chemically shifted two P 2p core level signals appearing at 130 and 132.8 eV show different dependencies on the photon energy; specifically, the peak with the lower *BE* of 130 eV clearly corresponds to a more surface species compared to the features at the higher *BE* of 132.8 eV. This fact, together with the observed

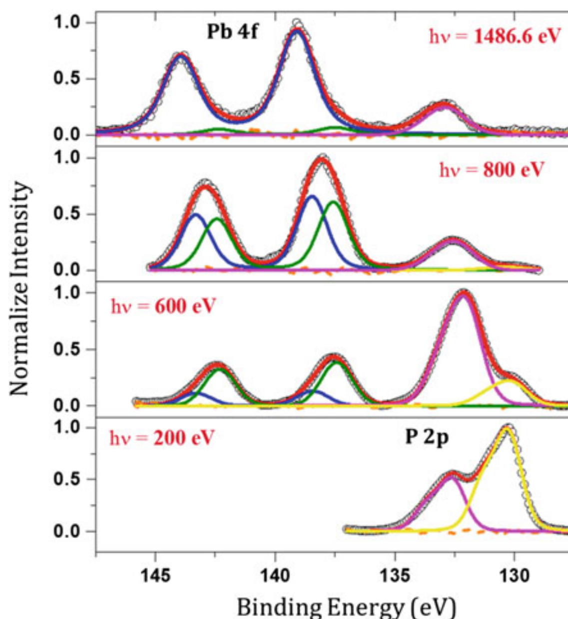

Fig. 13.3 High-resolution photoemission spectra of the Pb 4f and P 2p core levels collected at various photon energies from PbSe nanoparticles. Contributions to Pb 4f spectra arising from distinct Pb species are shown in *blue* and *green lines* along and those for P 2p are shown in *yellow* and *magenta lines*. Adapted from [109]

chemical shift, allows to assign the low *BE* feature to a physisorbed TOPO layer on top of the chemically bounded TOPO layer on the PbSe nanocrystal acting as the passivating agent. A careful analysis revealed [109] that the Pb 4f is also composed of two species of Pb with the one at lower BE being associate with the Pb near the nanocrystal surface and the other being located deeper into the volume of the nanocrystal. While this example makes clear the strength of this technique based on photoemission experiments with a variable energy source in providing unique insights in the internal structures of nanomaterials at a qualitative level, detailed examples are provided in the following section to illustrate how one may also extract quantitative information providing an accurate and detailed description of complex structures from such experiments.

13.6 Quantitative Determination of the Internal Structure

In the early days, XPS intensity ratios were extensively used to characterize as well as to estimate the thickness of various oxides formed on top of metallic samples [93, 94, 97, 110–113]. It was shown in [93] that with an increasing thickness of WO_3 layer deposited on top of metallic W the relative contribution to the W 4f XPS signal from the metallic W layer decreases with respect to WO_3 signal. While it was already suggested at that time that this relative change in the intensity ratio can be used to estimate the thickness of the top WO_3 layer; similar ideas were proposed

and pursued [110, 112, 113] to monitor quantitatively the progression of the oxidation process of various metals on increasing exposure to oxygen. Combining the concept of chemical shift, it was even possible to identify various species of oxides of Zr and follow their quantitative growth as a function of oxygen exposure in studies of oxidation of Zr and its alloys [94, 97]. Later this method of thickness estimation from the relative intensity ratios of photoemission signals was effectively implemented to determine the internal structure of various nanoparticles.

Nanda et al. [95] applied this method for a quantitative determination of the composition and the internal structure of different sized spherical CdS nanoparticles [95] capped with 1-thioglycerol. They investigated the internal structure using two different photon energy sources, namely, Al Kα (1486.6 eV) and Mg Kα (1253.4 eV). Both S 2s and 2p spectral features were found to be complex and could not be attributed to a single S species. Careful spectral decompositions of both S 2p and S 2s spectra showed evidence for three distinctive features suggesting three different S species present in the CdS nanoparticles. For example, three different S $2p_{3/2}$ peaks were found to be at about 161.8, 162.9 and 163.9 eV binding energies, representing three chemically shifted signals. These three S components were attributed to S in the bulk of the CdS nanoparticle, S at the surface layer of CdS and the S present in the thiol group of the capping agent, 1-thioglycerol, respectively. While the S species in the thiol group with a very different chemical environment is indeed expected to give rise to a strong chemical shift compared to S species in the nanoparticle as observed, the shift in the S 2p core levels from the S atoms at the surface of the nanoparticle compared to those in the bulk is known as the surface chemical shift. The surface nature of that specific S component was further confirmed by studying two different sizes of CdS nanoparticles synthesized in the same way. It was found that the second component of S species attributed to the surface layer had a higher contribution relative to the first component assigned to the bulk for the smaller nanoparticle, as should indeed be expected on the basis of an increasing surface to bulk ratio with a decrease in the size. Yet another validation of this interpretation was provide by the use of Mg Kα (1253.4 eV) as the photon source to carry out XPS with a slightly smaller photon energy on the same nanoparticles. The results with Mg Kα (1253.4 eV) again exhibited the same three components of S species, however, with an increased contribution of both second (surface) and third (thiol) components, relative to the first one. This is a consequence of the lower photon energy of Mg Kα (1253.4 eV) source compared to Al Kα (1484.6 eV) one, leading to a lower λ and consequently a higher surface sensitivity with Mg Kα (1253.4 eV) radiation. The internal structure of the CdS nanoparticles was modeled as a core/shell/shell structure with a CdS core, a surface CdS layer and finally, the capping layer of 1 thioglycerol as shown schematically in Fig. 13.4 with radii of r_0, r_1 and r_2, respectively, yielding the detailed structure of these nanoparticles. They modify and express (13.7) in a spherical polar coordinate to estimate the intensity ratios between different S components mentioned above. The exact values of the radii were calculated by varying these radii parametrically to simulate the experimentally obtained signal intensity ratio of three different components S 2p at different photon energies. In a different study [96] to determine

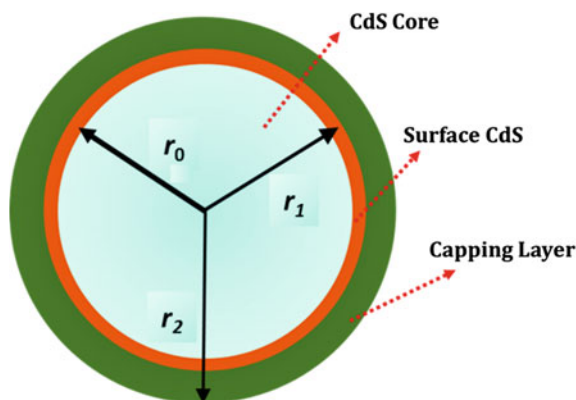

Fig. 13.4 Schematic model of CdS nanoparticles as derived from XPS analysis showing a CdS core region till r_0, followed by a thin shell of surface CdS layer of thickness $(r_1 - r_0)$. Surface S atoms exhibit a different core level binding energy due to what is known as surface core level shift. Finally, there is a protective layer of capping agent (thiol) of thickness $(r_2 - r_1)$ on the top. Adapted from [95]

the internal structure of ZnS nanoparticles passivated with 1-thioglycerol, XPS at various photon energies suggested the internal structure of these ZnS nanoparticles being similar to the internal structure of the above-mentioned CdS nanoparticles. The generality of this approach was demonstrated by Sapra et al. [109] who used variable energy XPS to determine the internal structure of luminescent PbSe nanopartcles as well as of nanorods by modifying (13.7) and expressing it in cylindrical polar coordinates. The variable energy XPS study [109] on different sized PbSe nanoparticles (Fig. 13.3) have suggested formation of Pb deficient $Pb_{1-x}Se$ layer on the surface of these nanoparticles. The thickness of this Pb deficient layer was found to be smaller for smaller sized nanoparticles. As the Pb deficient layer leads to the formation of trap states, which decreases the photoluminescence efficiency, they were able to explain the optoelectronic properties of the studied PbSe nanoparticles on the basis of internal structure and surface properties [109]. This later example illustrates the usefulness of the aforementioned variable energy XPS technique in correlating properties of lower dimensional materials with their internal structures.

Similar analyses can also be performed on nanoparticles with complex heterostructures with complicated variations in the composition. Unlike in the examples cited above, more complicated multicomponent structures require monitoring photoelectron signals of more than one element to accurately profile the composition through the nanoparticle, as has been discussed in previous sections. In recent times, there has been many reports [19, 20, 33, 114–116] using high quality and continuously tunable synchrotron photon sources on complex nanostructures. For example, Santra et al. [20] determined the internal structure of a targeted core/shell/shell ZnS/CdSe/ZnS quantum dot–quantum well (QDQW) structure. They analyzed the intensity ratio of S 2p and Se 3p core level spectra collected at

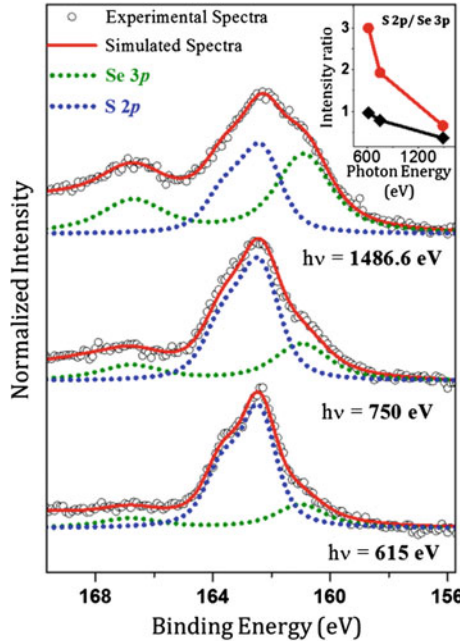

Fig. 13.5 High-resolution photoemission spectra of the S 2p and Se 3p core levels at various energies. At each energy, the experimental data are shown by the *black circles* and the total fit by the *red line*. The independent component functions, S 2p and Se 3p are shown as *blue* and *olive dotted lines*, respectively. The *inset* shows the S 2p/Se 3p intensity ratios obtained with (*red circles*) and without (*black square*) consideration of the photoemission cross-section (the lines are guides to the eye). Adapted from [20]

three different energies. These two core levels were specifically chosen in view of the fact that binding energies of S $2p_{1/2}$ and $2p_{3/2}$ are very close to those of Se $3p_{1/2}$ and $3p_{3/2}$, as shown in Fig. 13.5. Having the similar binding energies, the *KE* of the S 2p and Se 3p photoelectrons are also similar, which allows recording of both the S 2p and Se 3p core levels simultaneously at any given *hv*. In view of very similar *KE* for both peaks at a given *hv*, it is reasonable to assume that *K*, *P* and *T,* mentioned in (13.3), are same for both S 2p and Se 3p core level at a given *hv*, and are exactly cancelled in the intensity ratio between S 2p and Se 3p core level spectra. The inset to Fig. 13.5 shows the experimental intensity ratio obtained by the decomposition of the recorded spectra in terms of S 2p and Se 3p contributions, as shown in the main frame by dotted lines. Equation (13.8) can be derived from (13.6), in a spherical polar coordinate for the intensity ratio of S 2p and Se 3p as:

$$\frac{I_S}{I_{Se}} = \frac{\int_v dI_S}{\int_v dI_{Se}} = \frac{\sigma_S}{\sigma_{Se}} \frac{\int_0^R \int_0^\pi \int_0^{2\pi} N_S\,(r)\ \exp\left(-\frac{f(r,\theta)}{\lambda}\right)\ r^2 \sin(\theta)\ d\theta\ d\varphi\ dr}{\int_0^R \int_0^\pi \int_0^{2\pi} N_{Se}\,(r)\ \exp\left(-\frac{f(r,\theta)}{\lambda}\right)\ r^2 \sin(\theta)\ d\theta\ d\varphi\ dr} \tag{13.8}$$

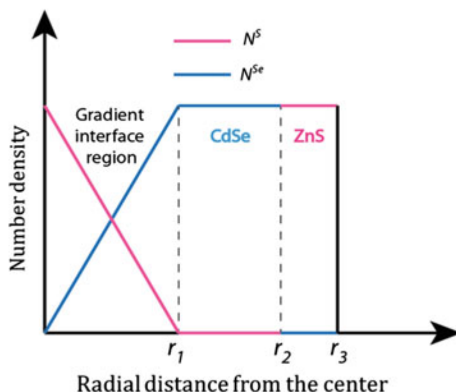

Fig. 13.6 Schematic representation of the variation of the chemical composition for the best fitted structure, which has three main layers: a gradient alloy in the core $(0 < r < r_1)$ followed by a thick shell of CdSe $(r_1 < r < r_2)$ and a thinner shell of ZnS $(r_2 < r < r_3)$. Adapted from [20]

where, R is the total radius of the nanoparticle, mean free paths (λ_S and λ_{Se}) of S 2p and Se 3p photoelectrons with almost the same KE for any given $h\nu$ are essentially the same and therefore, has been replaced with λ $(= \lambda_S = \lambda_{Se})$ in (13.8). The quantity $f(r,\theta)$ is given by $f(r,\theta) = (R^2 - r^2 Sin^2\theta)^{1/2} - r\ Cos\theta$. Equation (13.8), shows that the experimental intensity ratio obtained from the decomposition, after a suitable correction for the respective cross-sections, namely $(I_S/\sigma_S)/(I_{Se}/\sigma_{Se})$, is dependent on the elemental composition profile for S and Se, as expressed by $N_S(r)$ and $N_{Se}(r)$. Quantitative analyses of the photoemission data reveal that S and Se number densities for these QDQW nanoparticles varied as shown in Fig. 13.6, exhibiting the core region to be a graded alloy of ZnS and CdSe rather than pure ZnS as targeted. The solution based reaction to place a shell of CdSe on preformed ZnS nanocrystals is found to cause diffusion of Se ions towards the center of the nanoparticle, leading to the formation of such a gradient core. However, the outermost ZnS layer was found to form a sharp interface on top of the outer CdSe. The radius, r_3, obtained from the analysis which corresponds to the total size of the nanoparticle was found to be in good agreement with results from TEM measurements. Also the chemical composition based on the model in Fig. 13.6 and extracted values of r_1, r_2 and r_3, was found to be consistent with results from Inductively coupled plasma atomic emission spectroscopy (ICP-AES), thereby validating the photoemission analysis and estimates of r_1 and r_2 that would not be possible to obtain by any other technique.

In another interesting work to understand the extraordinarily high photoluminescence behavior of ternary CdSeS nanoparticles, the internal structure of these samples were determined [19] by analyzing the relative intensity variation of S 2p and Se 3p core levels at different photon energies in much the same way as in the previous example of QDQW. With additional information about the total size obtained from TEM and chemical composition from ICP-AES, internal structures

of such highly luminescent CdSeS nanoparticles were invariably found to consist of a gradient alloy structure of $CdSe_xS_{1-x}$ where x varies from 0 near the center of the nanoparticle to 1 near the surface of the nanoparticle. Depending upon the concentration ratio of S and Se used during the synthesis, the radius of the gradient core could be tuned to provide PL emission of different wavelengths spanning the visible spectrum. It was pointed out [19] that such a graded structure avoids any interface defect formation that tends to be present in systems with a sharp interface in core-shell structure due to the lattice mismatch. The absence of such interfacial defects in gradient structured CdSeS allows these nanoparticles to have a quantum yield as high as 80 %.

13.7 Hard X-ray Photoemission Spectroscopy (HAXPES)

While X-rays of very high energies, for example Cu Kα, have been used in photoemission experiments at very early days, the usage was limited due to the poor resolutions at that time [60]. The advancement in the third generation synchrotron radiation sources in recent times allows sufficiently high photon flux (P) with photon energies as high as 12 keV to carry out photoemission experiments with a good energy resolution. Therefore, it is now possible to tune the mean free path (λ) of the photoelectron up to ~10 nm. Such large mean free paths of the photoelectrons have opened up the possibility [51–61] of probing much greater depths and much larger nanocrystals that would have been otherwise impossible to probe with more conventional XPS.

Recently, Mukherjee et al. [117] employed such high energy XPS with $h\nu$ up to 4 keV in combination with surface sensitive lower energy XPS ($h\nu \geq 475$ eV) to elucidate the internal structure of inverted core-shell CdS-CdSe nanoparticles with an average diameter of 6 nm. Standard lab source (e.g. Al K α (1486.6 eV)) can generate photoelectrons with a mean free path of ~2 nm which is smaller than the size of these nanoparticles and therefore can give only restricted information. Instead, they [117] used a wide range of photon energies between 475 eV (thereby emphasizing the surface components) and 4000 eV (making the probe bulk sensitive) to study the core level intensity variation of overlapping S 2p and Se 3p spectra as shown in Fig. 13.7a. The benefit of using overlapping S 2p and Se 3p spectra has already been presented in the previous section of this book chapter. At lower photon energies, a distinct peak at 161.2 eV with a shoulder at 162.3 eV is dominant in the spectra. These binding energies correspond to $2p_{3/2}$ and $2p_{1/2}$ spin-orbit split 2p core levels of sulfur. There are also two low intensity peaks at 159.8 and 165.6 eV which correspond to Se $3p_{3/2}$ and Se $3p_{1/2}$ spectra with a spin orbit splitting of 5.8 eV. Interestingly, with an increase in $h\nu$, the Se 3p signal intensity increases significantly relative to the S 2p signal. This is most clearly evident when we follow the growth of the Se $3p_{1/2}$ spectral feature at 159.8 eV *BE* with changing $h\nu$; the corresponding enhancement of the Se $3p_{3/2}$ peak is less clear, as a worsening resolution with the increasing $h\nu$ makes it difficult to visually judge

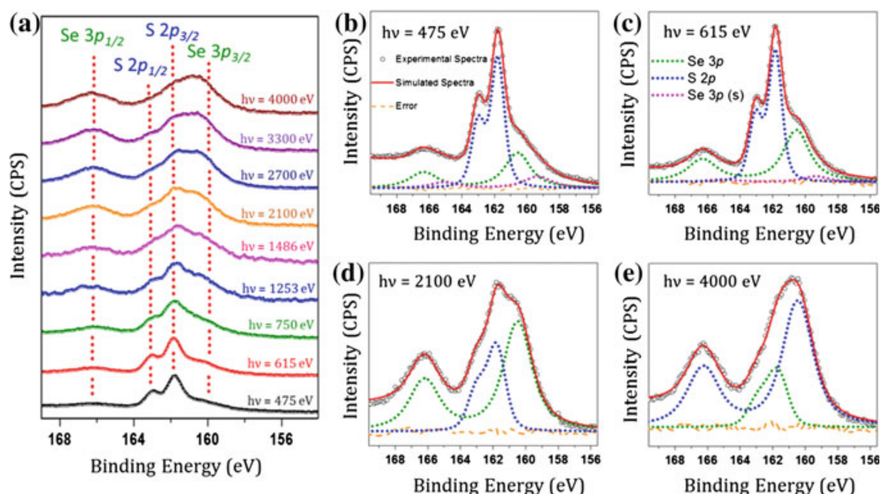

Fig. 13.7 **a** Photoelectron spectra of S 2p and Se 3p core levels collected at various photon energies from an inverted CdS/CdSe core–shell sample. **b–e** Decomposition of the experimental spectra (*empty black circles*) to different components, namely, the surface of Se 3p (*olive*), S 2p (*blue*), and Se 3p (s) (*magenta*). *Red solid lines* are the resulting fits, while the *orange dashed lines* are the residues. (Adapted from [117])

the contribution of Se $3p_{3/2}$ separate from those of S $2p_{3/2}$ and S $2p_{1/2}$ within the broadened main group around 160 eV *BE* (see Fig. 13.7a). However, it is easy to decompose each of the spectra in Fig. 13.7a in terms of contributions arising from S $2p_{3/2}$, S $2p_{1/2}$, Se $3p_{3/2}$ and Se $3p_{1/2}$ components as illustrated in Fig. 13.7b–e for a few selected photon energies [117]. Such spectral decompositions allow one to determine quantitatively the relative contributions of S and Se core levels in the overall spectra at different photon energies (Fig. 13.7a). Thus determined intensity ratio of the contributions from Se 3p and S 2p core level spectra is shown as a function of the photon energies in Fig. 13.8a by the solid blue squares, referred to the right axis, clearly showing the rapidly increasing Se 3p intensity relative to S 2p with an increasing *hv*. At this stage, it is important to note that the variation in the spectral intensities cannot be directly related to the variation in $N_S(r)$ and $N_{Se}(r)$ within the probing depth of the technique [see (13.8)], because the photoemission cross-section, σ, itself changes rapidly with *hv* and its dependence on *hv* is both element and core level specific. Therefore, we need to normalize the raw intensity ratio with the ratio of the photoemission cross-sections of Se 3p and S 2p levels for each of the photon energies [see (13.8)]. The corresponding cross-section corrected intensity ratios of Se 3p and S 2p are shown as a function of *hv* in Fig. 13.8a with filled circles, referred to the left axis. Clearly, the corrections arising from the changing σ qualitatively alter the trend of the intensity ratio as a function of the *hv* from an increasing to a decreasing function underlining the crucial importance of accounting for changes in $\sigma(hv)$ even for a qualitative understanding of chemical composition as a function of the probing depth in any given material.

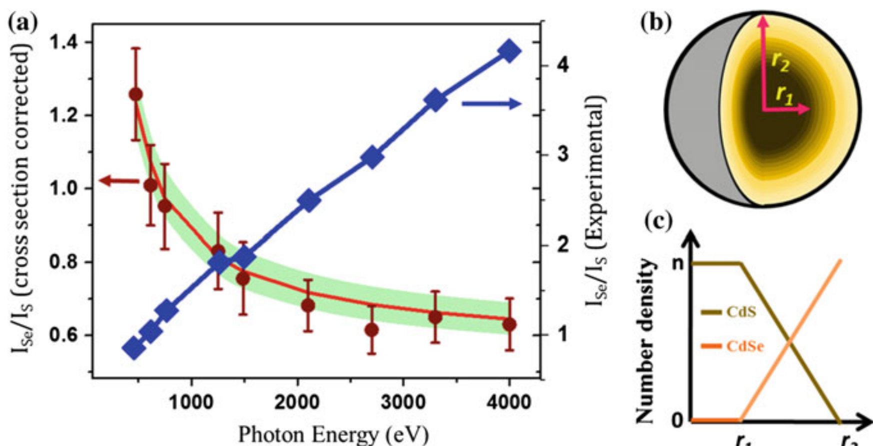

Fig. 13.8 **a** Variation of the experimental (*blue squares* joined by a *blue line*) and σ corrected (*filled circles*) relative intensity of Se 3p to S 2p at different photon energies. The error *bars* represent the errors in the intensity ratios estimated from the errors in the decomposition of the experimental photoelectron spectra. The region shaded in *green* shows the region over which the fitting of the experimental intensity ratio was performed, and the *red solid line* shows the best fitting. **b** Modeled structure, which gives the best agreement with the experimentally obtained results from XPS, TEM, and ICP-AES. **c** Variation of the number density of S (*dark yellow*) and Se (*orange*) as a function of the radius of the nanoparticles for the best fit structure. (Adapted from [117])

In the specific example of CdS/CdSe core-shell sample, the $\sigma(h\nu)$ corrected intensity ratio I_{Se}/I_S decreases with increase in $h\nu$ (solid circles in Fig. 13.8a) qualitatively suggesting that the Se is relatively more abundant on the outer regions of the nanoparticle and S is present deeper towards the core, as targeted in the synthesis [117].

It is possible to obtain a quantitative description of the internal structure of these CdS/CdSe inverted core/shell nanoparticles by determining $N_S(r)$ and $N_{Se}(r)$ that would be consistent with the experimentally observed dependence of I_{Se}/I_S on $h\nu$, shown in Fig. 13.8a. By proper modeling of $N_S(r)$ and $N_{Se}(r)$ to simulate the experimentally obtained I_{Se}/I_S using (13.8), the quantitative structure was found [117] to have a core consisting of pure CdS followed by a gradient alloy of CdS and CdSe as shown as a schematic in Fig. 13.8b, c shows the variation of $N_S(r)$ and $N_{Se}(r)$ as a function of, r, the radial distance from the center of the nanoparticle to the surface. The calculated intensity variation for this particular structure is shown by the solid red line in Fig. 13.8a, which matches very well with the $\sigma(h\nu)$ corrected experimental intensity variation shown by the filled circles. The total size obtained from TEM and the overall chemical composition determined independently from ICP-AES match well with the quantitative model obtained from the analysis of the XPS data, firmly establishing the efficacy of using variable photon energy up to hard X-ray to determine the internal structure of such large sized nanoparticles [117].

13.8 Heterostructure Determination of Thin Films

Heterostructure determination by variable energy XPS can be easily extended to any structure with a spatial homogeneity along the x and y directions, representing a two-dimensionally homogeneous system and any arbitrary variation along the z direction; in other words, the number density function $N(x, y, z)$ appearing in (13.3) or in (13.6) can be replaced by $N(z)$, which is only a function of z. The depth into the material that can be probed and $N(z)$ determined in such a heterostructure in naturally limited by the mean free path, λ, of the photoelectron, indicating the obvious merit of employing hard X-ray photoemission spectroscopy in such cases. A beautiful demonstration [118] of this powerful technique with hard X-ray sources has been realized recently in determining the position of the two dimensional electron gas (2DEG) formed at the interface of two insulating oxides $LaAlO_3$ (LAO) and $SrTiO_3$ (STO). In the original discovery of this phenomenon [48], it was proposed that the polar discontinuity present across the $SrTiO_3$−$LaAlO_3$ interface results in a diverging potential with a growing thickness of LAO, leading to electron transfers from the top $LaAlO_3$ layer to the interface $SrTiO_3$ layer at a critical thickness of LAO [45, 90], leading to the observed 2DEG carriers at the interface.

In order to demonstrate the efficacy of HAXPES in probing quantitatively the internal structure of such heterostructured oxide materials [52, 57, 59, 90, 118–121], we describe in some details results obtained in [118]. We show the variation in the La 3d/Sr 3d intensity ratio (I_{La}/I_{Sr}) corrected for the photoemission cross-section as a function of the photon energy in Fig. 13.9a for two samples, denoted as 6H and 6L. Here the number 6 corresponds to the targeted number of LAO unit cells (uc) grown on top of STO and H and L denote high and low oxygen partial pressure (pO_2), respectively, at the time of the growth of the STO and LAO layers. The 6H sample, grown at 10^{-4} Torr pO_2 is known to have a very low concentration of doped electrons [118], thereby serving the purpose of a reference sample; on the contrary, the 6L sample grown at 10^{-7} Torr pO_2 is known to be highly conducting with a large concentration of doped electrons [118]. The decreasing $\sigma(h\nu)$ corrected I_{La}/I_{Sr} with an increasing $h\nu$ in Fig. 13.9a in conjunction with the experimental geometry defined in the inset implies LAO is indeed the over-layer and a systematic increase in $h\nu$ makes increasing depth into STO to become visible to the HAXPES technique, thereby increasing the Sr 3d intensity and decreasing I_{La}/I_{Sr}. Knowing that there are 6 layers of LAO on top of STO, the experimental geometry allows one to calculate the expected variation in the $\sigma(h\nu)$ corrected I_{La}/I_{Sr} as a function of $h\nu$ using (13.6). This calculated curve is shown in Fig. 13.9a as green shade, with the width of the band arising from estimated errors in calculating the intensity ratio due to uncertainties in α, thickness of the LAO layer etc. Evidently, the calculated dependence and the experimentally obtained values are in excellent agreement, validating the approach and the data analysis.

Electrons doped in $SrTiO_3$ is necessarily accommodated in the Ti 3d conduction band of $SrTiO_3$, thereby showing up as a Ti^{3+} spectral signature in contrast to Ti^{4+} spectral feature of undoped $SrTiO_3$. Since the Ti^{3+} spectral features, with a lower

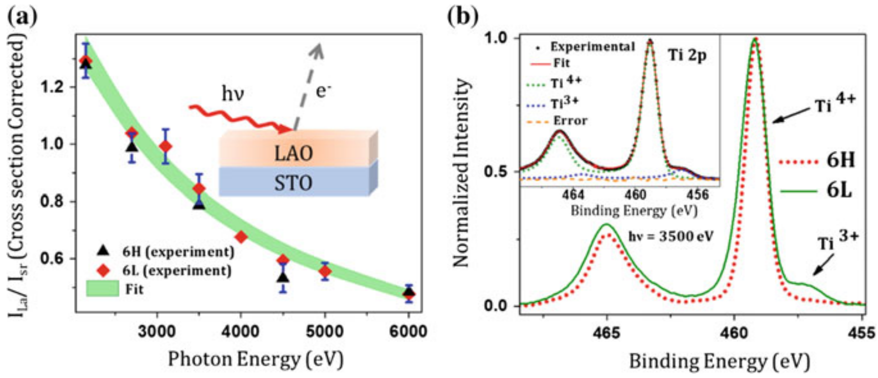

Fig. 13.9 **a** Experimentally obtained intensity ratio between La 3d and Sr 3d core levels spectra as a function of *hv* for 6H and 6L samples are shown as *triangles* and *diamonds* respectively. The *blue bars* represent typical errors in the estimation of the intensity ratio. Simulation of the experimentally obtained intensity ratio between La 3d and Sr 3d of 6 uc samples to obtain the thickness of the *top* LAO layer is shown as *green shade*. **b** High resolution X-ray photoelectron spectra of Ti 2p core levels collected from the high pO_2 grown (6H) and low pO_2 grown (6L) samples with $hv = 3500$ eV. The *inset* of Fig. 13.9b shows the decomposition of the Ti 2p spectra collected from 6L sample at $hv = 3500$ eV to obtain the intensity of the Ti^{4+} and Ti^{3+} components. (Adapted from [118])

BE than those of Ti^{4+} are distinctly observed in Ti 2p spectra, it can be used to map the spatial distribution of doped carriers in the sample. Ti 2p core level spectra collected from 6L and 6H LAO-STO samples with $hv = 3500$ eV are shown in the main frame of Fig. 13.9b. The presence of Ti^{3+} feature at the lower *BE* side of the main Ti^{4+} peak only for the 6L sample with a charge carrier concentration $\sim 10^{17}$ cm^{-2} (obtained from Hall measurements [118]) is clearly visible in comparison to the spectrum from the 6H reference sample. The inset to Fig. 13.9b shows the decomposition of the Ti 2p spectrum from the 6L sample in terms of its Ti^{3+} and Ti^{4+} contributions, allowing a quantitative estimate of Ti^{3+}/Ti^{4+} intensity ratio $I_{Ti^{3+}}/I_{Ti^{4+}}$ observed at different *hv*. One may at once anticipate that a systematic increase of *hv* will allow us to explore how $I_{Ti^{3+}}/I_{Ti^{4+}}$ changes as we probe increasingly deeper into the heterostructure, thereby allowing us to map out how Ti^{3+}, or in other words the doped electron in $SrTiO_3$ is distributed as a function of the depth from the LAO-STO interface. It is interesting to note here that this intensity ratio, involving the same core level (2p) of the same element (Ti), does not require any correction from changes in the cross-sections with *hv*, as this quantity varies exactly the same way for Ti^{3+} and Ti^{4+}, and therefore, cancelling each other and consequently, reducing the uncertainty in the analysis [see (13.7)]. The absolute variation of $I_{Ti^{3+}}/I_{Ti^{4+}}$ for the 6L sample with *hv* is shown in Fig. 13.10a. The gentle decrease in $I_{Ti^{3+}}/I_{Ti^{4+}}$ qualitatively suggests the presence of Ti^{3+} closer to the surface. When an attempt is made to describe the doped electron distribution as a single function at the interface, such as a Gaussian, Lorentzian or a rectangular function, with any arbitrary width, the best description obtained for $I_{Ti^{3+}}/I_{Ti^{4+}}$ as a

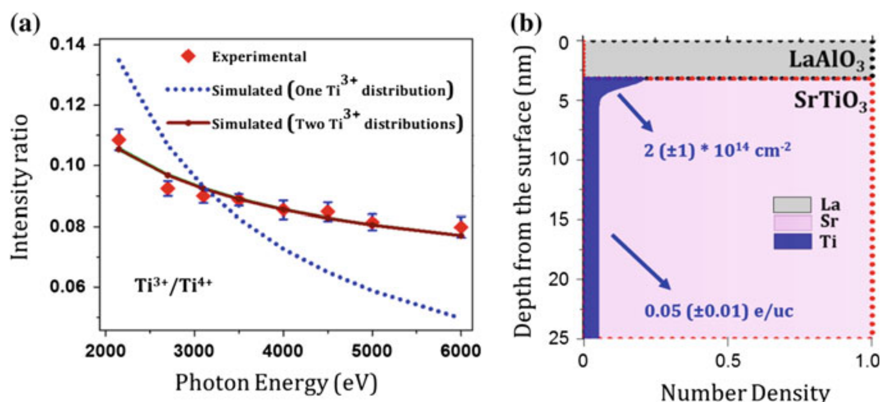

Fig. 13.10 **a** Intensity ratio (*red squares*) between Ti^{3+} and Ti^{4+} obtained from the decomposition of Ti 2p photoelectron spectra obtained from 6L samples at various photon energies. The errors in obtaining the intensity ratio are marked as *blue bars*. The wine *solid lines* shows the best fit to these intensity ratio. Ti^{3+} concentration distributions (*blue shade*) within the LAO-STO samples, that gives the best fitting to the experimentally obtained intensity ratios, are shown in Fig. 13.10b for 6L sample. The color code *grey* and *light pink* represents the LAO and STO layers, respectively, as obtained from the simulation of I_{La}/I_{Sr} intensity ratio. (Adapted from [118]) (Color figure online)

function of *hv* is shown in Fig. 13.10a as the blue dotted line [118]. Clearly such a single distribution of the electron gas is grossly inadequate to describe the experimental data that exhibit a much weaker dependency on *hv*. Interestingly, the experimental data can be very well described when we assume two separate electron distributions (bimodal distribution), as shown by the good agreement between the calculated behavior (shown by the solid lines) and experimental data (filled diamonds). The corresponding bimodal charge carrier distribution within the sample is shown in Fig. 13.10b. This figure shows that a charge carrier distribution is tied to the interface with approximately 2×10^{14} cm^{-2} density, whereas the other charge carrier distribution appears to be an almost homogeneous bulk doping of STO with about 0.05 electrons per unit cell. Evidently, there is no other technique that can provide such critical and detailed information on these unusual systems with extraordinary properties.

The variable high-energy photoemission spectroscopic measurements have recently been used [122–125] to understand the interface structure of a magnetic tunnel junction (MTJ) consisting of thin CoFeB (CFB) layers as ferromagnetic electrodes and MgO as the insulating layer in-between. In the following, we describe results from [125] to underline the ability of HAXPES to provide quantitative description of internal structures even in such complex, multicomponent systems. The overall structure of the two MTJ investigated consists of the stacking as Si(substrate)/Ta(5)/Ru(10)/Ta(5)/$Co_{20}Fe_{60}B_{20}$(5)/MgO(2) with the numbers in the brackets indicating the thickness of the corresponding layers in nm. High energy photoemission spectra collected for Fe 2p and B 1s at *hv* between 2500 and

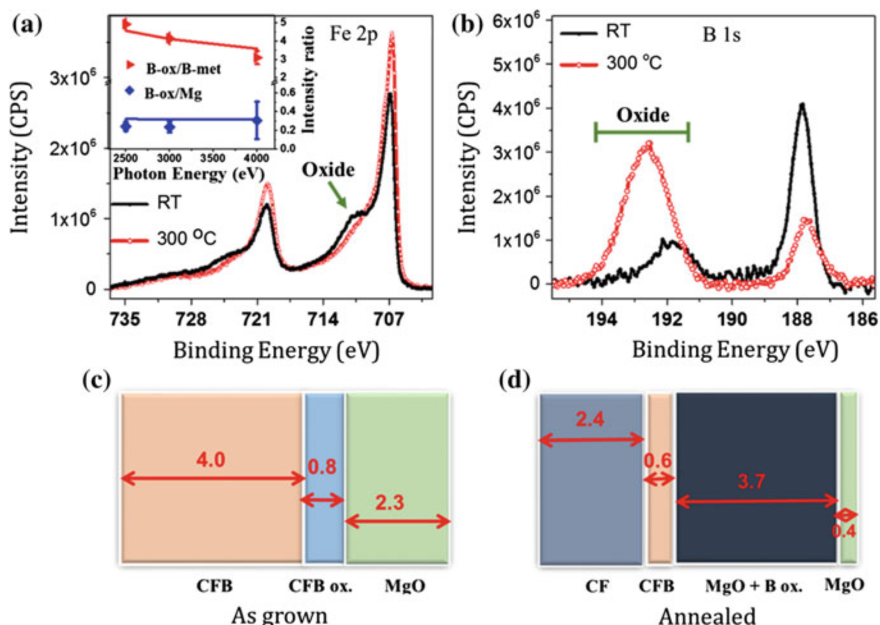

Fig. 13.11 **a** and **b** show Fe 2p and B 1s core level spectra collected from the uncapped bilayer MTJ sample at $h\nu$ = 3000 eV photon energy before (*black*) and after (*red*) annealing the sample at 300 ± 5 °C for 20 min. The *inset* of Fig. 13.11a shows the intensity ratio between B-oxide to B-metal (*red triangles*) and B-oxide to Mg (*blue square*) obtained from 300 ± 5 °C annealed sample at different photon energies. The *lines* represent the simulated intensity ratios for the best fitted structure, shown in Fig. 13.11d. The thickness and nature of various layers in the unannealed and annealed uncapped bilayer sample are shown in Fig. 13.11c, d. The numbers shown in the figures are in nanometer. (Adapted from [125])

4000 eV from this MTJ sample are shown in Fig. 13.11a, b, respectively, for two different cases. First, the sample as grown was investigated; then the sample was annealed at 300 °C for 20 min to understand the effect of annealing that is involved in processing of MTJ layers for device applications. This annealed sample was also investigated in an identical manner to understand the consequence of annealing [125]. The spin-orbit split metallic peaks of Fe 2p can be seen at *BE* of 706.8 and 720 eV and the B 1s metallic peak appears at *BE* of 187.8 eV. Along with the characteristic metallic features, both Fe 2p and B 1s spectra contain additional features at higher binding energies arising from corresponding oxide species, as indicated in the Figs. 13.10b, 13.11a. For Fe 2p, the oxide species appears at 3.6 eV higher *BE* from the main peaks, whereas it is at *BE* of about 191.8 eV for B 1s. The intensity ratio of the B-oxide and B-metallic 1s peak for the annealed sample is shown in the inset to Fig. 13.11a as a function of $h\nu$. It is clear from this plot that the intensity of the oxide species decreases with respect to the metallic peak when the spectra are collected with higher photon energies, suggesting presence of the oxide species closer to the surface compared to the metallic counterparts; a similar

observation was also made for the Fe-oxide signal. Such intensity ratios, not only for the oxide and metallic signals of the same elements, but also spectral intensity of different elements, such as B-oxide 1s/Mg 1s (shown in the inset to Fig. 13.11a for the annealed sample), Fe 2p/Mg 1s, Fe 2p/Co 2p (not shown here) were also obtained in this study for both samples as a function of the *hν*. These experimentally obtained intensity variations with the photon energy help to understand the internal structure of these two samples in detail [125]. For example, the relative insensitivity of the B-oxide/Mg intensity ratio on *hν* for the annealed sample shown in the inset suggests that boron oxide is spread nearly homogeneously in the MgO layer, as has also been reported in [122, 123]. Taking into account the intensity variation of various core levels at different photon energies, it was possible to obtain a quantitative description of the internal structure [125] of this bilayer MTJ sample before and after annealing, as shown in Fig. 13.11c and d, respectively. This study also reports the internal structure of a tri-layer sample (with an additional $C_{20}F_{60}B_{20}$ layer on top of MgO), in contrast to the bilayered one discussed here, resolving controversy on the behavior of B diffusion on annealing the sample, illustrating the tremendous usefulness of this technique.

13.9 Conclusion and Future Outlook

In this chapter, we have detailed how one may extract in-depth knowledge of the internal geometric and electronic structures of heterogeneous materials with the use of variable photon energy available at synchrotron radiation centers to carry out depth resolved X-ray photoelectron spectroscopy. Competing techniques to obtain such information are typically based on microscopic approaches, such as transmission electron microscopy (TEM) together with its ability to perform space resolved elemental identification via energy dispersive X-ray analysis and electron energy loss spectroscopy, and scanning tunneling microscopy (STM). In general, STM is extremely surface sensitive and it is impossible to obtain depth resolved information from such a technique. There have been attempts reported in the literature to obtain information beyond the surface by carrying out cross-sectional studies; this requires cutting through the sample in a direction perpendicular to the surface, thereby exposing the deeper part of the sample to the STM probe. However, strictly speaking, any information so obtained continues to be a surface related information, since the act of making the cross-sectional cut introduces a new surface in the sample. Since the surface electronic structure may be different from those from beyond the surface, cross-sectional studies to that extent may alter the electronic structure being probed compared to that in the deeper part of the system in an uncontrolled manner. This may limit the usefulness and applicability of such cross-sectional studies. Similar cross-sectional studies are also popular in conjunction with TEM. Obvious advantage of the technique discussed here based on photoelectron spectroscopy is its nondestructive nature. It has the ability of investigating the sample as such without the need to introduce any new surfaces to

access deeper parts of the sample. The other advantage of the present technique is that it naturally provides depth (or vertically) resolved information into the sample, starting from the surface, with the help of a changing mean free path of photoelectrons with a change in their kinetic energy brought about by changing the photon energy; this is in contrast to the laterally resolved information from all microscopic techniques mentioned above. Of course, there are several limitations of the present technique as well. For example, the depth that can be probed effectively using this technique is limited severely by ultra-short mean free paths of photoelectrons. Even with the advent of hard X-rays up to about 10 keV to carry out photoelectron spectroscopy, it is not possible to reliably probe beyond a depth of $\sim$15–20 nm. We note that this is not a limitation on the sample thickness; even a macroscopically thick sample may be investigated without any need to thin down the sample unlike in the case of TEM. However, the depth-resolved information will be restricted to within the first 15–20 nm of the surface at best using this technique. Since most of the nanocrystals investigated have sizes below 20 nm, the present technique is an ideal tool to probe their internal structures. Also, any heterostructures can be probed as long as the interface of interest is not buried deeper than the above-mentioned limit, as discussed in specific examples in this chapter.

It is important to keep in mind the uncertainties inherent in this technique. As has been explained in detail, a quantitative determination of the internal structure of any sample requires the knowledge of several parameters that are not very well controlled, thereby introducing uncertainties in the derived quantitative estimates. One such uncertainty arises from the estimate of the mean free path which is never easy to determine a priori with a great accuracy. The second source of uncertainty is the photon energy dependent cross-section of various levels that are analyzed to extract the depth resolved information. Other parameters, such as the photon flux and other experimental factors, can be largely taken care of by analyzing only intensity ratios and opting for core level signals that have similar binding energies, as explained in this chapter. It is also to be realized that the analysis of the intensity ratio as a function of the photon energy to extract the internal structure is based on a presumed parameterized model of the internal structure, such that the internal parameters of the assumed model are optimized to provide the best description of the intensity variation. Thus, the analysis can be hoped to provide reasonable estimates only if the assumed model is realistic. This implies that it is important to have some basic ideas of the shape and the internal symmetry of the sample.

The above mentioned limitations point to the fact that the present technique, instead of being viewed as a competing technique, should be more viewed as a complimentary one to other techniques that can provide any clue to the internal structure. Thus, it is important to start the analysis with a prior knowledge of the shape and overall dimension of the sample in case of nanomaterials. This information is easily obtained from TEM studies and helps to build up the model for the analysis. Similarly, in many spherical nanocrystals synthesized via the solution route, it is also reasonable to assume a spherical symmetry of the composition, helping to bring down the number of parameters in the model. The overall size

determined from the TEM study then provides a critical test for the model, since the analysis of the photoelectron spectroscopic results must be consistent with that of TEM in terms of the total size of the nanocrystal. Similarly, elemental analysis using ICP-AES or atomic absorption spectroscopy provides important restrictions on the model, since each optimized model corresponds to a well-defined average composition. Using every such available information on the system, one may substantially reduce the uncertainties associated with the analysis of the internal structure based on the present technique.

Since the electronic structure of any material is crucially dependent on the elemental distribution within the sample, it is clear that understanding the internal structure of low dimensional systems is of great importance, as has been discussed in this chapter. With an increasing number of beamlines becoming available around the world where one may carry out high resolution photoelectron spectroscopy over a wide range of photon energies, it appears that this technique, in conjunction with all other complimentary techniques, will play a unique and powerful role in unraveling the internal geometric and electronic structures of such systems.

References

1. G. Schmid (ed.), *Nanoparticles*: *From Theory to Application*, 2nd edn (Wiley-VCH Verlag GmbH & Co. KGaA: Weinheim, Germany, 2010)
2. H. Weller, Colloidal semiconductor Q-particles: chemistry in the transition region between solid state and molecules. Angew. Chem. Int. Ed. Engl. **32**(1), 41–53 (1993)
3. D. Bera et al., Quantum dots and their multimodal applications: a review. Materials **3**(4), 2260–2345 (2010)
4. T. Trindade, P. O'Brien, N.L. Pickett, Nanocrystalline semiconductors: synthesis, properties, and perspectives. Chem. Mater. **13**(11), 3843–3858 (2001)
5. B.O. Dabbousi et al., (CdSe)ZnS core-shell quantum dots: synthesis and characterization of a size series of highly luminescent nanocrystallites. J. Phys. Chem. B **101**(46), 9463–9475 (1997)
6. S. Sapra, D.D. Sarma, Evolution of the electronic structure with size in II–VI semiconductor nanocrystals. Phys. Rev. B **69**(12), 125304 (2004)
7. C.B. Murray, D.J. Norris, M.G. Bawendi, Synthesis and characterization of nearly monodisperse CdE (E = sulfur, selenium, tellurium) semiconductor nanocrystallites. J. Am. Chem. Soc. **115**(19), 8706–8715 (1993)
8. R. Viswanatha, D.D. Sarma, Study of the growth of capped ZnO nanocrystals: a route to rational synthesis. Chem. A Eur. J. **12**(1), 180–186 (2006)
9. X. Peng et al., Shape control of CdSe nanocrystals. Nature **404**(6773), 59–61 (2000)
10. C.J. Murphy, N.R. Jana, Controlling the aspect ratio of inorganic nanorods and nanowires. Adv. Mater. **14**(1), 80–82 (2002)
11. S. Acharya et al., Shape-dependent confinement in ultrasmall zero-, one-, and two-dimensional PbS nanostructures. J. Am. Chem. Soc. **131**(32), 11282–11283 (2009)
12. C. Burda et al., Chemistry and properties of nanocrystals of different shapes. Chem. Rev. **105** (4), 1025–1102 (2005)
13. A.R. Tao, S. Habas, P. Yang, Shape control of colloidal metal nanocrystals. Small **4**(3), 310–325 (2008)

14. M.A. Hines, P. Guyot-Sionnest, Synthesis and characterization of strongly luminescing ZnS-capped CdSe nanocrystals. J. Phys. Chem. **100**(2), 468–471 (1996)
15. X. Peng et al., Epitaxial growth of highly luminescent CdSe/CdS core/shell nanocrystals with photostability and electronic accessibility. J. Am. Chem. Soc. **119**(30), 7019–7029 (1997)
16. J.-S. Lee, E.V. Shevchenko, D.V. Talapin, Au−PbS core-shell nanocrystals: plasmonic absorption enhancement and electrical doping via intra-particle charge transfer. J. Am. Chem. Soc. **130**(30), 9673–9675 (2008)
17. P. Reiss, J. Bleuse, A. Pron, Highly luminescent CdSe/ZnSe core/shell nanocrystals of low size dispersion. Nano Lett. **2**(7), 781–784 (2002)
18. P. Reiss, M. Protière, L. Li, Core/shell semiconductor nanocrystals. Small **5**(2), 154–168 (2009)
19. D.D. Sarma et al., Origin of the enhanced photoluminescence from semiconductor CdSeS nanocrystals. J. Phys. Chem. Lett. **1**(14), 2149–2153 (2010)
20. P.K. Santra et al., Investigation of the internal heterostructure of highly luminescent quantum dot—quantum well nanocrystals. J. Am. Chem. Soc. **131**(2), 470–477 (2008)
21. A. Eychmüller, A. Mews, H. Weller, A quantum dot quantum well: CdS/HgS/CdS. Chem. Phys. Lett. **208**(1–2), 59–62 (1993)
22. D. Battaglia, B. Blackman, X. Peng, Coupled and decoupled dual quantum systems in one semiconductor nanocrystal. J. Am. Chem. Soc. **127**(31), 10889–10897 (2005)
23. S. Sengupta et al., Long-range visible fluorescence tunability using component-modulated coupled quantum dots. Adv. Mater. **23**(17), 1998–2003 (2011)
24. J.J. Li et al., Large-scale synthesis of nearly monodisperse CdSe/CdS core/shell nanocrystals using air-stable reagents via successive ion layer adsorption and reaction. J. Am. Chem. Soc. **125**(41), 12567–12575 (2003)
25. U. Resch-Genger et al., Quantum dots versus organic dyes as fluorescent labels. Nat. Meth. **5** (9), 763–775 (2008)
26. A.B. Greytak et al., Alternating layer addition approach to CdSe/CdS core/shell quantum dots with near-unity quantum yield and high on-time fractions. Chem. Sci. **3**(6), 2028–2034 (2012)
27. J.-S. Lee et al., "Magnet-in-the-semiconductor" FePt−PbS and FePt−PbSe nanostructures: magnetic properties, charge transport, and magnetoresistance. J. Am. Chem. Soc. **132**(18), 6382–6391 (2010)
28. R. Ghosh Chaudhuri, S. Paria, Core/shell nanoparticles: classes, properties, synthesis mechanisms, characterization, and applications. Chem. Rev. **112**(4), 2373–2433 (2011)
29. S. Kim et al., Type-II quantum dots: CdTe/CdSe(Core/Shell) and CdSe/ZnTe(Core/Shell) heterostructures. J. Am. Chem. Soc. **125**(38), 11466–11467 (2003)
30. R.E. Bailey, S. Nie, Alloyed semiconductor quantum dots: tuning the optical properties without changing the particle size. J. Am. Chem. Soc. **125**(23), 7100–7106 (2003)
31. X. Zhong et al., Alloyed $Zn_xCd_{1-x}S$ nanocrystals with highly narrow luminescence spectral width. J. Am. Chem. Soc. **125**(44), 13559–13563 (2003)
32. A. Nag, S. Chakraborty, D.D. Sarma, To dope Mn^{2+} in a semiconducting nanocrystal. J. Am. Chem. Soc. **130**(32), 10605–10611 (2008)
33. H. Borchert et al., Photoemission study of onion like quantum dot quantum well and double quantum well nanocrystals of CdS and HgS. J. Phys. Chem. B **107**(30), 7486–7491 (2003)
34. S. Sapra et al., Bright white-light emission from semiconductor nanocrystals: by chance and by design. Adv. Mater. **19**(4), 569–572 (2007)
35. F. García-Santamaría et al., Breakdown of volume scaling in auger recombination in CdSe/CdS heteronanocrystals: the role of the core-shell interface. Nano Lett. **11**(2), 687–693 (2011)
36. N. Tschirner et al., Interfacial alloying in CdSe/CdS heteronanocrystals: a raman spectroscopy analysis. Chem. Mater. **24**(2), 311–318 (2011)
37. W.K. Bae et al., Controlled alloying of the core-shell interface in CdSe/CdS quantum dots for suppression of auger recombination. ACS Nano **7**(4), 3411–3419 (2013)

38. X. Wang et al., Non-blinking semiconductor nanocrystals. Nature **459**(7247), 686–689 (2009)
39. M. Benoit et al., Towards non-blinking colloidal quantum dots. Nat. Mater. **7**(8), 659–664 (2008)
40. J. Mathon, A. Umerski, Theory of tunneling magnetoresistance of an epitaxial Fe/MgO/Fe (001) junction. Phys. Rev. B **63**(22), 220403 (2001)
41. C. Tusche et al., Oxygen-induced symmetrization and structural coherency in Fe/MgO/Fe (001) magnetic tunnel junctions. Phys. Rev. Lett. **95**(17), 176101 (2005)
42. F. Bonell et al., Spin-polarized electron tunneling in bcc FeCo/MgO/FeCo (001) magnetic tunnel junctions. Phys. Rev. Lett. **108**(17), 176602 (2012)
43. S. Ikeda et al., Tunnel magnetoresistance of 604 % at 300 K by suppression of Ta diffusion in CoFeB/MgO/CoFeB pseudo-spin-valves annealed at high temperature. Appl. Phys. Lett. **93** (8) (2008)
44. S.S.P. Parkin et al., Giant tunnelling magnetoresistance at room temperature with MgO (100) tunnel barriers. Nat. Mater. **3**(12), 862–867 (2004)
45. H.Y. Hwang et al., Emergent phenomena at oxide interfaces. Nat. Mater. **11**(2), 103–113 (2012)
46. J. Chakhalian, A.J. Millis, J. Rondinelli, Whither the oxide interface. Nat. Mater. **11**(2), 92–94 (2012)
47. A. Tsukazaki et al., Quantum hall effect in polar oxide heterostructures. Science **315**(5817), 1388–1391 (2007)
48. A. Ohtomo, H.Y. Hwang, A high-mobility electron gas at the $LaAlO_3/SrTiO_3$ heterointerface. Nature **427**(6973), 423–426 (2004)
49. N. Reyren et al., Superconducting interfaces between insulating oxides. Science **317**(5842), 1196–1199 (2007)
50. A. Brinkman et al., Magnetic effects at the interface between non-magnetic oxides. Nat. Mater. **6**(7), 493–496 (2007)
51. M. Gorgoi et al., The high kinetic energy photoelectron spectroscopy facility at BESSY progress and first results. Nucl. Instrum. Methods Phys. Res. Sect. A **601**(1–2), 48–53 (2009)
52. R. Knut et al., High energy photoelectron spectroscopy in basic and applied science: Bulk and interface electronic structure. J. Electron Spectrosc. Relat. Phenom. **190**(Part B 0), 278–288 (2013)
53. S. Ueda, Application of hard X-ray photoelectron spectroscopy to electronic structure measurements for various functional materials. J. Electron Spectrosc. Relat. Phenom. **190** (Part B 0), 235–241 (2013)
54. E. Ikenaga et al., Development of high lateral and wide angle resolved hard X-ray photoemission spectroscopy at BL47XU in SPring-8. J. Electron Spectrosc. Relat. Phenom. **190**(Part B 0), 180–187 (2013)
55. D. Céolin et al., Hard X-ray photoelectron spectroscopy on the GALAXIES beamline at the SOLEIL synchrotron. J. Electron Spectrosc. Relat. Phenom. **190**(Part B 0), 188–192 (2013)
56. H. Wadati, A. Fujimori, Hard X-ray photoemission spectroscopy of transition-metal oxide thin films and interfaces. J. Electron Spectrosc. Relat. Phenom. **190**(Part B 0), 222–227 (2013)
57. R. Claessen et al., Hard X-ray photoelectron spectroscopy of oxide hybrid and heterostructures: a new method for the study of buried interfaces. New J. Phys. **11**, 125007 (2009)
58. F. Borgatti et al., Interfacial and bulk electronic properties of complex oxides and buried interfaces probed by HAXPES. J. Electron Spectrosc. Relat. Phenom. **190**(Part B 0), 228–234 (2013)
59. C. Caspers et al., Chemical stability of the magnetic oxide EuO directly on silicon observed by hard X-ray photoemission spectroscopy. Phys. Rev. B **84**(20), 205217 (2011)
60. M. Gorgoi et al., Hard X-ray high kinetic energy photoelectron spectroscopy at the KMC-1 beamline at BESSY. Eur. Phys. J. Special Topics **169**(1), 221–225 (2009)

61. C. Weiland et al., NIST high throughput variable kinetic energy hard X-ray photoelectron spectroscopy facility. J. Electron Spectrosc. Relat. Phenom. **190**(Part B 0), 193–200 (2013)
62. S. Hufner, *Photoelectron Spectroscopy, Principles and Applications* (Springer, Berlin, New York, 1995)
63. K. Siegbahn et al., ESCA: atomic, molecular, and solid state structure studies by means of electron spectroscopy. Nova Acta Regiae Soc. Sci. Ups. Ser. IV, 1967. 20
64. A. Fujimori et al., Core-level photoemission measurements of the chemical potential shift as a probe of correlated electron systems. J. Electron Spectrosc. Relat. Phenom. **124**(2–3), 127–138 (2002)
65. E. Hao et al., Synthesis and optical properties of CdSe and CdSe/CdS nanoparticles. Chem. Mater. **11**(11), 3096–3102 (1999)
66. I. Tunc et al., XPS characterization of Au (Core)/SiO_2 (Shell) nanoparticles. J. Phys. Chem. B **109**(16), 7597–7600 (2005)
67. P.A. Mangrulkar et al., Throwing light on platinized carbon nanostructured composites for hydrogen generation. Energy Environ. Sci. **7**(12), 4087–4094 (2014)
68. H. Jensen et al., XPS and FTIR investigation of the surface properties of different prepared titania nano-powders. Appl. Surf. Sci. **246**(1–3), 239–249 (2005)
69. J.S. Owen et al., Reaction chemistry and ligand exchange at cadmium–selenide nanocrystal surfaces. J. Am. Chem. Soc. **130**(37), 12279–12281 (2008)
70. A. Roy et al., Photoemission study of porous silicon. Appl. Phys. Lett. **61**(14), 1655–1657 (1992)
71. A. Roy, D.D. Sarma, A.K. Sood, Spectroscopic studies on quantum dots of PbI_2. Spectrochim. Acta Part A **48**(11–12), 1779–1787 (1992)
72. J. Jasieniak, P. Mulvaney, From Cd-rich to Se-rich—the manipulation of CdSe nanocrystal surface stoichiometry. J. Am. Chem. Soc. **129**(10), 2841–2848 (2007)
73. J.E.B. Katari, V.L. Colvin, A.P. Alivisatos, X-ray photoelectron spectroscopy of CdSe nanocrystals with applications to studies of the nanocrystal surface. J. Phys. Chem. **98**(15), 4109–4117 (1994)
74. U. Winkler et al., Detailed investigation of CdS nanoparticle surfaces by high-resolution photoelectron spectroscopy. Chem. Phys. Lett. **306**(1–2), 95–102 (1999)
75. S.K. Kulkarni et al., Investigations on chemically capped CdS, ZnS and ZnCdS nanoparticles. Appl. Surf. Sci. **169–170**, 438–446 (2001)
76. K.B. Subila et al., Luminescence properties of CdSe quantum dots: role of crystal structure and surface composition. J. Phys. Chem. Lett. **4**(16), 2774–2779 (2013)
77. V. Vijayakrishnan et al., Metal-insulator transitions in metal clusters: a high-energy spectroscopy study of palladium and silver clusters. J. Phys. Chem. **96**(22), 8679–8682 (1992)
78. B.M. Reddy, B. Chowdhury, P.G. Smirniotis, An XPS study of the dispersion of MoO_3 on TiO_2–ZrO_2, TiO_2–SiO_2, TiO_2–Al_2O_3, SiO_2–ZrO_2, and SiO_2–TiO_2–ZrO_2 mixed oxides. Appl. Catal. A **211**(1), 19–30 (2001)
79. N. Kruse, S. Chenakin, XPS characterization of Au/TiO_2 catalysts: Binding energy assessment and irradiation effects. Appl. Catal. A **391**(1–2), 367–376 (2011)
80. A.V. Baranov et al., Effect of ZnS shell thickness on the phonon spectra in CdSe quantum dots. Phys. Rev. B **68**(16), 165306 (2003)
81. F. Todescato et al., Investigation into the heterostructure interface of CdSe-based core-shell quantum dots using surface-enhanced raman spectroscopy. ACS Nano **7**(8), 6649–6657 (2013)
82. W.W. Yu et al., Experimental determination of the extinction coefficient of CdTe, CdSe, and CdS nanocrystals. Chem. Mater. **15**(14), 2854–2860 (2003)
83. S. Tougaard, Surface nanostructure determination by X-ray photoemission spectroscopy peak shape analysis. J. Vac. Sci. Technol. A **14**(3), 1415–1423 (1996)
84. I. Doron-Mor et al., Controlled surface charging as a depth-profiling probe for mesoscopic layers. Nature **406**(6794), 382–385 (2000)

85. B.J. Tyler, D.G. Castner, B.D. Ratner, Regularization: a stable and accurate method for generating depth profiles from angle-dependent XPS data. Surf. Interface Anal. **14**(8), 443–450 (1989)
86. S. Hajati, S. Tougaard, Non-Destructive depth profiling by XPS peak shape analysis. J. Surf. Anal. **15**(3), 220–224 (2009)
87. S.H. Yang et al., Depth-resolved photoemission spectroscopy with soft X-ray standing waves. J. Electron Spectrosc. Relat. Phenom. **114–116**, 1089–1095 (2001)
88. D.D. Sarma et al., X-ray photoelectron spectroscopy: a unique tool to determine the internal heterostructure of nanoparticles. Chem. Mater. **25**(8), 1222–1232 (2013)
89. E. Holmström et al., Sample preserving deep interface characterization technique. Phys. Rev. Lett. **97**(26), 266106 (2006)
90. M. Sing et al., Profiling the interface electron gas of $LaAlO_3/SrTiO_3$ heterostructures with hard X-ray photoelectron spectroscopy. Phys. Rev. Lett. **102**(17), 176805 (2009)
91. W.A.M. Aarnink, A. Weishaupt, A. van Silfhout, Angle-resolved X-ray photoelectron spectroscopy (ARXPS) and a modified Levenberg-Marquardt fit procedure: a new combination for modeling thin layers. Appl. Surf. Sci. **45**(1), 37–48 (1990)
92. C. Weiland et al., Nondestructive compositional depth profiling using variable-kinetic energy hard X-ray photoelectron spectroscopy and maximum entropy regularization. Surf. Interface Anal. **46**(6), 407–417 (2014)
93. T.A. Carlson, G.E. McGuire, Study of the X-ray photoelectron spectrum of tungsten—tungsten oxide as a function of thickness of the surface oxide layer. J. Electron Spectrosc. Relat. Phenom. **1**(2), 161–168 (1972)
94. L. Kumar, D.D. Sarma, S. Krummacher, XPS study of the room temperature surface oxidation of zirconium and its binary alloys with tin, chromium and iron. Appl. Surf. Sci. **32**(3), 309–319 (1988)
95. J. Nanda, B.A. Kuruvilla, D.D. Sarma, Photoelectron spectroscopic study of CdS nanocrystallites. Phys. Rev. B **59**(11), 7473–7479 (1999)
96. J. Nanda, D.D. Sarma, Photoemission spectroscopy of size selected zinc sulfide nanocrystallites. J. Appl. Phys. **90**(5), 2504–2510 (2001)
97. P. Sen et al., An electron spectroscopic study of the surface oxidation of glassy and crystalline Cu–Zr alloys. J. Phys. F: Met. Phys. **14**(2), 565–577 (1984)
98. D.A. Shirley, High-resolution X-ray photoemission spectrum of the valence bands of gold. Phys. Rev. B **5**(12), 4709–4714 (1972)
99. R. Hesse et al., Comparative study of the modelling of the spectral background of photoelectron spectra with the Shirley and improved Tougaard methods. J. Electron Spectrosc. Relat. Phenom. **186**, 44–53 (2013)
100. S. Tanuma, C.J. Powell, D.R. Penn, Calculations of electron inelastic mean free paths (IMFPS). IV. Evaluation of calculated IMFPs and of the predictive IMFP formula TPP-2 for electron energies between 50 and 2000 eV. Surf. Interface Anal. **20**(1), 77–89 (1993)
101. C.S. Fadley, S. Nemšák, Some future perspectives in soft- and hard-X-ray photoemission. J. Electron Spectrosc. Relat. Phenom. **195**, 409–422 (2014)
102. B. Pal, S. Mukherjee, D. D. Sarma, Probing internal structures using hard X-ray photoelectron spectroscopy (HAXPES). J. Electron Spectrosc. Relat. Phenom. **200**, (2015). doi: 10.1016/j.elspec.2015.06.005
103. S. Tanuma, C.J. Powell, D.R. Penn, Calculations of electron inelastic mean free paths for 31 materials. Surf. Interface Anal. **11**(11), 577–589 (1988)
104. S. Tanuma, C.J. Powell, D.R. Penn, Calculations of electron inelastic mean free paths. III. Data for 15 inorganic compounds over the 50–2000 eV range. Surf. Interface Anal. **17**(13), 927–939 (1991)
105. C. Cancellieri et al., Interface fermi states of $LaAlO_3/SrTiO_3$ and related heterostructures. Phys. Rev. Lett. **110**(13), 137601 (2013)
106. J.J. Yeh, I. Lindau, Atomic subshell photoionization cross sections and asymmetry parameters: $1 \leqslant Z \leqslant 103$. At. Data Nucl. Data Tables **32**(1), 1–155 (1985)

107. J. H. Scofield, Theoretical photoionization cross sections from 1 to 1500 keV. Lawrence Livermore National Laboratory Rep (1973)
108. R. Hesse, P. Streubel, R. Szargan, Improved accuracy of quantitative XPS analysis using predetermined spectrometer transmission functions with UNIFIT 2004. Surf. Interface Anal. **37**(7), 589–607 (2005)
109. S. Sapra et al., Unraveling internal structures of highly luminescent PbSe nanocrystallites using variable-energy synchrotron radiation photoelectron spectroscopy. J. Phys. Chem. B **110**(31), 15244–15250 (2006)
110. D. D. Sarma, P. Sen, XPS and Auger studies of the surface oxidation of Manganese. Proc. Indian Natn. Sci. Acad. **49(A)**(3) (1983)
111. P. Sen, M.S. Hegde, C.N.R. Rao, Surface oxidation of cadmium, indium, tin and antimony by photoelectron and Auger spectroscopy. Appl. Surf. Sci. **10**(1), 63–74 (1982)
112. D.D. Sarma, M.S. Hegde, C.N.R. Rao, Study of surface oxidation of rare-earth metals by photoelectron spectroscopy. J. Chem. Soc. Faraday Trans. 2: Mol. Chem. Phys. **77**(9), 1509–1520 (1981)
113. M. Ayyoob, D.D. Sarma, XPS and UVPES studies of the surface oxidation of Gd and Yb. Ind. J. Chem. **22 (A)** (1983)
114. H. Borchert et al., Relations between the photoluminescence efficiency of CdTe nanocrystals and their surface properties revealed by synchrotron XPS. J. Phys. Chem. B **107**(36), 9662–9668 (2003)
115. F. Bernardi et al., Unraveling the formation of core-shell structures in nanoparticles by S-XPS. J. Phys. Chem. Lett. **1**(6), 912–917 (2010)
116. K. Huang et al., Internal structure of InP/ZnS nanocrystals unraveled by high-resolution soft X-ray photoelectron spectroscopy. ACS Nano **4**(8), 4799–4805 (2010)
117. S. Mukherjee et al., Determination of internal structures of heterogeneous nanocrystals using variable-energy photoemission spectroscopy. J. Phys. Chem. C **118**(28), 15534–15540 (2014)
118. S. Mukherjee et al., Distribution and nature of charge carriers in $LaAlO_3$-$SrTiO_3$ oxide heterostructures. Unpublished results
119. M. Paul et al., Probing the interface of Fe_3O_4GaAs thin films by hard X-ray photoelectron spectroscopy. Phys. Rev. B **79**(23), 233101 (2009)
120. E. Slooten et al., Hard X-ray photoemission and density functional theory study of the internal electric field in $SrTiO_3/LaAlO_3$ oxide heterostructures. Phys. Rev. B **87**(8), 085128 (2013)
121. C. Weiland et al., Hard X-ray photoelectron spectroscopy study of As and Ga out-diffusion in $In_{0.53}Ga_{0.47}As/Al_2O_3$ film systems. Appl. Phys. Lett. **101**(6), 061602 (2012)
122. A.A. Greer et al., Observation of boron diffusion in an annealed Ta/CoFeB/MgO magnetic tunnel junction with standing-wave hard X-ray photoemission. Appl. Phys. Lett. **101**(20), 202402 (2012)
123. A.K. Rumaiz et al., Boron migration due to annealing in CoFeB/MgO/CoFeB interfaces: a combined hard X-ray photoelectron spectroscopy and X-ray absorption studies. Appl. Phys. Lett. **99**(22), 222502 (2011)
124. X. Kozina et al., A nondestructive analysis of the B diffusion in Ta–CoFeB–MgO–CoFeB–Ta magnetic tunnel junctions by hard X-ray photoemission. Appl. Phys. Lett. **96**(7), 072105 (2010)
125. S. Mukherjee et al., Role of boron diffusion in CoFeB/MgO magnetic tunnel junctions. Phys. Rev. B **91**(8), 085311 (2015)

Chapter 14
Probing Perovskite Interfaces and Superlattices with X-ray Photoemission Spectroscopy

Scott A. Chambers

Abstract The use of X-ray photoemission spectroscopy (XPS) in the soft, intermediate and hard X-ray regimes in probing complex oxide interfaces and superlattices is reviewed. Core-level line shapes are briefly discussed, followed by a case study of several aspects of the $LaAlO_3/SrTiO_3(001)$ heterojunction. These include how XPS in both angle-integrated and angle-resolved modes has been used to probe the physical cause of interface conductivity, the origin of itinerant electrons, the valence band offset, and the extent of cation mixing. The chapter concludes with a brief discussion of other perovskite interfaces which have been successfully investigated with XPS.

14.1 Introduction

Complex oxides exhibit an exceedingly wide range of electronic, magnetic and optical properties, giving these materials considerable potential for interesting basic science investigations, as well as possible utility in a range of technological applications. Complex oxides have been vigorously investigated as epitaxial films over the past two decades, in part because of the discovery of high-T_c superconductivity in cuprates [1]. A second reason for this interest is the rich and varied property set, including colossal magnetoresistance [2], exhibited by the doped manganites, $AE_xRE_{1\text{-}x}MnO_3$, where *AE* and *RE* represent alkaline earth and rare earth metals, respectively. The observations of many interesting and often unexpected phenomena have captured the attention and imagination of a growing community of condensed matter scientists who wants to explore the fundamental physics of these materials, as well as novel technological concepts.

One important class of complex oxides is the perovskites which have the general formula ABO_3. The A (B) metal cation sites are twelve- (six-) fold coordinated to

S.A. Chambers (✉)
Fundamental and Computational Sciences Directorate, Physical Sciences Division,
Pacific Northwest National Laboratory, Richland, WA 99352, USA
e-mail: sa.chambers@pnnl.gov

© Springer International Publishing Switzerland 2016

J.C. Woicik (ed.), *Hard X-ray Photoelectron Spectroscopy (HAXPES)*,
Springer Series in Surface Sciences 59, DOI 10.1007/978-3-319-24043-5_14

oxygen anions. The high degrees of solubility of different metal cations on the A and B sites result in a rich phase space of compositions and electronic and magnetic structures. The added flexibility resulting from state-of-the-art epitaxial film growth enables the preparation of multilayers and superlattices which yield an additional degree of freedom not found in bulk material synthesis. One particularly popular experiment has been to prepare digital superlattices of the form $(ABO_3)_n/(A'BO_3)_m$, and compare the resulting properties with those of a random solid solution of the same composition, $A_xA'_{1-x}BO_3$, where $x = n/(n + m)$ [3].

In order to elucidate defensible structure-composition-property relationships for epitaxial films and interfaces of these materials, adequate materials characterization must be done. Several techniques are currently available and in frequent use. In situ reflection high-energy electron diffraction (RHEED) and ex situ high-resolution X-ray diffraction (XRD) yield important information on structural properties. Scanning transmission electron microscopy (STEM) in combination with electron energy loss spectroscopy (EELS) yield detailed structural and compositional information on a local scale [4]. Ex situ Rutherford backscattering spectrometry (RBS) provides useful volume averaged information on composition for most elements, subject to the uncertainties resulting from film peaks overlapping the broad plateaus associated with backscattering from elements in the substrate, and weak backscattering from elements of lower atomic number. The physics of RBS is relatively simple, the scattering cross sections are known in an absolute sense [5], and accurate models have been developed that allow the user to extract absolute areal densities for individual elements [6]. If carried out with a lower incident ion energy and higher energy resolution in the analyzer, the depth resolution of RBS can be significantly increased to yield useful information of elemental profiles at buried perovskite interfaces. This method is referred to as high-resolution RBS (HRRBS) or medium energy ion scattering (MEIS) [7].

Core-level X-ray photoemission spectroscopy (XPS) at intermediate and high X-ray energies readily can yield quantitative compositional information to depths that increase with increasing X-ray energy [8, 9]. Quantitative accuracy in the extracted concentrations requires the use of appropriate standard materials, or calibration against RBS data. In contrast to RBS, the physics of photoemission is rather involved, and published theoretical cross sections typically do not take into account the many-body effects discussed below. Such cross sections are thus of only semi-quantitative value. Nevertheless, significant insight into the electronic and magnetic properties of the emitting atom can be gained from absolute binding energies, multiplet fine structure, and shake-up/shake-down peak positions and intensities when accompanied with sufficiently accurate theoretical simulations. Due to the open shell valence *d* orbital electron configurations exhibited by many transition metal cations, core-level spectra can be exceedingly complex due to spin and orbital angular momentum coupling of the core hole to unpaired valence electrons (multiplet splitting), as well as valence charge rearrangement in the final state accompanying core-hole photoemission (shake processes) [10–12]. Significantly, the traditional view of shake up in oxides involving pure metal *d*-derived and O 2*p* states, and integral charge transfer between, has been shown to

be inadequate for accurate theoretical prediction of metal oxide core-level spectra. Rather, the extent of covalency in metal oxides requires that considerable mixing of these states be included in the theoretical description of many body effects, and that changes in the amount of covalency as a result of creating a core hole be considered [10]. These effects, together with spin-orbit splitting, makes the interpretation of XPS of oxides much more challenging than that associated with other inorganic compound materials, such as Group IV, III-V and II-VI semiconductors.

If the oxide of interest is a semiconductor or an insulator, its surfaces, films and buried interfaces can also exhibit band bending, which is directly measurable by XPS through shifts and broadening of core peaks measured against standards. Moreover, band offsets at buried interfaces can be extracted from a combination of core-level and valence band spectra for pure specimens of the materials which constitute the heterojunction [13, 14]. These quantities can be readily measured within the deposition system prior to air exposure (which can obscure or modify the sought-after property), provided the necessary hardware is appended to the growth chamber.

Finally, angle-resolved XPS (ARXPS) can yield insight into the abruptness (or lack of same) of buried perovskite interfaces [15]. Unlike MEIS, ARXPS typically has adequate sensitivity to all elements (other than H and He) so as to be useful for a wide range of perovskite interfaces. The drawback, however, is a lack of depth resolution; in general, unique atomic profiles cannot be extracted from ARXPS data. However, it is straightforward to determine if cation mixing at interfaces occurs by comparing experimental polar-angle intensity profiles with those from model calculations for which an abrupt interface is assumed, provided the surface is atomically flat. For epitaxial systems, angle-resolved data also exhibits diffraction modulation, giving rise to X-ray photoelectron diffraction (XPD), which is a useful source of information on the local crystallographic environment for specific elements [16].

Taken together, core-level and valence band XPS and XPD yield information on elemental abundances, valence states, and atom positions relative to the surface, as well as electronic structure for complex oxide multilayers. In addition to RHEED, XPS is in the opinion of this author the most broadly useful in situ characterization technique one can have in a thin-film deposition system. Here we review how XPS can be used to gain a variety of physical insights into perovskite interfaces and superlattices, with an emphasis on the fascinating topic of conductivity at polar/nonpolar heterojunctions, a topic currently of considerable interest. For the purposes of this article, spectra taken at an X-ray energy $h\nu < 1000$ eV will be referred to as soft X-ray XPS (SXPS), 1000 eV < $h\nu$ < 2000 eV will be dubbed intermediate X-ray XPS (INTXPS), and $h\nu > 2000$ eV will be called hard X-ray XPS (HAXPS). For SXPS and INTXPS, the surface sensitivity is fairly high, and having in situ capability within the ultrahigh vacuum environment of the deposition chamber is important. However, the influence of the surface becomes negligible at sufficiently high X-ray energy, and in situ capability is not as important. The XPS probe depth is directly related to the photoelectron inelastic mean free path (IMFP), which is in turn a sensitive function of the material properties of the specimen and the X-ray energy [17–22]. In XPS energy regimes in general, the IMFP scales

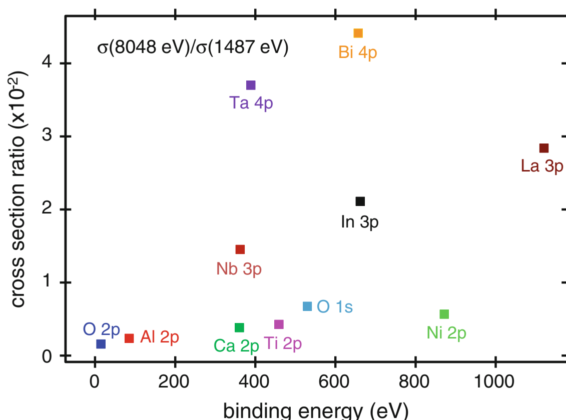

Fig. 14.1 Ratio of calculated atomic subshell photoionization cross sections at X-ray energies of 8048 and 1487 eV for different elements and orbitals as a function of orbital binding energy. Taken from [23]

approximately as $E_k^{0.5}$, where E_k, the photoelectron kinetic energy, is given by the Einstein relation $E_k = h\nu - E_b - \phi_A$, E_b and ϕ_A being the binding energy and analyzer work function, respectively. For wide-gap complex oxides, a typical IMFP for an electron with binding energy ~100 eV is ~1.5 nm at $h\nu = 1.5$ keV [15], leading to a probe depth of ~5 nm for an electron emission angle of 90° relative to the surface plane (normal emission). The same core level can be probed to a depth of ~18 nm at $h\nu = 8$ keV.

Another effect associated with moving into the hard X-ray regime is an across-the-board reduction in the photoelectric cross sections, $\{\sigma_{n,l}\ (h\nu)\}$. Figure 14.1 shows a selection of atomic subshell photoionization cross section ratios for 8 and 1.5 keV photons plotted for various elements from across the periodic chart that are of interest in complex oxide research [23]. In general, the cross sections at $h\nu = 8048$ eV (CuKα_1) range from a few tenths up to a few percent of the corresponding values at $h\nu = 1487$ eV (AlK$\alpha_{1,2}$). The higher the atomic number for the element of interest, the larger the HAXPS cross section for a given X-ray energy. In contrast, the sensitivities for shallow core levels in first and second row elements are quite low. However, the high brightness that can be found at hard X-ray beam lines relative to that for monochromatic AlKα lab sources generally more than compensates for the lower cross sections.

14.2 Core-Level Binding Energies and Line Shapes in Complex Oxides

As mentioned above, core-level photoemission in metal oxides is frequently accompanied by multiplet splitting and final-state effects (shake up and shake down) which, when combined with spin-orbit splitting and chemical shifts resulting from different metal valences, can result in significant complexities in the measured line shapes. Understanding the influence of these various phenomena on line shapes

is essential for correct assignment of measured spectral features. For example, in oxides of transition metals in which the cation is not in its higher oxidation state, final-state satellites can be mistaken for the presence of higher oxidation states. For instance, in RuO_2, the high-resolution Ru 3*d* spectrum exhibits weak features 1.8(1) eV to higher binding energy from both primary spin-orbit peaks that some groups have interpreted as being due to the presence of a RuO_3 impurity near the surface. Yet, scanned-angle XPD measurements for epitaxial $RuO_2/TiO_2(110)$ revealed that these features were due to final-state effects for Ru^{4+} at the cation site of the rutile lattice, and not some secondary phase [24], in agreement with a previous UPS study on polycrystalline RuO_2 [25]. Later dynamical mean-field calculations for RuO_2 and several ruthenates corroborated that the higher binding energy shoulders are best assigned to the unscreened core-hole final state whereas the more intense peaks correspond to the shake-down events in which the core hole is screened by quasiparticles on the Fermi surface [26]. The complex multiplet structure occurring when there are unpaired electrons in the valence band is often unresolved, resulting in a broader peak than might otherwise be expected. Moreover, the effect of bond covalency vis a vis ionicity and computed Madelung potential can influence the binding energies of metal cations in interesting ways [27]. In addition to having a significant influence on line shape, these different effects, which arise as a result of the bonding environment of the metal, can have an apparent impact on the magnitude of the spin-orbit splitting, which as an isolated phenomenon is primarily an atomic effect.

These effects are well illustrated by examining Ti 2*p* and Cr 2*p* spectra for different oxides and the pure metals from which they come. It is instructive to start with a comparison of $SrTiO_3(001)$ (STO) and Ti metal. Ti^{4+} in STO is formally a d^0 cation, although covalency and thus hybridization with O are expected to result in a higher electron density surrounding Ti cations via formation of completely filled bonding states, as has been seen in rutile TiO_2 [28]. The absence of unpaired valence electron spin density near Ti means there is no multiplet splitting in STO, and the Ti 2*p* line shape is relatively simple, as seen in Fig. 14.2a. Here, a Shirley background subtraction has been performed to remove the contributions of extrinsic energy loss processes [29]. The bulk of the STO spectrum consists of four peaks of comparable width, two weak and two strong, and three peaks are seen for Ti metal, one being considerably broader and weaker than the other two. There is a third much weaker peak ~31 eV to higher binding energy from the $j = 3/2$ peak for STO (not shown) which is due to inelastic scattering of the latter [30]. For Ti metal and STO, the two stronger peaks are typically assigned to the spin-orbit split pair—$2p_{3/2}$ at lower binding energy and $2p_{1/2}$ at higher binding energy. The branching ratio, which we define as the ($j = 1/2$):($j = 3/2$) peak area ratio, should be close to 0.5, the ratio of the number of magnetic sub-states associated with $j = 1/2$ and $j = 3/2$, respectively. In the absence of other effects, the magnitude of the spin-orbit (SO) splitting should be equal to the 2*p* orbital energy difference for $j = 1/2$ and $j = 3/2$, and be independent of chemical environment. The branching ratio for Ti metal is 0.46 and the SO splitting is 6.1 eV. However, in STO, the *apparent* branching ratio and SO splitting are 0.42 and 5.7 eV, respectively. The reason for

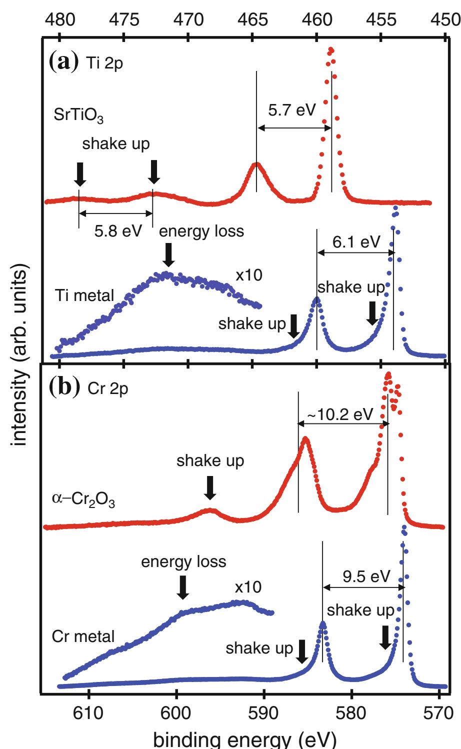

Fig. 14.2 Ti 2*p* (**a**) and Cr 2*p* (**b**) spectra excited with monochromatic AlKα X-rays ($h\nu$ = 1486.6 eV) and a normal emission geometry for a clean Nb-doped $SrTiO_3$(001) single crystal and an in situ evaporated film of polycrystalline Ti metal (**a**), along with MBE-grown α-Cr_2O_3(0001) on α-Al_2O_3(0001), and an evaporated polycrystalline Cr metal film (**b**)

the considerable differences in these two quantities between Ti and STO has to do with the other peaks in the spectra, which are often ignored in surface and interface analytical work. The broad feature centered at ∼472 eV in the Ti metal spectrum is due to an energy-loss process that is both intrinsic and extrinsic to core photoemission. The extrinsic effects result from energy loss stemming from a coupling of the longitudinal electric field of the ejected photoelectron to electron density fluctuations in the metal as the photoelectron traverses to the surface, otherwise known as a plasma excitation [31]. This effect can be elucidated by measuring and modeling the energy loss spectrum of an externally generated electron beam of the same kinetic energy as the photoelectron of interest [32]. The intrinsic effect is thought to result from energy loss associated with valence electron excitations *within* the photoemitting atom. Using the curve fitting method outlined in [32] to remove the extrinsic effects, it has been shown that the energy separation between the intrinsic energy loss feature and the corresponding "no-loss" photoelectron peak increases with the number of *d* band electrons in going from Sc to Co [33]. In contrast, the width of this loss feature was found to decrease with the number of unpaired electrons in the *d* band. Shake up in transition metals, including Ti, typically appears in the form of asymmetries on the higher binding energy sides of the two primary SO features which result from the population of low-lying excited states in the conduction band accompanying core-level photoejection [34].

Returning to the STO spectrum, the j = 1/2 feature is slightly broader than the j = 3/2 peak. Based on semi-empirical theory, an early paper claims that this result can be accounted for based on multiplet effects accompanying ligand-to-metal charge transfer in the ground state [35]. However, there is also an energy loss feature associated with the more intense j = 3/2 photoelectrons which overlaps the j = 1/2 feature and influences the line shape for the latter [30]. Additionally, Coster-Kronig Auger decay, which is possible only for the j = 1/2 orbital, results in lifetime broadening [36]. The two weaker peaks in the STO spectrum have been assigned to ligand-to-metal charge-transfer shake up events and can be accounted for in a semi-empirical way with a sufficiently large Coulomb interaction between the core hole and the valence d band (U_{dc} = 6 eV) [35]. The energy difference between the two shake-up peaks is 5.8 eV, quite close to the SO splitting for the primary SO split peaks, 5.7 eV. This similarity suggests that the two shake-up peaks in STO can be assigned as charge-transfer satellites associated with final-state j values of 3/2 and 1/2, respectively. With this assignment, the *actual* branching ratio for STO can be approximated as the total j = 1/2 intensity (sum of peak areas at 478.4 eV and 464.6 eV) divided by the total j = 3/2 intensity (sum of peak areas at 472.6 eV and 459.0 eV), or 0.47, in what is probably fortuitously good agreement with the value for the metallic Ti spectrum. Moreover, if the more intense j = 3/2 peaks for the two materials are aligned at 0 eV relative binding energy, the intensity weighted average relative binding energies, which represent averages over all final states, are nearly the same, 4.4 and 4.2 eV for Ti and STO, respectively. This result is expected based on the Manne-Åberg sum rule [37], but requires that the broad intrinsic loss peak at 471 eV be included, as rightly it should be. Thus, the *apparent* difference in SO splitting for Ti and STO is the result of a redistribution of photoelectron intensity across all final states. A key point here is that the *entire* spectrum needs to be taken into consideration to capture all the physics, as well as to insure the most accurate quantification when using theoretical cross sections.

The situation is more complex for Cr 2p, as seen in Fig. 14.2b, where we compare spectra for α-Cr_2O_3 and Cr metal. Cr^{3+} is a d^3 system, and multiplet splitting leads to several final states, resulting in fine structure and significant broadening of the primary j = 1/2 and j = 3/2 peaks relative to those for Cr metal which can be largely accounted for using a simple atomic multiplet model [38]. Moreover, a single shake-up feature is visible at ~596.2 eV for α-Cr_2O_3. As with Ti metal, Cr metal exhibits shake up in the form of asymmetries on the high binding energy sides of the j = 1/2 and j = 3/2 peaks, as well as a broad, relatively weak feature resulting from a mix of intrinsic and extrinsic energy loss events. The apparent SO splittings are also different—9.5 eV for Cr metal and ~10.2 eV for α-Cr_2O_3, although precise values are difficult to determine for the oxide due to the complex line shapes. Again, in the spirit of the Manne-Åberg sum rule [37], the apparent difference in the SO splitting is due to a redistribution of intensity over all final states, and the way those states partition according to j. However, the complexities added by multiplet splitting preclude a simple analysis, as can be done for Ti 2p spectra.

It is useful to see how the different effects play out over a wide range of Cr charge states. To this end, Fig. 14.3 shows Cr 2*p* spectra for several oxides with Cr ranging from Cr^{6+} to Cr^{3+}, as well as for Cr metal. Of these, only the Cr metal and α-Cr_2O_3 specimens were well grounded to the spectrometer; the latter was an epitaxial film grown on Pt(111) [38]. All others were either electrically insulating, or conductive, but not well grounded. For these, surface charging distorts the true line shapes. Low-energy electron flood gun charge compensation restores the true line shape, but typically leads to artificially low binding energies. Thus, for these samples, the binding energies were shifted in such a way that the associated O 1s peaks align at a constant binding energy of 530.0 eV, the value measured for thin epitaxial films of α-Cr_2O_3(0001) on Pt(111) [38]. The total chemical shift from Cr metal to La_2CrO_6 is 4.8 eV. La_2CrO_6 and $LaCrO_4$ do not exhibit much if any multiplet splitting due to the d^0 and d^1 electron counts, respectively, and the SO splitting is the same, 9.2 eV. The peak widths and SO splittings for La_2CrO_6 and $LaCrO_4$ are similar to those of the metal. $SrCrO_3$ (d^2), $LaCrO_3$ (d^3), and α-Cr_2O_3 (d^3) exhibit considerable multiplet splitting by virtue of their large number of Russell-Saunders configurations that couple to the core hole, with the resultant broadening effect on the SO split peaks, and the apparent change in SO splitting: ~9.7 eV for $SrCrO_3$ and ~10.2 eV for $LaCrO_3$ and α-Cr_2O_3. The $SrCrO_3$ surface contains some Cr^{6+}, as revealed by the weak peak at ~580.0 eV which is always present to some extent, depending on the level of oxygen to which the surface has been exposed.

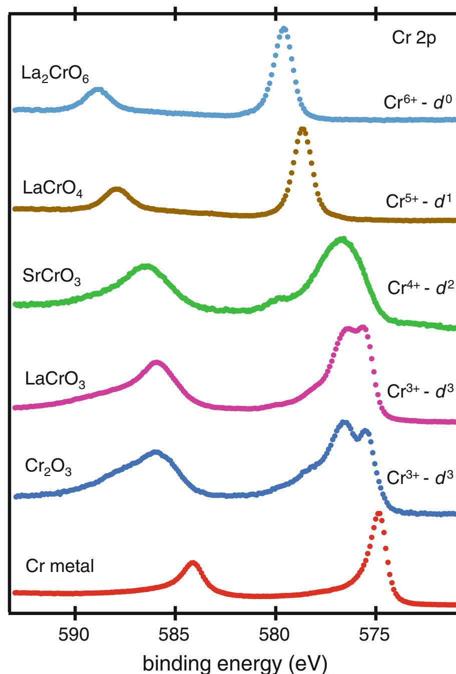

Fig. 14.3 Cr 2*p* spectra (monochromatized AlKα X-rays, normal emission) for several Cr-containing oxides with Cr in different charge states—Cr metal, epitaxial α-Cr_2O_3(0001)/Pt(111), polycrystalline $LaCrO_3$/a-SiO_2, $SrCrO_3$ bulk polycrystal, polycrystalline $LaCrO_4$/a-SiO_2, and polycrystalline La_2CrO_6/a-SiO_2. The binding energy scale is accurate in an absolute sense

Historically, attempts to theoretically account for these complex line shapes have consisted of semi-empirical approaches based on, for example, the Anderson impurity model [35, 39]. However, in order to do so in a fully satisfactory way, more rigorous first-principles calculations must be carried out. For instance, Nelin et al. [40] have shown that the configuration interaction calculations based on relativistic wave functions from solution of the Dirac-Fock equation can quantitatively account for the Ce 4*s* and 3*d* line shapes in CeO_2. Additionally, Kas et al. [41] have developed a novel many-body method which treats the interaction of the transient core hole with the electron density of the host oxide dynamically using a cumulant representation of the core-hole Green's function within the context of real-time, time-dependent density functional theory. This approach yields unique insight into the temporal response of the material to the creation of a core hole. A Fourier transform of the response function yields a strong feature at the energy predicted for the shake-up satellites relative to the main spin-orbit peaks corresponding to the ground state of the ion. The method is shown to predict the Ti 2*p* line shape for TiO_2(110) rutile, which is virtually identical to that for STO(001) shown in Fig. 14.2a, rather well, as seen in Fig. 14.4a. The only experimental input beyond structural parameters is the spin-orbit splitting. The satellite energies and intensities are accurately predicted. Significantly, a definitive assignment of the two satellite features as originating from metal-to-ligand charge transfer within the j = 1/2 and j = 3/2 spin-orbit channels results, as revealed by Fig. 14.4b. Here we see how the charge density is predicted to change in the vicinity of the photo-emitting Ti atom following 2*p* hole creation. The decrease in charge density at the Ti site is accompanied by increases at the nearest-neighbor O ligand sites. In order for charge transfer to occur in this direction (metal → ligand), it is clear that the valence of Ti is not actually 4 + ($3d^0$), but rather (4-δ) + ($3d^\delta$), reflecting some degree of covalency in TiO_2 and $SrTiO_3$ [28].

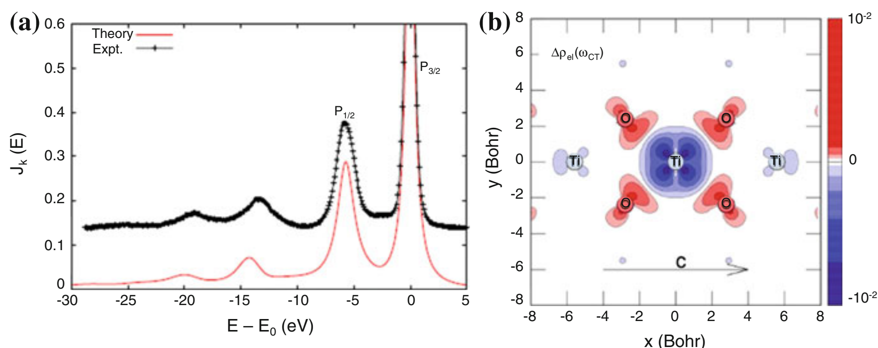

Fig. 14.4 **a** Measured and calculated Ti 2*p* spectrum for rutile TiO_2(110) based on a cumulant representation of the core-hole Green's function within the context of real-time, time-dependent density functional theory; **b** Change in charge density in the vicinity of the Ti cation that absorbs the X-ray following core-hole creation. Taken from [41]

14.3 XPS-Based Investigations of the $LaAlO_3/SrTiO_3(001)$ Heterojunction

One of the subtopics of considerable interest to the oxide materials science community in recent years is the phenomenon of conductivity at certain interfaces of polar and non-polar perovskite insulators. The most heavily studied system is the $LaAlO_3/SrTiO_3(001)$ heterojunction, typically prepared by on-axis pulsed laser deposition. As we shall see in what follows, XPS has been extensively used to investigate properties of this, and other polar/nonpolar interfaces. Thus, this subtopic serves as a good case study to illustrate the power of XPS to gain insight into properties including charge states of transition metal cations, interface atomic distributions, band alignment, and the presence (or absence) of built-in potentials within the polar oxide.

14.3.1 On the Physical Cause of Interface Conductivity at the $LaAlO_3/SrTiO_3(001)$ Interface

Inspired by the original observation of conductivity at this interface of two band insulators [42], a multitude of groups worldwide have embarked on studies of this unexpected phenomenon. The original explanation given for this unexpected result is that conductivity results from an electronic reconstruction that alleviates the problem of a diverging potential within the polar $LaAlO_3$ (LAO) phase resulting from the creation of a polar (LAO)/non-polar (STO) interface (the co-called "polar catastrophe") [43]. Significantly, conductivity occurs only when the epitaxial LAO is deposited on TiO_2-terminated STO. LAO consists of alternating layers of LaO, which have a formal charge of +1 per two-dimensional formula unit, and AlO_2, with a formal charge of −1 per two-dimensional formula unit. In contrast, STO consists of alternating layers of charge-neutral SrO and TiO_2. The original authors argued that the polarity discontinuity results in a built-in potential within the LAO phase which diverges with thickness, unless electronic rearrangement occurs to screen this potential [43]. When the built-in potential is sufficiently large, the argument goes, half an electron per unit cell (3.3×10^{14} e^-/cm^2) is thought to be transferred from the interfacial LaO plane to the STO. This charge, in addition to screening the polar discontinuity at the interface, would also effectively dope the STO near the interface *n*-type, leading to conductivity.

Inasmuch as the bottom of the STO CB is largely Ti 3*d* derived, this charge transfer should result in a partial screening of Ti^{4+} near the interface. That is, some fraction of the Ti ions near the interface will have an itinerant electron sufficiently close to be formally Ti^{3+} in a temporal sense (i.e. over the time scale of photoemission well above threshold, $\sim 10^{-16}$ s), as seen in studies of bulk La- and Nb-doped STO(001) [44]. The Ti 2*p* chemical shift in going from Ti^{4+} to Ti^{3+} is $\sim$2 eV. Thus, XPS is a useful way to determine whether or not Ti^{3+} is present at a

buried LAO/STO interface. It should be noted that Ti^{3+} will also be present if certain kinds of defects are present at the interface. These include oxygen vacancies (V_O) and La dopants at Sr sites (La_{Sr}), which are both known *n*-type dopants in STO.

Despite years of research, there is still controversy in the literature as to whether the observed conductivity is due to electronic reconstruction immediately following film growth in some form, or defect generation in the STO. Proponents of the electronic reconstruction model point to the existence of a critical LAO thickness (typically 4 u.c.) required to trigger conductivity [45], and a doubling of the critical thickness for conductivity when the A-site sublattice of the LAO is mixed with Sr to make $La_{0.5}Sr_{0.5}AlO_3$ [46]. In these arguments, it is commonly assumed that electronic reconstruction does not occur until the built-in potential is large enough that the top of the LAO valence band (VB) crosses the bottom of the STO conduction band (CB), leading to a dielectric breakdown from the LAO surface to the interface. However, this conceptualization of the electronic reconstruction misses an essential piece of the physics. Figure 1a of [43] schematically shows an atomically abrupt, perfectly stoichiometric interface structure …$(Sr^{2+}O^{2-})^0(Ti^{4+}O_2{}^{2-})^0(La^{3+}O^{2-})^{+1}(Al^{3+}O_2{}^{2-})^{-1}$ … without electronic reconstruction and, thus, with a diverging potential within the LAO film. Figure 1c of [43] then shows the same structure, with the same formal charges in the LAO layers, except that electronic reconstruction has occurred. Here each LaO layer has donated half an electron per u.c. to the BO_2 layers above and below it, including the interfacial TiO_2 layer. This panel shows that the potential no longer diverges, and that the polar catastrophe is resolved by this manner of charge transfer. The problem is that in order for the alternating charged layer structure $(La^{3+}O^{2-})^{+1}(Al^{3+}O_2{}^{2-})^{-1}$ to exist at all, as in Fig. 1a of [43], *the charge transfer must already have occurred*. Simple chemical reasoning makes this clear. Without charge transfer to adjacent layers, each LaO and AlO_2 atomic plane would consist of $(La^{2+}O^{2-})^0$ and $(Al^{4+}O_2{}^{2-})^0$, respectively. If this was the correct electronic structure, there would be no polarity within the LAO, and no polar discontinuity at the interface. However, $(La^{3+}O^{2-})^{+1}(Al^{3+}O_2{}^{2-})^{-1}$ is established *only* when the charge transfer described above is in effect, which means the situation depicted in Fig. 1a in [43] cannot exist. In contrast, Fig. 1c in [43] shows the electronic structure as it must exist for a perfect interface, independent of LAO film thickness. Thus, the polar discontinuity should occur and be resolved, and the interface made conductive, in principle upon completion of the first u.c. of LAO. The $(La^{3+}O^{2-})^{+1}$ plane at the interface can be thought of as a sheet of donors for STO [47, 48]. Complete resolution of the polar catastrophe also requires that the polar discontinuity at the surface be eliminated by surface composition alteration [49] or H chemisorption, as occurs with bulk crystals of polar materials such as MgO(111) [50] or α-Al_2O_3(0001) [51]. If this occurs, as it should, there would be no built-in potential across the LAO film. Practical considerations resulting from surface reactivity of 1 u.c. structures most likely preclude the experimental realization of conductivity with less that 2 or 3 u.c. However, several u.c of the polar oxide should not be required and, in fact, are not required for other polar/nonpolar interfaces, as described in Sect. 14.4. Thus, the common observation

of a conductivity threshold of several u.c., not only for LAO/STO along the (001) orientation [52], but also along the (111) and the (110) orientations [53], is fundamentally inconsistent with the electronic reconstruction picture, as described in this paragraph. Therefore, it would appear that another mechanism resulting in interface conductivity is operative.

Proponents of defect-driven conductivity argue that unless the interface is *demonstrably* atomically abrupt and defect free, the influence of the various kinds of defects present must be evaluated in order to extract defensible cause-and-effect relationships [15, 54]. However, accurate characterization of the kinds, quantities and spatial extents of defects at the interface is exceedingly difficult. For example, in considering the possibility of conductivity by means of La doping of the STO, it is important to note that if Al also diffuses into the STO and occupies Ti sites, these deep-acceptor defects will compensate La donors. Also, if deep acceptor-like defects are present on the LAO side of the interface, donor electrons from La doping of the STO could spill over and become trapped there. In either case, the extent of interfacial mixing must be determined for each kind of cation, along with the O vacancy concentration, in order to accurately assess the influence of these kinds of defects on conductivity.

The vast majority of the papers describing the observation of conductive LAO/STO interfaces have utilized on-axis pulsed laser deposition (PLD) as the film growth method. For oxide targets, the laser ablation plume that strikes the substrate in on-axis PLD contains ions of energy equal to at least $\sim$5 eV and up to hundreds of eV. Higher ion energies occur when the gas pressure is sufficiently low to preclude energy loss by inelastic scattering, as is typical in the most popular PLD growth conditions [55, 56]. On-axis PLD film growth of LAO in the low-pressure regime can thus result in vacancy generation in the STO substrate, leading to conductivity by V_O creation, and potentially more extensive cation mixing than might otherwise occur. In contrast, magnetron sputtering, off-axis PLD with high ambient pressure, and molecular beam epitaxy (MBE) produce beams that are much lower in energy, well below the threshold for point defect generation in oxides. Moreover, when using an LAO single crystal as the ablation target in PLD, as is typically the case, the La to Al flux ratio depends strongly on plume angle, working distance, and laser power density, leading to potential variations in film composition for different PLD process parameters and chamber geometries [57]. In light of these well-known issues, it is surprising that the majority of papers reporting interface conductivity do not describe any attempt to measure film composition; it is typically assumed that the film composition is the same as in bulk LAO single crystals, $La_{0.987}Al_{1.000}O_3$ [58].

There are, however, some recent studies in which process parameters have been systematically varied and the resulting effect on conductivity monitored, and XPS is often used to characterize the interface. For instance, Breckenfeld et al. [54] used ex situ INTXPS and RBS to determine the composition of LAO films grown by on-axis PLD over a range of laser power levels and oxygen chamber pressures. These authors made several interesting observations. First, they found a systematic variation in La to Al cation ratio with laser fluence, which was in turn strongly

correlated with sheet resistance and carrier concentration. The La cation percent (defined as [La]/([La] + [Al])), determined by XPS and calibrated using bulk LAO (001) single crystal standards, was found to vary between 56(2) % and 46(2) % in going from 1.2 to 2.0 J/cm^2, as seen in Fig. 14.5. The sheet resistance at 2 K dropped by up to seven orders of magnitude in going from La-rich to stoichiometric to Al-rich films grown in a relatively high O_2 pressure of 1×10^{-3} Torr. Moreover, the temperature dependences of sheet resistance, carrier concentration, and electron mobility measured in Al-rich films prepared at 1×10^{-3} Torr were found to be quite similar to those reported in many other papers using much lower O_2 pressures (mid 10^{-6} Torr) during deposition plus post-growth annealing in O_2 (up to 300 Torr) for which film composition was not determined, as reviewed in [52]. At a minimum, these results reveal that deviations in film stoichiometry of just a few percent can have a profound effect on interface electronic properties. This work also suggests

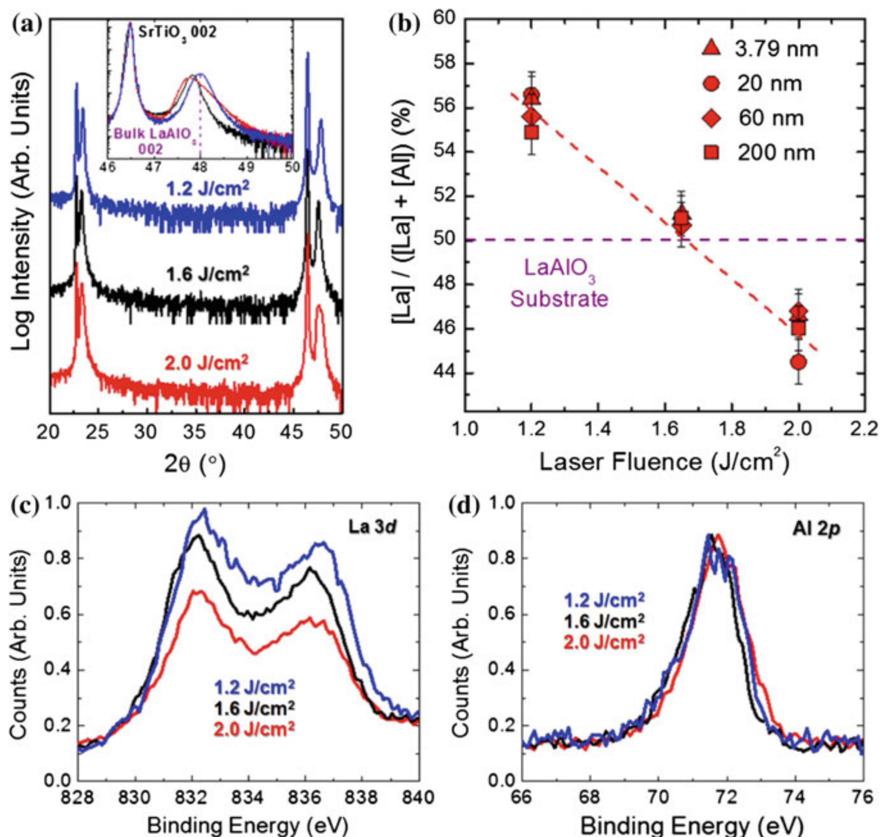

Fig. 14.5 **a** $\theta - 2\theta$ scans of the (002) reflection for 60 nm of PLD-grown LAO on STO(001) prepared with different laser fluences showing that the *c* lattice parameter increases with increasing power density; **b** Percent La within the A- and B-cation sublattices as a function of laser fluence; **c** La 3*d* and **d** Al 2*p* core peaks for the different laser fluences. Taken from [54]

that at least some of the conductive behavior published by so many groups that use a rather common set of on-axis PLD process parameters may be caused either directly or indirectly by excess Al in the LAO films.

A La:Al ratio less than unity has also been found to be essential for conductivity in MBE-grown LAO/STO(001). Warusawithana et al. [59] used the natural combinatorial spread resulting from placing La and Al in effusion cells on opposite sides of an MBE chamber to systematically vary the La:Al ratio. Two sets of experiments were done—one with small, discrete substrates mounted on a heater block, and one with single, large substrates on which multiple metallization pad arrays were subsequently fabricated. All films were grown in ozone at a chamber pressure of 1×10^{-6} Torr. RBS was done on LAO films grown on MgO(001) to determine the compositional spread in the film without interference from backscattering in the substrate. The conductivity was correlated with La:Al < 1 in the discrete substrate study, although there were exceptions (some insulating samples with La:Al < 1). For the continuous, large-substrate study, the room-temperature sheet resistance jumped from a range of relatively low values (10^5–10^8 Ω/square) up to the instrumental limit of 1×10^{11} Ω/square at a La:Al ratio of 0.97(3) or higher, with no listed exceptions. Interestingly, Breckenfeld et al. [54] measured sheet resistances of the order of 10^4 Ω/square on PLD-grown films that were either stoichiometric or La rich while Warusawithana et al. [59] measured 10^{11} Ω/square over the same composition range on MBE-grown films. Additionally, Dildar et al. [60] found that high-oxygen-pressure RF sputtering under their particular set of process conditions resulted in La rich films (La:Al = 1.07) that were also decidedly nonconductive. These results reveal that on-axis PLD growth promotes defect formation leading to conductivity in samples that are *not* Al rich, whereas MBE and RF sputtering do not. Both Warusawithana et al. and Dildar et al. interpreted the absence of conductivity in La-rich specimens in terms of the polar discontinuity being screened by B-site cation vacancies at the interface, while appealing to what is essentially the original electronic reconstruction model to account for conductivity in Al-rich samples. However, this logic does not explain why the stoichiometric samples were insulating in the study by Warusawithana et al. [59]. That is, if the original electronic reconstruction model can account for conductivity in the Al-rich samples (c.a. Figs. 5 and 6 in [59], it also leads us to expect conductivity in stoichiometric samples. Some speculation is made in [59] about there being random variations in composition across stoichiometric films, resulting in a patchwork of conductive (Al rich) and nonconductive (La rich) regions. But, no data are provided to support this notion.

In a seemingly unrelated experiment, Chen et al. [61] have shown that the deposition of epitaxial γ-Al_2O_3(001) on STO(001) by PLD at 7.5×10^{-5} Torr O_2 pressure leads to interface conductivity, as well as the appearance of $Ti^{3+\delta}$ in ex situ angle-resolved Ti 2*p* spectra. The reduced Ti was found to be localized to the first ~1 nm of the STO substrate. A summary of these results is shown in Fig. 14.6. ARXPS to track specific ions in the vicinity of the interface, such as is illustrated in Fig. 14.6b, is a useful method for detecting charge transfer processes and diffusion across oxide heterojunctions. A more complete discussion is given in Sect. 14.3.4.

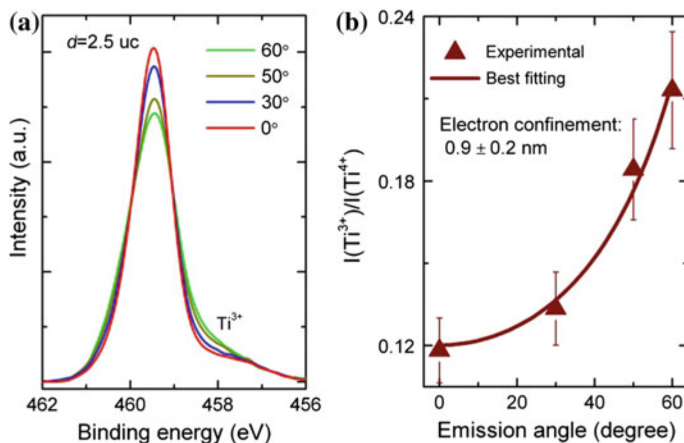

Fig. 14.6 **a** Ti 2*p* spectra excited with monochromatic AlKα X-rays for 2.5 u.c. of PLD-grown γ-$Al_2O_3/SrTiO_3(001)$ at various collection angles relative to the surface normal. The films were oxygen deficient as grown, resulting in oxygen gettering from the substrate; **b** Ti^{3+}/Ti^{4+} ratio versus emission angle and fit to a simple model aimed at estimating the depth below the interface to which the itinerant electrons from O vacancies are confined. Taken from [61]

A threshold film thickness for conductivity of ~2 u.c. was found. γ-Al_2O_3 (001) exhibits a spinel structure with along the (001) direction, pointing to the possible applicability of the polar catastrophe to explain its conductivity. Interestingly, the maximum low-temperature mobility for conductive state of this system is considerably higher than the best values reported for LAO/STO(001), and the highest carrier concentration is close to the value expected based on the electronic reconstruction model. However, the interface becomes insulating, and the $Ti^{3+\delta}$ peak disappears, after annealing in 0.75 Torr O_2, inconsistent with the expectations of the electronic reconstruction model. In a related study, Delahaye and Grenet [62] showed that evaporation of polycrystalline, oxygen-deficient alumina as well as "granular Al", a composite of nanometer-sized Al metal particles and amorphous alumina, results in a conductive interface with STO(001). The polar catastrophe model cannot explain these results because these Al films are not uniformly polar due to their heterogeneity and/or disorder.

However, these recent studies, together with those in [54] and [59], have one observation in common—*deposition of films with insufficiently oxidized Al on STO (001) consistently results in interface conductivity*. These results suggest that oxygen gettering by incompletely oxidized Al can drive interface conductivity in STO. In support of this conclusion is the fact that the standard free energy of formation of Al_2O_3 is exceedingly large and negative (−1661 kJ/mol) [63]. This value is among the most negative of any binary oxide, and is much more negative than that for either TiO_2 (−929 kJ/mol) or SrO (−576 kJ/mol) [63]. The feasibility of oxygen gettering by Al in Al-rich LAO/STO is dependent on how the excess Al is accommodated in the LAO lattice. If Al is expelled from the epitaxial lattice to

balance the A- and B-site cations, but retained as a secondary phase in the film, oxygen gettering is likely because the thermodynamic drive to form Al_2O_3 is so strong. If instead excess Al is accommodated by Al_{La} anti-site formation, as suggested by first-principles calculations [59], oxygen gettering might not occur. More exacting materials characterization of off-stoichiometry LAO is required to answer this question in a more definitive fashion.

As the investigation of cause continues, XPS in its various forms remains a valuable tool in determining solid-state chemistry and electronic properties, as well as the distribution of atoms in the vicinity of the interface. In the original conceptualization of the electronic reconstruction model, a potential drop across the LAO is expected to be present and act as the driving force for charge transfer from LAO to STO, as discussed above. A sharp potential drop is also expected within the STO near the interface if the conductive plane is truly two dimensional in nature due to the need for carrier confinement. Many papers tacitly assume these potential drops are present and interpret their data accordingly (see, for example, [64]). But, are these built-in potentials actually present, and, if so, how large are they? Such potential drops are readily detectable by XPS, provided the total potential drop is comparable to the core peak width. In this case, a built-in potential over the XPS probe depth will result in peak broadening, and a monotonic shift in binding energy with film thickness, relative to the same material in a flat-band condition.

Several investigators have looked for these effects in the LAO/STO system. For instance, Segal et al. [65] used in situ INTXPS with non-monochromatic MgKα X-rays ($h\nu$ = 1253.4 eV) to measure both potential drops within the LAO, and interface band alignment in MBE-grown LAO/STO(001), as a function of film thickness. These authors found that the binding energy differences between LAO core peaks (La $4d_{5/2}$ and Al $2p$) and the Sr $3d_{5/2}$ peak, which would reveal a potential drop in the LAO, showed no measureable change with film thickness above and below the critical thickness for conductivity. The data are shown in Fig. 14.7a, b. These results reveal that the bands are essentially flat in the LAO. Moreover, the core peak widths did not change with thickness (Fig. 14.7c), as expected if a built-in potential is actually present in the LAO. Similarly, potential drops across the LAO film based on energy differences between Al $2p$ and Sr $3d_{5/2}$ core peaks were an order of magnitude smaller than expected (based on the polar catastrophe model), as found by Takizawa et al. [66] for on-axis PLD-grown LAO/STO(001). The observed energy differences were of the same sign for TiO_2- and SrO-terminated STO(001), also contrary to the expectations of the polar catastrophe model. In contrast, Segal et al. [65] measured Sr $3d_{5/2}$ − La $4d_{5/2}$ energy differences of opposite sign for the two STO terminations, revealing important, yet poorly understood differences between MBE and PLD grown LAO/STO heterojunctions. Based on INTXPS, Chambers et al. [15] found a negligible potential drop across the LAO film in PLD-grown LAO/STO(001). There was only very slight broadening in the La $4d$ and Al $2p$ core peaks for 4 u.c. films relative to flat-band 25 u.c. LAO/STO(001), as seen in Fig. 14.8.

Berner et al. [67] measured Fermi surface (FS) maps for a conductive 4 u.c. LAO/STO(001) specimen under Ti $2p$ core-excitation resonance conditions. They

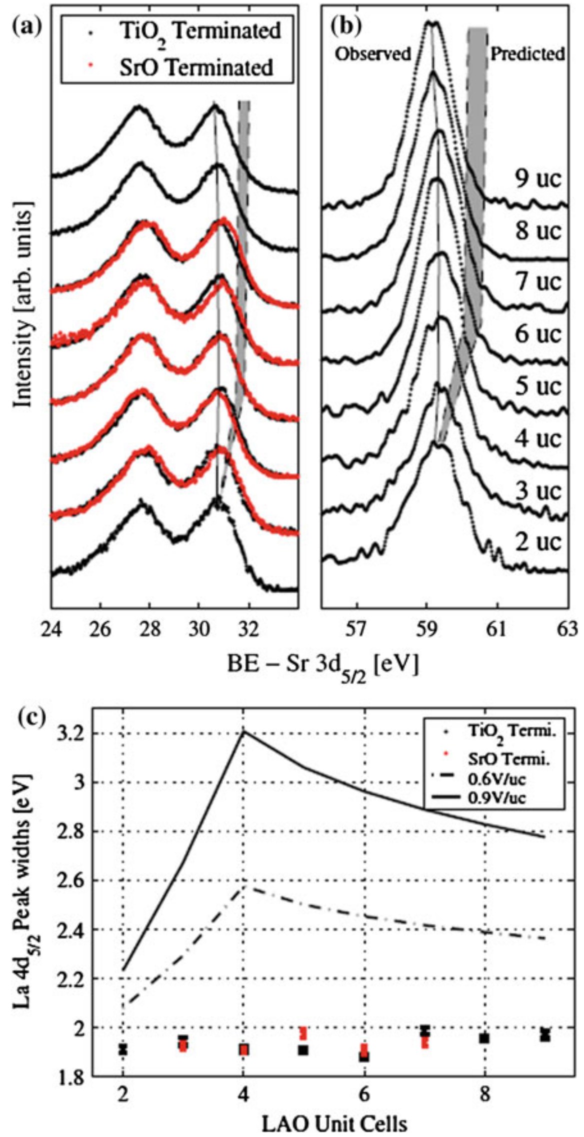

Fig. 14.7 **a** La 4d and **b** Al 2p spectra excited with non-monochromatic MgKα X-rays ($h\nu$ = 1253.4 eV) for various thicknesses of MBE-grown LAO on TiO_2-terminated $SrTiO_3$(001) plotted against binding energy relative to that of the Sr 3$d_{5/2}$ peak; **c** La 4$d_{5/2}$ peak width versus $LaAlO_3$ layer thickness for deposition on both TiO_2- and SrO-terminated $SrTiO_3$. Taken from [65]

noted the conspicuous absence of a hole-like FS around the M points in the Brillouin zone predicted by DFT for stoichiometric interfaces if the expected built-in potential is indeed present. Berner et al. [68] have also carried out HAXPS and INTXPS core-level and VB measurements, and their spectra were consistent with a flat-band condition for the LAO. Peak broadening is characteristic of a built-in potential within the LAO film, but the Al 1s measured at $h\nu$ = 3.5 keV showed negligible broadening over a range of film thickness. The absence of any

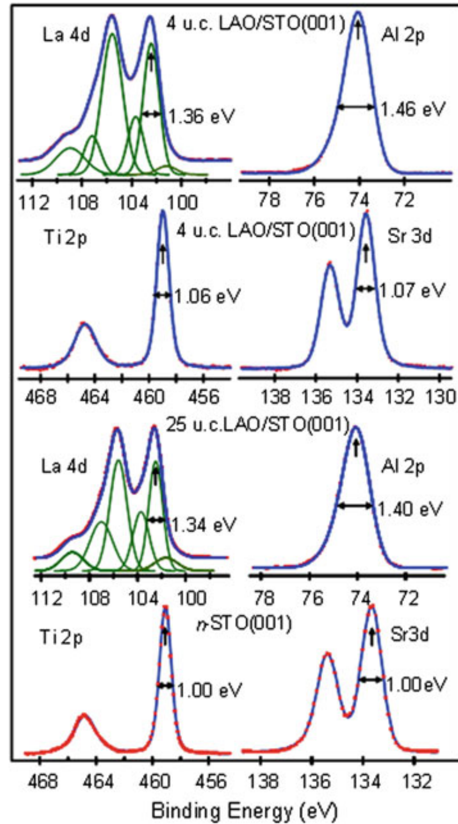

Fig. 14.8 Core-level spectra excited with monochromatic AlKα X-rays for 4 u.c. and 25 u.c. PLD-grown $LaAlO_3$ on $SrTiO_3(001)$, as well as clean Nb-doped $SrTiO_3(001)$. A comparison of the peak widths for the 4 u.c. heterojunction relative to those for the 25 u.c. heterojunction and the clean $SrTiO_3$ substrate yield information on any potential drops present in the $LaAlO_3$ and in the $SrTiO_3$ near the interface. There are no appreciable potential drops in either material. Adapted from [15]

change in spectral line shapes with X-ray intensity over two orders of magnitude suggests that X-ray induced band flattening was not a major effect.

Slooten et al. [69] used HAXPS to measure core-level spectra for on-axis PLD-grown LAO/STO(001) samples in an attempt to find a built-in potential in the LAO. While these authors did measured binding energy shifts for the La $4d_{5/2}$ and Al 2*s* peaks as a function of LAO film thickness in the right direction to indicate a built-in potential, there were two problems: (i) the magnitudes of the shifts were much smaller than the ~0.9 eV per u.c. required to resolve the polar catastrophe by 4 u.c., and, (ii) the shifts were not linear with the number of LAO u.c. as expected based on the polar catastrophe model. Additionally, there was essentially no broadening of the La $4d_{5/2}$ peak with increasing LAO film thickness, as expected if a built-in potential is present.

In order to explain the lack of a built-in potential, Takizawa et al. [66], Berner et al. [67, 68] and Slooten et al. [69] suggest the presence of charged defects, specifically V_O, on the LAO film surface. The electrons associated with such defects, if present, could in principle transfer to the interface, giving rise to an electronic reconstruction in the absence of a built-in potential. The driving force

behind their formation was suggested to be a lowering of the total energy of the heterojunction. No data were presented to support the actual presence of V_O on the LAO surface, but such defects may be present at such a low concentration (a few %) so as to be difficult to detect, as explained below. If V_O are present on the LAO surface immediately following film growth, one wonders if such defects would survive air exposure. Exposure of LAO/STO(001) surfaces with V_O to the terrestrial atmosphere might result in immediate oxidation as well as hydroxylation of the surface via dissociative chemisorption of water vapor. There is a strong driver for OH to occupy any V_O present on oxide surfaces in general. Chambers et al. [15] measured the O 1*s* polar angle distribution for 4 u.c. LAO/STO(001) exposed to air. The total spectrum at each angle was fit to two peaks—one associated with lattice O at 530.3 eV and one from OH at 532.3 eV—and the OH/lattice O peak area was successfully fit to a simple model in which five-coordinate surface Al cations were bound to OH, and the residual H atoms from water dissociation were bound to nearby surface O anions. If surface O vacancies are reoxidized upon air exposure, the interface should become insulating again. Theoretical investigations have modeled a rather high concentration of V_O in the top AlO_2 layer (25 %) in order to account for electron doping of the interface at the level of 0.5 e^- per u.c. [70–73]. Such a high concentration of vacancies would be easy to detect by SXPS, or angle-resolved INTXPS for in situ studies in which the surface was not exposed to air. The O 1*s* peak area would be significantly reduced relative to that measured for bulk LAO(001), but no such observations have been reported. However, the fact that the actual carrier concentration is typically an order of magnitude smaller than 0.5 e^- per u.c. means that the surface V_O concentration would be of the order of 2 %, which would be hard to detect. A more straightforward explanation for the absence of a detectable potential drop across the LAO film is simply that an electric field is not present, as discussed above.

It is also typically assumed that downward band bending is present on the STO side of the interface. In combination with the conduction band offset, such downward band bending on the STO side would confine the carriers to the interfacial region. If sufficiently large, band bending is readily detectable by core-level XPS in the form of peak broadening and shifting, provided the core peaks are sufficient sharp. Indeed, the individual spin-orbit components of the Sr 3*d* and Ti 2*p* core levels with their characteristics widths of ~1 eV should exhibit measurable broadening if at least a few tenths of an eV are dropped over a few atomic planes near the interface. The charge neutrality level in STO has been calculated using the tight binding method to be 0.7 eV below the CBM [74]. Therefore, downward band bending of the order of a least ~0.8 to 0.9 eV is expected to occur within a few nm of the interface if a two-dimensional electron liquid (2DEL) forms at the LAO/STO interface, *and* if the chemical potential within the STO does not climb closer to the CBM due to V_O formation during deposition. For example, Fig. 14.9a shows a simulation of the expected AlKα-excited Ti $2p_{3/2}$ line shape at normal emission if the STO bands bend downward by 0.9 eV toward the interface with 4 u.c. LAO over a distance of 1.2 nm. Here we use an attenuation length of 1.3 nm and a binding energy shift of 0.3 eV per TiO_2 layer for the first three below the interfacial

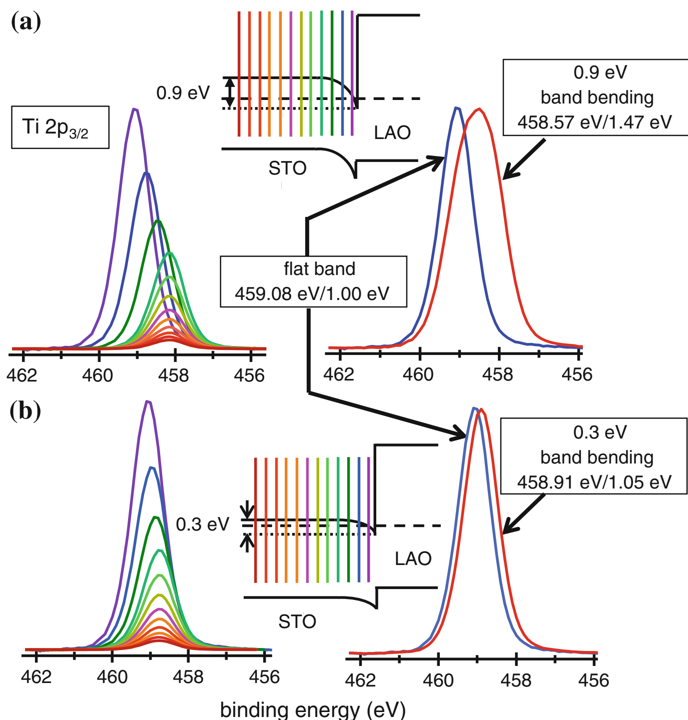

Fig. 14.9 Simulation of the effect of band bending on the Ti $2p_{3/2}$ line shape for 4 u.c. $LaAlO_3$/$SrTiO_3$(001): **a** 0.9 eV built-in potential over the first 1.2 nm of the $SrTiO_3$, **b** 0.3 eV over the same dimension. For each composite spectrum on the right, the binding energy and full width at half maximum are given, along with the modeled extent of band bending. See text for details

layer. The sum of all layers which contribute an intensity of ~1 % or more of that from the surface layer constitutes the simulated line shape. This extent of band bending results in an increase in full width at half maximum (FWHM) and a binding energy decrease of ~0.5 eV relative to the flat-band spectrum, and should be readily detectable. In contrast, if the band bending is 0.1 eV per layer, the FWHM increase and the binding energy decrease are only ~0.08 and ~0.05 eV, respectively, as seen in Fig. 14.9b. Therefore, we take ~0.3 eV as the detection limit for STO band bending.

Yoshimatsu et al. [75] used SXPS to look for such a notched potential in the STO for PLD-grown LAO/STO(001), and their results were interpreted as signaling ~0.25 eV of band bending near the interface based on absolute binding energies. These authors grew what they presumed were undoped STO buffer layers on a Nb-doped STO(001) substrate prior to depositing LAO, and thought that subsequent LAO deposition on TiO_2-terminated STO buffer layers leads to a strongly notched potential and 2DEL formation. However, this conclusion was subsequently challenged [76]. Here it was pointed out that not accounting for the effect of

instrumental broadening resulted in an inaccurate determination of the valence band maximum (VBM) relative to the Fermi level, and that STO buffer layers were actually inherently *n*-type, possibly as a result of V_O formation. Not only must one take into consideration instrumental broadening when attempting to locate the VBM in complex oxides, but a quantitative comparison to a properly broadened theoretical density of states modulated by appropriate photoemission cross sections should also be done to check the accuracy of simpler methods for determining the VBM [28]. In the case of complex oxides for which the VB is dominated by O 2*p* states, such as STO, a simple linear extrapolation of the leading edge to the energy axis yields the same VBM as does a detailed comparison of experiment to a Gaussian broadened theoretical density of states calculated by self-consistent GW theory [77, 78].

Chambers et al. [15] found evidence for at most a few tenths of an eV of downward band bending on the STO side of PLD-grown 4 u.c. LAO/STO(001). There was only very slight broadening in the Sr 3*d* and Ti 2*p* core peaks relative to those for bulk Nb-doped STO(001), as seen in Fig. 14.8. Berner et al. [68] also observed Sr 3*d* peak broadening consistent with ~0.3 eV of band bending on the STO side of the interface. The results of these three groups point to the common conclusion that the Fermi level in STO away from the interface is much closer to the CBM than expected based on the calculated charge neutrality level. This conclusion in turn points to the high likelihood that V_O form in the STO at some level during film growth by on-axis PLD in low O_2 pressure at a substrate temperature of 750–800 °C, and that these defects are not healed by post-annealing in oxygen. Quantum transport measurements suggest the potential drop within the STO is even smaller. A recent experimental investigation has succeeded in resolving several subbands in the Shubnikov de Haas (SdH) oscillations of LAO/STO and showed that the band edges are within a few meV of the Fermi level [79]. Subsequent theoretical modelling revealed quantitatively accounted of these observations, but only by modeling an electric field within the STO of ~0.1 meV/Å, which amounts to less than 2 meV over a 4 u.c. film [80].

Throughout this dialog in the literature, it has been suggested that the absence of a measurable polar field in the LAO by XPS may be due to electron-hole pair ($e^- - h^+$) creation by the X-rays during measurement, accompanied by a surface photovoltage effect in which the e^- and h^+ separate in and screen the polar field. A simple test of this hypothesis is to vary the X-ray intensity to see if there is any change in peak widths and binding energies. This test was performed and no effect was seen for either monochromatic AlKα X-rays from a lab source [15] or hard (3 keV) X-rays at a synchrotron [68, 69, 81]. This effect cannot be completely eliminated from consideration because it might occur and saturate at X-ray intensities below the lowest ones used in these studies. Moreover, the observation of a built-in potential using monochromatic AlKα X-rays for another polar/nonpolar perovskite interface—$LaCrO_3/SrTiO_3$(001)—shows that at least with this lab X-ray source, X-ray induced photo-voltage does not preclude the measurement of built-in potentials [82].

14.3.2 On the Origin and Characteristics of Itinerant Electrons at the LAO/STO Interface

Based on the STO band structure, it is expected that 2DEL formation at the LAO/STO interface will result in measurable Ti^{3+} using XPS, as discussed in Sect. 14.3.1. The carrier densities measured by electrical transport should result in a measureable Ti^{3+} feature alongside the dominant Ti^{4+} peak in the Ti 2*p* spectrum, provided the carriers are confined within the XPS probe depth. Moreover, the dependence of the Ti^{3+}/Ti^{4+} peak area ratio on photoelectron take-off angle yields information on carrier depth distributions. Sing et al. [83] first reported such observations for on-axis PLD grown samples using HAXPS. Although grown at a relatively low O_2 pressure of 1.5×10^{-5} Torr, one set of heterojunctions (denoted Augsburg) were cooled from growth temperature ($\sim$800 °C) to room temperature in 300 Torr O_2, as well as being subjected to post-growth annealing in O_2, in order to insure full oxidation. The other single 5 u.c. sample (denoted PSI) was deposited using similar conditions, but was not subjected to the post-growth oxidation process. Figure 14.10a shows Ti 2*p* spectra measured as a function of polar angle (relative to the surface normal) for conductive samples prepared by on-axis PLD from the two laboratories (PSI and Augsburg). The Ti^{3+}/Ti^{4+} peak area ratio increases with increasing polar angle, revealing that the Ti^{3+} is confined to the near-surface region. Figure 14.10b shows a comparison of the measured angular dependence of the Ti^{3+}/Ti^{4+} peak area ratio to a simple calculation based on a continuum model of the film, as discussed in more detail in Sect. 14.3.3. Here p is the fraction of the total intensity due to Ti^{3+} and d is the thickness of the 2DEL. The large error bars on the Ti^{3+}/Ti^{4+} peak area ratio propagate to a sizeable error bar for d, as seen in Fig. 14.10b. Nevertheless, from p and d, the electron concentrations were estimated, and the values differed from those determined by transport measurements in two ways. First, some Ti^{3+} and, therefore, some interface electrons, were detected at 2 u.c., below the 4 u.c. threshold for conduction in the Augsburg samples. Second, for thicknesses above 4 u.c., the electron concentration inferred from XPS increased with increasing thickness for the Augsburg samples, whereas the carrier concentration measured by transport is constant above threshold [84]. These differences were ascribed to two possible effects: (i) the presence of some density of X-ray generated carriers, and, (ii) the possibility of two kinds of interface electrons—mobile and immobile. Both would be manifested by the appearance of Ti^{3+} in XPS, but only the former would be detected by transport. Independent measurements on 4 u.c. samples from Augsburg using INTXPS (with monochromatic AlKα X-rays—see Fig. 14.8, lower left panel) [15] resulted in no evidence for Ti^{3+}. It has been claimed that there is not sufficient intensity in lab X-ray sources to result in a measurable Ti^{3+} signal for LAO/STO heterojunctions. However, Drera et al. [85] see clear evidence for Ti^{3+} in a 5 u.c., but not a 3 u.c. PLD-grown film using non-monochromatic MgKα X-rays which generate much higher background levels than do monochromatic AlKα X-rays, resulting in lower sensitivity. There is thus adequate sensitivity with lab sources to detect Ti^{3+}, if indeed Ti^{3+} is present at

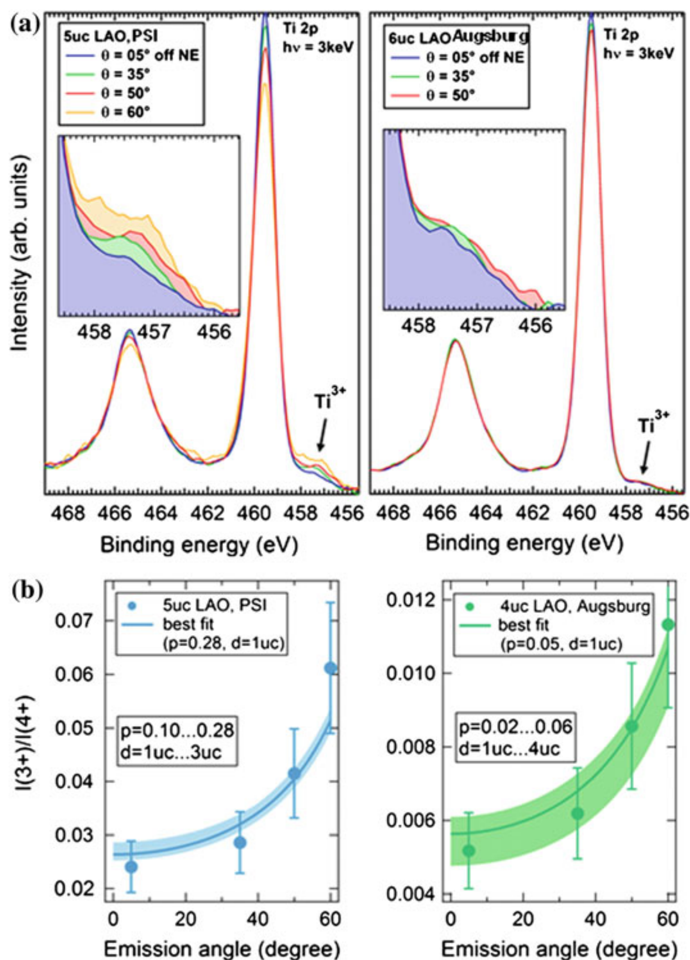

Fig. 14.10 **a** Ti 2*p* HAXPS (*hv* = 3 keV) for PLD-grown, conductive $LaAlO_3/SrTiO_3(001)$ heterojunctions at various angles off the normal emission (NE) geometry, and, **b** comparison of the dependence of the Ti^{3+}/Ti^{4+} peak area ratio on emission angle to a simple model from which the thickness of the Ti^{3+}—containing layer can be estimated. Taken from [83]

sufficiently high concentrations to result in conductivity. If, however, the carriers are not confined to the interface region due to the absence of a notched potential (i.e. no 2DEL), the Ti^{3+} concentration would fall below the detection limit.

The hypothesis of mobile and immobile interface electrons associated with Ti^{3+} was further explored in a recent resonant SXPS study by Berner et al. [67]. These authors measured the in-gap Ti^{3+} 3*d* photoemission near the chemical potential (E_b = 0) from heterojunctions prepared in Augsburg (growth process described above) as the X-ray energy was swept through the Ti L_3 edge. Once the threshold for Ti L_3 edge X-ray absorption was reached, Ti^{3+} 3*d* photoemission was enhanced

by the constructive interference of the direct photoemission channel, Ti $2p^63d^1 \rightarrow$ Ti $2p^63d^0 + e^-$, and the Auger decay channel accompanying excitation of the core electron, Ti $2p^63d^1 \rightarrow$ Ti $2p^53d^2 \rightarrow$ Ti $2p^63d^0 + e^-$ [86]. Figure 14.11a shows spectra in the vicinity of the chemical potential for a range of X-ray energies that sweep through the Ti L_3 edge for both Ti^{3+} and Ti^{4+}; the corresponding X-ray absorption spectra (XAS) for the two Ti charge states are shown in Fig. 14.11b. Figure 14.11c shows the entire VB spectrum along with the very weak feature associated with Ti^{3+} near $E_b = 0$. Two features are visible in Fig. 14.11a: one at $E_b = \sim 1.3$ eV which appears at $h\nu = 458.25$ eV (marked A), and one at $E_b = \sim 0.2$ eV which appears at $h\nu = 459.0$ eV (marked B). Both A and B are enhanced at X-ray energies corresponding to core excitation of Ti^{3+}. However, feature B is present over a wider range of X-ray energies than feature A. Accordingly, features A and B were interpreted as being due to localized and delocalized Ti^{3+} states, respectively, and were dubbed "trapped state" (A) and "metallic band" (B). These authors assigned B to itinerant electrons transferred to STO from LAO. As discussed in Sect. 14.3.1, the absence of a hole-like Fermi surface near the M points in the Brillouin zone led these authors to conclude that

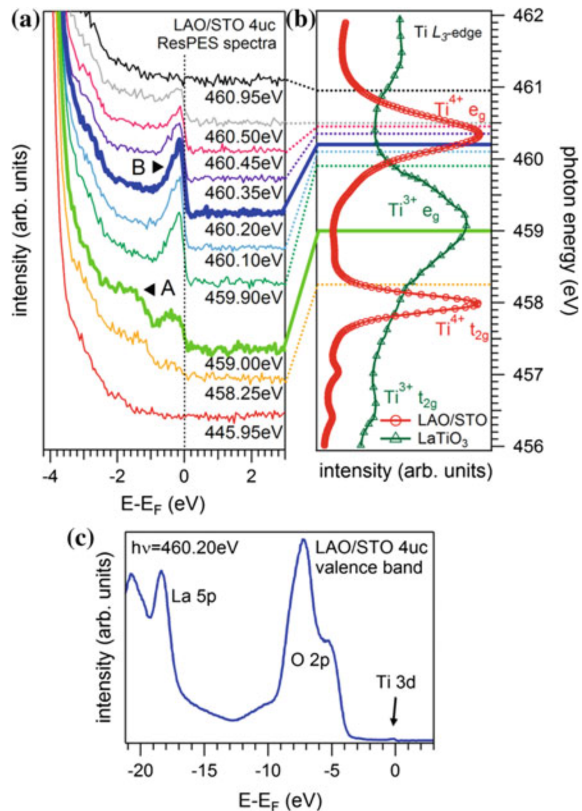

Fig. 14.11 **a** Resonant SXPS data for 4 u.c. $LaAlO_3$/$SrTiO_3$(001) as the X-ray energy is swept through the Ti L_3 edge; **b** Ti L edge XAS for Ti^{3+} and Ti^{4+}; **c** the full VB and in-gap spectrum at $h\nu = 460.2$ eV. Taken from [67]

there is no built-in potential in the LAO film, but rather that the metallic band (feature B) originated from a V_O band on the LAO surface. Moreover, Berner et al. concluded that A originated from V_O in the STO. In this way of thinking, V_O in STO would not lead to electrical conductivity, but rather only to localized trapped states. Yet, it is known from ARPES investigations of doped and undoped STO (001) single crystals that prolonged exposure to the intense X-ray beam from a synchrotron results in a surface 2DEL. These 2DELs were most likely the direct result of V_O creation, possibly via photon stimulated desorption [87, 88].

Slooten et al. [69] also used HAXPS to investigate electron confinement at the interface for samples deposited by on-axis PLD-grown LAO/STO(001) in 1.5×10^{-3} Torr O_2, a sufficiently high pressure to mitigate V_O formation, according to conventional wisdom. These authors also found spectral evidence for Ti^{3+}. However, their angle-dependent results revealed Ti^{3+} formation at thicknesses below the 4 u.c. conductivity threshold, and little confinement near the interface; the estimated d value was $\sim$20 u.c. for a 6 u.c. LAO film. Figure 14.12a shows spectra collected at normal emission for 0, 2 and 6 u.c. films, and Fig. 14.12b shows spectra

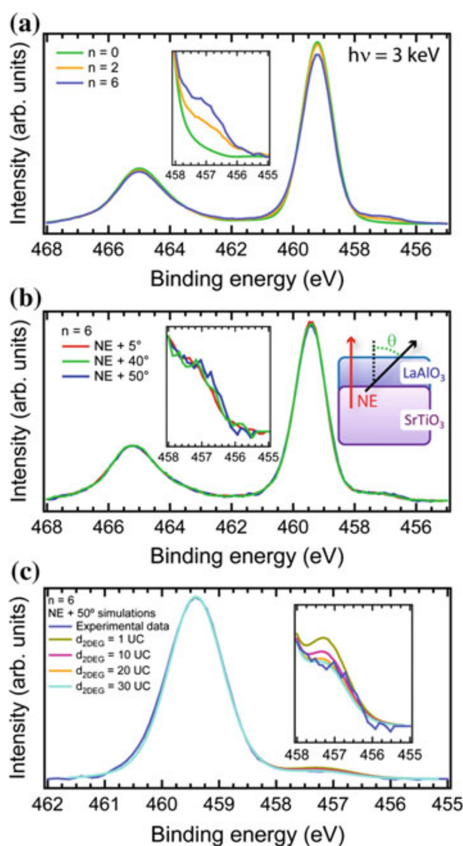

Fig. 14.12 **a** Ti 2p HAXPS ($h\nu$ = 3 keV) for PLD-grown $LaAlO_3/SrTiO_3$(001) heterojunctions of various LAO thicknesses measured at normal emission (NE); **b** Ti 2p spectra measured at various angles off normal emission for a 6 u.c. sample; **c** simulated spectra 50° off normal for a 6 u.c. sample with different thicknesses of the Ti^{3+}—containing layer modeled, along with a comparison to experiment (inset). Taken from [69]

collected 5°, 40°, and 50° off normal for a 6 u.c. film. The Ti^{3+} spectral intensity changes little as the polar angle is changed, indicating that the Ti^{3+} penetrates deep into the STO. Figure 14.12c shows simulations for a range of *d* values and a 6 u.c. film, along with a comparison to experiment in the inset, from which the large value of *d* is determined. Interestingly, these authors also obtained angle-dependent data consistent with stronger confinement (2DEG thickness of ∼6 u.c.), but only when the LAO film was grown on a highly defective substrate (see Fig. 4 in [69]). In another study, Cencellieri et al. [89] observed no Ti^{3+} in Ti 2*p* spectra for either LAO/STO(001) or $(LAO)_x(STO)_{1-x}$/STO(001) heterojunctions below the respective critical thicknesses. These authors post-annealed in 150 Torr of O_2 to insure complete oxidation. Resonant SXPS similar to that used by Berner et al. [67] was employed and no in-gap photoemission intensity was found at the chemical potential for 2.5 and 4 u.c. samples. However, a clear signal that was resonantly enhanced at the Ti L_3 edge for Ti^{3+} was observed for 4.5 and 6 u.c. samples. These data are shown in Fig. 14.13. Additionally, the angle dependent data presented by these authors were consistent with electron confinement within one or a few u.c. of the interface.

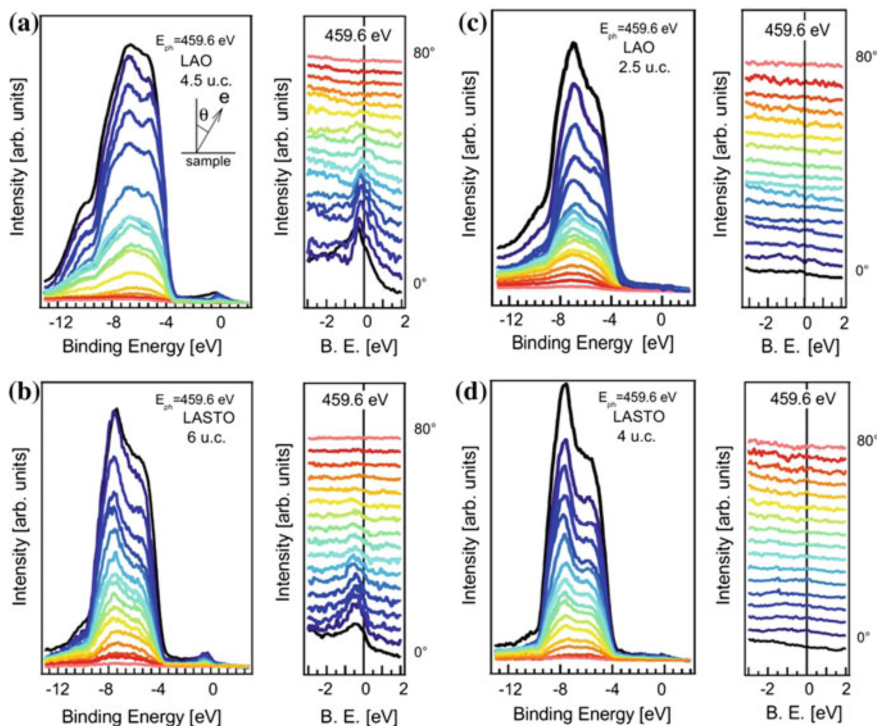

Fig. 14.13 Resonant SXPS at the Ti^{3+} L_3 absorption edge for LAO and $Sr_{0.5}La_{0.5}AlO_3$ (LASTO) films deposited on $SrTiO_3$(001) by on-axis PLD above (**a**, **b**) and below (**c**, **d**) the critical thickness for conductivity. Taken from [89]

The lack of reproducibility in the published results to date is troubling, particularly in light of the oft-made claim that LAO/STO interfaces can be routinely fabricated with atomic layer control and precision [52, 90, 91]. Implied in these kinds of descriptors is the ability to monitor and control stoichiometry, as well as defect densities. We have already discussed the possibility that Al rich films create V_O in the STO, leading to conductivity by means of vacancy doping that is not prevented by growing at high O_2 pressure. Regarding the $\sim$4 u.c. threshold film thickness required to trigger macroscopic conductivity despite the appearance of Ti^{3+} at lower film thicknesses, the possibility that 4 u.c. LAO are required before a defect-generated, *electrically continuous* conductive layer forms in the STO cannot be discounted. Another possibility rarely discussed is vacancy creation by the energetic particles in the laser plume that are incident on the STO substrate during on-axis PLD at lower pressures. Until these possibilities are more thoroughly investigated, a convincing case for the origin of Ti^{3+}, and any specific mechanism of interface conductivity, will be difficult to make.

14.3.3 On LAO/STO Band Offsets

It has been known for years that a combination of core-level and valence-band XPS can be used to determine valence band offsets (VBO) at semiconductor interfaces [13, 14]. By referencing appropriate core-level binding energies to the valence band maximum (VBM) for bulk crystals or thick (compared to the photoelectron attenuation length) films of the two semiconductors, the VBO can be determined by measuring core-level binding energy differences for the heterojunction. If the heterojunction (*HJ*) consists of materials *A* and *B*, with *A* (*B*) exhibiting an isolated core-level peak denoted by *CL*1 (*CL*2), the general formula for the VBO (ΔE_V) is given by

$$\Delta E_V = (E_{CL1} - E_{CL2})_{HJ} - (E_{CL1} - E_V)_A + (E_{CL2} - E_V)_B \tag{14.1}$$

where E_V is the VBM for bulk-like *A* and *B*. An important criterion for success in using this method is that there are no substantial changes in core-level line shapes due to interface chemistry; any changes in binding energy and line shape must be due entirely to changes in electrostatic potential at the heterojunction. It is also critically important that the quantity $E_{CL1} - E_V$ be measured with an accuracy of a few hundredths of an eV for each core level of interest, using a clean, well-ordered surface of the appropriate bulk-like material. Making this measurement correctly requires that the spectrometer energy dispersion be accurately calibrated over the binding energy range of interest. Additionally, specimen charging resulting from the build-up of positive charge in the X-ray irradiation area can prevent binding energy measurements of sufficient accuracy to allow VBOs to be determined. This

problem frequently occurs when using bright synchrotron x-radiation, particularly in the soft X-ray regime in which the cross sections are larger and higher charge densities can occur, as discussed for the case of $LaNiO_3/SrTiO_3(001)$ by Conti et al. [92]. Here, dynamic charging, in which all binding energies increase with time precludes accurate measurements of binding energies and line shapes. The problem is not nearly so acute when using lab X-ray sources. In this case, the use of a low-energy electron flood gun allows spectra to be obtained with static charging, in which all binding energies are shifted to values that are lower than their true values, but are constant over time. Since VBO determination is based on binding energy *differences*, absolute binding energies are not required, and static charging does not pose any limitation whatsoever.

Application of this method to the LAO/STO(001) interface has been carried out by a few groups. For comparative purposes, we will adopt the sign convention that a positive VBO denotes the LAO VBM being above (i.e. at lower binding energy) the STO VBM (i.e. $\Delta E_V = E_V^{STO} - E_V^{LAO}$). Based on La $4d_{5/2}$ and Sr $3d_{5/2}$ spectra such as those shown in Fig. 14.7, Segal et al. [65] carried out in situ measurements on MBE-grown specimens and found that the VBO for LAO deposited on TiO_2-terminated STO(001) substrates ranged from −0.35(18) eV for 2 u.c. of LAO to −0.60(18) eV for 9 u.c. of LAO. In contrast, based on spectra such as those shown in Fig. 14.8, Chambers et al. [15] ex situ measured on-axis PLD-grown 4 u.c. LAO/TiO_2:STO(001) samples from two laboratories (Universities of Augsburg and Tokyo), with and without in situ O_2 plasma cleaning. The measured VBO values ranged from −0.06(10) to +0.34 (10) eV, depending on which lab the film came from, and whether or not the surface was cleaned with activated oxygen once inside the XPS system. This analysis was based on the average of four pairs of core levels (La $4d_{5/2}$ and Sr $3d_{5/2}$, La $4d_{5/2}$ and Ti $2p_{3/2}$, Al $2p$ and Sr $3d_{5/2}$, and Al $2p$ and Ti $2p_{3/2}$), and for each sample. The resulting VBOs were well within experimental error (±0.08 eV for each measurement). Qiao et al. [93] also carried out measurements using the same four pairs of core levels for samples prepared by off-axis PLD in 10 mTorr O_2 at PNNL and obtained an average VBO of +0.17(8) eV. In contrast, Drera et al. [94] did not find consistency when using multiple pairs of core levels for PLD-grown heterojunctions, but rather found that the use of the Ti $3p$ line led to larger binding energy differences across the interface, sometimes by as much as 0.9 eV. These authors rationalized this result as being due to the effect of Ti^{3+} states perturbing the local electronic environment, even though the largest effect was observed for a 5 u.c. LAO/STO sample that was insulating, and for which the Ti^{3+} component was almost negligible. These authors measured values of −0.6 to −0.7 eV for 3 and 5 u.c. LAO films, although the error bars were quite large. Segal et al. [65] obtained results for LAO on SrO-terminated STO(001) substrates and observed that the VBO trend with LAO thickness goes in the opposite direction as that for LAO onTiO_2-terminated STO, as expected based on the polar catastrophe model. In contrast, Takizawa et al. [66] found the same trend for PLD-grown LAO on the two substrate terminations. Berner et al. [68] used HAXPS to measure the

VBO as a function of on-axis PLD-grown LAO film thickness and found the value to be +0.35 eV, independent of thickness. This value is in good agreement with that measured by Chambers et al. [15] for films prepared the same way [84].

It is also possible to extract the VBO directly from VB spectra for the heterojunction by utilizing reference VB spectra for thick films or bulk specimens of the two materials. The reference VB spectra are scaled by factors appropriate for the film thickness in the heterojunction, and then summed for different offset values and compared to experiment [95]. Both Qiao et al. [93] and Berner et al. [68] used this method and obtained VBO values in excellent agreement with those obtained using the combined VB and core-level method described above. In contrast, Drera et al. [94] did not report good agreement between the two methods.

The VBO results discussed above are summarized in Table 14.1. Although significant differences exist in the VBO values depending on the growth method and process parameters used, it is clear that a substantial built-in potential (at least ~0.7 eV per u.c.) is required for the LAO VBM to cross the STO conduction band minimum (CBM) at an LAO thickness of 4 u.c. Yet, the actual built-in potentials are much smaller, as discussed in Sects. 14.3.1 and 14.3.2. These results unambiguously show that the electronic reconstruction model as originally described does not explain the observation of interfacial conductivity. In the opinion of this author, the preponderance of evidence suggests that defects are required for conductivity. However, it is not clear if defects trigger an electronic reconstruction of a different kind, or are themselves the direct cause of conductivity via unintentional doping. In either case, XPS in its various forms will continue to be a useful tool in the ongoing investigation.

Table 14.1 Valence band offsets for the LAO/STO(001) interface as measured by XPS

Sample	Method	Clean?	ΔE_v (eV) core levels	ΔE_v (eV) valence bands	Reference
2 to 9 u.c. (cond ≥ 4 uc)	MBE	No	−0.35(18) to −0.60(18)	–	[65]
4 u.c. (cond) Augsburg	On-axis PLD	No Yes	+0.20(10) +0.34(10)	–	[15]
4 u.c. (cond) Tokyo	On-axis PLD	No Yes	−0.06(10) +0.14(10)	–	[15]
3 u.c. (ins)	Off-axis PLD	Yes	+0.17(10)	+0.14(10)	[93]
3 u.c. (ins) 5 u.c. (ins) 5 u.c. (cond)	On-axis PLD	No No No	−0.67(10) −0.57(38) −0.72(24)	−0.10 +0.17 −0.04	[94]
4 to 12 u.c.	On-axis PLD	No	+0.3 to +0.4	+0.3 to +0.4	[68]

Notes (i) "cond" denotes interface conductivity whereas "ins" denotes an insulating interface. (ii) "clean?" refers to whether or not some form of in situ cleaning to remove adventitious carbon prior to XPS measurements was done

14.3.4 On the extent of interfacial mixing at the LAO/STO interface

Regarding the state-of-the-art in perovskite heterojunction growth, it has been claimed that, "*the chemical abruptness and crystalline perfection of oxide multilayers now rival those of semiconductor multilayers; it is possible to change from one material to another over a distance of a single unit cell*" [90]. While this statement may be true for some perovskite superlattices prepared by MBE, it is in general not true for LAO/STO, at least based on published work. Although there is one study in which the authors claim to have made a completely abrupt PLD-grown LAO/STO interface based on a comparison of EELS data with simulations, the abrupt interface simulation clearly reveals a sharper interface than does the experimental profile (see Fig. 1d in [96]). Elsewhere in the literature when interface structure is investigated, it is usually found that cation mixing occurs, and often over distances greater than 1 u.c., even in MBE-grown material [59, 97]. Inasmuch as chemical disorder at the interface can affect electronic and magnetic properties, assessing the extent of intermixing is important. There are several analytical methods that can be brought to bear on this problem, each with strengths and weaknesses. ARXPS is one of these tools, and was used for determining Ti^{3+} depth profiles, as discussed in Sect. 14.3.2. A detailed discussion of these techniques with application to LAO/STO(001) has been published elsewhere [15]. Here we summarize the salient points associated with the use of ARXPS to study the LAO/STO (001) heterojunction [15, 93].

As is well known, the dependence of photoelectron intensities on take-off angle (θ_t) for a film-on-substrate specimen can be modeled using a simple continuum approach which takes into account only inelastic scattering, and does so assuming that scattering rates are isotropic. This approach completely ignores photoelectron diffraction (PED) effects, which can lead to rather large variations with emission angle—up to a few tens of percent—depending on the angular acceptance of the analyzer and the crystallographic perfection of the sample [16]. PED effects typically add intensity modulation to what would otherwise be a monotonically increasing intensity vs. take-off angle (θ_t) curve. The continuum model yields semi-quantitative insight into the extent of interfacial mixing, provided the surface is atomically flat.

Figure 14.14 shows polar scans of Sr 3*d*, Ti 2*p*, La 4*d* and Al 2*p* intensities in the (010) azimuth for 4 u.c. LAO/STO(001) prepared in Augsburg by on-axis PLD. Also shown are simulations of an abrupt 4 u.c. sample based on scans measured for a 25 u.c. LAO/STO(001) sample prepared under the same conditions as used for the 4 u.c. sample, and a bulk STO(001) single crystal. In light of XPS probe depths at the AlKα X-ray energy, a 25 u.c. LAO film yields the same XPS intensities as bulk LAO. The simulated scans for Sr 3*d* and Ti 2*p* are given by

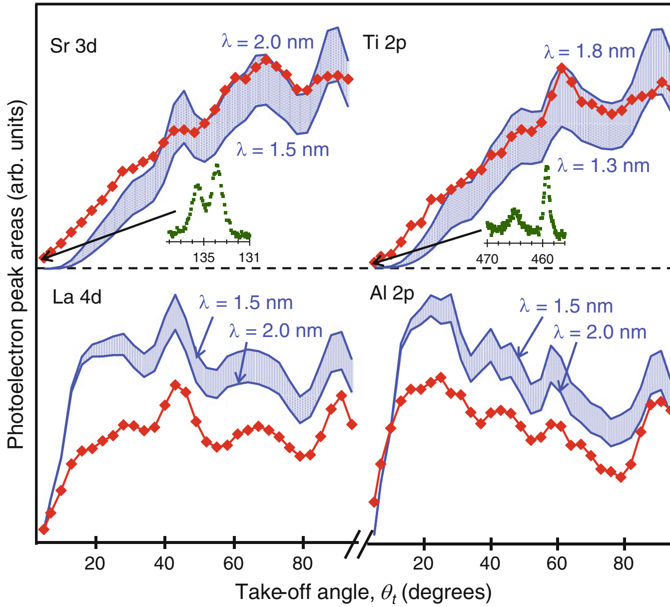

Fig. 14.14 ARXPS polar scans in the (010) azimuth for 4 u.c. $LaAlO_3/SrTiO_3(001)$ prepared by on-axis PLD (*diamonds*), along with simulations of the corresponding abrupt-interface polar scans calculated using (14.2) and (14.3) (*blue bands*). The deviations reveal the presence of interfacial mixing involving all four cations. The ranges of electron attenuation lengths used to generate the simulations are shown. *Insets* Sr 3*d* and Ti 2*p* spectra measured at the extremely surface sensitive angle of 5°. Taken from [15] (Color figure online)

$$I_{4uc}(\theta_t) = I_{STO}(\theta_t)\exp\left(-\frac{d}{\lambda \sin\theta_t}\right) \tag{14.2}$$

and those for La 4*d* and Al 2*p* are given by

$$I_{4uc}(\theta_t) = I_{25uc}(\theta_t)\left[1 - \exp\left(-\frac{d}{\lambda \sin\theta_t}\right)\right] \tag{14.3}$$

Here d and λ are the film thickness and electron attenuation length, respectively. Uncertainty in the exact value of λ leads to the use of a range of values, consistent with the NIST data base [98], but also reasonable for this particular material system [15]. Significantly, the Sr 3*d* and Ti 2*p* intensities exceed those for the abrupt simulation for θ_t values below $\sim 30°$, revealing that Ti and Sr diffuse out into the film. In fact, the presence of Sr 3*d* and Ti 2*p* peaks at $\theta_t = 5°$, as seen in the insets in Fig. 14.14, can only occur if these cations are present in the top u.c. of the LAO film, presumably as substitutional impurities on the A and B sites, respectively. Likewise, the La 4*d* and Al 2*p* intensities are less than those for the abrupt

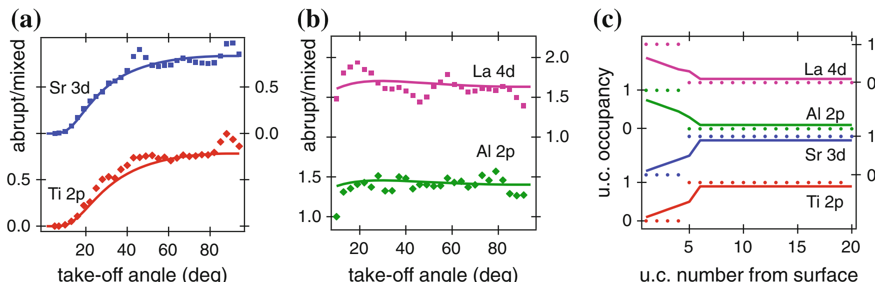

Fig. 14.15 **a**, **b** Measured (*discrete symbols* determined from the data from Fig. 14.12) and simulated (*continuous curves*) ratios of polar scans (*abrupt/mixed*). The simulated ratios are based on optimized values of atom occupancies in each of the layers for 4 u.c. $LaAlO_3/SrTiO_3(001)$. **c** Atom profiles (*solid curves*) which yield the optimized simulated polar scan ratios in **a** and **b**. The *dots* represent atom profiles for the abrupt interface. Taken from [15]

simulation at all angles, as expected for a non-abrupt interface in which both La and Al have diffused out into the STO.

Semi-quantitative atom profiles can be extracted from these angle scans, but the intensity modulation due to photoelectron diffraction must first be removed to the greatest possible extent. This was done by dividing the abrupt simulations by the actual 4 u.c. scans for each core level prior to analyzing the latter. These experimental intensity profile ratios can then be directly compared to a model intensity profile ratio calculation in which the fractional occupancies of each layer are systematically varied until optimal agreement is reached [15]. The results are shown in Fig. 14.15 for the angular distributions displayed in Fig. 14.14. Panels a and b show the experimental (discrete symbols) and model (continuous curves) profiles, and panel c shows the atom profiles which give the best agreement with experiment. The lack of depth resolution in ARXPS means that these best-fit atom profiles are not unique solutions. However, they do yield semi-quantitative information that is useful when trying to assess the extent of cation mixing at the interface, and the results are in qualitative agreement with those from medium energy ion scattering and other techniques [15].

14.4 Other Polar-Nonpolar Perovskite Heterojunctions—$GdTiO_3/SrTiO_3(001)$, $NdTiO_3/SrTiO_3(001)$ and $LaCrO_3/SrTiO_3(001)$

It is of interest to explore other heterojunctions comprised of insulating III-III and II-IV perovskites to see if interface conductivity occurs, and what XPS can contribute to our understanding of the electronic properties. Moetakef et al. [99] used metal-organic, or "hybrid" MBE to prepare $GdTiO_3/SrTiO_3/(LaAlO_3)_{0.3}(Sr_2AlTaO_6)_{0.7}(001)$ (GTO/STO/LSAT) heterojunctions and superlattices and found

interface conductivity with sheet carrier concentrations of ~0.5 e^{-}/u.c. for each GTO/STO interface. GTO is a ferrimagnetic Mott insulator with band gap of ~1 eV. In this MBE variant, a metal organic precursor is used to bring Ti and O to the substrate, and a conventional effusion cell is used for the rare earth metal. No oxygen is supplied from the gas phase, and a fairly high substrate temperature (800–900 °C) is used to insure complete decomposition of the metal organic. This group also found that the carrier concentration was reduced in proportion to the mole fraction of Sr added to the AO sublattice, up to the point that the $Sr_xGd_{1-x}O_3$ became metallic [100]. Additionally, conductivity occurs for GTO thicknesses as small as 2 u.c. [101]. These results are consistent with the electronic reconstruction model revisited, as discussed in Sect. 14.3.1. The GdO layer at the interface acts a donor sheet, leading to resolution of the polar discontinuity there, and effective doping of the STO near the interface. The formally positive charge on this GdO layer keeps the itinerant electrons close to the interface, resulting in 2DEG behavior [102].

Conti et al. [92] used SXPS and HAXPS to measure the VBO for MBE-grown GTO/STO(001) as well as $LaNiO_3/SrTiO_3(001)$ (LNO/STO) heterojunctions, also prepared by MBE. LNO is a correlated metal that exhibits a metal-to-insulator transition as a strained, thin epitaxial film. These authors used 6 keV X-rays in order to obtain maximum probe depth, and measured the VBO to range between 2.94 and 3.5 eV for different GTO/STO samples (two multilayers with $\Delta E_V = 2.94(5)$ and 3.3 (1) eV and two bilayers with ΔE_V = 3.5(1) and 3.2(1) eV). STEM images are consistent with an abrupt interface and that the growth conditions were nominally the same for all samples, making it difficult to understand why the spread of values is as large as it is. The LNO/STO VBO values measured using HAXPS differed considerably compared to those measured using SXPS. The authors concluded that HAXPS yielded more accurate results because of greater depth sensitivity and less extensive charging.

A very similar set of results have been found for $NdTiO_3$ (NTO)/STO(001) interfaces. Xu et al. [103] also used hybrid MBE to prepare NTO/STO and STO/NTO/STO heterojunctions on LSAT(001) substrates. Unlike GTO, NTO is an antiferromagnetic Mott insulator with a Mott Hubbard gap of 0.8 eV. These authors found interface conductivity in STO/NTO/STO structures for NTO layer thicknesses of as small as 2 u.c. Moreover, the sheet carrier concentration was found to be 3×10^{14} cm^{-2} per interface for NTO thicknesses up to 6 u.c., and went above this value for NTO thicknesses greater than 6 u.c., reaching a value of 1.5×10^{15} cm^{-2} at 25 u.c. [104]. INTXPS measurements made ex situ reveal that the valence band offset is of the broken type-II kind, resulting in spontaneous charge transfer from NTO to STO layers, giving rise to the additional carriers above and beyond the concentration expected based on electronic reconstruction. Additionally, there was no evidence found for a built-in potential within the NTO layers based on core-level peak broadening [104]. This material system thus provides additional direct evidence for the interface dipole being screened by charge transfer of half an electron per u.c. from the first NdO layer to STO near the interface, as discussed in Sect. 14.3.1.

Although the GTO/STO(001) and NTO/STO(001) interfaces behave as nearly ideal III-III/II-IV heterojunctions, other material systems have been also been investigated and found to deviate considerably from ideality. For instance, Qiao et al. [105] have used MBE to prepare $LaCrO_3/SrTiO_3(001)$ (LCO/STO) heterojunctions, but these were not found to be conductive for any LCO thickness. Chambers et al. [82] used monochromatic AlKα X-rays to measure potential drops across the LCO and band offsets as a function of LCO layer thickness. LCO is a wide gap insulator with a charge transfer gap of 4.75–4.95 eV, depending on strain [106]. Interestingly, these authors found evidence for a built-in potential within the LCO layer from XPS peak widths equal to ∼0.5 eV per u.c. at 2 u.c. which dropped with LCO layer thickness, going to zero at 15 u.c. Moreover, the VBO was measured to be 1.9 eV at 2 u.c., and found to increase with LCO layer thickness, saturating at 2.6 eV at 7 u.c. The dependences of the core-level peak widths, the build-in potential, and the VBO on LCO layer thickness are shown in Fig. 14.16a, b and c, respectively. The combination of the thickness-dependent VBO and potential drop across the LAO should lead to a crossing of the LCO VBM with the STO CBM at ∼7 u.c. resulting in conductivity, as depicted in Fig. 14.16d.

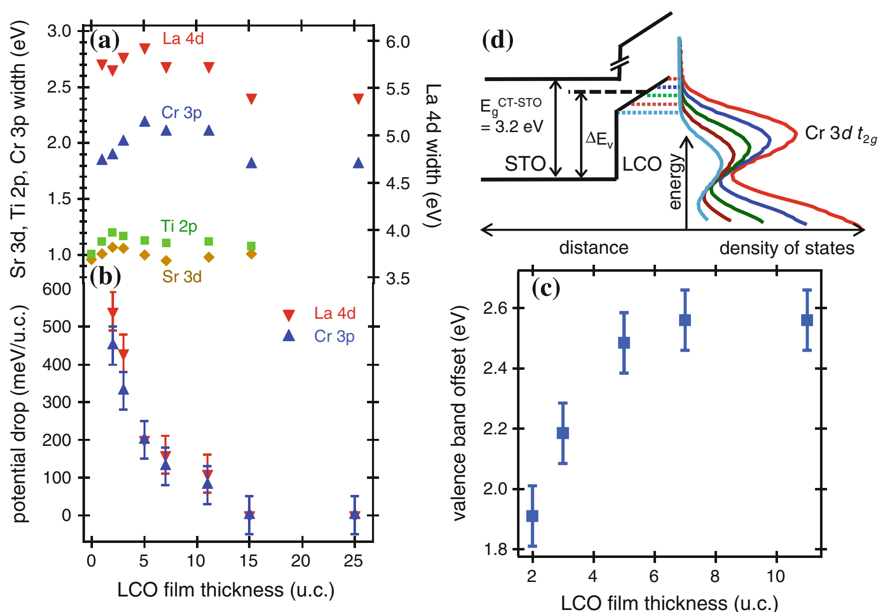

Fig. 14.16 **a** Core-level full width at half maximum values, **b** potential drop across the $LaCrO_3$ layer, and **c** valence band offsets for the $LaCrO_3/SrTiO_3$ (001) interfaces as a function of $LaCrO_3$ layer thickness; **d** schematic energy diagram showing how the combination of band offset and built-in potential across the $LaCrO_3$ layer can lead to interface conductivity via electronic reconstruction. Taken from [82]

However, there is no conductivity at any LCO layer thickness. The electronic properties, which differ strongly from those for both LAO/STO and GTO/STO, most likely have to do with the structural and compositional complexities of the interface. These have been examined using a combination of high-angle annular dark-field scanning transmission electron microscopy (HAADF-STEM), energy dispersive X-ray spectroscopy (EDS) and electron energy loss spectroscopy (EELS), along with RBS [97]. The interface is not abrupt, despite the superficial appearance of abruptness based on HAADF images. Intensity profiles and spectroscopy show that the *A*-site cations diffuse across the interface to a greater extent than *B*-site cations. The *B*-site cations are partially reduced on the LCO of the interface based on analysis of EELS near-edge structures. The location and direction of these electronic modifications do not intuitively compensate the charge imbalance imposed by uneven cation interdiffusion. However, based on first principles calculations, the feasibility that charge redistribution would occur within BO_2 layers of the LCO, enabled by low-lying *d* states within $LaCrO_3$, was established. Moreover, it was shown that such a charge rearrangement could suppress an electronic reconstruction of the type discussed in Sect. 14.3 [82]. These results highlight the importance of carefully considering both the physical and electronic structure of such complex interfaces in the process of interpreting transport results.

14.5 Novel HAXPS Investigations of Perovskite Interfaces

Finally, we briefly mention the use of HAXPS to make novel measurements on buried interfaces involving perovskites. For instance, Gray et al. [107, 108] have used X-ray standing-wave excitation to probe momentum resolved electronic structure and core-level chemical shifts resulting from crystal-field distortions at PLD-grown $La_{0.7}Sr_{0.3}MnO_3/SrTiO_3(001)$ superlattices. Additionally, Gray et al. [109] have probed changes in the VB density of states as a function of thickness for MBE-grown $LaNiO_3$ films on LSAT(001) and LAO(001) and shown how the DOS just below the Fermi level is suppressed in the thinnest films for which a metal-to-insulator transition is known to occur. These measurements illustrate the power of HAXPS, particularly when combined with the depth tunability of the standing-wave technique, to probe electronic structure at buried perovskite interfaces. Finally, Kaiser et al. [110] have used HAXPS to probe buried layers of delta-doped La:STO(001) epitaxial films prepared by MBE. These authors compared core-level and VB spectra for a 3-nm $La_{0.06}Sr_{0.94}TiO_3$ film capped with a 4.5 nm film of pure STO to those for a reference, bulk-like 300 nm film of $La_{0.06}Sr_{0.94}TiO_3$ and found comparable binding energies, line shapes and peak widths. These results indicate no detectable band bending or band offset associated with formation of the buried delta-doped layer, and establish the utility of HAXPS to probe electronic structure at buried perovskite interfaces.

14.6 Summary

This chapter focuses on the use of XPS in the various X-ray energy regimes (soft, intermediate and hard) to probe a variety of properties at interfaces of perovskite oxides. The versatility of the technique and the breadth of understanding that can be gained make XPS arguably the most valuable single technique one can use in trying to understand complex oxide interfaces. SXPS and INTXPS are especially valuable when incorporated as in situ tools within an ultrahigh vacuum oxide film deposition system, because they allow a wealth of data to be obtained without the often deleterious effects of air exposure on surfaces and shallow interfaces. Of the three photon energy regimes discussed here, HAXPS is relatively unexplored compared to the other two. Its principal advantages include greater probe depth, thereby enabling more deeply buried interfaces to be probed, and less extensive charging. The primary disadvantage is lower photoemission cross sections, particularly for lower Z elements. However, this disadvantage is more than compensated for by the high X-ray brightness available at advanced synchrotron facilities where these measurements are typically carried out.

The use of XPS to probe the chemical, electronic and structural properties of polar/nonpolar perovskite interfaces has been the principal focus of the chapter. The same attributes that give perovskites their amazing range of properties (different structural motifs, mutual cation solubilities at the A and B sites, and the ease with which O vacancies are created) also generate a range of outcomes accompanying interface formation which if not properly characterized, can lead to false conclusions about cause-and-effect relationships. No one experimental technique can answer all the relevant and important questions about these properties; a judiciously chosen combination of methods is needed. However, XPS in its various forms has in the past, and will in the future continue to provide important insight into the properties of these fascinating material systems.

Acknowledgements The author is indebted to Tiffany Kaspar and Ryan Comes for critical readings of this manuscript, and Joe Woicik, Susanne Stemmer, Ralph Claessen and Michael Sing for helpful comments. The writing of this chapter was supported by the U.S. Department of Energy, Office of Basic Energy Sciences, Division of Materials Sciences and Engineering under Award #10122, and Chemical Sciences, Geosciences and Biosciences Division under Award #48526. Some of the work described in this review was conducted in the William R. Wiley Environmental Molecular Sciences Laboratory (EMSL), a national scientific user facility sponsored by DOE's Office of Biological and Environmental Research and located at PNNL. PNNL is operated by Battelle for the DOE under Contract DE-AC05-76RLO1830.

References

1. J.G. Bednorz, K.A. Mueller, Eur. Phys. J. B **64**, 189 (1986)
2. G.J. Snyder, R. Hiskes, S. DiCarolis, M.R. Beasley, T.H. Geballe, Phys. Rev. B **53**, 14434 (1996)

3. T.S. Santos, S.J. May, J.L. Robertson, A. Bhattacharya, Phys. Rev. B **80**, 155114 (2009)
4. A.B. Shah, Q.M. Ramasse, X.F. Zhai, J.G. Wen, S.J. May, I. Petrov, A. Bhattacharya, P. Abbamonte, J.N. Eckstein, J.M. Zuo, Adv. Mater. **22**, 1156 (2010)
5. K. Oura, V.G. Lifshits, A.A. Saranin, A.V. Zotov, M. Katayama, *Surface Science: An Introduction* (Springer, Berlin, 2003)
6. M. Mayer, SIMNRA User's Guide 6.04. Max-Planck-Institut für Plasmaphysik. http://www2.if.usp.br/~lamfi/guia-simnra.pdf
7. M.H. Mendenhall, R.A. Weller, Nucl. Instrum. Methods Phys. Res. B **59**, 120 (1991)
8. K. Kobayashi, Nucl. Instrum. Methods Phys. Res. Sect. A **601**, 32 (2009)
9. N. Benito, R.E. Galindo, J. Rubio-Zuazo, G.R. Castro, C. Palacio, J. Phys. D: Appl. Phys. **46** (2013)
10. P.S. Bagus, E.S. Ilton, J.R. Rustad, Phys. Rev. B **69**, 205112 (2004)
11. P.S. Bagus, E.S. Ilton, Phys. Rev. B **73**, 155110 (2006)
12. L. Hozoi, A.H. de Vries, R. Broer, C. de Graaf, P.S. Bagus, Chem. Phys. **331**, 178 (2006)
13. E.A. Kraut, R.W. Grant, J.W. Waldrop, S.P. Kowalczyk, Phys. Rev. Lett. **44**, 1620 (1980)
14. E.A. Kraut, R.W. Grant, J.W. Waldrop, S.P. Kowalczyk, Phys. Rev. B **28**, 1965 (1983)
15. S.A. Chambers, M.H. Engelhard, V. Shutthanandan, Z. Zhu, T.C. Droubay, L. Qiao, P.V. Sushko, T. Feng, H.D. Lee, T. Gustafsson, E. Garfunkel, A.B. Shah, J.-M. Zuo, Q.M. Ramasse, Surf. Sci. Rep. **65**, 317 (2010)
16. S.A. Chambers, Adv. Phys. **40**, 357 (1991)
17. A. Jablonski, C.J. Powell, Phys. Rev. B **76**, 085123 (2007)
18. A. Jablonski, C.J. Powell, J. Vac. Sci. Technol. A **27**, 253 (2009)
19. A. Jablonski, C.J. Powell, Surf. Sci. **604**, 327 (2010)
20. A. Jablonski, C.J. Powell, Surf. Sci. **606**, 644 (2012)
21. C.J. Powell, A. Jablonski, Nucl. Instrum. Methods Phys. Res. Sect. A **601**, 54 (2009)
22. C.J. Powell, A. Jablonski, J. Electron Spectrosc. Relat. Phenom. **178**, 331 (2010)
23. J.J. Yeh, I. Lindau, At. Data Nucl. Data Tables **32**, 1 (1985)
24. Y.J. Kim, Y. Gao, S.A. Chambers, Appl. Surf. Sci. **120**, 250 (1997)
25. P.A. Cox, J.B. Goodenough, P.J. Tavener, D. Telles, R.G. Egdell, J. Solid State Chem. **62**, 360 (1986)
26. H.D. Kim, H.J. Noh, K.H. Kim, S.J. Oh, Phys. Rev. Lett. **93**, 126404 (2004)
27. G. Pacchioni, P.S. Bagus, Phys. Rev. B **50**, 2576 (1994)
28. J.C. Woicik, E.J. Nelson, L. Kronik, M. Jain, J.R. Chelikowsky, D. Heskett, L.E. Berman, G. S. Herman, Phys. Rev. Lett. **89**, 077401 (2002)
29. D.A. Shirley, Phys. Rev. B **5**, 4709 (1972)
30. A.E. Bocquet, T. Mizokawa, K. Morikawa, A. Fujimori, S.R. Barman, K. Maiti, D.D. Sarma, Y. Tokura, M. Onoda, Phys. Rev. B **53**, 1161 (1996)
31. W.J. Pardee, G.D. Mahan, D.E. Eastman, R.A. Pollak, L. Ley, F.R. McFeely, S. P. Kowalczyk, D.A. Shirley, Phys. Rev. B **11**, 3614 (1975)
32. S. Tougaard, J. Kraaer, Phys. Rev. B **43**, 1651 (1991)
33. N. Moslemzadeh, G. Beamson, P. Tsakiropoulos, J.F. Watts, S.R. Haines, P. Weightman, J. Electron Spectrosc. Relat. Phenom. **152**, 129 (2006)
34. S. Doniach, M. Sunjic, J. Phys. C **3**, 285 (1970)
35. K. Okada, A. Kotani, J. Electron Spectrosc. Relat. Phenom. **62**, 131 (1993)
36. J. Zaanen, G.A. Sawatzky, Phys. Rev. B **33**, 8074 (1986)
37. R. Manne, T. Aberg, Chem. Phys. Lett. **7**, 282 (1970)
38. S.A. Chambers, T. Droubay, Phys. Rev. B **64**, 075410 (2001)
39. R. Zimmermann, P. Steiner, R. Claessen, F. Reinert, S. Hufner, P. Blaha, P. Dufek, J. Phys.: Condens. Matter **11**, 1657 (1999)
40. C.J. Nelin, P.S. Bagus, E.S. Ilton, S.A. Chambers, H. Kuhlenbeck, H.J. Freund, Int. J. Quantum Chem. **110**, 2752 (2010)
41. J.J. Kas, F.D. Vila, J.J. Rehr, S.A. Chambers, Phys. Rev. B **91**, 121112(R) (2015)
42. A. Ohtomo, H.Y. Hwang, Nature **427**, 423 (2004)
43. N. Nakagawa, H.Y. Hwang, D.A. Muller, Nat. Mat. **5**, 204 (2006)

44. M.S.J. Marshall, D.T. Newell, D.J. Payne, R.G. Egdell, M.R. Castell, Phys. Rev. B **83**, 035410 (2011)
45. D.G. Schlom, J. Mannhart, Nat. Mat. **10**, 168 (2011)
46. M.L. Reinle-Schmitt, C. Cancellieri, D. Li, D. Fontaine, M. Medarde, E. Pomjakushina, C. W. Schneider, S. Gariglio, P. Ghosez, J.M. Triscone, P.R. Willmott, Nat. Comm. **3**, 1936 (2012)
47. M. Stengel, Phys. Rev. Lett. **106**, 136803 (2011)
48. A. Janotti, L. Bjaalie, L. Gordon, C.G. Van de Walle, Phys. Rev. B **86**, 241108 (2012)
49. C. Noguera, J. Phys. Condens. Matter **12**, R367 (2000)
50. V K. Lazarov, R. Plass, H.C. Poon, D.K. Saldin, M. Weinert, S.A. Chambers, M. Gajdardziska-Josifovska, Phys. Rev. B **71** (2005)
51. S.A. Chambers, T. Droubay, D.R. Jennison, T.R. Mattsson, Science **297**, 827 (2002)
52. M. Huijben, A. Brinkman, G. Koster, G. Rijnders, H. Hilgenkamp, D.H.A. Blank, Adv. Mater. **21**, 1665 (2009)
53. G. Herranz, F. Sanchez, N. Dix, M. Scigaj, J. Fontcuberta, Sci. Rep. **2**, 758 (2012)
54. E. Breckenfeld, N. Bronn, J. Karthik, A.R. Damodaran, S. Lee, N. Mason, L.W. Martin, Phys. Rev. Lett. **110**, 196804 (2013)
55. L. Wiedeman, H. Helvajian, J. Appl. Phys. **70**, 4513 (1991)
56. G.C. Tyrrell, T. York, N. Cherief, D. Givord, J. Lawlel, J.G. Lunney, M. Buckley, I.W. Boyd, Microelectron. Eng. **25**, 247 (1994)
57. T.C. Droubay, L. Qiao, T.C. Kaspar, M.H. Engelhard, V. Shutthanandan, S.A. Chambers, Appl. Phys. Lett. **97**, 124105 (2010)
58. G.W. Berkstresser, A.J. Valentino, C.D. Brandle, J. Cryst. Growth **128**, 684 (1993)
59. M.P. Warusawithana, C. Richter, J.A. Mundy, P. Roy, J. Ludwig, S. Paetel, T. Heeg, A.A. Pawlicki, L.F. Kourkoutis, M. Zheng, M. Lee, B. Mulcahy, W. Zander, Y. Zhu, J. Schubert, J.N. Eckstein, D.A. Muller, C. Stephen Hellberg, J. Mannhart, D.G. Schlom, Nat. Comm. **4**, 2351 (2013)
60. I.M. Dildar, D.B. Boltje, M.H.S. Hesselberth, J. Aarts, Q. Xu, H.W. Zandbergen, S. Harkema, Appl. Phys. Lett. **102**, 121601 (2013)
61. Y.Z. Chen, N. Bovet, F. Trier, D.V. Christensen, F.M. Qu, N.H. Andersen, T. Kasama, W. Zhang, R. Giraud, J. Dufouleur, T.S. Jespersen, J.R. Sun, A. Smith, J. Nygard, L. Lu, B. Buchner, B.G. Shen, S. Linderoth, N. Pryds, Nat. Comm. **4**, 2394 (2013)
62. J. Delahaye, T. Grenet, J. Phys. D Appl. Phys. **45**, 315301 (2012)
63. NIST Chemistry WebBook, Standard Reference Database # 69 (2011)
64. G. Singh-Bhalla, C. Bell, J. Ravichandran, W. Siemons, Y. Hikita, S. Salahuddin, A.F. Hebard, H.Y. Hwang, R. Ramesh, Nat. Phys. **7**, 80 (2011)
65. Y. Segal, J.H. Ngai, J.W. Reiner, F.J. Walker, C.H. Ahn, Phys. Rev. B **80**, 241107(R) (2009)
66. M. Takizawa, S. Tsuda, T. Susaki, H.Y. Hwang, A. Fujimori, Phys. Rev. B **84**, 245124 (2011)
67. G. Berner, M. Sing, H. Fujiwara, A. Yasui, Y. Saitoh, A. Yamasaki, Y. Nishitani, A. Sekiyama, N. Pavlenko, T. Kopp, C. Richter, J. Mannhart, S. Suga, R. Claessen, Phys. Rev. Lett. **110**, 247601 (2013)
68. G. Berner, A. Muller, F. Pfaff, J. Walde, C. Richter, J. Mannhart, S. Thiess, A. Gloskovskii, W. Drube, M. Sing, R. Claessen, Phys. Rev. B **88**, 115111 (2013)
69. E. Slooten, Z.C. Zhong, H.J.A. Molegraaf, P.D. Eerkes, S. de Jong, F. Massee, E. van Heumen, M.K. Kruize, S. Wenderich, J.E. Kleibeuker, M. Gorgoi, H. Hilgenkamp, A. Brinkman, M. Huijben, G. Rijnders, D.H.A. Blank, G. Koster, P.J. Kelly, M.S. Golden, Phys. Rev. B **87**, 085128 (2013)
70. Z.C. Zhong, P.X. Xu, P.J. Kelly, Phys. Rev. B **82**, 165127 (2010)
71. N.C. Bristowe, P.B. Littlewood, E. Artacho, Phys. Rev. B **83**, 205405 (2011)
72. Y. Li, S.N. Phattalung, S. Limpijumnong, J. Kim, J. Yu, Phys. Rev. B **84**, 245307 (2011)
73. N. Pavlenko, T. Kopp, E.Y. Tsymbal, J. Mannhart, G.A. Sawatzky, Phys. Rev. B **86**, 064431 (2012)
74. J. Robertson, C.W. Chen, Appl. Phys. Lett. **74**, 1168 (1999)

75. K. Yoshimatsu, R. Yasuhara, H. Kumigashira, M. Oshima, Phys. Rev. Lett. **101**, 026802 (2008)
76. S.A. Chambers, Phys. Rev. Lett. **102**, 199703 (2009)
77. S.A. Chambers, T. Droubay, T.C. Kaspar, M. Gutowski, J. Vac. Sci. Technol. B **22**, 2205 (2004)
78. S.A. Chambers, T. Droubay, T.C. Kaspar, M. Gutowski, M. van Schilfgaarde, Surf. Sci. **554**, 81 (2004)
79. A. McCollam, S. Wenderich, M.K. Kruize, V.K. Guduru, H.J.A. Molegraaf, M. Huijben, G. Koster, D.H.A. Blank, G. Rijnders, A. Brinkman, H. Hilgenkamp, U. Zeitler, J.C. Maan, arXiv:1207.7003v1 (2012)
80. L.W. van Heeringen, G.A. de Wijs, A. McCollam, J.C. Maan, A. Fasolino, arXiv:1303.7095v1 (2013)
81. M.S. Golden, private communication
82. S.A. Chambers, L. Qiao, T.C. Droubay, T.C. Kaspar, B. Arey, P.V. Sushko, Phys. Rev. Lett. **107**, 206802 (2011)
83. M. Sing, G. Berner, K. Goss, A. Muller, A. Ruff, A. Wetscherek, S. Thiel, J. Mannhart, S.A. Pauli, C.W. Schneider, P.R. Willmott, M. Gorgoi, F. Schafers, R. Claessen, Phys. Rev. Lett. **102**, 176805 (2009)
84. S. Thiel, G. Hammerl, A. Schmehl, C.W. Schneider, J. Mannhart, Science **313**, 1942 (2006)
85. G. Drera, F. Banfi, F.F. Canova, P. Borghetti, L. Sangaletti, F. Bondino, E. Magnano, J. Huijben, M. Huijben, G. Rijnders, D.H.A. Blank, H. Hilgenkamp, A. Brinkman, Appl. Phys. Lett. **98**, 052907 (2011)
86. C. Guillot, Y. Ballu, J. Paigne, J. Lecante, K.P. Jain, P. Thiry, R. Pinchaux, Y. Petroff, L.M. Falicov, Phys. Rev. Lett. **39**, 1632 (1977)
87. W. Meevasana, P.D.C. King, R.H. He, S.K. Mo, M. Hashimoto, A. Tamai, P. Songsiriritthigul, F. Baumberger, Z.X. Shen, Nat. Mat. **10**, 114 (2011)
88. A.F. Santander-Syro, O. Copie, T. Kondo, F. Fortuna, S. Pailhes, R. Weht, X.G. Qiu, F. Bertran, A. Nicolaou, A. Taleb-Ibrahimi, P. Le Fevre, G. Herranz, M. Bibes, N. Reyren, Y. Apertet, P. Lecoeur, A. Barthelemy, M.J. Rozenberg, Nature **469**, 189 (2011)
89. C. Cancellieri, M.L. Reinle-Schmitt, M. Kobayashi, V.N. Strocov, T. Schmitt, P.R. Willmott, S. Gariglio, J.M. Triscone, Phys. Rev. Lett. **110**, 137601 (2013)
90. J. Mannhart, D.G. Schlom, Science **327**, 1607 (2010)
91. H.Y. Hwang, Y. Iwasa, M. Kawasaki, B. Keimer, N. Nagaosa, Y. Tokura, Nat. Mat. **11**, 103 (2012)
92. G. Conti, A.M. Kaiser, A.X. Gray, S. Nemsak, G.K. Palsson, J. Son, P. Moetakef, A. Janotti, L. Bjaalie, C.S. Conlon, D. Eiteneer, A.A. Greer, A. Keqi, A. Rattanachata, A.Y. Saw, A. Bostwick, W.C. Stolte, A. Gloskovskii, W. Drube, S. Ueda, M. Kobata, K. Kobayashi, C.G. Van de Walle, S. Stemmer, C.M. Schneider, C.S. Fadley, J. Appl. Phys. **113** (2013)
93. L. Qiao, T.C. Droubay, T.C. Kaspar, P.V. Sushko, S.A. Chambers, Surf. Sci. **605**, 1381 (2011)
94. G. Drera, G. Salvinelli, A. Brinkman, M. Huijben, G. Koster, H. Hilgenkamp, G. Rijnders, D. Visentin, L. Sangaletti, Phys. Rev. B **87**, 075435 (2013)
95. S.A. Chambers, Y. Liang, Z. Yu, R. Droopad, J. Ramdani, K. Eisenbeiser, Appl. Phys. Lett. **77**, 1662 (2000)
96. C. Cantoni, J. Gazquez, F.M. Granozio, M.P. Oxley, M. Varela, A.R. Lupini, S. J. Pennycook, C. Aruta, U.S. di Uccio, P. Perna, D. Maccariello, Adv. Mater. **24**, 3952 (2012)
97. R. Colby, L. Qiao, V. Shutthanandan, J. Ciston, H.K.L. Zhang, B. Kabius, S.A. Chambers, Phys. Rev. B **88**, 155325 (2013)
98. NIST data base of electron attenuation lengths. http://www.nist.gov/srd/nist82.cfm
99. P. Moetakef, T.A. Cain, D.G. Ouellette, J.Y. Zhang, D.O. Klenov, A. Janotti, C.G. Van de Walle, S. Rajan, S.J. Allen, S. Stemmer, Appl. Phys. Lett. **99**, 232116 (2011)
100. T.A. Cain, P. Moetakef, C.A. Jackson, S. Stemmer, Appl. Phys. Lett. **101**, 111604 (2012)
101. S. Stemmer, private communication

102. S. Raghavan, S.J. Allen, S. Stemmer, Appl. Phys. Lett. **103**, 212103 (2013)
103. P. Xu, D. Phelan, J.S. Jeong, K.A. Mkhoyan, B. Jalan, Appl. Phys. Lett. **104**, 082109 (2014)
104. P. Xu, T.C. Droubay, J.S. Jeong, K. Andre Mkhoyan, P.V. Sushko, S.A. Chambers, B. Jalan, Submitted (2015)
105. L. Qiao, T.C. Droubay, M.E. Bowden, V. Shutthanandan, T.C. Kaspar, S.A. Chambers, Appl. Phys. Lett. **99**, 061904 (2011)
106. P.V. Sushko, L. Qiao, M.E. Bowden, G.E. Exarhos, F.K. Urban III, D. Barton, S.A. Chambers, Phys. Rev. Lett. **110**, 077401 (2013)
107. A.X. Gray, C. Papp, B. Balke, S.H. Yang, M. Huijben, E. Rotenberg, A. Bostwick, S. Ueda, Y. Yamashita, K. Kobayashi, E.M. Gullikson, J.B. Kortright, F.M.F. Groot, G. Rijnders, D. H.A. Blank, R. Ramesh, C.S. Fadley, Phys. Rev. B **82**, 205116 (2010)
108. A.X. Gray, J. Minár, L. Plucinski, M. Huijben, A. Bostwick, E. Rotenberg, S.-H. Yang, J. Braun, A. Winkelmann, D. Eiteneer, A. Rattanachata, A. Greer, G. Rijnders, D.H.A. Blank, D. Doennig, R. Pentcheva, J.B. Kortright, C.M. Schneider, H. Ebert, C.S. Fadley, Europhys. Lett. **104**, 17004 (2013)
109. A.X. Gray, A. Janotti, J. Son, J.M. LeBeau, S. Ueda, Y. Yamashita, K. Kobayashi, A.M. Kaiser, R. Sutarto, H. Wadati, G.A. Sawatzky, C.G. Van de Walle, S. Stemmer, C.S. Fadley, Phys. Rev. B **84**, 075104 (2011)
110. A.M. Kaiser, A.X. Gray, G. Conti, B. Jalan, A.P. Kajdos, A. Gloskovskii, S. Ueda, Y. Yamashita, K. Kobayashi, W. Drube, S. Stemmer, C.S. Fadley, Appl. Phys. Lett. **100**, 4731642 (2012)

Chapter 15
HAXPES Measurements of Heterojunction Band Alignment

Conan Weiland, Abdul K. Rumaiz and Joseph C. Woicik

Abstract Heterojunctions, the abrupt change of materials at interfaces, are an integral feature of modern electronic devices. The alignment of electronic energy levels at a heterojunction can be used to tailor charge transfer across the interface, for example to improve carrier injection or to block leakage current. An overview of the understanding of heterojunction energy-level alignment with specific examples of the unique contributions that hard X-ray photoelectron spectroscopy (HAXPES) provides to the understanding of this topic is presented in this chapter. Many theoretical approaches have been applied to heterojunction band alignment, and have had some success in predicting band-alignment values in some but not all cases. Band-alignment measurements have been made using electronic measurements such as internal photoemission, as well as photoelectron spectroscopy either measuring valence bands directly or through the use of core levels. Examples of measurements made by these techniques is presented. HAXPES measurements provide a greater analysis depth, which provides the advantage of measuring "real" heterojunctions fabricated by industrially-relevant techniques. HAXPES has been used to query the fundamental limitations on interlayer thickness for band-offset engineering, and the use of new materials for photovoltaic applications. These and other applications are presented.

C. Weiland (✉) · J.C. Woicik
Materials Measurements Laboratory, National Institute of Standards and Technology,
Gaithersburg, MD, USA
e-mail: cweiland@bnl.gov

J.C. Woicik
e-mail: joseph.woicik@nist.gov

A.K. Rumaiz
National Synchrotron Light Source II, Brookhaven National Laboratory,
Upton, NY, USA
e-mail: rumaiz@bnl.gov

© Springer International Publishing Switzerland 2016

J.C. Woicik (ed.), *Hard X-ray Photoelectron Spectroscopy (HAXPES)*,
Springer Series in Surface Sciences 59, DOI 10.1007/978-3-319-24043-5_15

15.1 Introduction

The constant production of faster and smaller electronic devices has ushered in the digital age. A central feature of modern electronics architectures is the heterojunction, or the abrupt change in material and electronic structure at the interface of dissimilar materials. Heterojunctions can be employed for a variety of applications; for example, controlling the strain present at an interface allows the tailoring of electron mobility and band gaps. Energy-level discontinuities at the heterojunction can be used to manipulate the transfer of charge across interfaces to optimize performance in applications such as transistors for computer processing and memory, photovoltaics, light-emitting diodes, and a host of others. The continued improvement of device performance has required the scaling of features to ever smaller dimensions, as well as the employment of a diverse range of new materials. This profusion of materials and complex architectures has led to the need for advanced measurement methodologies.

The theory of heterojunction band alignment has been extensively studied since the early days of semiconductor research. The early work of Shockley [1] established the conditions for one dimensional homojunctions, namely: (1) the Fermi level remains constant across the junction, and (2) the electric field remains continuous at the junction. It was then attempted to adapt these conditions for heterojunctions; thus it was understood that charge transfer across a heterojunction occurs to satisfy these rules. Anderson [2] used the vacuum level as reference for the electric potential; under this assumption the difference in electron affinities (φ) will be equal to the conduction-band offset, ΔE_C, as shown in Fig. 15.1. The discontinuity in valence band, ΔE_V, can be computed knowing the band gaps. This so called Anderson's rule gives an understanding of the "natural" band line ups and was used to predict band alignment in Ge/GaAs [2] and GaAs/AlGaAs [3] heterojunctions. Anderson's rule, however, implies that dipoles which form at the interface are non-interacting.

Alternative approaches were later developed by von Ross [4] and Adams and Nussbaum [5]. Both of these models were based on electrostatic calculations and intended to correct for inaccuracies in Anderson's model. Adams and Nussbaum's

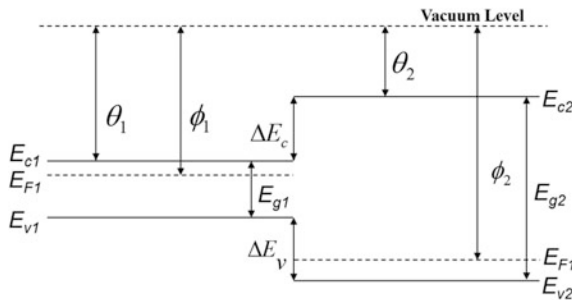

Fig. 15.1 Energy-band diagram for two semiconductors following Anderson's model. Figure adapted from [2]

calculations determined the intrinsic Fermi level to be continuous across a heterojunction, while the von Ross model found the conduction band to be continuous. Both models had some justification from other theoretical works, but experimental confirmation was limited.

The earliest attempts to solve the heterojunction band discontinuity problem using ab initio quantum mechanical calculations were done by Frensley and Kroemer [6]. The predictions made using pseudopotential calculations agreed with the observed experimental results and also supported Anderson's simplistic model. In their subsequent work, Frensley and Kroemer [7] laid down a conceptual framework to study heterojunction band alignment. The procedure relied on ab initio pseudopotential-based calculations of the band structure and the microscopic electrostatic potential across the junction. The interface dipoles were treated with simple estimates based on chemical bonds. A more rigorous ab initio approach was further developed by Baraff et al. [8]. Harris [9] used linear combination of atomic orbitals-based calculations to determine heterojunction band alignment, arguing that pseudopotential-based calculations gave misleading trends for lattice-mismatched heterojunctions.

For comparison of the different models, detailed synchrotron photoemission measurements of valence-band offsets on a variety of substrates with Si and Ge overlayers were performed by Katnani and Margaritondo [10]. Detailed comparison of the measured alignments with calculated alignments using the electron affinity (Anderson [2]), the Adams and Nussbaum [5], the von Ross [4], the Harrison [11], and the Frensley and Kroemer [6] models were made. Their results suggested no clear trend, with no theory universally providing close agreement with the experimental results.

A different approach to the heterojunction problem was put forward by Tersoff [12]. Using the concept of "zero-dipole" band lineup, Tersoff obtained quantitative predictions for both heterojunction band offsets as well as Schottky-barrier heights. Tersoff argued that band discontinuities at the heterojunction lead to the formation of gap states analogous to metal induced gap states at metal/semiconductor interfaces; thus when a heterojunction is formed, it is expected that the gap-state values across the junction will align, shifting the bands to bring the heterostructure into equilibrium with a minimum number of dipoles. This is schematically shown in Fig. 15.2. If one of the semiconductors was replaced with a metal, then the Schottky-barrier height would be obtained by lining up the gap state with the Fermi level of the metal. Thus apart from giving a framework to treat both semiconductor heterojunction band alignment and Schottky-barrier height within a single theory, the Tersoff model implies that heterojunction band alignment between two semiconductors can also be determined from the Schottky-barrier heights of the individual semiconductors with respect to a common reference metal.

A pseudopotential-based theoretical approach to determine heterojunction band alignment was later developed by Van de Walle and Martin [13]. Here it was recognized that many previous theoretical descriptions of band alignment depended on referencing energies from separate calculations of the bulk properties of the individual materials in the heterojunction, yet the calculations were not capable of

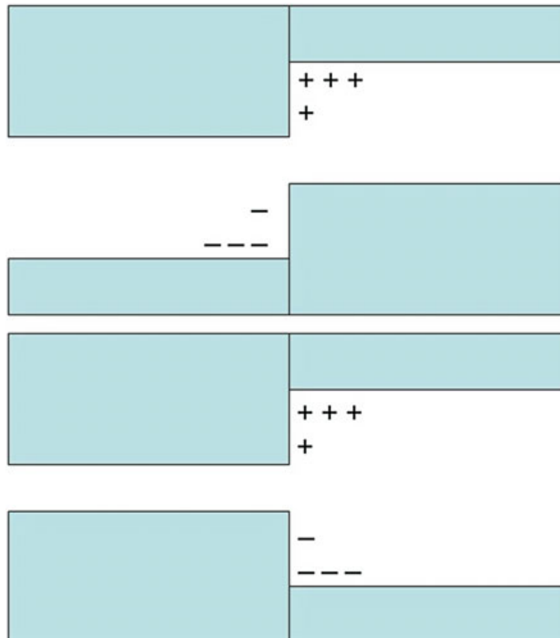

Fig. 15.2 Two simple examples of the relation between the band alignment and interface dipole. Net charge associated with gap states is shown schematically as + (electron deficit) and − (electron excess), where states at the bottom and top of the band gap are occupied or unoccupied, respectively. The *top section* shows a single semiconductor in which a band discontinuity is artificially induced (e.g. using a step potential). The *bottom section* shows an interface between two semiconductors, both with "symmetric" valence and conduction bands, but with unequal band gaps. Figure adapted from [12]

providing an absolute energy scale through which the individual calculations could be compared. The authors thus performed self-consistent ab initio pseudopotential-based calculations of multilayer systems so that the electron distribution at the interface could be directly calculated. The average potential at each side of the heterojunction was taken as a reference by which the band-alignment could be determined by considering the energies of the valence and conduction bands relative to this average potential. This theoretical treatment allowed for the incorporation of strain effects into the calculations, using as an example the Si/Ge interface, where it was found that the presence and location (i.e. strain on the Si side vs. strain on the Ge side) could have an effect on the band-alignment by as much as 0.5 eV.

Van de Walle and Martin [14] extended this work, performing calculations on a series of non-polar lattice-matched heterojunctions and compared their results with those from earlier experiments and theory. Reasonable agreement between theory and experiment were found in many cases, and the similarities and differences between the theoretical approaches were discussed. From their self-consistent interface calculations, they noted that interface properties for the materials calculated

seemed to depend primarily on bulk properties. This allowed them to construct a "model surface" approach to heterojunction band-alignment calculations, where the average pseudopotential on an absolute energy scale is used as a reference.

15.2 Measurements of Heterojunction Band Alignment

15.2.1 *The Natural Valence-Band Offset*

The early theoretical work led to the concept of the natural valence-band offset (NVBO); i.e., the valence-band offset due solely to intrinsic properties of the bulk semiconductors. Shih and Spicer [15] established that the NVBO can be measured from core-level shifts for compound semiconductors with a common element, using as an example the pseudobinary $Hg_{1-x}Cd_xTe$ alloy system. Their method determines the NVBO for the *AC/BC* heterojunction using measurements from the $A_{1-x}B_xC$ alloy. As the chemical bonding in the $A_{1-x}B_xC$ system is identical to the *AC* and *BC* semiconductors, i.e. *A*–*C* and *B*–*C* bonds, core-level shifts for *A* and *B* in the $A_{1-x}B_xC$ system should thus exclusively reflect the NVBO.

Figure 15.3 shows the Hg 5*d* and Cd 4*d* core levels for CdTe, HgTe, and $Hg_{0.7}Cd_{0.3}Te$. The valence-band maximum was aligned for all samples, as shown in the inset. A 0.1 ± 0.03 eV shift to higher binding energy is observed for the Hg

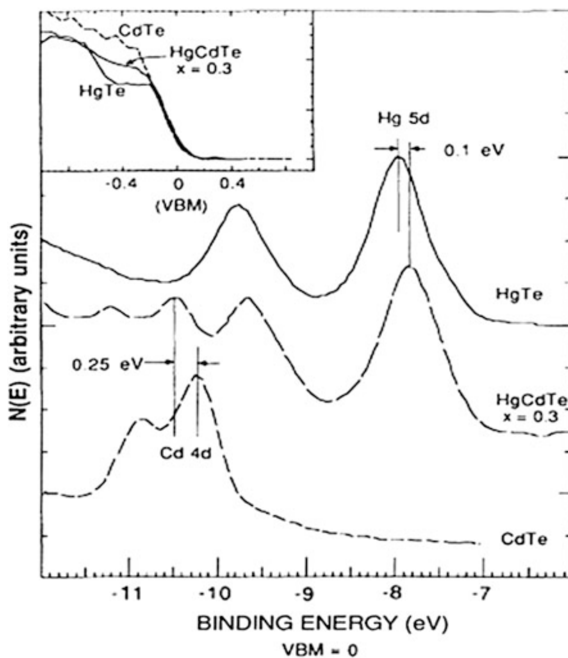

Fig. 15.3 X-ray photoelectron spectroscopy measurements of Hg 5d and Cd 4d core levels for HgTe, CdTe, and $Hg_{0.7}Cd_{0.3}Te$. The energy scale is referenced to the valence-band maximum, shown in the *inset*. Figure reprinted with permissions from [15]

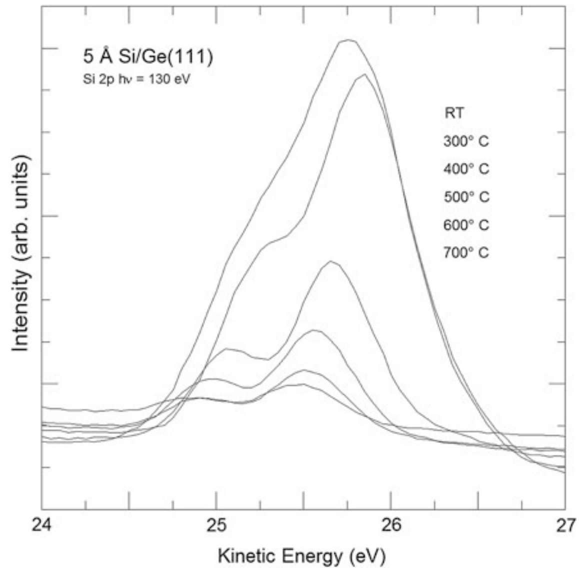

Fig. 15.4 Si 2p core level for 5 Å Si deposited on Ge (111) at room temperature (RT) followed by annealing. Figure reprinted with permissions from [19]

5*d* between the HgTe and the alloy, and a shift of 0.25 ± 0.03 eV to lower binding energy is observed for the Cd 4*d* between the CdTe and the alloy. An NVBO of 0.35 eV is therefore determined. This value was found to be in excellent agreement with earlier measurements on actual HgTe/CdTe heterostructures [16, 17] measured using Kraut's method [18], that we will describe below.

Similar behavior was also observed for the Si/Ge system, as demonstrated by Woicik and Pianetta [19]. While the true binary $Si_{1-x}Ge_x$ alloy differs from the pseudobinary alloys of Shih and Spicer [15], the electronegativities of Si and Ge are similar enough that the core-level shifts in $Si_{1-x}Ge_x$ alloys should not be due to chemical shifts but rather should reflect the NVBO between Si and Ge. Figure 15.4 shows the Si 2*p* core level for Si deposited on Ge (111) (2 × 1) at room temperature and followed by anneal. As the anneal temperature increases, the Si is driven into the Ge substrate, and a large Si core-level shift is observed. This shift shows an NVBO of 0.43 ± 0.07 eV, which is in excellent agreement with earlier measurements made by Mahowald et al. [20] on the actual heterojunction itself.

15.2.2 Ultraviolet-Photoelectron Spectroscopy

The NVBO derives the heterojunction band alignment from bulk properties of the semiconductors alone, while extrinsic factors can also play a significant role in band alignment and require the direct measurement of band offsets. Using Shih and Spicer's method [15], Hwang et al. determined the NVBO for InAs/GaAs using $In_xGa_{1-x}As$ with $x = 0.2$, 0.7, and 0.9 [21]. The energy difference between the Ga

3d and In 4d core levels was found to be approximately constant as a function of x, and the InAs/GaAs NVBO was determined to be 0.11 ± 0.05 eV. Previous measurements made by Kowalcyk et al. [22] on the actual heterojunctions found the valence-band offset to be 0.17 ± 0.07. The small difference between the NVBO and actual heterojunction valence-band offset was attributed to interfacial strain that arises from the 7 % lattice mismatch between InAs and GaAs, and it demonstrates the importance of measurements of the actual heterojunction band alignment for practical applications.

Figure 15.5a shows a band diagram of a clean semiconductor substrate. The valence- and conduction-band edges, E_V and E_C, respectively, the Fermi level, E_F, and two core levels, CL, are shown along with some slight band bending at the substrate/vacuum interface. As a semiconductor overlayer is deposited on top of the original substrate to create a heterojunction, some changes in band bending may occur, as shown in Fig. 15.5b. Shifts in the substrate E_V and E_C are due to this band bending that arises from new states created at the interface. Substrate core-level shifts are also affected by the band bending, and they may contain contributions from chemical shifts due to the different chemical bonding at the interface as compared to the bulk of the semiconductors, as highlighted in the lower CL of Fig. 15.5b.

Figure 15.5 highlights the practical details and complications of heterojunction band alignment measurements by photoelectron spectroscopy. The valence-band maximum can often be directly and uniquely probed, typically using an ultraviolet excitation source, allowing for the direct measurement of the valence-band offset.

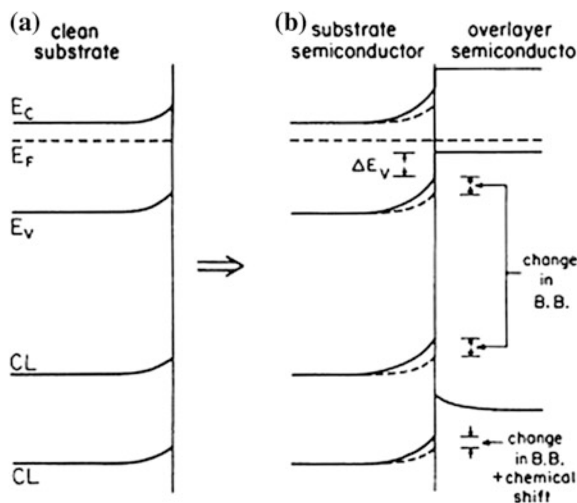

Fig. 15.5 Schematic band diagram for bare surface (**a**) and heterojunction interface (**b**). In (**b**), final band positions are shown with *solid lines* while the *dashed lines* represent the positions of the bare surface. These changes are due to differences in band bending for the valence band, conduction band, and one of the core levels. The second core level is also influenced by a chemical shift. Figure reprinted with permissions from [10]

This measurement requires first measuring the valence-band maximum for the clean substrate, followed by measuring the valence-band maximum of the overlayer. To account for band bending in the substrate, the overlayer must be deposited layer-by-layer in situ while a substrate core level is tracked. Chemical shifts may complicate this analysis, but as they often manifest as peak-shape changes, they can be accounted for. Katnani and Margaritondo [10] elegantly demonstrated this measurement technique using the interface of Si deposited on clean CdS, as shown in Fig. 15.6. Here, the valence-band maximum was determined from linear extrapolation of the leading edge of the valence-band spectrum to the zero-level background. A large ΔE_V of 1.55 eV is observed between the clean CdS and 20 Å of Si deposited on top. Additionally, at intermediate coverages, features from both CdS and Si are observed, allowing for the band bending to be accurately tracked. Clearly, such a measurement can only be so straightforward when such a large valence-band offset exists at the heterojunction.

Band alignment from such direct valence-band methods have been performed by many research groups on a variety of semiconductor systems. A few examples are presented below.

Maholwald et al. [20] explored the interface of Si and Ge (111) using photoelectron spectroscopy from both lab and synchrotron sources. Comparisons were made between the interface of Si deposited on cleaved Ge (111) at room temperature and at 300 °C. The two different deposition temperatures were found to give rise to different morphological structures, with the 300 °C deposition resulting in more epitaxial films according to low-energy electron diffraction measurements. Ge intermixing was also found with 300 °C deposition, as determined from the Ge substrate Auger electron decay with increasing silicon coverage; intensities for the

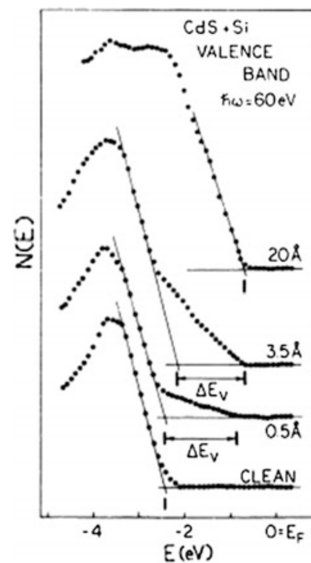

Fig. 15.6 Valence-band spectra for clean CdS and CdS with various coverages of Si. Figure reprinted with permissions from [10]

room temperature deposition decayed exponentially according to the expected escape depths, while at 300 °C a shallower decay was observed. The evolution of the Si valence-band alignment for the 300 °C deposition is shown in Fig. 15.7. Even with the significant differences in interface structure, no difference in valence-band alignment was found for the two temperatures, and a valence-band offset of 0.4 ± 0.1 eV is determined.

This was not the case, however, for silicon deposited on GaAs (110) [23]. Again, Si was deposited to different thicknesses at room temperature and 300 °C, this time on cleaved GaAs (110) surfaces. As on Ge (111), the different deposition temperatures led to different interface structures, with Ga and As segregation observed at 300 °C, while an abrupt interface was found at room temperature. With room temperature deposition, low-energy electron diffraction patterns showed the deposited Si to be disordered at all thicknesses, while at 300 °C, the Si was presumed pseudomorphic. Here, though, a significant difference was observed in the valence-band offset, shown in Fig. 15.8, with a valence-band offset of 0.6 ± 0.1 eV for room temperature depositions, but 0.3 ± 0.1 eV for 300 °C depositions. The difference in valence-band offset was attributed to differences in crystalline order which results in defect states for the room temperature deposited Si.

It is interesting to note the close agreement between the direct Si/Ge band-alignment measurements and the later NVBO measurements by Woicik and Pianetta [19]. This demonstrates that Si/Ge heterojunction band alignment is dominated by intrinsic effects, whereas for Si on GaAs (110), the more complicated morphology of the ionic IV/V versus the covalent IV/IV heterojunction plays a more significant role in the band alignment.

Differences in band alignment due to chemical changes were also probed by Mahowald et al. [24] using Si on InP (100) heterojunctions. As in the work on Si deposited on Ge (111) and GaAs (110), two deposition temperatures were used, room temperature and 280 °C. The intensities of the In and P Auger lines were

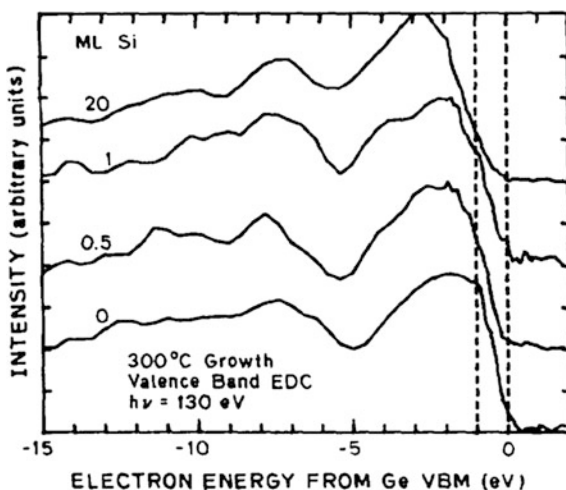

Fig. 15.7 Valence-band spectra for different thicknesses of Si (ML = monolayer) deposited on cleaved Ge (111) at 300 °C. Figure reprinted with permissions from [20]

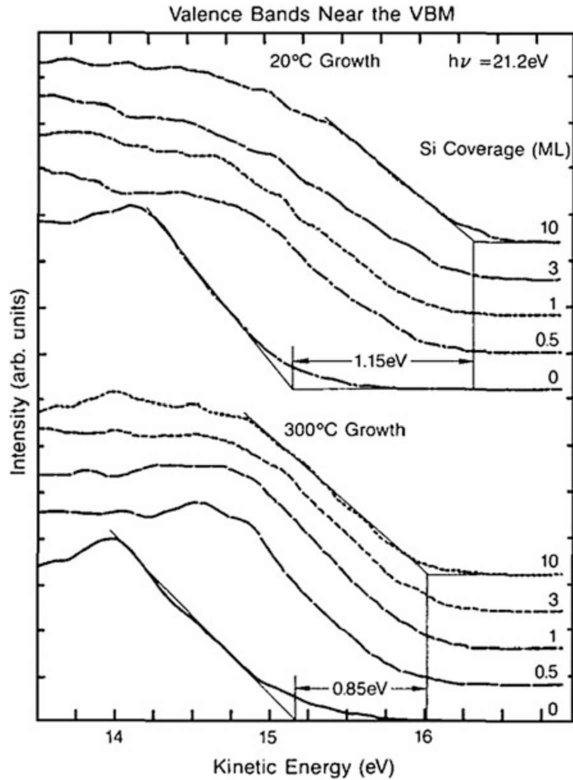

Fig. 15.8 Valence band of different thicknesses of Si (ML = monolayer) deposited on cleaved GaAs (110). Figure reprinted with permissions from [23]

tracked as a function of Si coverage; they were found to be linear with lower coverages (i.e. laminar growth), but leveled off with higher coverages, indicating the presence of In at the surface. The In 4*d* core level also showed additional features indicating multiple binding sites. The 280 °C growth showed higher in incorporation at the surface. This difference led to a subtle but significant difference in the valence-band offset, which was measured to be 0.56 ± 0.1 eV for the room temperature and 0.46 ± 0.1 eV for the 280 °C growth. These and above results for Si/GaAs interfaces demonstrate the role of the heterojunction fabrication in the ultimate band alignment.

Ultraviolet photoelectron spectroscopy is still frequently used for heterojunction band alignment measurements. Two technologically relevant examples used the method to determine the valence-band offsets at Si/SiO_2/HfO_2 heterostructures. Hf-based high dielectric constant (high-κ) oxides have been in use in devices since about 2007, and understanding the interface properties between Si and these oxides is essential for optimizing device performance. Sayan et al. [25] used synchrotron soft X-ray photoelectron spectroscopy to measure the valence-band offset of HfO_2 deposited on SiO_2/Si and SiO_xN_y/Si samples, finding an offset of −1.05 ± 0.1 eV between HfO_2 and SiO_2. The conduction-band offset was suggested to be 1.25 eV, but with a large uncertainty as the band gap of the HfO_2 layer was not measured.

A later paper combined photoemission, inverse photoelectron spectroscopy, and first-principles calculations to measure the band offsets of similar structures [26]. Here the valence- and conduction-band offsets between Si and HfO_2 were found to be 3.61 and 1.97 eV, respectively. These large offset values confirm HfO_2 can be used as a high-κ oxide for Si technologies as such a large offset will inhibit current leakage across the device.

15.2.3 Electrical Measurements: Internal Photoemission

As discussed in the previous section, heterojunction band alignment can be determined from measurements of valence-band shifts. However, the accuracy of these measurements can be limited when valence-band offsets are small. For example, the measurements by Katnani and Margaritondo [10] were only possible due to the large band offset between the CdS and Si (Fig. 15.6). Additionally, these measurements require in situ fabrication of the heterostructure, which may not accurately reflect either the properties of heterostructures fabricated by industrial techniques or those used in real devices. A further limitation of ultraviolet photoelectron spectroscopy-based heterojunction band-alignment measurements is the challenge introduced when similar materials are in the heterojunction, such as amorphous silicon and crystalline silicon. These problems can be better addressed with electrical measurements such as internal photoemission (IPE) spectroscopy. In IPE, a bias is placed across the heterojunction, and one side is illuminated with monochromatic photons. The photon energy is scanned; when it exceeds the barrier height, a photocurrent is induced. The measurement is repeated with various external biases, and the barrier height is found by the extrapolation of the photocurrent threshold to zero electric field [27]. Figure 15.9 shows a schematic of the IPE process.

Using IPE, Haase et al. [28] determined the conduction-band offset for GaAs/GaInP to be 0.108 eV. This technique was later used by Afanas'ev et al. [29]

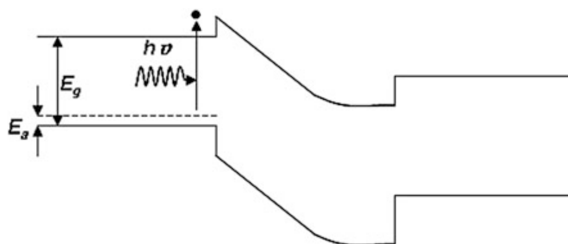

Fig. 15.9 Band diagram of a heterojunction showing the internal photoemission process. A bias, E_a, is applied across the heterojunction, and carriers are photoexcited over the barrier. The photocurrent threshold is measured, and the extrapolation of the threshold to zero electric field yields the energy barrier. Figure adapted from [28]

to measure the band offsets at HfO_2/Si (100) interfaces with thin (<2 nm) Si_3N_4, SiON, and SiO_2 interlayers. These measurements found the valence-band offset to be 3.1 ± 0.1 eV independent of the interlayer; a similar value was later found by Sayan et al. [26] in ultraviolet photoelectron spectroscopy of HfO_2/Si heterojunctions with no interlayer. Later, Afanas'ev and Stesmans [30] used IPE to measure the valence- and conduction-band offsets at HfO_2/Ge interfaces to be 3.0 ± 0.1 and 2.0 ± 0.1 eV, respectively.

15.2.4 Kraut's Method

While electronic measurements such as IPE can determine band offsets, they are not sensitive to the chemical details of an interface that can be elucidated using photoelectron spectroscopy. Photoelectron spectroscopy is therefore preferable when a more detailed understanding of interface formation is necessary. A photoemission method for heterojunction band alignment measurement that does not require in situ deposition is attributed to Kraut et al. [18]. This method is predicated on the fact that, for a given material, the energy difference between a core level and the valence-band maximum is a physical quantity, in analogy to core-level binding energies for noble gases that are referred to the vacuum level. Thus any shift in the valence-band maximum will likewise shift the core levels equivalently. An example band diagram is shown in Fig. 15.10. Three materials are indicated: semiconductors "A" and "B," and metal "M."

It can be seen that if the energy difference between the core level, E_{CL}, and the valence band, $E_{V,}$ are measured, the band alignment can be determined according to the following equations. For semiconductors:

$$\Delta E_V = \left(E_{CL}^A - E_V^A\right) - \left(E_{CL}^B - E_V^B\right) - \left(E_{CL}^A - E_{CL}^B\right), \quad (15.1)$$

Fig. 15.10 Example band diagram. Figure adapted from [18]

and if the band gap, E_g, is known

$$\Delta E_C = E_g^A - E_g^B + \Delta E_V; \tag{15.2}$$

for metals, the Schottky-barrier height, φ_B, is given by:

$$\varphi_B = \left(E_{CL}^B - E_V^B\right) - \left(E_{CL}^M - E_F\right) - \left(E_{CL}^B - E_{CL}^M\right). \tag{15.3}$$

Thus for band-alignment measurements, three photoemission measurements are made: first the core-level energy relative to the valence-band maximum for the reference materials identical to those in the heterostructure, then the core levels of the two materials in the actual junction. Changes in these values determine the band alignment.

An important aspect of Kraut's method is the accurate determination of the valence-band maximum in photoelectron spectroscopy. For a metal, the Fermi level is simply the inflection point of the Fermi foot. For semiconductors, however, that technically have zero density of states at the valence-band maximum, the situation is more complex. Linear extrapolation of the band edge can be used (see e.g. [10, 23] and discussion above); however, this simplification can introduce a high level of uncertainty into the band-edge determination. Kraut's method determines the valence-band maximum by fitting the valence-band spectrum with a theoretical density of states convoluted with a broadening function to account for experimental effects. It is important to note, however, that photoemission measures the sum of the angle-resolved partial densities of states modulated by their relative photoionization cross sections [31]:

$$I(E, h\nu) \propto \sum_{i,l} \rho_{i,l}(E)\sigma_{i,l}(E, h\nu). \tag{4}$$

Here, E is the photoelectron binding energy, hν is the incident photon energy, $\rho_{i,l}(E)$ are the angular momentum l-resolved partial density of states for the "i" atom, and $\sigma_{i,l}(E,h\nu)$ are the photoionization cross sections. The importance of the proper use of this equation for valence-band reconstruction has been demonstrated by Woicik et al. [32] for rutile TiO_2.

Figure 15.11 shows the valence-band reconstruction for diamond. The theoretical partial density of states calculated using the local-density approximation of density-functional theory shows that the valence-band maximum is comprised primarily of C 2p and not 2s states; however, due to the extremely low photoelectron cross section for C 2p states at this photon energy (2139 eV), the shape of the experimental valence band is considerably different. After accounting for the cross sections [33] and an experimental broadening of 0.3 eV, however, excellent agreement is achieved between the theoretical and experimental valence-band spectra, and the valence-band maximum can now be determined by fitting the theory to the measured data, shown by the line in the Fig. 15.11. It is evident that a simple linear extrapolation of the valence-band maximum to zero intensity would

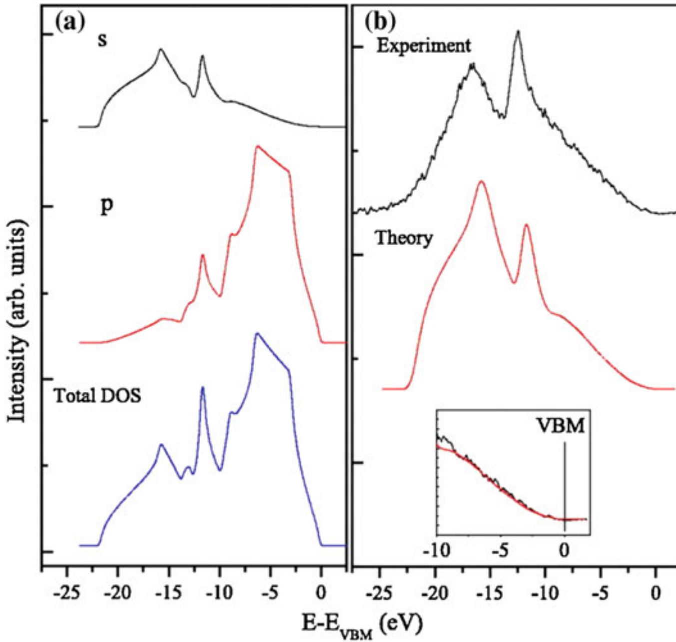

Fig. 15.11 Determination of the valence-band maximum for single-crystal diamond. Theoretically determined valence-band partial and total density of states are shown in (**a**). A theoretical valence-band spectrum is constructed by first normalizing the partial density of states to the photoelectron cross sections and then broadening the sum with a Guassian to account for experimental resolution. The experimental valence band, collected at hν = 2139 eV, and the theoretical reconstructed valence band are shown in (**b**). The valence-band maximum, determined by fitting the data to theory (see text), is highlighted in the *inset*. Figure reprinted with permissions from [35]

produce a valence-band maximum on the order of several eV lower than what is found by fitting the reconstructed density of states because the 2s density of states has so little intensity in this region. For additional accuracy, Kapilashrami et al. [34] have shown that GW approximation theory can be used to more properly account for the width of the valence band.

Kraut's method has been used for heterojunction band-alignment measurements, providing results of both industrial and fundamental importance. Waldrop et al. [36] measured and compared literature values of the band alignment for a series of heterojunctions, focusing specifically on the effect of crystallographic orientation, growth sequence (i.e. semiconductor A on B vs. B on A), and transitivity (ΔE_V (A − B) = ΔE_V (A − C) − ΔE_V (B − C)). They found that the band alignment is not always unique to the bulk properties of the materials, but that it may also depend on the specific interface. Small shifts were observed when comparing Ge/GaAs interfaces with different GaAs orientations; these differences were attributed to different electrostatic dipoles at the interface due to the differing polarities of the GaAs surfaces. Different valence-band offsets were also observed for GaAs/AlAs

versus AlAs/GaAs interfaces, as well as Ge/ZnSe versus ZnSe/Ge interfaces. Transitivity, which is predicted by various theories, e.g. [2, 6, 12], was found for the interface pairs ZnSe/GaAs and Ge/GaAs as well as GaAs/AlAs and Ge/GaAs, but it did not hold for the interface pairs CuBr/GaAs and Ge/GaAs, ZnSe/GaAs and Ge/GaAs, and AlAs/GaAs and Ge/GaAs.

One practical problem solved using Kraut's method was the band alignment of GaN, AlN, and InN heterojunctions. Group III–N materials have a multitude of applications in optoelectronic materials, including blue light emitting diodes, and understanding the band alignment between these materials is necessary for device design. Using Kraut's method, Martin et al. [37] measured the valence-band offset at GaN/AlN interfaces and found a valence-band offset of 0.8 ± 0.3 eV. Later, the same group measured InN/GaN, GaN/InN, GaN/AlN, AlN/GaN, InN/AlN, and AlN/InN interfaces. Here they found strong asymmetry in the band discontinuities based on the growth sequence, and they attributed their findings to strain-induced piezoelectric effects.

15.3 Band-Alignment Measurements Using HAXPES

15.3.1 Band Alignment at Ge/High-κ Interfaces

In practice, Kraut's method can and has been used in UPS, conventional lab-based XPS, and HAXPES, but HAXPES offers several advantages over the other techniques. First and foremost is the greater probing depth afforded due to the higher kinetic energies of the emitted photoelectrons, which permits the analysis of core levels in deeply buried interfaces in samples of technologically relevant film thicknesses, i.e. real heterojunctions. Thicknesses in devices may range from 1 nm for the thinnest oxides on Si to several tens of nm for metal contacts. The use of higher photon energies thus allows the study of real devices fabricated by industrial techniques.

The constant scaling of devices to decreased engineering dimensions raises the issue of tunneling as a fundamental limit to performance. For example, it is well known that tunneling through the gate oxide in SiO_2/Si transistors leads to significant energy loss due to leakage current and has necessitated the introduction of new materials in such architectures. Thickness dependence in heterojunction band alignment may also be an issue. As seen above in the IPE measurements of Afanas'ev et al. [29] and photoemission measurements of Sayan et al. [26], the presence of a thin (<2 nm) interlayer has no significant effect on the overall band alignment between HfO_2 and Si. This issue was raised more directly in the work of Rumaiz et al. [38], who measured the band alignment of HfO_2/Ge interfaces with and without N_2O-plasma passivation of the Ge substrate.

The two determining factors in heterojunction band alignment are generally considered to be the bulk electronic structure of the two materials (consider, for example, the NVBO [15] and the Anderson model [2]), and interface charge/dipoles (e.g. the

Tersoff model [12]). Ge treated with a N_2O plasma prior to HfO_2 deposition significantly alters the interface charge density, as shown by C-V measurements displayed in Fig. 15.12. However, the overall band alignment determined from the energy difference between the Ge 3d and Hf 4f core levels across the interlayer (Fig. 15.13) is not significantly affected, with valence-band offsets determined to be 3.3 ± 0.1 and 3.2 ± 0.1 eV for the treated and clean surfaces, respectively. Similar effects were seen at interfaces of $LaAlO_3$, $LaScO_3$, and Sc_2O_3 on Si with and without a 1 nm SiO_2 interlayer [39], as well as the interface between Au and a conductive polymer, poly [2-methoxy-5-(2′-ethyl-hexyloxy)-1,4-phenylene vinylene (MEH-PPV), with and without an interlayer of polar alkane-thiol monolayers [40]. These results can be attributed to the tunneling of the density of states through the thin interlayer.

The dependence of the interlayer thickness and possible effects of tunneling on band alignment was further probed using Ge/TiO_2 interfaces with varying thicknesses of a HfO_2 interlayer [41]. This is extremely important topic for establishing a fundamental lower limit to device thicknesses for band engineering. The bulk of the effort in the field of high-κ oxides on Ge has focused mainly on HfO_2 and ZrO_2, both of which can be fabricated using atomic layer deposition. High quality films of these materials with good interface properties have been successfully grown on pure and modified Ge surfaces [42–44]; theory and photoelectron spectroscopy measurements have shown favorable band offsets on Ge. However, HfO_2 and ZrO_2 both have $\kappa = 24$; based on the current scaling trend, it is evident that an oxide with κ near 40 would be ideal. Among the common oxides, TiO_2 is promising due to its high

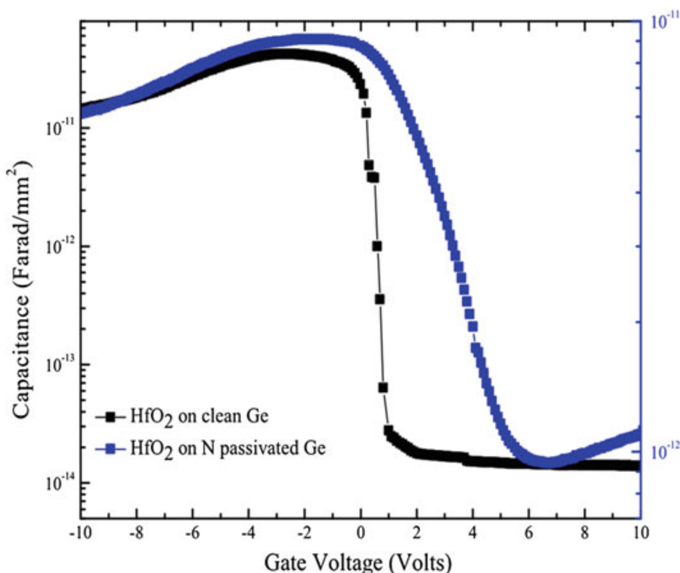

Fig. 15.12 Capacitance-voltage measurements taken at 100 kHz for HfO_2 on clean and N-passivated Ge. Aluminum was used as the top electrode. Figure reprinted with permissions from [38]

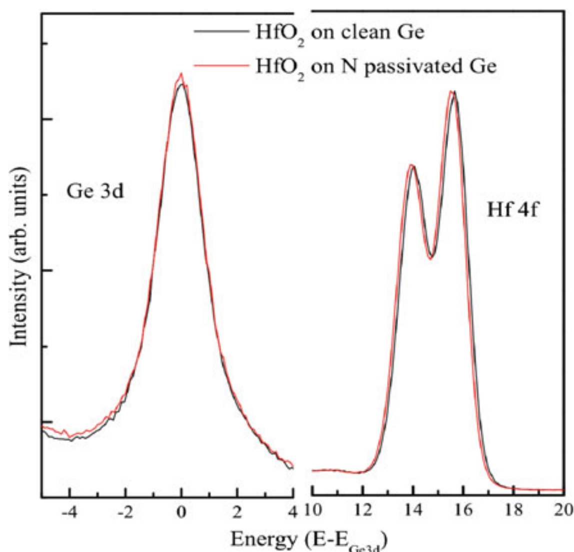

Fig. 15.13 HAXPES Ge 3d and Hf 4f core levels for HfO_2 collected at hν = 2139 eV for HfO_2 deposited on clean and N-passivated Ge. Figure reprinted with permissions from [38]

dielectric constant [45] and easy fabrication via atomic layer deposition. However, TiO_2 is known to have a small (poor) conduction-band offset with Ge, rendering it impractical as a gate oxide due to large leakage current. This problem has been addressed by introducing a suitable interlayer with higher conduction-band offset to introduce a potential step, and promising results using Al_2O_3 and HfO_2 as the interlayer have been published [46, 47]. The thickness of the interlayer depends on the choice of material; for example, it was shown that for Al_2O_3, to generate sub-nanometer effective oxide thickness with TiO_2, the thickness of the interlayer Al_2O_3 must be less than 0.8 nm [48].

TiO_2/HfO_2/Ge heterostructures were synthesized for HAXPES analysis using plasma enhanced atomic layer deposition with commercially available precursors. HAXPES Ge 3d, Ti 2p, and Hf 4f core levels recorded with photon energy hν = 2139 eV are shown in Fig. 15.14. Analysis of the Ge 3d core level shows decreasing elemental Ge and increasing GeO_x with increasing interlayer thickness. Interestingly, the Ti 2p and Hf 4f core levels show contrasting behavior. While the Ti 2p shows negligible change in peak width for different interlayer thicknesses, the Hf 4f shows a clear increase in the peak width with increasing interlayer thickness. This is a strong indication of chemical intermixing at the HfO_2/Ge interface. The Hf 4f core level can be modeled as a combination of a pure HfO_2 component and a Hf-germanate component.

The valence-band offset between HfO_2 and TiO_2 was determined using Kraut's method. Analyzing the GeO_x/HfO_2 interface is not straightforward, due to the unknown chemical state of the GeO_{x-}, and thus lack of relevant reference material. Also, to add to the complexity, the oxidation state of the GeO_x increases with the interlayer thickness. However, HAXPES allows determination of the core-level energy of the substrate Ge 3d, thereby producing the offsets between Ge and the

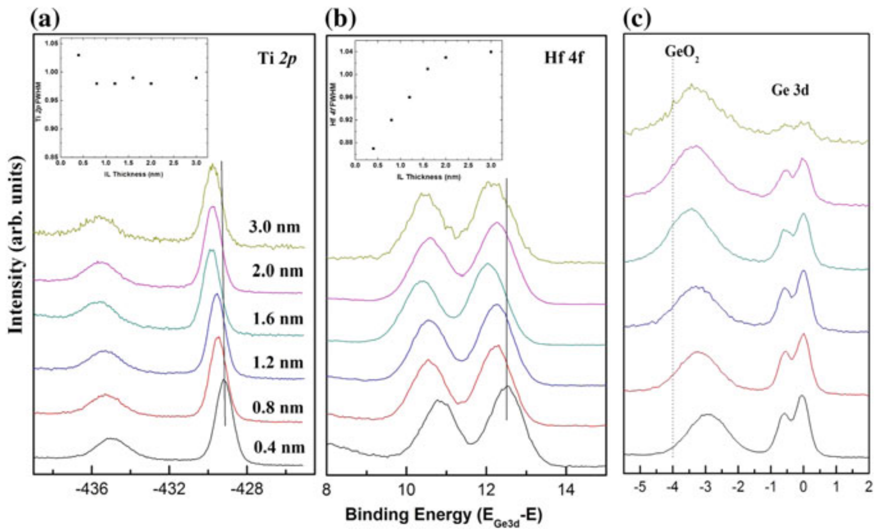

Fig. 15.14 Ti 2p, Hf 4f, and Ge 3d core levels in the structure $TiO_2/HfO_2/Ge$, with different thicknesses of HfO_2. The spectra were collected with photon energy hν = 2139 eV. The position of the Ge 3d line was set to 0. *Insets* show the core-level full width at half-maximum (FWHM) as a function of HfO_2 interlayer thickness. Figure adapted from [41]

HfO_2 interlayer; this is made feasible by the clear difference between the Ge substrate and oxide components. The valence-band offset decreases from 0.42 eV for the 3 nm interlayer thickness, to 0.22 eV for the smallest, 0.4 nm thickness. The resulting Ge/TiO_2 valence-band offset is shown in Fig. 15.15. The offset is seen to increase with thicknesses less than 2 nm, but it saturates at about 3.1 eV for HfO_2 thicknesses greater than 2 nm. These results demonstrate the dramatic role that

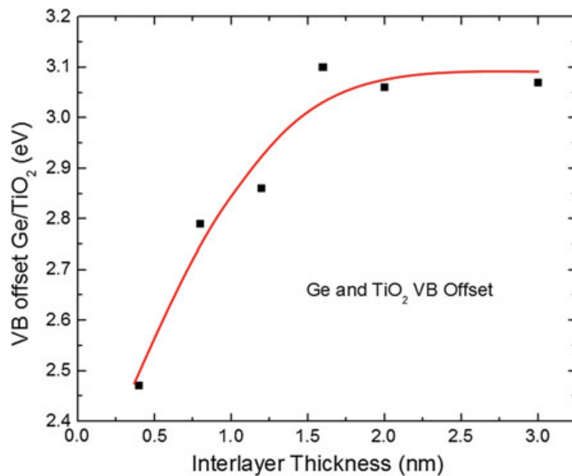

Fig. 15.15 Ge/TiO_2 valence-band offsets with different thicknesses of HfO_2 interlayer. Figure adapted from [41]

interlayer thickness can play in overall band alignment and indicate that ~1 nm may be the fundamental thickness limit to significantly affect band alignment.

15.3.2 Schottky-Barrier Heights at Diamond/Metal Interfaces

Another example of the use of HAXPES for heterojunction band-alignment measurements is found in the work of Gaowei et al. [35] measuring the Schottky-barrier heights of Ag and Pt contacts on diamond. Diamond is of interest for high-flux beamline monitors [49], but for proper function, high-quality blocking contacts must be employed. The study was performed to better understand the material and thermal load dependence of the diamond/metal contact.

5 and 10 nm Pt and 5 nm Ag films were sputter deposited on O-terminated diamond shards. The 5 nm Pt film was subsequently flash annealed to 600 °C. After annealing, the samples showed regions of high photo-conductivity, suggesting reduced barrier height between the diamond and the electrode. The effect of annealing on the Schottky-barrier height was determined by HAXPES. Due to the high density of Pt, hard X-rays are necessary to probe beneath films even as thin as 5 nm. For an Al Kα source (hν = 1486.6 eV), the inelastic mean free path (IMFP) for a C 1s photoelectron in Pt is only 1.4 nm, as calculated by the NIST IMFP database [50].

HAXPES valence band and C 1s, Ag $3d_{5/2}$, and Pt $4f_{7/2}$ core levels were collected for clean diamond, Ag, and Pt films. Data were collected with photon energy hν = 2139 eV. Determination of the diamond valence-band maximum was shown in Fig. 15.11 and discussed above. Using Kraut's method, the Schottky-barrier heights were found to be 2.3 eV for both the 5 and 10 nm unannealed Pt films on diamond, 2.1 eV for the annealed Pt film, and finally 1.87 eV for the Ag film. These values agree with the observed trends in the blocking nature of the contacts.

15.3.3 Band Bending in Metal-Oxide-Semiconductor Systems

HAXPES may also be used to measure band bending and Fermi-level pinning in metal-oxide-semiconductor systems. An examples of these measurements were published by Walsh et al. [51, 52] for Ni and Al on SiO_2/Si (100), and Al_2O_3 on GaAs (100). HAXPES provides a more direct route for the measurement of band bending as compared to capacitance-voltage measurements, which can be advantageous for systems with high density of interface states (D_{it}), such as GaAs.

In this work, band shifting was accomplished by the deposition of a high work-function metal, Ni, to act as a positive bias, and a low work-function metal,

Al, to act as a negative bias. A photon energy hν = 4150 eV provided an analysis depth of approximately 23 nm. Binding energies were referenced to the Fermi level of a gold foil measured immediately before and after the measurements for each sample.

For Si/SiO_2/metal systems, the application of the high/low work-function metals resulted in the downward/upward shifts of the Si 1s core level compared to the uncapped Si/SiO_2 interface, as shown in Fig. 15.16. The direction of these shifts is consistent with the expected changes in band bending from the applied metal contact; that is, the high work-function metal will act like a positive bias, shifting bands downward, while the low work-function metal will act like a negative bias and shift the bands upward. The magnitude of the shifts, however, were found to be less than expected, evidencing partial Fermi-level pinning due to the untreated Si/SiO_2 interface.

HAXPES was also used to measure band bending in the Si substrate. The location of the Si valence-band maximum below the Fermi level can be measured directly with careful calibration of the spectrometer work function. The valence-band maximum was found to be 0.95 eV for the n-type Si and 0.66 eV for the p-type relative to the calibrated Fermi level. The valence-band maximum was found to shift to 1.03 and 0.73 eV with Al and Ni electrodes, respectively on n-type Si and 0.8 and 0.45 eV for Al and Ni electrodes, respectively on p-type Si as determined from shifts in the Si 1s core level. These values were found in good agreement with electrical measurements.

The authors extended this work to GaAs/Al_2O_3 films, for which capacitance-voltage characteristics are more difficult to interpret due to the high D_{it} typically present [52]. The HAXPES measurement of the band bending is shown in Fig. 15.17. Much smaller band bending is observed in the GaAs compared with the Si. A total valence-band maximum shift of only 0.11 eV is observed between the Ni and Al capped n-type GaAs, and a shift of 0.15 is observed for the p-type GaAs.

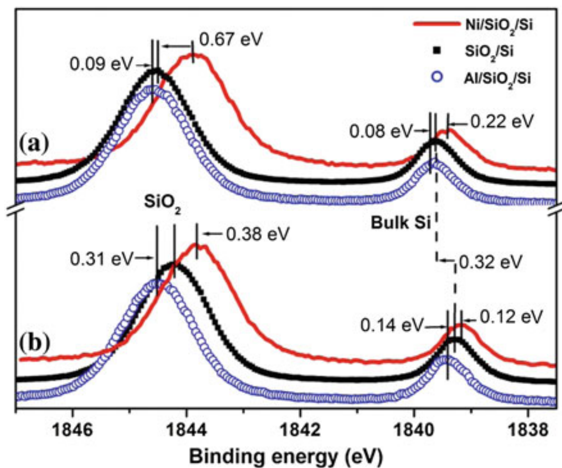

Fig. 15.16 Si 1s core levels measured with photon energy hν = 4150 eV, showing shifts and potential changes with metal deposition. Binding energies are referenced to the Fermi level. Measurements were made for n-type (**a**) and p-type (**b**) Si. Figure reprinted with permissions from [51]

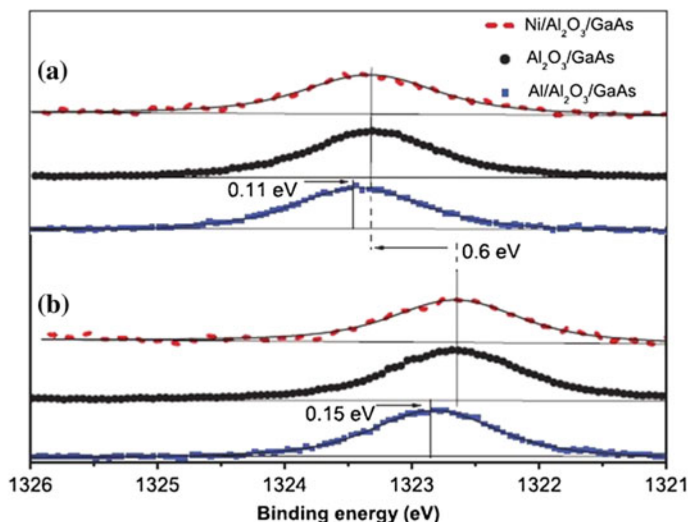

Fig. 15.17 As $2p_{3/2}$ core level measured with photon energy hν = 4150 eV, showing band bending with high and low work-function metal deposition. Measurements were made for n-type (**a**) and p-type (**b**) GaAs. Figure reprinted with permissions from [52]

These results suggest that the Fermi level is pinned between 0.8 and 1.11 eV above the valence-band maximum for Al_2O_3 on n-type GaAs, and between 0.4 and 0.75 eV above the valence-band maximum for Al_2O_3 on p-type GaAs.

15.3.4 Band Alignment in Ferroelectric Tunnel Junctions

Ferroelectric materials exhibit a spontaneous, switchable electric polarization that can be used for various device structures. The ability to scale down the ferroelectric while maintaining switchable polarization has opened the door to ferroelectric tunnel junctions [53–55]. Here, an ultra-thin ferroelectric film is used as a tunnel barrier between two metal electrodes and the polarization reversal is used to block/allow electron transport between them. Zenkevich et al. [56] made band-alignment measurements of ferroelectric $BaTiO_3$ (BTO) films sandwiched between Pt and Cr electrodes.

Measurements were performed using photon energy hν = 6 keV. BTO on Pt heterojunctions were investigated both with and without a Cr top electrode, so that both BTO/Pt and Cr/BTO interfaces could be probed. Band-alignment measurements were made using the Pt $4f_{7/2}$, Cr $2p_{3/2}$, and Ti $2p_{3/2}$ core levels. HAXPES measurements were made only on the heterostructures with spontaneous polarization towards the Pt electrode. Band offsets of 1.42 and 1.34 eV were found at the BTO/Pt and Cr/BTO interfaces, respectively. Using electrical measurements, the

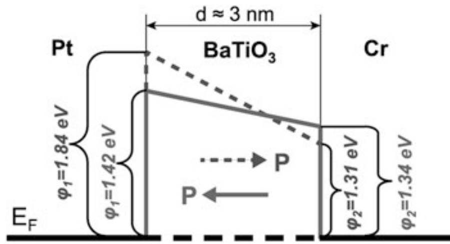

Fig. 15.18 Band offsets for Cr/BTO/Pt ferroelectric tunnel junctions with polarization towards the Pt (*solid lines*) or Cr (*dashed lines*) electrodes. Figure reprinted with permissions from [56]

offsets for the opposite polarization (towards the Cr electrode) were found to be 1.84 and 1.31 eV for the BTO/Pt and Cr/BTO interfaces, respectively. Results are summarized in Fig. 15.18.

Similar measurements were made using tender XPS (hν = 1100 eV) by Rault et al. [57], but with in situ biasing so that both polarizations could be probed by photoemission. Here a Nb-doped $SrTiO_3$ (NSTO) electrode was used in place of Cr. Band-alignment measurements were made at the top (Pt) electrode using the Pt $4f_{7/2}$, Ba $3d_{5/2}$ and Ti $2p_{3/2}$ core levels. Band offsets at the bottom (NSTO) were determined by electrical characterization. When polarization was towards the Pt electrode, band offsets of 0.4 and 0.45 eV were found at the Pt/BTO and BTO/NSTO interfaces, respectively, but in the reverse polarization, the offsets were 0.85 and 0.0 eV. These results and those of Zenkevich et al. [56] are important in verifying theoretical models describing the interfacial electronic structure at metal/ferroelectric interfaces.

15.3.5 Band Alignment in Photovoltaic Devices

In a photovoltaic device, photons are absorbed in a semiconductor, exciting a valence electron into the conduction band. Efficient electron and hole transport to low and high work-function electrodes is essential to produce current and avoid recombination. Consequently, band alignment is critical in the design of photovoltaic devices. In Si-based photovoltaics, charge separation can be assured using an n-type to p-type doping profile through the Si layer, but the same effect can be achieved using a uniformly-doped active layer and electrodes with proper band alignment. Ideally, the low work-function electrode would have a Fermi level close to the conduction-band minimum of the active layer for electron collection, while the Fermi level of the high work-function electrode would be close to the valence-band maximum of the active layer. Degenerately-doped semiconductors may also be used as electrodes, in which case the valence-band offset on the electron collection side must be large enough to block hole transport, while the conduction-band offset on the high work-function hole collection electrode should be large enough to block electron transport.

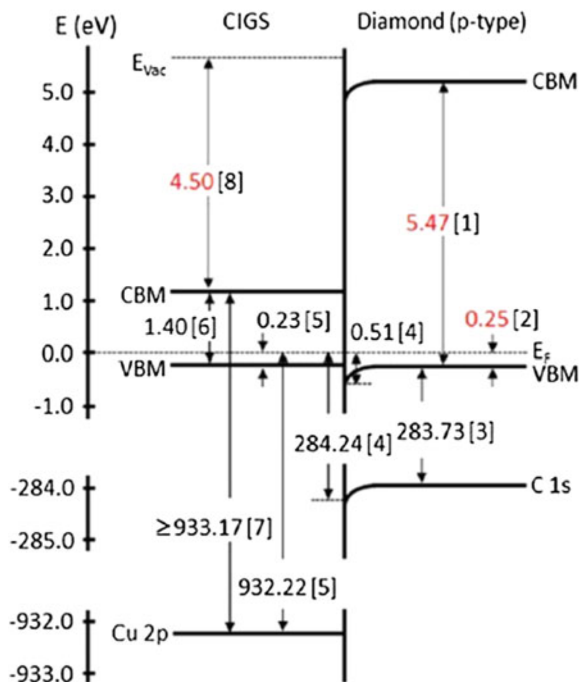

Fig. 15.19 Band alignment between $Cu_{0.78}(In_{0.32},Ga_{0.68})Se_2$ and B-doped diamond, measured by HAXPES and X-ray absorption spectroscopy. Figure reprinted with permissions from [34]

Recently, Kapilashrami et al. [34] used a combined HAXPES/X-ray absorption spectroscopy/first principles analysis to measure the band alignment at the interface between $Cu_{0.78}(In_{0.32},Ga_{0.68})Se_2$ (CIGS) and B-doped diamond films. CIGS is a commonly used photovoltaic absorber layer, with a band gap that can be tuned to the optimal range for the solar spectrum. Highly B-doped diamond was chosen as it is transparent to solar radiation. Figure 15.19 shows the resulting band alignment. Valence-band offsets were determined using Kraut's method, with the valence-band maximum fit from a GW calculated density of states, while band gaps were determined from the X-ray absorption measurements. A very slight valence-band offset and a large conduction-band offset is observed between the diamond and the CIGS films, which demonstrates the applicability of the B-doped diamond as an electrode for CIGS-based photovoltaics.

15.4 Summary and Outlook

This chapter has provided a brief overview of the various theoretical and experimental approaches to understanding heterojunction band alignment. While direct valence-band measurements of in situ-fabricated heterojunctions has been effective for some systems, the use of core-level shifts to determine band alignment has proven to be more applicable for measuring the band offsets and electronic structure

of "real-world" samples, as the measurement allows the heterojunctions to be fabricated ex situ using industrial techniques.

Band-alignment measurements using HAXPES provide the benefit of greater analysis depth and reduced surface sensitivity compared to low-energy methods, allowing for measurements of films over a wide range of thicknesses. This has become especially important as the dimensions of many layers in modern electronic devices coincide with the analysis depth of HAXPES measurements. With the increasing use and availability of HAXPES facilities at synchrotrons around the world, as well as the development of lab-based hard X-ray sources, further advances will be made in the understanding of semiconductor heterojunctions.

References

1. W. Shockley, Bell Syst. Tech. J. **28**, 435 (1949)
2. R. Anderson, Solid-State Electronics **5**, 341 (1962)
3. R. Dingle, W. Wiegmann, C.H. Henry, Phys. Rev. Lett. **33**, 827 (1974)
4. O. von Ross, Solid State Electron. **23**, 1069 (1980)
5. M.J. Adams, A. Nussbaum, Solid State Electron. **22**, 783 (1979)
6. W.R. Frensley, H. Kroemer, J. Vacuum Sci. Technol. **13**, 810 (1976)
7. W. Frensely, H. Kroemer, Phys. Rev. B **16**, 2642 (1977)
8. G.A. Baraff, J.A. Applebaum, D.R. Hamann, Phys. Rev. Lett. **38**, 237 (1977)
9. W.A. Harris, J. Vacuum Sci. Technol. **14**, 1016 (1977)
10. A.D. Katnani, G. Margaritondo, Phys. Rev. B **28**, 1944 (1983)
11. W. Harrison, J. Vacuum Sci. Technol. **14**, 1066 (1977)
12. J. Tersoff, Phys. Rev. B **30**, 4874 (1984)
13. C.G. Van de Walle, R.M. Martin, Phys. Rev. B **34**, 5621 (1986)
14. C.G. Van de Walle, R.M. Martin, Phys. Rev. B **35**, 8154 (1987)
15. C.K. Shih, W.E. Spicer, Phys. Rev. Lett. 58, 2594
16. S.P. Kowalczyk, J.T. Cheung, E.A. Kraut, R.W. Grant, Phys. Rev. Lett. **56**, 1605 (1986)
17. T.M. Duc, H. Hsu, J.P. Faurie, Phys. Rev. Lett. **58**, 1127 (1987)
18. E.A. Kraut, R.W. Grant, J.R. Waldrop, S.P. Kowalczyk, Phys. Rev. Lett. **44**, 1620 (1980)
19. J.C. Woicik, P. Pianetta, in Synchrotron Radiation Research: Advances in Surface and Interface Analysis, vol. 2, ed. by R.Z. Bachrach (Plenum Press, New York, 1992). (Chap. Studies of Si–Ge interfaces with surface EXAFS and photoemission, pp. 211–266)
20. P.H. Mahowald, R.S. List, W.E. Spicer, J. Woicik, P. Pianetta, J. Vac. Sci. Technol., B **3**, 1252 (1985)
21. J. Hwang, P. Pianetta, C.K. Shih, W.E. Spicer, Y.-C. Pao, J.S.H. Jr, Appl. Phys. Lett. **51**, 1632 (1987)
22. S.P. Kowalczyk, W.J. Schaffer, E.A. Kraut, R.W. Grant, J. Vacuum Sci. Technol. **20**, 705 (1982)
23. R.S. List, P.H. Mahowald, J. Woicik, W.E. Spicer, J. Vacuum Sci. Technol. **4**, 1391 (1986)
24. P.H. Mahowald, R.S. List, J.C. Woicik, P. Pianetta, W.E. Spicer, Phys. Rev. B **34**, 7069 (1986)
25. S. Sayan, E. Garfunkel, S. Suzer, Appl. Phys. Lett. **80**, 2135 (2002)
26. S. Sayan, T. Emge, E. Garfunkel, X. Zhao, L. Wielunski, R.A. Bartynski, D. Vanderbilt, J.S. Suehle, S. Suzer, M. Banaszak-Holl, J. Appl. Phys. **96**, 7485 (2004)
27. V. Adamchuk, V. Afanasev, Prog. Surf. Sci. **41**, 111 (1992)
28. M.A. Haase, M.J. Hafich, G.Y. Robinson, Appl. Phys. Lett. **58**, 616 (1991)

29. V.V. Afanasev, A. Stesmans, F. Chen, X. Shi, S.A. Campbell, Appl. Phys. Lett. **81**, 1053 (2002)
30. V.V. Afanasev, A. Stesmans, Appl. Phys. Lett. **84**, 2319 (2004)
31. S. Hüfner, Photoelectron Spectroscopy—Principles and Applications (Springer, Berlin, 1996)
32. J.C. Woicik, E.J. Nelson, L. Kronik, M. Jain, J.R. Chelikowsky, D. Heskett, L.E. Berman, G.S. Herman, Phys. Rev. Lett. **89**, 077401 (2002)
33. M. Trzhaskovskaya, V. Nefedov, V. Yarzhemsky, At. Data Nucl. Data Tables **77**, 97 (2001)
34. M. Kapilashrami, G. Conti, I. Zegkinoglou, S. Nemsak, C.S. Conlon, T. Torndahl, V. Fjallstrom, J. Lischner, S.G. Louie, R.J. Hamers, L. Zhang, J.H. Guo, C.S. Fadley, J.F. Himpsel, J. Appl. Phys. **116**, 143702 (2014)
35. M. Gaowei, E.M. Muller, A.K. Rumaiz, C. Weiland, E. Cockayne, J. Jordan-Sweet, J. Smedley, J.C. Woicik, Appl. Phys. Lett. **100**, 201606 (2012)
36. J.R. Waldrop, R.W. Grant, S.P. Kowalczyk, E.A. Kraut, J. Vacuum Sci. Technol. **3**, 835 (1985)
37. G. Martin, S. Strite, A. Botchkarev, A. Agarwal, A. Rockett, H. Morkoc, W.R.L. Lambrecht, B. Segall, Appl. Phys. Lett. **65**, 610 (1994)
38. A.K. Rumaiz, J.C. Woicik, G.A. Carini, D.P. Siddons, E. Cockayne, E. Huey, P.S. Lysaght, D.A. Fischer, V. Genova, Appl. Phys. Lett. 242108 (2010)
39. V. Afanasev, A. Stesmans, L. Edge, D. Schlom, T. Heeg, J. Schubert, Appl. Phys. Lett. **88**, 032104 (2006)
40. K. Demirkan, A. Mathew, C. Weiland, Y. Yao, A.M. Rawlett, J.M. Tour, R.L. Opila, J. Chem. Phys. **128**, 074705 (2008)
41. A.K. Rumaiz, J.C. Woicik, C. Weiland, Q. Xie, D.P. Siddons, G.H. Jaffari, C. Detavernier, Appl. Phys. Lett. **101**, 222110 (2012)
42. Q. Xie, S. Deng, M. Schaekers, D. Lin, M. Caymax, A. Delabie, X.-P. Qu, Y.-L. Jiang, D. Deduytsche, C. Detavernier, Semicond. Sci. Technol. **27**, 074012 (2012)
43. C.O. Chui, H. Kim, P.C. McIntyre, K. Saraswat, IEEE Electron Device Lett. **25**, 274 (2004)
44. N. Wu, Q. Zhang, C. Zhu, D.S.H. Chan, M.F. Li, N. Balasubramanian, A. Chin, D.-L. Kwong, Appl. Phys. Lett. **85**, 4127 (2004)
45. J. Robertson, Eur. Phys. J. Appl. Phys. **28**, 265 (2004)
46. Q. Xie, J. Musschoot, M. Schaekers, M. Caymax, A. Delabie, D. Lin, X.-P. Qu, Y.-L. Jiang, SVd Berghe, C. Detavernier, Electrochem. Solid-State Lett. **14**, G27 (2011)
47. S. Swaminathan, M. Shandalov, Y. Oshima, P.C. McIntyre, Appl. Phys. Lett. **96**, 082904 (2010)
48. Q. Xie, D. Deduytsche, M. Schaekers, M. Caymax, A. Delabie, X.-P. Qu, C. Detavernier, Appl. Phys. Lett. **97**, 112905 (2010)
49. E.M. Muller, J. Smedley, J. Bohon, X. Yang, M. Gaowei, J. Skinner, G. De Geronimo, M. Sullivan, M. Allaire, J.W. Keister, L. Berman, A. Hroux, J. Synchrotron Radiat. **19**, 381 (2012)
50. C.J. Powell, A. Jablonski, NIST Electron Inelastic-Mean-Free-Path Database, version 1.2 ed. (National Institute of Standards and Technology, Gaithersburg, MD, 2010)
51. L.A. Walsh, G. Hughes, P.K. Hurley, J. Lin, J.C. Woicik, Appl. Phys. Lett. **101**, 241602 (2012)
52. L.A. Walsh, G. Hughes, J. Lin, P.K. Hurley, T.P.O. Regan, E. Cockayne, J.C. Woicik, Phys. Rev. B **88**, 045322 (2013)
53. M.Y. Zhuravlev, R.F. Sabirianov, S.S. Jaswal, E.Y. Tsymbal, Phys. Rev. Lett. **94**, 246802 (2005)
54. H. Kohlstedt, N.A. Pertsev, J.R. Contreras, R. Waser, Phys. Rev. B **72**, 125341 (2005)
55. E.Y. Tsymbal, H. Kohlstedt, Science **313**, 181 (2006)
56. A. Zenkevich, M. Minnekaev, Y. Matveyev, Y. Lebedinskii, K. Bulakh, A. Chouprik, A. Baturin, K. Maksimova, S. Thiess, W. Drube, Appl. Phys. Lett. **102**, 062907 (2013)
57. J.E. Rault, G. Agnus, T. Maroutian, V. Pillard, P. Lecoeur, G. Niu, B. Vilquin, M.G. Silly, A. Bendounnan, F. Sirotti, N. Barrett, Phys. Rev. B **87**, 155146 (2013)

Chapter 16
HAXPES Studies of Advanced Semiconductors

Patrick S. Lysaght and Joseph C. Woicik

Abstract During the past decade, the semiconductor industry has experienced an unprecedented paradigm shift toward focused materials screening in order to keep pace with the rapid rate of device scaling dictated by Moore's Law. In addition, new device architectures have evolved that place greater demands on physical characterization techniques to interrogate subtle materials intermixing at buried interfaces. In this chapter, we demonstrate the general utility of HAXPES to probe sample materials representative of advanced semiconductor devices, thereby elucidating specific bonding configurations that limit electrical performance. HAXPES provides several distinct advantages for the analysis of advanced semiconductor devices; notably, the ability to probe structures of technologically relevant thicknesses and to tune the photoelectron depth sensitivity to measure changes with depth. Studies presented here include the influence of anneal temperature on transistor high-*k* gate dielectric layers deposited on both Si and high mobility SiGe and InGaAs substrates, substrate passivation processes, novel low resistivity metal contact formation, and the oxygen redistribution phenomenon associated with advanced memory structures. As materials and devices continue to evolve, it is clear that HAXPES will play a significant role in the successful integration of advanced devices into high volume manufacturing.

P.S. Lysaght (✉)
SEMATECH, Albany, NY 12203, USA
e-mail: pat.lysaght@sematech.org

J.C. Woicik
Materials Measurement Laboratory, National Institute of Standards and Technology,
Gaithersburg, MD 20899, USA
e-mail: joseph.woicik@nist.gov

© Springer International Publishing Switzerland 2016

J.C. Woicik (ed.), *Hard X-ray Photoelectron Spectroscopy (HAXPES)*,
Springer Series in Surface Sciences 59, DOI 10.1007/978-3-319-24043-5_16

16.1 High-*K* Gate Dielectrics

The grand challenge associated with the scaling of complementary metal oxide semiconductor (CMOS) devices beginning at the end of the 20th century was to develop a thin transistor gate insulator layer with a dielectric constant, k, higher (in the 10–25 range) than that of conventional silicon dioxide SiO_2 (k = 3.9) and with an equivalent oxide thickness (EOT) less than that of SiO_2 (1.0 nm) [1–4]. Compositional variations of the candidate material, metal-organic chemical vapor deposited (MOCVD) hafnium silicate $(HfO_2)_x + (SiO_2)_{1-x}$, have been evaluated by several techniques including high-resolution transmission electron microscopy (HRTEM), high angle annular dark field scanning transmission electron microscopy (HAADF-STEM), X-ray photoelectron spectroscopy (XPS), and secondary ion mass spectrometry (SIMS) in an effort to identify the chemical interactions at the high-*k*/Si substrate interface that must be controlled in order to achieve electrical performance requirements. Evaluation of the thermal stability of candidate high-*k* materials at that time involved a source/drain thermal activation process of 1000 °C for 10 s in a N_2 atmosphere. This requirement is above the crystallization temperature of binary oxide HfO_2, and it changes the material microstructure; i.e., phase segregation and crystallization occur, as is evident by HAXPES analysis of the O 1*s* binding energy shifts in Hf silicate relative to reference HfO_2 and SiO_2 samples as functions of composition and thermal processing [5–9].

By alloying HfO_2 with SiO_2 to form Hf silicate, $(HfO_2)_x + (SiO_2)_{1-x}$, the onset temperature of crystallization may be significantly increased to values that scale inversely with the HfO_2:SiO_2 ratio. A previously reported set of Hf silicate films (4.0 nm physical thickness) consisting of 60 mol.% HfO_2 and 40 mol.% SiO_2, annealed over a range of 800–1000 °C, revealed the onset of crystallization temperature to be 1000 °C by glancing-incidence X-ray diffraction (GI-XRD) measurements [7]. However, plan-view images of this sample set produced by HRTEM clearly illustrate evidence of crystallite formation at 800 °C. By comparison, (non-alloyed) HfO_2 films have been reported as polycrystalline (by XRD) following deposition at temperatures as low as 300 °C [8]. It is expected that Hf-silicate films transform to a phase separated microstructure upon cool down from rapid-thermal anneal (RTA) processing whereby the phase separation can take place in a manner that is large in degree and small in spatial extent as with the relatively large polycrystalline grains ($\sim$10 nm) illustrated in Fig. 16.1a. These grains result from nucleation and growth; they are small in degree and large in spatial extent [10]. The former material consists of a crystalline HfO_2-rich phase embedded in an amorphous silica-rich matrix. The latter mechanism corresponds to spinodal decomposition that is evident in the more dilute Hf silicate sample of Fig. 16.1c. Depending on composition and temperature, films in the amorphous phase will spontaneously phase separate and crystallize if they lie within the metastable spinodal or nucleate HfO_2 crystallites out of the amorphous phase [11].

The observed microstructures have been explained with a liquid miscibility gap in the ZrO_2–SiO_2 system shown in Fig. 16.2 [12, 13]. This region of liquid

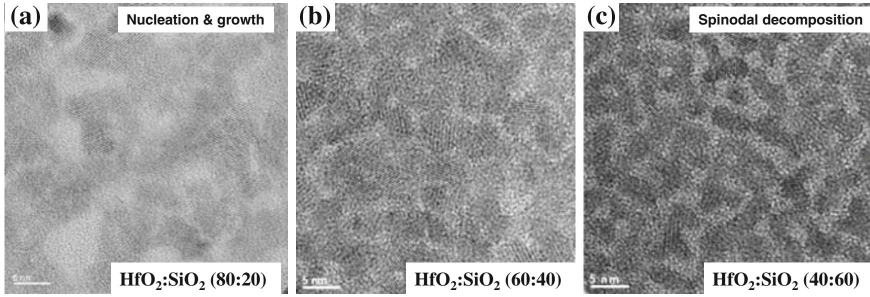

Fig. 16.1 Plan-view HRTEM images indicating Hf silicate compositional correlation of polycrystalline microstructure differences following RTA processing at 1000 °C for 10 s in N_2. **a** Nucleation and growth of crystals for 80 mol.% HfO_2, **b** 60 mol.% HfO_2 and **c** spinodal decomposition of 40 mol.% HfO_2 which results in crystals of smaller average grain size

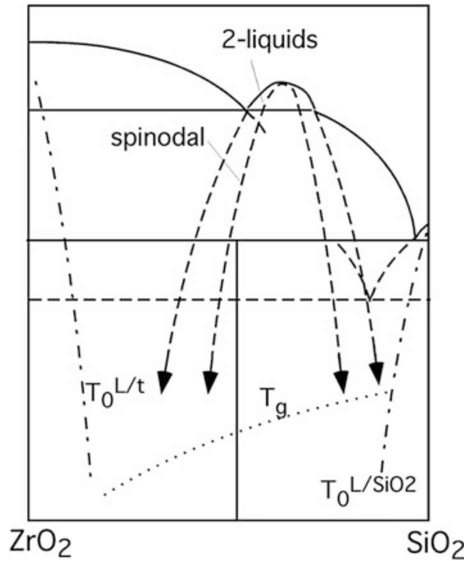

Fig. 16.2 Qualitative metastable phase diagram of the ZrO_2–SiO_2 system. Shown are the extensions of the liquid miscibility gap and spinodal (*dashed*), the glass transition temperature (*dotted line*), and T_0 curves (*dash-dotted line*). The metastable extensions of the liquidus lines become unstable in the spinodal and are not shown. Some of the stable phase fields were also excluded for clarity

immiscibility in the ZrO_2–SiO_2 system is assumed highly relevant to HfO_2–SiO_2 film systems and can extend as a metastable miscibility gap to lower temperatures and cause an amorphous film to lower its Gibbs free energy by separating into two phases with compositions defined by the extension of the metastable liquidus lines

[11, 14]. In addition, kinetic suppression of the crystalline silicate ($HfSiO_4$) has also been suggested for the short times associated with typical source/drain anneal processing as the formation of polycrystalline HfO_2 is thermodynamically preferred over formation of the complex Hf silicate structure [11, 12].

16.1.1 HAXPES Analysis of Hf Silicate

In order to obtain information pertaining to film partitioning and segregating into polycrystalline HfO_2 and SiO_2 and whether or not silicate remains in the film (perhaps at grain boundary regions), the XPS binding energy (BE) shifts of different films as a function of material composition and anneal temperature with minimal influence from interfacial roughness were studied.

The XPS binding energies have been referenced to the C 1*s* peak for adventitious carbon, (284.84 eV). Figure 16.3a shows the Hf 4*f* spectra from the binary metal oxide HfO_2 standard showing the Hf $4f_{7/2}$ and $4f_{5/2}$ at 18.54 and 16.88 eV, respectively. These values agree with previous reports for HfO_2 [9, 15–18]. The energy difference between these two peaks is ~1.7 eV. The Hf 4*f* BE is greater for the silicate than HfO_2 due to the higher electronegativity of the second nearest-neighbor silicon (Hf–O–Si bond) relative to hafnium (Hf–O–Hf bond) in the two materials [15]. Shifts in the BE of the Si 2*p* also reflect the effect of the second-nearest neighbor but the Si^{4+} 2*p* and the O 1*s* peaks are more difficult to interpret, as shown in Fig. 16.3b. Both spectra may illustrate evidence of Hf silicate

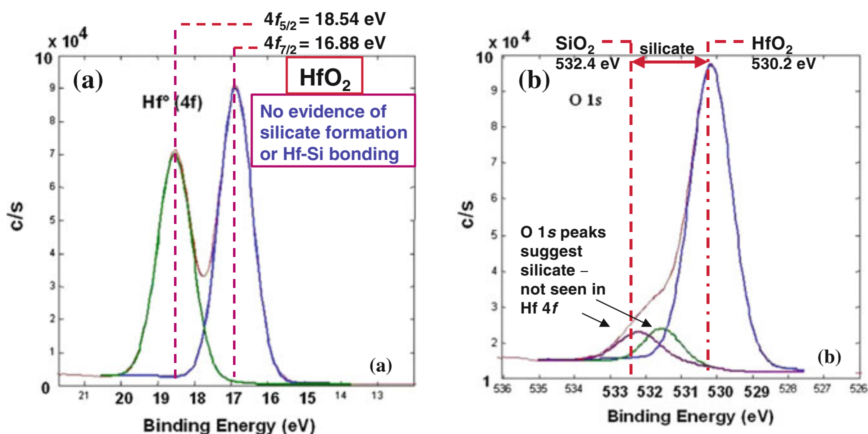

Fig. 16.3 XPS spectra for the HfO_2 reference annealed at 1000 °C for 10 s **a** Hf $4f_{7/2}$ at 18.54 eV and $4f_{5/2}$ at 16.88 eV and **b** the O 1*s* peak position at 530.2 eV with a *dashed reference line* at 532.4 eV for comparison to the O 1*s* peak identifying the Hf silicate (or sub-stoichiometric oxide) range

by shifts to lower BE relative to the reference SiO_2; however, this BE shift remains indistinguishable from sub-stoichiometric oxide ($SiO_{<2}$) and, therefore, inconclusive as evidence for Hf silicate. The apparent "silicate" peaks are not expected in the HfO_2 standard and may indicate silicate formation in the interface between the Si substrate and its unintentional oxide. This point is critical as there was much debate in the literature regarding indistinguishable substoichiometric SiOx and real Hf-silicate formation due to mixing of the HfO_2 with SiO_x. It is also clarified in discussions pertaining to Fig. 16.12, etc.

The chemical shift of the metal core level (Hf 4*f*) and Si 2*p* level with respect to the BE of the pure metal and Si oxides, respectively, vary as a function of the metal fraction in the silicate [15]. The Hf 4*f* spectra in Fig. 16.4 corresponds to 40 mol.% HfO_2 silicate. The BE peaks of Fig. 16.4a (560 °C/120 min anneal) are shifted higher relative to the Hf 4*f* spectra corresponding to HfO_2 (Fig. 16.3). By contrast, Fig. 16.4b illustrates the Hf 4*f* spectra of 40 mol.% HfO_2 silicate annealed at 1000 °C for 10 s where both XRD and plan-view HRTEM indicate evidence of polycrystalline HfO_2. The two-peak simulation utilized to produce an accurate fit of the data consists of a pair of Hf 4*f* doublets; (1) one corresponding to the BE of the 560 °C sample (Fig. 16.3a) and (2) the other corresponding to the binary metal oxide suggesting the material has phase segregated into HfO_2 and Hf silicate (Fig. 16.4b).

A comparison between the O 1*s* core level for the 40 and 60 % SiO_2 Hf silicate films of Fig. 16.5 illustrates the matched ratio of 60:40 for both the Hf-rich and the Si-rich compositions and the peak intensity ratios observed in Fig. 16.5a, b agree with the expected energy response.

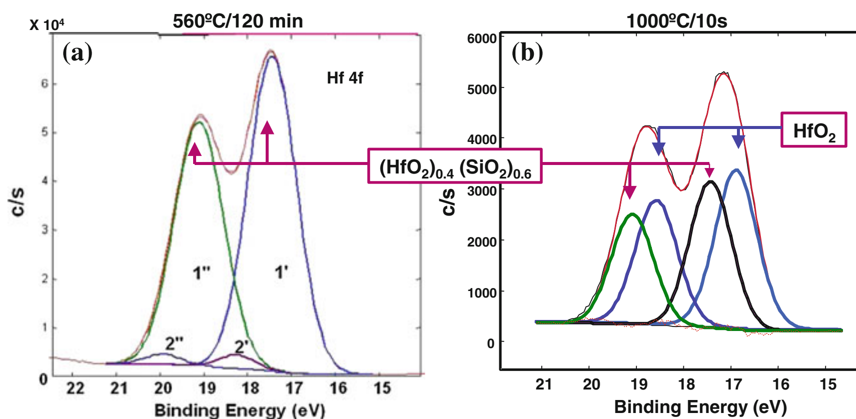

Fig. 16.4 XPS spectra of two 40 mol.% HfO_2 (60 mol.% SiO_2) film samples **a** annealed for 120 min at 560 °C and **b** annealed to 1000 °C for 10 s. The simulated Hf 4*f* spectra common to both samples ($4f_{7/2}$–17.4 eV, $4f_{5/2}$–19.1 eV) is indicative of the silicate composition

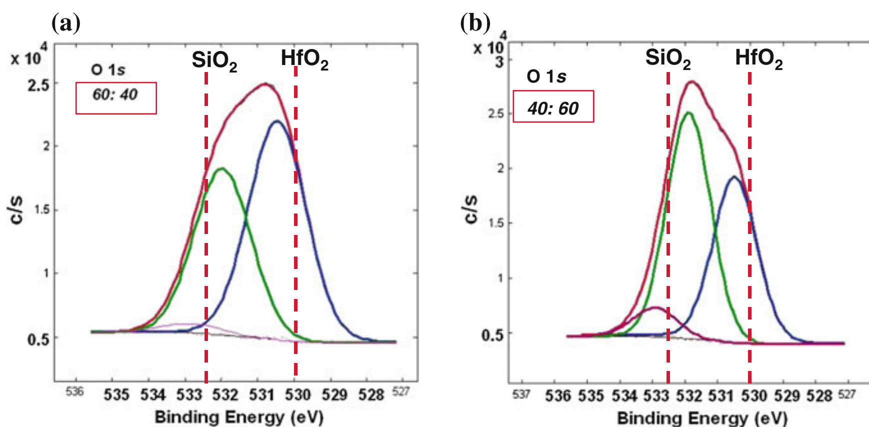

Fig. 16.5 O 1*s* spectra of two Hf silicate films following 1000 °C at 10 s RTA **a** 60 mol.% HfO_2 (40 mol.% SiO_2) indicating greater intensity toward the HfO_2 reference BE and **b** 40 mol.% HfO_2 (60 mol.% SiO_2) indicating greater intensity toward the SiO_2 reference BE

16.1.2 XANES Analysis of Hf Silicate

X-ray absorption near-edge fine-structure (XANES) analysis of the oxygen *K*-edge in combination with HRTEM has been used to further investigate phase separation of Hf-silicate thin films subjected to high-temperature annealing. Of particular interest was the relationship between phase separation and the unoccupied states, using HRTEM and XANES analysis. XANES is a sensitive tool to probe unoccupied states, complementary to the occupied state analysis of XPS, and it can be used to detect bonding changes as might be associated with phase separation. The lowest unoccupied states determine the conduction band offsets with silicon and the barrier heights for electrons, an important criterion for the suitability of the material as a gate dielectric [19].

The O *K*-edge of transition metal (TM) oxides and silicates show two sharp features near threshold due to hybridization with the TM *nd* states (the $s \rightarrow d$ transition is forbidden by the dipole selection rule) [20]. This double-peak structure is attributed to the crystal field splitting of the TM *d*-orbitals in non-spherical coordination with the ligand. XANES and electron energy loss near edge-fine structure (ELNES) data of the cubic, tetragonal, and monoclinic modifications of crystalline ZrO_2 [21], $ZrSiO_4$ [22, 23], and HfO_2 [24, 25], and of amorphous as well as crystalline SiO_2 [26, 27] have been reported. Peaks at higher energy in the O *K*-edge spectra of ZrO_2 and HfO_2 are due to excitations into bands formed by TM *s* and *p* states hybridized with the oxygen 2*p* level. In $ZrSiO_4$, additional peaks at higher energies are due to states from silicon, in particular, 3*s*3*p*3*d* orbitals hybridized with oxygen 2*p*. In SiO_2, the main features are due to transitions into oxygen 2*p* states hybridized with Si 3*s*, 3*p*, and 3*d* states.

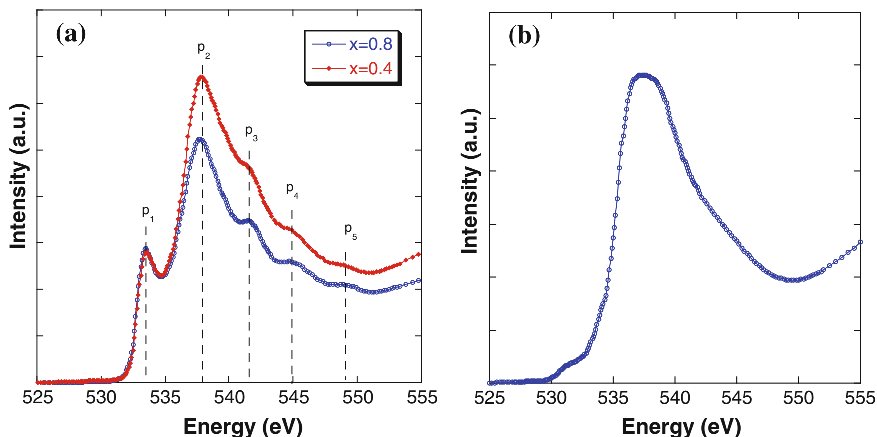

Fig. 16.6 Oxygen *K*-edge XANES of **a** the film with 80 mol.% HfO_2 (*open circles*) and the film with 40 mol.% HfO_2 after rapid thermal annealing at 1000 °C for 10 s (*filled diamonds*), and **b** an amorphous SiO_2 thermal oxide film on Si. No absolute energy calibration was performed. The spectra were shifted so that the peaks coincided with literature values

Figure 16.6 compares O *K*-edge XANES obtained from films with 80 mol.% HfO_2 and 40 mol.% HfO_2 after annealing at 1000 °C for 10 s in flowing nitrogen to an amorphous SiO_2 film. The near-edge fine structures of the oxygen *K*-edges of the two Hf-silicate films are similar, yet the relative intensities of peaks p_1 and p_2 are different.

The oxygen *K*-edge fine-structure can, in a first approximation to the segregated microstructure, be interpreted simply as the addition of spectra from amorphous silica and pure crystalline hafnia. Increasing amounts of silica in the samples result in an increase of bulk silica-like features in the oxygen *K*-edge. Peak p_1, at approximately 533.5 eV, reflects transitions into the lowest O 2*p*-Hf *d* hybridized band. The energy position of the second *d*-state feature of HfO_2, at about 537.2–537.5 eV [24, 25, 28], also corresponds to the energy position of the main peak in amorphous SiO_2 (Si 3*s*3*p* states) [26, 28]. Peak p_2 therefore represents an overlap of the second *d*-state peak from HfO_2 with the main peak of silica. This interpretation is supported by the increased intensity ratio of p_2 to p_1 in the film with $x = 0.4$. The O *K*-edge XANES of crystalline HfO_2 shows peaks at ~541 eV and ~544 eV [24], due to Hf *s* and *p* states hybridized with O 2*p*, at the energies of p_3 and p_4 in the film spectra. The origin of peak p_5 could not be identified unambiguously. In both samples, the peak positions are nearly identical. The widths of the Gaussian fit curves of p_3 and p_4 are somewhat narrower in the film with $x = 0.4$. Crystalline zircon shows four distinct features in the region after the first two peaks, which should also be observed for the isostructural hafnia. The phase separated films show only three peaks in this energy region.

The absence of silicate-type bonding becomes apparent by adding together the O *K*-edge spectra of an amorphous silica film with that of the $x = 0.8$ sample which

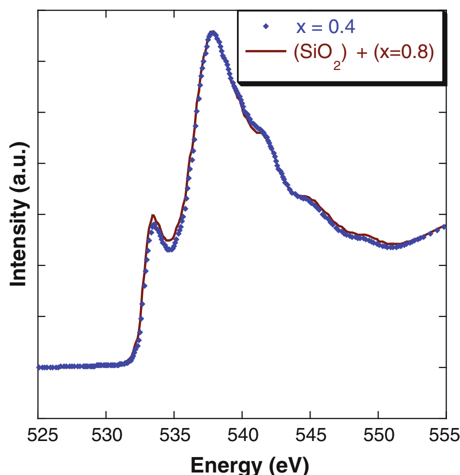

Fig. 16.7 Sum of the oxygen *K*-edges of the sample with $x = 0.8$ and SiO_2 (*solid line*) and comparison with the spectrum of the sample with $x = 0.4$ (*diamonds*)

reproduces the O *K*-edge of the sample with $x = 0.4$ (Fig. 16.7). The additional SiO_2 in the sample with $x = 0.4$ therefore has mostly bulk silica electronic structure and bonding. Even for an abrupt interface, this result is somewhat surprising, given the small length scale of the microstructure of this sample ($\sim$5 nm), in which a significant fraction of the microstructure is composed of interfacial silica and hafnia that might not have the bulk electronic structure [28, 29].

Considering the conduction band offset with silicon, the XANES spectra show that, due to the phase separation, the lowest unoccupied states of the alloyed film correspond to those of the *d*-states of pure HfO_2; i.e., the edge onset in both films occurs at the same energy. Therefore, in terms of increasing the conduction band offsets with Si, and given the typical device annealing temperatures above the onset of phase separation, the HfO_2–SiO_2 films have no advantage over the binary oxides.

16.2 Nitridation of HfO_2

Due to chemical phase separation and crystallization of the HfO_2, it is clear that there is no electrical performance advantage of Hf-silicate over HfO_2. Therefore, performance advantages associated with nitrogen incorporation into HfO_2 have been evaluated since N reduces the diffusion rate of boron (as well as all other elements). N incorporation also elevates the crystallization temperature since crystallization is a diffusion-limited phase transition where the rate depends on the Gibbs free-energy difference of the phases and the diffusion rate of the species involved.

The samples have been prepared to enable direct comparison of the influence of the Si ⟨100⟩ substrate starting conditions on subsequent NH_3 nitridation. Si treatment consisted of an in situ steam generated (ISSG) 2 nm thick thermal SiO_2 reference (sample A) and H-terminated substrates (samples B and C) exposed to an

Table 16.1 Sample set indicating NH_3 exposure both pre and post HfO_2 deposition and the resultant N dose measured by nuclear reaction analysis using $^{14}N(d,\alpha)^{12}C$

Sample	Interface	Pre-treatment	HfO_2 (nm)	Post-anneal	[N] 1E15/cm^{-2}
A	2 nm SiO_2	None	3	NH_3 PDA	3.566
B	HF-Last	NH_3-Pre-DA	3	None	2.137
C	HF-Last	NH_3-Pre-DA	3	NH_3 PDA	5.907

NH_3 chemical anneal process. Sample A did not receive NH_3 chemical treatment prior to HfO_2 deposition while samples B and C were exposed to NH_3 directly on the H-terminated Si substrate. These chemical treatments were followed by atomic-layer deposition (ALD) of HfO_2 (3 nm thick) and characterized as-deposited and with an NH_3 post deposition anneal (PDA) process, as per the process splits indicated in Table 16.1. Sample B maintained the HfO_2 film as-deposited, without the NH_3 PDA.

The N dose difference between sample B and C shows the N incorporation efficiency of the NH_3 PDA process with the final N dose ranging from approximately 7.6–20 at.%. STEM, EELS and Energy Dispersive X-ray Spectroscopy (EDXS) were used to further study the samples. The EDXS element profiles are plotted in the lower portion of Fig. 16.8. They were acquired along a straight line from the Si substrate, through the interface layer (IL), and then through the uncapped HfO_2 layer of the stack. The physical separation and slope of the Hf and O signals within the IL region are consistent with previous reports that claim Hf is not present in measurable quantities in the IL near the Si substrate. The influence of the starting Si substrate chemical treatment is clearly illustrated by the position and relative intensity of the N profile of each sample. The HF-last (H-terminated) substrate condition of sample B and C results in (substrate) Si–N bond formation which does not occur for sample A where the Si–N bonding is due to SiO_xN_y formation of the oxidized substrate. Sample A represents a reference film system in that the 3 nm HfO_2 was deposited on

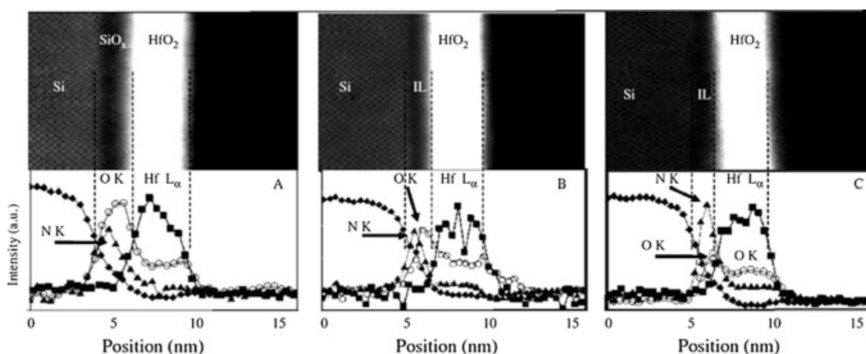

Fig. 16.8 HAADF-STEM Z-contrast images and corresponding EELS chemical scan element profiles illustrating the position and relative abundance of N incorporation as a function of NH_3 processing and starting substrate condition for samples A, B and C as specified in Table 16.1

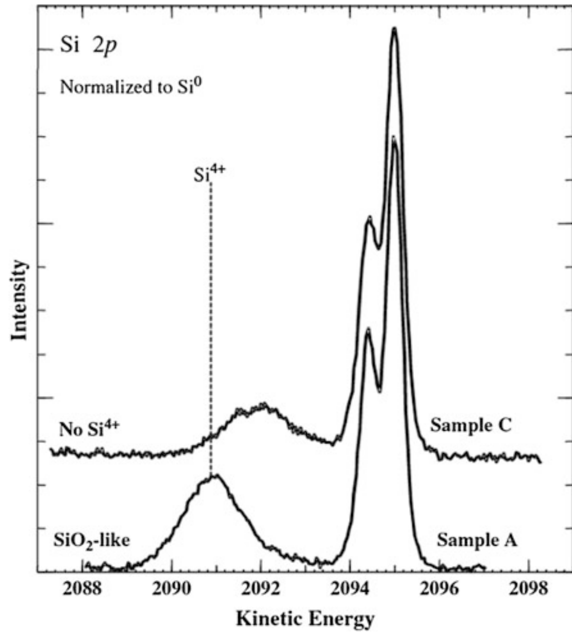

Fig. 16.9 Si 2*p* core-level spectra indicating the starting Si substrate process of HF-last results in H-terminated Si which restricts Si from achieving four coordination (Si^{4+}) with O (sample C). The reference thermal oxide (sample A) exhibits a significant Si^{4+} peak although N is detected in its bottom interface resulting from NH_3 PDA

a standard ISSG SiO_2 followed by the NH_3 PDA process. Beginning in the Si substrate and following the EELS profiles outward across the film system in cross section reveals an oxidized substrate which evolves into a SiO_xN_y IL between Si and HfO_2.

The Si 2*p* spectra shown in Fig. 16.9 provide additional information regarding the significant difference in Si coordination in the bottom IL. As shown in the EELS spectra of Fig. 16.8, nitrogen is detected with a peak profile in the bottom interface of sample A due to the NH_3 PDA process. This apparent SiO_xN_y IL between Si and HfO_2 appears much like thermal SiO_2 from the perspective of Si coordination and the evidence of the strong Si^{4+} peak associated with sample A in Fig. 16.9. By comparison, the hydrogen terminated (HF-last) Si substrate (sample C) which was exposed to NH_3 processing both pre and post HfO_2 deposition, clearly does not exhibit much of a Si^{4+} peak and therefore does not consist of significant amounts of stoichiometric SiO_2. Films exposed to a PDA process consisting of NH_3 exhibit a significant amount of N in the bulk film, which has been quantified by nuclear reaction analysis (NRA) and corroborated by the identification of Hf–N and Si–N bonding in XPS spectra.

By comparing films exposed to the NH_3 PDA process with otherwise identical films exposed to an N_2 PDA (which does not incorporate an appreciable amount of N into the bulk high-*k* film), for the same time and temperature, the effect of N incorporation has been decoupled from that of the thermal cycle alone. It is important to note that N incorporation resulting from NH_3 dissociation at the PDA temperature likely consists of NH_2^- and a proton H^+. Further dissociation of the

NH_2 molecule may lead to the formation of NH species where NH^0 is stable while NH^- is unstable, suggesting the likely final products of the NH_3 PDA process are NH_2^-, NH^0 and H^+, H^- [30]. Nitrogen may exchange for O via displacement of lattice oxygen ions in the grain structures of HfO_2 films and/or incorporate in lattice interstitials as excess N. In contrast to the N_2 molecule, the atomic N interstitial has no affinity for a second electron and is also stable as a positive ion. Additionally, grains consisting of Hf–N bonds are not consistent with metal bonds but behave much like the dielectric Hf_3N_4, since the permittivity of these films remains high, although shorter Hf–N bond lengths will contribute local strain in tetragonal and monoclinic HfO_2 [30].

Electrical properties of the dielectric films and interfaces have been characterized by metal-oxide semiconductor field-effect transistor (MOSFET) measurements. Transistors were fabricated using 3 nm HfO_2 gate dielectrics with 10 nm TiN/poly-Si gate electrodes formed by chemical vapor deposition (CVD) of tetrakis (diethylamido)titanium (TDEAT) with NH_3 followed by 180 nm of phosphorus doped poly-Si. The relationship between gate current density Jg at V_{fb-1} (where V_{fb} is the flatband voltage) and EOT for the gate dielectric stacks with several types of bottom interfacial oxides, with and without NH_3 treatment, is shown in Fig. 16.10a. For each bottom interfacial oxide studied, incorporating NH_3 resulted in slightly lower EOT relative to the same interfacial oxide without NH_3. This finding is consistent with the higher permittivity reported for silicon oxynitride relative to SiO_2 [31]. The influence of the NH_3 treatment on Jg is more difficult to isolate since

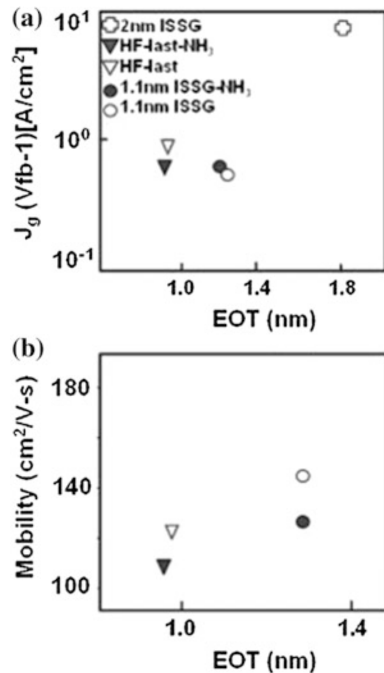

Fig. 16.10 Plot of **a** gate leakage current Jg versus EOT and **b** high field mobility vs EOT for transistors with 3 nm HfO_2 and several types of bottom interfacial oxides compared with and without NH_3 treatment

leakage current is a strong function of EOT. Figure 16.10b shows the plot of EOT versus effective high field electron mobility at 1 MV/cm. Formation of a high-quality thermal SiO_2 interface between the Si substrate and high-k dielectric enhances electrical performance and more specifically electron mobility [32]. There have been numerous reports that identify various specific components of mobility degradation with HfO_2, including phonon scattering [33], Coulomb scattering [34], transient charge trapping [35], and surface roughness [36, 37]. Coulomb scattering has been shown to dominate low field mobility, while phonon scattering and surface roughness dominate mid- and high-field nobilities, respectively [38]. Kirsch et al. investigated improvements in peak- and high-field electron mobility corresponding to physical scaling of the HfO_2 layer and attributed the results to reduced charge trapping and Coulomb scattering in the thinner films [39]. The general trend of mobility degradation with aggressive scaling of the bottom interface thickness is observed in Fig. 16.10b, which compares an HF-last chemically treated Si substrate with a 1.1 nm thick ISSG SiO_2 interface with and without NH_3 treatment. The mobility degradation associated with the NH_3 treated interfacial oxide may correspond to a combination of nonstoichiometric SiO_2 and the remote Coulomb scattering (RCS) contribution from the HfO_2 film in closer proximity to the substrate.

The Hf 4*f* core-level spectra of samples A, B and C are shown in Fig. 16.11. They clearly demonstrate the influence of the NH_3 PDA on the local coordination of the Hf atoms in these thin HfO_2 films. The well resolved transition metal core-level doublet (Hf $4f_{7/2}$ and Hf $4f_{5/2}$) of sample B corresponds to as-deposited HfO_2 while

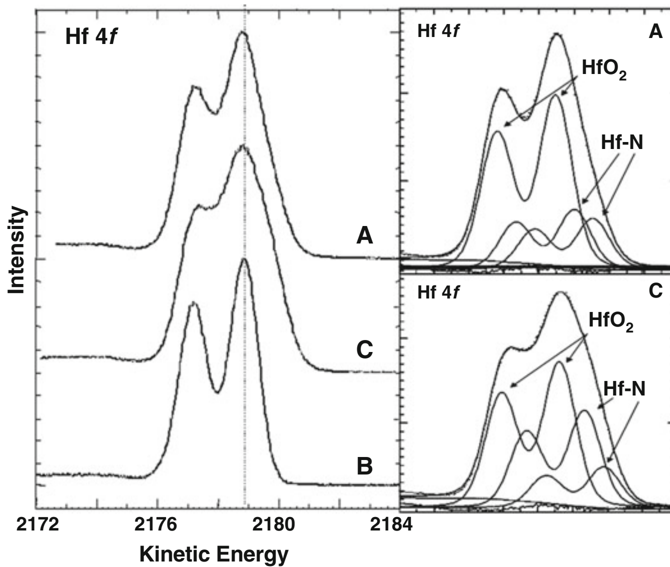

Fig. 16.11 Hf 4*f* core-level spectra of samples A, B and C. Samples A and C have been exposed to NH_3 PDA which introduces Hf-N bonding and accounts for the peak broadening. Sample A has a 2 nm SiO_2 bottom interface while samples B and C where both processed on HF-last substrates

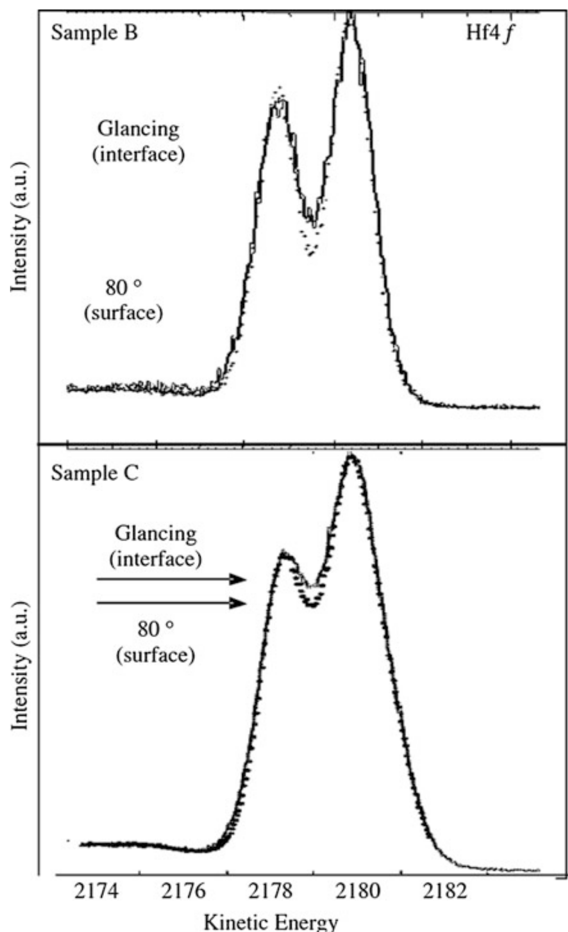

Fig. 16.12 Hf 4*f* core-level spectra recorded at glancing and near-normal incidence for samples B and C that emphasize the interface and surface regions of the HfO_2 layer, respectively. The result is consistent with HfO_2 and not Hf silicate formation at the interface with SiO_2

the relatively poorly resolved doublet of samples A and C result from the exposure to the NH_3 PDA process. Core-level fitting for samples A and C using the lineshape of sample B reveals the contribution of Hf–N bonding (lower binding-energy shift) to the spectra. Although sample A reveals a significant degree of crystallinity by HRTEM, Hf–N bonds broaden the line to lower binding energy following exposure to NH_3 relative to the as-deposited 3 nm HfO_2 sample B. Similarly, sample C exhibits additional peak broadening due to increased Hf–N bond formation from an additional NH_3 process (pre-deposition of HfO_2).

The Hf 4*f* spectra shown for samples B and C in Fig. 16.12 include two orientations of the sample relative to the incident-photon beam and electron analyzer and hence different photo-electron path lengths. Although there is a difference between the Hf 4*f* lineshapes obtained in the more surface sensitive (80°-incidence) and interface-sensitive (glancing-incidence) spectra, the apparent absence of a binding energy shift between the two indicates that no Hf silicate is formed.

The substitution of N for O in the unit cell leads to a hole in the valence band (*p*-type material) and also favors the formation of anion vacancies. This process can be represented as a formal reaction between oxygen in the HfO_2 unit cell (O_0) and interstitial nitrogen leading to the substitution of nitrogen for oxygen at an anion site (N_0), vacancy formation (V_0), and oxygen release: $3O_0 + 2N = 2N_0 + V_0 + 3O$. Hafnium oxynitride may be formed by nitridation of the oxide or oxidation of the nitride. The nitridation of HfO_2 increases the barrier for oxygen and boron diffusion. The nitridation reaction of $HfO_2 + ½N_2 = HfN + O_2$ is thermodynamically unfavorable. Hf_2N_2O has the simplest stoichiometric formula and may be prepared by 1:1 mixing of HfO_2 and Hf_3N_4 as: $½\ HfO_2 + ½Hf_3N_4 = Hf_2N_2O$, which has the cubic bixbyite-type crystal structure. This structure is close to the fluorite-type structure of cubic HfO_2 in which one-fourth of the anion positions are unoccupied and two-thirds of the remaining oxygen atoms are replaced by nitrogen atoms [40].

The N 1*s* core level data for sample A, B, and C are shown in Fig. 16.13. As already discussed, sample B was exposed only to the pre-DA process, and clearly there is evidence for only Si–N bonding in this sample. Sample A was exposed only to the PDA NH_3 process, and it exhibits only Hf–N bonds with no evidence for Si–N bonding (although EELS data for this sample does indicate N in the bottom interface). Finally, sample C shows N 1*s* spectra indicating both Si–N and Hf–N components; the Si–N corresponding to the pre-DA and the Hf–N resulting from the PDA. No appreciable N–O or N–H bond formation was captured for this sample set utilizing high resolution synchrotron XPS.

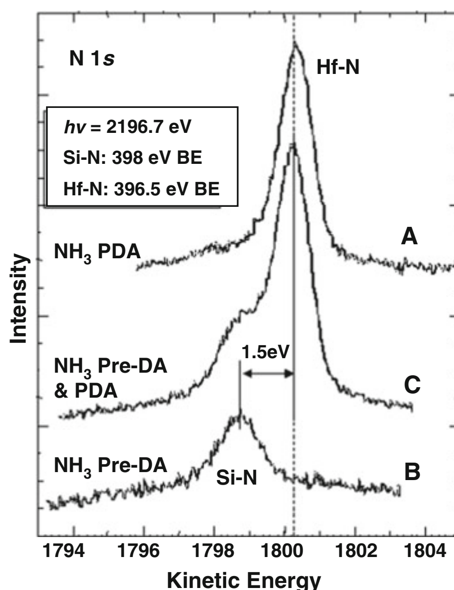

Fig. 16.13 N 1*s* core-level spectra for samples A (PDA only), C (pre-DA and PDA), and B (pre-DA only)

16.2.1 Depth Profiling by VKE-XPS

Figure 16.14 illustrates the use of variable-kinetic energy hard X-ray photoelectron spectroscopy (VKE-HAXPES) to study the chemical-depth profile of Si through the thin IL. The Si 1*s* core level was recorded at different photon energies between 2100 eV ≤ *hν* ≤ 3500 eV. The intensity of the Si 1*s* spectrum at the Si/SiO_2 interface recorded at *hν* = 3500 eV is dominated by the substrate (Si^0) signal. Correspondingly, at the low photon energy, *hν* = 2100 eV, few substrate Si–Si bonds (Si^0) are detected, and the spectrum consists primarily of oxidized Si at the HfO_2/SiO_2 interface. Based on the Si^{4+} peak shift to lower binding energy with decreasing photon energy, it is clear that the Si in the IL is less oxidized closest to the HfO_2 layer following NH_3 PDA. This is because lower kinetic energy electrons probe less of the IL region while favoring the HfO_2 rich surface region. Although the observed shift may be consistent with Hf silicate formation, it is not thermodynamically favorable for HfO_2 to mix with SiO_2 during thermal processing. As discussed in detail previously, various compositions of Hf silicate films demix and form HfO_2 grains embedded in amorphous SiO_2 upon exposure to anneal processing sufficient to induce crystallization [41–43].

As the 3 nm thick HfO_2 layer is too thin for effective VKE-XPS depth profiling at these photon energies using the low binding energy Hf 4*f* core line, Fig. 16.15 shows Hf 4*f* spectra recorded at glancing and near-normal incidence geometries.

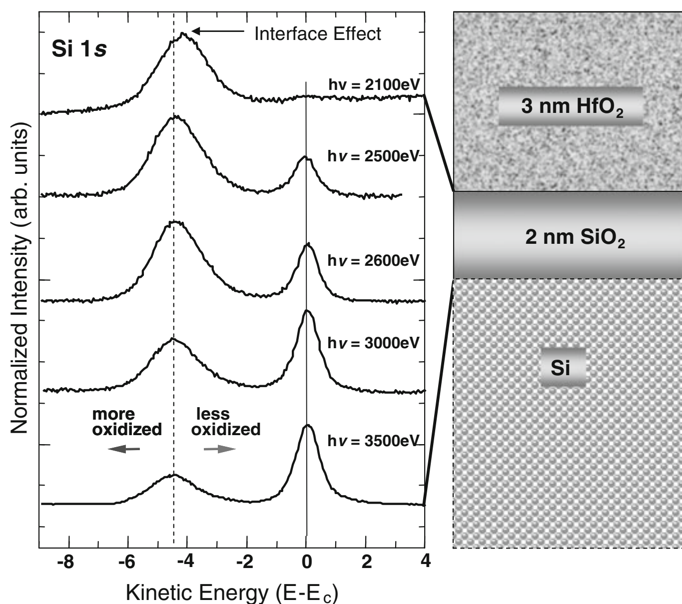

Fig. 16.14 Si 1*s* core-level spectra from sample A recorded with variable kinetic energy XPS and their dominant regions of depth sensitivity

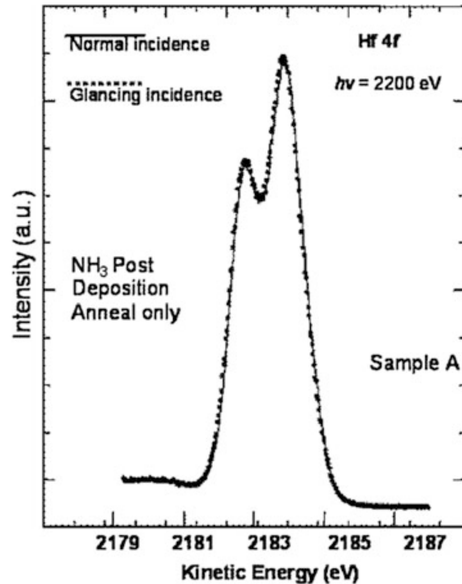

Fig. 16.15 Hf 4*f* core-level spectra of sample A recorded with photon energy *hv* = 2200 eV. The lineshape of the Hf 4*f* core level is the same at both glancing and normal photon-incident angles, indicating the uniformity of the Hf–N bonding throughout the film

The equivalence of these data suggest that the chemical composition around the Hf atoms is uniform throughout the film, and there is little if any detectable change in Hf bonding at the IL relative to the outer surface. The data are therefore consistent with no Hf silicate formation at the interface, since Hf silicate would have a significant Hf 4*f* core-level binding-energy shift to higher energy relative to the HfO_2 [9].

Because the Hf core line does not show a concomitant "interface effect" to that observed for the Si core line, it is clear that Hf has scavenged O and reduced the Si–O coordination near the HfO_2/Si interface. This conclusion is consistent with the mechanistic pathways proposed for electrical performance of advanced MOSFET devices described previously [44].

16.3 Spectroscopic Analysis of Al and N Diffusion in HfO_2

Many experiments have been conducted to address CMOS requirements to achieve both *n*-MOS and *p*-MOS electrode work-function (WF) values with electrode materials that exhibit Si band gap-edge WF behavior of approximately 4 and 5 eV for *n*-type and *p*-type, respectively [45, 46]. Concurrent with this initiative, considerable effort has been focused on controlled introduction of discrete donor and acceptor doping of Hf-based gate dielectrics to produce an *effective* work function (EWF) applicable to both *n*-type (La doping) and *p*-type (Al doping) with a common electrode layer, typically a nitrided transition metal [47–53]. Several groups have reported that alloying HfO_2 with Al results in significant improvements in performance properties [54–56]. Positive charges in high-*k* film systems that elevate the

EWF toward the conduction band of Si have been attributed to Al, which has also been shown to retard HfO_2 crystallization. This is a highly desirable characteristic as the presence of grain boundaries in crystallized HfO_2 can act as fast diffusion paths for metal gate constituents to convey into the oxidized substrate interfacial layer and the silicon channel region and degrade device performance [57, 58].

HAXPES, SIMS, spectroscopic ellipsometry, and EXAFS measurements have been employed to distinguish the effects of Al and N diffusion on the local bonding and microstructure of HfO_2 and its interface with the Si substrate in (001)Si/SiO_x/2 nm HfO_2/1 nm AlO_x film structures. HAXPES results will be discussed in detail here. The diffusion of Al from a thin cap layer deposited on both annealed and unannealed HfO_2 has been observed following a subsequent anneal in N_2 and NH_3 ambient. As pure N_2 gas is nonreactive, comparison between samples subjected to N_2 and NH_3 anneals serves to decouple the effect of incorporated nitrogen from the thermal reactions alone. Causal variations in the HfO_2 microstructure combined with the dependence of Al and N diffusion on initial HfO_2 conditions are presented with respect to anneal temperature and ambient. This work therefore addresses the impact of Al and N on the evolution of HfO_2 crystalline polymorphs; i.e., the different phases of the HfO_2, which strongly influence the resultant dielectric constant (monoclinic: *m*-HfO_2 = 16–18, tetragonal: *t*-HfO_2 = 28–29) [59]. By capturing elemental depth distribution profiles, chemical state changes, and microstructure variations following each process step, the impact of Al and N diffusion and redistribution is observed.

The blanket film samples identified in Table 16.2 were fabricated by ALD, using a process that has been described in detail previously [60]. All HfO_2 films are 2 nm thick and all AlO layers were processed to produce 1 nm thick cap layers. The 700 °C PDA process consists of N_2 (samples *a*, *b*, and *c*) versus NH_3 (samples *a′*, *b′*, and *c′*) ambient.

Figure 16.16 shows XPS shallow core-line survey scans acquired from the six samples recorded with photon energy $h\nu = 2133$ eV. The photoemission peaks are labeled. All spectra have been overlaid and aligned to the Si substrate core line and normalized to the intensity of the Si $2p_{3/2}$ feature. The Si 2*p* core-level spectra of Fig. 16.17a shows the Si^0 feature at 2034 eV along with its corresponding oxide peak at ∼2030 eV (shifted to ∼4 eV higher binding energy (BE), lower kinetic energy (KE)). The smaller oxide-energy shift exhibited by sample *a′* (3.5 eV) is due

Table 16.2 Six sample set designed to illustrate the dependence of Al diffusion into HfO_2 as a function of anneal sequence and ambient (N_2 vs. NH_3)

Sample	Core stack	Anneal 1	Cap layer	Anneal 2
a	Si/SiO/HfO	700 °C/N_2		
b	Si/SiO/HfO	700 °C/N_2	AlO	700 °C/N_2
c	Si/SiO/HfO		AlO	700 °C/N_2
a′	Si/SiO/HfO	700 °C/NH_3		
b′	Si/SiO/HfO	700 °C/NH_3	AlO	700 °C/NH_3
c′	Si/SiO/HfO		AlO	700 °C/NH_3

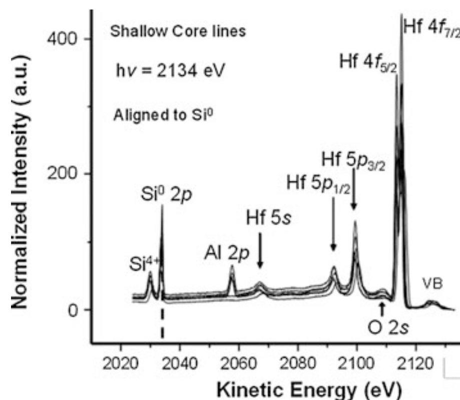

Fig. 16.16 Shallow core-line spectra of all six samples aligned to the Si^0 feature of Si 2*p*

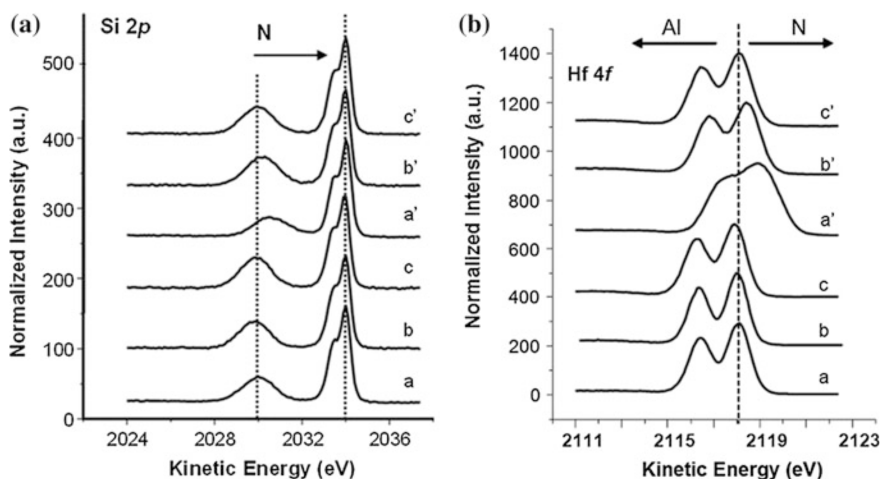

Fig. 16.17 **a** Si 2*p* core-level spectra showing the Si^{4+} oxide peak shifted with respect to Si^0 due to N (and opposite energy direction due to Al) and **b** Hf 4*f* core-level spectra referenced to sample a by the *dotted line*. The chemical state of Hf may be shifted in the directions indicated by N and Al

to incorporated nitrogen (shift direction indicated by the arrow), which substitutes for oxygen bound to Si. It has been shown that in Si/SiO_2 annealing in NH_3 incorporates nitrogen throughout the bulk of the oxide, while displacing oxygen from the film [61]. Interestingly, with respect to the oxide peak centroid of reference sample *a* (dashed line), the oxide peak of sample *b* is shifted 0.1 eV toward lower KE indicative of a Si–O–Al constituent in the bottom interface (BIF), consistent with the notion that HfO_2 grain boundaries offer effective diffusion pathways for Al. Regarding the Hf 4*f* spectra of Fig. 16.17b, the arrows at the top indicate the BE shift direction corresponding to the influence of Al (higher) and N (lower) on the

chemical state of Hf. Relative to the HfO_2/N_2 PDA reference (sample *a*), sample *b* appears similar, but perhaps slightly more resolved (peak-to-trough ratio) due to the additional anneal process and hence additional crystallization.

It is interesting to note that, while the Hf 4*f* core line appears unaffected, Al has diffused through the HfO_2 layer into the bottom interface, to some degree, as mentioned previously. This finding may be explained in that HfO_2 annealed in N_2 at 700 °C results in stoichiometric, stable, *m*-HfO_2, rendering it less likely to bond with Al from the AlO cap layer subsequently annealed in N_2. Hence, Al may transition to the SiO interface and reside as a trace precipitate in the grain boundary discontinuities of the HfO_2 layer of sample *b*. In sample *c*, the Hf 4*f* displays a 0.1 eV shift due to Al, while samples *a′* (0.9 eV shift) and *b′* (0.3 eV shift) exhibit evidence of Hf–N bonding [62]. The shift of the Hf 4*f* core line of sample *c* toward higher binding energy is due to the increased contribution of electron density of the Al–O bond in Hf–Al–O compared with the electron density of Hf-O. This is consistent with the Pauling electronegativity scale difference between Hf, Al, and O (1.30, 1.60, and 3.44, respectively) [63].

The Hf 4*f* spectra of *c′* ($HfO_2/AlO/NH_3$) is nearly coincident in energy with sample *a* due to the offsetting energy shift combination of Hf–O–Al and Hf–N bonding requiring additional evidence for accurate clarification. The O 1*s* spectrum of Fig. 16.18a for reference sample *a* shows a two component peak, characteristic of HfO_2 (BE ~530 eV) and SiO_2 (BE ~532 eV). In addition to the energy separation of the two components, the arrows designate the energy shift direction owing to Al and N incorporation. Strong N influence is evident in sample *a′* such that the two components are more distinguished and shifted 0.2 eV to lower BE. Clear Al and N effects are seen in samples *b* and *b′*, respectively, which shift contrarily by 0.1 eV relative to sample *a*.

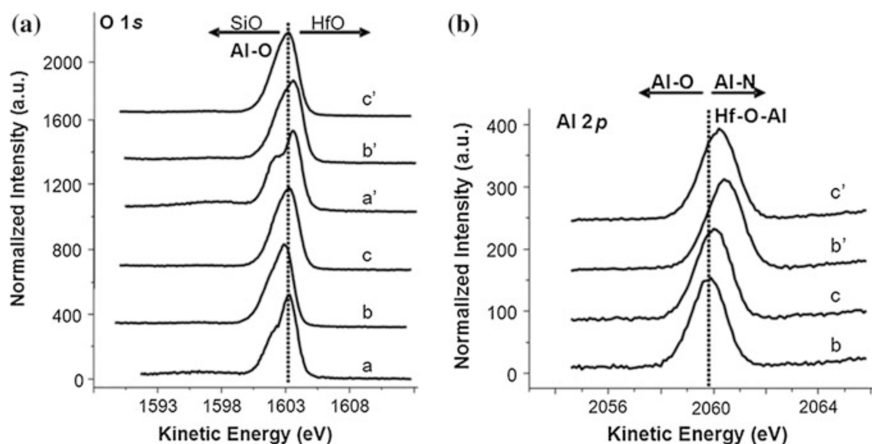

Fig. 16.18 **a** O 1*s* core-level spectra showing the relative energy position of Hf–O and Si–O and **b** Al 2*p* core-level spectra of the four Al-bearing samples. Shifts to lower BE (higher KE) are in the same direction for Hf–O–Al and Al–N

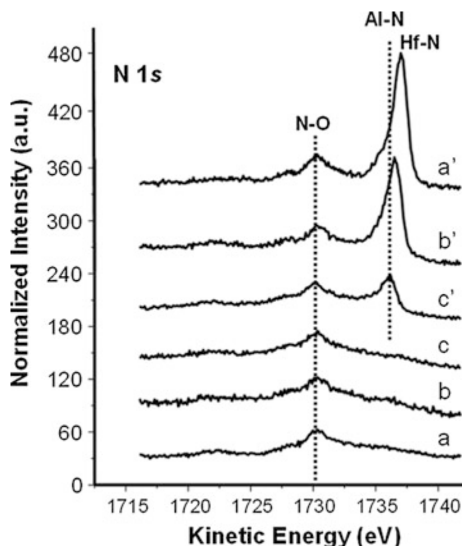

Fig. 16.19 N 1*s* core-level spectra of all six samples although only the NH_3 PDA samples exhibit a significant N signal. The spectra are aligned to the N–O feature in energy and intensity to illustrate the relative nitrogen concentration corresponding to Al–N and Hf–N bond formation

Consider the Al 2*p* spectra of the four Al-bearing samples plotted in Fig. 16.18b that have been referenced to the Si $2p_{3/2}$ core-level energy. Relative to sample *b* ($HfO_2/N_2/AlO/N_2$), the 0.2 eV shift to lower BE of sample *c* cannot be due to N and, therefore, denotes an Hf–O–Al network arising from Al diffusion into the unannealed HfO_2. This finding is consistent with the Hf 4*f* spectra of Fig. 16.17b. Additionally, the Al 2*p* core level is shifted to lower BE by 0.6 eV for sample *b*′ and 0.4 eV for sample *c*′ consistent with both Hf–O–Al formation and Al–N bonding.

In order to distinguish the constituents contributing to the measured binding energy shifts, the N 1*s* core line spectra was also acquired. In Fig. 16.19 the samples annealed in NH_3 ambient exhibit distinguishable Al–N and Hf–N bonding features while all 6 samples show a more subtle feature concomitant with N–O bond formation. The spectra were normalized to the intensity of the N–O peak to most accurately display the relative abundance of incorporated N. The prominent peak at ~1736 eV KE (BE ~397 eV) in sample *a*′ (without Al) corresponds to Hf-N exclusively. Sample *b*′ has a similar, yet somewhat diminished nitrogen peak shifted to higher BE indicative of an Al–N component. The N 1*s* spectrum of sample *c*′ appears to be mostly comprised of Al–N with little evidence of Hf-N bond formation.

16.3.1 Bandgap Analysis of HfAlON

Figure 16.20 shows valence-band (VB) spectra for the six samples again aligned in energy relative to the Si $2p_{3/2}$ core level. The VB consists mainly of O 2*p* non-bonding orbitals of π symmetry. By comparing the total density of states (DOS) in

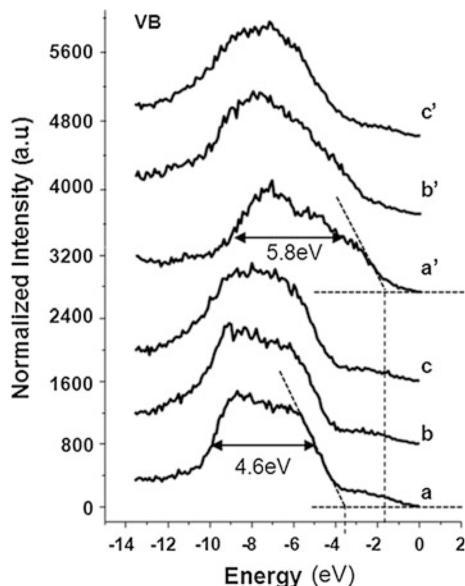

Fig. 16.20 Valence-band spectra showing the effect on the VBM and the consequent narrowing of the band gap due to N incorporation. Samples *a* and *a′* show the ~1.92 eV shift in the VBM due to the HN_3 anneal processing

HfO_2 with $Hf_8O_{10}N_4$, Shang et al. determined that the addition of N to HfO_2 reduces the band gap by approximately 1.2 eV due to raising the VB edge [64]. The local DOS shows that the added N 2*p* states reside 1.1 eV above the O 2*p* states in free atoms. The width of the O 2*p* states, taken at approximately half the maximum peak height is 4.6 eV for reference sample *a*. The O 2*p* broadens to 5.8 eV for samples *a′* and *b′*, owing to N incorporation, as theoretically predicted. This broadening due to N is accompanied by shifts in the O 2*p* (and Si 3*s*) core lines to lower BE. The enhanced N 2*p* feature is evident in the three NH_3 PDA samples, most obviously in samples *a′* and *b′*. The conduction band minimum (CBM) is due to nonbonding Hf 5*d* states which lie at a fixed energy above the VB edge of HfO_2.

To further understand the implications of the change in the VBM indicated by HAXPES, vacuum ultra-violet spectroscopic ellipsometry (VuV-SE) measurements were performed on the six samples to directly investigate their bandgaps. The data were modeled by first determining the total dielectric thickness and refractive index in the non-absorbing region of the spectrum using a Cauchy model. The total dielectric absorption was then analytically solved using a point-by-point data extraction method described in detail previously [64]. To first order, the absorption onset differences for HfO_2 correspond to N incorporation as indicated in the VB spectra of Fig. 16.20. The SE spectra compare sample *a versus a′* and *b versus b′*, respectively, where *a′* and *b′* illustrate a distinct narrowing of the bandgap by >1.9 eV (from 6.42 to 4.5 eV) and >1.3 eV (from 6.38 to 5.0 eV), respectively, owing to N incorporation. In contrast, the VuV-SE results for sample *c versus c′* indicates a rather similar bandgap (*c*: Eg = 6.24 eV, *c′*: Eg = 5.9 eV) consistent with the similar VB spectrum of Fig. 16.20.

The samples measured by XPS were subsequently characterized by SIMS to compare N and Al ionic profiles as a function of sputter depth. Regarding sample *a* and *a*′ (without Al), the SIMS profiles (not shown) were as expected with a significant difference in the amount of N detected. By assessing the relative concentration of nitrogen (NO signal) for samples with and without NH_3 processing, the evidence for Al–N bond formation, especially near the sample surface, was clear for samples *b*′ and *c*′, as indicated previously in the Al 2*p* spectra of Fig. 16.18b. Samples *b* and *c* exhibit a somewhat greater Al signal at the deepest diffusion depth which is consistent with the evidence for Al diffusion into the bottom interface as exhibited by these samples in the Si 2*p* spectra of Fig. 16.17a. The SIMS profiles reinforce the XPS data such that Al diffuses into unannealed HfO_2 forming an Hf–O–Al network regardless of the final drive-in anneal ambient. Al diffuses through HfO_2 annealed in N_2 ambient with much less impact on the HfO_2 layer. As for the NH_3 annealed samples (*b*′ and *c*′), it may be assumed that incorporation of N in HfO_2 during the initial anneal process restricts Al diffusion along grain boundaries since no net evidence of Al is detected in the bottom interface (Al and N could offset chemical shifts of the oxidized Si 2*p* level) of sample *b*′ or *c*′.

16.4 Hf-Based Materials on High Mobility Substrates

Comprehensive investigations of thin high-*k* gate-dielectric films have determined that the Hf-based materials, HfO_2, HfSiO, and HfSiON, are the most ubiquitous candidate successors of SiO_2 owing to their thermal stability in contact with Si [65, 66]. Additionally, in recent years, continued equivalent oxide-thickness (EOT) scaling has included efforts focused on extreme reduction and elimination of the unintentional SiO_x low-*k* IL between Si and the Hf-based layer [67]. Thinning the SiO_x brings the high-*k* layer in close proximity to the Si channel region which results in degradation of the carrier mobility in MOSFET devices [68, 69]. One avenue of compensation involves epitaxial growth of $Si_{1-x}Ge_x$ on Si as a channel layer with hole mobility several times greater than that of Si *p*-type MOSFETs due to a compressive strain effect [70]. However, many groups have reported the phenomenon of Ge enhanced Si oxidation: During conventional thermal oxidation of SiGe substrates, preferential Si oxidation produces a Ge-rich layer (GRL) at the SiGe/oxide interface which causes serious degradation of the oxide properties [71]. Furthermore, this exclusive oxidation of Si is expected according to the theory of binary alloy oxidation [72, 73] such that, under any set of conditions, selective oxidation, where only one component is oxidized exclusively, will take place only above a critical composition (50 at.% Si) of the more active alloy [74]. For the case of SiGe, and in particular for the $Si_{0.7}Ge_{0.3}$ composition reported in this article, Si is the more active component.

In addition to utilizing high-resolution photoemission spectroscopy to illustrate the significant process driven oxygen exchange phenomenon that takes place between bulk and surface constituents of Si and Ge, successful control of Si(Ge)

oxidation has been demonstrated. The impact of introducing an experimentally optimized nitrogen plasma (N*) treatment of the substrate/dielectric continuum has been captured through TEM with EELS elemental profiling and is presented along with corresponding performance data. This work illustrates the change in oxidation of Si and Ge at each process step in the fabrication of Si/$Si_{0.7}Ge_{0.3}$/HfO_2/TaN structures in order to elucidate the oxidation kinetics that need to be controlled for enhanced performance. To that end, TEM cross-sections with EELS element profiles of the gate stack have verified the effectiveness of a N* process that gives rise to an appreciable EOT reduction with only a slight increase in gate-leakage current density. The optimized N* process has resulted in improved EOT scaling, low sub-threshold voltage swing, low off-state leakage current, and a significant threshold voltage (Vt) reduction without requiring introduction of a Si cap layer for oxidation control in surface channel SiGe *p*FET devices.

Device representative blanket film samples were processed for HAXPES measurements. Following HF-last Si surface clean, selective 30 nm thick epitaxial $Si_{0.7}Ge_{0.3}$ was grown in a rapid thermal chemical vapor deposition (RTCVD) system and capped with ALD 2 nm thick HfO_2, annealed, and capped with 2.5 nm thick TaN which enabled X-ray photon probing through the entire stack into the SiGe layer. In addition to the enhanced energy and spatial resolution provided by synchrotron photoemission, the ability to simultaneously probe both deep and shallow core levels to provide bulk and surface sensitive spectra for each substrate element is particularly instructive when investigating oxygen redistribution phenomena.

Figure 16.21 shows HAXPES data acquired from a bare reference $Si_{0.7}Ge_{0.3}$ sample with native oxidation. The bulk sensitive Si 2*p* (binding energy (BE) ~99 eV) and surface sensitive Si 1*s* (BE ~1840 eV) are shown in Fig. 16.21a, b, respectively. It can be seen that the Si^0 (Si–Si substrate) feature and the Si^{4+} oxidized Si feature at approximately 4 eV lower kinetic energy [75, 76] (higher BE) indicate much more surface rather than bulk Si oxidation. The increased surface oxidation revealed by the Si 1*s* core line together with the large

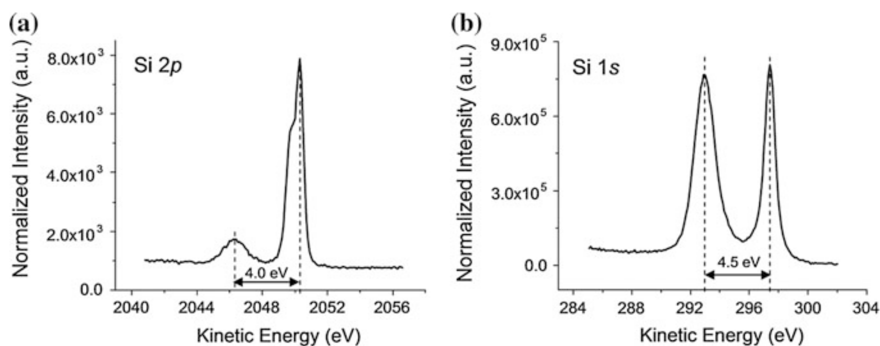

Fig. 16.21 **a** Bulk sensitive Si 2*p* and **b** surface sensitive Si 1*s* core-level spectra of native oxide on the reference $Si_{0.7}Ge_{0.3}$ sample indicating a large degree of surface oxidation of the Si

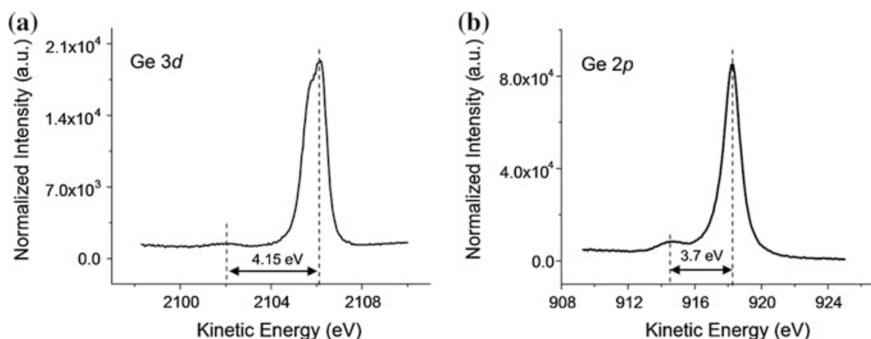

Fig. 16.22 **a** Bulk sensitive Ge 3*d* and **b** surface sensitive Ge 2*p* core-level spectra of native oxide on the reference $Si_{0.7}Ge_{0.3}$ sample indicating an overall lower degree of Ge oxidation than Si oxidation. The slight amount of Ge 3*d* oxidation appears to be more stoichiometric GeO_2-like than the surface sensitive Ge 2*p* oxidation

separation between the Si^0 and Si^{4+} peaks indicate as well a more stoichiometric (4-fold coordinated Si) SiO_2 at the surface. Unlike Si, however, Ge is only slightly oxidized as seen in Fig. 16.22a, b. Note as well the reversal of binding-energy shift difference between the bulk and surface sensitive Ge and Ge oxide peaks compared to Si.

In order to obtain a more complete interpretation of the XPS data from the $Si_{0.7}Ge_{0.3}$ reference sample, Fig. 16.23a shows the X-ray reflectivity and intensity of the Ge K_α fluorescence yield acquired simultaneously during an angular scan of the 30 nm thick bare $Si_{0.7}Ge_{0.3}$ layer epitaxially grown on a Si(100) substrate. The peak of the reflectivity curve indicates the critical angle occurring at approximately 0.15° where the incident X-ray photon beam penetration depth into the sample is

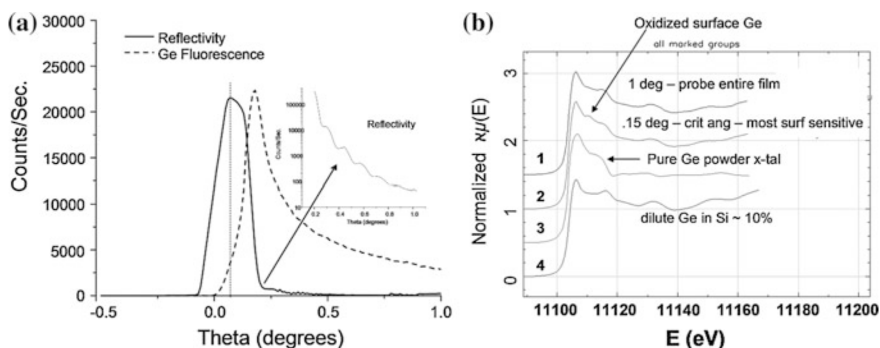

Fig. 16.23 **a** Angular dependence of the reflectivity and fluorescence-yield curves of the reference $Si_{0.7}Ge_{0.3}$ sample with respect to the incident X-ray photon beam angle. **b** Comparison of Ge *K*-edge bulk and surface-sensitive absorption scans with pure crystalline Ge powder and a dilute SiGe (10 at.% Ge) reference sample clearly identify the formation of a GRL at the $Si_{0.7}Ge_{0.3}$ surface

approximately 2.5–5 nm. Below the critical angle, total external reflection occurs. Beginning at 0°, the Ge fluorescence ramps up and at the critical angle, and only a small fraction of the total signal is observed. This angular orientation is the most surface sensitive. The diminished reflectivity orientation beginning at approximately 0.3–0.4° (a portion of the reflectivity curve is magnified in the inset) correlates to increased probe depth such that the fluorescence yield probes the entire thickness of the SiGe film. Figure 16.23b shows a series of Ge *K*-edge near edge X-ray absorption scans. Traces 1 and 2 shows the bulk $Si_{0.7}Ge_{0.3}$ absorption and the surface sensitive $Si_{0.7}Ge_{0.3}$ absorption acquired at 1° and at the critical angle of 0.15°, respectively. The arrow indicates surface oxidation; i.e., the bump located at approximately 4 eV above the absorption edge. This feature is not present in the bulk Ge absorption taken at 1°. Profiles 3 and 4 were acquired from reference samples where the arrow points to a shoulder characteristic of crystalline Ge, approximately 10 eV above the absorption edge of pure crystalline Ge powder for comparison. Trace 4, on the other hand, shows the Ge *K*-edge data from a dilute crystalline SiGe (10 at.% Ge) reference-alloy sample. The feature occurring approximately 13 eV above the edge originates from Si backscattering; it is also evident in traces 1 and 2. By comparing these absorption features, it is evident that there is GRL formation at the surface of the $Si_{0.7}Ge_{0.3}$ layer with a slight degree of Ge-O oxidation. Combining this result with the XPS findings of Fig. 16.21, it may be concluded that the $Si_{0.7}Ge_{0.3}$ reference sample consists of surface SiO_2 residing on a GRL on SiGe and that the GRL is slightly surface oxidized. SIMS was also utilized (not shown) to verify the existence of the GRL between the Si oxide surface layer and the SiGe layer.

16.4.1 HAXPES of $Si_{0.7}Ge_{0.3}/HfO_2/TaN/950$ °C

Figures 16.24, 16.25 and 16.26 show photoemission spectra of four samples; the bare $Si_{0.7}Ge_{0.3}$ reference, discussed previously, $Si_{0.7}Ge_{0.3}/HfO_2$ as deposited, $Si_{0.7}Ge_{0.3}/HfO_2/950$ °C anneal, and $Si_{0.7}Ge_{0.3}/HfO_2/TaN/950$ °C anneal. The substrate oxidation and its changes are apparent for each step. The sample order (top to bottom) varies from figure to figure for clearer illustration. Si 2*p* and Si 1*s* core-level spectra are shown in Fig. 16.24a, b, respectively. From the bulk Si 2*p* spectra, it is seen that the amount of bulk Si oxidation increases with each process step in the fabrication sequence as exhibited from the bottom to the top spectra displayed in Fig. 16.24a. As indicated in the figure, the Si oxide stoichiometry decreases as the bulk Si oxidation increases. For example, the $Si_{0.7}Ge_{0.3}$ reference exhibits an oxide peak at ~2046.2 eV which represents the most stoichiometric bulk Si oxidation detected in this sample set. It may be observed that depositing the HfO_2 and subsequently annealing at 950 °C produces incrementally slightly more oxidation but the centroid of the oxide peak shifts to lower BE with each process. This finding is consistent with numerous reports signifying that the cause of this decrease in SiO_2 stoichiometry is driven by Hf gettering of oxygen

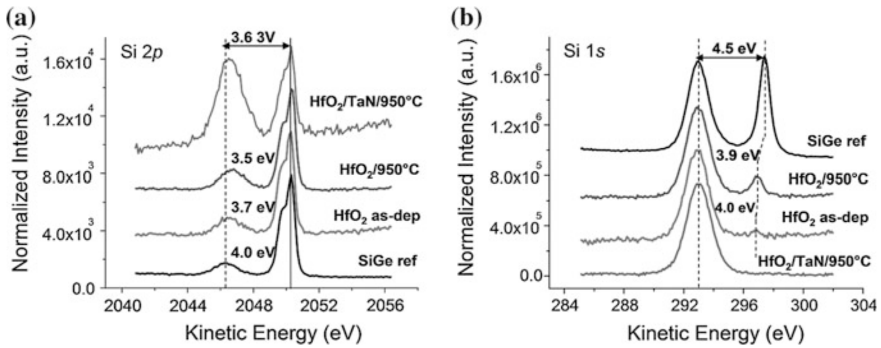

Fig. 16.24 **a** Si 2*p* and **b** Si 1*s* core-level spectra. The Si 2*p* spectra have been normalized to the Si^0 energy and intensity to emphasize variations in the relative oxidation of the four samples: The bare $Si_{0.7}Ge_{0.3}$ reference, $Si_{0.7}Ge_{0.3}/HfO_2$ as-deposited, $Si_{0.7}Ge_{0.3}/HfO_2$/950 °C anneal, and $Si_{0.7}Ge_{0.3}/HfO_2$/TaN/950 °C anneal. Bulk Si oxidation increases with each process step and is less SiO_2-like than the $Si_{0.7}Ge_{0.3}$ reference, but note that there is a much greater degree of surface than bulk Si oxidation for each sample

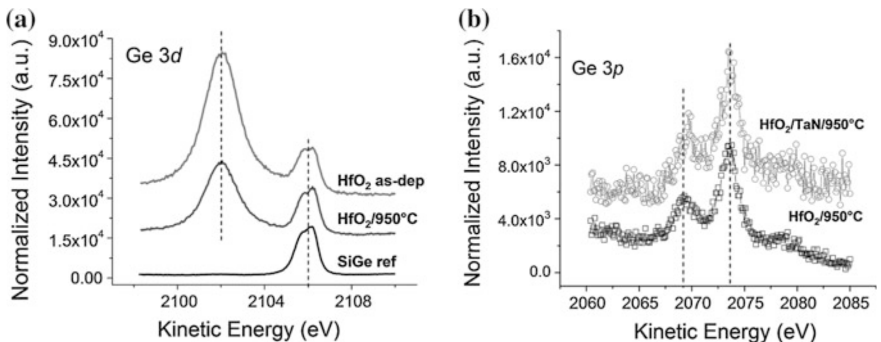

Fig. 16.25 **a** Ge 3d core-level spectra. The TaN covered sample could not be included in (**a**) due to interference of the Ta $5p_{3/2}$ core line with the Ge 3*d*. The slightly oxidized Ge 3*d* spectrum of the $Si_{0.7}Ge_{0.3}$ reference becomes significantly oxidized to bulk GeO_2-like upon deposition of HfO_2. Subsequent annealing then significantly reduces the bulk GeO_2 contribution. **b** Ge $3p_{3/2}$ core-level spectra recorded at similar kinetic energy to the Ge 3*d* spectra of (**a**) illustrating a strong similarity of oxidation with and without the TaN layer, but with slightly less stoichiometric GeO_2 for the TaN covered sample

from SiO_2 during both deposition and anneal processing [60, 77]. Regarding the increase in bulk Si oxidation with processing, the intensity of the oxide peak is found to be 1.8, 2.4, and 4.2 x the SiGe reference sample for HfO_2 as-deposited, HfO_2/950 °C anneal, and HfO_2/TaN/950 °C anneal, respectively. Core-level photoemission studies performed in order to determine the oxidation state of substoichiometric GeO_2 and SiO_2 have indicated that the increase in Si atoms in intermediate oxidation states (Si^{1+}, Si^{2+}, and Si^{3+}) correlates with a higher density

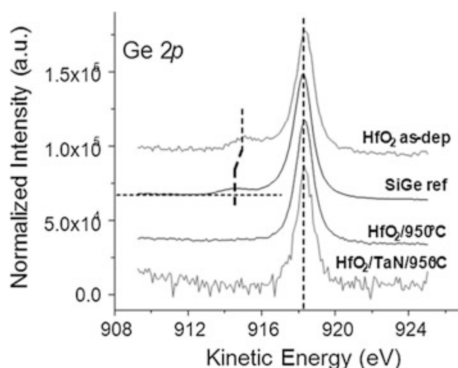

Fig. 16.26 Surface sensitive Ge 2*p* core-level spectra of the four samples indicate a shift to lower BE of the Ge oxide feature from the $Si_{0.7}Ge_{0.3}$ reference to the $Si_{0.7}Ge_{0.3}/HfO_2$ as-deposited sample with the apparent complete reduction of Ge 2*p* oxide for the two annealed samples

of electrically active interface states [78]. The most noteworthy oxidation increase occurs during TaN deposition and anneal at 950 °C. This process progression exacerbates bulk Si oxidation which expounds the urgency with which substrate oxidation must be rigorousness controlled or circumvented altogether to address *p*-FET EOT scaling and mobility targets in a timely manner. The Si 1*s* spectra of the sample set in Fig. 16.24b has been normalized to the Si^{4+} oxide-peak energy and intensity since the elemental Si^0 feature was not detected through the TaN layer. The amount of surface Si oxidation increases from the top to the bottom spectra; however, the HfO_2 as-deposited and HfO_2/950 °C anneal samples have reversed the amount of oxide found in the Si 2*p* spectra in Fig. 16.24a. Overall, there is a much greater degree of surface Si oxidation than the corresponding Si 2*p* bulk spectra for each of the four samples, while the energy shift of the oxide peak for the as-deposited and annealed HfO_2 samples is similar to that of the Si 2*p* substoichiometric oxide peak.

Acquiring Ge 3*d* core-level spectra for this sample set was challenging due to the close proximity of the Hf $5p_{3/2}$ and Ta $5p_{3/2}$ core lines (BE's approximately 30 eV) that necessitated acquisition of the Ge $3p_{3/2}$ core line (BE approximately 122 eV) for the sample with TaN. As seen from Fig. 16.25a, which does not include data from the TaN covered sample, the very slightly oxidized reference sample (see Fig. 16.22a) becomes significantly oxidized to GeO_2 upon HfO_2 deposition. However, subsequent annealing greatly reduces the bulk GeO_2 signal. Measuring photoemission from SiGe through 2 nm thick HfO_2 and 2.5 nm thick TaN resulted in noisy spectra.

For comparison, the Ge $3p_{3/2}$ core line was also acquired for the HfO_2/950 °C anneal sample (without TaN), at the same kinetic energy as shown in Fig. 16.25b. The degree of Ge oxidation appears quite similar for the two samples shown in Fig. 16.25b, however the TaN sample exhibits a 0.35 eV energy shift of the oxide feature relative to the GeO peak from the HfO_2/950 °C sample which is indicative

of decreased GeO_2 stoichiometry. The surface sensitive Ge 2*p* core lines are shown in Fig. 16.26. Again, HfO_2 deposition is seen to slightly increase the Ge oxidation while both annealed samples appear to exhibit completely reduced surface Ge. Initially, the $Si_{0.7}Ge_{0.3}$ reference exhibits a moderate bulk and significant surface Si oxidization along with un-oxidized bulk and only slightly surface oxidized Ge. Relative to the initial reference sample, deposition of HfO_2 generates slightly more bulk and significantly more surface Si oxide that is less stoichiometric in both cases. An appreciable amount of bulk Ge oxide also develops during HfO_2 deposition while only a slight degree of sub-stoichiometric surface GeO_x is detected. Annealing the HfO_2 at 950 °C slightly increases the bulk and reduces the surface Si oxide while shifting the oxide peak to lower BE with respect to the as-deposited sample. Conversely, the anneal process reduces bulk Ge oxide and appears to completely reduce surface Ge to elemental Ge.

These results are consistent with the findings of Jang et al. [79], who used EELS in a scanning transmission-electron microscope to characterize the SiGe/HfO_2 IL. They claimed that Ge atoms which diffused into the IL during film deposition moved back to the region close to the substrate during the anneal process. Regarding Si, however, they conclude that Si atoms which concurrently diffused to the IL during HfO_2 deposition remained there and oxidized during annealing. In our work, the Si^{4+} component of the Si 2*p* spectra shifts 0.3 and 0.5 eV lower in BE relative to the SiGe reference sample, for the HfO_2 as-deposited and HfO_2/950 °C anneal samples, respectively. The anneal process is seen to generate thermal driven gettering of oxygen by Hf as HfO_2 evolves to its lowest free energy state, monoclinic, and produces a highly stoichiometric binary metal oxide (*m*-HfO_2). The coincident energy shift of the oxidized Si peak indicates a net reduction of stoichiometric SiO_2. Cho et al. [80] reported similar findings using XPS to conclude that a layer composed of a mixture of SiO_x and GeO_x was observed in as-grown HfO_2 films on SiGe and they used medium energy ion scattering (MEIS) to determine from the Ge peak profile and position that Ge is included in the interfacial layer of an SiGe/HfO_2 as-grown sample [80]. They reported that the GeO_x layer became significantly reduced with increasing anneal temperature. Our results concur that there is significant Si–O and Ge–O corresponding to the HfO_2 as-deposited sample and post 950 °C anneal. Oxidation of the bulk Si slightly increases while oxidation of the surface Si slightly decreases. Although the Ge 2*p* spectra of Fig. 16.26 clearly indicates rather complete reduction of surface GeOx upon 950 °C anneal, some bulk GeO_2 remains as evident in the Ge 3*p* spectra of Fig. 16.27a. The GeO typically formed in the oxidation process is less stable than SiO_2 and is subsequently reduced by Si to form Ge and SiO_2. This is consistent with several reports [78, 81–84] claiming Ge acts as a catalyst; that is, it is neither oxidized nor incorporated into the growing SiO_2. As Si oxidizes at a faster rate than Ge, Ge is rejected from the growing Si oxide resulting in production of a GRL between the SiGe and the Si oxide [85]. During (Si) oxidation, the segregated Ge is almost completely reduced to its elemental form. Si atoms from the underlying SiGe network must diffuse through the GRL to bond with oxygen diffusing in through the growing Si oxide layer. At high Si concentration, only Si is oxidized

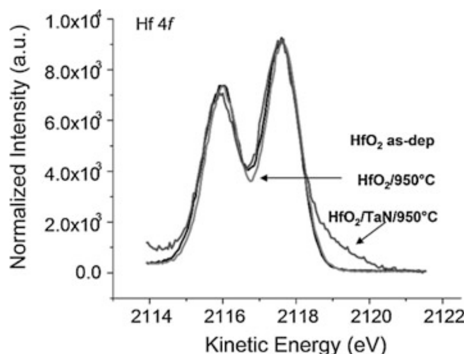

Fig. 16.27 Hf 4*f* core-level spectra of the three Hf-bearing samples. The best resolved core line is found for the $Si_{0.7}Ge_{0.3}/HfO_2$/950 °C anneal sample, and Ta is observed on the low BE side of the spectrum for the $Si_{0.7}Ge_{0.3}/HfO_2$/TaN/950 °C anneal sample

initially. Paine et al. [86] showed that only SiO_2 will form under virtually all experimental conditions due to the significantly more negative free energy of formation of SiO_2 relative to GeO_2 (GeO_2: −580 J/mol, SiO_2: −911 J/mol, and HfO_2: −1118 J/mol). These findings are consistent with the studies of LeGoues et al. [84] who reported that oxidation of SiGe alloys resulted in the formation of a pure SiO_2 layer on top of a Ge enriched SiGe alloy. As the SiO_2 layer grows, the Ge is "snow-plowed" in front of the growing oxide forming a GRL relative to the initial SiGe composition. Using Rutherford backscattering, they determined that no diffusion or injection of Ge into the underlying Si substrate occurs. One concern with respect to substrate defectivity and its impact on carrier (hole) mobility is that as the concentration and thickness of the GRL increases, it eventually becomes energetically more favorable to generate threading misfit dislocations between the GRL and the SiGe layer to accommodate the generated stress [87–89].

Comparison of the Hf 4*f* spectra for the three Hf bearing samples shown in Fig. 16.27 indicates only slight variation. The HfO_2/950 °C anneal sample is somewhat better resolved with sharper line shape exhibiting the maximum peak-to-trough ratio. The TaN covered sample, although annealed, shows some broadening on the low BE side of the base of the Hf 4*f* feature likely related to Ta core-line interference rather than indicating any reduced Hf or other Hf-metal contribution since there is an appreciably high abundance of (Si) oxide in close proximity to Hf in that sample.

16.4.2 HAXPES of Al_2O_3 on $In_{0.53}Ga_{0.47}As$

InGaAs has also been investigated as a high-mobility substrate for advanced logic-device applications. However, due to the lack of a stable, low-defect native oxide, such as SiO_2/Si, understanding and controlling oxide behavior is essential for

optimal device design and performance [90–96]. While control of interfacial oxidation has been extensively studied for high-*k* oxides on InGaAs and other III-V semiconductors [97–105], to date little attention has been paid to the possible 'out-diffusion' of elements from the semiconductor into the high-*k* film due to thermal instability. Understanding out-diffusion is important for CMOS devices as it may lead to defects and hence lower mobility in the channel region and changes in the electronic structure of the gate oxide. Ga out-diffusion from InGaAs and GaAs has been reported [106, 107], and in other instances As out-diffusion has been reported as well [108]. These studies relied on cross-sectional TEM with EELS or energy dispersive X-ray spectroscopy, where analysis is complicated by destructive sample preparation techniques and the low concentrations of the diffusing elements. For these reasons, we performed HAXPES on $In_{0.53}Ga_{0.47}As/Al_2O_3$ gate stacks as deposited and annealed at 400, 500, and 700 °C to test for out-diffusion of substrate elements.

As noted by many authors, HAXPES is an ideal, non-destructive structural probe that provides chemical depth-sensitive information; consequently, it is a useful tool for analyzing thin-film structures due to the inherent surface sensitivity of the photoelectrons and the unique ability to tune the electron inelastic mean free path (IMFP) to technologically relevant thicknesses [61]. The depth distribution of an element under investigation will play a significant role in the relative intensity of the measured photoelectron signal [109]; therefore careful analysis of HAXPES data can provide excellent non-destructive evidence for out-diffusion. For further confirmation, HAXPES spectra can be recorded at various photon energies giving different surface sensitivities.

A 150 nm *n*-type $In_{0.53}Ga_{0.47}As$ (Si doped, 1×10^{17} cm^{-3}) film was deposited by molecular beam epitaxy on an *n*-type InP wafer (Si doped, 9×10^{17} cm^{-3}) with a 100 nm *n*-type $In_{0.53}Ga_{0.47}As$ (Si doped, 5×10^{17} cm^{-3}) buffer layer. After appropriate surface cleaning, a nominally 5 nm thick Al_2O_3 film was deposited by ALD using H_2O as an oxidizer. The wafer was then diced and the shards were annealed under inert N_2 atmosphere at different temperatures: 25 (as-deposited), 400, 500 and 700 °C. After anneal, total-oxide (Al_2O_3 + interlayer) thickness was measured by spectroscopic ellipsometry (SE). SE data was modeled using a parameterized optical model accounting for changes in optical properties of the oxide film, making thickness results independent of changes in composition or crystallinity of the film (Al_2O_3 + interlayer). The 25 and 400 °C films were measured to be 5.3 ± 0.2 nm thick, the 500 °C film 5.8 ± 0.2 nm and the 700 °C film 6.1 ± 0.2 nm. The As-deposited amorphous Al_2O_3 film is expected to begin crystallization by the 700 °C PDA, which would lead to more dense and hence thinner films, so the increase in film thickness with increasing anneal temperature cannot be explained by structural changes within the Al_2O_3 film itself. Instead, it may reflect the evolution of a thicker InGaAs-oxide interlayer or may be an indication of out-diffusion of substrate elements into the Al_2O_3 film.

For consistent reference, In, Ga, and As photoelectron-peak intensities were normalized to overlayer peak intensities with similar binding energies (BE); i.e., an overlayer of constant thickness and chemical structure is assumed. This assumption

is used as annealing was performed in inert atmosphere at temperatures well below the temperature Al_2O_3 is expected to evaporate—possible errors in this assumption will be discussed below. Specifically, the Ga $2p_{3/2}$ (BE ~1120 eV) and As $2p_{3/2}$ (BE ~1320 eV) are referenced to the Al 1*s* (BE ~1560 eV), while the In $3d_{5/2}$ (BE ~440) is referenced to O 1*s* (BE ~530 eV). Additionally, Ga $2p_{3/2}$ and Al 1*s* BEs are determined with respect to the As $2p_{3/2}$ = 1323.6 eV reference [106], while O 1*s* is referenced to In $3d_{5/2}$ = 444.2 eV [110]. To account for different excitation probabilities at different beam energies, the peak intensities were divided by the photoelectron cross-section [111] and IMFP as calculated by the TPP-2M equation [112]. Figure 16.28 shows the normalized peaks, measured at hν = 4000 eV. The In $3d_{5/2}$ region shows a strong peak indicative of In–As bonds with a trace signal of

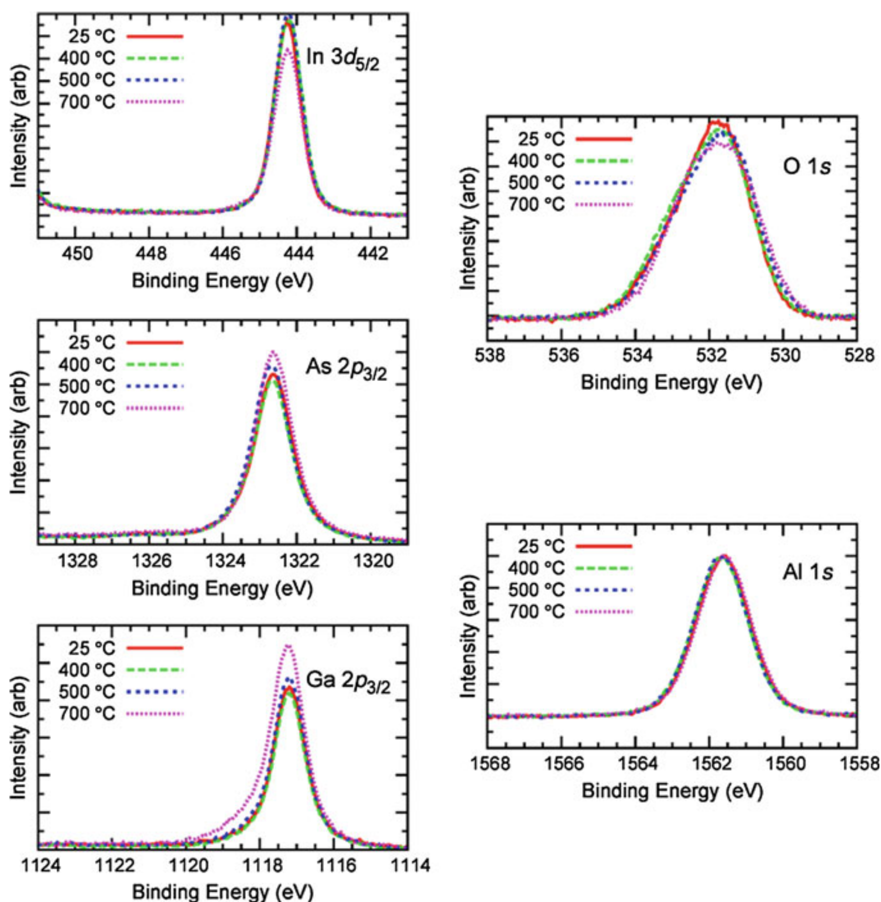

Fig. 16.28 In $4d_{5/2}$, As $2p_{3/2}$, Ga $2p_{3/2}$, O 1*s*, and Al 1*s* HAXPS core-level spectra taken at 4000 eV beam energy. In $4d_{5/2}$ and O 1*s* peak areas are normalized to the total O 1*s* peak area. All other peaks are normalized to the Al 1*s* peak area

oxidation shown by the high binding energy tail at about 445.5 eV. The In $3d_{5/2}$ intensity stays relatively constant until 700 °C, where it is diminished. The Ga $2p_{3/2}$ and As $2p_{3/2}$ signals show greater evidence of oxidation; Ga with the large tail around 1118.5 eV and As with a small second peak centered at 1326 eV, consistent with the literature [113]. The intensity of both peaks increase consistently with increasing anneal temperature. As $2p_{3/2}$ shows an increase in the main As–In/Ga component, while the small As–O component remains relatively constant with anneal temperature. Note that both the main Ga peak and the Ga–O should increase with anneal temperature. The O 1*s* signal shows significant changes with anneal temperature. The peak at 25 °C is composed of a main O feature with a high BE shoulder. With increasing anneal temperature, the contribution to the total peak area of the high BE component increases. The Al 1*s* shows no changes in peak shape though very subtle shifts in the peak position are observed; between 25 and 400 °C the peak shifts 0.1 eV to higher binding energy, then shifts back to the initial position between 500 and 700 °C. The Al and O spectra demonstrate changes in the Al_2O_3 overlayer during anneal, complicating interpretation of the Ga, In, and As intensity changes.

The measurements were repeated at lower X-ray energy, hν = 2200 eV, to provide more surface sensitive spectra for comparison. Results are shown in Fig. 16.29. The same general trends are observed for all regions: In $3d_{5/2}$ decreases in intensity while As $2p_{3/2}$ and Ga $2p_{3/2}$ increase with anneal temperature. The increase in Ga $2p_{3/2}$ -signal intensity at this beam energy is significantly higher than at the more “bulk”-sensitive beam energy, with a 136 % increase between 25 and 700 °C at 2200 eV beam energy versus a 39 % increase at 4000 eV. The In $3d_{5/2}$ decrease and As $2p_{3/2}$ increase are much more similar between beam energies. If the increases in Ga and As peak intensity are due to changes in the overlayer film alone, such as densification or crystallization, the As increase should be similar or slightly greater to that for Ga, since As $2p_{3/2}$ has only a slightly lower IMFP than Ga $2p_{3/2.}$ These results are strong evidence of Ga out-diffusion with a 700 °C anneal.

The O 1*s* signal at 2200 eV beam energy again shows the growth of the high BE component with annealing temperature. This component is more prominent in the more surface-sensitive measurements, suggesting that it is located towards the surface. Multiple chemical structures could give rise to this high BE feature. The binding-energy shift from the main O–Al peak, approximately 1.4 eV, is consistent with the shift between interfacial O–Al and O–As [15]; however, there is no corresponding growth in the As–O in the As $2p_{3/2}$ region, ruling out O–As as the sole contributor. It is tempting to thus assign the high BE feature to O–Ga, considering the large increase in Ga–O from the Ga $2p_{3/2}$ region. Interfacial O–Ga has been reported at 0.8 eV lower BE than an O–Al overlayer [15]; however, considering the measured O 1*s* peak widths of 1.75 eV, the O–Ga feature, which is expected to be small, may be masked by the main O–Al peak. Furthermore, the measured BE depends on interfacial dipoles and band alignment; if Ga-oxide has diffused into the Al_2O_3 film, the O–Ga BE should not be expected to be the same as an interfacial O–Ga. It is further possible, though, that the high BE component comes from adsorbed

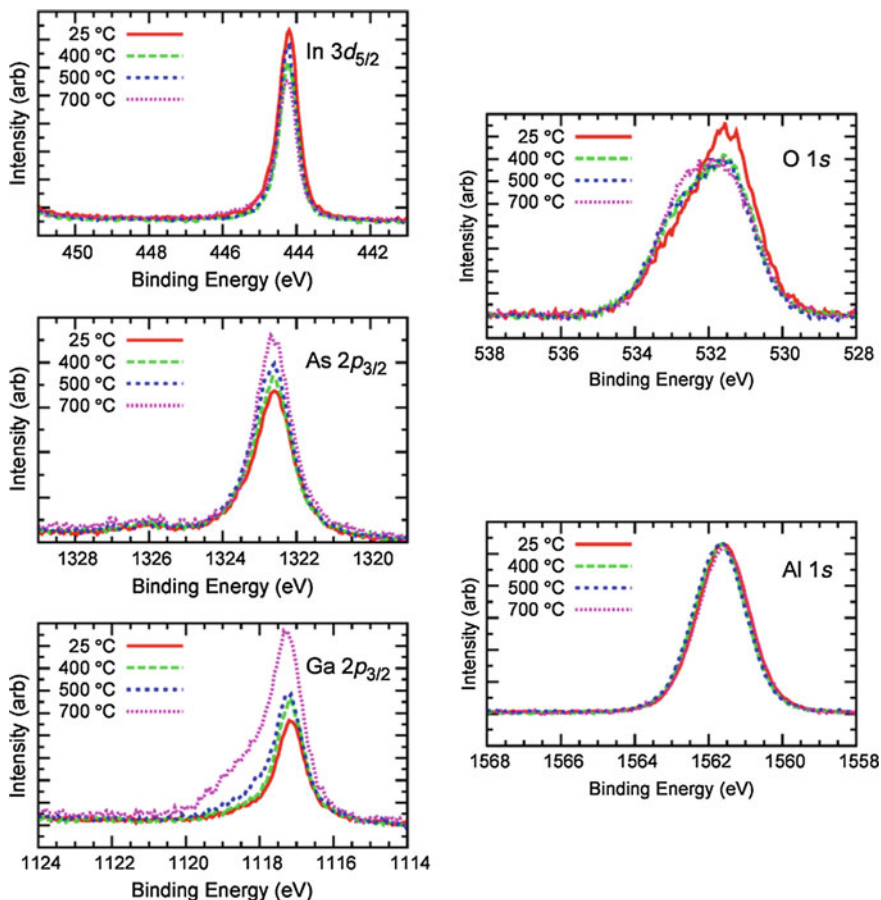

Fig. 16.29 In $4d_{5/2}$, As $2p_{3/2}$, Ga $2p_{3/2}$, O 1*s*, and Al 1*s* HAXPES core-level spectra taken at 2200 eV beam energy. In $4d_{5/2}$ and O 1*s* peak areas are normalized to the total O 1*s* peak area. All other peaks are normalized to the Al 1*s* peak area

hydroxyls or other surface contamination, leaving characterization of this component ambiguous.

As mentioned above, the composition and structure of the Al_2O_3 film is assumed to be constant with annealing, yet the SE, Al 1*s*, and O 1*s* results show that clearly it is not the case. However, calculations performed for different Al_2O_3 phases show only subtle changes for IMFP values, far too small to account for the different HAXPES peak intensities observed.

Comparison of the photoemission peak intensities measured at different beam energies can provide information about the depth distribution of elements within the analyzed region. Intensity in XPS is dependent on the depth distribution in the sample among other factors and can be estimated as [113]:

$$I \approx F\lambda\sigma n \int_{0}^{\infty} c(t)\exp\left(-{}^{t}/_{\lambda \sin\theta}\right)\mathrm{d}t \tag{16.1}$$

Instrument and geometry specific terms such as the detector transmission function and X-ray flux, are taken into the constant F; λ is the IMFP of the electron in the sample, σ is the photoelectron cross section, n is the density of the material under investigation, $c(t)$ is the relative depth distribution, and θ is the takeoff angle between sample and detector. The depth, t, is defined from 0 at the surface increasing into the sample. As the measured intensities were normalized to the overlayer signal with similar binding energy as well as scattering cross section and IMFP, F, σ and λ are accounted for in the equation. Taking the ratio of the peak intensity measured at different beam energies further eliminates the dependence on material density, leaving only dependence on the depth-distribution dependent integral term.

A summary of the intensity ratios, R_i, for the measured photoemission peaks is shown in Fig. 16.30; i.e., where:

$$R_i = {}^{I_{i,2200}}/_{I_{i,4000}} \tag{16.2}$$

$I_{i,j}$ is the peak intensity for core level ‘i’ measured at photon energy ‘j’. As discussed above, $R_{Ga2p3/2}$ shows a clear increasing trend with anneal temperature. The $R_{As2p3/2}$ trend shows a subtle increase to 400 °C, and levels off thereafter. $R_{In3d5/2}$ displays a slight decrease with increasing anneal temperature. According to calculations based on (16.1) (discussed further below), the decreasing $R_{3d5/2}$ trend suggests In moves away from the as-deposited interface; the intensity values are consistent with the increase in total oxide thickness as measured by SE. Also included in the figure are $R_{Ga3d5/2}$ and $R_{As3d5/2}$ (peaks not shown). Due to their lower BE, the Ga $3d_{5/2}$ (BE ~20 eV), and As $3d_{5/2}$ (BE ~40 eV) core levels are more “bulk”-sensitive even at hν = 2200 eV, leading to the higher ratio than seen in

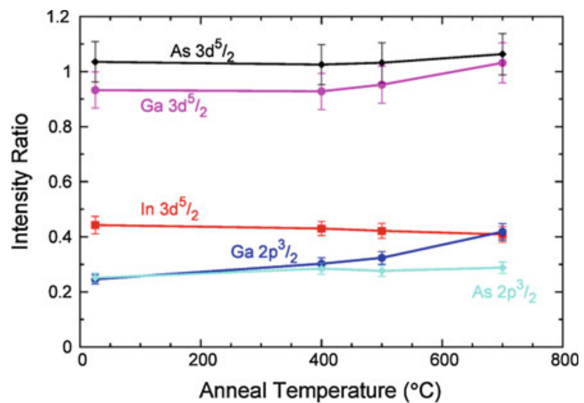

Fig. 16.30 Core-level intensity ratios, R, for As, Ga, and In as indicated

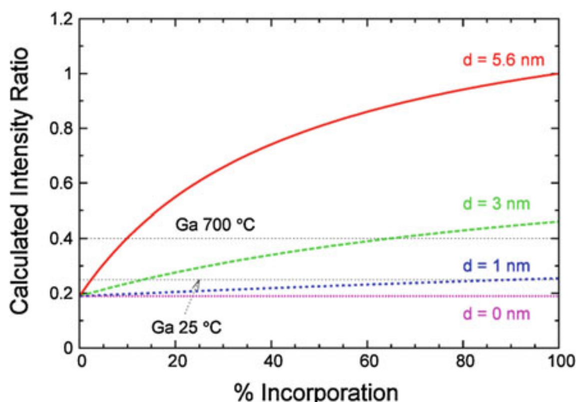

Fig. 16.31 Calculated $R_{Ga2p3/2}$ as a function of % incorporation in an interlayer with thickness ranging from d = 0 nm to d = 5.6 nm, and Al_2O_3 top layer, assuming total overlayer thickness of 5.6 nm. The *horizontal lines* show the measured $R_{Ga2p3/2}$ at 25 and 700 °C, showing an upper and lower bound on Ga incorporation. $R_{As2p3/2}$ intensity ratio would follow the same curves due to the similar Ga $2p_{3/2}$ and As $2p_{3/2}$ IMFPs

the Ga $2p_{3/2}$ and As $2p_{3/2}$. However, these low BE cores show the same general trends, within error, of increasing Ga but relatively constant As.

To further understand these trends, calculations were performed according to (16.1) based on a simple three layer model. The model consists of an InGaAs substrate, interlayer consisting of Ga and As oxides with adjustable thickness *'d'*, and a top Al_2O_3 layer. The total overlayer thickness, i.e. the thickness of the interlayer plus the thickness of the remaining Al_2O_3, is held at 5.6 nm, the average value measured by SE. The interlayer consists of an adjustable percentage of the element under consideration. Because there is only a single data point per two variables (interlayer thickness and incorporation) in the calculation, it is not possible to determine values for both variables.

Figure 16.31 shows the calculated $R_{Ga2p3/2}$ as a function of Ga incorporation in the interlayer for various interlayer thicknesses. The horizontal lines show the measured Ga $2p_{3/2}$ ratio at 25 and 700 °C, demonstrating the limits for Ga interlayer thickness and incorporation at these temperatures. Since the IMFPs for the As $2p_{3/2}$ and Ga $2p_{3/2}$ regions are so close, calculation results should be approximately the same for both core levels. The $R_{Ga2p3/2}$ and $R_{As2p3/2}$ at 25 °C, approximately equal to 0.25, are slightly higher than the calculated value for no out-diffusion (approximately equal to 0.2). This is likely due to the presence of a thin interlayer consisting of Ga and As oxides. Interlayers of 1 nm have been previously observed under similar depositions conditions [114]. $R_{As2p3/2}$ (Fig. 16.30) reaches approximately 0.3 at 400 °C and then remains constant within experimental error. Comparing with the calculations in Fig. 16.31, this ratio suggests an interlayer thickness greater than 1 nm or at most 5 % diffusion of As throughout the overlayer. Note that the SE results showed an increase in the total overlayer thickness with anneal temperature, consistent with growth in interlayer thickness. $R_{Ga2p3/2}$ increases to approximately

0.4. For this value, the interlayer thickness would need to be at least 2 nm, and would correspond to a pure Ga film. However, for Ga dispersed throughout the overlayer, the Ga incorporation would be approximately 10 %.

As stated above, it is not possible to determine both interlayer thickness and incorporation from the calculations; however, it is clear that more Ga diffuses out from the InGaAs substrate than As, and that In does not out-diffuse at all. We propose the following model: during deposition, a thin interlayer consisting primarily of As and Ga oxides is formed, as evidenced by the presence of Ga and As oxides in the photoelectron spectra. After annealing between 400 and 500 °C, the interlayer thickens, and draws more Ga, seen in the increase in the Ga-oxide shoulder. Some As and Ga may also diffuse into the Al_2O_3 at this point. However, annealing to 700 °C causes Ga to out-diffuse further into the Al_2O_3 layer, while the interlayer thickness, as seen in the As $2p_{3/2}$ intensity ratio, remains relatively constant. This proposed model is consistent with both the HAXPES and SE data.

16.5 Summary

HAXPES has been critically important to the understanding of local-bonding configurations of various high-*k* gate dielectric thin films. HAADF-STEM *Z*-contrast images with element profiles showing changes in the integrated intensities from EELS and EDXS data recorded for a series of points across representative gate stacks have been correlated with HAXPES Si 2*p* and N 1*s* spectra to identify substrate Si–N bond formation associated with HF-last + NH_3 substrate treatments. The NH_3 anneal ambient has been shown to produce Hf–N bond formation and influence the crystallographic microstructure of thin HfO_2 films. The Si 1*s* spectra obtained with VKE-XPS, however, reveal a shift to higher binding energy of the Si^{4+} peak at the HfO_2/SiO_2 interface with increasing photon energy, while the Hf 4*f* core level spectra, obtained over a wide range of incident angles, exhibited no observable change in binding energy or line shape. It is difficult to distinguish chemical intermixing corresponding to Hf silicate from micro-roughness of the crystalline-amorphous interface, since both conditions are characterized as a transition region of intermediate electron density between stoichiometric amorphous SiO_2 and crystalline HfO_2. However, the combination of the Si 1*s* spectra recorded via VKE-XPS depth profiling and the Hf 4*f* spectra recorded at different electron take-off angles (at $h\nu$ = 2200 eV) shows that the N content and chemistry in the HfO_2 film are uniform throughout the thickness of the film and that the underlying SiO_2 becomes O deficient in contact with HfO_2. In addition, evidence of Ga and As out-diffusion has been observed under non-destructive HAXPES analysis by utilizing the dependence of photoemission intensity on in-depth concentration profiles. HAXPES analysis shows significant Ga diffusion into the Al_2O_3 film, with a smaller amount of As diffusion, which may be constrained to a thin interlayer. The In signal shows no evidence of out-diffusion, and in fact is seen to move away from the initial interface, likely due to the thickening of the oxide overlayers.

References

1. International Technology Roadmap for Semiconductors, vol. **105** Semiconductor Industry Association, Austin, TX, SEMATECH (1999)
2. D.G. Schlom, J.H. Haeni, MRS Bull. **27**, 198 (2002)
3. G.D. Wilk, R.M. Wallace, J.M. Anthony, J. Appl. Phys., **89**, 5243–5275 (2001)
4. A.I. Kingon, J.-P. Maria, S.K. Streiffer, Nature **406**, 2001 (1032)
5. T.S. Jeon, J.M. White, D.L. Kwong, Appl. Phys. Lett., **78**, 368 (2001)
6. Y.-M. Sun, J. Lozano, H. Ho, H.J. Park, S. Veldman, J.M. White, Appl. Surf. Sci., **161**, 115 (2000)
7. P.S. Lysaght, B. Foran, R.S. Tichy, L. Larson, R.W. Murto, H.R. Huff, **745**, N IEEE RTP (2002)
8. P.S. Lysaght, P.J. Chen, R. Bergmann, T. Messina, R.W. Murto, H.R. Huff, J. Non-Cryst. Solids **303**, 54 (2002)
9. P.D. Kirsch, C.S. Kang, J. Lozano, J.C. Lee, J.G. Ekerdt, J. Appl. Phys., **91**, 4353 (2002)
10. J.W. Gibbs, *Scientific Papers*, vol. 1 (Dover Publications, New York, 1961)
11. S. Stemmer, Z. Chen, C.G. Levi, P.S. Lysaght, B. Foran, J.A. Gisby, J.R. Taylor, Jpn. J. Appl. Phys. **42**, 3593 (2003)
12. A.I. Kingon, J.-P. Maria, D. Wicaksaana, C. Hoffmann, S. Stemmer, Extended Abstracts of the International Workshop on Gate Insulators, (2001)
13. J.-P. Maria, D. Wicaksana, A.I. Kingon, B. Busch, H. Schulte, E. Garfunkel, T. Gustafsson, J. Appl. Phys. **90**, 3476 (2001)
14. S. Ramanathan, P.C. McIntyre, J. Luning, P.S. Lysaght, Y. Yang, Z. Chen, S. Stemmer, J. Electrochem. Soc. **150**, F173 (2003)
15. G.D. Wilk, R.M. Wallace, J.M. Anthony, J. Appl. Phys **87**, 484 (2000)
16. H.J. Kato, App. Phys., **92**, 1106 (2002)
17. J.H. Lee, N.I. Lee, K. Fujihara, App. Phys. Lett. **81**, 472–474 (2002)
18. P.S. Lysaght, B. Foran, S. Stemmer, G. Bersuker, J. Bennett, R. Tichy, L. Larson, H.R. Huff, J. Microelect. Eng., **69**, 182–189, 3516 (2003)
19. P.W. Peacock, J. Robertson, J. Appl. Phys. **92**, 4712–4721 (2002)
20. R.F. Egerton, *Electron Energy-Loss Spectroscopy in the Electron Microscope*, 2nd edn. (Plenum Press, New York, 1996)
21. D.W. McComb, Phys. Rev. B **54**, 7094–7102 (1996)
22. D.W. McComb, R. Brydson, P.L. Hansen, R.S. Payne, J. Phys. Conden. Mat. **4**, 8363–8374 (1992)
23. Z. Wu, F. Seifert, Solid State Commun. **99**, 773–778 (1996)
24. L. Soriano, M. Abbate, J.C. Fuggle, M.A. Jimenenz, J.M. Sanz, C. Mythen, H.A. Padmore, Solid State Commun. **87**, 699–703 (1993)
25. J.G. Chen, Surf. Sci. Rep. **30**, 1–152 (1997)
26. L.A.J. Garvie, P. Rez, J.R. Alvarez, P.R. Buseck, A.J. Craven, R. Brydson, Amer. Mineral., **85**, 732 (2000)
27. D.J. Wallis, P.H. Gaskell, R. Brydson, J. Microsc. **180**, 307–312 (1995)
28. D.A. Muller, Private communication (2002)
29. J.B. Neaton, D.A. Muller, N.W. Ashcroft, Phys. Rev. Lett. **85**, 1298–1301 (2000)
30. J.L. Gavartin, A.L. Shluger, A.S. Foster, G.I. Bersuker, J. Appl. Phys. **97**, 53704 (2005)
31. D.I. Bazhanov, A.A. Knizhnik, A.A. Safonov, A.A. Bagaturyants, M.W. Stoker, A.A. Korkin, J. Appl. Phys. **97**, 44108 (2005)
32. M.L. Green, E.P. Gusev, R. Degraeve, E.L. Garfunkel, J. Appl. Phys. **90**, 2057 (2001)
33. J. Barnett et al., Mater. Res. Soc. Symp. Proc. **811**, E1.4 (2004)
34. M.V. Fischetti, D.A. Neumayer, E.A. Cartier, J. Appl. Phys. **90**, 4587 (2001)
35. M. Hiratani, S. Saito, Y. Shimamoto, K. Torii, Jpn. J. Appl. Phys. **41**(1), 4521 (2002)
36. H. Lee, in *Technical Digest—International Electron Devices Meeting*, vol. 2004, p. 859 (2004)

37. S. Saito, D. Hisamoto, S. Kimura, H. Hiratani, in T*echnical Digest - International Electron Devices Meeting*, vol. 797 (2003)
38. S. Takagi, A. Toriuni, M. Iwase, H. Tango, IEEE Trans. Electron Devices **41**, 2357 (1994)
39. P.D. Kirsch et al., J. Appl. Phys. **99**, 023508 (2006)
40. S.G. Lim, S. Kriventsov, T.N. Jackson, J.H. Haeni, D.G. Schlom, A.M. Balbashov, R. Uecker, P. Reiche, J.L. Freeouf, G. Lucovsky, J. Appl. Phys. **91**, 4500 (2002)
41. H. Kim, P.C. McIntyre, J. Appl. Phys. **92**, 5094 (2002)
42. S. Ramanathan, P.C. McIntyre, J. Luning, P.S. Lysaght, Y. Yang, Z. Chen, S. Stemmer, J. Electrochem. Soc. **150**, F173 (2003)
43. S. Stemmer, Y. Li, B. Foran, P.S. Lysaght, S.K. Streiffer, P. Fuoss, S. Seifert, Appl. Phys. Lett. **83**, 3141 (2003)
44. G. Bersuker, J. Peterson, J. Barnett, J. Sim, R. Choi, B.H. Lee, P. Lysaght, H.R. Huff, J. Electrochem. Soc. **501**, 623 (2006)
45. T.-H. Cha, D.-G. Park, T.-K. Kim, S.-A. Jang, I.-S. Yeo, J.-S. Roh, J.-W. Park, Appl. Phys. Lett. **81**, 4192 (2002)
46. Z.B. Zhang, S.C. Song, C. Huffman, J. Barnett, N. Moumen, H. Alshareef, P. Majhi, M. Hussain, M.S. Akbar, J.H. Sim, S.H. Bae, B. Sassman, B.H. Lee, in *VLSI Symposium on Technical Digest*, vol. **50** (2005)
47. S. Guha, E. Cartier, M.A. Gribelyuk, N.A. Bojarczuk, M.C. Copel, Appl. Phys. Lett. **77**, 2710 (2000)
48. P.D. Kirsch, P. Sivasubramani, J. Huang, C.D. Young, M.A. Quevedo-Lopez, H.C. Wen, H. Alshareef, K. Choi, C.S. Park, K. Freeman, M.M. Hussain, G. Bersuker, H.R. Harris, P. Majhi, R. Choi, P. Lysaght, B.H. Lee, H.H. Tseng, R. Jammy, T.S. B€ocke, D. J. Lichtenwalner, J.S. Jur, A.I. Kingon, Appl. Phys. Lett. **92**, 092901 (2008)
49. M. Bosman, Y. Zhang, C.K. Cheng, X. Li, X. Wu, K.L. Pey, C.T. Lin, Y.W. Chen, S.H. Hsu, C.H. Hsu, Appl. Phys. Lett. **97**, 103504 (2010)
50. K. Choi, H.-C. Wen, G. Bersuker, R. Harris, B. Hun, Lee. Appl. Phys. Lett. **93**, 133506 (2008)
51. M. Kadoshima, Y. Sugita, K. Shiraishi, H. Watanabe, A. Ohta, S. Miyazaki, K. Nakajima, T. Chikyow, K. Yamada, T. Aminaka1, E. Kurosawa1, T. Matsuki, T. Aoyama, Y. Nara, and Y. Ohji, in *Technical Digest VLSI Symposium*, vol. 66 (2007)
52. A. Toriumi, K. Kita, K. Tomida, Y. Zhao, J. Widiez, T. Nabatame, H. Ota, M. Hirose, in *Technical Digest—International Electron Devices Meeting*, vol. **53** (2007)
53. S.C. Song, Z.B. Zhang, M.M. Hussain, C. Huffman, J. Barnett, S.H. Bae, H.J. Li, P. Majhi, C.S. Park, B.S. Ju, H.K. Park, C.Y. Kang, R. Choi, P. Zeitzoff, H.H. Tseng, B.H. Lee, R. Jammy, in *Technical Digest VLSI Symposium*, vol. **13** (2006)
54. V. Mikhelashvili, R. Brener, O. Kreinin, B. Meyler, J. Shneider, G. Eisenstein, Appl. Phys. Lett. **85**, 5950 (2004)
55. H.Y. Yu, N. Wu, M.F. Li, C.X. Zhu, B.J. Cho, D.L. Kwang, C.-L. Tung, J.S. Pan, J.W. Chai, W.D. Wang, D.Z. Chi, C.H. Ang, J.Z. Chi, S. Ramanathan, Appl. Phys. Lett. **81**, 3618 (2002)
56. M.-H. Cho, Y.S. Roh, C.N. Whang, K. Jeong, H.J. Choi, S.W. Nam, D.-H. Ko, J.H. Lee, N.I. Lee, K. Fujihara, Appl. Phys. Lett. **81**, 1071 (2002)
57. M. Koyama, Y. Kamimuta, M. Koike, M. Suzuki, A. Nishiyama, Jpn. J. Appl. Phys., Part 1 **43**, 1788 (2004)
58. M.A. Quevedo-Lopez, M.R. Visokay, J.J. Chambers, M.J. Bevan, A. LiFatou, L. Colombo, M.J. Kim, B.E. Gnade, R.M. Wallace, J. Appl. Phys. **97**, 043508 (2005)
59. P.S. Lysaght, J.C. Woicik, M.A. Sahiner, B.-H. Lee, R. Jammy, Appl. Phys. Lett. **91**, 122910 (2007)
60. P.S. Lysaght, J.C. Woicik, D. Fischer, G.I. Bersuker, J. Barnett, B. Foran, H.-H. Tseng, R. Jammy, J. Appl. Phys. **101**, 024105 (2007)
61. R. Koba, R.E. Tressler, J. Electrochem. Soc. **135**, 144 (1988)
62. G. He, L.D. Zhang, G.W. Meng, G.H. Li, Q. Fang, J.P. Zhang, J. Appl. Phys. **102**, 094103 (2007)

63. G. Shang, P.W. Peacock, J. Robertson, Appl. Phys. Lett. **84**, 106 (2004)
64. J. Price, G. Bersuker, P.S. Lysaght, J. Vac. Sci. Technol. B **27**, 310–312 (2009)
65. K.J. Hubbard, D.G. Schlom, J. Mater. Res. **11**, 2757 (1996)
66. J. Price, M. Lei, P.S. Lysaght, G. Bersuker, M.C. Downer, J. Vac. Sci. Technol. B **29**(4), 04D101 (2011)
67. J. Huang, D. Heh, P. Sivasubramani, P.D. Kirsch, G. Bersuker, D.C. Gilmer, M.A. Quevedo-Lopez, M.M. Hussain, P. Majhi, P. Lysaght, H. Park, N. Goel, C. Yong, C.S. Park, C. Park, M. Cruze, V. Diaz, P.Y. Hung, J. Price, H.H. Tseng, R. Jammy, in *Digest Technical Papers—Symposium on VLSI Technology*, vol. 34 (2009)
68. S. Barraud, O. Bonno, M. Casse, J. Appl. Phys. **104**, 073725 (2008)
69. M. Casse, L. Thevenod, B. Guillaumot, L. Tosti, F. Martin, J. Mitard, O. Weber, F. Andrieu, T. Ernst, G. Reimbold, T. Billon, M. Mouis, F. Boulanger, IEEE Trans. Electron Devices **50**, 1665 (2006)
70. Y.-C. Yeo, Q. Lu, T.-J. King, C. Hu, T. Kawashima, M. Oishi, S. Mashiro, J. Sakai, in *Technical Digest—International Electron Devices Meeting*, vol. 753 (2000)
71. C.G. Ahn, H.S. Kang, Y.K. Kwong, S.M. Lee, B.R. Ryum, B.K. Kang, J. Appl. Phys. **86**, 1542 (1999)
72. C. Wagner, J. Electrochem. Soc. **99**, 369 (1952)
73. C. Wagner, J. Electrochem. Soc. **103**, 627 (1956)
74. H.K. Liou, P. Mei, U. Gennser, E.S. Yang, Appl. Phys. Lett. **59**, 1200 (1991)
75. M.M.B. Holl, S. Lee, F.R. McFeely, Appl. Phys. Lett. **65**, 1097 (1994)
76. S. Toyoda, J. Okabayashi, H. Kumigashira, M. Oshima, K. Ono, M. Niwa, K. Usuda, G.L. Liu, Appl. Phys. Lett. **84**, 2328 (2004)
77. G. Bersuker, C.S. Park, J. Barnett, P.S. Lysaght, P.D. Kirsch, C.D. Young, R. Choi, B.H. Lee, B. Foran, K. van Benthem, S.J. Pennycook, P.M. Lenahan, J.T. Ryan, J. Appl. Phys. **100**, 094108 (2006)
78. F.K. LeGoues, R. Rosenberg, T. Nguyen, F. Himpsel, B.S. Meyerson, J. Appl. Phys. **65**, 1724 (1989)
79. J. Jang, T.J. Park, J.-H. Kwon, J.H. Jang, C.S. Hwang, M. Kim, Appl. Phys. Lett. **92**, 232906 (2008)
80. M.-H. Cho, H.S. Chang, D.W. Moon, S.K. Kang, B.K. Min, D.-H. Ko, H.S. Kim, P. McIntyre, J.H. Lee, J.H. Ku, N.I. Lee, Appl. Phys. Lett. **84**, 1171 (2004)
81. D. Fathy, O.W. Holland, C. White, Appl. Phys. Lett. **51**, 1337 (1987)
82. O.W. Holland, C. White, D. Fathy, Appl. Phys. Lett. **51**, 520 (1987)
83. G.L. Patton, S.S. Iyer, S.L. Delage, R.C. McIntosh, E. Gannin, Mater. Res. Soc. Symp. Proc. **102**, 295 (1988)
84. F.K. LeGoues, R. Rcsenberg, B.S. Meyerson, Appl. Phys. Lett. **54**, 644 (1989)
85. B.-G. Min, Y.H. Pae, K.S. Jun, D.-H. Ko, H. Kim, M.-H. Cho, T.-W. Lee, J. Appl. Phys. **100**, 016102 (2006)
86. D.C. Paine, C. Caragianis, A.F. Schwartzman, J. Appl. Phys. **70**, 5076 (1991)
87. J.-H. Yoo, S.-W. Kim, B.-G. Min, H. Sohn, D.-H. Ko, M.-H. Cho, J. Vac. Sci. Technol. B **28** (6), 1298 (2010)
88. D. Nayak, K. Kamjoo, J.S. Park, J.S. Woo, K.L. Wang, Appl. Phys. Lett. **56**, 66 (1990)
89. D.K. Nayak, K. Kamjoo, J.S. Park, J.C.S. Woo, K.L. Wang, Appl. Phys. Lett. **57**, 369 (1990)
90. G. Brammertz, H.C. Lin, K. Martens, D. Mercier, C. Merckling, J. Penaud, C. Adelmann, S. Sioncke, W.E. Wang, M. Caymax, M. Meuris, M. Heyns, J. Electrochem. Soc. **155**, H945 (2008)
91. C.L. Hinkle, M. Milojevic, B. Brennan, A.M. Sonnet, F.S. Aguirre-Tostado, G.J. Hughes, E. M. Vogel, R.M. Wallace, Appl. Phys. Lett. **94**, 162101 (2009)
92. C.-W. Cheng, G. Apostolopoulos, E.A. Fitzgerald, J. Appl. Phys. **109**, 023714 (2011)
93. L.K. Chu, C. Merckling, A. Alian, J. Dekoster, J. Kwo, M. Hong, M. Caymax, M. Heyns, Appl. Phys. Lett. **99**, 042908 (2011)
94. L. Lin, J. Robertson, Appl. Phys. Lett. **98**, 082903 (2011)
95. J. Robertson, L. Lin, Appl. Phys. Lett. **99**, 222906 (2011)

96. W. Wang, K. Xiong, R.M. Wallace, K. Cho, J. Phys. Chem. C **114**, 22610–22618 (2010)
97. C.-H. Chang, Y.-K. Chiou, Y.-C. Chang, K.-Y. Lee, T.-D. Lin, T.-B. Wu, M. Hong, J. Kwo, Appl. Phys. Lett. **89**, 242911 (2006)
98. Y.H. Chang, M.L. Huang, P. Chang, C.A. Lin, Y.J. Chu, B.R. Chen, C.L. Hsu, J. Kwo, T.W. Pi, M. Hong, Microelectron. Eng. **88**, 440–443 (2011)
99. M. El Kazzi, L. Czornomaz, D.J. Webb, C. Rossel, D. Caimi, H. Siegwart, J. Fompeyrine, C. Marchiori, Appl. Phys. Lett. **99**, 052102 (2011)
100. M.M. Frank, G.D. Wilk, D. Starodub, T. Gustafsson, E. Garfunkel, Y.J. Chabal, J. Grazul, D. A. Muller, Appl. Phys. Lett. **86**, 152904 (2005)
101. T. Gougousi, J.W. Lacis, Thin Solid Films **518**, 2006–2009 (2010)
102. C.L. Hinkle, A.M. Sonnet, E.M. Vogel, S. McDonnell, G.J. Hughes, M. Milojevic, B. Lee, F. S. Aguirre-Tostado, K.J. Choi, H.C. Kim, J. Kim, R.M. Wallace, Appl. Phys. Lett. **92**, 071901 (2008)
103. C.H. Hou, M.C. Chen, C.H. Chang, T.B. Wu, C.D. Chiang, Electrochem. Solid-State Lett. **11**, D60–D63 (2008)
104. M. Milojevic, F.S. Aguirre-Tostado, C.L. Hinkle, H.C. Kim, E.M. Vogel, J. Kim, R.M. Wallace, Appl. Phys. Lett. **93**, 202902 (2008)
105. M. Tallarida, C. Adelmann, A. Delabie, S. Van Elshocht, M. Caymax, D. Schmeisser, Appl. Phys. Lett. **99**, 042906 (2011)
106. H.-S. Kim, I. Ok, M. Zhang, C. Choi, T. Lee, F. Zhu, G. Thareja, L. Yu, J.C. Lee, Appl. Phys. Lett. **88**, 252906 (2006)
107. S.A. Suleiman, H.J. Oh, A. Du, C.M. Ng, S.J. Lee, Electrochem. Solid-State Lett. **13**, H336–H338 (2010)
108. G.K. Dalapati, Y. Tong, W.-Y. Loh, H.K. Mun, B.J. Cho, IEEE Trans. Electron Devices **54**, 1831–1837 (2007)
109. S. Tougaard, H. Hansen, M. Neumann, Surf. Sci. **244**, 125–134 (1991)
110. M. Procop, J. Electron Spectrosc. Relat. Phenom. **59**, 1–10 (1992)
111. I.M. Band, Y.I. Kharitonov, M.B. Trzhaskovskaya, At. Data Nucl. Data Tables **23**, 443–505 (1979)
112. S. Tanuma, C.J. Powell, D.R. Penn, Surf. Interface Anal. **35**, 268–275 (2003)
113. A.K. Livesey, G.C. Smith, J. Electron Spectroscopy and Related Phenomena **67**, 439–461 (1994)
114. Y.T. Chen, J. Huang, J. Price, P. Lysaght, H. Madan, D. Veksler, C. Weiland, J.C. Woicik, P. Y. Hung, S. Datta, R. Droopad, G. Bersuker, J.C. Lee, P. Majhi, P.D. Kirsch, N. Goel, R. Jammy, in *Digest Technical Papers—Symposium on VLSI Technology* (2011)

Chapter 17
Liquid/Solid Interfaces Studied by Ambient Pressure HAXPES

Z. Liu and H. Bluhm

Abstract The investigation of liquid/solid interfaces using X-ray photoelectron spectroscopy is still in its infancy, but several viable approaches for the characterization of these interfaces have been proposed over the last few years. Most of these schemes require the use of ambient pressure X-ray photoelectron spectroscopy (APXPS) due to the high vapor pressure of the liquids of interest. APXPS at high kinetic energies is especially valuable due to the extended mean free path of electrons at higher energies, which allows measuring liquid/solid interfaces in the presence of thicker solution layers. In this chapter we describe the basics of high-energy APXPS and review current schemes as well as application examples for the measurement of liquid/solid interfaces using photoelectron spectroscopy.

17.1 Introduction

Liquid/solid interfaces are ubiquitous in nature and play an important role in many technological applications. Examples are electrochemical reactions, the photo-catalytic reduction of CO_2, corrosion processes, and the weathering of rocks.

Z. Liu (✉)
Advanced Light Source, Lawrence Berkeley National Laboratory,
Berkeley, CA 94720, USA
e-mail: zliu2@lbl.gov

Z. Liu
State Key Laboratory of Functional Materials for Informatics, Shanghai Institute
of Microsystem and Information Technology, Chinese Academy of Sciences,
Shanghai 200050, China

Z. Liu
Condensed Matter Physics and Photon Science Division, School of Physical Science
and Technology, ShanghaiTech University, Shanghai 200031, China

H. Bluhm (✉)
Chemical Sciences Division, Lawrence Berkeley National Laboratory,
Berkeley, CA 94720, USA
e-mail: hbluhm@lbl.gov

© Springer International Publishing Switzerland 2016

J.C. Woicik (ed.), *Hard X-ray Photoelectron Spectroscopy (HAXPES)*,
Springer Series in Surface Sciences 59, DOI 10.1007/978-3-319-24043-5_17

For a fundamental understanding of the reactions at liquid/solid interfaces it is paramount to measure the chemical composition and structure in particular of the electric double layer, which spontaneously forms at a liquid/solid interface, and where—depending on the nature of the solid surface, the constituents of the liquid and an applied bias voltage—the structure and chemical composition of the interlayer with the solid is distinct from the average liquid composition in the bulk. It is thus imperative to develop new tools for the investigation of liquid/solid interfaces at the molecular level [1], in particular techniques as routine, versatile and sensitive for interfaces as X-ray photoelectron spectroscopy [2]. A full characterization of the liquid/solid interface requires the measurement of the properties of the solid bulk, the bulk liquid, and the thin interface layer between the solid and liquid phases. The measurement of the properties of the interface layer is the most difficult task, yet the interface is the most important part of the liquid/solid system. Furthermore, a liquid/solid interface, such as that in an electrochemical cell, needs to be characterized in situ or *operando* to capture the true makeup of the interfacial layer under operating conditions. A number of different methods have been used to investigate liquid/solid interfaces, among them scanning probe microscopy [3, 4], infrared spectroscopy [5], non-linear optical spectroscopies (sum-frequency generation [6], second harmonic generation [7]), surface X-ray diffraction [8], X-ray absorption spectroscopy [9] as well as X-ray standing wave fluorescent yield (XSW-FY) spectroscopy [10]. A comprehensive overview of the different techniques and their relative advantages can be found in a recent review by Zaera [11].

X-ray photoelectron spectroscopy is in principle an excellent method for the investigation of liquid/solid interfaces since it has elemental and chemical sensitivity and allows measuring local electrical potentials (without mechanically contacting the sample) through the detection of rigid kinetic energy shifts in all core and valence levels. It thus provides simultaneous chemical and potential imaging at a lateral resolution determined either by the incident X-ray beam size or the area detector of the spectrometer (in the latter case in one direction). This capability of XPS makes it ideally suited to determine the chemical composition and electrical potentials across the electric double layer at a liquid/solid interface.

Due to the high vapor pressure of most liquids of interest, differential pumping schemes have to be used in XPS experiments to minimize the elastic and inelastic scattering of electrons in the gas phase above the liquid. This technique is commonly referred to as ambient (or high) pressure XPS [12, 13] (APXPS, HPXPS) and was pioneered in the early 1970s by Siegbahn and coworkers [14, 15]. Current instruments are able to work at pressures above 20 Torr, the equilibrium vapor pressure of water at 20 °C, with good signal-to-noise ratios at acceptable acquisition times [12, 13, 16]. The further extension of APXPS to the high kinetic energy (KE) range, i.e. ambient pressure HAXPES, has two main advantages: On the one hand the reduced scattering of photoelectrons in the gas phase provides higher signal intensity at higher vapor pressure. On the other hand, high KE photoelectrons have an increased mean free path in the liquid and thus enable the measurement of liquid/solid interfaces at increased liquid film thicknesses.

Apart from the challenge that working at ambient pressures poses in photoelectron spectroscopy, and which has been addressed in APXPS designs, a main technical obstacle is the preparation of liquid films that are thick enough to be viable model systems to mimic the real liquid/solid interfaces, but thin enough to permit photoelectrons from the liquid/solid interface to penetrate the liquid on their path to the photoelectron spectrometer. Another method is the use of ultrathin solid films in contact with a bulk liquid reservoir, where the electrons traverse the solid membrane on their way to the electron spectrometer and thus the preparation of the electron-transparent solid film is the main challenge. Several approaches that address these challenges have been proposed over the past years and will be discussed in detail below.

A third challenge concerns the enhancement of the photoelectron signal from the narrow interfacial region over that from the bulk materials on either side of the interface. This problem can be addressed by the use of standing wave methods, where the X-rays are tailored into a standing wave by interference of the incident with the reflected wave at the first order Bragg reflection, often using multilayer mirror substrates which determine the wave length of the standing wave (see Chapter by Zegenhagen et al. in this book [17]). This approach, which was recently for the first time applied to APXPS measurements of liquid/solid interfaces, will be discussed at the end of this chapter, together with the results of several other recent APXPS investigations of liquid/solid interfaces.

17.2 Technical Aspects

17.2.1 Optimum Photon Energy Range for Liquid/Solid Interface Studies

In this section we address the optimum photon energy range for ambient pressure HAXPES. Figure 17.1 shows the inelastic mean free path (IMFP) of photoelectrons (PEs) in water [18], with the expected increase of the IMFP with increasing KE; thus, for a given core level, the use of hard X-ray photons permits measurements at increased depth into the sample. This is beneficial for the investigation of buried interfaces, such as liquid/solid interfaces. Unfortunately, this large probing depth will reduce the relative contribution from the key interface region (typically ~ 1 nm thick) with respect to that of the bulk liquid and solid. In addition, the photo-ionization cross-section decreases with increasing photon energy, thus further reducing the absolute photoemission signal from the interface region. Therefore, an optimal photon energy range exists for a given core level of interest in studies of the liquid/solid interface. In general, the binding energies (BE) of most core levels of interest in these studies are below 1 keV.

In the following we will discuss why “tender” X-rays (2–7 keV) result in optimal kinetic energies for PEs from core levels with binding energies below 1 keV to

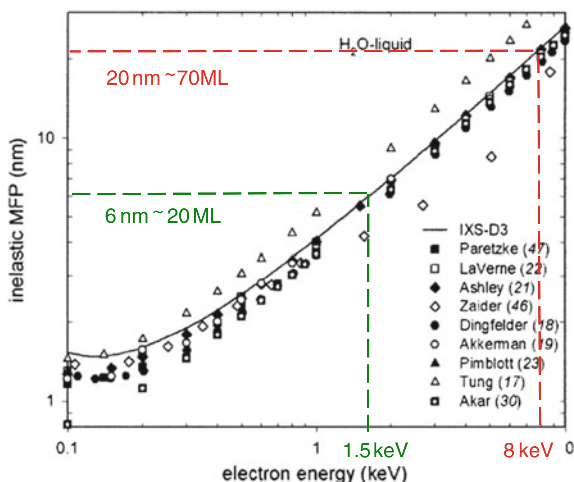

Fig. 17.1 Dependence of the inelastic mean free path of electrons in liquid water on electron kinetic energy. For a standard X-ray anode (Al K-alpha, 1486.7 eV) the inelastic mean free path is about 6 nm ($\sim$20 monolayers of water) for electrons with the highest KE. The increase of the probing depth is about threefold when the excitation energy is increased to 8 keV. Adapted and reproduced with permission from [18]

extract information from the liquid/solid interface region [19]. The optimum photon energy window for the detection of elements from buried interfaces is given by the competing effects of increased probing depth at increased kinetic energies, and decreased photoelectron cross section with increasing incident photon energy. To illustrate this, we use the SESSA software package [20, 21] (also discussed by Powell in this book [22]) to simulate a model system consisting of a carbon over-layer of variable thickness to mimic thin electrolyte films. As shown in Fig. 17.2 (insert), we use a 1 nm layer of iron to represent the interface region (a typical thickness for the electrical double layer) between the carbon overlayer and silicon substrate.

Figure 17.2 shows the intensity of the Fe $2p_{3/2}$ core (BE $\sim$710 eV) level signal at the buried interface as a function of incident photon energy for 10, 20, and 30-nm thick carbon over-layers. For a 10 nm carbon overlayer, the Fe $2p_{3/2}$ signal increases sharply at $\sim$1 keV photon energy. It reaches a maximum intensity at around 3 keV, upon which the intensity decreases gradually as the photon energy increases. The sharp rise of the photoelectron yield at $\sim$1 keV is due to the probing depth effect, where at low photon energies (<1 keV) the IMFP (<3 nm) is shorter than the thickness of the 10 nm carbon overlayer and thus only a small portion of the iron Fe $2p_{3/2}$ interface signal is detected. As the photon energy increases, the IMFP of the PEs increases as well and with it the signal from the Fe at the interface, as the IMFP approaches the thickness of the carbon overlayer. With a further increase of the photon energy the photo-ionization cross-section of Fe $2p_{3/2}$ decreases significantly, resulting in the decrease of the Fe $2p_{3/2}$ signal. Since the

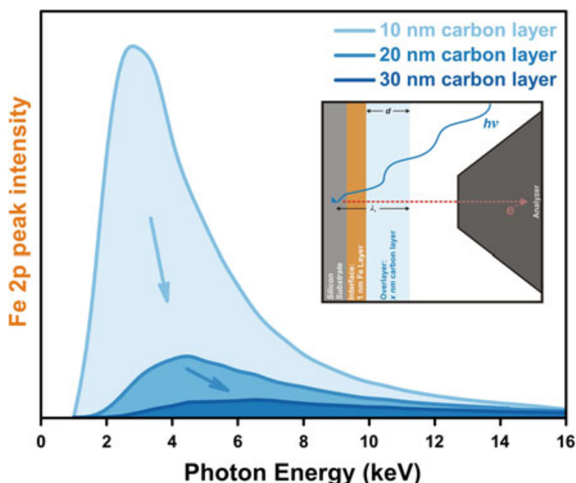

Fig. 17.2 Integrated area of Fe *2p* for a 1 nm Fe interface layer as a function of photon energy buried under various thicknesses of carbon to illustrate the ideal photon energy region for studying interface phenomena in systems on the order of 10s of nm in thickness. The *inset* is a representation of the electrolyte, electrode, and electrolyte-electrode interface layer used in the SESSA simulation used to generate the data for this plot

dependence of the IMFP and photo-ionization cross-section on the photon energy are qualitatively the same for all core levels, we expect to see similar trends (Fig. 17.2) for the detection of other elements from buried interfaces. As the thickness of the carbon overlayer increases to 20 and 30 nm, both the onset photon energies for the detection of a photoelectron signal and the optimal incident photon energies shift to higher energies due to these same IMFP and photo-ionization cross-section effects. In addition, the absolute Fe $2p_{3/2}$ signal at the optimal photon energy also decreases significantly for the thicker films because of the decreased photo-ionization cross-section (from the higher photon energy) and the increased attenuation of the photoelectrons by the thicker over-layer.

The SESSA XPS simulation results have two implications: (1) To probe the buried solid-liquid or solid-solid interface, the photon energy and model system used (overlayer thickness) need to be evaluated simultaneously. For the model system based on this nanometers thick thin-film overlayer, “tender” X-ray photons with energies between 2 and 7 keV offer the best signal to noise ratio. (2) For model systems with more than ~30 nm over-layer (either liquid or solid), XPS may lose its advantage over other methods, such as sum-frequency vibrational spectroscopy [23–25] and second harmonic generation [26, 27], which may become more attractive options.

Many of the liquids of interest are typically low Z materials where the electron IMFPs are significantly larger than those of solid materials with higher Z value. This makes it in many cases advantageous to probe the liquid/solid interface from the liquid side. This is particularly important for aqueous solutions since the PEs

have a longer IMFP in water than in most other materials. For example, the electron IMFP in water is about 20 % longer than that in carbon.

The preceding discussion demonstrates the tradeoffs between surface and bulk sensitivity when probing the narrow, buried interface region. It also highlights the main technical challenge for using photoelectron spectroscopy. An ultrathin (on the order of a few tens of nanometers) liquid or solid thin film is needed for the effective measurement of the interface region either from the liquid or from the solid side of the interface.

17.2.2 Electron Optic Considerations for Ambient Pressure HAXPES

Since the voltages in the electrostatic lens of a photoelectron analyzer in general increase with the electron kinetic energy, it is challenging to detect high kinetic energy electrons at high pressures due to the threat of gas discharge (arcing). Overcoming this problem requires the design of differentially pumped electrostatic lens systems where the voltage differences between the adjacent lens elements and common ground are reduced in the high pressure region, without sacrificing the overall efficiency of electron detection.

Currently, two commercial vendors (Scienta and SPECS) provide solutions to ambient pressure HAXPES applications. To our knowledge, both commercial analyzers use a shaped mesh as one of first lens elements in the pre-lens. As discussed in detail in [28], using a shaped mesh lens allows to collect high energy electrons from a high pressure environment and has several advantages: A large angular range can be collected without having extreme spherical aberrations; the electron optical properties of the mesh electrode allow for a relatively long working distance between the sample and the first electrostatic lens section with strong electrical field gradients, which is beneficial for suppressing corona discharge [29]. Using a shaped mesh lens also allows for smaller opening angles of the entrance aperture to the lens system, which improves maneuverability of the sample in the vicinity of the aperture without scarifying electron collection performance. This is very important for the operation at high kinetic energies because the lens voltages can be kept relatively low.

It should be noted that there are also disadvantages to using mesh electrodes. Electric fields at the shaped mesh interface produce micro lens effects for each individual transparent part of the mesh. This effect cannot be removed by changing the thickness, or the wire density, of the mesh. Fortunately, current theory can estimate many of the side effects with high accuracy. By improving the manufacturing techniques and the use of carefully designed lens tables, the micro lens effects have only small effects on the overall analyzer performance, except for the spatial and angular resolution, which is lower for analyzers using shaped mesh electrodes compared to traditional designs using only cylindrical lenses [28].

However, the new pre-lens designs have already enabled the reliable and stable detection of high kinetic energy electrons in ambient pressure HAXPES at pressures up to 100 Torr [28].

17.2.3 Accessing Liquid/Solid Interfaces Using Photoelectron Spectroscopy

The biggest challenge in the investigation of liquid/solid interfaces using APXPS is to create either an ultrathin solid film or a thin liquid film for the effective detection of electrons from the interface region. Currently both approaches are being pursued by several groups. The film thickness should be of the order of the inelastic mean free path of photoelectrons at the given kinetic energy, e.g. for water about 6 nm for KE ∼1.5 keV and about 20 nm for KE ∼8 keV (see Fig. 17.1) [18]. Preparing ultrathin liquid or solid films that are stable for the duration of the measurements (often several hours) is not straightforward. Several different strategies are being developed, each with their own advantages but also shortcomings.

Perhaps the most straightforward way to prepare a thin liquid film is through adsorption of the liquid from the vapor. For the case of water this requires raising the relative humidity to values close to saturation (100 %), when on hydrophilic surfaces a multilayer water film is present, with the film thickness dependent on the relevant humidity (RH). Figure 17.3 shows an example for the case of TiO_2(110) [30]. The challenges of this approach are the control of pH or solute concentration in the film, the necessity to precisely control temperature and water vapor pressure due to the high adsorption/desorption rates at ambient temperatures, and the control of electrical potentials across the interface, which requires the presence of control and reference electrodes in the solution film. These boundary conditions limit the use of this method to a certain subset of experiments, where the potentials do not need to be actively controlled and the chemical composition and the pH are not changed during the experiments [31, 32].

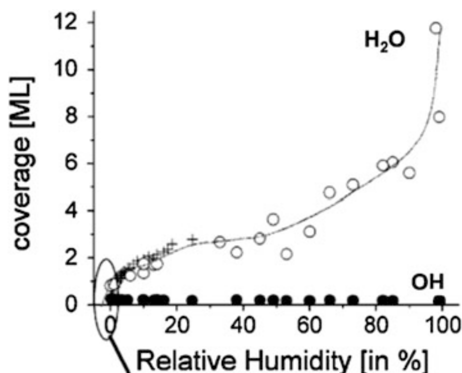

Fig. 17.3 Thickness of the water layer on rutile TiO_2(110) as a function of relative humidity. Reproduced with permission from [30]

A second strategy to prepare liquid/solid interfaces is the use of liquid jets [33], which contain small (sub-micron) particles of the solid of interest. Some of these particles will reside sufficiently close to the liquid jet surface so that photoelectrons emitted from the liquid/solid interface can be detected (see Fig. 17.4) [34, 35]. The advantage of this method is that the pH and the concentration of the solution can be tuned during the measurements. A drawback is the difficulty to control electrical potentials across the solid/liquid interface. Using this approach, e.g. the surface potential of silica particles as a function of particle size and pH of the solution was successfully determined [36].

Another intriguing approach is the use of ultrathin membranes, where one side of the membrane is part of a liquid cell, while the other side faces the electron spectrometer (see Fig. 17.5). Membrane materials used so far are silicon [37], Nafion [38], and graphene/graphene oxide [39, 40]. The electrons from the liquid/solid interface traverse the membrane on the way to the electron spectrometer. Similar to in-situ X-ray photon-in photon-out environmental cells [41], these ultrathin membrane windows are increasingly being fabricated as low-cost, single-use environmental cells that are compatible with many electron based characterization techniques. There are several advantages to this technique: (i) In a flow cell setup the solution concentration and pH can be changed during the experiment, (ii) full potential control across the interface is possible, with reference and counter electrodes inside the liquid cell and the membrane as working electrode, and (iii) the absence of a gas phase since the liquid is contained behind the membrane. In the ideal case of a leak-tight membrane, it would not even be necessary to use a differentially-pumped electron spectrometer (although it might be safer given the chance of the evolution of leaks in the membrane). The drawback of

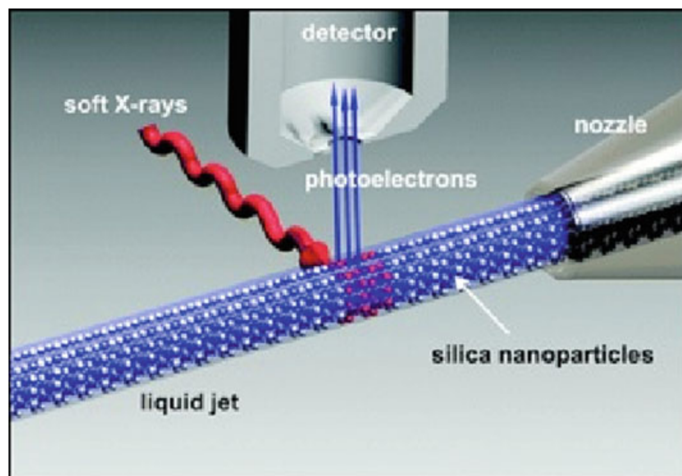

Fig. 17.4 Preparation of liquid/solid interfaces using the liquid-jet technique, where solid particles are suspended in the liquid, with some of the particles residing sufficiently close to the jet surface to detect photoelectrons from the liquid/solid interface. Reproduced with permission from [34]

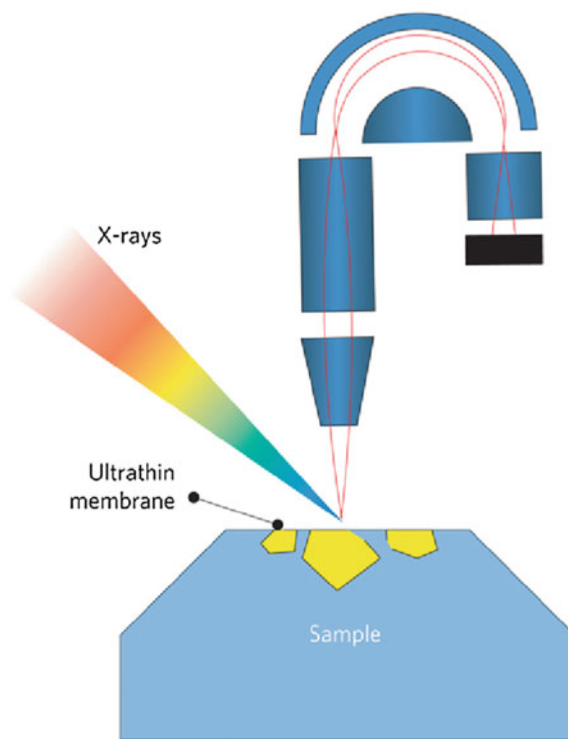

Fig. 17.5 Detection of photoelectrons from the liquid/solid interface of an ultrathin membrane, where the electrons transverse the whole of the membrane on their way to the electron spectrometer. Reproduced with permission from [39]

this approach is the fabrication and mounting of ultrathin membranes, and the possible limitation of this approach to certain classes of materials which lend themselves to forming ultrathin membranes or can be deposited onto an ultrathin membrane template.

The last technique we discuss here is the so-called “dip & pull” method, which has recently been developed to create an ultrathin liquid film on a solid surface. This approach is inspired by the previous works by Bockris and Cahan [42] and Siegbahn [43]. We will describe this new technique in detail here. As reported in [28], a flat working electrode (WE, here Pt foil) is placed close to the conical entrance aperture to the differentially pumped lens system, as shown in Fig. 17.6a. The sample (WE), Ag/AgCl reference electrode (RE) and a Pt foil counter electrode (CE) are mounted on an electrically insulating polyether ether ketone (PEEK) holder that is attached to a multi-axis manipulator. Electrical feedthroughs at the manipulator connect the WE, RE, and CE to an external potentiostat to perform *operando* electrochemistry measurements. When an aqueous electrolyte is used, the water vapor pressure in the main chamber is controlled up to about 20 Torr through a ultra-high vacuum (UHV) leak valve connected to a heated water reservoir. At the equilibrium condition, this allows the electrolyte level in the glass electrolyte container to remain constant during the experiment.

In the example shown in Fig. 17.6a, a Pt WE is placed in front of the analyzer cone where XPS spectra of the bare electrode in vacuum or a gas environment can be collected. Representative Pt *4f* and O *1s* XPS spectra from the Pt WE under water vapor are depicted in Fig. 17.6a as well. In Fig. 17.6b, the electrodes are moved away from the analyzer cone so that they can be fully immersed into the electrolyte. Under this condition, the sample can be electrochemically characterized in situ by, e.g., cyclic voltammetry (CV).

After the immersion of all three electrodes into the electrolyte, a solid-liquid interface can be created on the sample (WE) by slowly extracting the sample from

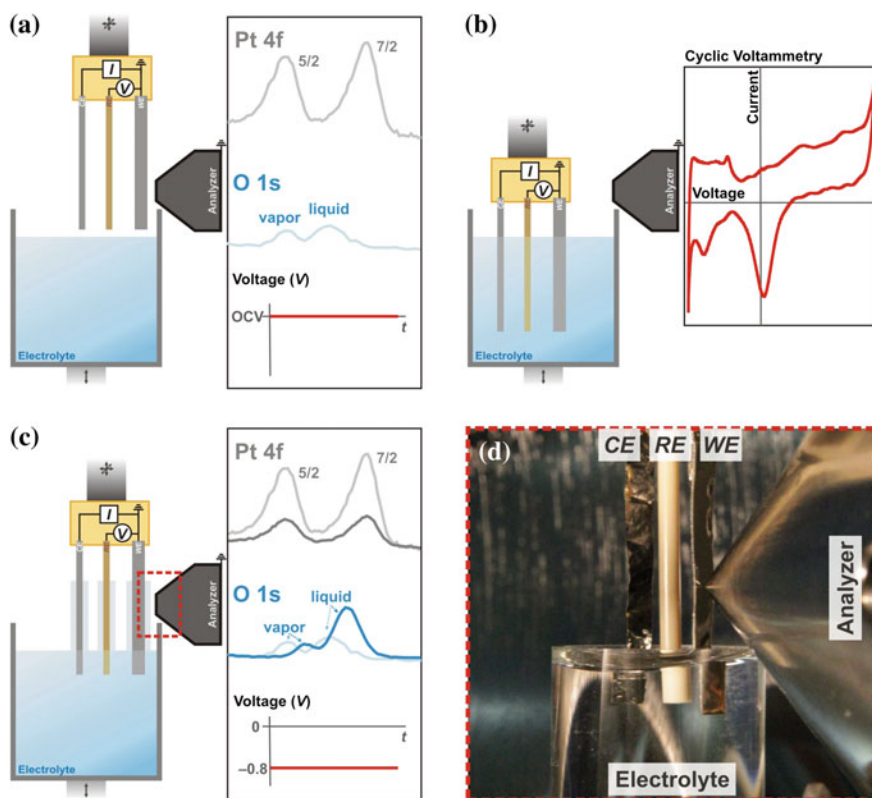

Fig. 17.6 Schematic of three-electrode electrochemistry setup in the AP-XPS chamber. **a** Position of electrodes before immersion and corresponding representative Pt 4*f*, O 1*s* spectra and electrochemical profile. **b** Electrodes are immersed in the electrolyte, where any electrochemical treatment can be performed within the APXPS chamber. Shown is a representative Pt foil capacitive-voltage (CV) curve in 6 M KF aqueous electrolyte. **c** Electrodes are placed at the AP-XPS measurement position, and corresponding representative Pt 4*f* and O 1*s* of the partially removed electrodes are overlaying the representative vapor exposed electrode spectra (shown in Fig. 17.4a). **d** Image of the 3-electrode apparatus that has been first dipped into and then pulled from the electrolyte in the beaker and placed into XPS position while ensuring all three electrodes are in contact with the electrolyte within the beaker. Reproduced with permission from [28]

the solution either by raising the three electrodes or by lowering the electrolyte container. Following this procedure, a thin layer of liquid electrolyte film is formed on the Pt electrode. This layer is stabilized by the close-to equilibrium vapor pressure in the chamber. By moving the three-electrodes and electrolyte container accordingly, this thin film can be positioned at the focal point of the electron analyzer and studied using APXPS (Fig. 17.6c). The liquid film thickness depends on a number of factors, among them the height of the measurement position with respect to the bulk electrolyte surface. During the measurement, all three electrodes are kept in contact with the bulk electrolyte, thus allowing the simultaneous collection of spectra from the WE (Pt *4f*), electrolyte (O *1s*) and water vapor gas phase (O *1s*) at varying holding potentials (see Fig. 17.6c). Figure 17.6d shows an image of the 3-electrode apparatus that has been partially emerged from the electrolyte in the beaker and placed into XPS position.

Using this method, stable KF and KOH liquid films of nanometer thickness have been created on both a Pt electrode [28] and a Ni thin film [44] electrode. It has been demonstrated that the thin liquid layer (10–30 nm thick) is continuous and can carry the electrical potential of the bulk electrolyte. Using this technique, the electrochemical oxidation of Pt [28] and Ni [44] has been measured in situ. While this approach shows great promise there are still a number of technical challenges that need to be overcome, such as possible limitations to the ionic/mass transport from the bulk solution reservoir to the measurement position due to the limited film thickness. This mass transport limitation can, in principle, affect the ion concentrations of the solution, such as pH value, at different vertical position. However, the ability to measure the relative concentration of different ionic species as well as the total solution thickness as a function of position above the solution reservoir using XPS allows identifying and characterizing possible mass transport related issues.

17.3 Application Examples

In the following we will discuss several examples of APXPS measurements of liquid/solid interfaces. The examples were chosen to demonstrate the breadth of possible applications of photoelectron measurements at liquid/solid interfaces, as well as to show the utility of the different approaches to preparing liquid/solid interfaces, provided in the previous section.

17.3.1 Measurement of the Surface Potential of Silicon Oxide Particles in Solution

One of the basic properties of the liquid/solid interface is its surface potential, which is caused by the presence of surface charges at the interface, such as protonated or deprotonated hydroxyl groups. The measurement of the surface potential

has proven to be elusive for a long time. Using XPS in combination with the liquid microjet technique, Brown et al. [36] performed a pioneering measurement of the surface potential of SiO_2 nanoparticles in a 0.05 M NaCl solution. SiO_2 is arguably one the most important oxides due to its ubiquity in nature as part of minerals and rocks as well as in technology.

Figure 17.7 shows Si 2*p* spectra taken with a photon energy of 510 eV, i.e. a kinetic energy of ~400 eV, under acidic (pH 0.3, lower panel) and basic (pH 10.0, upper panel) conditions [36]. Aside from the main peak which is due to Si in the bulk of the nanoparticle, there are small shoulders on the high (low) binding energy side of the main peak under acidic (basic) conditions, which are due to protonated (deprotonated) silanol groups at the SiO_2 particle/solution interface. In addition, there is a shift of 0.3 eV in the main Si 2*p* peak towards higher binding energy as the pH is decreased from 10.0 to 0.3. Brown et al. interpret this shift as a direct result of the increase of the surface charge towards more positive values at low pH, i.e. upon protonation of the surface. This phenomenon is akin to the application of a positive bias to the surface, or charging of the surface in the case of electrically insulating materials, which both also lead to apparent binding energy shifts towards higher values. The XPS data in Fig. 17.7 thus provide a direct measure of the surface potential change at the liquid/solid interface. The versatility of the use of

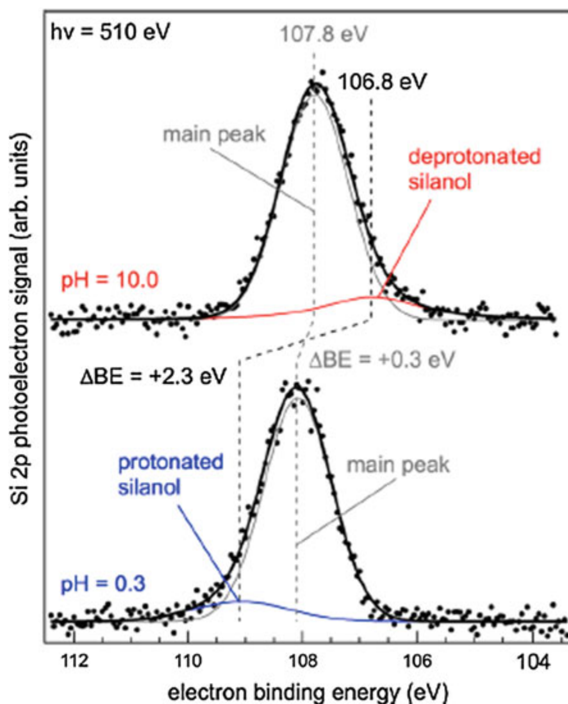

Fig. 17.7 Si 2p XPS spectra measured from a liquid micro jet, containing silica particles with an average diameter of 9 nm. The lower panel shows the spectrum at a pH of 0.3, the upper at a pH of 10.0. The main peak is due to Si in the bulk of the nanoparticles, while the small shoulders at either the high (low) binding-energy sides are due to protonated (deprotonated) silanol groups at the liquid/solid interface. The binding energy axis is referenced to the $1b_1$ orbital of liquid water. Reproduced with permission from [36]

suspended nanoparticles in liquid microjets will allow measuring a wide range of combinations of solid materials with solutions of varying composition, concentration and pH values.

17.3.2 Measurement of Liquid/Solid Interfaces Using Ultrathin Solid Membranes

Recently, Kolmakov et al. [39] demonstrated successfully that in situ environmental cells using graphene oxide as an electron-transparent window can be used for photoelectron spectroscopy (see Fig. 17.5). Membranes as thin as one layer of graphene-oxide are used to separate the liquid cells and the electron spectrometer. The electrons from the liquid/solid interface traverse the membrane on the way to the electron spectrometer. In this proof-of-principle experiment, the authors also show that graphene oxide windows are transparent to low-energy electrons (down to 400 eV), and they demonstrate the feasibility of X-ray photoelectron spectroscopy measurements on model samples such as gold nanoparticles and aqueous salt solution placed on the back side of a window.

Around the same time as Kolmakov et al.'s work [39], an electrochemical cell based on an ultrathin Si membrane window (15 nm) was developed at the Japanese synchrotron facility SPring 8. APXPS studies of electrochemical reactions on the Si membrane were conducted using a traditional hemispherical electron analyzer, located on the vacuum side of the Si membrane window [37]. The authors used the silicon membrane itself as one electrode and Cu tape as the counter electrode. The aqueous electrolyte is sealed inside a micro-cavity between the Si-membrane and the Cu tape. Using this two electrode system, both current-voltage (I-V) measurements and HAXPES experiments (at 5950 eV) were performed [37]. As shown in Fig. 17.8a, the observed anodic current in the cell starts to increase at about 0.8 V. Due to the two electrode limitation, the electrode potentials cannot be unambiguously determined for both the Si electrode and the Cu electrode, but Si oxidation and hydrogen evolution reactions are still expected to take place at the Si membrane and Cu tape, respectively, in the presence of an anodic current. Figure 17.8b–d shows Si 2*p* spectra taken at different positive potentials (700–1500 meV). The oxide peak observed around 104.5 eV increases as the potential becomes more positive (Fig. 17.8c), providing quantitative information on the oxide growth as a function of potential [37].

In addition, Takagi et al. recently performed one of the first in-situ ambient pressure HAXPES experiments at a photon energy of 7.94 keV [38]. Using a special designed Nafion membrane polymer electrolyte fuel cell, the authors performed X-ray photoelectron spectroscopy measurements of a Pt/C electrode under working conditions. Instead of the membrane-sealed liquid cell, they used a two chamber flow cell separated by a Nafion membrane. The anode side H_2/N_2 gas mix was kept up to atmospheric pressure and the cathode side H_2O pressure was up to 21 Torr, which corresponds to the saturated vapor pressure of water around room

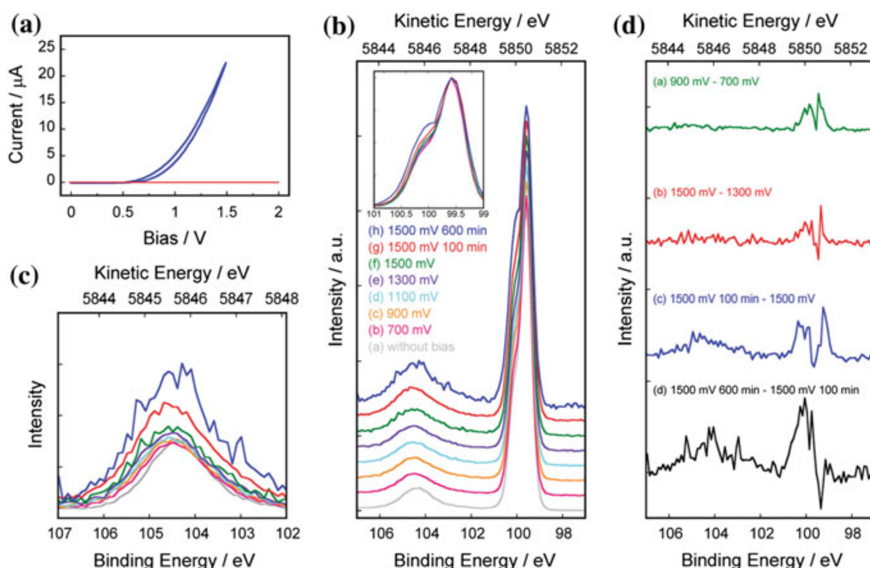

Fig. 17.8 **a** Current-voltage (I-V) relationships of a micro-volume cell with (*blue*) and without water (*red*). **b** Si $2p_{3/2}$ XPS spectra in the region of the Si membrane measured (a) without bias and (b) at 700 mV, (c) 900 mV, (d) 1100 mV, (e) 1300 mV, and (f) 1500 mV. Spectrum (g) was taken after holding the potential at 1500 mV for 100 min and (h) after 600 min. The *inset* in (**b**) shows a magnified image of (**b**) in the region between 101 and 99 eV. **c** Detailed view of the Si $2p_{3/2}$ binding-energy region between 107 and 102 eV, corresponding to Si^{4+}. **d** Several difference spectra of the data in (**b**). Reproduced with permission from [37]

temperature. Under these conditions, the Pt $3d_{5/2}$ level showed oxidation of the Pt nanoparticles at the cathode, with a clear dependence of the oxidation on the applied voltage between the anode and cathode. Although this is not strictly a liquid/solid experiment, it is a clear demonstration that ambient pressure HAXPES is a valuable in situ tool for the investigation of the electronic states and the adsorbed species of polymer electrolyte fuel-cell electrode catalysts under reaction conditions. The ambient pressure HAXPES results by Tagaki et al. [38] show no evidence of the various oxygen species (e.g., H_2O, H_2O–OH, and OH–O) on the Pt surface that were observed in previous soft X-ray APXPS measurements on Pt at lower pressures [45, 46]. The reason for this discrepancy is not obvious, but could be related to the difference in total water vapor pressure or the difference in surface sensitivity.

17.3.3 Operando *Measurement of Pt Oxidation in KF Solution*

Using the "dip & pull" method, Axnanda et al. [28] measured in situ the oxidation of a Pt WE to demonstrate that the thin film created can be used as a functional

electrolyte. In the experiment, the Pt WE is immersed into 6 M KF followed by cyclic voltammetry from −0.8 to 0.8 V (vs. Ag/AgCl). Once the Pt CV has stabilized, the Pt electrode is pulled from the electrolyte and moved to the analysis position (as shown in Fig. 17.6c) while holding the potential at −0.8 V. After the electrolyte film is formed, the applied voltage is changed to 0.0–1.2 V while keeping the Pt WE electrode at the APXPS measurement position.

The Pt $4f_{7/2}$ spectrum at a holding potential of 0.0 V shows only a peak at a BE of 71.2 eV due to metallic Pt (Fig. 17.9, lower panel). Upon changing the holding potential to 1.2 V, new features appear on the higher binding energy side of the metallic Pt peak. To fit the Pt $4f_{7/2}$ spectrum at 1.2 V, two additional peaks at BE of 72.6 eV (shown in purple color) and 74.1 eV (shown in black color) are needed, which have a BE that is higher by 1.4–2.9 eV than that of the metallic Pt peak.

The 72.6 eV Pt 4*f* peak is in agreement with a Pt^{+2} oxidation state, while the 74.1 eV Pt 4*f* is assigned to Pt^{+4}, based on literature values [47, 48]. This leads to the conclusion that the Pt interfacial species observed at oxygen evolution reaction potentials are a mixture of both the Pt divalent and Pt tetravalent state, which is different from the pure tetravalent state suggested by the Pourbaix diagram at this pH range [49]. It is interesting to note that the Pt oxidation conditions in this experiment are similar to those in the Pt oxidation experiment performed by Takagi et al. [38], there using a model in-situ polymer electrolyte fuel cell. The assignment of the Pt oxidation-state peaks are different in these two studies. Because the signal-to-noise ratio in the Pt 4*f* spectrum is less than ideal in the "dip & pull" experiment, the data are not sufficient to provide qualitative analysis of the Pt

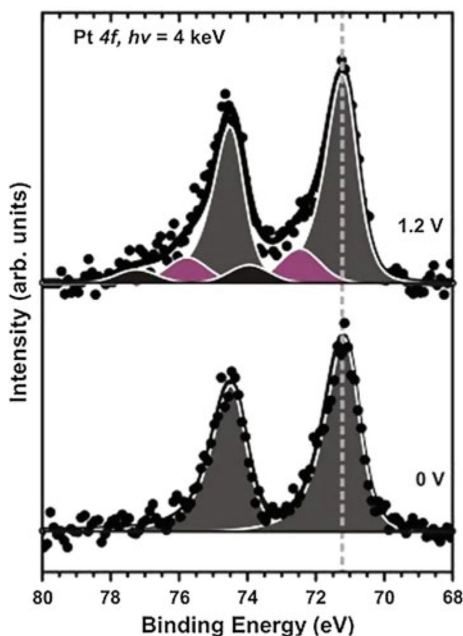

Fig. 17.9 Pt 4*f* XPS spectra of a Pt foil in a 6 M KF solution, at holding potentials of 0 V and 1.2 V during the XPS measurement. All of the potentials are reported with respect to Ag/AgCl reference electrode. Reproduced with permission from [28]

oxidation state under oxygen-evolution reaction conditions. Nevertheless, this study shows that the thin electrolyte layer formed on the surface of Pt maintains an electrical potential across the electrode-electrolyte interface, indicating that this method can potentially be used to perform *operando* studies on electrochemical systems using the AP-XPS system. Clearly, more studies are urgently needed to clarify some important details of this method, such as the ion mass transport along the film, the pH values and ion concentrations of the film solutions.

17.3.4 Depth-Dependent Concentration Profiles from Standing Wave APXPS

One of the big challenges in the study of liquid/solid interfaces using photoelectron spectroscopy is the large contribution of the bulk solid and bulk liquid to the overall signal which can strongly interfere with the detection of the signal from the relatively narrow interfacial region. A promising approach to enhancing the signal from the interface is standing-wave ambient-pressure photoemission spectroscopy (SWAPPS). This method is based on standing wave photoemission spectroscopy, where incident X-rays illuminate the sample under the first order Bragg diffraction condition of either a lattice plane or a multilayer mirror and interfere with the reflected X-rays, thus forming a standing-wave in the interference volume. The standing wave propagates perpendicular to the interface and has a period close to that of the lattice spacing or the multilayer grating [50, 51]. The standing wave approach provides a built-in ruler, i.e., the period of the standing wave, to determine absolute depth distributions of chemical species throughout the probed volume, which is a considerable improvement over other approaches to depth-profiling in XPS, where either the kinetic energy or the takeoff angle of the photoelectrons are varied to change the probing depth.

An example for the application of SWAPPS to the measurement of the ion distribution at the interface of a thin, mixed NaOH/CsOH film is given in Fig. 17.10. A thin film of a mixed NaOH/CsOH solution is drop-cast onto a hematite substrate, dried, and then rehydrated inside the in situ cell of the APXPS chamber through condensation of water from the gas phase at $\sim$7 % relative humidity. The hematite sample was deposited onto a Mo/Si multilayer with a period of 3.4 nm (80 repeats). For the incident photon energy of 910 eV, used in these experiments, the first order Bragg angle is about 12° from the sample surface. Rocking curves around the first order Bragg diffraction peak were taken for all elements in the sample: Fe, O, Cs, Na, as well as C from adventitious contamination. The rocking curves for O 1s are displayed in Fig. 17.10b and clearly show similarities in the peak position and shape of the rocking curve for OH and adsorbed water, indicating that these components are co-located at the sample surface. Strong differences between the rocking curves of these overlayer species and the hematite oxygen are also observed, as expected. Figure 17.10c shows the rocking curves for Cs 4d and Na 2p, where a small but reproducible shift in the

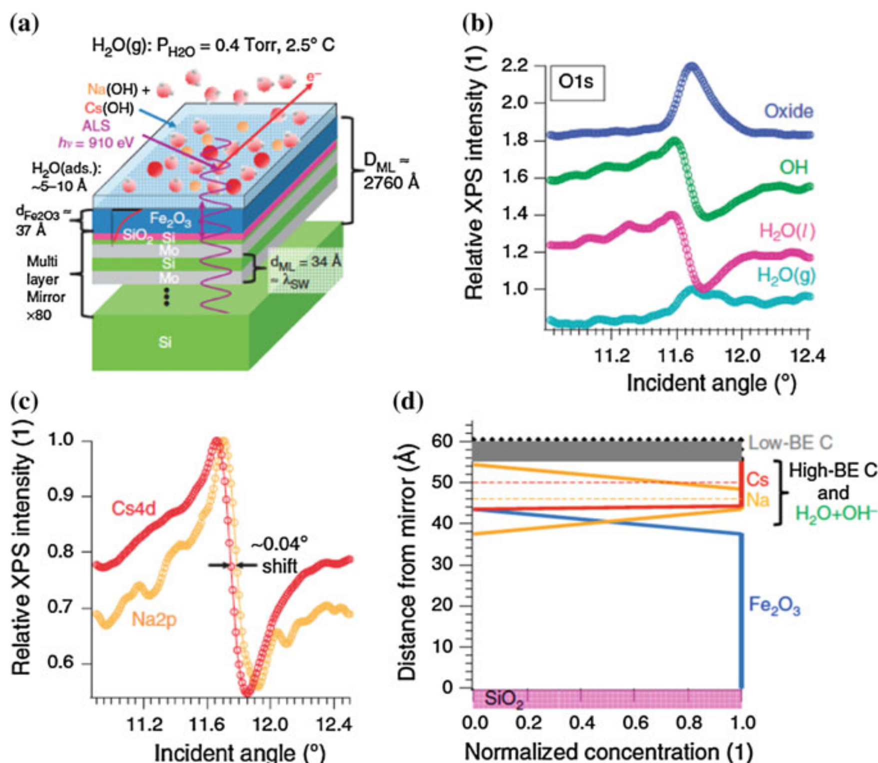

Fig. 17.10 **a** Principal setup of the standing-wave APXPS experiment. The thin film (3.7 nm) hematite sample is grown onto a Mo/Si multilayer structure with a periodicity of 3.4 nm. A mixed NaOH and CsOH solution is drop cast onto the hematite film outside the vacuum chamber, allowed to dry and then rehydrated inside the in situ measurement cell through exposure to water vapor at a relative humidity of ~7 %. **b** O 1*s* rocking curves taken at an incident photon energy of 910 eV. The peak positions and shapes of the rocking curves indicate that OH and adsorbed H_2O are co-located, with a clear separation to the oxide. **c** Rocking curves for Cs 4*d* and Na 2*p* which show that Na and Cs are located at different distances from the substrate. **d** Calculated concentration profiles for hematite, Cs^+, Na^+, adsorbed water, hydroxyls, as well as hydrophilic (high-BE C) and hydrophobic (low-BE C) carbon contamination. Adapted and reproduced with permission from [32]

peak position indicates that Na is located closer to the interface with hematite compared to Cs. A detailed analysis of the rocking curves for all elements yields a concentration profile across the hematite substrate and the adsorbed species (Fig. 17.10d). The profile shows that Na is indeed in close contact with the hematite substrate, while Cs is excluded from the interface. It also shows that there are two carbon contamination components, which interact very differently with the interface region: While the hydrophilic component (carbonate or carboxylic acid, according to its binding energy) is mixed with the adsorbed water and hydroxyls, the aliphatic, hydrophobic carbon forms a narrow layer on top of the hydrated film. This example

shows that SWAPPS allows to identify and map all components of a liquid/solid interface with sub-nanometer resolution in the direction perpendicular to the interface. SWAPPS has also recently been used in proof-of-principle investigation for the reaction of Ni immersed in a 0.1 M KOH solution under oxidizing conditions [44].

17.4 Summary

Photoelectron spectroscopy, in particular when operated using high photon energies (i.e., high-KE photoelectrons), is a promising method for the study of the elemental composition and potential distribution at liquid/solid interfaces. It is applicable to a wide variety of research areas, including electrochemistry and geochemistry. The obstacles due to the operation of a high KE electron spectrometer under elevated pressure conditions have for the most part been overcome, and commercial spectrometers are available. The biggest challenge is currently the preparation of liquid/solid interfaces that are accessible to electron spectroscopy, which requires either the preparation of very thin ($\sim$10 nm) thick solution layers, or the use of ultrathin solid films through which the electrons from the liquid/solid interface are detected. There are several approaches to tackling this problem, as we have discussed above, all with their own advantages as well as complications. All of these techniques are still in their infancy, and further innovations and optimizations are urgently needed to develop ambient pressure HAXPES measurements of liquid/solid interfaces into a mature characterization method. Furthermore, the combination of APXPS with other complimentary techniques, such as infrared and non-linear optical spectroscopy, will be crucial in the quest to map the chemical and potential distribution across liquid/solid interfaces with high spatial resolution.

Acknowledgements This work was supported by a Laboratory Directed Research and Development project through Lawrence Berkeley National Laboratory. The ALS and the MES beamline 11.0.2 are supported by the Director, Office of Science, Office of Basic Energy Sciences, Division of Chemical Sciences, Geosciences, and Biosciences and Materials Sciences Division of the US Department of Energy at the Lawrence Berkeley National Laboratory under Contract No. DE-AC02-05CH11231. Z. Liu thanks the support form National Natural Science Foundation of China under Contract No. 11227902.

References

1. F. Zaera, Surf. Sci. **605**, 1141 (2011)
2. A. Gross, K. Wandelt, Surf. Sci. **631**, 1 (2014)
3. O.M. Magnussen, Chem. Rev. **102**, 679 (2002)
4. F. Ohnesorge, G. Binnig, Science **260**, 1451 (1993)
5. J. Kubota, Z. Ma, F. Zaera, Langmuir **19**, 3371 (2003)
6. Y.R. Shen, PNAS **93**, 12104 (1996)

7. F.M. Geiger, Annu. Rev. Phys. Chem. **60**, 61 (2009)
8. V.R. Stamenković, M. Arenz, C.A. Lucas, M.E. Gallagher, P.N. Ross, N.M. Marković, J. Am. Chem. Soc. **125**, 2736 (2003)
9. J.-J. Velasco-Velez, C.H. Wu, T.A. Pascal, L.F. Wan, J. Guo, D. Prendergast, M. Salmeron, Science **346**, 831 (2014)
10. M.J. Bedzyk, D. Bilderback, J. White, H.D. Abruna, G.M. Bommarito, J. Phys. Chem. **90**, 4926 (1986)
11. F. Zaera, Chem. Rev. **112**, 2920 (2012)
12. D.E. Starr, Z. Liu, M. Haevecker, A. Knop-Gericke, H. Bluhm, Chem. Soc. Rev. **42**, 5833 (2013)
13. M. Salmeron, R. Schlögl, Surf. Sci. Rep. **63**, 169 (2008)
14. H. Siegbahn, K. Siegbahn, J. Electron Spectrosc. Rel. Phenom. **2**, 319 (1973)
15. H. Siegbarn, L. Asplund, P. Kelfve, K. Hamrin, L. Karlsson, K. Siegbahn, J. Electron Spectrosc. Rel. Phenom. **5**, 1059 (1974)
16. A. Shavorskiy, O. Karslioglu, I. Zegkinoglou, H. Bluhm, Synchrotron Radiat. News **27**, 14 (2014)
17. J. Zegenhagen et al., in *Photoelectron Emission Excited by a Hard X-ray Standing Wave this Book*, ed. by J. Woicik. Hard X-ray Photoelectron Spectroscopy (HAXPES) (Springer, Berlin, 2015)
18. D. Emfietzoglou, H. Nikjoo, Rad. Res. **167**, 110 (2007)
19. J.J. Yeh, I. Lindau, At. Data Nucl. Data Tables **32**, 1 (1985)
20. W. Smekal, W.S.M. Werner, C.J. Powell, Surf. Interface Anal. **37**, 1059 (2005)
21. W.S.M. Werner, Surf. Interface Anal. **31**, 141 (2001)
22. C.J. Powell et al., in Inelastic Mean Free Paths, Mean Escape Depths, Information Depths, and Effective Attenuation Lengths for Hard X-ray Photoelectron Spectroscopy, ed. by J. Woicik. Hard X-ray Photoelectron Spectroscopy (HAXPES) (Springer, Berlin, 2015)
23. Y.R. Shen, J. Opt. Soc. Am. B **28**, A56 (2011)
24. J.A. McGuire, Y.R. Shen, Science **313**, 1945 (2006)
25. W.-T. Liu, Y.R. Shen, PNAS **111**, 1293 (2014)
26. K.B. Eisenthal, Chem. Rev. **96**, 1343 (1996)
27. S. Ong, X. Zhao, K.B. Eisenthal, Chem. Phys. Lett. **191**, 327 (1992)
28. S. Axnanda, E.J. Crumlin, B. Mao, S. Rani, R. Chang, P.G. Karlsson, M.O.M. Edwards, M. Lundqvist, R. Moberg, P.N. Ross, Z. Husssain, Z. Liu, Sci. Rep. **5**, 9788 (2015)
29. H. Matsuda, H. Daimon, M. Kato, M. Kudo, Phys. Rev. E **71**, 066503 (2005)
30. G. Ketteler, S. Yamamoto, H. Bluhm, K. Andersson, D.E. Starr, D.F. Ogletree, H. Ogasawara, A. Nilsson, M. Salmeron, J. Phys. Chem. C **111**, 8278 (2007)
31. K. Arima, P. Jiang, X. Deng, H. Bluhm, M. Salmeron, J. Phys. Chem. C **114**, 14900 (2010)
32. S. Nemšák, A. Shavorskiy, O. Karslioglu, I. Zegkinoglou, P.K. Greene, E.C. Burks, K. Liu, A. Rattanachata, C.S. Conlon, A. Keqi, F. Salmassi, E.M. Gullikson, S.-H. Yang, H. Bluhm, C.S. Fadley, Nat. Comm. **5**, 5441 (2014)
33. M. Faubel, B. Steiner, J.P. Toennies, J. Chem. Phys. **106**, 9013 (1997)
34. M.A. Brown, N. Duychkaerts, A. Beloqui Redondo, I. Jordan, F. Nolting, A. Kleibert, M. Ammann, H.J. Wörner, J.A. van Bokhoven, Z. Abbas, Langmuir **29**, 5023 (2013)
35. I. Jordan, A. Beloqui Redondo, M.A. Brown, D. Fodor, M. Staniuk, A. Kleibert, H.J. Wörner, J.B. Giorgi, J.A. van Bokhoven, Chem. Comm. **50**, 4242 (2014)
36. M.A. Brown, A. Beloqui Redondo, M. Sterrer, B. Winter, G. Pacchioni, Z. Abbas, J.A. van Bokhoven, Nanoletters **13**, 5403 (2013)
37. T. Masuda, H. Yoshikawa, H. Noguchi, T. Kawasaki, M. Kobata, K. Kobayashi, K. Uosaki, Appl. Phys. Lett. **103**, 111605 (2013)
38. Y. Takagi, H. Wang, Y. Uemura, E. Ikenaga, O. Sekizawa, T. Uruga, H. Ohashi, Y. Senba, H. Yumoto, H. Yamazaki, S. Goto, M. Tada, Y. Iwasawa, T. Yokoyama, Appl. Phys. Lett. **105**, 131602 (2014)
39. A. Kolmakov, D.A. Dikin, L.J. Cote, J. Huang, M.K. Abyaneh, M. Amati, L. Gregoratti, S. Günther, M. Kiskinova, Nat. Nanotechn. **6**, 651 (2011)

40. A. Knop-Gericke, M. Hävecker, R. Schlögl, private communication
41. J. Guo, J. Elec. Spectrosc. Rel. Phenom. **188**, 71 (2013)
42. J. O'M. Bockris and B.D. Cahan, J. Phys. Chem. **50**, 1307 (1969)
43. H. Siegbahn, J. Phys. Chem. B **89**, 897 (1985)
44. O. Karslıoğlu, S. Nemsak, I. Zegkinoglou, A. Shavorskiy, M. Hartl, F. Salmassi, E.M. Gullikson, M.L. Ng, Ch. Rameshan, B. Rude, D. Bianculli, A.A. Cordones, S. Axnanda, E. J. Crumlin, P.N. Ross, C.M. Schneider, Z. Hussain, Z. Liu, C.S. Fadley, H. Bluhm, Faraday Discuss. (2015). doi:10.1039/C5FD00003C
45. R. Arrigo, M. Hävecker, M.E. Schuster, C. Ranjan, E. Stotz, A. Knop-Gericke, R. Schlögl, Ang. Chem. Int. Ed. **52**, 11660 (2013)
46. H.S. Casalongue, S. Kaya, V. Viswanathan, D.J. Miller, D. Friebel, H.A. Hansen, J.K. Nørskov, A. Nilsson, H. Ogasawara, Nat. Commun. **4**, 2817 (2013)
47. D.R. Butcher, M.E. Grass, Z. Zeng, F. Aksoy, H. Bluhm, W.-X. Li, B.S. Mun, G.A. Somorjai, Z. Liu, J. Am. Chem. Soc. **133**, 20319 (2011)
48. D. Miller, H. Sanchez Casalongue, H. Bluhm, H. Ogasawara, A. Nilsson, S. Kaya, J. Am. Chem. Soc. **136**, 6340 (2014)
49. M. Pourbaix, *Atlas of Electrochemical Equilibria in Aqueous Solutions* (National Association of Corrosion Engineers, 1974)
50. C.S. Fadley, J. Electron Spectrosc. Relat. Phenom. **190**, 165 (2013)
51. A.X. Gray, J. Electron Spectrosc. Relat. Phenom. **195**, 399 (2014)

Chapter 18
HAXPES Applications to Advanced Materials

Keisuke Kobayashi

Abstract The application of HAXPES to the study of the electronic structure, chemical bonding state, and geometric structure of advanced materials of industrial importance is presented. Topics include phase-change memory, transparent amorphous-oxide thin-film transistors, dilute magnetic semiconductors, strongly correlated magnetic materials, advanced shape memory, Au nanoclusters dispersed in ceria, hard disc lubricants, and Li-ion battery electrode degradation. Examples of applications of HAXPES to operando measurements for Si-MOS gate stack structure, and electrochemical reactions at solid-solid as well as solid-liquid interfaces are also introduced. It is demonstrated that the extended probing depth of HAXPES and its unique ability to determine bulk electronic structure and its depth dependence can solve many of the relevant materials issues affecting current advanced device performance. Together with first principles electronic structure calculations, these studies successfully reveal the origin of the functionalities of the advanced materials. In the last part of this chapter, a laboratory HAXPES system with a monochromatic Cr K_α (5.4 keV) X-ray source and several typical examples of its application are introduced. Future development of laboratory HAXPES are also briefly discussed.

K. Kobayashi (✉)
Hiroshima Synchrotron Radiation Center, Hiroshima University, Kagamiyama 2-313, Higashi-Hiroshima City 739-0046, Japan
e-mail: koba_kei@spring8.or.jp

K. Kobayashi
Quantum Beam Science Directorate, Japan Atomic Energy Agency, Kouto 1-1-1, Sayo-Cho, Hyogo 679-5148, Japan

K. Kobayashi
Research Institute of KUT, Kochi University of Technology, Miyanokuchi 185, Tosayamada-Cho, Kami City, Kochi 782-8502, Japan

© Springer International Publishing Switzerland 2016

J.C. Woicik (ed.), *Hard X-ray Photoelectron Spectroscopy (HAXPES)*,
Springer Series in Surface Sciences 59, DOI 10.1007/978-3-319-24043-5_18

18.1 Introduction

The development of HAXPES as an important analytical method began at the beginning of the 21st century. Here it will be described how the development proceeded at SPring-8, and what pushed its application to advanced materials science. By the end of the 20th century progress in the field of synchrotron radiation (SR) was striking. At the same time it was clear that the application of SR spectroscopy was limited in the physical sciences. Photoelectron spectroscopy is an invaluable method to obtain electronic structure and chemical-bonding information, but its high surface sensitivity severely limits research in fields other than surface science. Suga and coworkers showed that "bulk sensitive photoelectron spectroscopy" was possible at the soft X-ray beamline BL25SU of SPring-8 through measurements of the 3d-4f resonant photoelectron spectra of rare earth compounds [1]. However, for excitation photon energies less than 1 keV typically available at soft X-ray beamlines, data are not free from surface effects. Ultra-high vacuum and in situ surface preparation remain a significant hindrance for all but the most adamant surface scientist. Meanwhile, research and development was focusing on novel materials, and it was clear that a more bulk-sensitive photoelectron spectroscopy method was needed to allow SR to become widely applicable. Clearly, the only solution was to increase the photon energy of the measurement. In collaboration with the RIKEN/SPring-8 group, a series of HAXPES test experiments were initiated at the RIKEN undulator beamline BL29XU in June 2002, and the results were promising [2]. Various research groups engaged in Si-CMOS, compound semiconductor materials, strongly correlated spin electronic materials, etc., were encouraged to participate in these early experiments. Some of these results were presented at the first international workshop HAXPES 2003 (September 11–12, 2003, ESRF, France) [3, 4]. In order to further open the field to new users, a HAXPES end station at the JASRI R&D beamline BL47XU was constructed. It was available to nano-technology research in 2004 and to general users in 2005 [5]. In 2006, development began at the National Institute for Materials Science (NIMS) of the HAXPES end station at the NIMS beamline BL15XU for advanced materials research. New users conducted experiments at the two beamlines, research flourished, and it soon became clear that the available SR beamtime was too limited to satisfy the growing community [6]. Consequently, a laboratory based HAXPES system to satisfy this growing demand was planned. The JST "sentan" project was initiated in 2005. It lasted for 5 years and resulted in the Cr K_{α} lab-based HAXPES system [7]. The following will discuss HAXPES applications for advanced materials conducted at the SPring-8 beamlines (BL29XU, BL47XU, and BL15XU) and demonstrate its versatile potential.

18.1.1 Phase-Change Memory Materials

Elements in groups V and VI (including As, Sb, S, Se and Te) readily form disordered structures [8] that are often short lived at room temperature (RT). On the

other hand, compounds containing other elements, including Ag and In or Ge, can remain amorphous at RT for several decades. The crystallization process in these compounds can be accelerated greatly by laser irradiation or electric heating to a rapid transformation within tens of nanoseconds in amorphous $Ge_2Sb_2Te_5$ (GST225) and $Ag_{3.5}In_{3.8}Sb_{75.0}Te_{17.7}$ (AIST) materials, [9, 10] leading to phase change (PC) memories with both long-term stability and rapid switching [11].

PC recording is used extensively in rewritable high-density storage media, particularly in optical recording discs, for example digital versatile disc-random access memory (DVD-RAM), digital versatile disc-rewritable (DVD-RW) and Blue-ray disc-rewritable (BD-RE) [12]. Intensive efforts for the development of PCRAM, which is competing with other types of RAM such as ReRAM (Resistance RAM) and MRAM (magnetic RAM), as a candidate of non-volatile computer memory have been initiated world-wide [13]. In all of these PC memory devices, information is stored as a row of nano-sized amorphous marks in a polycrystalline layer or as cell arrays and accessed by the difference between either the optical or electrical properties in the amorphous (*a*-) and crystalline (*c*-) phases [12, 14].

$(GeTe)_{1-x}(Sb_2Te_3)_x$ pseudobinary compounds (GST) and related compounds, which take the NaCl structure in the crystalline phase, are widely used as the memory layer in rewritable phase-change optical discs [11]. Various modifications of compounds have been investigated in order to satisfy the essential requirements of nanosecond scale rewritable speeds, extremely good reversibility between the *a*- and *c*-phases over 10^5 cycles, and long thermal stability over scores of years for these optical as well as electronic memory devices. Typically, GST with $x = 1/3$ composition ($Ge_2Sb_2Te_5$, GST225) exhibits suitable crystallization and melting temperatures for laser-induced phase changes and rapid phase transition times [11, 15, 16]. GeTe-rich compositions such as $x = 1/9$ ($Ge_8Sb_2Te_{11}$) are adopted for the blue-ray disk on which as much as 50 GB of information can be recorded using a blue-violet laser [17].

Applications of PC materials to commercial devices were started without the clear understanding of the PC mechanism. In 2004, Kobolov et al. [18] proposed the umbrella flip model, in which the six to four coordination change of Ge plays a key role to introduce randomness without long distance atomic diffusion. In 2006, Wełnic et al. [19] proposed a spinel structure for amorphous GST based on density functional theory (DFT) calculations.

A systematic investigation of the electronic structures and chemical states of amorphous as well as crystalline $(GeTe)_{1-x}(Sb_2Te_3)_x$ ($x = 0$–$1/3$) pseudobinary compounds using high resolution HAXPES were reported in 2007 by Kim et al. [20]. Samples were prepared by sputtering on polycarbonate disc substrates and capped with 2–3 nm of carbon at Matsushita Electric Industrial Company, Ltd. Valence band spectra of crystalline phase GST's are compared with Sb_2Te_3 (blue) and Sb (red) in Fig. 18.1a (Backgrounds were subtracted using Shirley's method [21]). The similarity of the overall spectral features of GST with Sb, GeTe, and Sb_2Te_3 is clear.

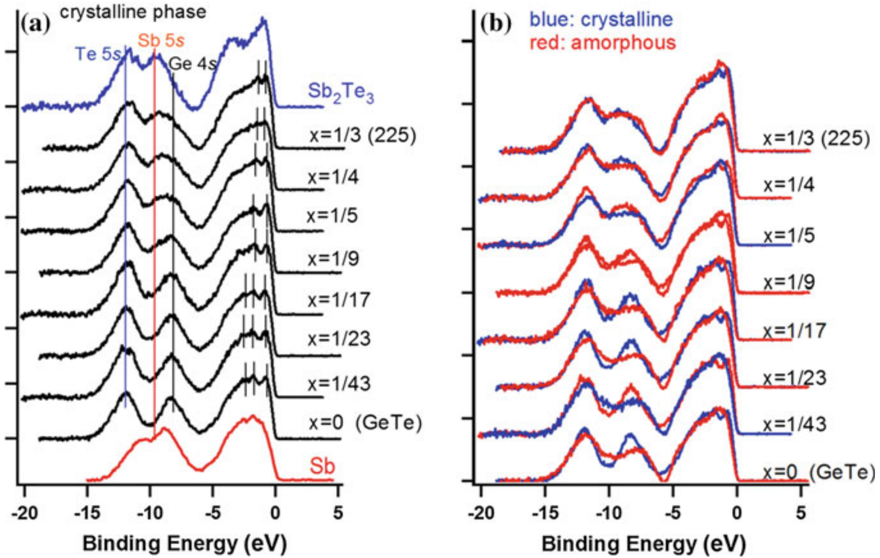

Fig. 18.1 **a** Valence-band spectra of crystalline $(GeTe)_{1-x}(Sb_2Te_3)_x$ (x = 0–1/3), each showing the three-peak structure corresponding to Te 5*s*, Sb 5*s*–Ge 4*s* overlapped, and Te 5*p*, Sb 5*p*, and Ge 4*p* mixed band from the higher binding-energy side, respectively. *Vertical bars* show fine structure due to bands. **b** Comparisons between the valence-band spectra of the amorphous (*red*) phases and those of the crystalline (*blue*) phases. In all of the spectra, a Shirley background [21] was subtracted, and the binding energies are set to zero at the VBM. The spectra are normalized to the area of the Te 4*d* core-level spectra

These valence band spectra are explained as follows. The valence-electron configuration of Sb is $5s^2 5p^3$, where the two s^2 electrons form a lone-pair band. The remaining three *p* electrons sustain the crystal bonding of the distorted cubic (rhombohedral) structure by forming half-filled resonance bonding of p_x, p_y and p_z orbitals resulting in a semimetal band structure. Corresponding to this valence-electron configuration, the Sb valence-band spectrum shows a 5*s* band, which splits into two peaks at 8 and 12 eV corresponding to the long and short bond states in the rhombohedral structure. The topmost *p* band, which is distributed in energy from 0 to 6 eV, is well separated from the *s* band. In the case of GeTe (green), which on average has 5 valence electrons per atom, also forms the rhombohedral structure and behaves as a narrow gap semiconductor. Peaks at around 12 and 8 eV are assigned to Te 5*s* and Ge 4*s* orbitals, respectively, whereas the *p* band intensities are distributed in energy similar to that of Sb. The Ge 4*p* band is also well separated from the Ge 4*s* band. The separation of the *p* bands from the *s* bands in Sb and GeTe evidence that the *s*-*p* hybridization is weak in these materials as discussed above. The Sb_2Te_3 spectrum shows two peaks that correspond to Te 5*s* states at 12 eV and Sb 5*s* states at around 10 eV. Evidently the top most band of Sb_2Te_3 is also well separated from the *s* bands, and distributes almost in the same binding-energy region as those of Sb and GeTe. Sb_2Te_3 consists of

stacking of Te–Sb–Te–Sb–Te layers sustained by long and short *p*-like bonds in the quintuple layers and weak Te–Te bonds at the interfaces of the quintuple layers.

Rewriting the chemical formula of GST, $((GeTe)_{1-x}(Sb_2Te_3)_x)$ as $(GeTe)_{1-x}2(SbTe)_x(\Upsilon Te)_x$, where Υ denotes vacancies, the unit cell of crystalline GST is understood to inevitably contains vacancies to form the NaCl structure. For instance, GST225 ($x = 1/3$) needs 0.8 vacancies at the cation sites with 1.6 Ge, 1.6 Sb, and 4 Te atoms in one NaCl cubic unit cell. We have 9.6 valence electrons in average per molecular unit in the formula for GST225, suggesting that GST's may be regarded as members of the average 5 valence ($\langle 5 \rangle$ valence) electron family. If we assume that one excess electron for each of the two Sb atoms is transferred to the adjacent (ΥTe) unit, then all the molecular units contain 6 *p* electrons to sustain half-filled *p*-like bonding in addition to closed *s* subshells. This fact gives a sound basis for understanding the results in Fig. 18.1a where all the valence bands of the GST alloys show similar features to GeTe and Sb, and Sb_2Te_3.

Figure 18.1b compares valence-band spectra of crystalline (blue) and amorphous (red) GST. The most striking feature of this figure is that the *a*- and *c*-phases closely resemble each other for all GST samples. This makes a clear contrast to amorphous Si (*a*-Si), into which broken bonds are inevitably introduced because the rigid sp^3 tetrahedral bonds do not allow flexible bond deformations. *a*-Si is therefore extremely defective without hydrogenation termination of the broken bonds to form *a*-Si:H. The resultant valence-band densities of states in *a*-Si and *a*-Si:H differ significantly from *c*-Si. In GeTe, differences between the valence-band spectra of *a*- and *c*-films are recognizable by presence/absence of fine features (denoted by bars in Fig. 18.1a) of band structure origin, which appear near the top of the valence band. Although the similarity of the *c*- and *a*-phase spectra is enhanced with increasing *x*, the two fine features still remain distinguishable in the *c*-phase at $x = 1/3$, indicating that overall translational symmetry in the crystal is maintained in spite of the random distribution of vacancies. The fact that the three band feature of the whole valence band is maintained indicates that there are no drastic changes in the s^2p^3 valence configuration during the phase transition. The almost perfect resemblance between the *a*- and *c*-phases with increasing *x* to 1/3 suggests that increasing vacancies bring a similar degree of local disorder into the crystalline structure as in the amorphous phase. The bandgap between the *s*-band and the *p*-band becomes clearer in the amorphous spectrum as *x* increases, suggesting enhancement of the *s*-*p* de-hybridization.

Figure 18.2 shows the Te 4*d*, Sb 4*d*, and Ge 3*d* core-level spectra of the crystalline (closed circles) and amorphous (open circles) films with $x = 0$–$1/3$. The Ge 3*d* spectra of the *a*-phase samples show a single broad peak, whereas those in the *c*-phase exhibit a doublet due to the spin-orbit splitting of 0.6 eV. Only the Sb 4*d* spectra of the *a*-phase show a chemical shift of 0.2 eV toward lower binding energy that is independent of *x*. Another interesting feature in this figure is the additional weak component with a 1 eV chemical shift observed in the Sb 4*d* in the crystalline phase with $x = 1/23$ as marked by arrows. The same chemical shift is more clearly observed in the Sb 3*d* core-level spectra of larger photoionization cross section [22], (inset of Fig. 18.2) for samples with $x = 1/45$–$1/17$. This shift is not

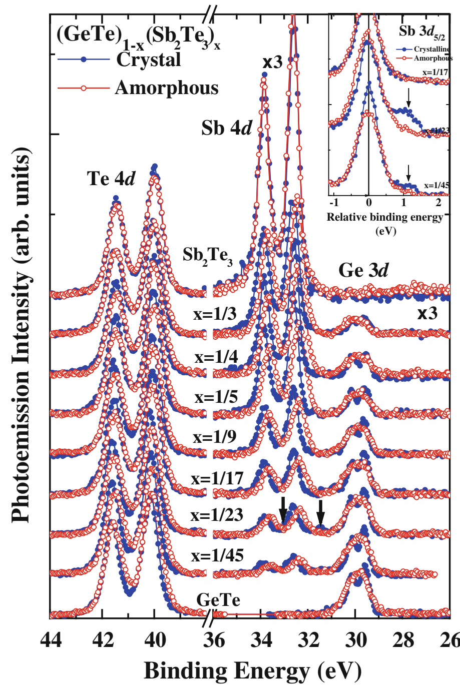

Fig. 18.2 Te 4*d*, Sb 4*d*, and Ge 3*d* core-level spectra of the crystalline (*closed circles*) and amorphous (*open circles*) $(GeTe)_{1-x}$ $(Sb_2Te_3)_x$ with $x = 0–1/3$. In all spectra, a Shirley background was subtracted [21] and the binding energies are set to zero at the VBM. A set of weak components about 1 eV lower binding energy than the Sb 4*d* main doublet is indicated by *arrows*. The spectra are normalized to the area of the Te 4*d* core level. The *inset* shows Sb $3d_{5/2}$ spectra of x = 1/45, 1/23, and 1/17 between −1 and 2 eV. The weak 1 eV chemically shifted component is clearly seen in the spectra with x = 1/23 and 1/45

observed in the *a*-phase. The binding energy of this weak peak in the Sb 3*d* spectra was 527.7 eV from the Fermi level E_F, and it is equivalent to the binding energy of the neutral Sb compound (528 eV) [23]. The main peak at 1 eV higher-binding energy is then reasonably assigned to Sb^{1+}. In the case of dilute Sb concentrations, the Sb atoms substitute for Ge atoms as randomly distributed donor impurities in the GeTe matrix. No filling of the vacancies by the extra Sb takes place [17]. When the compensation of residual holes (as-grown GSTs including GeTe are usually *p*-type) is completed, a fraction of the Sb impurities could remain neutral. In the high Sb_2Te_3 composition alloys, the material is regarded as a $(GeTe)_{1-x}$ $2(SbTe)_x(\Upsilon Te)_x$ mixed crystal, in which Sb atoms are ionized and donated electrons are considered to localize around vacancies as discussed above. The observation of neutral Sb components shown in Fig. 18.2 suggests that the boundary between these two cases is considered to be somewhere around $x = 1/23–1/17$.

Figure 18.3a shows the photoemission spectra of the crystalline (closed circles) and amorphous (open circles) $(GeTe)_{1-x}(Sb_2Te_3)_x$ near the valence-band maximum

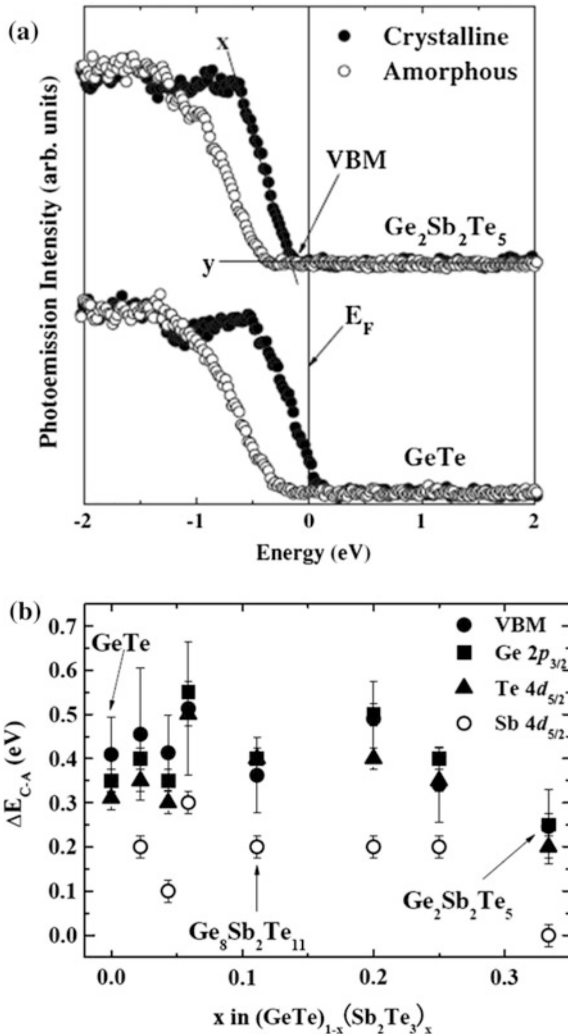

Fig. 18.3 **a** HAXPES spectra near the VBM of crystalline (*closed circles*) and amorphous (*open circles*) GeTe and $Ge_2Sb_2Te_5$ films. The Fermi level is taken as the energy zero. **b** The binding-energy differences between the crystalline and amorphous phases ΔE_{C-A}'s of the VBM's (*filled circles*), Ge $2p_{3/2}$ (*filled squares*), Te$4d_{5/2}$ (*filled triangles*), and Sb $4d_{5/2}$ (*open circles*) core-level spectra as functions of *x*. The error bars of the ΔE_{C-A}'s for valence and core levels correspond to the total-energy resolution and the energy step of the measured spectra, respectively

(VBM). The Fermi energy is indicated as zero. The energy differences between the crystalline and amorphous phases (ΔE_{C-A}'s) for the VBM (filled circles) and core-level spectra Ge $2p_{3/2}$ (filled squares), Te $4p_{5/2}$ (filled triangles), and Sb $4d_{5/2}$ (open circles)] are plotted as functions of x in Fig. 18.3b. All the ΔE_{C-A}'s except those of the Sb $4d_{5/2}$, nearly coincide, indicating that there are equivalent energy shifts for the VBM of Ge and Te during the *c*-*a* phase transition. These parallel energy shifts are understood to be due to the shift of E_F into the band gap. The VBM positions shift to 0.4 and 0.35 eV below E_F for *a*-GeTe and *a*-GST225, respectively. Assuming that both *a*-GeTe and *a*-GST225 behave as intrinsic semiconductors with E_F located in the middle of the band gap as generally

known in amorphous semiconductors [24], the band gap values coincide with the reported optical band gap values of 0.8 eV [25] and 0.7 eV [26] for a-GeTe, and a-GST225 (x = 1/3), respectively. The opening of the bandgap is also verified by DFT calculations discussed in this section. Only the Sb core levels show a chemical shift of about 0.2 eV, as seen in Fig. 18.2. The Sb atoms are identified to be in a singly ionized state in the *c*-phase, and, in a simple picture, each of the vacancies traps two electrons to maintain charge neutrality. The ionized Sb core levels show 0.2 eV chemical shifts toward the lower binding energy side in the *a*-phase, implying that the ionized Sb atoms partly recover their charge from the vacancies in the amorphous phase.

It is known that elemental group-V materials (As, Sb, Bi) and IV–VI compounds (such as the chalcogenides of Ge, Sn, Pb, and their mixed compounds) show polymorphism in their crystalline structures. This polymorphism is well pigeon holed by taking the averaged atomic number of the constituent atoms or Harrison's metallicity [27] in the vertical axis and the electronegativity difference [28] of the constituent cation and anion in the horizontal axis as shown in Fig. 18.4a, b [29–31]. As mentioned above, the crystals of the ⟨5⟩ valence-electron family is sustained by p_x, p_y, and p_z orbitals which form three half-filled chains of resonance bonding orthogonal to each other [20, 32, 33, 34]. Thus the cubic structure is the basic crystalline structure, which suffers from an inherent Peierls instability. The two different types of dimerization; i.e., to rhombohedral and orthorhombic structures, are possible [35], resulting in the polymorphism. A similar phase diagram is

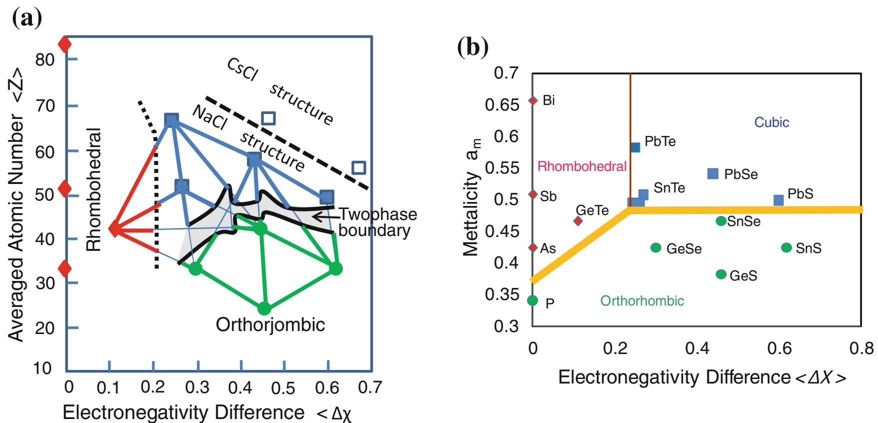

Fig. 18.4 **a** Mapping of crystal structures in ⟨5⟩ valence-electron crystals with averaged electronegativity difference $\langle \Delta\chi \rangle$ in the *horizontal* and averaged atomic number $\langle Z \rangle$ in the *vertical axes*. Here $\langle \Delta\chi \rangle$ and $\langle Z \rangle$ are defined as $\{1/2(\chi_{Pb} \times (1 - x) + \chi_{Sn} \times x) - \chi_{Te}\}$ and $1/2[\{Z_{Pb} \times (1 - x) + Z_{Sn} \times x\}/2 + Z_{Te}]$ for $Pb_{1-x}Sn_xTe$ as an example. The electronegativity as defined by St. John and Bloch is used in this mapping [28]. **b** Phase diagram of polymorphism in ⟨5⟩ valence-electron family converted from Fig. 18.4a. Electronegativity differences and Harrison's metallicity are taken for the *horizontal* and *vertical axes*, respectively. The linear relation between Harrison's metallicity and $\langle Z \rangle$ are given as $m = 4.67 \times 10^{-3}\langle Z \rangle$ by Suski et al. [31]

also shown by Littlewood [36]. Cubic-rhombohedral transformation takes place in the high metallicity region. Electronegativity difference breaks inversion symmetry, and introduces a bandgap at the Fermi level that stabilizes the cubic structure [37] as in the case of lead salts. If this effect is not sufficient, crystals deform along the $\langle 111 \rangle$ direction by synchronous dimerization along three $\langle 100 \rangle$ axes, introducing the further break of inversion symmetry to increase the bandgap. The dimerization is described by the interband electron-TO zone-center phonon coupling [38]. In the low metallicity region, where the *s*-*p* hybridization tends to be significant, crystals take another mode of dimerization to result in the somewhat complicated orthorhombic double layered structure. It is noteworthy that GST's sit around the rhombohedral-cubic-orthorhombic phase boundaries as marked in Fig. 18.4b.

Consideration of the HAXPES results based on this phase diagram leads to an intuitive picture for the PC phenomenon. In the crystalline phase, GST's take the NaCl structure by the long range resonance bonding as discussed above. Upon quenching from the melt, the resonance bonding is fragmented due to hindrance by intrinsic vacancies. Considerable parts of the 6 fold *p*-like resonance bonds are frozen into 3 fold bonds, and this generates local randomness leading to the amorphous structure. When the amorphous GST's are annealed, the nucleation and growth mechanism in the solid state, in which the remaining 6 fold bonding units act as nuclei, takes place by the reconstruction of the resonance bonding by the transformation of 3 fold bonds to 6 fold bonds. The phase change is not expected to include long-range atomic movement.

The atomic structure and the electronic band structure should be consistently understood in the crystalline and amorphous phases. The experimental data on GST by X-ray absorption fine structure (XAFS) [18, 39, 40], electron diffraction [40], neutron-diffraction, X-ray diffraction [39], and reverse Monte Carlo (RMC) analysis of synchrotron radiation high-energy X-ray diffraction (XRD) data [41] provide an ideal database for testing structural models. However, there had been little consensus on the atomic structure of *a*-GST. Akola et al. pursued large-size computational calculations to obtain a consistent picture of amorphous GST by combining data from high-energy XRD [41] and HAXPES measurements [20] on *a*- and *c*-GST by a combined molecular dynamics (MD)-DF simulation of a large sample [42–45] over hundreds of picoseconds with the melt-quench method.

The RMC optimization of structure combined with the molecular MD-DFT calculations yielded a structure factor $S(Q)$ in excellent agreement with the XRD results, with only small differences in amplitude near the first two peaks [42]. The calculated partial pair distribution functions $g(r)$ also followed the experimental curve almost perfectly with minor deviations near the first peak, and the total energy was only 0.079 eV/atom higher than the DFT energy minimum. The structure and cavities, which were important components of the *a*-phase, are obtained by RMC optimization. The cavity volume percentage in the *a*-phase, which made up 13.7 % of its total volume, was slightly more than found in [46, 47], and also higher than the vacancy concentration of *c*-GST (10 %). The material comprises cubic subunits, many of which (including *ABAB* squares) show perfect *AB* alternation. These features support the idea of a nucleation-driven phase change [10], where cubic

subunits act as nucleation centers and cavities provide space for the concerted rearrangement of square units to form a cubic lattice. The measured EXAFS bond lengths agreed well with the calculated peaks or shoulders in $g_{ij}(r)$ obtained from the RMC-optimized structure [48]. The RMC geometry was finally optimized to find the nearest DFT minimum for comparing the electronic structures of the *a*- and *c*-phases [20].

As shown in Fig. 18.5a, both the resultant electronic structures of *a*-GST and *c*-GST are semiconducting, with band gaps near 0.2 eV, and the calculated DOS closely reproduces the HAXPES valence-band spectra for both for *a*-GST and *c*-GST. The experimental and calculated difference spectra between *a*-GST and *c*-GST (Fig. 18.5b) also coincide remarkably well. For the resultant amorphous structure, the following is concluded; (i) ring structures play an essential role in the phase change, and *ABAB* squares, the structural units in *c*-GST, are dominant in *a*-GST; (ii) numerous cavities provide space for the phase change to occur without breaking many bonds; and (iii) over-coordinated Sb and Te and a small number of "wrong bonds" indicate that *a*-GST is a poor glass former. These features are keys to the rapid phase change in GST. It is also noticed that Ge in *a*-phase has both (distorted) octahedral and tetrahedral configurations with different bond lengths, and three- and five-fold Ge configurations occur frequently. Broadening of Ge 3d core-level spectra in the *a*-phase shown in Fig. 18.3 is interpreted as an indication of these varieties of the local bonding of Ge atoms in this phase.

The Sb–Te binary compounds with small amounts of In, Ag and/or Ge, for example $Ag_{3.5}In_{3.8}Sb_{75.0}Te_{17.7}$ (AIST), are another type of commonly used PC

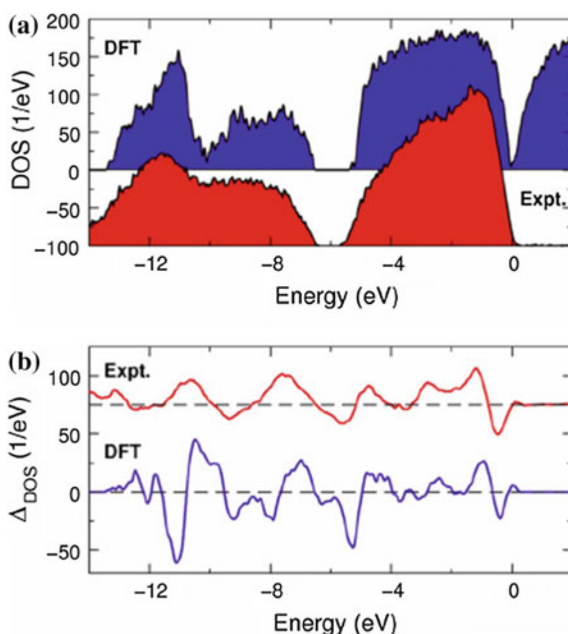

Fig. 18.5 **a** HAXPES valence-band spectrum of *a*-GST225 (*lower curve* filled by *red*) and the calculated electronic DOS (*upper curve* filled by *blue*). The *vertical axes* units are electrons/eV for calculated DOS. **b** Differences between the calculated (*blue*) and experimental HAXPES (*red*) DOS of the *c*- and *a*-phases

materials. The average number of *p* electrons is also close to three in AIST, suggesting orthogonal bonds with neighboring atoms and octahedral coordination sustaining the near-simple-cubic high-temperature structures of AIST crystals similar to *c*-GST [49]. Nevertheless, the recrystallization in GST and AIST is known to be strikingly different: in the former it proceeds mainly by way of nucleation inside the amorphous marks, in the latter by way of crystal growth from the rim. In order to understand the differences between the PC mechanisms and to obtain an atomistic understanding of the crystallization process, Matsunaga et al. performed a combined experimental and theoretical investigation of AIST and discussed the results in comparison with those obtained for GST discussed above [50]. The same technique used for *a*-GST discussed above was applied to determine the amorphous and crystalline structures of an AIST alloy. The resulting $S(Q)$ and the total correlation function $T(r)$, which was obtained from Fourier transforming the $S(Q)$, agreed well with experiment with minor differences. A prominent difference in $T(r)$s for the AIST and GST (determined by fitting the calculations with the experimental results) was that the first peak in *a*-AIST (2.86 Å) was only slightly shorter than that found in *c*-AIST (2.93 Å), whereas the first peak in *a*-GST (2.79 Å) was much shorter than that in *c*-GST (2.97 Å). Another distinguishable difference was that the shoulder of the $T(r)$ curve on the second peak in *a*-AIST (3.5 Å, arrowed) was near that observed in the crystalline form (3.30 Å). These differences between the diffraction patterns of AIST and GST evidently indicated that they crystallize differently. The total energy of RMC-refined *a*-AIST was only 68 meV/atom above the minimum DFT energy. The total volume of the individual cavities was 7 %, significantly less than 14 % in *a*-GST. This may be related to the fact that crystalline AIST has no intrinsic vacancies (cavities) in contrast with *c*-GST (ca. 10 %).

The density of states (DOS) were then calculated for the DF-RMC structure, keeping consistency with both the X-ray diffraction (XRD) and the extended X-ray absorption fine structure (EXAFS) data. Figure 18.6a, b show the HAXPES valence-band spectra of *c*- and *a*-AIST, respectively. The upper panels show the experimental spectra and their least squares fits using a linear combination of the calculated partial density of states (p-DOS). The amorphous and crystalline phases of AIST resemble the HAXPES spectra, as for GST. Narrower bandgaps in calculated DOS (in case of *c*-AIST, DOS at E_F is apparently nonzero) than those in experimental spectra are due to the well know tendency of DFT calculations to underestimate the gaps between occupied and unoccupied states [51]. The lower panels show contributions to the valence-band spectra of the *p*-DOS of the four constituent atoms. The 5*s* states of Sb and Te observed at lower energies are well separated from their 5*p* states with larger energy gaps in both *c*- and *a*-AIST, comparing to the GST case. This indicates that the orthogonal p^3-type bonds should dominate the bonding in both phases. A narrow band of states originating from the Ag 4*d* appears near the bottom of the *p* band (−5.5 eV). The low in concentration and the small photo-ionization cross-section of the In 5*s* level results in much less contribution to the *p* band in the observed spectra than the Ag 4*d*. The valence-band maximum was found to be 0.26 eV below the Fermi level in *c*-AIST, and it was an

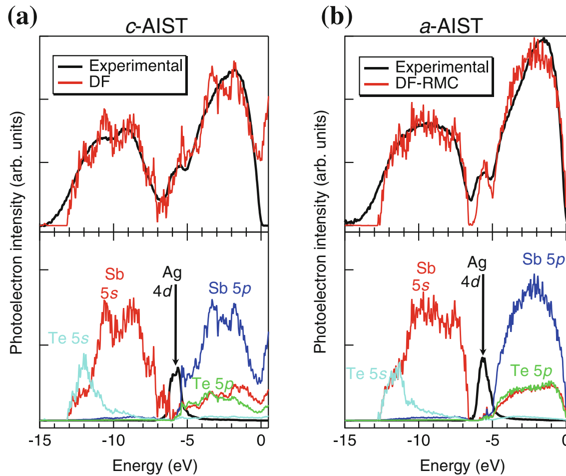

Fig. 18.6 Experimental (*black*) and theoretical (*red*) valence-band spectra of *c*-AIST (**a**) and *a*-AIST (**b**). Contributions of the *p*-DOS are shown in the *lower panels* for the Sb 5*p*, Sb 5*s*, Te 5*p*, Te 5*s* and Ag 4*d*. In 4*d* (not shown due to their low contribution) and Ag 4*d* peaks in the calculated DOS are shifted by −3.09 and −1.25 eV (*c*-AIST) and −2.96 and −1.09 eV (*a*-AIST) to coincide with the experimental peaks

additional 0.3 eV lower in *a*-AIST as determined by HAXPES measurements. As the Fermi level is considered to be located at the gap center, this shift of the valence-band maximum means that the gap in AIST decreases from 1.12 to 0.52 eV upon crystallization. The bond-order profiles of Sb–Sb and Sb–Te bonds were calculated and found strikingly similar in *a*-AIST and *c*-AIST, with a shift toward the covalent side in *a*-AIST compared to *c*-AIST. Shifts of bond orders toward the covalent value of unity were also observed for the other elements. These are consistent with the larger bandgap mentioned above. The small change in structure between covalent bonds in *a*-AIST and resonant bonds in *c*-AIST should therefore provide adequate optical contrast between them [33]. This situation is similar to that in GST, where angular disorder breaks the resonant bonds in *a*-GST and provides sufficient optical contrast between *a*-GST and *c*-GST [52].

Bonding in *a*-AIST and *c*-AIST are now compared to understand the mechanism of the rapid phase change. The local environment around Sb atoms, which is deduced from the structure (bond lengths and bond angles) and the chemical coordination numbers obtained by the RMC-refined DFT calculations, is depicted in Fig. 18.7a. Both *a*-AIST (left panel) and *c*-AIST (right panel) resemble a (distorted) 3C3 octahedron. Each vector shown is defined as the sum of (typically three) short bonds and has been computed for each atom by summing bond vectors. The vectors are analogous to a “pseudo spin” in phase-transition models. In *a*-AIST, they are randomly oriented. The PC is then suggested to be realized simply by a small displacement of the central atom as it interchanges one short (red) and one long (dashed) bond, analogous to the SN2 reaction or “interchange mechanism”

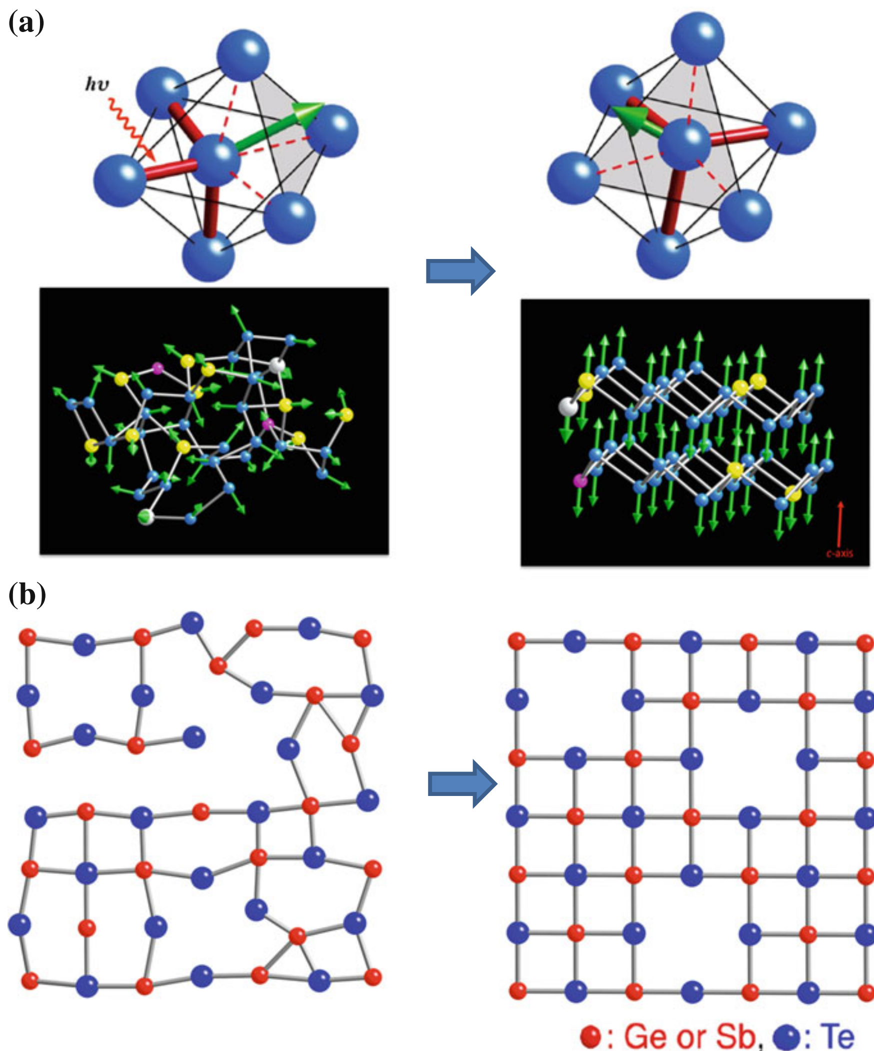

Fig. 18.7 **a** The distorted octahedron in AISTT has a central atom with three short (*red*) and three long (*dashed*) bonds. The *green* vector is defined as the sum of short bonds, which can change the direction by interchanging a short with a long bond. The bond interchange reaction allows reconstruction of the ordered alignment of the *green* vectors, resulting in resonant bonding between periodic short and long bonds of the crystalline A7 network. The *grey sticks* (*lower panels*) correspond to the *red bonds* (*upper panels*). **b** In the case of GST, the ABAB fragments act as nuclei for growth of A7 structure as shown schematically in 2 dimensions. The cavities turn to vacancies in this phase change process

discussed extensively in the inorganic chemistry of molecular reactions [53, 54]. Figure 18.7a schematically shows how the vectors, randomly oriented in a fragment of *a*-AIST, become aligned along the *c* axis upon laser irradiation or electric heating. The small atomic displacement simply interchanges a strong bond and a

weak bond, requiring neither bond breaking nor diffusion, and the process is a sequential, collective motion of Sb atoms, the main component of *a*-AIST. The octahedrons become ordered so the entire amorphous mark takes on the A7 structure. This "bond-interchange" model was proposed as the origin of "growth-dominated" crystallization of *a*-AIST as schematically shown in the lower panels of Fig. 18.7a. The presence of other elements (Ag, In, and Te) and other bond types (for example Sb–Te) in AIST is conjectured to hinder the sequential alignment of Sb atoms and ensure the long-term stability of amorphous marks at RT. The crystallization process in GST is depicted in Fig. 18.7b. Many four- and six-fold rings (NaCl type fragments) in *a*-GST act as nuclei for crystallization and require larger atomic displacements than in *a*-AIST. Crystallization starts simultaneously from such nuclei distributed in the amorphous mark and leads to an aggregation of small crystal grains, aided by the higher concentrations of cavities and also of Te atoms, which favor low coordination.

As discussed above, reversible fast PC phenomena in materials with 3*p* electrons/atom on average are essentially the electronic transitions which couple with the inherent lattice instabilities due to the specific electron configuration of this family. The approach discussed in this section successfully provided a total understanding of the PC mechanism and crystallization processes of GST and AIST. The bulk sensitivity and electronic structural information gained by HAXPES was an indispensable part of this approach. It will also play a key role in the characterization of electronic structure and chemical bonding as part of the design-synthesis-experimental-characterization-verification feedback loop in the quest for new functional materials.

18.1.2 Transparent Amorphous Oxide Semiconductors

Due to strong requirements for high-precision flat-panel and flexible-display devices from the commercial PC, TV, mobile-phone, and wearable device markets, conducting materials for transparent thin-film transistors (TFT) have been actively researched and developed [55, 56]. A number of wide band-gap-oxide semiconductors were investigated for their use as the channel in conventional TFT structures: Sb-doped SnO_2 [57], ZnO [58, 59], $InGaO_3(ZnO)$ [56] and Sn-doped In_2O_3 [60] as crystalline channels, and Zn–Sn–O [61] and In–Ga–Zn–O [62] as amorphous channels.

Among them, amorphous In–Ga–Zn–O (*a*-IGZO), which can produce TFT's exhibiting good performance with field-effect mobilities $\sim 10\ cm^2\ V^{-1}\ s^{-1}$, sub threshold voltage swings (S) < 0.20 V/decade, and excellent process stability [62–64], has been proposed to be one of the best candidates. The carrier transport properties and the device performance of transparent-amorphous-oxide semiconductor (TAOS) films are known to be strongly affected by the existence of tail states and in-gap states, which are inevitably introduced by structural disorder and defects [65]. Consequently, control of these states is needed to improve the performance

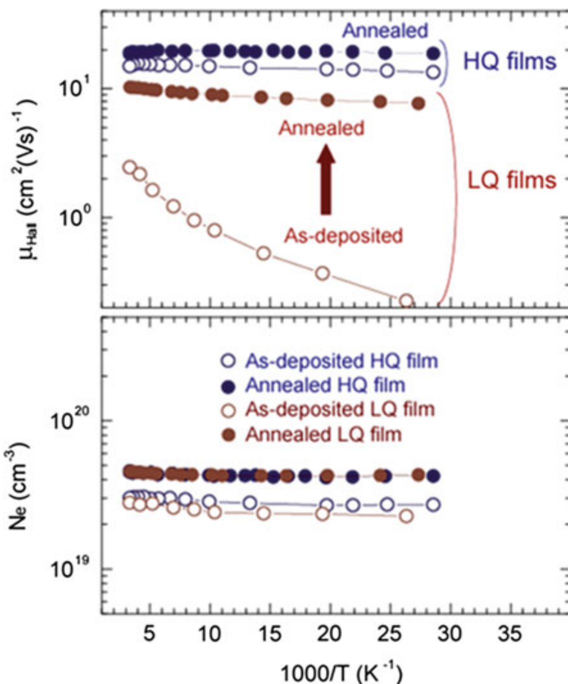

Fig. 18.8 Temperature dependence of μ_{Hall} and Ne for the *a*-IGZO films. The *open symbols* represent the temperature dependence for the as-deposited films, while the *solid symbols* represent the temperature dependence for the annealed films

and to establish stable fabrication processes of these devices. HAXPES is a unique bulk-sensitive spectroscopic tool able to investigate the energy distribution of the occupied in-gap-state densities of film samples. Therefore Nomura et al. [66] used HAXPES to study the effect of tail and in-gap states on the transport properties of *a*-IGZO films.

A lower Hall mobility (μ_{Hall}) of 2.5 cm^2 V^{-1} s^{-1} (low-quality (LQ) films) and a higher Hall mobility of 15 cm^2 V^{-1} s^{-1} (high-quality (HQ) films) IGZO films with molar ratio of ~1:1:1 were prepared by deposition on silica glass substrates by PLD (pulsed laser deposition). Carrier concentration N_e was tuned at ~10^{19} cm^{-3} by the laser excitation pulse energy. Thermal annealing at 400 °C for 0.5 h in vacuum improved the μ_{Hall} from 15 to 19 cm^2 V^{-1} s^{-1} in high quality (HQ) films and from 2.5 to 10 cm^2 V^{-1} s^{-1} in low quality (LQ) films, as shown in Fig. 18.8. The μ_{Hall} values were temperature independent for all films except the as-deposited LQ film, indicating that conduction carriers are degenerated in extended states. Only the as-deposited LQ film exhibited a thermally activated behavior suggesting effects of shallow trap states or low potential barriers.

Valence-band (VB) HAXPES spectra of these as-deposited and annealed films are composed of three bands which are dominantly of O 2*s*, Ga 3*d*, In 4*d*, Zn 3*d* and O 2*p* character, as shown in Fig. 18.9a. It is clear that these state densities are not affected by film quality. Two additional components are recognized in the VBM-band gap region as shown in Fig. 18.9b. One is tailing into the band gap region (in-gap state I) up to ca. 1.5 eV above the VBM. The other is distributed in

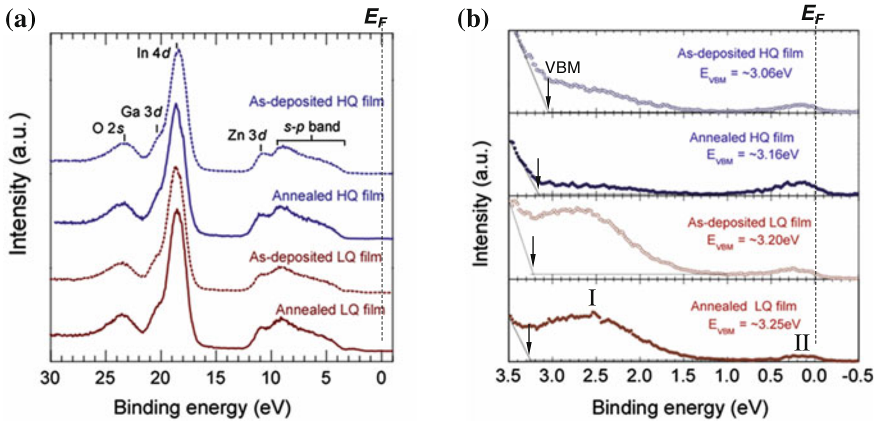

Fig. 18.9 **a** Valence-band HAXPES spectra for the *a*-IGZO films. **b** Valence-band HAXPES spectra around the band-gap region. Intensities are normalized with the *s-p* band observed in (**a**). Two different types of in-gap states are recognized as denoted by I and II

energy from E_F to ca. 0.5 eV below E_F. The latter consists of two different contributions; i.e., from the occupied conduction-band state and the in-gap state below the conduction-band minimum (in-gap state II), as will be discussed in detail below.

To analyze the in-gap state II quantitatively, the apparatus function of the HAXPES system was determined by measuring the Fermi-edge spectrum of gold [67]. Then an In-rich heavily doped film (a-I_2GZO, In:Ga:Zn $\sim$2:1:1) (with a free carrier density of $N_{e,\mathrm{Hall}} = 1.8 \times 10^{20}$ cm^{-3}) was used to obtain a calibration factor to convert the integrated area of the conduction band (CB) signal to an electron density. The CB DOS $N(E)$ can be calculated as $N(E) = N_0(E - E_{CB})^{1/2}$ (E_{CB} being the CB edge energy) [68], assuming a parabolic CB for *a*-IGZO, which is composed primarily of In 5*s* orbitals determined by ab initio calculations [69]. Taking E_{CB} and a fitting parameter to adjust the signal intensity, the spectral weight due to occupied electrons in the conduction band was calculated for the a-I_2GZO by convoluting $N(E)$ with both the Fermi-Dirac distribution and apparatus function. The best fit for the Fermi-edge region was obtained with the $E_F - E_{CB}$ value of 0.2 eV, which agreed well with the Burstein–Moss shift E_{BM} $\sim$0.17 eV calculated from the $N_{e,\mathrm{Hall}}$ value and the effective mass $\sim$0.35m_0 which was obtained with the optical model analysis of free carrier absorption.

The same procedure was adapted to the analyses of the as-deposited HQ and LQ films resulting in excellent agreement in Fermi-edge shape. A large extra DOS of $\sim$5 × 10^{19} cm^{-3} was clearly visible in the region from E_{CB} down to about 0.5 eV below E_{CB}. It is noteworthy that *a*-IGZO TFT's operate with low off currents, <1 pA, and small S values [70], which cannot be explained if a large DOS exists near the CB. In addition, device simulations and capacitance-voltage measurements show that in-gap DOS beneath CB is less than 10^{18} cm^{-3} [71, 72].

The DOS of in-gap state I (near the VBM state) is the largest in the as-deposited LQ film. It is much weaker in the HQ film. Thermal annealing reduces the DOS of this state without changing its shape both in the LQ and HQ films. Using the same calibration factor used for the DOS of in-gap state II, the DOS of in-gap state I observed in Fig. 18.9b is estimated as 9.3×10^{20} cm^{-3} for the as-deposited HQ film and 2.6×10^{21} cm^{-3} for the as-deposited LQ films. The thermal annealing reduced these values to 5.0×10^{20} and 1.6×10^{21} cm^{-3}, respectively. The above results correlate with the improvements of the Hall mobility by annealing, suggesting that in-gap state I is related to carrier scattering centers. The in-gap state I densities are more than two orders of magnitude greater than a hole density induced by a gate voltage (V_g) in a typical TFT structure ($\sim 4 \times 10^{18}$ cm^{-3} for $V_g = 50$ V for a 100 nm-thick SiO_2 gate insulator, and a 30 nm-thick channel). This means that the E_F in the channel is pinned at this in-gap state, and free holes are not induced in extended states in the valence band by the practical range of gate-voltage application in this situation. This observation provides a potential explanation why the *p*-type inversion operations in oxide TFT's have never been established in oxide films including ZnO and *a*-IGZO TFT's.

Weak Urbach absorption tails with the Urbach width of 22 meV were observed in as-deposited as well as in annealed HQ films. In contrast, the as-deposited LQ film exhibits a stronger and broader Urbach tail in the photon-energy region between E_g and 1.8 eV. Thermal annealing reduced the intensity of the tail; however, the shape and width of the absorption band were not changed. These results coincide with the behavior of the in-gap state I shown in Fig. 18.9b, indicating that the Urbach tails are due primarily to excitations of electrons from in-gap state I [66]. The correlation between the DOS of in-gap state I and the photo-response of *a*-IGZO TFT's upon light illumination by sub gap photons was recognized, suggesting that it is due to excitations of carriers from this deep lying in-gap state. The reduction of the DOS of in-gap state I must therefore be indispensable for satisfying practical performances of the transparent TFT's.

The above results provided useful information for the development of transparent TFT's; however, doping levels of the sample films used in the experiments are too high compared to films used in actual TFT's. Thus further investigations using low doped (in other words, highly resistive) TFT films was required. It is also necessary to clarify if the in-gap states are either surface states or bulk states, and what the origin of the near-CBM states is. In order to answer these questions, Nomura et al. also conducted HAXPES experiments on device grade *a*-IGZO films [73].

A set of *a*-IGZO films with In:Ga:Zn $\sim$1:1:1 atomic ratio were prepared by PLD [74]. Carrier concentrations N_e were controlled at $\sim 10^{15}$ cm^{-3}. The films were subjected to thermal annealing in dry O_2 or wet O_2 gas partial pressure to systematically change N_e from 10^{19} to $<10^{15}$ cm^{-3}. Three different types of samples, i.e., epitaxial (*epi*)-ZnO films on (111) surfaces of yttria-stabilized zirconia (YSZ) single crystal by PLD, single crystal (*sc*)-IGZO films on YSZ (111) single-crystal substrates, and highly doped *sc*-IGZO films with N_e of $\sim 10^{19}$ cm^{-3} were used as references for HAXPES measurements.

The depth distribution of the in-gap states were investigated by film thickness dependence and takeoff angle (*TOA*) dependence measurements (from 5° to 88° from the film surface). In-gap state I decreased with increasing film thickness, suggesting that this state is located in the near surface region. The DOS of in-gap state I is the largest at $\sim 7.1 \times 10^{20}$ cm^{-3} for the un-annealed film. It is reduced to $\sim 5.0 \times 10^{20}$ cm^{-3} by the dry O_2 annealing. The wet O_2 annealing further reduced it to $\sim 2.0 \times 10^{20}$ cm^{-3}, which is comparable to that of the *sc*-IGZO film ($\sim 2 \times 10^{20}$ cm^{-3}). Take-off angle dependence in the region of θ = 88°–5° (corresponding to the effective escape depths $\delta = \delta_0 \sin\theta$ of 5.8–0.5 nm) of near VBM spectra were investigated. For the un-annealed films, the in-gap state I (near the VBM) increased close to the film surface (i.e., decreasing δ). Its density reached 6.0×10^{21} cm^{-3} at δ ~ 0.5 nm, which is nine times larger than that at δ ~ 5.8 nm. Both the dry and wet-annealed films also exhibited the same trends. The in-gap state I densities near the surface region at δ ~ 0.5 nm were as high as 3.3×10^{21} and 1.0×10^{21} cm^{-3} for the dry and the wet-annealed films, respectively. This result clearly shows that the in-gap state I is due to the existence of a higher density of defects in the near-surface region than in the bulk region, which can be reduced by thermal annealing. The *TOA* dependence of the photoelectron signals were successfully analyzed by assuming a simple exponential distribution $D(x) = a \cdot \exp(-x/l)$ for the depth distribution of in-gap state I density.

The in-gap state II (near-CBM states) density did not decrease monotonically with increasing effective attenuation length δ for the un-annealed, the dry annealed, and the wet annealed films. The results indicated smaller densities in the surface region (δ = 0.5 nm) than in the intermediate δ regions (δ = 1.0–2.9 nm), suggesting that this type of in-gap state annihilates in the top surface region. Similar results were also obtained in the crystalline oxide semiconductors (i.e., the *sc*-IGZO film, the ZnO single crystal, and the *epi*-ZnO film) as shown in Fig. 18.10a. Their shapes and widths are similar for all the samples irrespective of the film qualities (i.e., the different annealing treatments), degrees of order/disorders in atomic structure (crystals or amorphous), and also materials. It should be noted that similar near-CBM states have also been reported in oxide crystalline materials such as Sb-doped SnO_2, ITO, CdO, and $CdSnO_4$ by Egdell and coworkers, and amorphous In–Zn–O [75–80].

Figure 18.10b, c show the electron concentration (N_e) dependence of in-gap state II for the *a*-IGZO and *sc*-IGZO. In IGZO the carrier concentration exceeds 10^{17} cm^{-3}, and most of the shallow donors are considered to be ionized and carriers are degenerated near the CBM. This means that occupied shallow donor states should not appear in photoelectron spectra. The in-gap state II density increases with increasing N_e in samples with N_e lower than 10^{16} cm^{-3}. The densities of states are estimated as $\sim 5 \times 10^{19}$ cm^{-3} for the highest-quality film with the lowest N_e of $\sim 10^{16}$ cm^{-3}. More than three-orders-of-magnitude difference between these two values evidently indicates that the near CB minimum spectral weight cannot be attributed to free carriers in the conduction band. It should be noted that the integrated areas of in-gap state II are nearly unchanged in the N_e region from 10^{17}–10^{19} cm^{-3}. It should also be pointed out again that DOS values of in-gap state II are

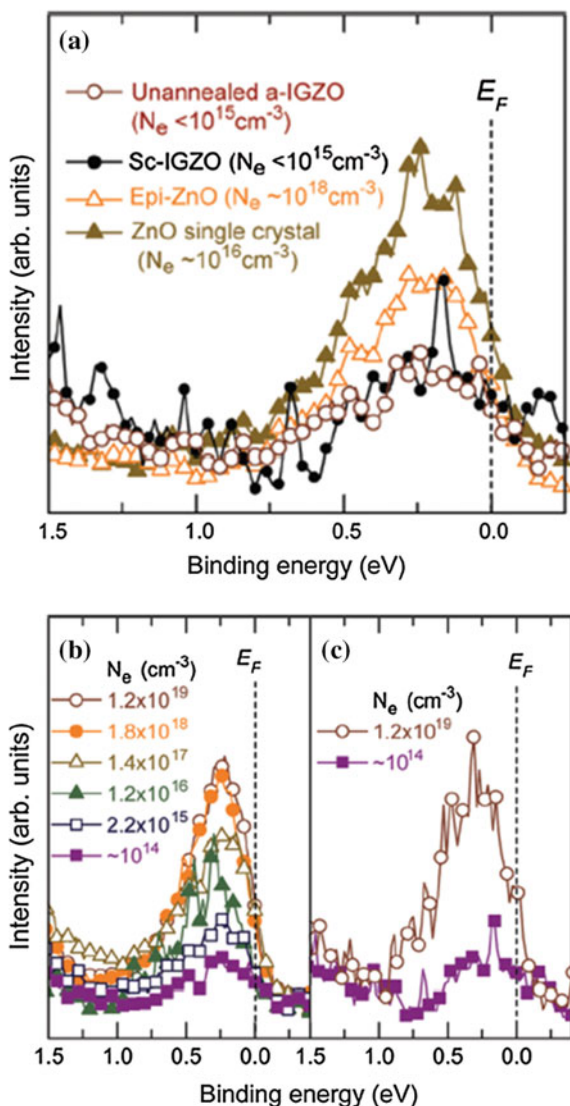

Fig. 18.10 **a** Comparison of HAXPES spectra of near-CBM states for *a*-IGZO film, *sc*-IGZO film, ZnO single crystal, and *epi*-ZnO film. Carrier concentration dependence of HAXPES spectra of near-CBM states for **b** unannealed *a*-IGZO and **c** *sc*-IGZO film

too high to be compatible with the FET operation. Indeed Nomura et al. performed simulations mimicking the observed in-gap states, and found that it was not possible to reproduce the FET characteristics [73].

There can be several candidates to explain the appearance of in-gap state II. One possibility would be that it is formed in the vacuum chamber and does not exist in the channel region of the actual TFT's. However, results of the *TOA* dependence measurements indicate that the near-CBM states have smaller density in the surface region, and exist continuously in the bulk regions of the *a*-IGZO films at least as deep as 5.8 nm from the surface, proving inconsistency with this model. Excitations

of electrons from metastable defects in the band gap by X-rays may be another candidate. The *a*-IGZO has been found to exhibit very slow decay of photoconductivity with time constants $\tau \gg 10^3$ s. This phenomenon has been assigned to the formation of metastable defects by sub-gap photons [74]. Similar phenomena have also been observed in wide band-gap semiconductors including ZnO. The high-density excitation of photoelectrons at $>5 \times 10^{19}$ cm^{-3} would be possible in semiconductors with extremely large τ as long as $>10^3$ s [73]. This model can explain the decrease in the in-gap state II in the top surface region because in general electrons and holes recombine faster at the surface than in the bulk region of many semiconductors. X-ray flux density dependence of the in-gap state II spectral intensity would be key in judging the applicability of this model. However, no sign of X-ray flux dependence of the in-gap state II intensity has been observed by varying the X-ray flux [81]. All the experimental results mentioned above can be consistently explained by assuming the existence of in-gap states that remain neutral with trapped electrons irrelevant to the position of the Fermi level due to high local barriers between the in-gap states and bulk conduction band states. It is possible to consider trap states with large local lattice distortions which provide high potential barriers described by the configuration coordinate similar to DX center in III–V compounds [82]. Transfer of the trapped electrons to bulk conduction-band states is exhibited even when their energies are above the Fermi level during the gate bias applications. However, this explanation remains to be speculative at present, and the origin of the in-gap state II is still open to further investigations.

18.1.3 Dilute Magnetic Semiconductors

Hole-mediated ferromagnetism based on the Zener model [83, 84] has produced reliable estimates of Curie temperature T_c for dilute magnetic semiconductors (DMS) such as GaMnAs. This is a mean-field theory with the assumption that the ferromagnetism occurs through interactions between the local moments of the transition-metal (TM) atoms, which are mediated by the itinerant holes in the material. Okabayashi et al. reported experimental results supporting the theoretical approximation of hole-mediated ferromagnetism by using soft X-ray photoemission spectroscopy to classify the GaMnAs as a charge-transfer insulator [85]. They also reported that the Mn 3*d* component overlaps with the GaAs valence band and a significant amount of Mn 3*d* character is mixed in the doped holes by using resonant photoemission spectroscopy at the photon energies below 70 eV [86]. Recently Mn 3*d* derived states in GaAsMn have been re-examined by angle resolved HAXPES and also by magnetic circular dichroism (MCD) HAXPES, and these results are discussed in different chapters in this book.

Room temperature (RT) ferromagnetism is the target development for spin-electronics applications. It has not been realized in GaMnAs until the present. On the other hand, GaMnN was predicted to have a T_c above RT, if doped with a

high hole concentration at about 1×10^{20} cm^{-3} [84, 87]. Experimentally, a wide range of values from 10 to 940 K has been reported for the T_c of Mn-doped GaN [88–92] through the measure of magnetic properties. However, the observed ferromagnetism in Mn-doped GaN was argued to possibly arise from ferromagnetic Ga-Mn or Mn-N clusters [93–95]. Even in the case where the ferromagnetism in GaMnN is due to the Mn substituted for Ga, it may be difficult to apply the hole-mediated ferromagnetism model to wide band-gap semiconductor based DMS such as GaN. This is because the doped transition metals introduce deep levels in which carriers are localized. Indeed, the experimentally confirmed $Mn^{3+/2+}$ acceptor level in GaN appears very deep in the band gap at 1.8 eV from valence-band maximum [87], and thus it would be an ineffective *p*-type dopant under most conditions. Therefore, the magnetism of Mn-doped GaN remains controversial.

While the magnetism of Mn-doped GaN remains in question, the stable RT ferromagnetism of Cr doped GaN is predicted by first principles calculation [96], and confirmed experimentally [97–100]. In order to understand the origin of the ferromagnetism in the transition-metal doped wide-gap semiconductors, the electronic structure of Cr-doped GaN was studied by HAXPES at an excitation energy of 5.95 keV by Kim et al. [101]. Epitaxial films of wurtzite $Ga_{1-x}Cr_xN$ were grown by NH_3-assisted molecular beam epitaxy (MBE) on ZnO substrates. The Cr atoms substituted for the Ga sites without any other secondary phases up to a CrN composition of $x = 0.101$, which was determined by electron probe microanalysis. The films were confirmed to show ferromagnetic behavior above RT. Details about the MBE growth process and $Ga_{1-x}Cr_xN$ magnetic properties were reported elsewhere [99].

All of the HAXPES spectra (N 1*s*, Ga $2p_{3/2}$, and valence-band spectra) exhibit a shift toward the low-binding energy (BE) by 1.1 and 1.2 eV compared to the undoped GaN spectra, for the $Ga_{0.937}Cr_{0.063}N$ and the $Ga_{0.899}Cr_{0.101}N$ samples, respectively. E_F is located very near the conduction-band minimum in as-grown undoped GaN, as the unintentionally doped electron concentration is 8×10^{19} cm^{-3}. Cr doping results in high resistivity due to the compensation of electrons by Cr induced deep levels, in which hopping conduction takes place [100]. The uniform shifts of the spectra are then interpreted as caused by Fermi-level pinning in the partially filled Cr 3*d* localized in-gap state, which yields ionized impurity centers. In the comparison of spectra of $Ga_{1-x}Cr_xN$ with that of undoped GaN hereafter, the binding-energy origin is set at the VBM, and all spectra for the doped samples are shifted to have their VBM's equal.

Black and red curves in Fig. 18.11a show the normalized valence-band spectrum for undoped GaN and that of $Ga_{0.899}Cr_{0.101}N$, respectively. The lower solid curve shows the difference spectrum between them which clearly indicates that Cr doping introduces new electronic states (**A**) in the band-gap region, and causes decreases in state densities below the VBM (**B** and **C**). As shown in Fig. 18.11b, the density of the in-gap states of the $Ga_{1-x}Cr_xN$ ($x = 0$, 0.063–0.101) increases with increasing Cr concentration, evidencing that the in-gap states are closely related to the Cr 3*d* orbitals. For quantitative analysis, the N 1*s* core-level spectra were normalized to equal area, and the Ga $2p_{3/2}$ core-level and valence-band spectra were scaled by this

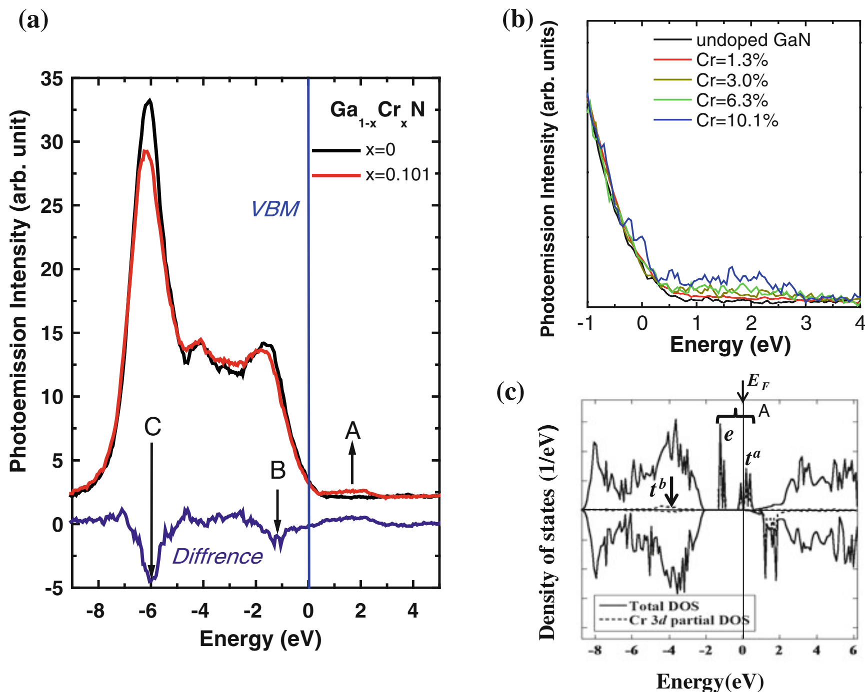

Fig. 18.11 **a** Superposition of valence-band spectra for undoped GaN (*black*) and $Ga_{0.899}Cr_{0.101}N$ (*red*) at $h\nu = 5.95$ keV corrected for background. The *solid line* at the bottom shows the difference spectrum between the two. **b** Electron-distribution curves (EDC's) near the VBM of the undoped GaN (*black*) and the $Ga_{1-x}Cr_xN$ [$x = 0.013$ (*red*), 0.03 (*yellow*), 0.063 (*green*), 0.101 (*blue*)]. The intensity of the new energy state in the band gap depends on the Cr concentration. **c** Calculated total DOS and Cr 3d p-DOS based on the DFT with GGA

same factor. This scaling is valid because Cr is confirmed to substitutionally occupy the Ga sites by X-ray diffraction and angular dependent N 1s X-ray absorption [99, 102].

In order to elucidate the origin of the in-gap states, DFT band-structure calculations based on the generalized gradient approximation (GGA) [51, 103] have been performed. The crystal structures of GaN with periodic boundary conditions using a super cell in which one of the 16 Ga sites is replaced by a Cr site. The cell is optimized with the Vienna ab initio simulation package (VASP) (based on the projector-augmented-wave approach [104, 105]). The resultant total density of states (DOS) and Cr 3d partial DOS are shown in Fig. 18.11c. In the band gap, there are two sharp up-spin bands which are explained by a Cr cluster model as follows. Since the Cr atoms in the Ga sites are tetrahedrally bonded with four nitrogen atoms, the $3d_\varepsilon$ (d_{xy}, d_{yz}, and d_{zx} orbitals) and $3d_\gamma$ ($d_{x^2-y^2}$ and d_{z^2} orbitals) states split into nonbonding ($\boldsymbol{e}$), bonding ($\boldsymbol{t}_b$), and antibonding ($\boldsymbol{t}_a$) states in the tetrahedral crystal field. The two sharp up-spin bands correspond to the $\boldsymbol{e}$ and $\boldsymbol{t}_a$ states. The $\boldsymbol{t}_b$

state is merged in the VB and the down-spin band overlaps the CB. Because E_F is positioned at $\boldsymbol{t}_a$, and the up- and down-spin states are separated, the material is spin polarized. This calculated result is similar to the DOS calculated by the Korringa–Kohn–Rostoker method combined with the coherent-potential approximation (CPA) [96]. The Cr 3*d* contribution to the in-gap states is evident; however, the first-principles calculations reveal that the second-nearest-neighbor Ga 4*s* states also contribute to the in-gap states by hybridization with the Cr 3*d* levels. The atomic subshell photoionization cross section of Cr 3*d* (4×10^{-7} Mb for $Ga_{0.899}C_{r0.101}N$) is very small compared to Ga 4*s* (5.4×10^{-5} Mb for $Ga_{0.899}Cr_{0.101}N$) at the high excitation energy [22]. Therefore, the question arises which is the main contribution to the observed in-gap states.

Two different estimates were done to solve the problem. First, the partial DOS for Ga 4*s* and Cr 3*d* of the in-gap states were multiplied by the atomic subshell photoionization cross sections at 6 keV [22], and in the case of the Ga 4*s* contribution, it was also multiplied by 12, considering the 12-fold coordination of Ga around the Cr atoms. The ratio of the Ga 4*s* to Cr 3*d* contributions to the area of the in-gap state was estimated to be 3.7. Second, the ratio of the area of the observed in-gap state to that of the valence band in the region of 0 to −8 eV, where the Ga 4*s* contribution is dominant, was estimated to be 0.021 for $x = 0.1$. This ratio is to be compared with the ratio of the calculated Ga 4*s* *p*-DOS of the in-gap state to that of the total valence band. The calculation for $x = 0.07$ gave a value of 0.015 for this ratio. After scaling by the Cr concentration, both the experimental and calculated ratios nearly coincide at approximately 0.02 for $x = 0.1$. The above analysis assures that the in-gap states are dominated by the Ga 4*s* contribution.

Cr doping also causes changes in the valence band (**B** and **C** in Fig. 18.11a). Since Cr atoms substitute into Ga sites, the Ga 4*s* contribution in the Cr-doped GaN decreases compared to the undoped GaN. Thus the negative values of the **B** and **C** peaks in the difference spectrum are primarily due to the decrease of Ga content in the matrix. However, the difference spectrum in the energy region from ~2 to ~5 eV is dissimilar to the Ga 4*s* partial DOS, indicating that the $\boldsymbol{t}_b$ state, which distributes in the same energy region as shown in Fig. 18.11c, is also responsible for the valence-band spectral change.

The experimentally observed in-gap state shows a broader spectral-density distribution which covers the energy region of the two sharp calculated Ga 4*s* states corresponding to the $\boldsymbol{e}$ and $\boldsymbol{t}_a$. This discrepancy is reasonably understood by considering randomly distributed ionized-impurity potentials. As a result of compensation of unintentionally doped *n*-type impurities by Cr doping, the ionized-impurity concentration then reaches a value near 1×10^{20} cm^{-3}. This value is considered to introduce a large enough spatial fluctuation of the ionized-impurity potential to cause the broadening of the in-gap states.

Figure 18.12a shows N 1*s* spectra of undoped GaN (open circles), $Ga_{0.937}Cr_{0.063}N$ (solid gray circles), and $Ga_{0.899}Cr_{0.101}N$ (solid black triangle). The lower binding-energy tail at around 393.8 eV of the main peak (394.5 eV) increases with increasing Cr doping. As clearly seen in the difference spectra between the undoped GaN and $Ga_{1-x}Cr_xN$ ($x = 0.063$ and 0.101) in the bottom of the figure by

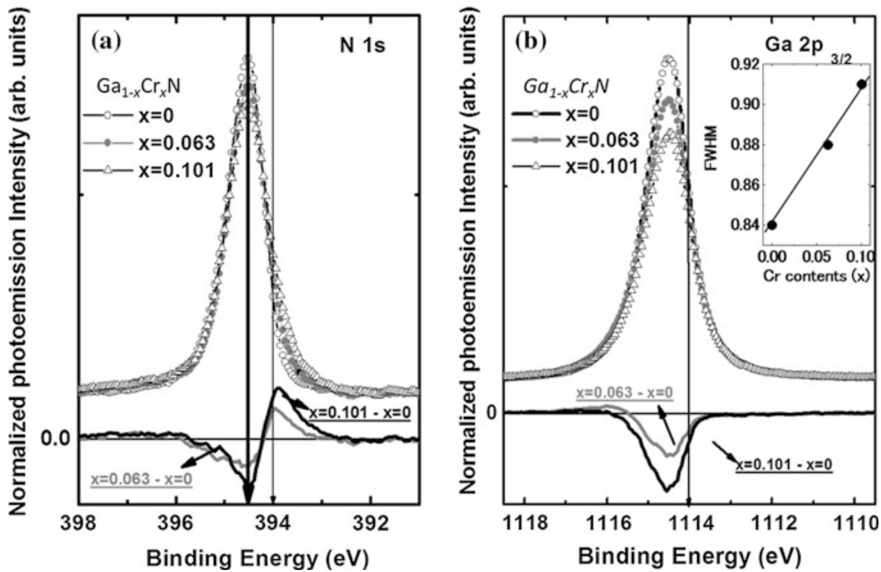

Fig. 18.12 **a** N 1 *s* and **b** Ga $2p_{3/2}$ HAXPES core-level spectra of the undoped GaN (*open circles*) and the $Ga_{1-x}Cr_xN$ [x = 0.063 (*filled gray circles*), 0.101 (*open black triangles*)]. The *lower panel* shows the difference spectra between GaN and $Ga_{1-x}Cr_xN$ [x = 0.063 (*gray*), 0.101 (*black*)]. The *right inset* in (**b**) shows the FWHM variation of the Ga $2p_{3/2}$ spectra with Cr concentration. The width increases as x increases

gray and black solid lines, the Cr doping causes a decrease of the N 1*s* in the matrix and introduces a new chemically shifted component at the lower binding energy. Considering that the electronegativity difference ($\Delta\chi$) of the Cr-N bond (1.51) is larger than that of Ga–N bond (1.26) [106], this chemically shifted component is assigned as originating from N atoms in the Cr-N bonds. The intensity of the Ga $2p_{3/2}$ core-level spectra decreases as shown in Fig. 18.12b, whereas the full width at half maximum (FWHM) increases with increasing Cr content x (insertion of Fig. 18.12b). The line shape of the difference spectra is evidently asymmetric. These results suggest that an unresolved chemically shifted component at the lower binding energy of the main peak due to Ga-Cr hybridization gives a contribution to the spectra. This is consistent with the DFT calculation result in which the Cr 3*d* orbital is not only hybridized with the nearest N but also the second nearest neighbor Ga atom by Cr–N chemical bond formation. In 6 % Cr doping, the Cr–N–Ga–N–Cr network makes a large island by percolation in the crystal. These islands possibly play an important role in the ferromagnetism of $Ga_{1-x}Cr_xN$.

As discussed above, the Cr induced band in GaCrN is apparently detached from the valence band and shows a localized nature. However, arguments still remain concerning the GaMnAs electronic structure and the nature of states, from which ferromagnetic coupling is originated [87, 107–117]. Grey et al. have exploited hard X-ray angle resolved photoelectron spectroscopy (HARPES) to solve this

controversy by studying the differences between the bulk electronic structures of a parent semiconductor GaAs and a dilute ferromagnetic semiconductor derived from it [118]. As discussed in another chapter of this book by Grey, these results strongly favor a model of $Ga_{1-x}Mn_xAs$ in which the Mn-induced impurity band is centered about 400 meV below the Fermi level, and is not detached from the GaAs valence bands. It is also suggested that the magnetism originates from the coexistence of the two different mechanisms of the double exchange and *p-d* exchange based on the above model and recently suggested by theory [119]. HAXPES investigation by Fujii et al. also leads to the consistent conclusion [120].

18.1.4 LBMO

Perovskite manganites, which have been intensively investigated as promising candidate materials for spintronic applications, show a rich variety of physical properties such as colossal magnetoresistance [121], ferromagnetism with metallic conduction [122], and perfect spin polarization [123]. Charge and/or orbital ordering [124] due to the strong coupling between spin and charge and orbital–lattice–degrees of freedom is also an interesting feature of this compound system [125]. Among them, $La_{1-x}Sr_xMnO_3$ (LSMO), and related compounds, which show ferromagnetic phase transitions accompanied by metal-insulator transitions near room temperature, have attracted much interest due to potential applicability to the spin electronic devices.

As described in another chapter by Taguchi and Panaccione, HAXPES investigations on these perovskites and related materials exhibit an additional sharply peaked feature in the metallic phase. Horiba et al. first observed this well-screened feature in bulk-sensitive HAXPES Mn 2*p* core-level spectra of $La_{1-x}Sr_xMnO_3$ (LSMO) thin films whereas it had not been observed in surface-sensitive SXPES measurements [126]. This feature is explained as due to nonlocal screening of core holes by the itinerant carriers in the strongly correlated states originating from transition metal 3*d* states. Introducing an additional hybridization term (V^*), which represents the hybridization strength between Mn 3*d* states and coherent states at the Fermi level and thus the degree of itineracy of the carriers, the single-site cluster model by Taguchi et al. was successful in reproducing the transition metal 2*p* HAXPES spectral features in $(La_{1-x}Sr_x)MnO_3$ thin films displaying metallic states in the core-level HAXPES spectra [126–128]. The take-off angle (*TOA*) dependence of the HAXPES clarified that the well-screened feature is indeed of a bulk nature and strongly correlated with the electronic structure near the Fermi level, the metal-insulator transition, and the appearance of the ferromagnetism.

It was found that tensile strain from the substrate due to lattice mismatch stabilizes the double exchange ferromagnetism in lightly doped $(La_{1-x}Ba_x)MnO_3$ thin films [129, 130]. Ultra-thin films down to 5 nm thickness displayed room-temperature ferromagnetism, whereas the ferromagnetic Curie temperature (T_c) in unstrained systems is 260 K [131]. This opens the possibility of spintronic devices such as a

ferromagnetic (La,Ba)MnO_3/Sr(Ti,Nb)O_3 *p-n* diode [132] and a ferromagnetic (La,B) MnO_3/Pb(Zr,Ti)O_3 field-effect transistor [133] operating at room temperature. Tanaka et al. [134] conducted HAXPES investigations of the well-screened satellite of the Mn 2*p* core-level HAXPES spectra of tensile strained $La_{0.85}Ba_{0.15}MnO_3$ (LBMO) thin films of 3, 20, and 300 nm thicknesses grown epitaxially on Nb-doped $SrTiO_3$ (001) single-crystal substrates using a pulsed laser deposition (PLD) technique. They found that the dependence of the Mn $2p_{3/2}$ satellite peak on film thickness systematically agreed with the ferromagnetic order in the bulk part of the films. The V^* of the strained (La,Ba)MnO_3 films systematically evolved with decreasing film thickness from 300 to 20 nm, supporting strain induced ferromagnetism. They also showed that the temperature dependence of the satellite intensity varied as the square of the magnetization.

In order to clarify the relationship between the well screened satellite spectral weight and the magnetization quantitatively, Ueda et al. [135, 136] analyzed the temperature dependence of the Mn $2p_{2/3}$ HAXPES spectra for films with t = 5 and 20 nm thickness in the temperature range between 28 and 340 K. As seen in Fig. 18.13a, b, the satellite intensity for the 5 nm thick LBMO film is apparently less distinct than that for the 20 nm-thick LBMO film at low temperature. The normalized satellite intensity $I_S(T)$ increased with decreasing temperature,

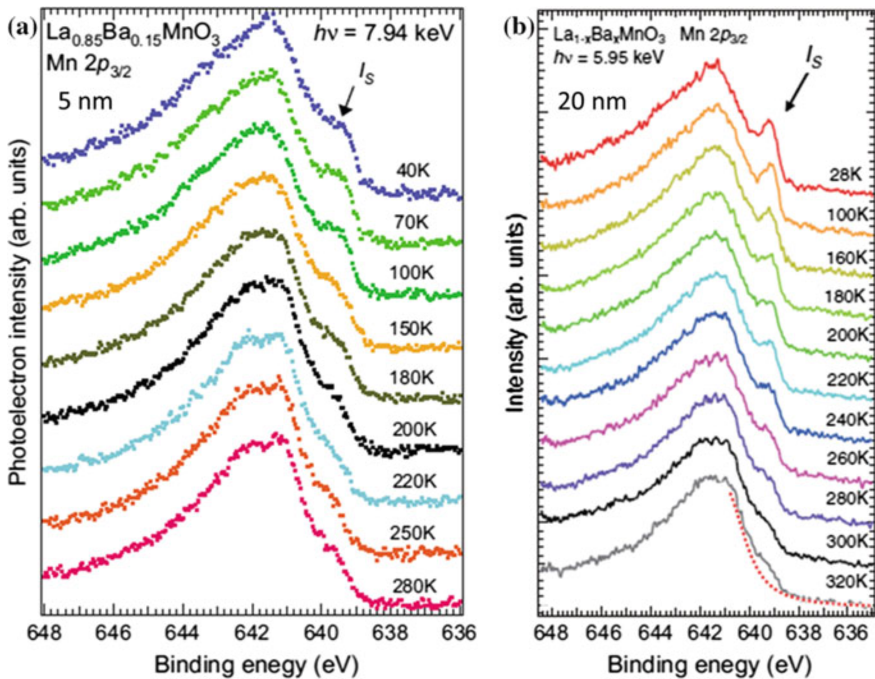

Fig. 18.13 Mn 2*p* core-level HAXPES spectra of the 5 nm thick (**a**) and 20 nm thick (**b**) $La_{0.85}Ba_{0.15}MnO_3$ films taken at various temperatures

correlating with increasing ferromagnetic order and metallicity. Using the same single-cluster calculations that were used by Taguchi et al. [126–128] for LSMO, they could reproduce the intensity and position of the satellite peaks of the experimental Mn 2*p* HAXPES spectra for the $t = 20$ and 5 nm films. The V^* of the 20 and 5 nm-thick LBMO was then estimated at various temperatures. The resultant V^* increased with developing ferromagnetic ordering as the temperature decreased, showing a linear relation between $(V^*)^2$ and the well-screened peak intensity ($I_S(T)$) [135]. The experimental $I_S(T) - T$ curve resembled the $M(T)^2 - T$ curve as measured by the SQUID magnetometer, indicating that HAXPES can be used to investigate ferromagnetism in strongly correlated materials.

To deduce the magnetization M from the Mn 2*p* HAXPES spectra, Ueda et al. [135, 136] employed the double-exchange model [137] under the assumption that the Hund coupling J_H was strong between the Mn $\boldsymbol{e}_g$ and $\boldsymbol{t}_{2g}$ states. The double-exchange model should be simplified to the *t*-*J* model in this case [138], and J is proportional to t^2/U, where U is the Mn 3*d*-3*d* Coulomb interaction. V^* is taken to be proportional to the Mn 3*d*-3*d* transfer integral, and consequently t is proportional to V^*. J is then proportional to the square of V^*. The Bloch $T^{3/2}$ law gives the relation between M and J [139], and the temperature-dependent normalized magnetization, $m(T)$, is given as follows:

$$m(T) = 1 - A\left[k_B T/(V^*)^2\right]^{3/2}. \quad (18.1)$$

Here A is a coefficient and k_B is the Boltzmann constant.

Figure 18.14a, b show the normalized magnetization curves obtained by SQUID and the calculated $m(T)$'s using (18.1) below T_c for the 5-nm and for the 20-nm-thick LBMO films, respectively. The temperature-dependent parameter V^* was determined experimentally by fitting the Mn 2*p* spectra as described above. The calculated $m(T)$ reproduces the magnetization curve in both cases. Note that the $m(T)$ curves deviate from the magnetization curves when V^* in (18.1) is constant as shown in the same figures. These results indicate that the ferromagnetism of LBMO is governed by $(V^*)^2$. On the basis of the Anderson-impurity model, the density of states at E_F ($D(E_F)$) is proportional to $(V^*)^2$ as discussed in [132–135], suggesting that a mobile carrier mediated double-exchange interaction model is reasonable for this material.

The $D(E_F)$ decreases with increasing temperature as discussed. Consequently, carrier scattering processes are also expected to be temperature dependent because they dependent on $D(E_F)$. Indeed, the Hall mobility of LBMO strongly depends on temperature, whereas the carrier density for LBMO is only weakly temperature dependent [140]. Figure 18.14c, d show the temperature dependence of the normalized conductivity with the calculated $m(T)$ for the 5 and 20 nm-thick LBMO films. The normalized conductivity curves agree well with the calculated $m(T)$ below T_c [136]. According to the Anderson-Hasegawa model [141], the nearest-neighbor Mn 3*d*-3*d* transfer integral (t) decreases by magnon excitations with increasing temperature, giving rise to the decrease of magnetization with increasing temperature. The similarity of the temperature behavior of the

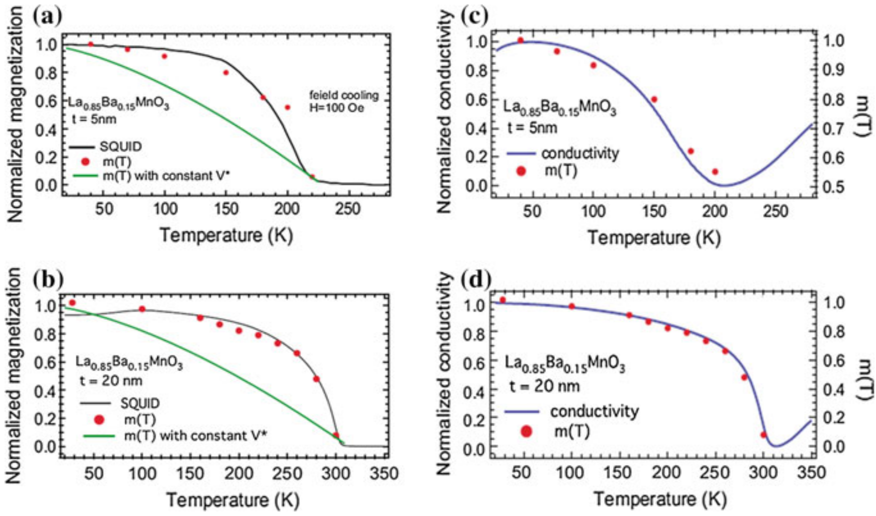

Fig. 18.14 Normalized magnetization curves of the 5 nm thick (**a**) and 20 nm thick (**b**) $La_{0.85}Ba_{0.15}MnO_3$ films measured by SQUID magnetometry. The calculated $m(T)$ curves using (18.1) are also shown in the figure. Normalized conductivity curves of the 5 nm thick (**a**) and 20 nm thick (**b**) $La_{0.85}Ba_{0.15}MnO_3$ films are shown as *solid lines*. The calculated $m(T)$ curves using (18.1) are also plotted in the figure

conductivity with magnetization suggests that the same magnon excitations contribute to the carrier scattering process.

Regarding the observed thickness dependence of the ferromagnetism, the strain introduced in the LBMO epitaxial layer by lattice mismatch modifies the Mn derived $\boldsymbol{e}_{g.}$ state to decrease the split between the $d_{x^2-y^2}$ and $d_{z^2-r^2}$ orbitals and increase the bandwidth, resulting in the large V^* ($D(E_F)$) in the 20 nm thick film. In the 300 nm thick film, the strain is relaxed due to introduction of mismatch dislocations, consequently further enhancement of $D(E_F)$ and V^* are not expected. On the other hand, it is seen in Fig. 18.14a, b that T_c of 5 nm thick LBMO is suppressed compared with 20 nm thick LBMO. Further suppression of T_c and I_s was found in the 3 nm thick LBMO film as seen in [134]. These suppressions of T_c in the thin LBMO films, in which the LBMO lattice is not relaxed (thus the $\boldsymbol{e}_{g.}$ state modification is the same as the 20 nm thick film) are considered to be mainly related to the carrier concentration modulation due to an interface effect [129].

Horiba et al. conducted a systematic HAXPES investigation of changes in the electronic structure due to deformation in $La_{1-x}Sr_xMnO_3$ thin films on substrates with different lattice mismatches [138]. Epitaxial LSMO thin films, which were grown on atomically flat surfaces of $LaAlO_3$ (LAO), $(LaAlO_3)_{0.3}(SrAl_{0.5}Ta_{0.5}O_3)_{0.7}$ (LSAT), and Nb-doped $SrTiO_3$ (STO) substrates by PLD were used for the investigation. These authors found that the application of compressive (c/a = 1.05) and tensile (c/a = 0.98) strain results in the formation of a gap at the Fermi level (E_F) and suppression of spectral weight at E_F, respectively, across the phase

transition. Detailed discussion of the electronic-structure changes due to applied substrate stress is given in [142], referring to the *c*/*a*-*x* phase diagram [143].

18.1.5 A New Type of Shape Memory Alloy

A new type of shape-memory alloy (SMA) showing a large magnetic-field induced strain (MFIS) has attracted much attention as a magnetic actuator material [144, 145], since the ferromagnetic Ni–Mn–GA compound was proposed as a candidate [146]. The first report of ferromagnetic Ni–Mn–Ga explains that the MFIS is due to a rearrangement of martensite variants by an external magnetic field induced through a strong coupling between magnetic and mechanical variables [147].

Ni–Mn–In, Ni–Mn–Sn, and Ni–Mn–Sb alloy systems are different types of magnetic SMA's, of which the crystalline structure changes from the cubic Heusler $L2_1$ structure to the layered structure upon martensitic phase transition (MPT). The magnetization in the martensite phase of this system is significantly smaller than that in the austenite one [148]. A shape recovery of about 3 % has been confirmed for a pre-deformed single crystal of Co-doped Ni–Mn–In alloy due to a magnetic-field-induced phase transition (MFIT) from a weak-magnetic martensite to a ferromagnetic austenite phase at 298 K [149]. This suggest that the stress due to the MFIT is extremely large (over 100 MPa) [149, 150]. Indeed the value is several decades larger than that generated in the conventional ferromagnetic SMA's. This group of alloys also shows many other interesting properties, such as an inverse magnetocaloric effect [151], a giant magnetoresistance effect [152], giant magnetothermal conductivity [153], and an exchange bias effect [154], thus attracting interest as a new advanced functional material. Behaviors of electrical resistivity [155] and thermoelectric properties [156] in the martensite phase of the Ni–Mn–Sn alloy suggest that the density of states in the vicinity of the Fermi energy changes upon the MPT. First-principles calculations, particularly on Ni–Mn–Ga systems, have provided different interpretations of the origin of the MPT, such as a Jahn–Teller distortion [157] and Fermi surface nesting [158].

Ye et al. conducted HAXPES investigations of electronic-structure change of polycrystalline $Ni_2Mn_{1+x}Sn_{1-x}$ ($0 \le x \le 0.42$) during the MPT, and discussed the results based upon DFT calculations [159]. The samples were confirmed to crystallize in the $L2_1$ structure at room temperature by structure refinement using standard Rietvelt analysis of powder diffraction measurements. The excess Mn atoms in these samples occupy the vacant Sn sites consistent with the reported results [160, 161]. HAXPES valence-band spectra of samples with $x = 0.42$ and 0.36 for temperatures from 300 to 20 K showed a sharp peak around 0.3 eV below E_F, which was attributed to the Ni 3*d* $\boldsymbol{e}_{g.}$ minority-spin states as in Ni_2MnGa and found to be temperature dependent. It remained unchanged from 300 K down to 240 K for the $x = 0.42$ sample, and down to 80 K for the $x = 0.36$ sample. However, a sudden reduction of the peak intensity was clear when the temperature was decreased across the MPT temperature (230 K for $x = 0.42$ and 80 K for $x = 0.36$

samples). No change in either structure was observed, upon further decrease of the sample temperature down to 160 K for $x = 0.42$ sample, indicating that the electronic and lattice structures were stabilized in the martensite phase. A sample with $x = 0.40$ which showed MPT at 190 K also exhibited similar temperature behavior. Two additional samples with lower concentrations ($x = 0.12$ and 0.00), which did not show MPT, exhibited no noticeable change near E_F between 300 and 20 K. All these results evidence the important role of the electronic structure near the Fermi level in producing lattice deformations.

Figure 18.15a shows the valence-band spectra in the austenite phase (300 K) for x = 0.00–0.42. The systematic shift of the peak towards E_F is observed with increasing x. The peak in the samples which do not show MPT ($x = 0.0$ and 0.12) is located away from E_F, whereas it approaches E_F in the samples which show MPT ($x = 0.36$, 0.4, and 0.42). This behavior is understood to be important for triggering the MPT in the ferromagnetic state. The substitution of Sn atoms by Mn atoms increases the valence-electron numbers, which results in an upward shift of E_F, contrary to the observation. A pure rigid-band model is apparently not applicable to explain the peak shift.

The first-principles calculations using the VIENNA ab initio simulation package [105] was carried out to elucidate the role of excess Mn atoms in the MPT of the Ni–Mn–Sn alloys. A peak structure, which was revealed to be predominantly composed of Ni 3d $\boldsymbol{e}_g$. ($d_{x^2-y^2}$ and $d_{3z^2-r^2}$) orbitals as pointed out for Ni_2MnGa by several authors [158, 162–164], was found at about 0.51 eV below E_F in the minority-spin band of Ni_2MnSn. This peak structure was broadened and shifts

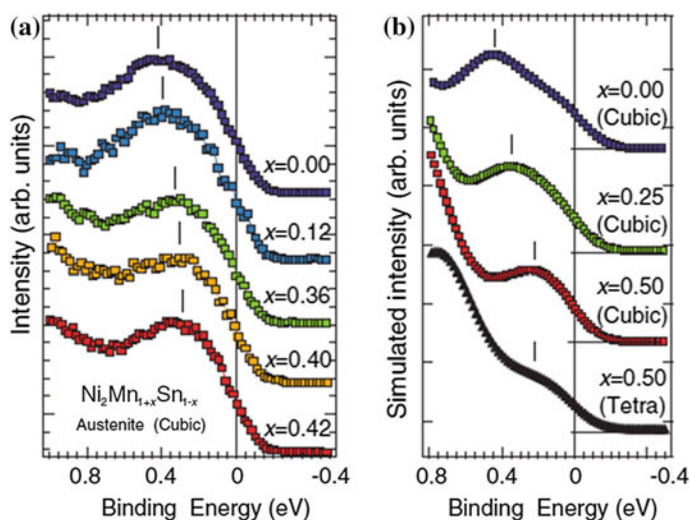

Fig. 18.15 **a** Near E_F valence-band spectra of $Ni_2Mn_{1+x}Sn_{1-x}$ as a function of x in the cubic Heusler $L2_1$ phase at 300 K. **b** The simulated spin-integrated X-ray photoelectron spectra by DFT calculation

towards E_F with increasing Mn composition. The spin integrated DOS which are broadened by a Gaussian function with a FWHM of 240 meV reproduce the experimental results as shown in Fig. 18.15b. The peak shift can be explained as the result of the hybridization between the Ni 3*d* orbitals and the 3*d* orbitals of the Mn atoms which occupy the Sn sites. The magnetic moment of the excess Mn at the Sn sites (denoted by "Mn_{Sn}" hereafter) is antiparallel to that of Mn at the ordinary sites. The same antiferromagnetic coupling between the excess Mn and the ordinary Mn magnetic moments has also been predicted theoretically for Ni–Mn–Ga alloys [165]. This coupling locates the occupied Mn_{Sn} 3*d* states on the lower-energy (or higher-binding energy) side of the Ni 3*d* states in the minority-spin band, giving rise to the hybridization between the Mn_{Sn} 3*d* and the Ni 3*d* orbitals that causes the energy shift of the Ni 3*d* bands towards E_F.

The calculation of the net magnetization due to the antiparallel arrangement of the Mn magnetic moment agreed with magnetization measurements [166]. The total energy variation due to a tetragonal distortion from the cubic phase for each Mn composition was also calculated fixing the cell volume at that of the cubic phase. In the tetragonal structure with $c/a > 1$, the degenerate Ni 3*d* $\boldsymbol{e}_{g.}$ level splits into two bands composed of $3d_{x^2-y^2}$ orbitals at higher energy and $3d_{3z^2-r^2}$ orbitals at lower energy. The total energy gain due to the tetragonal distortion is then expected to be large in $Ni_2Mn_{1.5}Sn_{0.5}$ ($x = 0.5$) as E_F is located between the two split-off levels. However, it is subtle as both split-off levels are completely occupied in the case of Ni_2MnSn ($x = 0$). This explains why the martensite phase is stabilized only for Ni–Mn–Sn alloys having larger amounts of excess Mn atoms. The substitution of Sn atoms by Mn atoms increases the valence-electron number and the excess electrons occupy the Ni 3*d* $\boldsymbol{e}_{g.}$ state. At the half filling of the Ni 3*d* $\boldsymbol{e}_{g.}$ state, the cubic structure becomes most unstable and tends to deform to the tetragonal structure to gain energy by splitting the Ni 3*d* $\boldsymbol{e}_{g.}$ state into the $3z^2 - r^2$ and the $x^2 - y^2$ states. This essential understanding of the MPT in $Ni_2Mn_{1+x}Sn_{1-x}$ has been obtained by the combination of the HAXPES observation and the first principle calculations.

18.1.6 Au^+ and Au^{3+} Ions in Au/CeO_2 Thin Films as an Example of a Functional Nanocluster

Gold nanoclusters supported on various oxide supports have been reported to be significantly active catalysts [167, 168]. The high activities observed for various catalytic reactions such as CO oxidation [169–172], 2-propanol oxidation [173], water gas-shift reaction (WGS) suggest the presence of cationic gold [174, 175]. Gold nanoclusters supported by ceria are expected to have high catalytic activity due to redox properties of ceria.

To investigate the interaction of gold with CeO_2 layers, Matolín et al. [176] conducted comparative photoelectron spectroscopy studies on samples prepared by simultaneous magnetron sputtering of gold and cerium oxide with various excitation photon energies from 180 to 6 keV. Two Au doped samples labelled Au L and

Au H with 6.5 and 16.9 at.% Au in ceria, respectively, were prepared on Si(100) wafer substrates by using non-reactive radio-frequency (rf) magnetron sputtering from composite target of CeO_2 and Au wires. This method provides CeO_2 layers continuously doped with Au atoms during the growth. The Au concentrations were determined from Ce 3*d* and Au 4*f* peak areas by using the XPS atomic sensitivity factors. The Au concentration determined in this way corresponded to an average Au concentration in the surface layer probed by XPS, which is approximately 2 nm thick, and could differ from that of the film bulk. The high resolution Ce 3*d* core-level HAXPES (5946.8 eV) spectrum evidenced the formation of CeO_2 [171, 172, 177, 178]. Comparison of HAXPES Ce 3*d* spectra obtained for a pure cerium oxide film with those of the Au L and Au H films indicated that there was no measurable influence of added gold on the cerium oxide stoichiometry.

Figure 18.16 compares the Au 4*f* spectra recorded at 180, 500, and 5946.8 eV photon energies. The inelastic mean-free path in CeO_2 is estimated as $\lambda = 7$, 0.5 and 0.9 nm, for HAXPES, $h\nu$ = 180 and 500 eV, respectively [173–181]. The comparison for Au L is shown in Fig. 18.16a. At $h\nu$ = 180 eV, the spectrum consists of a dominant spin-orbit doublet corresponding to Au^0 with an additional doublet due to Au^+ at higher binding energy. A trace contribution from Au^{3+} is also observed at 0.85 eV higher binding energy than the Au^0 doublet. At $h\nu$ = 500 eV, increases in the Au^{1+} and Au^{3+} signals are distinguishable, and the increase in the Au^{3+} signal is prominent in the high-energy HAXPES spectrum. As shown in Fig. 18.16b, manifestation of Au^{3+} component is more evident in Au H. The Au^{3+}/Au^0 ratio

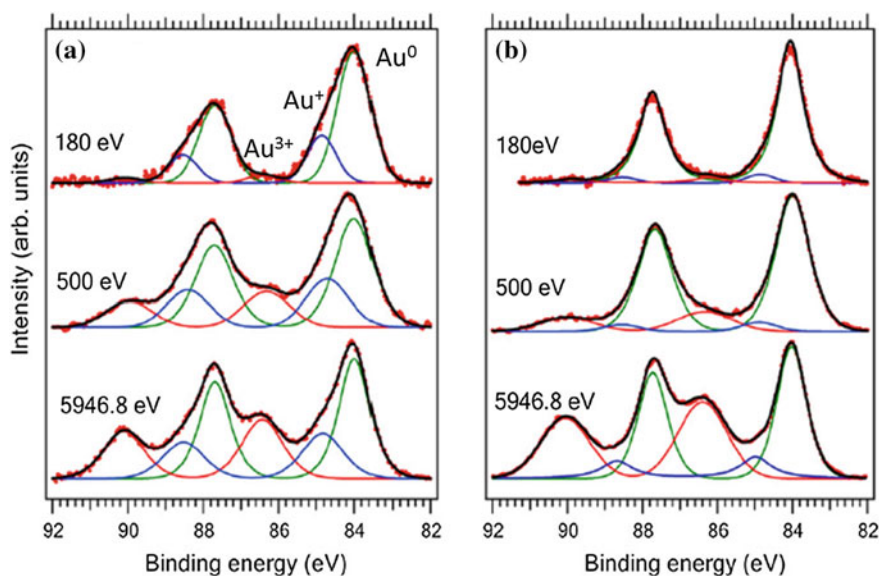

Fig. 18.16 Soft X-ray ($h\nu$ = 180 and 500 eV) and hard X-ray ($h\nu$ = 5946.8 eV) Au 4*f* spectra for Au L sample (**a**) and Au H sample (**b**)

increases dramatically with increase in probing depth for both the Au L and Au H samples, evidencing that Au^{3+} distributes deep in the bulk region of the sample. The Au^{1+}/Au^{0} ratio shows more moderate variation, demonstrating that the Au^{1+} and Au^{0} are localized near the surface.

It is surprising that high concentration of $Au^{1+,3+}$, with Au^{3+} content exceeding 50 %, exist in the co-sputtered Au/CeO_2 system. A simple estimate based on the attenuation of the Au^{1+} and Au^{3+} signal as functions of λ leads to a structural model with metallic gold on the surface, Au^{1+} at the gold–ceria interface and Au^{3+} dispersed in the ceria film bulk. The gold is expected to form three-dimensional islands with average height above 1 nm. Particles with larger thickness contribute to reduce the total Au^{1+} signal, especially for 180 eV photon energy. The low values of the Au^{1+}/Au^{0} ratio for photon energies 180 and 500 eV (high surface sensitivity) suggest that the Au^{1+} species are localized at the Au/oxide interface perimeter [182] and also at the bottom of the gold particles. On the other hand, for $h\nu = 5946.8$ eV ($\lambda = 7$ nm) the Au^{1+} signal notably increases, which could correspond to the increasing contribution of Au^{1+} species due to increasing probing depth. The Au^{3+}/Au^{0} ratio increases from 0.04 for 180 eV up to 0.91 for HAXPES. This behavior can be satisfactorily explained by a model of Au^{3+} ions dispersed in the cerium-oxide film bulk. The SEM image of the Au H surface showed structure with average grain size of 25 nm, different from that of the pure ceria film.

For the Au L sample, the Au^{1+}/Au^{0} intensity ratio showed the same value of 0.31 for 180 and 500 eV photon energies. This fact fits with a model of very small gold particles giving a high contribution of the interface Au^{1+} species at the Au/oxide interface perimeter. Similarly to the Au H sample, the Au^{1+}/Au^{0} intensity ratio increases at $h\nu = 5946.8$ eV excitation because the Au^{1+} species belonging to the whole interface are detected. The higher Au^{1+}/Au^{0} intensity ratio for the Au L sample than that for the Au H one reflects a higher relative concentration of gold atoms at the interface for smaller particles. The Au^{3+}/Au^{0} ratio shows an increase as the photon energy increases similar to the Au H case, confirming that Au^{3+} ions are dispersed in the cerium-oxide film sub-surface region.

The most probable picture of the Au–CeO_2 rf-sputtered film structure based on the experimental observations corresponds to the Au^{3+} cations embedded in the growing film and of a partial segregation of metallic Au at the surface. The amount of surface Au increases with increasing concentration of the Au dopant, and it forms particles which are separated from the ceria film by the Au^{1+} rich interface; i.e., a Ce–O–Au structure is formed. Each of the atomically dispersed Au atoms, which are supposed to substitute in Ce sites [183], has eight neighboring oxygen atoms. These oxygen atoms can be easily released in spite of the strong interaction with Au due to the oxygen storage capacity of cerium oxide to form the Au oxide. The overall cerium-oxide reduction, however, is slight because of low Au concentration. Oxidation of Au atoms, which are atomically dispersed in oxygen rich CeO_2, leads to the formation of a new functional material: Au–Ce mixed oxide.

The above results clearly illustrate the usefulness of HAXPES for the study of nanoclusters. Matolín and his coworkers have applied HAXPES to CeO_2 substrates dispersed with Pt, Sn, and Pt–Ti nanoclusters as well to reveal the specific

electronic and chemical interactions of the doped metal-CeO_2 system in relation with the development of advanced fuel cells [184–186]. A study on N-containing carbon-based cathode catalysts for polymer electrolyte fuel cells by Niwa et al. is also an example of HAXPES successfully applied to the advanced fuel-cell research and development [187]. HAXPES investigations of various catalysts has also been reviewed by Yoshikawa et al. [188].

18.1.7 Hard Disc Lubricants

As a result of the continuous demands for increasing the areal density of hard discs (HD), the gap between the read-write head and the magnetic recording disk has been reduced to the sub 10-nm range. To reduce the friction and resulting damage from high-speed moving contact between the two surfaces, the magnetic recording disk and the head are typically coated with an amorphous diamond-like carbon (DLC) film, and the surface of the disk is lubricated with a molecularly thin film of a perfluoropolyether (PFPE) oil. A noble lubricant has been designed and synthesized to obtain high temperature resistivity and self-repair in case the main chain of the molecule is damaged. This consists of a PFPE structure terminated on one chain by a hydroxyl end group and on the other by a cyclotriphosphazene derivative [189, 190]. It is important to know the electronic structures and chemical adsorption states for the further improvement in the tribological reliability of future HD devices; however, it was not clear how this material sticks to the diamond-like carbon (DLC) surface.

In order to clarify the adsorption states of the lubricant molecules to the DLC substrate, Ikenaga et al. conducted HAXPES investigations on the cyclotriphosphazene-terminated PFPE lubricant [191], which was synthesized and purified by the Matsumura Oil Research Co. Japan. Ltd. and was designated “A20H”. The A20H has an end-functionalized PFPE based on the “Fomblin Z-Dol” backbone (random copolymer of perfluoroethylene oxide and perfluoromethylene oxide repeat units). The “S-3500”, which is organized by only cyclotriphosphazene, was also investigated as a reference. These monomer units of chemical structure are shown in the right panel of Fig. 18.17. Monolayers of these lubricants were prepared on substrates, which were structured as 5 nm amorphous-carbon films with diamond-like carbon (DLC) on NiP (200 μm)/Al plate, using standard dip-coating techniques [192].

The C1*s* spectrum (a) of a thin A20H film in Fig. 18.17 reveals the presence of two groups of broad peaks. In the same figure, the C1*s* spectrum of (b) thin S-3500 film, (c) thin Z-Dol film and (d) the DLC substrate are shown for comparison. The dominant peak S is assigned as due to C–C bonding states of the DLC substrate, because a similar strong peak is commonly observed in all spectra including the DLC. Characteristic features, denoted 1, are observed at 286.6 eV as higher-binding energy shoulders of peaks S in spectra (a) and (b). These shoulder features 1 are

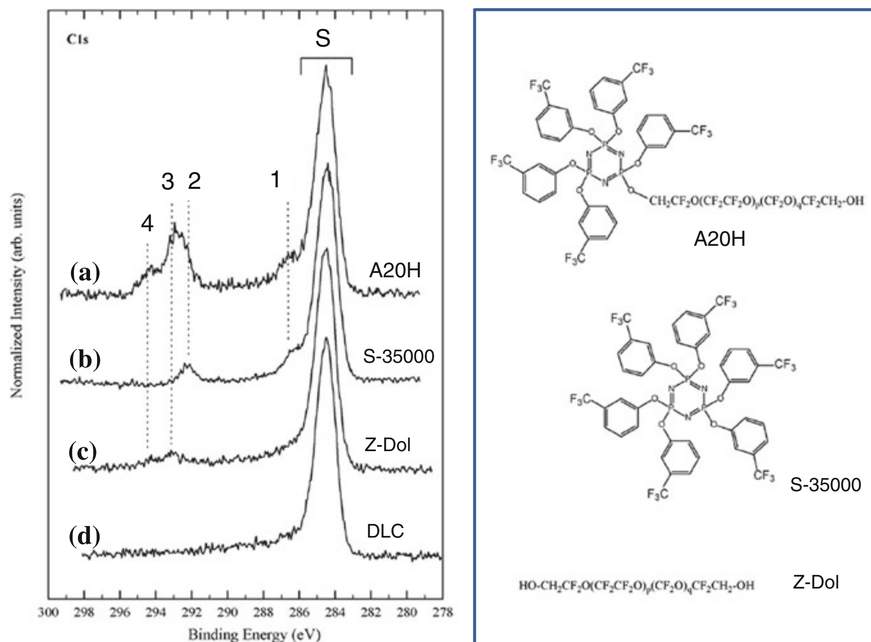

Fig. 18.17 *Left panel* Comparison of HAXPES C 1*s* spectra in thin A20H film (**a**), S-3500 (**b**), Z-Dol (**c**) and DLC (**d**). Intensities are normalized to the intensity of peaks S which originate from C–C bonding in the DLC (**d**) substrate. A Shirley background has been subtracted. *Right panel*, *top* to *bottom* Monomer units of "A20H", which is an end-functionalized PFPE based on the "Fomblin Z-Dol" backbone (random copolymer of perfluoroethylene oxide and perfluoromethylene oxide repeat units), "S-3500", which is organized by only cyclotriphosphazene, and Z-Dol

attributed to the cyclotriphosphazene group as they are not seen in Z-Dol and DLC as shown in spectra (c) and (d).

Waltman et al. [193, 194] reported a similar XPS spectrum to that of (a) in A20H/CN_x, and proposed assignments based on comparison to FTIR and SCF/3-21G[d] calculation. The peaks 3 and 4 at higher binding energies were assigned to perfluoroethylene oxide $C–F_2$ and $C–(F_2O_2)$ of the main chain. They also suggested that $C–F_3$ trifluoromethyl in the cyclotriphosphazene group component appears around these peaks, but it is not observed by HAXPES. The feature 2 is seen clearly as peaks in S-3500 whereas it appears as a shoulder in A20H spectrum. No corresponding peak is seen in Z-Dol and the DLC spectra. The peak 2 can be assigned to $C-F_3$ trifluoromethyl in the cyclotriphosphazene group, which overlaps the main chain in peak 3 in A20H. No chemical shift is observed between peak 2 of S-3500 and that of the A20H spectra, indicating that the adsorption states of the cyclotriphosphazene of S-3500 and A20H are in an equivalent environment on the DLC surface.

In order to discuss these assignments in detail, the A20H spectrum was de-convoluted by Voigt function fitting. The S components, which are assigned to

C–C bonding of the DLC substrate, were resolved into 3 components. The S-1 and S-2, which appear at 284.4 eV and at 285.2 eV, were assigned to sp^2 and sp^3 hybridized carbon atoms, respectively. The sp^2 and sp^3 components in clean DLC surfaces were reported [195–197] to appear at the same binding energies with Lorenzian-lifetime width of 215 meV. Using this lifetime value in the Voigt function fitting procedures of the A20H spectra, the resultant Gaussian width of both components are 1.06 eV, which is much larger than the instrumental broadening of 294 meV. This additional broadening is likely due to the chemical adsorption and phonon broadening. The broad S-3 peak at 286.3 eV was attributed to C–O contamination formed at the surface of samples due to air exposure.

Figure 18.18a shows take-off angle dependence of P 1*s* spectra for A20H. The most prominent feature of this figure is that the P 1*s* peak can be seen in a very narrow *TOA* region of ±8° around the surface normal as shown in Fig. 18.18b. This result provides important information on the adsorption configuration of A20H on the DLC. Each spectrum consists of two peaks at 2143.7 and 2148.6 eV, which are assigned to the P 1*s* peak of the substrate NiP and that of adsorbed cyclotriphosphazene, respectively. The P 1*s* spectrum was similar to that of S-3500, suggesting

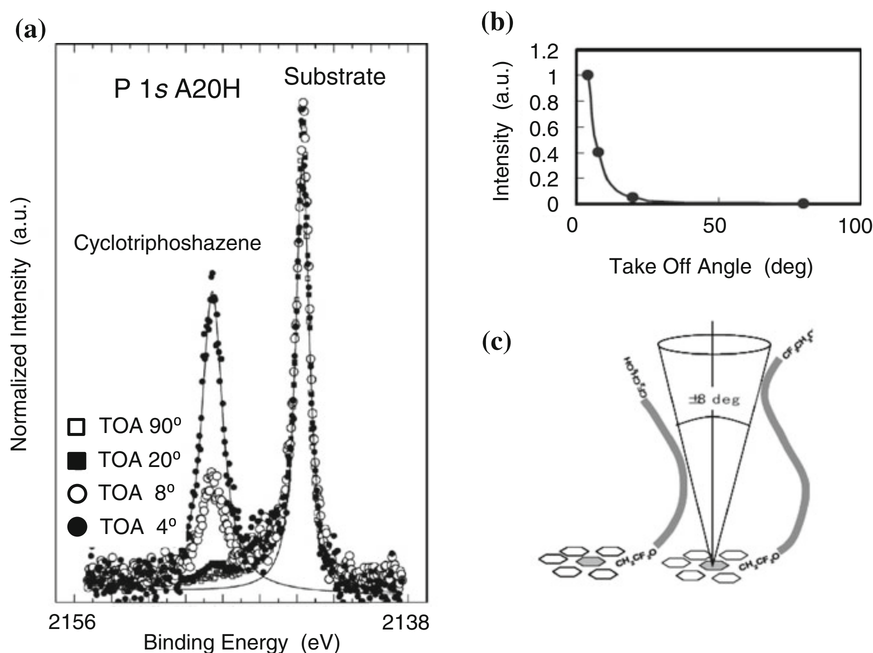

Fig. 18.18 **a** Take-off angle dependence (*TOA*) of P 1*s* spectra for A20H normalized at the P 1*s* peak from NiP. The higher binding-energy peak, which originates from cyclotriphosphazene P, shows a significant *TOA* dependence. **b** Intensity of the A20H P 1*s* plotted as function of *TOA* measured from the surface normal. **c** Model structure of A20H adsorption on the DLC surface based on the experimental results

that the configuration of the adsorbed cyclotriphosphazene-end group is similar to that in S-3500. The P 1*s* spectrum (at *TOA* of 4°) of cyclotriphosphazene is nicely fit with a single, symmetric component with broader width than that of the substrate NiP as shown in Fig. 18.18a by the solid curves. This demonstrates that three phosphorus atoms in the cyclotriphosphazene group adsorb in equivalent environments. Calculations indicate that the binding energy of N = P (N 1*s*) in cyclotriphosphazene is ~1 eV smaller than the nitrogen in the model CN_x cluster due to accumulation of excess negative charge in the ring-shaped P–N group [198]. This result provides a qualitative explanation for the additional broadening of the P 1*s* peak. Combining all of these results leads to a model of the adsorption configuration of A20H on DLC as proposed in Fig. 18.18c. Here the ring-shaped P–N group in cyclotriphosphazene preferentially lays down, and the chains which consist of copolymer of perfluoroethylene-oxide and perfluoromethylene-oxide repeated units are raised outward from the DLC surface. The chains repel each other due to their electrostatic charge, and the ring-shaped P–N group can be seen only in a very narrow angular region of ca. ±8° around the surface normal. The proposed configuration explains the high performance of A20H as a lubricant for the high-density hard disc.

18.1.8 Li Ion Batteries

Due to the incentive of reduced carbon-dioxide emissions, innovative developments in high-power battery technology are required for hybrid-electric and fuel-cell vehicles. In order to achieve the necessary high wattage, improvement of the interfaces between the electrolyte and both the positive and negative electrodes is essential. This is particularly true for the positive electrode [199]. The power-fade of lithium batteries, which is one of the most essential problems to be solved, has been found to result from the degradation of the positive electrode [199–201]. The crystal structure of $LiNiO_2$-based materials near the positive-electrode surface is changed to a cubic structure from a layered rock-salt structure, with the concomitant charge-transfer resistance increase between the positive electrode and the electrolyte.

Lithium nickel-oxide ($LiNiO_2$) based materials are one of the promising materials for high-power Li-ion cell positive electrodes due to their high power-to-energy ratio [198–202]. Nevertheless, many problems remain to be solved in order to meet the requirements necessary for advanced applications. Of particular importance is the problem of power fading, which is due to a variety of obstructing chemical reactions that occur at the interface between the electrode and electrolyte. Robust surface and interface characterization is therefore necessary to improve electrodes in the Li ion batteries [201–208].

Shikano et al. conducted HAXPES ex situ investigations of the changes in positive electrodes and their interfaces during the standard cycle tests (modified) in real Li-ion battery cells at BL47XU in SPring-8 [209]. Cylindrical cells with a

capacity of ca. 420 mAh were used in the study. The positive electrodes consisted of a mixture of $LiNi_{0.73}Co_{0.17}Al_{0.10}O_2$ (LMO), acetylene black (AB), and polyvinylidene fluoride (PVDF) as active material, conductive material and binder, respectively, and the negative electrode was comprised of non-graphitizable carbon (hard carbon) and a PVDF binder. Each cell was characterized using a modified version of the cycle-test procedure in the PNGV Battery Test Manual [200, 206, 207]. Details of cell chemistry and characterization are described elsewhere [200]. Positive electrodes were removed from cells under state-of-charge (SOC) control before and after cycle testing, and they were washed with dimethyl carbonate and dried under vacuum at room temperature for more than 10 h. The surface species present were characterized by XPS (JEOL JPS-9010MX spectrometer using MgK_α radiation) and HAXPES ($h\nu$ = 8 keV) at BL47XU of SPring-8.

Figure 18.19 shows typical HAXPES (O 1*s*) spectra for the LiNiCoO-based positive electrode before the cycle test. The two peaks in the O 1 *s* spectra at 529.3 and 531.3 eV correspond to LMO and Li_2CO_3, respectively [210–212]. Peaks at 532.9 and 534.5 eV can be assigned to $ROCO_2Li$ and a polycarbonate-type compound [211–218]. The other two higher binding-energy components, which manifest in the 0 % SOC with higher *TOA* of 60° (higher surface sensitivity), are assigned to oxygen in carbonyl and alkyl carbonate bonding. The result clearly shows that the carbonyl and alkyl carbonate are abundant near the positive electrode surface, and the amount of Li_2CO_3 on the surface clearly decreases with increasing SOC.

Bulk sensitive (*TOA* = 10°) HAXPES C 1*s* and O 1*s* spectra from a positive electrode from a cell before and after cycle tests are shown in Fig. 18.20. SOC was kept at 0 % to assure that the charge–discharge effect is negligible. After the tests at 40, 60 and 80 °C, the relative capacities were decreased to 99.7, 95.0 and 81.2 %, and the relative dc resistances were increased to 1.1, 1.3 and 1.8, respectively [199, 200]. The strong peak at 284.3 eV in the C 1*s* spectra (Fig. 18.20a) was assigned to AB (acetylene black). The intensities of all spectra are normalized to this peak.

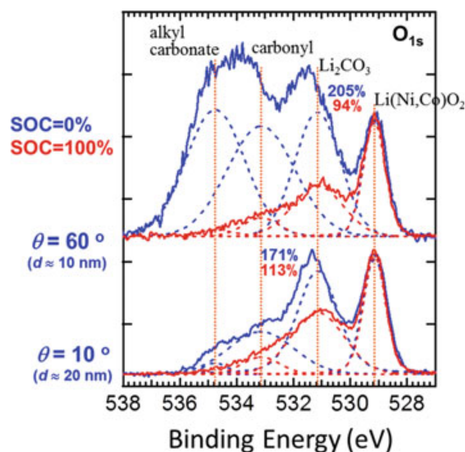

Fig. 18.19 HAXPES O 1*s* spectra for LiNiCoO-based positive electrode before the cycle test. Spectra with different SOC and *TOA* (measured from surface normal) are compared

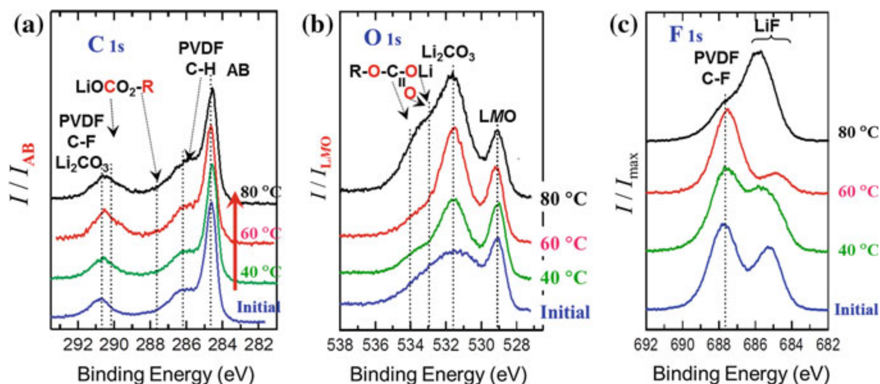

Fig. 18.20 HAXPES (θ = 10°) spectra of a positive electrode from a cell before and after cycle tests at 40, 60 and 80 °C: **a** C 1*s*, **b** O 1*s* and **c** F 1*s* core levels. SOC was kept at 0 %

Peaks at 286.5 and 290.4 eV are assigned to C–H and C–F of PVDF, respectively [212, 214, 215]. The other peaks are assigned to Li_2CO_3 and organic species, such as hydrocarbons, $ROCO_2Li$ and polycarbonate-type compounds. Bulk sensitive HAXPES (*TOA* = 10°) C 1*s* data indicated that the hydrocarbon signal was not significant, indicating that hydrocarbons are present only on the surface of the positive electrode.

Figure 18.20b shows O 1*s* HAXPES spectra. Only Li_2CO_3 increases after the test at 40 °C. It significantly increases at 60 °C, whereas increases in $ROCO_2Li$ and polycarbonate-type compounds are still slight at this temperature. The signals from all carbonates, such as Li_2CO_3, $ROCO_2Li$, and polycarbonate-type compounds, become distinguishable after the 80 °C cycle test, indicating that the electrolyte decomposition took place during testing above 60 °C. The highly resistive Li_2CO_3 forming reaction causes a decrease of the Li supply. Consequently, the increase of Li_2CO_3 should relate to both power and capacity fades. The electrolyte (mixture of $LiPF_6$ in propylene carbonate and dimethyl carbonate) decomposition also induces power fade due to the high resistivity of the organic products.

HAXPES F 1 *s* spectra of the positive electrode with SOC of 0 % after the cycle test exhibited peaks at 687.3 and 684.6 eV as shown in Fig. 18.20c. The 687.3 eV peak was assigned to come from PVDF. The 684.6 eV peak was identified to come from LiF, evidencing formation of LiF on the positive electrode.

Ni $2p_{3/2}$ spectra give information about changes in the valence state of Ni at the surface of LiNiCoO-based positive electrode. Almost all reported Ni $2p_{3/2}$ core-level XPS spectra after Ar sputtering are very similar to the NiO spectrum [216], which means that the surface of LMO is easily reduced under vacuum and changes to a NiO-like structure. Without sputtering, Ni $2p_{3/2}$ XPS spectra, which were decomposed into 854.5, 856.0, 860.6 and 863.0 eV peaks, (not shown here) exhibited different shapes from those of NiO [216] and $LiNiO_2$ [217], while the binding energies of the peaks were very close to those of NiO [216]. Abraham et al. suggested the thickness of a NiO-like film on the electrode surface to be around

2–4 nm [214]. In the bulk sensitive HAXPES spectra, the component due to the NiO-like structure is minor, because its thickness is much smaller than the HAXPES probing depth. Figure 18.21a shows bulk sensitive HAXPES Ni $2p_{3/2}$ spectra of the positive electrode before the cycle test. Two components at 855.2 and 855.8 eV are recognizable in the Ni $2p_{3/2}$ HAXPES spectra, with a broader satellite at ca. 6 eV higher binding energy. The intensity ratio of the peaks at 855.8 and 855.2 eV seems to vary corresponding to changes in SOC. The FWHM of the peak at 855.8 eV is also apparently dependent on SOC. This might be due to an overlap with $Ni^{3+/4+}$ in the intermediate state at the surface of the positive electrode. If the NiO-like structure is the same as $Ni^{2+}O$, the NiO feature should appear independent of SOC; however, this is not the case. The peak at 855.2 eV was assigned to come from a Li-deficient cubic phase, namely $Li_{0.5-x}(Ni,Co,Al)_{0.5}O$, which was considered to exist between the surface and the LMO layer. The 855.8 eV peaks were assigned as overlap of $Ni^{3+/4+}$ in LMO and in the intermediate state of LMO and the Li-deficient cubic phase. This assignment is consistent with the fact that the 855.8 eV peak is stronger in the case of SOC = 100 % than in the case of SOC = 0 %. Figure 18.21b shows superposition of the bulk sensitive HAXPES Ni $2p_{3/2}$ spectra of the positive electrode for all samples, before and after the cycle tests at 40 and 60 °C with SOC of 0 and 100 %. The spectra of both SOC equal 0 and 100 % coincide well regardless of whether or not the cycle test had been performed, and also regardless of the temperature of the test. This result clearly shows that the valence state of Ni, even after the cycle test at 40 and 60 °C, was the same as that before the test. These results agree with Ni *K*-edge XANES results showing that the

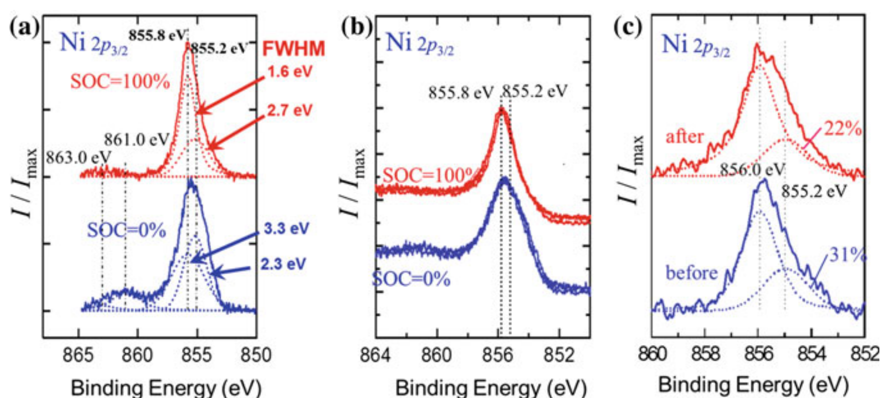

Fig. 18.21 **a** Ni $2p_{3/2}$ core-level HAXPES spectra at the surface of $LiNi_{0.8}Co_{0.2}O_2$-based positive electrode before cycle test for *TOA* = 10°. **b** Superposition of bulk sensitive Ni $2p_{3/2}$ core-level spectra of the positive electrode from a cell before and after cycle testing at 40 and 60 °C. SOC was kept at 0 and 100 %. The spectra of both SOC equal 0 and 100 % coincide well regardless of whether or not the cycle test had been performed and also regardless of the temperature of the test. **c** Ni $2p_{3/2}$ core-level HAXPES spectra of $LiNi_{0.8}Co_{0.2}O_2$-based positive electrode after the cycle test (60 °C) for *TOA* = 60°)

Ni ions in the bulk of the electrodes are not disturbed by cycle testing [200]. On the other hand, surface sensitive HAXPES spectra (*TOA* = 60°) indicated that the valence state of Ni after the cycle test is slightly higher than before the test as shown in Fig. 18.21c. This result also agrees with the surface sensitive TEY (total electron yield) XANES data indicating that not NiO but rather a Li-deficient cubic phase was formed around the surface of the positive electrode.

Based on the above analyses, a model of the surface of the positive electrode can be made. A Li-deficient cubic phase, namely $Li_{0.5-x}(Ni,Co,Al)_{0.5}O$, is changing its Li deficiency x continuously from the surface to the bulk of the positive electrode. Carbonates and LiF exist on the surface. The compositional slope between the Li-deficient cubic phase and LMO is steep in the case of 0 % SOC, resulting in greater inhomogeneous broadening of the corresponding component in the Ni 2*p* core line. Near the surface, Ni ions in the Li-deficient cubic phase remain in the same environment, thus their FWHM is independent of SOC. After the cycle tests, the Li deficiency develops near the surface region corresponding to the capacity fade. On the other hand, the valence state of Ni ions in the bulk remains in the same condition after testing. Li conductivity in the Li-deficient cubic phase is considered to be lower than that of LMO, which is caused by the random occupation of the same site by Li ions, transition-metal ions, and vacancies in the cubic phase. The thickness of the Li-deficient cubic phase therefore should be related to the power fade of the cells.

In conclusion, the large probing depth of HAXPES clarified the mechanism of the capacity and power fade in a Li-ion battery. The investigations revealed that the amount of carbonates increased after cycle testing. Decomposition of electrolyte was detected at temperatures above 60 °C. Growth of the Li-deficient cubic phase near the surface of the positive electrode with circle test was observed. Capacity and power fade can be related to the amount of species such as carbonates and LiF on the surface and to the thickness of the Li-deficient cubic phase near the surface.

18.2 Operando Observations for Advanced Materials by HAXPES

In the developments of advanced devices, it is essential to gain a comprehensive understanding of the evolution of chemical state and electronic structure in the functional layers and interfaces of a device during actual operation. The necessity for spectroscopic methods capable of these operando observations is therefore a driving focus of research. The large probing depth of HAXPES provides opportunity to monitor the electronic and chemical variations in the target layers beneath thin electrodes of ~10 nm thickness under applied voltage, opening new applications of photoelectron spectroscopy to the study of electronic and chemical devices. Here several examples are discussed that demonstrate the potential of HAXPES.

18.2.1 Detection of Interface States in MOS Structures

Control of interface state density in individual MOS transistors has been one of the most essential challenges to reduce the dispersion of threshold voltages in large-scale integration (LSI). As the downsizing of MOS transistors proceeded, gate insulator thickness has decreased to a few nm [219]. The high-k gate-stack structures with materials of high dielectric constant (k) composed of metal/high-k/ultra-thin-oxide/semiconductor substrate, have been introduced to reduce the leakage current due to the material limit of SiO_2. However, evaluation of the interface states by standard CV measurements at the ultra-thin-oxide/Si interface in the high-k gate stack structure becomes difficult due to the tunneling current flowing through the thin oxide layer which disturbs the electrical measurements [215, 219, 220].

In order to demonstrate that HAXPES can solve this problem, operando observation of Si MOS structures under applied electric field have been conducted in order to measure interface states using a laboratory HAXPES system with monochromatic Cr K_α (5.4 keV) X-rays as the excitation source [7, 221]. Description of the system is given in the last section of this chapter. MOS samples, with structures as shown in the insert of Fig. 18.22c, were fabricated 3.9/5.6 nm thermal SiO_2 and top 10 nm Au electrode on a p-type substrate at Toray Research Center [222].

Au $3d_{5/2}$ and Si $1s$ spectra were recorded while increasing the applied voltage between the top and bottom electrodes at 50 mV steps while keeping the top electrode grounded. The data are plotted in Fig. 18.22a, b with the applied voltage taken as the vertical axis. The Au $3d_{5/2}$ peak from the top Au electrode shifts linearly with the bias voltage V. On the other hand, the two Si $1s$ peaks, originating from the substrate Si and SiO_2, exhibit nonlinear behavior. The nonlinear shift is attributed to the Fermi-level pinning at the interface states until they are filled.

Replacing the carrier distribution function as unity (low temperature approximation), the density of interface states under bias application is expressed as

$$\begin{aligned} D_{it}(E_F^f) &= (\varepsilon_{ox}/de)(\mathrm{d}\Delta V_{ox}/\mathrm{d}E) \\ &= (\varepsilon_{ox}/de)(\mathrm{d}\Delta V_{ox}/\mathrm{d}V)\{1/(1-(\mathrm{d}\Delta V_{ox}/\mathrm{d}V))\} \end{aligned} \quad (18.2)$$

where E_F^f is the Fermi-level position measured from the metal electrode Fermi level under the bias V, ΔV_{ox} is the potential difference across the SiO_2 layer, $\varepsilon_{\mathrm{ox}}$ is the dielectric constant of SiO_2, and d is the SiO_2 thickness. The ΔV_{ox} can be derived from the difference in energy positions between the Au $3d_{5/2}$ and substrate Si $1s$ peaks as a function of V. Taking the derivative of the $\Delta V_{\mathrm{ox}} - V$ curve in Fig. 18.22c, interface-state distribution curves were determined from (18.2) for two MOS samples with different SiO_2 thicknesses as shown in Fig. 18.22d. Three interface states are recognized in the band-gap region of Si independent of the SiO_2 thickness, as denoted by arrows in the figure.

Similar experiments were also performed using the NIMS undulator beamline BL15XU at SPring-8 by Yamashita et al. for Ru/SiON/Si(100) structures with

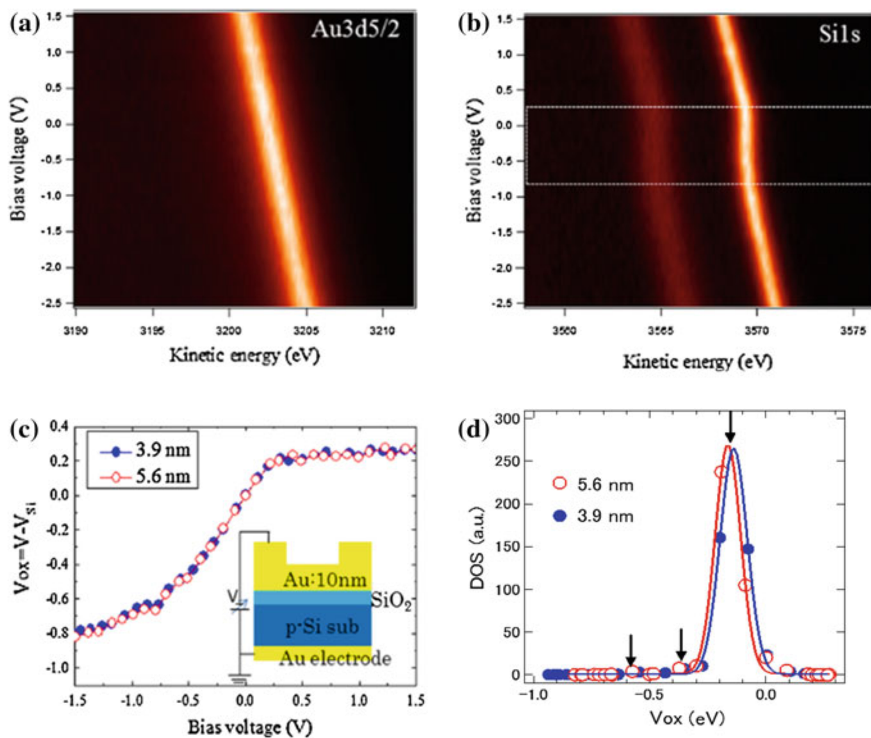

Fig. 18.22 **a** and **b** Bias dependence of Au $3d_{5/2}$ and Si 1*s* spectra in an Au (10 nm)/SiO_2 (3.9 nm)/p-Si(0 0 1)MOS structure. The Si 1*s* core line from both the SiO_2 (low kinetic energy) and Si substrate (high kinetic energy) show a nonlinearity with bias voltage in (**b**). **c** Bias dependence of voltage across the SiO_2 layer, which can be derived from the shifts of the Au $3d_{5/2}$ and Si 1*s* peaks. The *inset* shows a schematic of the sample structure. **d** Interface-state densities derived from (18.2) for two samples with SiO_2 thicknesses of 3.9 nm (*solid circles*) and 5.6 nm (*open circles*), respectively

different N concentrations [223]. A similar interface-state peak near the center of the band gap was observed. They also observed two additional interface states at higher and lower binding energies relative to the dangling-bond state. The intensities of these states increased with nitrogen concentration. The interface states near the mid gap were attributed to isolated Si dangling bonds, whereas the interface states near the VBM and CBM were identified to be due to weakened bonding, and anti-bonding Si–O and/or Si–Si states, respectively. It should be noted that N related in-gap states are not formed in the Si band gap according to theoretical calculation [224].

18.2.2 Electrochemical Reactions at Solid-Solid Interfaces

For the development of advanced semiconductor devices and solid-state batteries, ion migration phenomenon in oxide thin films has become an important problem. It

is a key issue for understanding the mechanisms of the elementary electrochemical processes involved in the metal-oxide semiconductor interface. In the oxide-metal junction systems, not only the electrochemical reactions of oxygen ions and host cations in oxide thin films, but also dissolutions and migrations of hetero-cations, such as copper and silver ions introduced by reversible electrochemical reaction of electrodes, as well as protons incorporated by hydration, are now recognized to play important roles in time-dependent dielectric breakdown (TDDB) of interconnect materials [225–228] and mechanisms of resistance random access memory (ReRAM) [229–231], an atomic switch [232–236], and other nano electronics devices. Among these, efforts have been dedicated to the research and development of ReRAM devices [237–241], which utilize reversible electric-field induced resistance switching behavior in meta-oxide-metal sandwich structures.

HfO_2, which is used as a high-*k* gate insulator for advanced complementary metal-oxide-semiconductor (CMOS) technology [241, 242], was found to exhibit resistance switching phenomena [239, 240]. Two mechanisms have been proposed to explain this: the filament model and oxygen vacancy nucleation [238–246]. Nagata et al. have conducted HAXPES operando observations of changes in the composition and electronic states at the interfaces of Pt/HfO_2/Pt (metal–oxide–metal) devices [247]. The sample studied has a 100-nm-thick Pt bottom-electrode layer deposited on an insulating *c*-plane sapphire substrate. A 30-nm-thick HfO_2 layer was then deposited on the Pt bottom electrode. Patterned 10 nm thick Pt top electrodes were deposited on the HfO_2 film. The measurement setup is shown in Fig. 18.23a. The dc bias voltages were applied to the sample with a voltage current source/monitor through Au wires fixed to the top and the bottom electrodes. HAXPES measurements were conducted at the SPring-8 BL15XU with incident X-ray energy of 5.95 keV and a total energy resolution of 240 meV.

Current-voltage characteristic (Fig. 18.23b) of the device in the early stage of the ReRAM actions already exhibits weak nonlinearity. Figure 18.23c shows O 1*s* spectra taken at several *TOA*'s (measured from the sample surface) to obtain initial compositional depth information at 0 V. Steep inclined backgrounds are due to the superposition of the high binding-energy tail of the Pt $4p_{3/2}$ states. The peak around 530.5 eV, which is attributable to O–Hf bonding [248], is most prominent at *TOA* of 85° (large probing depth). As the *TOA* is decreased (smaller probing depth), the intensity of the O–Hf peak decreases whereas a peak around 532.8 eV grows [249]. The latter peak is attributed to O–Pt bonding, indicating existence of PtO at the interface and/or surface. When the thickness of the Pt layer increased, the O–Pt peak intensity decreased, suggesting that PtO is predominantly formed at the interface.

Voltage application causes a clear difference in the O–Pt and O–Hf components of O 1*s* spectra at a *TOA* of 20° (low bulk sensitivity) as shown in Fig. 18.23d. The O–Pt peak increased, whereas the O–Hf peak decreased at an applied voltage of 150 mV, where the current was 15 mA, indicating that the Pt interface layer was oxidized and oxygen vacancies were formed in the HfO_2 layer. When the bias was reversed, the O–Pt peak became more pronounced than when under a forward bias,

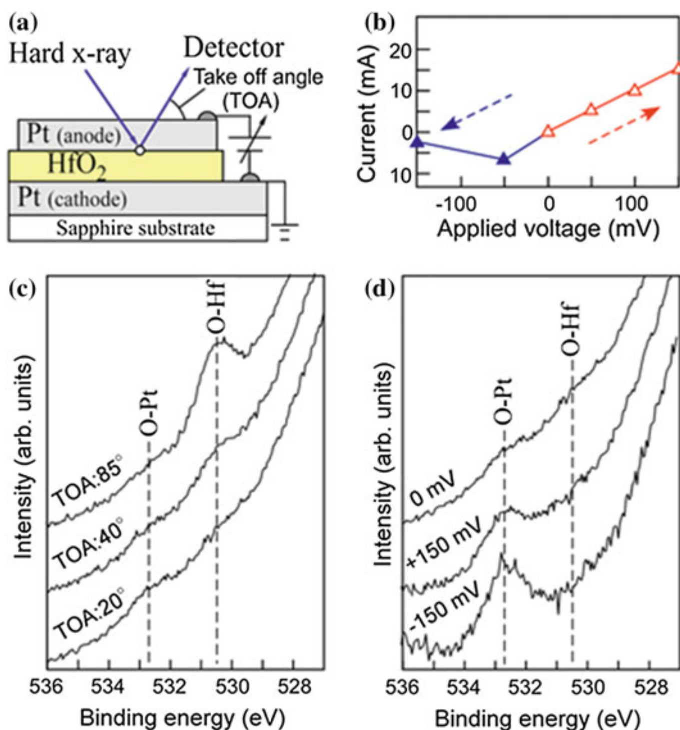

Fig. 18.23 **a** Schematic illustration of the measurement. **b** *I-V* property for Pt film on HfO_2 film. *Open symbols* show forward bias conditions and *solid symbols* show reverse bias conditions. **c** HAXPES of O 1*s* as a function of *TOA* under zero bias, and **d** as a function of bias at a *TOA* of 20°

suggesting that an additional PtO layer was formed at the interface by the reversed bias application to the PtO layer formed by the first bias application.

After background removal by the Shirley function [21], Pt 4*f* and Hf $3d_{5/2}$ peaks were fitted by Voigt functions with Doniach and Šunjić electron-hole pair creation losses [250]. Figure 18.24 shows Pt 4*f* and Hf $3d_{5/2}$ spectra at a *TOA* of 20° under a bias of −150 mV. Weak components in the Pt 4*f* spectrum, which peak at 72.2 and 75.5 eV and are attributed to PtO [23], appear in addition to the main peaks that are due to the metallic Pt at 71.0 and 74.3 eV. The Pt 4*f* and Hf $3d_{5/2}$ HAXPES spectra were found to be dependent on the applied voltage. As the forward bias is increased, the Pt–O intensity increases as shown in Fig. 18.25a, indicating that the forward bias voltage drives oxygen toward the anode and induces Pt oxidization, in spite of the higher energy required to oxidize Pt compared to Hf [251, 252]. Upon removal of the forward bias, the Pt–O intensity recovers slightly, but it still remains at higher intensity than its initial intensity at zero bias. This result indicates that Pt–O bonding remains at the interface after removal of the bias voltage.

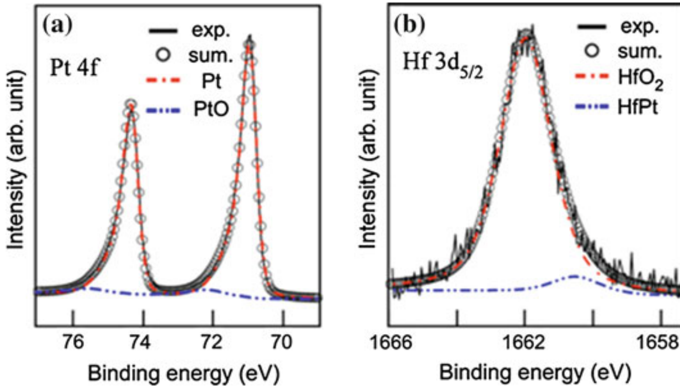

Fig. 18.24 HAXPES of **a** Pt 4*f* and **b** Hf $3d_{5/2}$ for the Pt/HfO_2/Pt diode under a reverse bias of −150 mV at a *TOA* of 20°. *Solid lines* show observed spectra. *Open circles* are curve fit results. *Dashed curves* show deconvoluted components corresponding to bonding of Pt, PtO, HfO_2, and HfPt

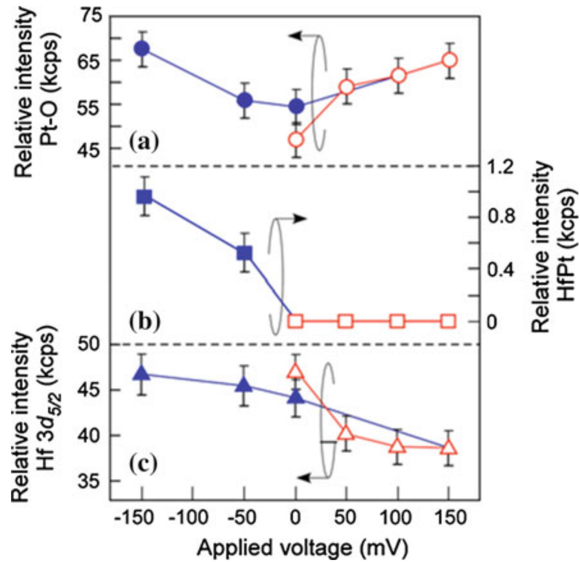

Fig. 18.25 Applied bias dependences of **a** Pt 4*f* normalized intensity of PtO (*circles*), **b** Hf $3d_{5/2}$ intensity ratio of HfPt (*squares*), and **c** normalized intensity of Hf $3d_{5/2}$ (*triangles*). Spectra have been normalized with respect to the Pt 4*f* intensity of Pt at 0 V (initial state). *Open symbols* show forward-bias conditions and *solid symbols* show reverse-bias conditions

In Fig. 18.24b, the Hf $3d_{5/2}$ peak at 1662.0 eV corresponds to HfO_2 [2]. When the bias is inverted, an additional peak, which is assigned to the Hf–Pt bonds, appears at the lower binding-energy position. The Hf–Pt intensity shows a monotonic increase under the reversed bias as shown in Fig. 18.25b. To examine the bias-induced variation in the Hf density at the interface, the Hf $3d_{5/2}$/Pt $4f_{7/2}$ elemental intensity ratio at *TOA* = 20° was plotted as a function of the bias voltage in

Fig. 18.25c. The ratio decreases with increasing forward bias, and increases with increasing negative reverse bias reverting to the initial intensity ratio at −150 mV. This indicates that the biases drive the Hf atoms along the field direction. The Hf drawing toward the anode is accompanied with Pt oxidization as evidenced by the Pt–O intensity increase in Fig. 18.25a. This further suggests that the diffusion of Hf into the Pt anode produces a Pt–Hf mixed oxide and stabilized oxygen atoms in the negatively biased anode. This result is consistent with the observation of Matolin et al. that the rare-earth transition metal affected the valence of Pt to form the Pt–rare earth–O bonding [190].

Based upon the above results, changes in the Pt/HfO_2/Pt sandwich structure under positive and inverted biases are described as follows: the application of a forward bias diffuses oxygen into the Pt layer, thus forming PtO. When the bias is reversed, the PtO layer remains at the interface. Hf moves to the interface, leaving O vacancies and forming Pt–Hf bonds in the interface region. The O vacancies percolate to form conduction filaments in a high electric field during ReRAM actions [234, 244, 245]. This O-vacancy formation is also consistent with the report on electrical properties, in which the O vacancies act as trap centers for charge carriers causing deterioration in the metal/HfO_2 interface during CMOS application [253, 254]. The most important finding of this study, however, is that detectable O migration already begins at lower bias voltages than the threshold.

Similar operando HAXPES experiments and analysis have been conducted in a Cu/HfO_2/Pt ReRAM device by Nagata et al. [255]. A different relationship between the interface structures and the chemical states in the Cu/HfO_2/Pt system from that obtained at the Pt/HfO_2/Pt system was elucidated. The application of a bias reduces the interfacial natural oxide (Cu_2O) layer, contrary to the Pt/HfO_2 case where the oxidization of the Pt layer occurs. The reduction is caused by the lower standard reduction potential of Cu ions ($Cu^+ + e^- \rightarrow Cu + 0.52$ V) than Pt ions ($Pt^{2t} + 2e^- \rightarrow Pt + 1.19$ V) [256]. Cu diffuses into HfO_2 more easily than Pt [257] thus forming Cu–Hf–O, segregating into Cu filaments in the HfO_2 layer during bias application.

When the partial conductivity of ions is not negligible, the charge and potential distributions drastically change from those in ordinary semiconductors under the application of an external field. The development of the electrochemical polarization by the ion migration results in the variation of the chemical potential of electrons $\mu_{e'}$ which corresponds to the variation of redox states near the cathode and anode due to charge/discharge of ions as discussed by Tsuchiya et al. [258]. If only the oxide ions (O^{2-}) migrated, the redox state is simply related to the variation of oxygen non stoichiometry. On the other hand, when migration of foreign cations is not negligible, the increase/decrease in the concentration corresponds to the reduction/oxidation of the oxide thin film. The ion migration gives rise to the electrochemical polarization, and the Fermi energy (E_F) shifts toward the conduction band (CB) or to the valence band (VB) corresponding to the oxidation or reduction of the film, respectively. The redox window is defined as a range of E_F variation between the two extreme limits of reduction and oxidation. Pinning of E_F is caused by static chemical origins, such as the presence of a large density of state

(DOS) due to donor and acceptor levels, which buffer the charge-transfer reaction by chemical redox reactions, such as $Mn^{+} + e \rightarrow M^{(n-1)+}$ for the donor formation and $O^{2} + h^{+} \rightarrow O^{-}$ for the acceptor formation. Chemical buffer reactions such as oxygen gas evolution and metal precipitation also contribute to the E_F pinning. In addition, kinetic origins such as depletion of ionic carriers or the irreversibility of the electrode reaction between gaseous species and component ions eventually limit the redox state. The electrical-potential gradient induced by an applied voltage across the film is greatly reduced and severe band bending results due to E_F variation in the redox window. These strongly affect the charge transport across the film as well as the electrochemical processes at the electrode/oxide interface.

Direct observation of the above phenomena was demonstrated by Tsuchiya et al. who studied the reduction/oxidation (redox) state in an oxide electrolyte film at a hetero-interface in a carbon/amorphous tantalum oxide (a-TaO_x) electrochemical cell using in situ HAXPES under applied dc bias voltage [258]. They found a surprising result that even chemically stable a-TaO_x can be electrochemically polarized. The reduction limit observed in unintentionally proton doped samples was found to be due to pinning of the Fermi level in an in-gap donor state. It was also found that a-TaO_x showed an asymmetric shift of core levels with respect to the applied bias that is not expected when the migration of intrinsic ions such as Ta^{5+} or O^{2-} is dominant.

In order to verify the role of polarization by protons as a migrating mediator, these authors examined a heavily hydrated a-TaO_x thin film with 14.7 at.% of protons (measured by RBS) by in situ HAXPES. The hydrated film exhibited the same behavior as the unintentionally hydrated film under the cathodic polarization (reducing direction). An expansion of the redox window to the oxidation side when compared to the unintentionally hydrated a-TaO_x case which reached up to 2.4 eV was clearly observed. This drastic change in the oxidation side demonstrated the increased de-protonation capacity due to an increase of proton concentration near the working electrode. However, the observed redox-window width of $\sim$2.4 eV was much smaller than the estimated band gap of 3.9 eV [259], suggesting that the E_F pinning level was located near the middle of the bang gap due to the Ta^{4+} donor state.

Since the electrochemical properties determine the dielectric properties as well as the electronic breakdown in the MIM-type cell, the above result must be accounted for in order to understand the charge-transfer reaction at the metal/oxide hetero-interface. In addition, the results clearly demonstrated the possibility of designing various chemical functionalities by controlling the density of protons or other mobile ions as a mediator to the redox modulation. These findings, which were obtained owing to the large probing depth of HAXPES, are important contributions to the research and development of materials and devices such as batteries, solid catalysts, and other electrochemical cells, and ReRAM and other nano-electronic devices.

18.2.3 Liquid-Solid Interfaces

Understand liquid-solid interfaces [260] at the atomic level is crucial for improving the performance of advanced energy-conversion devices such as fuel cells, Li air batteries, dye-sensitized solar cells, and photocatalysts. Observation of electrochemical processes at solid-liquid interfaces, however, faces the difficulty of preparing the liquid-layer/solid-electrode interface that photoelectrons can penetrate without inelastic scattering.

T. Masuda et al. have reported in situ photoelectron spectroscopy of an electrochemical reaction at a solid-liquid interface using hard X-rays (5950.1 eV) and a micro-volume cell having a window with an ultra-thin Si membrane through which the photoelectrons can escape from the cell [261]. This is the first trial for the "real" photoelectron spectroscopy, except XPS on non-volatile ionic liquids as the electrolyte solution [262–264]. A micro-volume cell filled with a liquid is sealed by a 15 nm thick Si membrane, which serves as a separator between vacuum and ambient, a window for X-rays and photoelectrons, and a working electrode. X-rays penetrate to the solution through the membrane, and about 14 % of the photoelectrons emitted from Si exposed to the solution; i.e., at the solid-liquid interface, are estimated from the IMFP of 7.5 nm to penetrate or escape the Si membrane without losing their kinetic energy [179–181].

After the surface of the Si membrane was made hydrophilic by plasma-ion treatment, a droplet of purified water was placed on the membrane and sealed by conductive Cu tape. A Au wire was fixed on the Si-membrane frame to make contact to the potentiostat for biasing the Si membrane to the Cu tape. Measurements were carried out with an incident X-ray energy of 5950.1 eV with high-photon flux of $\sim 10^{11}$ photons/s and incident angle from the membrane surface of 4° at the beamline BL15XU at SPring-8. *I-V* curves of the micro-volume cell with and without water (red) inside were measured by the two-terminal method. Anodic current started to increase from about 0.8 V when the cell was filled by water, whereas no detectable current was observed even under greater positive potential without water, showing that the Si and Cu film were insulated from each other by the adhesive of the Cu tape.

Figure 18.26a shows Si $2p$ photoelectron spectra, which were normalized at the Si $2p_{1/2}$ peak, at various potentials. A broad peak due to native oxide was observed around 104.5 eV in the spectrum without potential application. The oxide peak intensity monotonically increases with the increasing positive potential. After the measurement of spectrum (g), synchrotron radiation (SR) was turned off and the potential was kept at 1500 mV during the collection of spectrum (h). The largest growth of Si oxide was observed in this period between (g) and (h). These results evidence that Si oxide grows by electrochemical oxidation at the Si membrane-water interface, giving evidence against the SR-induced etching [265] and reduction of Si oxide [266].

Figure 18.26b, c schematically show the electrochemical oxidation at the Si membrane. Before the oxidation (b), a cross section of the 15 nm thick Si

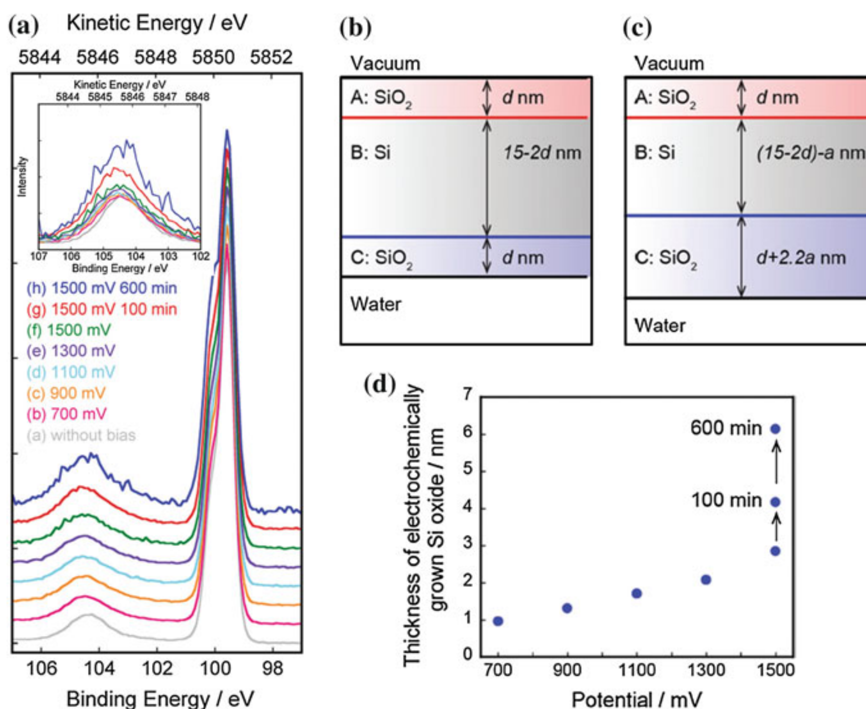

Fig. 18.26 **a** Si $2p_{3/2}$ HAXPES spectra of the Si membrane measured without bias, and at 700, 900, 1100, 1300, 1500 mV, and after keeping the potential at 1500 mV for 100 and 600 min. The *inset* shows the spectra plotted on the same scale in the region between 107 and 102 eV. **b** Models of the Si membrane **a** before and **b** after the oxidation. **c** Thickness of electrochemically grown Si oxide derived from the data

membrane is modeled by three layers based on the assumption that both the vacuum and solution sides are covered by native-oxide layers with a thickness of d nm. When the Si membrane is positively biased (Fig. 18.26c), the thickness of Si layer (B) is decreased by a nm. The Si-oxide layer thickness (C) is increased by $2.2a$ nm due to the lower Si density in SiO_2 than in Si [267]. The photoelectron intensity ratio, $I(SiO_2)/I(Si)$, can be calculated based on a uniform layer model using the inelastic mean free paths of the Si $2p$ photoelectrons for Si oxide and Si estimated by TPP-2M formula [179–181]. Fitting the calculated values of $I(SiO_2)/I(Si)$ to the experimental values, the thickness of electrochemically grown Si oxide can be quantitatively determined, as shown in Fig. 18.26d.

The large probing depth of HAXPES has opened a new opportunity for the studies of gas-solid and liquid-solid interfaces as exemplified above. A flow-type cell which enables injection of additional reactants from outside of the vacuum apparatus will be realized, and other measurement techniques such as optical absorption, ellipsometry, and Raman scattering will be integrated into the cell to monitor the progress of the electrochemical reaction. However, improvements in

cell structures, including designs to prevent damage to the vacuum system and beamline in the event of damage to the cell, are needed to widen the variety of applications.

18.3 Lab HAXPES Development and Applications

Various hindrances including the low selection rate due to excessive demand and the general paucity of SR beamtime, the impossibility of prompt turnaround times, and the cost of travelling often make HAXPES at SR sources not practical for many would-be general users, especially those who are non-experts in the field. Development of laboratory based HAXPES systems with practical throughput, good energy resolution, and quick turn-around times is therefore extremely desirable to encourage research in a wide field of disciplines covering both academic, industrial, and government needs. It would also possibly relieve specific beamline restrictions for the general user such as the control of toxic and/or radioactive materials.

A laboratory HAXPES system, High Energy Angle Resolved X-ray Photoelectron Spectrometer for Laboratory (HEARP Lab) [7, 221], has been developed using monochromatic Cr K_{α} X-ray excitation (5.4 keV). It has been demonstrated to be not only complementary to the SR beamline HAXPES, but it also has been found indispensable for advanced research and development from the basic to the industrial sciences and technology [7]. As shown in Fig. 18.27a, the system is composed of a compact monochromatic Cr K_{α} X-ray source (b), and a high-energy, high-resolution hemispherical electron analyzer that has been coupled with a wide angular acceptance resolving objective lens (c) with a mesh electrode (d) [7, 221]. A thorough description of the system and its performance has been reported with a variety of applications, including bulk-sensitive valence-band and core-level spectroscopy of advanced materials [7], overlayers-thickness determination in the thickness range of up to 25 nm, and investigation of buried layers in MOS structures with thickness-graded SiO_2 interlayers [268].

Application to the interface in-gap state spectroscopy of MOS structures by electric-field application is also described in the preceding section of this chapter [7]. Here its application to bulk sensitive X-ray photoelectron diffraction [269], surface polarity determinations of ZnO single- as well as poly-crystalline films, [270] environmental cell developments [7], are demonstrated.

X-ray photoelectron diffraction (XPD) using a conventional XPS apparatus has been a useful tool as a surface sensitive probe for local atomic structure, atomic positions of adsorbates and overlayer growth, specifying both elemental and chemical states. The larger probing depth of the hard X-ray excited XPD (HAXPD) makes it possible to investigate the local structure of bulk materials. Piš et al. have reported the successful application of the HEARP Lab system to the observation of XPD patterns for H-terminated Si(001) and SiO_2/Si(001) with different SiO_2 layer thicknesses [269]. This technique can be applied to site determination of doped impurity atoms as already reported for GaAs:Mn by beamline HAXPES [271].

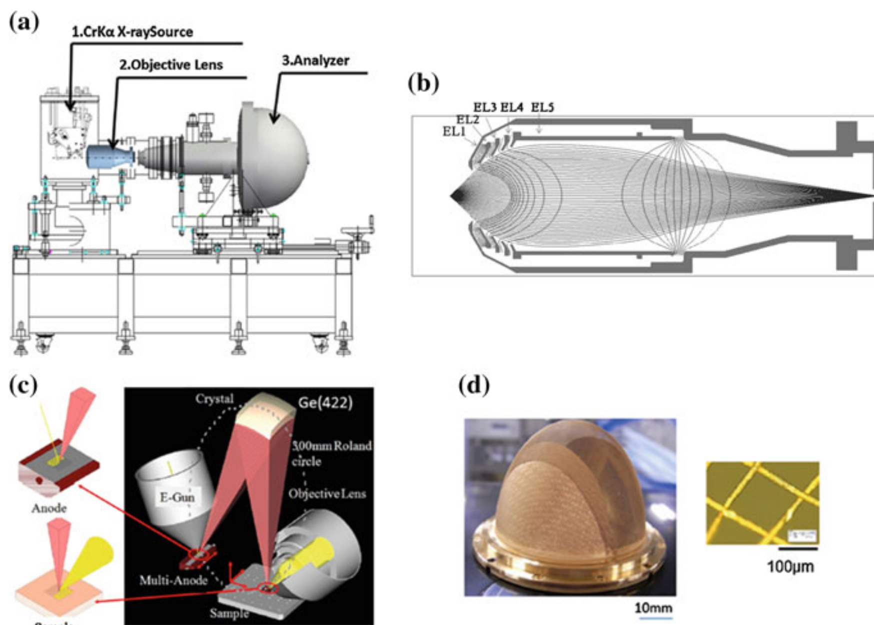

Fig. 18.27 **a** Lab HAXPES system (HEARP Lab). **b** Monochromatic Cr K_α source. Micro-focused electron beam is irradiated onto a water cooled Cr target. Cr K_α X-rays are monochromatized by an elliptically bent Ge crystal with 422 reflections and focused onto the sample surface. The X-ray spot can be scanned by rostering the electron beam on the target. **c** Cross sectional view of the wide-acceptance lens with simulated electron trajectories. **d** Photograph of the first-stage mesh electrode in the wide-acceptance objective lens

Detection of changes in local lattice configuration during phase transitions may be an interesting target of application. A more practical application of the bulk sensitive XPD to the polarity determination for ZnO (0001) and (000-1) surfaces has reported by Williams et al. [270]. They have obtained θ (polar angle)-ϕ (azimuth angle) mapping of the Zn 2p and O 1s spectral intensities, and compared with those simulated by a cluster model (CM) [272] and a dynamical calculation using Bloch waves (DBW) [273] as shown in Fig. 18.28a–d. The measured Zn $2p_{3/2}$ XPD patterns (a) and (b) show a clear distinction between the (0001) and (000-1) surfaces and resemble both the CM (c) and the DBW (d) simulations as a whole. It should be noticed that the Zn $2p_{3/2}$ XPD pattern from the (0001) polar surface shows a low intensity (black) ring in the θ region of 26°–27°, whereas the same black feature is recognized within the same angular region in the O 1s XPD pattern from the (000-1) surface. The origin of this dark ring is related to the relative positions of the cations and anions, which differ from each other when they are viewed from the (0001) and (000-1) surfaces in the wurtzite structure. For a detailed discussion see [270].

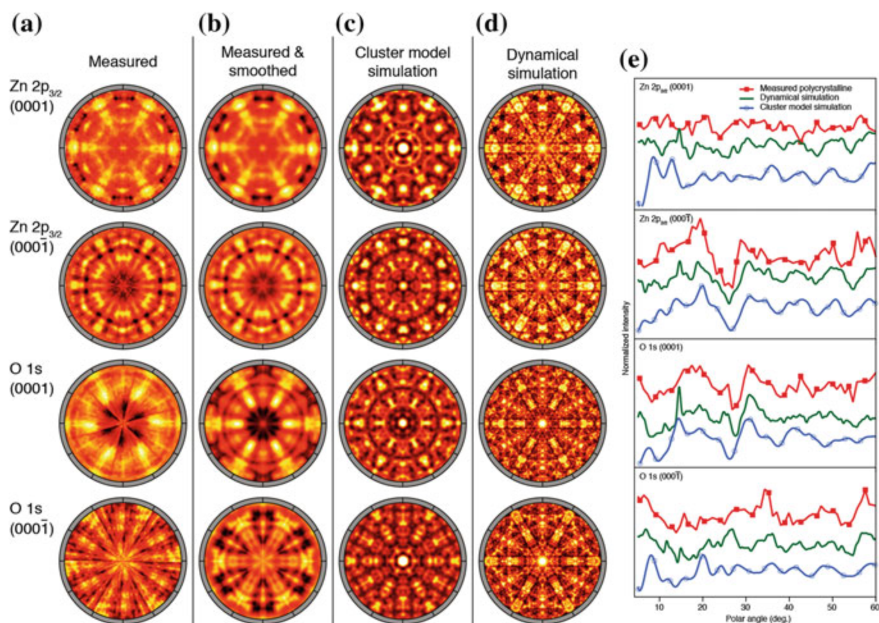

Fig. 18.28 **a** Measured photoelectron patterns of Zn and O from polar single-crystal ZnO surfaces at 5.4 keV photon-energy excitation. **b** The patterns have been interpolated and smoothed and are compared with simulated patterns by **c** cluster-model and **d** dynamical Bloch-wave simulations. **e** Polar angle (θ) dependence of the core-level peak intensities from the *c*-axis oriented polycrystalline films. The measured data is shown in the *top curve* of each plot. The dynamical Bloch-wave and cluster-model simulations obtained by averaging the intensity profiles about the azimuth angle are also shown following each experimental curve. The strongest polarity-dependent features are the diffraction minima found at θ = 26°–27° for the Zn $2p_{3/2}$ (0001) and O 1*s* (000-1) profiles

Polar angular dependences of Zn $2p_{3/2}$ and O 1*s* core-level spectra of ZnO thin films with (0001) and (000-1) preferred polarities with in-plain grain rotations prepared by sputtering on glass substrates were also measured as shown in the top curve of each plot in Fig. 18.28e. Since the specific intensity minima in the XPD θ-ϕ mapping is ring shaped in the single-crystal XPD patterns, the azimuthal averaging resulting from the in-plane grain rotation does not weaken it in the polycrystalline intensity profiles, resulting in the distinct intensity minimum found around θ = 26°–27° in the polycrystalline intensity profiles. The averages of the calculated polar angle dependences of Zn $2p_{3/2}$ and O 1 *s* spectral intensities over azimuth angles give excellent agreement with the experimental results for both CM and DBW calculations as shown in Fig. 18.28e. It is concluded that the black-ring feature in the XPD θ-ϕ mappings in single crystals and distinct minimum found in the θ dependence of the core-level intensity profiles are useful fingerprints for the determination of the surface polarity in the single crystals and c-axis-textured polycrystalline films of ZnO.

As already demonstrated by the above experiments, Lab based HAXPES is promising, and several future applications to advanced materials will now be described.

1. The environmental cell for HAXPES was designed in collaboration with Kawasaki and his coworkers by modifying the TEM environmental cell developed by his group [274]. Photograph and schematic cell cross sectional structure are shown in Fig. 18.29b, d [7]. The cell has a vacuum tight Si_3N_4 membrane of 14 nm thickness and an aperture of 0.1 × 2 mm^2 for photoelectron detection (Fig. 18.29c). The membrane can withstand pressure differences of 2 atmospheres (ATM). X-rays irradiate the sample surface through a Kapton-window on the sidewall of the cell. Ambient air was introduced into the cell with the distance between the Au sample surface and the membrane of 2.5 mm in this test device. Figure 18.29e shows Au $3d_{5/2}$ spectra at different cell pressures. Here the pressure values in the cell were taken as the pressure values measured at the inlet and outlet of the gas introduction pipes (Fig. 18.29a) when they became equal. The integrated intensity of the spectrum decreases exponentially with increasing

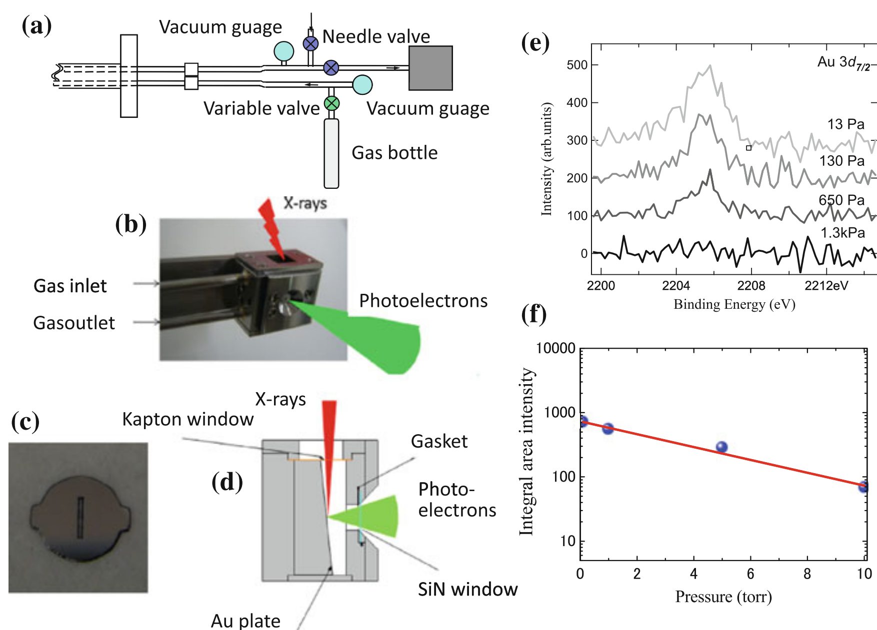

Fig. 18.29 **a** Gas-flow environmental cell system for in situ HAXPES. **b** Photographs of the environmental cell and **c** the Si_3N_4 thin film. Cross section of the environmental cell is schematically shown in (**d**). Au $3d_{5/2}$ spectra from an Au-plate sample in the environmental cell to which ambient air was introduced with pressures of 0.1, 1, 5, and 10 Torr are shown in (**e**). The gap between the Au surface and the Si_3N_4 window was 2.5 mm. **f** The logarithm of the Au $3d_{5/2}$ intensities has a linear dependence on the air pressure in the cell

pressure as shown in Fig. 18.29f. The air in the 2.5 mm gap between the window and Au sample causes significant photoelectron attenuation, which limits the highest pressure to 100–1000 Pa for photoelectron detection from the sample surface. The highest pressure could be increased by more than a factor of 10 by reducing the gap between the sample surfaces. The present cell method has the advantage that it can maintain a static pressure with exact pressure values while still being small and simple for different experimental configurations. Temperature control and external electric-field application to the sample inside the cell are planned for future development.

2. One of the most versatile methods to obtain a data set with systematic variation of composition and film thickness is to characterize films prepared with graded material parameters by PLD or sputtering with multiple sources. In combination with scanning probes of ca. 100 µm size, it is possible to characterize, for example, compositional dependences of sample properties over entire composition ranges. These methods were named "combinatorial" and have demonstrated their utility for advanced-device research [275, 276]. A multilayer sample with a wedged SiO_2 buried layer shown in Fig. 18.30 measured with an X-ray beam size of 100 µm using Lab HEARP gives a successful demonstration [7, 268, 277].

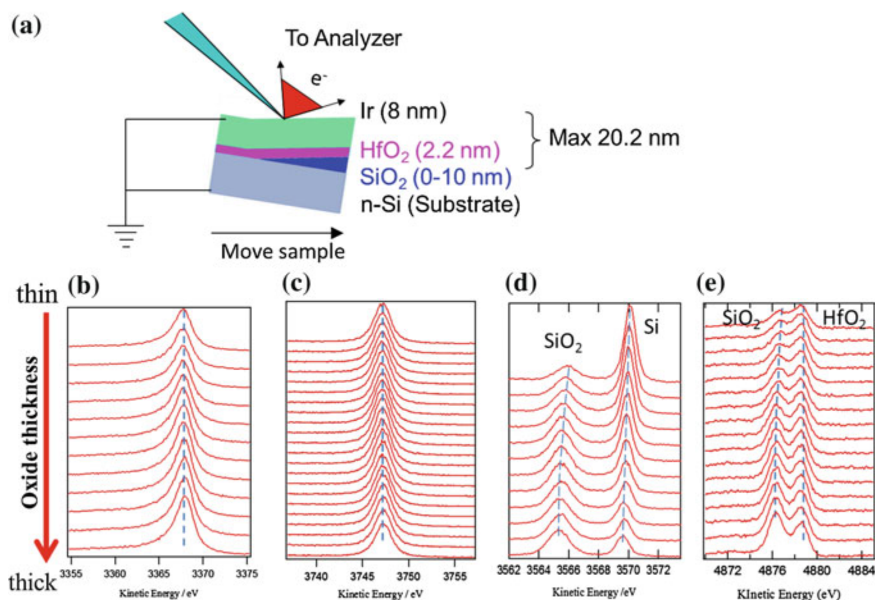

Fig. 18.30 **a** Schematic of multilayer wedged sample with overlayer thicknesses as indicated. **b** SiO_2 overlayer-thickness dependence of Ir $3d_{5/2}$, Hf $3d_{5/2}$, Si 1*s* and O 1*s* spectra of Ir (8 nm)/HfO_2 (2.2 nm)/wedge SiO_2 (0–10 nm)/Si(0 0 1) sample shown in (**a**). The SiO_2 thickness dependences of the spectra (**b**–**e**) were obtained by shifting the X-ray spot position along the thickness-varying direction of the wedge-shaped SiO_2 buried layer

3. Quartz and Ge bent crystals are used in Rowland configurations for monochromatizing Al and Cr K_α X-rays. If the sizes of the Rowland circles are different, however, it is possible to align a water cooled anode substrate with both Al and Cr anodes and a sample at each of the two intersections of the Rowland circles. By shifting the anode or by deflecting the electron beam to select either the Al or Cr target, it is possible to choose X-rays with energy of 1.49 keV (Al K_α) or 5.4 keV (Cr K_α) and focus them onto the sample surface without changing the sample position [278]. This type of switchable X-ray source will enable users to observe shallow core levels of lighter elements to deep core levels of heavy elements, thereby also improving the precision of depth profiling.

18.4 Summary

Examples of HAXPES applications to advanced materials were discussed. HAXPES experiments determine essential information on the electronic structures and chemical-bonding states relevant to actual advanced devices such as phase-change memory materials, InGaZnO transparent semiconducting thin films, hard-disc lubricants, and Li-ion battery positive-electrode materials. Combinations of HAXPES for electronic structure investigations, X-ray diffraction (XRD) for structural analyses, and large scale DFT-MD theoretical calculations were shown to be powerful methods for establishing material structure/function properties. Due to the large probing depth of HAXPES, operando observations of electronic and chemical-state variations under applied external-field conditions has also been made possible. Examples of solid-solid and solid-liquid interface systems were also given. The applicability of a Laboratory HAXPES system to the advanced material research and development were also presented, focusing on the development of an environmental cell for near-ambient pressure measurements, combinatorial approaches, and the plausibility of *in-house*, switchable monochromatic multiple-energy X-ray sources. The large variety of HAXPES experiments conducted using the SPring-8 beamline HAXPES end stations and the Lab HEARP system prove the general utility of HAXPES for the investigation of advanced materials.

Acknowledgements The author is grateful to T. Ishikawa, late Y. Takata of RIKEN and their co-workers for the collaborations during the incubation period of HAXPES development. M. Taniguchi and the staff of HiSOR are appreciated for the collaborations at BL15XU. The author is also thankful to the staff of BL29XU, BL47XU, and BL15XU for their devoted work. All collaborating users of the work discussed in this chapter are greatly appreciated. Development of the Cr K_α laboratory HAXPES system was performed in the framework of the JST “sentan” project. The author is thankful for the support. Finally, the author is thankful to Yoshiko Kobayashi for her encouragement and devoted help during this work.

References

1. A. Sekiyama, T. Iwasaki, K. Matsuda, Y. Saitoh, Y. Ônuki, S. Suga, Nature **403**, 396–398 (2000)
2. K. Kobayashi, M. Yabashi, Y. Takata, T. Tokushima, S. Shin, K. Tamasaku, D. Miwa, T. Ishikawa, H. Nohira, T. Hattori, Y. Sugita, O. Nakatsuka, S. Sakai, S. Zaima, Appl. Phys. Lett. **83**, 1005 (2003)
3. Y. Takata, M. Yabashi, K. Tamasaku, Y. Nishino, D. Miwa, T. Ishikawa, E. Ikenaga, K. Horiba, S. Shin, M. Arita, K. Shimada, H. Namatame, M. Taniguchi, H. Nohira, T. Hattori, S. Södergren, B. Wannberg, K. Kobayashi, Nuclear Instrum. Methods Phys. Res. **A547**, 50–55 (2005)
4. K. Kobayashi, Nuclear Instrum. Methods Phys. Res. **A547**, 98–112 (2005)
5. K. Kobayashi, E. Ikenaga, J.J. Kim, M. Kobata, S. Ueda, in *Proceedings of 9th International Conference on Synchrotron Radiation Instrumentation*, Daegu (Korea), 28 May–2 June 2006, ed by J.Y. Choi, S. Rah. AIP Conference Proceedings, vol. 879 (2006), pp. 1539–1544
6. K. Kobayashi, Nuclear Instrum. Methods Phys. Res. **A601**, 32–47 (2009)
7. K. Kobayashi, M. Kobata, H. Iwai, J Electron Spectrosc. Relat. Phenom. **190**, 210–221 (2013)
8. S.R. Elliott, *Physics of Amorphous Materials* (Longman Group Ltd., England, 1984)
9. B.S. Lee, G.W. Burr, R.M. Shelby, S. Raoux, C.T. Rettner, S.N. Bogle, K. Darmawikarta, S.G. Bishop, J.R. Abelson, Science **326**, 980–984 (2009)
10. Y. Fukuyama, N. Yasuda, J. Kim, H. Murayama, Y. Tanaka, S. Kimura, K. Kato, S. Kohara, Y. Moritomo, T. Matsunaga, R. Kojima, N. Yamada, H. Tanaka, T. Ohshima, M. Takata, Appl. Phys. Exp. **1**, 045001 (2008)
11. N. Yamada, E. Ohno, K. Nishiuchi, N. Akahira, M. Takano, J. Appl. Phys. **69**, 2849–2856 (1991)
12. E.R. Meinders, A.V. Mijiritskii, L. van Pieterson, M. Wuttig, *Optical Data Storage*, vol. 4 (Philips Research Book Series, Springer, 2006)
13. See for example, *Advance in Non-volatile Memory and Storage Technology*, ed. by Y. Nishi (Woodhead Publicing, Sawaston, Cambridge CB22 3HJ, UK, 2014) (© 2014 Elsevier Ltd. All right reserved)
14. M. Wuttig, N. Yamada, Nat. Mater. **6**, 824 (2007)
15. J.H. Coombs, A.P.J.M. Jongelis, W. van Es–Spiekman, B.A.J. Jacobs, J. Appl. Phys. **78**, 4906 (1995)
16. C. Trappe, B. Béchevet, B. Hyot, O. Winkler, S. Facsko, H. Kurtz, Jpn. J. Appl. Phys. Part 1 **39**, 766 (2000)
17. T. Matsunaga, N. Yamada, Jpn. J. Appl. Phys. Part 1 **43**, 4704 (2004)
18. A. Kobolov, P. Fons, A. Frenkel, A.L. Ankudinov, J. Tominaga, T. Uruga, Nat. Mater. **3**, 703 (2004)
19. W. Wełnic, A. Pamungkas, R. Detemple, C. Steimer, S. Blügel, M. Wuttig, Nat. Mater. **5**, 56–62 (2006)
20. J.J. Kim, K. Kobayashi, E. Ikenaga, M. Kobata, S. Ueda, T. Matsunaga, K. Kifune, R. Kojima, N. Yamada, Phys. Rev. B **76**, 115124 (2007)
21. D.A. Shirley, Phys. Rev. B **5**, 4709 (1972)
22. J.J. Yeh, I. Lindau, At. Data Nucl. Data Tables **32**, 1 (1985)
23. J.F. Moulder, W.F. Stickle, P.E. Sobol, K.D. Bomben, *Handbook of X-ray Photoelectron Spectroscopy* (Physical Electronics, Chanhassen, MN, 1995)
24. M.H. Cohen, H. Fritzsche, S.R. Ovshinsky, Phys. Rev. Lett. **22**, 1065 (1969)
25. K. Bahl, K.L. Chopra, J. Appl. Phys. **41**, 2196 (1970)
26. B.S. Lee, J.R. Abelson, S.G. Bishop, D.H. Kang, B.K. Cheong, K.B. Kim, J. Appl. Phys. **97**, 93509 (2005)
27. W.A. Harrison, Phys. Rev. B **8**, 4487 (1973)
28. J. St. John, A.N. Bloch, Phys. Rev. Lett. **33**, 1095 (1974)

29. K.L.I. Kobayashi, Y. Kato, K.F. Komatsubara, Butsuri **31**, 253–264 (1976). in Japanese
30. K.L.I. Kobayashi, Y. Kato, K.F. Kobatsubara, Prog. Crystal Growth and Charact. **1**, 117–149 (1978)
31. T. Suski, J. Karpinski, K.L.I. Kobayashi, K.F. Komatsubara, J. Phys. Chem. Solids **42**, 479–482 (1981)
32. G. Lucovski, P.M. White, Phys. Rev. B **8**, 660 (1973)
33. K. Shporto, S. Kremmer, M. Woda, D. Lencer, I. Robertson, M. Wuttig, Nat. Mater. **7**, 653–658 (2008)
34. K. Kobayashi, J.J. Kim, T. Matsunaga, K. Kifune, E. Ikenaga, M. Kobata, S. Ueda, R. Kojima, N. Yamada, in *Proceedings of 2008 MRS Spring Meeting* eds. by A.H. Edwards, P.J. Fons, S. Raoux, P.C. Taylor, M. Wuttig (Moscone West, San Francisco, 24–28 March 2008), pp. 1072-G02-07
35. K.A. Khachaturyan, Phys. Rev. B **36**, 4222 (1987)
36. P.B. Littlewood, J. Phys. C Solid St. Phys. **13**, 4855 (1980)
37. Y. Onodera, Solid State Comm. **11**, 1397 (1972)
38. K.L.I. Kobayashi, K. Kato, Y. Katayama, K.F. Komatsubara, Phys. Rev. Lett. **37**, 772 (1976)
39. P. Jóvári, I. Kaban, J. Steiner, B. Beuneu, A. Schöps, A. Webb, J. Phys. Condens. Matter **19**, 335212 (2007)
40. C. Lang, S.A. Song, D.N. Manh, D.J.H. Cockayne, Phys. Rev. B **76**, 054101 (2007)
41. S. Kohara, K. Kato, S. Kimura, H. Tanaka, T. Usuki, K. Suzuya, H. Tanaka, Y. Moritomo, T. Matsunaga, N. Yamada, Y. Tanaka, H. Suematsu, M. Takata, Appl. Phys. Lett. **89**, 201910 (2006)
42. J. Akola, R.O. Jones, S. Kohara, S. Kimura, K. Kobayashi, M. Takata, T. Matsunaga, R. Kojima, N. Yamada, Phys. Rev. B **80**, 020201(R) (2009)
43. J. Akola, R.O. Jones, Phys. Rev. B **76**, 235201 (2007)
44. J. Akola, R.O. Jones, J. Phys. Condens. Matter **20**, 465103 (2008)
45. J. Akola, R.O. Jones, Phys. Rev. Lett. **100**, 205502 (2008)
46. P. Biswas, R. Atta-Fynn, D.A. Drabold, Phys. Rev. B **76**, 125210 (2007)
47. P. Biswas, D.N. Tafen, F. Inam, B. Cai, D.A. Drabold, J. Phys. Condens. Matter **21**, 084207 (2009)
48. See EPAPS Document No. E-PRBMDO-80-R07926 for bond distances and bond angle distributions, partial coordination numbers, and frequently occurring Ge-centered configurations. $S(Q)$ for the DF optimized structure is also given. For more information on EPAPS, see http://www.aip.org/pubservs/epaps.html
49. T. Matsunaga, Y. Umetani, N. Yamada, Phys. Rev. B **64**, 184116 (2001)
50. T. Matsunaga, J. Akola, S. Kohara, T. Honma, K. Kobayashi, E. Ikenaga, R.O. Jones, N. Yamada, M. Takata, R. Kojima, Nature Mater. **10**, 129 (2011)
51. W. Kohn, L.J. Sham, Phys. Rev. **140**, A1133 (1965)
52. B. Huang, J. Robertson, Phys. Rev. B **81**, 081204 (2010)
53. S. Gronert, Acc. Chem. Res. **36**, 848–857 (2003)
54. J. Mikosch, S. Trippel, C. Eichhorn, R. Otto, U. Lourderaj, J.X. Zhang, W.L. Hase, M. Weidemüller, R. Wester, Science **319**, 183–186 (2008)
55. H. Hosono, M. Yasukawa, H. Kawazoe, J. Non-Cryst. Solids **203**, 334 (1996)
56. K. Nomura, H. Ohta, K. Ueda, T. Kamiya, M. Hirano, H. Hosono, Science **300**, 1269 (2003)
57. M.W.J. Prins, K.-O. Grosse-Holz, G. Müller, J.F.M. Cillessen, J.B. Giesbers, R.P. Weening, R.M. Wolf, Appl. Phys. Lett. **68**, 3650 (1996)
58. R.L. Hoffman, B.J. Norris, J.F. Wager, Appl. Phys. Lett. **82**, 733 (2003)
59. J. Nishii, F.M. Hossain, S. Takagi, T. Aita, K. Saikusa, Y. Ohmaki, I. Ohkubo, S. Kishimoto, A. Ohtomo, T. Fukumura, F. Matsukura, Y. Ohno, H. Koinuma, H. Ohno, M. Kawasaki, Jpn. J. Appl. Phys. **42**, L347 (2003)
60. T. Miyasako, M. Senoo, E. Tokumitsu, Appl. Phys. Lett. **86**, 162902 (2005)
61. H.Q. Chiang, J.F. Wager, R.L. Hoffman, J. Jeong, D.A. Keszler, Appl. Phys. Lett. **86**, 013503 (2005)
62. K. Nomura, H. Ohta, A. Takagi, T. Kamiya, M. Hirano, H. Hosono, Nature **432**, 488 (2004)

63. K. Nomura, A. Takagi, H. Ohta, T. Kamiya, M. Hirano, H. Hosono, Jpn. J. Appl. Phys. **45**, 4303 (2006)
64. H. Yabuta, M. Sano, K. Abe, T. Aiba, T. Den, H. Kumomi, K. Nomura, T. Kamiya, H. Hosono, Appl. Phys. Lett. **89**, 112123 (2006)
65. *Technology and Application of Amorphous Silicon*, ed. by R.A. Street (Springer, Berlin, 2000)
66. K. Nomura, T. Kamiya, H. Yanagi, E. Ikenaga, K. Yang, K. Kobayashi, M. Hirano, H. Hosono, Appl. Phys. Lett. **92**, 202117 (2008)
67. See EPAPS Document No. E-APPLAB-92-097819 for Fermi edge spectrum of the gold reference. For more information on EPAPS, see http://www.aip.org/pubservs/epaps.html
68. N.W. Ashcroft, N.D. Mermin, *Solid State Physics* (Saunders College Publishing, Philadelphia, 1976)
69. K. Nomura, T. Kamiya, H. Ohta, T. Uruga, M. Hirano, H. Hosono, Phys. Rev. B **75**, 035212 (2007)
70. H. Kumomi, K. Nomura, T. Kamiya, H. Hosono, Thin Solid Films **516**, 1516 (2008)
71. H.-H. Hsieh, T. Kamiya, K. Nomura, C.-C. Wu, H. Hosono, Appl. Phys. Lett. **92**, 133503 (2008)
72. M. Kimura, T. Nakanishi, K. Nomura, T. Kamiya, H. Hosono, Appl. Phys. Lett. **92**, 133512 (2008)
73. K. Nomura, T. Kamiya, E. Ikenaga, H. Yanagi, K. Kobayashi, H. Hosono, J. Appl. Phys **109**, 073726 (2011)
74. K. Nomura, A. Takagi, H. Ohta, T. Kamiya, M. Hirano, H. Hosono, Jpn. J. Appl. Phys. **45**, 4303 (2006)
75. C. Körber, V. Krishnakumar, A. Kleind, G. Panaccione, P. Torelli, A. Walsh, J.L.F. Da Silva, S.-H. Wei, R.G. Egdell, D.J. Payne, Phys. Rev. B **81**, 165207 (2010)
76. A. Walsh, J.L.F. Da Silva, S.-H. Wei, C. Körber, A. Klein, L.F.J. Piper, A. DeMasi, K.E. Smith, G. Panaccione, P. Torelli, D.J. Payne, A. Bourlange, R.G. Egdell, Phys. Rev. Lett. **100**, 167402 (2008)
77. Y. Dou, R.G. Egdell, Surf. Sci. **372**, 289 (1997)
78. Y. Dou, R.G. Egdell, T. Walker, D.S.L. Law, G. Beamson, Surf. Sci. **398**, 241 (1998)
79. R.G. Egdell, J. Rebane, T.J. Walker, Phys. Rev. B **59**, 1792 (1992)
80. T. Shibuya, M. Yoshinaka, Y. Shimane, F. Utsuno, K. Yano, K. Inoue, E. Ikenaga, J.J. Kim, S. Ueda, M. Kobata, K. Kobayashi, Thin Solid Films **518**, 3008 (2010)
81. T. Kamiya, Private communication
82. D.J. Chadi, K.J. Chang, Phys. Rev. B **39**, 10063 (1989)
83. T. Dietl, A. Haury, Y.M. d'Aubigné, Phys. Rev. B **55**, R3347 (1997)
84. T. Dietl, H. Ohno, F. Matsukura, J. Cibert, D. Ferrand, Science **287**, 1019 (2000)
85. J. Okabayashi, A. Kimura, O. Rader, T. Mizokawa, A. Fujimori, T. Hayashi, M. Tanaka, Phys. Rev. B **58**, R4211 (1998)
86. J. Okabayashi, A. Kimura, T. Mizokawa, A. Fujimori, T. Hayashi, M. Tanaka, Phys. Rev. B **59**, R2486 (1999)
87. T. Dietl, H. Ohno, F. Matsukura, Phys. Rev. B **63**, 195205 (2002)
88. M.E. Overberg, C.R. Abernathy, S.J. Pearton, N.A. Theodoropoulou, K.T. McCarthy, A.F. Hebard, Appl. Phys. Lett. **79**, 1312 (2001)
89. G.T. Thaler, M.E. Overberg, B. Gila, R. Frazier, C.R. Abernathy, S.J. Pearton, Appl. Phys. Lett. **80**, 3964 (2002)
90. N. Theodoropoulou, A.F. Hebard, M.E. Overg, C.R. Abernathy, S.J. Pearton, S.N. Chu, R.G. Wilson, Appl. Phys. Lett. **78**, 3475 (2001)
91. M.L. Reed, N.A. El-Masry, H.H. Stadelmaier, M.K. Ritums, M.J. Reed, C.A. Parker, Appl. Phys. Lett. **79**, 3473 (2001)
92. S. Sonoda, S. Shimizu, T. Sasaki, Y. Yamamoto, H. Hori, J. Cryst. Growth **237–239**, 1358 (2002)
93. Y. Shon, Y.H. Kwon, D.Y. Kim, X. Fan, D. Fu, T.W. Kang, Jpn. J. Appl. Phys. **40**, 5304 (2001). Part 1

94. S. Dhar, O. Brandt, A. Trampert, L. Däweritz, K.J. Friedland, K.H. Ploog, J. Keller, B. Beschoten, G. Güntherodt, Appl. Phys. Lett. **82**, 2077 (2003)
95. M. Zajac, J. Gosk, E. Grzanka, M. Kamiñska, A. Twardowki, B. Strojek, T. Szyszko, S. Podsiadlo, J. Appl. Phys. **93**, 4715 (2003)
96. K. Sato, H. KatayamaYoshida, Jpn. J. Appl. Phys. **40**, L485 (2001). Part 2
97. S.E. Park, H.J. Lee, Y.C. Cho, S.Y. Jeong, C.R. Cho, S.L. Cho, Appl. Phys. Lett. **80**, 4187 (2002)
98. M. Hashimoto, Y.K. Zhou, M. Kanamura, H. Asahi, Solid State Commun. **122**, 37 (2002)
99. J.J. Kim, M. Makino, P.P. Chen, T. Suzuki, D.C. Oh, H.J. Ko, J.H. Chang, T. Hanada, T. Yao, Phys. Status Solidi C **0**, 2869 (2003)
100. H.X. Liu, S.Y. Wu, R.K. Singh, L. Gu, D.J. Smith, N. Newman, N.R. Dilley, L. Montes, M.B. Simmonds, N. Newman, Appl. Phys. Lett. **85**, 4076 (2004)
101. J.J. Kim, H. Makino, K. Kobayashi, Y. Takata, T. Yamamoto, T. Hanada, M.W. Cho, E. Ikenaga, M. Yabashi, D. Miwa, Y. Nishino, K. Tamasaku, T. Ishikawa, S. Shin, T. Yao, Phys. Rev. B **70**, 161315(R) (2004)
102. T. Takeuchi, M. Taguchi, Y. Harada, T. Tokushima, Y. Takata, A. Chainani, J.J. Kim, H. Makino, T. Yao, T. Tsukamoto, S. Shin, K. Kobayashi, Jpn. J. of Appl. Phys **44**, L153–L155 (2005)
103. J.P. Perdew, *Electronic Structures of Solids*, vol. 91, eds. by P. Ziesche, H. Eschrig (Akademie Verlag, Berlin, 1991)
104. G. Kresse, J. Furthmüller, J. Furthmuller, Phys. Rev. B **54**, 11–169 (1996)
105. G. Kresse, D. Jöbert, Phys. Rev. B **59**, 1758 (1999)
106. A.L. Allred, E.G. Rochow, J. Inorg. Nucl. Chem. **5**, 264 (1958)
107. T. Dietl, Nature Mater. **9**, 965–974 (2010)
108. J. Mašek, F. Máca, J. Kudrnovský, O. Makarovsky, L. Eaves, R.P. Campion, K.W. Edmonds, A.W. Rushforth, C.T. Foxon, B.L. Gallagher, V. Novák, J. Sinova, T. Jungwirth, Phys. Rev. Lett. **105**, 227202 (2010)
109. D. Neumaier, M. Turek, U. Wurstbauer, A. Vogl, M. Utz, W. Wegscheider, D. Weiss, Phys. Rev. Lett. **103**, 087203 (2009)
110. K. Hirakawa, S. Katsumoto, T. Hayashi, Y. Hashimoto, Y. Iye, Phys. Rev. B **65**, 193312 (2002)
110. K.S. Burch, D.B. Shrekenhamer, E.J. Singley, J. Stephens, B.L. Sheu, R.K. Kawakami, P. Schiffer, N. Samarth, D.D. Awschalom, D.N. Basov, Phys. Rev. Lett. **97**, 087208 (2006)
112. V.F. Sapega, M. Moreno, M. Ramsteiner, L. Däweritz, K.H. Ploog, Phys. Rev. Lett. **94**, 137401 (2005)
113. K. Ando, H. Saito, K.C. Agarwal, M.C. Debnath, V. Zayets, Phys. Rev. Lett. **100**, 067204 (2008)
114. L.P. Rokhinson, Y. Lyanda-Geller, Z. Ge, S. Shen, X. Liu, M. Dobrowolska, J.K. Furdyna, Phys. Rev. B **76**, 161201(R) (2007)
115. K. Alberi, K.M. Yu, P.R. Stone, O.D. Dubon, W. Walukiewicz, T. Wojtowicz, X. Liu, J.K. Furdyna, Phys. Rev. B **78**, 075201 (2008)
116. S. Ohya, K. Takata, M. Tanaka, Nature Phys. **7**, 342–347 (2011)
117. M. Dobrowolska, K. Tivakornsasithorn, X. Liu, J.K. Furdyna, M. Berciu, K.M. Yu, W. Walukiewicz, Nature Mater. **11**, 444–449 (2012)
118. A.X. Gray, J. Minár, S. Ueda, P.R. Stone, Y. Yamashita, J. Fujii, J. Braun, L. Plucinski, C.M. Schneider, G. Panaccione, H. Ebert, O.D. Dubon, K. Kobayashi, C.S. Fadley, Nat. Mater. **11**, 957–962 (2012)
119. K. Sato, L. Bergqvist, J. Kudrnovský, P.H. Dederichs, O. Eriksson, I. Turek, B. Sanyal, G. Bouzerar, H. Katayama-Yoshida, V.A. Dinh, T. Fukushima, H. Kizaki, R. Zeller, Rev. Mod. Phys. **82**, 1633–1690 (2010)
120. J. Fujii, B.R. Salles, M. Sperl, S. Ueda, M. Kobata, K. Kobayashi, Y. Yamashita, P. Torelli, M. Utz, C.S. Fadley, A.X. Gray, J. Braun, H. Ebert, I. Di Marco, O. Eriksson, P. Thunström, G.H. Fecher, H. Stryhanyuk, E. Ikenaga, J. Minár, C.H. Back, G. van der Laan, G. Panaccione, Phys. Rev. Lett. **11**, 097201 (2013)

121. R. von Helmolt, J. Wecker, B. Holzapfel, L. Schultz, K. Samwer, Phys. Rev. Lett. **71**, 2331 (1993)
122. A. Urushibara, Y. Moritomo, T. Arima, A. Asamitsu, G. Kido, Y. Tokura, Phys. Rev. B **51**, 14103 (1995)
123. J.H. Park, E. Vescovo, H.J. Kim, C. Kwon, R. Ramesh, T. Venkatesan, Nature (London) **392**, 794 (1998)
124. H. Kuwahara, Y. Tomioka, A. Asamitsu, Y. Moritomo, Y. Tokura, Science **270**, 961 (1995)
125. M. Imada, A. Fujimori, Y. Tokura, Rev. Mod. Phys. **70**, 1039 (1998)
126. K. Horiba, M. Taguchi, A. Chainani, Y. Takata, E. Ikenaga, D. Miwa, Y. Nishino, K. Tamasaku, M. Awaji, A. Takeuchi, M. Yabashi, H. Namatame, M. Taniguchi, H. Kumigashira, M. Oshima, M. Lippmaa, M. Kawasaki, H. Koinuma, K. Kobayashi, T. Ishikawa, S. Shin, Phys. Rev. Lett. **93**, 236401 (2004)
127. M. Taguchi, A. Chainani, N. Kamakura, K. Horiba, Y. Takata, M. Yabashi, K. Tamasaku, Y. Nishino, D. Miwa, T. Ishikawa, S. Shin, E. Ikenaga, T. Yokoya, K. Kobayashi, T. Mochiku, K. Hirata, K. Motoya, Phys. Rev. **71**, 155102 (2005)
128. M. Taguchi, A. Chainani, N. Kamakura, K. Horiba, Y. Takata, E. Ikenaga, T. Yokoya, S. Shin, K. Kobayashi, K. Tamasaku, Y. Nishino, D. Miwa, M. Yabashi, T. Ishikawa, T. Mochiku, K. Hirata, K. Motoya, Cond-mat/0404200 (unpublished)
129. T. Kanki, H. Tanaka, T. Kawai, Phys. Rev. B **64**, 224418 (2001)
130. J. Zhang, H. Tanaka, T. Kanki, J.H. Choi, T. Kawai, Phys. Rev. B **64**, 184404 (2001)
131. T. Kanki, R.W. Li, Y. Naitoh, H. Tanaka, T. Matsumoto, T. Kawai, Appl. Phys. Lett. **83**, 1184 (2003)
132. H. Tanaka, J. Zhang, T. Kawai, Phys. Rev. Lett. **88**, 027204 (2002)
133. T. Kanki, Y.G. Park, H. Tanaka, T. Kawai, Appl. Phys. Lett. **83**, 4860 (2003)
134. H. Tanaka, Y. Takata, K. Horiba, M. Taguchi, A. Chainani, S. Shin, D. Miwa, K. Tamasaku, Y. Nishino, T. Ishikawa, E. Ikenaga, M. Awaji, A. Takeuchi, T. Kawai, K. Kobayashi, Phys. Rev. B **73**, 094403 (2006)
135. S. Ueda, H. Takami, T. Kanki, H. Tanaka, Phys. Rev. B **89**, 035141 (2014)
136. S. Ueda, H. Tanaka, E. Ikenaga, J.J. Kim, T. Ishikawa, T. Kawai, K. Kobayashi, Phys. Rev. B **80**, 092402 (2009)
137. C. Zener, Phys. Rev. **82**, 403 (1951)
138. P.W. Anderson, Science **235**, 1196 (1987)
139. C. Kittel, *Introduction to Solid State Physics*, 6th edn. (Wiley, New York, 1986)
140. T. Kanki, T. Yanagida, B. Vilquin, H. Tanaka, T. Kawai, Phys. Rev. B **71**, 012403 (2005)
141. P.W. Anderson, H. Hasegawa, Phys. Rev. **100**, 675 (1955)
142. K. Horiba, A. Maniwa, A. Chikamatsu, K. Yoshimatsu, H. Kumigashira, H. Wadati, A. Fujimori, S. Ueda, H. Yoshikawa, E. Ikenaga, J.J. Kim, K. Kobayashi, M. Oshimal, Phy. Rev. B **80**, 132406 (2009)
143. Y. Konishi, Z. Fang, M. Izumi, T. Manako, M. Kasai, H. Kuwahara, M. Kawasaki, K. Terakura, Y. Tokura, J. Phys. Soc. Jpn. **68**, 3790 (1999)
144. A.N. Vasil'ev, V.D. Buchel'nikov, T. Takagi, V.V. Khovailo, E.I Estrin, *Usp. Fiz. Nauk*, **173**, 577 (2003). (*Phys. Usp*. **46**, 559 (2003)
145. P. Entel, V.D. Buchelnikov, V.V. Khovailo, A.T. Zayak, W.A. Adeagbo, M.E. Gruner, H.C. Herper, E.F. Wassermann, J. Phys. D **39**, 865 (2006)
146. P.J. Webster, K.R.A. Ziebeck, S.L. Town, M.S. Peak, Philos. Mag. B **49**, 295 (1984)
147. K. Ullakko, J.K. Huang, C. Kantner, R.C. O'Handley, V.V. Kokorin, Appl. Phys. Lett. **69**, 1966 (1996)
148. Y. Sutou, Y. Imano, N. Koeda, T. Omori, R. Kainuma, K. Ishida, K. Oikawa, Appl. Phys. Lett. **85**, 4358 (2004)
149. R. Kainuma, Y. Imona, W. Ito, Y. Suto, H. Morito, S. Okamoto, O. Kitakami, K. Oikawa, A. Fujita, T. Kanomata, K. Ishida, Nature (London) **439**, 957 (2006)
150. A. Planes, L. Manosa, M. Acet, J. Phys. Condens. Matter. **21**, 233201 (2009)
151. T. Krenke, E. Duman, M. Acet, E.F. Wassermann, X. Moya, L. Mañosa, A. Planes, Nature Mater. **4**, 450 (2005)

152. S.Y. Yu, Z.H. Liu, G.D. Liu, J.L. Chen, Z.X. Cao, G.H. Wu, B. Zhang, and, X.X. Zhang, Appl. Phys. Lett. **89**, 162503 (2006)
153. B. Zhang, X.X. Zhang, S.Y. Yu, J.L. Chen, Z.X. Cao, G.H. Wu, Appl. Phys. Lett. **91**, 012510 (2007)
154. M. Khan, I. Dubenko, S. Stadler, N. Ali, Appl. Phys. Lett. **91**, 072510 (2007)
155. K. Koyama, H. Okada, K. Watanabe, T. Kanomata, R. Kainuma, W. Ito, K. Oikawa, K. Ishida, Appl. Phys. Lett. **89**, 182510 (2006)
156. K. Koyama, T. Igarashi, H. Okada, K. Watanabe, T. Kanomata, R. Kainuma, W. Ito, K. Oikawa, K. Ishida, J. Magn. Magn. Mater. **310**, e994 (2007)
157. S. Fujii, S. Ishida, S. Asano, J. Phys. Soc. Jpn. **58**, 3657 (1989)
158. C.P. Opeil, B. Mihaila, R.K. Schulze, L. Mañosa, A. Planes, W.L. Hults, R.A. Fisher, P.S. Riseborough, P.B. Littlewood, J.L. Smith, J.C. Lashley, Phys. Rev. Lett. **100**, 165703 (2008)
159. M. Ye, A. Kimura, Y. Miura, M. Shirai, Y.T. Cui, K. Shimada, H. Namatame, M. Taniguchi, S. Ueda, K. Kobayashi, R. Kainuma, T. Shishido, K. Fukushima, T. Kanomata, Phys. Rev. Lett. **104**, 176401 (2010)
160. P.J. Brown, A.P. Gand, K. Ishida, R. Kainuma, T. Kanomata, K.-U. Neumann, K. Oikawa, B. Ouladdiaf, K.R.A. Ziebeck, J. Phys. Condens. Matter **18**, 2249 (2006)
161. T. Krenke, M. Acet, E.F. Wassermann, X. Moya, L. Mañosa, A. Planes, Phys. Rev. B **72**, 014412 (2005)
162. S.R. Barman, S. Banik, A. Chakrabarti, Phys. Rev. B **72**, 184410 (2005)
163. A. Ayuela, J. Enkovaara, K. Ullakko, R.M. Nieminen, J. Phys. Condens. Matter **11**, 2017 (1999)
164. A. Ayuela, J. Enkovaara, R.M. Nieminen, J. Phys. Condens. Matter **14**, 5325 (2002)
165. J. Enkovaara, O. Heczko, A. Ayuela, R.M. Nieminen, Phys. Rev. B **67**, 212405 (2003)
166. T. Kanomata, K. Fukushima, H. Nishihara, R. Kainuma, W. Itoh, K. Oikawa, K. Ishida, K.U. Neumann, R.A. Ziebeck, Mater. Sci. Forum **583**, 119 (2008)
167. M. Haruta, N. Yamada, T. Kobayashi, S. Iijima, J. Catal. **115**, 301 (1989)
168. M. Haruta, S. Tsubota, T. Kobayashi, H. Kageyama, M.J. Genet, B. Delmon, J. Catal. **144**, 175 (1993)
169. G.J. Hutchings, M.S. Hall, A.F. Carley, P. Landon, B.E. Solsona, C.J. Kiely, A. Herzing, M. Makkee, J.A. Moulijn, A. Overweg, J.C. Fierro-Gonzalez, J. Guzman, B.C. Gatese, J. Catal. **242**, 71 (2006)
170. J. Guzman, S. Carrettin, A. Corma, J. Am. Chem. Soc. **127**, 3286 (2005)
171. M.A. Henderson, C.L. Perkins, M.H. Engelhard, S. Thevuthasan, C.H.F. Peden, Surf. Sci. **526**, 1 (2003)
172. A. Fujimori, Phys. Rev. B **28**, 2281 (1983)
173. S.Y. Liu, S.M. Yang, Appl. Catal. A Gen. **334**, 92 (2008)
174. Q. Fu, H. Saltsburg, M. Flytzani-Stephanopoulos, Science **301**, 935 (2003)
175. Q. Fu, S. Kudriavtseva, H. Saltsburg, M. Flytzani–Stephanopoulos Chem. Eng. J. **93**, 41 (2003)
176. V. Matolín, M. Cabala, I. Matolíınová, M. Škoda, J. Libra, M. Václavů, K.C. Prince, T. Skála, H. Yoshikawa, Y. Yamashita, S. Ueda, K. Kobayashi, J. Phys. D Appl. Phys. **42**, 115301 (2009)
177. D.R. Mullins, S.H. Overbury, S.H. Huntley, Surf. Sci. **409**, 307 (1998)
178. M. Engelhard, S. Azad, C.H.F. Peden, S. Thevuthasan, Surf. Sci. Spectra **11**, 73 (2004)
179. S. Tanuma, C.J. Powell, D.R. Penn, Surf. Interface Anal. **20**, 77 (1993)
180. S. Tanuma, C.J. Powell, D.R. Penn, Surf. Interface Anal. **21**, 165 (1994)
181. S. Tanuma, C.J. Powell, D.R. Penn, Surf. Interface Anal. **35**, 268 (2003)
182. J.G. Wang, B. Hammer, Top. Catal. **44**, 49 (2007)
183. Y. Chen, P. Hu, M.-H. Lee, H. Wang, Surf. Sci. **602**, 1736 (2008)
184. V. Matolín, I. Matolínnov, M. Václavu, I. Khalakhan, M. Vorokhta, R. Fiala, I. Piš, Z. Sofer, J. Poltierov-Vejpravová, T. Mori, V. Potin, H. Yoshikawa, S. Ueda, K. Kobayashi, Langmuir **26**(15), 12824–12831 (2010)

185. N. Tsud, T. Skala, K. Mašek, P. Hanyš, M. Takahashi, H. Suga, T. Mori, H. Yoshikawa, M. Yoshitake, K. Kobayashi, V. Matolin, Thin Solid Films **518**, 2206–2209 (2010)
186. V. Matolín, M. Cabalal, I. Matolíınová, M. Škodal, M. Václavů, K.C. Prince, T. Skála, T. Mori, H. Yoshikawa, Y. Yamashita, S. Ueda, K. Kobayashi, Fuel Cells **10**, 139–144 (2010)
187. H. Niwa, M. Kobayashi, K. Horiba, Y. Harada, M. Oshima, K. Terakura, T. Ikeda, Y. Koshigoe, J. Ozaki, S. Miyata, S. Ueda, Y. Yamashita, H. Yoshikawa, K. Kobayashi, J. Power Sources **196**, 1006–1011 (2011)
188. H. Yoshikawa, V. Matolín, I. Matolíınová, J. Electron Spectrosc. Relat. Phenom. **190**, 268–277 (2013)
189. R.J. Waltman, N. Kobayashi, K. Shirai, A. Khurshudov, H. Deng, Tribol. Lett. **16**, 151 (2004)
190. P.H. Kasai et al., J. Inf. Storage. Proc. Syst. **1**, 233–243 (1999)
191. E. Ikenaga, M. Kobata, J.J. Kim, A. Wakabayashi, Y. Nishino, K. Tamasaku, Y. Sakane, T. Ishikawa, S. Komiya, K. Kobayashi, J. Electron Spectrosc. Relat. Phenom. **156–158**, 336–339 (2007)
192. M.F. Toney, C.M. Mate, D. Pocker, I.E.E.E. Trans, Magn. **34**, 1774 (1998)
193. R.J. Waltman, D.J. Pocker, H. Deng, N. Kobayashi, Y. Fujii, T. Akada, K. Hirasawa, G.W. Tyndall, Chem. Mater. **15**, 2362 (2003)
194. R.J. Waltman, N. Kobayashi, K. Shirai, A. Khurshudov, H. Deng, Tribol. Lett. **16**, 151 (2004)
195. P. Merel, M. Tabbal, M. Chaker, S. Moisa, J. Margot, Appl. Surf. Sci. **136**, 105–110 (1998)
196. J. Diaz, G. Paolicelli, S. Ferrer, F. Comin, Phys. Rev. B **54**, 8064 (1996)
197. E. Riedo, F. Comin, J. Chevrier, F. Schmithusen, S. Decossas, M. Sancrotti, Surf. Coat. Technol. **125**, 124–128 (2000)
198. C.M. Breneman, K.B. Wiberg, J. Comput. Chem. **11**, 361 (1990)
199. N. Kihira, N. Terada, in *Proceedings of 22nd International Battery Hybrid and Fuel Cell Electric Vehicle Symposium and Exposition* (Yokohama, 2006)
200. H. Kobayashi, M. Shikano, S. Koike, H. Sakaebe, K. Tatsumi, J. Power Sources **174**, 380 (2007)
201. K. Amine, J. Liu, ITE Lett. **1**, 59–63 (2000)
202. K. Amine, C.H. Chen, J. Liu, M. Hammond, A. Jansen, D. Dees, I. Bloom, D. Vissers, G. Henriksen, J. Power Sources **97**(98), 684–687 (2001)
203. G.V. Zhuang, G. Chen, J. Shim, X. Song, P.N. Ross, T.J. Richardson, J. Power Sources **134**, 293–297 (2004)
204. Md. K. Rahman, Y. Saito, 208th ECS Meeting, abstract #198 (2005)
205. MdK Rahman, Y. Saito, J. Power Sources **174**, 889 (2007)
206. PNGV Battery Test Manual, Rev. 3, DOE/ID-10597 (2001)
207. N. Kihira, Abstracts of the 46th Battery Symposium in Japan, pp. 566–567 (2005)
208. N. Kihira, Y. Mita, E. Takei, Y. Kobayashi, H. Miyashiro, K. Kumai, N. Terada, T. Iwahori, 206th ECS Meeting, abstract #385 (2004)
209. M. Shikano, H. Kobayashi, S. Koike, H. Sakaebe, E. Ikenaga, K. Kobayashi, K. Tatsumi, J. Power Sources **174**, 795–799 (2007)
210. C.D. Wagner, A.V. Naumkin, A. Kraut-Vass, J.W. Allison, C.J. Powell, J.R. Rumble Jr., NIST X-ray photoelectron spectroscopy database, NIST Standard reference database 20, Version 3.4, 2007
211. A.M. Andersson, A. Henningson, H. Siegbahn, U. Jansson, K. Edström, J. Power Sources **119**(12), 1522–1527 (2003)
212. R. Dedryvère, L. Gireaud, S. Grugeon, S. Laruelle, J.M. Tarascon, D. Gonbeau, J. Phys. Chem. B **109**, 15868–15875 (2005)
213. H.C. Wen, P. Majhi, K. Choi, C.S. Park, H.N. Alshareef, H.R. Harris, H. Luan, H. Niimi, H.B. Park, G. Bersuker, P.S. Lysaght, D.L. Kwong, S.C. Song, B.H. Lee, R. Jammy, Microelectron. Eng. **85**, 2 (2008)
214. D. Bar-Tow, E. Peled, L. Burstein, J. Electrochem. Soc. **146**, 824–832 (1999)

215. A.M. Andersson, D.P. Abraham, R. Haasch, S. MacLaren, J. Liu, K. Amine, J. Electrochem. Soc. **149**, A1358–A1369 (2002)
216. A.N. Mansour, Surf. Sci. Spectra **3**, 231–238 (1996)
217. A.N. Mansour, Surf. Sci. Spectra **3**, 279–286 (1996)
218. D.P. Abraham, R.D. Twesten, M. Balasubramanian, J. Kropf, D. Fischer, J. McBreen, I. Petrov, K. Amine, J. Electrochem. Soc. **150**, A1450–A1456 (2003)
219. M.L. Green, E.P. Gusev, R. Degraeve, E.L. Garfunkel, J. Appl. Phys. **90**, 2057 (2001)
220. G.D. Wilk, R.M. Wallace, J.M. Anthony, J. Appl. Phys. **89**, 5243 (2001)
221. M. Kobata, I. Piš, Hideo Iwai, H. Yamazui, H. Takahashi, M. Suzuki, H. Matsuda, H. Daimon, K. Kobayashi, Anal. Sci. **26**, 227 (2010)
222. G.D. Wilk, R.M. Wallace, J.M. Anthony, J. Appl. Phys. **89**, 5243 (2001)
223. Y. Yamashita, H. Yoshikawa, T. Chikyow, K. Kobayashi, ECS Trans. **41**, 331 (2011)
224. L. Quan, H.W. Qi, W.X. Yun, M.X. Xiang, Acta Phys. Sin. **59**, 7880 (2010)
225. J.D. McBrayer, R.M. Swanson, T.W. Sigmon, J. Electrochem. Soc. **133**(6), 1242 (1986)
226. G. Raghavan, C. Chiang, P.B. Anders, S.-M. Tzeng, R. Villasol, G. Bai, M. Bohr, D.B. Fraser, Thin Solid Films **262**, 168 (1995)
227. H. Miyazaki, D. Kodama, N. Suzumura, J. Appl. Phys. **106**, 104103 (2009)
228. N. Suzumura, S. Yamamoto, D. Kodama, K. Makabe, J. Komori, E. Murakami, S. Maegawa, K. Kubota, *IEEE 44th Annual Intern. Reliab. Phys. Symp.* (2006)
229. R. Waser, M. Aono, Nat. Mater. **6**, 833 (2007)
230. Y. Watanabe, J.G. Bednorz, A. Bietsch, Ch. Gerber, D. Widmer, A. Beck, S.J. Wind, Appl. Phys. Lett. **78**, 3738 (2001)
231. K. Szot, W. Speier, G. Bihlmayer, R. Waser, Nat. Mater. **5**, 312 (2006)
232. K. Terabe, T. Hasegawa, T. Nakayama, M. Aono, Nature **433**, 47 (2005)
233. T. Sakamoto, H. Sunamura, H. Kawaura, T. Hasegawa, T. Nakayama, M. Aono, Appl. Phys. Lett. **82**, 3032 (2003)
234. T. Tsuchiya, Y. Oyama, S. Miyoshi, S. Yamaguchi, Appl. Phys. Express **2**, 055002 (2009)
235. T. Sakamoto, K. Lister, N. Banno, T. Hasegawa, K. Terabe, M. Aono, Appl. Phys. Lett. **91**, 092110 (2007)
236. T. Tsuruoka, K. Terabe, T. Hasegawa, I. Valov, R. Waser, M. Aono, Adv. Funct. Mater. **22**, 70–77 (2012)
237. Y.-M. Kim, J.-S. Lee, J. Appl. Phys. **104**, 114115 (2008)
238. T. Sakamoto, K. Lister, N. Banno, T. Hasegawa, K. Terabe, M. Aono, Appl. Phys. Lett. **91**, 092110 (2007)
239. S. Lee, W.-G. Kim, S.-W. Rhee, K. Yong, J. Electrochem. Soc. **155**, H92 (2008)
240. M. Haemori, T. Nagata, T. Chikyow, Appl. Phys. Express **2**, 061401 (2009)
241. J.F. Gibbons, W.E. Beadle, Solid-State Electron. **7**, 785 (1964)
242. G.D. Wilk, R.M. Wallace, Appl. Phys. Lett. **74**, 2854 (1999)
243. J. Robertson, Rep. Prog. Phys. **69**, 327 (2006)
244. J.J. Yang, F. Miao, M.D. Pickett, D.A.A. Ohlberg, D.R. Stewart, C.N. Lau, R.S. Williams, Nanotechnology **20**, 215201 (2009)
245. C. Yoshida, K. Kinoshita, T. Yamasaki, Y. Sugiyama, Appl. Phys. Lett. **93**, 042106 (2008)
246. H. Shima, F. Takano, H. Muramatsu, M. Yamazaki, H. Akinaga, A. Kogure, Phys. Status Solidi (RRL) **2**, 99 (2008)
247. T. Nagata, M. Haemori, Y. Yamashita, H. Yoshikawa, Y. Iwashita, K. Kobayashi, T. Chikyow, Appl. Phys. Lett. **97**, 082902 (2010)
248. D. Barreca, A. Milanov, R.A. Fischer, A. Devi, E. Tondello, Surf. Sci. Spectra **14**, 34 (2007)
249. G.M. Bancroft, I. Adams, L.L. Coatsworth, C.D. Bennewitz, J.D. Brown, W. Westwood, Anal. Chem. **47**, 586 (1975)
250. S. Doniach, M. Šunjić, J. Phys. C **3**, 285 (1970)
251. T.A. Lee, A. Navrotsky, J. Mater. Res. **19**, 1855 (2004)
252. Y. Nagano, J. Therm. Anal. Calorim. **69**, 831 (2002)
253. H. Takeuchi, D. Ha, T.-J. King, J. Vac. Sci. Technol. A **22**, 1337 (2004)

254. K. Ohmori, P. Ahmet, M. Yoshitake, T. Chikyow, K. Shiraishi, K. Yamabe, H. Watanabe, Y. Akasaka, Y. Nara, K.-S. Chang, M.L. Green, K. Yamada, J. Appl. Phys. **101**, 084118 (2007)
255. T. Nagata, M. Haemori, Y. Yamashita, H. Yoshikawa, Y. Iwashita, K. Kobayashi, T. Chikyow, Appl. Phys. Lett. **99**, 223517 (2011)
256. A.J. Bard, L.R. Faulkner, *Electrochemical Methods. Fundamentals and Applications*, 2nd edn. (Wiley, New York, 2001)
257. M. Yoshitake, Y.-R. Aparna, K. Yoshihara, J. Vac. Sci. Technol. A **19**, 1432 (2001)
258. T. Tsuchiya, S. Miyoshi, Y. Yamashita, H. Yoshikawa, K. Terabe, K. Kobayashi, S. Yamaguchi, Solid State Ionics **253**, 110–118 (2013)
259. Y. Abe, N. Itadani, M. Kawamura, K. Sasaki, H. Itoh, Vacuum **83**, 528–530 (2009)
260. H.D. Abruna, *Electrochemical Interfaces: Modern Techniques for Insitute Interface Characterization* (VCH Publishers, New York, Weinheim, Cambridge, 1991)
261. T. Masuda, H. Yoshikawa, H. Noguchi, T. Kawasaki, M. Kobata, K. Kobayashi, K. Uosaki, Appl. Phys. Lett. **103**, 111605 (2013)
262. A.W. Taylor, F.L. Qiu, I.J. Villar-Garcia, P. Licence, Chem. Commun. **45**, 5817 (2009)
263. D. Weingarth, A. Foelske-Schmitz, A. Wokaun, R. Kotz, Electrochem. Commun. **13**(6), 619 (2011)
264. R. Wibowo, L. Aldous, R.M.J. Jacobs, N.S.A. Manan, R.G. Compton, Chem. Phys. Lett. **517** (1–3), 103 (2011)
265. Q. Ma, N. Moldovan, D.C. Mancini, R.A. Rosenberg, J. Appl. Phys. **89**, 3033 (2001)
266. Y. Sugita, Y. Nara, N. Nakayama, T. Ito, Jpn. J. Appl. Phys. **30**, 3209 (1991)
267. F.J. Himpsel, F.R. Mcfeely, A. Taleb-ibrahimi, J.A. Yarmoff, G. Hollinger, Phys. Rev. B **38**, 6084 (1988)
268. M. Kobata, I. Piš, H. Nohira, H. Iwai, K. Kobayashia, Surf. Interface Anal. **43**, 1632–1635 (2011)
269. I. Piš, M. Kobata, T. Matsushita, H. Nohira, K. Kobayashi, Appl. Phys. Express **3**, 056701 (2010)
270. J.R. Williams, I. Piš, M. Kobata, A. Winkelmann, T. Matsushita, Y. Adachi, N. Ohashi, K. Kobayashi, J. Appl. Phys. **111**, 033525 (2012)
271. I. Bartoš, I. Piš, M. Kobata, K. Kobayashi, M. Cukr, P. Jĭrcĭek, T. Sugiyama, E. Ikenaga, Phys. Rev. B **83**, 235327 (2011)
272. T. Matsushita, F. Matsui, H. Daimon, K. Hayashi, J. Electron Spectrosc. Relat. Phenom. **178**, 195 (2010)
273. A. Winkelmann, C.S. Fadley, F.J. Garcia de Abajo, New J. Phys. **10**, 113002 (2008)
274. T. Kawasaki, K. Ueda, M. Ichihashi, T. Tanji, Rev. Sci. Instrum. **80**, 113701 (2009)
275. X.D. Xiang, X. Sun, G. Briceño, Y. Lou, K.A. Wang, H. Chang, W.G. Wallace-Freedman, S.W. Chen, P.G. Schultz, Science **268**, 1738 (1995)
276. H. Koinuma, I. Takeuchi, Nat. Mater. **3**, 429–438 (2004)
277. G. Panaccione, K. Kobayashi, Surf. Sci. **606**, 125–129 (2012)
278. K. Kobayashi, H. Iwai, M. Kobata, H. Yamazui, Patent, PCT/JP2011/001904

Chapter 19
Photoelectron Microscopy and HAXPES

Raymond Browning

Abstract High energy X-ray photoelectron spectroscopy (HAXPES) has emerged as an important materials analytical technique in several technology areas including semiconductor device analysis and in situ catalysis. The next instrumental challenge is taking development of the HAXPES technique beyond high-energy photoelectron spectroscopy to high-energy photoelectron microscopy. In this chapter we argue that a new symbiosis is possible that will integrate the rich chemical and structural information derived from HAXPES spectroscopy with the techniques of low-energy high spatial resolution photoelectron microscopy. This integration will produce a powerful materials analysis technology with a wide range of real world applications. It is expected that chemical-state analysis on the mesoscale enabled by HAXPES microscopy will make a significant contribution.

19.1 Introduction

This is an exciting time for photoelectron microscopy with developments across the board from new photon sources, advances in instrumentation, and new methods of analysis. High-energy X-ray photoelectron spectroscopy (HAXPES) has emerged as an important materials analytical technique in several technology areas including semiconductor device analysis and in situ catalysis. The key feature of HAXPES for these applications is the longer mean-free path (MFP) of the photoelectrons at high kinetic energies. The longer electron MFP is a tool for comparison of the surface and bulk of a sample so that a model of the near surface elemental and chemical distributions can be made or, in the case of catalysis, information can be extracted through a gas surrounding the catalyst. The next instrumental challenge is to develop the HAXPES technique beyond high-energy photoelectron spectroscopy to high-energy photoelectron microscopy. Microscopy has only played a minor role in

R. Browning (✉)
R. Browning Consultants, 1 Barnhart Place, Shoreham, NY 11786, USA
e-mail: ray@rbrowning.net

© Springer International Publishing Switzerland 2016

J.C. Woicik (ed.), *Hard X-ray Photoelectron Spectroscopy (HAXPES)*,
Springer Series in Surface Sciences 59, DOI 10.1007/978-3-319-24043-5_19

the development of HAXPES, although excellent results have so far been obtained, and new instrumental methods are promising. Also, we have a technology driver. There is a pressing need for chemical-state analysis on the mesoscale [1] for which HAXPES microscopy is an active and expanding field that can make a significant contribution. In this report I will demonstrate why HAPEXES microscopy as an instrumental technique is about to undergo rapid development, and how it fits into the general picture of photoelectron microscopy. I will also suggest the development path that should be productive for integrating HAXPES into photoelectron microscopy.

The relatively slower development of HAXPES microscopy is due to both physical factors, and the operational basis of the most popular types of photoelectron microscope. The main physical factor is simply that the signal from HAXPES is much lower for the same photon flux than at lower photon energies due to the reduced photoionization cross section at higher photon energies. By its nature, microscopy requires much more signal than spectroscopy so the loss of intensity in the characteristic electron signal is a serious penalty. The second issue is that the main class of high spatial resolution photoelectron microscope preferentially uses low-energy photoelectrons for imaging. The photoelectron emission microscope (PEEM) class of instruments is derived from the low-energy electron microscope (LEEM) [2, 3] which uses a strongly accelerating cathode lens with the sample as the cathode. While the recent development of the vector potential photoelectron microscope (VPPEM) [4, 5] does not use a cathode lens, the highest spatial resolutions are also achieved using low-energy electrons.

Other approaches to photoelectron microscopy include the different variants of the scanning X-ray microprobe. Of the two main approaches to forming the scanning probe, the focusing mirror systems seem intuitively more likely to have value for HAXPES imaging [6]. The zone-plate approach while not confined to lower energy X-rays does have other technical and design issues to overcome, such as probe formation over a wide energy range [7]. However, the physical limitation still remains that microscopy requires a large signal. It is for this reason that most high-energy microprobe imaging uses signal channels such as X-ray fluorescence, Bragg diffraction, or X-ray absorption which have large signal strengths in comparison to HAXPES photoelectrons [8]. However, we shall demonstrate below that the integration of different signal channels into HAXPES imaging is a route to overcome many of the difficulties, and it leads to new opportunities for photoelectron microcopy. For this reason, the low energy microscope looks most interesting as a basis for further development.

For HAXPES spectroscopy, the photoelectron that is directly emitted from a core level, the photoemission peak, or the XPS signal, is typically the information channel of interest. The information depth for this signal has become well understood [9, 10], and using both the change in MFP with energy and the change in detection angle give information on the chemical structure of buried layers. This direct high-energy signal also includes shakeup features, recoil effects, interatomic transitions, and other rich details of composition and structure. Although, for microscopy these additional features will be much weaker. Other signals created by

the high-energy photons, such as X-ray absorption spectra (XAS) [11] and its derivatives, near edge X-ray absorption fine structure (NEXAFS) [12] and extended X-ray absorption fine structure (EXAFS) [13], are more accessible for imaging as they have a significant low-energy partial yield (PAY). Both PEEM and VPPEM microscopies have an advantage at low energies where they can collect all the electrons emitted into 2π steradians. These low energy electrons again can be rich in composition details, but using a low-energy signal such as PAY NEXAFS brings up the question of what is the information depth.

In summary, there are several information channels that are considered to be HAXPES; they include the direct photoemission peak and the photoelectron-yield response to X-ray absorption. While there are several ways to create an image, we shall concentrate on the extension of the low-energy microscopies to high energies, neglecting the contributions from scanning probe systems.

19.2 HAXPEEM

At present, the number of examples of photoelectron microscopy using high-energy photons and the directly emitted HAXPES photoemission peak as an imaging channel are limited. While several groups have used PEEM with high-energy photons as the excitation, they image with low-energy electron signals [14–18]; this is not the same as using the long MFP of the photoelectrons directly. However, there is what may be considered the holotype experiment for HAXPES in a PEEM [19, 20]. This experiment was performed at PETRA III on an undulator beam line, and it gives us a clear indication of the orders of magnitude to be expected in spatial resolution, photon flux, and image collection times.

Basic PEEM is naturally a low-energy imaging technique, with photoelectrons in the energy range of 0–50 eV. The limit to using higher energies is the decrease in collection angle needed to make a high resolution image with energy filtering in an analyzer. The solid angle for a PEEM imaging several keV electrons is reduced to the order of 0.1 %. Taken with the decrease in sensitivity of HAXPES, this requires a very bright photon source to achieve submicron spatial resolution. Even so, imaging at PETRA III took an extended exposure time of 120 min. Figure 19.1 shows the results from an Au/Si calibration sample using 4294 eV Au photoelectrons [19, 20].

The line scan on the left of Fig. 19.1 shows better than 500 nm spatial resolution across an edge. Depth-profile data can also be obtained. Figure 19.2 shows results from Au islands on $SrTiO_3$ using 6.5 keV photons, and the Sr $2p_{3/2}$ transition [19]. From the intensity loss, a MFP at 4560 eV of 8.5 nm was estimated. The departure from the calculated value of 4.4 nm [21] is argued to be due to surface roughness. What perhaps is more interesting is the shift in the buried layer Sr peak position by 0.4 eV to lower binding energy. As this signal will more strongly represent the Au/$SrTiO_3$ interface, it shows that the interface states differ from the bulk, and this effect can be imaged.

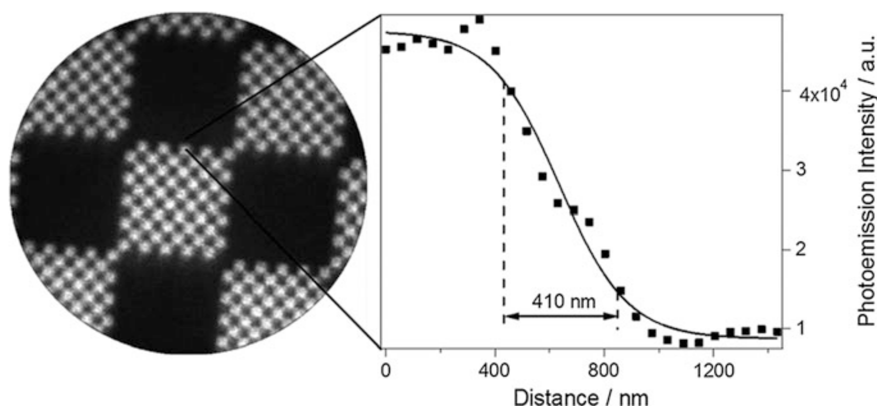

Fig. 19.1 Au/Si calibration sample imaged on the Au $3d_{5/2}$ photoemission line at a kinetic energy of 4294 eV (*left*). Line scan across a square edge and 16/84 % profile fit (*right*) [19, 20]

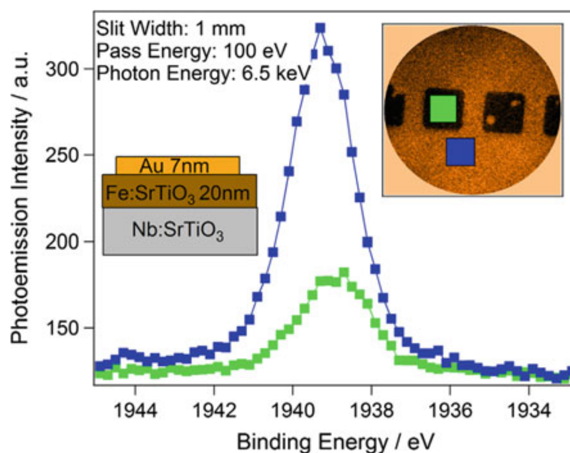

Fig. 19.2 Selected area hard X-ray photoemission spectra from Al/$SrTiO_3$. *Inset top right* definition of regions of interest. *Inset left* sample layer composition [19, 20]

The advantage of a PEEM instrument for this experiment is that both very low-energy imaging and HAXPES imaging can be performed on the same sample area. By switching focusing conditions and turning on a different light source, in this experiment a mercury-discharge lamp, a wide range of photoelectron energies can be collected.

The PEEM used for the results of Figs. 19.1 and 19.2 was operated with an accelerating electrostatic lens with 24 keV extraction voltage. An electrostatic electron lens operated under these conditions is a very good lens, having both low spherical and chromatic aberrations, although with high-energy electrons it is a low power lens with only a 6.6:1 accelerating ratio. This means that the solid angle of acceptance must be reduced to give a reasonable spatial resolution, in this case implying 0.15 % transmission. While this sensitivity is still relatively high, the low cross section of the HAXPES makes for lengthy collection times of 2 h per image.

The authors did not estimate the beam-flux density they used, but it would be expected to be on the order of 10^8 photons/s/μ^2 from the P09 beamline used. In comparison, an increase of at least two orders of magnitude might be expected from current beamline developments together with an improvement in the spatial resolution down to 50 nm, although a factor of 10 decrease in the exposure time taken with a factor 3 increase in spatial resolution is more likely given that sample-position stability may become an issue below 100 nm. The high flux does impose limitations on the types of samples that can be imaged, but the typical high-flux problem of space-charge broadening at the backplane crossover is not an issue for high energy imaging [22]. Note that we also expect a change in magnification going from low-energy operation to high-energy operation, but this change can be accurately compensated for.

An alternative to what could be called true HAXPES imaging is to use high-energy photons but image with low-energy electrons. The low-energy electron channel gives a much stronger signal, while still providing an enhanced probing depth over soft X-ray operation [16] together with reasonable spatial resolution at the solid surface. This enhanced probing depth is due to a longer MFP of the higher energy Auger electrons. The energy loss mechanisms for these electrons are largely plasmon losses which have low lateral-momentum loss but lead to an increase in secondary electrons at the surface [17]. Thus high-energy X-ray photons combined with low-energy PAY NEXAFS will have a similar probing depth to HAXPES with a spatial resolution that will depend on the information depth.

Images with good contrast and signal-to-noise have been be obtained by imaging the *K* edge of Co (7.71 keV) [17]. Also 200 nm spatial resolution was obtained using X-ray magnetic circular dichroism (XMDC) even with Pt L_2 (13.27 keV) in CoCrPt films [17]. This last result was obtained with only 10^7 photons/s/μ^2 (SPring8 BL39XU) [23]. Note that these low-energy results are from a direct imaging PEEM with no energy analysis, so that true HAXPES imaging would not have been possible. They do, however, demonstrate that extension of PEEM to higher photon energies is a natural development and important results can be obtained with current instruments. The SPring8 BL39XU has now been converted to a hard X-ray nanospectroscopy (XAFS and XMCD) station with a beam size of 100 nm and a flux density of 6×10^{11} photons/s/μ^2 using Kirkpatrick-Baez mirrors [23].

Clearly, from the PETRA results [19, 20] an extension to a true HAXPES PEEM (HAXPEEM) with a few 10's of nanometer resolution is possible with a higher beam brightness, but much more can be achieved. The HAXPEEM is essentially looking at a colored world through a monochrometer. In principle, the HAXPEEM has access to a wide range of photon energies, and it can detect electrons with energies from zero up to over 10 keV. In fact, the same instrument used for HAXPEEM was also used to image the checkerboard of Fig. 19.1 with the low energy Si 2*p* and Au $4f_{7/2}$ core levels and similar imaging quality [19]. This is not a trivial observation, bringing information together from across the photon- and electron-detection ranges creates new information, and this data fusion has been successfully implemented in several fields from remote sensing to medical imaging [24–27]. Image processing using correlations between low-energy spectral features

with strong signals and noisy high-energy features can improve the effective spatial resolution of the higher energy features. Binning of hyperspectral image pixels can separate out edge effects from feature centers in complex images, and very small volumetric densities can be isolated from a matrix. Image fusion across different image types can expose subtle correlations that would be otherwise overlooked. Taken together with higher beam-flux densities, hyperspectral imaging could push effective HAXPES spatial resolutions into the mid and low 10's of nanometers. For some applications the availability in the one instrument of a wide hyperspectral range might be the most important advantage of this class of microscope over the scanning microprobe. Also, in some circumstances the very low-energy and high-energy electron MFP's may be similar [28]. This makes data fusion much more direct, and the combination of information from the two ends of the spectrum very powerful. Taken with the fact that both PEEM and VPPEM have higher spatial resolution and much stronger signals at lower energies, there seems to be a case for combining HAXPES imaging with low electron-energy X-ray photoelectron spectroscopic imaging (LEEXPES) and with the extended probing depth of core-edge yields using high energy photons.

19.3 Photoelectron Microscopes

We are limiting our discussion to the low-energy full-field imaging photoelectron microscope of which there are two distinct types. The first type is based on the electrostatic cathode lens arrangement developed by Bauer [29] as the low-energy electron microscope (LEEM), and later authors as the photoelectron emission microscope (PEEM). The second is the magnetic-field type recently developed by Browning [4], the vector potential photoelectron microscope (VPPEM).

The PEEM type of microscope has been extremely successful, and it has developed into a wide range of powerful instruments. This development is still continuing with instruments becoming more and more sophisticated. Improvements over the last 50 years have included correction for chromatic and spherical aberration [2], and correction for angular dispersion in the energy analyzer [19]. Typically we can expect photoelectron imaging from PEEM in the 10–100 nm range, with imaged electrons in the 1–50 eV range. Contrast mechanisms include partial-yield absorption spectra, magnetic-dichromic imaging, and work-function changes. With improvements in electron optics it may be possible to image below 10 nm but there are some unknowns such as the effects of space charge [22]. The type of sample is somewhat limited as the sample is part of the electron optics of the cathode lens, and must necessarily be a good conductor, flat with little or no roughness.

VPPEM is still in its early stage of development, and as this is relatively unknown technique we will give an introduction to the instrument here. VPPEM uses the magnetic vector-potential field as a spatially resolved reference for image formation. A magnet with a uniform field region, such as a solenoid, is used to create a cylindrically symmetric vector-potential field which acts as a two

dimensional reference. The sample to be imaged is immersed in the center of the field, and illuminated by a UV or X-ray photon beam. The resultant photoelectrons are emitted into the vector-potential field, and travel down magnetic field lines in cyclotron orbits towards a ferromagnetic shield with an aperture. When the photoelectrons leave the vector-potential field by passing through the aperture in the ferromagnetic shield, the momentum in the magnetic field (the vector potential) is conserved, and forms an angular image of the electron emission. The photoelectrons have chemical information from the sample in the electron-energy spectrum and two dimensional spatial information from the magnetic vector-potential field. The resulting angular electron image can be passed through an electron energy analyzer to produce a photoelectron spectroscopic (PES) image.

We can illustrate the mechanics of VPPEM image formation with a simulation of the exit of electron trajectories from a simple magnetic circuit. Figure 19.3 shows a magnet set in a soft iron yoke with a tapered aperture for the exit of electrons from the field. The magnetic axis is rotationally symmetric around the horizontal axis. The volume near the magnet face has a constant magnetic field, and therefore the vector-potential field is a radially increasing circular vector field.

Figure 19.3 shows a set of electron trajectories which begin at equally spaced radial points just off the axis near the pole piece. The electron trajectories initially travel along parallel to the optical axis, and are constrained into a narrow beam by the magnetic field lines near the axis. There is a small magnification of the radial distances as the magnetic field weakens moving away from the pole piece. When the electrons exit the field through the aperture, they leave the field lines, and become deflected away from the axis by the change in the vector potential. The deflection produces an angular distribution dependent on the initial radial distribution in the vector potential field.

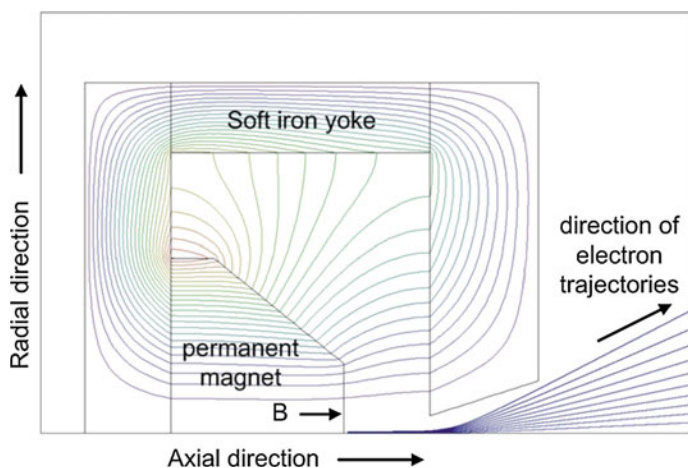

Fig. 19.3 Electron trajectories in a magnetic circuit composed of a permanent magnet in a ferromagnetic yoke with a tapered aperture from [5]

Only the radial distances are plotted in Fig. 19.3, the electron trajectories are rotated out of the plane of the diagram. The simulation shows the deflection angles are proportional to the radial positions at the origin for small and moderate angles.

If the electron trajectories are emitted at an angle relative to the magnetic axis they follow cyclotron orbits around the field lines until they exit the aperture where they are deflected into a final direction.

In the VPPEM, electrons of all energies from a sample are deflected into an angular image by the change in vector potential at the aperture. The angular image can be converted into a monochromatic real image focused at an image plane. Figure 19.4 illustrates the electrostatic elements needed. Diverging electron trajectories exiting the ferromagnetic aperture are focused into a concentric hemispherical analyzer (CHA) by a condenser lens. After energy analysis by the CHA, which is double focusing, the diverging monochromatic image is focused onto an image plane and an image detector.

The electron optics of the VPPEM produces major differences between how the microscope operates and the PEEM, or indeed many other types of electron microscope. It should be noted that the object and the image are not at conjugate planes. The microscope in effect does not image the object but rather the radial change in the vector-potential field. As the vector-potential field is cylindrical along the solenoid axis, the depth of field is very large, up to a centimeter in the proof-of-principle instrument [4]. This is clearly valuable for many samples with large topographic features.

The spatial resolution is determined by maximum radial size of the electron cyclotron orbits at the sample. The maximum radial size is for electrons leaving the sample surface at 90° to the field direction and depends on the energy of the electrons at the sample and the strength of the magnetic field. The point spread function (PSF) is shown in Fig. 19.5. As can be seen the PSF has a sharp central needle like part (aculeate) and a wide halo that stretches out to twice the maximum

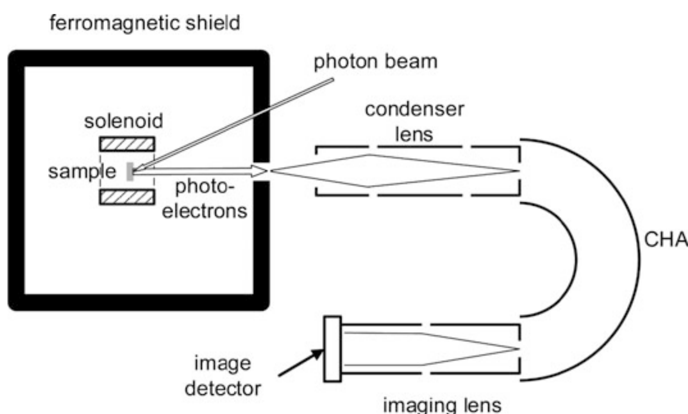

Fig. 19.4 Schematic of the VPPEM electron optics

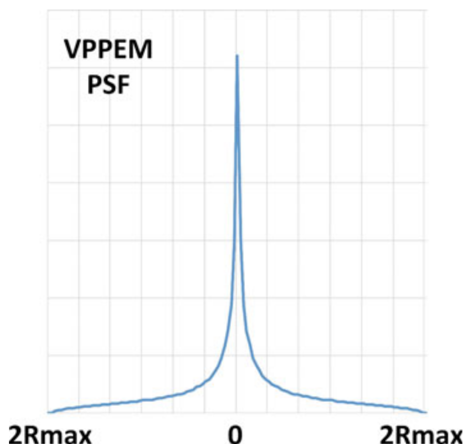

Fig. 19.5 VPPEM point spread function (PSF). This function is symmetric around the axis with a sharp central peak, but with 50 % of the signal at greater than 1 Rmax

radius. The halo dominates the edge resolution, and a good approximation to the resolution defined as the 20–80 % signal change measured over an edge is $3\sqrt{E}/B$ microns with E in electron volts and B in Tesla [5].

Electrons can be accelerated or decelerated within the magnetic field without distorting the image. Very low energy electrons, with energies below 1 eV, can be imaged by accelerating them off the sample to several tens of electron volts before they exit the field. As this gives the highest spatial resolution, and it is also a bulk signal, very low energy imaging is the normal mode of operation. Electrons emitted with 1 eV energy in a 2 T field can be imaged with an edge resolution of 1.5 μ. However, the edge resolution does not represent the achievable resolution of the instrument. Because the VPPEM PSF can be confidently calculated from the imaging conditions, recovery of a sharper image by image deconvolution is possible using this information. The Richardson-Lucy (RL) deconvolution method has been shown to be very successful for low contrast VPPEM images [30], and it has been adapted for multispectral imaging to provide over 10 times better spatial resolution than the basic edge resolution.

19.4 Low Energy Electron Mean Free Paths

To fully justify the low energy microscopy approach, and for it to become valuable in conjunction with high energy imaging, we need much more information about the electron mean free path. There is sufficient knowledge about low-energy electron MFP's to see how this region of the spectrum might start to be used. However, unlike high-energy MFP's where universal curves [9, 10] give a good guide for energies above 100 eV, for low energies, experimental data seems to be the most reliable source. There are large differences in low-energy MFP's depending on the details of the electronic structure near the Fermi level. Free-electron theory can give trends at

low energies [31, 32], but for calculations to be useful they must take the band structure of the material into account [33]. For example, the electron MFP for ytterbium 5–10 eV above the Fermi level is 1–2 nm [34], while for aluminum the MFP is 5–10 nm [35]. A big difference between ytterbium and aluminum is that ytterbium has a loss channel close to the Fermi level in the core 4*f* transitions [36].

The experimental data on low energy MFP's comes from a variety of sources; these include ultra-violet photoemission [37], ballistic-electron spectroscopy [38], and energy-loss spectroscopies in solids and gasses [39–43]. While much of this data is somewhat isolated at present, there is no real impediment to collecting it together for use with microscopy. Although putting the data together does not give the universal curves of higher energies, it does tell us that imaging of electrons within a few eV of the Fermi level in solids and between 0.5–2 eV in gases renders MFP's that are often comparable to those in the 2–10 keV HAXPES range. Further, these MFP's scale in a useful way with energy so that they can in principle be used for depth profiling as with HAXPES spectroscopy. Significant synergies could exist between data from high accuracy HAXPES depth profiles and high spatial resolution depth estimates from LEEXPES.

19.5 Low Energy Photoelectron Signal Sources

The information in low-energy electron spectromicroscopy images can originate from a number of signal sources. If we add this to high-energy image data it becomes very complex. While some of this information may be useful, other information may be noise and an impediment to a simple measurement of elemental spatial distributions. Some of the desired information such as chemical shifts may make image registration across a wide data range challenging, but as will be demonstrated below the strong signal can be used to make detailed and informative images.

The LEEXPES signal, besides having elemental and chemical content, may be sensitive to differential surface charging, surface topography, magnetic-substrate effects, and/or sample bias. In particular the spatial resolution may be dependent on the surface topography as is the case for cathode lens-based photoemission electron microscopy (PEEM) [44], although the VPPEM image contrast is less sensitive to many of these effects. If the photon illumination is not normal to the surface, there will also be some illumination and emission shadowing on rough surfaces. Roughness will also generate changes in the effective penetration depth of the X-rays with variations in the local angle of incidence to the sample surface normal.

In general, the LEEXPES signal will be a two dimensional spectral signal derived from both the secondary effect of X-ray absorption such as the core-edge absorption yield, and also the directly emitted photoelectrons [45, 46]. This information is mixed with the other contrast effects. The two dimensions in the LEEXPES signal are photon energy and detected electron energy. The LEEXPES signal will also consist of several spectral regions covering different core excitations. The LEEXPES signal is therefore a hyperspectral signal. When we are discussing imaging, our

initial analytic emphasis is towards signal processing. The first aim is to create and then partition an image into regions of interest using the structure of the hyper-spectral signal as a guide. Introducing imaging to photoelectron spectroscopy in this way tends to use the concepts of signals rather than spectra. This is because the underlying photoelectron spectral information, core level excitation, chemical state, and coordination, are mixed in with other contrast mechanisms. Therefore, our description will depart somewhat from conventional spectroscopy terms to describe this emphasis.

The LEEXPES signal consists of the absorption-yield signal and the photo-emission peak closely mixed together. Figure 19.6 illustrates these sources of the LEEXPES signal in a schematic photoelectron-emission energy-level diagram. This illustration is particular for VPPEM which uses a biased sample to set the energy of the detected electrons, but it is also relevant to the interpretation of PEEM data at very low energies where the analyzing energy is scanned and very similar results are obtained [47]. In Fig. 19.6 the vertical direction is energy, and the horizontal direction represents distance out of the sample surface. Figure 19.6 illustrates the case of an aluminum sample with an oxidized surface. The metal is on the left, and the VPPEM microscope is on the right.

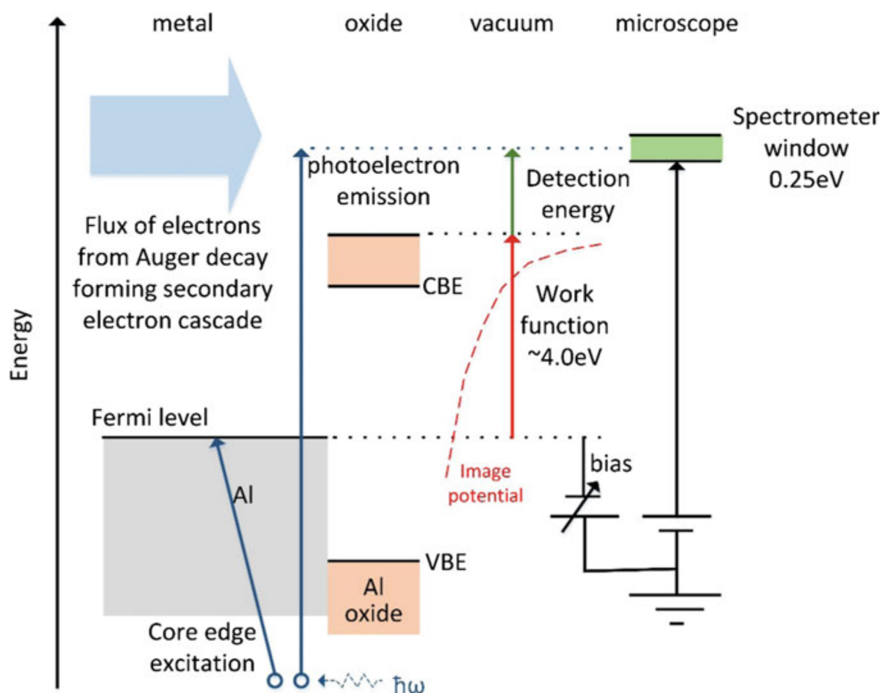

Fig. 19.6 Energy-level diagram of the VPPEM signals from an oxidized aluminum surface, from [28]

The sample is irradiated by X-ray photons, and if a photon, ħω, has sufficient energy it can create a core hole in the metal by removing an electron in a core state to an empty state above the Fermi level. In the case of an insulating oxide, the core electron is removed to the conduction band edge (CBE). We expect, in theory, the Fermi level in the oxide to be midway between the conduction-band edge and the top of the valence band (VBE) [48]. The photoelectron transitions in Fig. 19.6 are indicated by the blue vertical arrows beginning with a circle to represent the core-hole remaining. Only the aluminum metal transitions have been shown. After the initial photoelectron event, the remaining core hole is filled with an electron from a higher-energy level, and this initiates an Auger cascade. The Auger cascade creates a flux of inelastically scattered electrons over a wide energy range. These electrons form the secondary electron distribution when they leave the sample. The increase in the number of secondary electrons as the photon energy is swept from a low energy up across the core-absorption energy is detected by the spectrometer as a PAY NEXAFS signal with a prominent feature at the core-edge absorption energy.

As the photon energy is raised to several eV above the core absorption energy, the directly excited photoelectron, the XPS electron, ejected from the aluminum metal core can escape the surface directly. The directly emitted electron must have a kinetic energy in the solid that is greater than the workfunction. An aluminum metal photoelectron also has to travel through the oxide overlayer without being absorbed. If the potential bias of the sample has been set so that the energy of the directly excited electron in the vacuum coincides with the energy window of the spectrometer, then the electron is detected. If the sample bias is fixed and the photon energy is increased, the electron energy will move through the spectrometer window to produce a peak in the spectrometer signal. The photoemission peak will be superimposed on the higher-energy part of the PAY NEXAFS structure because the core edge and the photoemission peak are only a few eV apart.

Figure 19.7 shows a LEEXPES spectrum from a VPPEM. The spectrum is along the photon-energy axis for a fixed detection energy of 0.5 eV. The data are from an oxidized Al surface taken from a spectral image series with photon energies from 72.5 to 85.0 eV in 0.5 eV steps.

In Fig. 19.7 the Al 2*p* metallic-core absorption yield appears at 74.5 eV and the Al 2*p* metallic photoemission peak feature appears at 4.5 eV higher energy at 79.0 eV. The extra 4.5 eV binding energy being the sum of the 4.0 eV workfunction and the 0.5 eV electron-detection energy.

By changing the sample bias, the energy of the detected electrons can be changed, and the photoemission peaks will appear at different photon energies. Changing both the photon energy and the detected energy creates the two dimensional image data set. Spectra taken from an image data set from 65.0 to 95.0 eV in steps of 1.0 eV and with detection energies 1.0, 2.0, 5.0, and 10 eV are presented in Fig. 19.8. The background levels have been suppressed to arrange the individual spectra in the graph.

The spectra in Fig. 19.8a show that there is a 2p absorption edge in the region of 74.5 eV and there are two Al 2p photoemission peaks, the peak originating in the

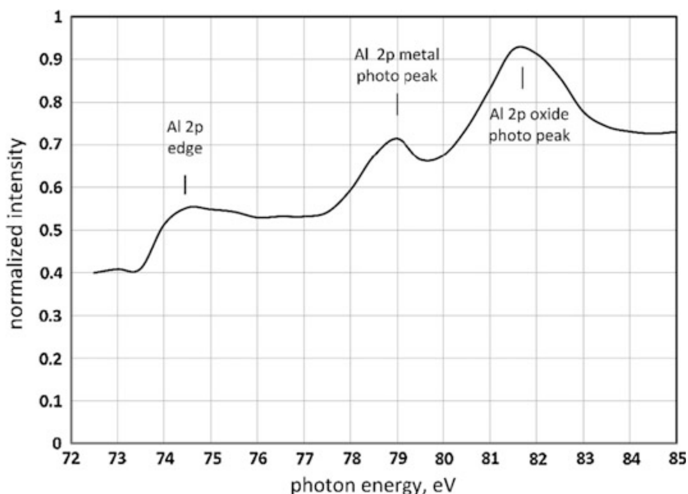

Fig. 19.7 VPPEM spectrum from oxidized aluminum, from [28]

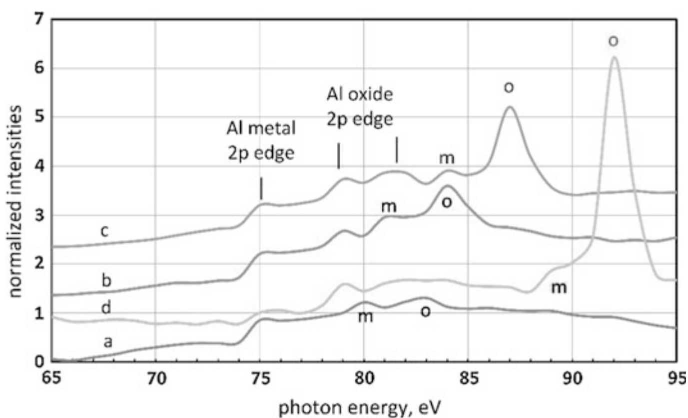

Fig. 19.8 Spectra from an aluminum foil with different detection energies. **a** 1.0 eV, **b** 2.0 eV, **c** 5.0 eV, **d** 10.0 eV. The spectra are shifted in the vertical direction to provide visual separation [28]

metal is indicated by the letter m and the one in the oxide by the letter o. As the detected energy is changed to a higher value (by reducing the sample bias) the two Al 2p photoemission peaks, m and o, move together to higher photon energy and get relatively larger.

As the Al metal 2p photoemission peak moves higher in energy with a higher detection energy, a further feature appears with a peak at 79.0 eV, just below the initial metal photo-peak position at 80.0 and 4.0 eV above the 2p edge. The binding energy of this new feature remains at 79.0 eV as we increase the detection energy to

10.0 eV. There also appears to be a third peak, 3.0 eV higher than the 79.0 eV peak, with the same general characteristics. These two additional features can be identified as Al 2p edges from amorphous aluminum oxide [49].

A clear feature of the spectral series in Fig. 19.8 is the change of relative intensity between the Al metal and the oxide photoemission peaks with detection energy. This change in relative intensity gives us data for depth profiling through changes in attenuation length with detection energy.

The Al 2*p* metal-absorption edge in Fig. 19.8 defines the Fermi-level energy for binding energies above it. This gives a direct measure of the energy above the Fermi energy of the photoelectrons in the aluminum. From the spectral series in Fig. 19.8, we have the Al 2p metal photoemission peaks (m) at 80.0, 81.0, 84.0, and 89.0 eV. The energies in the aluminum are the 5.0, 6.0, 9.0, and 14.0 eV respectively. If the Fermi energies of the oxide and the metal are aligned, we can expect the same energies in the oxide. The Al metal and oxide photoelectrons pass through the same surface potential barrier, with the same final energy, and their energies in the oxide will therefore be the same. At each of the detection energies, the surface barrier reflectivities for the metal and oxide peaks will also be the same.

To model the change in relative intensities between the Al metal and oxide photoemission peaks, we used mean-free paths based on simplified fits to theoretical curves in the literature [50, 51].

Figure 19.9 shows that electron energies in the 5–15 eV range are on the rapidly changing lower part of the curves. This makes relative peak intensities very sensitive to changes in thickness in the nanometer range. For 5.0 eV, the inelastic mean free path in the metal is 4.1 nm, and for 14.0 eV it is 1.7 nm. In the oxide, the mean free paths are 22.2 and 4.8 nm respectively.

The MFP equations ignore elastic scattering and are therefore not practical attenuation lengths. Above 50 eV, elastic scattering reduces the attenuation length

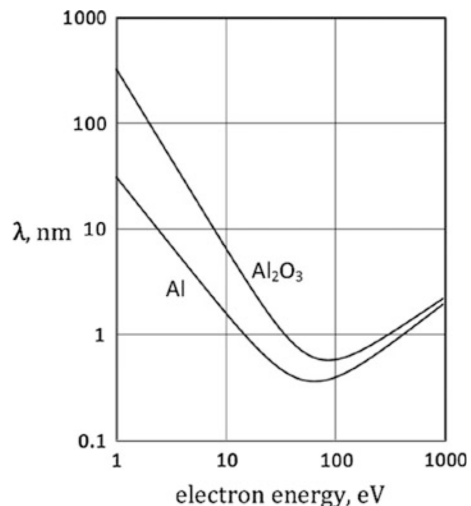

Fig. 19.9 Inelastic mean-free path lengths for electrons in Al and Al_2O_3 from [28] based on [46, 47]

typically by a factor 0.7–0.95 [52]. However, it may be expected that elastic scattering would play a different role at lower energies, changing the shape of the low-energy part of the curves in Fig. 19.9. This complication is passed over, and the factor fixed at 0.8.

There are some differences to the conventional angle-resolved XPS layer-thickness model where the take-off angle is specified [53–55]. The VPPEM collects 2π steradians, so that angles range from 0° to 90° to the (assumed) normal. This collection angle, and the low energy of the electrons add extra details to the model. The model of the emission process uses three processes. The first process is the electron flux travelling to the solid surface. The second process is a refraction and reflection at the surface barrier, where the critical angle limits the angular range of the model in the solid. This angular range changes with detection energy. The third process is the detection of a Lambertian distribution into the 2π solid angle collected by the VPPEM.

The results from Fig. 19.9 are fitted by trial varying overlayer thickness. Figure 19.10 shows the relative peak heights for the Al metal photoemission peaks, P_m, and the Al oxide photoemission peak, P_o, plotted against the energy of the electrons in the solid for an overlayer thickness of 3.5 nm [56].

The fit is normalized to the peak-height ratio at 14.0 eV. It can be seen from Fig. 19.10 that the results for 14.0, 9.0, and 6.0 eV are consistent with the model, but the fit underestimates the lower-energy peak-height ratio. This deviation from the model is outside what would be expected even with errors in the simple peak fitting used; clearly more work is needed to expand our understanding of the method.

Due to the many issues associated with the low-energy mean free path, it is unlikely that LEEXPEM based on either PEEM or VPPEM will ever reach the level of accuracy for depth profiling that is being obtained by angle resolved XPS and HAXPES. However, for VPPEM at least, its insensitivity to many common imaging artifacts gives a significant advantage being able to obtain depth-profile

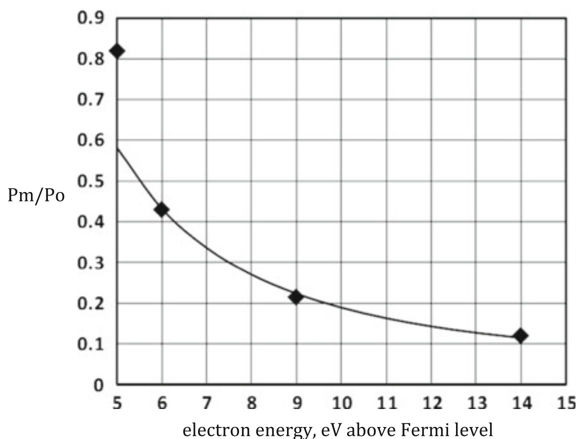

Fig. 19.10 Plot of relative VPPEM photoemission peak heights for the Al metal, P_m, and the Al oxide, P_o. Data points are from experiment, solid line from a model using a 3.5 nm oxide thickness [28]

estimates from uneven surfaces. This would include fibers, fracture surfaces, and recessed features on the nanometer scale. This suggests that low energy VPPEM would be a valuable technique to use in conjunction with data from these other methods.

From the HX-PEEM experiments [14–18] we can see that the information depth can be considerably increased by using hard X-rays and low-energy electron detection. For VPPEM this is an important observation. VPPEM is a technique that will be used for real world problems in the mesoscale range. If the depth of information is restricted to the surface the technique will have less relevance.

19.6 Image Analysis in Photoelectron Microscopy

The HAXPEEM images shown in Figs. 19.1 and 19.2 are only an indication of the information available from photoelectron microscopy. Much more can be achieved. Although there are no good examples of image processing with HAXPEEM, we have an example of using VPPEM in the LEEXPES mode with very low photon fluxes. With this example we can illustrate of the power of image processing in photoelectron microscopy. This example also shows how to combine images across spectral ranges and demonstrates that, even with the low signal levels expected from HAXPEEM, rich image data can be finessed.

In principle, LEEXPES has larger signals for imaging than does HAXPES. However, the low-energy signal is inherently more complex, and this in effect adds noise to the signal. But for both the low-energy and the high-energy signals, the possibility of recovering detailed information from noisy data by application of hyperspectral image data reduction has been demonstrated [57].

As we have indicated, using very low-energy photoelectrons for imaging raises many issues of signal interpretation. At very low energies, there are many specific surface effects to be considered in interpreting the signal. These include effects due to the surface image potential, changes in work function, local charging, and contamination. The image potential can lead to surface states that cause significant changes in transmission across the surface barrier as the take-off energy is changed. However, many of these effects will be somewhat averaged out because both the VPPEM and PEEM collect 2π steradians of the emitted electrons at low energies. Changes in workfunction across the sample will lead to a change in energy of the detected photo peak and also the inelastic mean-free path of the photoelectron. Thus, the issues of information depth and chemical state are factors that can be mixed together when considering image interpretation.

Imaging at low-electron energies with both PEEM and VPPEM on well characterized surfaces is effective because the signals are strong, and the microscopes collect 100 % of the signal. PEEM on an undulator beam line can image at video rates with 10’s of nanometer spatial resolutions. This would also be expected of VPPEM which up to now has only been used on a bending-magnet beamlines. While PEEM is not normally used for imaging specifically at electron energies at or

below 1.0 eV, the direct imaging of work function changes using these energies is possible [47]. VPPEM on the other hand has the highest spatial resolution at very low energies, and thus imaging at or below the secondary-peak maximum is the normal imaging mode.

Hyperspectral imaging is accomplished by scanning either the photon energy or the analysis energy, or both, over several spectral features of interest, and collecting a stack of images at a step size relevant to the problem. The resulting image stack may contain from 10's to 1000's of images. Even with fairly coarse step sizes and poor counting statistics, good quality images can be extracted, and contrast mechanisms separated out. The left-hand side of Fig. 19.11 shows part of a VPPEM image stack of a calcium/aluminum alloy after annealing [30]. The calcium/aluminum alloy is a distortion-strengthened alloy that has potential in high conductivity, self-supporting overhead electrical transmission lines. Overheating of the alloy causes the Ca and Al to react and form a range of intermetallics [58].

The VPPEM detection energy used for the images of Fig. 19.11 was 1.0 eV, and thus the electron energy above the Fermi level is approximately 5.0 eV. Therefore, we can expect the information depth to be greater than 1–2 nm, and the image visualizes more of the bulk alloy than the surface. The complete image stack was over two spectral ranges of photon energy. These ranges are 20–45 and 70–90 eV covering the Ca 3*p* and the Al 2*p* core levels with 1 eV step size. Normalized spectra from the complete image stack are shown on the right-hand side of Fig. 19.11. These spectra are obtained iteratively from different areas in the image stack with the aim of isolating the most different spectra, the endpoint spectra. The two most different spectra were determined for the image stack, and these are shown as the red and blue spectra, the endpoint spectra E1 and E2 in Fig. 19.11. These spectra are treated as signals, not photoelectron spectra, and they are uncorrected for the beamline monochrometer function which has broad peaks at 30 and 80 eV.

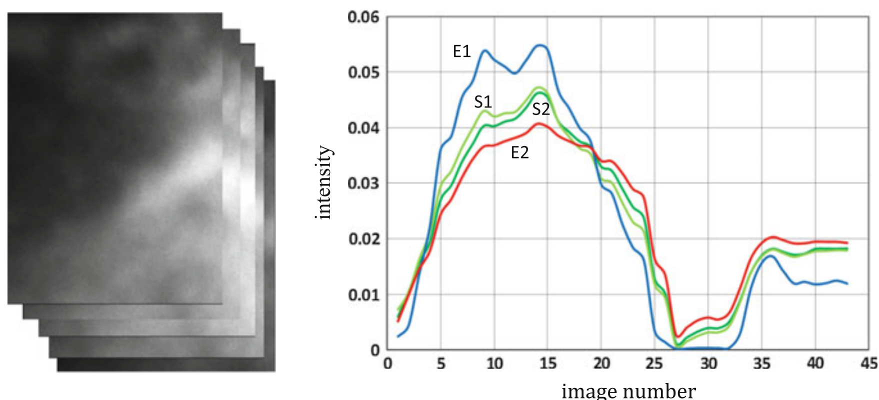

Fig. 19.11 VPPEM hyperspectral image stack and endpoint spectra [54]

Difference images were created using the endpoint spectra that measured the similarities of the images to the two end-point spectra. This was accomplished by a root-mean-square (RMS) comparison of each individual pixel spectrum with the E1 and E2 spectra. The image intensities are a linear function of fitting error, bright areas are a good fit to the spectra and dark areas a poor fit. Just the lower half of the spectra were used because of the difficulty of accurate image registration across the complete image stack.

Figure 19.12 shows the RMS endpoint images and scatter diagram. On the left (a) and (b) endpoint images E1 and E2. Images Fig. 19.12c, d are the endpoint images after 50 iterations of the Richardson-Lucy deconvolution [59, 60] using the theoretical VPPEM point-spread function [5]. A scatter diagram can be created from the deconvoluted endpoint images, and this is shown on the right of Fig. 19.12. The images E1 and E2 are largely anticorrelated so that the scatter diagram can be rotated 45° in the plane of the diagram, and a histogram can be taken across the long axis of the distribution. This histogram is shown below the scatter diagram.

The sample is complex, with at least nine different features in the field of view. By isolating smaller areas, it can be shown that there are six distinct features that represent the Ca and Al with four intermetallics across the compositional phase diagram. These features can be isolated by dividing up the histogram, and Fig. 19.13 shows the VPPEM image derived from this histogram. The four different intermetallics and the Ca and Al are shown as a six color false-color image. While

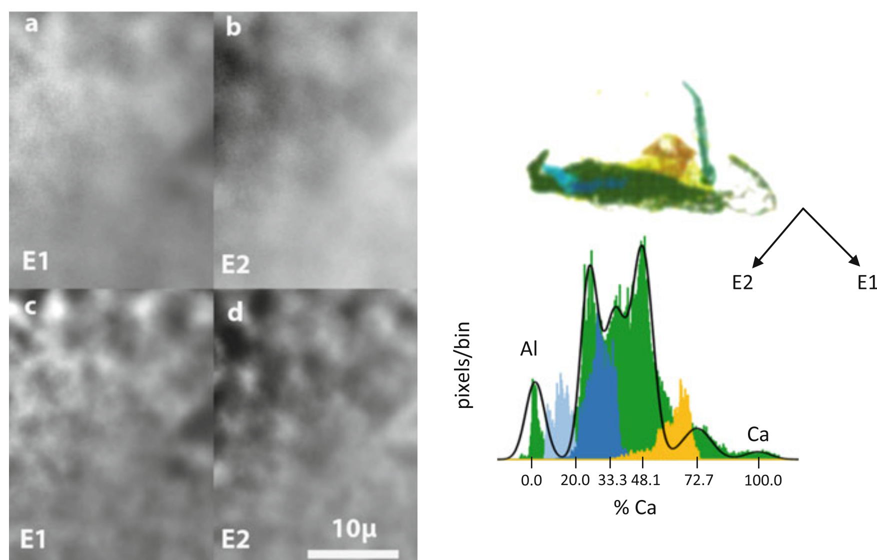

Fig. 19.12 Endpoint images and scatter diagram. On the *left* **a** and **b** endpoint images E1 and E2, **c** and **d** endpoint images after Lucy-Richardson deconvolution. On the *right* scatter diagram and histogram from images (**c**) and (**d**) [54]

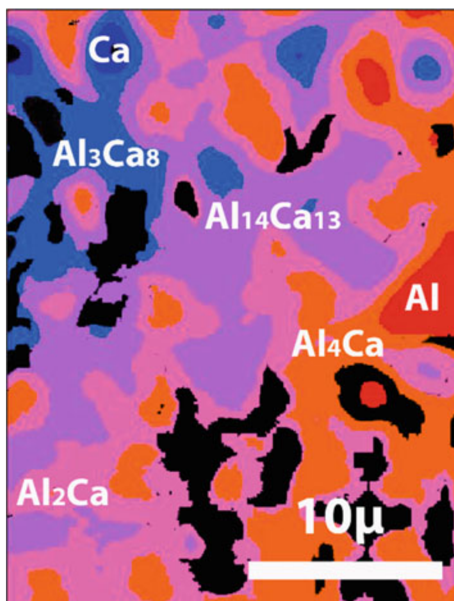

Fig. 19.13 Endpoint hyperspectral image of the reaction zones between Ca and Al [54]

Fig. 19.13 shows the Al–Ca intermetallics, there are other features that are a consequence of the distortion processing of the alloys. These additional features include voids and probably several of the many mineral phases with carbon and oxygen. Beamline U4A, where the data were taken, could not reach these additional core levels so they are shown as black areas in Fig. 19.10.

An important benchmark is that beamline U4A is a UV bending-magnet source, and the photon flux was only 10^3–10^4 photons/s/μ^2. This flux is quite low for photoelectron microscopy, yet highly detailed image data was recovered using hyperspectral image processing methods. With the current instrument using a 1.8 Tesla (T) field with 1.0 eV electrons and 2 s per image over a 25 image stack, a 0.12 μ resolution was obtained after Richardson-Lucy deconvolution.

This example demonstrates that HAXPES hyperspectral-imaging signal levels would likely be sufficient to present information-rich content, and they could also be combined with LEEXPES in an image stack. Hyperspectral imaging is effective for the analysis of complex multiphase materials because the signal-to-noise in the image can be thought of as being due to the volume of the data compared to the noise. Thus the signal-to-noise in each independent signal axis is multiplicative, not additive [61].

The current VPPEM is a prototype. Improvements can be made in both the instrumentation and the data collection. The 1.8 T field can be increased to 20 T with currently available magnets, and from our current benchmark this would imply a 10 nm resolution. This resolution would only require a factor 100 increase in brightness. We will be moving the instrument to NSLS II 7ID where the photon flux will be increased by six orders of magnitude at the NIST Soft and Tender

beamlines [62]. Also the photon-energy range (presently 20–45 eV, 65–90 eV) will be considerably extended from 100 to 7.5 keV. The imaging energy can be decreased to 0.25 eV, and an order of magnitude more data can be collected. These improvements will take the spatial resolution into the low 10's of nanometers, and LEEXPES and HX-VPPEM will be combined in the same data sets. The concept set out here for fusion between LEXPES and HX-PPEM can then be directly tested.

19.7 Conclusion

From the recent results from different photoelectron microscopes, a new synthesis is possible that includes four new developments. The first development is the proof-of-principle experiments with HAXPES microscopy, the second is the development of a new imaging photoelectron microscope, the third is new methods in image processing, and the fourth is the development of beamlines with a wide photon-energy range at third generation synchrotrons. While many of the high-energy microscopy experiments have been proof of principle demonstrations, the basis for developing a new microscopy has been firmly established. It is also important that LEEXPES and HAXPES can be combined in one instrument. Such an instrument will collect a wide range of spectroscopic information at one time, and the advantages of using hyperspectral methods and data fusion can be exploited.

With the technical basis for HAXPES imaging in place, what remains is to find the application driver for the technology to push it forward. Mesoscale analysis appears to be a natural fit, and there is a need for instrumentation in this area that can give detailed chemistry and coordination in complex materials.

The several versions of hard X-ray microscopy discussed here have different attributes. The direct high-energy photoelectron HAXPEEM imaging approach promises the highest spatial resolution, possibly down to 10 nm, but the HX-PEEM/VPPEM promises faster, more convenient imaging with LEEXPES imaging providing higher resolution from image fusion. VPPEM imaging also promises analysis of 3D-mesoscale structures with uneven features and conductivities.

In summary, recent developments in instrumentation and techniques are opening up the world of photoelectron microscopy to include HAXPES, and exciting advances in the near future will form a vital part of the tool set for materials analysis at the mesoscale.

References

1. G. Crabtree, J. Sarrao, P. Alivisatos, W. Barletta, F. Bates, G. Brown, R. French, L. Greene, J. Hemminger, M. Kastner, et al., From quanta to the continuum: opportunities for mesoscale science (2012). http://science.energy.gov/~/media/bes/pdf/reports/files/OFMS_rpt.pdf
2. E. Bauer, Rep. Prog. Phys. **57**, 895 (1994)

3. E. Bauer, J. Electron Spectrosc. Relat. Phenom. **185**, 314 (2012)
4. R. Browning, Rev. Sci. Instrum. **82**, 103703 (2011)
5. R. Browning, Rev. Sci. Instrum. **85**, 033705 (2014)
6. H. Mimura, S. Matsuyama, H. Yumoto, H. Hara, K. Yamamura, Y. Sano, M. Shibahara, K. Endo, Y. Mori, Y. Nishino, K. Tamasaku, M. Yabashi, T. Ishikawa, K. Yamauchi, Jpn. J. Appl. Phys. **44**, L539 (2005)
7. M. Suzuki, N. Kawamura, M. Mizumaki, Y. Terada, T. Uruga, A. Fujiwara, H. Yamazaki, H. Yumoto, T. Koyama, Y. Senba, T. Takeuchi, H. Ohashi, N. Nariyama, K. Takeshita, H. Kimura, T. Matsushita, Y. Furukawa, T. Ohata, Y. Kondo J. Ariake, J. Richter, P. Fons, O. Sekizawa, N. Ishiguro, M. Tada, S. Goto, M. Yamamoto, M. Takata, T. Ishikawa, J. Phys. Conf. Series **430**, 012017 (2013)
8. Y. Terada, S. Homma-Takeda, A. Takeuchi, Y. Suzuki, X-ray Optics. Instrum. **2010**, 317909 (2010)
9. K. Horiba, Y. Nakamura, N. Nagamura, S. Toyoda, H. Kumigashira, M. Oshima, K. Amemiya, Y. Senba, H. Ohashi, Rev. Sci. Instrum. **82**, 113701 (2011)
10. R.P. Winarski, M.V. Holt, V. Rose, P. Fuesz, D. Carbaugh, C. Benson, D. Shu, D. Kline, G.B. Stephenson, I. McNulty, J. Maser, J. Synchrotron Radiat. **19**, 1056 (2012)
11. C.J. Powell, A. Jablonski, Nuc. Instum. Method. Phys. Res. **A601**, 54 (2009)
12. M.P. Seah, Sur. Interface Anal. **44**, 497 (2012)
13. Y. Hwu, W.L. Tsai, B. Lai, J.H. Je, G.H. Fecher, M. Bertolo, G. Margaritondo, Surf. Sci. **480**, 188 (2001)
14. H. Yasufuku, H. Yoshikawa, M. Kimura, K. Ito, K. Tani, S. Fukushima, Suf. Int. Analy **36**, 892 (2004)
15. T. Wakita, T. Taniuchi, K. Ono, M. Suzuki, N. Kawamura, M.I. Takagaki, H. Miyagawa, F. Guo, T. Nakamura, T. Muro, H. Akinaga, T. Yokoya, Jpn. J. Appl. Phys. **45**, 1886 (2006)
16. T. Taniuchi, T. Wakita, M. Takagaki, N. Kawamura, M. Suzuki, T. Nakamura, K. Kobayashi, M. Kotsugi, M. Oshima, H. Akinaga, H. Muraoka, K. Ono, AIP Conf. Proc. **897**, 1353 (2007)
17. T. Kinoshita, E. Ikenaga, J. Kim, S. Ueda, M. Kobata, J.R. Harries, K. Shimada, A. Ino, K. Tamasaku, Y. Nishino, T. Ishikawa, K. Kobayashi, W. Drube, C. Kunz, Sur. Sci. **601**, 4754 (2007)
18. M. Kotsugi, T. Wakita, T. Taniuchi, H. Maruyama, C. Mitsumata, K. Ono, M. Suzuki, N. Kawamura, N. Ishimatsu, M. Oshima, Y. Watanabe, M. Taniguchi, IBM J. Res. Dev. **55**, 13 (2011)
19. C. Wiemann, M. Patt, S. Cramm, M. Escher, M. Merkel, A. Gloskovskii, S. Thiess, W. Drube, C.M. Schneider, Appl. Phys. Lett. **100**, 223106 (2012)
20. C.M. Schneider, C. Wiemann, M. Patt, V. Feyer, L. Plucinski, I.P. Krug, M. Escher, N. Weber, M. Merkel, O. Renault, N. Barrett, J. Elec. Spectros. Relat. Phenom. **185**, 330 (2012)
21. S. Tanuma, C.J. Powell, D.R. Penn, Surf. Interface Anal. **43**, 689 (2011)
22. T. Schmidt, A. Sala, H. Marchetto, E. Umbach, H.J. Freund, Ultramicroscopy **126**, 23 (2013)
23. http://www.spring8.or.jp/pdf/en/ann_rep/98/P67-68.pdf
24. Z. An, Z. Shi, Optik **125**, 3150 (2014)
25. R.A. Schowengerdt, *Remote Sensing,* Chap. 8, 355 (Academic Press, Waltham, 2007)
26. K. Artyushkova, J.O. Farrar, J.E. Fulghum, Surf. Interface Anal. **41**, 119 (2009)
27. J. Sui, T. Adali, Q. Yu, V.D. Calhoun, J. Neurosci. Methods **204**, 68 (2012)
28. R. Browning, J. Elec. Spectros. Relat. Phenom. **195**, 125 (2014)
29. E. Bauer, in *Proceedings of the Fifth International Congress on Electron Microscopy, Philadelphia*, vol. 1, ed. by S.S. Besse Jr (Academic, New York, 1962) D 11
30. R. Browning, Surf. Interface Anal. **47**, 63 (2015)
31. J.J. Quin, Phys. Rev. **126**, 1453 (1962)
32. D.R. Penn, Phys. Rev B **35**, 482 (1987)
33. V.M. Silkin, E.V. Chulkov, P.M. Echenique, Phys. Rev. B **68**, 205106 (2003)
34. F. Offi, S. Iacobucci, L. Petaccia, S. Gorovikov, P. Vilmercati, A. Rizzo, A. Ruocco, A. Goldoni, G. Stefani, G. Panaccione, J. Phys. Condens. Matter **22**, 305002 (2010)

35. H. Kanter, Phys. Rev. B **1**, 522–536 (1970)
36. V. P. Zhukov, E.V. Chulkov, P.M. Echenique, A. Marienfeld, M. Bauer, M. Aeschlimann, Phys. Rev. B **76**, 193107 (7007)
37. P. Jiricek, M. Cukr, I. Bartos, J. Sadowski, Sur. Sci. **566–568**, 1196 (2004)
38. A. Bauer, M.T. Cuberes, M. Prietsch, G. Kaindl, J. Vac. Sci. Technol. B **11**, 1584 (1993)
39. S. Hino, N. Sato, H. Inokuchi, Chem. Phys. Lett. **37**, 494 (1976)
40. F. Offi, S. Iacobucci, P. Vilmercati, A. Rizzo, A. Ruocco, A. Goldoni, M. Sacchi, G. Panaccione, Phys. Rev. B **77**, 201101 (2008)
41. Y. Ozawa, Y. Nakayama, S. Machida, H. Kinjo, H. Ishii, J. Elec, Spectros. Relat. Phenom. **197**, 17 (2014)
42. G.K.L. Marx, P.-O. Jubert, A. Bischof, R. Allenspach, Apppl. Phys. Let **83**, 2925 (2003)
43. K. Fedus, G.P. Karwasz, Z. Idziaszek, Phys. Rev. A **88**, 012704 (2013)
44. S.A. Nepijko, N.N. Sedov, G. Schönhense, M. Escher, X. Bao, W. Huang, Ann. Phys. **9**, 441 (2011)
45. A. Bianconi, R.Z. Bachrach, S.A. Flodstrom, Solid State Comm. **24**, 539 (1977)
46. A. Bianoconi, R.Z. Bachrach, Phys. Rev. Let. **42**, 104 (1979)
47. S.L. Christensen, B.M. Haines, U.D. Lanke, M.F. Paige, S.G. Urquhart, IBM J. Res. Dev. **55**, 5 (2011)
48. E.G. Kim, J.L. Brédas, Org. Electron. **14**, 569–574 (2013)
49. A.N. Buckley, A.J. Hartmann, R.N. Lamb, A.P.J. Stampfl, J.W. Freeland, I. Coulthard, Surf. Interface Anal. **35**, 922–931 (2003)
50. S. Tanuma, C.J. Powell, R. Penn, Surf. Interface Anal. **37**, 1–14 (2005)
51. B. Ziaja, R.A. London, J. Hajdu, J. Appl. Phys. **99**, 33514 (2006)
52. M.P. Seah, I.S. Gilmore, Surf. Interface Anal. **31**, 835–846 (2001)
53. S. Hajati, S. Tougaard, Anal. Bioanal. Chem. **396**, 2741–2755 (2010)
54. S. Oswald, R. Reiche, M. Zier, S. Baunack, K. Wetzig, App. Sur. Sci. **252**, 3–10 (2005)
55. S. Tougaard, J. Elect. Spect. Relat. Phenom. **178**, 128–153 (2010)
56. B.R. Strohmeier, Surf. Interface Anal. **15**, 51–56 (1990)
57. C.-I. Chang, *Hyperspectral Data Processing: Algorithm Design and Analysis*, Chap. 11 (Wiley, New York, 2013)
58. L. Tian, H. Kim, I. Anderson, A.M. Russell, Mat. Sci. Eng. A **570**, 106 (2013)
59. L.B. Lucy, Astron. J. **79**, 745 (1974)
60. W.H. Richardson, JOSA **62**, 55 (1972)
61. R. Browning, Surf. Interface Anal. **1993**(20), 495 (1993)
62. R. Reininger, J.C. Woicik, S.L. Hulbert, D.A. Fischer, Nucl. Instrum. Meth. Phys. Res. A **649**, 49 (2011)

Chapter 20
Femtosecond Time-Resolved HAXPES

Lars-Philip Oloff, Masaki Oura, Ashish Chainani and Kai Rossnagel

Abstract The problems, progress, and prospects of time-resolved hard X-ray photoelectron spectroscopy (TR-HAXPES) using X-ray free-electron laser (XFEL) radiation are discussed. This novel photoemission technique is characterized by a unique combination of femtosecond time resolution and bulk sensitivity with momentum selectivity and sensitivity to the atomic site-specific chemical and structural environment. TR-HAXPES will in particular enable us to simultaneously study the ultrafast electron and structural dynamics in the bulk of complex materials and electronic devices.

20.1 Introduction

Photoelectron spectroscopy in the extreme ultraviolet and soft X-ray spectral region (hν ≈ 20–2000 eV) comprises a powerful arsenal of tools for the comprehensive characterization of the chemical, structural, and electronic properties of solid *surfaces*. X-ray photoelectron spectroscopy (XPS) reveals the chemical identity and state of the atoms present, X-ray photoelectron diffraction (XPD) provides information on the local geometrical arrangement of the atoms, and angle-resolved photoelectron spectroscopy (ARPES) directly measures the energy and momentum distribution of the electrons dispersing in the atomic lattice [1]. The characterization

L.-P. Oloff · K. Rossnagel (✉)
Institute of Experimental and Applied Physics, University of Kiel, 24098 Kiel, Germany
e-mail: rossnagel@physik.uni-kiel.de

L.-P. Oloff
e-mail: oloff@physik.uni-kiel.de

L.-P. Oloff · M. Oura · A. Chainani · K. Rossnagel
RIKEN Spring-8 Center, Sayo-Cho, Hyogo 679-5148, Japan
e-mail: oura@spring8.or.jp

A. Chainani
e-mail: chainani@spring8.or.jp

© Springer International Publishing Switzerland 2016

J.C. Woicik (ed.), *Hard X-ray Photoelectron Spectroscopy (HAXPES)*,
Springer Series in Surface Sciences 59, DOI 10.1007/978-3-319-24043-5_20

of the surface electronic structure of a material without time resolution, however, can only be a first step in understanding the properties of a material. For a more complete understanding, we also need to elucidate the non-equilibrium electron dynamics in the bulk or at buried interfaces that gives rise to the functioning of complex materials or electronic devices, respectively.

Two recently developed advances in the technique of photoelectron spectroscopy separately address the two aspects of this problem. On the one hand, as extensively discussed in this book, hard X-ray photoelectron spectroscopy (HAXPES) carried out at incident photon energies in a range of about 2–15 keV offers the required bulk sensitivity with probing depths up to several 10 nm. On the other hand, time-resolved photoelectron spectroscopy (TR-PES) using ultrashort photon pulses in a pump-probe approach can directly track electronic and atomic structure dynamics on the femtosecond time scale [2]. Apparently, the combination of these two techniques, i.e., time-resolved HAXPES (TR-HAXPES), may solve the two-faced problem.

In principle, TR-HAXPES provides a unique combination of bulk sensitivity and femtosecond time resolution with element and atomic-site specificity, chemical sensitivity, sensitivity to the local atomic structure, as well as momentum selectivity. The technique can thus enable us to shoot combined bulk electronic and atomic structure movies that capture the motion of electrons in a solid (XPS) and of the atoms themselves (XPD) in real space, as well as the motion of electrons in energy-momentum space (ARPES) on the fundamental time scales of, e.g., electron-electron scattering, electron-lattice coupling, and lattice vibrations.

The well-known layered charge-density-wave (CDW) material 1*T*-TaS_2 may serve as a specific example [3]. TR-HAXPES would permit to simultaneously track and transiently disentangle the three intertwined order parameters of a CDW on the relevant femtosecond time scale: the CDW amplitude as reflected in the splitting of the shallow Ta 4*f* core levels in XPS [4], the amplitude of the Ta atom displacements in the periodic lattice distortion [5] as encoded in the XPD patterns of the deep Ta core levels, and the CDW energy gap in the Ta 5*d* conduction band structure directly visible in ARPES [6]. Such time-resolved and bulk-representative data could, for example, provide unique insights into the mechanism of CDW formation in layered materials, which is still a matter of some controversy [7]. Most importantly, using TR-HAXPES, the combined electronic and structural dynamics could be obtained from the same sample under identical conditions.

In practice, however, the realization of TR-HAXPES will be extremely challenging due to the notoriously low photoionization cross sections at high photon energies and the low repetition rates and fluctuating nature of the ultrashort-pulsed hard X-ray sources currently available. This puts particularly stringent requirements on the photoelectron detection scheme [8, 9].

Here, we first discuss the most important fundamental and practical challenges of TR-HAXPES, namely (i) vacuum space-charge effects, and (ii) use of FEL radiation. We then present first experimental results obtained at the X-ray free-electron laser (XFEL) SACLA that demonstrate the viability of the technique [9–11]. In particular, our results show that it is straightforward to quantify pump

pulse-induced space-charge effects. We conclude with an attempt to assess the prospects of TR-HAXPES using XFELs.

20.2 Challenges

Space-charge effects TR-HAXPES relies on the use of ultrashort photon pulses for pumping and probing of a solid sample. This implies a fundamental limitation: Whenever the absorption of a photon pulse leads to the emission of more than one electron into vacuum, the mutual Coulomb repulsion between the photoelectrons on their passage to the detector can distort the initial kinetic energy and emission angle distribution resulting in a loss of the effective energy and angle (momentum) resolution. The magnitude of these vacuum space-charge effects primarily depends on the density and shape of the emitted electron cloud and the kinetic energy distribution [12, 13]. These vacuum space-charge effects can occur due to the pump and/or the probe photon pulses in any given experiment. Accordingly, in the case of strong pumping, there will actually be two separate photoelectron clouds created: a "slow" one resulting from multiphoton absorption of the optical pump pulse, and a "fast" one generated by the hard X-ray probe pulse [11].

In TR-HAXPES, the pump and probe photon pulses will be short, $\tau < 100$ fs, the surface area from which photoelectrons are emitted will have a characteristic width d of a few 100 μm, and the initial photoelectron velocities v_0 will be in a range of about 10^5–10^8 m/s (corresponding to kinetic energies of 10^{-1}–10^4 eV). Since $d >> \tau v_0$, the photoelectron clouds initially have the shape of a quasi-two-dimensional disk, and the potential energy of an electron in such a charge distribution is proportional to the initial photoelectron density N/d, where N is the number of photoelectrons in the respective electron cloud. As it is this initial potential energy that is converted into the final kinetic energy gain at the detector, the space-charge-induced spectral shift will also be proportional to N/d.

A rough estimate of an acceptable electron density can be obtained as follows. The potential energy of an electron in the center of a homogeneously charged two-dimensional disk is

$$E_{pot} = 6 \times 10^{-6}\,N/d[\mathrm{mm}]\ \mathrm{eV}. \tag{20.1}$$

Thus, if space-charge-induced spectral distortions shall stay below 50 meV, the linear photoelectron density per photon pulse must be limited to fewer than about 10^4/mm.

An important point following from the above is that in typical TR-HAXPES experiments the absolute space-charge-induced energy shifts and broadenings will depend only weakly on the mean photoelectron kinetic energy and the photon pulse duration. So, somewhat counterintuitively, the high photoelectron kinetic energies in TR-HAXPES will not be an advantage. Figure 20.1 shows the results of N-body molecular-dynamics simulations [12, 13] illustrating this point: Upon increasing the

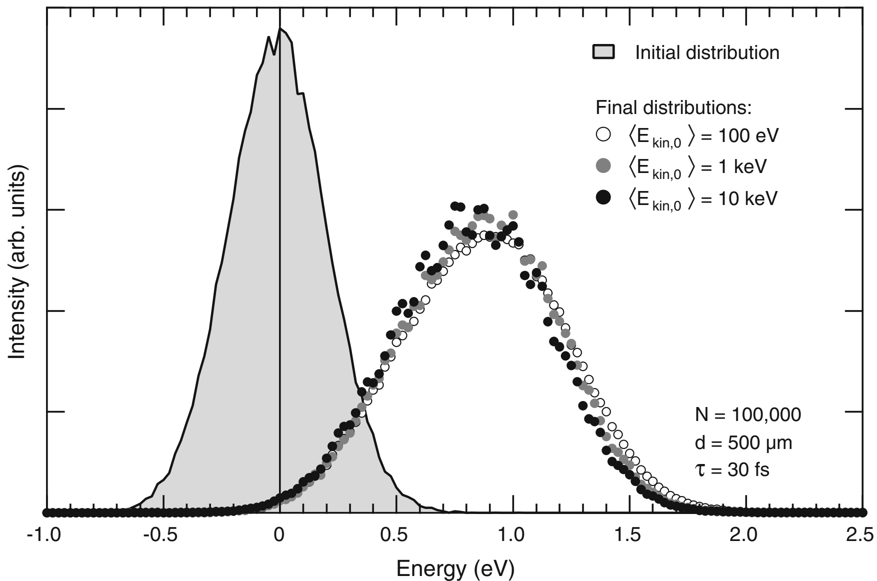

Fig. 20.1 Calculated kinetic energy distributions (*open and filled circles*) of a disk-shaped photoelectron cloud, after expansion due to mutual Coulomb repulsion of the electrons ("Coulomb explosion") in vacuum, as a function of the mean kinetic energy of an initial Gaussian energy distribution (*solid line with gray filling*). The space-charge-induced spectral shift and broadening depend only weakly on the kinetic energy. The key parameters of the numerical simulation are indicated ($\langle E_{kin,0}\rangle$: mean energy of initial Gaussian kinetic energy distribution; N: number of electrons; d: diameter of the circular emission area (FWHM of two-dimensional Gaussian distribution); τ: pulse duration (FWHM of Gaussian-shaped pulse)) [11–13]

mean photoelectron kinetic energy from 10^2 to 10^4 eV, while holding all other simulation parameters constant, the variation in the space-charge-induced energy shift and broadening of a Gaussian energy distribution is negligibly small. Note that the magnitude of the *ab initio* calculated space-charge effects, i.e., an energy shift and broadening in the range of 0.8–0.9 eV for $N = 10^5$ and d = 0.5 mm, agrees well with the 1.2 eV predicted by the simple formula (20.1) given above.

FEL radiation The central requirement for TR-HAXPES is a source of ultrashort-pulsed ($\tau < 100$ fs) hard X-ray ($h\nu > 2$ keV) radiation. Furthermore, because of the space-charge limit and the low photoionization cross sections at high photon energies, the source needs to have a high average brilliance rather than a high peak brilliance. Presuming a space-charge limit of about 10^4 electrons/pulse, the usable photon flux is roughly given by 10^6 photons/pulse times the pulse repetition rate. Here, we assume a photoemission quantum yield of 0.01 and note that the repetition rate cannot be much higher than 1 MHz because photoexcited samples may take up to 1 µs to relax back to equilibrium. The maximum usable photon flux is thus about 10^{12} photons/s.

Figure 20.2 compares different sources of ultrashort-pulsed radiation in the extreme ultraviolet to hard X-ray regime, including table-top high-harmonic-generation (HHG) sources [14, 15], a femtosecond slicing source at a third-generation storage ring, and several existing and planned FELs. The plot clearly suggests that presently, and probably also in the foreseeable future, XFELs are the only viable sources for TR-HAXPES. However, the plot also shows that the optimum source delivering the maximum usable photon flux for TR-HAXPES is not yet available.

The use of XFELs in TR-HAXPES has strong practical implications. Most existing XFELs produce the ultrashort X-ray pulses by self-amplified spontaneous emission (SASE). The problem with SASE FEL radiation is that it generally is stochastic in nature because it originates from shot noise in the electron beam. SASE FEL radiation is therefore generally characterized by strong shot-to-shot fluctuations in the pulse intensity, energy spectrum, and arrival time. This, together with the low repetition rate, makes XFEL-based TR-HAXPES considerably more challenging than conventional HAXPES using third-generation synchrotron radiation as well as TR-PES using HHG sources.

The average FEL pulse intensity and spectral fluctuations can be controlled relatively easily by the use of absorbers and a monochromator, respectively. But to

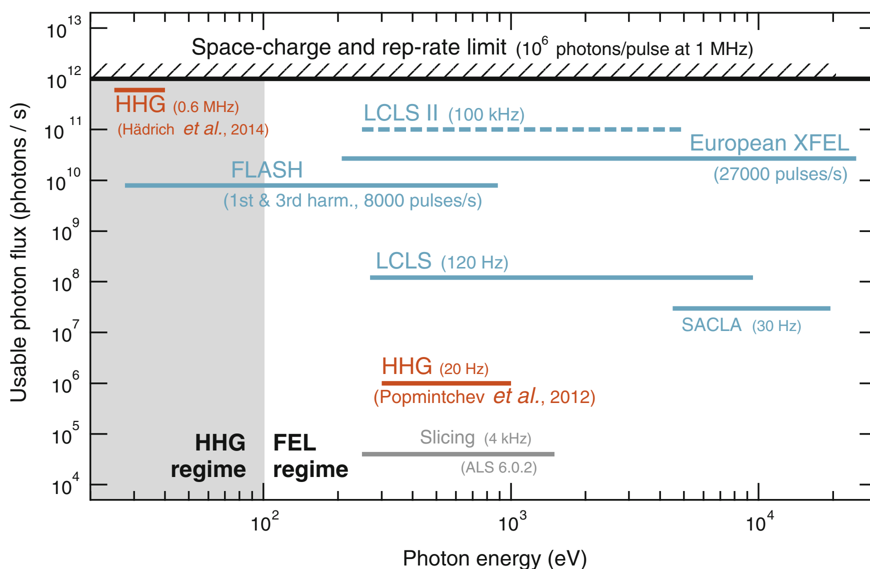

Fig. 20.2 Comparison of the usable photon flux of different ultrashort-pulsed sources of extreme ultraviolet, soft X-ray, and hard X-ray radiation. The maximally usable flux in time-resolved photoelectron spectroscopy is indicated at 10^{12} photons/s, corresponding to 10^6 photons/pulse at the space-charge limit times a maximum repetition rate of 10^6 pulses/s providing 1 μs for complete sample relaxation between pulses. The most promising X-ray light sources for TR-HAXPES are XFELs with a high repetition rate

cope with the shot-to-shot intensity fluctuations, arrival time jitter, and low repetition rate, one has to implement a single-shot ultrahigh-efficiency photoelectron detection scheme complemented by single-shot FEL pulse intensity and timing diagnostics [8, 9]. Photoemission spectroscopy and FEL diagnostics data can then be acquired for each individual FEL pulse so that the experimental data can later be binned into sets based on similar properties of the FEL pulse. The requirements on data acquisition may be relaxed when the stability of the FEL radiation increases, e.g., by FEL seeding.[1] However, the combined space-charge and repetition-rate limit remains a fundamental bottleneck.

To illustrate this bottleneck, consider commercially available photoelectron spectrometers that combine multi-angle imaging with time-of-flight energy measurement. With an angular acceptance $\Delta\Omega/2\pi \approx 0.025$ (corresponding to an acceptance angle of ±13°) and an energy window $\Delta E/E \approx 0.02$, these instruments will in principle be able to detect about 5 of the roughly 10^4 electrons emitted per pulse at the space-charge limit (if a multi-hit detector is used). The repetition rates of the existing and planned XFELs indicated in Fig. 20.2 will then provide effective count rates of about 150 Hz (SACLA) up to about 500 kHz (LCLS II). Despite the overall low detection efficiency of less than 10^{-3}, such count rates seem practical.

20.3 First Results

FEL-based TR-PES The technique of femtosecond TR-PES using FEL radiation was established at FLASH in the extreme ultraviolet region ($h\nu \approx$ 110–160 eV) around the year 2008 [4, 8, 16]. The pioneering experiments were performed at a monochromator beamline using a conventional hemispherical electron analyzer with a CCD detector, but without the use of timing tools. Thus, count rates of about 1 electron per FEL pulse at 150 pulses/s and effective energy and time resolutions of 300 meV and 700 fs (FWHM), respectively, could be achieved [4, 8].

The central experimental result obtained at FLASH from the layered reference charge-density-wave material 1*T*-TaS_2 is displayed in Fig. 20.3 [4]. At temperatures below about 180 K, pristine 1*T*-TaS_2 exhibits a commensurate $\sqrt{13} \times \sqrt{13}$ charge-density-wave [3]. In the accompanying periodic lattice distortion, the Ta atoms are grouped into 13-atom David-star clusters consisting of two 6-atom rings contracted towards the central atom (Fig. 20.3a). The atomic displacements and associated charge transfers are large, up to 7 % of the in-plane lattice constant and about 0.4 e^- from each Ta atom in the outer ring to the seven inner atoms, respectively. Thus, in each cluster, there are effectively two differently charged Ta atoms in the ratio

[1]FEL seeding is a technique in which the FEL is not operated in the SASE mode (amplifying the shot noise in the electron beam), but is instead used as an amplifier that is seeded by coherent radiation from another laser source, e.g., an optical laser, a higher harmonic source, or even a second SASE FEL.

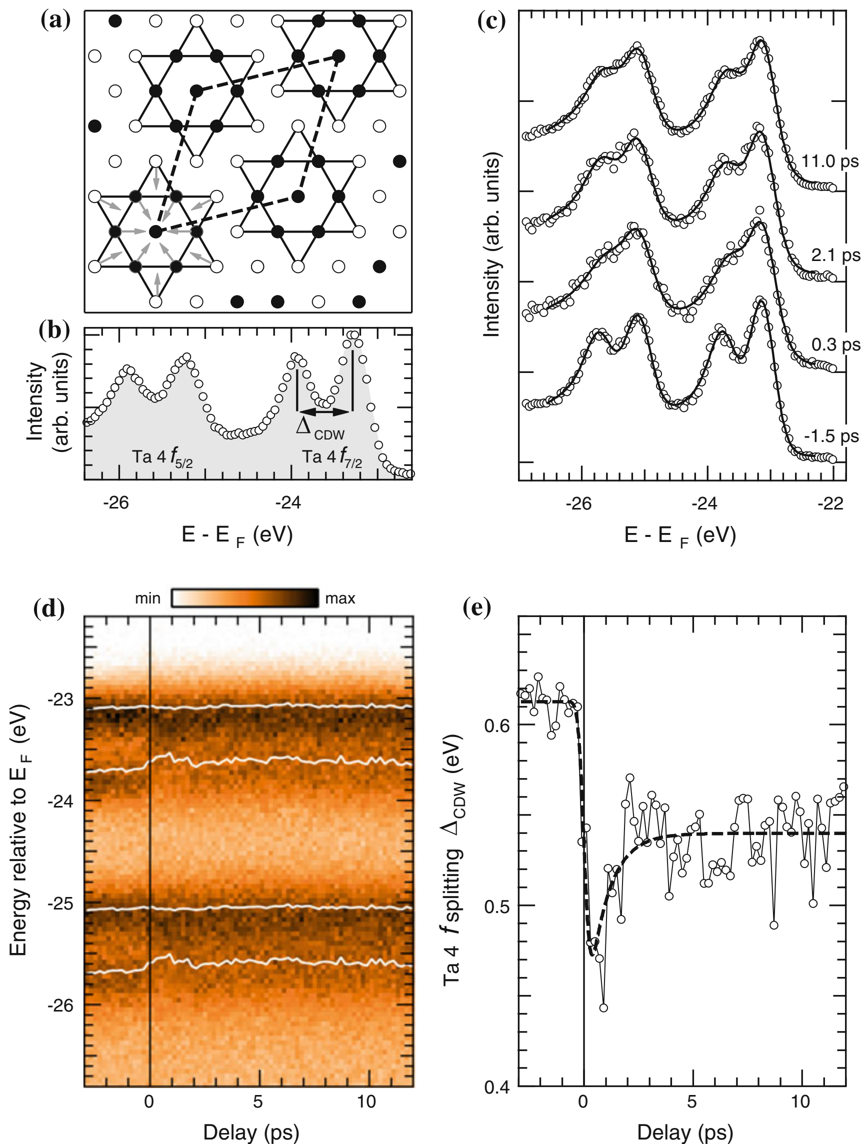

Fig. 20.3 **a** Schematic of the $\sqrt{13} \times \sqrt{13}$ reconstruction of layered 1*T*-TaS_2 (in the plane of the Ta atoms) showing the David-star clusters. The *arrows* indicate displacements of the Ta atoms from their original positions. *Open and filled circles* represent different charge states of the Ta atoms. **b** Ta 4*f* core-level photoemission spectrum of 1*T*-TaS_2 (hυ = 156 eV, T = 10 K, no laser pumping). The charge-density-wave-induced Ta 4*f* core-level splitting is indicated. **c**, **d** Ta 4*f* core-level photoemission spectra as a function of pump-probe delay ($h\upsilon_{pump}$ = 1.55 eV, $h\upsilon_{probe}$ = 156 eV, F_{inc} = 1.8 mJ/cm^2, T = 10 K). The *solid black lines* in (**c**) represent best fits to the experimental, whereas the *solid white lines* in (**d**) indicate fitted peak positions. **e** Time-dependence of the charge-density-wave-induced Ta 4*f* core-level splitting. The *open circles* represent experimental data. The *dashed line* is a fit to the experimental data using a single exponential starting at zero delay convoluted with a Gaussian representing the effective time resolution [4]

6:7 so that each of the two spin-orbit split Ta 4*f* levels is split into two peaks (Fig. 20.3b) (there are actually three different Ta species, but the different charge states of the central atom and the inner ring atoms cannot be resolved). This charge-density-wave induced core-level splitting can be regarded as an electronic order parameter for the system [4]. At the lowest temperatures, the splitting is larger than 0.6 eV.

The selected photoemission spectra in Fig. 20.3c and the full photoemission intensity map in Fig. 20.3d display the ultrafast dynamics in the Ta 4*f* core levels on the picosecond time scale. Upon impulsive near-infrared excitation, the charge-density-wave-induced Ta 4*f* splitting is quasi-instantaneously suppressed within the time resolution of the experiment. It is then partially restored with a time constant of ≈1 ps and remains stationary for at least 12 ps.

Figure 20.3e shows the extracted quantitative dynamics of the spectroscopic order parameter. The observed transient dynamics can be understood on the basis of the two-temperature model and the two-component nature of a charge-density wave [4]: First, the impulsive excitation rapidly suppresses the electronic charge-order component (the charge-density wave) by heating the electrons to a highly elevated temperature. During this process, the lattice-order component (the periodic lattice distortion) remains mostly intact. Then, on the time scale of electron-lattice thermalization, the lattice distortion is diminished, while charge order is partially restored, until at about 2 ps, a quasi-equilibrium state at elevated lattice temperature is attained with reduced charge and lattice order.

The results depicted in Fig. 20.3 clearly demonstrate that FEL-based TR-PES is not only feasible, but also useful. There is presently no other technique with which the ultrafast atomic site-specific charge-order dynamics in complex materials can be studied.

The extension of TR-PES into the hard X-ray regime, i.e., real TR-HAXPES, has recently been demonstrated at the SACLA XFEL [9–11]. Figure 20.4 shows a schematic illustration of the experimental setup, including the layout for realizing single-shot photoelectron detection. The measurements reported here were performed

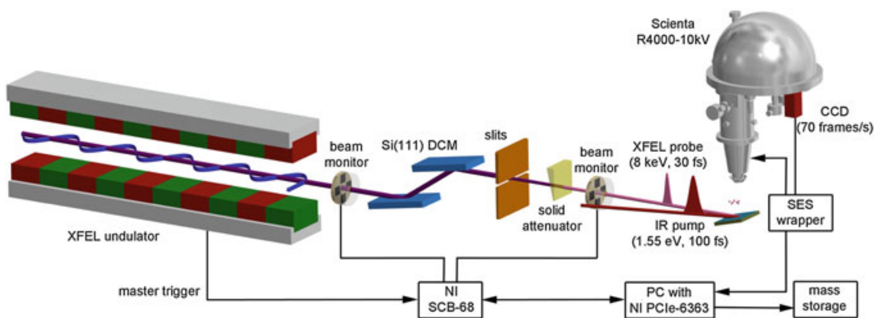

Fig. 20.4 Schematic illustration of the experimental setup and data acquisition concept for single-shot TR-HAXPES experiments at the SACLA XFEL [9, 11]

at beamline BL3 of SACLA using ultrashort ($\tau \approx 30$ fs), quasi-monochromatic ($\Delta h\nu \approx 1$ eV) hard X-ray ($h\nu = 8$ keV) pulses at a repetition rate of 20 Hz. The average XFEL pulse contained about 6×10^9 photons, with ≈10 % fluctuation over 30 shots, and the number of photons per pulse at the sample was adjusted down to about $(2–8) \times 10^8$ by inserting Si filters into the beam. Photoemission spectra were recorded with a Scienta R4000-10 kV electron analyzer. Notably, the stability of the XFEL radiation was sufficient to acquire the spectra in the conventional "sweep mode", i.e., single-shot detection was not used. The total instrumental energy resolution (photons plus electrons) was limited to 1.03 eV. In the time-resolved pump-probe measurements, 100-fs optical pump pulses were used.

Figure 20.5 shows a Ti 1*s* core-level spectrum measured at the XFEL SACLA in comparison to a Ti 1*s* spectrum measured at the storage ring SPring-8 [9–11]. Both spectra were taken from a La-doped $SrTiO_3$ sample at a photon energy of 8 keV. The instrumental energy resolutions and acquisition times were 1.03 eV FWHM versus 0.26 eV FWHM and 80 min versus 16 min, respectively. Not unexpectedly, the spectrum taken with XFEL radiation displays a lower signal-to-noise ratio and a larger width of the Ti 1*s* peak: 2.01 eV FWHM versus 1.43 eV FWHM for the spectrum taken at the storage ring. Yet, the spectral features and line shape are preserved and the remaining space-charge-induced broadening of 0.97 eV (after

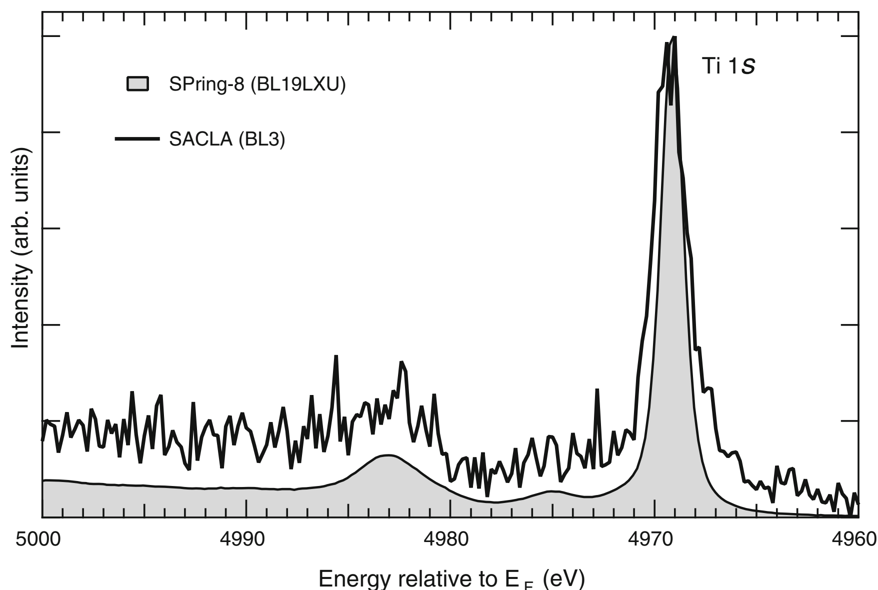

Fig. 20.5 Comparison of two Ti 1*s* core-level photoemission spectra of $SrTiO_3$ recorded at beamline BL19LXU of SPring-8 (*solid line with gray filling*) and beamline BL3 of SACLA (*thick solid line*), respectively ($h\upsilon = 8$ keV, T = 300 K). Instrumental energy resolutions (FWHM): 0.26 eV (SPring-8) versus 1.03 eV (SACLA). Acquisition times: 16 min (SPring-8) versus 80 min (SACLA) [9–11]

correction for the instrumental energy resolution, i.e., $[(2.01\ \text{eV})^2—(1.03\ \text{eV})^2—(1.43\ \text{eV})^2]^{1/2}$) is smaller than the experimental line width of 1.43 eV measured by high-resolution HAXPES.

This is all the more remarkable considering the low FEL repetition rate of only 20 Hz. The results therefore suggest that XFEL-based TR-HAXPES is not only feasible, but also practical as soon as kHz repetition rates become available.

Pump pulse-induced space-charge effects in TR-HAXPES The first real pump-probe TR-HAXPES measurements focused on studying the pump energy dependence and the dynamics of pump pulse-induced vacuum space-charge effects [11]. A La-doped $SrTiO_3$ sample was excited with optical pulses of two different photon energies (hν = 1.55 eV and hν = 3.10 eV) with pulse energies in the range of 40–550 μJ corresponding to incident fluence of about 1.6–22.5 mJ/cm^2. Such strong optical excitation generally leads to the nonlinear emission of a dense cloud of "slow" photoelectrons (with up to 1.3×10^6 particles in the present case [11]) that will interact with the "fast" photoelectron cloud emitted by the XFEL probe pulse.

Figure 20.6a shows how the Ti 1*s* emission is continuously shifted toward higher kinetic energies when the pump pulse energy is increased. This reflects the increase of the interaction strength between a probe photoelectron and a pump electron cloud of increasing density. The space-charge-induced energy shift is expected to be proportional to the number of pump electrons. But this number will depend non-linearly on the absorbed pump pulse energy because two or more photons have to be absorbed simultaneously for the emission of a photoelectron when the photon energy is lower than the work function. The pulse energy dependencies of the spectral shift, as measured for the two pump photon energies used, are shown in a log-log plot in Fig. 20.6b. The experimental data indicate power law dependencies consistent with dominant 2- and 3-photon electron emission processes, respectively, as expected from the photon energies used (3.10 and 1.55 eV) and the work function of $SrTiO_3$ (4.0 ± 0.2 eV).

The space-charge dynamics in the Ti 1*s* core-level spectrum resulting from the interaction of the probe photoelectrons with the pump electron cloud was measured for pump-probe delays in a range of −200 to +900 ps. Figure 20.7a shows the delay-dependent experimental spectra. The maximum spectral shift and broadening occur at zero delay, when the centers of the pump and probe pulses overlap in time. The space-charge-induced spectral distortions relax on a 100 ps time scale and the dynamics shows a characteristic asymmetry: The relaxation for positive delays (pump pulse before probe pulse) is significantly longer than for negative delays.

Figure 20.7b compares the extracted time dependence of the spectral shift to the results of a simulation based on the electrostatics of a homogeneously charged two-dimensional disk [11], as mentioned above. The simple analytical model can reproduce the temporal asymmetry in the spectral shift surprisingly well. The asymmetry directly reflects the distinct mean velocities of the "slow" pump and "fast" probe photoelectron cloud. The origin of the asymmetry is that the initial potential energy of the probe electrons, which is converted into the final kinetic

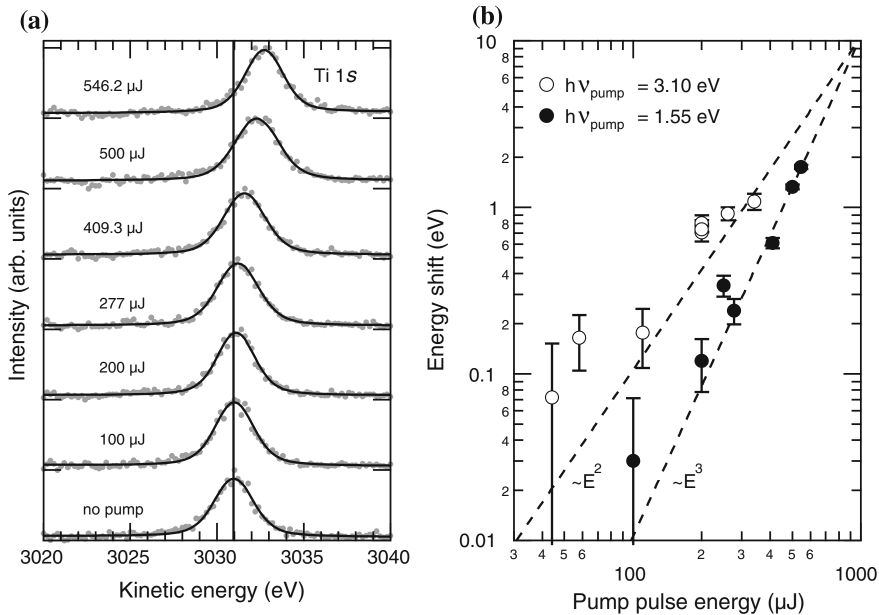

Fig. 20.6 **a** Ti 1*s* core-level photoemission spectra of $SrTiO_3$ taken at a fixed pump-probe delay of −80 ps as a function of pump pulse energy ($h\upsilon_{pump}$ = 1.55 eV, $h\upsilon_{probe}$ = 7998 eV, T = 300 K). The *gray dots* represent experimental data. *Solid lines* indicate best fits to the experimental spectra using Voigt profiles. The *vertical line* marks the peak position obtained for a blocked pump beam. **b** Spectral shift of the Ti 1*s* emission relative to the unpumped spectrum as a function of pump pulse energy for two different photon energies of the pump pulse: $h\upsilon_{pump}$ = 3.10 eV (*open circles*) versus $h\upsilon_{pump}$ = 1.55 eV (*filled circles*). *Dashed lines* represent linear fits to the experimental data in the double logarithmic plot. Power law dependencies on the pump pulse energy are indicated [11]

energy gain, is determined by the initial separation of the two electron clouds, and this initial separation is given by the propagation speed of the cloud emitted first. So, at the same absolute value of the delay, the initial distance between the clouds will be much shorter and, correspondingly, the kinetic energy gain much higher, when the pump electrons are emitted before the probe electrons (positive delay) as compared to the probe electrons coming first (negative delay).

These first real TR-HAXPES results show that pump pulse-induced space-charge effects in TR-HAXPES are easy to describe quantitatively and, because of the relatively long time constants, also easy to separate from the most interesting intrinsic dynamics happening on the sub-picosecond time scale. Although the high kinetic photoelectron energies in TR-HAXPES are not advantageous in terms of the magnitude of pump pulse-induced space-charge effects, they are advantageous in allowing for a clear spectral separation of the pump and probe electron energy distributions. Thus, indeed, TR-HAXPES may enable studies in the strong excitation regime that are not possible with TR-PES using extreme ultraviolet or soft X-ray radiation. More generally, the sharp peaking of the space-charge-induced

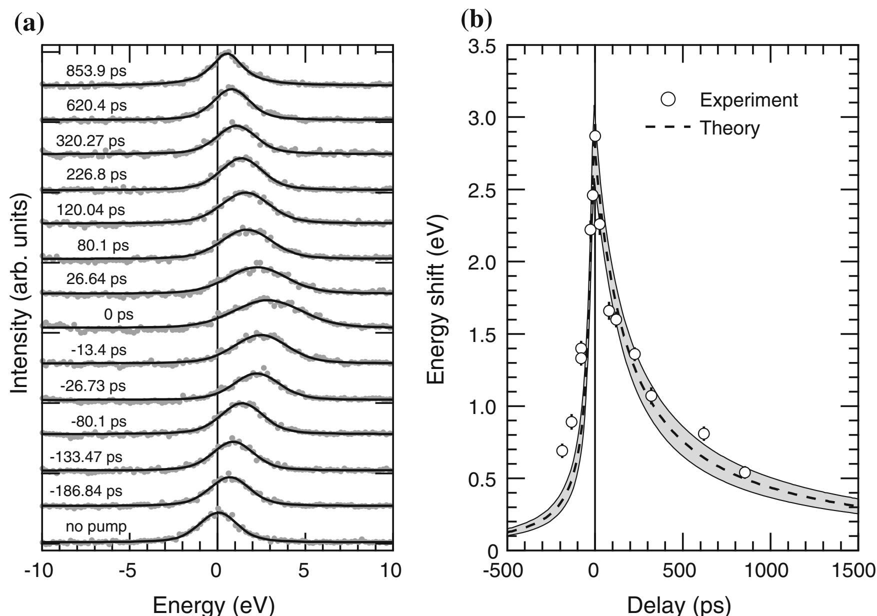

Fig. 20.7 **a** Ti 1*s* core-level photoemission spectra of $SrTiO_3$ as a function of pump-probe delay ($h\upsilon_{pump}$ = 1.55 eV, $h\upsilon_{probe}$ = 7998 eV, F_{inc} = 20 mJ/cm^2, T = 300 K). The *dots* represent experimental data. *Solid lines* indicate best fits to the experimental spectra using Voigt profiles. The *vertical line* marks the peak position for a blocked pump beam (E_{kin} = 3030.97 eV). **b** Spectral shift of the Ti 1*s* emission relative to the unpumped spectrum as a function of pump-probe delay. The *open circles* are experimental data. The *dashed line* is from a simple analytical model. The *shaded area* indicates a 68.3 % confidence band [11]

spectral shift for temporally overlapping pump and probe pulses can be used as a criterion to determine the experimental time zero at the sample with a precision of better than ±10 ps.

20.4 Outlook

The first TR-HAXPES results obtained at the SACLA XFEL [9–11], together with the results of the pioneering TR-PES experiments using extreme ultraviolet FEL radiation at FLASH [4, 8, 16], have established the general feasibility of FEL-based TR-PES, and specifically XFEL-based TR-HAXPES, at remarkably low FEL repetition rates of only 20–150 Hz. Thus, TR-HAXPES, in principle, opens the door to electronic and atomic structure dynamics in electronic devices and complex materials on the picosecond down to the femtosecond time scale. We envisage applications ranging from the charge carrier and band bending dynamics in space-charge layers at buried interfaces and, eventually, in electronic devices *in*

operando to the dynamics of laser-induced coherences and correlations in the bulk electronic structure of materials on the time scales of lattice vibrations and, ultimately, electron-electron interactions. However, in order to make TR-HAXPES a powerful and practical technique, a number of key developments in instrumentation need to come together.

The fundamental bottleneck in TR-HAXPES is the combined space-charge and repetition-rate limit, as illustrated in Fig. 20.2. To drive the maximum possible amount of data through this bottleneck requires a source delivering ultrashort hard X-ray pulses at a repetition rate as high as 1 MHz as well as a photoelectron detection scheme capable of detecting every emitted electron at the space-charge limit of about 10^4 electrons/pulse. Compare this with the repetition rate of 20 Hz and the count rate of about 1 electron/pulse at which the spectrum plotted in Fig. 20.5 was acquired. There are eight orders of magnitude room for improvement. Remarkably, already the use of the European XFEL foreseen to deliver 2.7×10^4 pulses/s combined with the use of a commercially available angle-resolving time-of-flight spectrometer without an analyzer slit will reduce the acquisition time for a high-resolution spectrum from about 1 h to less than 1 s. Nevertheless, the development of novel single-shot full-hemisphere photoelectron detection strategies will be inevitable, if the full potential of TR-HAXPES in simultaneously detecting ARPES Fermi surfaces and XPD diffraction patterns is to be realized.

Another important instrumentation need concerns the pump part of pump-probe TR-HAXPES. Once the probe part of TR-HAXPES has become practical and efficient, the full potential of the technique will be exploited only if the ultrashort ($\tau \approx 10$ fs) hard X-ray probe pulses are complemented by equally short pump pulses with tunable photon energy. Spectral tunability over the whole infrared region, from a few meV to about 1.7 eV, will, for example, allow us to selectively excite specific vibrational modes in complex materials or resonantly excite specific electronic transitions, in particular across energy gaps at the chemical potential. In contrast to the commonly used broad 1.5-eV pumping, energy-selective excitation will result in much cleaner experiments that are easier to understand, and it will provide ways to directly control material properties and transiently create novel phases. One may argue here that the most interesting (coherent electron) dynamics happens on the sub-100 fs time scale. To enter this time window will require 10-fs pump and probe pulses and synchronization to better than the pulse duration. Although this has not yet been achieved at existing FELs, it seems possible [17].

In conclusion, the experimental program for femtosecond TR-HAXPES sketched here is ambitious, but the goal is worthwhile: a "complete" solid-state photoemission experiment combining femtosecond time-resolved XPS, XPD, and ARPES with bulk sensitivity and, possibly, also spin resolution. The future will be bright for TR-HAXPES—as soon as the average XFEL brightness increases.

Acknowledgments The authors thank the operation and engineering staff of SACLA for their support during the TR-HAXPES experiments. The experiments were performed with the approval of JASRI (proposal nos. 2013A8050 and 2013A8067).

References

1. S. Hüfner, *Photoelectron Spectroscopy: Principles and Applications*, 3rd edn. (Springer, Berlin, 2003)
2. L. Perfetti, P.A. Loukakos, M. Lisowski, U. Bovensiepen, H. Berger, S. Biermann, P.S. Cornaglia, A. Georges, M. Wolf, Phys. Rev. Lett. **97**, 067402 (2006)
3. P. Fazekas, E. Tosatti, Philos. Mag. B **39**, 229 (1979)
4. S. Hellmann, M. Beye, C. Sohrt, T. Rohwer, F. Sorgenfrei, H. Redlin, M. Kalläne, M. Marczynski-Bühlow, F. Hennies, M. Bauer, A. Föhlisch, L. Kipp, W. Wurth, K. Rossnagel, Phys. Rev. Lett. **105**, 187401 (2010)
5. M. Eichberger, H. Schäfer, M. Krumova, M. Beyer, J. Demsar, H. Berger, G. Moriena, G. Sciaini, R.J.D. Miller, Nature **468**, 799 (2010)
6. S. Hellmann, T. Rohwer, M. Kalläne, K. Hanff, C. Sohrt, A. Stange, A. Carr, M.M. Murnane, H.C. Kapteyn, L. Kipp, M. Bauer, K. Rossnagel, Nat. Commun. **3**, 1069 (2012)
7. K. Rossnagel, J. Phys. Condens. Matter **23**, 213001 (2011)
8. S. Hellmann, C. Sohrt, M. Beye, T. Rohwer, F. Sorgenfrei, M. Marczynski-Bühlow, M. Kalläne, H. Redlin, F. Hennies, M. Bauer, A. Föhlisch, L. Kipp, W. Wurth, K. Rossnagel, New J. Phys. **14**, 013062 (2012)
9. M. Oura, T. Wagai, A. Chainani, J. Miyawaki, H. Sato, M. Matsunami, R. Eguchi, T. Kiss, T. Yamaguchi, Y. Nakatani, T. Togashi, T. Katayama, K. Ogawa, M. Yabashi, Y. Tanaka, Y. Kohmura, K. Tamasaku, S. Shin, T. Ishikawa, J. Synchrotron Rad. **21**, 183 (2014)
10. M. Oura, L.-P. Oloff, A. Chainani, K. Rossnagel, M. Matsunami, R. Eguchi, T. Kiss, T. Yamaguchi, Y. Nakatani, J. Miyawaki, K. Yamagami, M. Taguchi, T. Togashi, T. Katayama, K. Ogawa, M. Yabashi, T. Gejo, K. Myojin, K. Tamasaku, Y. Tanaka, T. Ebihara, T. Ishikawa, Trans. Mat. Res. Soc. Jpn. **39**, 469 (2014)
11. L.-P. Oloff, M. Oura, K. Rossnagel, A. Chainani, M. Matsunami, R. Eguchi, T. Kiss, Y. Nakatani, T. Yamaguchi, J. Miyawaki, M. Taguchi, K. Yamagami, T. Togashi, T. Katayama, K. Ogawa, M. Yabashi, T. Ishikawa, New J. Phys. **16**, 123045 (2014)
12. S. Hellmann, K. Rossnagel, M. Marczynski-Bühlow, L. Kipp, Phys. Rev. B **79**, 035402 (2009)
13. S. Hellmann, T. Ott, L. Kipp, K. Rossnagel, Phys. Rev. B **85**, 075109 (2012)
14. T. Popmintchev, M.-C. Chen, D. Popmintchev, P. Arpin, S. Brown, S. Ališauskas, G. Andriukaitis, T. Balčiunas, O.D. Mücke, A. Pugzlys, A. Baltuška, B. Shim, S.E. Schrauth, A. Gaeta, C. Hernández-García, L. Plaja, A. Becker, A. Jaron-Becker, M.M. Murnane, H.C. Kapteyn, Science **336**, 1287 (2012)
15. S. Hädrich, A. Klenke, J. Rothhardt, M. Krebs, A. Hoffmann, O. Pronin, V. Pervak, J. Limpert, A. Tünnermann, Nat. Photon. **8**, 779 (2014)
16. A. Pietzsch, A. Föhlisch, M. Beye, M. Deppe, F. Hennies, M. Nagasono, E. Suljoti, W. Wurth, C. Gahl, K. Döbrich, A. Melnikov, New J. Phys. **10**, 033004 (2008)
17. S. Schulz, I. Grguraš, C. Behrens, H. Bromberger, J.T. Costello, M.K. Czwalinna, M. Felber, M.C. Hoffmann, M. Ilchen, H.Y. Liu, T. Mazza, M. Meyer, S. Pfeiffer, P. Prędki, S. Schefer, C. Schmidt, U. Wegner, H. Schlarb, A.L. Cavalieri, Nat. Commun. **6**, 5938 (2015)

Index

A
Accelerator, 44, 47–49
Acceptance angle, 265
Advanced semiconductor devices, 408, 417
Ambient pressure X-ray photoelectron spectroscopy, 448, 449, 452, 453, 459, 464
Angle-resolved photoemission (ARPES), 8, 13, 24, 31
Angular distribution parameters, 267
Atomic multiplets, 270
Auger parameter, 220, 250, 252, 257, 258

B
Band structure calculations, 269
Binding energy shifts, 218, 248–250, 253, 255, 257
Bulk electronic structure, 143, 149, 152
Buried interfaces, 333, 417

C
Catalyst and battery materials, 497, 500
Chemical bonding, 270
CMOS, 408, 422, 436
Configuration interaction, 270
Core level, 52, 55, 57, 61
Core-level line shape, 367
Correlated electrons, 270
Correlated materials, 264
Cross section, 52, 57, 60

D
Databases, 111, 112, 136, 138
Density functional theory (DFT), 162, 167
DFT calculation, 474, 475, 477, 478, 490, 495, 496
Dilute ferromagnetic semiconductors, 153
Dilute magnetic semiconductors, 486
Diluted magnetic systems, 199, 211
Double core hole, 99
Dynamical mean field theory (DMFT), 164, 168, 171

E
Effective attenuation lengths, 124, 135
Electrochemistry, 455, 456, 464
Electronic structure, 264, 270, 300, 304, 468, 469, 476, 480, 487, 490, 491, 494, 496, 500, 507, 522
Electron screening, 201, 204, 212
Environmental science, 454, 459
ESCA, 35, 39, 41, 44
Escape depth, 53–55, 57

F
Final-state relaxation, 220, 249, 250, 254, 258
Fourier imaging, 298
Free-electron laser, 556

G
Gate stacks, 436, 442
Geometry, experimental, 264
Graphene, 292, 294, 295

H
Hard disc lubricant, 500
Hard X-ray, 556–559, 562, 567
Hard X-ray angle-resolved photoelectron spectroscopy (HARPES), 8, 24, 25, 27, 31, 141, 144, 146–151, 153–155, 160, 164, 168, 170, 171
Hard X-ray photoelectron diffraction (HXPD), 15, 16, 31
Hard X-ray photoelectron spectroscopy, 311, 325, 328
Hard X-ray photoemission, 1, 17, 19, 22, 31, 43, 263

© Springer International Publishing Switzerland 2016
J.C. Woicik (ed.), *Hard X-ray Photoelectron Spectroscopy (HAXPES)*,
Springer Series in Surface Sciences 59, DOI 10.1007/978-3-319-24043-5

HAXPEEM, 535, 537, 548
HAXPES, 1, 35, 38, 41, 43, 57, 59, 61, 144, 149, 176, 177, 179, 182, 183, 187–189, 193
HAXPES microscopy, 534, 552
HfO_2 high-k gate dielectric layers, 408
HXPS, 2–4, 7, 8, 11, 12, 14, 17, 24, 25, 31
Hybridization, 270

I
Inelastic mean free paths, 113, 116, 118, 135
Information depths, 113, 124
Interfaces, 2, 14, 19, 20, 22, 24, 31, 43, 53, 57, 61, 382, 383, 390, 392, 394–396, 399, 401, 402
Interference, 67, 82, 87, 89, 92, 93, 103
Ion recoil, 79

K
Korringa–Kohn–Rostoker method (KKR), 163, 171

L
Laboratory HAXPES, 508, 517, 522
LBMO, 491–494
LDA, 269
Localization of the valence-band hole, 188

M
Manganites, 200, 213
Mean escape depths, 121
Metal oxides, 198, 199
Momentum conservation, 185
Monochromator, 46, 47, 49, 50, 52, 58–60
Multiplet splitting, 218, 221, 222, 228, 229, 231, 232, 234, 244, 258
Multipole contributions, 279, 285, 286, 292, 300

N
Nano thin films and clusters, 487
NiO, 264
Nondestructive depth profiling, 313, 332
Non-dipole effects, 67, 82–85, 87, 88, 100, 101

O
One-step model of photoemission, 160, 164, 171
Operando observation, 507, 508, 510, 522
Orbital character, 273

P
Perovskite, 296, 298
Perovskite oxide interfaces, 341–343, 375, 376
Phase change, 469, 475, 476, 478, 479
Phase retarder, 264
Phase space, 50, 52
Photoelectron angular distribution, 267
Photoelectron microscopy, 533–535, 548, 551
Photoelectron spectroscopy, 386–388, 390, 392, 393, 396, 555, 556, 559
Photoemission, 2–5, 8, 13, 14, 17–19, 24, 27, 45, 49, 52, 55, 57, 60, 61
Photoionization cross section, 267, 269, 271
Polarization dependence, 264
Predictive equations, 112, 120, 138

R
Recoil effects, 176, 177, 183, 188, 192, 193

S
Scattering, 271
Semiconductors, 383, 385–387, 392, 393, 402
SLAC, 44, 45, 47
Solid/liquid interface, 454
Space-charge effects, 556–558, 564, 565
SPEAR, 43–47, 49, 51, 52
Spintronics, 20
Standing wave, 19, 20, 25, 31
Storage ring, 43–46, 50, 52, 58
Strongly correlated materials, 2
Structure, 292, 294, 295, 298, 299, 304
Surface sensitivity, 52, 53, 55, 57, 61
SW-HARPES, 25, 27
Synchrotron radiation, 1, 43–46, 48, 50–52

T
Theory of HAXPES, 169
Thin liquid films, 453, 455, 457
Time-resolved, 556, 559, 563, 567
Transition-metals, 258
Transition metal oxides, 303

U
Ultrafast nuclear motion, 80, 102, 103

V
Valence band, 44, 60, 61
Vanadates, 207, 213

Variable energy photoelectron spectroscopy, 311
Variable kinetic energy X-ray photoelectron spectroscopy (VKE-XPS), 421, 442
VPPEM, 534, 535, 538–545, 547–551

X

X-ray photoelectron spectroscopy (XPS), 3, 5, 13, 22, 24, 43, 52, 57, 111, 114, 136
X-ray photoemission, 342
X-ray standing wave, 277, 279, 282, 297
XPD, 15